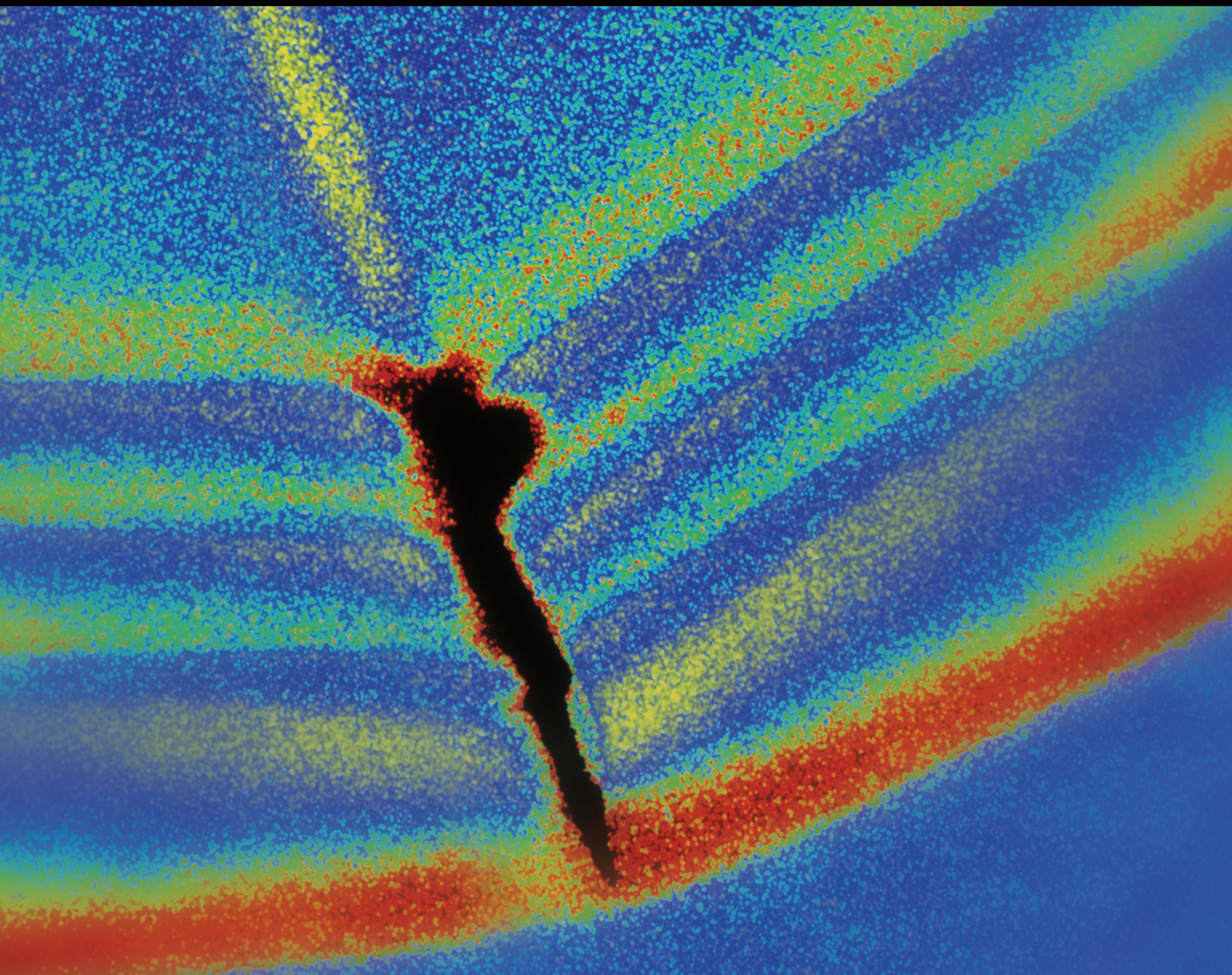


Shock and Vibration

# Modelling of Structures under Seismic, Impact, and Shock Vibrations

Lead Guest Editor: Abdul Qadir Bhatti

Guest Editors: Naveed Ahmad, Hugo Rodrigues, and Giuseppe Brandonisio





---

# **Modelling of Structures under Seismic, Impact, and Shock Vibrations**

Shock and Vibration

---

## **Modelling of Structures under Seismic, Impact, and Shock Vibrations**

Lead Guest Editor: Abdul Qadir Bhatti

Guest Editors: Naveed Ahmad, Hugo Rodrigues,  
and Giuseppe Brandonisio



---

Copyright © 2018 Hindawi. All rights reserved.

This is a special issue published in "Shock and Vibration." All articles are open access articles distributed under the Creative Commons Attribution License, which permits unrestricted use, distribution, and reproduction in any medium, provided the original work is properly cited.

## Editorial Board

- Brij N. Agrawal, USA  
Felix Albu, Romania  
Marco Alfano, Italy  
Sumeet S. Aphale, UK  
Hassan Askari, Canada  
Lutz Auersch, Germany  
Matteo Aureli, USA  
Mahmoud Bayat, Iran  
Marco Belloli, Italy  
Giosuè Boscato, Italy  
Francesco Braghin, Italy  
Rafał Burdzik, Poland  
Salvatore Caddemi, Italy  
Ivo Caliò, Italy  
Antonio Carcaterra, Italy  
Dumitru I. Caruntu, USA  
Cristina Castejón, Spain  
Nicola Caterino, Italy  
Gabriele Cazzulani, Italy  
Noel Challamel, France  
Athanasios Chasalevris, UK  
Xavier Chiementin, France  
Nawawi Chouw, New Zealand  
Simone Cinquemani, Italy  
Pedro A. Costa, Portugal  
Alvaro Cunha, Portugal  
Giorgio Dalpiaz, Italy  
Farhang Daneshmand, Canada  
Sergio De Rosa, Italy  
Silvio L.T. de Souza, Brazil  
Dario Di Maio, UK  
Luigi Di Sarno, Italy  
Longjun Dong, China  
Lorenzo Dozio, Italy  
Mohamed El Badaoui, France  
Mohammad Elahinia, USA  
Fiorenzo A. Fazzolari, UK  
Matteo Filippi, Italy  
Piotr Folegą, Poland  
Paola Forte, Italy  
Francesco Franco, Italy  
Juan C. G. Prada, Spain  
Pedro Galvín, Spain  
Gianluca Gatti, Italy  
Marco Gherlone, Italy  
Anindya Ghoshal, USA
- Gilbert R. Gillich, Romania  
Nere Gil-Negrete, Spain  
Adam Glowacz, Poland  
Itzhak Green, USA  
Hassan Haddadpour, Iran  
M.I. Herreros, Spain  
Hamid Hosano, Japan  
Reza Jazar, Australia  
Sakdirat Kaewunruen, UK  
Yuri S. Karinski, Israel  
Jeong-Hoi Koo, USA  
Georges Kouroussis, Belgium  
Mickaël Lallart, France  
Luca Landi, Italy  
Marco Lepidi, Italy  
Zhixiong Li, China  
Manuel Lopez Aenlle, Spain  
Nuno M. Maia, Portugal  
Stefano Manzoni, Italy  
Giuseppe Carlo Marano, Italy  
Stefano Marchesiello, Italy  
Francesco S. Marulo, Italy  
Jean-Mathieu Mencik, France  
Laurent Mevel, France  
Fabio Minghini, Italy  
Mahdi Mohammadpour, UK  
Rui Moreira, Portugal  
Emiliano Mucchi, Italy  
Peter Múčka, Slovakia  
Sara Muggiasca, Italy  
Tony Murmu, UK  
Pedro Museros, Spain  
Roberto Nascimbene, Italy  
Sundararajan Natarajan, India  
Toshiaki Natsuki, Japan  
Miguel Neves, Portugal  
Nicola Nisticò, Italy  
Roberto Palma, Spain  
A. Papageorgiou, Greece  
Francesco Pellicano, Italy  
Paolo Pennacchi, Italy  
Evgeny Petrov, UK  
Giuseppe Piccardo, Italy  
Antonina Pirrotta, Italy  
Franck Poisson, France  
Luca Pugi, Italy
- Mohammad Rafiee, Canada  
Carlo Rainieri, Italy  
José J. Rangel-Magdaleno, Mexico  
Didier Rémond, France  
Francesco Ripamonti, Italy  
Riccardo Rubini, Italy  
Salvatore Russo, Italy  
Giuseppe Ruta, Italy  
Edoardo Sabbioni, Italy  
Filippo Santucci de Magistris, Italy  
Onome E. Scott-Emuakpor, USA  
Roger Serra, France  
Chengzhi Shi, USA  
Vadim V. Silberschmidt, UK  
Kumar V. Singh, USA  
Jean-Jacques Sinou, France  
Isabelle Sochet, France  
Alba Sofi, Italy  
Jussi Sopanen, Finland  
Stefano Sorace, Italy  
Andrea Spaggiari, Italy  
Shuaishuai Sun, Australia  
Chao Tao, China  
Marco Tarabini, Italy  
Gloria Terenzi, Italy  
Mario Terzo, Italy  
Tai Thai, Australia  
Marc Thomas, Canada  
Hamid Toopchi-Nezhad, Iran  
Carlo Trigona, Italy  
Federica Tubino, Italy  
Nerio Tullini, Italy  
Angelo Marcelo Tusset, Brazil  
Jens Twiefel, Germany  
Filippo Ubertini, Italy  
Marcello Vanali, Italy  
F. Viadero, Spain  
M. Ahmer Wadee, UK  
Jörg Wallaschek, Germany  
Matthew J. Whelan, USA  
Agnieszka Wylomanska, Poland  
Davood Younesian, Iran  
Enrico Zappino, Italy  
Radoslaw Zimroz, Poland

# Contents

## **Modelling of Structures under Seismic, Impact, and Shock Vibrations**

Abdul Qadir Bhatti , Naveed Ahmad , Hugo Rodrigues , and Giuseppe Brandonisio  
Editorial (2 pages), Article ID 4105168, Volume 2018 (2018)

## **A Structural Pounding Formulation Using Systematic Modal Truncation**

Jianye Shi , Franz Bamer , and Bernd Markert  
Research Article (15 pages), Article ID 6378085, Volume 2018 (2018)

## **Developing Seismic Risk Prediction Functions for Structures**

Naveed Ahmad , Qaisar Ali, Muhammad Adil, and Akhtar Naeem Khan  
Research Article (22 pages), Article ID 4186015, Volume 2018 (2018)

## **Vibration Suppression of a Cantilever Plate Using Magnetically Multimode Tuned Mass Dampers**

Jae-Sung Bae , Jung-Sun Park, Jai-Hyuk Hwang, Jin-Ho Roh , Bong-do Pyeon, and Jong-Hyuk Kim  
Research Article (13 pages), Article ID 3463528, Volume 2018 (2018)

## **A Vibration Model of Ball Bearings with a Localized Defect Based on the Hertzian Contact Stress Distribution**

Fanzhao Kong, Wentao Huang , Yunchuan Jiang, Weijie Wang, and Xuezheng Zhao  
Research Article (14 pages), Article ID 5424875, Volume 2018 (2018)

## **IP Controller Design for Uncertain Two-Mass Torsional System Using Time-Frequency Analysis**

Jing Cui, Jiayu Ye, and Zhongyi Chu   
Research Article (9 pages), Article ID 1329876, Volume 2018 (2018)

## **Blast Responses and Vibration of Flood-Defense Structures under High-Intensity Blast Loadings**

Yonghee Ryu, WooYoung Jung , HoYoung Son, and Bu-Seog Ju   
Research Article (9 pages), Article ID 4750345, Volume 2018 (2018)

## **Parametric Study on Dynamic Response of FRP Masonry Structures under the Impacts of Debris Flow**

Peizhen Li , Tangzhenhao Li, Zheng Lu , and Jin Li  
Research Article (20 pages), Article ID 4527571, Volume 2018 (2018)

## **Development of a Multiaction Hybrid Damper for Passive Energy Dissipation**

Ji-Eun Roh , Moo-Won Hur, Hyun-Hoon Choi, and Sang-Hyun Lee   
Research Article (16 pages), Article ID 5630746, Volume 2018 (2018)

## **Deterministic and Probabilistic Serviceability Assessment of Footbridge Vibrations due to a Single Walker Crossing**

Cristoforo Demartino, Alberto Maria Avossa , and Francesco Ricciardelli  
Research Article (26 pages), Article ID 1917629, Volume 2018 (2018)

## **Seismic Response of Plan-Asymmetric Structures with Diaphragm Flexibility**

Hamed Eivani , Abdolreza S. Moghadam , Armin Aziminejad, and Masoud Nekooei  
Research Article (18 pages), Article ID 4149212, Volume 2018 (2018)

### **Lateral Torsional Buckling of Steel Beams under Transverse Impact Loading**

Wenna Zhang , Feng Liu, and Feng Xi 

Research Article (15 pages), Article ID 4189750, Volume 2018 (2018)

### **Influence of Wheel Eccentricity on Vertical Vibration of Suspended Monorail Vehicle: Experiment and Simulation**

Kaikai Lv, Kaiyun Wang, Zhihui Chen, Chengbiao Cai, and Lirong Guo

Research Article (10 pages), Article ID 1367683, Volume 2017 (2017)

### **Review of Blast Loading Models, Masonry Response, and Mitigation**

Eid Badshah, Amjad Naseer, Muhammad Ashraf, Feroz Shah, and Kareem Akhtar

Review Article (15 pages), Article ID 6708341, Volume 2017 (2017)

### **Dropping Shock Characteristics of the Suspension Cushioning System with Critical Components**

Hui Li, Anjun Chen, and Ningning Duan

Research Article (12 pages), Article ID 3164294, Volume 2017 (2017)

### **A Numerical Approach to the Dynamic Response of the Deployment System during a Circular Cylinder Crossing through the Wave Zone**

Xiaozhou Hu, Daojun Cai, and Yiyao Jiang

Research Article (13 pages), Article ID 7974057, Volume 2017 (2017)

### **Investigation of Axial Strengthened Reinforced Concrete Columns under Lateral Blast Loading**

Mohammad Esmailnia Omran and Somayeh Mollaei

Research Article (18 pages), Article ID 3252543, Volume 2017 (2017)

### **Dynamic Response Analysis of Cable of Submerged Floating Tunnel under Hydrodynamic Force and Earthquake**

Zhiwen Wu and Guoxiong Mei

Research Article (14 pages), Article ID 3670769, Volume 2017 (2017)

### **Normalized Study of Three-Parameter System in the Time Domain and Frequency Domain**

Xiao-Lei Jiao, Yang Zhao, and Wen-Lai Ma

Research Article (21 pages), Article ID 9153178, Volume 2017 (2017)

### **Experimental Investigation of Seismic-Induced Hydrodynamic Pressures on a Vertical Wall under Conditions of Wave Resonance**

YiLiang Zhou, LingKan Yao, MingYuan Gao, and Hongzhou Ai

Research Article (11 pages), Article ID 4542654, Volume 2017 (2017)

### **Modal and Vibration Analysis of Filter System in Petrochemical Plant**

Zhongchi Liu, Ji Wang, Wie Min Gho, Xiao Liu, and Xuebing Yu

Research Article (13 pages), Article ID 3685675, Volume 2017 (2017)

---

**Shock Mechanism Analysis and Simulation of High-Power Hydraulic Shock Wave Simulator**

Xiaoqiu Xu, Han Tao, and Junwei Han

Research Article (10 pages), Article ID 4361256, Volume 2017 (2017)

**Modeling and Analysis of a Multi-Degree-of-Freedom Micro-Vibration Simulator**

Xiaoming Wang, Zhenbang Xu, Shuai He, Qingwen Wu, Hang Li, Yaping Zhao, and Lei He Research

Article (17 pages), Article ID 4840514, Volume 2017 (2017)

**Sensitivity Analysis of a CPAM Inverse Algorithm for Composite Laminates Characterization**

Farshid Masoumi and Ahmad Ghasemi Ghalebahman

Research Article (14 pages), Article ID 2821873, Volume 2017 (2017)

**Numerical Evaluation on Dynamic Response of Existing Underlying Tunnel Induced by Blasting Excavation of a Subway Tunnel**

Jixue Zhou, Yi Luo, XinPing Li, Yunhua Guo, and Tingting Liu

Research Article (10 pages), Article ID 8628671, Volume 2017 (2017)

**Vibration of a Cylindrical Tunnel under a Centric Point-Source Explosion**

Yuetang Zhao, Cheng Chu, Anastasios Vafeidis, and Jie Li

Research Article (7 pages), Article ID 9152632, Volume 2017 (2017)

## Editorial

# Modelling of Structures under Seismic, Impact, and Shock Vibrations

**Abdul Qadir Bhatti** <sup>1,2</sup> **Naveed Ahmad** <sup>3</sup> **Hugo Rodrigues** <sup>4</sup>  
**and Giuseppe Brandonio**<sup>5</sup>

<sup>1</sup>Islamic University of Madinah, Madinah, Saudi Arabia

<sup>2</sup>International Islamic University, Islamabad, Pakistan

<sup>3</sup>University of Engineering and Technology, Peshawar, Pakistan

<sup>4</sup>Polytechnic of Leiria, Leiria, Portugal

<sup>5</sup>University of Studies of Naples “Federico II”, Naples, Italy

Correspondence should be addressed to Abdul Qadir Bhatti; [draqbhatti@iu.edu.sa](mailto:draqbhatti@iu.edu.sa)

Received 2 August 2018; Accepted 5 August 2018; Published 6 September 2018

Copyright © 2018 Abdul Qadir Bhatti et al. This is an open access article distributed under the Creative Commons Attribution License, which permits unrestricted use, distribution, and reproduction in any medium, provided the original work is properly cited.

The special issue is to address the state of knowledge in the areas of seismic behavior of structures; response of structures under blast, shock, and impact loads; material behavior under blast; impact and explosion tests; structural mechanism and damage evolution; protection concepts and design; and linear/nonlinear analytical/numerical modelling of structures and simulation. This issue will benefit structural engineers for modelling structural analysis and design for extreme loads (seismic, blast, and impact), in which the structure primarily behaves nonlinearly and inelastically. The investigators have been invited to contribute original research articles as well as review articles that have been stimulating the continuing efforts to understand the modelling of structures under the extreme loadings.

The modelling of materials and structural behavior under dynamic loading, including blast/shock-induced vibration, impact loading, and seismic actions, is a very challenging topic with several open questions that need to be addressed in order to obtain safer structures. The main reason to promote the present special issue was to promote a platform to share the recent advances that may be beneficial to structural engineers, who are facing challenges, when modelling structures for analysis and design for extreme loads.

64 papers have been submitted, from which a total of 25 papers have been finally selected to integrate the present issue, which shows the interest and importance of the special issue topic.

There are many severe conditions under which the vibration occurs under short duration impact loads within milliseconds of time history response such as falling-weight impact loading and rock fall on structures. The impact with very high response such as blast and shock vibration impact on structures of various types within microseconds have been added. Eight papers are focused on shock and blast in structures, and the topics covered are related with the response of building structural elements, as well as the effects in special infrastructures.

Eleven papers were submitted related to pure dynamic and vibration modelling strategies.

Since the last century, many developments have been made in understanding the seismic demand on structures due to earthquake-induced ground motions and structure response under dynamically varying loads. However, observations from the recent past earthquakes have demonstrated that structures designed to modern codes of practice and guidelines have not performed up to the expectations in reducing losses due to earthquakes. Furthermore, the recent earthquakes have demonstrated that the vulnerability of deficient; that is, noncomplaint, structures is higher than the previously known. All these are pointing to the growing interest in tools for modelling of structures under earthquake loading, to accurately account for the possible damage mechanisms and their implication on the structure response under earthquakes of

varying intensity, for example, frequent earthquakes, rare earthquakes, and very rare earthquake. With the advancement of experimental database, it is possible to test, validate, and calibrate tools for structure modelling and analysis, which can be in turn used both in research and practice. Six papers are focused in the study of earthquake impact in structures and infrastructures. In fact, the topics in several cases cross the boundaries mixing the advanced dynamic methods to study the seismic effects on structures or combining different hydrodynamic loads with the effects of earthquakes, and only with the proper advanced numerical strategies will be possible to have an accurate assessment of the structural behaviour.

The editorial team is sure that the papers reflect significant researches and developments the different topics addressed. We hope that readers will find all articles of the special issue useful and exciting and that the articles will stimulate further research activities in the area of damage assessment.

### **Conflicts of Interest**

The guest editors have no conflicts of interest regarding the publication of this special issue.

*Abdul Qadir Bhatti  
Naveed Ahmad  
Hugo Rodrigues  
Giuseppe Brandonisio*

## Research Article

# A Structural Pounding Formulation Using Systematic Modal Truncation

Jianye Shi , Franz Bamer , and Bernd Markert

*Institute of General Mechanics, RWTH Aachen University, Templergraben 64, 52062 Aachen, Germany*

Correspondence should be addressed to Franz Bamer; [bamer@iam.rwth-aachen.de](mailto:bamer@iam.rwth-aachen.de)

Received 28 July 2017; Revised 8 March 2018; Accepted 25 March 2018; Published 7 May 2018

Academic Editor: Naveed Ahmad

Copyright © 2018 Jianye Shi et al. This is an open access article distributed under the Creative Commons Attribution License, which permits unrestricted use, distribution, and reproduction in any medium, provided the original work is properly cited.

The evaluation of the response function of the structural pounding problem is generally time-consuming if high-order systems are applied. The well-known modal truncation strategy is outstandingly efficient for a single linear ground-accelerated structure. However, for the analysis of the structural pounding problem, the classical modal truncation technique turns out to be ineffective as additional higher frequency motion due to possible contact impact occurs. This makes the determination of how many modes should be taken into account in order to obtain a required level of accuracy more difficult. Therefore, in this paper, a systematically controlled modal truncation strategy adapted to the seismic pounding formulation under consideration of high nonlinearity and nonsmoothness of contact problems is introduced. A comparative study of the classical and the controlled modal truncation technique is presented and a comparison with the commercial software package ABAQUS<sup>®</sup> is provided. It is shown that the computational accuracy is significantly improved when applying the new systematically controlled modal truncation strategy.

## 1. Introduction

It has been observed that the motion of buildings due to earthquake excitation may not cause as much damage to buildings as the result of possible pounding between them [1–4]. Pounding occurs if the separation distance between adjacent buildings is not sufficient in order to compensate for their relative movements. It is dynamically complex and even chaotic behavior that occurs if the eigenfrequencies of the single buildings differ considerably [5]. Therefore, numerical simulations of the dynamic pounding problem are necessary in order to understand the characteristics of structures based on which guidelines for structural design can be provided [6–8].

Due to the high number of degrees of freedom and the nonlinearity as well as nonsmoothness of the contact problem, the evaluation of the multiple structure pounding is time-consuming [9, 10]. As a result, the evaluation of the response to a whole frequency range can be computationally disproportionately expensive. Thus, low-order models are necessary that guarantee a certain level of accuracy.

Some studies have investigated model order reduction techniques based on modal truncation strategies and the

proper orthogonal decomposition for structures with nonlinear materials. However, they applied those strategies only to dynamical single body systems without consideration of multibody pounding; see [11–17]. Only limited research studies have been conducted considering model reduction techniques for structural pounding problems. In the work of Zucca [18], another model order reduction technique based on dynamic substructuring technique is applied to the forced response of structures with contact interfaces. In the work of G eradin and Rixen [19], a nodeless dual-superelement is formulated to reduce the degrees of freedom of the unilateral contact problems. Most of the researches focus on the modeling and mitigation of the constitutive pounding law [1, 3, 8]; few of them attempt to apply model reduction techniques for the pounding problems.

The aim of this paper is to provide a low-order representation of structural pounding formulation by applying the classical and a systematically controlled modal truncation technique considering dynamic contact impact interaction. The theoretical principles and mathematical formulation as well as the solution methods in time domain are introduced in Section 2. A representative academic model, an ensemble of three adjacent frame structures, is demonstrated in

Section 2.2. In Section 3, the numerical investigations of the dynamic model are presented. In order to verify the in-house software, a comparison with the commercial software ABAQUS<sup>®</sup> for the solution is given. Convergence studies and frequency response analyses as well as error estimations are carried out. The full and the reduced solutions are compared concerning efficiency and error of the displacements, acceleration, and contact forces. The effectiveness of the improved method is verified by performing a frequency response analysis applying different number of considered modes for the reduced computation. Additionally, the proposed controlled modal truncation strategy is examined on three real earthquake records. Conclusions and outlook of the demonstrated methods are presented in Section 4.

## 2. Mechanical Formulation

### 2.1. Initial Boundary Value Problem (IBVP) for Multiple Pounding

**2.1.1. Strong Form.** The problem statement associated with the kinematic linear frictionless contact problem for the three demonstrated deformable bodies is summarized in the following equations. The IBVP for a dynamic system with finite deformation must be satisfied for each body (cf. [20]):

$$\begin{aligned} \operatorname{div} \mathbf{T}^{(i)} + \mathbf{b}_0^{(i)} &= \rho^{(i)} \ddot{\mathbf{u}}^{(i)} \quad \text{in } \Omega_t^{(i)} \times [0, T], \\ \mathbf{u}^{(i)} &= \widehat{\mathbf{u}}^{(i)} \quad \text{on } \gamma_u^{(i)} \times [0, T], \\ \mathbf{T}^{(i)} \mathbf{n}^{(i)} &= \widehat{\mathbf{t}}^{(i)} \quad \text{on } \gamma_\sigma^{(i)} \times [0, T], \\ \mathbf{u}^{(i)}(t_0) &= \widehat{\mathbf{u}}_0^{(i)} \quad \text{in } \widehat{\Omega}_0^{(i)}, \\ \dot{\mathbf{u}}^{(i)}(t_0) &= \widehat{\mathbf{v}}_0^{(i)} \quad \text{in } \widehat{\Omega}_0^{(i)}. \end{aligned} \quad (1)$$

The boundary  $\Gamma^{(i)}$  of each body is divided into three disjoint parts, shown in Figure 1:

$$\begin{aligned} \Gamma^{(i)} &= \Gamma_u^{(i)} \cup \Gamma_\sigma^{(i)} \cup \Gamma_c^{(i)}, \\ \Gamma_u^{(i)} \cap \Gamma_\sigma^{(i)} \cap \Gamma_c^{(i)} &= \emptyset, \end{aligned} \quad (2)$$

where the Dirichlet, Neumann, and contact boundary conditions are defined on  $\Gamma_u^{(i)}$ ,  $\Gamma_\sigma^{(i)}$ ,  $\Gamma_c^{(i)}$ , respectively. It should be pointed out that one body can have more contact surfaces; see Figure 1(b). Conventionally, one defines slave and master surfaces for the contact problem with superscripts <sup>(1)</sup> and <sup>(2)</sup>, respectively; see [20, 21]. Generally, the definition of master and slave is arbitrary. In the demonstrated formulation, Figure 1(b) plays a role as master with respect to both Figures 1(a) and 1(c). This convention will be kept to describe the academic test example and contact constraints in Sections 2.2 and 2.3.

Taking small deformation into consideration, the linearized Green-Lagrangian strain can be expressed as

$$\mathbf{E}^{(i)} = \frac{1}{2} (\operatorname{Grad} \mathbf{u}^{(i)} + \operatorname{Grad}^T \mathbf{u}^{(i)}). \quad (3)$$

Linear-elastic material is introduced; therefore, the constitutive relation between strain and displacement under small deformation is given as

$$\mathbf{T}^{(i)} = \mathcal{C}^{(i)} \mathbf{E}^{(i)}, \quad (4)$$

where  $\mathbf{T}$  is the Cauchy stress tensor and the tensor  $\mathcal{C}$  is the forth-order elasticity tensor. Karush-Kuhn-Tucker (KKT) conditions are applied to describe the contact constraints in a strong sense, which are in case of normal frictionless contact [21]

$$\begin{aligned} g_n &\geq 0, \\ p_n &\leq 0, \\ p_n g_n &= 0 \\ &\text{on } \gamma_c^{(i)} \times [0, T], \\ \mathbf{t}_\tau &= \mathbf{0} \quad \text{on } \gamma_c^{(i)} \times [0, T]. \end{aligned} \quad (5)$$

The scalar magnitude  $g_n$  is the gap function between two participants, which is determined by using the closest point projection. The magnitude  $p_n$  is the contact traction acting on the slave surfaces and the vector  $\mathbf{t}_\tau$  is the tangential traction describing the friction and other viscous tractions. In this paper, friction is neglected.

**2.1.2. Weak Form.** Based on the strong form of contact problems for multiple deformable bodies, the weak statement can be achieved in a variational sense using the principle of virtual displacement. By multiplying the virtual displacement as test functions with the local momentum balance in (1), one gets the weak form of the pounding system with frictionless contact

$$\begin{aligned} \delta \mathcal{W}_{\text{kin}}(\mathbf{u}^{(i)}, \delta \mathbf{u}^{(i)}) + \delta \mathcal{W}_{\text{int}}(\mathbf{u}^{(i)}, \delta \mathbf{u}^{(i)}) \\ - \delta \mathcal{W}_{\text{ext}}(\mathbf{u}^{(i)}, \delta \mathbf{u}^{(i)}) - \delta \mathcal{W}_{\text{con}}(\mathbf{u}, \delta \mathbf{u}) = 0, \end{aligned} \quad (6)$$

where  $\delta \mathcal{W}_{\text{kin}}$  stands for the virtual work of the inertia column forces,  $\delta \mathcal{W}_{\text{int}}$  is the virtual work of the internal stresses,  $\delta \mathcal{W}_{\text{ext}}$  is the virtual work of the external forces, and  $\delta \mathcal{W}_{\text{con}}$  stands for the virtual contact work. They are given as

$$\begin{aligned} \delta \mathcal{W}_{\text{kin}} &= \sum_1^3 \left[ \int_{\Omega_0^{(i)}} \rho_0^{(i)} \dot{\mathbf{u}}^{(i)} \cdot \delta \mathbf{u}^{(i)} dV_0 \right], \\ \delta \mathcal{W}_{\text{int}} &= \sum_1^3 \left[ \int_{\Omega_0^{(i)}} \mathbf{T}^{(i)} \cdot \delta \mathbf{E}^{(i)} dV_0 \right], \\ \delta \mathcal{W}_{\text{ext}} &= \sum_1^3 \left[ \int_{\Omega_0^{(i)}} \widehat{\mathbf{t}}^{(i)} \cdot \delta \mathbf{u}^{(i)} dV_0 + \int_{\Gamma_\sigma^{(i)}} \mathbf{b}_0^{(i)} \cdot \delta \mathbf{u}^{(i)} d\Gamma^{(i)} \right], \\ \delta \mathcal{W}_{\text{con}} &= \sum_1^3 \left[ \int_{\Gamma_c^{(i)}} \mathbf{t}_N^{(i)} \cdot \delta \mathbf{u}^{(i)} d\Gamma^{(i)} \right]. \end{aligned} \quad (7)$$

It should be pointed out that the weak form is also valid for each separate body  $\Omega^{(i)}$ . There are many possible ways to

TABLE 1: Cross sections columns ([m]), cross sections beams ([m]), Young's modulus of the columns ( $E_c$  [N/m<sup>2</sup>]), and Young's modulus of the beams ( $E_b$  [N/m<sup>2</sup>]) of the frame system (FS).

FS	Columns	$E_c$	Beams	$E_b$
1	Hollow $0.2 \times 0.2, t = 0.01$	$2.1e^{11}$	Full $0.3 \times 4.0$	$3.5e^{10}$
2	Hollow $0.3 \times 0.3, t = 0.03$	$2.1e^{11}$	Full $0.3 \times 0.3$	$2.1e^{11}$
3	Hollow $0.2 \times 0.2, t = 0.02$	$2.1e^{11}$	Full $0.3 \times 4.0$	$3.5e^{10}$

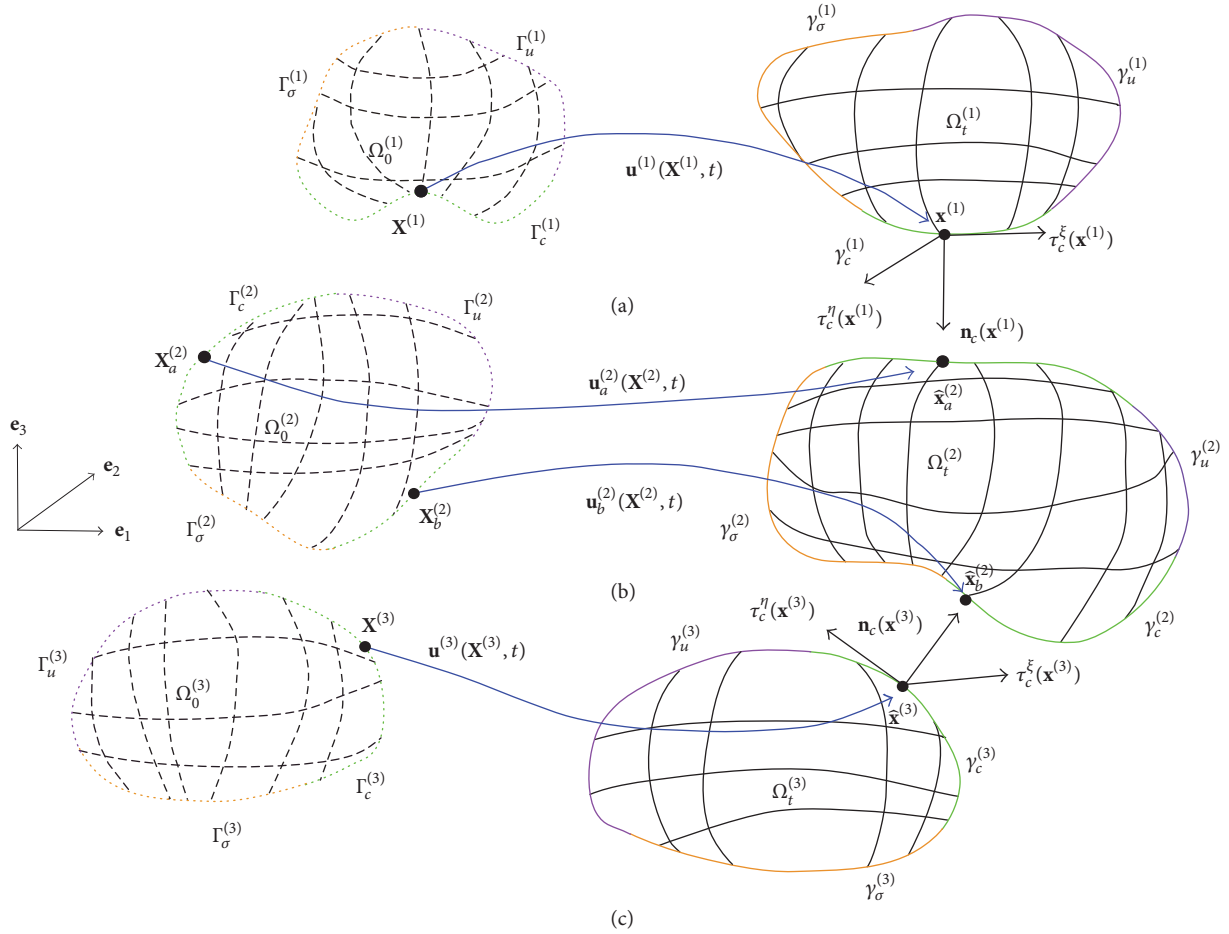


FIGURE 1: Kinematics of a multiple pounding problem.

contribute to the contact virtual work such as Lagrange multiplier method, augmented Lagrange multiplier method, or mortar method [20, 21]. In this work, the contact constraints are regularized by the penalty method, which is introduced in Section 2.3.

**2.2. An Academic Multiple Pounding Benchmark Example.** A system of two three-story frames and one higher four-story adjacent frame is selected to represent the academic pounding benchmark example. The selected frames are modeled by column-beam elements. The frames are arranged with an initial gap of  $g_{0,1} = g_{0,2} = 0.2$  m. The widths and the heights

of the frames are  $l_1 = 6.0$  m,  $l_2 = 5.0$  m, and  $l_3 = 5.0$  m and  $h_1 = 3.0$  m,  $h_2 = 3.2$  m, and  $h_3 = 3.4$  m. This is depicted in Figure 2. Different cross sections as well as different stiffness parameters are chosen for the columns and beams. The measurements and the material parameters of the cross sections are presented in Table 1.

The structures are discretized by two node structural beam/truss elements with three degrees of freedom per node, that is, axial and vertical local displacements and rotations (in total 978 degrees of freedom).

In order to keep the convention of indices for slave and master surfaces in Section 2.1, the contact domain between

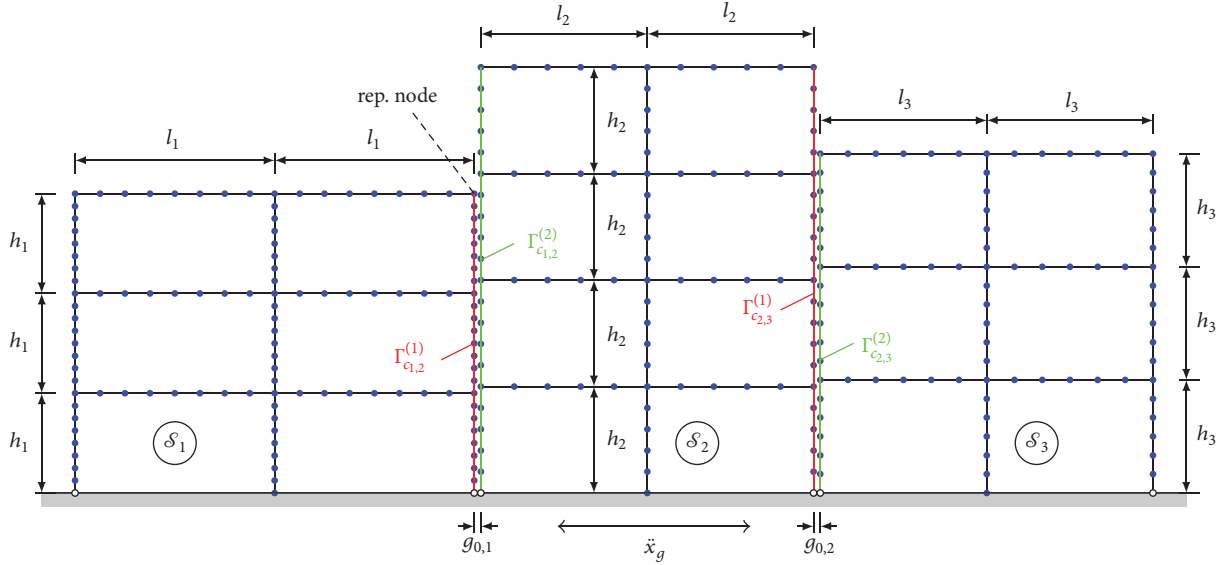


FIGURE 2: Dynamic system of adjacent structures; frame height measures  $h_1$ ,  $h_2$ , and  $h_3$ ; frame width measures  $l_1$ ,  $l_2$ , and  $l_3$ ; initial gap  $g_{0,1}$ ; initial gap  $g_{0,2}$ ; representative output node (rep. node); contact surfaces  $\Gamma_{c_{1,2}}^{(1)}$ ,  $\Gamma_{c_{1,2}}^{(2)}$ ,  $\Gamma_{c_{2,3}}^{(1)}$ , and  $\Gamma_{c_{2,3}}^{(2)}$ .

frame  $\mathcal{S}_1$  and frame  $\mathcal{S}_2$  will be marked as  $\Gamma_{c_{1,2}}^{(1)}$  (slave side) and  $\Gamma_{c_{1,2}}^{(2)}$  (master side) and, furthermore,  $\Gamma_{c_{2,3}}^{(1)}$  (slave side) and  $\Gamma_{c_{2,3}}^{(2)}$  (master side) for the contact domain between frame  $\mathcal{S}_2$  and frame  $\mathcal{S}_3$ , rather than  $\Gamma_c^{(1)}$ ,  $\Gamma_c^{(2)}$ , and  $\Gamma_c^{(3)}$ ; see Figure 2. An a priori master-slave separation is possible in this academic case.

**2.3. Method of Contact Constraint Enforcement.** Pounding between two adjacent objects is usually modeled by introducing the impact elements, which are widely used to describe the contact force if collision occurs (cf. [1, 3, 8, 22–24]). Mostly pounding elements with a linear or a nonlinear spring damper system, following the Hertz law, are applied (cf. [2, 25–29]). In this paper, a pounding element with a linear spring is chosen to describe the impact forces in both horizontal and vertical directions by interpolating the node tractions. This is equivalent to the penalty method, using the penalty parameter for the stiffness of the spring. This method enjoys the particular advantage of removing the constraints explicitly from the variational formulation; see [21]. The contact constraints, regularized by the penalty method, are briefly introduced.

As mentioned in Section 2.1, the slave side is labeled by index (1) and the master side by index (2), respectively. Based on the node-to-segment formulation, the gap function mentioned in Section 2.1 is defined by solving the problem of the minimum distance between the slave point  $\mathbf{x}_p^{(1)}$  and the opposite point on the master surface  $\gamma_c^{(2)}$  of the discretized system; see Figure 3. The possible element of the master surface can be defined through the equation

$$\mathbf{x}^{(2)}(\xi) = \mathbf{x}_1^{(2)} + (\mathbf{x}_2^{(2)} - \mathbf{x}_1^{(2)})\xi. \quad (8)$$

The gap function is then defined as

$$g_n = (\mathbf{x}_p^{(1)} - (1 - \xi^*)\mathbf{x}_1^{(2)} - \xi^*\mathbf{x}_2^{(2)}) \cdot \mathbf{n}^{(2)}, \quad (9)$$

where  $\xi^*$  is the parameter of the intersection point coordinate. The contact traction can be described as the product of the penalty parameter  $\varepsilon_n$  and the gap function  $g_n$ . The nonconform meshes between two bodies are combined in this sense. Inserting the gap function into the weak form (7), the virtual contact work can be formulated as

$$\delta \mathcal{W}_{\text{con}} = \sum_1^3 \left[ \int_{\Gamma_c^{(i)}} \varepsilon_n^{(i)} \langle g_n \rangle \delta g_n d\Gamma^{(i)} \right], \quad (10)$$

where the bracket  $\langle \cdot \rangle$  is the Macaulay bracket, which means

$$\langle x \rangle := \begin{cases} x, & \text{if } x \geq 0, \\ 0, & \text{if } x < 0. \end{cases} \quad (11)$$

Evaluation of the volume integration of the individual term in (7) delivers the explicit formulation of the set of equations of motion describing the discretized dynamic system

$$\mathbf{M}\ddot{\mathbf{u}} + \mathbf{C}\dot{\mathbf{u}} + \mathbf{K}\mathbf{u} + \mathbf{F}^c(\mathbf{u}) = \mathbf{F}(t), \quad (12)$$

where  $\mathbf{M}$ ,  $\mathbf{C}$ , and  $\mathbf{K}$  are the global mass and damping and stiffness matrices, respectively. Rayleigh-Damping is chosen for the damping matrix  $\mathbf{C}$ , which is proportional to the mass and stiffness matrix:

$$\mathbf{C} = \mu\mathbf{M} + \lambda\mathbf{K}, \quad (13)$$

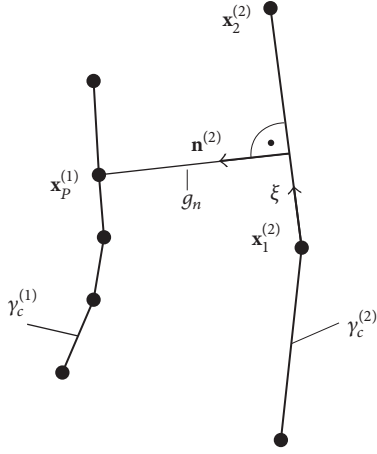


FIGURE 3: Illustration of the contact zone and the gap function.

where the second and the fifth modes are used to evaluate the coefficients  $\mu$  and  $\lambda$ :

$$\begin{aligned}\mu &= 2\xi \frac{\omega_2 \omega_5}{\omega_2 + \omega_5}, \\ \lambda &= \frac{2\xi}{\omega_2 + \omega_5},\end{aligned}\quad (14)$$

with a damping ratio  $\xi = 4\%$ ,  $\omega_2 = 1.796$  rad/s, and  $\omega_5 = 7.085$  rad/s. The contact force is then directly expressed as a function of the displacement field by the penalty method, which couples all degrees of freedom of all frames. The initial conditions are assumed to be zero for both the displacements and velocities.

**2.4. Modal Truncation Strategies.** The global set of equations of motion (12) is solved numerically. Dependent on the number of degrees of freedom and the performance of the contact search algorithms, this is generally time-consuming. Thus, the simulation of the system response for the whole range of frequencies is even much more challenging. Therefore, solution strategies applying the classical and a systematically controlled modal truncation technique are introduced.

**2.4.1. Classical Modal Truncation.** The undamped homogeneous set of equations of motion  $\mathbf{M}\ddot{\mathbf{u}} + \mathbf{K}\mathbf{u} = \mathbf{0}$  leads after inserting the solution ansatz function  $\mathbf{u} = \Phi e^{-i\omega t}$  to the eigenvalue problem  $[\mathbf{K} - \omega^2 \mathbf{M}]\Phi_i = \mathbf{0}$ . The solution of the eigenvalue problem leads then to the spectral matrix  $\Omega = \text{diag}[\omega_i^2]$ , with the eigenfrequencies  $\omega_i$  in ascending order and the corresponding eigenmatrix  $\Phi = [\Phi_1, \Phi_2, \dots, \Phi_n]$  (cf. [12]). The transformation into the reduced space is physically motivated by the fact that, dependent on the frequency range of the excitation force, the whole deformation energy of the vibrating system is associated with a low number of vibration modes. In case of seismic ground excitation, it can a priori be assumed that the whole deformation energy is stored in the first couple of low frequency modes of vibration (cf. [13]). Based on modal analysis, the transformation matrix

can be extracted from the sorted modal matrix according to correspondent eigenfrequencies of the full system with  $m \ll n$ , which means

$$\Phi = \left[ \underbrace{\Phi_1, \Phi_2, \dots, \Phi_m}_{\Phi_r}, \underbrace{\Phi_{m+1}, \Phi_{m+2}, \dots, \Phi_n}_{\text{truncated modes}} \right]. \quad (15)$$

The physical coordinate  $\mathbf{u}$  is transformed into the reduced space  $\mathbf{z}$  by

$$\mathbf{u} = \Phi_r \mathbf{z}. \quad (16)$$

Additionally, left transformation by  $\Phi_r^T$  leads to

$$\begin{aligned}\underbrace{\Phi_r^T \mathbf{M} \Phi_r}_{\mathbf{m} \in \mathcal{R}^{m \times m}} \ddot{\mathbf{z}} + \underbrace{\Phi_r^T \mathbf{C} \Phi_r}_{\mathbf{c} \in \mathcal{R}^{m \times m}} \dot{\mathbf{z}} + \underbrace{\Phi_r^T \mathbf{K} \Phi_r}_{\mathbf{k} \in \mathcal{R}^{m \times m}} \mathbf{z} + \underbrace{\Phi_r^T \mathbf{F}^c}_{\mathbf{f}^c \in \mathcal{R}^{m \times 1}} \\ = \underbrace{\Phi_r^T \mathbf{F}}_{\mathbf{f}(t) \in \mathcal{R}^{m \times 1}}(t).\end{aligned}\quad (17)$$

Concerning the multiple structural pounding problem, the matrices  $\mathbf{M}$  and  $\mathbf{K}$  are block-wise diagonal and only the contact force is responsible for possible interaction. The solution of the eigenvalue problem including these matrices provides eigenvalues, which can be sorted in increasing order, but it is not possible to assign these eigenvalues to the frame system which they belong to without visible check. Therefore, concerning the multiple pounding problem, this is an uncontrolled modal truncation strategy. The motivation is to divide the whole mechanical problem into subsystem coupled by a contact term and investigate each subsystem separately.

**2.4.2. Controlled Modal Truncation.** The observation of the afore presented classical uncontrolled modal truncation method is that the system modes do not necessarily cover the essential modes of all bodies within the overall number of considered modes. Applying a systematic modal truncation strategy, the system modes are picked in a controlled way, which means that the main modes of each body and the unessential modes are truncated. In other words, the truncation will be carried out for each separate body. Therefore, the system is decoupled into subsystems and for each subsystem the following set of equations of motion must hold:

$$\mathbf{M}^{(i)} \ddot{\mathbf{u}}^{(i)} + \mathbf{C}^{(i)} \dot{\mathbf{u}}^{(i)} + \mathbf{K}^{(i)} \mathbf{u}^{(i)} + \mathbf{F}^{c(i)}(\mathbf{u}) = \mathbf{F}^{(i)}(t). \quad (18)$$

For each body, the modal truncation technique is now separately executed with  $m^{(i)} \ll n^{(i)}$ ; that is,

$$\mathbf{u}^{(i)} = \Phi_r^{(i)} \mathbf{z}^{(i)}. \quad (19)$$

The set of equations of motion of one body is rewritten by left multiplication of the reduced modal matrix as

$$\begin{aligned}\underbrace{\Phi_r^{(i)T} \mathbf{M}^{(i)} \Phi_r^{(i)}}_{\mathbf{m}^{(i)}} \ddot{\mathbf{z}}^{(i)} + \underbrace{\Phi_r^{(i)T} \mathbf{C}^{(i)} \Phi_r^{(i)}}_{\mathbf{c}^{(i)}} \dot{\mathbf{z}}^{(i)} + \underbrace{\Phi_r^{(i)T} \mathbf{K}^{(i)} \Phi_r^{(i)}}_{\mathbf{k}^{(i)}} \mathbf{z}^{(i)} \\ + \underbrace{\Phi_r^{(i)T} \mathbf{F}^{c(i)}}_{\mathbf{f}^{c(i)}} = \underbrace{\Phi_r^{(i)T} \mathbf{F}^{(i)}}_{\mathbf{f}^{(i)}(t)}(t).\end{aligned}\quad (20)$$

Assembling all of the controlled modal truncation matrices, one obtains one controlled modal truncation matrix

$$\mathbf{u} = \begin{bmatrix} \mathbf{u}^{(1)} \\ \mathbf{u}^{(2)} \\ \mathbf{u}^{(3)} \end{bmatrix} = \begin{bmatrix} \widehat{\Phi}_r^{(1)} & \mathbf{0} & \mathbf{0} \\ \mathbf{0} & \widehat{\Phi}_r^{(2)} & \mathbf{0} \\ \mathbf{0} & \mathbf{0} & \widehat{\Phi}_r^{(3)} \end{bmatrix} \begin{bmatrix} \mathbf{z}^{(1)} \\ \mathbf{z}^{(2)} \\ \mathbf{z}^{(3)} \end{bmatrix} = \widehat{\Phi}_r \widehat{\mathbf{z}}, \quad (21)$$

and the controlled truncated set of equations of motion:

$$\underbrace{\widehat{\Phi}_r^T \mathbf{M} \widehat{\Phi}_r}_{\widehat{\mathbf{m}}} \ddot{\widehat{\mathbf{z}}} + \underbrace{\widehat{\Phi}_r^T \mathbf{C} \widehat{\Phi}_r}_{\widehat{\mathbf{c}}} \dot{\widehat{\mathbf{z}}} + \underbrace{\widehat{\Phi}_r^T \mathbf{K} \widehat{\Phi}_r}_{\widehat{\mathbf{k}}} \widehat{\mathbf{z}} + \underbrace{\widehat{\Phi}_r^T \mathbf{F}^c}_{\widehat{\mathbf{f}}^c} = \underbrace{\widehat{\Phi}_r^T \mathbf{F}(t)}_{\widehat{\mathbf{f}}(t)}. \quad (22)$$

Through this transformation, the global movement of the system is captured and, therefore, a more reliable low-order system is ensured.

**2.5. Time Integration.** The nonlinear dynamic system is solved using the central difference integration scheme (cf. [12]). Considering second-order Taylor forward and backwards expansion, the approximation of the velocity is obtained by the sum of the two expansions, and the approximation of the acceleration is obtained by the difference of the two expansions. Thus, the approximations of the velocity and acceleration by the central difference method are described by

$$\begin{aligned} \dot{\mathbf{u}}_k &= \frac{\mathbf{u}_{k+1} - \mathbf{u}_{k-1}}{2\Delta t}, \\ \ddot{\mathbf{u}}_k &= \frac{\mathbf{u}_{k-1} - 2\mathbf{u}_k + \mathbf{u}_{k+1}}{\Delta t^2}. \end{aligned} \quad (23)$$

Inserting the approximations in (12) leads to an explicit formulation for the displacement at the subsequent time step:

$$\begin{aligned} & \left( \frac{1}{\Delta t^2} \mathbf{M} + \frac{1}{2\Delta t} \mathbf{C} \right) \mathbf{u}_{k+1} \\ &= \mathbf{F}_k - \left( \mathbf{K} - \frac{2}{\Delta t^2} \mathbf{M} \right) \mathbf{u}_k - \left( \frac{1}{\Delta t^2} \mathbf{M} + \frac{1}{2\Delta t} \mathbf{C} \right) \mathbf{u}_{k-1} \\ & \quad + \mathbf{F}_k^c. \end{aligned} \quad (24)$$

As presented in (24), the displacement vector at time instant  $t_{k+1}$  is evaluated based on the already known displacement vectors at time instants  $t_{k-1}$  and  $t_k$ . Therefore, an additional value for  $\mathbf{u}_{-1}$  must be calculated before the start of the integration loop. This is realized by the second-order backwards Taylor extrapolation:

$$\mathbf{u}_{-1} = \mathbf{u}_0 - \dot{\mathbf{u}}_0 \Delta t + \ddot{\mathbf{u}}_0 \frac{\Delta t^2}{2}. \quad (25)$$

The initial acceleration  $\ddot{\mathbf{u}}_0$  is obtained by inserting the initial conditions  $\mathbf{u}_0$  and  $\dot{\mathbf{u}}_0$  into the global equation of motion (12). The coefficient matrix  $((1/\Delta t^2)\mathbf{M} + (1/2\Delta t)\mathbf{C})$  is positive definite and can be LU factorized a priori, which accelerates the solution procedure. The big advantage of explicit time integration schemes is that for each step no iteration is required. However, the disadvantage is that relatively small

time steps must be chosen in order to ensure convergence. In other words, if the chosen time step  $\Delta t$  exceeds a critical value, the solution function increases exponentially to infinity. The critical time step of the central difference integration scheme depends on the highest eigenfrequency of the dynamic system:

$$\Delta t \leq t_{\text{crit}} = \frac{2}{\omega_{\text{max}}}, \quad (26)$$

where  $\omega_{\text{max}}$  defines the highest eigenfrequency of the dynamic system. Applying the frequency based controlled modal truncation strategy, the highest eigenfrequency of the low-order system is significantly reduced. Thus, the critical time step is considerably enlarged. Applying this strategy, a much higher iteration time step can be chosen, which leads to a considerably smaller number of integration loops to be processed and a significant decrease of the total computational time.

The new strategy, presented in this paper, is a remarkably efficient explicit time integration scheme, as it is able to overcome the general downside of these types of methods, that is, computational instability. Implicit time integration schemes, as, for example, the Newmark method (cf. [12]), require, on the one hand, an iterative procedure within one time integration step, and, therefore, more computational effort within this integration step. On the other hand, in case of the right choice of certain parameters, they are unconditionally stable. Choosing an arbitrary large time step, generally, a converged solution function can be observed. However, applying very large time steps, a solution function is obtained, which converges to the static solution. This is caused by the numerical damping effect. Thus, in order to ensure response functions with sufficient accuracy, additional calculations can ensure a sufficiently accurate solution. In summary, a smaller number of integration steps must be applied, but the computational effort and storage per integration step are considerably higher compared to explicit time integration schemes.

Within one test calculation, the standard central difference scheme is compared with the new reduced integration strategy and, additionally, with the implicit Newmark method, using the commercial software package ABAQUS<sup>®</sup>. Through this approach, not only is the overall correctness of the implemented in-house code verified but also the computational efficiency is tested. The comparison of the three methods can be found in Section 3.5. A more detailed discussion on the advantages and disadvantages of the different time integration methods for the dynamic Signorini problem is given in the study of Doyen et al. [30].

### 3. Comparison of Methods

**3.1. System Modal Analysis.** The uncontrolled classical modes of vibration of the whole system are calculated. The first 10 modes are depicted in Figure 4. It is observed that, due to different stiffness and characteristics of frames, the system modes alter from one frame to another frame in an irregular pattern. The disadvantage of the classical modal truncation technique is obvious: if one takes, for example, the first 6

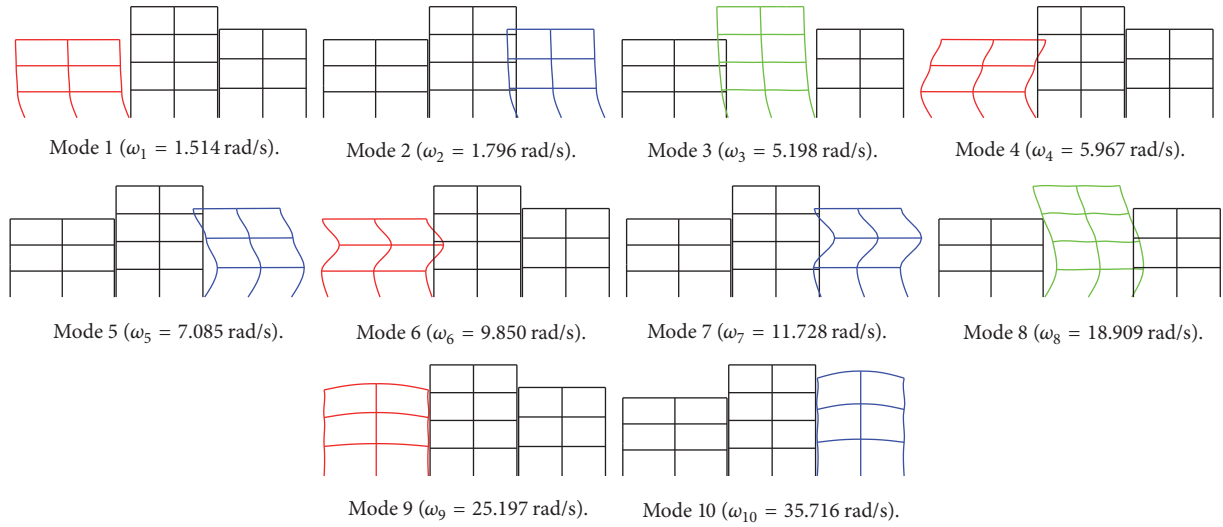


FIGURE 4: Presentation of the first 10 system modes.

modes and cuts the rest modes, the distribution of modes will be [3, 1, 2] concerning the substructures [ $\mathcal{S}_1$  (red),  $\mathcal{S}_2$  (green),  $\mathcal{S}_3$  (blue)]. A consistent distribution is therefore not achieved, which leads to an unsatisfactory low-order model.

The idea of the controlled modal truncation is motivated by the above introduced disorder of system modes. The aim of the systematic modal truncation is to decouple the whole nonlinear contact problem and to keep the important modes of each frame by executing the modal truncation for each frame subsystem separately. The choice of the modes can be empirically selected according to the number of stories of the frames or according to the frequency range of excitation. For instance, if the first ten modes are used and the rest of the modes are truncated, one can choose three modes for the first frame, four modes for the second frame, and three modes for the third frame. This is depicted in Figure 5. A consistent distribution of modes over the subsystem is achieved and a sufficient number of deformation patterns within the contact area is ensured in order to describe global contact behavior. These two methods are compared in detail applying harmonic and transient seismic excitations in the following sections.

**3.2. Sinusoidal Seismic Excitation.** The level of accuracy with respect to the number of considered modes for both the classical and the controlled modal truncation technique is studied under sinusoidal excitation. The results are focused on the displacement, the velocity, and the acceleration as well as the contact force of the horizontal degrees of freedom of the output node depicted in Figure 2. The ground acceleration is defined as  $\ddot{x}_g = a_0 \sin(\nu t)$  with  $a_0 = 2.5 \text{ m/s}^2$  and  $\nu = 4.0 \text{ rad/s}$ . In order to examine the accuracy of the strategies, six, ten, and fifteen modes of vibration are chosen and compared. We obtain unsatisfactory results for all values of interest if only the first six modes (with a mode distribution of [2, 2, 2] concerning [ $\mathcal{S}_1$ ,  $\mathcal{S}_2$ ,  $\mathcal{S}_3$ ] for the controlled modal truncation strategy) are chosen; see Figure 6. The deviation of the acceleration and the contact force is considerably

large. Consideration of only six modes for both classical and systematic modal truncation is obviously insufficient for a reliable approximation of the response outputs.

The results improve significantly if ten or more modes are taken into account. Regarding the classical modal truncation, if the first ten modes, illustrated in Figure 4, are chosen, the results improve considerably as shown in Figure 6 (red curves). However, noticeable errors for the acceleration and the contact forces are observed. By means of controlled modal truncation technique (with a mode distribution of [3, 4, 3] concerning [ $\mathcal{S}_1$ ,  $\mathcal{S}_2$ ,  $\mathcal{S}_3$ ]), which is depicted in Figure 5, the displacements and velocities are almost the same compared to the full system. It can be concluded that the systematically controlled modal truncation technique delivers much better results than the uncontrolled modal truncation for every quantity of interest; see Figure 7.

If 15 system modes (with a mode distribution of [4, 7, 4] concerning [ $\mathcal{S}_1$ ,  $\mathcal{S}_2$ ,  $\mathcal{S}_3$ ] for the controlled modal truncation strategy) are taken into consideration, the results between the full and the reduced systems agree almost; see Figure 8. The critical time step is smaller than the truncated system with ten modes. The convergence study with respect to the number of modes is carried out in the next section. Error analysis of the two techniques is given in Section 3.4.

**3.3. Frequency Response Analysis.** The frequency response analysis is essential for a better understanding of system characteristics in earthquake engineering. It is also the most commonly used method regarding the design of structures subject to earthquakes [31]. The frequency response analysis investigates how the maximum response of the displacement, the velocity, and the acceleration as well as the contact force of the structure behaviors subjected to harmonic excitations with different frequencies. For the demonstrated model, the driving angular frequencies vary from 0.1 rad/s to 5.0 rad/s. The results regarding the maximum displacements, the velocities, and the acceleration as well as the impact forces versus

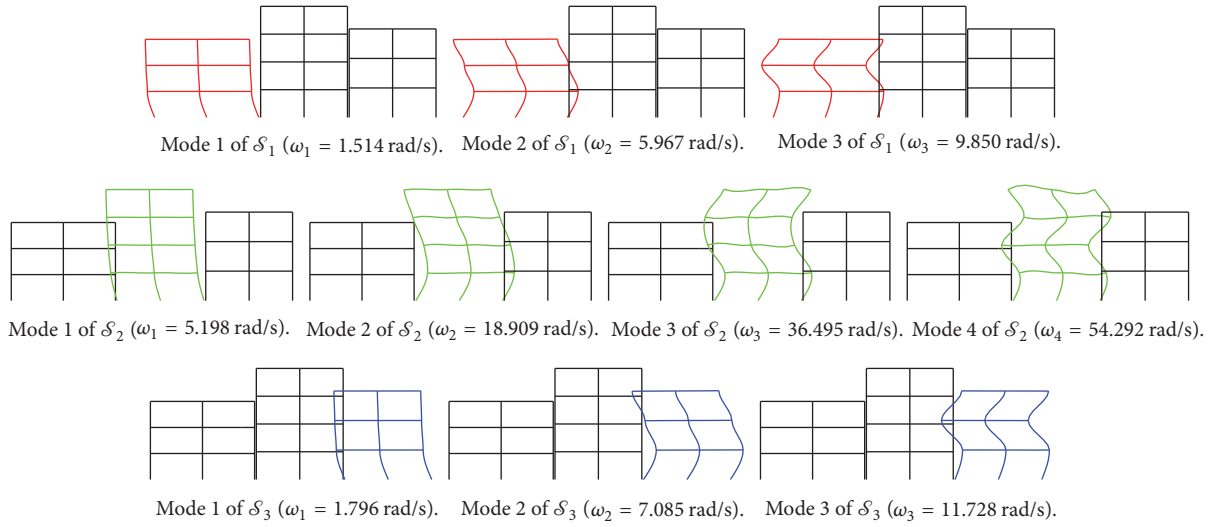
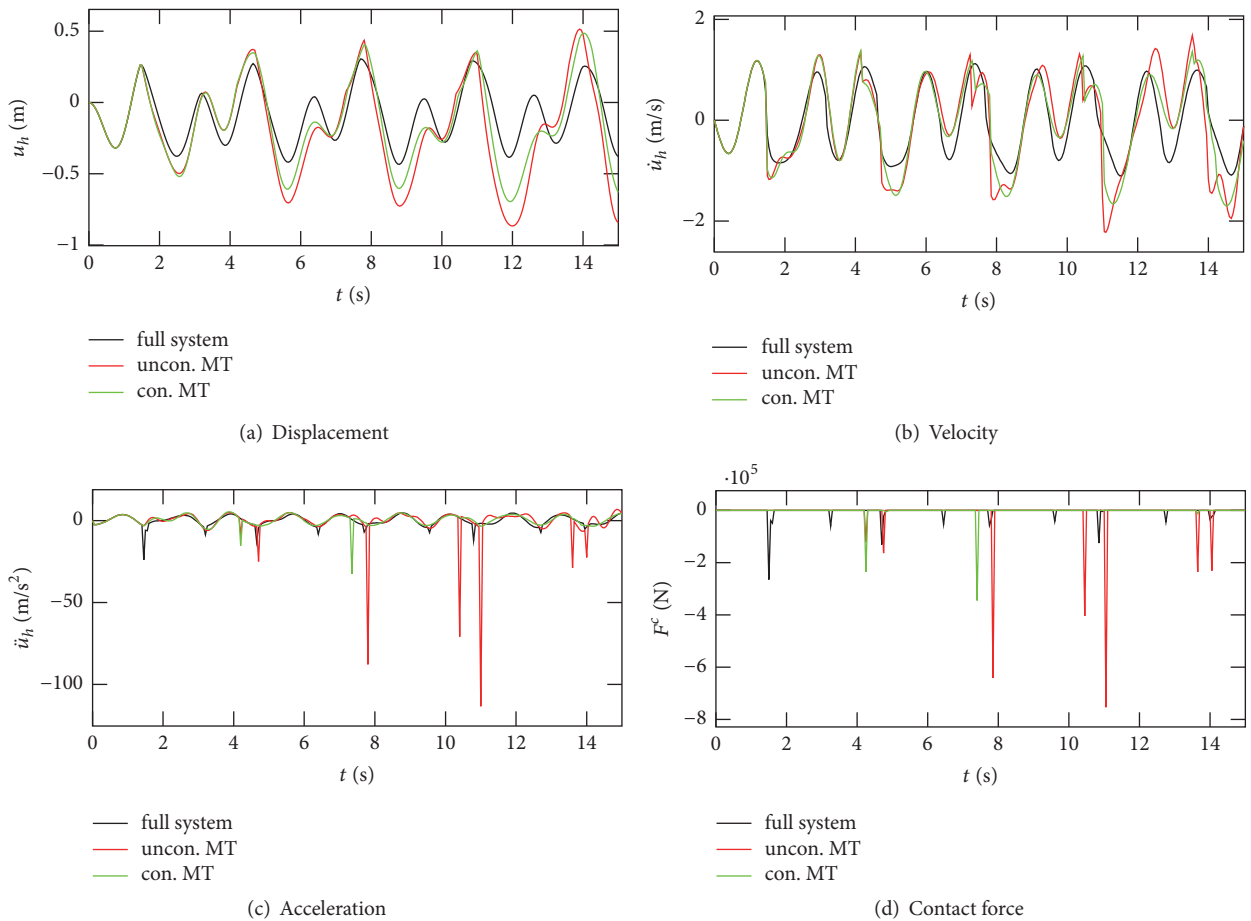


FIGURE 5: Presentation of the controlled modes.

FIGURE 6: Results for the displacement, the velocity, and the acceleration as well as the contact force with  $m = 6$ .

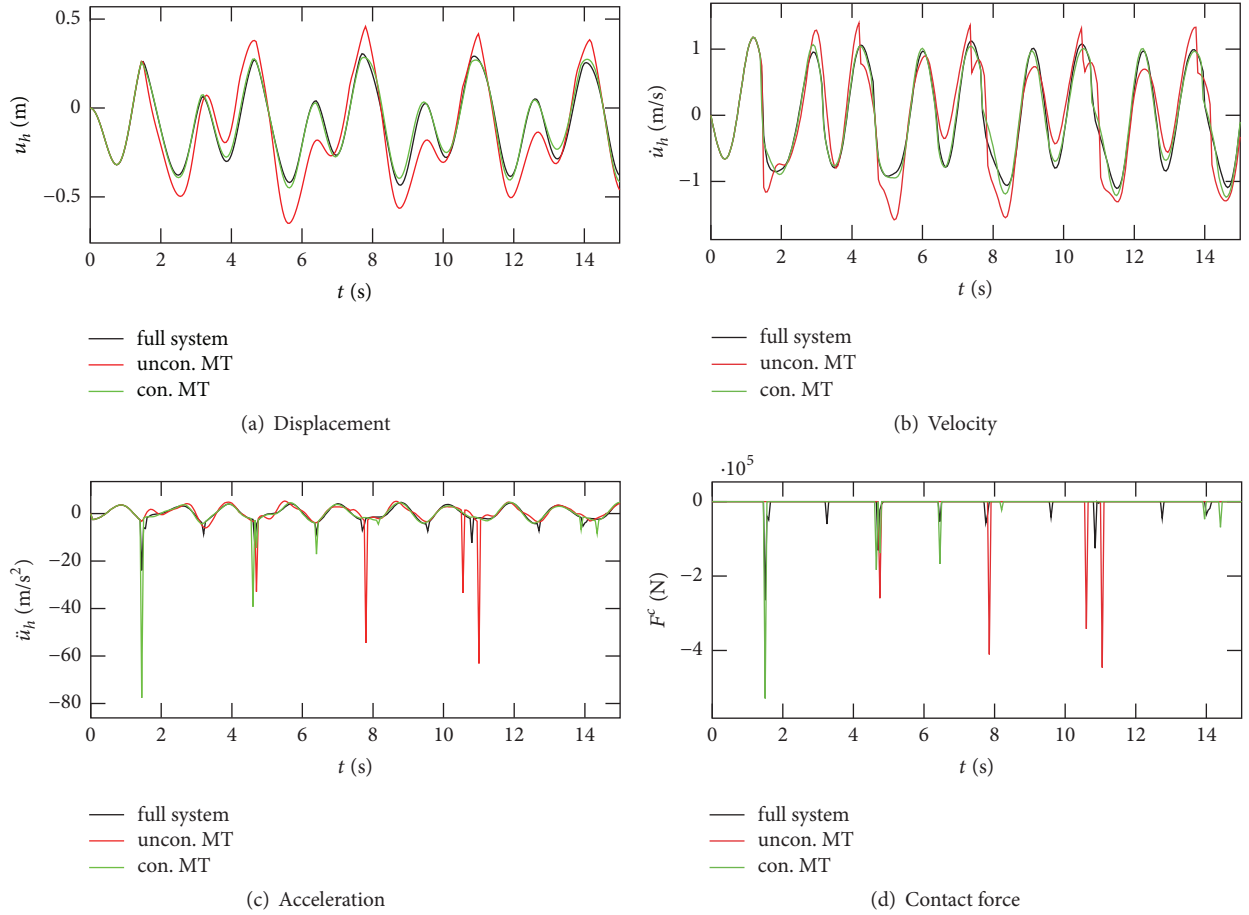


FIGURE 7: Results for the displacement, the velocity, and the acceleration as well as the contact force with  $m = 10$ .

driving angular frequencies applying the first ten modes are shown in Figure 9. It is observed that the extremal values are reached near  $\nu \approx 2.3$  rad/s. The numerical calculations of the first five eigenfrequencies are 1.514, 1.796, 5.198, 5.967, and 7.085 rad/s. The extremal values are not located near these frequencies as complex pounding interaction influences the overall system behavior.

It is observed that the controlled modal truncation technique approximates the results significantly better than the standard modal truncation technique. The maximum displacements, velocities, and contact forces for the whole range of interest of the excitation frequencies are well approximated by the controlled modal truncation method. The computational effort for each test frequency of the full system is about 315 seconds. However, the truncated system needs only 15 seconds. As the whole evaluation is based on the representative node, it is necessary to carry out a global error estimation, considering all degrees of freedom.

**3.4. Error Estimation.** As shown in Section 3.1, the results are mainly dependent on how many modes are chosen. The root-mean-square deviation (RMSD) of the node output histories is evaluated and plotted in Figure 10. The RMSD is defined as

$$\text{RMSD}(u_h) = \sqrt{\frac{\sum_{i=1}^n (u_{h,i} - \hat{u}_{h,i})^2}{n}}, \quad (27)$$

where  $\hat{u}_{h,i}$  is the reference solution of the full system and  $u_{h,i}$  is a reduced solution at the time step  $i$ . The RMSD errors of the standard method are larger than the controlled modal truncation if the applied number of modes  $m$  is smaller than 20. If more than 20 modes are taken into consideration, the RMSD of both methods are almost the same.

**3.5. Comparison of the New Strategy with the Commercial Software Package ABAQUS®.** In order to verify the correctness and efficiency of the implemented in-house software and the new strategy presented this paper, the full system response is compared with the commercial software package ABAQUS® and the reduced system using the new reduction strategy. Applying ABAQUS®, the same discretization compared to the in-house simulation is applied and the same penalty parameter, that is, stiffness parameter of the linear pounding element, is chosen within the contact module. The test is carried out in two steps.

In the first step, a statical analysis is performed. A horizontal force is applied at the top left node of the first frame system, where the magnitude of the force is chosen to be large enough in order to ensure contact between frames one and two and contact between frames two and three. The displacements of numerous representative nodes of the first, the second, and the last frame are evaluated by using ABAQUS®. The

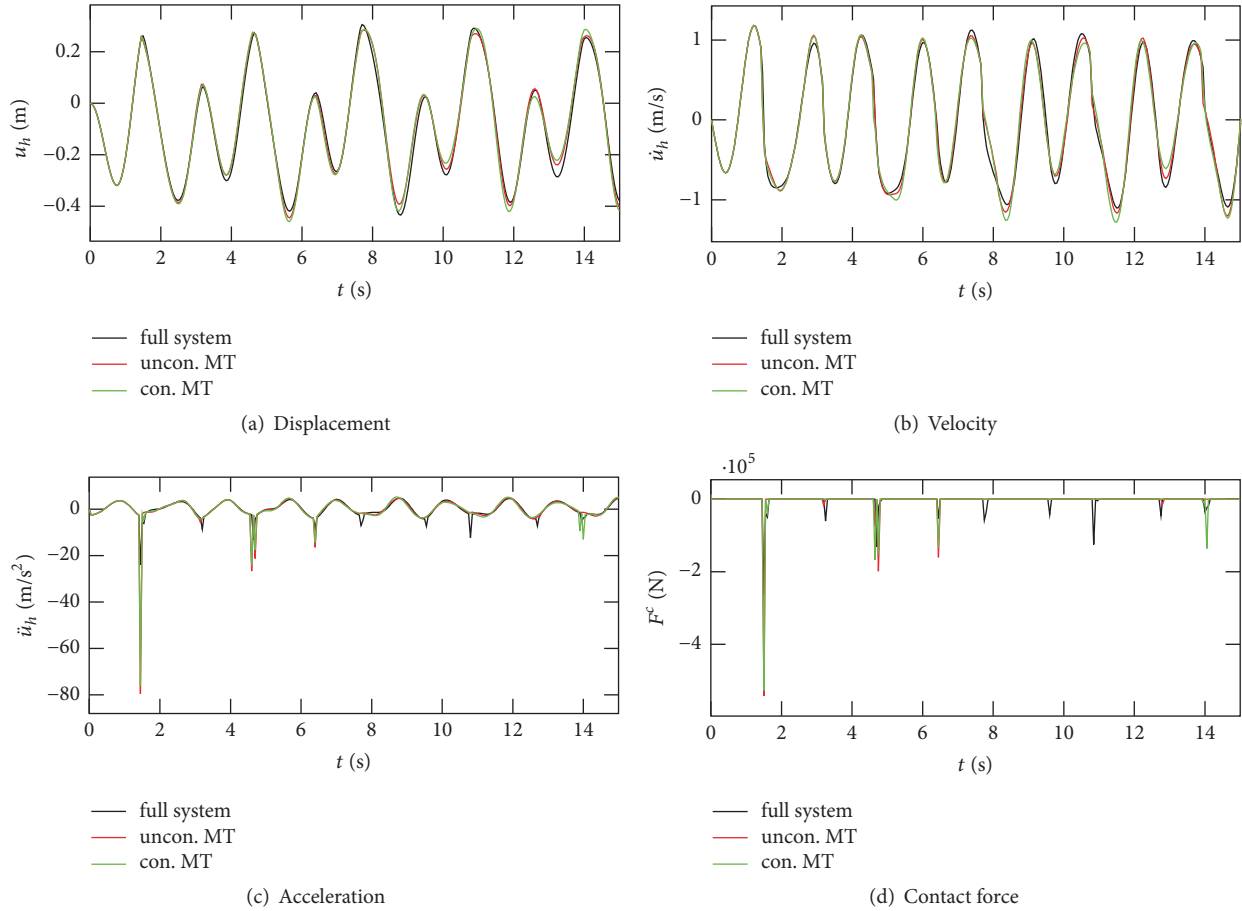


FIGURE 8: Results for the displacement, the velocity, and the acceleration as well as the contact force with  $m = 15$ .

results of the commercial software package agree perfectly with the in-house software tool. This verifies the correctness of the stiffness matrix and the contact formulation of the in-house software.

In the second step, the dynamic response of the structural system is evaluated, using the in-house implementation and the commercial software package ABAQUS<sup>®</sup>. The comparison of the displacement of the representative node, using ABAQUS<sup>®</sup> and the in-house software, is presented in Figure 11 by the blue dashed and black lines, respectively. Additionally, the solution of the new proposed controlled modal truncation strategy is depicted by the red dotted line in this figure.

In Figure 11, it can be seen that the in-house software agrees well with the result of the commercial software tool. Thus, the correctness of the calculation is verified. However, small deviations are observed, which are caused by the fact that, for the ABAQUS<sup>®</sup> simulation, the implicit Newmark integration is chosen, applying a time step of 0.001 seconds, and, for the in-house implementation, the explicit central difference method is used. It is also observed that, for the implicit integration scheme of the commercial software package, a maximum time step of 0.001 seconds must be chosen; otherwise, numerical damping is considerably high, and

an inaccurate solution is observed. Detailed comments about the advantages and disadvantages of the two methods are discussed in Section 2.5. The computational cost of the in-house software, using an integration time step of 0.0001 seconds for the explicit integration scheme, is comparable with the one of commercial software ABAQUS<sup>®</sup>. On the same machine, the calculation time using the in-house tool is about 315 seconds and the calculation time using the commercial software is about 297 seconds. However, the calculation time, applying the novel strategy, is only 15 seconds. It is observed that the new method shows an outstanding efficiency by preserving a required level of accuracy. Thus, the new method provides the possibility of evaluating high dimensional dynamic multiple pounding systems, which demand generally very high computational effort, using the standard integration scheme.

*3.6. Excitation under Different Earthquake Measurements.* Regarding general problems in earthquake engineering, ground excitations are not harmonic. They are transient. Therefore, the presented methods are verified applying different earthquake excitations. Two earthquake test samples depicted in Figure 12 are chosen. The calculation is performed taking into account ten modes (with a mode distribution

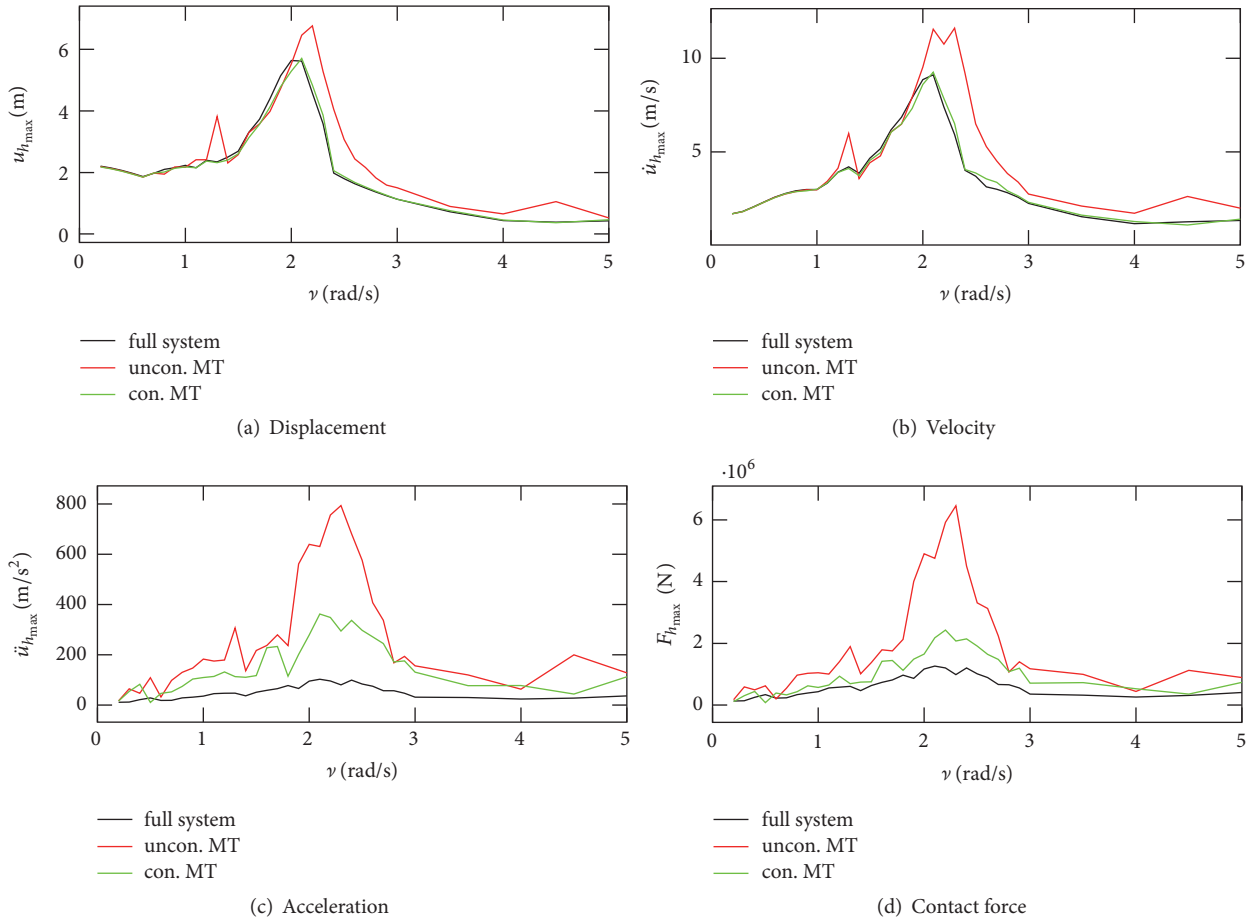


FIGURE 9: Frequency response of the maximum of the displacement, the velocity, and the acceleration as well as the contact force.

of  $[3, 4, 3]$  concerning  $[\delta_1, \delta_2, \delta_3]$  for the controlled modal truncation strategy). Data of the earthquake measurements are presented in Table 2.

The numerical results of the representative node, presented in Figures 13 and 14, reveal that the systematically controlled modal truncation technique provides reliable approximations of the system response. Taking into account the displacements and velocities compared to the full benchmark response, a higher accuracy is achieved by the controlled modal truncation technique. Concerning the acceleration and contact forces, especially at the contact time instants, the low-order model must be improved by taking more modes for both the classical and the controlled modal truncation methods.

#### 4. Conclusion and Outline

In this paper, the classical and a systematic modal truncation technique are studied, taking into account computational contact impact problem. Pounding is realized applying linear pounding elements within a node-to-surface contact formulation. Due to the pounding impact the classical modal truncation technique is not sufficient to approximate the system

response since the unconsidered higher frequency vibration modes play also an important role for the system response. The computational results show that the systematically controlled modal truncation is able to deliver a more reliable approximation of the full systems, especially for the displacements and velocities. This is also verified applying real earthquake excitations. The systematically controlled modal truncation technique makes the frequency response analysis for complex structural systems with a high number of degrees of freedom more feasible with consideration of the computational effort. It should be pointed out that the stated method is of course not limited to the seismic pounding problem only, but to a much broader field of dynamical contact and impact problems.

It must be added that the systematically controlled modal reduction technique is effective for materially linear systems. In the present paper, it is shown that it can also be efficiently applied for dynamic pounding problems. However, it is still necessary to increase the accuracy of the presented method, especially, with respect to the acceleration and the contact force functions. The next step concerning future research should also concentrate more on local vibration near the contact area. Here, it should be more focused on substructuring techniques, performed by, for example, the Craig-Bampton

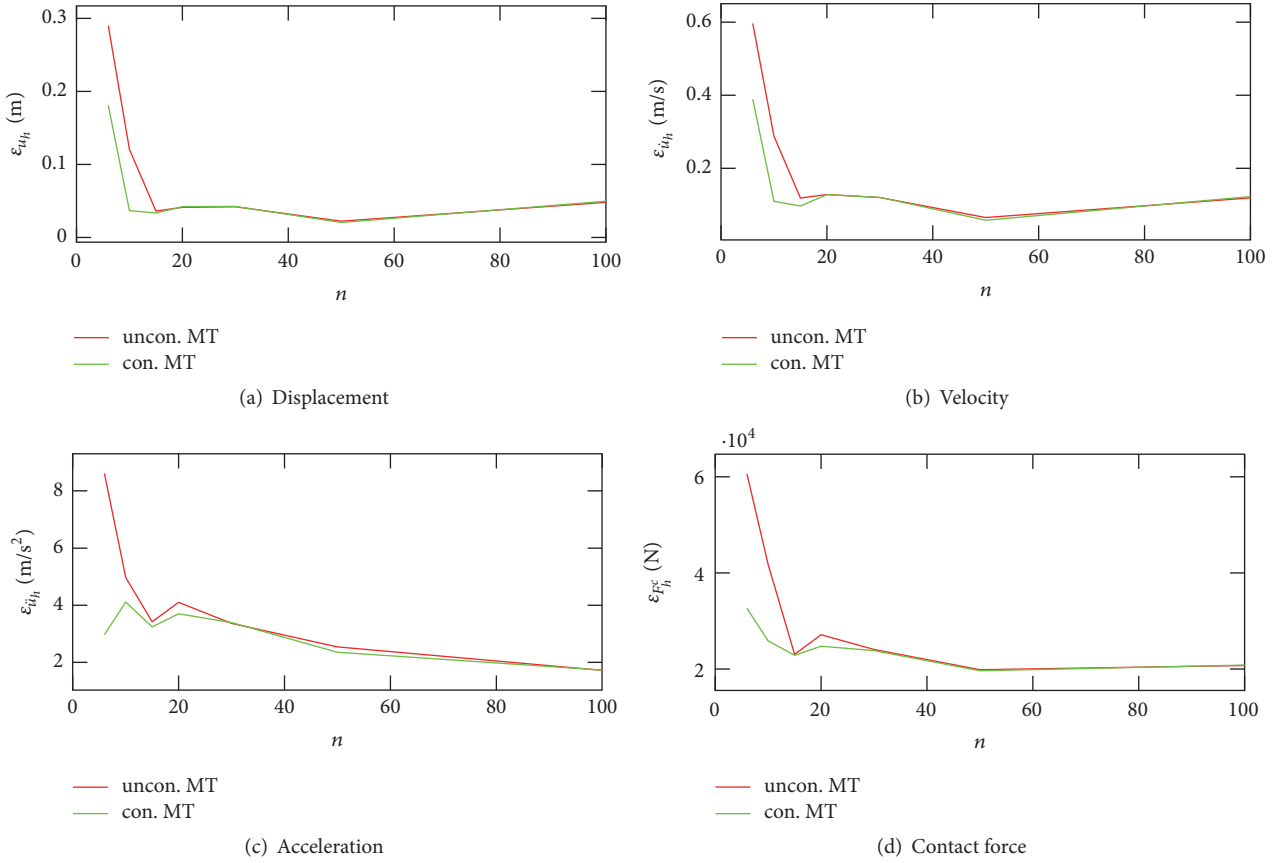


FIGURE 10: Error analysis using RMSD of the displacement, the velocity, and the acceleration as well as the contact force.

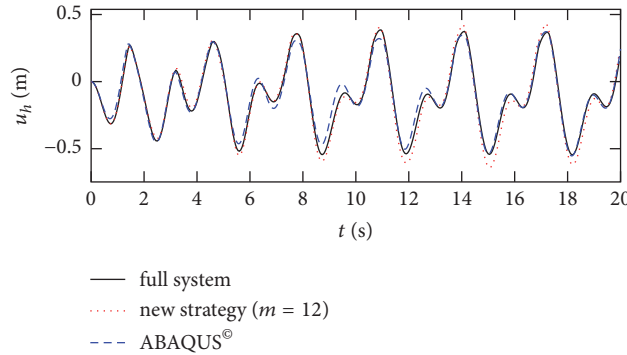


FIGURE 11: Comparison of the displacement between the in-house software and ABAQUS®.

method, where in this paper defined subsystems are again subdivided into substructures.

In case of material nonlinearity, further extensions of the above-mentioned strategies are necessary. Generally, the method of proper orthogonal decomposition was found to be useful for creating model order reduced descriptions, which are able to provide accurate approximations of nonlinear dynamic systems. The objective for upcoming studies, regarding the accurate low-order description of pounding problems, is to combine the proposed strategy with the Craig-Bampton method (cf. [18]) and with the proper orthogonal

decomposition (POD), which has been presented in recent studies [11, 12]. In particular, the frame subsystems, introduced in this paper, can be described by constraint modes, concerning the global motion of the structure, and internal modes, describing the local behavior of the structure within the contact area. Then, the nonlinear system behavior can be approximated using proper orthogonal modes, which are evaluated from an information matrix (snapshot matrix [13]), which contains already existing solution vectors of the materially nonlinear system and the constraint as well as the internal modes of the frame subsystems.

TABLE 2: Earthquake excitation list.

Event	Year	Location	$n_t$ [-]	$T$ [s]	$M$	PGA [ $m/s^2$ ]
Kobe	1995	Hanshin (Japan)	2001	20.000	7.2	6.81
Bam	2003	Bam (Iran)	400	19.950	6.6	3.58

$n_t$ : number of time steps,  $T$ : duration of the record,  $M$ : moment magnitude, and PGA: peak ground acceleration.

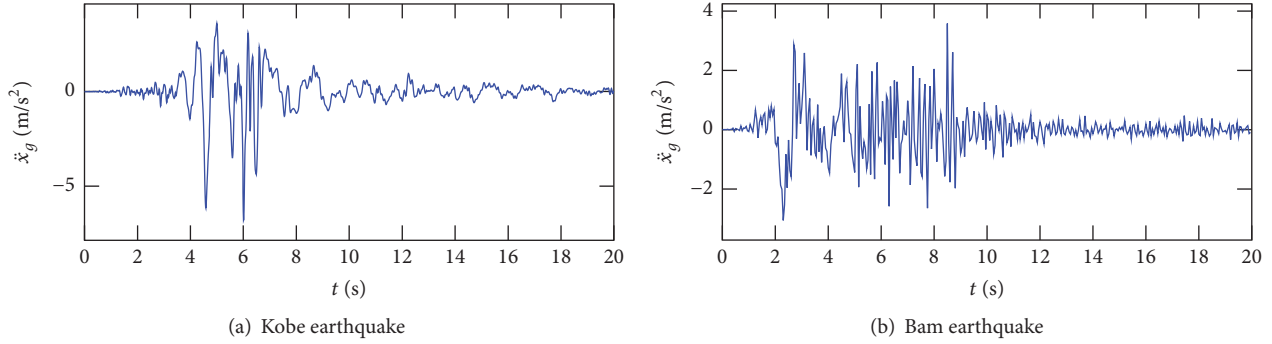


FIGURE 12: Acceleration time history of the Kobe and the Bam earthquake excitation.

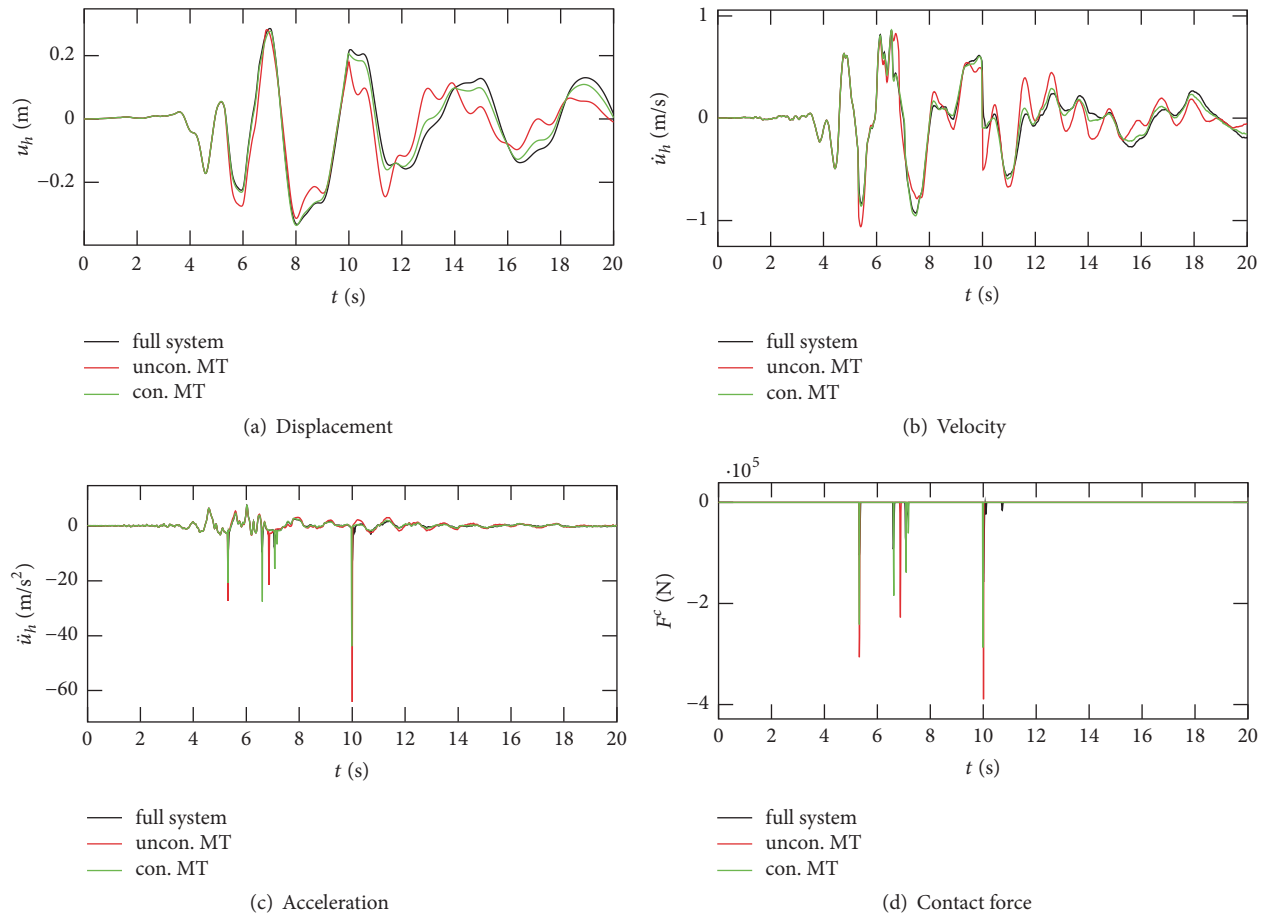


FIGURE 13: Results for the displacement, the velocity, and the acceleration as well as the contact force under seismic excitation (Kobe).

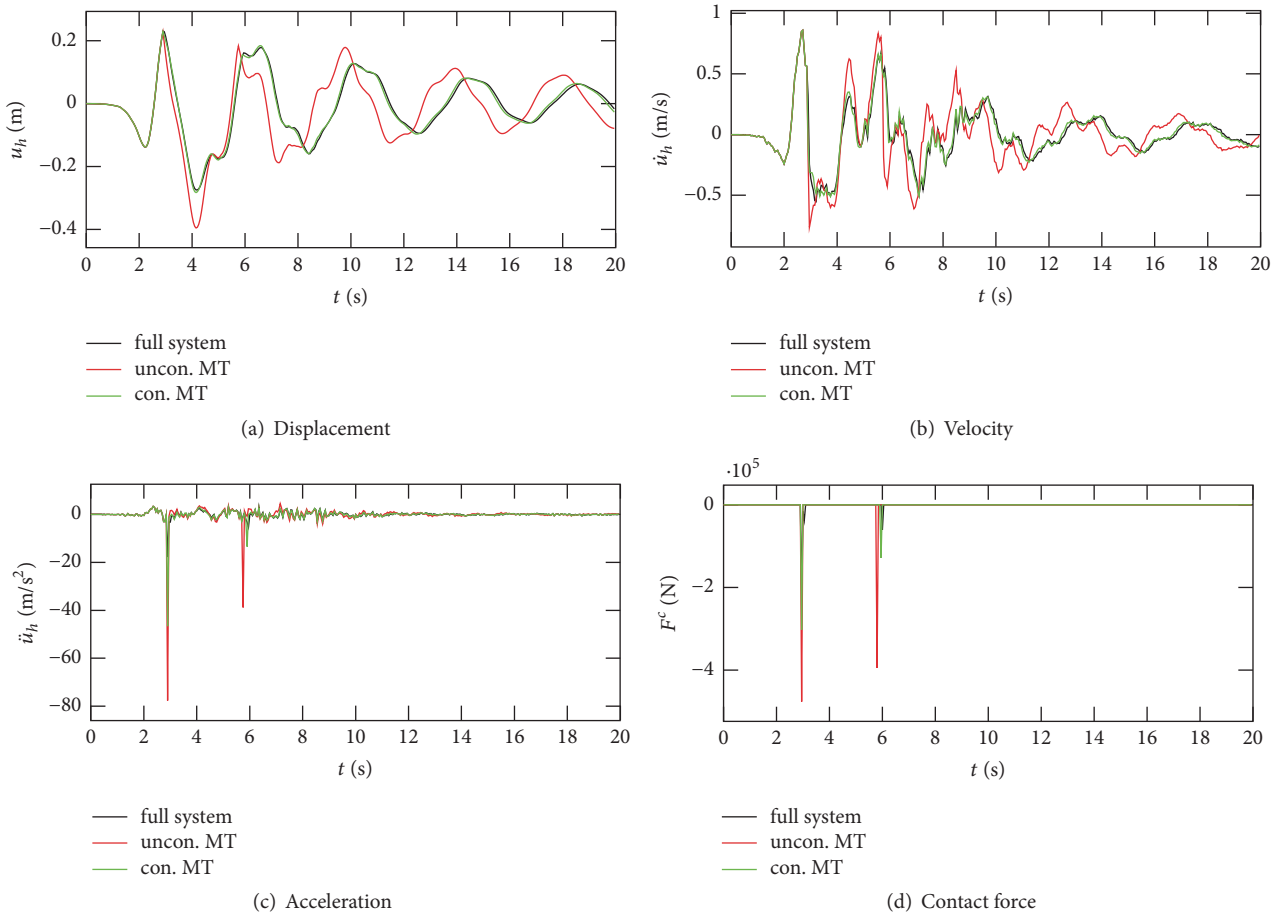


FIGURE 14: Results for the displacement, the velocity, and the acceleration as well as the contact force under seismic excitation (Bam).

## Conflicts of Interest

The authors declare that they have no conflicts of interest.

## References

- [1] R. Jankowski, "Assessment of damage due to earthquake-induced pounding between the main building and the stairway tower," *Key Engineering Materials*, vol. 347, pp. 339–344, 2007.
- [2] H. Naderpour, R. C. Barros, S. M. Khatami, and R. Jankowski, "Numerical study on pounding between two adjacent buildings under earthquake excitation," *Shock and Vibration*, vol. 2016, Article ID 1504783, 9 pages, 2016.
- [3] R. Jankowski and S. Mahmoud, "Linking of adjacent three-storey buildings for mitigation of structural pounding during earthquakes," *Bulletin of Earthquake Engineering*, vol. 14, no. 11, pp. 3075–3097, 2016.
- [4] S. T. Wasti and G. Ozcebe, *Seismic Assessment and Rehabilitation of Existing Buildings*, Kluwer Academic Publishers, Dordrecht, The Netherlands, 2003.
- [5] M. Ghandil and H. Aldaikh, "Damage-based seismic planar pounding analysis of adjacent symmetric buildings considering inelastic structure–soil–structure interaction," *Earthquake Engineering & Structural Dynamics*, vol. 46, no. 7, pp. 1141–1159, 2016.
- [6] B. F. Maison and K. Kasai, "Dynamics of pounding when two buildings collide," *Earthquake Engineering & Structural Dynamics*, vol. 21, no. 9, pp. 771–786, 1992.
- [7] B. F. Maison and K. Kasai, "Analysis for a type of structural pounding," *Journal of Structural Engineering*, vol. 116, no. 4, pp. 957–977, 1990.
- [8] S. A. Anagnostopoulos and K. V. Spiliopoulos, "An investigation of earthquake induced pounding between adjacent buildings," *Earthquake Engineering & Structural Dynamics*, vol. 21, no. 4, pp. 289–302, 1992.
- [9] S. Efraimiadou, G. D. Hatzigeorgiou, and D. E. Beskos, "Structural pounding between adjacent buildings subjected to strong ground motions: Part I: The effect of different structures arrangement," *Earthquake Engineering & Structural Dynamics*, vol. 42, no. 10, pp. 1509–1528, 2013.
- [10] S. Efraimiadou, G. D. Hatzigeorgiou, and D. E. Beskos, "Structural pounding between adjacent buildings subjected to strong ground motions: Part II: The effect of multiple earthquakes," *Earthquake Engineering & Structural Dynamics*, vol. 42, no. 10, pp. 1529–1545, 2013.
- [11] F. Bamer and C. Bucher, "Application of the proper orthogonal decomposition for linear and nonlinear structures under transient excitations," *Acta Mechanica*, vol. 223, no. 12, pp. 2549–2563, 2012.
- [12] F. Bamer, A. K. Amiri, and C. Bucher, "A new model order reduction strategy adapted to nonlinear problems in earthquake

- engineering,” *Earthquake Engineering & Structural Dynamics*, vol. 46, no. 4, pp. 537–559, 2017.
- [13] F. Bamer and B. Markert, “An efficient response identification strategy for nonlinear structures subject to nonstationary generated seismic excitations,” *Mechanics Based Design of Structures and Machines*, vol. 45, no. 3, pp. 313–330, 2017.
- [14] F. Bamer, J. Shi, and B. Markert, “Efficient solution of the multiple seismic pounding problem using hierarchical substructure techniques,” *Computational Mechanics*, pp. 1–22, 2017.
- [15] F. Bamer and B. Markert, “A Nonlinear Deterministic Mode Decomposition Strategy for High-Dimensional Monte Carlo Simulations,” *PAMM*, vol. 16, no. 1, pp. 187–188, 2016.
- [16] F. Bamer, A. Koeppe, and B. Markert, “An efficient Monte Carlo simulation strategy based on model order reduction and artificial neural networks,” *PAMM*, vol. 17, no. 1, pp. 287–288, 2017.
- [17] J. Shi, F. Bamer, and B. Markert, “An explicit reduced order integration scheme for contact problems in structural dynamics,” *PAMM*, vol. 17, no. 1, pp. 349–350, 2017.
- [18] S. Zucca, “On the dual Craig-Bampton method for the forced response of structures with contact interfaces,” *Nonlinear Dynamics*, vol. 87, no. 4, pp. 2445–2455, 2016.
- [19] M. Géradin and D. J. Rixen, “A “nodeless” dual superelement formulation for structural and multibody dynamics application to reduction of contact problems,” *International Journal for Numerical Methods in Engineering*, vol. 106, no. 10, pp. 773–798, 2016.
- [20] P. Wriggers, *Computational Contact Mechanics*, Springer-Verlag Berlin, Berlin, Heidelberg, Germany, 2006.
- [21] T. A. Laursen, *Computational Contact and Impact Mechanics: Fundamentals of Modeling Interfacial Phenomena in Nonlinear Finite Element Analysis*, Springer-Verlag Berlin, Berlin, Heidelberg, Germany, 2003.
- [22] A. K. Chopra, *Dynamics of Structures, Theory and Applications to Earthquake Engineering, Third Edition*, Prentice Hall, New Jersey, USA, 3rd edition, 2007.
- [23] G. Tecchio, M. Grendene, and C. Modena, “Pounding effects in simply supported bridges accounting for spatial variability of ground motion: A case study,” *Advances in Civil Engineering*, vol. 2012, Article ID 267584, 2012.
- [24] S. E. Abdel Raheem, “Mitigation measures for earthquake induced pounding effects on seismic performance of adjacent buildings,” *Bulletin of Earthquake Engineering*, vol. 12, no. 4, pp. 1–20, 2014.
- [25] D. Zhao and Y. Liu, “Improved damping constant of Hertz-Damp model for pounding between structures,” *Mathematical Problems in Engineering*, Article ID 9161789, 2016.
- [26] Y. Liu, W.-G. Liu, X. Wang, W.-F. He, and Q.-R. Yang, “New equivalent linear impact model for simulation of seismic isolated structure pounding against moat wall,” *Shock and Vibration*, vol. 2014, Article ID 151237, 10 pages, 2014.
- [27] Q. Xue, C. Zhang, J. He, G. Zou, and J. Zhang, “An updated analytical structural pounding force model based on viscoelasticity of materials,” *Shock and Vibration*, vol. 2016, Article ID 2596923, 15 pages, 2016.
- [28] X. Xu, X. Xu, W. Liu, and D. Zhou, “A new formula of impact stiffness in linear viscoelastic model for pounding simulation,” *Shock and Vibration*, vol. 2016, Article ID 5861739, 2016.
- [29] X. Cheng, W. Jing, J. Chen, and X. Zhang, “Pounding Dynamic Responses of Sliding Base-Isolated Rectangular Liquid-Storage Structure considering Soil-Structure Interactions,” *Shock and Vibration*, vol. 2016, Article ID 8594051, 2016.
- [30] D. Doyen, A. Ern, and S. Piperno, “Time-integration schemes for the finite element dynamic Signorini problem,” *SIAM Journal on Scientific Computing*, vol. 33, no. 1, pp. 223–249, 2011.
- [31] R. Jankowski, “Non-linear viscoelastic modelling of earthquake-induced structural pounding,” *Earthquake Engineering & Structural Dynamics*, vol. 34, no. 6, pp. 595–611, 2005.

## Research Article

# Developing Seismic Risk Prediction Functions for Structures

Naveed Ahmad , Qaisar Ali, Muhammad Adil, and Akhtar Naeem Khan

*Earthquake Engineering Center, UET Peshawar, Khyber Pakhtunkhwa, Pakistan*

Correspondence should be addressed to Naveed Ahmad; [naveed.ahmad@uetpeshawar.edu.pk](mailto:naveed.ahmad@uetpeshawar.edu.pk)

Received 23 July 2017; Accepted 13 March 2018; Published 29 April 2018

Academic Editor: Yuri S. Karinski

Copyright © 2018 Naveed Ahmad et al. This is an open access article distributed under the Creative Commons Attribution License, which permits unrestricted use, distribution, and reproduction in any medium, provided the original work is properly cited.

The paper presents the development of a nonlinear static displacement-based methodology for seismic risk assessment and loss estimation of stone masonry building stock of Pakistan. Experimental investigation of one-third scaled model, tested on shake table, is performed in order to obtain lateral strength and drift limits for stone masonry and develop damage scale for performance-based assessment. Prototype buildings are designed respecting the existing building stock and investigated through nonlinear static and dynamic time history analyses. Nonlinear static mechanical models, for both global and local vulnerabilities, are developed for the considered typology which are used to derive analytical structure-dependent fragility functions considering expected sources of uncertainties explicitly in contrary to the conventional procedures. Furthermore, seismic risk assessment is performed for different scenario earthquakes and presented in terms of structure-independent fragility functions to estimate the mean damage ratio, the repair cost as a fraction of replacement cost, and casualties, with the dispersion being quantified, given source-to-site distance and magnitude for an earthquake event. The methodology is tested for seismic risk assessment of the considered typology in recent 2005 Kashmir earthquake, which is reasonably predicted. Future development of the methodology is required with additional experimental tests on rubble stone masonry material in order to increase confidence in future applications.

## 1. Introduction

Stone masonry buildings constitute a substantial portion of urban and rural building stock of northern areas of Pakistan. Two wythes random rubble stone masonry walls (Figure 1) in dry or mud mortar or cement mortar with flat earthen roof (wooden beams and straw), wooden/steel truss with galvanized iron (GI) sheet roof, and reinforced concrete (rc) slab are the most common construction type in rural and urban settlements of Pakistan. Recent practices in the country, mainly in the recent earthquake affected areas (<http://www.erra.pk/>), make use of throw stones and vertical steel bars, 1.2 m apart, in order to improve the seismic performance of such systems which seems not to be dramatically different than the ordinary wall configuration. Nevertheless, the findings herein are conservative for the new structural systems. Furthermore, the overall contribution of old construction schemes is relatively more in Pakistan [1].

Such building systems have shown very poor performance in past earthquakes and lead to huge losses of life and economy. Collapse of such structures featured prominently

in the 2005 Kashmir earthquake [2, 3]. However, due to the abundant local availability of stone material, cheap labor cost, low economic status of the people, old traditions of construction, and lack of public awareness, stone masonry buildings are still in use in Pakistan. Stone masonry buildings are practiced, with little modifications (Figure 1), in the earthquake affected areas in the order of 50 percent of total building stock, which is about 500,000 housing units. Also, some parts of the country, which are not affected in the near past, have significant amount of old stone masonry buildings (Figure 1) [1]. Thus, the present study assesses the seismic performance of the considered building system using experimental and numerical investigations. Analytical methodology is developed for future applications in seismic risk assessment and loss estimation of stone masonry buildings on regional scale. Simplified charts are developed to estimate the socioeconomic impacts of earthquakes with the expected dispersion being quantified, given the magnitude and source-to-site distance of event, for earthquake preparedness and planning, decision-making, and risk mitigation in Pakistan. A test prediction of seismic risk is performed for the

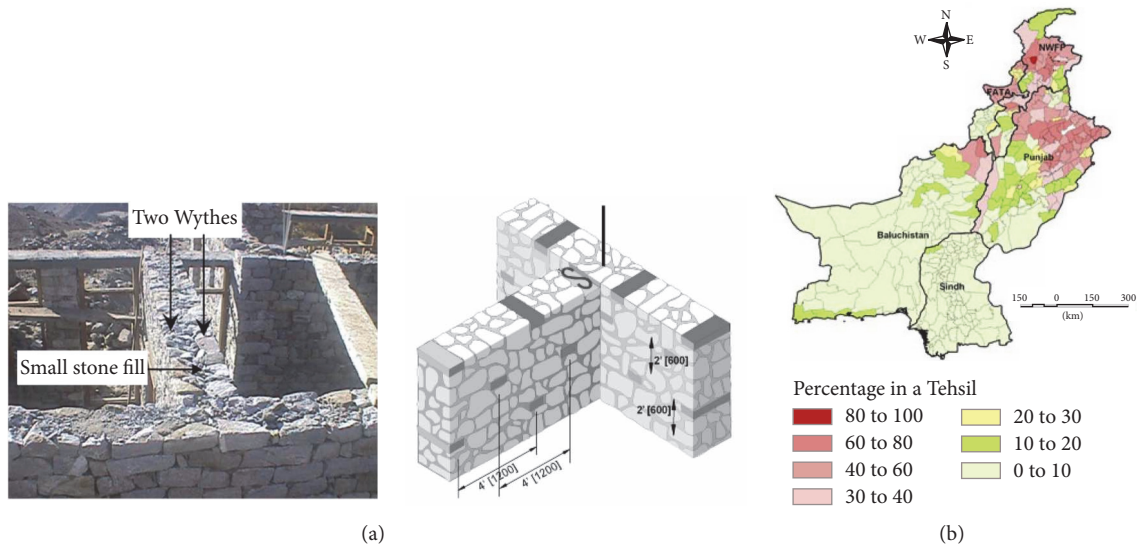


FIGURE 1: Typical rubble stone masonry building walls, existing buildings, and new structural schemes (a) and spatial distribution of stone masonry buildings in Pakistan [1] (b).

considered typology in the recent 2005 Kashmir earthquake which is reasonably predicted.

## 2. Displacement-Based Earthquake Loss Assessment Methodology (DBELA)

Seismic risk assessment and loss estimation of structures have developed from initial studies, in the past 30 years, which used empirical approaches to predict the socioeconomic impacts of earthquakes, to more recent methodologies based on numerical predictions of the capacity of buildings to resist strong ground shaking [4, 5]. There are various shortcomings with the use of empirical methodologies, which arise due to the use of ground motion intensity parameters, which do not take the relationship between the frequency content of the ground motion and the vibration characteristics of the building stock into account (e.g., peak ground acceleration). The ground motion uncertainties and spatial variabilities cannot be truly represented which can be different from earthquake-to-earthquake and site-to-site. Further problems exist with such methods due to the use of existing building damage, which thus precludes the possibility of accurately modeling the vulnerability of new or retrofitted buildings. In order to respond to these shortcomings and, perhaps more importantly, so as to allow the most recent developments in seismic hazard and ground motion prediction to be employed, newly emerging methodologies are based on the analytical assessment of building damage given an input response spectrum. Such methods have the additional advantage of allowing the vulnerability of the building stock to be predicted based on a limited amount of knowledge of the structural characteristics of the buildings under consideration and thus they can be easily calibrated around the world [5]. Furthermore, the vulnerability predictions with mechanics-based methods can be easily justified following a close inspection of the characteristics of the buildings. Thus, the present study performed

calibration of a nonlinear static analytical mechanics-based, mainly displacement-based, fully probabilistic method, presented herein, for seismic vulnerability and risk assessment of stone masonry building stock of Pakistan on regional scale. The displacement-based method is originally proposed and developed elsewhere for rc and masonry buildings [6–10]. However, it is further extended and developed to take different sources of uncertainties, involved in the evaluation of structural capacity and seismic demand, in an explicit and transparent manner and make use of analytical fragility functions, derived in a conceptual and transparent manner, to develop damage scenario for a given earthquake. Also, the methodology can be applied to both individual building and building aggregates considering their global and local vulnerabilities. The methodology is previously developed for other building stock of Pakistan [11–15] and further calibrated for stone masonry buildings of Pakistan herein.

**2.1. Fundamentals of the Methodology.** The methodology makes use of analytical fragility functions and a mathematical model for building stock, which is represented as a nonlinear static single degree of freedom (SDOF) system defined completely by secant vibration period, displacement capacity, and viscous damping, to assess the seismic risk and socioeconomic impacts of a given earthquake event. The seismic demand on building stock is defined by 5% damped displacement response spectrum using code-based (for intensity-based), GMPE-based (for scenario earthquakes), and/or UHS-based (for estimation of loss exceedance curve and annualized losses) spectrum representation depending on the scope of the study. GMPE stands for ground motion prediction equation and UHS stands for uniform hazard spectra. To better understand the methodology, it is depicted graphically (Figure 2).

In this methodology, the first step is to generate elastic displacement response spectrum for a given earthquake,

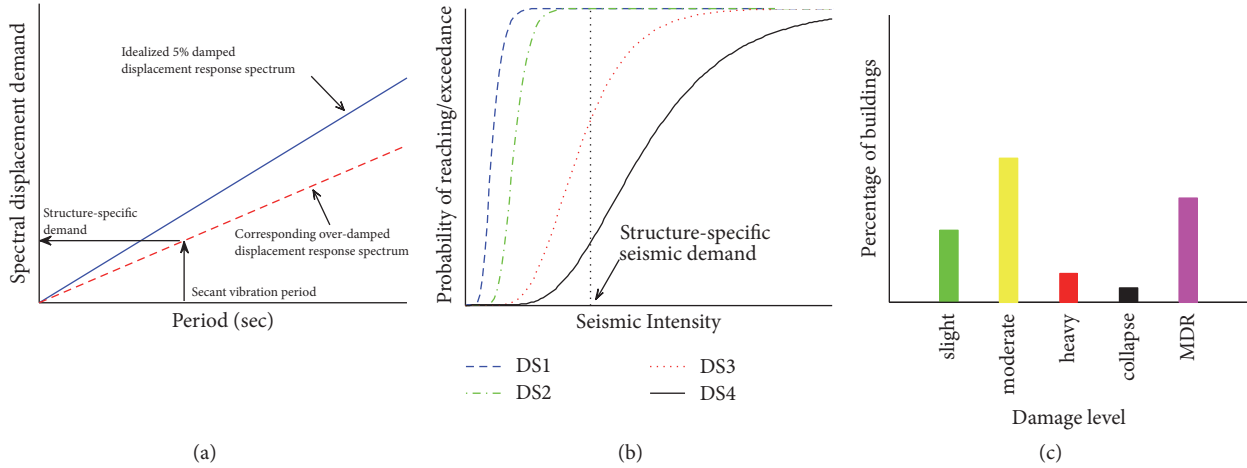


FIGURE 2: Graphical representation of DBELA: idealized displacement response spectrum (a), analytical fragility functions, global mechanism (b), and damage scenario (c).

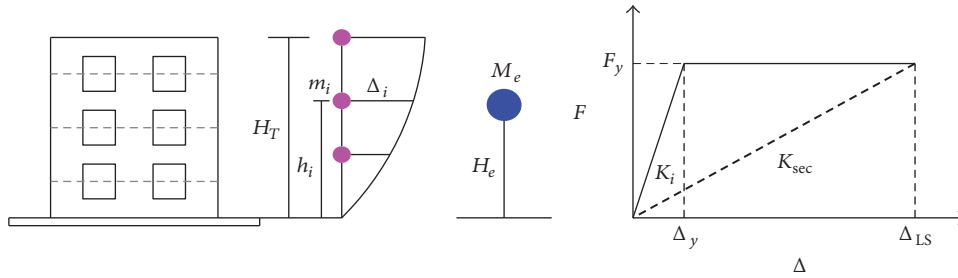


FIGURE 3: Nonlinear static SDOF idealization, mechanical model, of stone masonry buildings for global mechanism.

which is overdamped in an iterative fashion to compute the structure-specific seismic demand (seismic intensity). This seismic intensity is used to compute the number of buildings in different damage states from the analytical fragility functions in order to develop damage scenarios. The number of buildings in different damage states is transformed to mean damage ratio (MDR), which quantifies the regional seismic risk and gives an estimate of direct economic losses for the considered earthquake. The conversion of building damage states to MDR is performed using earthquake loss model [16]. However such models are needed to be calibrated for different regions in order to develop regional specific risk estimation tools and increase the confidence in future applications.

2.2. Mechanical Model for Stone Masonry Buildings. For seismic assessment, the stone masonry building stock of Pakistan is broadly classified in two major classes based on the predominant seismic response mechanism during an earthquake. Masonry buildings provide seismic resistance to ground shaking through the development of in-plane/out-of-plane forces/deformations in structural walls. The buildings that have enough structural integrity provide seismic resistance predominantly through in-plane shear/flexure response of structural walls (global mechanism) while buildings with less structural integrity respond primarily in out-of-plane response of walls (local mechanism). The methodology

uses SDOF systems to assess the seismic performance of each class of building stock. The SDOF system, called a mechanical model, has nonlinear lateral force-displacement response to assess the seismic performance of structures. The mechanical model simulates the response of the structural system in terms of its displacement capacity, energy dissipation, and secant vibration period for seismic assessment. The SDOF system derivation for each class of buildings are discussed as follows.

2.2.1. Global Mechanism (In-Plane Response). The seismic response of stone masonry buildings having rc slab, well-connected orthogonal walls, and ring beams is mainly governed by the global response of buildings, because of the in-plane integrity of walls provided by the rc slab, with shear failure dominated mechanism of in-plane walls [17–19]. Flexure rocking with compressed toe crushing is also a possible mechanism to resist lateral load. The structural system provides energy dissipation due to nonlinear behavior of masonry walls and limited ductility capacity. The current construction practice in the area is to include vertical steel bars and through stones in wall; although it may not increase the wall strength significantly, however, it will ensure sufficient in-plane integrity of the walls and whole system to respond through global mechanism. An equivalent SDOF system (Figure 3) is used to simulate the global response of building in terms of displacement capacity, viscous damping,

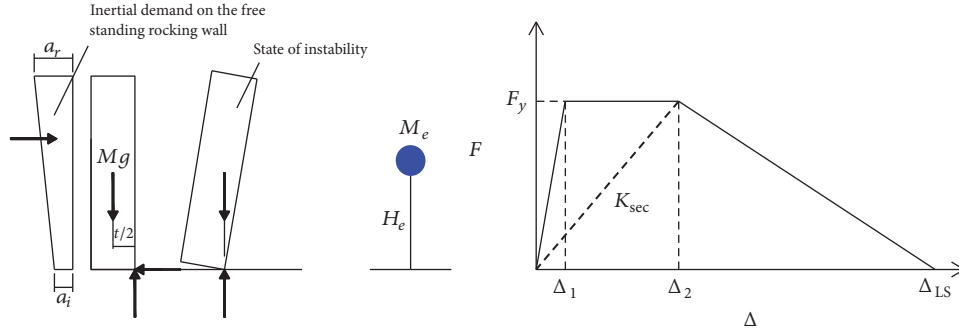


FIGURE 4: Nonlinear static SDOF idealization, mechanical model, of masonry wall for out-of-plane mechanism, modified.

and secant vibration period at different damage states for performance evaluation given an earthquake event, represented as 5% damped displacement response spectrum.

In this figure,  $H_T$  represents the total building height;  $h_i$  represents the  $i$ th floor height,  $\Delta_i$  represents the lateral displacement, and  $m_i$  represents the  $i$ th floor mass for a given deformed shape of building;  $M_e$  and  $H_e$  represent mass and height of the equivalent SDOF system;  $\Delta_y$  and  $\Delta_{LS}$  represent the equivalent yield and ultimate limit states displacements that represent the displacement capacity of the actual building at the center of seismic force for a specified deformed shape;  $K_i$  represents the initial preyield stiffness;  $F_y$  represents the yielding force;  $K_{sec}$  represents the secant stiffness.

For seismic assessment, the mechanical model is completely defined by secant vibration period, limit state displacement capacity, and energy dissipation characteristics of building represented as viscous damping:

$$T_{LS} = T_y \sqrt{\mu}, \quad (1)$$

$$\Delta_{LS} = \theta_y k_1 H_T + (\theta_{LS} - \theta_y) k_2 h_s, \quad (2)$$

$$\xi_{eq} = \xi_{el} + \xi_{hyst}, \quad (3)$$

where  $T_{LS}$  represents the limit state secant vibration period;  $T_y$  represents the yield vibration period;  $\mu = \Delta_{LS}/\Delta_y$  represents the limit state ductility;  $\Delta_y$  represents the yield displacement capacity;  $\Delta_{LS}$  represents the specified limit state displacement capacity;  $\theta_y$  represents the yield drift;  $\theta_{LS}$  represents the specified limit state drift;  $H_T$  represents the height of the system;  $k_1$  and  $k_2$  represent the displacement coefficients to convert multi-degree of freedom (MDOF) structural system to an equivalent SDOF system and simulate the displacement capacity of MDOF system at the center of seismic force [8];  $\xi_{eq}$  represents the equivalent viscous damping of the structural system [20];  $\xi_{el}$  represents the elastic damping of the system (preyield);  $\xi_{hyst}$  represents the hysteretic contribution of system damping due to nonlinear response of the structural components. The limit state parameter's values are selected to predict the corresponding damage states of structures for socioeconomic loss computation [16].

**2.2.2. Local Mechanism (Out-of-Plane Response).** Stone masonry buildings without rc slabs and ring beams having

orthogonal walls not properly connected, or due to loss of in-plane walls integrity during seismic excitations, respond in local out-of-plane collapse of portion or complete walls [18]. The mechanical model for this mechanism is formulated elsewhere [21] for brick masonry walls (Figure 4).

In Figure 4,  $a_i$  represents the peak acceleration of input excitation;  $a_r$  represents the response acceleration of wall;  $M$  represents total mass of wall;  $g$  represents acceleration due to gravity;  $t$  represents the wall thickness;  $\Delta_1$ ,  $\Delta_2$ , and  $\Delta_{LS}$  represent the limit state displacement capacities of wall.

The resistance of local out-of-plane mechanism to earthquake excitation is governed by the wall geometry, boundary condition, self-weight, and precompression level of rocking portion of wall while being less affected by the masonry material properties [22]. The out-of-plane stability of precracked wall can be relatively well assessed by using the secant stiffness, at the beginning of the third degrading branch of the mechanical model, and 5% damped response spectrum [22]. Thus, the secant period for out-of-plane mechanisms can be formulated as follows:

$$T_{out} = 2\pi \left( \frac{c \cdot t}{\lambda \cdot g \cdot (1 - c)} \right)^{0.5}, \quad (4)$$

where  $c = \Delta_2/\Delta_u$  represents the ratio of the limit state displacement capacity;  $\lambda = F/W$  represents the collapse multiplier;  $F$  represents the force at incipient rocking;  $t$  represents the wall thickness;  $W$  represents the total weight of the rocking wall. The ultimate displacement capacity of the out-of-plane wall is mainly governed by the thickness of the wall [21] which can be used with 5% viscous damping for seismic assessment and collapse prediction [22]. Nevertheless, the response of walls for out-of-plane loading in actual buildings is more complex than previously presented (Figure 4). Based on actual observations during earthquakes, various possible failure mechanisms are reported (Figure 5) [23] which are typical for most of the European historical towns. Collapse multiplier has been derived for different mechanisms using static analytical analysis to compute the lateral strength of out-of-plane loaded wall [23] which is further developed following detailed experimental investigation [24] on scaled models, typical for Italian dry stone masonry. The typologies of failure mechanisms for out-of-plane could be even more than the cases presented herein.

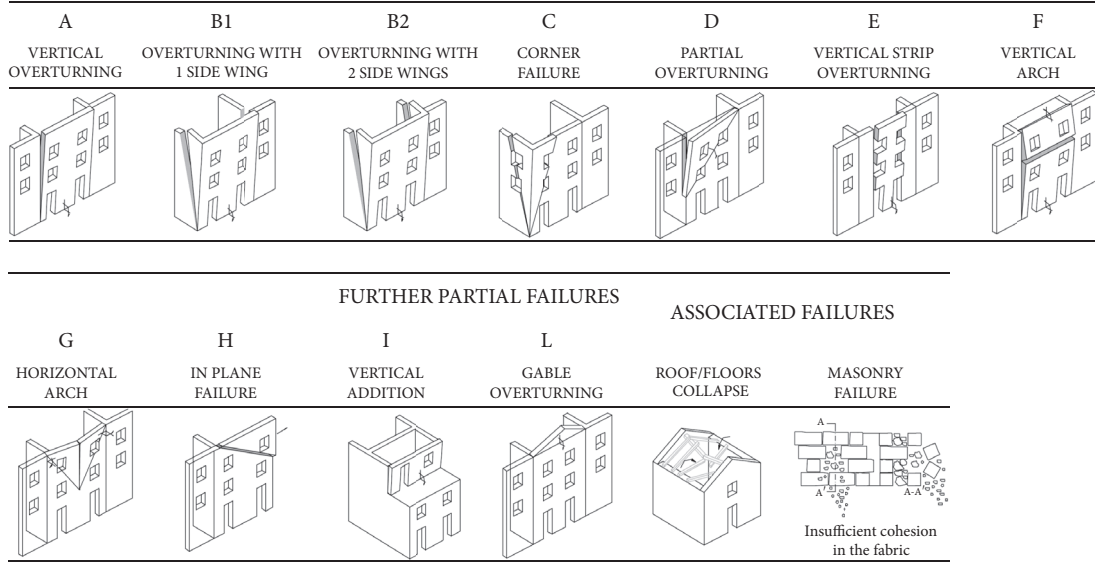


FIGURE 5: Observed out-of-plane mechanism of masonry buildings [23].

2.3. *Development of Analytical Fragility Functions.* Fragility functions, also called fragility curves, vulnerability curves, and/or building damage functions, describe the number of buildings reaching or exceeding a given damage state given the seismic intensity, represented as peak ground shaking parameters or spectral quantities [25]. Considering different possible damage states of buildings, there could be a number of fragility functions for a given typology which can be used to estimate the number of buildings in different damage level given the seismic intensity. Generally, for a given limit state, fragility function is derived considering a standard normal cumulative distribution function of the logarithmic difference of the seismic intensity and threshold capacity of limit states with certain level of standard deviation:

$$P \left[ D \geq \frac{d_{LS}}{SD = sd_{LS}} \right] = \Phi \left[ \frac{1}{\beta} \ln \left( \frac{SD}{sd_{LS}} \right) \right], \quad (5)$$

where  $P[...]$  represents the probability of reaching or exceeding a given limit state;  $\Phi$  represents the standard normal cumulative distribution function;  $SD$  represents the seismic intensity/demand;  $sd_{LS}$  represents the limit state capacity of the system;  $\beta$  represents the natural logarithmic standard deviation which defines the level of uncertainties in the fragility functions. The limit state capacity  $sd_{LS}$ , usually median value, is obtained experimentally or numerically using sophisticated numerical tools. The standard deviation  $\beta$  is obtained from the square root square sum or similar combination of individual uncertainties which do not have clear rationale and justification behind. Similar other procedures exist which make use of constraint criterion to derive analytical fragility functions.

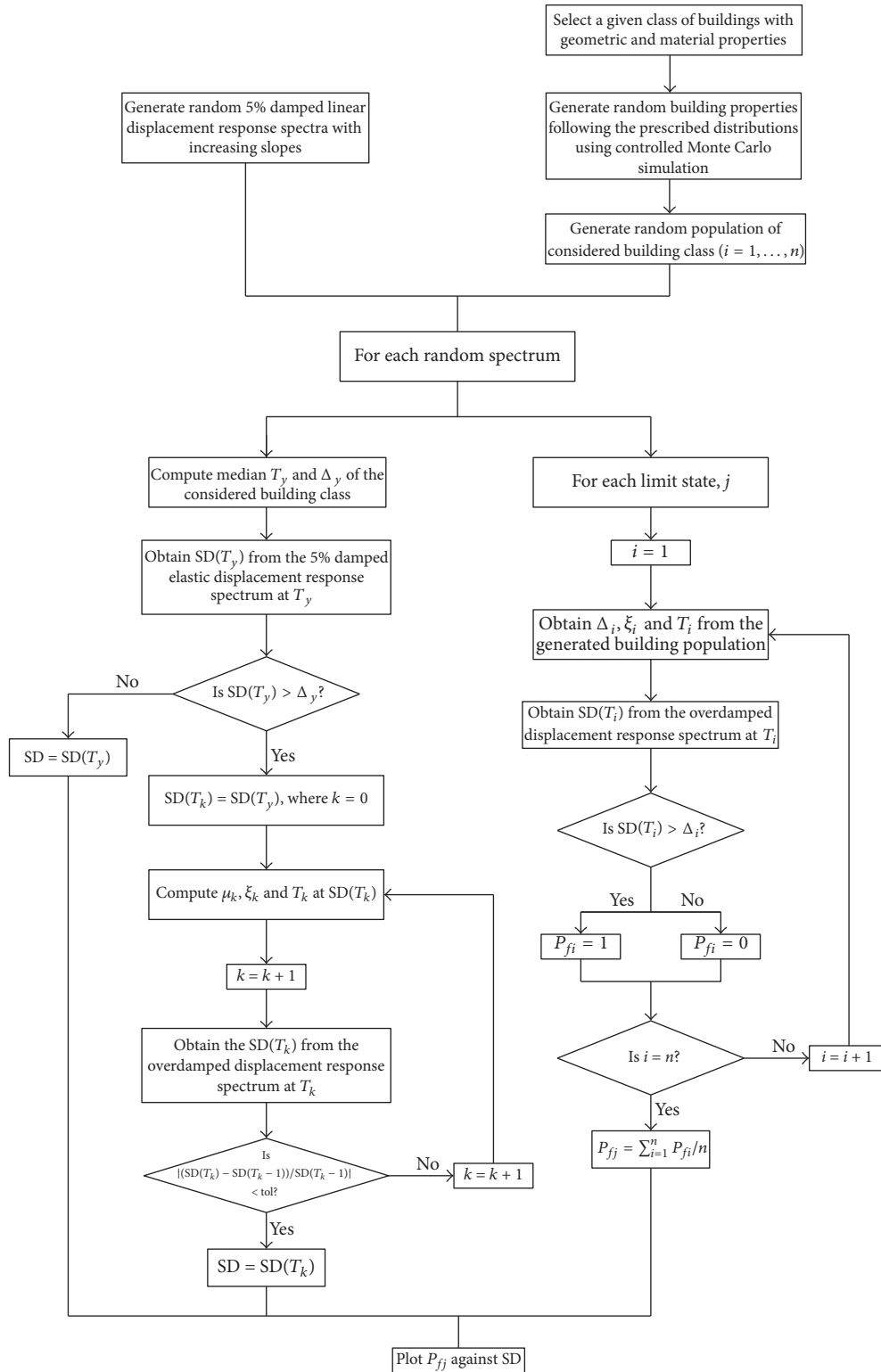
For loss estimation on regional scale, the uncertainties and variabilities in structural characteristics, geometrical and material uncertainties, can be obtained through on site survey of building stock and laboratory investigation of structural materials. The survey can better provide information on

the likelihood of different geometrical features of regional building stock, for example, beam/column depth, width, length, reinforcement details, and number of structure's storeys [16], which affect the seismic response of structural systems. No any hypothesis can give clear and conceptual information on how these local structural uncertainties can be truly represented in the fragility functional form, that is,  $\beta$ , using (5). Thus, a transparent and conceptual methodology is presented to derive analytical fragility functions for regional building stock, taking into account different sources of uncertainties explicitly, without making any constraint.

2.3.1. *Description of the Proposed Methodology.* The DBELA methodology makes use of displacement-based analytical fragility functions where the seismic intensity is defined as a vector-based inelastic displacement demand on the structural system due to its direct correlation with the structural expected performance level for a given seismic demand [8, 20]. The seismic intensity is obtained in an iterative fashion following the damage states of structural systems for a given displacement response spectrum. The random linear 5% displacement response spectra are used to assess the structural performance and derive fragility functions which have the advantage to avoid the problem of being specific to a given regional spectrum and which can be used later for any risk assessment study using scenario earthquakes, uniform hazard spectra, and/or code spectra. To better understand different steps involved in the methodology flow charts are provided for fragility function's derivation for both global and local mechanisms (Figures 6 and 7) while each of the major steps involved is described as follows.

#### (1) Global Mechanism

*Step 1.* The first step of the method is the generation of random population of buildings which represent a given class

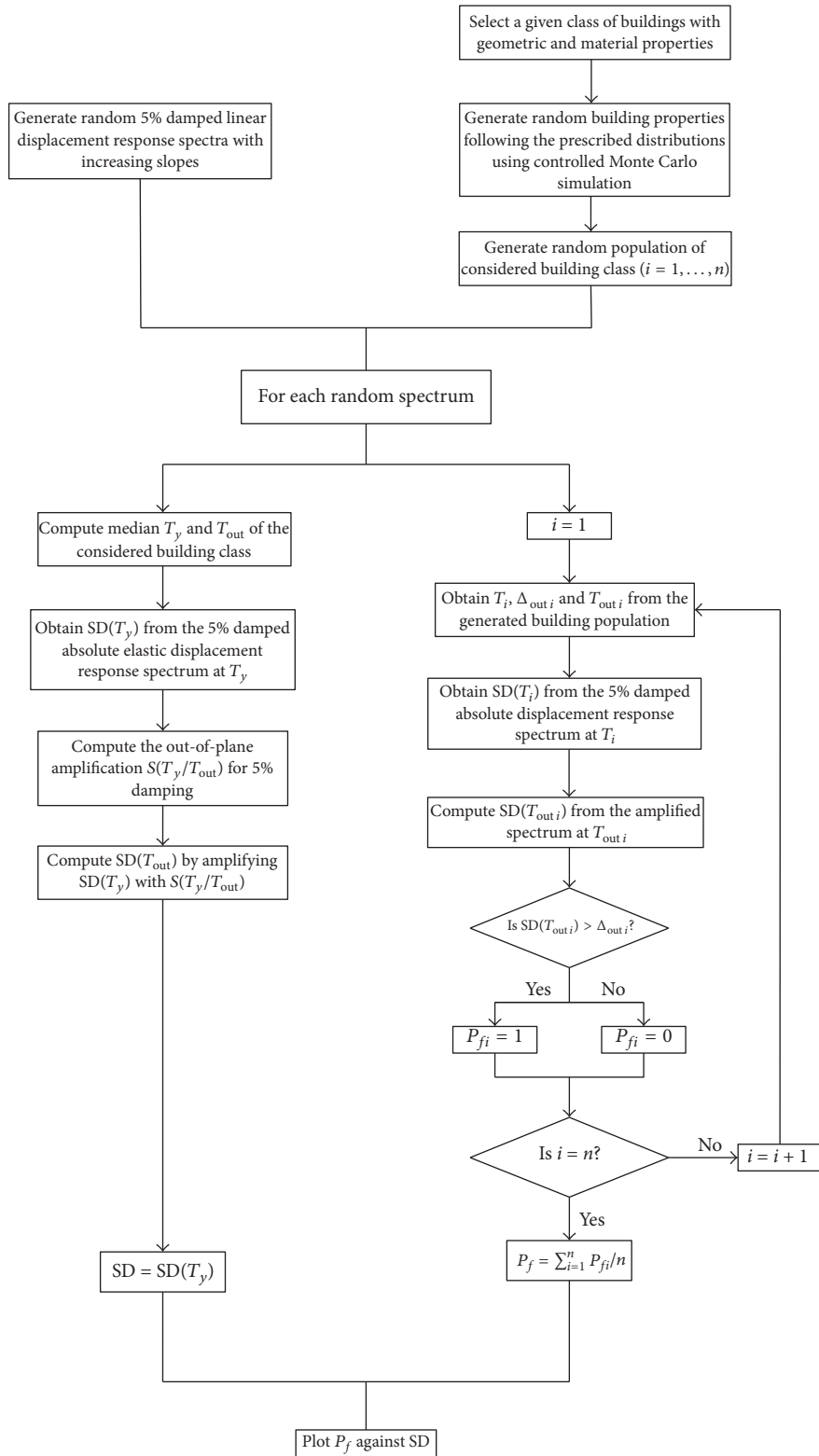


Symbols:

$n$  = number of generated buildings  
 $i$  = random building from generation  
 $j$  = limit state  
 $y$  = yield limit state  
 $k$  = iteration number  
 No = the condition is not satisfied

Yes = the condition is satisfied  
 $\Delta$  = displacement capacity  
 $\xi$  = viscous damping  
 $T$  = vibration period  
 $SD$  = spectral displacement demand  
 $P_f$  = probability of exceedance

FIGURE 6: Flow chart for the derivation of displacement-based analytical fragility functions, global mechanism.



Symbols:

$n$  = number of generated buildings  
 $i$  = random building from generation  
 $y$  = in-plane yield limit state  
 No = the condition is not satisfied  
 Yes = the condition is satisfied  
 $\Delta_{out}$  = out-of-plane displacement capacity

$T$  = in-plane vibration period  
 $T_{out}$  = out-of-plane vibration period  
 SD = spectral displacement demand  
 $S(T_y/T_{out})$  = floor amplification function  
 $P_f$  = probability of exceedance

FIGURE 7: Flow chart for the derivation of displacement-based fragility functions, local mechanism.

of building typologies within a given urban/rural exposure. Controlled Monte Carlo simulation is used to generate thousands of buildings, each with different geometrical and mechanical properties being defined using a complete probabilistic distribution with prescribed mean and coefficient of variation.

*Step 2.* The second step of the method is to define random seismic demand on the generated buildings which is performed through the use of random linear 5% damped displacement response spectrum. Special variability of ground motions is not considered in the fragility derivation which can be considered later in the application of fragility functions for developing damage scenarios for regional risk assessment and loss estimation.

*Step 3.* For each of the spectra, (a) for each limit state the secant vibration period, displacement capacity, and viscous damping of the buildings from the random populations are computed using calibrated structure-specific mathematical models, (b) the displacement demand on each of the buildings is obtained from the overdamped displacement response spectrum at the limit state vibration period of that building which is then compared with the displacement capacity of the building to predict its performance, and (c) the number of buildings having capacity less than the demand is summed and divided by the total number of the generated buildings to obtain the probability of exceedance of a given limit state. Similar hypotheses are used by other support methodologies [8–10] to compute the limit state probability of exceedance.

*Step 4.* For each of the spectra, (a) the median yield vibration period and median yield displacement capacity are obtained from the generated building stock, (b) the spectral displacement demand at the median yield vibration period is obtained from the 5% damped elastic displacement spectrum, (c) this is compared with the median yield displacement capacity, if in case the demand is less than the yield displacement (i.e., this defines the median spectral displacement demand on the structures), and (d) for spectral displacement demand greater than the median yield displacement, the performance point is obtained in an iterative fashion which defines the median spectral displacement demand (seismic intensity).

*Step 5.* The probability of exceedance for each limit state is plotted versus the median displacement demand (seismic intensity) for each of the random spectra. Available cumulative distribution functions are fit to the data and the unknowns of the functions are obtained to completely describe the fragility functions for future applications.

## (2) Local Mechanism

*Step 1.* The first step of the method is the generation of random population of buildings which represent a given class of building typologies within a given urban/rural exposure. Controlled Monte Carlo simulation is used to generate thousands of buildings, each with different geometrical and mechanical properties being defined using a

complete probabilistic distribution with prescribed mean and coefficient of variation.

*Step 2.* The second step of the method is to define random seismic demand on the generated buildings which is performed through the use of random linear 5% damped absolute displacement response spectra [20].

*Step 3.* For each of the absolute spectra, (a) vibration period, displacement capacity, and viscous damping of the buildings from the random populations can be computed for a given local mechanism at the collapse limit state using simplified empirical models, (b) the displacement demand on each of the buildings for local mechanism can be obtained from the 5% damped absolute displacement response spectrum at the global secant vibration period of building which is then amplified with the out-of-plane amplification spectrum/function at the vibration period of the considered local mechanism in order to compare the demand with the displacement capacity to predict its performance, and (c) the number of buildings having capacity less than the demand is summed and divided by the total number of generated buildings in order to obtain the probability of exceedance of local collapse mechanism.

*Step 4.* For each of the absolute spectra, (a) the yield vibration period for global response and median secant vibration period for local response are computed and (b) the spectral displacement demand at the median yield vibration period of the given class is obtained from the 5% damped absolute displacement spectrum which is amplified with the floor amplification function at the local mechanism's secant period in order to obtain the median spectral displacement demand (seismic intensity).

*Step 5.* The probability of exceedance for each limit state is plotted versus the median displacement demand (seismic intensity) for each of the random spectra. Available cumulative distribution functions are fit to the data and the unknowns of the functions are obtained to completely describe the fragility functions for future applications.

## 3. Experimental Test on Case Study Rubble Stone Masonry

*3.1. Model Description and Test Setup.* The DBELA assessment approach needs the basic material properties of masonry and geometric detailing to develop structure-specific mechanical models (in-plane/out-of-plane) for the assessment of global and local capacity of masonry structural systems. The essential material properties, compressive strength, elastic moduli, tensile strength, and so forth, of considered rubble stone masonry cannot be obtained reliably at the section level due to the difficulties in performing tests on masonry prism, reproducing the true replica of the field condition and huge scatter in the observed behavior, which is due to the fact that when stone-to-stone contact is found during the compression tests, very huge value of compressive strength is achieved which gets minimal value

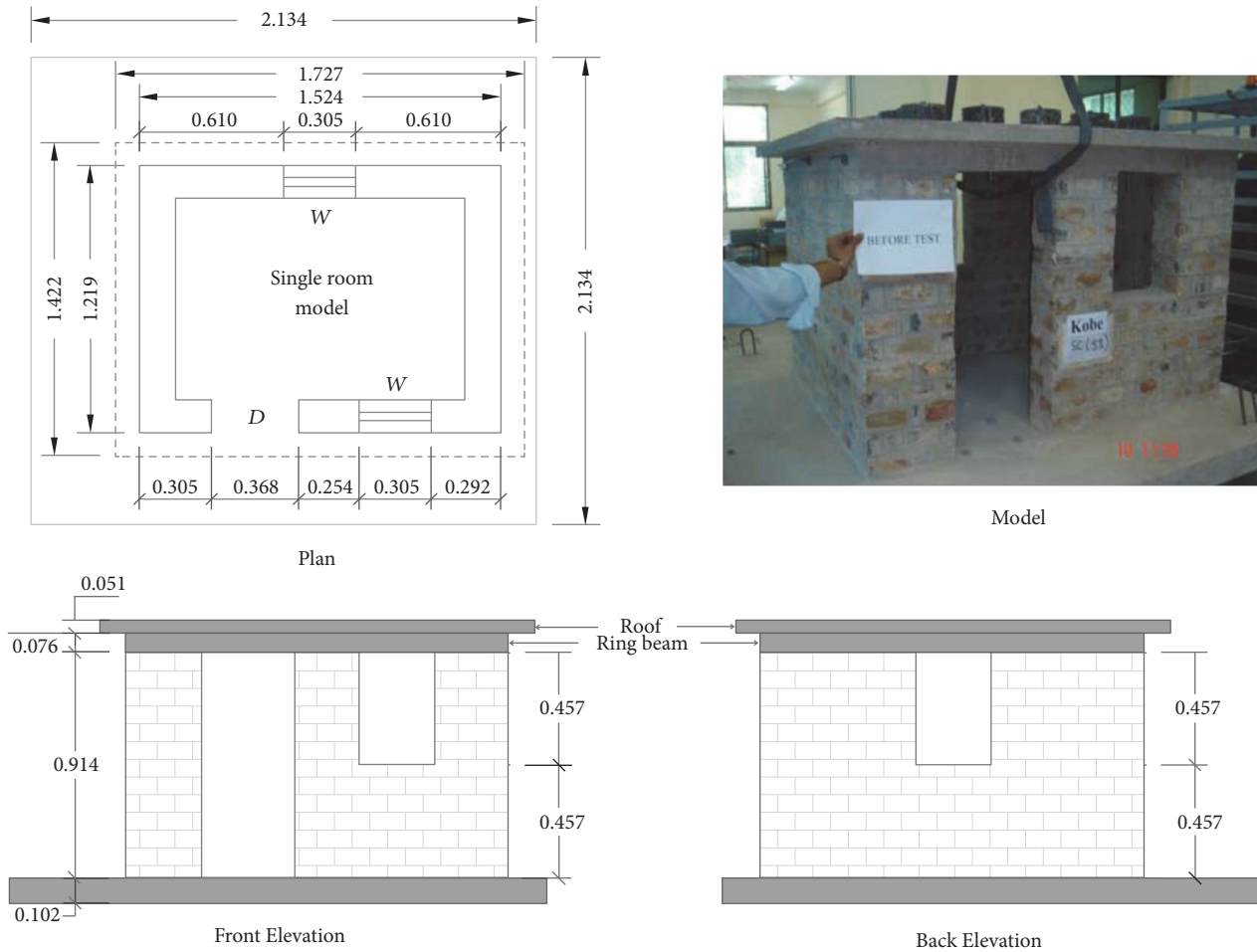


FIGURE 8: Details of the stone masonry structural model tested on shake table, plan view, elevation and actual model.

when stone-to-void possibility is found. Huge uncertainties in the material properties at the section level make the global response less reliable to be achieved. Also, the material properties at section level cannot directly provide guidance on the performance levels, damage scale, and predominant seismic response mechanism of a building. Thus, a full reduced scaled structural model is tested to obtain the global capacity parameters and develop damage scale in order to develop the DBELA tool for global seismic risk assessment of stone masonry buildings with rc slab in Pakistan.

One-third scaled structural model of single storey and single room is designed for corresponding prototype structure using the similitude principles (Figure 8). A comprehensive detail of the testing program and test results are published elsewhere [26]; the present paper will briefly describe the overview of the test and the main findings important within the scope of the present research work. The model is constructed of half-dressed stone masonry work in cement mortar with rc slab and ring beam which represents most of the existing urban building stock, public and private, in the region. The structural model is fixed to 130 mm thick concrete pad at the bottom which is mounted on the shake table, a single degree of freedom (SDOF) shake table at the Earthquake Engineering Center of University of

Engineering and Technology Peshawar Pakistan, and firmly secured using bolts. The structural model is tested in the weaker direction using natural accelerogram, Kobe 1995, and incremental excitations with linear scaling until the complete collapse of structural model. The model is instrumented with accelerometers and displacement transducers at the base of the model and top of the roof: two accelerometers at the base and one on the roof, two displacement transducers at the base, and two on the roof right above the walls.

**3.2. Observed Response of the Structural Model.** The structural model is subjected to 5% scaled Kobe record with linear amplitude scaling until the total collapse of structural model. The model is inspected for the observed damage after every run. The floor acceleration and displacements, on each in-plane wall and at the base of the model, are recorded and processed. The floor acceleration is normalized by the seismic mass of the structural model in order to obtain the base shear for the corresponding equivalent SDOF system. Also, the average floor displacement demand is obtained which is corrected with the base displacement demand in order to obtain the relative displacement demand on the system, which is normalized by the model height to compute the corresponding drift demand on the system. The observed



FIGURE 9: Observed damage states of tested structural model, from (a) to (d): DS1, DS2, DS3, and DS4.

TABLE 1: Capacity parameters and damage states of the corresponding prototype system.

Damage level	Equivalent base shear (m/sec <sup>2</sup> )	Drift demand (%)	Damage description
Minor (DS1)	1.67	0.05	Separation of reinforced concrete slab and ring beams from walls
Moderate (DS2)	3.92	0.48	Crack initiation in the masonry in-plane walls and around the openings
Major (DS3)	5.00	1.49	Widening of cracks and falling of stones from the out-of-plane walls
Collapse (DS4)	1.47	2.65	Complete collapse of the structural model

physical damage states of tested structural model are shown (Figure 9) at different run of input excitations and the capacity parameters, for the corresponding prototype buildings, along with the description of observed damage at different performance levels which are provided in Table 1.

#### 4. Derivation of Mechanical Models for Stone Masonry Buildings

**4.1. Characteristics of the Case Study Buildings.** Stone masonry buildings are practiced abundantly in the northern areas, urban and rural, of Pakistan due to large local availability of stone material and low cost of labor in construction. Stone masonry with earthen floor, wooden/steel truss with GI sheet, and/or rc floor are the common residential building construction practice for single storey in rural areas and up to three storeys with rc floors in urban areas. Stone masonry in cement mortar contributes 50% in overall to the total building stock in the recent earthquake affected areas (<http://www.erra.pk/>). The most prevailing building dimensions range from 8 m × 5 m to 15 m × 5 m with typical wall density, with the ratio of the cross-sectional area of the in-plane walls to the total floor area, ranging from 10% to 15% [27]. The buildings have 300 to 500 mm thick load bearing walls with rubble stone masonry, having 130 to 150 mm thick rammed earthen roof, wooden/steel truss GI sheet, or rc slab and interstorey height of 2.0 m to 3.0 m. The buildings are provided with a ring beam right above the walls, approximately 150 to 230 mm deep, and width equal to the wall thickness. The building rests on shallow strip type footing, with stepped stone work overlain compacted earth surface. The load bearing walls are perforated by doors, with typical dimensions of 1.00 m × 2.13 m, and windows, with typical dimensions of 1.00 m × 1.22 m to 1.83 m × 1.22 m, thus providing 70% effective cross-sectional area of walls for carrying both gravity and lateral loads. The primary seismic resistance mechanism for

stone masonry buildings with rc slab, as observed in the dynamic test, is in-plane global mechanism with diagonal shear cracks followed by bed-joint sliding in the short piers. However, the ultimate mechanism, collapse of the building, is governed by the combined in-plane and out-of-plane failure of masonry walls (Figure 9). Stone masonry buildings, which do not respect the minimum requirements to ensure in-plane integrity of walls, respond in local out-of-plane failure of portion of walls or complete walls and can be followed by the complete collapse of building [18].

#### 4.2. Prototype 2D Cases Study Structural Models

**4.2.1. Design of Prototype Buildings.** Due to unavailability of basic material properties for stone masonry, and the reasons mentioned earlier, it is not straightforward to develop numerical tools for future applications for global analysis. Thus, the present study considered the simplified equivalent frame approach, SD-SAM [11, 12] earlier proposed and employed in the regional seismic loss estimation study, for nonlinear static and dynamic time history analysis (global analysis) of masonry buildings, and developed herein for case study buildings of Pakistan. The method uses the idea of modeling masonry spandrels and piers as equivalent beam-column elements with bending and shear deformation with infinitely stiff joint element offsets at the ends of the pier and spandrel elements (Figure 10), as proposed earlier [28]. The effective deformable length of pier is approximately obtained taking the intersection of the element with a line making a 30-degree angle with the corners of the openings. Each of the elements is provided with lumped nonlinear hinge having an appropriate force-displacement response to simulate the lateral response of masonry wall, depending on the elements ultimate mechanism. The properties of hinge, force-displacement response, are obtained from the available empirical rules and/or experimental tests on masonry material and walls [10, 11]. The present study performed the

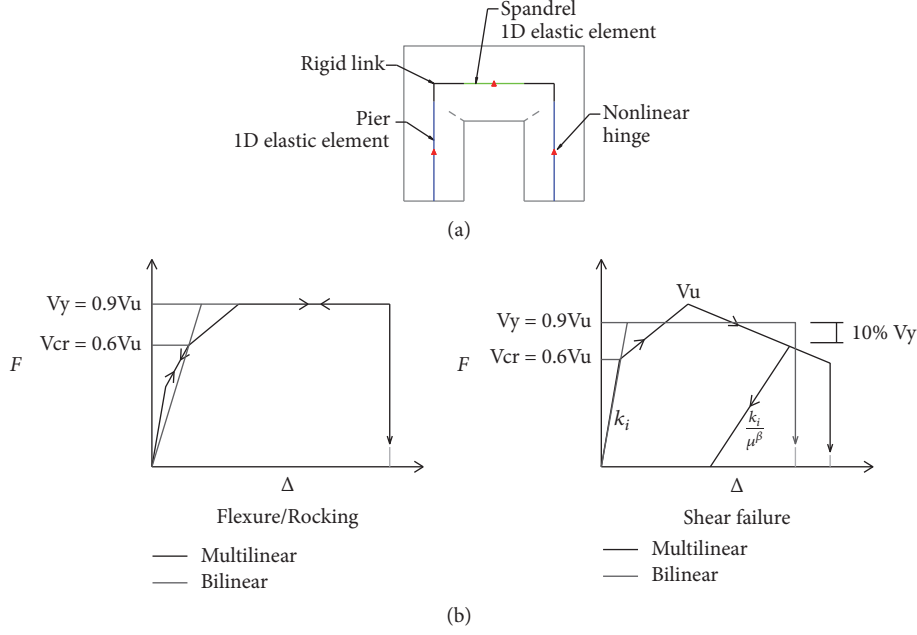


FIGURE 10: Equivalent frame idealization of masonry wall (a) and nonlinear force-displacement response of frame elements (b) [11, 12].

calibration of the SD-SAM approach for stone masonry with rc slab (global mechanism) as follows.

In the first step, a generic prototype of equivalent frame is generated for the tested structural model and designed, respecting the geometric detailing and loading conditions, with the available empirical shear strength models for masonry walls, previously developed [17, 29] and employed for brick masonry buildings [11, 12]. The beam-column element used for masonry idealization is completely defined by masonry Young modulus, shear modulus, wall sectional area, and the wall moment of inertia. The hinge is assigned with nonlinear force-displacement constitutive law to simulate the lateral capacity of the frame elements, that is, pier and spandrel. The total lateral displacement capacity of the element at any instant is the summation of the bending, which is contributed by the elastic flexure bending of beam-column element, and shear, which is contributed by the lateral translation of hinge, deformation developed in the element [11, 12]. The possible failure mechanisms considered for masonry piers are flexure mechanism and shear failure using the following strength models:

$$V_f = \frac{pD^2t}{2H_p\psi} \left( 1 - \frac{p}{0.85f_u} \right), \quad (6)$$

$$V_d = \frac{f_{tu}Dt}{b} \left( 1 + \frac{p}{f_{tu}} \right)^{1/2}, \quad (7)$$

$$V_s = \frac{Dt(1.5c + \mu p)}{(1 + 3(cH_p\psi/pD))}, \quad (8)$$

where  $V_f$  represents the ultimate strength for flexure failure mode;  $D$  and  $t$  represent the length and thickness of the

wall;  $p = P/(D \cdot t)$  represents the mean vertical stress due to axial load  $P$ ;  $H_p$  represents the total height of the pier;  $\psi$  is 1.0 for a cantilever pier and 0.5 for a pier fixed-fixed boundary conditions;  $f_u$  represents the compressive strength of masonry;  $V_d$  represents the ultimate strength for diagonal shear failure mode;  $f_{tu}$  represents the diagonal tensile strength of masonry;  $b = 1$  for  $H_p/D \leq 1$ ,  $b = H_p/D$  for  $1 < H_p/D < 1.5$ , and  $b = 1.5$  for  $1.5 \leq H_p/D$ ;  $V_s$  represents the ultimate strength for sliding shear failure;  $\mu$ , assumed as 0.4, and  $c$ , taken as  $0.4f_{tu}$ , represent the coefficient of friction and cohesion of masonry as global strength parameters. The strength computed is reduced by 10% in order to be conservative and respect the energy balance criterion [17, 29] which is observed to predict well the equivalent strength of masonry buildings [10].

In the second step, the tensile strength,  $f_{tu}$ , of masonry is selected, fixing the compressive strength to 4 Mpa, to achieve the equivalent yield strength,  $4.50 \text{ m/sec}^2$ , of the corresponding prototype systems. In the next step, the Young modulus,  $E$ , and shear modulus,  $G = 0.3E$ , are selected to achieve the corresponding drift limits at yield and the 1st modal period of structural system. The assumption made herein for compressive strength and shear modulus is typical for such type of masonry system [30]. The equivalent frame is designed, using SD-SAM, employed in OpenSees [31] with masonry walls represented by equivalent elastic beam-column element which is provided with zero-length element, hinge (Figure 10), with hysteretic material to define the nonlinearity, force-displacement constitutive law, of masonry walls with bilinear rule. The structural model is analyzed to obtain the capacity curve with displacement controlled pushover analysis which is compared with the observed capacity of the tested prototype building and is

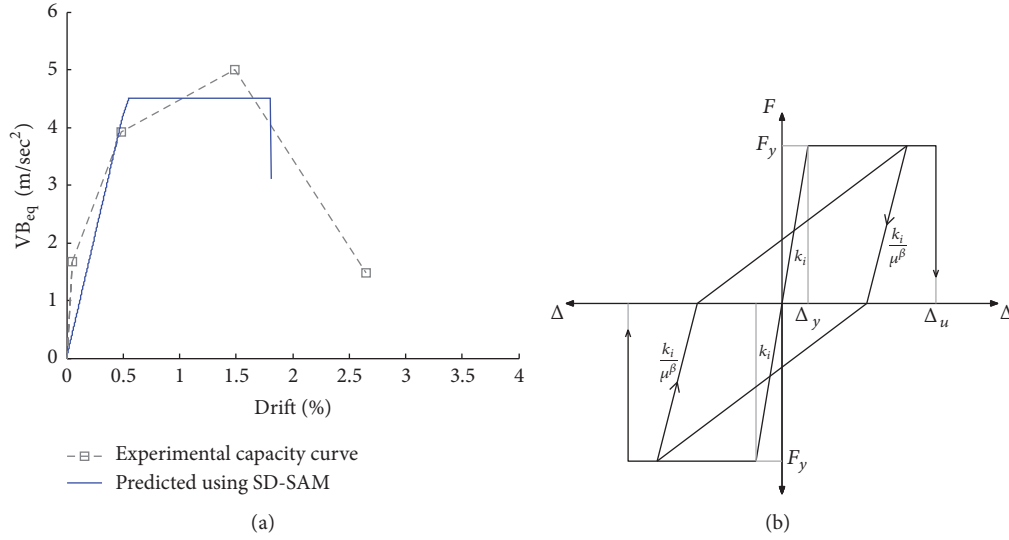


FIGURE 11: Comparison of the observed and predicted lateral capacity of tested stone masonry building (a) and phenomenological nonlinear hysteretic response of frame element (b).

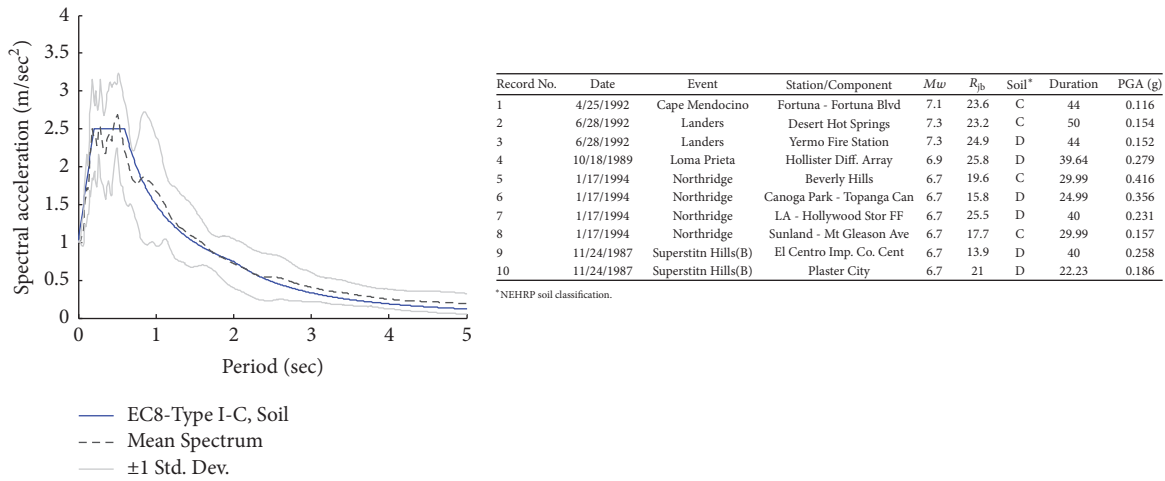


FIGURE 12: Mean of the acceleration spectra considered for NLTHA and details of the accelerograms used in the study.

found reasonable in terms of yield stiffness and equivalent bilinearised strength, respecting the energy balance criterion [17, 29] (Figure 11). The ultimate displacement capacity, and the corresponding drift limit of building, of the nonlinear hinge is obtained, when the lateral strength obtained from experimental results (see Table 1) drops by 20%.

#### 4.3. Dynamic Analysis of Case Study Structural Models.

The present study considered 125-case study 2D two-storey structural models, selected with different floor area, wall density, and material properties, in order to take into account the regional geometric and material uncertainties explicitly in the capacity evaluation, designed with the material sectional properties obtained in the previous section. The frame elements are assigned with bilinear Takeda type rule [32] (Figure 11) with Emori and Schnobrich [33] type of unloading stiffness and beta equal to 0.6 as proposed earlier [11, 12]

for masonry buildings. The case study structural models are analyzed dynamically using nonlinear time history analysis (NLTHA) with 10 natural accelerograms extracted from the PEER NGA database for soft soil condition with the mean spectrum compatible to EC8 Type I-C-soil spectrum [34] (Figure 12).

The accelerograms are linearly scaled in order to observe the postyield response of the models which is used then to derive static SDOF system, mechanical models, for the considered building typology in order to retrieve the dynamic characteristics of buildings in preyield and postyield limit states and develop empirical models for limit state's vibration period and displacement capacity. It is worth mentioning that the numerical tool used herein is simplified but respecting the fundamental structure's parameters, that is, stiffness, strength, ductility, and energy dissipation, sufficient to demonstrate the global structural performance for seismic

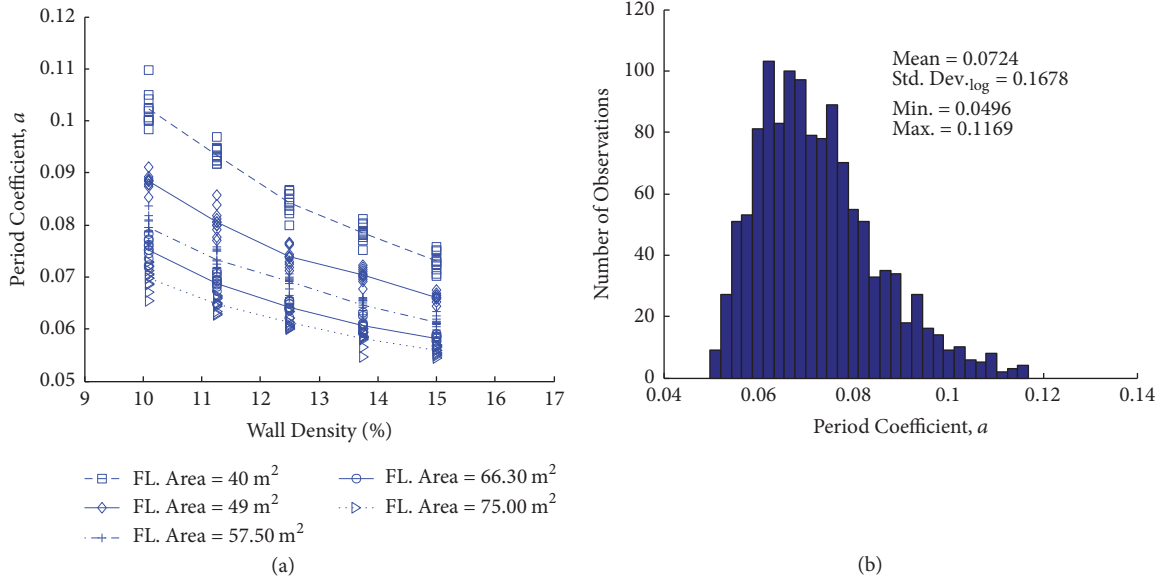


FIGURE 13: Period coefficient for different wall density and floor areas (a) and for all cases study structural models (b).

loading. Also, the findings of numerical tool are used for the risk assessment of buildings on regional scale where, apart from large case study structural models, the regional structural geometric and mechanical properties are approximately defined which makes the present tool as a reasonable choice for structural analysis.

The scope of the dynamic analysis is to compute the equivalent base shear and equivalent displacement demand at different limit states of masonry walls on the ground floor, since ground storey mechanism is governed for the considered typology, using the proposed SDOF derivation [11, 12], and computes the secant vibration period of considered building stock:

$$\begin{aligned}
 T_y &= 2\pi \sqrt{\frac{\Delta_{eq}}{VB_{eq}}}, \\
 \Delta_{eq} &= \frac{\sum_{i=1}^n m_i \Delta_i^2}{\sum_{i=1}^n m_i \Delta_i}, \\
 VB_{eq} &= \frac{VB}{M_{eq}}, \\
 M_{eq} &= \sum_{i=1}^n \frac{m_i \Delta_i}{\Delta_{eq}},
 \end{aligned} \tag{9}$$

where  $\Delta_{eq}$  represents the equivalent displacement of structural system;  $VB_{eq}$  represents the equivalent base shear for the corresponding SDOF system;  $m_i$  and  $\Delta_i$  represent the floor mass and floor displacement demand, respectively;  $VB$  represents the base shear demand;  $M_{eq}$  represents the equivalent mass of the structural system. The vibration periods obtained for the considered case study buildings are

used to develop the period model (10) for future applications in regional risk assessment using the DBELA methodology.

$$T_y = a \cdot \exp(\pm \varepsilon \beta) H_T^b, \tag{10}$$

where  $H_T$  represents the total height of the building;  $a$  and  $b$  are the coefficients obtained through regression analysis of the data;  $\beta$  represents the regional variability in the period computation due to geometric and material uncertainties and record-to-record variability. The period coefficient with  $b$  set to 0.75 obtained for 25 structural models with record-to-record variability and mean material properties is shown in Figure 13. Also, the period coefficients obtained for all the 125 structural models are obtained.

It is observed that for a given structural system the period reduces with increasing wall density. Similar trend of vibration period is also observed for increasing floor area. The period coefficient obtained for all the cases study structural models, 1250 cases, takes into account the geometric (floor area and wall density) and material uncertainties besides the variability introduced by earthquake excitations. Existing and conventional code-based formulae considered  $\beta$  in (10) equal to zero which gives the mean estimate of vibration period. However, the height dependent only formulae will neglect the floor area and wall density effect in the buildings period estimation for regional risk assessment.

Additionally, the structural models are analyzed to develop the limit states displacement capacity model (2) for different performance levels of the structures. In the first step, static analyses are performed for all 125 structural models to obtain the crack and yield limit state drift values using the shear strength, obtained using calibrated strength models ((6)~(8)), and stiffness at cracking and yielding, respectively, with 50% cracked sectional properties and 70%

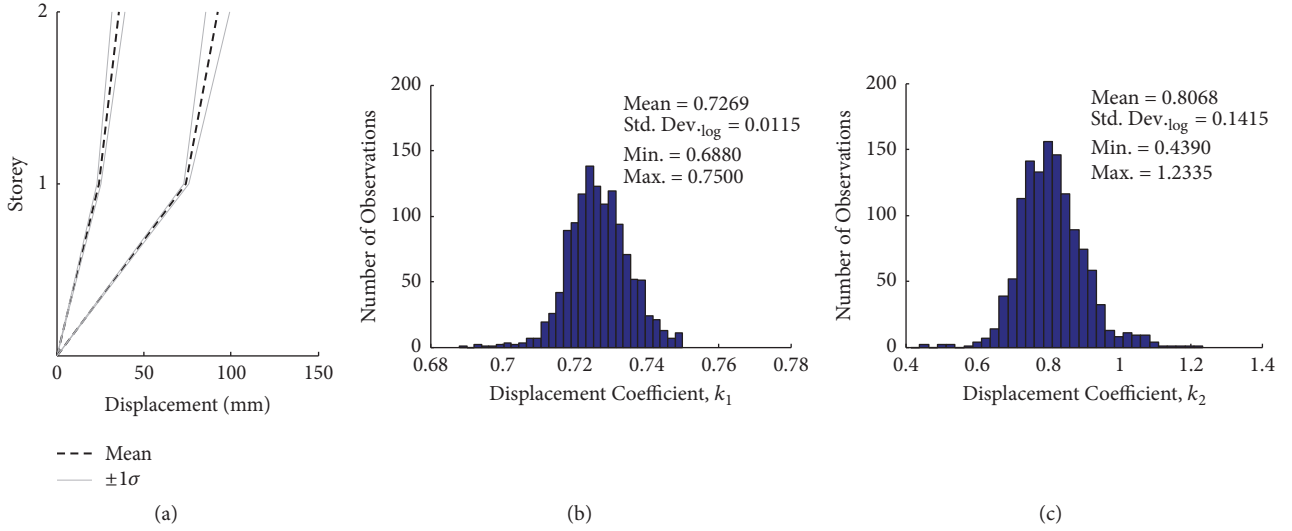


FIGURE 14: Limit states displacement profiles of a two-storey structural model (a); displacement coefficients at yielding (b) and near collapse limit state (c).

effective shear area, of masonry walls, respectively. The crack force is conservatively considered being 60% and the yield force being 90% of the maximum computed force [17, 29]. A mean value of 0.24% is obtained for crack limit state with logarithmic standard deviation of 0.16, min 0.16%, and max 0.33%. Similarly, for yield limit states, a mean value of 0.35% is obtained with logarithmic standard deviation of 0.15, min 0.24%, and max 0.50%. These values are less than the experimental results due to the fact that the tested model has wall density of 12.84%. The computed drift values take into account the geometric and material variability for rather broader range of wall density and floor area. Using the limit states ductility obtained in the experiment, which is reduced by 20% in order to be conservative, a mean value of 0.768% and 1.016% is obtained for major and collapse limit states, respectively, which nevertheless need to be updated once more experimental data on rubble masonry are made available. Also the structural models are analyzed to obtain the displacement coefficients,  $k_1$  and  $k_2$ , at the preyield and postyield limit states, which are used herein to take into account the record-to-record variability in the displacement capacity evaluation of the SDOF systems and make the model (2) treat different uncertainties, that is, geometric, material, and record-to-record, explicitly in the capacity evaluation. Each of the structural models is investigated to obtain the floor displacements and the corresponding base shear at the yielding of the ground floor walls for each NLTHA of a given structural model which is used to obtain the effective height of the SDOF system, following the recommendation of Priestley et al. [20]:

$$H_e = \frac{\sum_{i=1}^n m_i \Delta_i H_i}{\sum_{i=1}^n m_i \Delta_i}, \quad (11)$$

where  $H_e$  represents the effective height of the SDOF system, which corresponds to the center of seismic force;  $H_i$

represents the floor height. The displacement coefficient at yield limit state ( $k_1$ ) is obtained then by dividing  $H_e$  over the total height of the structural model,  $H_T$ . A mean value of 0.7269 is obtained with logarithmic standard deviation of 0.0115, and minimum value of 0.6880 and a maximum value of 0.7500 are obtained. Since the considered building typology has soft-storey ultimate mechanism with demand mostly concentrated at the ground storey level, thus the above hypotheses cannot be directly used to obtain displacement coefficient at postyield limit states ( $k_2$ ); hence the following procedure is used. NLTHA of all the structural models is performed, through linear scaling of accelerograms, to exceed the near collapse limit state of walls at the ground floor. The data is analyzed to obtain the equivalent displacement demand when the target ductility of 3 is exceeded at the ground floor level, which corresponds to the collapse limit state of structural model. In the next step (2) is used, inverting and rearranging, to obtain  $k_2$ :

$$k_2 = \frac{\Delta_{LS} - \Delta_y}{\theta_p h_s}, \quad (12)$$

where  $\Delta_{LS}$  represents the equivalent displacement at the near collapse limit state of ground floor walls;  $\Delta_y$  represents the equivalent displacement at the yielding limit state of ground floor walls;  $\theta_p$  represents the plastic drift demand on the ground floor walls, obtained by dividing the ground floor displacement demand over the ground floor height;  $h_s$  represents the ground floor height. A mean value of 0.8068 is obtained with logarithmic standard deviation of 0.1415, and minimum value of 0.439 and a maximum value of 1.2335 are obtained. Figure 14 shows the limit state displacement profiles of a two-storey structural model, 40 m<sup>2</sup> floor area and 10% wall density, for 10 accelerograms and the displacement coefficients,  $k_1$  and  $k_2$ , for all the 125-case study structural models.

TABLE 2: Parameters used in the random generation of stone masonry buildings of Pakistan.

Parameter	Mean value	C.O.V. (%)	Lower bound	Upper bound	Probability distribution type
$H_T$ (m)	3.00	30.00	2.50	3.50	Truncated lognormal
$h_s$ (m)	2.50	30.00	2.00	3.00	Truncated lognormal
Drift (%)					
LS1	0.240	16.10	0.16	0.33	Truncated lognormal
LS2	0.350	15.08	0.24	0.50	Truncated lognormal
LS3	0.768	30.00	0.53	1.10	Truncated lognormal
LS4	1.016	30.00	0.70	1.45	Truncated lognormal
$k_1$	0.727	01.15	0.69	0.75	Truncated lognormal
$k_2$	0.807	14.22	0.44	1.23	Truncated lognormal
$c$ (%)	0.400	20.00	0.28	0.50	Truncated lognormal
$t$ (mm)	400	20.00	300	500	Truncated lognormal
$\Psi$	0.8	10.00	0.50	1.00	Truncated lognormal
$\phi$	0.75	16.00	0.60	0.90	Truncated lognormal

## 5. Derivation of Analytical Fragility Functions

The proposed methodology is used herein to derive analytical fragility functions for urban rubble stone masonry buildings of Pakistan. Application of the methodology is also carried out for brick masonry urban building stock of NE Pakistan [35]. However application on the derivation of fragility functions for rural stone masonry building stock is shown also herein which exhibits mainly out-of-plane local failure of walls. The following section will briefly describe the global and local fragility functions derivation.

### 5.1. Displacement-Based Analytical Fragility Functions for Stone Masonry Buildings of Pakistan

**5.1.1. Global Mechanism.** Controlled Monte Carlo simulation is used to generate random building stock with different geometric and mechanical properties considering lognormal probability density function (pdf) for all the parameters involved in the capacity evaluation (Table 2). The lognormal pdf is considered for simplicity reasons and to be conservative in structural capacity estimation. The damage scale is selected as observed in the experimental test, Table 1. The displacement capacity and secant vibration period are obtained at each limit state, using the calibrated empirical models, that is, (1)~(2). Due to unavailability of material viscous damping, the damping model proposed for other masonry types [11] is considered herein.

**5.1.2. Local Mechanism.** Stone masonry buildings with rc slab did not show prominent out-of-plane failure in experimental test and during 2005 Kashmir earthquake but were damaged mainly due to diagonal cracks in wall, cracking around the corners of opening, horizontal cracks at the roof level, and complete collapse of buildings [36]. However stone masonry buildings with wooden/steel truss and GI sheet suffered major local out-of-plane failure of portion of walls or complete walls. Collapse of gables, corner wedge type of wall

failure, and complete overturning of exterior walls were the common out-of-plane failures [36]. Delamination of exterior wythe of walls was observed in few cases but this never caused serious problem to the overall stability of buildings [36]. Two-way vertical bending [22] of out-of-plane walls is not observed; thus the mechanical model (4) derived for the free standing out-of-plane rocking walls is considered only. The limit state displacement capacity of out-of-plane mechanical model is adopted from Doherty et al. [21]; however the ultimate displacement capacity of wall is considered with reduction factor ( $\psi$ ) in order to be conservative in capacity evaluation [8, 24, 37]. Following experimental investigation on the out-of-plane testing of several dry stone masonry walls at the University of Pavia [37], a reduction factor ( $\phi$ ) is proposed for the collapse multiplier obtained using rigid block behavior of out-of-plane responding walls. Different parameters involved in the in-plane/out-of-plane mechanical models are defined to generate regional building stock, both urban and rural building stock. Table 1 shows the values assigned to each parameter and the assumed distribution functions to generate random numbers using controlled Monte Carlo simulation.

Once the regional building stock is generated and the limit state capacities are evaluated in a probabilistic fashion, random linear 5% damped displacement response spectra are generated. The global in-plane assessment is performed through overdamping the linear spectrum, using overdamping factor [38] and the system viscous damping, for each limit state.

$$\eta = \sqrt{\frac{7}{2 + \xi_{eq}}}, \quad (13)$$

$$\xi_{eq} = 5 + 32 \left( \frac{\mu - 1}{\pi\mu} \right),$$

where  $\eta$  represents the overdamping factor;  $\xi_{eq}$  represents the masonry viscous damping [11]. The local out-of-plane

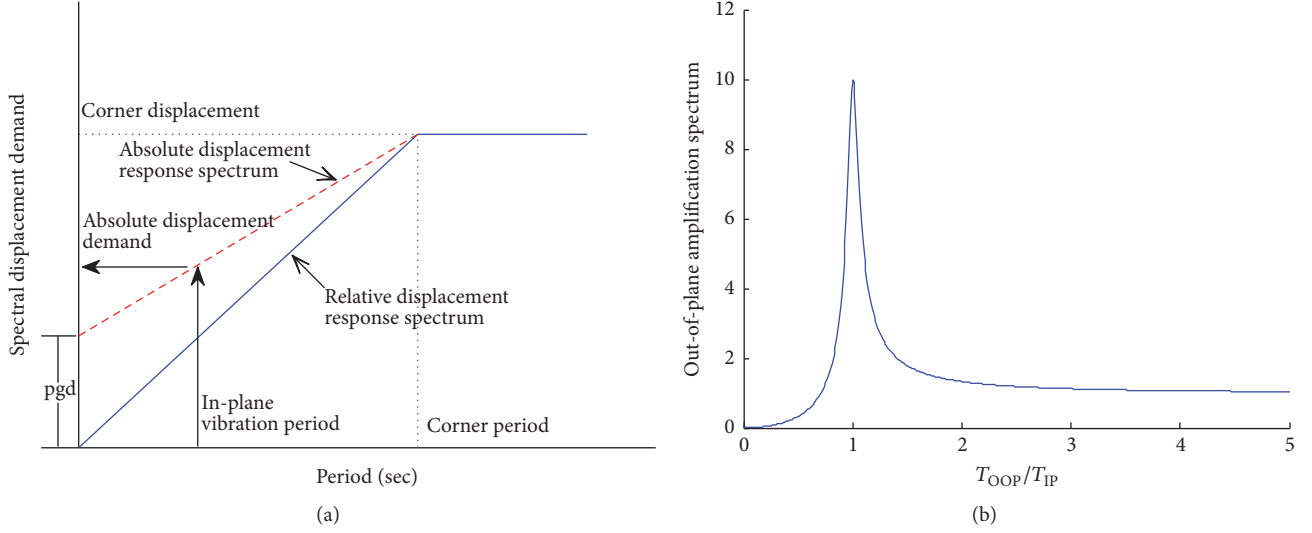


FIGURE 15: Definition of seismic demand on the out-of-plane walls: absolute spectrum (a) and out-of-plane amplification spectrum (b).

assessment is performed using absolute displacement spectrum along with the out-of-plane amplification spectrum [20]:

$$S_{\text{OOP}} = \frac{1}{\sqrt{(1 - (T_{\text{IP}}/T_{\text{OOP}})^2)^2 + 4\xi_{\text{OOP}}^2 (T_{\text{IP}}/T_{\text{OOP}})^2}}, \quad (14)$$

where  $T_{\text{OOP}}$  represents the period of out-of-plane wall;  $T_{\text{IP}}$  represents the in-plane secant period of building;  $\xi_{\text{OOP}}$  represents the viscous damping of out-of-plane wall, recommended as 5% [22]. The relative and absolute displacement spectrum and out-of-plane amplification spectrum used for in-plane and out-of-plane assessment are depicted in Figure 15.

The absolute spectrum is anchored at the peak ground displacement (pgd) and linearly increased to maximum displacement demand at corner period following the recommendation of Priestley et al. [20]. Different recommendations can be used to compute the pgd, corner period, and corner displacement for worldwide regions [34, 39–44]. However, for the out-of-plane fragility function's derivation the pgd and the slope of absolute displacement spectrum are randomly selected using Monte Carlo simulation while increasing the spectrum linearly, against the period, without any bound for convenience and to be conservative. Nevertheless, an appropriate displacement spectrum, both relative and absolute, has to be used for developing damage scenarios for intended loss estimation study. The procedure outlined in Figures 6 and 7 is used to derive the fragility functions for two-storey stone masonry building stock of Pakistan for both in-plane global mechanism and local out-of-plane mechanism as shown in Figure 16.

**5.2. Structure-Independent Fragility Functions.** It is mentioned that fragility functions are needed to be developed in terms of structure-dependent vector-based intensity measures (inelastic displacement demand in the present case

which is well correlated with the structural expected performance) and in order to avoid the problem of being specific to given assumed spectral shape and region, for example, code spectra and UHS for a given site which are not conceptual [45, 46] when losses are required for scenario earthquakes. However, for decision-making it will be of utmost importance to present the earthquake impacts as a function of convenient and easy to perceive structure-independent parameters, yet respecting the fundamentals of strong ground motions (frequency content, ground motion uncertainties, site soil characteristics, and correct spectral shape) and structures (strength, stiffness, ductility, and energy dissipation). Also, a prompt assessment for quick response and emergency planning soon after the earthquake could be much facilitated using fragility functions which need fewer parameters to estimate the socioeconomic impacts of an earthquake event. The simplest and readily available parameters to compute earthquake losses at a given site for an earthquake event are the magnitude of earthquake, source-to-site distance, site soil condition, site building typology, building content, and occupancy.

Thus fragility functions are derived for the MDR of stone masonry buildings of Pakistan expected at a site for a given scenario earthquake. Different possibilities of source-to-site distance and magnitude are selected, considering soft soil condition (type D of NEHRP soil classification as recommended for Pakistan [47]). The empirical ground motion prediction equation [44] of PEER NGA project [48] is used to generate ground motions for a given scenario earthquake with due consideration of ground motion uncertainties (both inter- and intraevent), 10,000 simulations for each scenario earthquake. The selected GMPE has the advantage to predict also pgd for scenario earthquakes. Figure 17 reports the structure-independent fragility functions for the considered building typology of Pakistan. The earthquake loss model of Bal et al. [16] is used to compute MDR. For a given site, knowing the MDR, the unit replacement cost of a building,

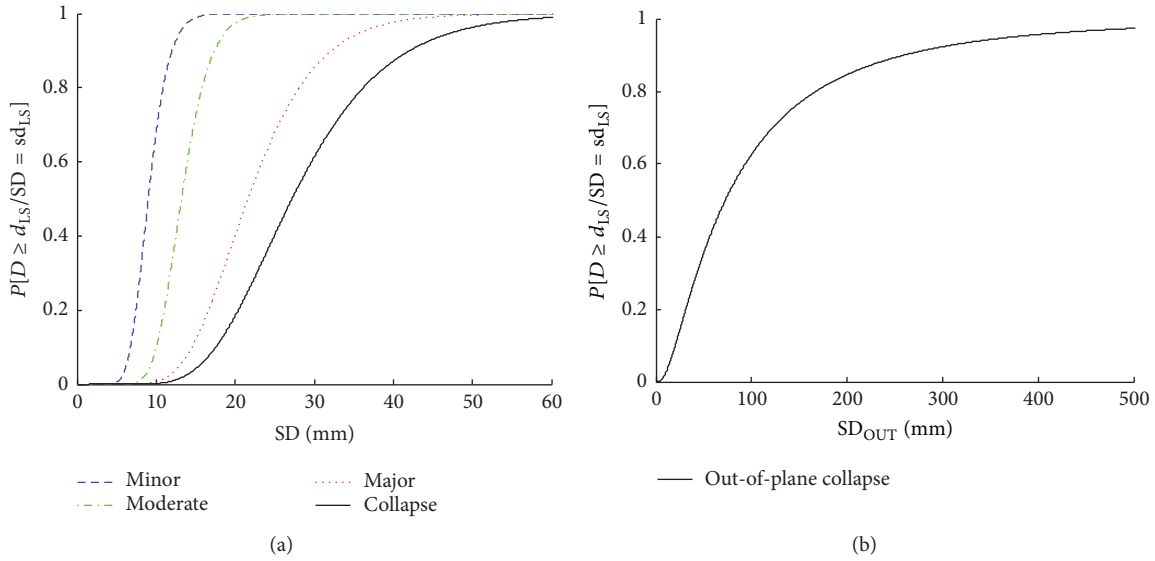


FIGURE 16: Analytical fragility functions for two-storey stone masonry building stock of Pakistan: in-plane global mechanism (a) and out-of-plane local mechanism (b).

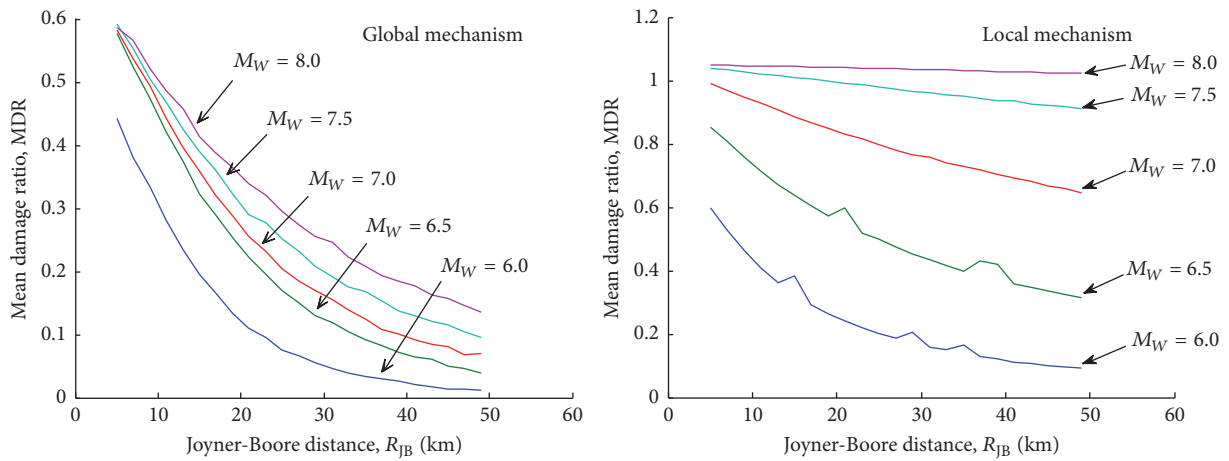


FIGURE 17: Charts for MDR of stone masonry buildings for scenario earthquakes.

and the total number of buildings in a given municipality, the expected economic loss can be easily obtained [11]. Different other loss models are available to compute the expected human casualties in heavily damaged and collapsed buildings [49]. However, fragility functions are derived herein for the trapped people along with their expected level of injuries using site-specific casualty model, derived from the recent 2005 Kashmir Earthquake [50].

As expected from the structural mechanics standpoint, the local out-of-plane mechanism results in relatively higher seismic risk and losses as compared to global in-plane mechanism of structural systems. Depending on the site building characteristics, if buildings are provided with rc slab and ring beams (like the present situation in the earthquake affected areas, <http://www.erra.pk/>, and some urban exposure) only the global mechanism's charts have to be used to compute

the regional seismic risk and losses for a given scenario earthquake, described only by the source-to-site distance and moment magnitude. If the regional buildings do not meet the minimum criterion to ensure the in-plane integrity of structural system and global seismic response mechanism [18], only the out-of-plane mechanism's charts have to be used for assessment. A weighting factor has to be applied to MDR in cases where both in-plane and out-of-plane mechanisms are expected in regions; that is, for a given scenario MDR can be obtained for both mechanisms which will be multiplied by the corresponding percentage of each buildings class (global mechanism/local mechanism).

The expected causality rate is presented in terms of the occupancy in a housing unit and the total number of building stocks in the region. Thus the number of housing units in a region and the likelihood function of occupancy per housing

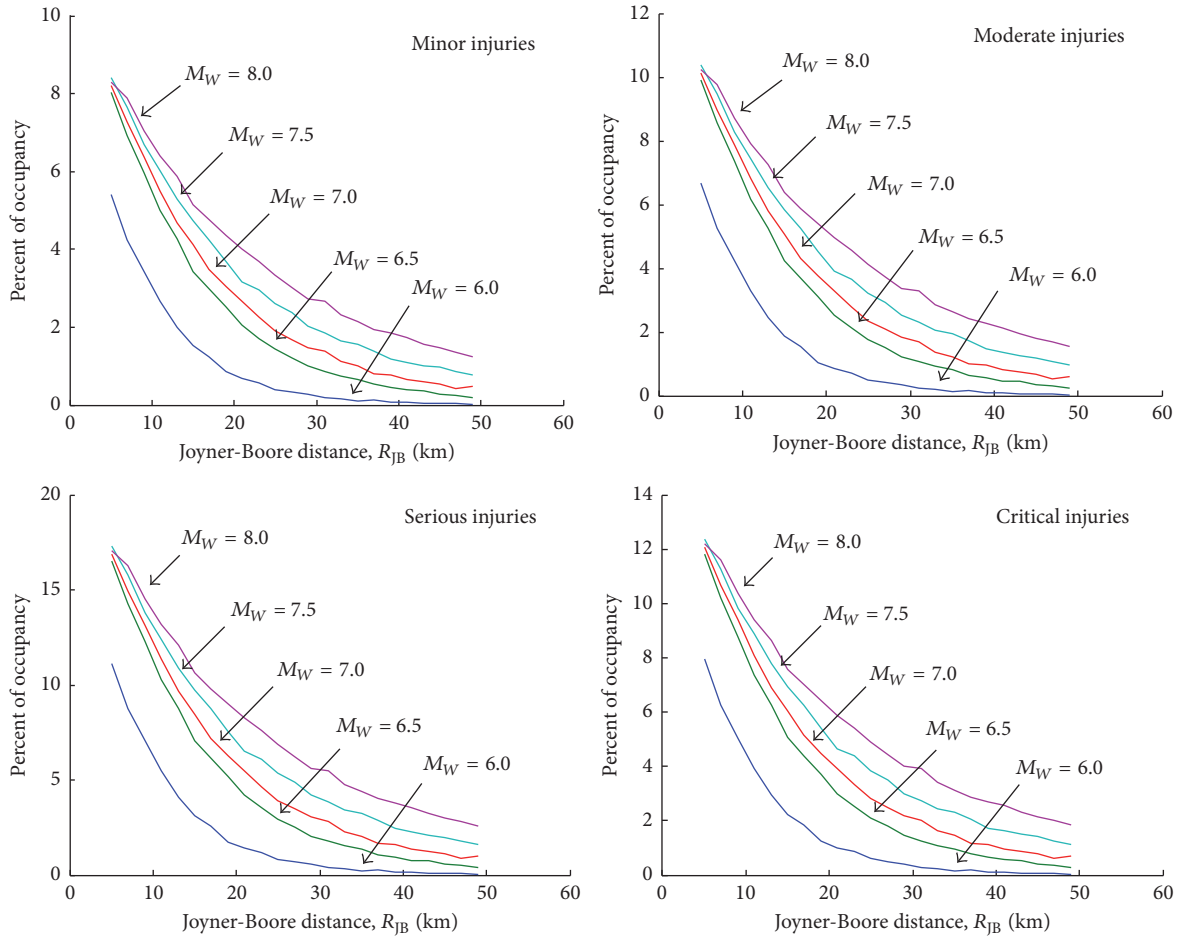


FIGURE 18: Charts for expected casualty rate in collapsed stone masonry buildings for scenario earthquakes, in-plane mechanism.

unit, 7 to 12 for the considered typology [27, 51], have to be multiplied with the number obtained from the casualty rate charts (Figures 18 and 19).

**5.3. Comparison with the Observed Response during 2005 Kashmir Earthquake.** The structure-independent fragility functions are used to assess the seismic risk of stone masonry buildings for a scenario earthquake that recently occurred in the country, that is, 2005 Kashmir Earthquake. The Kashmir earthquake has a moment magnitude of 7.6 that struck most of the northern areas of Pakistan on 8 October 2005 at 08:50 AM local time (<https://earthquake.usgs.gov/earthquakes/eventpage/usp000e12e#executive>). The epicenter of the main earthquake shock was located at Latitude 34.49N and Longitude 73.63E, approximately 19 km north east of Muzaffarabad city of Azad Jammu Kashmir. The earthquake event is the direct results of collision of the Indian plate, moving 40–50 mm/yr northward, with the Eurasian plate. The collision is crust to crust and thus produces large magnitude shallow earthquakes [52]. More than 780,000 buildings were either destroyed or damaged beyond repair during Kashmir earthquake and more rendered unusable and needed demolition and replacement ([http://www.eeri.org/lfe/pdf/kashmir\\_eeri\\_2nd\\_report.pdf](http://www.eeri.org/lfe/pdf/kashmir_eeri_2nd_report.pdf)).

The destruction was observed over an area of 30,000 sq-km causing severe loss of life and property [53].

Almost all the buildings, mainly stone and block masonry laid in cement sand mortar with rc slabs or GI sheet roofing, collapsed in the areas close to the epicenter [2]. In regions approximately 25 km away from the epicenter nearly 25 percent of the buildings collapsed and 50 percent of the buildings were severely damaged which gives a MDR of about 0.79 using the loss model of Bal et al. [16]. To test the proposed methodology and structure-independent scenario-based fragility functions, seismic risk is computed for considered buildings considering both local and global vulnerabilities. The structure-independent fragility functions are derived for individual mechanisms and also for the combined mechanism (Figure 20). The combined fragility function is derived using the weighting factor 0.20 for in-plane mechanism and 0.80 for out-of-plane mechanism as the building stock proportion in the earthquake affected regions was found to be 20 percent urban buildings (represented by in-plane mechanical model) and 80 percent rural buildings (represented by out-of-plane mechanical model) [3]. The site soil is considered as type D of NEHRP soil classification with shear wave velocity of 250 m/sec<sup>2</sup>.

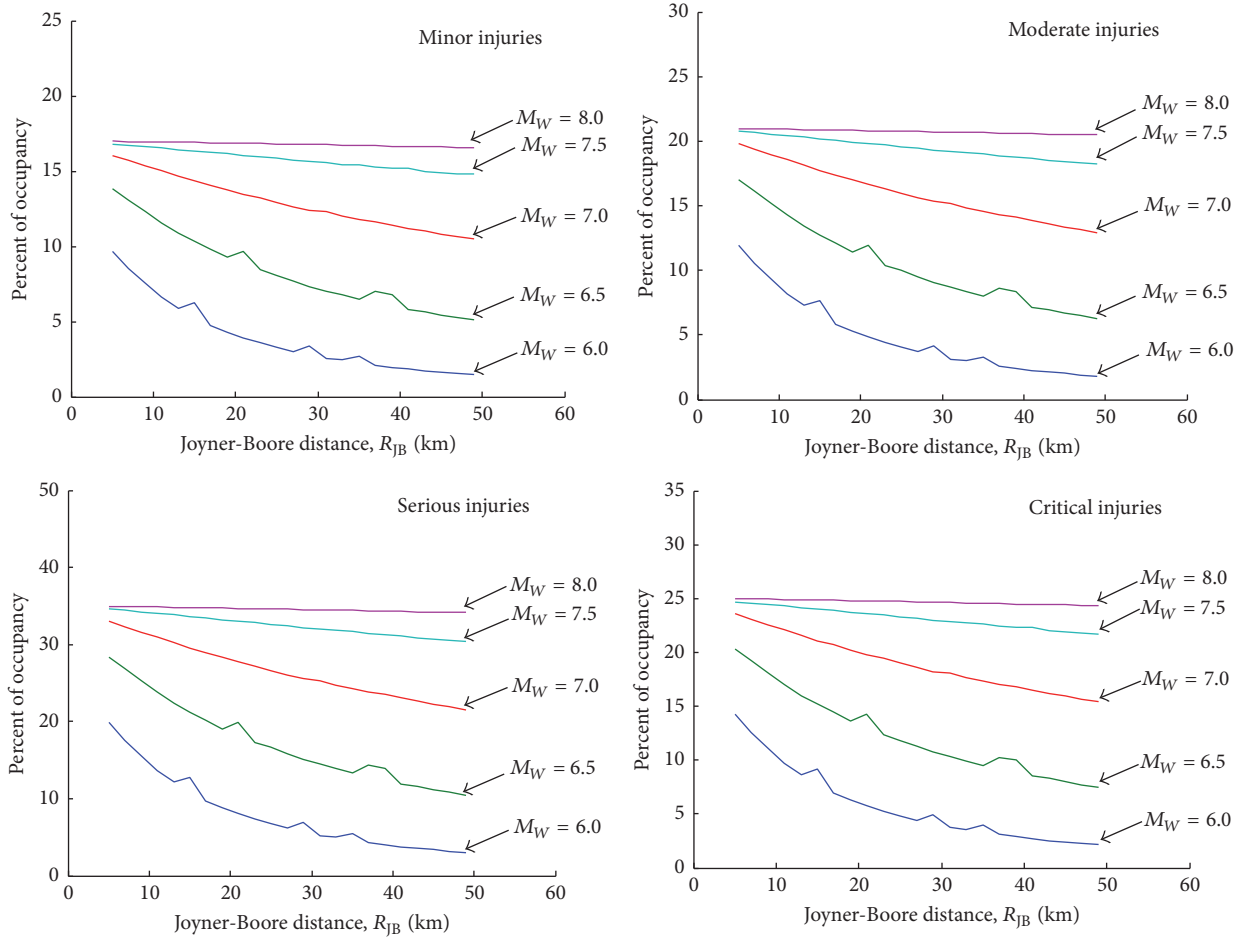


FIGURE 19: Charts for expected casualty rate in collapsed stone masonry buildings for scenario earthquakes, out-of-plane mechanism.

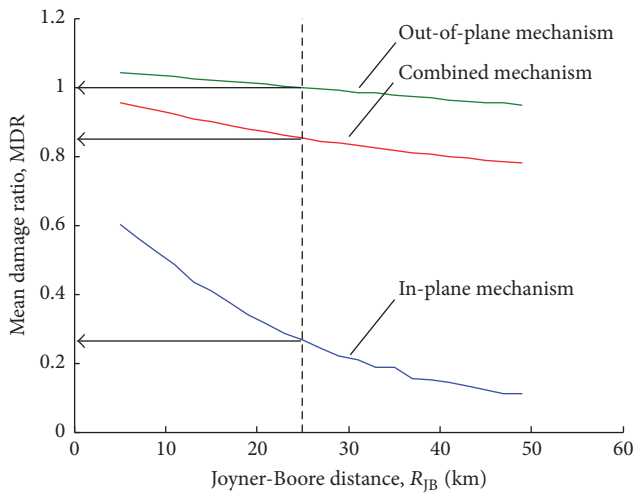


FIGURE 20: Chart for MDR of stone masonry buildings of Pakistan for scenario 2005 Kashmir earthquake.

Using only the in-plane fragility function gives an estimate of the MDR equal to 0.26 which gives an error of about +67.09 percent thus underestimating the risk, and the

out-of-plane fragility function gives estimate of MDR equal to 1.00 which gives an error of about -26.58 percent thus overestimating the seismic risk, and the combined fragility function gives an estimate of MDR equal to 0.85 which gives an error of about -7.60 thus overestimating the site risk. Nevertheless, the observed MDR is reasonably predicted in case of combined fragility function. Also, the proposed fragility functions are conservative, that is, giving slightly overestimated seismic risk and losses.

5.4. *Uncertainties in MDR.* The mean prediction for seismic risk can reasonably predict the observed response during earthquake, as observed in the previous section. Nevertheless, considerable uncertainties can result in loss estimation for a given region considering a single scenario earthquake [54] and/or fragility functions [55]. The present methodology is capable of providing analytical estimate of the uncertainties expected in the regional seismic risk assessment. Thus the uncertainties are quantified in MDR to provide better guidance in decision-making. Each of the scenarios is simulated considering 10,000 ground motion possibilities with the uncertainties defined by the ground motion prediction equation (total uncertainties are used) [44]. The coefficient of variation (COV) and standard deviation are obtained for

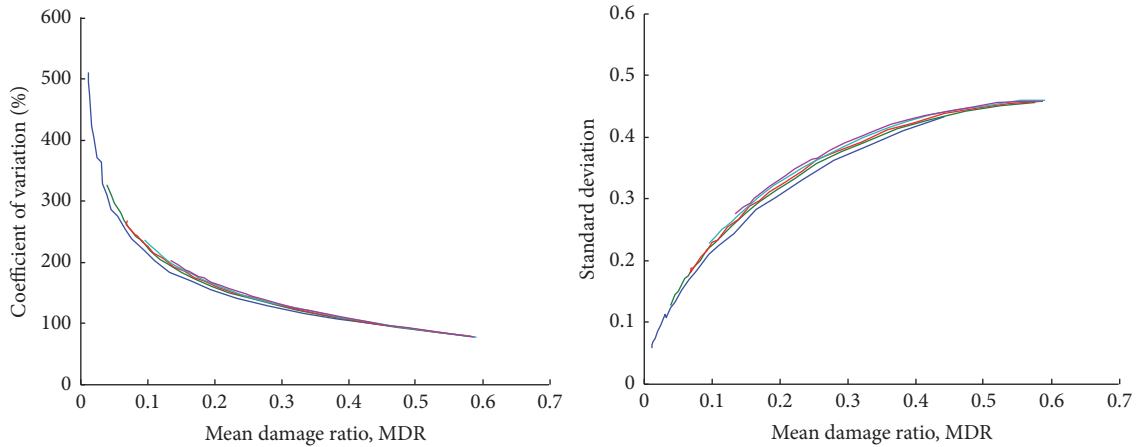


FIGURE 21: Trends in COV and standard deviation versus MDR for stone masonry building (global mechanism) of Pakistan.

each scenario and plotted to observe the trends, and quantify, in COV and standard deviation against the MDR (Figure 21).

It is observed that COV tends to decrease with increase in MDR, a similar trend also observed elsewhere [55], and there is little dependence on the magnitude of earthquakes. On the other hand the standard deviation is found to behave differently where initially the standard deviation increases with increasing MDR, as observed elsewhere [55], up to certain level but then tends to saturate when the MDR gets very higher. The values of COV and standard deviation at a given MDR are different than the reported one [55]. It is worth mentioning that other reported findings [55] are for different regions and structural systems which gives an indication that COV and standard deviation in loss estimation studies are structural and regional dependent.

## 6. Conclusions and Future Developments

Seismic risk assessment of stone masonry buildings of Pakistan is performed using an innovative and state-of-the-art nonlinear static methodology for seismic risk assessment and loss estimation of buildings on regional scale. The methodology takes different possible sources of uncertainties in an explicit and transparent manner to compute the structural capacity and assess the seismic performance of structural system. Analytical displacement-based fragility functions are derived for the considered buildings, for both local and global vulnerabilities, which are used to estimate the seismic risk and losses for scenario earthquakes and develop structure-independent fragility functions. Simplified charts are provided to compute the socioeconomic impacts of earthquakes given the magnitude and source-to-site distance of the event. Comparison of the methodology and derived fragility functions is performed with the recent earthquake observation, in predicting seismic risk of the considered typology, which is reasonably predicted. The methodology can provide also estimate of uncertainties in regional seismic risk to provide help in decision-making. However, from the derived structure-independent fragility functions it is possible to develop seismic risk prediction equations for regional

loss estimation. Comparison with large earthquake observation databases can provide estimate of inter- and intraevent uncertainties in seismic risk prediction in similar fashion as ground motion prediction equations do. It will make the regional loss estimation studies to assess the regional risk directly using the derived equations, once developed for a region. Similar studies will be performed on other regional building stocks of Pakistan once more experimental and reliable data are made available for the region. Additional data on stone masonry material and buildings can further improve the findings herein in order to increase confidence in future applications. The findings herein are the first of its kind for the considered region.

## Disclosure

The research work presented herein is the further extension of the methodology, adopted for the fragility functions derivation under the EU funded project SYNER-G (Systematic Seismic Vulnerability and Risk Analysis for Buildings, Lifelines Networks and Infrastructures Safety Gain), to derive functions for the direct seismic risk assessment of buildings given the scenario earthquake.

## Conflicts of Interest

The authors declare that there are no conflicts of interest regarding the publication of this paper.

## References

- [1] S. T. Maqsood and J. Schwarz, "Seismic vulnerability of existing building stock in Pakistan," in *Proceedings of the 14th World Conference on Earthquake Engineering*, 2008.
- [2] A. Naeem, Q. Ali, M. Javed et al., "A summary report on Muzaffarabad earthquake, Pakistan," Tech. Rep., Earthquake Engineering Center, NWFP University of Engineering and Technology, Peshawar, Pakistan, 2005.
- [3] A. Naseer, A. Naeem, Z. Hussain, and Q. Ali, "Observed seismic behavior of buildings in northern Pakistan during the 2005

- Kashmir earthquake," *Earthquake Spectra*, vol. 26, no. 2, pp. 425–449, 2010.
- [4] G. M. Calvi, R. Pinho, G. Magenes, J. J. Bommer, L. F. Restrepo-Vélez, and H. Crowley, "Development of seismic vulnerability assessment methodologies over the past 30 years," *ISET Journal of Earthquake Technology*, vol. 43, no. 3, pp. 75–104, 2006.
  - [5] H. Crowley and R. Pinho, "Using basic principles of mechanics of materials to assess the seismic risk of entire countries," *Environmental Semeiotics*, vol. 1, pp. 1–19, 2008.
  - [6] G. M. Calvi, "A displacement-based approach for vulnerability evaluation of classes of buildings," *Journal of Earthquake Engineering*, vol. 3, no. 3, pp. 411–438, 1999.
  - [7] S. Glaister and R. Pinho, "Development of a simplified deformation-based method for seismic vulnerability assessment," *Journal of Earthquake Engineering*, vol. 7, pp. 107–140, 2003.
  - [8] L. F. Restrepo-Velez and G. Magenes, "Simplified procedure for the seismic risk assessment of unreinforced masonry buildings," in *Proceedings of the 13th World Conference on Earthquake Engineering*, 2004.
  - [9] H. Crowley, R. Pinho, and J. J. Bommer, "A probabilistic displacement-based vulnerability assessment procedure for earthquake loss estimation," *Bulletin of Earthquake Engineering*, vol. 2, no. 2, pp. 173–219, 2004.
  - [10] B. Borzi, H. Crowley, and R. Pinho, "Simplified pushover-based earthquake loss assessment (SP-BELA) method for masonry buildings," *International Journal of Architectural Heritage*, vol. 2, no. 4, pp. 353–376, 2008.
  - [11] N. Ahmad, H. Crowley, R. Pinho, and Q. Ali, "Simplified formulae for the displacement capacity, energy dissipation and characteristic vibration period of brick masonry buildings," *Proceeding International Masonry Society*, vol. 11, pp. 1385–1394, 2010.
  - [12] N. Ahmad, H. Crowley, R. Pinho, and Q. Ali, "Displacement-based earthquake loss assessment of masonry buildings in Mansehra City, Pakistan," *Journal of Earthquake Engineering*, vol. 14, no. 1, pp. 1–37, 2010.
  - [13] N. Ahmad, H. Crowley, R. Pinho, and Q. Ali, "Displacement-based earthquake loss assessment of adobe buildings in Pakistan," in *Proceedings of the International Structural Engineering and Construction*, 2011.
  - [14] N. Ahmad, H. Crowley, R. Pinho, and Q. Ali, "Development of displacement-based method for seismic risk assessment of rc building stock of Pakistan," in *Proceedings of the International Conference on Earthquake Engineering and Seismology*, 2011.
  - [15] N. Ahmad, H. Crowley, R. Pinho, and Q. Ali, "Displacement-based seismic performance evaluation of Dhajji structural systems," in *Proceedings of the Masonry Society*, 2011.
  - [16] I. E. Bal, H. Crowley, R. Pinho, and G. Gulay, "Detailed assessment of structural characteristics of Turkish rc building stock for loss assessment models," *Soil Dynamics and Earthquake Engineering*, vol. 28, no. 10–11, pp. 914–932, 2008.
  - [17] M. Tomazevic, *Earthquake-Resistant Design of Masonry Buildings-Innovation in Structures and Construction*, Imperial College Press, London, UK, 1999.
  - [18] G. Magenes, "Masonry building design in seismic areas: recent experiences and prospects from a European standpoint," in *Proceedings of the 1st European Conference on Earthquake Engineering and Seismology, Keynote 9*, 2006.
  - [19] A. Galasco, G. Magenes, A. Penna, and M. Da-Pare, "In-plane cyclic shear tests of undressed double leaf stone masonry panels," in *Proceedings of the 14th European Conference on Earthquake Engineering*, 2010.
  - [20] M. J. N. Priestley, G. M. Calvi, and M. J. Kowalsky, *Displacement-Based Seismic Design of Structures*, IUSS Press, Pavia, Italy, 2007.
  - [21] K. Doherty, M. C. Griffith, N. Lam, and J. Wilson, "Displacement-based seismic analysis for out-of-plane bending of unreinforced masonry walls," *Earthquake Engineering & Structural Dynamics*, vol. 31, no. 4, pp. 833–850, 2002.
  - [22] M. C. Griffith, G. Magenes, G. Melis, and L. Picchi, "Evaluation of out-of-plane stability of unreinforced masonry walls subjected to seismic excitation," *Journal of Earthquake Engineering*, vol. 7, pp. 141–169, 2003.
  - [23] D. D'Ayala and E. Speranza, "Definition of collapse mechanisms and seismic vulnerability of historic masonry buildings," *Earthquake Spectra*, vol. 19, no. 3, pp. 479–509, 2003.
  - [24] L. F. Restrepo-Velez, *Seismic risk of unreinforced masonry buildings [Ph.D. Thesis]*, ROSE School-IUSS Pavia, Pavia, Italy, 2004.
  - [25] HAZUS-99, *Earthquake Loss Estimation Methodology*, FEMA, Washington, Wash, USA, 1999.
  - [26] Q. Ali, A. N. Khan, M. Ashraf et al., "Shaking table test on typical stone masonry buildings used in the Himalayan belt," in *Proceedings of the 9th US and 10th Canadian Conference on Earthquake Engineering*, 2010.
  - [27] Q. Ali and T. Muhammad, "Stone masonry residential buildings," World Housing Encyclopedia 138, World Housing Encyclopedia, Earthquake Engineering Research Institute, California, Calif, USA, 2007, <http://www.world-housing.net/WHEReports/wh100145.pdf>.
  - [28] G. Magenes and D. Fontana, "Simplified non-linear seismic analysis of masonry buildings," *Proceedings of British Masonry Society*, vol. 8, pp. 190–195, 1998.
  - [29] G. Magenes and G. M. Calvi, "In-plane seismic response of brick masonry walls," *Earthquake Engineering & Structural Dynamics*, vol. 26, no. 11, pp. 1091–1112, 1997.
  - [30] G. Magenes, A. Penna, A. Galasco, and M. Rota, "Experimental characterization of stone masonry mechanical properties," *Proceedings of International Masonry Society*, vol. 11, pp. 247–256, 2010.
  - [31] F. McKenna, G. L. Fenves, and M. H. Scott, *Open System for Earthquake Engineering Simulation: Version 2.2.2*, University of California Berkeley, California, Calif, USA, 2010, <http://opensees.berkeley.edu>.
  - [32] S. Otani, "SAKE, a computer program for inelastic response of R/C frames to earthquakes," Tech. Rep. UILU-Eng-74-2029, Civil Engineering Studies, University of Illinois at Urbana-Champaign, Illinois, Ill, USA, 1974.
  - [33] K. Emori and W. C. Schnobrich, "Analysis of reinforced concrete frame-wall structures for strong motion earthquakes," Structural Research Series No. 434 434, Civil Engineering Studies, University of Illinois at Urbana-Champaign, Illinois, Ill, USA, 1978.
  - [34] CEN, "Eurocode 8: Design of structures for earthquake resistance," in *Part I: General rules-Seismic actions and general requirements for buildings, prEN 1998-1-3*, Comité Européen de Normalisation, Brussels, Belgium, 2004.
  - [35] N. Ahmad, H. Crowley, R. Pinho, and Q. Ali, "Derivation of displacement-based fragility functions for masonry buildings," in *Proceedings of the 14th European Conference on Earthquake Engineering*, 2010.

- [36] M. Javed, A. Naeem, A. Penna, and G. Magenes, "Behavior of masonry structures during the Kashmir 2005 earthquake," in *Proceedings of the 1st European Conference on Earthquake Engineering and Seismology*, vol. 1077, 2006.
- [37] L. F. Restrepo-Velez and G. Magenes, "Static tests on dry stone masonry and evaluation of static collapse multiplier," Tech. Rep. 2, IUSS Press, Pavia, Italy, 2009.
- [38] CEN, "Eurocode8: Design provisions for earthquake resistance of structures," in *Part1-1: General rules- Seismic actions and general requirements for structures, prEN 1998-1-1*, Comite European de Normalisation, Brussels, Belgium, 1994.
- [39] N. J. Gregor and B. A. Bolt, "Peak strong motion attenuation relations for horizontal and vertical ground displacements," *Journal of Earthquake Engineering*, vol. 1, no. 2, pp. 275-292, 1997.
- [40] J. J. Bommer and A. S. Elnashai, "Displacement spectra for seismic design," *Journal of Earthquake Engineering*, vol. 3, no. 1, pp. 1-32, 1999.
- [41] S. V. Tolis and E. Faccioli, "Displacement design spectra," *Journal of Earthquake Engineering*, vol. 3, no. 1, pp. 107-126, 1999.
- [42] E. Faccioli, R. Paolucci, and J. Rey, "Displacement spectra for long periods," *Earthquake Spectra*, vol. 20, no. 2, pp. 347-376, 2004.
- [43] N. Lam and A. Chandler, "Peak displacement demand of small to moderate magnitude earthquakes in stable continental regions," *Earthquake Engineering & Structural Dynamics*, vol. 34, no. 9, pp. 1047-1072, 2005.
- [44] K. W. Campbell and Y. Bozorgnia, "NGA ground motion model for the geometric mean horizontal component of PGA, PGV, PGD and 5% damped linear elastic response spectra for periods ranging from 0.01 to 10 s," *Earthquake Spectra*, vol. 24, no. 1, pp. 139-171, 2008.
- [45] J. Bommer, R. Spence, M. Erdik et al., "Development of an earthquake loss model for Turkish catastrophe insurance," *Journal of Seismology*, vol. 6, no. 3, pp. 431-446, 2002.
- [46] H. Crowley and J. J. Bommer, "Modelling seismic hazard in earthquake loss models with spatially distributed exposure," *Bulletin of Earthquake Engineering*, vol. 4, no. 3, pp. 249-273, 2006.
- [47] BCP, *Building Code of Pakistan-Seismic Provisions-2007*, Ministry of Housing and Works, Islamabad, Pakistan, 2007.
- [48] B. S. J. Chiou, R. Darragh, and W. Silva, "An Overview of the NGA databas," *Earthquake Spectra*, vol. 24, no. 1, pp. 23-44, 2008.
- [49] R. Spence, *Earthquake Disaster Scenario Predictions and Loss Modelling for Urban Areas, LESSLOSS Report*, IUSS Press, Pavia, Italy, 2007.
- [50] E. So, R. Spence, A. Khan, and T. Lindawati, "Building damage and casualties in recent earthquakes and tsunamis in Asia: a cross-event survey of survivors," in *Proceedings of the 14th World Conference on Earthquake Engineering 01-0007*, 2008.
- [51] Q. Ali, *Building construction, vulnerability and inventory (Pakistan)*, WHE-Pager Project, Earthquake Engineering Research Institute, California, Calif, USA, <http://pager.world-housing.net/wp-content/uploads/2009/08/Pakistan1.pdf>.
- [52] R. Bilham, "Earthquakes in India and the Himalaya: tectonics, geodesy and history," *Annals of Geophysics*, vol. 47, no. 2-3, pp. 839-858, 2004.
- [53] ADB-WB, "Pakistan 2005 Earthquake: Preliminary damage and needs assessment," Tech. Rep., Asian Development Bank and World Bank, Islamabad, Pakistan, 2005.
- [54] H. Crowley, P. J. Stafford, and J. J. Bommer, "Can earthquake loss models be validated using field observations?" *Journal of Earthquake Engineering*, vol. 12, no. 7, pp. 1078-1104, 2007.
- [55] K. Porter, "Cracking an open safe: Uncertainty in HAZUS-based seismic vulnerability functions," *Earthquake Spectra*, vol. 26, no. 3, pp. 893-900, 2010.

## Research Article

# Vibration Suppression of a Cantilever Plate Using Magnetically Multimode Tuned Mass Dampers

Jae-Sung Bae , Jung-Sun Park, Jai-Hyuk Hwang, Jin-Ho Roh ,  
Bong-do Pyeon, and Jong-Hyuk Kim

*School of Aerospace and Mechanical Engineering, Korea Aerospace University, 200-1 Hwajeon-dong, Deogyang-gu, Goyang-si, Gyeonggi-do 412-791, Republic of Korea*

Correspondence should be addressed to Jae-Sung Bae; jsbae@kau.ac.kr

Received 15 July 2017; Accepted 20 February 2018; Published 12 April 2018

Academic Editor: Abdul Qadir Bhatti

Copyright © 2018 Jae-Sung Bae et al. This is an open access article distributed under the Creative Commons Attribution License, which permits unrestricted use, distribution, and reproduction in any medium, provided the original work is properly cited.

For a few decades, various methods of suppressing structural vibration have been proposed. The present study proposes and exploits an effective method of suppressing the vibration of cantilever plates similar to the solar panels of a satellite. Magnetically tuned mass dampers (mTMDs) are a tuned mass damper (TMD) with eddy current damping (ECD). We introduce the mTMD concept for the multimode vibration suppression of the cantilever plate. The design parameters of the mTMD are determined based on the parametric study of the theoretical four-degree-of-freedom model, which was derived for a cantilever plate with TMDs. Two TMDs are optimized for the first bending mode and first torsion mode of the plate, and they are verified analytically and experimentally. To increase the damping performance of the TMDs, ECD is introduced. Its damping ratios are estimated analytically and verified experimentally.

## 1. Introduction

The suppression of structural vibrations has significant applications in engineering fields such as machine tool industries, as well as with civil, automotive, and aerospace structures. Over the past few decades, significant research effort has been applied to suppressing vibrations in engineering structures and machines. Traditionally, passive methods have been used to attenuate structural vibrations. Recent advances in digital signal processing and sensor/actuator technology have resulted in a substantial focus on using active methods [1]. In addition, semiactive methods have filled the gap between the two.

Eddy currents are generated when a conducting plate moves in the stationary magnetic field or the magnetic field varies on the stationary conducting plate. The relative motion between the conducting plate and the magnetic field induces the eddy currents within the conducting plate. These currents induce their own magnetic field with the opposite polarity of the applied magnetic field so that the resistive electromagnetic force is generated. This electromagnetic force eventually disappears due to the electrical resistance and is proportional

to the velocity of oscillating conductor. Hence the ECD can be allowed to function as a form of viscous damping.

A lot of studies on various applications utilizing eddy currents for damping dynamic systems have been developed in past decades [2–8]. Sodano and Bae [9] and Bae et al. [10, 11] have already presented a good literature review. Kwak et al. [12] introduced an eddy current damper (ECD) and applied it to the vibration suppression of a cantilever beam. Their experiments showed that an ECD was very effective for the vibration suppression of a cantilever beam. Bae et al. [13] developed a mathematical model for the ECD of Kwak et al. [12]. Using this model, they have investigated the ECD damping characteristics and performed the simulation of the vibration suppression of a cantilever beam with Kwak's ECD. Sodano et al. [14–16] proposed the new concept of ECD device to attenuate the vibration of a cantilevered beam. Cheng and Oh [17, 18] studied multimode vibration suppression using a permanent magnet and a coil with a shunt circuit for semiactive control.

Recently, Bae et al. [10] proposed using a magnetically tuned mass damper (mTMD), as shown in Figure 1, to increase the damping performance of a conventional TMD

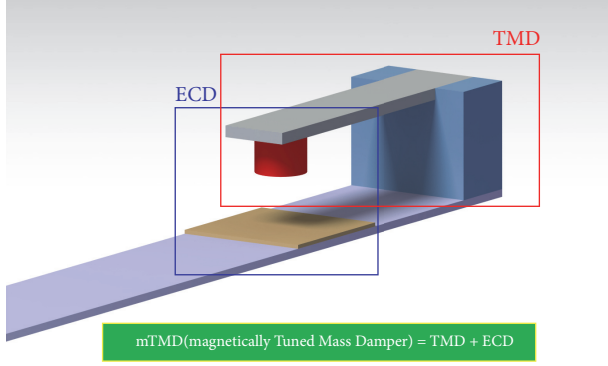


FIGURE 1: Schematic of magnetically tuned mass damper [10].

by using eddy current damping (ECD). Their study used simulations and experiments to show that the proposed method significantly increased the damping performance of the TMD if not adequately tuned. Wang et al. [19] derived the theoretical formulation of ECD in a horizontal TMD. They constructed a large-scale horizontal TMD with ECD and investigated its characteristics experimentally. Yan et al. [20] proposed and studied the multimode vibration suppression method employing a permanent magnet stacked electromagnetic absorber with negative resistance and negative inductance negative resistance shunt impedances. They showed numerically that the proposed absorber could absorb the multimode vibration of a beam and provide considerable damping over a relatively wider bandwidth. Yan et al. [21] proposed an electromagnetic shunt damping vibration isolator consisting of a box-shaped spring, a permanent magnet, an electromagnet, and a shunt circuit. Their numerical results showed that the proposed isolator could attenuate the vibration of a plate considerably. Xie et al. [22] proposed and developed an electromagnetic shunt damping absorber (EMSDA) employing an electromagnetic shunt damping mechanism. They derived the theoretical model of the EMSDA and showed numerically and experimentally that the proposed absorber could suppress the structural vibration significantly. Zihao et al. [23] proposed a beam-like semiactive electromagnetic vibration absorber (EVA) consisting of a flexible ferromagnetic cantilever beam, a ferromagnetic mass, and an E-shaped electromagnet. Their numerical and experimental results showed that the proposed EVA effectively suppressed vibrations under both steady-state excitation and sweeping frequency excitation. Bae et al. [24] proposed a relatively lightweight TMD to attenuate the vibration of a large beam structure by introducing eddy current damping to a TMD. This method was an application of their previous work [10]. The experimental results showed that the proposed method was simple but effective in suppressing the vibration of a large beam structure without a substantial weight increase.

The lowest two modes of a cantilever plate are generally the first bending mode and the first torsion mode. Both modes could be important in the vibration suppression of the plate. The present study introduces the mTMD concept for the multimode vibration suppression of a plate. The four-degree-of-freedom model of a cantilever plate with TMDs is

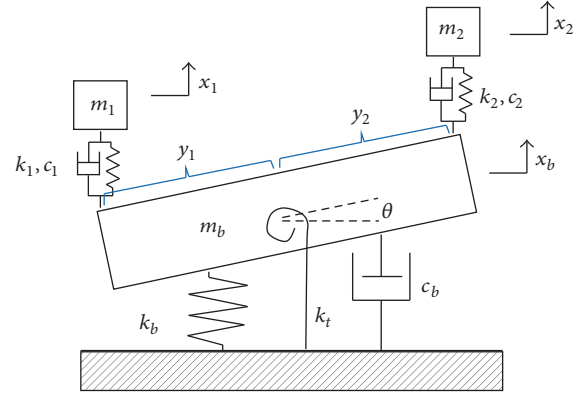


FIGURE 2: Schematic of a multimode TMD (4-DOF).

employed for a theoretical analysis. Two TMDs are optimized for the first bending mode and first torsion mode of the plate, and they are verified analytically and experimentally. ECD is introduced to increase the damping performance of the TMDs. Its damping ratios are estimated analytically and verified experimentally.

## 2. Theoretical Analysis

**2.1. Theoretical Modeling of a Multimode TMD.** The schematic of a multimode TMD with damping in both the base and adaptive mass system is shown in Figure 2. From this schematic, the relative displacement between the base and each adaptive mass ( $m_1$  and  $m_2$ ) is calculated using (1). The rotational angle ( $\theta$ ) of the base is assumed to be small.

$$\begin{aligned} x_1 - x_b + y_1\theta &: \text{between the base and } m_1 \\ x_2 - x_b - y_2\theta &: \text{between the base and } m_2. \end{aligned} \quad (1)$$

To obtain the equations of motion from Lagrange's equation, the kinetic energy and the potential energy of the system can be written as

$$\begin{aligned} T &= \frac{1}{2}m_b\dot{x}_b^2 + \frac{1}{2}(J_b + m_1y_1^2 + m_2y_2^2)\dot{\theta}^2 + \frac{1}{2}m_1\dot{x}_1^2 \\ &\quad + \frac{1}{2}m_2\dot{x}_2^2 \\ V &= \frac{1}{2}k_bx_b^2 + \frac{1}{2}k_t\theta^2 + \frac{1}{2}k_1(x_1 - x_b + y_1\theta)^2 \\ &\quad + \frac{1}{2}k_2(x_2 - x_b - y_2\theta)^2. \end{aligned} \quad (2)$$

The generalized force can be defined as

$$\begin{aligned} F &= \frac{1}{2}c_b\dot{x}_b^2 + \frac{1}{2}c_t\dot{\theta}^2 + \frac{1}{2}c_1(\dot{x}_1 - \dot{x}_b + y_1\dot{\theta})^2 \\ &\quad + \frac{1}{2}c_2(\dot{x}_2 - \dot{x}_b - y_2\dot{\theta})^2. \end{aligned} \quad (3)$$

TABLE 1: Plate properties.

Length	Width	Thickness	Young's modulus	$\nu$	$\rho$
280 mm	290 mm	2 mm	72 GPa	0.32	2630 kg/m <sup>3</sup>

From the Lagrange's equation, the equations of motion are presented as

$$\begin{aligned}
 & \begin{bmatrix} m_b & 0 & 0 & 0 \\ 0 & J_b + m_1 y_1^2 + m_2 y_2^2 & 0 & 0 \\ 0 & 0 & m_1 & 0 \\ 0 & 0 & 0 & m_2 \end{bmatrix} \begin{bmatrix} \ddot{x}_b \\ \ddot{\theta}_b \\ \ddot{x}_1 \\ \ddot{x}_2 \end{bmatrix} \\
 & + \begin{bmatrix} c_b + c_1 + c_2 & -c_1 y_1 + c_2 y_2 & -c_1 & -c_2 \\ -c_1 y_1 + c_2 y_2 & c_t + c_1 y_1^2 + c_2 y_2^2 & c_1 y_1 & -c_2 y_2 \\ -c_1 & c_1 y_1 & c_1 & 0 \\ -c_2 & -c_2 y_2 & 0 & c_2 \end{bmatrix} \begin{bmatrix} \dot{x}_b \\ \dot{\theta}_b \\ \dot{x}_1 \\ \dot{x}_2 \end{bmatrix} \\
 & + \begin{bmatrix} k_b + k_1 + k_2 & -k_1 y_1 + k_2 y_2 & -k_1 & -k_2 \\ -k_1 y_1 + k_2 y_2 & k_t + k_1 y_1^2 + k_2 y_2^2 & k_1 y_1 & -k_2 y_2 \\ -k_1 & k_1 y_1 & k_1 & 0 \\ -k_2 & -k_2 y_2 & 0 & k_2 \end{bmatrix} \begin{bmatrix} x_b \\ \theta_b \\ x_1 \\ x_2 \end{bmatrix} \\
 & = \begin{bmatrix} F \\ 0 \\ 0 \\ 0 \end{bmatrix} \sin \omega t.
 \end{aligned} \quad (4)$$

To verify the equation of motion, a comparison with the results of a commercial FEM program is carried out. The analysis is performed according to the mass ratio of the plate and TMD. Figure 3 shows the frequency results of the modeling and program, and it indicates that the two models are in good agreement with the error at 1%. Table 1 presents the properties and specifications used in the analysis.

**2.2. Modeling of Eddy Current Damping.** A few concepts of the ECD devices are proposed by researchers in decades. The concept of the ECD used in the present study is presented in Figure 4 and is proposed by Sodano et al. [14–16] and Bae et al. [10]. The damping force ( $F_z$ ) in the  $z$  (vertical) direction due to the eddy current in Figure 4 yields

$$\begin{aligned}
 F_z &= -2\pi\sigma\delta\nu \int_0^{r_c} y B_y^2(y, l_g) dy \\
 &= -2\pi\sigma\delta\nu \left( \frac{\mu_0 M_0 b}{4\pi} \right)^2 \\
 &\cdot \int_0^{r_c} \int_{-L}^0 y (l_g - z_1) I_1^2(b, y, l_g - z_1) dz_1 dy,
 \end{aligned} \quad (5)$$

where the details of (5) are referred to [10].

**2.3. Cantilever Plate with Magnetically Tuned Mass Dampers.** Figure 5 shows a TMD with ECD applied to a cantilever

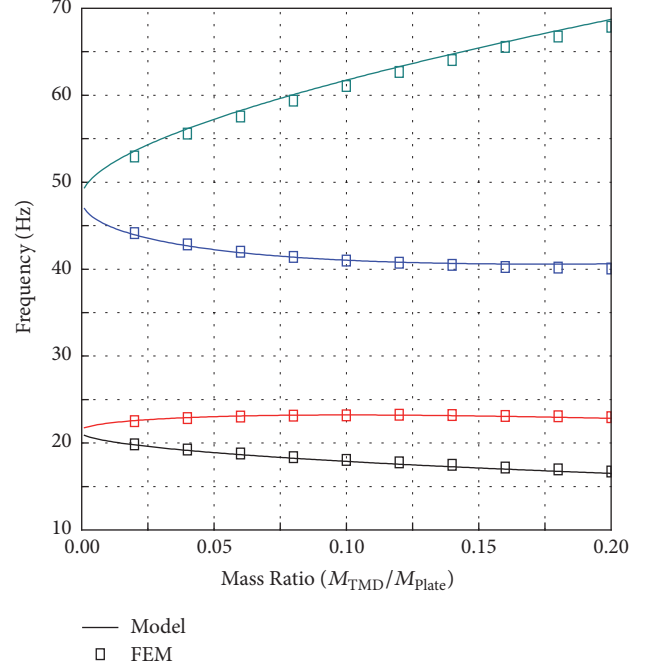


FIGURE 3: Comparison of frequency results for the presented modeling and commercial FEM program for various mass ratios.

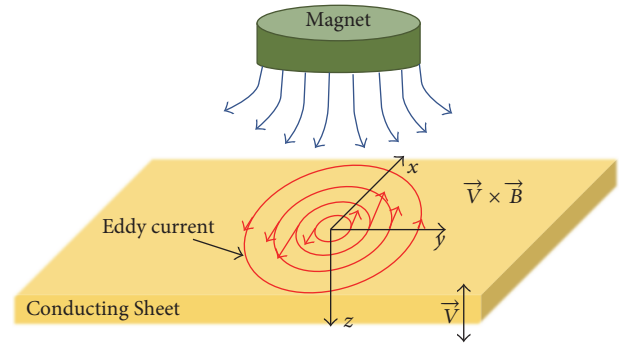


FIGURE 4: Schematic of eddy currents [10].

plate. This TMD with ECD is called a magnetically tuned mass damper (mTMD). The mTMD consists of a permanent magnet, a cantilevered beam, and a conducting plate of sheet. Two mTMDs are implemented via the attachment of an additive structure on both sides of the cantilever plate. One is used to suppress the first bending vibration, and the other is used to suppress the first torsional vibration. In terms of performance, TMDs offer excellent vibration absorption in a particular frequency range, but they are unsatisfactory outside of that range. In the present study, ECD is used to improve the performance of a TMD in a wide frequency range. In the present study, TMDs are first

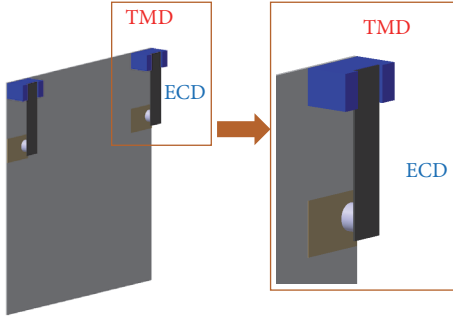


FIGURE 5: Schematic of magnetically tuned mass damper.

designed to suppress the vibrations of a cantilevered plate, and the vibration absorption performance is verified via experiments and simulations. ECD is subsequently applied to the TMDs to improve their performance, and the mTMDs are verified via experiments.

### 3. Numerical and Experimental Results

**3.1. TMD Design Parameters.** Generally, as the mass ratio  $\mu$  of the TMD mass to the primary mass increases, the damping performance of a TMD on the vibration of the primary structure becomes more effective. However, it causes the mass increase of the system. Therefore, it is necessary to limit the value of  $\mu$ . Since the value of  $\mu$  is practically assumed to be from 0.05 to 0.25 the largest value must be selected to improve TMD performance.

When  $\mu = 0.25$  and  $\zeta = 0.01$ , the normalized magnitude of the primary structure for various  $\beta$  and  $\zeta$  values is presented in Figure 6. In Figure 6(a), the TMD shows good vibration absorption performance at  $\beta = 0.85$ , so this value is selected. Figure 6(b) shows the normalized magnitude of the primary structure for various  $\zeta$  values, and it is known that an optimized damping ratio exists at which the performance of the vibration absorption reaches its maximum value.

However, the optimal parameters of the TMD change when multimode TMDs are employed. To determine the effects of absorber frequency, the mass ratios of two TMDs are fixed at 0.1. Figure 7(a) shows the tendency according to frequency ratio. As the frequency ratio increases, the amplitude peak of the primary structure increases. Also, Figure 7(b) shows that the frequency ratio is fixed at 0.9 for the parameter study. Changing the mass ratio causes the gap between peaks to increase.

When the mass ratio is 0.1, the frequency ratio of the TMD in terms of suppressing the bending vibration is 0.96. Figure 8(a) shows the frequency response for this case. The TMD tuned for the bending mode affects the peak of the bending vibration, but the torsion vibration only changes the frequency of the peak; it does not diminish the amplitude. Figure 8(b) shows the frequency response when the frequency ratio for the torsion is 0.95.

Using optimal parameters for each TMD, the suppression performance tends not to be optimized due to the

coupling effect. That is why additional tuning is required. Considering that the bending and torsion vibrations are suppressed optimally, the TMD frequency ratios are tuned at  $\beta_1 = 0.91$  and  $\beta_2 = 0.92$ . Figures 9(a) and 9(b) show the frequency responses when TMDs are tuned individually and simultaneously, respectively. The damping performance of TMDs tuned for both bending and torsion is more excellent as shown Figure 9(b).

### 3.2. TMD Experimental Setup and Results

**3.2.1. Theoretical and Experimental Results.** First, mathematical modeling was verified in Section 2 before the TMD experiment. Figure 10 shows the experimental results for the frequency response function for the theoretical modeling of the plate. The boundary conditions of the two results are that the bottom of the plate is fixed and TMD (absorber) system is not installed.

The first and second natural frequencies obtained in theoretical modeling are 19.91 Hz and 44.95 Hz. And the mode natural frequencies obtained by the experiment are 19.96 Hz and 45.02 Hz, respectively. Since the error of each mode frequency is about 0.25%, 0.16%, which is less than 1%, the validity of mathematical modeling has been verified.

**3.2.2. TMD Experimental Setup and Results.** Figure 11 shows the experimental setup with the TMDs attached to a plate. Acrylic connectors are used to construct the TMDs, and the mass is 5.8 g. For convenience, the plate is designated as the primary structure, the TMD tuned for bending vibrations is called the first TMD, and the TMD tuned for torsional vibrations is called the second TMD. The experiments are carried out on the basis of the design parameter  $\mu = 0.1$ , and they are performed using a laser displacement sensor and impact hammer.

The experiments are performed according to a series of procedures. To compare the results, the first vibration test is conducted only on the primary structure. In order to reduce the vibration for the bending mode, the first TMD is applied to the primary structure and the second TMD is applied to reduce the vibration for the torsional mode. Figure 12 shows the FRF results. The FRF of the primary structure is denoted using a black line for comparison with other results. In the first mode, which is the bending mode, the frequency is about 19.91 Hz. In the second mode, the torsion mode, the frequency is about 44.86 Hz. When only the first TMD is attached, the bending vibration is effectively attenuated at about 16.2 dB, but the torsional vibration is not suppressed. When only the second TMD is attached, similarly, only the torsional vibration is suppressed at about 16.19 dB. From these results, the vibration absorption performance of the TMDs is verified as being suitable for each mode. However, when the TMD is only applied for a single mode, the other mode is not affected.

In order to suppress the bending and torsion vibrations together, the first and second TMDs are applied simultaneously. Each TMD is seated on the basis of the design parameter of the optimized single mode. Figure 13 shows the FRF results. The FRF results in Figure 13(a) show that the

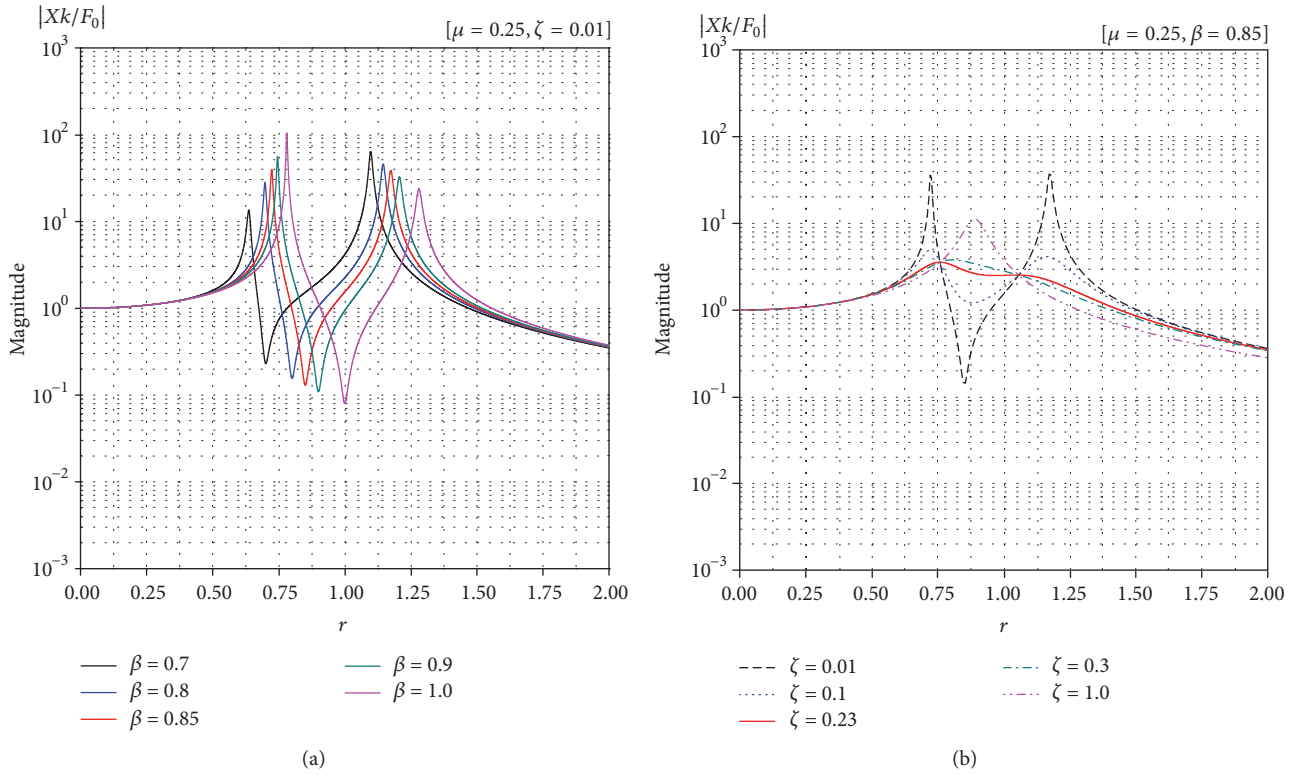


FIGURE 6: Normalized magnitude of the primary structure: (a) for various  $\beta$  values when  $\mu = 0.25$ ; (b) for various  $\zeta$  values when  $\mu = 0.25$ ,  $\beta = 0.85$ .

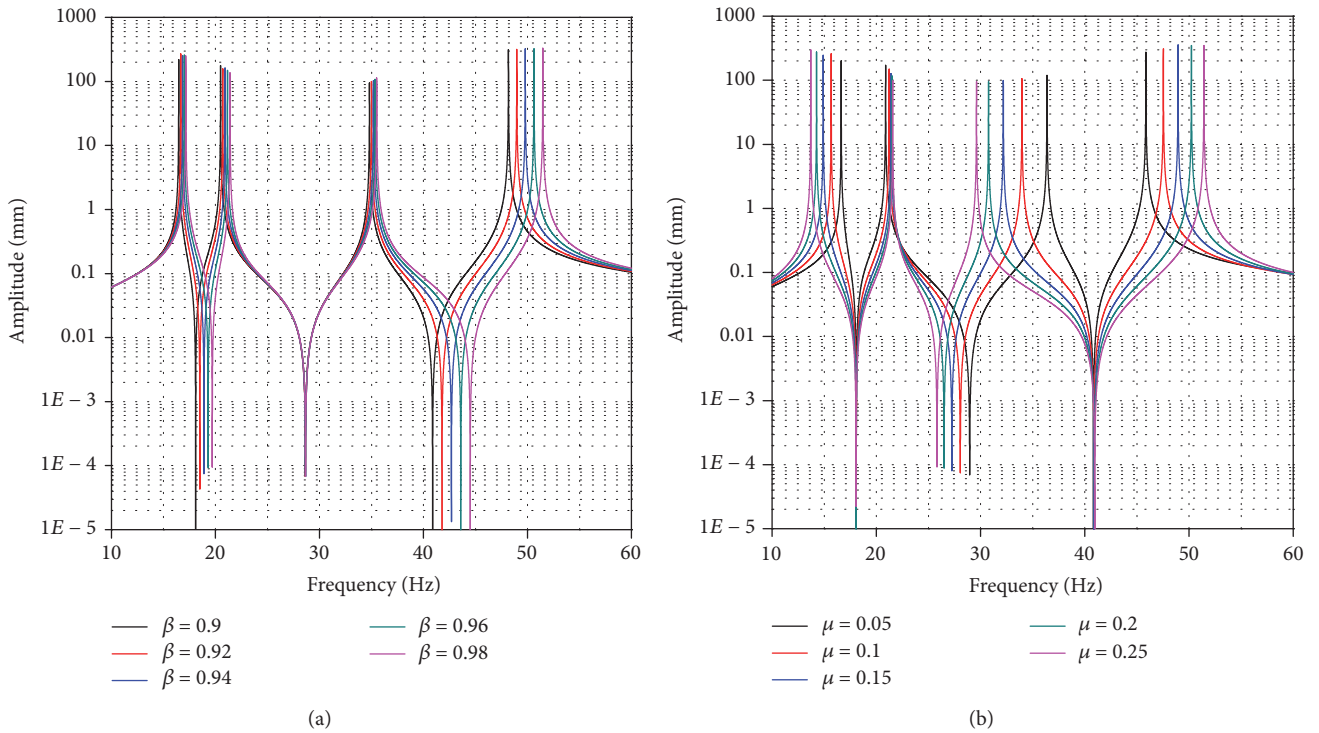


FIGURE 7: Normalized magnitude of the primary structure: (a) for various  $\beta$  values when  $\mu = 0.1$  and (b) for various  $\mu$  values when  $\beta = 0.9$ .

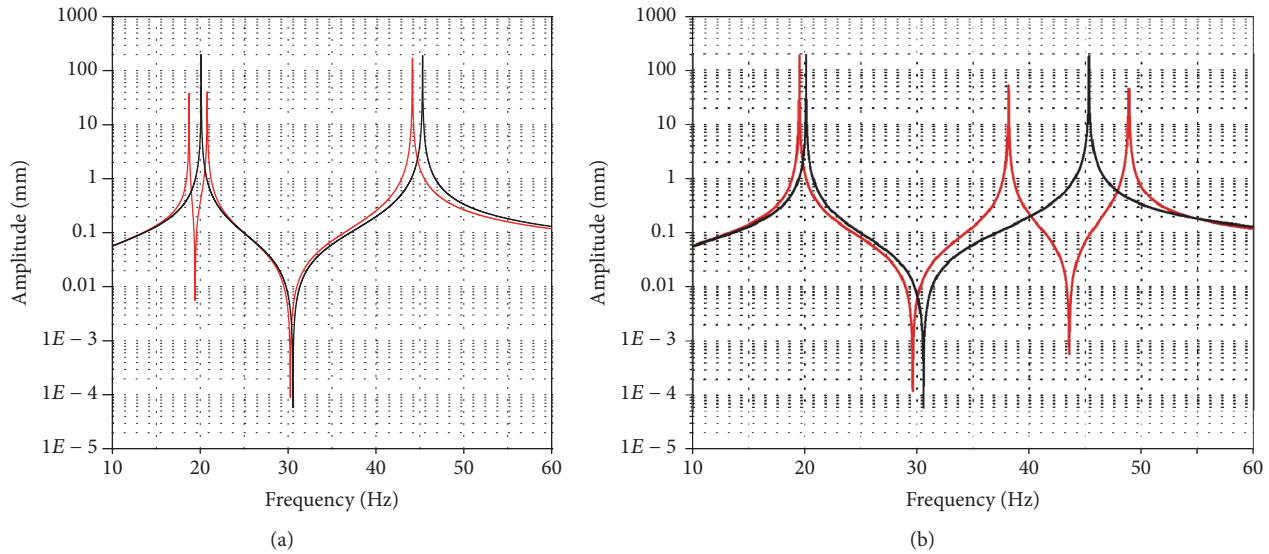


FIGURE 8: Normalized magnitude of the primary structure: (a) with the bending TMD and (b) with the torsion TMD (Key: black line, Primary; red line, TMD.).

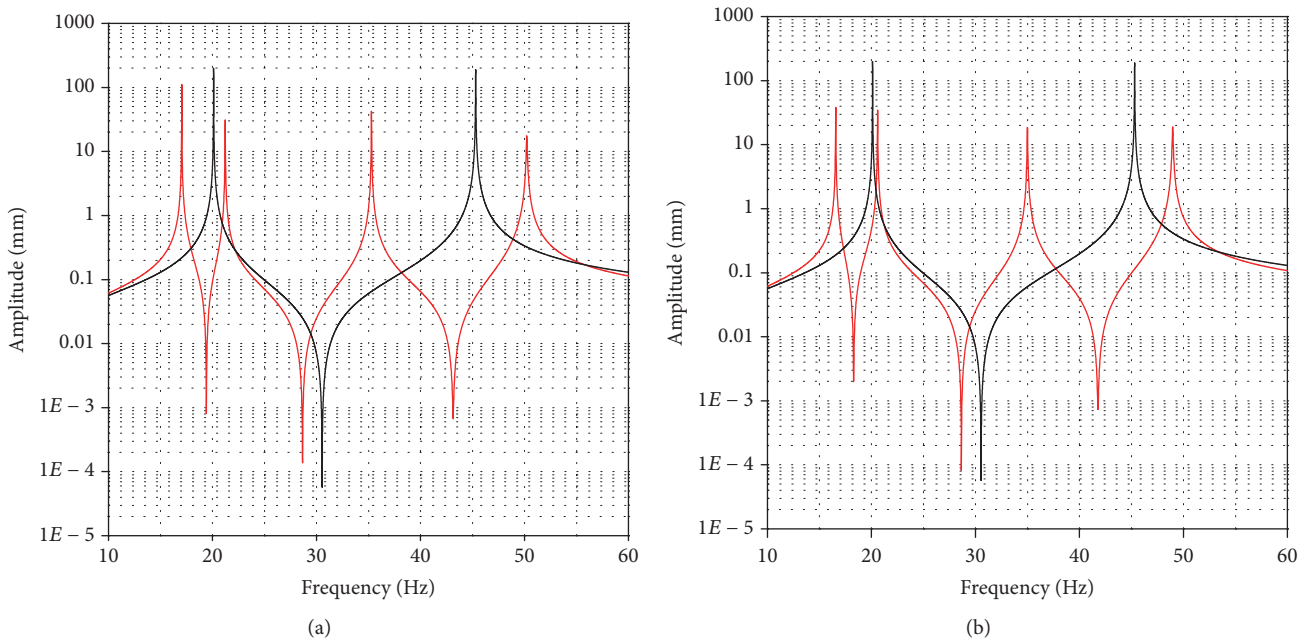


FIGURE 9: Frequency response functions of the plate with the TMDs: (a) with the TMDs tuned individually and (b) with the TMDs tuned for both bending and torsion (Key: black line, Primary; red line, TMD.).

TMDs are not optimized because the coupling effect does not correspond with the peak values. Therefore, it can be seen that a new optimal design parameter is needed.

Using a new optimal parameter that considers the coupling effect, vibration tests are carried out repeatedly. The results are shown in Figure 13(b). The bending vibration suppresses about 9.75 dB to 10.52 dB, and the torsional vibrations are attenuated at about 14.05 dB to 14.15 dB. Each TMDs is optimized and suppresses the vibrations effectively.

*3.3. Experimental Results and Simulations of Magnetically TMD.* Figure 14 shows the experimental setup of the mTMD using magnetic effects to improve the vibration absorption performance of the TMD. The conducting sheet is located in the magnetic field generated by a cylindrical permanent magnet used as a concentrated TMD mass.

The eddy currents circulate on the conducting sheet via the relative motion between the magnet and the conducting sheet. In addition, ECD can be generated. The thickness of

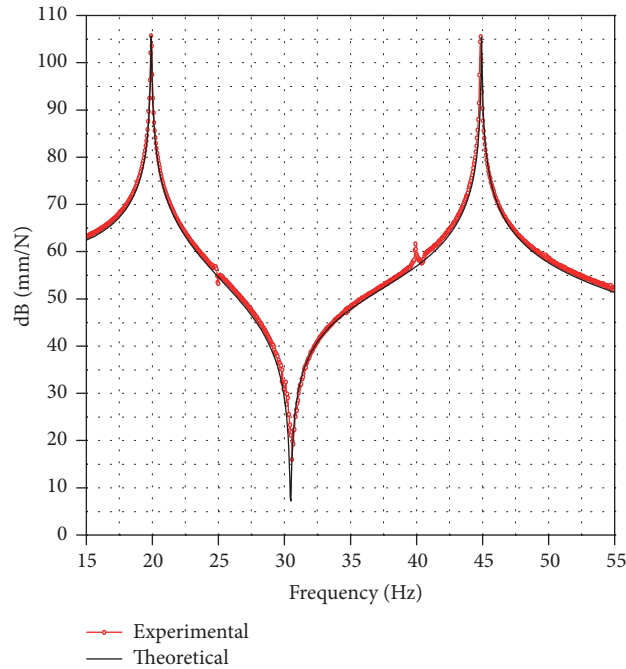


FIGURE 10: Comparison of theoretical and experimental results for only plate.

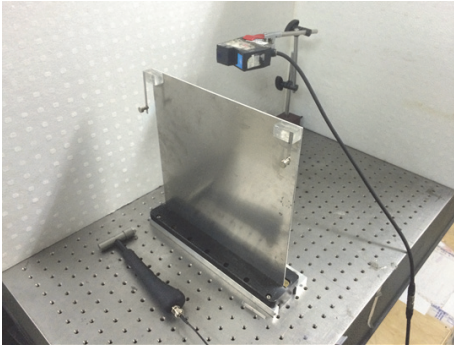


FIGURE 11: TMD experimental setup.

the conducting sheet is 0.4 mm. The gap between the magnet and conductive sheet can be changed by using externally fixed blocks. Figure 15 shows the experimental results when the gap between the first TMD magnet and the conductive sheet is 3 mm and the second TMD's gap is 1 mm. From these results, it is known that the performance of the present mTMD surpasses that of the TMD. The mTMD shows excellent damping effects in a wide frequency range.

**3.4. Effects of Gap on Magnetically TMD Performance.** As shown in Figure 16, the theoretical results of the mTMD show how the gap between the magnet and the conductive sheet affects the performance of the vibration absorption of the mTMD. The gap size is reduced from 5 mm to 1 mm by moving fixed blocks between the magnet and the beam of the TMD during the experiments. To verify the damping effect according to the gap, first, the gap of the first TMD

is fixed. The experiments are then performed for various gaps of the second TMD. The experiments are subsequently repeated with the same procedure after changing the gap of the first TMD. Figure 16 shows the FRF results for in each case. However, as shown in Figure 7, TMD performance is not proportional to the damping ratio ( $\zeta$ ), and the optimal value of the damping ratio is about 0.23. The optimal value of the gap size in the present mTMD system is 3 mm as shown in Figure 17 and Table 2 (the theoretical approach used to calculate the damping ratio of the mTMD will be presented in the next section.) Table 2 shows the degree of attenuation in dB of each order of natural frequency. Each datum in Table 2 represents the maximum reduction width. The 3 mm gap is chosen because it has the largest energy in the first bending mode, so the gap of the first TMD with the maximum reduction width is set at 3 mm. In addition, the gap of the second TMD shows a gradual decrease in the vibration reduction width when the first TMD gap is increased by 3 mm. Based on these results, it can be known that the gap of the TMDs optimized for vibration suppression performance are 3 mm and 1 mm, respectively.

**3.5. Theoretical Analysis of mTMD Damping Coefficient.** Previous experiments confirm that the damping ratio of an mTMD can be controlled by changing the gap between the magnet and conductive sheet. These damping characteristics can be explained by (5).

Equation (5) calculates the amount of ECD force generated during the relative motion between the magnet and conductor, so the magnetic damping coefficient can be obtained by eliminating the term of velocity ( $v$ ) in the equation. Regarding the various gap sizes from 1 to 5 mm,

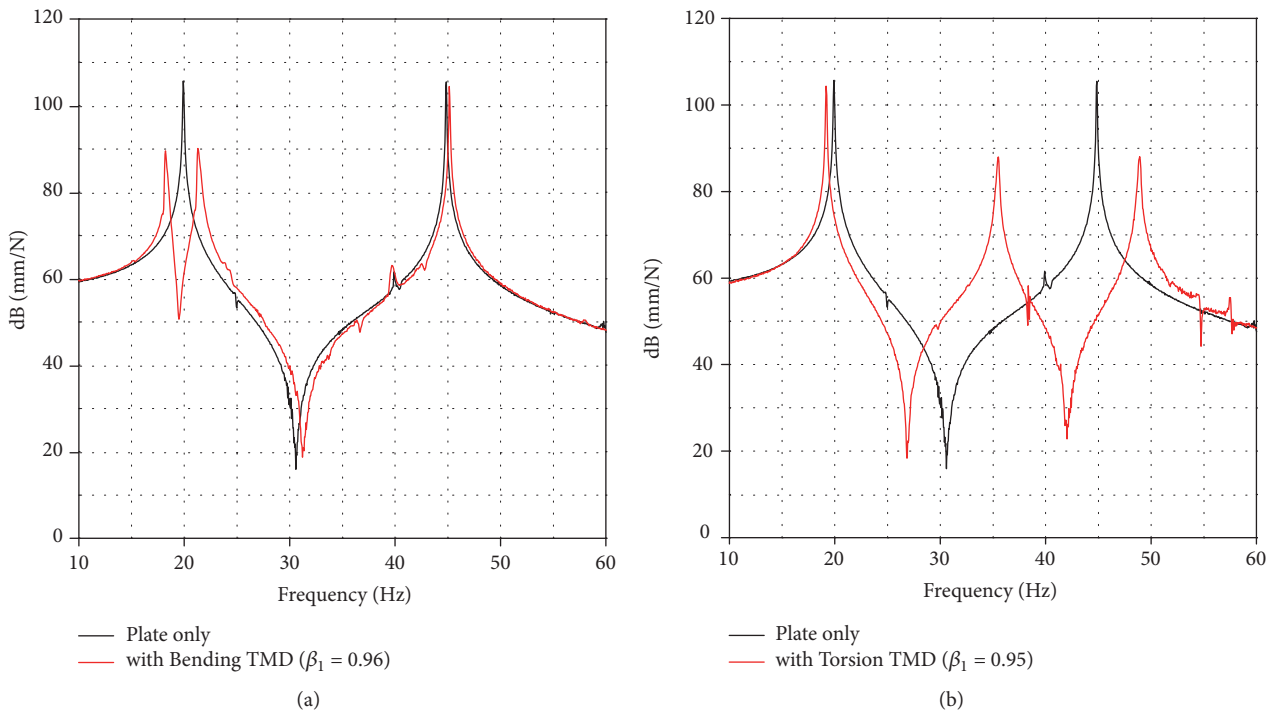


FIGURE 12: Experimental FRF results of the primary structure with each TMD: (a) with the first TMD only and (b) with the second TMD only (Key: black line, Primary: red line, TMD).

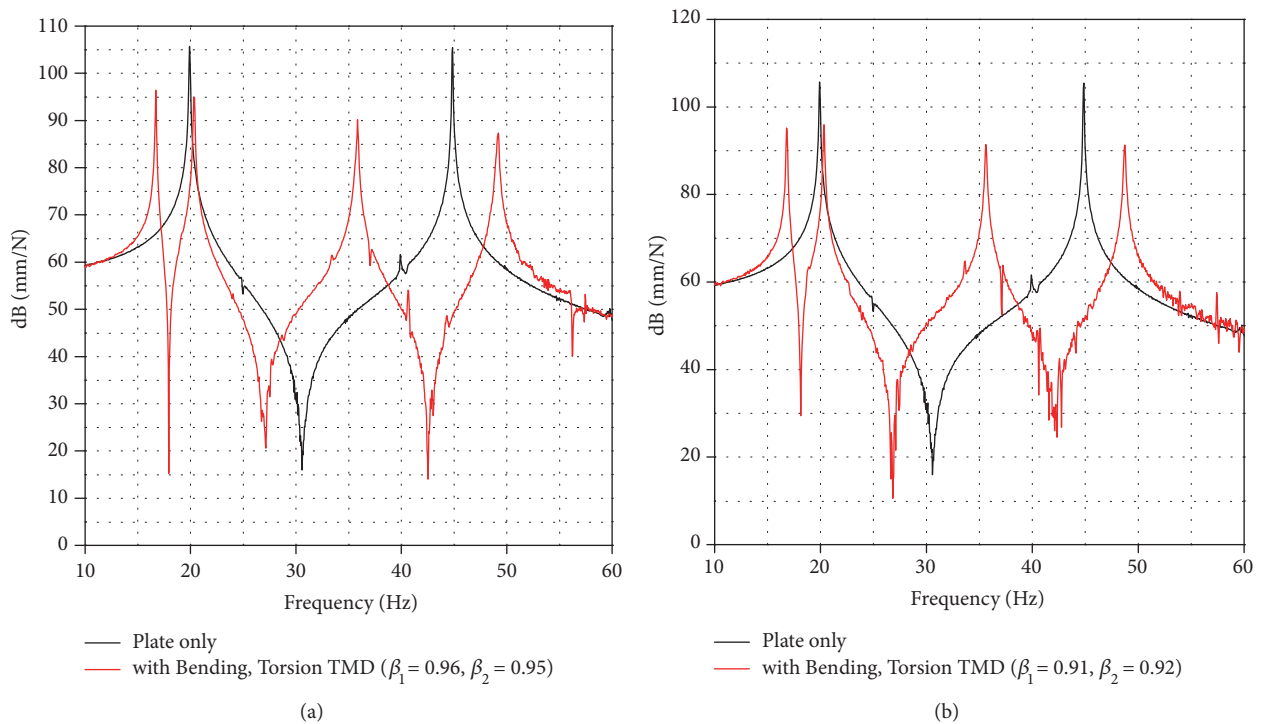


FIGURE 13: Experimental FRF results of the primary structure with TMDs: (a) with the TMDs tuned individually and (b) with the optimized TMDs (Key: black line, Primary: red line, TMD).

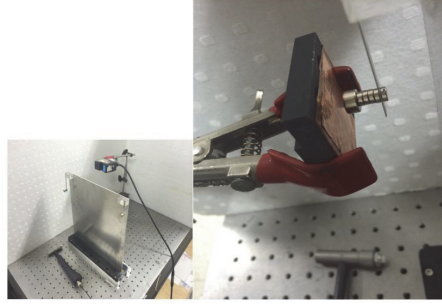


FIGURE 14: Experimental setup of the mTMD.

TABLE 2: Experimental results of the mTMD with respect to gap interval [Unit: dB].

Gap of second TMD	Gap of first TMD				
	1 mm	2 mm	3 mm	4 mm	5 mm
1 mm	-31.59/-35.97	-32.96/-37.21	-37.21/-36.48	-33.99/-36.45	-33.67/-36.69
2 mm	-30.41/-34.42	-31.22/-34.19	-34.19/-34.17	-32.82/-34.62	-32.01/-33.71
3 mm	-28.98/-32.12	-30.41/-32.13	-32.13/-32.22	-31.32/-31.23	-30.35/-30.83
4 mm	-28.13/-30.08	-29.65/-29.62	-30.63/-29.85	-30.58/-29.51	-29.09/-28.86
5 mm	-27.52/-27.64	-28.89/-28.16	-30.05/-27.58	-29.94/-27.02	-28.31/-25.883

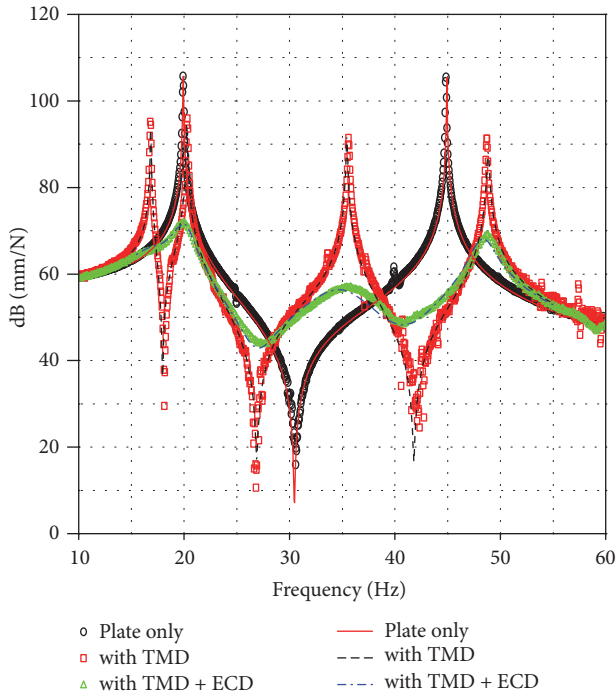


FIGURE 15: Experimental FRF results of the primary structure with the mTMD.

the magnetic coefficients calculated using (5) are presented in Table 3. These results theoretically verify the fact that the decrease in the gap causes the magnetic damping coefficient to increase. This can be proven with experiments using only the mTMD. Table 3 compares the damping ratio between the experiments and theoretical analyses.

For the first TMD, the optimal value of the gap size in the simulation results (3 mm) is identical to the value in the experimental results. Figure 17 shows the damping ratio of the first mode for various gap sizes. The simulation and experimental results are in good agreement. From the results described above, the present method of calculating the magnetic damping coefficients can be verified.

#### 4. Conclusions

The present study proposed the mTMD concept to suppress the multimode vibration of a cantilevered plate. The four-degree-of-freedom model is employed to theoretically describe the vibration of a cantilevered plate with TMDs. Two TMDs are optimized for the first bending mode and first torsion mode of the plate, and they are verified analytically and experimentally. ECD is introduced to increase the damping performance of the TMDs. The damping model of ECD in [10] is used to calculate the damping force of mTMD. Its damping ratios are estimated analytically and verified experimentally.

For the multimode vibration suppression, two mTMDs are introduced to the cantilevered plate. The damping performance of the plate with two mTMD is estimated analytically. To verify the analytical results, the experimental setup is constructed. The results show that the mTMDs to be optimized for both the bending and torsion modes could attenuate the multimode vibration of the plate efficiently in a wide frequency range. The gap size between the magnet and the conductor is one of important parameters to determine the damping ratio of ECD. The present estimations of the damping ratios for various gap sizes are in good agreement with the experimental results.

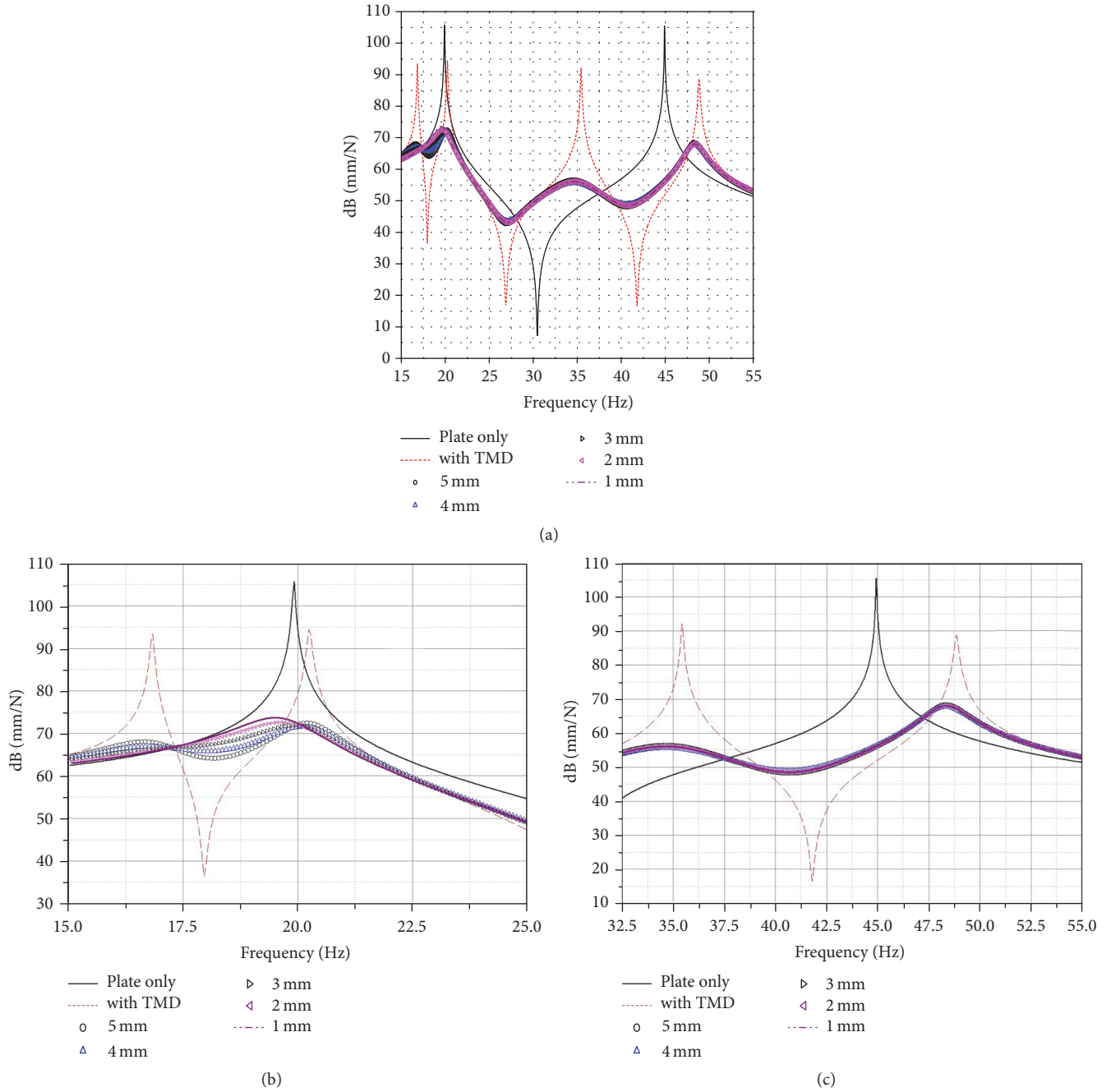


FIGURE 16: Effect of the gap size of the primary structure: (a) with the mTMD, (b) with the mTMD in bending mode, and (c) with the mTMD in torsion mode.

TABLE 3: Comparison of damping coefficients for the gap change between experiments and theoretical analyses.

Gap	Bending		Torsion	
	Experiment	Theoretical analysis	Experiment	Theoretical analysis
5 mm	0.08151	0.0739	0.0299	0.0289
4 mm	0.09727	0.0998	0.0372	0.0365
3 mm	0.1347	0.1388	0.0512	0.0480
2 mm	0.2094	0.2009	0.0644	0.0663
1 mm	0.2730	0.2702	0.0850	0.0868

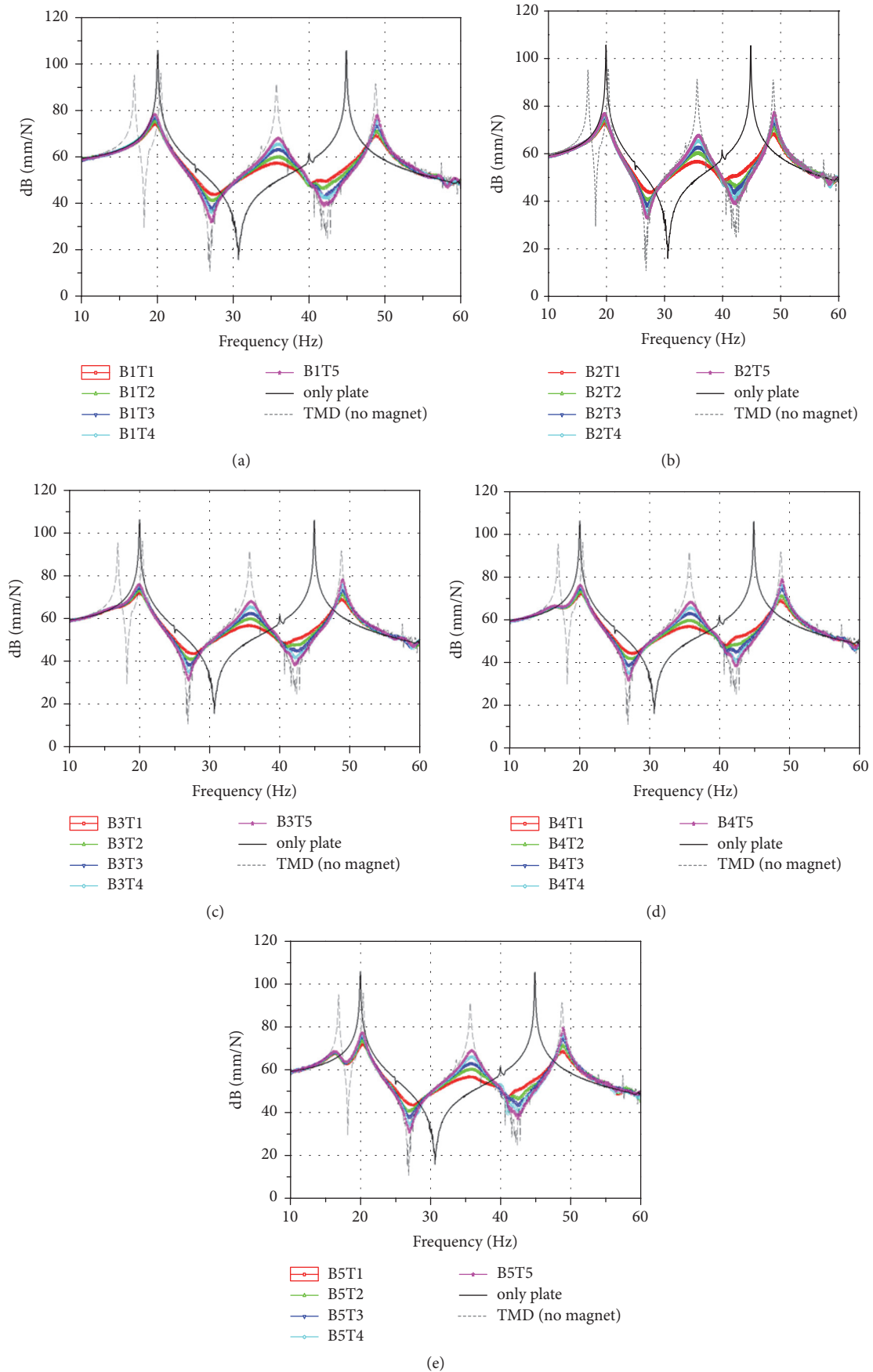


FIGURE 17: FRF results of mTMD with respect to the gap change when  $\mu = 0.1$  and  $\beta = 0.85$ : (a) first TMD gap at 1 mm, (b) first TMD gap at 2 mm, (c) first TMD gap at 3 mm, (d) first TMD gap at 4 mm, and (e) first TMD gap at 5 mm.

## Nomenclature

- $b$ : Radius of magnet  
 $B$ : Magnetic flux density  
 $c$ : Damping coefficient of system  
 $F_0$ : External force  
 $F_z$ : Damping force  
 $k$ : Spring coefficient of system  
 $m$ : Mass of system  
 $M_0$ : Magnetization  
 $r_c$ : Equivalent radius of copper tube  
 $v$ : Velocity of magnet  
 $\beta$ : Natural frequency ratio of system  
 $\delta$ : Thickness of copper  
 $\mu$ : Mass ratio of system  
 $\mu_0$ : Permeability of free space  
 $\varsigma$ : Damping ratio of system  
 $\sigma$ : Conductivity of copper.

## Subscripts

- $b$ : Base.

## Conflicts of Interest

The authors declare that there are no conflicts of interest regarding the publication of this paper.

## Acknowledgments

This work was supported by the New & Renewable Energy Core Technology Program of the Korea Institute of Energy Technology Evaluation and Planning (KETEP), a financial resource granted by the Ministry of Trade, Industry & Energy, Republic of Korea (no. 20143030021130). The first and second authors gratefully acknowledge the support in part provided by the Global Surveillance Research Center (GSRC) program funded by the Defense Acquisition Program Administration (DAPA) and Agency for Defense Development (ADD).

## References

- [1] R. Alkhatib and M. F. Golnaraghi, "Active structural vibration control: a review," *Shock and Vibration*, vol. 35, no. 5, pp. 367–383, 2003.
- [2] T. Takagi, J. Tani, S. Matsuda, and S. Kawamura, "Analysis and Experiment of Dynamic Deflection of a Thin Plate with a Coupling Effect," *IEEE Transactions on Magnetics*, vol. 28, no. 2, pp. 1259–1262, 1992.
- [3] J. S. Lee, "Dynamic stability of conducting beam-plates in transverse magnetic fields," *Journal of Engineering Mechanics*, vol. 122, no. 2, pp. 89–94, 1996.
- [4] D. A. Kienholtz, S. C. Pendleton, and K. E. Richards, "Demonstration of solar array vibration suppression," in *Proceedings of SPIE's Conference on Smart Structures and Materials*, 72, pp. 2193–59, 1994.
- [5] G. L. Larose, A. Larsen, and E. Svensson, "Modelling of tuned mass dampers for wind-tunnel tests on a full-bridge aeroelastic model," *Journal of Wind Engineering & Industrial Aerodynamics*, vol. 54–55, no. C, pp. 427–437, 1995.
- [6] H. Teshima, Tanaka, K. Miyamoto, K. Nohguchi, and K. Hinata, "Effect of eddy current dampers on the vibrational properties in superconducting levitation using melt-processed YBaCuO bulk superconductors," *Physica C*, vol. 274, pp. 17–23, 1997.
- [7] Y. Matsuzaki, D. Ishikubo, T. Kamita, and T. Ikeda, "Vibration control system using electromagnetic forces," *Journal of Intelligent Material Systems and Structures*, vol. 8, no. 9, pp. 751–756, 1997.
- [8] Y. Matsuzaki, T. Ikeda, A. Nae, and T. Sasaki, "Electromagnetic forces for a new vibration control system: Experimental verification," *Smart Materials and Structures*, vol. 9, no. 2, pp. 127–131, 2000.
- [9] H. A. Sodano and J.-S. Bae, "Eddy current damping in structures," *The Shock and Vibration Digest*, vol. 36, no. 6, pp. 469–478, 2004.
- [10] J.-S. Bae, J.-H. Hwang, J.-H. Roh, J.-H. Kim, M.-S. Yi, and J. H. Lim, "Vibration suppression of a cantilever beam using magnetically tuned-mass-damper," *Journal of Sound and Vibration*, vol. 331, no. 26, pp. 5669–5684, 2012.
- [11] J.-S. Bae, J.-H. Hwang, J.-H. Roh, and M.-S. Yi, "Development of an electromagnetic shock absorber," *International Journal of Applied Electromagnetics and Mechanics*, vol. 49, no. 1, pp. 157–167, 2015.
- [12] M. K. Kwak, M. I. Lee, and S. Heo, "Vibration Suppression Using Eddy Current Damper," *Korean Society for Noise and Vibration Engineering*, vol. 23, pp. 441–453, 2003.
- [13] J.-S. Bae, M. K. Kwak, and D. J. Inman, "Vibration suppression of a cantilever beam using eddy current damper," *Journal of Sound and Vibration*, vol. 284, no. 3–5, pp. 805–824, 2005.
- [14] H. A. Sodano, J.-S. Bae, D. J. Inman, and W. Keith Belvin, "Concept and model of eddy current damper for vibration suppression of a beam," *Journal of Sound and Vibration*, vol. 288, no. 4–5, pp. 1177–1196, 2005.
- [15] H. A. Sodano, J.-S. Bae, D. J. Inman, and W. K. Belvin, "Modeling and application of eddy current damper for suppression of membrane vibrations," *AIAA Journal*, vol. 44, no. 3, pp. 541–549, 2006.
- [16] H. A. Sodano, J.-S. Bae, D. J. Inman, and W. K. Belvin, "Improved concept and model of eddy current damper," *Journal of Vibration and Acoustics*, vol. 128, no. 3, pp. 294–302, 2006.
- [17] T.-H. Cheng and I.-K. Oh, "A current-flowing electromagnetic shunt damper for multi-mode vibration control of cantilever beams," *Smart Materials and Structures*, vol. 18, no. 9, Article ID 095036, 2009.
- [18] T.-H. Cheng and I.-K. Oh, "Vibration suppression of flexible beam using electromagnetic shunt damper," *IEEE Transactions on Magnetics*, vol. 45, no. 6, pp. 2758–2761, 2009.
- [19] Z. Wang, Z. Chen, and J. Wang, "Feasibility study of a large-scale tuned mass damper with eddy current damping mechanism," *Earthquake Engineering and Engineering Vibration*, vol. 11, no. 3, pp. 391–401, 2012.
- [20] B. Yan, Y. Luo, and X. Zhang, "Structural multimode vibration absorbing with electromagnetic shunt damping," *Journal of Vibration and Control*, vol. 22, no. 6, pp. 1604–1617, 2016.
- [21] B. Yan, X. Zhang, and Y. Luo, "Investigation of negative resistance shunt damping for the vibration control of a plate," *International Journal of Applied Electromagnetics and Mechanics*, vol. 45, pp. 93–100, 2014.
- [22] S. Xie, P. Li, X. Zhang, and B. Yan, "Vibration suppression of structure with electromagnetic shunt damping absorber," *International Journal of Applied Electromagnetics and Mechanics*, vol. 45, pp. 395–402, 2014.

- [23] L. Zihao, L. Wanyou, and Y. Yali, "A study of a beam-like electromagnetic vibration absorber," *Journal of Vibration and Control*, vol. 22, no. 11, pp. 2559–2568, 2014.
- [24] J. S. Bae, J. H. Hwang, D. G. Kwag, J. Park, and D. J. Inman, "Vibration suppression of a large beam structure using tuned mass damper and eddy current damping," *Shock & Vibration*, 10 pages, 2014.

## Research Article

# A Vibration Model of Ball Bearings with a Localized Defect Based on the Hertzian Contact Stress Distribution

Fanzhao Kong, Wentao Huang , Yunchuan Jiang, Weijie Wang, and Xuezheng Zhao

*School of Mechatronics Engineering, Harbin Institute of Technology, 92 West Dazhi Street, Harbin 150001, China*

Correspondence should be addressed to Wentao Huang; [hwt@hit.edu.cn](mailto:hwt@hit.edu.cn)

Received 27 July 2017; Revised 5 February 2018; Accepted 28 February 2018; Published 1 April 2018

Academic Editor: Naveed Ahmad

Copyright © 2018 Fanzhao Kong et al. This is an open access article distributed under the Creative Commons Attribution License, which permits unrestricted use, distribution, and reproduction in any medium, provided the original work is properly cited.

To study the vibration mechanism of ball bearings with localized defects, a vibration model of a ball bearing based on the Hertzian contact stress distribution is proposed to predict the contact force and vibration response caused by a localized defect. The calculation of the ball-raceway contact force when the ball passes over the defect is key to establishing a defect vibration model. Hertzian contact theory indicates that the contact area between the ball and the raceway is an elliptical contact surface; therefore, a new approach is used to calculate the ball-raceway contact force in the defect area based on the stress distribution and the contact area. The relative motion between the inner ring, the outer ring, and the balls is considered in the proposed model, and the Runge-Kutta algorithm is used to solve the vibration equations. In addition, vibration experiments of a bearing with an outer ring defect under different loads are performed. The numerical signals and experimental signals are compared in the time and frequency domains, and good correspondence between the numerical and experimental results is observed. Comparisons between the traditional model and the proposed model reveal that the proposed model provides more reasonable results.

## 1. Introduction

The failure of a properly installed and lubricated bearing occurs in the form of surface fatigue cracks, such as spalls and pits [1]. In a ball bearing, spalls and pits often form on the contact surfaces between the raceways and balls. The variation of the contact deformation between the ball and the raceway when the ball passes over a defect causes a sudden change in the contact force, which causes periodic vibration of the bearing. How to describe and explain this process using mathematical and physical models is a major area of research on bearings with defects.

In early studies [2, 3], the variation of the fault signals of bearing defects in the frequency domain was analysed in detail. Subsequently, a vibration model of bearings was introduced. The research focused on the periodic vibration phenomenon in bearings, and an impulse was used to describe the impact force caused by a localized defect. Rafsanjani et al. [4] developed a vibration model of ball bearings, studied the vibration characteristics of localized defects on the inner ring, outer ring, and balls, and established a pulse function that contains several parameters, such as the position, angle,

and depth of the defects. Tandon and Choudhury [5, 6] used a rectangular pulse, a triangular pulse, and a half-sine pulse to express the impact force caused by localized defects, correlated the severity of the defect and the defect generation time with the amplitude of the pulse, and calculated the width of the pulse from the width of the defect. The results showed that the vibration amplitude of the outer raceway's defect expressed by the rectangular pulse is greater than that expressed by the half-sine pulse.

Although the periodic vibration of a bearing due to a fault can be simulated somewhat by pulse functions, the geometric morphology of defects cannot be adequately described, and the generation of the impact force cannot be adequately explained; thus, current research focuses on simulating the impact process via mechanical calculations. In previous studies [7–17], scholars suggested that when a ball passes over a defect on the raceway, the ball will sink to a certain depth, and the contact deformation between the ball and raceway will change, resulting in a change in the ball-raceway contact force; this process causes periodic vibration of the bearings. Sawalhi and Randall [7, 8] presented a gearbox model with bearing faults and compared it with the model

in [9]. In [9], when the rolling element enters or exits the spall region, the contact force between the elements and the raceways will change instantly, which can cause sharp vibrations in the gearbox system. This model predicts very large impulsive forces in the system as a result of the sharp increase in acceleration required to maintain a balance within the system. Thus, they updated the model to reflect the actual path of the rolling element and defined the depth of the defect as a gradient function associated with the width of the defect, the rolling element's radius, and the race radius. Patel et al. [10] reported a dynamic model of ball bearings with single and double defects on the raceways; a fixed sinking depth of the balls was obtained based on the defect width and the ball radius. Patel et al. [11] updated the model by considering the profile of a localized defect and assigning a variable defect depth based on the variable size of the defect and the ball radius. The simulation results in these two papers are generally consistent with the experimental results. Patil et al. [12] proposed a ball bearing model with a localized defect to predict the vibration response. In this model, the defect is modelled as a circumferential half sinusoidal wave, and the vibration amplitude of the ball is calculated based on the angle of the defect, the rotational speed of the balls, and the defect width. The experimental results showed that the greater the defect width is, the larger the vibration amplitude of the fault signal is. Moazen Ahmadi et al. [13] established a nonlinear dynamic model of roller bearings with a wider range of defects. The model considers the finite size of the rollers, the contact force, and the damping force between the rolling elements and raceways to calculate the path and contact force of rollers in the defect region. Comparisons between the proposed model, the point mass model, and experimental results were performed and showed that the proposed model is more reasonable than the point model; the numerical results are more consistent with the experimental results. Liu et al. [14] proposed that the vibration amplitude and duration of the impact force are determined by the geometric profile and size of the defects. Based on the geometric profile and size of the defects, ball-defect contacts were divided into five types; moreover, the sinking depth of the ball was expressed by piecewise functions according to the number of contact points between the balls and the defects, and the contact stiffness of each type was calculated to obtain the contact force. Gomez et al. [15] presented a deep groove ball bearing model with localized defects to study the instantaneous angular speed variations of the balls. This model used a simple localized defect model with a rigidly defect depth, and the defect depth is also regarded as the variation of the contact deformation when the balls pass over the defect. Mishra et al. [16] proposed three different ball bearing defect models, a 5-DOF vibration model developed in MATLAB Simulink, a multibody dynamics model using bond graph by SYMBOLS software, and a multibody CAD model using ADAMS software. The simulated and the experimental vibration signals of different bearing faults are also compared. However, the ball-raceway contact deformation has a constant value when the balls pass over the defect in the vibration model. Chen and Kurfess [17] proposed a new rolling element bearing model to estimate the defect size on the outer raceway. The vibration

signal from the time domain is used to estimate the defect size. The experiment results showed that this model provides accurate estimation.

In the studies described above, the contact forces between the balls and the defects are calculated based on the sinking depth of the balls, which is related to the defect width and the ball radius. The advantage of this approach is that it can calculate the impact forces of defects with different sizes; however, the disadvantage of this approach is that regardless of how the load applied to the bearing changes, the rigidly sinking depth of the ball is unchanged in the defect area. To solve this problem, a vibration model of a bearing with a defect that uses Hertzian contact stress distribution is proposed. The new model considers the contact area and the stress distribution. It includes several important parameters, the defect width and the ball radius, as well as the bearing load, the defect geometry, and the shaft rotational speed. In the new model, the load on the bearings can affect the sinking depth of the balls, and the geometric relationship between the balls, raceways, and defects is different from that in the traditional models.

This paper is divided into six sections. The second section presents the analysis of the contact process between a ball and a defect, and the third section introduces the contact model of balls and raceways. An experiment is presented in the fourth section. In the fifth section, the numerical results of the proposed model are analysed, and the experimental results and the numerical results are compared. The last section presents the conclusions.

## 2. Analysis of the Contact Process between the Ball and Defect Area

Hertzian contact theory is used to calculate the contact force between the ball and the raceway over a long period, as shown in the following:

$$Q = K \cdot \delta^n, \quad (1)$$

where  $Q$  is the contact force,  $K$  is the contact stiffness,  $\delta$  is the contact deformation, and  $n = 1.5$  for a ball bearing.

The sinking depth of the ball in defect area is shown in Figure 1. The model in Figure 1(a) is the traditional model; [7–11, 15–17] used this model. However, all the sinking depths of the balls in Figure 1 are possible in the proposed model; the sinking depth is affected by the applied load.

In Figure 1(a), the sinking depth  $\Delta$  of the ball is obtained from the width of the defect, as shown in the following:

$$\Delta = r - \sqrt{r^2 - L^2}, \quad (2)$$

where  $r$  is the radius of the ball and  $2L$  is the width of the defect.

As mentioned previously,  $\delta$  is the contact deformation between the ball and the raceways before the ball reaches the defect. When the ball passes over the defect, the remaining deformation between the ball and the raceways is  $\delta - \Delta$ ; thus, according to (1), the ball-defect contact force is

$$Q = K \cdot (\delta - \Delta)^{3/2}. \quad (3)$$

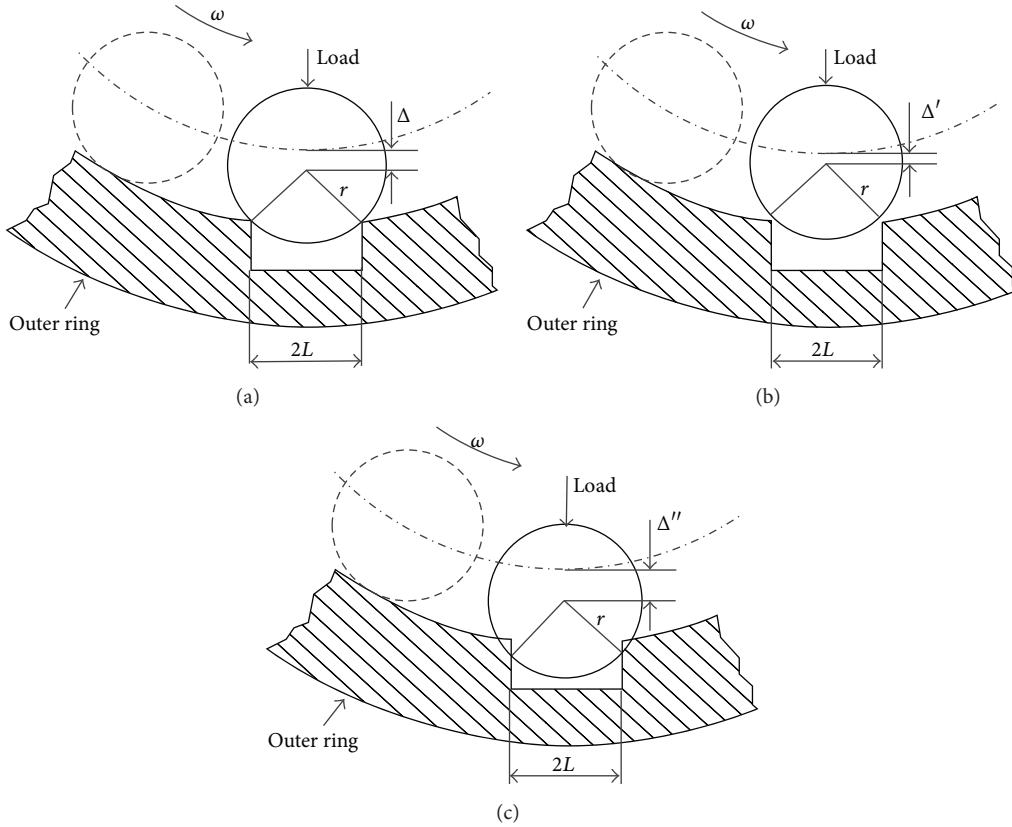


FIGURE 1: The sinking depth of the ball.

This method can be considered an approximate method. For details, refer to [11]. This traditional model has the following disadvantages.

(1) The sinking depth of the ball is a function of only the ball radius and the defect width, and it is independent of the applied load on the bearing. Moreover, after the sinking depth of the ball is determined, the path of the ball is also limited.

(2) When the ball contacts the raceways or the defect, a small contact area is simplified as a line contact or a point contact, which results in an inaccurate contact force.

To address these problems, a Hertzian contact stress distribution is applied to the calculation of the contact force in the defect area. In the proposed model, the sinking depth of the ball is related to the load applied on the bearing, and the contact area between the ball and defect is also considered.

### 3. Bearing System Model

**3.1. Vibration Model of the Bearing.** A vibration model of the bearing is presented in Figure 2. The ball bearing (Type 6204) is mounted at the end of a shaft. The inner ring is fixed rigidly to the motor shaft, and the outer ring is fixed to the housing. A constant additional load  $F_l$  is applied to the housing in the vertical direction, and an accelerometer is mounted onto the housing to measure the vibration of the outer ring. The ball-raceway contact can be considered a spring-mass system. The proposed model incorporates the following realistic assumptions and considerations.

(1) The balls rotate with the cage; that is, the balls do not slip.

(2) The forces act in the radial direction only; the contact is an elastic contact and follows Hertzian contact theory.

(3) The forces act only in the radial plane of the bearing.

(4) When the ball passes over the localized defect on the raceway, the stress distribution between the ball and the raceway follows Hertzian contact theory.

(5) Because of the centrifugal force, the balls, cage, and outer ring have the same rotational frequencies.

(6) Grease is used in the bearing; the damping due to the lubricating film between the ball and the raceways and the damping of the shaft and the housing are considered.

**3.2. Kinematics of the Balls.** The inner and outer centres of the rolling element bearings are not concentric because of the applied load and the bearing clearance. Figure 3 illustrates the relationships between the motions of the components of the ball bearing, where  $O_{in}(x_i, y_i)$  and  $O_{out}(x_o, y_o)$  are the centres of the raceways,  $P_j(p_{x,j}, p_{y,j})$  is the centre of the  $j$ th ball, the raceway radii are  $R_i$  and  $R_o$ , the angular positions of the  $j$ th ball on the raceways are  $\alpha_{in,j}$  and  $\alpha_{out,j}$ , and  $\alpha_{out,j}$  can be described as follows:

$$\alpha_{out,j} = 2\pi \cdot f_c \cdot t + \frac{\pi}{4} (j - 1) + \alpha_0. \quad (4)$$

In Figure 3, the geometrical relationships of  $\alpha_{in,j}$  and  $\alpha_{out,j}$  are as follows:

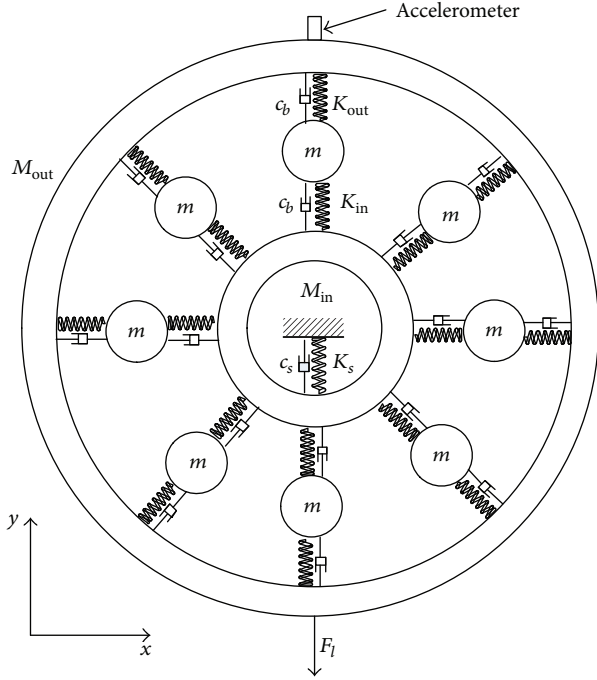


FIGURE 2: The bearing system model.

$$\cos \alpha_{in,j} = \frac{(x_o + OP_{out,j} \cdot \cos \alpha_{out,j} - x_i)}{OP_{in,j}},$$

$$\sin \alpha_{in,j} = \frac{(y_o + OP_{out,j} \cdot \sin \alpha_{out,j} - y_i)}{OP_{in,j}}, \quad (5)$$

$$\cos(\alpha_{in,j} - \alpha_{out,j}) = \cos \alpha_{in,j} \cdot \cos \alpha_{out,j} + \sin \alpha_{in,j} \cdot \sin \alpha_{out,j},$$

where  $f_c$  is the cage frequency,  $\alpha_0$  is the initial angular position of the cage,  $OP_{in,j} = \sqrt{(p_{x,j} - x_i)^2 + (p_{y,j} - y_i)^2}$ ,  $OP_{out,j} = \sqrt{(p_{x,j} - x_o)^2 + (p_{y,j} - y_o)^2}$ , and the ball-raceway deformations are denoted as follows:

$$\delta_{in,j} = r + R_i - OP_{in,j},$$

$$\delta_{out,j} = r - R_o - OP_{out,j}. \quad (6)$$

### 3.3. Defect Model Based on the Hertzian Contact Stress Distribution

**3.3.1. Hertzian Contact Stress Distribution.** The analysis of the contact type of the bearing is presented below. In Figure 4, when a ball contacts the raceway, the contact is a point contact if the load is zero, as shown in Figure 4(a). After a load is applied to the ball, the contact point expands to an ellipse, as shown in Figure 4(b).

The Hertzian contact force calculation of a ball bearing was simplified. For the contact area between the ball and the raceway (both of which are made of steel),  $a$  is the semimajor

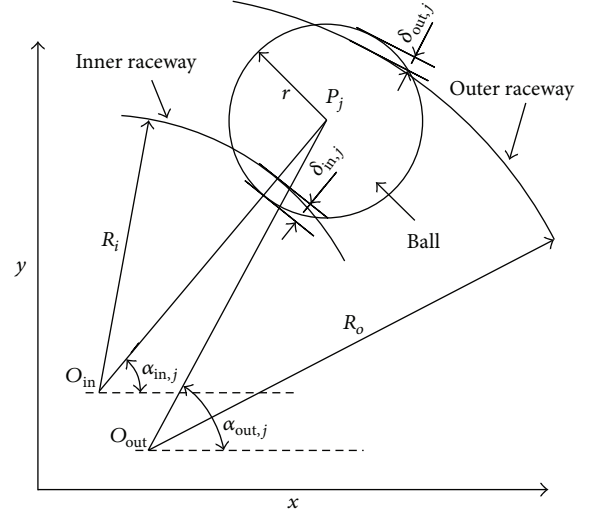


FIGURE 3: Relationships between the motions of the components of a ball bearing.

axis, and  $b$  is the semiminor axis; they can be obtained as follows:

$$a = 0.0236a^* \left( \frac{Q}{\sum \rho} \right)^{1/3},$$

$$b = 0.0236b^* \left( \frac{Q}{\sum \rho} \right)^{1/3}, \quad (7)$$

where  $\sum \rho$  is the sum of the curvatures of the ball and the raceway and  $a^*$  and  $b^*$  can be obtained from [18].

The stress on the elliptical contact area is shown in Figure 5, and the normal stress within the contact area is given by the following:

$$\sigma = \frac{3Q}{2\pi ab} \sqrt{1 - \frac{x^2}{a^2} - \frac{y^2}{b^2}}. \quad (8)$$

**3.3.2. Localized Defect Contact Force.** When a ball passes over the localized defect (Figure 6), the shape of the ball-defect contact area changes as the ball moves. Figure 7 illustrates the geometry of the contact area in Figure 6 with coordinates, where the size of the localized defect is  $2L$ ; when the  $j$ th ball moves from left to right, the contact area can be described as follows:

$$\frac{x^2}{a^2} + \frac{(y - y_j)^2}{b^2} = 1, \quad (9)$$

where  $y_j$  is the  $y$ -axis coordinate of the ellipse centre. According to (8) and (9), the compressive stress distribution of the contact ellipse is

$$\sigma = \frac{3Q}{2\pi ab} \sqrt{1 - \left( \frac{x}{a} \right)^2 - \left( \frac{y - y_j}{b} \right)^2}. \quad (10)$$

Figure 7 illustrates the variation of the ball-raceway contact area at the defect edge. As the ball begins to enter the

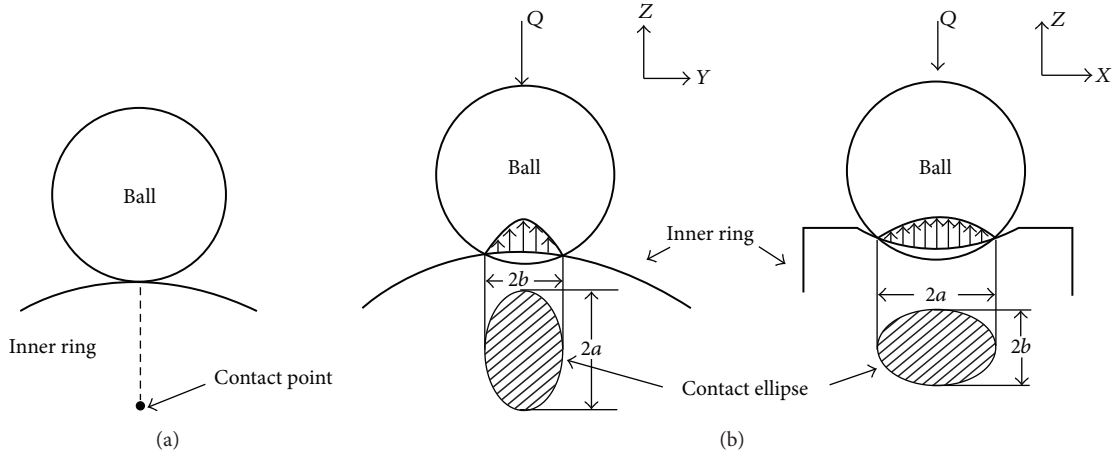


FIGURE 4: The contact area between the ball and raceway. (a) The contact point under no load conditions; (b) the contact ellipse under an applied load [18].

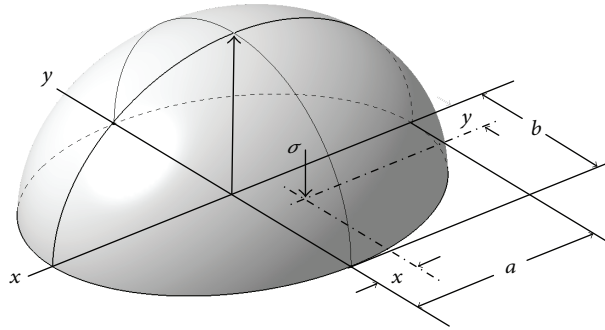


FIGURE 5: Compressive stress distribution of the ball-raceway contact.

defect (Figure 7(a)), the ball-raceway contact area at the left edge of the defect becomes smaller; at this stage, the range of  $y_j$  is  $-L - b \leq y_j \leq b - L$ , and the contact force  $Q_{j,f}$  between the  $j$ th ball and the left edge of the defect (contact force of the shadow area) is

$$Q_{j,f} = \int_{y_j-b}^{-L} dy \int_{-a\sqrt{1-((y-y_j)/b)^2}}^{a\sqrt{1-((y-y_j)/b)^2}} \sigma dx, \quad (11)$$

$$-L - b \leq y_j \leq b - L.$$

Figure 7(b) shows that there is no contact between the ball and the edge of the defect. When a ball enters the defect, if the contact force of the inner raceway is smaller, the speed of the bearing is faster, or the defect is larger, the sinking depth of the ball decreases, and the ball is unable to contact the edges of the defect. Thus, the contact force is zero. For this condition ( $b < L$ ), the contact force is

$$Q_{j,f} = 0, \quad b - L \leq y_j \leq L - b. \quad (12)$$

Figure 7(c) shows that the ball is in contact with both edges of the defect; this condition is the opposite of that in Figure 7(b). For this condition ( $b > L$ ), the contact force is

$$Q_{j,f} = \int_{y_j-b}^{-L} dy \int_{-a\sqrt{1-((y-y_j)/b)^2}}^{a\sqrt{1-((y-y_j)/b)^2}} \sigma dx$$

$$+ \int_{y_j+b}^L dy \int_{-a\sqrt{1-((y-y_j)/b)^2}}^{a\sqrt{1-((y-y_j)/b)^2}} \sigma dx, \quad (13)$$

$$L - b \leq y_j \leq b - L.$$

In Figure 7(d), as the ball exits the defect, the contact area becomes larger, the range of  $y_j$  is  $L - b \leq y_j \leq L + b$ , and the contact force between the ball and the right edge of the defect is

$$Q_{j,f} = \int_{y_j+b}^L dy \int_{-a\sqrt{1-((y-y_j)/b)^2}}^{a\sqrt{1-((y-y_j)/b)^2}} \sigma dx, \quad (14)$$

$$L - b \leq y_j \leq L + b.$$

For the ball bearing with a localized defect on the raceway, the centre of the contact ellipse is  $y_j$ , its angular position on the outer raceway is equal to the angular position of the ball centre, and the angular position of the defect on the outer raceway is  $\alpha_{out,f}$ . When the ball moves near the defect, the relationship between  $y_j$  and  $\alpha_{out,f}$  is as follows:

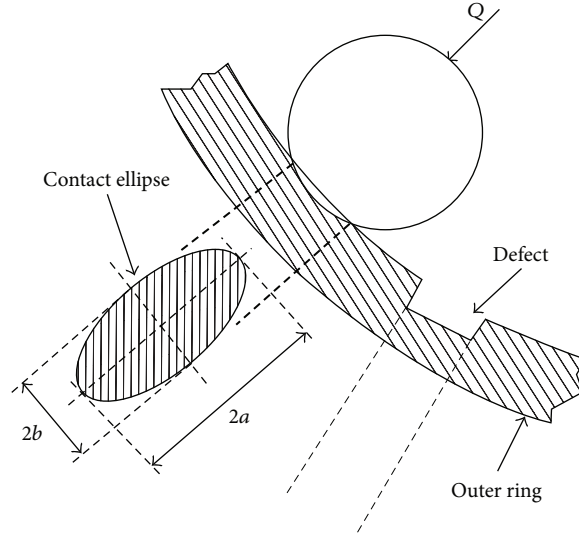


FIGURE 6: The ball-raceway contact area and a defect on the outer ring.

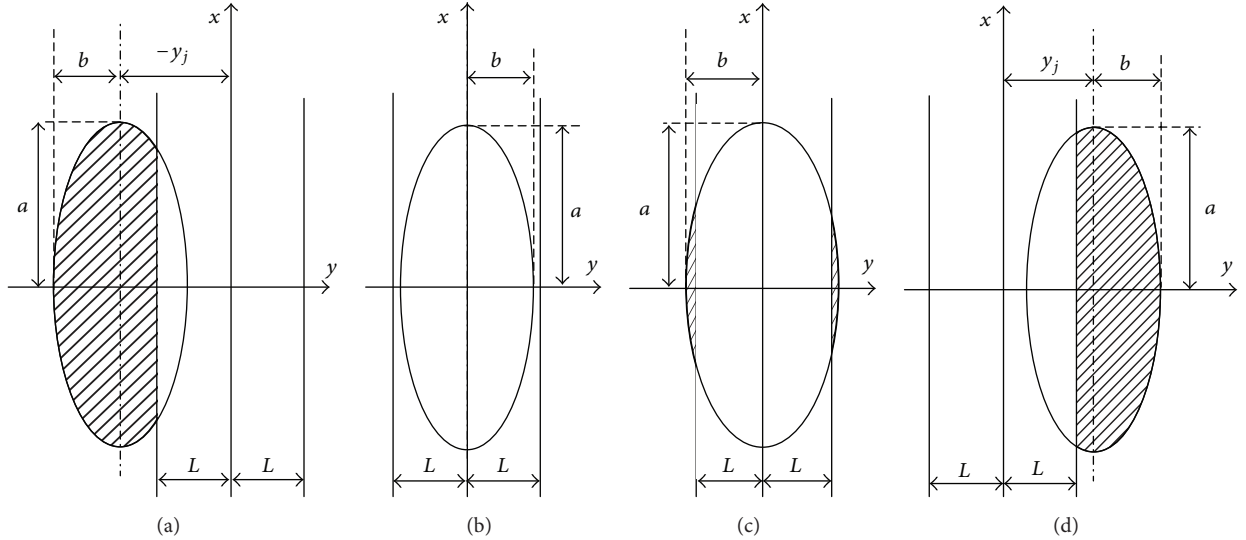


FIGURE 7: The variation of the ball-raceway contact area at the defect edge.

$$\alpha_{out,j} = \alpha_{out,f} + \frac{y_j}{R_o}, \quad y_j \ll R_o. \quad (15)$$

3.4. *Calculation of the Contact Force.* The contact forces between the  $j$ th ball and the raceways are given by  $Q_{in,j}$  and  $Q_{out,j}$ :

$$\begin{aligned} Q_{out,j} &= K_{out} \delta_{out}^{3/2}, \\ Q_{in,j} &= K_{in} \delta_{in}^{3/2}. \end{aligned} \quad (16)$$

When a ball passes the defect, the contact force between the ball and the outer raceway in the defect area is given by

$$\begin{aligned} Q_{out,j} &= Q_{j,f}, \\ \alpha_{out,f} - \frac{(L+b)}{R_o} &\leq \alpha_{out,j} \leq \alpha_{out,f} + \frac{(L+b)}{R_o}. \end{aligned} \quad (17)$$

The sums of the contact forces between the balls and the raceways in the  $x$ -axis and  $y$ -axis directions are as follows:

$$\begin{aligned} Q_{in,y} &= \sum_{j=1}^n Q_{in,j} \cdot \sin \alpha_{in,j}, \\ Q_{in,x} &= \sum_{j=1}^n Q_{in,j} \cdot \cos \alpha_{in,j}, \\ Q_{out,y} &= \sum_{j=1}^n Q_{out,j} \cdot \sin \alpha_{out,j}, \\ Q_{out,x} &= \sum_{j=1}^n Q_{out,j} \cdot \cos \alpha_{out,j}. \end{aligned} \quad (18)$$

3.5. *Damping.* The damping coefficient  $c_b$  of the balls resulting from the built-up oil film during rotation is as follows [19]:

$$0.25 \times 10^{-5} \times K_{\text{lin}} \leq c_b \leq 2.5 \times 10^{-5} \times K_{\text{lin}}. \quad (19)$$

The shaft and housing damping coefficients are calculated using the following [20]:

$$c_s = \frac{LF \cdot K_s}{\omega_{\text{ext}}}, \quad (20)$$

where  $K_{\text{lin}}$  is the linear stiffness of the bearing, the loss factor LF depends on the material,  $\omega_{\text{ext}}$  is the excitation frequency, and  $K_s$  is the stiffness of the support shaft, which can be calculated by the finite element software ANSYS. The values of the parameters in (19) and (20) are  $K_{\text{lin}} = 3.34 \times 10^4$  N/mm,  $LF = 0.01$ ,  $K_s = 3.70 \times 10^4$  N/mm, and  $\omega_{\text{ext}} = 30$ .

The damping forces between  $j$ th ball and the raceways can be expressed as  $F_{d,\text{in},j} = c_b \cdot \dot{\delta}_{\text{in},j}$  and  $F_{d,\text{out},j} = c_b \cdot \dot{\delta}_{\text{out},j}$ , and the total contact damping forces acting on the inner and outer raceways in the  $x$ -axis and  $y$ -axis directions are given by

$$\begin{aligned} F_{d,\text{in},x} &= \sum_{j=1}^n F_{d,\text{in},j} \cdot \cos \alpha_{\text{in},j}, \\ F_{d,\text{out},x} &= \sum_{j=1}^n F_{d,\text{out},j} \cdot \cos \alpha_{\text{out},j}, \\ F_{d,\text{in},y} &= \sum_{j=1}^n F_{d,\text{in},j} \cdot \sin \alpha_{\text{in},j}, \\ F_{d,\text{out},y} &= \sum_{j=1}^n F_{d,\text{out},j} \cdot \sin \alpha_{\text{out},j}. \end{aligned} \quad (21)$$

3.6. *Vibration Equations of the Bearings.* According to the bearing system model shown in Figure 2, the vibration equations for the inner and outer rings of the ball bearing in the  $x$ -axis and  $y$ -axis directions are as follows:

$$\begin{aligned} M_{\text{in}} \cdot \ddot{y}_{\text{in}} + c_s \cdot \dot{y}_{\text{in}} + K_s \cdot y_{\text{in}} + Q_{\text{in},y} + F_{d,\text{in},y} \\ = -M_{\text{in}}g, \\ M_{\text{in}} \cdot \ddot{x}_{\text{in}} + c_s \cdot \dot{x}_{\text{in}} + K_s \cdot x_{\text{in}} + Q_{\text{in},x} + F_{d,\text{in},x} = 0, \\ M_{\text{out}} \cdot \ddot{x}_{\text{out}} + F_{d,\text{out},x} - Q_{\text{out},x} = 0, \\ M_{\text{out}} \cdot \ddot{y}_{\text{out}} + F_{d,\text{out},y} - Q_{\text{out},y} = -M_{\text{out}}g - F_l, \end{aligned} \quad (22)$$

where  $M_{\text{in}}$  is the mass of the inner ring and shaft,  $M_{\text{out}}$  is the mass of the outer ring and housing, and  $F_l$  is the gravitational load. The vibration equation of the  $j$ th ball in the outer ring's radial direction is given by

$$\begin{aligned} m \cdot \ddot{\delta}_{\text{out},j} + F_{d,\text{out},j} + F_{d,\text{in},j} \cdot \cos(\alpha_{\text{in},j} - \alpha_{\text{out},j}) \\ = -Q_{\text{out},j} + Q_{\text{in},j} \cdot \cos(\alpha_{\text{in},j} - \alpha_{\text{out},j}) - m\omega^2 r, \end{aligned} \quad (23)$$

where  $\omega = 2\pi f_c$ , the initial coordinates, velocities, and acceleration of the raceways and balls are set to reasonable

TABLE 1: Parameters of the type 6204 bearing.

Inner groove radius	4.088 mm
Outer groove radius	4.168 mm
Inner raceway radius	13.281 mm
Outer raceway radius	21.226 mm
Number of balls	8
Ball radius	3.969 mm
Radial clearance	3.25 $\mu\text{m}$

values, and the angular positions of the balls vary according to (4). The fourth-order Runge-Kutta algorithm is used to solve (22) and (23) with the commercial software MATLAB to calculate the motion parameters of each component. The damping and stiffness values in the numerical model are given as follows:  $c_s = 0.74$  Ns/mm,  $c_b = 0.8$  Ns/mm,  $K_i = 8.98 \times 10^5$  N/mm<sup>3/2</sup>, and  $K_o = 8.98 \times 10^5$  N/mm<sup>3/2</sup>. The flow chart of the numerical computation is shown in Figure 8.

## 4. Experimental Setup

The experimental rig and the bearing (Type 6204) are shown in Figure 9. The mass of the housing is 1.345 kg; additional loads of 4.9 N, 9.8 N, 14.7 N, and 19.6 N are applied to the housing in the vertical direction. When a ball passes over the defect on the outer raceway, the periodic vibration response is recorded by the acceleration sensor above the bearing housing. The experimental vibration signals and the numerical signals are analysed by the resonance demodulation method, which is used to diagnose early fault defects of rolling bearings; [21] introduces the theory of this method in detail.

The type 6204 bearing shown in Figure 9(b) has a localized defect on the outer raceway. The defect is 0.2 mm wide, 14.0 mm long, and 1.0 mm deep, and it is located vertically in the loaded region. The rotational frequency of the bearing is 1800 rpm. The bearing parameters are given in Table 1.

## 5. Experimental and Numerical Results

5.1. *Comparison between Experimental Signals and Numerical Signals.* Figure 10 shows the vibration responses of the experimental and numerical signals under the different load conditions. The results show that, with an increase of the additional load, the amplitude of the vibration signals increases; because the bearing has a random vibration, the vibration amplitude of the numerical signals coincides somewhat with the mean vibration amplitude of the experimental signals.

Figure 11 shows the frequency spectra of the experimental and numerical signals under the different load conditions. For the ball bearing with a localized defect on the outer raceway, the theoretical fault characteristic frequency (ball pass frequency for the outer race) is 92.39 Hz. The vibration amplitude and frequency of the fault signals are given in Table 2. The fault characteristic frequencies of the

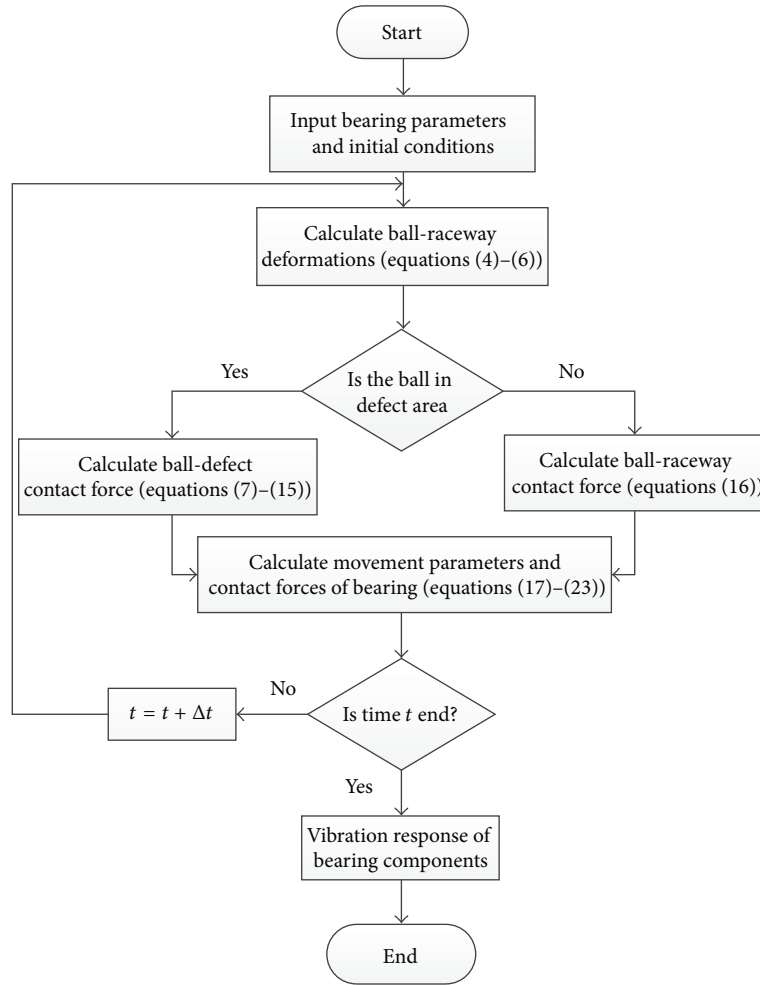
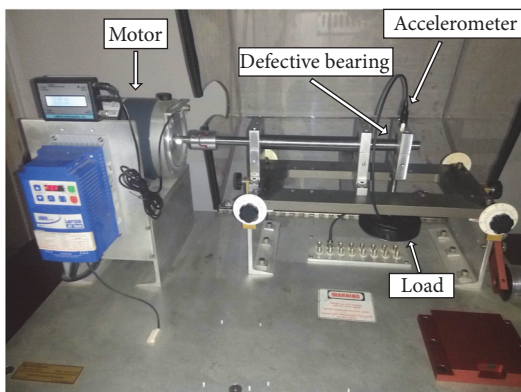
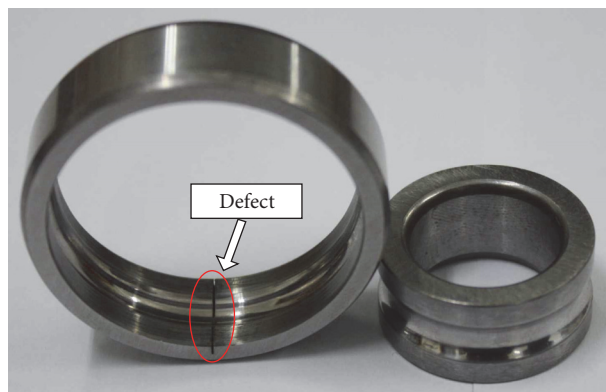


FIGURE 8: Flow chart of the numerical computation.



(a) Experimental rig



(b) Localized defect on the outer raceway

FIGURE 9

experimental signals and the numerical signals are consistent and are very similar to the theoretical fault characteristic frequency. The vibration amplitudes of the experimental and numerical signals both increase with increases of the additional load because a greater load will cause the impact

forces between the balls and the defect to increase, which will increase the vibration amplitudes of the signals. In addition, the vibration amplitudes of the numerical signals are slightly greater than those of the experimental signals. The defect's surface morphology may have an effect on the distribution of

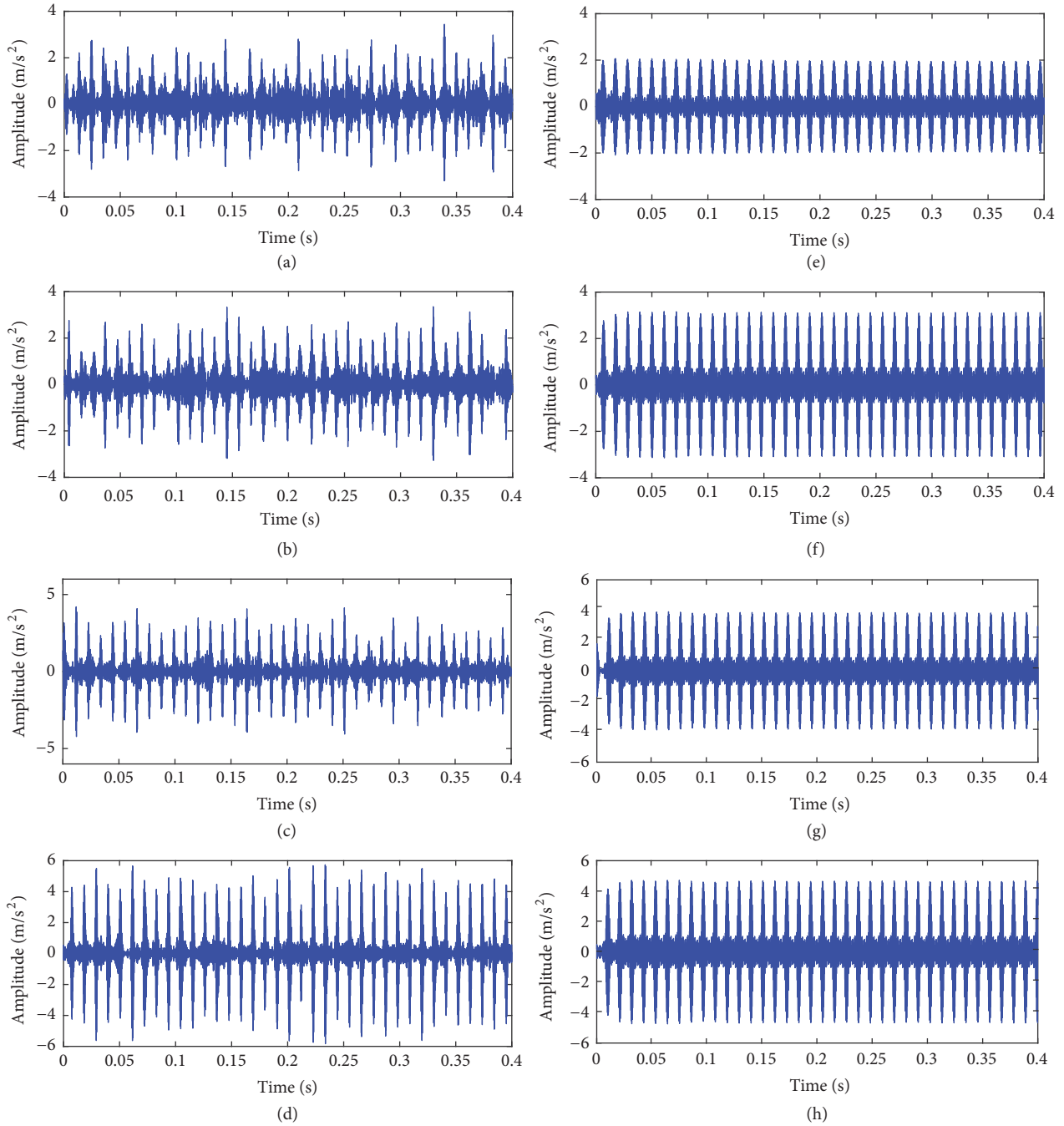


FIGURE 10: Vibration responses of the experimental signals and the numerical signals under different loads. Experimental signals: (a) 4.9 N, (b) 9.8 N, (c) 14.7 N, and (d) 19.6 N. Numerical signals: (e) 4.9 N, (f) 9.8 N, (g) 14.7 N, and (h) 19.6 N.

TABLE 2: Comparison of the fault signals in Figure 11.

Load (N)	Numerical signals		Experimental signals	
	Frequency (Hz)	Amplitude ( $m/s^2$ )	Frequency (Hz)	Amplitude ( $m/s^2$ )
4.9	92.19	85.92	92.19	60.49
9.8	92.19	119.7	92.19	74.69
14.7	92.19	150.1	92.19	93.74
19.6	92.19	184.9	92.97	169.4

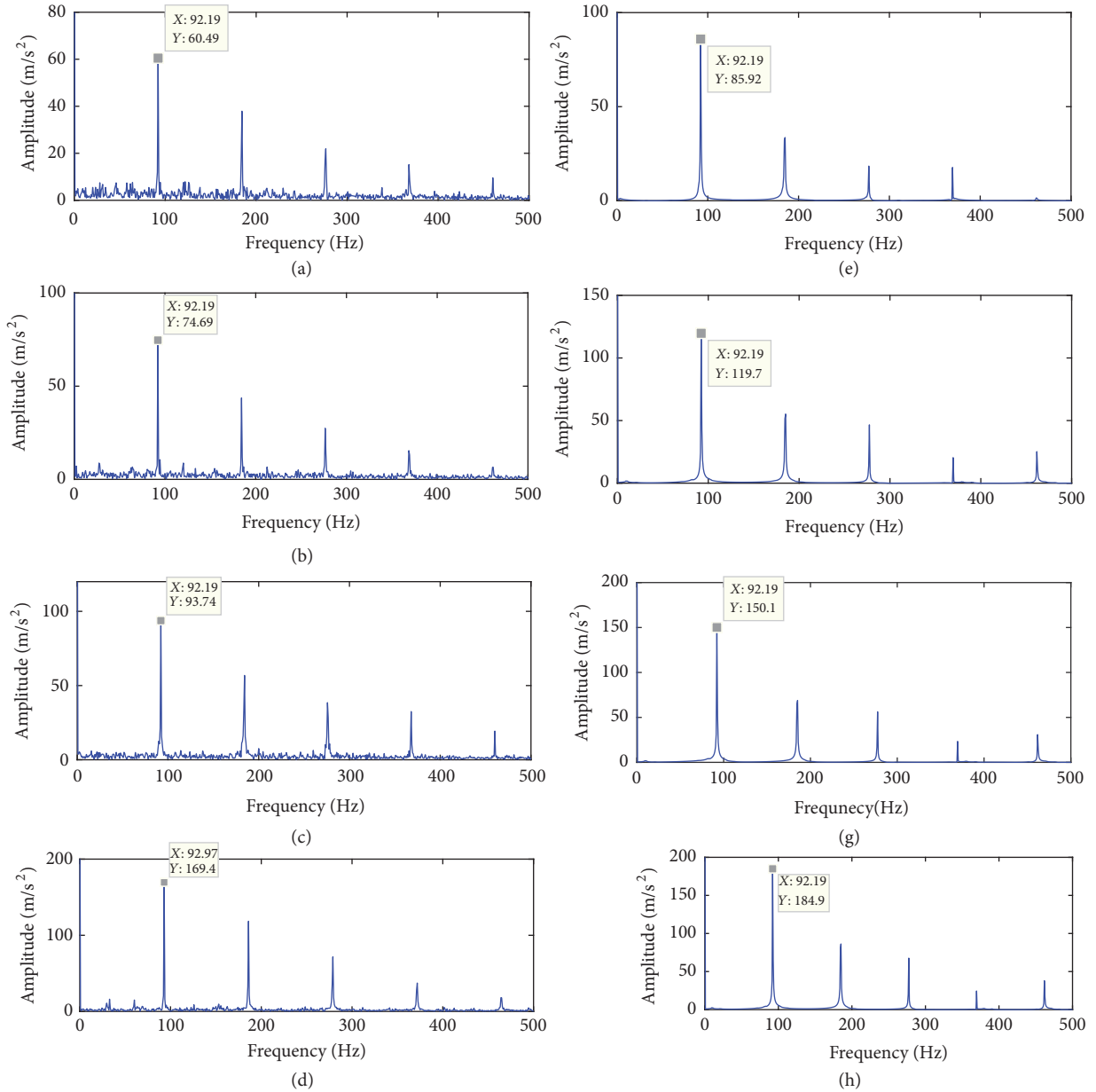


FIGURE 11: Frequency spectra of the experimental signals and the numerical signals under different loads. Experimental signals: (a) 4.9 N, (b) 9.8 N, (c) 14.7 N, and (d) 19.6 N. Numerical signals: (e) 4.9 N, (f) 9.8 N, (g) 14.7 N, and (h) 19.6 N.

the contact stress and the shape of the contact area; this effect will be studied in future articles.

## 5.2. Comparison between the Proposed Model and the Traditional Model

### 5.2.1. Sinking Depth of the Balls.

In contrast to the traditional model, which only considers the effect of the defect size on the sinking depth of balls in the defect area, the model proposed in this paper considers both the defect size and the load. Figure 12 shows the relationships among the maximum sinking depth of the balls, the size of the defect, and the load for the traditional model and the proposed model. The sinking depth of the ball in the traditional model is

independent of the load, whereas, in the proposed model, the maximum sinking depth increases with increases of the load and the size of the defect.

The paths of the balls passing through the defect area under different loads calculated with the proposed model are shown in Figure 13. The sinking depths of the balls increase with increasing load. The sinking depths of the balls shown in Figure 13 are listed in Table 3; the trend is consistent with that in Figure 12(b) because a greater applied load causes greater acceleration and velocity of the balls, as shown in Figures 14 and 15.

Table 4 shows the relationships between the contact ellipse and the sinking depth of the ball. In Figure 13, the sinking depth of the ball ranges between  $0.8 \times 10^{-3}$  mm and

TABLE 3: Relationship between the additional load and the change of the sinking depth of the balls in Figure 13.

Additional load (N)	Change of sinking depth $\Delta$ ( $10^{-3}$ mm)	
	Traditional model	Proposed model
4.9		0.70
9.8	1.26	0.80
14.7		0.91
19.6		1.02

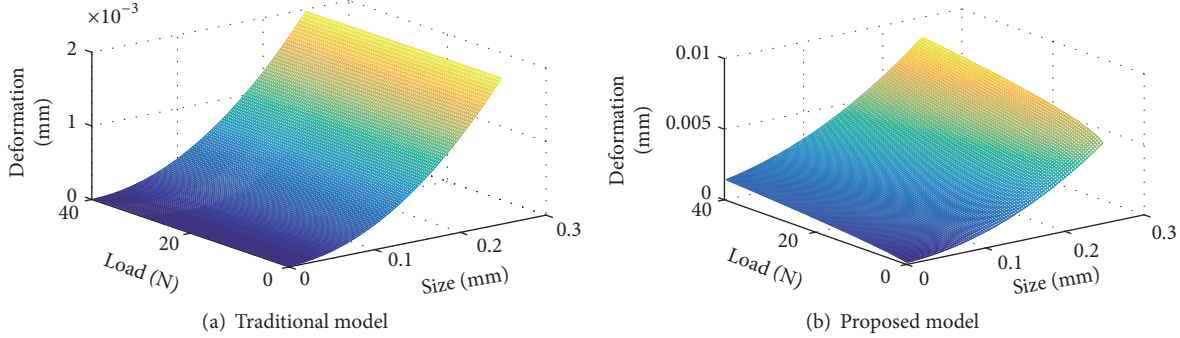


FIGURE 12: Maximum sinking depth of the balls at the centre of the defect.

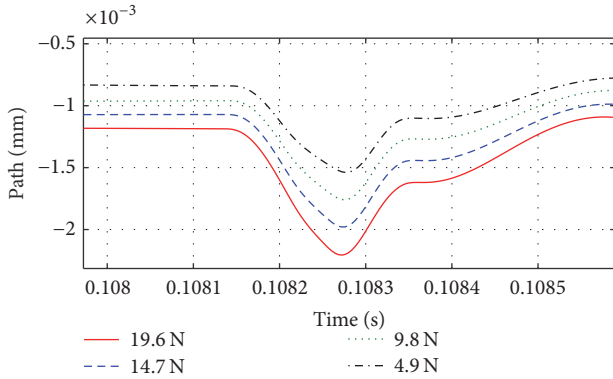


FIGURE 13: Paths of the balls passing through the defect area under different loads.

$2.2 \times 10^{-3}$  mm; the values of the semimajor and semiminor axes of the contact ellipse based on this range are given in Table 4. When the sinking depth of the ball is  $0.8 \times 10^{-3}$  mm, the ball does not enter the defect; at this stage, the semiminor axis of the contact area is  $0.0485 \times 2 = 0.097$  mm, and the width of the defect is 0.2 mm. The size of the contact ellipse is clearly nonnegligible because the ball-raceway contact force was affected by the defect before the ball enters the defect.

When the sinking depth of the ball is  $2.2 \times 10^{-3}$  mm, the semiminor axis of the contact area is  $0.0805 \times 2 = 0.1610$  mm, which is smaller than the width of the defect, so there is no contact between the ball and the defect edges when the ball is in the centre of the defect; at this stage, contact force between the ball and the outer raceway is zero. The ball has left the defect area on the outer raceway before it reaches the maximum sinking depth  $6 \times 10^{-3}$  mm.

In general, the sinking depth in Figure 12(b) is the maximum sinking depth when the ball stays at the defect area. In Figure 13, the ball has a velocity when it passes through the defect area, the movement of the ball will affect the paths of the balls.

**5.2.2. Contact Force.** The ball-raceway contact forces of the traditional and proposed models in the defect area under different loads are shown in Figure 16. In the traditional model, the contact force changes suddenly when the ball enters and leaves the defect area, whereas there is a continuous and gradual change in the proposed model. The traditional model presented in this paper is only a basic model; the contact forces of the traditional models in [11, 12] also have nonabrupt changes. We do not compare the differences between the changing processes of the contact forces in the proposed model and the traditional models. Whether the traditional model or the proposed model is used, the change of the contact forces increases with an increase in the applied load. There are two other differences between these two models.

(1) The duration of the change in the contact force in the defect area in the proposed model is greater than that in the traditional models.

(2) The change of the contact force in the traditional model is smaller than that in the proposed model; when the ball is at the centre of the defect, the contact force between the ball and the raceway is zero in the new model.

The reasons for these differences are as follows.

(1) The traditional model neglects the contact areas between the ball and the raceways; a change occurs only when the centre of the ball enters the defect.

(2) When the minor axis of the contact ellipse is smaller than the size of the defect, the ball cannot come into contact with the raceway when it passes over the defect; thus, the contact force becomes zero.

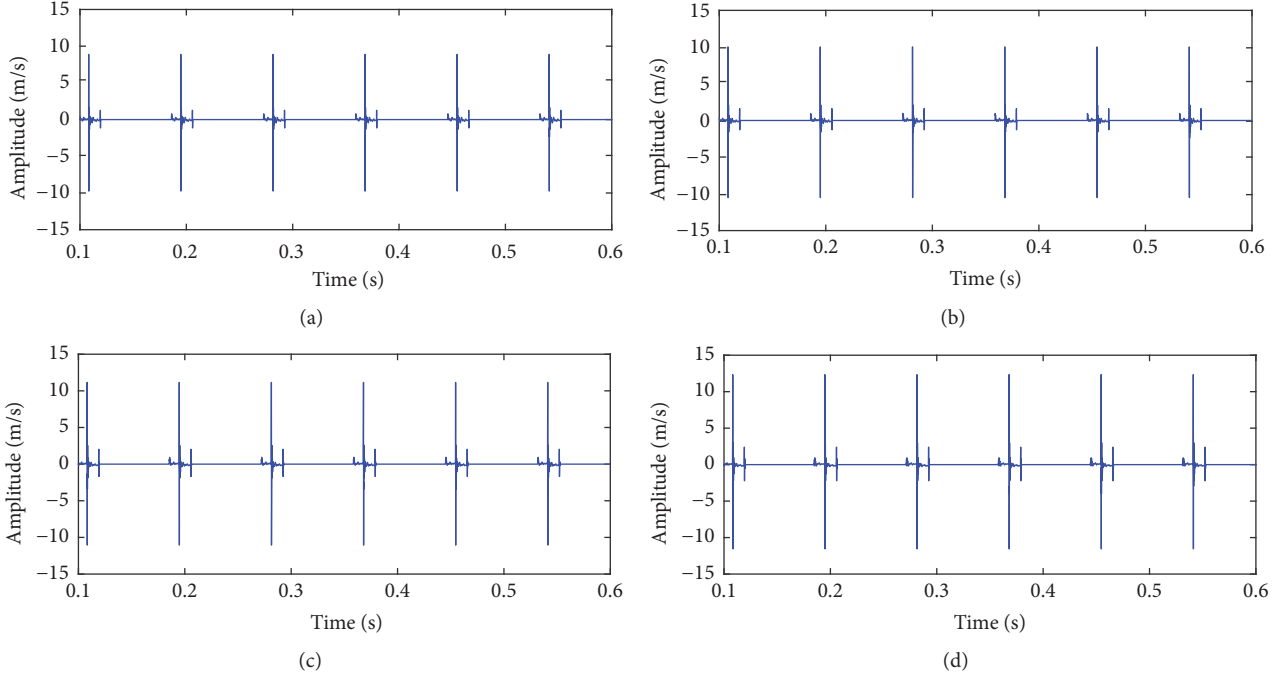


FIGURE 14: Velocities of the balls in the radial direction in the defect area under different loads: (a) 4.9 N, (b) 9.8 N, (c) 14.7 N, and (d) 19.6 N.

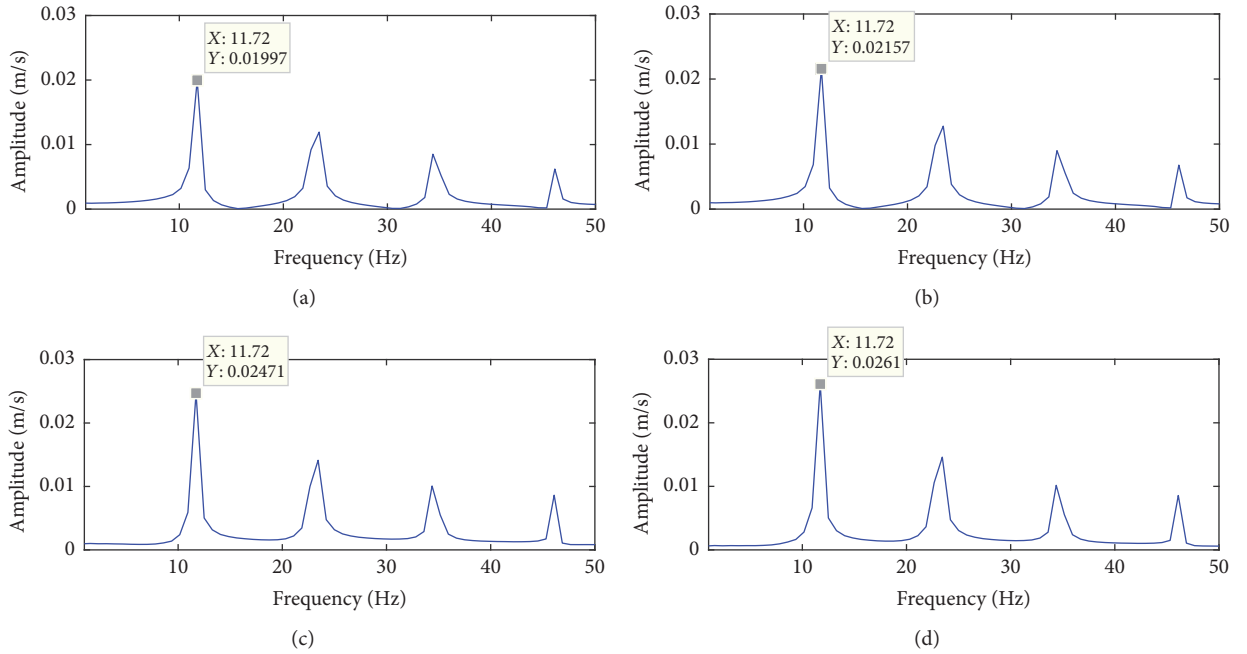


FIGURE 15: The spectra of velocities of the balls in the radial direction in the defect area under different loads: (a) 4.9 N, (b) 9.8 N, (c) 14.7 N, and (d) 19.6 N.

In Figure 16(a), the duration of the change in the contact force is the time required for the ball to pass over the defect. The width of the defect is  $2L$ , and the velocity of the ball is  $2\pi f_c R_o$ ; therefore, the duration of the change in the contact force in the defect area is  $L/\pi f_c R_o$ . For the experiment in this article, the duration is  $1.298 \times 10^{-4}$  s.

As shown in Figure 16(b), the duration of the change in the contact force is greater than that in the traditional model.

When the ball is still far from the defect edge, the contact force decreases. In the proposed model, this distance is the semiminor axis of the contact ellipse, the time for the ball to travel this distance is  $b/2\pi f_c R_o$ , and the total duration of the change in the contact force when the ball passes over the defect is  $(L + b)/\pi f_c R_o$ . The value of the semiminor axis of the contact ellipse is constantly changing and is determined by the applied load on the ball. Therefore, with an increase of

TABLE 4: Relationships of  $\Delta$ - $a$ - $b$ .

Sinking depth ( $10^{-3}$ mm)	Semimajor axis $a$ (mm)	Seminor axis $b$ (mm)
0.8	0.3046	0.0485
1.0	0.3405	0.0543
1.2	0.3730	0.0595
1.4	0.4029	0.0642
1.6	0.4307	0.0687
1.8	0.4569	0.0728
2.0	0.4816	0.0768
2.2	0.5051	0.0805

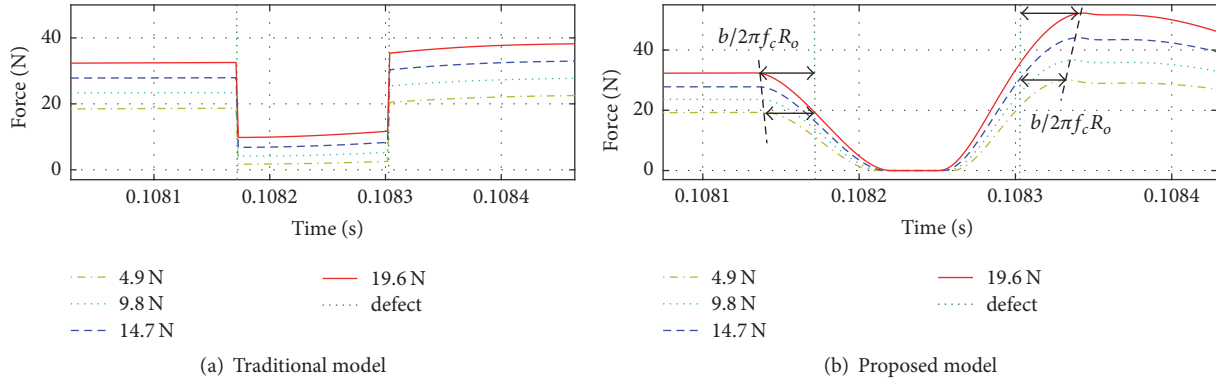


FIGURE 16: Ball-raceway contact forces in the defect area under different loads.

the applied additional load (from 4.9 N to 19.6 N), the total duration of the change in the contact force becomes longer.

## 6. Conclusions

A model for predicting the vibration response of ball bearings with a localized defect based on the Hertzian contact stress distribution is proposed. The mechanism of the vibration response in the defect area and the solution method of the traditional model are analysed. The Hertzian contact stress distribution and the contact area are used to calculate the ball-raceway contact force in the defect area. An experiment using a ball bearing with a defect in the outer raceway is performed, and the vibration responses of the experimental and numerical signals are compared to verify the applicability of the proposed model. Comparisons between the traditional model and the proposed model show that, unlike in the traditional model, in the proposed model, with an increase in the applied load, the sinking depth of balls in the defect area increases, and the contact force begins to change before the ball enters the defect region and stops changing after the ball leaves the defect region.

## Conflicts of Interest

The authors declare that they have no conflicts of interest.

## Acknowledgments

This work was supported by the National Natural Science Foundation of China (51175102) and the Fundamental

Research Funds for the Central Universities (Grant no. HIT.NSRIF.201638).

## References

- [1] S. Singh, C. Q. Howard, and C. H. Hansen, "An extensive review of vibration modelling of rolling element bearings with localised and extended defects," *Journal of Sound and Vibration*, vol. 357, pp. 300–330, 2015.
- [2] P. D. McFadden and J. D. Smith, "Model for the vibration produced by a single point defect in a rolling element bearing," *Journal of Sound and Vibration*, vol. 96, no. 1, pp. 69–82, 1984.
- [3] P. D. McFadden and J. D. Smith, "The vibration produced by multiple point defects in a rolling element bearing," *Journal of Sound and Vibration*, vol. 98, no. 2, pp. 263–273, 1985.
- [4] A. Rafsanjani, S. Abbasion, A. Farshidianfar, and H. Moeenfar, "Nonlinear dynamic modeling of surface defects in rolling element bearing systems," *Journal of Sound and Vibration*, vol. 319, no. 3–5, pp. 1150–1174, 2009.
- [5] N. Tandon and A. Choudhury, "An analytical model for the prediction of the vibration response of rolling element bearings due to a localized defect," *Journal of Sound and Vibration*, vol. 205, no. 3, pp. 275–292, 1997.
- [6] A. Choudhury and N. Tandon, "Vibration response of rolling element bearings in a rotor bearing system to a local defect under radial load," *Journal of Tribology*, vol. 128, no. 2, pp. 252–261, 2006.
- [7] N. Sawalhi and R. B. Randall, "Simulating gear and bearing interactions in the presence of faults. Part I. The combined gear bearing dynamic model and the simulation of localised bearing faults," *Mechanical Systems and Signal Processing*, vol. 22, no. 8, pp. 1924–1951, 2008.

- [8] N. Sawalhi and R. B. Randall, "Simulating gear and bearing interactions in the presence of faults. Part II. Simulation of the vibrations produced by extended bearing faults," *Mechanical Systems and Signal Processing*, vol. 22, no. 8, pp. 1952–1966, 2008.
- [9] N. S. Feng, E. J. Hahn, and R. B. Randall, "Using transient analysis software to simulate vibration signals due to rolling element bearing defects," *Applied Mechanics*, pp. 689–694, 2002.
- [10] V. N. Patel, N. Tandon, and R. K. Pandey, "A dynamic model for vibration studies of deep groove ball bearings considering single and multiple defects in races," *Journal of Tribology*, vol. 132, no. 4, Article ID 041101, 10 pages, 2010.
- [11] V. N. Patel, N. Tandon, and R. K. Pandey, "Vibration studies of dynamically loaded deep groove ball bearings in presence of local defects on races," in *Proceedings of the 2013 International Conference on Design and Manufacturing, IConDM 2013*, pp. 1582–1591, India, July 2013.
- [12] M. S. Patil, J. Mathew, P. K. Rajendrakumar, and S. Desai, "A theoretical model to predict the effect of localized defect on vibrations associated with ball bearing," *International Journal of Mechanical Sciences*, vol. 52, no. 9, pp. 1193–1201, 2010.
- [13] A. Moazen Ahmadi, D. Petersen, and C. Howard, "A non-linear dynamic vibration model of defective bearings - The importance of modelling the finite size of rolling elements," *Mechanical Systems and Signal Processing*, vol. 52-53, no. 1, pp. 309–326, 2015.
- [14] J. Liu, Y. Shao, and T. C. Lim, "Vibration analysis of ball bearings with a localized defect applying piecewise response function," *Mechanism and Machine Theory*, vol. 56, pp. 156–169, 2012.
- [15] J. L. Gomez, A. Bourdon, H. André, and D. Rémond, "Modelling deep groove ball bearing localized defects inducing instantaneous angular speed variations," *Tribology International*, vol. 98, pp. 270–281, 2016.
- [16] C. Mishra, A. K. Samantaray, and G. Chakraborty, "Ball bearing defect models: A study of simulated and experimental fault signatures," *Journal of Sound and Vibration*, vol. 400, pp. 86–112, 2017.
- [17] A. Chen and T. R. Kurfess, "A new model for rolling element bearing defect size estimation," *Measurement*, vol. 114, pp. 144–149, 2018.
- [18] T. A. Harris, *Rolling Bearing Analysis*, Wiley, 1984.
- [19] S. Khanam, J. K. Dutt, and N. Tandon, "Impact force based model for bearing local fault identification," *Journal of Vibration and Acoustics*, vol. 137, no. 5, Article ID 051002, 2015.
- [20] G. Genta, "On a persistent misunderstanding of the role of hysteretic damping in rotordynamics," *Journal of Vibration and Acoustics*, vol. 126, no. 3, pp. 459–461, 2004.
- [21] D. R. Harting, "Incipient failure detection by demodulated resonance analysis," *Instrumentation Technology*, vol. 9, pp. 59–63, 1977.

## Research Article

# IP Controller Design for Uncertain Two-Mass Torsional System Using Time-Frequency Analysis

Jing Cui,<sup>1</sup> Jiayu Ye,<sup>1</sup> and Zhongyi Chu <sup>2</sup>

<sup>1</sup>College of Mechanical Engineering and Applied Electronics Technology, Beijing University of Technology, Beijing 100022, China

<sup>2</sup>School of Instrument Science and Opto-Electronics, Beihang University, Beijing 100191, China

Correspondence should be addressed to Zhongyi Chu; [chuzystar@gmail.com](mailto:chuzystar@gmail.com)

Received 20 July 2017; Revised 28 November 2017; Accepted 26 February 2018; Published 29 March 2018

Academic Editor: Naveed Ahmad

Copyright © 2018 Jing Cui et al. This is an open access article distributed under the Creative Commons Attribution License, which permits unrestricted use, distribution, and reproduction in any medium, provided the original work is properly cited.

With the development of industrial production, drive systems are demanded for larger inertias of motors and load machines, whereas shafts should be lightweight. In this situation, it will excite mechanical vibrations in load side, which is harmful for industrial production when the motor works. Because of the complexity of the flexible shaft, it is often difficult to calculate stiffness coefficient of the flexible shaft. Furthermore, only the velocity of driving side could be measured, whereas the driving torque, the load torque, and the velocity of load side are immeasurable. Therefore, it is inconvenient to design the controller for the uncertain system. In this paper, a low-order IP controller is designed for an uncertain two-mass torsional system based on polynomial method and time-frequency analysis (TFA). IP controller parameters are calculated by inertias of driving side and load side as well as the resonant frequency based on polynomial method. Therein, the resonant frequency is identified using the time-frequency analysis (TFA) of the velocity step response of the driving side under the open-loop system state, which can not only avoid harmful persistent start-stop excitation signal of the traditional method, but also obtain high recognition accuracy under the condition of weak vibration signal submerged in noise. The effectiveness of the designed IP controller is verified by groups of experiments. Experimental results show that good performance for vibration suppression is obtained for uncertain two-mass torsional system in a medium-low shaft stiffness condition.

## 1. Introduction

Drive systems have a pivotal position in the field of modern industry including robots, rolling mills, textile, or paper machines [1]. Most of these systems can be reduced to a model whose motor and load machine are connecting through a shaft. With the increasing levels of industrial production, these systems are demanded for larger inertias of motors and load machines, whereas shafts should be lightweight. In this case, the model is turned into a two-mass torsional system, as the shafts could no longer be regarded as rigid. Excessive shaft twists will be generated easily when the motor has just been started and exciting mechanical vibrations not only are affecting the performance of drive systems greatly, but also are able to lead to instability of the entire drive system [2].

On the other hand, for these industrial drive systems, usually the velocity of driving side can be measured, whereas the driving torque, the load torque, and the velocity of load

side are immeasurable [3]. In this case, torsional vibrations of the load side must be suppressed by only using the velocity feedback of the driving side, such as using PI speed controller and additional feedback [4],  $H_\infty$  feedback controller and IP-position controller [5], neural network speed controller [6], and controllers based on polynomial method [7]. Herein, low-order IP controllers occupied an important position in engineering application due to the characteristics of simple structure, convenient parameters calculation, and easy application. However, the system models are generally considered to be known when controllers are designed and flexible shaft stiffness and resonant frequency of the system are given directly in the parameter list, or the resonance frequency is obtained by drawing the Bode plot based on certain open-loop system model [4–6].

According to the actual engineering applications, like rolling machines, machine tools, injection molding machines, and other mechanical systems using flexible

connection, the resonant frequency of the system is difficult to measure due to the unknown stiffness coefficient of the flexible shaft that makes the system uncertain. Therefore, it is inconvenient to design the controller with the unknown resonant frequency of the system, especially only with the measured driving side velocity.

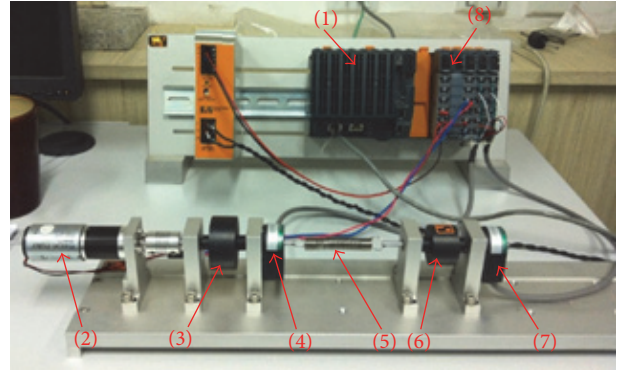
To solve this problem, many studies of frequency identification had been implemented: the Fast Fourier Transform (FFT) is one of the most widely used and well-established methods for frequency domain analysis. Nonetheless, owing to the characteristic of the velocity step response of drive side in which tiny vibration is submerged in noise, using the FFT cannot identify the resonance frequency definitely. Meanwhile, frequency response of the system can be obtained by using Welch-Method in current and speed signal with Pseudo-Random Binary Signals (PRBS) excitation [8, 9], the measured frequency response functions (FRFs) of drive-side and load-side velocities with Random Binary Signal (RBS) excitation [10]. Nevertheless, regardless of whether the excitation signal is PRBS or RBS, persistent start-stop excitation will do more harm to the system than using step signal.

In this paper, a low-order IP controller is designed based on polynomial method for uncertain two-mass torsional system. Parameters of IP controller are calculated by inertias of driving side and load side as well as the resonant frequency. Therein, owing to the uncertain system, the resonant frequency of the system as a necessary parameter for calculating IP controller parameters is recognized by using time-frequency analysis (TFA) and the conducted signal is only the velocity step response of the drive side. The effectiveness of designed IP controller is verified by groups of experiments. Experiment results show that the vibrations of the load side are well suppressed.

This paper is outlined as follows. The experimental set-up and modeling of the two-mass system are introduced in Section 2. In Section 3, the design method of IP controller for the uncertain system is briefly implemented, while it emphasizes identifying the resonant frequency of the system especially only with the measured driving side velocity. Groups of experiments are conducted in Section 4. Experiments verify that, with this approach, vibrations of the load side are suppressed very well. Finally, conclusions and future work are given in Section 5.

## 2. Experimental Set-Up and Modeling of the Two-Mass System

**2.1. Experimental Set-Up.** The experimental platform is shown in Figure 1. The test platform is controlled by the control programs which are written in AS 3.0.90 (B&R Automation Studio) on a personal computer (PC). A voltage regulator module (VRM) is used to actuate the direct current (DC) brush motor. A mass which is rigidly connected with the motor (after a planetary gear reducer) can be seen as the drive side. The drive side and load side of the system are coupled by a spring as the flexible shaft. There are two same-type encoders attached to the drive side and the load side, respectively. The resolution ratio of each encoder is



- (1) Programmable computer controller (PCC)
- (2) DC motor
- (3) Drive-side mass
- (4) Drive-side encoder
- (5) Spring
- (6) Load-side mass
- (7) Load-side encoder
- (8) Voltage regulator module (VRM)

FIGURE 1: The experimental platform.

4000 pulses/rev. The drive-side encoder is used to carry out the feedback control and to gain the velocity of the drive side for identifying the resonance frequency. The performance of IP controller is reflected by the velocity of load side, which is collected by the load-side encoder. All the experiments are implemented under the sampling time of 10 ms. The structure of the whole experimental system is shown in Figure 2.

**2.2. Modeling of the Two-Mass System.** The model of the two-mass system can be abstracted as in Figure 3. The damping has been omitted. The following formulas can be listed according to the dynamic theory:

$$\begin{aligned}
 T_s &= K_s * \int (\omega_m - \omega_l) \\
 T_m + T_s &= d\omega_m * J_m \\
 T_l - T_s &= d\omega_l * J_l.
 \end{aligned} \tag{1}$$

$J_m, J_l$  are inertias of the drive side (including the drive motor) and the load side, respectively

$T_m, T_l$  are torques of the drive side and the load side, respectively

$\omega_m, \omega_l$  are velocities of the drive side and the load side, respectively

$T_s$  is torque generated by the shaft during rotation

$K_s$  is spring coefficient.

According to (1), the block diagram of the system can be drawn as in Figure 4.

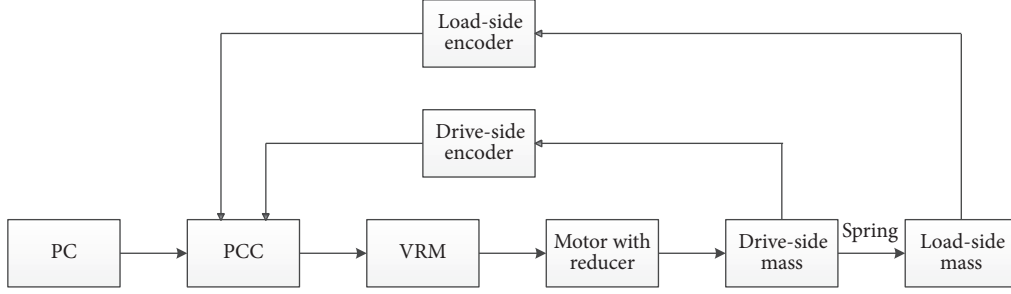


FIGURE 2: The structure of the experimental system.

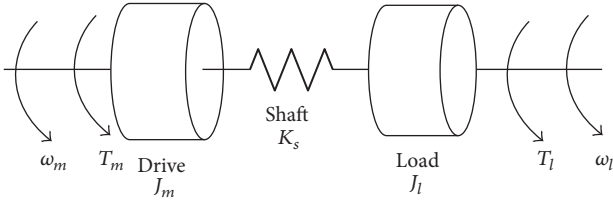


FIGURE 3: Model of the two-mass system.

From the block diagram, the transfer function between  $T_m$  and  $\omega_m$  can be written as

$$P(s) = \frac{s^2 + \omega_{\text{ares}}^2}{J_m s (s^2 + \omega_{\text{res}}^2)}, \quad (2)$$

where  $\omega_{\text{res}}$  and  $\omega_{\text{ares}}$  are the resonance frequency and antiresonance frequency, respectively.

$$\omega_{\text{res}} = \sqrt{\frac{K_s (J_m + J_l)}{J_m J_l}} \quad (3)$$

$$\omega_{\text{ares}} = \sqrt{\frac{K_s}{J_l}} \quad (4)$$

$$\omega_{\text{ares}} = \sqrt{q} \omega_{\text{res}} \quad (5)$$

$$q = \frac{J_m}{J_m + J_l}. \quad (6)$$

$q$  is defined as the inertia ratio as shown in (6).

For a generalized discussion, (2) can be standardized by replacing the complex variable  $s$  with  $s^* = s/\omega_{\text{ares}}$ .

$$P(s^*) = \frac{q(s^{*2} + 1)}{J_m \omega_{\text{ares}} (q s^{*3} + s^*)}. \quad (7)$$

For the sake of simplicity, the standardized two-mass system transfer function can be taken as

$$P_n(s^*) = \frac{s^{*2} + 1}{q s^{*3} + s^*}. \quad (8)$$

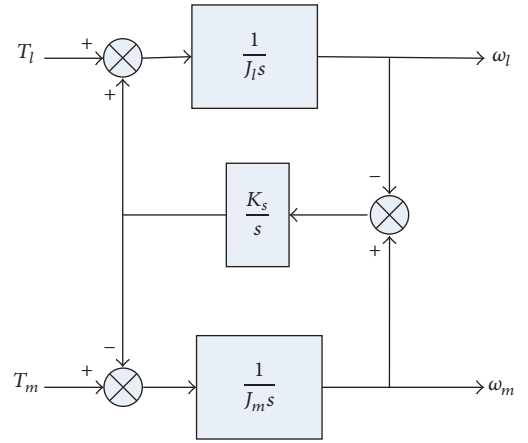


FIGURE 4: Block diagram of the two-mass system.

### 3. IP Controller Design

**3.1. IP Controller Design.** The block diagram of the closed-loop system with IP feedback controller is shown in Figure 5. The closed-loop system transfer function can be derived from the block diagram.

$$G_n(s^*) = \frac{K_i^* (s^{*2} + 1)}{q s^{*4} + K_p^* s^{*3} + (1 + K_i^*) s^{*3} + K_p^* s^* + K_i^*}. \quad (9)$$

Comparing (7) and (8), IP controller parameters  $K_p$ ,  $K_i$  can be derived as

$$K_p = \frac{K_p^* J_m \omega_{\text{ares}}}{q} \quad (10)$$

$$K_i = \frac{K_i^* J_m \omega_{\text{ares}}^2}{q},$$

where  $K_p^*$ ,  $K_i^*$  are the standardized controller parameters. By substituting (5) into (10), IP controller parameters  $K_p$ ,  $K_i$  can be rewritten as

$$K_p = \frac{K_p^* J_m \omega_{\text{res}}}{\sqrt{q}} \quad (11)$$

$$K_i = K_i^* J_m \omega_{\text{res}}^2.$$

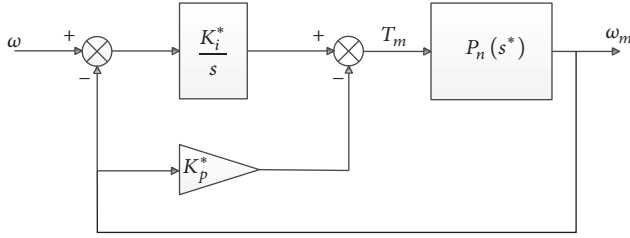


FIGURE 5: Block diagram of the closed-loop system.

According to [11, 12], IP controller is applied when inertia ratio  $q < 1/3$  and  $K_p^*$ ,  $K_i^*$  can be selected as follows in order to have a good performance with sufficient damping provided:

$$\begin{aligned} K_p^* &= \frac{4}{5\sqrt{2}}, \\ K_i^* &= \frac{1}{4}. \end{aligned} \quad (12)$$

From (11), the inertias of drive side (including the drive motor) and load side as well as the resonance frequency are needed to calculate IP controller parameters. The inertias can be obtained by conventional calculating or 3D modeling software.

**3.2. Identification of the Resonance Frequency.** As mentioned in Section 1, for a two-mass torsional system, usually the velocity of the drive side can be measured. So, vibration suppression of the load side is only able to use the velocity feedback of the driving side. The velocity step responses of the drive side and the load side are given in Figures 6(a) and 6(b). Using the FFT to identify them is attempted and their results are given in Figures 6(c) and 6(d), respectively. According to the results, it is obvious that only the FFT can identify the resonance frequency from the velocity step responses of the load side (shown in Figure 6(d)). While for the drive-side velocity, it just does not have any effect (shown in Figure 6(c)). In this case, for the system in which only the drive-side velocity can be measured, the FFT does not apply to resonance frequency analysis. So, a more efficient analytical method is needed.

Because of the tiny vibration of the velocity step response of the drive side (shown in Figure 6(a)), time-frequency analysis (TFA) is used for obtaining the resonance frequency of the system by revealing the energy size of drive-side velocity in each time period. One of the most popular methods of TFA is the short-time Fourier transform (STFT) [13]. When the STFT is used, it is considered that a certain width of window sliding in the nonstationary signal is assumed to be piecewise stationary. The signal intercepted by the window is processed by the traditional Fourier transform [14]. The discrete form of STFT is able to be obtained by using the time-frequency grid point  $(m\Delta t, n\Delta f)$  of equal interval sampling the signal  $z(k\Delta t)$ .

The signal  $z(k\Delta t)$  is represented by the velocity response of the drive side, as shown in Figure 6(a):

$$\begin{aligned} \text{STFT}_z(m\Delta t, n\Delta f) \\ = \sum_{k=-\infty}^{\infty} z(k\Delta t) \eta[(m-k)\Delta t] e^{-j2\pi(n\Delta f)k\Delta t} \Delta t. \end{aligned} \quad (13)$$

$m\Delta t$  is time point

$n\Delta f$  is frequency point

$\Delta t$  is sampling interval of the time variable

$\Delta f$  is sampling interval of the frequency variable

$\eta(\Delta t)$  is time window function.

It is important to choose a suitable window function for the STFT to play the best performance [15]. The narrower the main-lobe of the window, the higher the frequency resolution that can be got and the faster the attenuation of the side-lobe of the window, the less the energy leakage. Considering the signal obtained from the velocity of drive side, whose resonance point is concerned but not energy size, the Hanning-window is selected because of its characteristic of less energy leakage and better frequency resolution.

Velocity step response of the drive side as the test signal is processed by using Hanning-window in MATLAB. According to the experimental data, for example, as in Figure 6(a), the sampling frequency is set as 100 Hz (equivalent to  $\Delta t = 10$  ms in (13)) and sampling as 30 s. In this case, tiny vibration is shown in the first 500 data points out of 3000 data points ( $k = 0, 1, 2, \dots, 2999$ ). The window width  $m$  is set as 512 considering the length of the vibration signal and an optimal frequency resolution. On this basis, the overlapping width between each two windows is set as 500 in order to have a better time aggregation [12]. So, the time-frequency spectrum can be obtained as shown in Figure 7. There are two obvious yellow lines in Figure 7. The long yellow line (around 7 Hz) stands for the system backlash which is formed by the connecting way of spring and load. The short one (around 1.9 Hz) represents the resonant frequency which is marked in Figure 7. Comparing Figure 7 with the FFT result of the load-side velocity (shown in Figure 6(d)), it is testified that the STFT can effectively extract the resonance frequency from the velocity step responses of the drive side.

## 4. Experiment Results

To verify the validity of the method, experiments are carried out on the experimental platform. For the sake of simplicity, only the drive side inertia, the load side inertia, and the spring coefficient are adjustable. There are three kinds of weight of masses. Their inertias as well as other components are shown in Table 1. The equivalent inertias of drive side  $J_m$  and load side  $J_l$  can be calculated as follows:

$$\begin{aligned} J_m &= J_{m1} + J_{m2} + J_{m3} + J_{\text{mass}} \\ J_l &= J_{m3} + J_{\text{mass}}. \end{aligned} \quad (14)$$

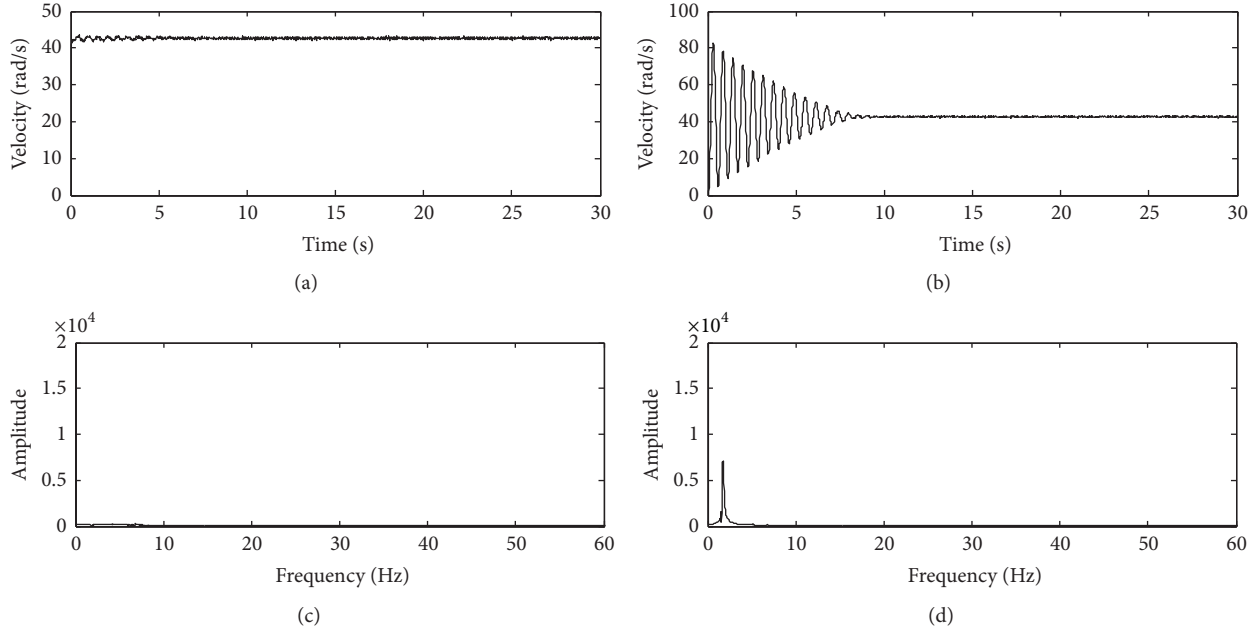


FIGURE 6: The velocity step responses of the drive side and the load side as well as their results of the FFT: (a) velocity step response of drive side, (b) velocity step response of load side, (c) FFT result of velocity step response of drive side, and (d) FFT result of velocity step response of load side.

TABLE 1: Inertias of DC motor, coupler, stiff shaft, and three masses.

Parameter	Inertia ( $\times 10^{-6} \text{ kg}\cdot\text{m}^2$ )	Description
$J_{m1}$	1.361	Inertia of the DC motor with a reducer
$J_{m2}$	0.562	Inertia of the coupler
$J_{m3}$	0.019	Inertia of the stiff shaft
$J_{\text{mass}}$		
$J_{\text{mass1}}$	5.303	Inertias of masses. $J_{\text{mass}}$ stands for any one of the three inertias
$J_{\text{mass2}}$	16.281	
$J_{\text{mass3}}$	44.196	

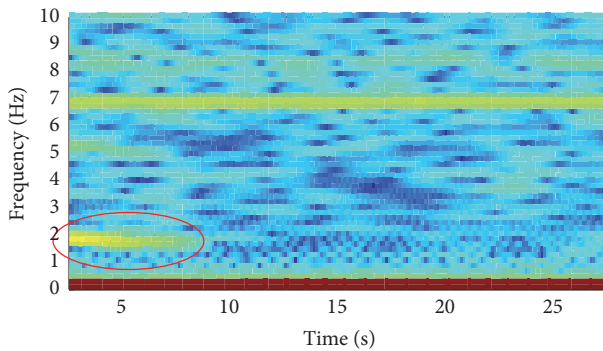


FIGURE 7: Time-frequency spectrum of the drive-side velocity using the STFT.

There are four springs of stainless steel with different sizes used in experiments to verify the applicability of this method. The sizes of springs are given in Table 2. The stiffness of springs are arrayed from small to large. The first experiment is to determine the inertia ratio  $q = 0.285$ , by changing the

TABLE 2: Various sizes of the springs.

Number	Wire diameter * outside diameter (mm)
(1)	0.8 * 10
(2)	1 * 10
(3)	1 * 8
(4)	1.2 * 10

different types of springs to verify the feasibility of the method mentioned in Section 3.

The time-frequency spectra of the velocity of drive side with different springs are given in Figure 8. Referring to Figure 8, resonant frequencies are marked by red arrows with different springs and IP controller parameters  $K_p$ ;  $K_i$  can be calculated by (11). Calculation results of IP controller parameters  $K_p$ ,  $K_i$  are given in the caption of Figure 9. The experimental velocity responses of both drive side and load side are shown in Figure 9. In the process of experiments, the stiffness of springs always remains unknown. Only the velocity response of the drive side is used when extracting

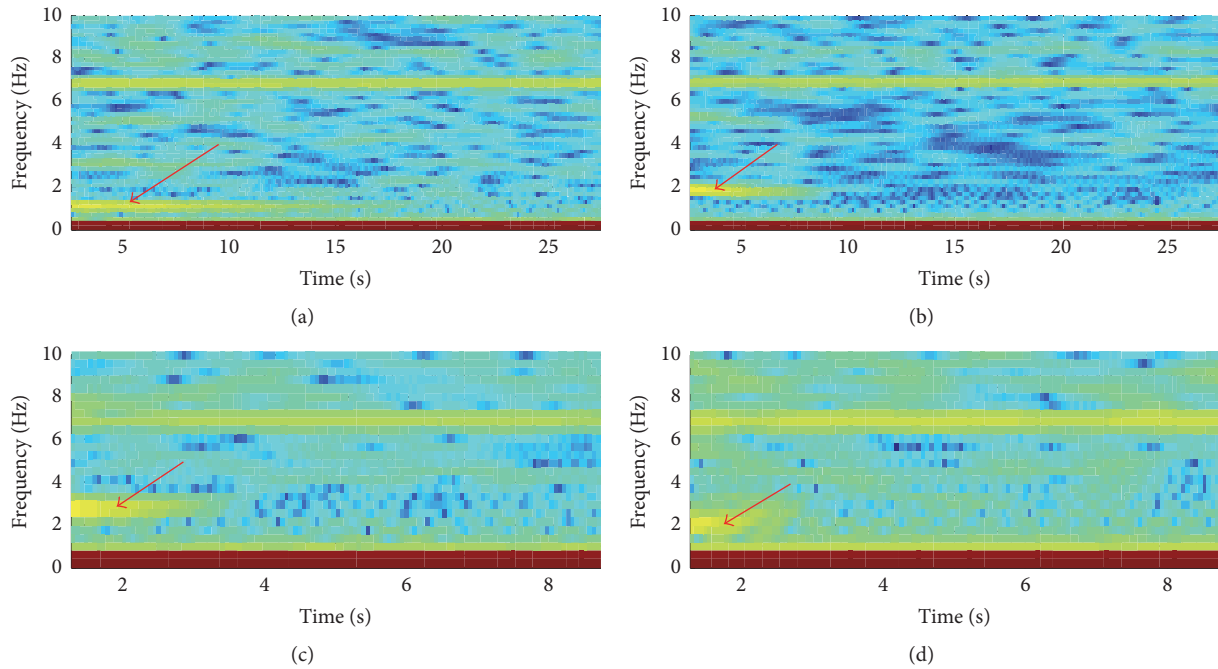


FIGURE 8: The time-frequency spectra of the velocity of drive side with different springs ( $q = 0.285$ ): (a) spring 1, (b) spring 2, (c) spring 3, and (d) spring 4.

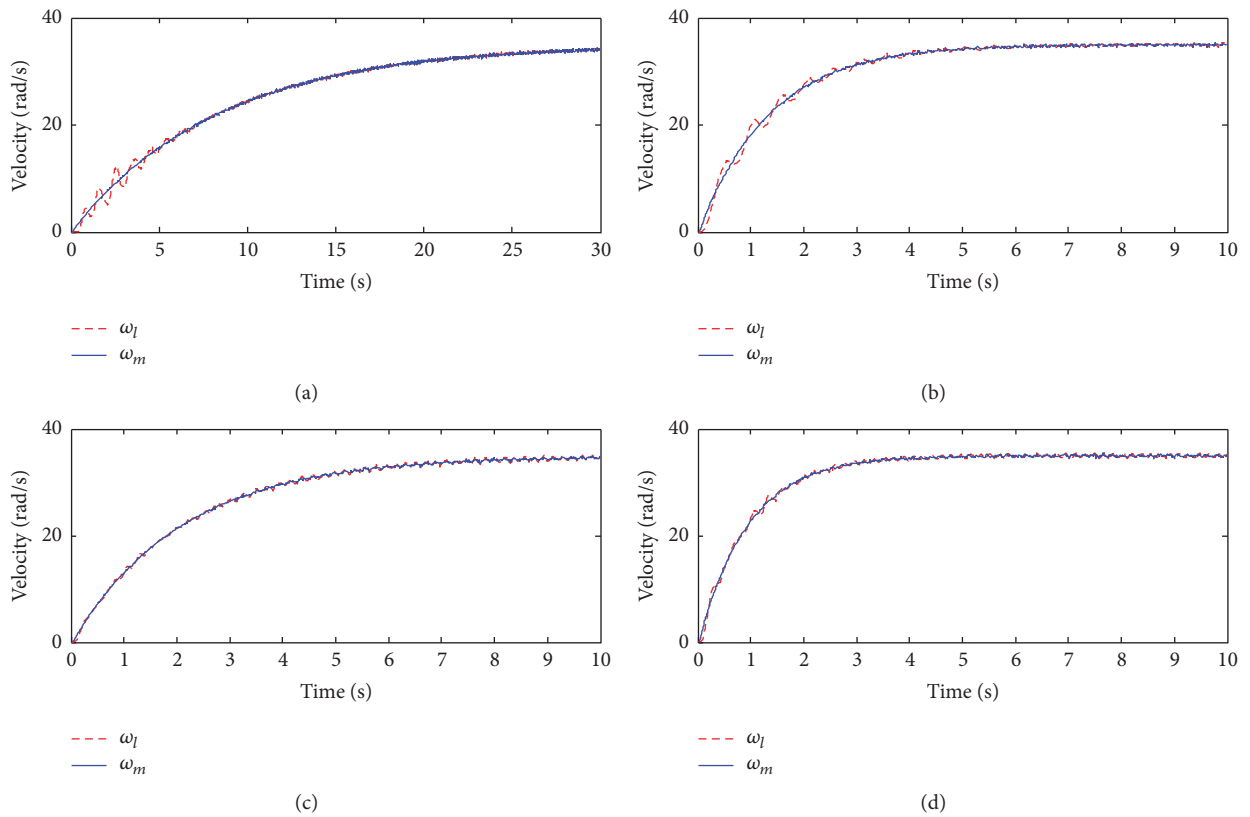


FIGURE 9: The experimental velocity responses of load side with different springs ( $q = 0.285$ ): (a) spring 1,  $K_p = 0.0175$ ,  $K_i = 1.5771$ ; (b) spring 2,  $K_p = 0.0276$ ,  $K_i = 3.9537$ ; (c) spring 3,  $K_p = 0.032$ ,  $K_i = 5.3$ ; (d) spring 4,  $K_p = 0.0393$ ,  $K_i = 7.984$ .

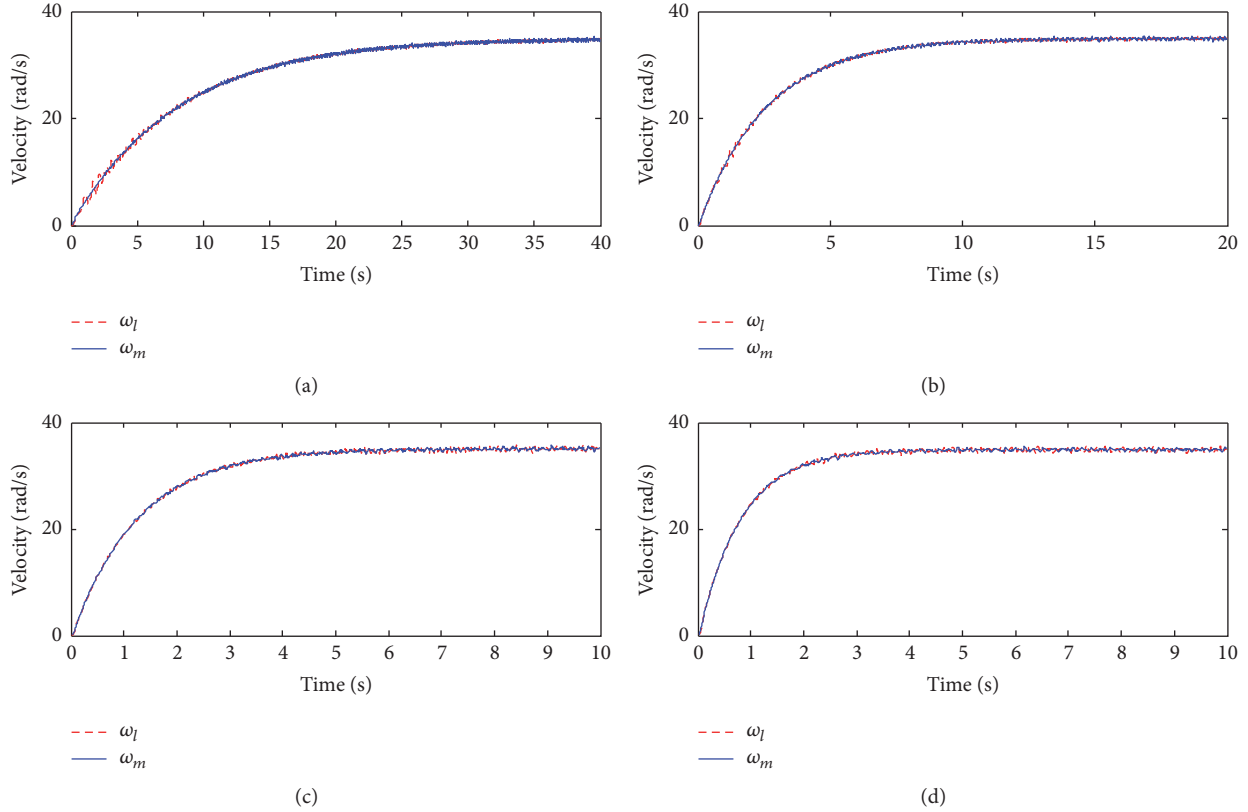


FIGURE 10: The experimental velocity responses of load side with different springs ( $q = 0.290$ ): (a) spring 1,  $K_p = 0.0093$ ,  $K_i = 1.1943$ ; (b) spring 2,  $K_p = 0.0163$ ,  $K_i = 3.7193$ ; (c) spring 3,  $K_p = 0.0276$ ,  $K_i = 4.7772$ ; (d) spring 4,  $K_p = 0.0397$ ,  $K_i = 9.922$ .

TABLE 3: The combination of masses.

Drive side	Load side	Inertia ratio $q$
Mass 2	Mass 3	0.285
Mass 1	Mass 2	0.290
Mass 1	Mass 3	0.131

the resonant frequency by STFT. Experimental results show nonovershoot in Figure 9. The velocity response of the load side which is sampled by a load-side encoder is almost overlapping together with the velocity response of the drive side. Nevertheless, there are still tiny vibrations when the motor is started due to the low stiffness of the springs as shown in Figures 9(a) and 9(b).

Other experiments are also conducted by changing inertia ratio  $q$  and repeating the above steps. The inertia ratio  $q$  can be altered by changing the mass on the drive and load sides. In order to satisfy the condition that inertia ratio  $q < 1/3$ , three kinds of combinations can be permitted and inertia ratio  $q$  is calculated, respectively, which are given in Table 3. The results are shown in Figures 10, 11, and 12. Although tiny vibrations exist when the motor just starts in the 5 s (shown in Figures 10(a), 10(b), 11(a), and 11(b)), the IP controller designed in the case of system uncertainty still shows a good performance with controller parameters designed by using the STFT. Nonovershoot is still performed and the velocity

response of the load side follows up the velocity response of the drive side very well. Even then, one experiment result (shown in Figure 12) is not as expected. Because of the high shaft stiffness, the speed of vibration attenuation of the load side response is very fast (shown in Figure 12(a)). The STFT is not able to analyze the resonance frequency of the system because the vibration signal is covered by window width (shown in Figure 12(b)).

## 5. Conclusion and Future Work

In this paper, a low-order IP controller of the two-mass system with model uncertainty has been designed for vibration suppression. The controller is designed based on polynomial method. Parameters of IP controller are calculated by inertias of drive side and load side as well as the resonant frequency. In case the shaft stiffness coefficient is unknown, the resonant frequency of the system is identified by using STFT in velocity step response of the drive side under the open-loop system. The effectiveness of this method is verified through three groups of experiments by changing the inertia ratio  $q$ . Referring to experimental results, the designed IP controller shows good performance for vibration suppression. However, when the shaft stiffness is high, the speed of vibration attenuation of the load side response is very fast (shown in Figure 12(a)). The STFT is not able to analyze the resonance frequency of the system because the vibration signal is covered by window

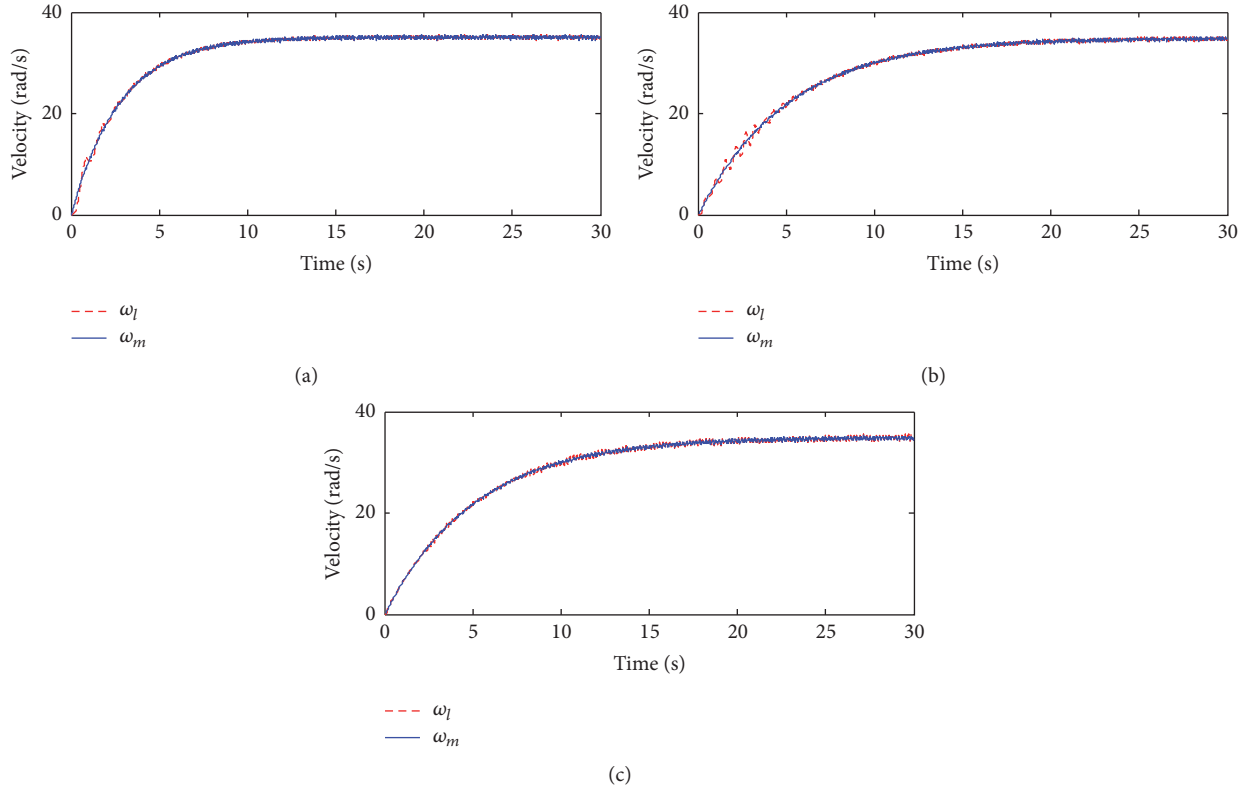


FIGURE 11: The experimental velocity responses of load side with different springs ( $q = 0.131$ ): (a) spring 1,  $K_p = 0.0089$ ,  $K_i = 0.5$ ; (b) spring 2,  $K_p = 0.0138$ ,  $K_i = 1.1943$ ; (c) spring 3,  $K_p = 0.0162$ ,  $K_i = 1.653$ .

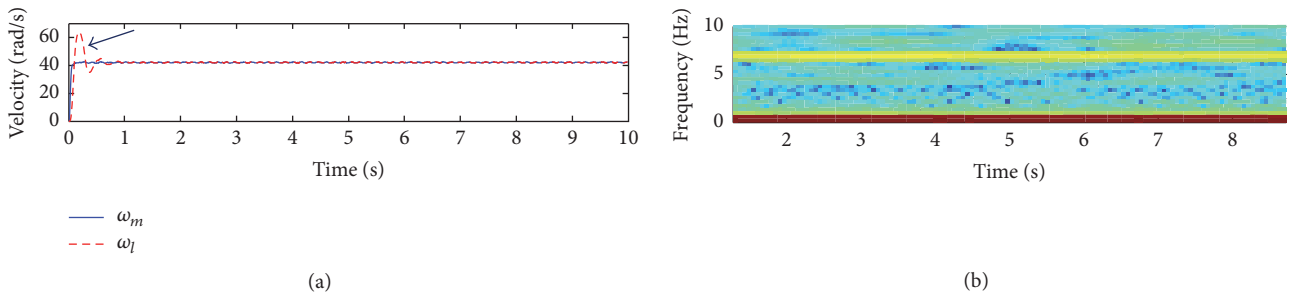


FIGURE 12: (a) Velocity response of the drive side and the load side when  $q = 0.131$  and spring 4 are chosen. (b) The time-frequency spectra of the velocity of the drive side.

width (shown in Figure 12(b)), while shortening the window width will decrease the frequency resolution. Therefore, the controller parameters cannot be calculated in this case.

According to the phenomenon found in this paper, in order to enhance the performance of the two-mass torsional system further, future work will focus on the following aspects. (1) First one is determining the scope of the application mentioned above quantitatively. The reason why the use of STFT has a limitation is that the window width may cover the vibration signal in settling time. In this case, encoders with higher resolution can be used to obtain more data of vibration signal. Then, the frequency resolution of STFT can be improved with wider window and parameters of a

two-mass torsional system with high-stiffness shaft can be identified indirectly. (2) Other TFA methods or frequency extracting methods will be considered. For example, wavelet transform (WT) is a powerful method in signal processing. The window width of WT is variable depending on the signal frequency. Therefore, its frequency-related window can improve the frequency extraction ability in two-mass torsional system with different shaft stiffness.

### Conflicts of Interest

The authors declare that there are no conflicts of interest regarding the publication of this manuscript.

## Acknowledgments

The authors acknowledge the financial support from the Natural Science Foundation of China (61773028), the Natural Science Foundation of Beijing (4172008), and the National Science and Technology Major Project of China (2013ZX04008-021).

## References

- [1] W. Li and Y. Hori, "Vibration suppression using single neuron-based PI fuzzy controller and fractional-order disturbance observer," *IEEE Transactions on Industrial Electronics*, vol. 54, no. 1, pp. 117–126, 2007.
- [2] X. Xie, J. Huang, and Z. Liang, "Vibration reduction for flexible systems by command smoothing," *Mechanical Systems and Signal Processing*, vol. 39, no. 1-2, pp. 461–470, 2013.
- [3] K.-B. Lee and F. Blaabjerg, "An improvement of speed control performances of a two-mass system using a universal approximator," *Electrical Engineering*, vol. 89, no. 5, pp. 389–396, 2007.
- [4] K. Szabat and T. Orłowska-Kowalska, "Vibration suppression in a two-mass drive system using PI speed controller and additional feedbacks - Comparative study," *IEEE Transactions on Industrial Electronics*, vol. 54, no. 2, pp. 1193–1206, 2007.
- [5] D. Xie, D. Qu, and F. Xu, "Design of H $\infty$  feedback controller and IP-position controller of PMSM servo system," in *Proceedings of the IEEE International Conference on Mechatronics and Automation, ICMA 2005*, pp. 578–583, can, August 2005.
- [6] M. Kaminski, "Neural network speed controller for drive system with elastic joint," in *Proceedings of the IEEE EuroCon 2013*, pp. 2080–2085, Croatia, July 2013.
- [7] Y. Qiao, L. Zhou, and C. Ma, "Polynomial-based inertia ratio controller design for vibration suppression in two-mass system," in *Proceedings of the 39th Annual Conference of the IEEE Industrial Electronics Society, IECON 2013*, pp. 3687–3692, Austria, November 2013.
- [8] S. Villwock and M. Pacas, "Application of the welch-method for the identification of two- and three-mass-systems," *IEEE Transactions on Industrial Electronics*, vol. 55, no. 1, pp. 457–466, 2008.
- [9] H. Zoubek and M. Pacas, "An identification method for multi-mass-systems in speed-sensorless operation," in *Proceedings of the 2011 IEEE International Symposium on Industrial Electronics, ISIE 2011*, pp. 1895–1900, Poland, June 2011.
- [10] M. Ruderman, W. Maebashi, and M. Iwasaki, "Semi-dual loop control of two-mass actuator system using Luenberger state observer," in *Proceedings of the 39th Annual Conference of the IEEE Industrial Electronics Society, IECON 2013*, pp. 6563–6568, Austria, November 2013.
- [11] C. Ma, J. Cao, and Y. Qiao, "Polynomial-method-based design of low-order controllers for two-mass systems," *IEEE Transactions on Industrial Electronics*, vol. 60, no. 3, pp. 969–978, 2013.
- [12] J. Ye, J. Cui, and Z. Chu, "Experimental study of vibration suppression for uncertain two-mass torsional system," in *Proceedings of the 12th IEEE International Conference on Control and Automation, ICCA 2016*, pp. 996–1001, npl, June 2016.
- [13] B. Liang, S. Iwnicki, A. Ball, and A. E. Young, "Adaptive noise cancelling and time-frequency techniques for rail surface defect detection," *Mechanical Systems and Signal Processing*, vol. 54-55, pp. 41–51, 2015.
- [14] Z. K. Peng, W. M. Zhang, Z. Q. Lang, G. Meng, and F. L. Chu, "Time-frequency data fusion technique with application

to vibration signal analysis," *Mechanical Systems and Signal Processing*, vol. 29, pp. 164–173, 2012.

- [15] F. Al-Badour, M. Sunar, and L. Cheded, "Vibration analysis of rotating machinery using time-frequency analysis and wavelet techniques," *Mechanical Systems and Signal Processing*, vol. 25, no. 6, pp. 2083–2101, 2011.

## Research Article

# Blast Responses and Vibration of Flood-Defense Structures under High-Intensity Blast Loadings

Yonghee Ryu,<sup>1</sup> WooYoung Jung ,<sup>2</sup> HoYoung Son,<sup>3</sup> and Bu-Seog Ju <sup>3</sup>

<sup>1</sup>Samsung Heavy Industries, Pangyo, Bundang-gu, Sungnam-si, Gyungki-do 13486, Republic of Korea

<sup>2</sup>Department of Civil Engineering, Gangneung-Wonju National University, Gangneung 25457, Republic of Korea

<sup>3</sup>Department of Civil Engineering, Kyung Hee University, Yongin-si, Gyeonggi-do 17104, Republic of Korea

Correspondence should be addressed to Bu-Seog Ju; [bj2@khu.ac.kr](mailto:bj2@khu.ac.kr)

Received 25 July 2017; Accepted 31 January 2018; Published 27 February 2018

Academic Editor: Giuseppe Brandonisio

Copyright © 2018 Yonghee Ryu et al. This is an open access article distributed under the Creative Commons Attribution License, which permits unrestricted use, distribution, and reproduction in any medium, provided the original work is properly cited.

This study presented the blast behavior of flood-defense structures subjected to high-intensity loadings such as blast shock waves. In order to understand the blast behavior of weir structures, PHAST program was used to predict blast loadings in consideration of material reactivity and congestion levels. Environment factors such as weather data and atmospheric parameters were also considered in this study. Then, nonlinear dynamic analyses were performed using the ABAQUS platform to evaluate structural responses and blast vibration of concrete weir structures subjected to various types of blast loadings, due to uncertainties of the magnitude and durations of blast loads as a function of distance from the explosion. It was shown that the blast damage to concrete weir structure was significantly influenced by congestion levels or material reactivity. Also, the stress concentration under blast loading was observed at the connection area between the concrete weir body and stilling basin.

## 1. Introduction

Critical infrastructures such as bridges, dams, nuclear power plants, lifelines, and buildings can be exposed to terrorist attacks and chemical explosions. The Pentagon and World Trade Center in 2001, the Australian Embassy in Jakarta, Indonesia in 2004, and Bangkok City, Thailand in 2015, are the sites of infamous terrorist attacks. Representing a much higher likelihood of explosion than terrorist conspiracy are chemical and petrochemical plants, due to explosive materials and hot work which is frequent ignition sources. In China, for example, there have been two recent major explosions at petrochemical plants: in Jilin in 2005, which killed six people and necessitated the evacuation of thousands more, and in Guangxi in 2008, which killed 16 people (<https://en.wikipedia.org/>). Moreover, and more recently still, the devastation due to the strongest recent explosion at Tianjin in China occurred at a warehouse containing hazardous materials such as calcium carbide, sodium cyanide, and sodium nitrate, killing more than 100 people and hospitalizing about 100 others.

Many researchers [1–3] have recognized the need to address, in the design stage, the problem of the protection for critical structures from high-intensity dynamic events generated by strong explosions. Nog et al. [4] studied blast-loading effects on structures and the blast-wave mechanism in free air. Dharmasena et al. [5] evaluated the dynamic and mechanical responses of metallic honeycomb sandwich panel structures under high-intensity loading using ABAQUS/Explicit based on experimental tests. Also, reliability analyses of reinforced concrete subjected to blast loadings have been conducted, by Low and Hao [6]. In addition, Xiangdi et al. [7] introduced a new, computational fluid dynamics- (CFD-) based method of risk determination for gas-explosion hazards in China. Furthermore, in recent years, infrastructure systems were designed to withstand extreme loads such as earthquake or blast. Fujikura et al. [8] described the behavior of bridge pier systems under multihazard scenarios such as seismic and blast loadings based on FEMA [9] and FHWA [10]. The inelastic deformation of bridge pier was experimentally and numerically investigated by using a simplified single degree of freedom system. Li et al. [11] evaluated the performance



Gangjeong-Goryeong weir system

FIGURE 1: Gangjeong-Goryeong weir system near Daegu Seongseo Industrial Complex in Korea.

of overhead protection structures subjected to blast loads following the procedures in ASCE guidelines in which finite element analysis (FEA) was conducted by the ABAQUS platform. In Korea, on the other hand, performance evaluation of flood-defense dam/weir structures subjected to blast loads has seldom been carried out. The focus of the present study, therefore, was the characterization of the performance of weir-infrastructure systems under various types of blast loads. More specifically, blast-loading explosive weight and stand-off distance were considered as intensity uncertainties in evaluating soil-structure interaction in accordance with material uncertainties in Finite Element (FE) models. Additionally, in order to generate a scenario involving blast loads related to man-made hazards, PHAST [12] as a consequence-modeling program was employed for several important factors such as humidity, temperature, material reactivity, and congestion. This validated program [13–15] is widely used to calculate the blast loadings using a Baker-Strehlow-Tang (BST) model in which the blast model is also validated by experimental data [16, 17]. Three types of quantitative explosion analyses, low, medium, and high material reactivity and congestion levels, were performed, and PHAST-based blast time histories corresponding to those levels were derived. Finally, the sensitivity studies were conducted to address the relative effects of material uncertainties on the weir structure as modeled in ABAQUS [18].

## 2. Selected Target Areas and Flood-Defense Structures

Extreme loads can cause failure of flood-defense structures such as dams and weir systems. The 2011 Japan earthquake and massive tsunami, for example, the most destructive natural catastrophe in that country's history, caused extensive damage to an entire regional area even though there had been a seawall in place for protection of infrastructure. In recent years in Korea, several concrete weir structures for flood (or drought) control have been constructed, some of which are located nearby major industrial complexes including petrochemical plants and Liquefied Petroleum Gas (LPG) stations. To assess damage to weir structures and improve the performance of flood-defense structures under blast loads, the Gangjeong-Goryeong weir system located near the Daegu Seongseo Industrial Complex in Korea was selected for evaluation in this study (see Figure 1). The Gangjeong-Goryeong hydraulic system's designed pool elevation is 19.50 m for the

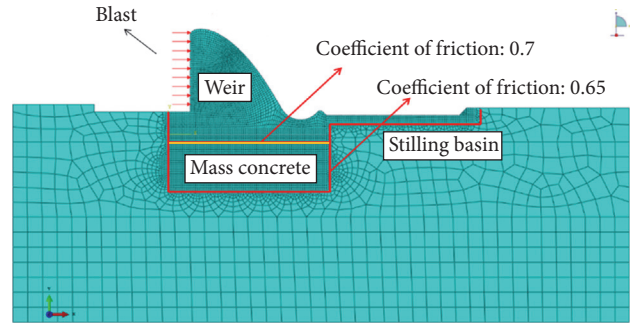


FIGURE 2: The figure shows FE model of Gangjeong-Goryeong weir hydraulic system reproduced from Ju and Jung [19, 20], [under the Creative Commons Attribution License/Public Domain].

nonoverflow section and 9.47 m for the overflow section, and the storage capacity for generation of electric power and flood/drought control is 92.3 million  $\text{m}^3$ . The material properties of the weir structures and soil foundations are as follows: elastic modulus of weir body and mass concrete, 26,637 MPa and 24,579 MPa, respectively; elastic modulus of steel, 200,000 MPa; unit weight of weir and mass concrete, 2350  $\text{kg}/\text{m}^3$ ; design strength of weir body and mass concrete, 24 MPa and 18 MPa; Poisson's ratio for both weir and mass concrete, 0.167. Further details on some of those material properties are provided in Table 1 [19, 20].

## 3. Numerical Model of Weir Structures

In order to understand the behavior of weir structure as a flood-defense structure subject to high-intensity loadings such as explosions, a numerical FE model was developed using the ABAQUS [18] platform in this study. The FE model of the Gangjeong-Goryeong weir hydraulic system shown in Figure 2 was completed according to the 4-node bilinear plane strain quadrilateral element (CPE4R) for the weir, mass concrete, and soil foundations. The dam/weir is a continuous structure in which the performance of the dam/weir against the blast loading can be assumed to be the plain strain behavior. As one dimension is very large compared to the other dimensions, the principal strain in the direction of the longest dimension is constrained and assumed as zero. For the steel rebar, a 2D truss element was used. The soil foundations specifically were modeled based on Mohr-Coulomb material with perfectly plastic behavior. Accordingly, there were two classifications of FE model: (1) a 2D linear elastic model for the weir and (2) a 2D nonlinear model for soil-structure interaction based on the isotropic Coulomb friction material in ABAQUS. It should be noted that any FE model of a weir-structure system for blast or explosion must take into account hydrostatic and dynamic forces such as uplift pressure of piecewise liner distribution, hydrostatic pressure corresponding to the water level, and hydrodynamic pressure based on Westergaard's added-mass method [21]. The fundamental frequency of the weir structure is 1.24 Hz. The detail discussions regarding the FE modeling of the weir-structure system can be found in Ju and Jung [19].

TABLE 1: Material properties of weir structures (after Ju and Jung [19, 20]).

Structures	Elastic modulus (MPa)	Poisson's ratio	Density (t/mm <sup>3</sup> )
Weir body	26,637	0.167	$2.4E - 9$
Mass concrete	24,579	0.167	$2.4E - 9$
Steel	200,000	0.25	$7.85E - 9$
Soil layer I	2	0.4	$1.7E - 9$
Soil layer II	25	0.4	$1.9E - 9$
Soil layer III	2,000	0.3	$2.4E - 9$

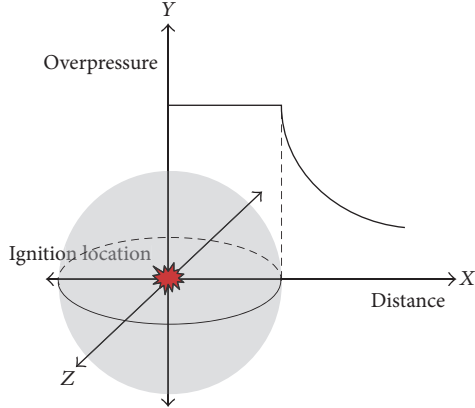


FIGURE 3: BST blast curve based on idealized vapor cloud explosion.

#### 4. Blast Loading from Gas Explosion

An explosion is a sudden extreme energy release generating high temperatures and blast pressures. Deflagration leads to high pressure (~5 bar) and flame propagating at the speed of sound via heat transfer in congested areas. Detonation is a more severe explosion leading to very high pressure (~20 bar) and flame speed (1,600~2,000 m/s), not only inside congested areas but also outside [22]. Such high pressures can result, even at long distances, in structural damage. The Buncefield disaster in December 2005 was a major accident caused by a series of explosions at storage tanks in England. Serious damage associated with blast overpressures was observed in facilities and buildings surrounding the explosion site [23]. The Texas City Refinery explosion in March 2005 was one of the worst industrial disasters in recent US history; indeed, houses as far away as 1.2 km from the refinery incurred damage [24].

Blast-loading prediction has been performed by researchers using experimental tests and computational fluid dynamic (CFD) simulations. Baker et al. [25] proposed an explosion model for calculation of blast pressures from vapor cloud explosions (VCE), defining potential explosion sites with respect to the explosion size and severity as well as the maximum flame speed on the basis of fuel reactivity (burning velocity), confinement (degrees of freedom), and congestion (density). A new version of this model incorporating updated blast curves was renamed the Baker-Strehlow-Tang (BST) model [26]. This model was developed based on three-dimensional numerical CFD simulations of VCE (see Figure 3), with overpressure and impulse curves of positive

TABLE 2: Flame speed table for BST model (after Pierorazio et al. [16]).

Material reactivity	Congestion		
	Low	Medium	High
High	0.59	DDT*	DDT*
Medium	0.47	0.66	1.60
Low	0.079	0.47	0.66

\*Deflagration-to-detonation transition.

and negative phases provided as functions of distance for various flame speeds covering deflagration to detonation. The BST model's table of flame speed was revised based on experimental results and updated according to a confinement of 2.5D, as shown in Table 2. A series of medium-scale VCE tests were conducted to measure the flame speed for a given fuel reactivity/confinement/congestion set. 2.5D values were introduced by averaging between the 2D and 3D confinement values for the same set of conditions [16].

#### 5. Prediction of Blast Pressure Using PHAST

The BST model predicts explosion load and impulse with reference to the flame speed table and blast curves in terms of the fuel reactivity, confinement, and congestion in the region around the release. The explosive energy is determined by the total flammable mass under the given environmental conditions. In the current study, the PHAST [12] program (v7.1) was used as the modeling environment for the evaluation of blast. The explosion scenarios involving major accidents were assumed to occur at an onshore production platform. The catastrophic rupture for various sizes of storage tanks filled with propane (flash point  $-104^{\circ}\text{C}$ ) was considered to be the worst case for major accidents. The weather data and atmospheric parameters in Table 3 were adapted from a study on a procedure for evaluating the consequences of accidents [27]. The ground correction factor for each scenario in the present simulations was chosen as 2 on the recommendation of a ground-effect study [17]. Figures 4 and 5 plot the results of pressure and impulse at specified distances for the various flammable masses 5, 10, 20, 40, 60, 80, 100, and 200 tons. The degree of confinement was assumed to be 2D, solid decks on multilevel process units, and more than 80% blockage by piping structures [25]. A total of 9 scenarios for three levels, high, medium, and low, of congestion and material reactivity, respectively, were considered in this study. 2.0HM, for example, indicates 2.0 degrees of confinement, high

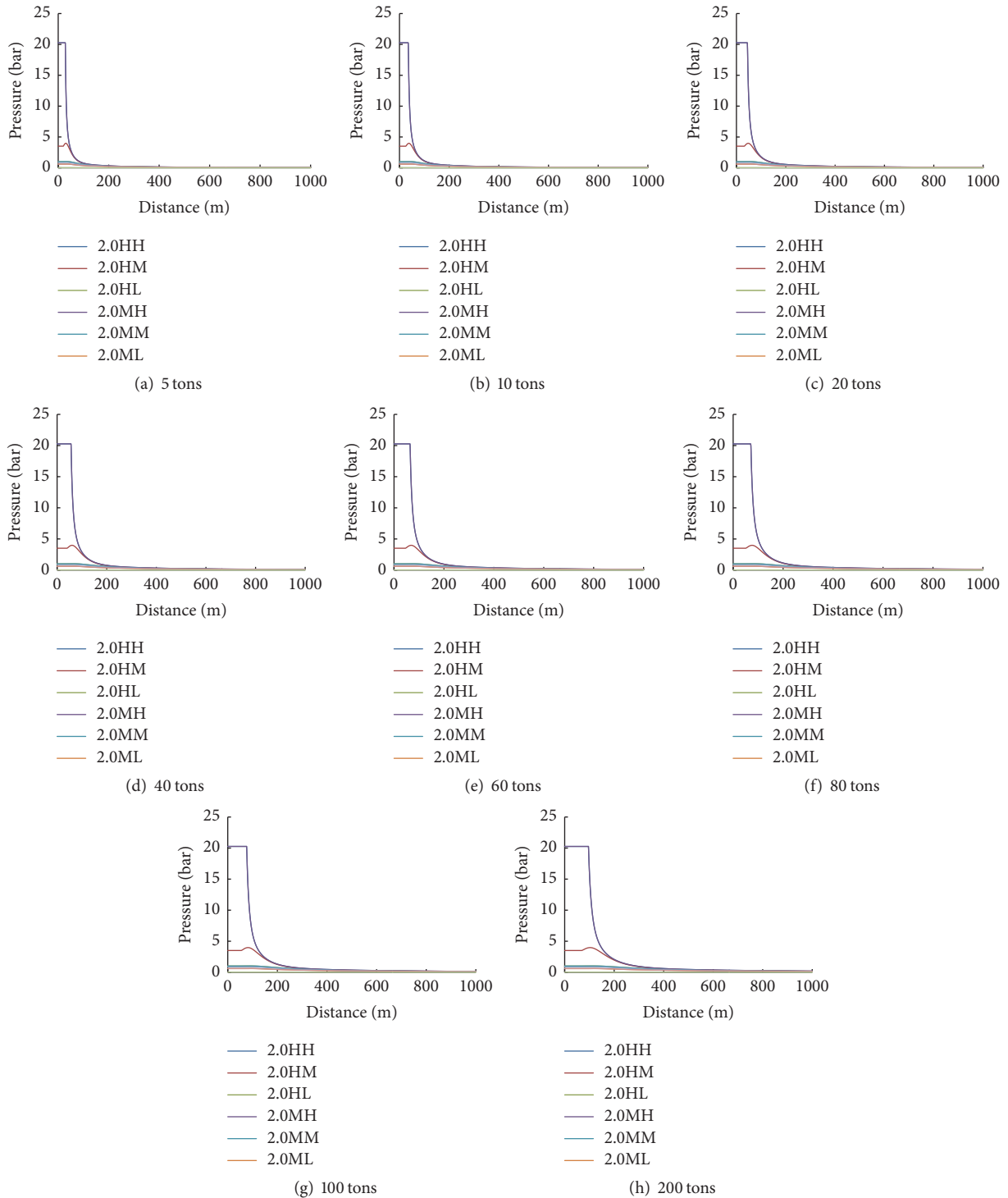


FIGURE 4: Pressure versus distance for various flammable masses.

level of congestion, and medium level of material reactivity. Figure 6 represents the blast pressure results based on the BST method. The impulse is the integral of the pressure over time interval. Therefore, the blast pressure duration was simply calculated as two times the right-angled-triangle area divided by the maximum pressure at a certain distance.

### 6. Blast Response and Vibration of Flood-Defense Structures under High-Intensity Blasts

An explosion is a rapid increase in volume and release of energy in very short duration. Explosive force is released in

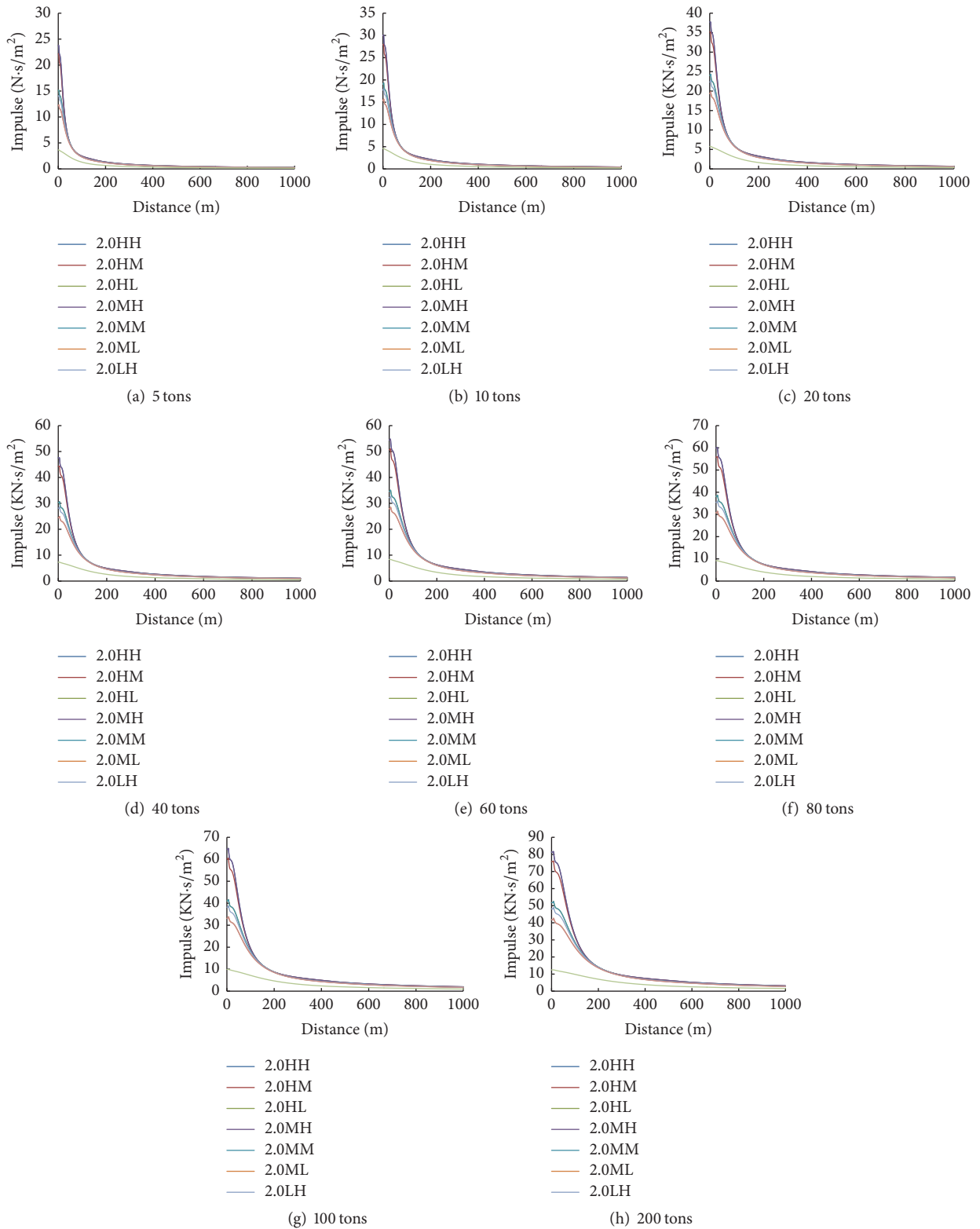


FIGURE 5: Impulse versus distance for various flammable masses.

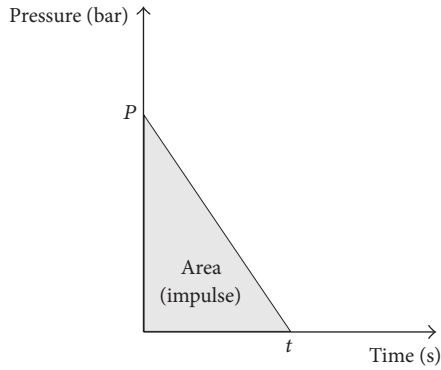


FIGURE 6: Representative blast pressure model.

TABLE 3: Weather and atmospheric conditions for Spring season (after Pintarič [27]).

Wind speed	2 m/s
Pasquill stability	D, neutral, little sun and high wind
Atmospheric temperature	13
Relative humidity	0.7

a direction perpendicular to the surface of the explosive and can be assumed to reach in the left front side of the structure (see Figure 2). In order to understand the blast behavior of the weir structure in terms of flame speed based on the BST model, nine (9) blast-load scenarios with various congestion and material reactivity conditions were considered in the linear elastic FE weir model with the nonlinear soil-structure interaction model based on the isotropic Coulomb friction material. For instance, Figure 7 shows stress-time history for the blast-wave expansion process with time domain using the distance and flammable masses selected as zero meters and 5 tons with high congestion and material reactivity conditions for more rigorous and conservative analysis. At the very beginning of the explosion, the maximum principal stress due to the strong shockwave was 4.0 MPa, and subsequently the high blast shockwave stress occurred on the area of the weir. And, then the maximum stress was significantly concentrated on the area of connection between the weir body and the stilling basin as time went by. It tells us that the initial crack may develop the left side of the weir, and the significant damage can occur at the right side of the weir hitting the stilling basin by the shockwave. Figure 8 shows the simulation results on the tensile and compressive stresses for the weir using various types of congestion levels and material relativities: HH, HM, HL, MH, MM, ML, LH LM, and LL. The maximum tensile and compressive stresses for were found 16.38 MPa and 11.61 MPa under the HH (MH) and LM (ML) conditions, respectively. As for the absolute maximum displacement (LL condition), it was 16.83 mm at the end of the stilling basin, as can be seen in the figure. Correspondingly, the nonlinear response of displacements for the stilling basin should be checked independently from the pressure-time-history data for a strong shockwave analysis since the maximum displacement was not obtained as

the same congestion and material reactivity conditions as the maximum pressure.

Furthermore, in order to understand the blast behaviors of the system according to the uncertainties of flammable mass and stand-off distance, eight flammable masses (5, 10, 20, 40, 60, 80, 100, and 200 tons) and six stand-off distances (100, 200, 400, 600, 800, and 1000 m) under the high congestion and material reactivity conditions were considered in this study. For the low-flammable-mass levels, the tensile stresses were greater than the compressive stresses, and then tensile and compressive stresses became closed as mass levels increased as shown in Figure 9(a). The relationships between tensile and compressive stresses as a function of  $x$  (mass) were found to be  $0.033x + 19.44$  and  $0.025x + 16.01$ , respectively. Figure 9(b) shows the maximum tensile and compressive stresses versus various types of stand-off distances. Both tensile and compressive stresses increased as the stand-off distances increased, and stresses were converged at the distance of 800 m. The relationships between tensile and compressive stresses as a function of  $x$  (distance) were found to be  $-1E - 5x^2 + 0.021x + 2$  and  $-1E - 5x^2 + 0.020x + 2$ , respectively. It should be noted that the tensile stress, compressive stress, and displacement were gradually increased with increasing explosive mass and stand-off distance.

Figure 10 shows the results in terms of the shockwave ( $5t$ , HH)-induced stress changes of the weir in the linear and nonlinear soil-structure interaction models. As seen in the time histories, the compressive stress at the connection area shows similar trends, whereas the tensile stress was significantly different between the two models. Specifically, the tensile stress of the linear soil-structure interaction model was much higher than that of the nonlinear model. It shows us some amount of energy was consumed in nonlinear behavior under the blast loading with nonlinear soil-structure interaction. Finally, sensitivity study for the effects of the friction for the weir system were conducted as shown in Figure 11. The friction coefficients were increased from 0.7 to 0.9 considering the uncertainty of concrete on concrete frictional condition. The results showed the friction effect on the weir structure subjected to high-intensity blast loading was not significant as shown the mean tensile and compressive stress values were 3.96 MPa and 4.36 MPa with mean plus one standard deviation indications, respectively.

## 7. Conclusions

This study evaluated the blast response and possible damage locations of weir structures under high-intensity loadings such as blast shock waves. In order to define the blast loads and account for the material reactivity and congestion levels, the PHAST program was used. Also, the parameters for the BST models represented the relevant weather data and atmospheric factors for a given area of explosion. Additionally, for structural simulation under blast shockwave, the ABAQUS platform was adapted to develop the linear elastic FE weir model with the nonlinear soil-structure interaction model based on the isotropic Coulomb friction material. Various parametric studies were conducted to investigate the different blast responses of the concrete flood-defense system under

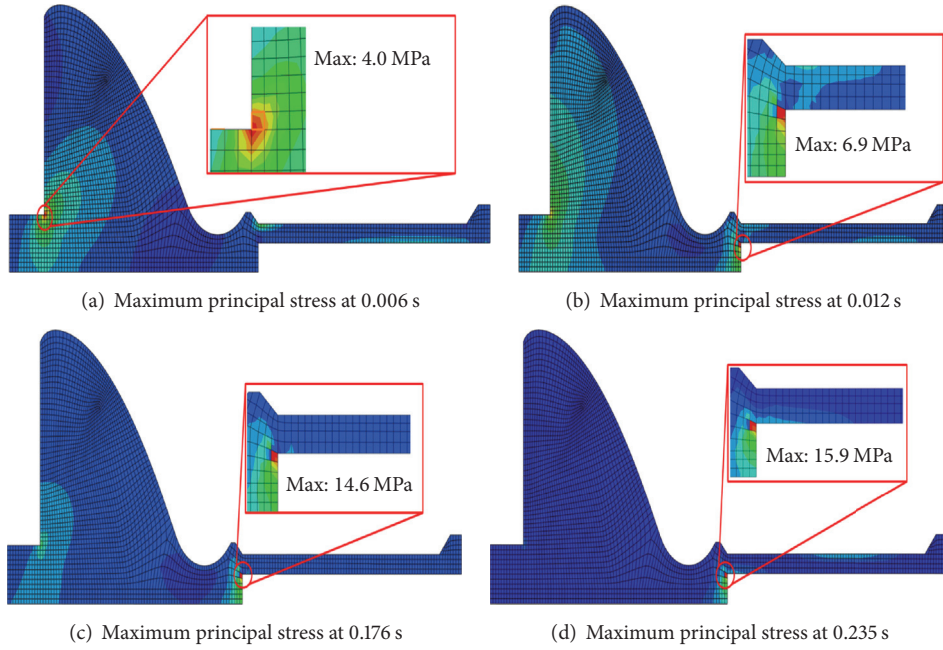


FIGURE 7: Blast-wave expansion process with time domain (5 tons, HH).

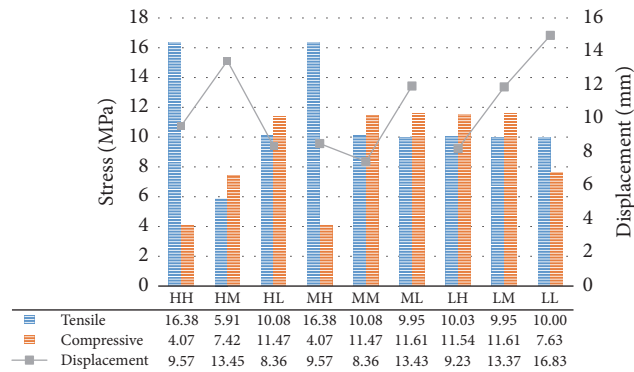


FIGURE 8: Results' comparison based on material reactivity and congestion levels.

different blast conditions, stand-off distance, and friction coefficients: nine blast-load scenarios with various congestion and material reactivity conditions (HH, HM, HL, MH, MM, ML, LH LM, and LL), eight flammable masses (5, 10, 20, 40, 60, 80, 100, and 200 tons), six stand-off distances (100, 200, 400, 600, 800, and 1000 m), and three friction coefficients (0.7, 0.8, and 0.9). The blast shockwave data and observations obtained in this study and presented herein can be used to support the development of comprehensive regulatory design guidelines for the design and development of concrete weir structures subject to various threat-scenario uncertainties. The primary research results in this study are listed as follows:

- (i) The initial crack may develop the left side of the weir, and the significant damage can occur at the right side of the weir (between the concrete weir body and stilling basin) hitting the stilling basin by the shockwave.
- (ii) The blast damage to concrete weir structure was significantly influenced by congestion levels or material reactivity.
- (iii) The tensile and compressive stress levels were sensitive to the flammable-mass levels, and both tensile and compressive stresses increased as the stand-off distances increased and were converged at the certain distance. The tensile stress, compressive stress, and displacement were gradually increased with increasing explosive mass and stand-off distance.
- (iv) Some amount of energy was consumed in nonlinear behavior under the blast loading when nonlinear soil-structure interaction was considered in an analytical model.
- (v) Sensitivity study was conducted for the effects of using the different value of friction coefficients for the weir

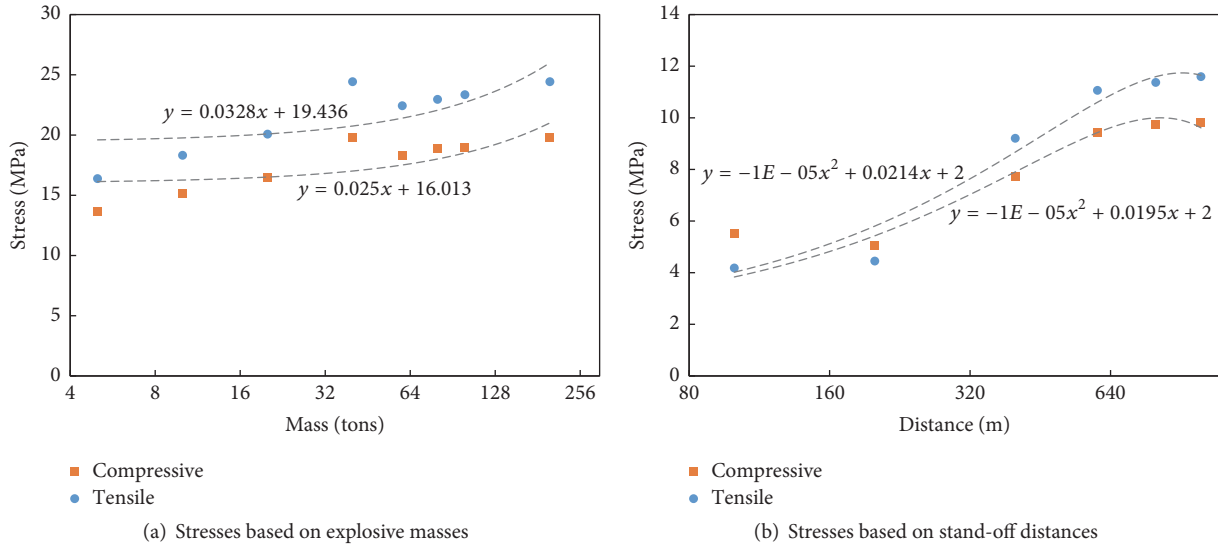


FIGURE 9: Stress changes of the weir in accordance with explosive masses and stand-off distances.

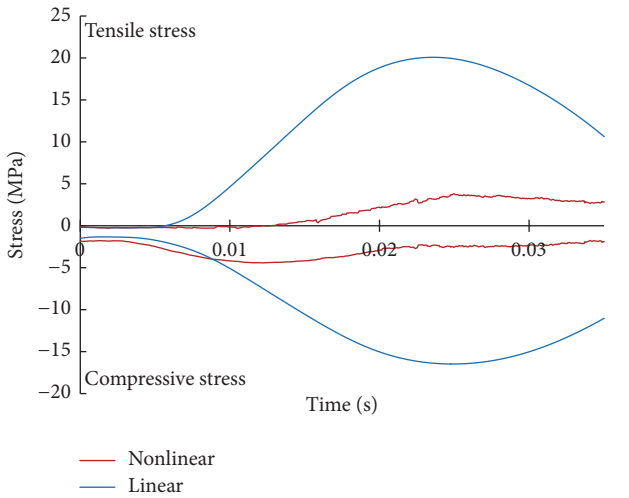


FIGURE 10: Blast vibration of the weir associated with linear and nonlinear soil-structure interaction models.

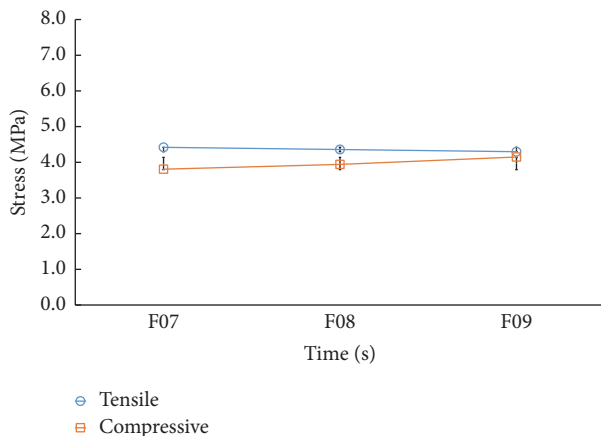


FIGURE 11: Sensitivity study with respect to friction coefficients.

system. As a result, it was revealed that the effect of the friction on the weir system under the blast loading was not significant.

**Conflicts of Interest**

The authors declare that there are no conflicts of interest regarding the publication of this paper.

**Acknowledgments**

This work was supported by a grant from Kyung Hee University in 2016 (KHU-20161374).

**References**

- [1] G. Razaqpur, W. Mekky, and S. Foo, "Fundamental concepts in blast resistance evaluation of structures," *Canadian Journal of Civil Engineering*, vol. 36, no. 8, pp. 1292–1304, 2009.
- [2] E. Jacques, A. Lloyd, and M. Saatcioglu, "Predicting reinforced concrete response to blast loads," *Canadian Journal of Civil Engineering*, vol. 40, no. 5, pp. 427–444, 2013.
- [3] C. Viau and G. Doudak, "Investigating the behaviour of typical and designed wall-to-floor connections in light-frame wood stud wall structures subjected to blast loading," *Canadian Journal of Civil Engineering*, vol. 43, no. 6, pp. 562–572, 2016.
- [4] T. Nog, P. Mendis, A. Gupta, and J. Ramsay, "Blast loading and blast effects on structures-an overview," *EJSE Special Issue: Loading on Structure*, pp. 76–91, 2007.
- [5] K. P. Dharmasena, H. N. G. Wadley, Z. Xue, and J. W. Hutchinson, "Mechanical response of metallic honeycomb sandwich panel structures to high-intensity dynamic loading," *International Journal of Impact Engineering*, vol. 35, no. 9, pp. 1063–1074, 2008.
- [6] H. Y. Low and H. Hao, "Reliability analysis of reinforced concrete slabs under explosive loading," *Structural Safety*, vol. 23, no. 2, pp. 157–178, 2001.

- [7] Z. Xiangdi, J. Chunming, W. Yanping, Y. Jiwu, and W. Zheng, "Simulation study on an explosion accident in China," *Process Safety Progress*, vol. 33, no. 1, pp. 56–63, 2014.
- [8] S. Fujikura, M. Bruneau, and D. Lopez-Garcia, "Experimental investigation of multihazard resistant bridge piers having concrete-filled steel tube under blast loading," *Journal of Bridge Engineering*, vol. 13, no. 6, pp. 586–594, 2008.
- [9] Federal Emergency Management Agency (FEMA), *Reference Manual to Mitigate Potential Terrorist Attacks against Buildings*, FEMA 426, Washington D.C, Wash, USA, 2003.
- [10] Federal Highway Administration (FHWA), *Recommendations for Bridges and Tunnel Security*, the Blue Ribbon Panel on Bridge and Tunnel Security, Washington D.C, Wash, USA, 2003.
- [11] G. Li, P. Summers, K. Clutter, and D. Bonaventure, "Blast and impact resistant design of overhead protection structures," in *Proceedings of the Structures Congress 2012*, pp. 167–176, USA, March 2012.
- [12] "PHAST Professional Version 7.1; Risk Management software; DNV Technica, London".
- [13] H. W. M. Witlox, M. Harper, and A. Oke, "Phast validation of discharge and atmospheric dispersion for carbon dioxide releases," in *Proceedings of the 15th Annual Symposium, Mary Kay O'Connor Process Safety Centre*, Texas A&M University College Station, Texas, TX, USA, 2012.
- [14] H. W. M. Witlox and A. Oke, *Verification and Validation of Consequence Models for Accidental Releases of Hazardous Chemicals to the Atmosphere*, vol. 154 of *Institution of Chemical Engineers Symposium Series*, Institution of Chemical Engineers; 1999, 2008.
- [15] DNV software, "Obstructed Region Explosion Model Validation," Phast 7.1 technical documentation, 2010.
- [16] A. J. Pierorazio, J. K. Thomas, Q. A. Baker, and D. E. Ketchum, "An update to the Baker-Strehlow-Tang vapor cloud explosion prediction methodology flame speed table," *Process Safety Progress*, vol. 24, no. 1, pp. 59–65, 2005.
- [17] Y. Xu, D. Worthington, and A. Oke, *Correcting the Predictions by Baker-Strehlow-Tang (BST) Model for the Ground Effect*, Symposium Series No. 155, IChemE, 2009.
- [18] ABAQUS, "Ver 6.13, Dassault Systemes".
- [19] B. S. Ju and W. Jung, "Evaluation of seismic fragility of weir structures in South Korea," *Mathematical Problems in Engineering*, vol. 2015, Article ID 391569, 10 pages, 2015.
- [20] B. S. Ju and W. Y. Jung, "Evaluation of seismic performance of weir structures in Korea," *International Journal of Engineering and Technology (IJET)*, vol. 7, no. 2, pp. 808–816, 2015.
- [21] H. M. Westergaard, "Water pressure on dams during earthquakes," *Transactions of the American Society of Civil Engineers*, vol. 98, pp. 418–433, 1933.
- [22] O. R. Hansen, R. Martini, J. Choi, and Y. Ryu, "Impact of DDT on FPSO explosion risk assessment," *Process Safety Progress*, vol. 34, no. 1, pp. 44–57, 2015.
- [23] G. Atkinson, "Blast damage to storage tanks and steel clad buildings," *Process Safety and Environmental Protection*, vol. 89, no. 6, pp. 382–390, 2011.
- [24] CSB, "Final Investigation Report Refinery Explosion and Fire, US Chemical Safety and Hazard Investigation Board," 2007, <http://www.csb.gov/assets/1/19/csbfinalreportbp.pdf>.
- [25] Q. A. Baker, C. M. Doolittle, G. A. Fitzgerald, and M. J. Tang, *Recent Developments in the Baker-Strehlow VCE Analysis Methodology*, Loss Prevention Symposium, AIChE, 31st edition, 1997, paper 42f.
- [26] M. J. Tang and Q. A. Baker, "A new set of blast curves from vapor cloud explosion," *Process Safety Progress*, vol. 18, no. 4, pp. 235–240, 1999.
- [27] Z. N. Pintarič, "Assessment of the consequences of accident scenarios involving dangerous substances," *Process Safety and Environmental Protection*, vol. 85, no. 1 B, pp. 23–38, 2007.

## Research Article

# Parametric Study on Dynamic Response of FRP Masonry Structures under the Impacts of Debris Flow

Peizhen Li <sup>1,2</sup>, Tangzhenhao Li,<sup>2</sup> Zheng Lu <sup>1,2</sup> and Jin Li<sup>2</sup>

<sup>1</sup>State Key Laboratory of Disaster Reduction in Civil Engineering, Tongji University, Shanghai, China

<sup>2</sup>Research Institute of Structural Engineering and Disaster Reduction, Tongji University, Shanghai, China

Correspondence should be addressed to Zheng Lu; luzheng111@tongji.edu.cn

Received 10 July 2017; Accepted 8 January 2018; Published 8 February 2018

Academic Editor: Naveed Ahmad

Copyright © 2018 Peizhen Li et al. This is an open access article distributed under the Creative Commons Attribution License, which permits unrestricted use, distribution, and reproduction in any medium, provided the original work is properly cited.

The aim of this study was to investigate the influences of different parameters on the performance of fiber reinforced polymer (FRP) masonry structures under debris flow using finite element models that were established using the software LS-DYNA. The overall structural responses under the impacts of viscous debris flows were analyzed based on an in-depth parametric study of some key factors (fiber types, relative impact positions, etc.). The results show that the diagonal and intersecting parallel types of FRP arrangements elicit better performances than horizontal types. Use of wider fiber cloths leads to the minimization of the structural response after its impact by debris flow. In addition, glass fiber reinforced polymer (GFRP) yields the best results among all studied materials in reducing local damage, while carbon fiber reinforced polymer (CFRP) yields a better overall structural response. Impact positions at the center of the wall are more unfavorable than those at the corners.

## 1. Introduction

Debris flow, usually caused by blizzards or heavy rains, is a solid-liquid, two-phase fluid, containing a large number of sand and gravel particles [1]. Mountain areas, where debris flow is generated from frequent eruptions [2], account for two-thirds of China's land area [3]. In these areas, masonry structures constitute one of the main structural forms used in inhabited areas. According to published statistical data, masonry bricks are used to occupy 70% of construction materials in China. Besides, 80% of houses in mountainous areas have been built using bricks [4]. However, the resistance of such masonry structures to geological disasters is generally quite weak, and these parts of China have not been well developed economically [5]. Thus, debris flow has posed a great threat to the economic development and personnel safety in mountain areas. As a line of defense against debris flow, structures play an important role in ensuring the safety of residents' lives and their properties. Additionally, according to the "National Comprehensive Disaster Prevention and Reduction Plan" promoted by the Chinese government, disaster prevention and reduction is one of the most important

national strategies [6]. Consequently, taking effective measures to strengthen the structures in areas threatened by debris flow is of significant importance.

In order to decrease losses caused by debris flow, many scholars all over the world have been expending efforts to study debris flow, as well as propose various reinforcing methods, for example, energy dissipation methods [7–14]. Wu [15] used a cantilever beam, or a simply supported beam, to simulate the dam and other structures and obtained an equation of impact force based on material mechanics. This method assumed that rocks and structures were elastic and ignored the plastic deformation which might have occurred under debris impact. Accordingly, this assumption resulted in an overestimation of the impact force of rocks. Based on such studies, scholars began to consider viscoelastic and elastoplastic behaviors of the material during collisions and developed other formulations and equations [16]. The contact stiffness method was based on a spring-mass system in which an effective contact stiffness was needed. This method was recommended in the Highway Bridge Design Specification published by the National Association of Australian State Road Authorities [17]. Some scholars established calculation

methods on the debris flow force under rock impacts from the viewpoint of energy conversion. Hungr [18] analyzed the relationship between the impact energy of debris flow and the bending deformation energy of a beam, by simplifying the representation of the support scheme to a cantilever scheme. In addition, he introduced a structural stiffness coefficient and proposed a practical calculation formula for the debris flow force.

In regard to the reinforcing method, FRP plays an important role in repairing and reinforcing building structures because of its high strength, light weight, convenience in construction, and abilities of corrosion and aging resistance [19]. In a seismic test, the load-bearing capacity of a brick wall, reinforced by carbon fiber reinforced polymer (CFRP), was significantly improved in the elastic stage [20]. Seible [21] proved that the ductility of a brick wall reinforced by CFRP can be improved under earthquake actions. Based on the experiment of damaged masonry walls strengthened by CFRP under low-cyclic reversal tests, Wang [22] proved that the function of CFRP was similar to that of the rod in the truss model. CFRP delayed or prevented the development of cracks and improved the dynamic response of masonry walls.

Based on these studies, it can be concluded that FRP reinforcement can effectively increase the structural stiffness to resist seismic loads. However, the performances of conventional and FRP-reinforced structures under debris flow impact have been rarely investigated [23]. In fact, in poor mountainous area, there are plenty of masonry structures which are vulnerable to debris flow loads [24]. According to the study of Guo et al. [25], FRP is favorable for masonry walls for its impact resistance. Hence, this FRP strengthening method may constitute a cost-effective way to increase the structural resistance to debris flow. However, such a reinforcement method cannot be applied in construction without determining its parameters since they are key factors in influencing the structural performance. Consequently, this study mainly focuses on the dynamic response of FRP-reinforced masonry structures under debris flow impacts, based on an extensive parametric study of some of key factors, including fiber reinforcement arrangement, width and types of the FRP material, and relative impact positions. Simulations are developed herein in accordance with the following steps. (1) Select proper material models and element types based on relevant research experience. (2) Establish structural models. To complete this study, thirteen two-story models are established based on four assumptions. (3) Analyze structural response under dead load by dynamic relaxation method. This is a necessary step to consider the influence of the dead load and the slurry load. (4) Investigate failure process. The parametric study is developed mainly at this step by focusing on the rock impact time history curves, damage of the wall, and the displacement of the structure.

## 2. Numerical Stimulation

*2.1. Debris Flow Model.* The impact of large rocks in debris flow is the main cause of structural damage [26]. The most popular method used to calculate the impact force of rocks in debris flow is the quasi-static method. However, this method

does not take into account the time effect and complex contacts. By using the LS-DYNA software, these defects can be solved [27]. LS-DYNA is a general-purpose, finite element program, which is suitable for solving nonlinear collision problems. The modeled and calculated numerical results have been shown to be in good agreement [28–30]. Wei [31] simulated clay brick unreinforced masonry walls through the use of LS-DYNA software. It is pointed out that the numerical model can reasonably predict the damage levels by comparing them with field test data. According to Elsanadedy [32], FRP can be well-simulated through LS-DYNA by studying reinforced concrete one-way slabs upgraded with FRP composites.

Impact position and velocity are two core parameters of the rock in debris flow. According to Proske [33], the largest impact force of debris flow concentrates in regions corresponding to the range of 20–33% of flow depths. He [34] found that rocks concentrated at 1/2 of the maximum depth are more unfavorable to debris flow. Based on Zeng's study [35], the typical velocity of boulders in debris flow ranges between 3.5 m/s and 5 m/s. Based on these studies, it is assumed herein that the velocity of the rock is 5 m/s, and the impact position—whose depth is equal to the height of the first floor of the structure—is at 1/2 of the depth of the debris flow. The density is selected as 2000 kg/m<sup>3</sup>. Furthermore, the rock's size is 0.5 m × 0.5 m × 0.5 m, and its density is defined as 2800 kg/m<sup>3</sup>, resulting in the total mass of approximately 350 kg.

*2.2. Masonry Structural Model.* The masonry structural model comprises a typical two-story masonry structure designed based on Chinese codes [36] and consists of clay bricks with a thickness of 240 mm. The story height is 3.3 m and the layouts are shown in Figure 1. The compressive strengths of mortar and brick are 7.5 MPa and 15.0 MPa, respectively. The FRP is arranged at the wall of axis ③, and every piece of FRP comprises only one layer.

For FRP structures, including the column, ring beam, and masonry wall, the minimum element mesh size was 0.03 m, and the maximum element mesh size was 0.12 m. For slab and the roof, the element mesh size was 0.12 m. In addition, for steel, the minimum element mesh size was 0.1 m, and the maximum element mesh size was 0.2 m. Full 3D finite element model with the boundary conditions is shown in Figure 2. All freedom of the bottom nodes of the model is constrained.

The construction of the masonry model was based on the following assumptions.

(a) FRP behaves as an elastic material during the impact. (b) The masonry walls and FRP share the same nodes in the constructed model [37]. (c) The hydrostatic pressure is ignored in the simulation. (d) The slurry of the debris flow is assumed to behave as a one-dimensional Newtonian fluid, and it impacts the wall perpendicularly.

*2.3. Material Model.* The anisotropic brittle damage model (MAT96) is selected to simulate masonry materials [38, 39]. This an anisotropic brittle damage model which admits progressive degradation of tensile and shear strengths across

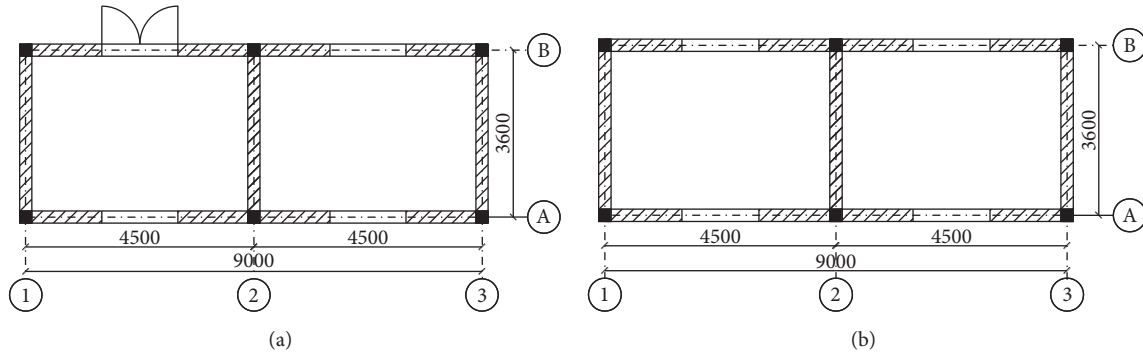


FIGURE 1: Layouts of the model: (a) first floor and (b) second floor.

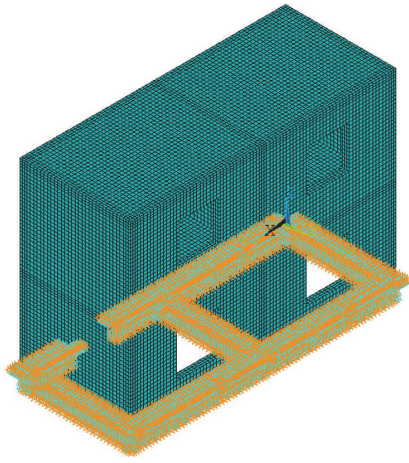


FIGURE 2: Full finite element model.

smear cracks that are initiated under tensile loadings [40]. The continuous surface cap model (CSCM), which considers the hardening, damage, and strain rate effects of the material [41], is used to simulate concrete. According to the results of Xu and Fang [42], carbon fiber has a large elastic modulus, and the tensile properties of this material were not affected by the strain rate. Accordingly, carbon fiber could be treated as an ideal elastomeric material. The constitutive relationship of carbon fiber is modeled by the stress–strain relationship corresponding to a linearly elastic material [43]. Moreover, the stiffness of rock is much larger than that of the structure, and further considerations of this matter are beyond the main focus of this study. Therefore, the rock is assumed to be rigid.

### 3. Comparative Analyses of Reinforced and Unreinforced Models

Before conducting a parametric study on the dynamic response of FRP-reinforced masonry structures under debris flow, it is necessary to evaluate the effectiveness of the FRP-reinforced masonry structure. Hence, the corresponding comparative analyses of reinforced and unreinforced models are discussed in this section. As it is shown in Figure 3, the

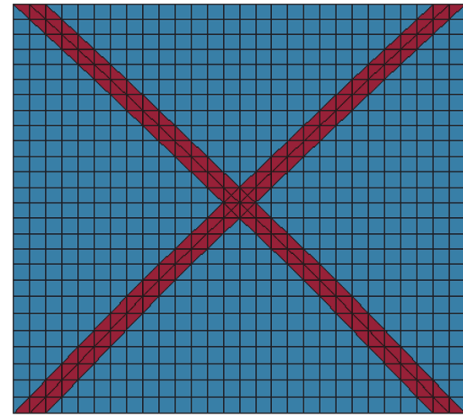


FIGURE 3: Arrangement of FRP.

FRP is arranged in a diagonal arrangement in the reinforced model. The width of FRP of the model is 150 mm, and its thickness is 0.167 mm. The unreinforced model is regarded as the control model. The rock impact occurs at the center of the wall.

**3.1. Dynamic Relaxation Analyses.** Dynamic relaxation is a numerical method aiming to find a geometry where all forces are in equilibrium. It is a step employed to consider the influences of the dead load and the slurry load before the rock impact.

According to Tang et al.'s study [44], hydrodynamic pressure of the slurry can be calculated using the formula  $F = K\rho v^2$ . The empirical coefficient  $K$  depends on the type and stage of debris flow.  $\rho$  is the density of slurry.  $v$  is the velocity of slurry. The slurry load can be simplified as uniformly distributed load [39], which is loading on the impacted cross wall. In this article, the slurry load is considered only in stationary stage. Hence, the empirical coefficient equals to 0.5. The parameters of hydrodynamic pressure of the slurry are shown in Table 1.

In simulation process, loading curve was defined by key word \*DEFINE-CURVE. Then, the uniformly distributed load was applied on the surface elements of impacted wall

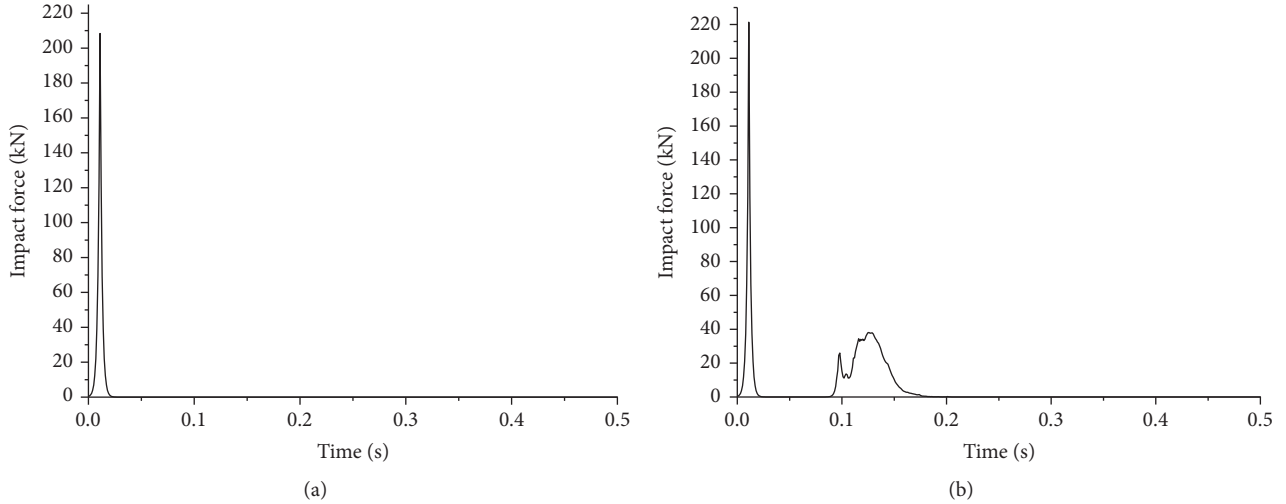


FIGURE 4: Impact force of the two models: (a) control model and (b) reinforced model.

TABLE 1: The parameters of hydrodynamic pressure of the slurry.

Type of debris flow	Density ( $\text{kg/m}^3$ )	Velocity (m/s)	Stationary stage empirical coefficient
Viscous debris flow	2000	5	0.5

by defining key word \*SET-SEGM and \*LOAD-SEGMENT-SET. Dynamic relaxation was completed by defining key word \*CONTROL\_DYNAMIC\_RELAXATION.

In this step, the maximum stress of the control model is 1.61 MPa, while the corresponding maximum stress value for the reinforced model is 1.45 MPa. For the entire model, the stress of the reinforced model is relatively smaller. Similar to the stress distribution, the displacement of the reinforced model is smaller than that of the control model. The maximum displacement of the control model is 2.52 mm, while that for the reinforced model is 1.39 mm.

**3.2. Rock Impact Time History Curves.** After the dynamic relaxation analysis, the rock began to move to the masonry wall at a speed of 5 m/s when  $T = 0$  s. As shown in Figure 4, the collision between the rock and the wall triggered the impulsive force.

It can be seen that the impact force reaches its maximum value within 10 ms. The peak forces for the control and reinforced models are 208 kN and 218 kN, respectively. The reason for this finding is that the stiffness of the reinforced model is larger than that of the control model, since the FRP contributes to the increase of the stiffness. Moreover, owing to the impedance of the FRP, there are two successive impulses in the reinforced model. However, a second impact on FRP is favorable since the rest of the structure can be made full use of. In other words, an increased proportion of the energy of the rock is absorbed by the reinforced model. Consequently, the damage in the reinforced house that is expected to be caused by the rock could be reduced. Figure 5 shows the

condition during the impact at  $T = 15$  ms. It can be seen that the rock has crashed into the structure in the control model at this moment, while the rock is stopped by the FRP of the reinforced model. This result also indicates that the reinforced model performs better than the unreinforced one.

**3.3. Displacement Response.** Four typical nodes are selected to analyze the overall displacement response of the structure. The position and number of the nodes are shown in Figure 6. Figure 7 shows the displacement time history curves of these typical nodes. It can be seen that the fluctuation of the displacement of the reinforced model is much smaller than that of the control model. In addition, as it is shown in Table 2, the maximum displacement of the control model is a little larger than that of the reinforced model. This is because FRP absorbs part of the energy of the rock, and because the masonry walls of the reinforced model are fully used.

In summary, the reinforced model performs better than the unreinforced model. Therefore, a parametric study on the dynamic response of FRP-reinforced masonry structures under debris flow impact is necessary.

## 4. Parametric Study on Dynamic Responses

### 4.1. Fiber Reinforcement Arrangement

**4.1.1. Scheme of Reinforcement.** Three finite element models are established. They are reinforced by FRP and classified in three types, namely, the diagonal type, the intersecting parallel type, and the horizontal type. The reinforcement scheme is shown in Table 3, and the corresponding finite element models are shown in Figure 8.

### 4.1.2. Dynamic Response

**(a) Rock Impact Time History Curves.** Figure 9 shows the impact time history curves for models 1 to 3. It can be seen that the peak values of the impact forces of models 1 to 3 are

TABLE 2: Maximum displacement (mm) of the control and reinforced models.

Node	Model		
	Control model	Reinforced model	Percentage reduction
1	2.14	2.03	5.1%
2	2.16	2.02	6.5%
3	1.69	1.58	6.5%
4	0.35	0.32	8.6%

TABLE 3: Reinforcement scheme with different FRP arrangements.

Number	Width (mm)	Thickness (mm)	Paste type	Area (m <sup>2</sup> )
1	340	0.167	Diagonal type	3.08
2	240	0.167	Intersecting parallel type	3.08
3	240	0.167	Horizontal type	3.08

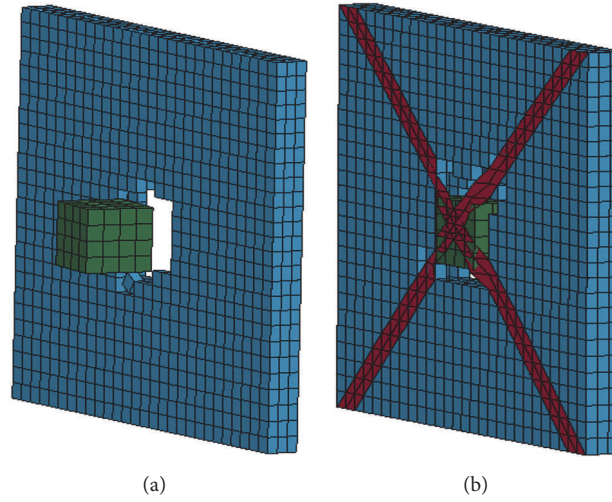


FIGURE 5: The condition of the two models at  $T = 15$  ms: (a) control model and (b) reinforced model.

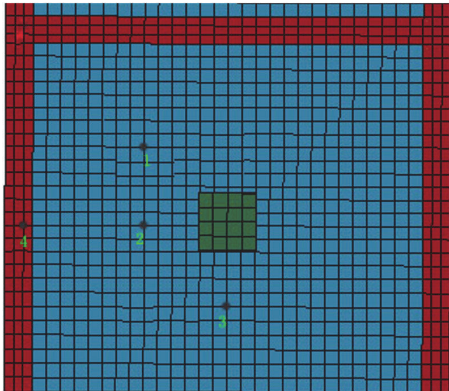


FIGURE 6: Locations of nodes in the impacted transverse wall.

209 kN, 212 kN, and 211 kN, respectively. In addition, based on the irregular pattern of the curves upon rock impact with the FRP, it can be noticed that the impact force is complex. This is because the vibration of the model caused by the

impact triggers the interaction between the rock and the FRP. As it is shown in Figure 9, the arrangement of carbon fiber has influenced the magnitude of the impact force and the duration of the interaction. Among these arrangement types, the horizontal FRP arrangement reduces the force and prolongs the interaction between the rock and the fiber.

(b) *Damage Response.* Figure 10 shows the stress contours for models 1 to 3 at  $T = 300$  ms. It can be seen that local damage is the main failure mode. A certain degree of stress concentration occurs at the four corners of the rectangular hole and at the bottom of the wall. Maximum stress appears at the locations of the fixed supports that are connected to the ground. The maximum stress values of models 1 to 3 are 1.06 MPa, 0.94 MPa, and 1.15 MPa, respectively. Based on the stress contours, it can be deduced that the stress values of the diagonal and the intersecting parallel types are smaller, because the stress of the wall distributes more uniformly in these two types. Consequently, these two types of arrangements are more favorable for debris flow resistance. Moreover, it can also be noted that there is variation in

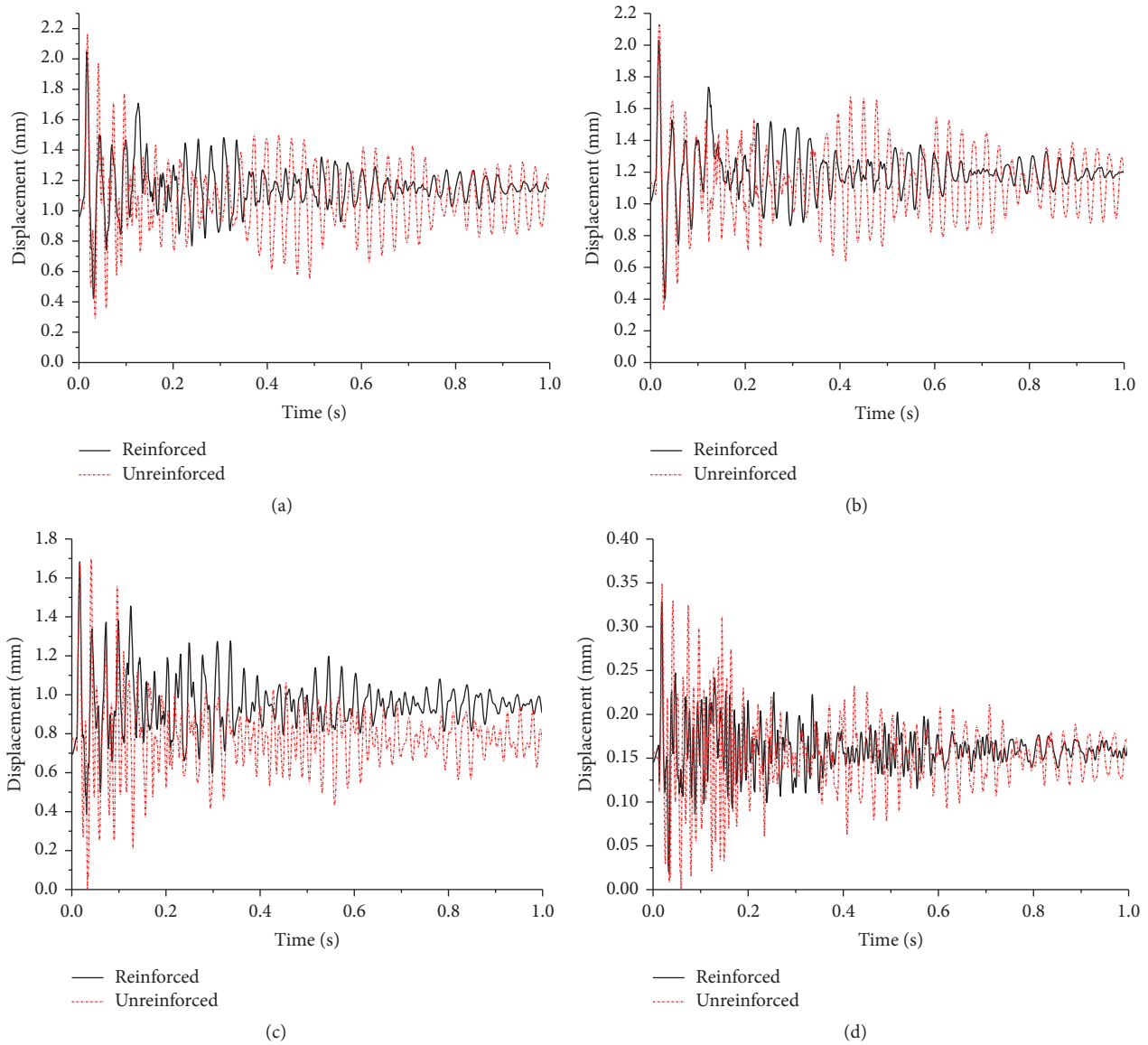


FIGURE 7: Displacement time history curves of nodes: (a) node 1, (b) node 2, (c) node 3, and (d) node 4.

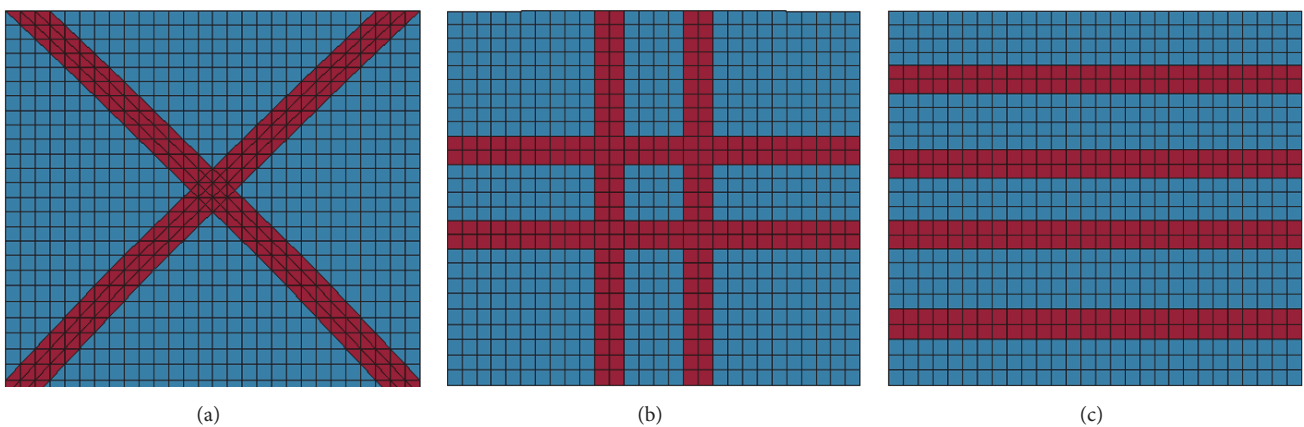


FIGURE 8: Fiber reinforcement arrangements: (a) model 1, (b) model 2, and (c) model 3.

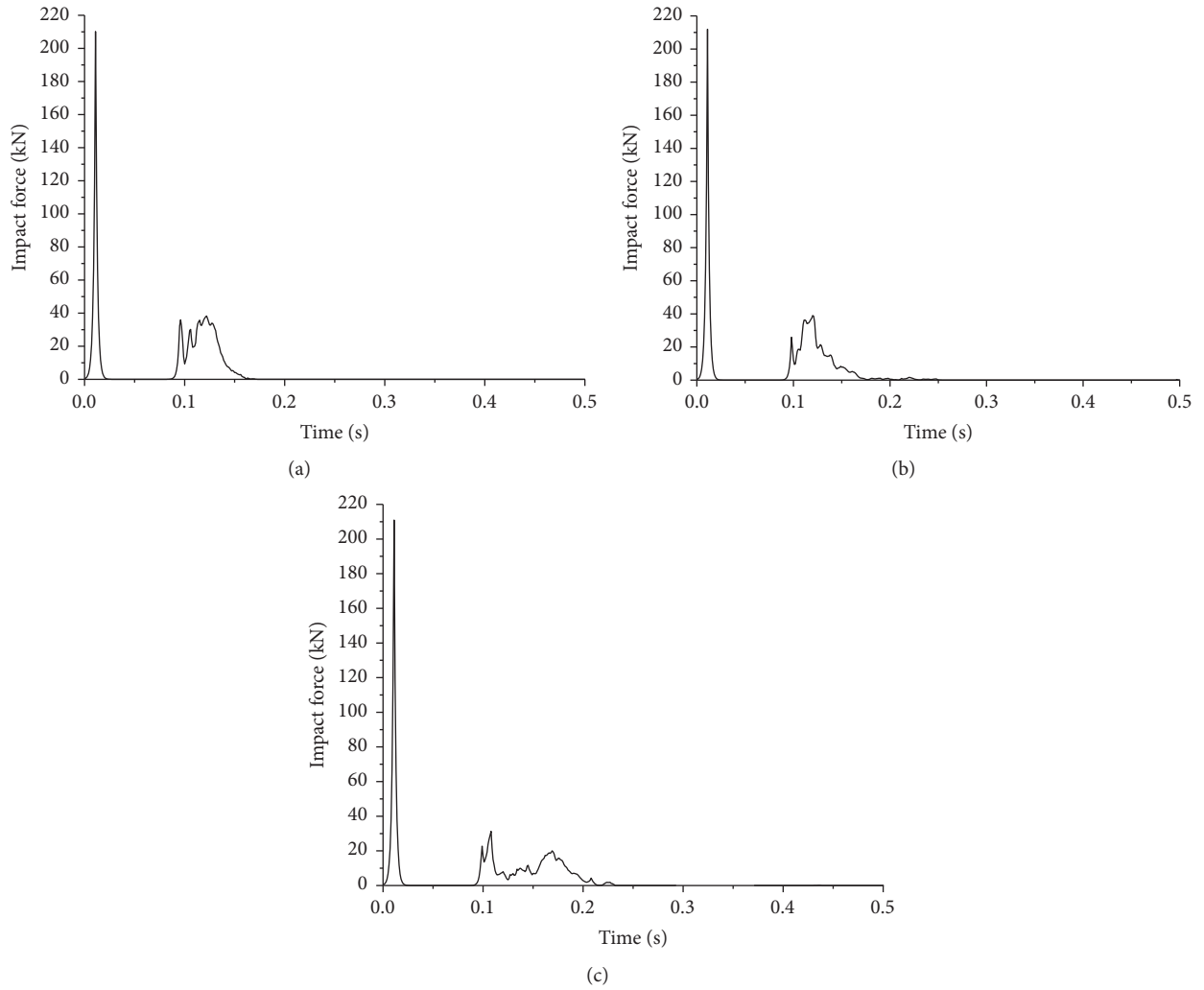


FIGURE 9: Impact time history curves: (a) model 1, (b) model 2, and (c) model 3.

the way local damage develops, in accordance with the arrangement type. It can be seen that the local damage develops along the direction of fiber arrangements. This damage results owing to the change of stiffness, which is affected by FRP. These bricks have a higher stiffness and tend to absorb more energy during the interaction, which results in the local damage.

(c) *Displacement Response.* Four typical nodes are selected to analyze the overall displacement response of the structure. The position and number of the nodes are the same as those shown in Figure 6. Figure 11 shows the displacement time history curves of these typical nodes. It can be seen that the displacement patterns of the nodes in these three models are basically the same. Model 3 yields the largest displacement amplitude, and the largest final residual strain, while model 1 yields the smallest. This is because the arrangement types of models 1 and 2 make the stress distribute uniformly on the wall. In addition, the wave of the time history curve of node 4 is denser than the others, indicating that node 4 has

TABLE 4: Maximum displacements (mm) of models 1 to 3.

Node	Model		
	1	2	3
1	2.00	2.08	2.05
2	2.60	2.54	2.63
3	1.49	1.52	1.56
4	0.23	0.27	0.28

a higher vibration frequency. This is because node 4 is on the structural column, whose out-of-plan stiffness is larger than that of the masonry wall. A higher stiffness leads to a higher vibration frequency.

Table 4 lists the maximum displacement of each typical node. The results from these data are consistent with the elicited results shown in Figure 11. According to these analyses, the diagonal and the intersecting parallel types of FRP arrangements elicit better performances in resisting debris flow than the horizontal type.

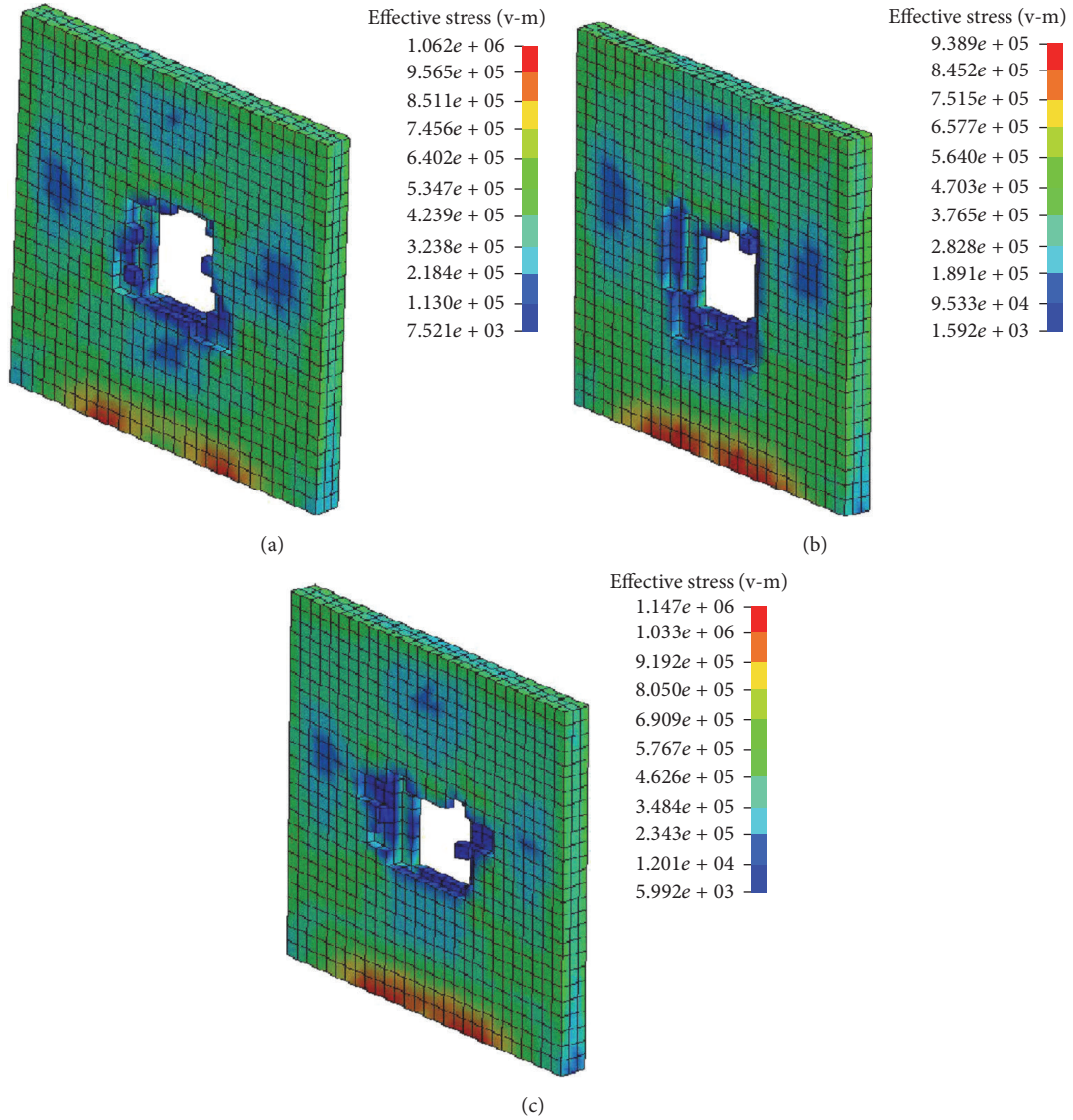


FIGURE 10: Stress contours of impacted walls at  $T = 300$  ms: (a) model 1, (b) model 2, and (c) model 3.

TABLE 5: Scheme of reinforcement at different FRP widths.

Number	Width (mm)	Thickness (mm)	Paste type	Area (m <sup>2</sup> )
4	150	0.167	Diagonal	1.35
5	250	0.167	Diagonal	2.25
6	250	0.167	Diagonal	3.15

## 4.2. Fiber Width

**4.2.1. Scheme of Reinforcement.** Three finite element models are established. The FRP of these models are all arranged in a diagonal arrangement, but with different widths. The scheme of reinforcement is shown in Table 5, and the corresponding finite element models are shown in Figure 12.

### 4.2.2. Dynamic Response

**(a) Rock Impact Time History Curves.** Figure 13 shows the impact time history curves from model 4 to model 6. It can be

seen that the peak values of the impact forces of models 4 to 6 are 202 kN, 208 kN, and 209 kN, respectively. The differences of the force values result from the different wall stiffness values, which are affected by the width of the FRP. As it is mentioned in Section 4.1.2, irregular curve patterns result from the vibration of the model.

**(b) Damage Response.** Figure 14 shows the stress contours for models 4 to 6 at  $T = 300$  ms. It can be found that local damage is the main failure mode. A certain degree of stress concentration occurs at the four corners of the hole, and at

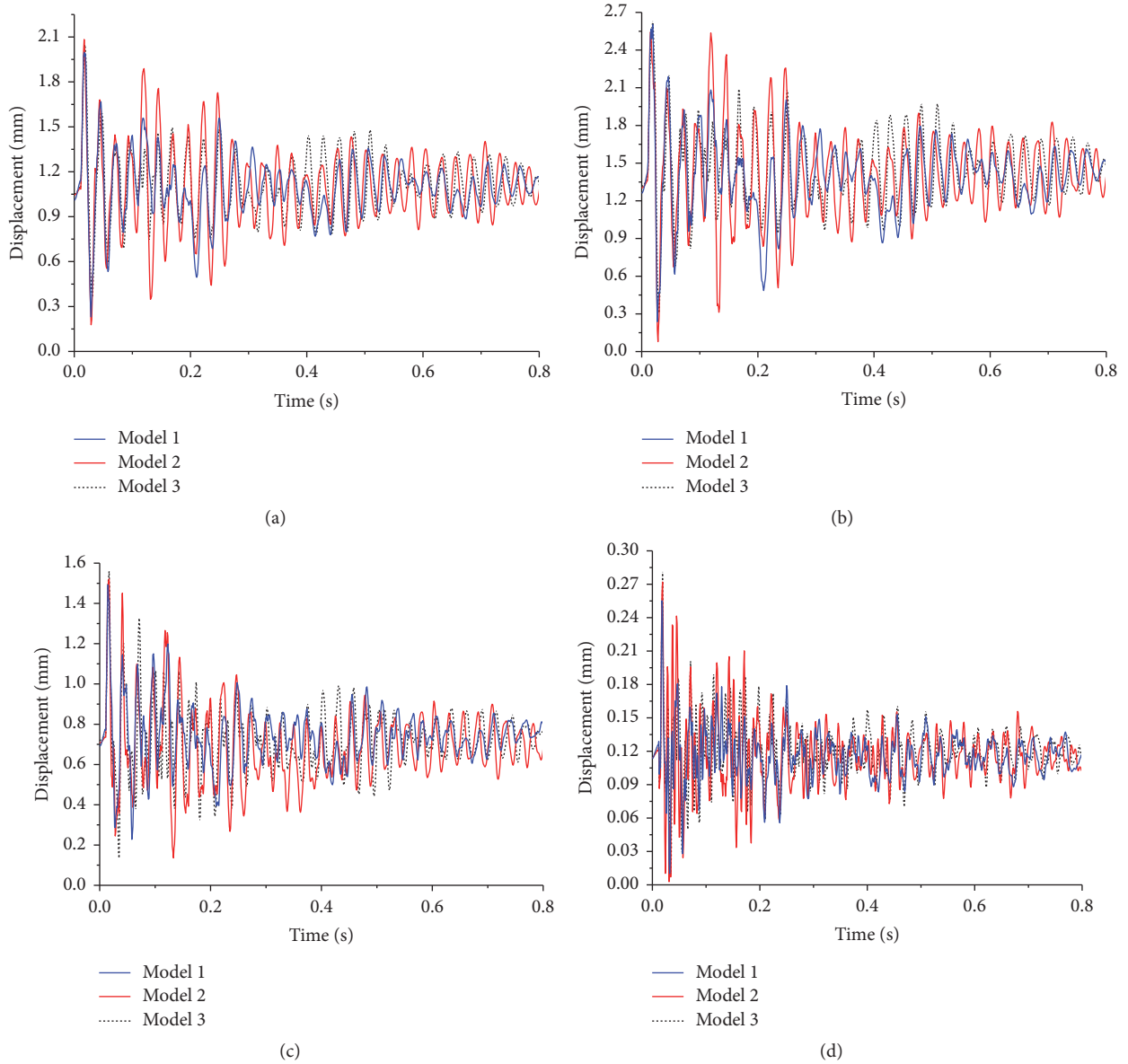


FIGURE 11: Displacement time history curve of nodes: (a) node 1, (b) node 2, (c) node 3, and (d) node 4.

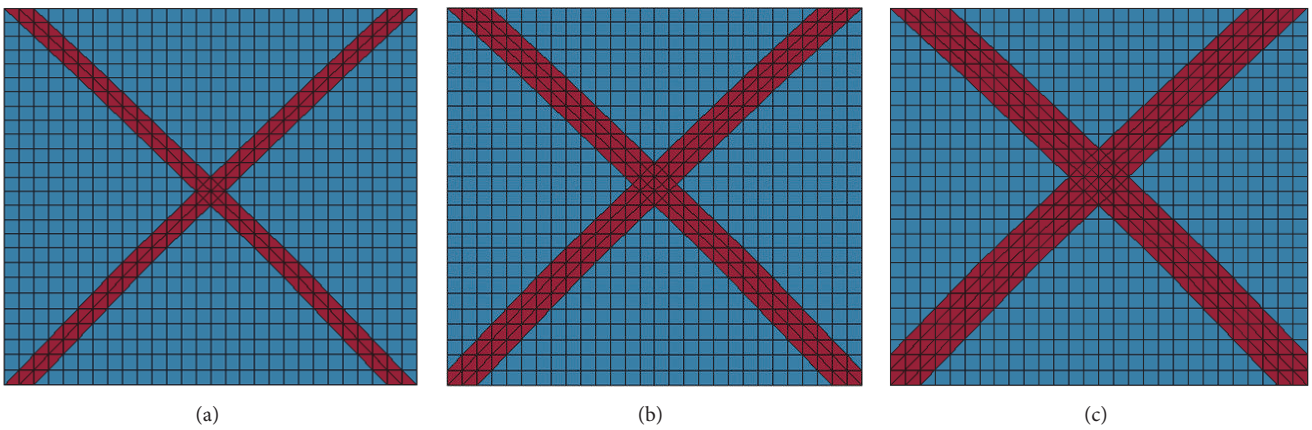


FIGURE 12: Carbon fiber layouts: (a) model 4, (b) model 5, and (c) model 6.

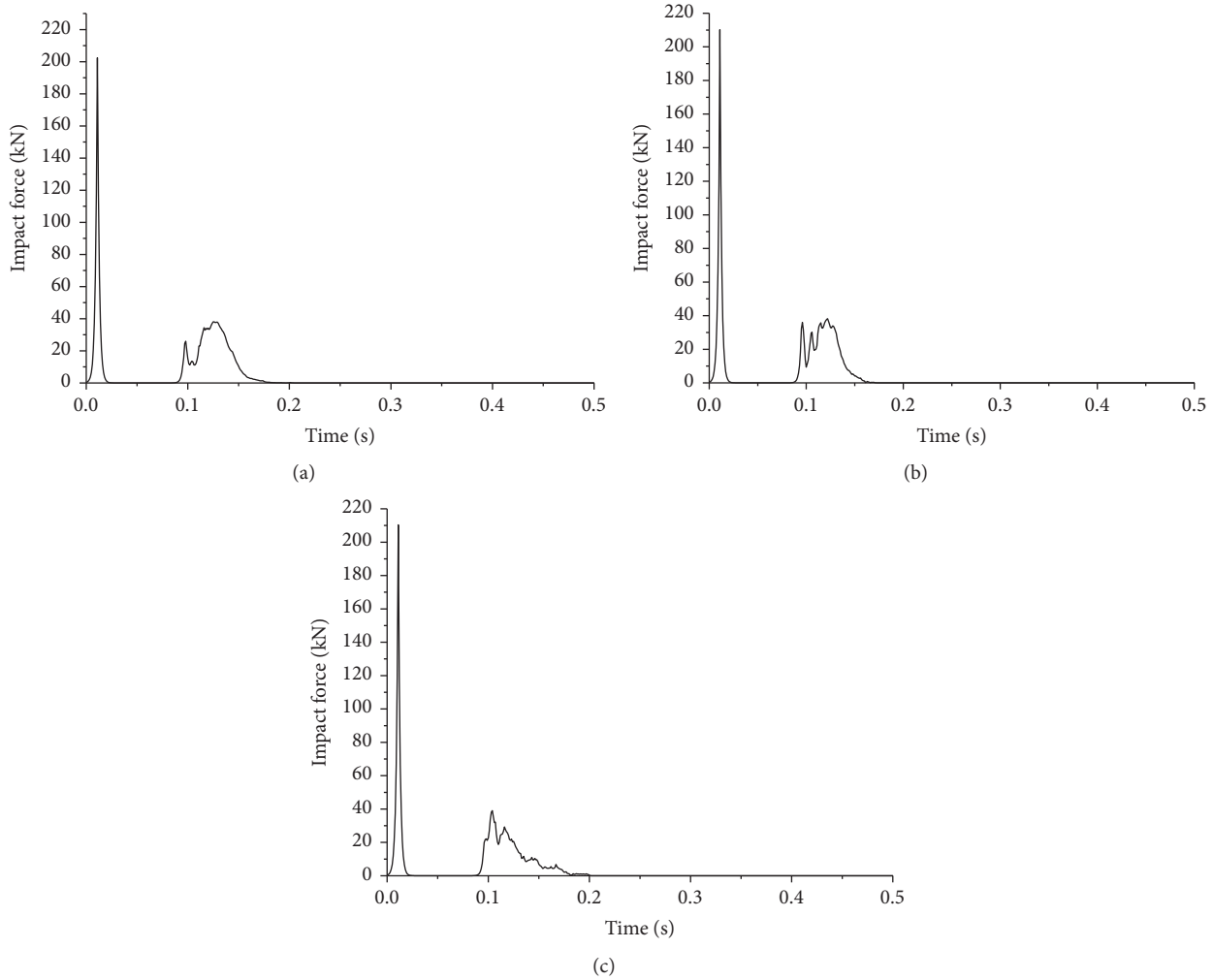


FIGURE 13: Impact time history curves: (a) model 4, (b) model 5, and (c) model 6.

the bottom of the wall. The maximum stress appears at the fixed supports connected to the ground.

By comparing the damage of the three models, model 4 yields the smallest final damage, while model 6 yields the largest. There are two main reasons for this. First, at increasing FRP widths, the duration of the interaction between the rock and FRP becomes longer. Second, the stiffness of the wall increases when the width of the carbon fiber cloth increases. According to  $F = \sqrt{mv^2k}$  (where  $F$  is the impact force,  $m$  is the mass,  $v$  is the velocity, and  $k$  is the stiffness), the impact force increases with increases in stiffness. Consequently, an increased energy is absorbed by the wall when the fiber cloth is wider, which results in an increased damage.

(c) *Displacement Response.* Figure 15 shows the displacement time history curves of selected typical nodes. From these curves, the displacement patterns of the nodes in the three models are generally the same. Model 4 has the largest displacement amplitude, and the largest final residential strain, while model 6 has the smallest. This is because the deformation of the FRP cloth contributes to energy absorption, which results in decreases of the wall displacement. In

addition, the time history curve of node 4 is denser than the others, indicating that node 4 has a higher vibration frequency. As it was mentioned before, node 4 is on the structural column, whose out-of-plan stiffness is larger than that of the masonry wall. A higher stiffness leads to a higher vibration frequency.

Table 6 lists the maximum displacement of each typical node. The results from these data are consistent with the elicited results shown in Figure 15. In general, a wider fiber cloth minimizes the response of the structure after its impact by debris flow.

4.3. *Fiber Types.* To analyze the effect of different fiber types on the reinforced structure under debris flow, carbon fiber reinforced polymer (CFRP), glass fiber reinforced polymer (GFRP), and aramid fiber reinforced polymer (AFRP) were chosen. The main differences of these FRPs exist in their physical parameters, including their elastic moduli, tensile strengths, and ultimate elongation rates.

4.3.1. *Scheme of Reinforcement.* Some of the main physical parameters of the CFRP, GFRP, and AFRP are listed in

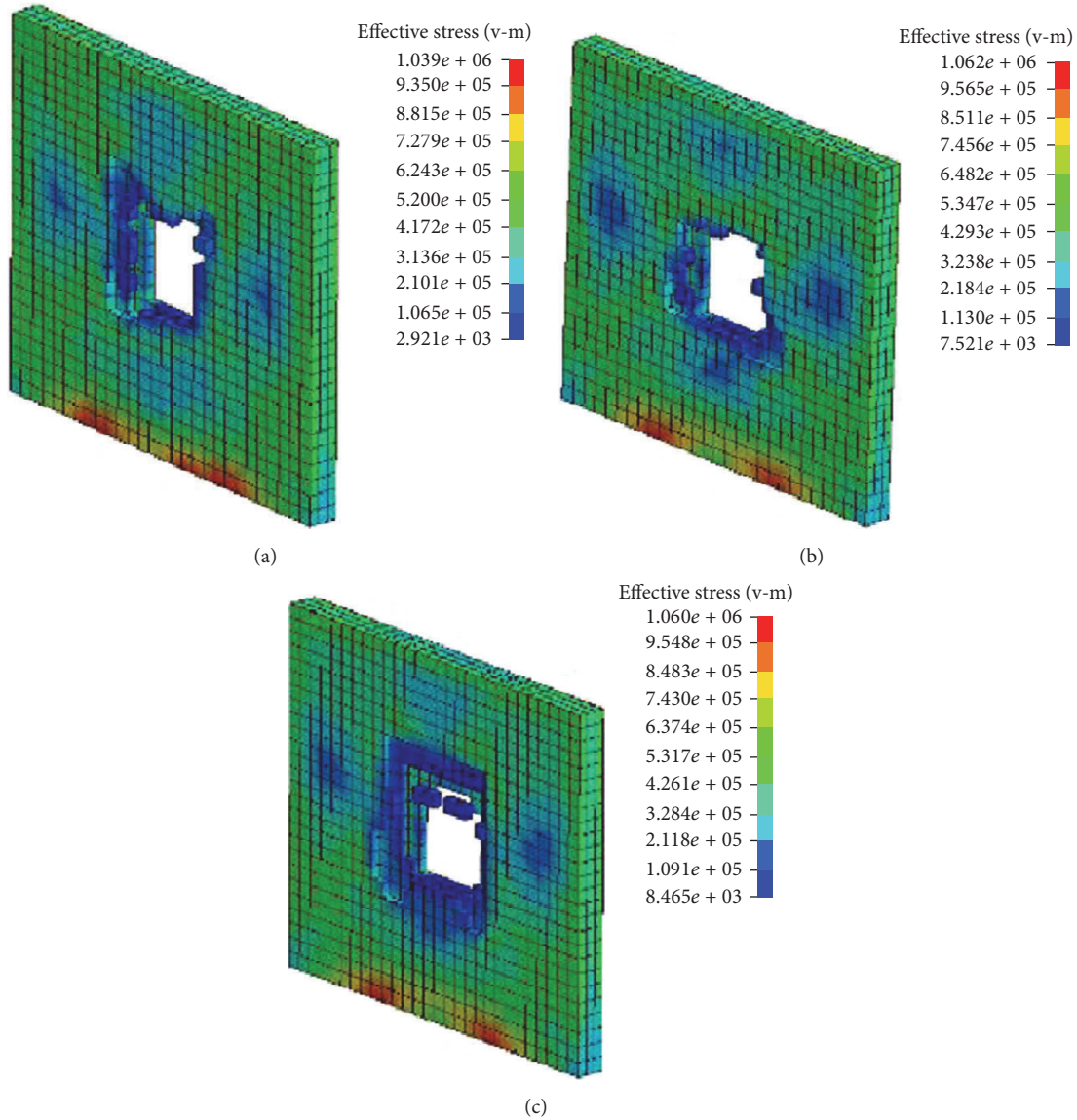


FIGURE 14: Stress contours of impacted walls at  $T = 300$  ms: (a) model 4, (b) model 5, and (c) model 6.

TABLE 6: Maximum displacements (mm) elicited by the three models.

Node	Model		
	4	5	6
1	2.03	1.99	1.96
2	2.65	2.60	2.47
3	1.67	1.49	1.47
4	0.27	0.25	0.24

Table 7. It can be found that CFRP has the largest tensile and elastic modulus values, whereas GFRP has the largest density and AFRP the largest ultimate elongation rate. The adopted scheme of reinforcement is shown in Table 8.

#### 4.3.2. Dynamic Response

(a) *Rock Impact Time History Curves.* Figure 16 shows the impact time history curves for models 7 to 9. It can be seen that the peak values of the impact force of models 7 to 9 are 221 kN, 219 kN, and 213 kN, respectively. The magnitude of the impact forces and the duration of the interactions exhibit minor differences in these models. This is primarily owing to the different elastic moduli of the three FRP materials. Furthermore, as previously mentioned, the generated irregular patterns of the curves after the rock penetrates the wall are complex, and this is an outcome of the induced vibration owing to the specific model.

(b) *Damage Response.* Figure 17 shows the stress contours of models 7 to 9 at  $T = 300$  ms. It can be seen that the local damage is the main failure mode of the walls. In

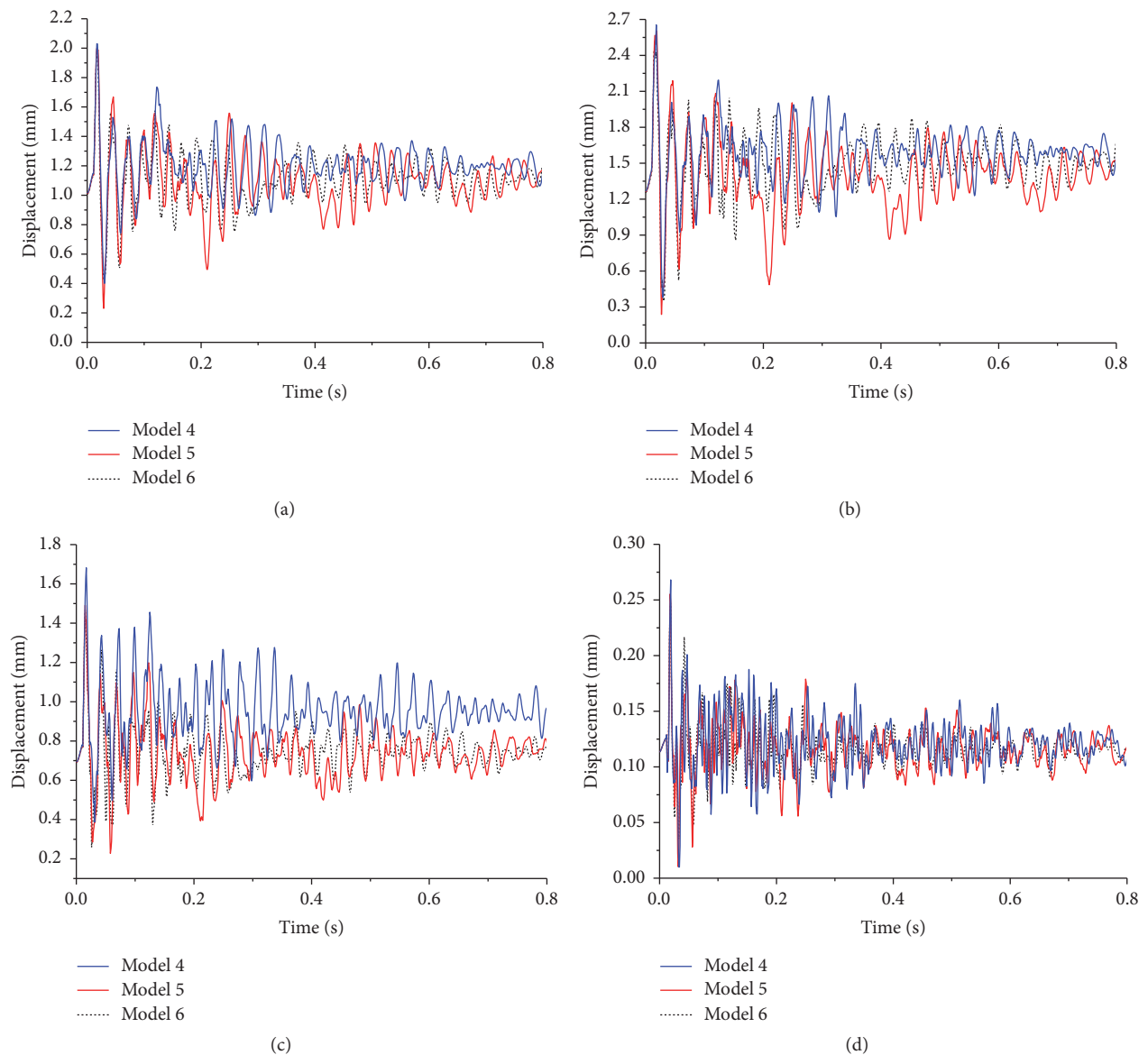


FIGURE 15: Node displacement-time curve: (a) node 1, (b) node 2, (c) node 3, and (d) node 4.

TABLE 7: Main physical parameters of CFRP, GFRP, and AFRP.

FRP	Density ( $\text{g/cm}^3$ )	Tensile strength (MPa)	Elastic modulus (GPa)	Ultimate elongation rate (%)
CFRP	1.8	3500	230	1.5
GFRP	2.5	3100	72.5	2.7
AFRP	1.45	2900	125	2.8

TABLE 8: Adopted scheme of reinforcement for different FRP types.

Model number	FRP	Width (mm)	Thickness (mm)	Arrangement type
7	Carbon fiber reinforced polymer (CFRP)	200	0.170	Diagonal
8	Glass fiber reinforced polymer (GFRP)	200	0.170	Diagonal
9	Aramid fiber reinforced polymer (AFRP)	200	0.170	Diagonal

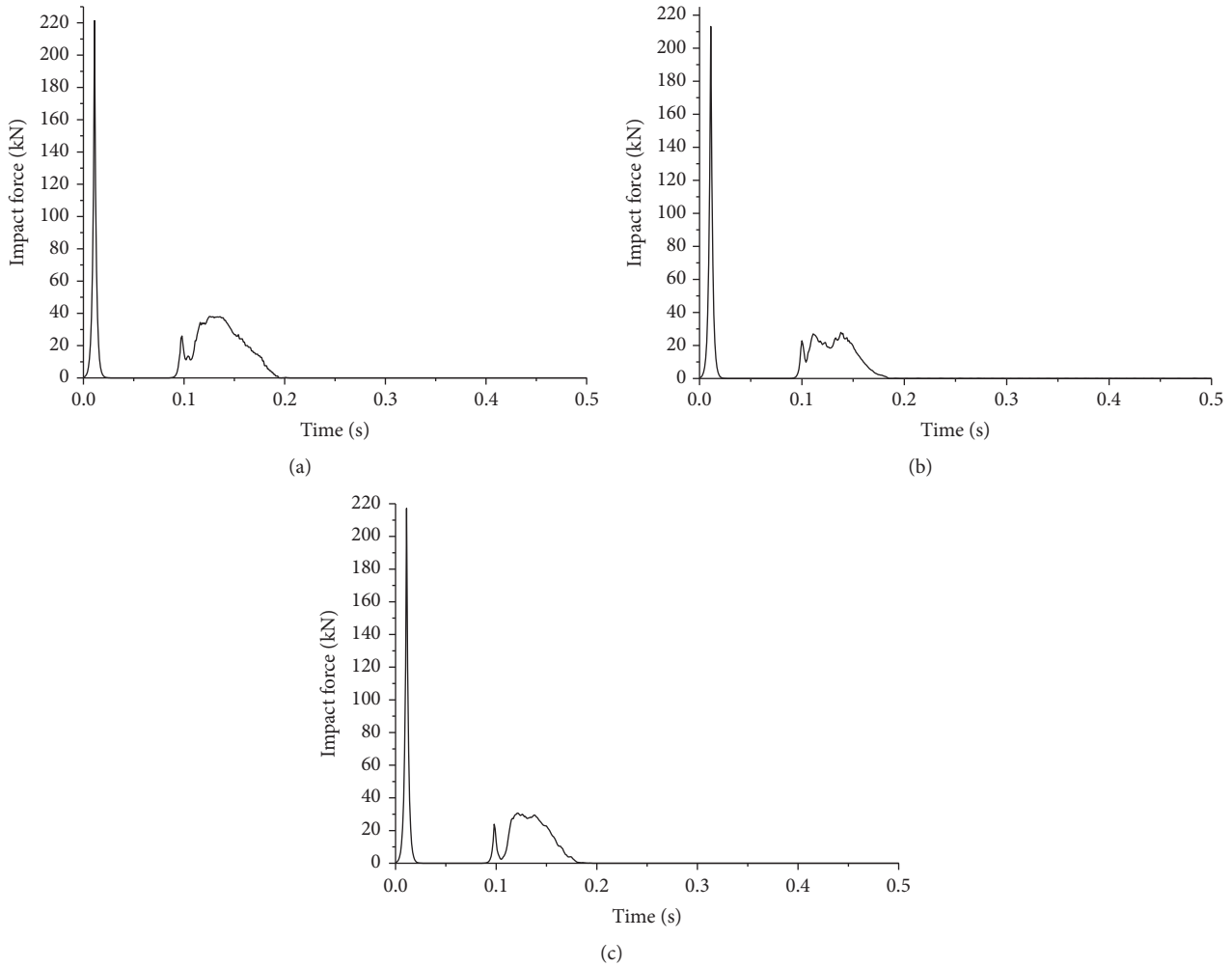


FIGURE 16: Impact time history curve: (a) model 7, (b) model 8, and (c) model 9.

addition, a certain degree of stress concentration occurs at the four corners of the hole and at the bottom of the wall. By comparing the damage of these three models, model 8 yields the smallest final damage, while model 7 yields the most severe final damage. This finding possibly relates to the elastic modulus of the FRP. As it is shown in Tables 7 and 8, model 7 is reinforced by GFRP whose elastic modulus is 72.5 GPa, and model 8 is reinforced by CFRP whose elastic modulus is 230 GPa.

(c) *Stress–Strain Response.* Figure 18 shows the stress fields for models 7 to 9 when the velocity of the rock is reduced to zero upon impact. Figure 19 shows the strain of each model at the same instant in time. At that moment, the fiber stress and strain reach their maximum values. It can be seen that the stress values of the elements around the impact position also reach the value of the largest stress. The maximum stresses of models 7 to 9 are 290 MPa, 180 MPa, and 230 MPa, respectively. These values are much smaller than the tensile strengths of the fibers. The magnitude distribution pattern of the strain is coincident with that of stress. The maximum strain values of models 7 to 9 are 0.005, 0.012, and 0.009, respectively, which are also smaller than the FRPs' ultimate

strain. The conclusion that can be inferred is that increased energy is absorbed by the fiber, and increased fiber stress is developed when the elastic modulus is increased.

(d) *Displacement Response.* Figure 20 shows the displacement time history curves of selected typical nodes. From these curves, the displacement patterns of the nodes in three models are generally the same. Model 8 yields the largest displacement amplitude, and the largest final residual strain, while model 7 yields the smallest displacement amplitude and final residual strain. Because model 8 is reinforced by CFRP with a larger elastic modulus, it can absorb more energy upon deformation, resulting in the reduction of the displacement of the entire model. In addition, the time history curve of node 4 is also denser than the others, which means that node 4 has a higher vibration frequency. As it was mentioned before, node 4 attains a higher stiffness than other nodes.

Table 9 lists the maximum displacement of each typical node. The results from these data are consistent with the results presented in Figure 20. In general, CFRP performs better under debris flow, because of its high elastic modulus.

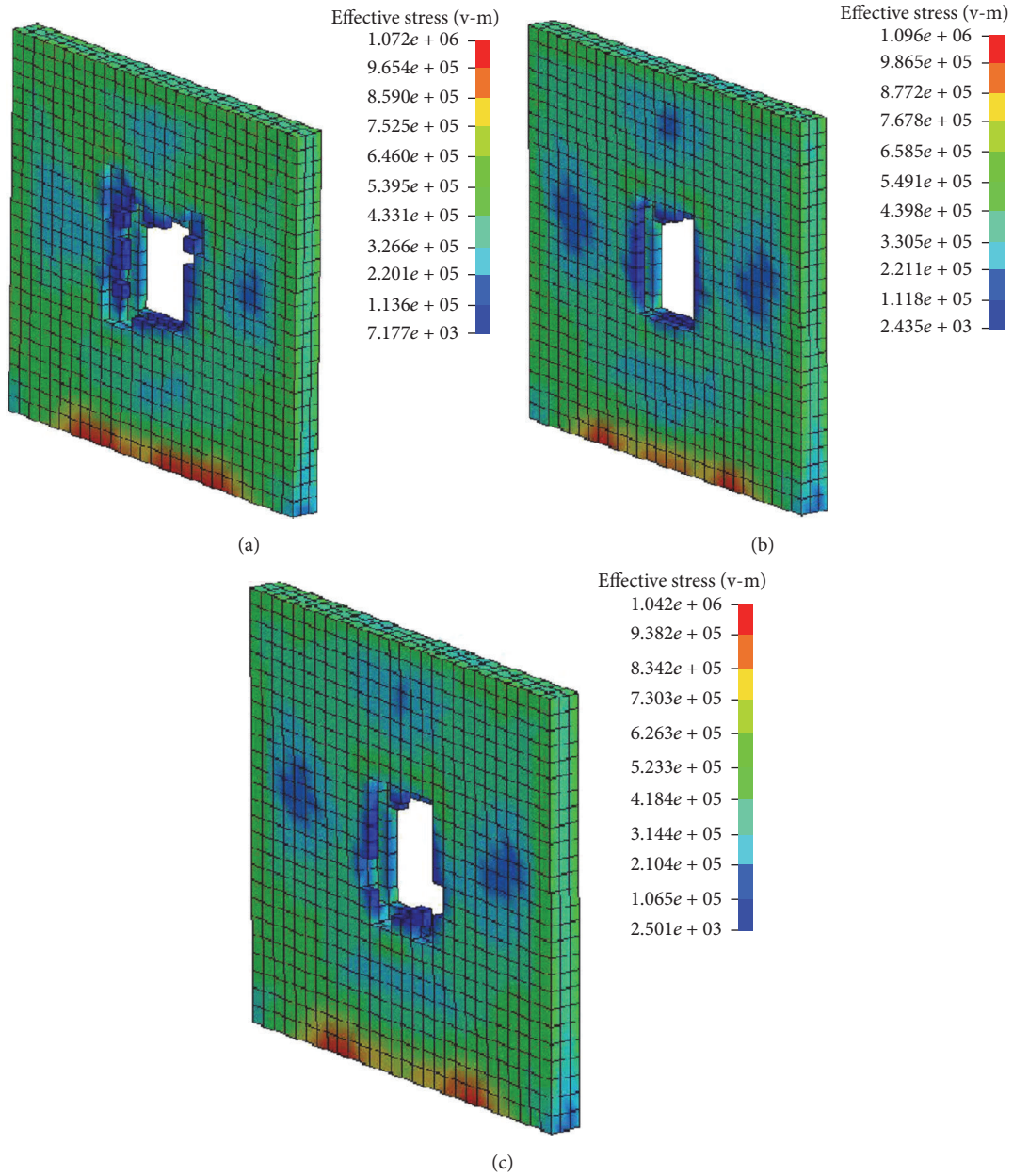


FIGURE 17: Stress contours of impacted wall at  $T = 300$  ms: (a) model 7, (b) model 8, and (c) model 9.

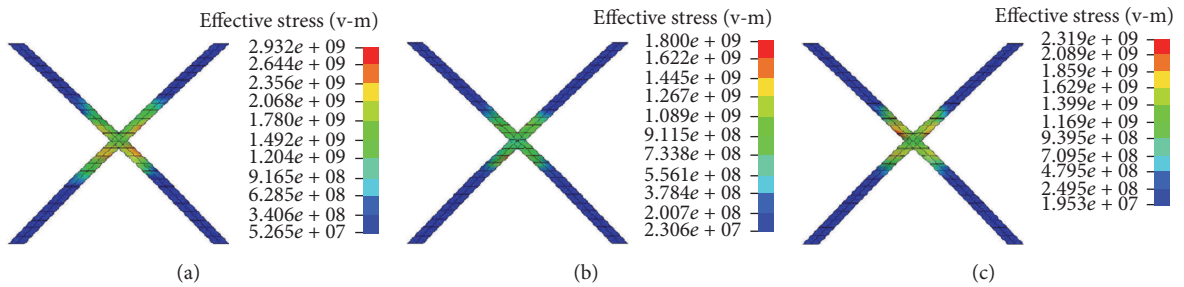


FIGURE 18: Stress contours of three models: (a) model 7, (b) model 8, and (c) model 9.

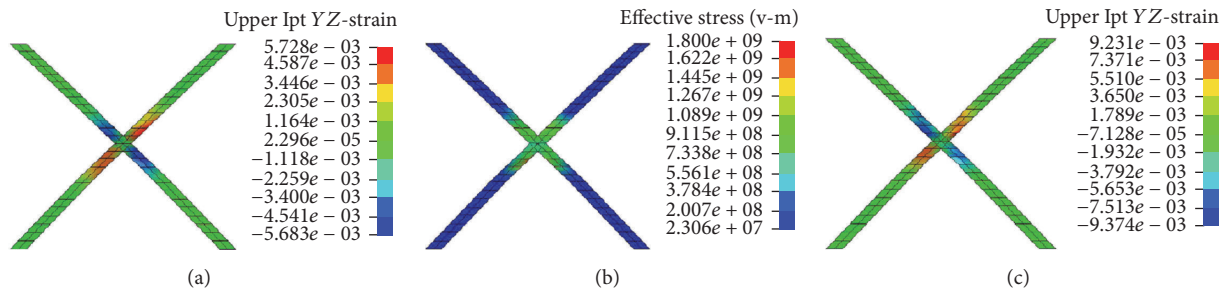


FIGURE 19: Strain contours of the three models: (a) model 7, (b) model 8, and (c) model 9.

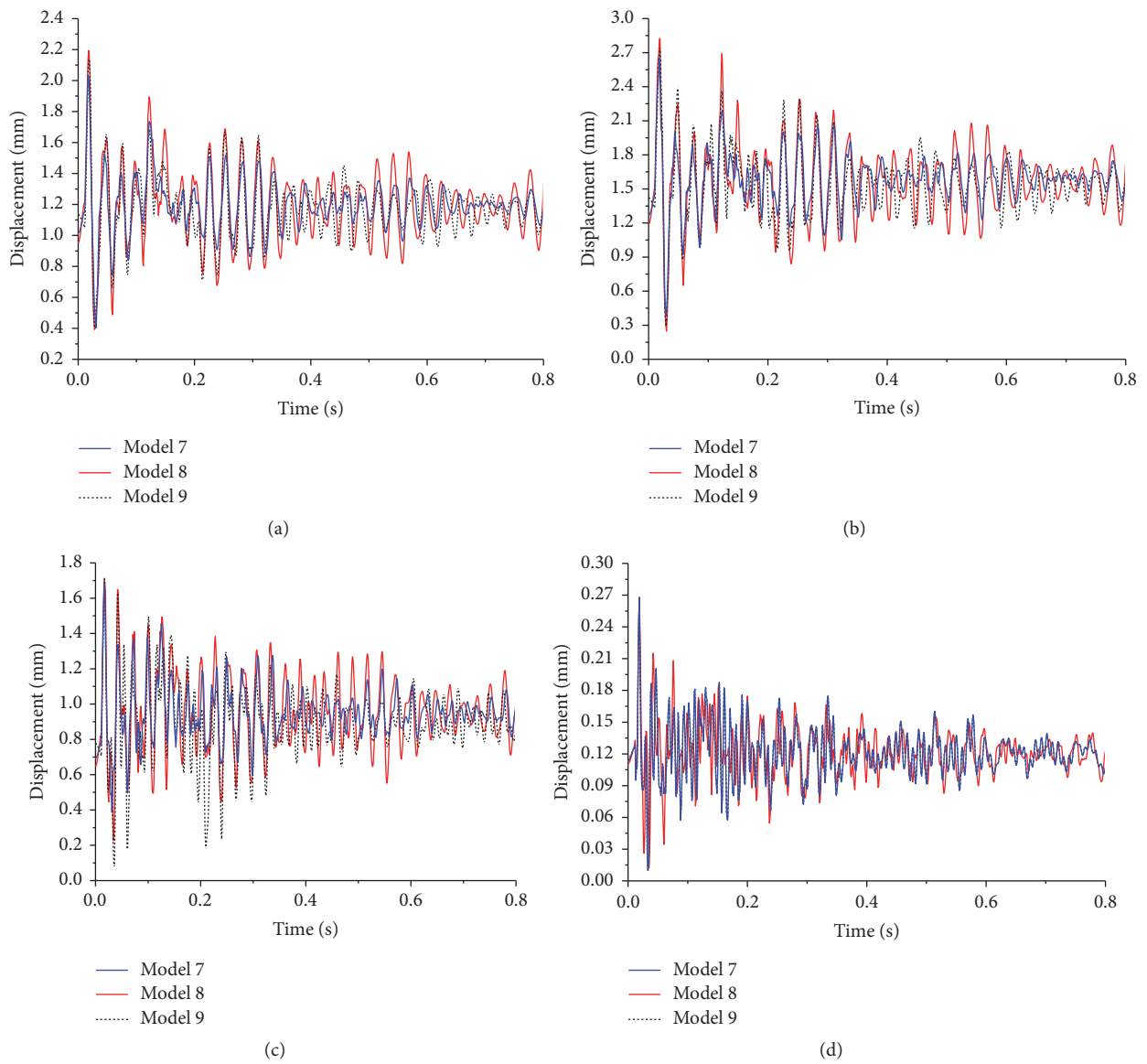


FIGURE 20: Node displacement-time curve: (a) node 1, (b) node 2, (c) node 3, and (d) node 4.

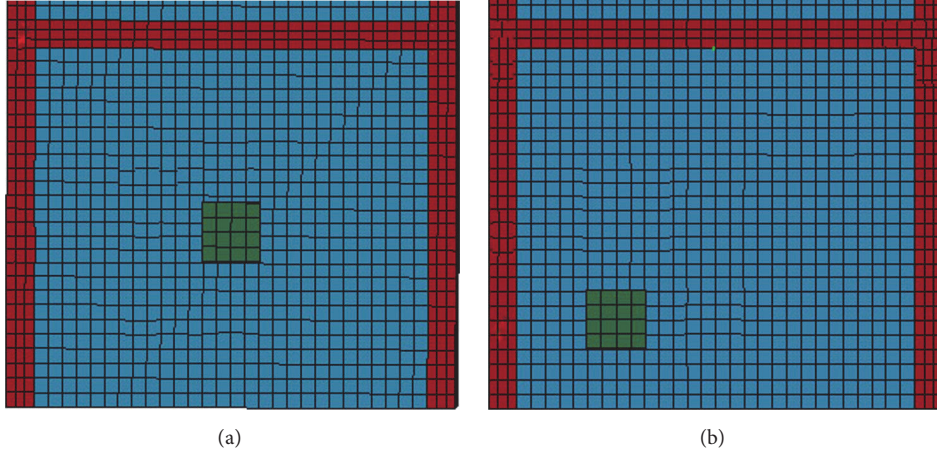


FIGURE 21: Relative impact positions: (a) model 10 and (b) model 11.

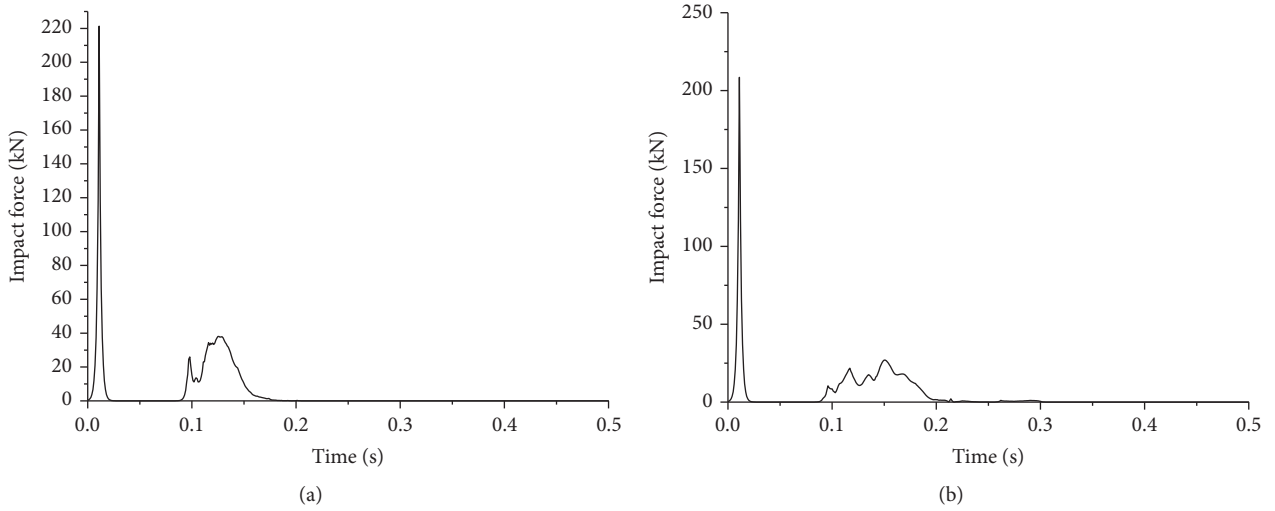


FIGURE 22: Impact time history curves: (a) model 10 and (b) model 11.

TABLE 9: Maximum displacements (mm) elicited by the three models.

Node	Model		
	7	8	9
1	2.03	2.14	2.20
2	2.62	2.83	2.74
3	1.68	1.78	1.71
4	0.26	0.27	0.27

#### 4.4. Relative Impact Position

**4.4.1. Scheme of Reinforcement.** To analyze the effect of different impact positions, two models were established. As shown in Figure 3, a diagonal FRP arrangement is adopted. The widths of the FRP of the two models are 150 mm, and the thickness values are 0.167 mm. The reinforcement scheme is shown in Table 10. Figure 21 shows the relative impact positions of the two models.

TABLE 10: Scheme of reinforcement at different impact positions.

Number	Distance from the center of the impact to the bottom (mm)	Distance from the center of the impact to axis A (mm)
10	1530	1680
11	710	960

#### 4.4.2. Dynamic Response

**(a) Rock Impact Time History Curves.** Figure 22 shows the impact time history curves for models 10 to 11. It can be seen that the peak values of the impact force of models 10 and 11 are 218 kN and 209 kN, respectively. This difference results from the different stiffness. The stiffness of the wall is a little larger at the center, because the area of the FRP at the cross-position is larger than that of other parts. Furthermore, as mentioned above, irregular curve patterns are elicited after the rock penetrates the wall owing to the model vibrations.

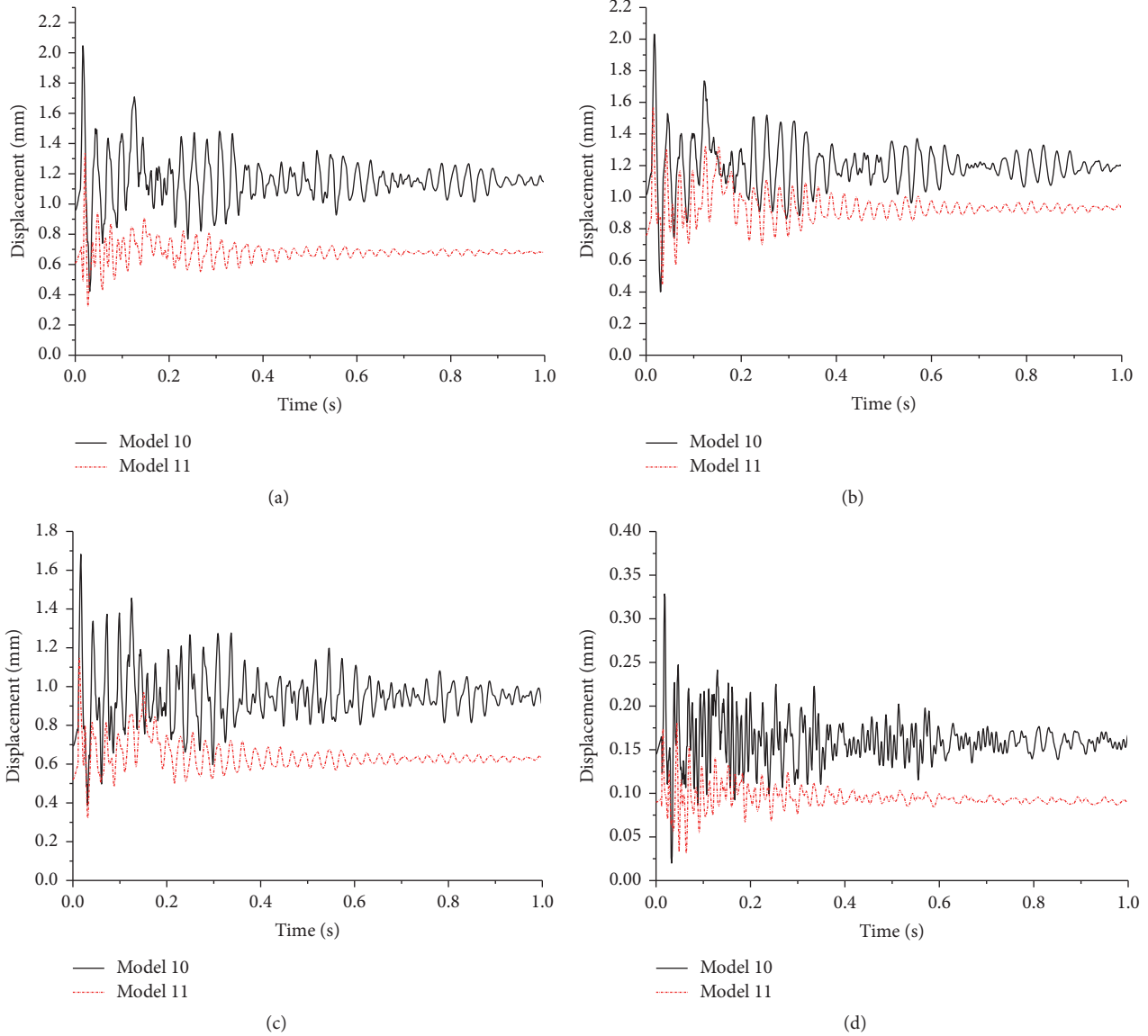


FIGURE 23: Node displacement-time curve: (a) node 1, (b) node 2, (c) node 3, and (d) node 4.

(b) *Displacement Response.* Figure 23 shows the displacement time history curves of four typical nodes. As seen, the displacement patterns of the nodes in the two models are generally the same. However, the value of the displacement in model 11 is much smaller than that of model 10. This is because the impact position of model 11 is close to the foundation of the structure. In terms of mechanics, for the forces that have the same value, the force that is closer to the anchorage end causes a smaller displacement. Table 11 lists the maximum displacements for each of the studied nodes. The results from these data are consistent with the results plotted in Figure 23.

(c) *FRP Response.* Figure 24 shows the stress distribution of FRP for the two models when maximum stress occurs. It can be seen that the maximum stress concentrates at the impact position. The maximum stress of FRP in model 10 is 293 GPa

TABLE 11: Maximum displacements (mm) elicited by the two models.

Node	Model	
	10	11
1	2.03	1.34
2	2.02	1.57
3	1.58	1.16
4	0.32	0.18

when  $T = 130$  ms, while its corresponding value is 340 GPa in model 11 when  $T = 150$  ms. This is because the impact is burdened by two FRP strips in model 10, but by one FRP strip in model 11. Figure 25 shows the stress time history curves of the maximum stress element in the two models. Based on the curves, it can be concluded that FRP is in the elastic stage of its

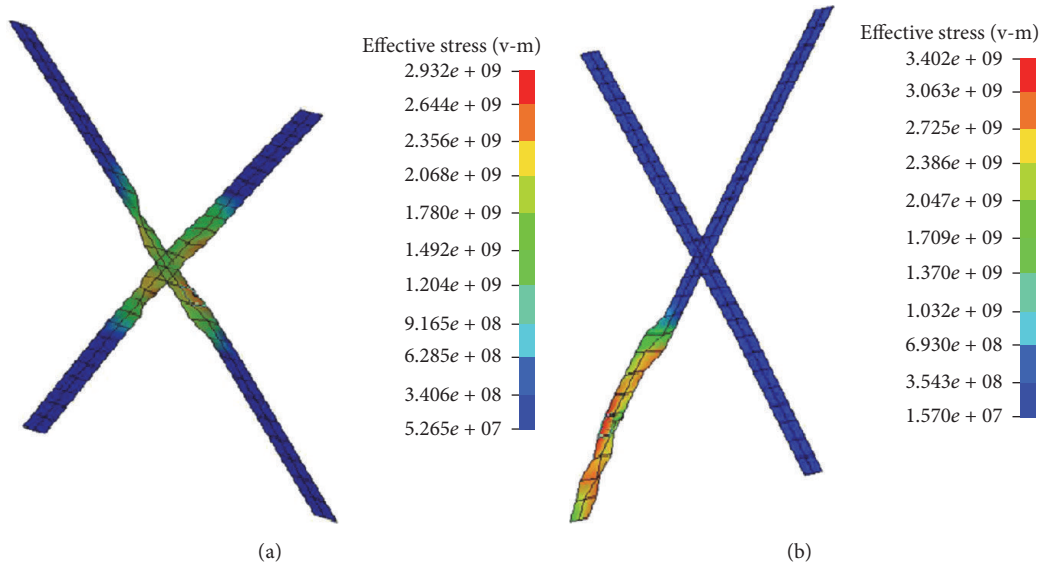


FIGURE 24: Stress distribution of FRP: (a) model 10,  $T = 130$  ms, and (b) model 11,  $T = 150$  ms.

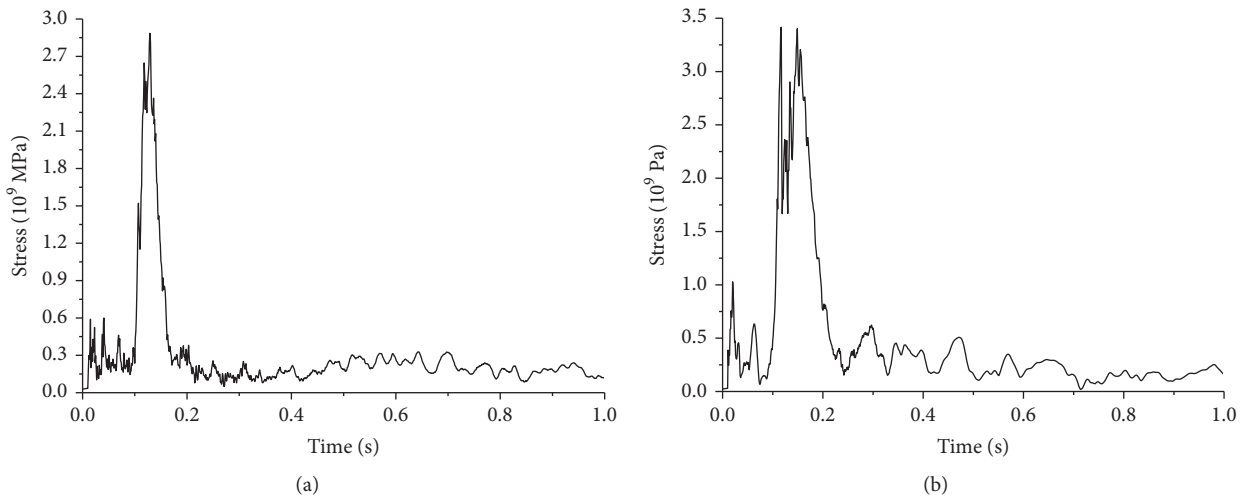


FIGURE 25: Stress time history curves of the maximum stress element in the two models: (a) model 10 and (b) model 11.

deformation during the impact. The strain is calculated to be more than 0.0002, which is far lower than the ultimate tensile strain. Accordingly, FRP is not exposed to tensile failure. In other words, the assumption that FRP is elastic is proven.

In general, it can be concluded that the impact at the center is more unfavorable than at the corner. Consequently, it is reasonable to simulate the constructed models using an impact position set at the center of the wall.

### 5. Application Proposals

Based on the detailed parametric study and the discussion on the corresponding mechanism introduced in Section 4, some suggestions of engineering applications in debris flow hazard areas can be proposed:

(1) For FRP-reinforced masonry structures, the dynamic performance under debris flow varies based on different FRP

arrangements and FRP material types. The importance of these differences should be reflected in the design codes in the future. However, further studies should be carried out to determine the details of these parameters.

(2) The width of FRP is an essential parameter for reinforcing masonry structures. If civil engineers need to control local damage, narrower widths of FRPs are favorable, but wider FRP widths are more suitable in controlling the overall displacement. However, the achievement of a consistent one-to-one match between values of the FRP width and the degrees of local damage, or the overall displacements, requires further studies.

(3) Although there is a reinforcement code in China, FRP reinforcement regulations for masonry structures under debris flow cannot be referred. These regulations, such as the ones pertaining to failure criteria, demand more in-depth studies. Suggestions on the failure criteria can be determined

by the destruction of walls, failure of FRP, or by surpassing the limitation of the overall displacement.

## 6. Conclusion

In this study, the influences of different parameters on the dynamic response of FRP-reinforced masonry structures under viscous debris flow are discussed. Because the application of FRP in resisting debris flow has been seldomly studied before, this study is valuable and necessary for its further application in masonry structures in resisting debris flow. The following conclusions are obtained based on parametric studies by analyzing the numerical simulation results:

(1) The reinforced model performed better than the unreinforced model under debris flow. The parametric study on the dynamic response of FRP-reinforced masonry structures under debris flow impacts was necessary.

(2) The arrangement of reinforced FRP was an important parameter that influenced responses of masonry structures under debris flow. Generally, the diagonal and the intersecting parallel types of FRP arrangements yielded better performances than the horizontal type. The carbon fibers arranged in diagonal and intersecting parallel arrangements induced a more uniform wall stress distribution. Additionally, different arrangements also led to different shapes of local damage of masonry walls.

(3) The widths of the reinforced FRP materials had a profound influence on the structural behavior. A wider fiber cloth led to a minimized structural response impacted by debris flow, and resulted in more severe local damage.

(4) The elastic modulus was the dominant physical parameter that influenced the dynamic response of the masonry structure reinforced by different types of FRP. GFRP yielded the smallest elastic modulus value among all the three types and had the most significant effect in reducing the local damage, while the CFRP yielded a better structural response under debris flow because of its high elastic modulus, which ultimately helped the fiber absorb more energy.

(5) The impact at the center was more unfavorable than that at the corner. Consequently, it was reasonable to conduct a parametric study on the dynamic response of FRP-reinforced masonry structures with the debris impact at the center of the wall.

## Conflicts of Interest

The authors declare that they have no conflicts of interest.

## Acknowledgments

The financial support that was received from the National Key Technology R&D Program through Grant 2014BAL05B01 is highly appreciated.

## References

- [1] X. Tang, *Debris Flows in China*, The Commercial Press, Beijing, China, 2000.
- [2] B.-H. Jun, "Numerical simulation of the topographical change in Korea mountain area by intense rainfall and consequential debris flow," *Advances in Meteorology*, vol. 2016, Article ID 9363675, 11 pages, 2016.
- [3] W. Zhang, Q. Wang, J. Chen, H. Li, J. Que, and Y. Kong, "Grain-size analysis of debris flow alluvial fans in Panxi Area along Jinsha River, China," *Sustainability*, vol. 7, no. 11, pp. 15219–15242, 2015.
- [4] F. Tang, "Finite element analysis of seismic resistance of masonry structure in rural China," *Advanced Materials Research*, vol. 827, pp. 328–333, 2014.
- [5] Z. Lu, Y. Yang, X. Lu, and C. Liu, "Preliminary study on the damping effect of a lateral damping buffer under a debris flow load," *Applied Sciences*, vol. 7, no. 2, article no. 201, 2017.
- [6] S. Q. Yang, "Introduction of National Comprehensive Disaster Prevention and Reduction Plan," *Disaster Reduction in China*, no. 1, pp. 20–22, 2017.
- [7] Z. Lu, D. Wang, S. F. Masri, and X. Lu, "An experimental study of vibration control of wind-excited high-rise buildings using particle tuned mass dampers," *Smart Structures and Systems*, vol. 18, no. 1, pp. 93–115, 2016.
- [8] Z. Lu, X. Chen, D. Zhang, and K. Dai, "Experimental and analytical study on the performance of particle tuned mass dampers under seismic excitation," *Earthquake Engineering & Structural Dynamics*, vol. 46, no. 5, pp. 697–714, 2017.
- [9] Z. Lu, X. Lu, H. Jiang, and S. F. Masri, "Discrete element method simulation and experimental validation of particle damper system," *Engineering Computations*, vol. 31, no. 4, pp. 810–823, 2014.
- [10] K. Dai, J. Wang, R. Mao, Z. Lu, and S.-E. Chen, "Experimental investigation on dynamic characterization and seismic control performance of a TLPD system," *The Structural Design of Tall and Special Buildings*, vol. 26, no. 7, Article ID e1350, 2017.
- [11] Z. Lu, X. Chen, X. Lu, and Z. Yang, "Shaking table test and numerical simulation of an RC frame-core tube structure for earthquake-induced collapse," *Earthquake Engineering & Structural Dynamics*, vol. 45, no. 9, pp. 1537–1556, 2016.
- [12] Z. Lu, Z. Wang, S. F. Masri, and X. Lu, "Particle impact dampers: Past, present, and future," *Structural Control and Health Monitoring*, vol. 25, no. 1, article e2058, 2018.
- [13] Z. Lu, X. Chen, and Y. Zhou, "An equivalent method for optimization of particle tuned mass damper based on experimental parametric study," *Journal of Sound and Vibration*, 2017.
- [14] Z. Lu, B. Huang, and Y. Zhou, "Theoretical study and experimental validation on the energy dissipation mechanism of particle dampers," *Structural Control and Health Monitoring*, 2017.
- [15] J. Wu, *Debris-Flow and Comprehensive Management*, Science Press, Beijing, China, 1993.
- [16] G. Kuwabara and K. Kono, "Restitution coefficient in a collision between two spheres," *Japanese Journal of Applied Physics*, vol. 26, no. 8R, pp. 1230–1233, 1987.
- [17] American Association of State Highways and Transportation Officials, "LRFD bridge design specifications," Washington, DC, USA, 1998.
- [18] O. Hungr, G. C. Morgan, and R. Kellerhals, "Quantitative analysis of debris torrent hazards for design of remedial measures," *Canadian Geotechnical Journal*, vol. 21, no. 4, pp. 663–677, 1984.
- [19] J. Xie, *Study on the new technique of repairing and strengthening masonry walls with continuous carbon fiber sheet*, Doctor's Thesis, Tianjin University, Tianji, China, 2005.

- [20] G. Schwegler, "Masonry construction strengthened with fiber composites in seismically endangered zones," in *Proceedings of the 10th European Conference on Earthquake Engineering*, vol. 3, pp. 2299–2303, Vienna, Austria, 1994.
- [21] F. Seible, "Repair and seismic retest of a full-scale reinforced masonry building," in *Proceedings of the 6th International Conference on Structural Faults and Repair*, vol. 3, pp. 229–236, Edinburgh, UK, 1995.
- [22] X. Wang, Z. Lu, and X. Lu, "An investigation of the aseismic behavior of masonry structures strengthened by carbon fiber reinforced plastics," *Industrial Construction*, vol. 33, no. 9, pp. 11–13, 2003.
- [23] D. Laigle, P. Lachamp, and M. Naaim, "SPH-based numerical investigation of mudflow and other complex fluid flow interactions with structures," *Computational Geosciences*, vol. 11, no. 4, pp. 297–306, 2007.
- [24] C. Zeng, P. Cui, and Y. Ge, "Characteristic and mechanism of buildings damaged by debris flows on 11 July, 2013 in Qipangou of Wenchuan, Sichuan," *Journal Earth Science and Environment*, vol. 36, no. 2, pp. 81–91, 2014.
- [25] Y. Guo, Z. Yu, and L. Guo, "Impacting testing methods for masonry wall based on the drop hammer," *Structural Engineering*, vol. 28, no. 6, pp. 123–127, 2012.
- [26] P. Li, T. Li, Z. Lu, and J. Li, "Study on dynamic response of novel masonry structures impacted by debris flow," *Sustainability*, vol. 9, no. 7, article no. 1122, 2017.
- [27] T.-L. Teng, C.-C. Liang, and T.-T. Tran, "Development and validation of a finite element model for road safety barrier impact tests," *Simulation-Transactions of the Society for Modeling and Simulation International*, vol. 92, no. 6, pp. 565–578, 2016.
- [28] O. I. Abdelkarim and M. A. ElGawady, "Dynamic and static behavior of hollow-core FRP-concrete-steel and reinforced concrete bridge columns under vehicle collision," *Polymer*, vol. 8, no. 12, article no. 432, 2016.
- [29] C. Reuter, K.-H. Sauerland, and T. Tröster, "Experimental and numerical crushing analysis of circular CFRP tubes under axial impact loading," *Composite Structures*, vol. 174, pp. 33–44, 2017.
- [30] G. S. Chandekar and A. D. Kelkar, "Experimental and numerical investigations of textile hybrid composites subjected to low velocity impact loadings," *The Scientific World Journal*, vol. 2014, Article ID 325783, 14 pages, 2014.
- [31] X. Wei and M. G. Stewart, "Model validation and parametric study on the blast response of unreinforced brick masonry walls," *International Journal of Impact Engineering*, vol. 37, no. 11, pp. 1150–1159, 2010.
- [32] H. M. Elsanadedy, T. H. Almusallam, S. H. Alsayed, and Y. A. AL-Salloum, "Experimental and FE study on RC one-way slabs upgraded with FRP composites," *KSCE Journal of Civil Engineering*, vol. 19, no. 4, pp. 1024–1040, 2015.
- [33] D. Proske, J. Suda, and J. Hubl, "Debris flow impact estimation for breakers," *Georisk Assessment & Management of Risk for Engineered Systems & Geohazards*, vol. 5, no. 2, pp. 143–155, 2011.
- [34] N. He, N. S. Chen, and C. Zeng, "Current situation and tendencies of debris flow initiation mechanism," *Journal of Catastrophology*, vol. 28, no. 1, pp. 121–125, 2013.
- [35] C. Zeng, P. Cui, Z. Su, Y. Lei, and R. Chen, "Failure modes of reinforced concrete columns of buildings under debris flow impact," *Landslides*, vol. 12, no. 3, pp. 561–571, 2015.
- [36] *Ministry of Housing and Urban-Rural Construction of the People's Republic of China. Code for design of masonry structures GB 5003-2011*, China Architecture & Building Press, Beijing, China, 2011.
- [37] S. Zhang, D. Yang, Y. Sheng, S. W. Garrity, and L. Xu, "Numerical modelling of FRP-reinforced masonry walls under in-plane seismic loading," *Construction and Building Materials*, vol. 134, no. Supplement C, pp. 649–663, 2017.
- [38] G. Wang, *Debris flow impact pressure signal processing by the wavelet analysis, Doctoral Thesis*, University of Science and Technology of China, Hefei, China, April 2017.
- [39] P. Li, J. Li, and T. Li, "The failure mechanism of masonry structure under debris flow impact," *Journal of Huazhong University of Science and Technology (Natural Science Edition)*, vol. 45, no. 7, p. 1-5+29, 2017.
- [40] S. Govindjee, G. J. Kay, and J. C. Simo, "Anisotropic modelling and numerical simulation of brittle damage in concrete," *International Journal for Numerical Methods in Engineering*, vol. 38, no. 21, pp. 3611–3633, 1995.
- [41] "LS-DYNA Theoretical Manual," Livermore Software Technology Corporation, May 2007, [http://ftp.lstc.com/anonymous/outgoing/jday/manuals/ls-dyna.971\\_manual\\_k\\_rev1.pdf](http://ftp.lstc.com/anonymous/outgoing/jday/manuals/ls-dyna.971_manual_k_rev1.pdf).
- [42] S.-L. Xu and Q. Fang, "Numerical analysis on blast-resistant capacity of masonry walls retrofitted with elastomeric polymer and CFRP," *Journal of PLA University of Science and Technology (Natural Science Edition)*, vol. 11, no. 3, pp. 306–311, 2010.
- [43] Y. R. Guo and H. Zheng, "Numerical simulation of CFRP strengthened perforated masonry walls under blast loading," *Advanced Materials Research*, vol. 640, no. 1, pp. 727–731, 2012.
- [44] J. B. Tang, K. H. Hu, G. D. Zhou, H. Y. Chen, X. H. Zhu, and C. Ma, "Debris flow impact pressure signal processing by the wavelet analysis," *Journal of Sichuan University (Engineering Science Edition)*, vol. 45, pp. 8–13, 2013.

## Research Article

# Development of a Multiaction Hybrid Damper for Passive Energy Dissipation

Ji-Eun Roh <sup>1</sup>, Moo-Won Hur,<sup>1</sup> Hyun-Hoon Choi,<sup>2</sup> and Sang-Hyun Lee <sup>1</sup>

<sup>1</sup>Department of Architectural Engineering, Dankook University, Yongin, Republic of Korea

<sup>2</sup>Heun Deul Lim Corporation, Seongnam, Republic of Korea

Correspondence should be addressed to Sang-Hyun Lee; [lshyun00@dankook.ac.kr](mailto:lshyun00@dankook.ac.kr)

Received 28 July 2017; Revised 11 December 2017; Accepted 2 January 2018; Published 31 January 2018

Academic Editor: Abdul Qadir Bhatti

Copyright © 2018 Ji-Eun Roh et al. This is an open access article distributed under the Creative Commons Attribution License, which permits unrestricted use, distribution, and reproduction in any medium, provided the original work is properly cited.

A multiaction hybrid damper (MHD) is designed to have independent hysteretic characteristics under small and large loading conditions, and its control performance for building structures excited by wind or earthquake load is verified. The MHD is composed of steel elements, two friction pads, and two lead rubber bearings (LRBs). Because the friction pads and the LRBs are in series connection, only the LRBs deform before the friction pad slippage occurs. After the friction slippage, the damper deformation concentrates on the friction pads. The initial stiffness and hysteresis are dependent on the properties of the LRB, and the maximum force is determined by the friction pad. Accordingly, the load-deformation behaviors before/after the friction slippage can be independently designed to show optimal performance for a building structure subject to wind and earthquake loads. The cyclic loading tests of a full scale MHD were conducted to evaluate the multiaction behaviors and energy dissipation capacity of the MHD. The control performance of the MHD damper is analytically investigated by using a 20-story steel structure subject to wind loads and a 15-story RC structure excited by earthquake loads. The MHD damper showed good performance for reducing both the linear wind-induced and nonlinear earthquake-induced responses.

## 1. Introduction

A variety of research on developing passive dampers has been conducted for the purpose of reducing the earthquake- or wind-induced response of building structures. The passive dampers are classified as either displacement-dependent or velocity-dependent. Metallic yield or friction type damper is displacement-dependent because the force response is mainly a function of the relative displacement between each end of the device and is independent of the relative velocity or excitation frequency. Viscous or viscoelastic or mass type damper is velocity-dependent because the force response is primarily a function of the relative velocity and the properties vary according to the excitation frequency. Both the displacement-dependent and the velocity-dependent dampers have been commonly used for the earthquake-resistant design while the velocity-dependent dampers have been generally used for the wind-resistant design.

The force-displacement mechanism of the metallic yield damper is based on elastic and plastic deformations of the

metal such as steel. Added damping and stiffness (ADAS) consisting of multiple X-shaped steel plates was first introduced by Bergman. The ADAS uniformly distributes the yielding mechanism along the steel plate [1]. Other configurations of the metallic yield damper include triangular added damping and stiffness (TADAS), honeycomb, and slit dampers [2–4]. Metallic yield damper is inexpensive to manufacture and its yielding force can be easily modulated by changing the thickness or the number of the steel plates. The metallic damper, however, has some undesirable features such as permanent deformation after the steel yielding and no energy dissipation before the yielding. If the failure of the steel plate occurs during the event, the damper should be replaced by new one after the event.

Friction dampers dissipate structural energy through slippage mechanism between two elements and the slip force level can be easily adjusted by controlling the clamping force. The friction damper was proposed by Pall and Marsh and it was a device installed at the crossing joint of the X-brace to avoid the compression in the brace member [5].

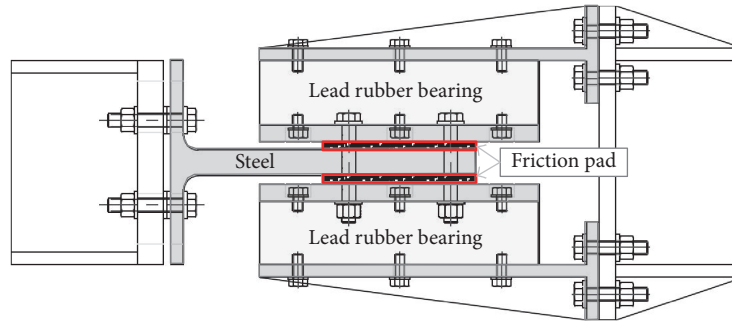


FIGURE 1: Section of the proposed MHD.

Two typical types of the friction dampers are rotational one proposed by Mualla [6] and slotted-bolted one proposed by FitzGerald et al. [7]. Friction dampers dissipate a lot of energy in comparison with other ones with the identical maximum force, since it generates rectangular hysteresis loops. In the design of the friction damper for improving seismic performance of building structures, it is the most important factor to determine the slip load of the damper and brace stiffness. Filiatrault and Cherry have developed design procedure for equally distributed friction dampers minimizing the sum of normalized displacements and dissipated energy through parametric study on the natural period of the structure, the frequency content of an earthquake, and the slip load of the friction damper [8]. Fu and Cherry proposed a design procedure of the friction dampers using a force normalization coefficient [9]. Lee et al. proposed the seismic design methodology of the friction dampers based on the story shear force distribution of a building structure [10].

Lead rubber bearing (LRB) proposed by Robinson was manufactured by drilling a hole through the center of the rubber plate and filling the hole with a lead insert. This material has viscoelastic characteristics of restoring and damping forces [11]. LRB is widely used for the seismic isolation installed at the base of the building.

General passive dampers utilize single material for achieving the energy dissipation mechanism and the capacity of the material governs the damper performance. The metallic or friction damper does not show any energy dissipation mechanism before yielding or slippage. Consequently, the metallic or friction damper is almost useless for small load which does not excite the structure over a specific loading level causing yielding or slippage of the dampers. On the other hand, the LRB has initial stiffness and damping, so the LRB can be used under both the small and large loading conditions. However, the LRB does not have larger energy dissipation during one cycle when compared with the friction or yield damper having rectangular hysteretic curve.

Recently, research on developing hybrid damper for wind and earthquake loads has been carried out. Hybrid passive control damper (HPCD) consisting of high-damping rubber damper in series with a buckling-restrained brace (BRB) was developed to dissipate multilevel seismic energy [12]. Christopoulos and Montgomery suggested that viscoelastic coupling damper (VCD) consists of VE material, steel plate,

and anchor to reduce both the wind and earthquake response of tall shear wall buildings [13]. A hybrid damper which combines a friction damper and steel strip damper is proposed for improving the seismic performance of structures at multiple levels by Lee et al. [14].

In this study, a multi-action hybrid damper (MHD) is proposed to provide independent hysteretic characteristics for small and large loading conditions. The major components of the MHD are steel elements, two friction pads, and two lead rubber bearings. The lead rubber bearing and friction pad, respectively, govern the initial and subsequent hysteretic behaviors of the MHD for the small and large amplitudes of loading. The cyclic loading tests using a 200 kN MHD were conducted for the verification of the damper performance. Also, numerical analyses were conducted for a 20-story steel building structure excited by wind load and a 15-story RC apartment structure under seismic load.

## 2. Configuration and Mechanism of the MHD

The MHD consists of three main parts, steel plates, two LRBs, and two friction pads as shown in Figure 1. Three T-shaped angles and two steel plates are used for connecting the LRBs and friction pads. All the steel elements are manufactured by using rolled section for cost reduction of the MHD. Clamping force of the friction pad is controlled by the number of the high-tensile bolts and torque applied to the bolts.

Figure 2(a) shows the configuration of the typical MHD, and Figure 2(b) is the MHD without LRBs. As shown in Figure 2(b), the MHD can be utilized as a simple friction damper if the LRB is not used and the steel plates on friction pads are directly connected to the T-shaped angle. When the considered load is large enough to cause the slippage of the friction damper and the additional damping is not required for small load, the MHD can be used as a friction damper for economical efficacy.

Figure 3 illustrates the mechanism of the MHD. The steel plates, the LRBs, and the friction pads are in series connection with regard to the horizontal axis movement. If the slippage in the friction pad does not occur, only the LRB and steel element deform. Particularly, when the stiffness of the steel element is comparatively larger to that of the LRB, the initial

TABLE 1: Slip load according to the number of bolts and tightening torque.

The number of high-tensile bolts	Tightening torque per bolt, $T$ (N·m)	Tension per bolt, $F$ (kN)	Slip load per bolt, $R$ (kN)	Slip load (kN)
4	60	20.9	23.0	91.9
4	120	41.8	46.0	183.9
8	60	20.9	23.0	183.9
8	120	41.8	46.0	367.8

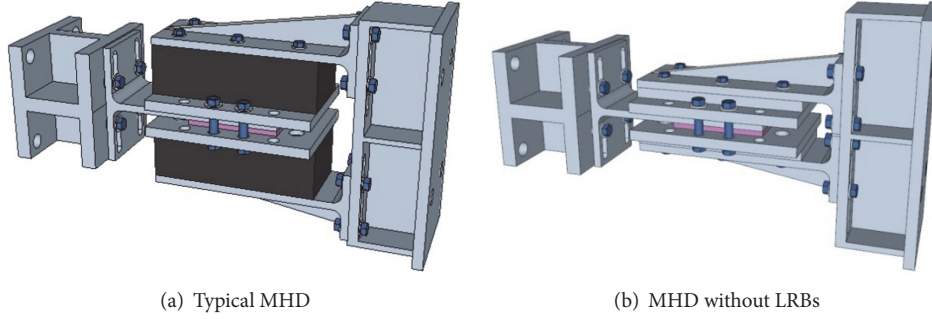


FIGURE 2

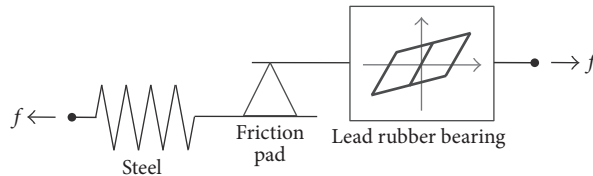


FIGURE 3: Mechanism of the MHD.

deformation induced by the external force  $f$  mainly concentrates on the LRB. The damper ends shall be connected to the structural system such as brace or beam or column. When the force level generated by the LRB reaches the maximum static frictional force of the friction pads, the slippage of the friction pads occurs and all the subsequent deformation concentrates on the friction pads. This implies that the initial deformation and energy dissipation are governed by the LRB while the subsequent deformation and maximum force are dependent on the friction pads.

### 3. Experimental Study

**3.1. Slip Load of the Friction Pad.** The slip load of the friction pad is dependent on normal clamping force, which is determined by the number of the high-tensile bolts and their tightening torques applied to the bolts. ASTM A490-M16 (with 16 mm diameter and 2 mm pitch) bolts were used for the connections. Formula (1) is interaction between slip load ( $R$ ) and normal force ( $F$ ).

$$R = \mu \times h_{sc} \times F \times N_s, \quad (1)$$

where  $\mu$  is a friction coefficient between the friction pad and the steel plate;  $h_{sc}$  is a factor depending on the shape of the bolt hole;  $N_s$  is the number of slip planes;  $h_{sc}$  is 1.0 for standard bolt hole; and  $N_s = 2$  are used in the MHD.

The normal force  $F$  is determined by tightening torque ( $T$ ) based on the following [15].

$$F = T \times \frac{1}{0.161p + 0.583d_m \times k_1 + 0.5D_k \times k_2}, \quad (2)$$

where  $T$  is tightening torque ( $N \cdot m$ ),  $p$  is screw pitch,  $d_m$  is average diameter of the screw,  $k_1$  is friction coefficient between threads of bolt and nut, and  $D_k$  and  $k_2$  are, respectively, the average diameter and friction coefficient between head of the bolt and contacted nut. Table 1 shows the calculated slip load with regard to the number of high-tensile bolts and tightening torque.

**3.2. Test of the MHD without the LRB.** The cyclic loading tests on the MHD without the LRB were first conducted in order to investigate the characteristics of frictional behavior of the MHD. The test configuration is shown in Figure 4. Two reaction frames were used for the installation of the hydraulic actuator and the damper, and the actuator controls the movement of the one end of the damper. A hydraulic actuator with maximum loading capacity 250 kN and 150 mm stroke was used.

The cyclic loading tests were carried out with variables of the number of high-tensile bolts and tightening torques. The maximum displacement was 5 mm, and the excitation frequency was 0.1 Hz. Figure 5(a) shows the force-displacement

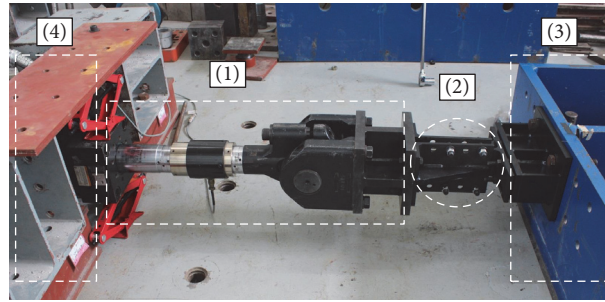


FIGURE 4: Test configuration; (1) hydraulic actuator, (2) the MHD without the LRB, and (3) and (4) reaction frames.

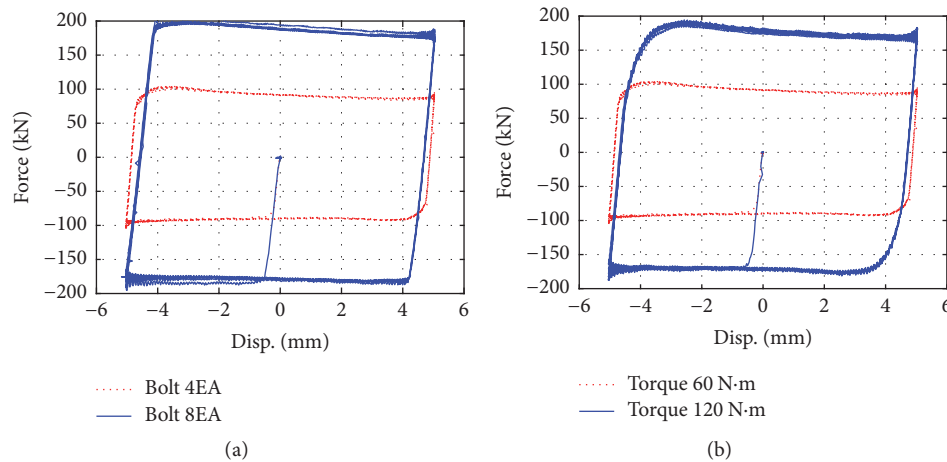


FIGURE 5: Force-displacement curves of the MHD without the lead rubber bearing; friction variation according to (a) the number of high-tensile bolts and (b) tightening torques.

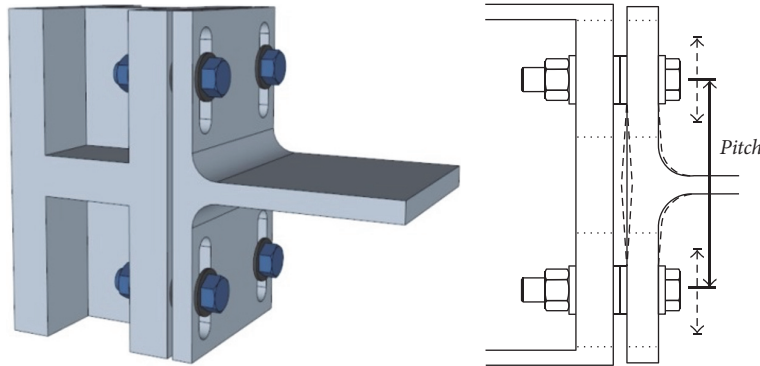


FIGURE 6: The bolt pitch in the T-shaped element.

curve obtained by using the specimens with 4 bolts and 8 bolts. The tightening torque of 60 N·m was applied to each bolt. The friction pad slip occurred at 94 kN with 4 friction bolts and at 188 kN with 8 friction bolts. The slip load increased in proportion to the number of high-tensile bolts. Another test was carried out by doubling the torque from 60 N·m to 120 N·m for the specimen with 4 bolts. Figure 5(b) shows that the slip load increased from 94 kN to 188 kN with increasing the torque.

The initial stiffness of the MHD without the LRB can be controlled by varying the pitches on the flange of the

T-shaped steel element as shown in Figure 6. The initial stiffness and the slip load of the MHD can be independently determined. The flange of the T-shaped element used in the experiment has 21 mm of thickness and 140 mm of width; the flexural stiffness of the hinge supported beam with concentrated load at midspan,  $48EI/l^3$ , was used.

As shown in Figure 7, changes in initial stiffness were experimentally evaluated for the different pitches of 90 mm, 150 mm, and 200 mm. Figure 8 shows the force-displacement curves obtained from the three specimens with different bolt pitches. It is observed that the initial stiffness decreases with

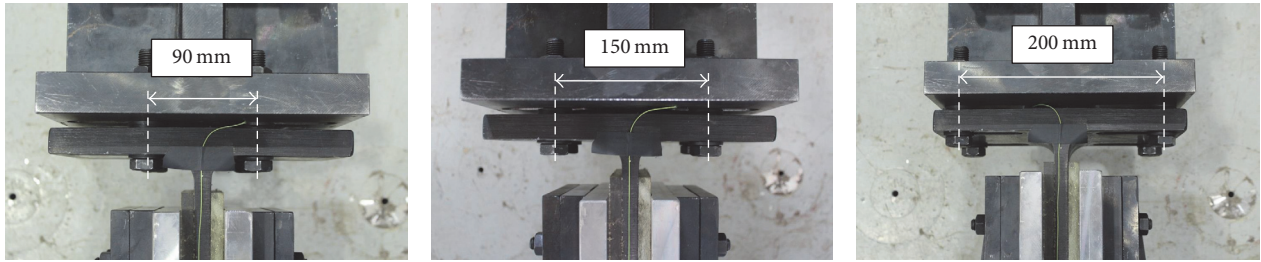


FIGURE 7: Three specimens with different bolt pitches.

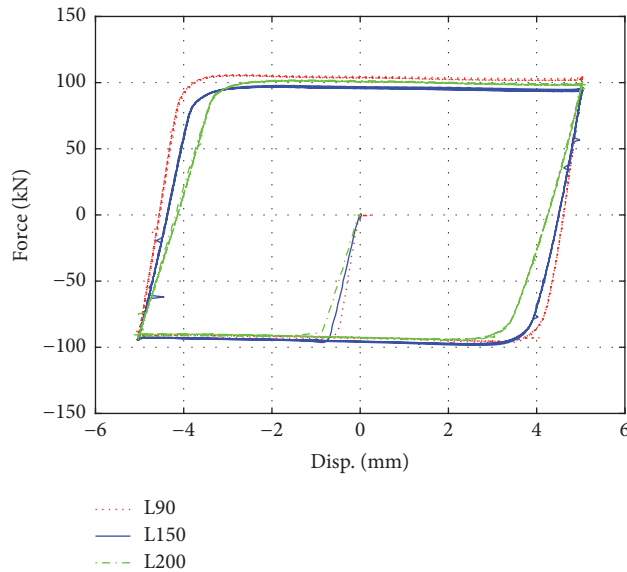


FIGURE 8: Force-displacement curves of the three specimens with different bolt pitches.

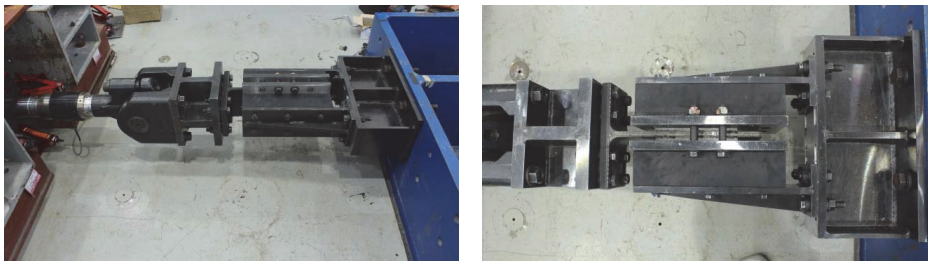


FIGURE 9: Cyclic loading tests of the typical MHD.

increasing pitches. From Table 2, it is noted that the calculated initial stiffness is very close to them from the experiments. The slip loads for all the cases are almost identical.

**3.3. Test of the Typical MHD with the LRB.** The hysteresis curves of the typical MHD with the LRB were obtained by conducting the cyclic loading tests as shown in Figure 9. In order to investigate the displacement-dependent characteristics of the MHD, force-displacement curves were obtained by changing the amplitude of the peak displacement.

Figure 10 shows the force-displacement curves under displacement-controlled cyclic loads with amplitudes of

3 mm, 5 mm, and 10 mm displacement. The friction pad was clamped by using the 4 high-tensile bolts fastened with torque 120 N·m. The loading frequency was 0.1 Hz and 5 cycle tests were conducted. It is observed that the slip of the friction did not occur and only the LRB deformed. The maximum values of the restoring force induced by the LRB were about 50 kN, 70 kN, and 100 kN for the amplitudes of 3 mm, 5 mm, and 10 mm, respectively. Because the restoring force of the LRB did not reach the slip load of the friction pad, the hysteresis characteristics of the MHD were determined only by the LRB. Table 3 shows the positive and negative force levels at the zero or 10 mm displacement per each cycle. All the values are within an error of 10%, which implies that the deviation

TABLE 2: Initial stiffness according to different pitches of bolts on the flange of the T-steel.

Pitches of bolts on the flange of the T-steel (mm)	Net length of bolts (mm)	Initial stiffness (kN/mm)		Error rate (%)
		Calculated	Experiment	
90	60	210.6	211.92	0.6
150	120	162.1	161.89	0.1
200	170	109.1	110.08	0.9

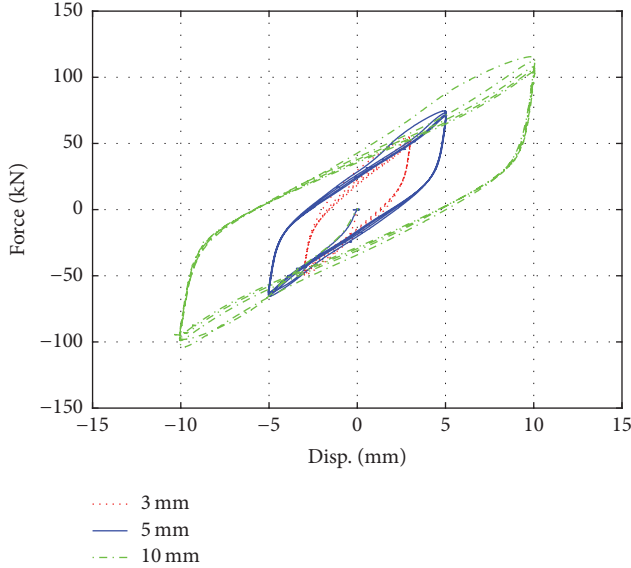


FIGURE 10: Force-displacement curves of the typical MHD for small deformation.

from the average value is small and the LRB has stable hysteretic characteristics. Because the friction pad and the LRB are in series connection, only the LRB deforms when the displacement is small and the restoring force of the LRB is not large enough to cause the slippage of the friction pad.

Another test was conducted when the slip load of the friction pad was reduced to about 100 kN by loosening the torque to 60 N·m. And then the peak displacement of the cyclic loading was set to be 40 mm. The curve shown in Figure 11 with legend “40 mm” is the result. The initial stiffness and hysteresis obtained within the displacement smaller than about 10 mm are identical to those of the LRB. When the restoring force reached about 100 kN, the slippage of the friction pad started and the force level with increasing displacement is almost constant, which is the typical characteristics of a friction damper. When the slippage of the friction pad occurred, the LRB did not show any deformation, which implies that the large deformation behavior of the typical MHD is governed by the friction pad. The curve shown in Figure 11 with legend “60 mm” is the results from test conducted by doubling the torque from 60 N·m to 120 N·m and increasing the peak displacement to 60 mm. It is identified that the slip load increases to about 200 kN and the slippage the friction pad occurs at 14.1 mm. Also, the energy dissipation per cycle increases by the increase of the slip load and the maximum displacement. Table 4 shows the forces at

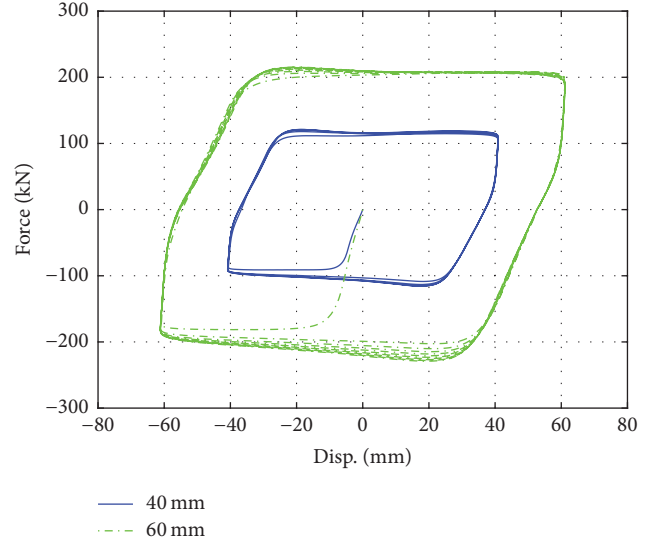


FIGURE 11: Force-displacement curves of the typical MHD for large deformation.

the zero or 60 mm displacement of the MHD. The maximum deviation from average value is just 6.8%, which implies that the MHD has the stable hysteresis for the repeated loadings.

Table 5 shows the energy dissipated by the MHD per each loading cycle. The average of the dissipated energy increased significantly from 1238.5 kN·m to 41743.6 kN·m by increasing the peak displacement and force. The deviation from average was maximum 11.4% at the first cycle of the loading tests. After the first cycle, the deviation decreased and the MHD showed stable hysteresis.

#### 4. Application of the MHD for Wind Vibration Mitigation

**4.1. Structural Outline of a 20-Story Steel Structure.** In order to evaluate the vibration control performance of the MHD for a building structure under wind loads, numerical analysis was conducted using a 20-story steel structure. The building is designed according to Korean Building Code (KBC2016) [15]. The building is supposed to be constructed in Seoul and it has 58.6 m height and 24 m × 18 m plan. The used materials are SS400 for beams and SM490 for girder and column. MIDAS GEN was used as a design and analysis program [16]. The slab is modeled as a rigid diaphragm, and Figure 12 shows plan and elevation.

TABLE 3: Forces at the zero or peak displacements of the MHD under cyclic loading (10 mm peak displacement).

Cycle No.	Positive force at zero disp.		Negative force at zero disp.		Positive force at +10 mm disp.		Negative force at -10 mm disp.	
	$F_{i,0}^+$ (kN)	Deviation from average (%)	$F_{i,0}^-$ (kN)	Deviation from average (%)	$F_{i,M}^+$ (kN)	Deviation from average (%)	$F_{i,M}^-$ (kN)	Deviation from average (%)
(1)	39.4	8.6	-31.1	9.9	104.8	0.2	-99.0	4.6
(2)	37.8	4.3	-29.5	4.5	107.9	3.2	-96.4	1.9
(3)	36.4	0.5	-28.4	0.5	105.6	0.9	-94.7	0.1
(4)	35.4	2.4	-27.5	2.7	103.9	0.7	-91.0	3.8
(5)	34.6	4.6	-26.8	5.3	102.8	1.7	-93.5	1.2
Average	36.7		-28.7		105.0		-94.9	

TABLE 4: Forces at the zero and peak displacements of the MHD under cyclic loading (60 mm peak displacement).

Cycle No.	Positive force at zero disp.		Negative force at zero disp.		Positive force at +60 mm disp.		Negative force at -60 mm disp.	
	$F_{i,0}^+$ (kN)	Deviation from average (%)	$F_{i,0}^-$ (kN)	Deviation from average (%)	$F_{i,M}^+$ (kN)	Deviation from average (%)	$F_{i,M}^-$ (kN)	Deviation from average (%)
(1)	203.4	2.3	-199.1	6.8	202.2	2.4	-174.4	6.1
(2)	205.8	1.1	-205.4	3.8	200.9	1.8	-183.6	1.1
(3)	207.3	0.4	-209.3	2.0	199.3	1.0	-185.5	0.1
(4)	208.2	0.0	-212.2	0.7	198.4	0.5	-186.4	0.4
(5)	208.8	0.3	-214.6	0.5	197.6	0.1	-187.1	0.8
Average	206.7		-208.1		199.7		-183.4	

TABLE 5: Dissipated energy per each loading cycle.

Cycle number	10 mm peak displacement (about 100 kN peak force)		60 mm peak displacement (about 200 kN peak force)	
	Dissipated energy (N·m)	Deviation from average (%)	Dissipated energy (N·m)	Deviation from average (%)
(1)	1362.3	11.4	39152.4	7.9
(2)	1261.6	3.1	41809.6	1.7
(3)	1217.1	0.5	42531.7	0.0
(4)	1187.0	2.9	42618.0	0.2
(5)	1164.4	4.8	42706.4	0.4
Average	1238.5		41763.6	

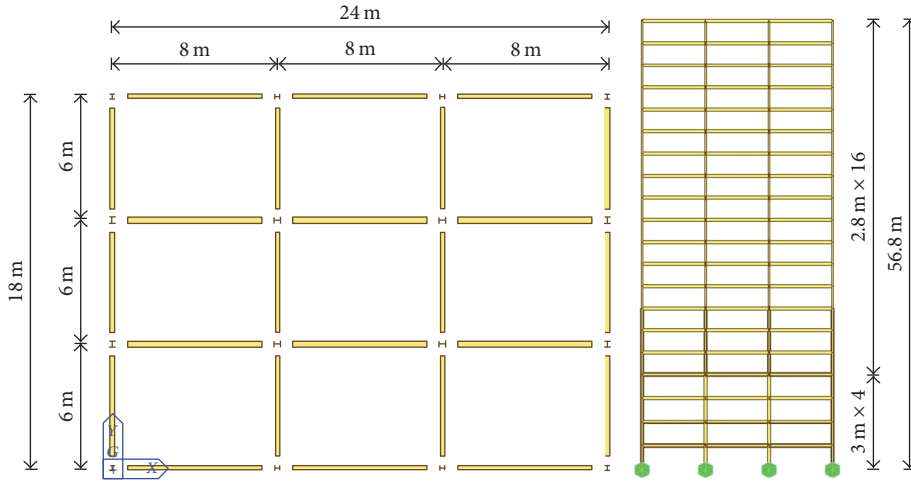


FIGURE 12: Plan and elevation of a 20-story steel structure.

4.2. *Modal Analysis and Wind Load Generation.* Figure 13 shows the first 3 mode shapes. The period of the first mode in  $X$ -direction was 4.14 sec., 4.34 sec. in  $Y$  direction, and 3.75 sec. in torsion. The 1% modal damping ratio was used for all modes, and the only the fluctuation component in  $X$ -directional response was considered. The fluctuation component of the along-wind load was generated by using the method proposed by Wu et al. [17]. The method is to generate the time histories of along-wind loads based on the cross-power spectrum of the story wind loads. Figure 14 shows the time histories of the generated wind loads, and Figure 15 shows the wind-induced peak interstory drifts of the 20-story steel structure without the MHD. It is noted that the peak interstory drift is smaller than 13 mm at which the slippage of the friction occurs. Accordingly, if the 200 kN MHD shown in Figure 11 is used, only the lead rubber bearing plays a role of dissipating energy, and the slippage of the friction pad is not expected.

4.3. *Preliminary Design of the MHD.* In this section, the MHD is preliminarily designed by using the concept of the equivalent damping ratio added by the MHD and gust factor. The gust factor for the flexible structure is given as [15]

$$G_f = 1 + g_f \cdot \gamma_f \sqrt{B_f + R_f}, \quad (3)$$

where  $g_f$  is peak factor,  $\gamma_f$  is coefficient of variation of wind speed,  $B_f$  is nonresonance factor, and  $R_f$  is resonance factor

The peak and resonance factors are related with the structural damping ratio. Also, in gust factor, 1 is related with the mean component of the wind load and the remainder is related with the fluctuation component. Accordingly, the reduction ratio of the fluctuation component in the gust factor with regard to the increase of the damping ratio is given by

$$RF_{f,D} = \frac{G_f(\xi_0) - 1}{G_f(\xi_0 + \xi_\alpha) - 1}, \quad (4)$$

where  $\xi_0$  is the damping ratio of the original structure and  $\xi_\alpha$  is damping ratio added by the damper.

Figure 16 shows the variation of  $RF_{f,D}$  with regard to  $\xi_\alpha$ . It is observed that  $RF_{f,D}$  is decreasing with increasing  $\xi_\alpha$ .

If the effect of the damper can be expressed as an equivalent damping ratio added by the damper, the fluctuation component in along-wind directional response of a structure with the damper can be estimated by simply multiplying  $RF_{f,D}$  and one structure without the damper. Added damping ratio,  $\xi_\alpha$ , by the damper is estimated by the following [18].

$$\xi_\alpha = \frac{\sum W_j}{4\pi \sum W_k}, \quad (5)$$

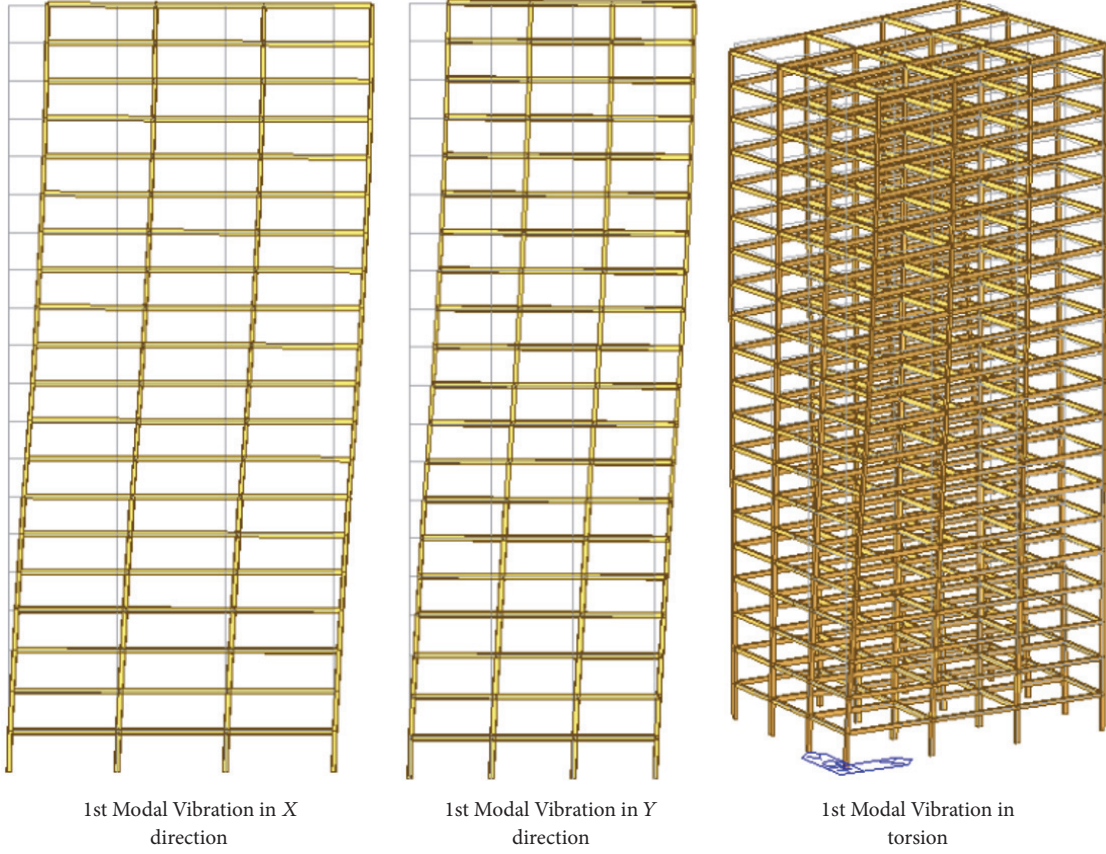


FIGURE 13: Mode shapes of a 20-story steel structure.

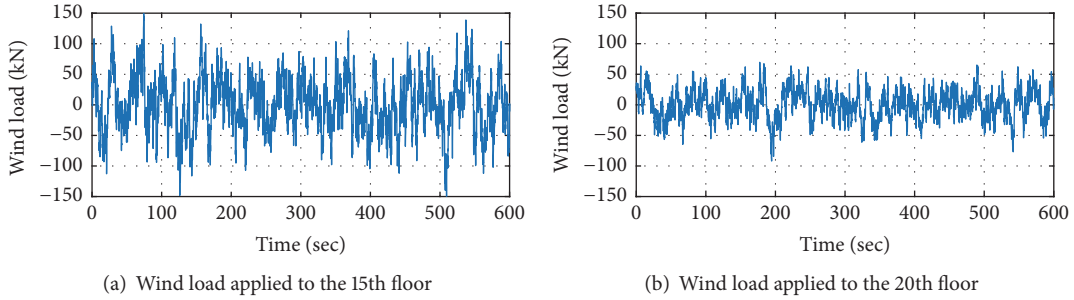


FIGURE 14: Generated wind loads.

where  $W_j$  is the work done by  $j$ th damper during one complete cycle and  $W_k$  is the maximum strain energy of the structure.

The hysteresis of the MHD shown in Figure 10 for small deformation can be idealized by using a bilinear curve as shown in Figure 17. Bilinear curve is represented by initial stiffness  $k_{d1}$ , yield strength  $f_y$ , and postyield stiffness  $k_{d2}$ .  $\alpha$  is the postyield stiffness ratio to the initial stiffness,  $D_y$  is the yield displacement,  $D_r$  is the target displacement, and  $\mu$  is the ratio of  $D_r$  to  $D_y$ .

$\sum W_k$  is the sum of the strain energy of a structure itself and the strain energy due to the addition of the damping device by

$$\sum W_k = \frac{1}{2} \sum_{i=1}^N F_i \cdot D_i + \frac{1}{2} \sum_{j=1}^{N_d} K_{eqj} \cdot D_{rj}^2, \quad (6)$$

where  $N$  is the number of building stories,  $F_i$  is  $i$ th story wind load,  $D_i$  is  $i$ th story displacements,  $N_d$  is the number of the dampers,  $D_{rj}$  is the relative displacement between two ends of the  $j$ th damper, and  $K_{eqj}$  shall be taken by the following equation, as the equivalent stiffness of the damper.

$$K_{eqj} = \frac{f_{yj} (1 + \alpha_j \mu_j - \alpha_j)}{D_{rj}}. \quad (7)$$

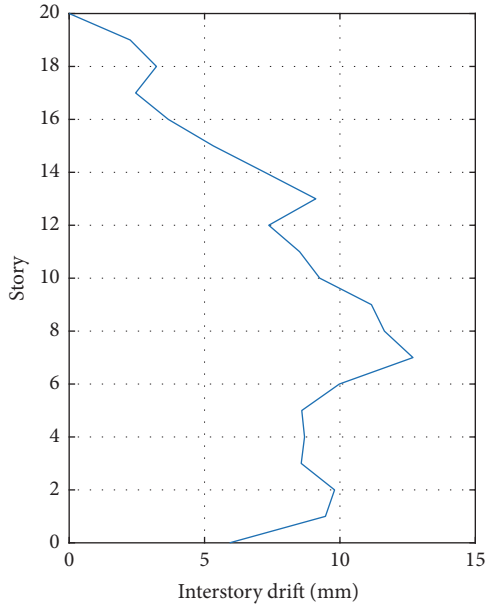


FIGURE 15: Peak interstory drifts.

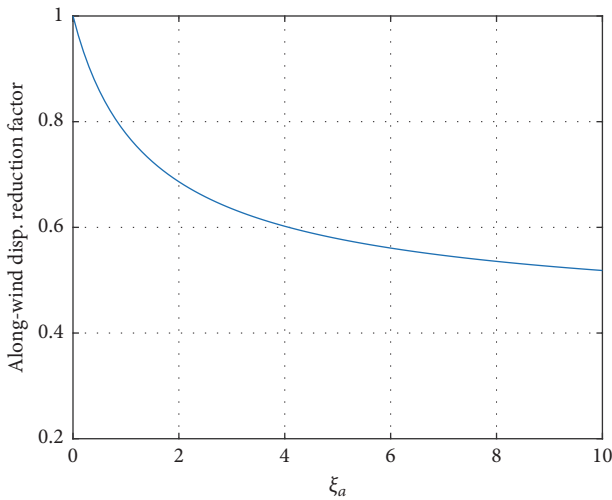


FIGURE 16: Reduction ratio of the fluctuation component in the gust factor.

$\sum W_j$  shall be taken by following equation, using the sum of the work done during one complete cycle by the  $j$ th damper.

$$\sum_{j=1}^{N_d} W_j = \sum_{j=1}^{N_d} 4(D_{rj} \cdot f_{yj} - D_{yj} \cdot f_{yj}(1 + \alpha_j \mu_j - \alpha_j)). \quad (8)$$

Because  $D_{rj}$  is the value obtained for the damper-installed structure, the equivalent damping ratio cannot be explicitly obtained in the preliminary design stage where only the response of a structure without the damper can be used. When  $D_{rj}$  of the structure without the damper is used, the corresponding equivalent damping ratio becomes different from the actual value which shall be obtained by using  $D_{rj}$  of the structure with the damper.

In this study, when the number of the dampers, the installation location, and the properties of the damper are given, the added damping ratio is estimated by using the wind load reduction factor and the response of a structure without the damper. The wind load reduction factor of a structure without the damper is just 1, and then the resulting uncontrolled structural response is calculated by just static wind load or generated dynamic wind load. Based on the calculated the response, the equivalent damping ratio added by the damper whose number, location, and the properties are given can be estimated. Obviously, the first estimated damping ratio gives other wind load reduction factors than 1. And then the structural response of a structure with the dampers is estimated by multiplying the given wind load reduction factor and the uncontrolled response. This procedure is repeated until two damping ratios become the same; one is calculated by the wind load reduction factor itself, and the other one is based on the structural response obtained by multiplying the wind load reduction factor and the uncontrolled response. Figure 18 shows the damper installation configuration. Totally, 18 dampers are installed at the 1st, 2nd, and 3rd floors. In this section, yield strength  $f_y = 50$  kN, initial stiffness  $k_{d1} = 50$  kN/mm, and postyield stiffness  $k_{d2} = 10$  kN/mm were used for modeling the hysteresis of the LRB shown in Figure 10. Figure 19 shows the damping ratio added by installing the 18 dampers. Two damping ratios, which are previously mentioned, are compared. The cross point corresponds to 4.22% damping ratio and 0.596 wind load reduction factor.

Nonlinear time history analysis using the generated wind loads shown in Figure 14 was conducted to calculate the actual response reduction by the damper installation. Figure 20 shows the comparison between uncontrolled and controlled roof displacement. The average response reduction ratios in the floor displacement and interstory drift are, respectively, 0.585 and 0.525, which are close to the wind load reduction factor 0.596 estimated in the preliminary design. This indicates that the proposed method can be effectively used for estimating the effect of the MHD. Figure 21 shows the hysteretic curve of the MHD installed at the first floor. The MHD shows bilinear behavior and the peak displacement of the MHD is smaller than 5 mm and the force is smaller than 80 kN, which is appropriate for the assumption that only the LRB of the MHD plays a role of dissipating energy when the maximum force does not reach the friction force.

## 5. Application of the MHD for Seismic Design

**5.1. Structural Outline.** A 15-story reinforced concrete apartment building is considered for verifying the seismic response control performance of the MHD. The structure has the dimensions of 48.6 m (length)  $\times$  14.8 m (width)  $\times$  45 m (height) as shown in Figure 22. The gravity load is resisted entirely by the moment frame and the lateral load is resisted by the shear walls in core. The structure with the MHD is designed based on the 75% base shear force of the structure without the MHD. Beams, columns, and walls are modeled by nonlinear elements using PERFORM 3D program [19]. The

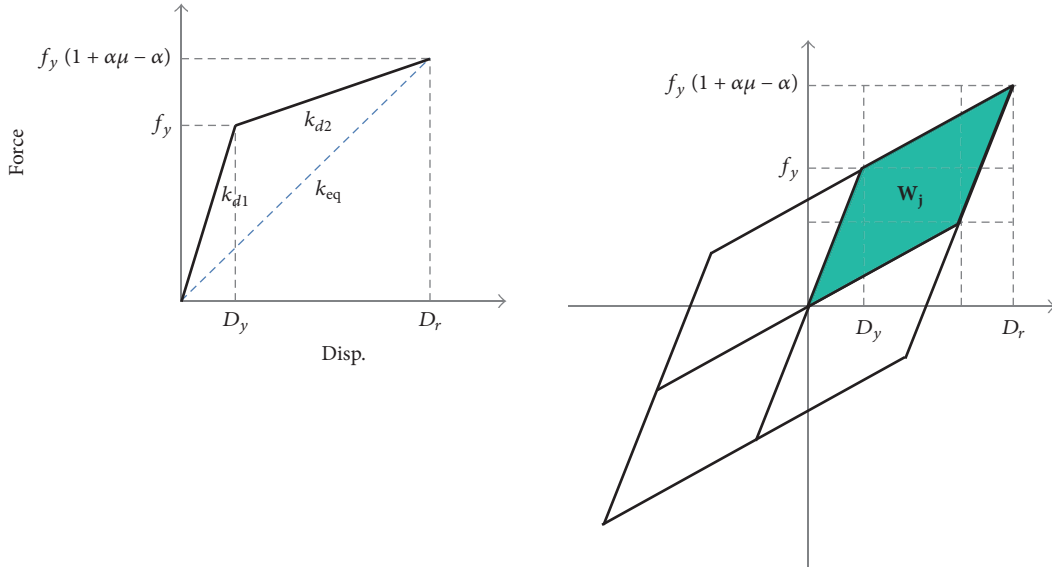


FIGURE 17: Bilinear idealization of the hysteretic curve of the MHD for small deformation.

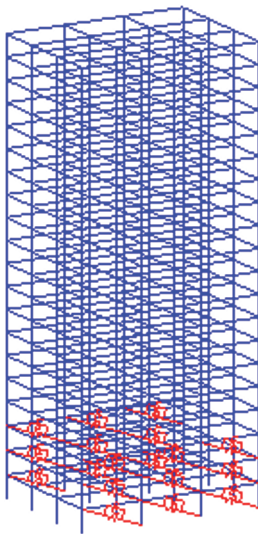


FIGURE 18: Damper installation configuration in a 20-story steel structure.

structure without the dampers is designed according to KBC2016 [15].

5.2. *Damper Installation and Nonlinear Analysis.* The slip load of friction pad and hysteresis of the LRB (initial stiffness and yield strength) can be adjusted according to the demand by changing the material properties. The 110 kN MHD are installed on the 3rd, 9th, and 15th floors. Yield strength  $f_y = 80$  kN, initial stiffness  $k_{d1} = 50$  kN/mm, and postyield stiffness  $k_{d2} = 1$  kN/mm were used for modeling the hysteresis of the LRB. And slip load of friction pad was 110 kN. Four MHDs at each floor are inserted between the moment frame and shear wall at the location shown in Figure 22. The total summation of the damper friction force is 1,320 kN (110 kN  $\times$

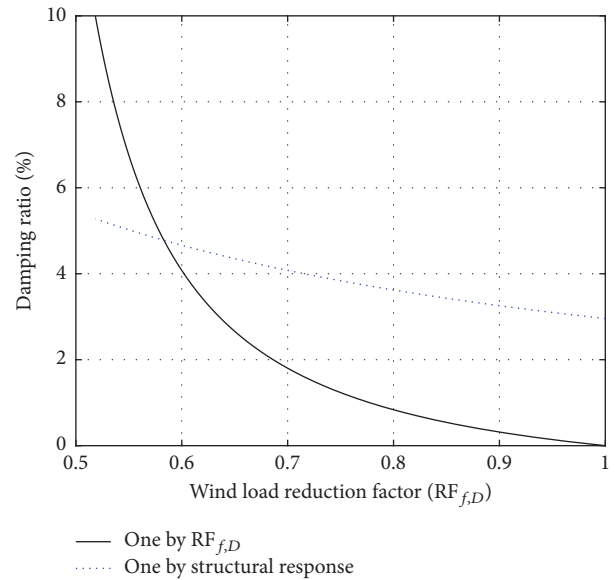


FIGURE 19: Added damping ratio and wind load reduction factor.

3 stories  $\times$  4 dampers) and this is about 10% of the base shear force.

Fourteen ground accelerations measured from three earthquakes were used for numerical analyses. The earthquakes records are Loma Prieta (1989), Chi-Chi (1999), and Cacaeli (1999). The magnitude of the earthquake records was scaled according to the design spectrum presented by Korean Building Code (KBC2016). Figure 23 shows that the peak displacement, drift ratio, and story shear force could be reduced significantly by applying the MHD to the 15-story building structure. Figure 24 illustrates the hysteretic curves of the LRB, the friction pad, and the combined MHD located on the 15 floor when Chi-Chi earthquake load was used as ground acceleration. LRB showed bilinear hysteresis and the

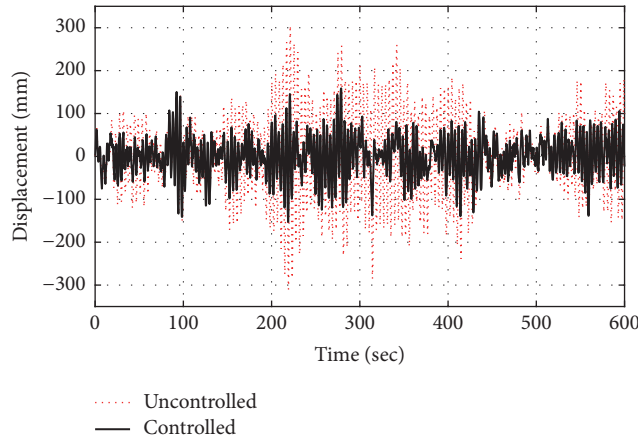


FIGURE 20: Roof floor displacement.

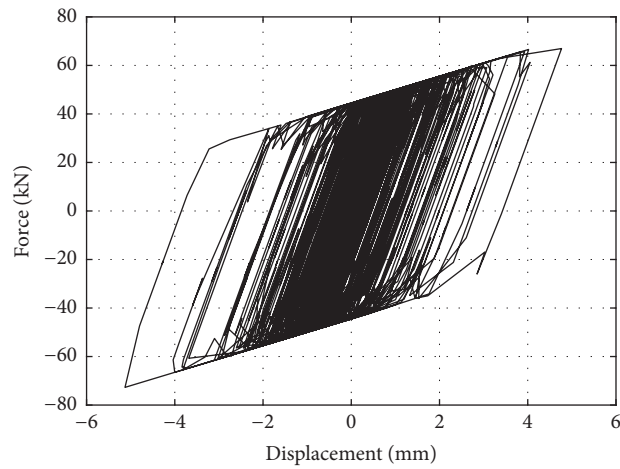


FIGURE 21: Hysteretic curve of a MHD installed at the first floor.

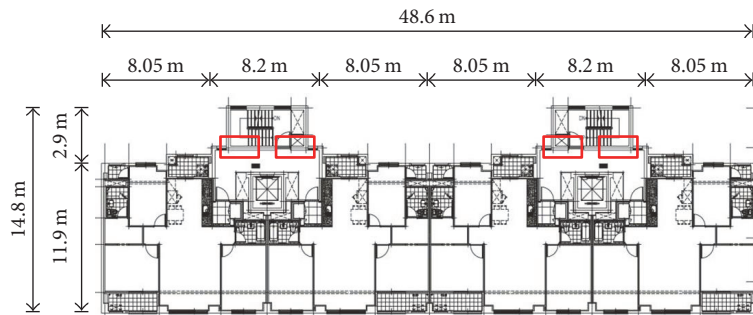


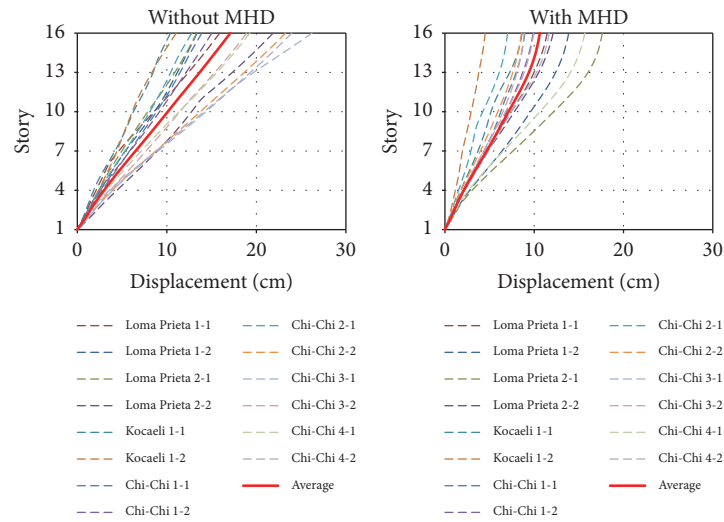
FIGURE 22: A 15-story apartment RC structure and damper installation location.

friction pad slipped at 110 kN, and the combined hysteresis of the MHD was trilinear. It is observed that the MHD shows similar behaviors to the experimentally obtained hysteresis shown in Figure 11.

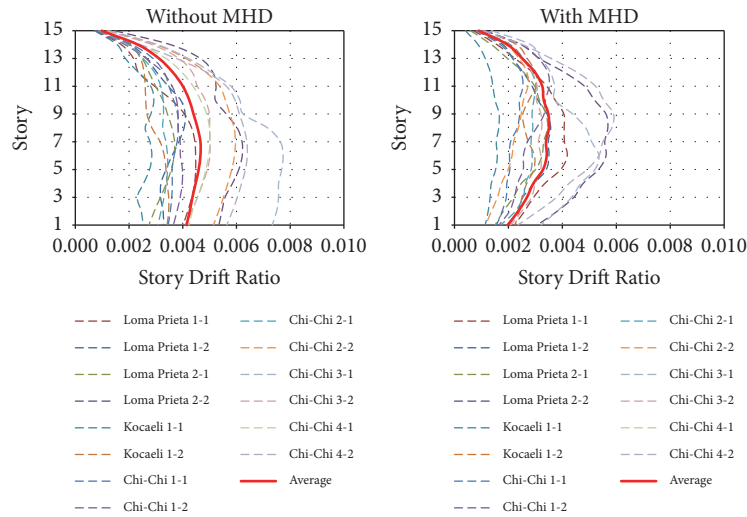
### 6. Conclusions

In this study, a multi-action hybrid damper (MHD) composed of friction pads, lead rubber bearings, and steel plates was

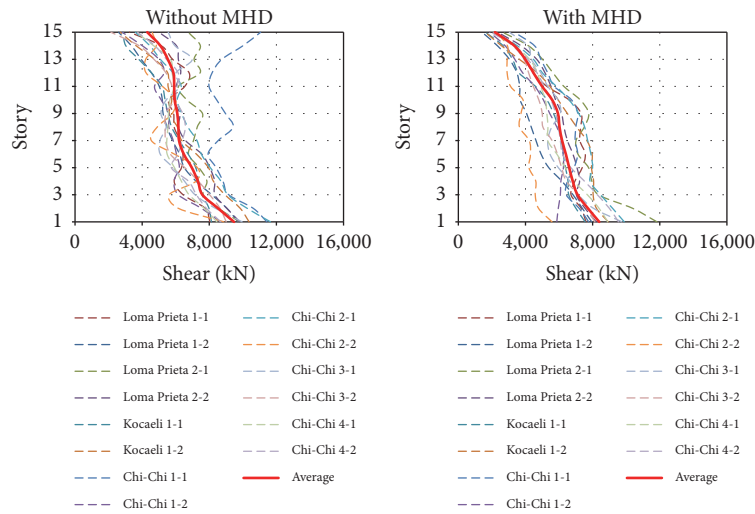
proposed. Full scale cyclic tests were conducted for identifying the hysteretic characteristics of the MHD. The test results indicate that only lead rubber bearing initially deforms until the restoring force of the MHD reaches the slip load of the friction pad because the lead rubber bearing and the friction pad are in series connection. After the slippage of the friction pad, the additional deformation in the direction of the increasing displacement of the MHD concentrates on the friction pad. Consequently, the MHD shows independent behaviors of the lead rubber bearing and the friction pad



(a) Peak story displacement



(b) Peak story drift ratio



(c) Peak story shear force

FIGURE 23: Response comparison between structures with/without MHD.

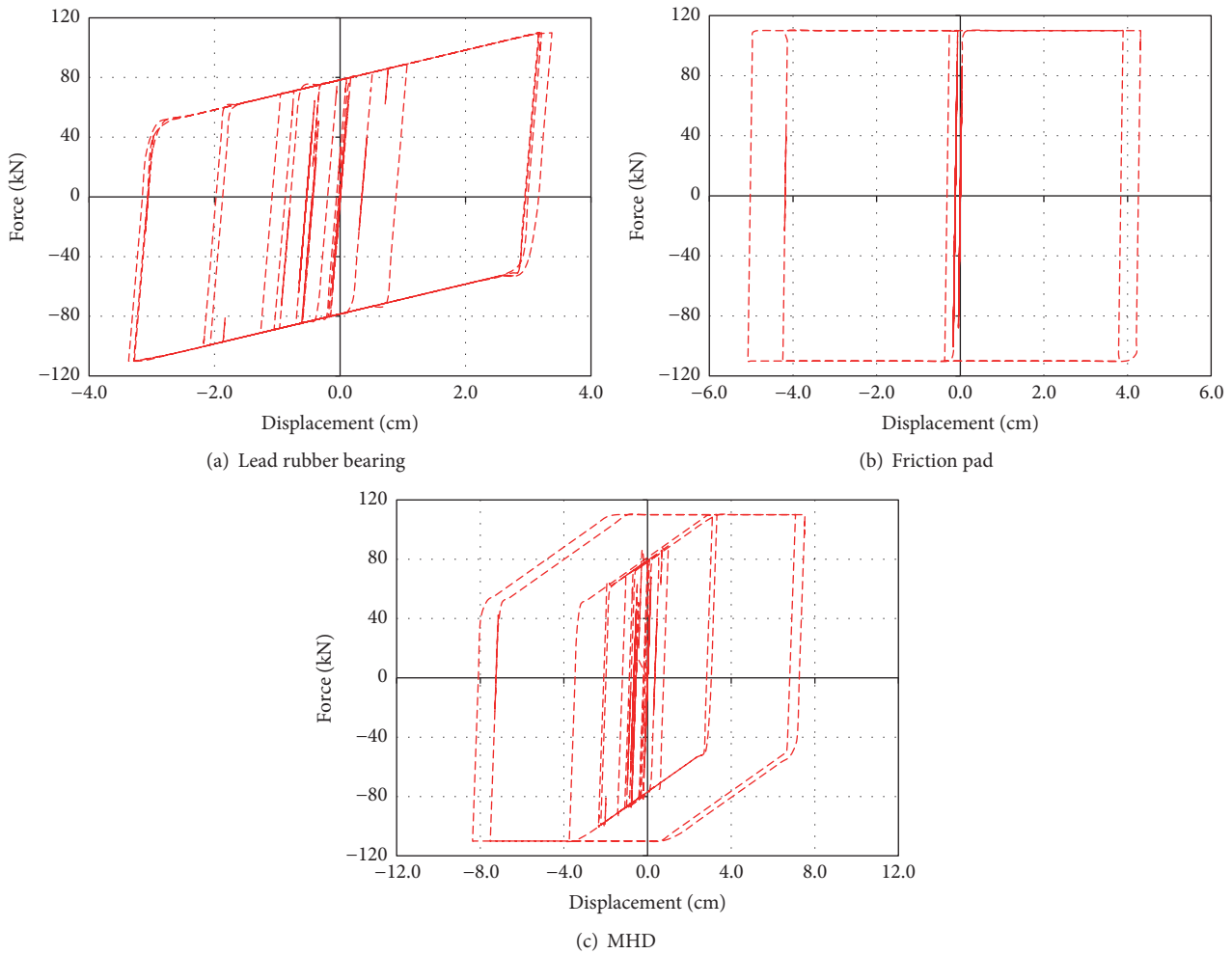


FIGURE 24: Hysteresis behavior from nonlinear analysis.

according to the amplitude of the deformation. The proposed MHD showed very stable hysteretic behaviors and any undesirable variation of the hysteretic curve in the progress of the cyclic loading was not observed. Numerical analyses results from a 20-story steel structure and 15-story RC apartment structure showed that the proposed MHD can be used for mitigating both the relatively small wind-induced and the relatively large seismically induced responses.

### Conflicts of Interest

The authors declare that they have no conflicts of interest.

### Acknowledgments

This work was supported by the National Research Foundation of Korea (NRF) grant funded by the Korea government (MSIP) (no. NRF-2015RIA2A1A10054506).

### References

- [1] D. M. Bergman and S. C. Goel, "Evaluation of cyclic testing of steel plate devices for added damping and stiffness," Report no. UMCE87-10. Ann Arbor (MI,USA): The University of Michigan, 1987.
- [2] K.-C. Tsai, H.-W. Chen, C.-P. Hong, and Y.-F. Su, "Design of steel triangular plate energy absorbers for seismic-resistant construction," *Earthquake Spectra*, vol. 9, no. 3, pp. 505–528, 1993.
- [3] T. Kobori, Y. Miura, E. Fukusawa, T. Yamada, T. Arita, and Y. Takenake, "Development and application of hysteresis steel dampers," in *Proceedings of the 11th World Conference on Earthquake Engineering*, pp. 2341–2346, 1992.
- [4] P. W. Clark, I. D. Aiken, F. Tajirian, K. Kasai, E. Ko, and I. Kimura, "Design procedures for buildings incorporating hysteretic damping devices," In: Proc. int. post-SmiRT conf. seminar on seismic isolation. Passive energy dissipation and active control of vibrations of structures, 1999.
- [5] A. S. Pall and C. Marsh, "Response of friction damped braced frames," *Journal of the Structural Division*, vol. 108, no. 6, pp. 1313–1323, 1982.
- [6] I. H. Mualla, *Experimental and computational evaluation of a novel friction damper device [Ph.D. thesis]*, Department of Structural Engineering and Materials, Technical University of Denmark, 2000.
- [7] T. F. FitzGerald, T. Anagnos, M. Goodson, and T. Zsutty, "Slot- ted bolted connections in aseismic design for concentrically

- braced connections,” *Earthquake Spectra*, vol. 5, no. 2, pp. 383–391, 1989.
- [8] A. Filiatrault and S. Cherry, “Seismic design spectra for friction-damped structures,” *Journal of Structural Engineering*, vol. 116, no. 5, pp. 1334–1355, 1990.
- [9] Y. Fu and S. Cherry, “Design of friction damped structures using lateral force procedure,” *Earthquake Engineering & Structural Dynamics*, vol. 29, no. 7, pp. 989–1010, 2000.
- [10] S.-H. Lee, J.-H. Park, S.-K. Lee, and K.-W. Min, “Allocation and slip load of friction dampers for a seismically excited building structure based on storey shear force distribution,” *Engineering Structures*, vol. 30, no. 4, pp. 930–940, 2008.
- [11] W. H. Robinson, “Lead-rubber hysteretic bearings suitable for protecting structures during earthquakes,” *Earthquake Engineering & Structural Dynamics*, vol. 10, no. 4, pp. 593–604, 1982.
- [12] J. D. Marshall and F. A. Charney, “A hybrid passive control device for steel structures, I: Development and analysis,” *Journal of Constructional Steel Research*, vol. 66, no. 10, pp. 1278–1286, 2010.
- [13] C. Christopoulos and M. Montgomery, “Viscoelastic coupling dampers (VCDs) for enhanced wind and seismic performance of high-rise buildings,” *Earthquake Engineering & Structural Dynamics*, vol. 42, no. 15, pp. 2217–2233, 2013.
- [14] C.-H. Lee, J. Kim, D.-H. Kim, J. Ryu, and Y. K. Ju, “Numerical and experimental analysis of combined behavior of shear-type friction damper and non-uniform strip damper for multi-level seismic protection,” *Engineering Structures*, vol. 114, pp. 75–92, 2016.
- [15] KBC2016, Korean Building Code, 2016, Korean Architectural Institute.
- [16] Midas Gen Analysis Manual. 2016, Midas IT.
- [17] J. C. Wu, J. N. Yang, and W. E. Schmitendorf, “Reduced-order H<sub>∞</sub> and LQR control for wind-excited tall buildings,” *Engineering Structures*, vol. 20, no. 3, pp. 222–236, 1998.
- [18] Building Seismic Safety Council. NEHRP guidelines for the seismic rehabilitation of building. FEMA 273. Washington, DC: Building Seismic Safety Council, 1997.
- [19] Perform-3D User Guide: Nonlinear Analysis and Performance Assessment for 3D Structures. 2006, Computers & Structures Inc.

## Research Article

# Deterministic and Probabilistic Serviceability Assessment of Footbridge Vibrations due to a Single Walker Crossing

Cristoforo Demartino,<sup>1</sup> Alberto Maria Avossa ,<sup>2</sup> and Francesco Ricciardelli<sup>2</sup>

<sup>1</sup>College of Civil Engineering, Nanjing Tech University, Nanjing 211816, China

<sup>2</sup>DICDEA, Università della Campania Luigi Vanvitelli, Via Roma 9, 81031 Aversa, Italy

Correspondence should be addressed to Alberto Maria Avossa; [albertomaria.avossa@unicampania.it](mailto:albertomaria.avossa@unicampania.it)

Received 9 July 2017; Revised 5 September 2017; Accepted 12 November 2017; Published 17 January 2018

Academic Editor: Hugo Rodrigues

Copyright © 2018 Cristoforo Demartino et al. This is an open access article distributed under the Creative Commons Attribution License, which permits unrestricted use, distribution, and reproduction in any medium, provided the original work is properly cited.

This paper presents a numerical study on the deterministic and probabilistic serviceability assessment of footbridge vibrations due to a single walker crossing. The dynamic response of the footbridge is analyzed by means of modal analysis, considering only the first lateral and vertical modes. Single span footbridges with uniform mass distribution are considered, with different values of the span length, natural frequencies, mass, and structural damping and with different support conditions. The load induced by a single walker crossing the footbridge is modeled as a moving sinusoidal force either in the lateral or in the vertical direction. The variability of the characteristics of the load induced by walkers is modeled using probability distributions taken from the literature defining a Standard Population of walkers. Deterministic and probabilistic approaches were adopted to assess the peak response. Based on the results of the simulations, deterministic and probabilistic vibration serviceability assessment methods are proposed, not requiring numerical analyses. Finally, an example of the application of the proposed method to a truss steel footbridge is presented. The results highlight the advantages of the probabilistic procedure in terms of reliability quantification.

## 1. Introduction

Vibrations of footbridges due to human loading have recently received much attention, due to the increasing number of vibrations incidents occurring worldwide. The main cause of these large vibrations is the low stiffness and damping of recently built footbridges. As a matter of fact, if only static dead and live loads are considered in the design process, footbridges can prove unable to meet serviceability requirements against vibrations.

In particular, the significant amount of research produced in the last one and a half decades has been triggered by the two vibration incidents of the Paris Passerelle Solferino on December 15, 1999, and of the London Millennium Bridge on July 10, 2000, that played a similar role in the public opinion and in the scientific community to that played by the collapse of the Tacoma Narrows bridge in November 1940 [1]. Nevertheless, crowd-related failures of bridges have occurred over the centuries with much more devastating effects, the first of which being documented is probably that of the bridge

over river Ouse in England, in 1154 [2]. In spite of the long series of failures, to the authors' knowledge the first paper to have appeared dealing with the effects of human movements on structural loading is that of Tilden [3]. This is a pioneering work where many aspects of the human loading of structures seem to have already been recognized, though not quantified.

The vibrations are generated by the “quasi” harmonic load induced by walkers and joggers. If the central frequency of the load and a natural vibration frequency of the footbridge are similar, resonant vibrations can occur. The latter is a rather common condition [4]. However, this apparently simple mechanism is in fact not easy to quantify. First of all, walkers do not induce a perfectly periodic load due to the intrasubject variability gait, and this load differs from one subject to another (intersubject variability). Finally, two forms of feedback can take place: (i) interwalker interaction and (ii) walker-structure interaction [5]. The first refers to gait modifications due to the presence of neighboring walkers, whereas the second is the adjustment of gait as an effect of the floor vibration.

Standards and guidelines have been developed to help the designer in the evaluation of the vibration serviceability based on simplified loading models, simulating different possible scenarios [5, 6]. In broad terms, the design of footbridges against pedestrian-induced vibrations requires the knowledge of [7] (i) the characteristics of the pedestrian action, (ii) a response evaluation method, and (iii) a comfort criterion. The interested reader is referred to [5, 6, 8, 9]. Design guidelines outline procedures for vibration serviceability checks, but it is noticeable that most of these assume that the action is deterministic [10], yet this is stochastic, and it would be reasonable to incorporate its variability in the loading models. However, it should be mentioned that other loads on bridges should be considered in the design procedures such as seismic, wind, and impact loads (e.g., [11–16]).

Different authors have tried to characterize the randomness of the pedestrian action in either time or frequency domain, considering both intrasubject and intersubject variability. Brownjohn et al. [17] for the vertical direction and Pizzimenti and Ricciardelli [18] and Ricciardelli and Pizzimenti [19] for the lateral direction gave Power Spectral Density Functions (PSDFs) of the load induced by a walker, for use in the evaluation of the stationary response to a stream of walkers, including intrasubject and intersubject variability of gait.

Subsequently, Butz [20] presented a spectral approach for the evaluation of the peak acceleration induced by unrestricted pedestrian traffic. The PSDFs of the modal force were approximated through a Gaussian function, fitting data coming from Monte Carlo simulations. These were carried out for different bridge geometries and for four different pedestrian densities. Step frequency, pedestrian mass, force amplitude, and pedestrian arrival time were randomly selected from given probability distributions. The PSDF of the acceleration was evaluated from the PSDF of the modal force, and the 95th fractile peak modal acceleration was derived as the product of the RMS acceleration and a peak factor. The latter was evaluated to be around 4. All the coefficients required for the application of the procedure were expressed in a parametric form. This model has then been incorporated into HIVOSS guidelines [21].

Živanović et al. [22] presented a multiharmonic force model for calculation of the multimode structural response to a crossing, accounting for inter- and intrasubject variability in the walking force. The model is again based on Monte Carlo simulations, with pedestrian characteristics also selected from given distributions. The intrasubject variability was accounted for describing the force in the frequency domain and then converting it to the time domain. No parametric form of the peak response as a function of the different parameters and no procedure for the serviceability assessment are given.

Ingólfsson et al. [23] proposed a Response Spectrum approach inspired by earthquake engineering. Through Monte Carlo simulations, they evaluated a reference vertical acceleration to the action of a flow of 1 walker/s with probabilistically modeled characteristics, to which empirical correction factors are applied to account for return period, modal mass, mean arrival rate, structural damping,

footbridge span, and mode shape. A total of 97 windows, 300 s long, were used to establish the peak acceleration Generalized Extreme Value (GEV) distribution parameters. Two reference populations were considered, with step frequencies of 1.8 and 2.0 Hz, with STD of 0.1 Hz and Poisson distributed arrivals. The input force was modeled as a harmonic load and the intersubject variability was considered varying the characteristics of each pedestrian according to given distributions. All the parameters contained in the procedure are given in parametric form, and the GEV distribution of the peak acceleration is found to tend to a Gumbel distribution (i.e., the shape parameter tends to 0).

Piccardo and Tubino [24] studied the vertical vibration serviceability of footbridges, based on a probabilistic characterization of pedestrian-induced forces taking into account intersubject variability and considering only one mode of vibration. Only the 95th fractile peak modal acceleration was derived and expressed in two nondimensional forms: (a) the Equivalent Amplification Factor, that is, the ratio between the maximum dynamic response to a realistic loading scenario and the maximum dynamic response to a single resonant pedestrian; (b) the Equivalent Synchronization Factor, that is, the ratio between the maximum dynamic response to a realistic loading scenario and the maximum dynamic response to uniformly distributed resonant pedestrians. Comparison of their procedure with similar methods contained in standards and design guidelines has pointed out that the latter are generally conservative (often largely conservative) and can become only slightly nonconservative in particular cases. They concluded that further investigations on the evaluation of the PDF of the maximum dynamic response are required.

Živanović et al. [25] reviewed different time-domain design procedures for vibration serviceability assessment of footbridges exposed to streams of pedestrians and evaluated their performance in predicting the vertical vibration response of two existing footbridges. They compared the procedures contained in Eurocode 5 [26], ISO 10137 [27], Sétra [28], BSI [29], Brownjohn et al. [30], Butz [20], Ingólfsson et al. [23], and Živanović et al. [22]. They found some discrepancies between the predicted and measured vibration levels and discussed their potential causes, among which are interwalker and walker-structure interaction.

Pedersen and Frier [10] evaluated the effect of the probabilistic modeling of the parameters describing walking loads: step frequency, stride length, Dynamic Load Factor (DLF), and walker weight. A literature review revealed a variety of probability distributions through which the walking parameters can be modeled, and these were used for exploring the sensitivity of the 95th fractile of midspan acceleration. They observed that the step frequency distribution can have a strong influence, whereas the DLF, the walker weight, and stride length have a much lower influence. No interactions were considered in this study.

Ingólfsson and Georgakis [31] presented a probabilistic lateral load model in which the forces are given as the sum of an external component and a frequency and amplitude-dependent self-excited component; the latter is quantified through equivalent pedestrian damping and mass coefficients measured from experiments. They found that the peak

response of a footbridge to a pedestrian flow is very sensitive to the selection of the pacing rate distribution.

Piccardo and Tubino [32] introduced an equivalent spectral model for the analysis of the dynamic response of footbridges to unrestricted pedestrian traffic (i.e., no interwalker interaction) using a complete probabilistic representation of pedestrians. They provided simple closed-form expressions for the evaluation of the maximum dynamic response for use in vibration serviceability analyses, similarly to classical procedures adopted in wind engineering. These expressions are based on the definition of the peak factor found by Davenport [33].

Recently, Ricciardelli and Demartino [5] compared background hypotheses, fields of applicability, and results obtained through a number of different loading and response evaluation models. In particular, they compared single walker models, multiple walkers models, interaction models (interwalker and walker-structure), and instability models, together with current design procedures incorporated into standards and guidelines. Avossa et al. [34] applied the design procedures to various steel footbridges highlighting the large differences that they bring in the results. They concluded that a critical revision of design procedures is needed as these, even though inspired by the same principles and applying the same rules, show different results; this should also be done through validation with the available full-scale data. Finally, Avossa et al. [35] evaluated through Monte Carlo simulations the probability distribution of the footbridge peak acceleration to single and multiple crossing walkers for two specific footbridge configurations.

In combination with a probabilistic definition of the load, criteria for the probabilistic definition of the structural capacity must be set. For instance, Eurocode 0 [36] requires that a structure is designed to have adequate (i) resistance, (ii) serviceability, and (iii) durability. In particular, the limit state of vibrations causing discomfort to people and/or limiting the functional effectiveness of the structure must be considered. Moreover, it establishes that when the structure is prone to significant acceleration, dynamic analyses must be performed. Similarly, ISO 2394 [37] specifies general principles for the reliability assessment of structures subjected to known or foreseeable types of actions, providing more or less similar requirements for safety, serviceability, and durability. In Annex E of ISO 2394 [37], principles of reliability-based design are given specifying the requirements in terms of probability of failure for different limit states.

ISO 10137 [27] contains structural acceleration limits for different situations. ISO 10137 recognizes the vibration source, path, and receiver as three key elements which require being identified when dealing with vibration serviceability. In the context of walking-induced vibrations in footbridges, the walkers are the vibration source, the footbridge is the path, and the walkers are again the receivers. According to ISO 10137, an analysis of the response requires a calculation model that incorporates the characteristics of the source and of the transmission path, which must be solved for the vibration response of the receiver; in doing so, the dynamic action of one or more walkers can be described as force time histories. This action varies in time and space as the walkers

move on the footbridge. It is recommended that the following scenarios are considered: (i) one person walking across the bridge, (ii) an average pedestrian flow (group size of 8 to 15 walkers), (iii) streams of walkers (significantly more than 15 walkers), and (iv) occasional festive choreographic events (when relevant).

However, although many authors have derived probabilistic models to describe the vibration response induced by pedestrian loads, a fully probabilistic procedure for the serviceability assessment of footbridge vibrations due to a single walker crossing and a comparison with deterministic approaches is not yet available. In particular, the studies reviewed above do not allow for variation of the reliability levels, as they take as demand parameter the 95th fractile of the peak acceleration response. It is important to notice that although the research interest is nowadays mainly oriented towards the multipedestrian case, the need for analyzing the single pedestrian case stems from at least three different reasons: (i) this case can induce the largest acceleration, especially for short low-damped footbridges, (ii) many standards and codes of practices refer to this load scenario, and (iii) vibration assessment procedures for multipedestrian loading are often derived from the single pedestrian case.

This study presents criteria for the deterministic and probabilistic vibration serviceability assessment of footbridges to the crossing of one walker. In Section 2, the load induced by a single walker is modeled as a moving harmonic force having lateral and vertical components, whose characteristics derive from a Standard Population (SP) of walkers. The latter is defined based on data available in the literature, concerning the probabilistic distribution of walker characteristics and gait parameters. In Section 3, the dynamic characteristics of a single span footbridge (span length, natural frequencies, mass, structural damping, and support conditions) are defined and a modal dynamic model is presented. In Section 4, numerical analyses of the transient response to a moving harmonic load are presented, through which the peak response is evaluated in both a deterministic and probabilistic way. In Section 5, closed-form deterministic and probabilistic vibration serviceability methods are proposed, whose applications do not require numerical analyses. These incorporate the acceleration limits of ISO 10137 [27] and the required reliability level of ISO 2394 [37], leading to a method which also complies with Eurocode 0 [36]. As an example, in Section 6, the deterministic and probabilistic methods are applied to a prototype truss steel footbridge. Finally, some conclusions and prospects are drawn (Section 7).

## 2. Single Walker Behavior

Ground Reaction Forces (GRFs) are defined as the forces induced on the ground by walkers. The measurement of GRFs has advanced considerably over the recent decades. It first became a useful clinical tool starting from the pioneering work of Beely [38] and Elftman [39]. Nowadays, observational gait analysis is regularly performed by physical therapists to determine treatment goals and is used as an evaluation tool during rehabilitation [40]. In Medical Sciences, the main goal is the identification of the kinematic characteristics

of a subject. Differently, in civil engineering it is of interest to characterize GRFs, with the final aim of evaluating the structural response for comfort assessment [9, 41].

GRFs are characterized by different magnitudes and frequency content in the vertical, lateral, and longitudinal directions. Based on the existing knowledge of GRFs, several loading models have been developed for footbridges, some of which consider the crossing of a single pedestrian [5]. A common approach is that of periodic loading, assuming that a walker generates identical footfalls with constant frequency neglecting intrasubject variability. In this case, the dynamic part of the GRF is expanded in Fourier series:

$$F_i(t) = W \cdot \sum_{j=1}^{\infty} \text{DLF}_{i,j} \left( \sin(j \cdot \pi \cdot f_{w,i} \cdot t) - \psi_{i,j} \right), \quad (1)$$

where the subscript  $i = V, L$  indicates the vertical or lateral direction (the longitudinal component is neglected) and where  $W$  is the weight of the walker,  $\text{DLF}_{i,j}$  is the  $j$ th Dynamic Load Factor (DLF), that is, the  $j$ th harmonic load amplitude normalized by the body weight,  $f_{w,i} = f_w$  when  $i = V$  and  $f_{w,i} = 0.5 \cdot f_w$  when  $i = L$ ,  $f_w$  being the step frequency, and  $\psi_{i,j}$  is the phase lag of the  $j$ th harmonic. Moreover, in the following, only the first harmonic will be retained, and accordingly subscript  $j$  will be omitted. This representation of the load is consistent with different standards such as UK Annex to EC1 [29] and ISO 10137 [27].

When the walker crosses a footbridge of span  $L$ , the modal load associated with the first bending mode is

$$f_i(t) = \int_0^L \phi_i(x) \cdot F_i(t) \cdot \delta(x - v \cdot t) \cdot [H(t) - H(t - T_p)] dx, \quad (2)$$

where  $\phi_i(x)$  is first mode shape (Section 3),  $\delta(\bullet)$  is the Dirac Function,  $x$  defines the position of the walker on the bridge,  $H(\bullet)$  is the Heaviside function, and  $T_p = L/v$  is the crossing time,  $v = f_w l_w$  being the walking speed,  $L$  the span length, and  $l_w$  the step length.

**2.1. Standard Population of Walkers.** The definition of a Standard Population (SP) of walkers is needed to characterize intersubject variability probabilistically. This is not trivial due to the large scatter of the data available in the literature, and one must be aware of the fact that changing the population will lead to a different vibration response [10].

The parameters governing the excitation generated by a walker are (i) the walking speed  $v$ , (ii) the step frequency  $f_w$ , (iii) the Dynamic Load Factors  $\text{DLF}_V$  and  $\text{DLF}_L$ , (iv) the weight of the walker  $W$ , and (v) the phase angles  $\psi_V$  and  $\psi_L$ . The data mainly come from the Biomechanics and Transportation fields, although recent results have also been published in the area of structural engineering. The SP defined in this section is based on research developed in European countries.

Humans can walk up to 4 m/s [42], but the speed of roughly 2.2 m/s represents a natural transition from walking to running [43, 44]. In spite of this, the walking speed is

usually considered as normally distributed, and a large scatter in the mean value is found in the literature. This is due to physiological and psychological factors, such as biometric characteristics of the walker (body weight, height, age, and gender), cultural and racial differences, travel purpose, and type of walking facility [45]. In the following, the walker speed is assumed as [46]

$$v = \mathcal{N}(1.41, 0.224) > 0.41 \text{ [m/s]}. \quad (3)$$

Equation (3) is truncated at 0.41 m/s as smaller values lead to negative STDs in (4).

It is agreed that walking occurs at an average step frequency of approximately  $f_w = 2$  Hz (e.g., [28]). Biomechanics studies established that walkers tend to adjust their step frequency and therefore step length,  $l_w$ , so to minimize energy consumption at a given walking speed [47]. The step length (and its double, the stride length) varies with the physical characteristics of the subject (height, weight, etc.) and from one country to another due to the different traditions and lifestyle. Accordingly, the correlation between the walking speed and the step frequency has been reported in literature with a large scatter [45, 48–50]. Many researchers have considered the step frequency as normally distributed [41, 48, 51]. In this study, it is assumed that the mean and STD of the normal distribution of  $f_w$  are linearly dependent on the walking speed [52]:

$$f_w = \mathcal{N}(0.7868 \cdot v + 0.7886, 0.0857 \cdot v - 0.035) > 0 \text{ [Hz]}. \quad (4)$$

Negative values are truncated as meaningless. The mean value of  $f_w$  associated with the mean walking speed (i.e., 1.41 m/s) is 1.898 Hz, and the standard deviation is 0.086 Hz.

Values of the DLFs have been reported in many publications and have been incorporated into design guidelines. These are usually derived from force measurements on instrumented floors or treadmills [53]. In this study, only fixed floor conditions are considered since walker-structure interaction effects are neglected. This interaction is significant in the lateral direction [54] and less in the vertical direction. DLFs measured on a rigid floor are therefore assumed to be the same as those that would be measured on a moving floor if the displacements are small. Moreover, DLFs can also be derived using analytical models that are usually inspired by biomechanics as the inverted pendulum model [55, 56]. Živanović et al. [8] reported a review of the DLFs used in single walker force models. The mean values of  $\text{DLF}_V$  are approximately in the range of 0.257 [57] to 0.5 [58]. Generally, the dynamic part of the vertical GRF is found to be dependent on  $f_w$ . The first study revealing this issue is that of Kajikawa [59] (reported in [60]). It is now widely accepted that  $\text{DLF}_V$  increases with  $f_w$  up to a maximum of approximately 0.5 [61, 62]. Accordingly, in this study, the SP is described through a  $\text{DLF}_V$  depending on  $f_w$  (see (4)) as [62]

$$0 < \text{DLF}_V = 0.37 \cdot (f_w - 0.95) \leq 0.5. \quad (5)$$

According to (5),  $\text{DLF}_V$  is described by a normal distribution with mean equal to 0.35 and STD 0.07.

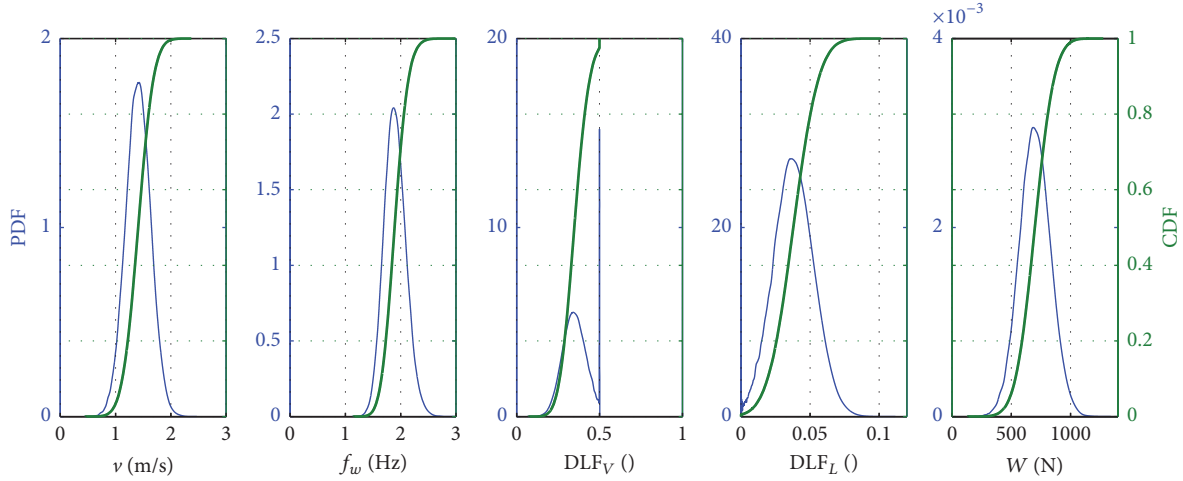


FIGURE 1: Probability Density Function (PDF, thin line) and Cumulated Distribution Function (CDF, thick line) of the random variables defining the SP:  $v$ ,  $f_w$ ,  $DLF_V$ ,  $DLF_L$ , and  $W$ .

On the other hand, the mean values of  $DLF_L$  are approximately in the range of 0.039 [63] to 0.1 [58]. Accordingly, in this study, the SP is assumed to have a  $DLF_L$  described through a normal distribution [52]:

$$DLF_L = \mathcal{N}(0.03792, 0.01459) > 0. \quad (6)$$

In (5) and (6), negative values are truncated as meaningless. Moreover, in (5) an upper bound was set at 0.5.

The body weight is very much dependent on height; therefore, in medical applications, it is preferred to refer to the Body Mass Index (BMI), that is, the body mass divided by the square of the height [64]. For each country, Walpole et al. [65] used available data on BMI and height distribution to estimate average adult body mass. In particular, they reported the average body mass by world regions as in 2005. The average body mass ranges between 57.7 kg for Asia and 80.7 kg for North America. Indeed, load models (e.g., (1)) require the definition of the walker weight,  $W$ ; that is, the body weight increased by the weight of clothing and other items carried by the walker. The walker weight is taken equal to 700 N by many loading models (e.g., [28, 57]). In this study, the weight of the SP is assumed to be normally distributed as in HIVOSS [21]:

$$W = \mathcal{N}(744, 130) \geq 0 \text{ [N]}. \quad (7)$$

The mean value in (7) is 7% larger than that of 695 N corresponding to the average body mass 70.8 kg reported by Walpole et al. [65] for Europe since the latter lacks clothing and other items carried by the walker. Negative values are truncated as meaningless.

Finally, the distribution of phase lags,  $\psi_i$ , between walkers is a measure of the correlation of the forces they exert. For a continuous PDF of walking frequencies, phase lags are characterized by the PDF of the phase spectrum. If this is uniformly distributed between 0 and  $2\pi$ , then the walkers and the walking forces are uncorrelated. Correlation increases when the PDF of the phase spectrum is peaked around a given

value as this value approaches 0; the forces tend to be in phase. In the case of a single walker, all this loses its meaning and will be neglected in the following.

In Figure 1, the Probability Density Functions (PDFs) and the Cumulative Distribution Functions (CDFs) of the random variables defining the SP previously described are shown.

### 3. Footbridge Characteristics and Mechanical Model

In this study, single span beam footbridges are considered. The dynamic response of the footbridge is analyzed by means of modal analysis, considering only the first lateral and vertical modes. The latter assumption is made since (i) in common footbridges torsional vibrations are not an issue, with the exception of some research aimed at the mitigation of torsional vibrations on suspended footbridges [66] and (ii) usually only one mode, either vertical or lateral, is responsible for the footbridge liveliness [67].

Referring to Figure 2, the footbridge response is governed by the two uncoupled differential equations ( $i = V, L$ ):

$$\begin{aligned} m\ddot{u}_i(x, t) + c_i\dot{u}_i(x, t) + EI_i u_i^{IV}(x, t) \\ = F_i(t) \cdot \delta(x - v \cdot t), \end{aligned} \quad (8)$$

where  $m$  is the footbridge uniform mass per unit length,  $c_i$  is the viscous damping per unit length and  $EI_i$  is the bending stiffness, and  $u_i(x, t)$  are the displacements in the vertical,  $u_V(x, t)$ , and lateral,  $u_L(x, t)$ , directions.  $F_i(t)$  and  $\delta(x - v \cdot t)$  have been defined in Section 2. The viscous damping is related to the inherent structural damping and to that based on isolation or supplemental energy dissipation devices (e.g., [68, 69]).

Considering only one mode of vibration, the vertical and lateral deflection of the footbridge is written as

$$u_i(x, t) = \phi_i(x) \eta_i(t), \quad (9)$$

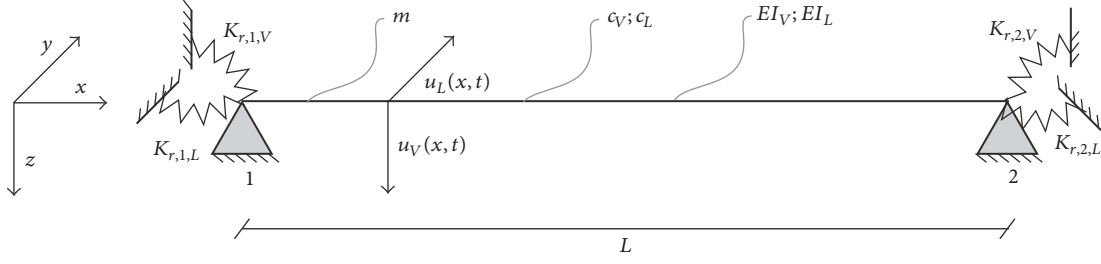


FIGURE 2: Beam characteristics: dynamic model.

where  $\phi_i(x)$  is the mode shape and  $\eta_i(t)$  the associated generalized coordinates in the vertical,  $\eta_V(t)$ , and lateral,  $\eta_L(t)$ , directions.

For a single span beam, the mode shape takes the general form:

$$\begin{aligned} \phi_i(x) = & c_{1i} \sin\left(\lambda_i \frac{x}{L}\right) + c_{2i} \cos\left(\lambda_i \frac{x}{L}\right) \\ & + c_{3i} \sinh\left(\lambda_i \frac{x}{L}\right) + c_{4i} \cosh\left(\lambda_i \frac{x}{L}\right), \end{aligned} \quad (10)$$

where  $\lambda_i$  is the first eigenvalue of the secular equation and  $c_{1i}$ ,  $c_{2i}$ ,  $c_{3i}$ , and  $c_{4i}$  depend on the supports rotational stiffness  $K_{r,1,i}$  and  $K_{r,2,i}$  (Figure 2). For example, for a simply supported beam ( $K_{r,1,i} = K_{r,2,i} = 0$ ),  $c_{1i} = 1$  and  $c_{2i} = c_{3i} = c_{4i} = 0$  and  $\lambda_i = \pi$ . The mode shape is normalized, so as to have maximum value equal to one.

The modal equations of motion are

$$\ddot{\eta}_i(t) + 4\pi\xi_i f_i \dot{\eta}_i(t) + 4\pi^2 f_i^2 \eta_i(t) = m_i^{-1} f_i(t), \quad (11)$$

where  $\xi_i$  is the modal damping ratio,  $f_i$  is the natural frequency, and  $m_i$  is the modal mass in the vertical and lateral directions.

Assuming that the motion starts from rest (i.e.,  $\eta_i(0) = \dot{\eta}_i(0) = 0$ ), the solution of (11) is

$$\eta_i(t) = \frac{1}{m_i} \int_0^t f_i(\tau) \cdot h_i(t - \tau) \cdot d\tau, \quad (12)$$

where  $h_i(t - \tau)$  is the unit-impulse response function.

The governing parameters of the dynamic response are (i) the span length  $L$ , (ii) the natural frequencies  $f_V$  and  $f_L$ , (iii) the structural damping ratios  $\xi_V$  and  $\xi_L$ , and (iv) the modal shapes  $\phi_V(x)$  and  $\phi_L(x)$ . The footbridge mass per unit length,  $m$ , also influences the response. However, this parameter appears as a linear factor in the equations and accordingly it plays the role of a scale parameter in the results.

In the analyses, values of the span length  $L$  in the wide range of 10 m to 200 m were considered, where the smallest value corresponds to a simple road crossing and the largest is assumed as an upper limit for beam footbridges.

The vertical and lateral natural frequencies are expressed in terms of frequency ratios:  $\alpha_i = \bar{f}_{w,i}/f_i$ . Here and in the following, the overbar indicates a mean value of the distribution. The range of interests for vibration serviceability assessments is  $0.3 \leq \alpha_i \leq 1.7$ , which approximately corresponds to

the external boundaries of Range 3 (low risk of resonance for standard loading situations) as defined in S etra [28].

The damping ratio can vary in the wide range of 0.1% to 2.0% [70]. In particular, standards and guidelines, such as S etra [28], Heinemeyer et al. [21], ISO 10137 [27], and Eurocodes (EC1 [71], EC3 [72], and EC5 [26]), suggest minimum and mean values depending on construction material (Table 1). The lower values apply to steel bridges (0.2% ÷ 0.5%), whereas the largest values are for timber bridges (1.5% ÷ 3%). In particular, the values given by FIB [73] are the result of the combination of material, bridge type, and support conditions. According to the values given in Table 1, damping ratios in the range of 0.1% to 1.5% were considered in this study. It is worth mentioning that it is difficult to accurately predict (during the design process) and estimate (during the assessment process) this parameter and accordingly fairly large uncertainties are associated with it.

Finally, the mode shapes (i.e., the supports rotational stiffness values  $K_{r,1,i}$  and  $K_{r,2,i}$ ) influence the dynamic response of the footbridge. In particular, the mode shapes vary the modal masses,  $m_V$  or  $m_L$ , and the modal loads (see (2)). Mode shapes (see (10)), in turn, depend on the rotational stiffness of the supports,  $K_{r,1,i}$  and  $K_{r,2,i}$ . In this study, only symmetric support conditions have been considered, that is,  $K_{r,1,i} = K_{r,2,i} = K_{r,i}$ .

In general, the mode shapes are a function of  $K_{r,i}$ . However, when the mode shape is evaluated from a FE model, the evaluation of the end rotational stiffness can be cumbersome and also a direct comparison to fit (10) is not immediate. Accordingly, in the following, a simplified and approximate procedure is proposed to define the mode shapes of the equivalent beam model (i.e., (10)) using static analysis from the FE model of the footbridge. The only reason for this simplified procedure is to provide practitioners with a simple tool to apply the proposed method. This method is accurate if the FE model meets the assumptions of (10), that is, constant mass and stiffness. To this aim, the support condition is expressed in terms of a nondimensional restrained level (RL), defined as the ratio of the end moment for the particular support condition (i.e., value of  $K_{r,i}$ ) due to an arbitrary symmetric load,  $M_i(K_r)$ , to that of the clamped beam subjected to the same load,  $M_i(K_r \rightarrow \infty)$ :

$$RL_i = \frac{M_i(K_{r,i})}{M_i(K_{r,i} \rightarrow \infty)}. \quad (13)$$

TABLE 1: Suggested damping ratios  $\xi$  [%] for different construction material, as given by different standards and guidelines.

Type	Damping ratios $\xi$ [%]							
	Sétra		Hivoss		ISO 10137	Eurocodes <sup>1</sup>	FIB	
	Min	Mean	Min	Mean	Mean	Mean	Min	Mean
Reinforced concrete	0.8	1.3	0.8	1.3	0.8	1.5	0.8	1.2
Prestressed concrete	0.5	1.0	0.5	1.0		1.0	0.7	1.0
Steel	0.2	0.4	0.2	0.4	0.5	0.2/0.4 <sup>2</sup>	0.5	1.0
Composite steel-concrete	0.3	0.6	0.3	0.6	0.6	0.6	0.6	1.0
Timber	1.5	3.0	1.0	1.5	-	1/1.5 <sup>3</sup>	0.8	1.4

<sup>1</sup>EC1 [71], EC3 [72], and EC5 [26]; <sup>2</sup>0.2/0.4% if welded/bolted connection are present; <sup>3</sup>1% if no mechanical joints are present and 1.5% otherwise.

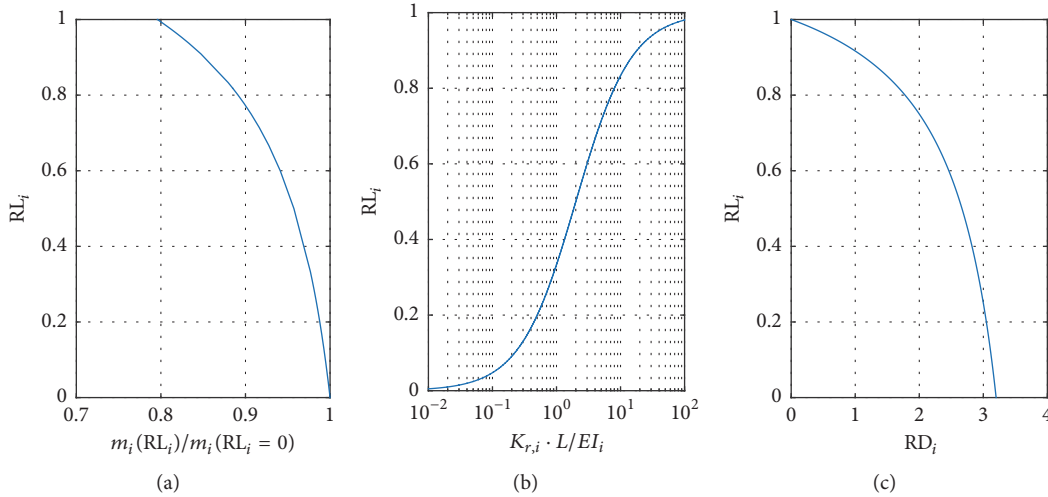


FIGURE 3: Restraint level  $RL_i$  as a function of  $m_i(RL_i)/m_i(RL_i = 0)$  (a),  $K_{r,i}L/EI_i$  (b), and  $RD_i$  (c).

Therefore,  $RL_i$  is in the range of 0 (supported case,  $K_{r,i} = 0$ ) to 1 (clamped case,  $K_{r,i} \rightarrow \infty$ ). The relationship between  $K_{r,i}$  and  $RL_i$  can be simply obtained as

$$K_{r,i} = 2 \cdot \frac{RL_i}{1 - RL_i} \cdot \frac{EI_i}{L}. \quad (14)$$

The relationship between  $K_{r,i}$  and  $RL_i$  is shown in a nondimensional form in Figure 3. The derivation of (14) is given in Appendix C.1.

On the other hand, the static deformation due to an arbitrary uniform load of the Finite Element model is expressed as the nondimensional Rotation-to-Deflection ratio ( $RD_i$ ):

$$RD_i = \frac{\Theta_i \cdot L}{\delta_i}, \quad (15)$$

where  $\theta_i$  and  $\delta_i$  are the end rotation and midspan deflection. The relationship between  $RL_i$  and  $RD_i$  can be simply obtained as

$$RL_i = \frac{4 - 1.25 \cdot RD_i}{4 - RD_i} \quad (16)$$

which is also shown in Figure 3. Finally, the parameters of (10) are chosen in order to have the same value of  $RD_i$  as that obtained from the FE model. The derivation of (16) is given in Appendix C.2.

To conclude, the simplified and approximated procedure to evaluate the mode shape using static analysis of the FE model of the footbridge requires the following steps: (i) evaluation of  $RD_i$  (see (15)) using the FE model of the footbridge (i.e., evaluation of the end rotation and midspan deflection,  $\theta_i$  and  $\delta_i$ , due to a uniform load), (ii) conversion of  $RD_i$  to an equivalent  $RL_i$  using (16) (Figure 3), (iii) evaluation of  $K_{r,i}$  using (14) (Figure 3), and (iv) evaluation of the mode shapes (see (10)) using as input the obtained  $K_{r,i}$  in the boundary conditions and solving the eigenvalue problem obtaining  $\lambda_i$ ,  $c_{1i}$ ,  $c_{2i}$ ,  $c_{3i}$ , and  $c_{4i}$ . Finally, by integrating the mass per unit length,  $m$ , over the mode shape, the modal mass can be obtained. The ratio of the modal mass for the generic boundary,  $m_i(RL_i)$ , to the modal mass of the supported beam,  $m_i(RL_i = 0)$ , is shown as a function of  $RL_i$  in Figure 3. This was obtained by numerically solving the eigenvalue problem for different values of  $RL_i$ . As expected, the modal mass reduces when the rotational stiffness of the supports increases (i.e.,  $RL_i$ ). The latter ratio will be used in Section 4.1.2.

## 4. Response Evaluation

In this section, the response evaluation procedure is presented. This is summarized in Figure 4. The aim of the assessment is to verify that the acceleration induced by the crossing of a single walker is not causing discomfort to the walker

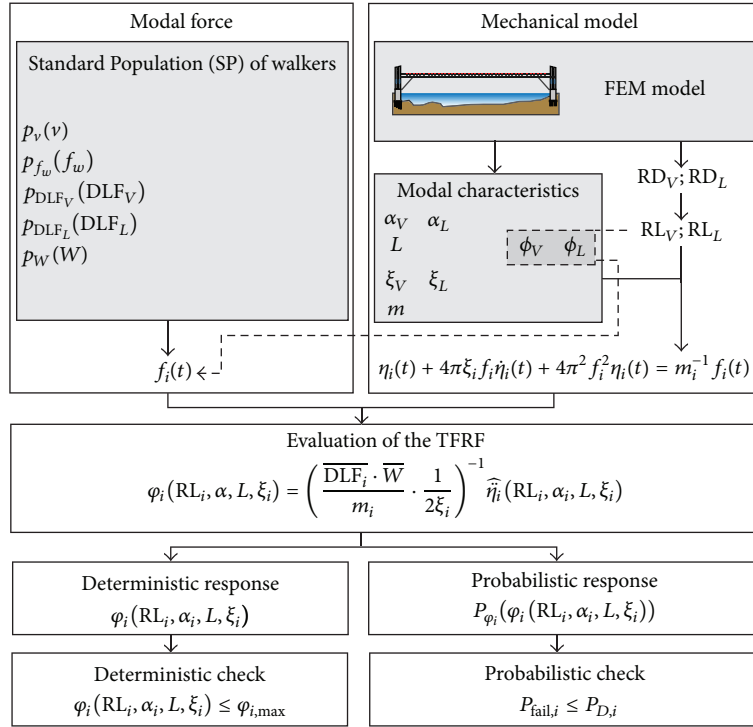


FIGURE 4: Deterministic and probabilistic assessment procedures.

himself/herself or other people standing on the footbridge. The engineering demand parameter chosen to assess this scenario is the peak acceleration, as it will be shown in Section 5. A deterministic and a probabilistic approach will be used.

The input parameters are characteristics of the walker (modal force) and the dynamic properties of the footbridge (mechanical model). The SP described in Section 2.1 is used to describe the characteristics of the walker and of the induced modal force. The deterministic response is evaluated referring to the SW (i.e., the walker having mean characteristics of the SP). The probabilistic response is evaluated referring to the SP defined in Section 2.

The output is expressed through the Transient Frequency Response Function (TFRF), that is, the ratio between the modal peak nonstationary response induced by a given walker crossing the bridge and the corresponding stationary response induced by the SW. In this way, the peak modal acceleration,  $\hat{\eta}_i$ , can be expressed in terms of a TFRF [5, 75]:

$$\hat{\eta}_i(RL_i, \alpha_i, L, \xi_i) = \frac{DLF_i \cdot \bar{W}}{2\xi_i} \cdot \frac{1}{m_i} \cdot \varphi_i(RL_i, \alpha_i, L, \xi_i), \quad (17)$$

where  $\varphi_i$  is the TFRF. Here and in the following, the hat,  $\hat{\cdot}$ , indicates the peak response and the overline,  $\bar{\cdot}$ , indicates the mean value. The mechanical model of the footbridge is deterministic and the response is expressed as a function of its input parameters:

$RL_i \rightarrow$  mode shape,

$\alpha_i \rightarrow$  frequency ratio,

$\xi_i \rightarrow$  damping ratio,

$L \rightarrow$  number of loading cycles.

(18)

The arrow indicates to which characteristics of the mechanical model or modal force the input parameters are referred. In particular, the first three are nondimensional parameters, defining the dynamic properties of the structure. The last is the dimensional footbridge span, which is a measure of the number of loading cycles (see (2)). The number of cycles is the ratio of  $L$  to the wavelength, the latter being the ratio of the walking speed to the walking frequency. Accordingly, for a given value for the wavelength, increasing of the span length will correspond to larger values of the response tending to those of a stationary system; this also depends on the structural damping [75–77].

The TFRF can be evaluated in both deterministic and probabilistic forms, and the two approaches are discussed in Sections 4.1 and 4.2, respectively. On the other hand, the deterministic and probabilistic check procedures will be presented in Section 5.

The sources of uncertainty and error were discussed in Sections 2.1 and 3. The interested reader is referred to [10] for a discussion on the sensitivity of footbridge vibrations to stochastic walking parameters.

**4.1. Deterministic Approach.** The modal response to a harmonic load crossing a beam at a constant speed can be obtained as the superposition of forced and of free-decay responses. Different authors derived the closed-form solution

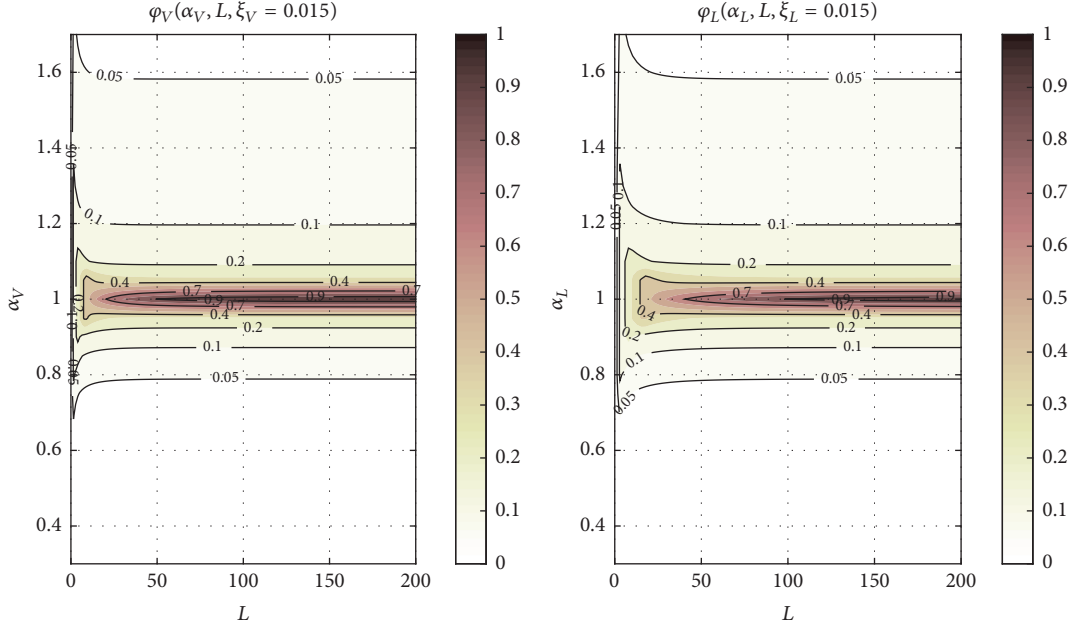


FIGURE 5:  $\varphi_V(\alpha_V, L, \xi_V = 0.015)$  and  $\varphi_L(\alpha_L, L, \xi_L = 0.015)$  for the simply supported beam evaluated using (19).

TABLE 2: Limits of validity and availability of closed-form peak modal response from different authors.

Reference	$\alpha$	$RL_i$	Peak modal response
Abu-Hilal and Mohsen [74]	All	All	
Ricciardelli and Briatico [75]	All	0	✓
Piccardo and Tubino [76]	1	All	✓

to this problem. First, Abu-Hilal and Mohsen [74] derived a closed-form solution of the resonant and nonresonant response for any support condition. Subsequently, limited to the simply supported beam, Ricciardelli and Briatico [75] derived an approximated closed-form solution of the resonant and nonresonant response, together with a closed-form solution of the peak modal response. Then, Piccardo and Tubino [76] derived an approximated closed-form solution

only of the resonant response, but for any support conditions, together with a closed-form solution of the peak modal response. A synthesis of the limits of validity and of the availability of closed-form peak modal response for different authors is reported in Table 2.

In the following, the case of a simply supported beam ( $RL_i = 0$ ) will be analyzed in Section 4.1.1, while the effects of the change of the support conditions will be described in Section 4.1.2.

**4.1.1. Simply Supported Beam ( $RL_i = 0$ ).** For the case of a simply supported beam, different closed-form solutions for the TFRF are available in the literature (see Table 2), and a comparison for the resonant case can be found in [5, 34]. The most accurate solution proves to be that of Ricciardelli and Briatico [75]:

$$\varphi_i(RL_i = 0, \alpha_i, L, \xi_i) = \min \left\{ \begin{array}{l} \xi_i \cdot \frac{2\alpha_i^2}{|1 - \alpha_i^2|} \left[ 1 + \frac{1}{n_i} \frac{2}{|1 - \alpha_i^2|} \cdot \exp \left[ -\frac{\pi \cdot n_i(L) \cdot \xi_i}{2\alpha_i} \right] \right] \\ \frac{n_i(L) \cdot \xi_i}{1 + n_i^2(L) \cdot \xi_i^2} \left[ \sqrt{1 + n_i^2(L) \cdot \xi_i^2} + \exp \left[ -n_i(L) \cdot \xi_i \left( \frac{\pi}{2} + \arctan \frac{1}{n_i(L) \cdot \xi_i} \right) \right] \right] \end{array} \right\}, \quad (19)$$

where  $n_i(L)$  is twice the number of load cycles imposed by the walker to the footbridge and is defined as

$$n_i(L) = \frac{2 \cdot \bar{f}_{w,i}}{\bar{v}} \cdot L = \begin{cases} 2.70 \text{ m}^{-1} \cdot L & \text{for } i = V \\ 1.35 \text{ m}^{-1} \cdot L & \text{for } i = L. \end{cases} \quad (20)$$

Equation (19) for the resonant case is quite consistent with that of Piccardo and Tubino [76].

An example of the vertical and lateral TFRF for  $\xi_i = 0.015$  is shown in Figure 5, where it is visible that the maximum response is obtained for the resonant conditions. At resonance, the TFRF increases increasing the span length, due to the larger number of loading cycles. In particular, the TFRF increases with  $L$  only for relatively low values of  $L$  (around 20 m for  $i = V$  and 40 m for  $i = L$ ), while, for larger beam lengths, the TFRF remains constant. Out of resonance, the two figures are almost identical.

4.1.2. *Effects of Different Support Conditions* ( $RL_i > 0$ ). Change of support conditions influences mode shapes and thus acceleration response. In order to account for general support conditions, a boundary factor,  $BF_i$ , is defined as the ratio of the modal peak acceleration on beam with arbitrary  $RL_i$  to that of a simply supported beam (i.e., for  $RL_i = 0$ ):

$$BF_i(RL_i, \alpha_i, L, \xi_i) = \frac{\hat{\eta}_i(RL_i, \alpha_i, L, \xi_i)}{\hat{\eta}_i(RL_i = 0, \alpha_i, L, \xi_i)}. \quad (21)$$

Substituting (17) in (21), it can be observed that the boundary factor can be split into two parts:

$$\begin{aligned} BF_i(RL_i, \alpha_i, L, \xi_i) &= BF_{m,i}(RL_i) \cdot BF_{\varphi,i}(RL_i, \alpha_i, L, \xi_i) \\ &= \frac{m_i(RL_i = 0)}{m_i(RL_i)} \\ &\quad \cdot \frac{\varphi_i(RL_i, \alpha_i, L, \xi_i)}{\varphi_i(RL_i = 0, \alpha_i, L, \xi_i)}, \end{aligned} \quad (22)$$

where  $\varphi_i(RL_i = 0, \alpha_i, L, \xi_i)$  and  $m_i(RL_i = 0)$  are the TFRF (see (19)) and the modal mass of a simply supported beam and  $\varphi_i(RL_i, \alpha_i, L, \xi_i)$  and  $m_i(RL_i)$  are those for a generic symmetric support conditions (i.e., arbitrary value of  $RL_i$ ). The derivation of (22) is given in Appendix C.3. According to (22),  $BF_i(RL_i, \alpha_i, L, \xi_i)$  accounts for the variation of modal mass through a mass boundary factor,  $BF_{m,i}(RL_i)$ , and of mode shape through a TFRF boundary factor,  $BF_{\varphi,i}(RL_i, \alpha_i, L, \xi_i)$ .

The variation of modal mass with  $RL_i$ , that is,  $BF_{m,i}(RL_i)$ , was shown in Figure 3 as  $m_i(RL_i)/m_i(RL_i = 0)$ , that is, the inverse of  $BF_{m,i}(RL_i)$ . This contribution only depends on the mode shape: with increasing  $RL_i$ , the modal mass reduces. The second term in (22),  $BF_{\varphi,i}(RL_i, \alpha_i, L, \xi_i)$ , depends on all the variables, as in (19).

Using the definition of  $BF_{\varphi,i}(RL_i)$  given in (22), the TFRF for general support conditions can be expressed as

$$\begin{aligned} \varphi_i(RL_i, \alpha_i, L, \xi_i) &= BF_{\varphi,i}(RL_i, \alpha_i, L, \xi_i) \\ &\quad \cdot \varphi_i(RL_i = 0, \alpha_i, L, \xi_i). \end{aligned} \quad (23)$$

At resonance  $BF_i(RL_i, \alpha_i = 1, L, \xi_i)$  can be evaluated using the solution of Piccardo and Tubino [76] while for nonresonant conditions the numerical solution of Abu-Hilal and Mohsen [74] must be used (see Table 2).

In the following, the trend of the boundary factor is only reported for the vertical direction for the sake of brevity, although similar conclusions apply to the case of lateral vibrations. The variation of  $BF_V(RL_V, \alpha_V = 1, L, \xi_V = 0.015)$  (solid lines) and  $BF_{\varphi,V}(RL_V, \alpha_V = 1, L, \xi_V = 0.015)$  (dashed lines) is shown in Figure 6 for  $RL_V$  equal to 0 (simply supported beam), 0.25, 0.5, 0.75, and 1 (clamped beam). The value of  $BF_{\varphi,V}$  increases with reducing rotational stiffness,  $K_{r,V}$  (i.e., reducing  $RL_V$ ). The increase of the modal peak acceleration with increasing  $RL_V$  (i.e., increasing  $K_{r,V}$ ) is due to the choice of considering the mass per unit length,  $m$ , and the natural frequency,  $f_V$ , as input parameters. The latter result derives from having calculated the modal masses (i.e.,

$m_V(RL_V)$  and  $m_V(RL_V = 0)$ ) starting from the same values of mass per unit length,  $m$ . Accordingly, for the same value of  $m$ , the increase of  $RL_V$  leads to a decrease of modal mass,  $m_V$ , as reported in Figure 3. The reduction of modal mass is followed by a reduction of stiffness of the beam,  $EI_V$  (see (8)), to keep  $f_V$  constant, being the frequency proportional to the ratio of the stiffness and modal mass. Accordingly, the reduction of stiffness brings an increase of the peak response, thus explaining the increase of  $BF_V(RL_V, \alpha_V = 1, L, \xi_V)$  with increasing of  $RL_V$ .

On the other hand, if the modal mass,  $m_V$  (instead of the mass per unit length,  $m$ ), and the natural frequency,  $f_V$ , are used as input parameters, the beam will be characterized by the same stiffness,  $EI_V$ , so as to have the same value of  $f_V$ . If the same modal mass is considered (i.e.,  $m_V(RL_V)$  is the same for all  $RL_V$ ), then  $BF_{m,V}(RL_V) = 1$ . Accordingly, the peak response is reduced with increasing  $RL_V$ , as intuitively it should behave. This can be observed looking only at the effect of  $RL_V$  on the TFRF, that is,  $BF_{\varphi,V}(RL_V, \alpha_V = 1, L, \xi_V)$  (dashed line) in Figure 6, since  $BF_{m,V}(RL_V) = 1$ . In this case, the peak response reduction increases with increasing  $RL_V$ .

Away from resonance, the variation of  $BF_V(RL_V = 1, \alpha_V, L, \xi_V = 0.015)$  is also shown in Figure 6.  $BF_V$  shows a marked dependence on  $L$  for  $L \leq 50$  m, whereas it is almost constant for  $L \geq 50$  m, especially away from resonance.

Finally,  $BF_i(RL_i = 1, \alpha_i, L, \xi_i)$  for different values of  $\xi_i$  is reported in Appendix A for the vertical and lateral directions.

4.2. *Probabilistic Approach.* The PDF of the peak acceleration as a function of the footbridge characteristics (i.e.,  $\alpha_i, L$ , and  $\xi_i$ ) is obtained through the convolution of the response for the vertical and lateral directions:

$$\begin{aligned} P_{\hat{\eta}_i}(\hat{\eta}_i(\alpha_i, L, \xi_i)) &= \int_0^\infty \int_0^\infty \int_0^\infty \int_0^\infty P_{\hat{\eta}_i, W, DLF_i, v, f_{w,i}} \\ &\quad \cdot dW \cdot dDLF_i \cdot dv \cdot df_{w,i}, \end{aligned} \quad (24)$$

where the PDF of the peak acceleration reported in the integral can be found applying the chain rule:

$$\begin{aligned} P_{\hat{\eta}_i, W, DLF_i, v, f_{w,i}} &= P_{\hat{\eta}_i}(\hat{\eta}_i(\alpha_i, L, \xi_i) | W, DLF_i, v, f_{w,i}) \\ &\quad \cdot P_W(W) \cdot P_{DLF_i}(DLF_i | f_{w,i}) \\ &\quad \cdot P_{f_{w,i}}(f_{w,i} | v) \cdot P_v(v), \end{aligned} \quad (25)$$

where  $P_A(a | b)$  is the conditional probability of  $a$  given  $b$ . All the variables describing the SP (see Section 2.1) are statistically independent, except for  $v$  and  $f_{w,V}$ . Accordingly, in the derivation of (25), only the conditional probability of  $f_{w,i}$  given  $v$  and  $DLF_V$  given  $f_{w,V}$  was considered.

The multiple integral in (24) combined with (25) was solved through Monte Carlo simulations, using the following procedure in the vertical and lateral directions:

- (1) Evaluation of the integral for  $0.3 \leq \alpha_i \leq 1.7$  (step 0.1),  $10 \text{ m} \leq L \leq 200 \text{ m}$  (step 10 m), and  $0.001 \leq \xi_i \leq 0.015$  (step 0.001) and for  $RL_i = 0$  and 1
- (2) Random generation of 10,000 walkers, whose characteristics ( $W, DLF_i, v$ , and  $f_w$ ) follow the PDFs of the SP of Section 2.1

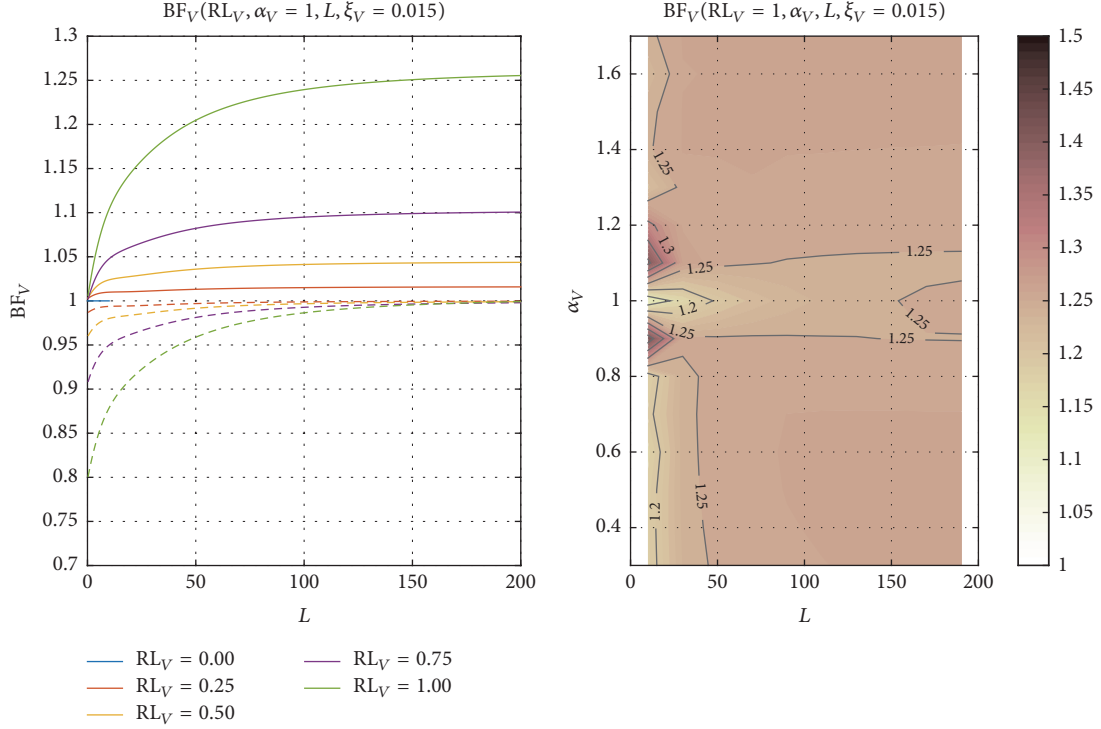


FIGURE 6: Boundary factor  $BF_V(RL_V, \alpha_V = 1, L, \xi_V = 0.015)$  (solid lines) and TFRF boundary factor  $BF_{\varphi_V}(RL_V, \alpha_V = 1, L, \xi_V = 0.015)$  (dashed lines) for different values of  $RL_V$  evaluated using the solution of Piccardo and Tubino [76].  $BF_V(RL_V = 1, \alpha_V, L, \xi_V = 0.015)$  evaluated numerically using the solution of Abu-Hilal and Mohsen [74].

- (3) Evaluation of the modal vertical and lateral acceleration time histories,  $\ddot{\eta}_i(t)$ , for  $RL_i = 0$  and  $RL_i = 1$  using the model of Abu-Hilal and Mohsen [74] (see (12)) for the population of walkers generated in (2) (a time step of 0.01 s was used in the simulations)
- (4) For each walker, evaluation of the lateral and vertical peak acceleration and evaluation of  $\varphi_i(RL_i, \alpha_i, L, \xi_i)$  (see (17))
- (5) Evaluation of the empirical PDF of the TFRF,  $P_{\varphi_i}(\varphi_i(RL_i, \alpha_i, L, \xi_i))$
- (6) Fit of the empirical PDF to a GEV distribution.

The distributions of the TFRF are fitted using the GEV distribution with the following CDF:

$$P_{\varphi_i}(\varphi_i(RL_i, \alpha_i, L, \xi_i)) = \exp \left\{ - \left[ 1 + k_i \left( \frac{\varphi_i - \mu_i}{\sigma_i} \right) \right]^{-1/k_i} \right\}, \quad (26)$$

where the location parameter,  $\mu_i$ , the scale parameter,  $\sigma_i$ , and the shape parameter,  $k_i$ , are all dependent on  $RL_i$ ,  $\alpha_i$ ,  $L$ , and  $\xi_i$ . A preliminary convergence study showed that the number of 10,000 simulations ensures a good accuracy and repeatability of the results.

The estimated GEV parameters for lateral and vertical vibrations for supported ( $RL_i = 0$ ) and clamped ( $RL_i = 1$ ) beams are shown in Appendix B. In all the cases investigated, the GEV parameters were found to depend on  $\alpha_i$  and  $\xi_i$ ,

whereas a dependency on  $L$  was found only for  $L \leq 20$  m for lateral vibrations and for  $L \leq 40$  m for vertical vibrations. The explanation of this difference can be found observing the results of the deterministic approach reported in Section 4.1. Observing Figure 5, it can be seen that the variation of  $\varphi_i$  is noticeable up to 50 m while for larger values it is negligible. Accordingly, also the probabilistic model exhibits small variations of the GEV parameters for values of  $L$  associated with  $L \leq 50$  m. In Appendix B, the GEV parameters are shown for  $L = 10$  m, 20 m, 30 m, and 40 m and for  $L$  in excess of 50 m; the latter are the average value obtained varying  $L$  from 50 m to 200 m. In order to verify the accuracy of the mean GEV parameter representation, the STD of the GEV parameters in the range of  $L$  from 50 m to 200 m was calculated finding very low values of the standard deviation (compared with the values assumed by the variables reported in Appendix B):  $1 \times 10^{-2}$  for  $\mu_i$ ,  $2 \times 10^{-3}$  for  $\sigma_i$ , and  $2 \times 10^{-3}$  for  $k_i$ .

In all the cases investigated,  $k_i$  broadly ranges from  $-0.4$  to 1.2 taking the largest values around resonance. Moreover, at resonance  $k_i$  slightly increases with decreasing structural damping, while it is approximately constant away from resonance. The maximum value of  $k_i$  is reached for  $\alpha = 0.9$  for the lowest structural damping.  $k_i$  takes approximately the same values for  $RL = 0$  and  $RL = 1$ . Globally,  $k_V$  takes larger values compared with  $k_L$ , with small exceptions.  $k_V$  is less dependent on damping than  $k_L$ . The variation of  $k_V$  and  $k_L$  with  $L$  is in agreement with the previous observations.

In all the cases investigated,  $\sigma_i$  and  $\mu_i$  broadly range from 0 to 0.2 taking larger values at resonance and both increasing

TABLE 3: Probabilistic design values  $\beta_D[P_D]$ , after ISO 2394 [37].

Relative costs of safety measures	Consequences of failure			
	Small	Some	Moderate	Great
High	0 [ $5 \cdot 10^{-1}$ ]	1.5 [ $7 \cdot 10^{-2}$ ]	2.3 [ $1 \cdot 10^{-2}$ ]	3.1 [ $1 \cdot 10^{-3}$ ]
Moderate	1.3 [ $1 \cdot 10^{-1}$ ]	2.3 [ $1 \cdot 10^{-2}$ ]	3.1 [ $1 \cdot 10^{-3}$ ]	3.8 [ $7 \cdot 10^{-5}$ ]
Low	2.3 [ $1 \cdot 10^{-2}$ ]	3.1 [ $1 \cdot 10^{-3}$ ]	3.8 [ $7 \cdot 10^{-5}$ ]	4.3 [ $8 \cdot 10^{-6}$ ]

with damping. Globally,  $\sigma_L$  is larger than  $\sigma_V$  for  $\alpha_i > 1$  especially for low damping, and the two quantities are quite similar for  $\alpha_i < 1$ . For both vertical and lateral directions, both  $\sigma_i$  and  $\mu_i$  are larger for the clamped case than for the supported case; this is in agreement with the variation of  $BF_i$  (Figures 7 and 8). The same observations can be made regarding the dependence on  $L$  of  $\sigma_i$  and  $\mu_i$ , as those made for  $k_i$ .

## 5. Reliability Analysis: Deterministic and Probabilistic Approaches

In this section, first (deterministic) and third (probabilistic) level safety assessments methods will be applied. In particular, it is assessed that the acceleration induced by the crossing of a walker is not causing loss of comfort for a receiver.

In the application of the first level safety assessment method, it is assumed that the basic variables are summarized into a deterministic value of capacity (the maximum tolerable acceleration),  $C_i$ , and a deterministic value of demand (the peak acceleration induced by a single walker),  $D_i$ . Capacity and demand are expressed in terms of TFRFs:

$$D_i = \varphi_i(\text{RL}_i, \alpha_i, L, \xi_i) \leq \varphi_{i,\max} = C_i \quad \forall i, \quad (27)$$

where  $D_i$  is expressed as in (23) and the limit acceleration is expressed in terms of equivalent TFRF:

$$\begin{aligned} C_i &= \varphi_{i,\max} \\ &= \left( \text{BF}_{m,i}(\text{RL}_i) \cdot \frac{\overline{\text{DLF}}_i \cdot \overline{W}}{2\xi_i} \cdot \frac{1}{m_i} \right)^{-1} \hat{\eta}_{i,\max}, \end{aligned} \quad (28)$$

where  $m_i$  is the modal masses evaluated considering  $\text{RL}_i = 0$  (simply supported beam),  $\text{BF}_{m,i}(\text{RL}_i)$  is the mass boundary factor correcting the modal masses for support condition, and  $\hat{\eta}_{i,\max}$  is the maximum tolerable acceleration.

Application of the third level method requires either numerical integration or approximate analytical methods (such as first- and second-order reliability methods) or simulation methods [78]; the latter was used in this study (Section 4.2). Given the Joint Probability Density Function (JPDF),  $p_{C,D}(c, d)$ , of capacity and demand, then the probability of failure  $P_{\text{fail},i}$  is given as

$$P_{\text{fail},i} = \int_{C-D \leq 0} p_{C_i, D_i}(c_i, d_i) \cdot dc_i \cdot dd_i. \quad (29)$$

$C_i$  has a negligible variability compared to  $D_i$ ; then it is reasonable to consider it as deterministic. Under this

assumption,  $P_{\text{fail},i}$  can be evaluated as the Complementary Cumulative Distribution Function (CCDF):

$$P_{\text{fail},i} = 1 - \int_0^{\varphi_{i,\max}} p_{\varphi_i}(\varphi_i(\text{RL}_i, \alpha_i, L, \xi_i)) \cdot d\varphi_i, \quad (30)$$

where the integration limit is equal to the maximum tolerable acceleration reported in the capacity value (see (28)).

Equivalently, the reliability index can be considered:

$$\beta_i = -\Phi_U^{-1}(P_{\text{fail},i}), \quad (31)$$

where  $\Phi_U^{-1}$  denotes the inverse standardized normal distribution function.

The acceptance condition is based on the requirement that the probability of failure does not exceed the design value  $P_{D,i}$ , or that the reliability index is greater than its corresponding design value  $\beta_{D,i} = -\Phi_U^{-1}(P_{D,i})$  [37]:

$$\begin{aligned} P_{\text{fail},i} \leq P_{D,i} &\iff \\ \beta_i &\geq \beta_{D,i}. \end{aligned} \quad (32)$$

In Eurocode 0 [36] and ISO 2394 [37], reliability requirements are expressed in terms of the reliability index  $\beta_D$ ; these are related to the expected social and economic consequences. In particular, ISO 2394 [37] gives the probabilistic design values as a function of the relative costs of safety measures and of the consequence of failure (Table 3).

The consequence classes in Table 3 are quantified through the ratio between the failure costs and the costs of construction. In the case of footbridge vibrations, the consequence of vibrations is small, as no damage to things or people occurs. ISO 2394 [37] suggests  $\beta_D = 0$  [ $P_D = 5 \cdot 10^{-1}$ ] for reversible limit states (Table 3). However, based on performance demand and on the outcome of cost-benefit analyses, the designer may find it appropriate to increase or reduce the probabilistic design values, that is, to increase or reduce reliability. As reported by ISO 2394 [37], the probabilistic design values are “*formal or notional numbers, intended primarily as a tool for developing consistent design rules, rather than giving a description of the structural failure frequency.*” In the same manner, Eurocode 0 [36] gives a target reliability index  $\beta_D$  of 1.5 for serviceability irreversible limit state not providing any indication for the serviceability reversible one.

For both levels of assessment (deterministic and probabilistic), it is necessary to quantify capacity, that is, to set the maximum tolerable acceleration; reference values can be found in the literature [8]. The interested reader is also referred to [79, 80] for further information. ISO 10137 [27] states that “*the designer shall decide on the serviceability*

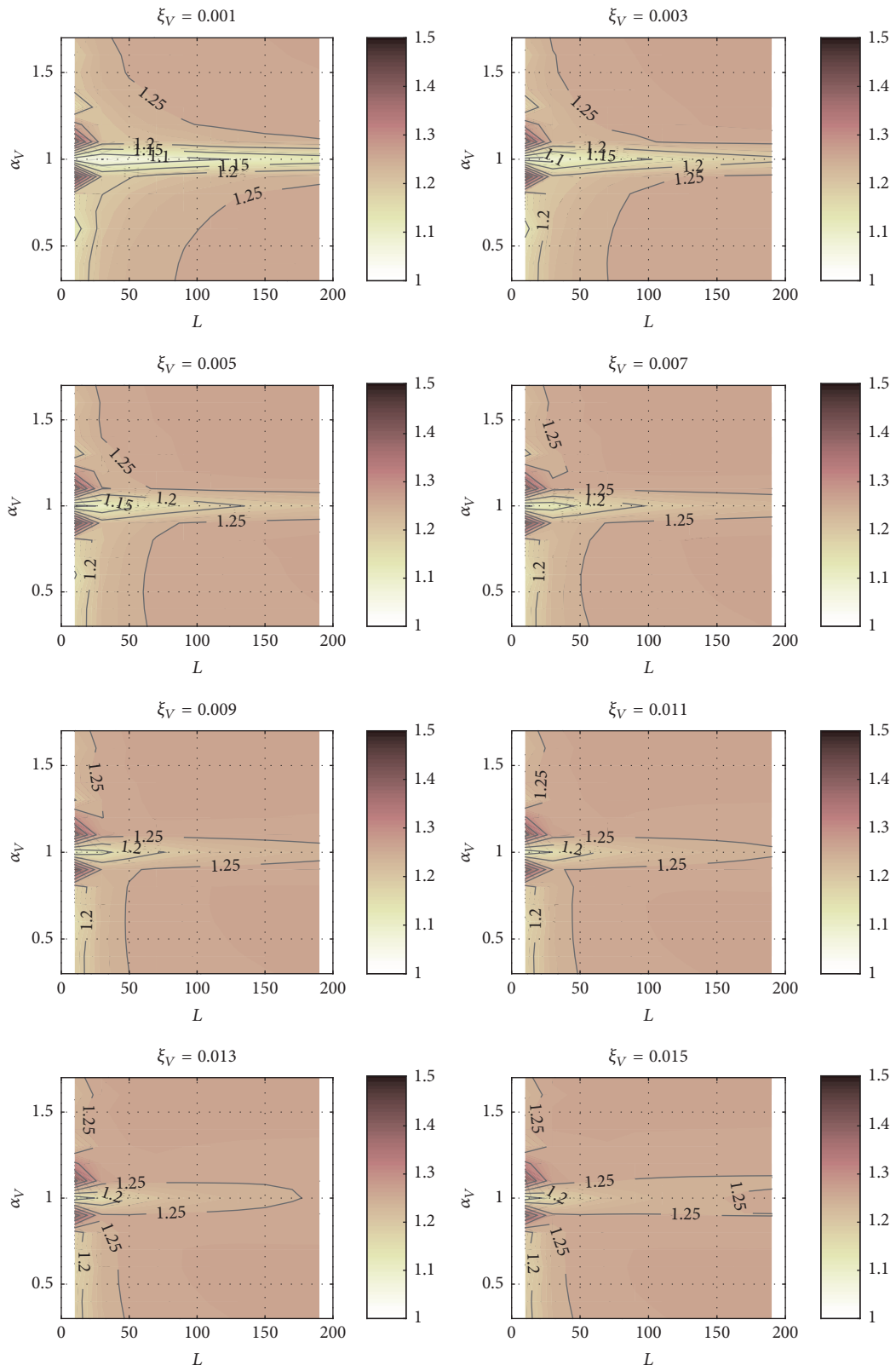


FIGURE 7:  $BF_V(RL_V = 1, \alpha_V, L, \xi_V)$  for different values of  $\xi_V$  numerically evaluated using the solution of Abu-Hilal and Mohsen [74].

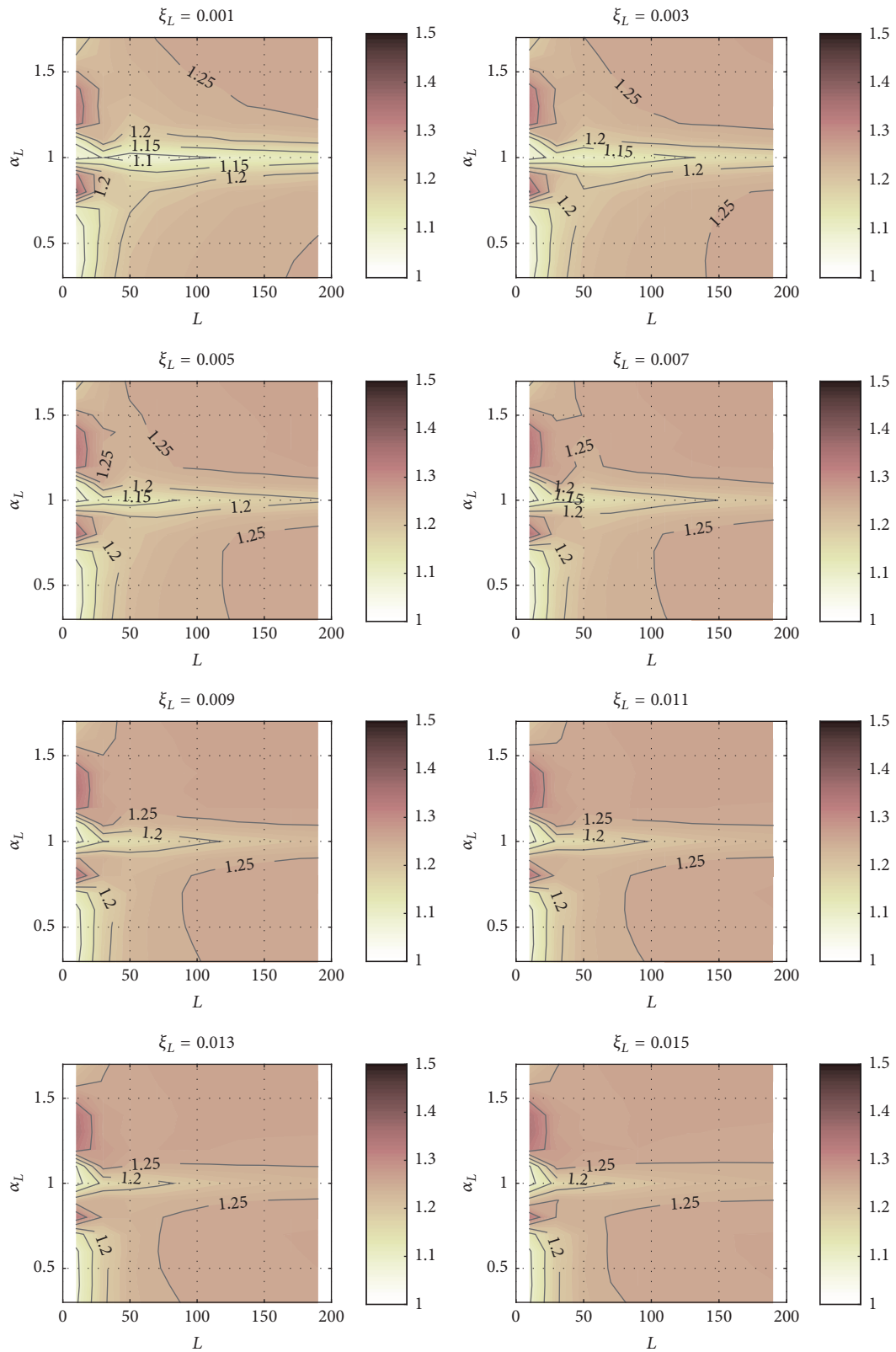


FIGURE 8:  $BF_L(RL_L = 1, \alpha_L, L, \xi_L)$  for different values of  $\xi_L$  numerically evaluated using the solution of Abu-Hilal and Mohsen [74].

*criterion and its variability.*” Further, ISO 10137 [27] states that footbridges “shall be designed, so that vibration amplitudes from applicable vibration sources do not alarm potential users.” In particular, Annex C to ISO 10137 [27] provides limiting criteria for human comfort on footbridges in the range of frequency of 1 to 80 Hz. The capacity is expressed in terms of RMS acceleration evaluated on a 1s window (running RMS method, ISO 2631 [81]); the limit values are given as a function of the vibration frequency (base curves), for the lateral (side to side and back to chest) and vertical directions. For footbridges, the base curves must be multiplied by a factor of 30 in the vertical directions and by a factor of 60 in the lateral direction. The factor of 30 applies only to pedestrians standing still on the bridge, because sensitivity to vibration decreases when walking. Finally, the results of the numerical simulations show that, for the range of the input parameters considered, the ratio between the peak values and the 1s RMS peak values of the acceleration (Maximum Transient Vibration Value, ISO 2631 [81]) is around  $\sqrt{2}$  (1.13 to 1.57 in the lateral direction and 1.30 to 1.51 in the vertical direction), similar to the peak factor of a stationary sinusoidal process.

The maximum tolerable acceleration is therefore evaluated from the ISO 10137 base curves:

$$\begin{aligned} \hat{\eta}_{V,\max}(\alpha_V) &= \sqrt{2} \cdot 30 \cdot \hat{\eta}_{V,\text{rms}}(\alpha_V) \\ &= \begin{cases} 0.21 & \text{if } \alpha_V \leq 0.47 \\ 0.140 + 0.150 \cdot \alpha_V & \text{if } \alpha_V > 0.47, \end{cases} \\ \hat{\eta}_{L,\max}(\alpha_L) &= \sqrt{2} \cdot 60 \cdot \hat{\eta}_{L,\text{rms}}(\alpha_L) \\ &= \begin{cases} 12.52 - 25.75 \cdot \alpha_L & \text{if } \alpha_L \leq 0.47 \\ 0.30 & \text{if } \alpha_L > 0.47, \end{cases} \end{aligned} \quad (33)$$

where  $\hat{\eta}_{V,\max}(\alpha_V)$  and  $\hat{\eta}_{L,\max}(\alpha_L)$  are the peak acceleration thresholds and  $\hat{\eta}_{V,\text{rms}}(\alpha_V)$  and  $\hat{\eta}_{L,\text{rms}}(\alpha_L)$  are the corresponding 1s RMS peak acceleration thresholds (base curves) in  $\text{m/s}^2$ . The acceleration thresholds are given in terms of generalized coordinates (i.e.,  $\hat{\eta}_{V,\max}(\alpha_V)$  and  $\hat{\eta}_{L,\max}(\alpha_L)$ ), which applies to the case where mode shapes are normalized to one (Section 3).

Equations (33) are shown in Figure 9, limited to the frequency range of interest for footbridges. For  $\alpha_L \geq f_{w,L}$  (i.e.,  $f_L \leq 1$  Hz), the acceleration threshold has been extrapolated to a constant value. For the resonant case, where the acceleration is larger, the vertical and lateral acceleration thresholds are similar and equal to  $\hat{\eta}_{V,\text{rms}}(\alpha_V = 1) = 0.29 \text{ m/s}^2$  and  $\hat{\eta}_{L,\text{rms}}(\alpha_L = 1) = 0.30 \text{ m/s}^2$ , respectively. In the vertical direction,  $\hat{\eta}_{V,\text{rms}}(\alpha_V)$  increases in almost the entire range of  $\alpha_V$ . In the lateral direction,  $\hat{\eta}_{L,\text{rms}}(\alpha_L)$  is taken as constant for  $\alpha_L \geq 0.47$  and strongly increases for  $\alpha_L < 0.47$  reducing the risk of loss of comfort.

## 6. Application to a Steel Truss Footbridge

As an example, the proposed procedure is applied to a prototype steel truss footbridge with an overall length of 101.90 m

TABLE 4: Dynamic characteristics of the truss footbridge.  $m_V$  and  $m_L$  are evaluated considering a simply supported beam; that is,  $\text{RL}_i = 0$ .

Variable	Dimension	$i = V$	$i = L$
$L$	[m]		90
$m$	[kg/m]		1,495
$m_i$	[kg]	67,275	67,275
$\xi_i$	[%]	0.5	0.5
$\alpha_i$	[-]	1.061	0.507
$\text{RD}_i$	[-]	2.694	0.357
$\text{RL}_i$	[-]	0.48	0.975
$\text{BF}_i$	[-]	1	1.21
$\text{BF}_{m,i}$	[-]	1	1.25
$\text{BF}_{\varphi,i} = (\text{BF}_i/\text{BF}_{m,i})$	[-]	1	0.97

(central span of 90.00 m with two lateral cantilevers of 6.20 m and 5.70 m, resp.), a width of 3.50 m, and a height of truss of 4.45 m. The structural members, designed according to the Italian Code provisions [82], are made of grade S355 steel.

The footbridge was modeled using the FE software package SAP2000 [83] as a 3D truss beam simply supported at four nodes. In particular, fixed bearings were placed on one side of the beam and longitudinally sliding bearings on the other side. The mean mass per unit of length of the footbridge is 1,495 kg/m corresponding to a modal mass of 67,275 kg in both directions, considering simply support ( $\text{RL}_i = 0$ ) conditions. Damping ratio was set to 0.5% in both directions. Modal analysis was performed, and the first two modes of vibration were found to be the first vertical bending mode ( $f_V = 1.789$  Hz) and the first lateral bending mode ( $f_L = 1.873$  Hz), respectively (Figure 10). The natural frequencies correspond to  $\alpha_V = 1.06$  and  $\alpha_L = 0.51$ , both indicating possible walking-induced vibrations.

To evaluate the actual support condition in terms of  $\text{RL}_i$  using (16), evaluation of  $\text{RD}_i$  defined through (15) is required; this was done by applying a uniform load in lateral and vertical directions to the FE model and evaluating the corresponding end rotation  $\theta_i$  and midspan deflection  $\delta_i$ . It should be pointed out that the uniform load coming from the deck is allocated to the nodes of the FE model using a tributary area load criterion. Finally,  $\text{RD}_i$  was converted into an equivalent  $\text{RL}_i$  using (16). A synthesis of the footbridge dynamic characteristic is given in Table 4. The RL (Table 4) correspond to a clamped beam in the lateral direction and to an intermediate condition between the simply supported and clamped beam for the vertical direction. In this application, considering that the boundary factor corresponding to  $\text{RL}_i = 0.5$  is quite similar to that corresponding to  $\text{RL}_i = 0$  (Figure 6), the condition  $\text{RL}_L = 1$  is used for the lateral direction and  $\text{RL}_V = 0$  for the vertical direction. The last assumption is also made because the procedure proposed in this study is only given for  $\text{RL}_i = 0$  and  $\text{RL}_i = 1$ . The variation of the support conditions with respect to the simply supported case in the lateral direction makes it necessary to evaluate  $\text{BF}_L$ ,  $\text{BF}_{m,L}$ , and  $\text{BF}_{\varphi,L}$ . In particular, from Figure 8 one can find  $\text{BF}_L = 1.21$ , while  $\text{BF}_{m,L} = 1.25$  was found from Figure 3. Moreover,  $\text{BF}_{\varphi,L} = 0.968$  was estimated dividing  $\text{BF}_L$  by  $\text{BF}_{m,L}$  using the definition of (22).

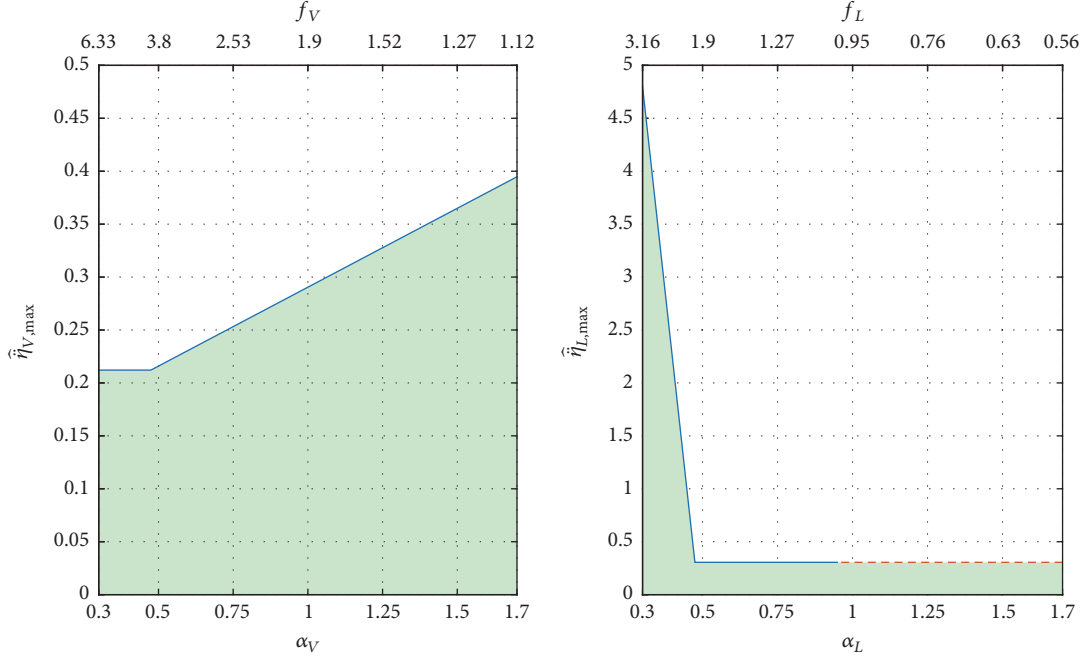


FIGURE 9: Threshold vertical and lateral peak acceleration using (33). The red dashed line indicates extrapolated values for  $f_L \leq 1$  Hz. Green areas indicate the region of acceptable comfort.

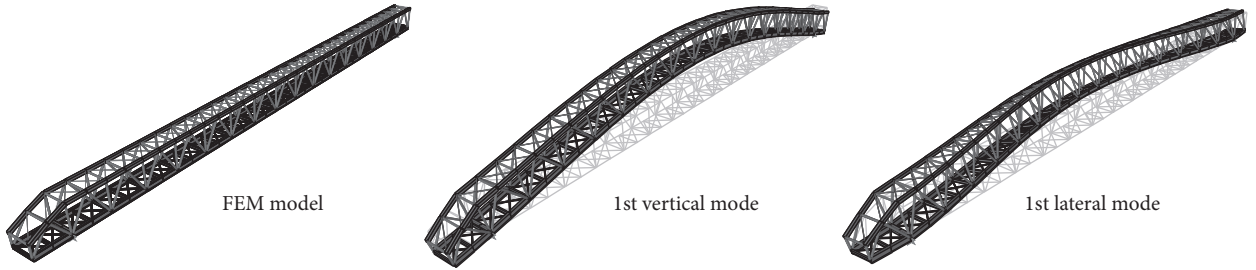


FIGURE 10: 3D SAP2000 Finite Element model of the truss footbridge, and first lateral and vertical mode shapes.

The limit acceleration was calculated according to ISO 10137 [27] using (33) (see Figure 9) and the design value of  $P_D$  and  $\beta$  considering small consequences of failure and moderate relative costs of safety measures according to ISO 2394 [37] (see Table 3). For both, vertical and lateral directions,

$$\begin{aligned} \hat{\eta}_{\max} &= 0.3 \text{ m/s}^2, \\ P_D &= 0.1, \\ \beta_D &= -\Phi_U^{-1}(P_D) = 1.3. \end{aligned} \quad (34)$$

The acceleration capacity is expressed in terms of equivalent TFRFs using (28):

$$\begin{aligned} C_V &= \left( \text{BF}_{m,V} \cdot \frac{\overline{\text{DLF}}_V \cdot \overline{W}}{2\xi_V} \frac{1}{m_V} \right)^{-1} \cdot \hat{\eta}_{V,\max} = 0.775, \\ C_L &= \left( \text{BF}_{m,L} \cdot \frac{\overline{\text{DLF}}_L \cdot \overline{W}}{2\xi_L} \frac{1}{m_L} \right)^{-1} \cdot \hat{\eta}_{L,\max} = 5.723. \end{aligned} \quad (35)$$

The acceleration demand TFRFs are evaluated for the simply supported beam using (19), and these values are corrected to account for the mode shape using BF as reported in (23):

$$\begin{aligned} D_V &= \varphi_V(\text{RL}_V, \alpha_V, L, \xi_V) = 1 \cdot 0.0904 = 0.0904, \\ D_L &= \varphi_L(\text{RL}_L, \alpha_L, L, \xi_L) = 0.97 \cdot 0.0035 = 0.0034. \end{aligned} \quad (36)$$

The deterministic check is performed using the inequality condition expressed in (27):

$$\begin{aligned} D_V &= 0.0904 < 0.775 = C_V, \\ D_L &= 0.0034 < 5.723 = C_L. \end{aligned} \quad (37)$$

Using the deterministic approach, it is found that maximum acceleration induced by the SW is lower than the acceptable threshold. In the lateral direction, the demand is much smaller than the capacity indicating large reliability. Conversely, in the vertical direction, the demand and the capacity are closer showing lower safety.

The probabilistic reliability analysis is based on the definition of the GEV parameters (see (26)); these are given in Appendix B. The lateral GEV parameters are evaluated considering  $RL_L = 1$  and using Figure 11, whereas the vertical GEV parameters are evaluated considering  $RL_V = 0$  and using Figure 12:

$$\begin{aligned}
 k_V (RL_V = 0, \alpha_V, L, \xi_V) &= 0.6718, \\
 \mu_V (RL_V = 0, \alpha_V, L, \xi_V) &= 0.05067, \\
 \sigma_V (RL_V = 0, \alpha_V, L, \xi_V) &= 0.05588, \\
 k_L (RL_L = 1, \alpha_L, L, \xi_L) &= -0.0129, \\
 \mu_L (RL_L = 1, \alpha_L, L, \xi_L) &= 0.001828, \\
 \sigma_L (RL_L = 1, \alpha_L, L, \xi_L) &= 0.003309.
 \end{aligned} \tag{38}$$

The value of the CDF corresponding to TFRF predicted using the deterministic procedure (i.e., (36)) is equal to

$$\begin{aligned}
 P_{\varphi_V} (D_V) &= 0.565, \\
 P_{\varphi_L} (D_L) &= 0.379.
 \end{aligned} \tag{39}$$

The PDF and CDF of  $\varphi_i$  for the vertical and lateral direction evaluated using the GEV parameters reported in (38) are shown in Figure 13, together with the deterministic acceleration demand TFRFs (see (36)). This result shows that, using the SW (i.e., walker having the mean characteristics of the SP), the cumulative probability is either higher or lower than the median of the probability distribution. In other words, this means that using mean characteristics of the SP characteristics can lead to unconservative evaluations as the obtained probability of exceeding can be different from the median, that is, 0.5.

$P_{\text{fail},i}$  can be evaluated as the Complementary Cumulative Distribution Function (CCDF) associated with a TFRF equal to either  $C_V$  or  $C_L$ :

$$\begin{aligned}
 P_{\text{fail},V} &= 0.0296 \iff \\
 \beta_V &= 1.887, \\
 P_{\text{fail},L} &\rightarrow 0.0 \iff \\
 \beta_L &\rightarrow \infty.
 \end{aligned} \tag{40}$$

The 0 probability of failure in the lateral direction of (40) is due to the negative values of  $k_L$  (see (38)) leading to a reversed Weibull distribution that is characterized by an upper limit. Accordingly, also the reliability index assumes infinitive value.

The acceptance condition is based on a requirement that the probability of failure  $P_{\text{fail},i}$  does not exceed the design

value  $P_{D,i}$  or the reliability index  $\beta_i$  is greater than its design value  $\beta_{D,i}$  [37]:

$$\begin{aligned}
 P_{\text{fail},V} &= 0.0296 < 0.1 = P_{D,V} \iff \\
 \beta_V &= 1.887 > 1.3 = \beta_D, \\
 P_{\text{fail},L} &= 0.0 < 0.1 = P_{D,L} \iff \\
 \beta_L &= \infty > 1.3 = \beta_D.
 \end{aligned} \tag{41}$$

Application of the probabilistic approach shows that the probability of failure is lower than the design probability. In particular, in the lateral direction, the check is satisfied in all cases (it can be considered a deterministic safety condition), while in the vertical direction the ratio between the capacity and the demand is lower. Approximately in 2.96% (see (40)) of the cases, the vertical acceleration induced by a single walker crossing the footbridge is larger than the threshold value.

## 7. Conclusions

Prior work has evaluated the dynamic effects induced by a single walker crossing a footbridge. The research available focuses on the definition of force characteristics and on the related dynamic response. No complete procedure is available for the probabilistic assessment of footbridges against the crossing of single walkers.

In this paper, a procedure for the deterministic and probabilistic assessment of footbridges against the crossing of single walkers was presented. This scenario is considered by different standards and design guidelines, such as ISO 10137. The procedure presented complies with Eurocode 0 [36] and ISO 2394 [37] and allows controlling the reliability level. The flow diagram of the procedure is given in Figure 4. First, the definition of the walker and footbridge dynamic characteristics is needed: a study of the data available in the literature allowed the definition of a Standard Population of walkers. Only walking conditions were considered. The common beam-type footbridge characteristics were evaluated and a dynamic modal model according to Abu-Hilal and Mohsen [74] was presented. All the variables defining the footbridge characteristics were chosen as such to obtain a simple procedure suitable for design implementation. The peak acceleration was chosen as the engineering demand parameter and it was derived with both a deterministic and a probabilistic approach. Using the deterministic approach, the serviceability check is carried out comparing the peak acceleration induced by a walker having the mean characteristics of the Standard Population, with the acceleration thresholds of ISO 10137 [27]. With the probabilistic approach, the exceedance probability of the threshold acceleration must be lower than the reliability levels defined in ISO 2394 [37]. This study, therefore, indicates that the use of the deterministic approach without the knowledge of the real reliability levels can lead to unconservative evaluations. Finally, application of deterministic and probabilistic approaches to a prototype steel footbridge showed how it can be easily used in the engineering practice.

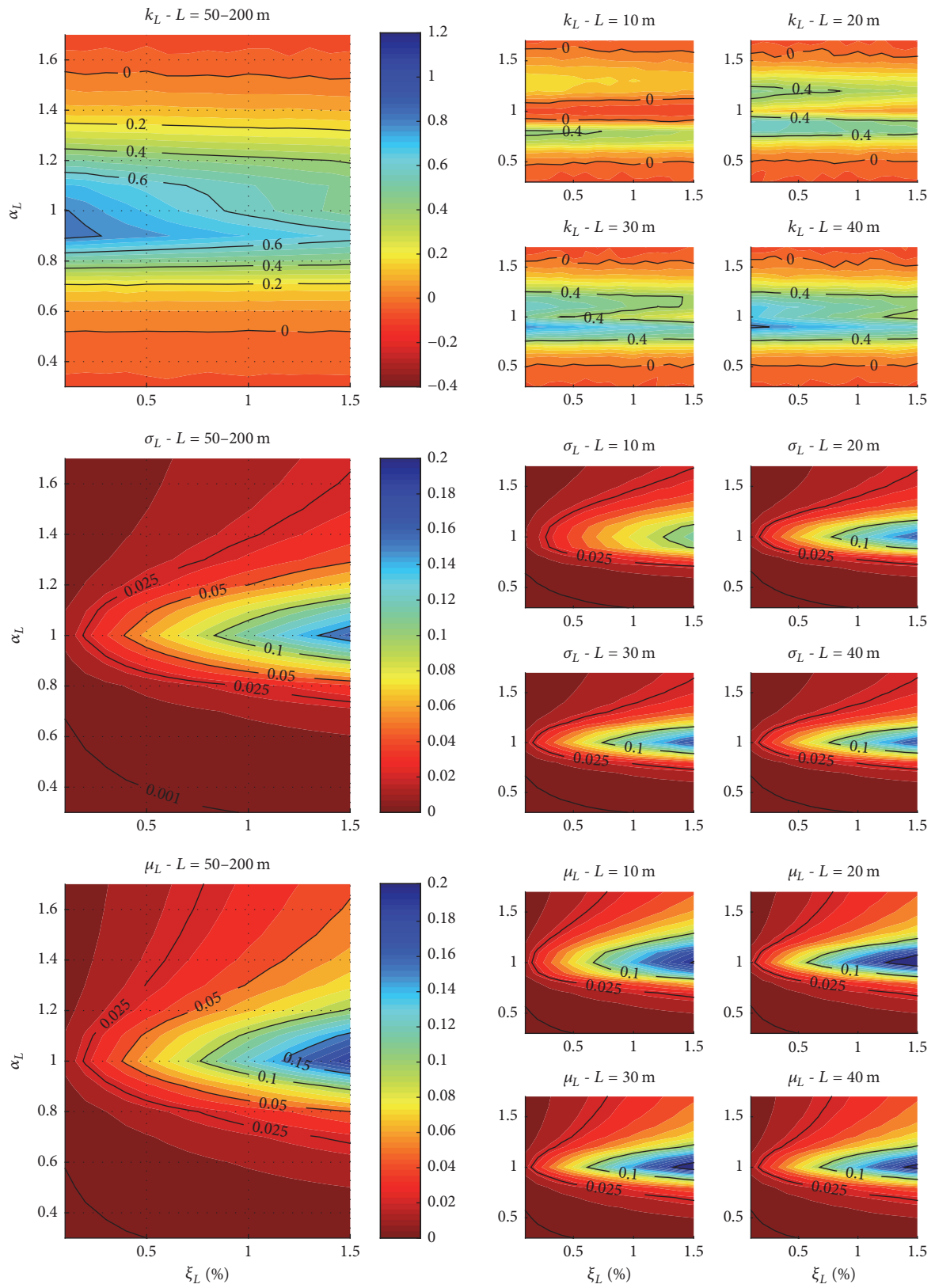


FIGURE 11: GEV parameters of  $P_{\varphi_L}(\varphi_L(RL_L = 1, \alpha_L, L, \xi_L))$ : double clamped case in lateral direction.

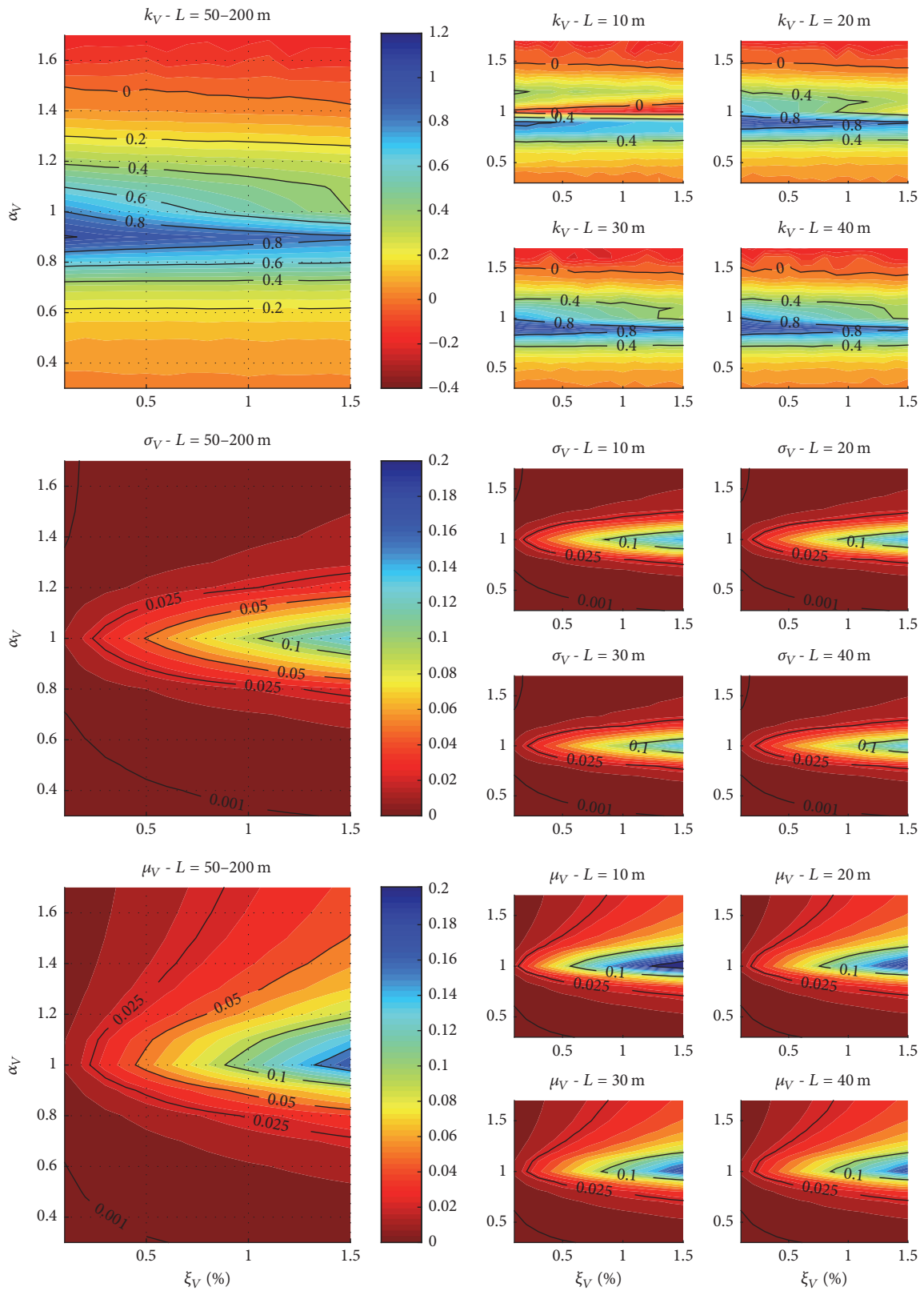


FIGURE 12: GEV parameters of  $P_{\varphi_V}(\varphi_V(RL_V = 0, \alpha_V, L, \xi_V))$ : simply supported case in vertical direction.

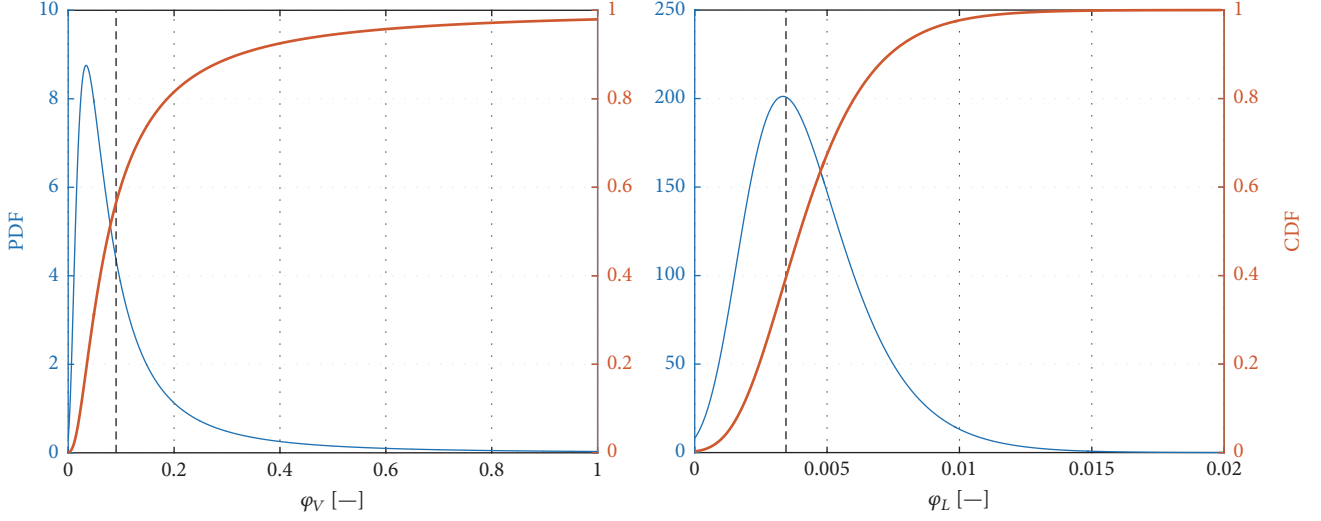


FIGURE 13: Probability Density Function (PDF, thin line) and Cumulated Distribution Function (CDF, thick line) of  $\phi_i$  for the vertical and lateral direction (GEV parameters are reported in (38)). The vertical dashed line indicates the deterministic acceleration demand TFRFs,  $D_V$  and  $D_L$  (see (36)).

## Appendix

### A. Boundary Factor for the Clamped Case $RL = 1$

See Figures 7 and 8.

### B. GEV Parameters for $RL = 1$ and $RL = 0$

See Figures 15 and 11 for  $RL = 1$ . See Figures 12 and 14 for  $RL = 0$ .

### C. Derivation of (14), (16), and (22)

*C.1. Derivation of (14).* Let us consider a beam supported at both ends by fixed vertical constraints and with variable rotational stiffness (Figure 2). In this study, only symmetric support conditions will be considered:

$$K_{r,1,i} = K_{r,2,i} = K_{r,i}, \quad (C.1)$$

where the subscript  $i = V, L$  indicates the vertical and lateral direction, respectively. The following derivation will be done for a generic direction  $i$ .

If we consider the beam loaded by an arbitrary symmetric load, the rotation at the two ends will be the same:

$$\Theta_{1,i} = \Theta_{2,i} = \Theta_i. \quad (C.2)$$

Let us define a nondimensional restrained level ( $RL_i$ ), defined as the ratio of the end moment for the particular support condition (i.e., value of  $K_{r,i}$ ) due to an arbitrary symmetric load,  $M_i(K_{r,i})$ , to that of the clamped beam subjected to the same load,  $M_i(K_{r,i} \rightarrow \infty)$ :

$$RL_i \equiv \frac{M_i(K_{r,i})}{M_i(K_{r,i} \rightarrow \infty)} = \frac{M_i(RL_i)}{M_i(RL_i \rightarrow 1)}. \quad (C.3)$$

Therefore,  $RL_i$  is in the range of 0 (supported case,  $K_{r,i} = 0$ ) to 1 (clamped case,  $K_{r,i} \rightarrow \infty$ ). The bending moment at the two ends can be expressed according to

$$\begin{aligned} M_i(RL_i) &= K_{r,i}(RL_i) \cdot \Theta_i(RL_i) \\ &= RL_i \cdot M_i(RL_i \rightarrow 1). \end{aligned} \quad (C.4)$$

Using the assumptions of symmetric load and boundary conditions, the rotation at the end for a generic value of  $RL_i$ ,  $\Theta_i(RL_i)$ , can be written as

$$\begin{aligned} \Theta_i(RL_i) &= \Theta_i(RL_i = 0) - \frac{M_i(RL_i)L}{3EI_i} - \frac{M_i(RL_i)L}{6EI_i} \\ &= \Theta_i(RL_i = 0) - \frac{M_i(RL_i)L}{2EI_i}, \end{aligned} \quad (C.5)$$

where  $\Theta_i(RL_i = 0)$  is the rotation at one end of a simply supported beam and  $M_i(RL_i)$  is the bending moment at one end (the two bending moments at the two ends are the same due to the symmetry in the load and constraints).

Substituting (C.4) in (C.5), the following can be obtained:

$$\begin{aligned} \Theta_i(RL_i) &= \Theta_i(RL_i = 0) - \frac{M_i(RL_i)L}{2EI_i} \\ &= \Theta_i(RL_i = 0) - \frac{K_{r,i} \cdot \Theta_i(RL_i) \cdot L}{2EI_i}. \end{aligned} \quad (C.6)$$

Then, solving by  $\Theta_i(RL_i)$ , the following relation as a function of  $K_{r,i}$  can be found:

$$\Theta_i(RL_i) = \Theta_i(RL_i = 0) \cdot \left( 1 + \frac{2EI_i}{K_{r,i} \cdot L} \right). \quad (C.7)$$

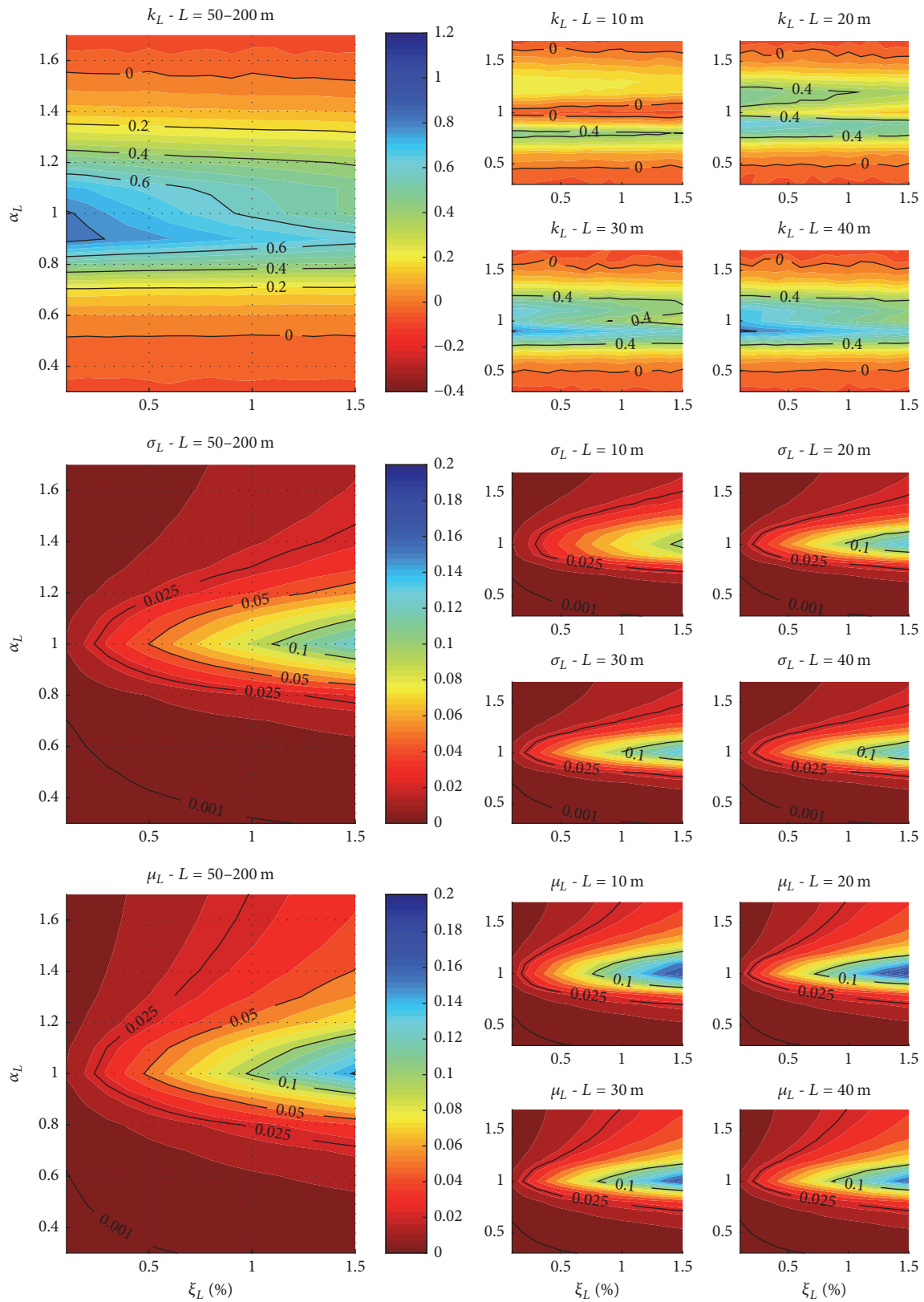


FIGURE 14: GEV parameters of  $P_{\varphi_L}(\varphi_L(RL_L = 0, \alpha_L, L, \xi_L))$ : simply supported case in lateral direction.

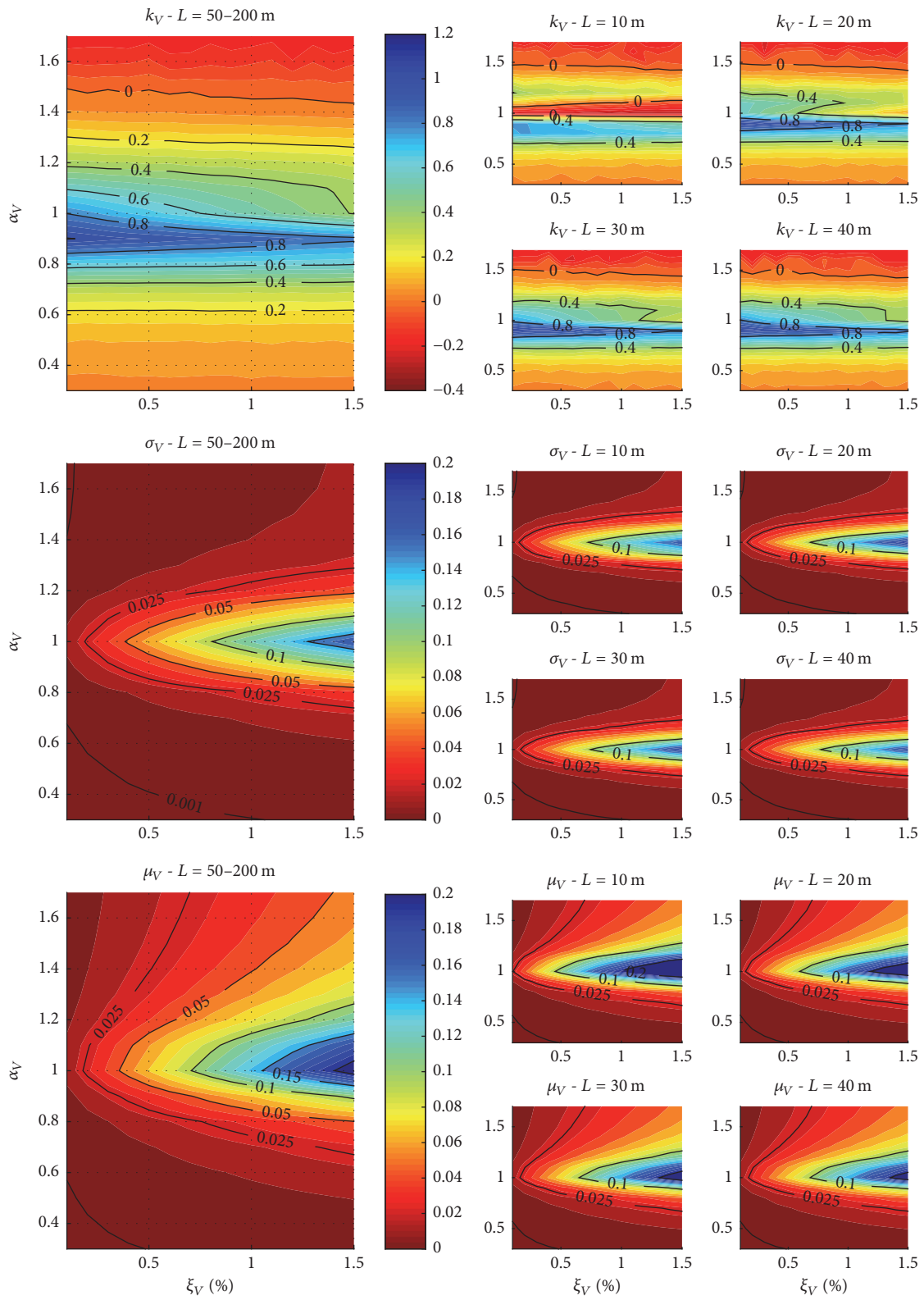


FIGURE 15: GEV parameters of  $P_{\varphi_V}(\varphi_V(RL_V = 1, \alpha_V, L, \xi_V))$ : double clamped case in vertical direction.

Substituting (C.4) and (C.7) in (C.3), the restrained level  $RL_i$  can be expressed as a function of the rotational stiffness,  $K_{r,i}$ :

$$\begin{aligned} RL_i &= \frac{K_{r,i} \cdot \Theta_i(RL_i)}{M_i(RL_i \rightarrow 1)} \\ &= K_{r,i} \frac{\Theta_i(RL_i) \cdot 2EI_i}{2EI_i + K_{r,i} \cdot L} \cdot \frac{1}{M_i(RL_i \rightarrow 1)}. \end{aligned} \quad (C.8)$$

Solving (C.8) by the rotational stiffness  $K_{r,i}$ , the following relation as a function of the restrained level  $RL_i$  can be found:

$$K_{r,i} = 2 \cdot \frac{EI_i}{L} \cdot RL_i \cdot \frac{1}{((\Theta_i(RL_i = 0) \cdot 2EI_i) / (M_i(RL_i \rightarrow 1) \cdot L) - RL_i)}. \quad (C.9)$$

For a symmetric load applied on a symmetric constrained beam, it can be simply demonstrated that

$$M_i(RL_i \rightarrow 1) = \frac{\Theta_i(RL_i = 0) \cdot 2EI_i}{L}. \quad (C.10)$$

Using the previous equation in (C.9), the rotational stiffness as a function of  $RL_i$  can be expressed and simplified as

$$K_{r,i} = 2 \cdot \frac{EI_i}{L} \cdot \frac{RL_i}{(1 - RL_i)}. \quad (C.11)$$

That is the demonstration of (14).

*C.2. Derivation of (16).* Let us define a nondimensional Rotation-to-Deflection ratio, (RD)<sub>i</sub>:

$$RD_i = \frac{\Theta_i(RL_i) \cdot L}{\delta_i(RL_i)}, \quad (C.12)$$

where  $\Theta_i(RL_i)$  and  $\delta_i(RL_i)$  are the end rotation and the midspan deflection due to a uniform load. The last deflection term can be expressed as sum of simply supported midspan beam deflection  $\delta_i(RL_i = 0)$  and midspan deflection due to the end moments  $M_i(RL_i \rightarrow 1)$  as follows:

$$\delta_i(RL_i) = \delta_i(RL_i = 0) - \frac{M_i(RL_i) \cdot L^2}{8EI_i}. \quad (C.13)$$

Substituting (C.7), (C.11), and (C.13) in (C.12), the nondimensional Rotation-to-Deflection ratio can be expressed as

$$RD_i = \frac{\Theta_i(RL_i = 0) \cdot (1 - RL_i) \cdot L}{\delta_i(RL_i = 0) - (RL_i \cdot M_i(RL_i \rightarrow 1) \cdot L^2) / 8EI_i}. \quad (C.14)$$

Solving (C.14) by the restrained level,  $RL_i$ , the following relation as a function of the Rotation-to-Deflection ratio  $RD_i$  can be derived:

$$RL_i = \frac{(1 - (RD_i \cdot \delta_i(RL_i = 0)) / (\Theta_i(RL_i = 0) \cdot L))}{(1 - (RD_i \cdot M_i(RL_i \rightarrow 1) \cdot L) / (\Theta_i(RL_i = 0) \cdot 8EI_i))}. \quad (C.15)$$

Finally, substituting the expression of  $\delta_i(RL_i = 0)$ ,  $\Theta_i(RL_i = 0)$ , and  $M_i(RL_i \rightarrow 1)$  due to a uniform load pattern, the parameter  $RD_i$  can be expressed more simply as

$$RL_i = \frac{4 - 1.25 \cdot RD_i}{4 - RD_i}. \quad (C.16)$$

That is the demonstration of (16).

*C.3. Derivation of (22).* The peak modal acceleration,  $\widehat{\eta}_i(RL_i, \alpha_i, L, \xi_i)$ , is expressed in terms of a TFRF ( $RL_i, \alpha_i, L, \xi_i$ ):

$$\widehat{\eta}_i(RL_i, \alpha_i, L, \xi_i) = \frac{\overline{DLF_i} \cdot \overline{W}}{2\xi_i} \cdot \frac{1}{m_i} \cdot \varphi_i(RL_i, \alpha_i, L, \xi_i). \quad (C.17)$$

Since change of support conditions influences mode shapes and thus acceleration response, a boundary factor,  $BF_i(RL_i, \alpha_i, L, \xi_i)$ , is defined as

$$BF_i(RL_i, \alpha_i, L, \xi_i) = \frac{\widehat{\eta}_i(RL_i, \alpha_i, L, \xi_i)}{\widehat{\eta}_i(RL_i = 0, \alpha_i, L, \xi_i)}. \quad (C.18)$$

The boundary factor is the ratio between the peak modal acceleration evaluated for arbitrary boundary conditions,  $\widehat{\eta}_i(RL_i, \alpha_i, L, \xi_i)$ , and that evaluated for simply supported conditions,  $\widehat{\eta}_i(RL_i = 0, \alpha_i, L, \xi_i)$ . Substituting (C.17) in (C.18), the following can be obtained:

$$\begin{aligned} BF_i(RL_i, \alpha_i, L, \xi_i) &= \frac{(\overline{DLF_i} \cdot \overline{W}) / 2\xi_i \cdot 1/m_i(RL_i) \cdot \varphi_i(RL_i, \alpha_i, L, \xi_i)}{(\overline{DLF_i} \cdot \overline{W}) / 2\xi_i \cdot 1/m_i(RL_i = 0) \cdot \varphi_i(RL_i = 0, \alpha_i, L, \xi_i)}. \end{aligned} \quad (C.19)$$

Rearranging the previous equation,

$$\begin{aligned} BF_i(RL_i, \alpha_i, L, \xi_i) &= \frac{(\overline{DLF_i} \cdot \overline{W}) / 2\xi_i}{(\overline{DLF_i} \cdot \overline{W}) / 2\xi_i} \cdot \frac{1/m_i(RL_i)}{1/m_i(RL_i = 0)} \cdot \frac{\varphi_i(RL_i, \alpha_i, L, \xi_i)}{\varphi_i(RL_i = 0, \alpha_i, L, \xi_i)} \\ &= \frac{m_i(RL_i = 0)}{m_i(RL_i)} \cdot \frac{\varphi_i(RL_i, \alpha_i, L, \xi_i)}{\varphi_i(RL_i = 0, \alpha_i, L, \xi_i)} \\ &= \frac{m_i(RL_i = 0)}{BF_{m,i}(RL_i)} \cdot \frac{\varphi_i(RL_i, \alpha_i, L, \xi_i)}{BF_{\varphi,i}(RL_i, \alpha_i, L, \xi_i)} \end{aligned} \quad (C.20)$$

obtaining

$$\begin{aligned} BF_i(RL_i, \alpha_i, L, \xi_i) &= BF_{m,i}(RL_i) \cdot BF_{\varphi,i}(RL_i, \alpha_i, L, \xi_i) \\ &= \frac{m_i(RL_i = 0)}{m_i(RL_i)} \cdot \frac{\varphi_i(RL_i, \alpha_i, L, \xi_i)}{\varphi_i(RL_i = 0, \alpha_i, L, \xi_i)}. \end{aligned} \quad (C.21)$$

That is the demonstration of (22).

## Conflicts of Interest

The authors declare that they have no conflicts of interest.

## Acknowledgments

The authors express their personal thanks and appreciation to the Consorzio Interuniversitario di Ricerca Me.S.E. for having funded the publication and dissemination of these research results.

## References

- [1] H. Petroski, *To Engineer Is Human: The Role of Failure in Successful Design*, Vintage books New York, New York, NY, USA, 1992.
- [2] B. Wolmuth and J. Surtees, "Crowd-related failure of bridges," *Proceedings of the Institution of Civil Engineers: Civil Engineering*, vol. 156, no. 3, pp. 116–123, 2003.
- [3] C. Tilden, "Kinetic effects of crowds," *Transactions of the American Society of Civil Engineers*, vol. 76, no. 1, pp. 2107–2126, 1913.
- [4] Á. Cunha and C. Moutinho, "Active control of vibrations in pedestrian bridges," in *Proceedings of the Conference of the European Association for Structural Dynamics (Eurodyn '99)*, 1999.
- [5] F. Ricciardelli and C. Demartino, "Design of footbridges against pedestrian-induced vibrations," *Journal of Bridge Engineering*, Article ID C4015003, pp. 1–13, 2016.
- [6] K. Van Nimmen, G. Lombaert, G. De Roeck, and P. Van den Broeck, "Vibration serviceability of footbridges: evaluation of the current codes of practice," *Engineering Structures*, vol. 59, pp. 448–461, 2014.
- [7] J. Wheeler, "Prediction and control of pedestrian-induced vibration in footbridges," *Journal of the Structural Division*, vol. 108, no. 9, pp. 2045–2065, 1982.
- [8] S. Živanović, A. Pavić, and P. Reynolds, "Vibration serviceability of footbridges under human-induced excitation: a literature review," *Journal of Sound and Vibration*, vol. 279, no. 1–2, pp. 1–74, 2005.
- [9] E. T. Ingólfsson, C. T. Georgakis, and J. Jönsson, "Pedestrian-induced lateral vibrations of footbridges: a literature review," *Engineering Structures*, vol. 45, pp. 21–52, 2012.
- [10] L. Pedersen and C. Frier, "Sensitivity of footbridge vibrations to stochastic walking parameters," *Journal of Sound and Vibration*, vol. 329, no. 13, pp. 2683–2701, 2010.
- [11] A. Avossa, R. Di Camillo, and P. Malangone, "Performance-based retrofit of a prestressed concrete road bridge in seismic area, Life-Cycle and Sustainability of Civil Infrastructure Systems," in *Proceedings of the 3rd International Symposium on Life-Cycle Civil Engineering (IALCCE '12)*, CRC Press, Vienna, Austria, 2012.
- [12] A. M. Avossa and P. Malangone, "Seismic retrofit of a prestressed concrete road bridge," *Ingegneria Sismica (International Journal of Earthquake Engineering)*, vol. 29, no. 4, pp. 5–25, 2012.
- [13] C. Demartino and F. Ricciardelli, "Aerodynamic stability of ice-accreted bridge cables," *Journal of Fluids and Structures*, vol. 52, pp. 81–100, 2015.
- [14] C. Demartino, H. H. Koss, C. T. Georgakis, and F. Ricciardelli, "Effects of ice accretion on the aerodynamics of bridge cables," *Journal of Wind Engineering & Industrial Aerodynamics*, vol. 138, pp. 98–119, 2015.
- [15] C. Demartino, J. Wu, and Y. Xiao, "Experimental and numerical study on the behavior of circular RC columns under impact loading," *Procedia Engineering*, vol. 199, pp. 2457–2462, 2017.
- [16] C. Demartino, J. Wu, and Y. Xiao, "Response of shear-deficient reinforced circular RC columns under lateral impact loading," *International Journal of Impact Engineering*, vol. 109, pp. 196–213, 2017.
- [17] J. M. W. Brownjohn, A. Pavić, and P. A. Omenzetter, "A spectral density approach for modelling continuous vertical forces on pedestrian structures due to walking," *Canadian Journal of Civil Engineering*, vol. 31, no. 1, pp. 65–77, 2004.
- [18] A. Pizzimenti and F. Ricciardelli, "Experimental evaluation of the dynamic lateral loading of footbridges by walking pedestrians," in *Proceedings of the EURO DYN '05*, vol. 1, pp. 435–440, 2005.
- [19] F. Ricciardelli and A. D. Pizzimenti, "Lateral walking-induced forces on footbridges," *Journal of Bridge Engineering*, vol. 12, no. 6, pp. 677–688, 2007.
- [20] C. Butz, *Beitrag zur Berechnung fußgänger induzierte Brückenschwingungen [Ph.D. thesis]*, Shaker Verlag Aachen, Aachen, Germany, 2006.
- [21] C. Heinemeyer, C. Butz, A. Keil et al., "Design of lightweight footbridges for human induced vibrations," in *Background Document in Support to The Implementation, Harmonization and Further Development of The Eurocodes*, 2009.
- [22] S. Živanović, A. Pavić, and P. Reynolds, "Probability-based prediction of multi-mode vibration response to walking excitation," *Engineering Structures*, vol. 29, no. 6, pp. 942–954, 2007.
- [23] E. Ingólfsson, C. Georgakis, and M. Svendsen, "Vertical footbridge vibrations: details regarding and experimental validation of the response spectrum methodology," in *Proceedings of the 3rd international conference on footbridge*, 2008.
- [24] G. Piccardo and F. Tubino, "Simplified procedures for vibration serviceability analysis of footbridges subjected to realistic walking loads," *Computers & Structures*, vol. 87, no. 13–14, pp. 890–903, 2009.
- [25] S. Živanović, A. Pavić, and E. T. Ingólfsson, "Modeling spatially unrestricted pedestrian traffic on footbridges," *Journal of Structural Engineering*, vol. 136, no. 10, pp. 1296–1308, 2010.
- [26] CEN, Eurocode 5: Design of timber structures, Comité Européen de Normalisation, 2005.
- [27] ISO, Bases for design of structures-Serviceability of buildings and walkways against vibration, 2007.
- [28] Sétra, Technical guide-Footbridges: Assessment of vibrational behaviour of footbridges under pedestrian loading, 2006.
- [29] BSI, U.K. national annex to Eurocode 1, 2008.
- [30] J. Brownjohn, P. Fok, M. Roche, and P. Omenzetter, "Long span steel pedestrian bridge at Singapore Changi Airport—part 2: crowd loading tests and vibration mitigation measures," *The Structural Engineer*, vol. 82, no. 16, pp. 28–34, 2004.
- [31] E. T. Ingólfsson and C. T. Georgakis, "A stochastic load model for pedestrian-induced lateral forces on footbridges," *Engineering Structures*, vol. 33, no. 12, pp. 3454–3470, 2011.
- [32] G. Piccardo and F. Tubino, "Equivalent spectral model and maximum dynamic response for the serviceability analysis of footbridges," *Engineering Structures*, vol. 40, pp. 445–456, 2012.
- [33] A. G. Davenport, "Note on the distribution of the largest value of a random function with application to gust loading," in *Proceedings of the ICE*, vol. 28, pp. 187–196, 1964.
- [34] A. M. Avossa, C. Demartino, and F. Ricciardelli, "Design procedures for footbridges subjected to walking loads: comparison

- and remarks," *The Baltic Journal of Road and Bridge Engineering*, vol. 12, no. 2, pp. 94–105, 2017.
- [35] A. M. Avossa, C. Demartino, and F. Ricciardelli, "Probability distribution of footbridge peak acceleration to single and multiple crossing walkers," *Procedia Engineering*, vol. 199, pp. 2766–2771, 2017.
- [36] CEN, Eurocode 0: Basis of structural design, Comité Européen de Normalisation, 2002.
- [37] ISO, 2394 General Principles on Reliability for Structures, 1998.
- [38] F. Beely, "Zur Mechanik des Stehens," *Langenbeck's Archiv Für Klinische Chirurgie*, vol. 27, pp. 457–471, 1882.
- [39] H. Elftman, "A cinematic study of the distribution of pressure in the human foot," *The Anatomical Record*, vol. 59, no. 4, pp. 481–491, 1934.
- [40] C. J. T. Van Uden and M. P. Besser, "Test-retest reliability of temporal and spatial gait characteristics measured with an instrumented walkway system (GAITRite)," *BMC Musculoskeletal Disorders*, vol. 5, no. 1, article 13, 2004.
- [41] S. Zivanovic, A. Pavic, P. Reynolds, and P. Vujovic, "Dynamic analysis of lively footbridge under everyday pedestrian traffic," in *Proceedings of the 6th European Conference on Structural Dynamics*, vol. 1, pp. 453–459, 2005.
- [42] N. A. Borghese, L. Bianchi, and F. Lacquaniti, "Kinematic determinants of human locomotion," *The Journal of Physiology*, vol. 494, no. 3, pp. 863–879, 1996.
- [43] L. Li, E. C. H. Van Den Bogert, G. E. Caldwell, R. E. A. Van Emmerik, and J. Hamill, "Coordination patterns of walking and running at similar speed and stride frequency," *Human Movement Science*, vol. 18, no. 1, pp. 67–85, 1999.
- [44] J. L. Lelas, G. J. Merriman, P. O. Riley, and D. C. Kerrigan, "Predicting peak kinematic and kinetic parameters from gait speed," *Gait & Posture*, vol. 17, no. 2, pp. 106–112, 2003.
- [45] F. Venuti and L. Bruno, "Crowd-structure interaction in lively footbridges under synchronous lateral excitation: a literature review," *Physics of Life Reviews*, vol. 6, no. 3, pp. 176–206, 2009.
- [46] F. Ricciardelli, C. Briatico, E. Ingólfsson, and C. Georgakis, "Experimental validation and calibration of pedestrian loading models for footbridges," *Experimental Vibration Analysis for Civil Engineering Structures*, 2006.
- [47] M. Y. Zarrugh, F. N. Todd, and H. J. Ralston, "Optimization of energy expenditure during level walking," *European Journal of Applied Physiology*, vol. 33, no. 4, pp. 293–306, 1974.
- [48] A. Pachi and T. Ji, "Frequency and velocity of people walking," *The Structural Engineer*, vol. 83, no. 3, pp. 36–40, 2005.
- [49] S. Zivanovic, V. Racic, I. El-Bahnasy, and A. Pavic, "Statistical characterisation of parameters defining human walking as observed on an indoor passerelle," in *Proceedings of the Experimental Vibration Analysis for Civil Engineering Structures, EVACES '07*, pp. 219–225, 2007.
- [50] E. T. Ingólfsson, C. T. Georgakis, F. Ricciardelli, and J. Jönsson, "Experimental identification of pedestrian-induced lateral forces on footbridges," *Journal of Sound and Vibration*, vol. 330, no. 6, pp. 1265–1284, 2011.
- [51] Y. Matsumoto, T. Nishioka, H. Shiojiri, and K. Matsuzaki, "Dynamic design of footbridges," in *Proceedings of the IABSE Proceeding*, 1978.
- [52] C. Butz, M. Feldmann, C. Heinemeyer et al., "Advanced load models for synchronous pedestrian excitation and optimised design guidelines for steel foot bridges (SYNPEX)," *Endbericht und Zwischenberichte zum RFCS Projekt RFS-CR*, vol. 3, article 19, 2007.
- [53] V. Racic, A. Pavic, and J. M. W. Brownjohn, "Experimental identification and analytical modelling of human walking forces: literature review," *Journal of Sound and Vibration*, vol. 326, no. 1–2, pp. 1–49, 2009.
- [54] F. Ricciardelli, M. Mafrici, and E. T. Ingólfsson, "Lateral pedestrian-induced vibrations of footbridges: characteristics of walking forces," *Journal of Bridge Engineering*, vol. 19, no. 9, Article ID 04014035, 2014.
- [55] J. H. Macdonald, "Lateral excitation of bridges by balancing pedestrians," *Proceedings of the Royal Society A Mathematical, Physical and Engineering Sciences*, 2008.
- [56] Q. S. Yang, J. W. Qin, and S. S. Law, "A three-dimensional human walking model," *Journal of Sound and Vibration*, vol. 357, pp. 437–456, 2015.
- [57] J. Blanchard, B. Davies, and J. Smith, "Design criteria and analysis for dynamic loading of footbridges," in *Proceedings of the Proceeding of a Symposium on Dynamic Behaviour of Bridges at the Transport and Road Research Laboratory*, 1977.
- [58] H. Bachmann, A. Pretlove, and J. Rainer, Dynamic forces from rhythmic human body motions.
- [59] Y. Kajikawa, "Some considerations on ergonomical serviceability analysis of pedestrian bridge vibrations," in *Proceedings of the JSCE*, vol. 325, pp. 23–33, 1982 (Japanese).
- [60] M. Yoneda, "A simplified method to evaluate pedestrian-induced maximum response of cable-supported pedestrian bridges," in *Proceedings of the International Conference on the Design and Dynamic Behaviour of footbridges*, 2002.
- [61] S. Kerr, *Human induced loading on staircases [Ph.D. thesis]*, University of London, London, UK, 1998.
- [62] P. Young, "Improved floor vibration prediction methodologies," in *Proceedings of the ARUP vibration seminar*, vol. 4, 2001.
- [63] H. Bachmann and W. Ammann, "Vibrations in structures: induced by man and machines," *Vibrations in structures: induced by man and machines*, vol. 3, 1987.
- [64] M. Fareed and M. Afzal, "Evidence of inbreeding depression on height, weight, and body mass index: a population-based child cohort study," *American Journal of Human Biology*, vol. 26, no. 6, pp. 784–795, 2014.
- [65] S. C. Walpole, D. Prieto-Merino, P. Edwards, J. Cleland, G. Stevens, and I. Roberts, "The weight of nations: an estimation of adult human biomass," *BMC Public Health*, vol. 12, no. 1, article 439, 2012.
- [66] L. Bruno, F. Venuti, and V. Nascé, "Pedestrian-induced torsional vibrations of suspended footbridges: proposal and evaluation of vibration countermeasures," *Engineering Structures*, vol. 36, pp. 228–238, 2012.
- [67] H. Bachmann, *Vibration Problems in Structures: Practical Guidelines*, Springer, Berlin, Germany, 1995.
- [68] M. Ferraioli, A. M. Avossa, and F. Formato, "Base isolation seismic retrofit of a hospital building in Italy: design and construction," in *Proceedings of the Final Conference on COST Action C26: Urban Habitat Constructions under Catastrophic Events*, pp. 835–840, September 2010.
- [69] A. M. Avossa and G. Pianese, "Damping effects on the seismic response of base-isolated structures with LRB devices," *Ingegneria Sismica*, vol. 34, no. 2, pp. 3–29, 2017.
- [70] Y. Kubota and T. Kishimoto, "Structural continuity and relativity for footbridge design," in *Proceedings of the Footbridges 2008: Third International Conference*, 2008.
- [71] CEN, Eurocode 1: Actions on structures, Comité Européen de Normalisation, 2003.

- [72] CEN, Eurocode 3: Design of Steel Structures, Comité Européen de Normalisation, 2005.
- [73] FIB, Guidelines for the design of footbridges, Fédération Internationale du Béton, Lausanne, Switzerland, 2005.
- [74] M. Abu-Hilal and M. Mohsen, "Vibration of beams with general boundary conditions due to a moving harmonic load," *Journal of Sound and Vibration*, vol. 232, no. 4, pp. 703–717, 2000.
- [75] F. Ricciardelli and C. Briatico, "Transient response of supported beams to moving forces with sinusoidal time variation," *Journal of Engineering Mechanics*, vol. 137, no. 6, pp. 422–430, 2011.
- [76] G. Piccardo and F. Tubino, "Dynamic response of Euler-Bernoulli beams to resonant harmonic moving loads," *Structural Engineering and Mechanics*, vol. 44, no. 5, pp. 681–704, 2012.
- [77] A. Palmeri, F. Ricciardelli, G. Muscolino, and A. De Luca, "Random vibration of systems with viscoelastic memory," *Journal of Engineering Mechanics*, vol. 130, no. 9, pp. 1052–1061, 2004.
- [78] H. Karadeniz and T. Vrouwenvelder, Overview reliability methods, vol. 5, 2003.
- [79] M. Griffin, Handbook of human vibration, 1990.
- [80] N. Mansfield, *Human Response to Vibration*, CRC Press, Boca Raton, Fla, USA, 2004.
- [81] ISO, ISO 2631: Mechanical vibration and shock-Evaluation of human exposure to whole-body vibration-Part 1: General requirements, 1997.
- [82] MIT, *Ministerial Decree: NTC 2008-Norme tecniche per le costruzioni*, Ministero delle Infrastrutture, Italy, 2008.
- [83] S. CSI, Ver. 14.00, integrated finite element analysis and design of structures basic analysis reference manual, 2010.

## Research Article

# Seismic Response of Plan-Asymmetric Structures with Diaphragm Flexibility

Hamed Eivani <sup>1</sup>, Abdolreza S. Moghadam <sup>2</sup>, Armin Aziminejad,<sup>1</sup> and Masoud Nekooei<sup>1</sup>

<sup>1</sup>Department of Civil Engineering, Science and Research Branch, Islamic Azad University, Tehran, Iran

<sup>2</sup>International Institute of Earthquake Engineering and Seismology (IIEES), Tehran, Iran

Correspondence should be addressed to Abdolreza S. Moghadam; moghadam@iiees.ac.ir

Received 28 June 2017; Revised 30 October 2017; Accepted 3 December 2017; Published 15 January 2018

Academic Editor: Naveed Ahmad

Copyright © 2018 Hamed Eivani et al. This is an open access article distributed under the Creative Commons Attribution License, which permits unrestricted use, distribution, and reproduction in any medium, provided the original work is properly cited.

The seismic behavior of asymmetric structures with a flexible diaphragm was studied by conducting inelastic dynamic time-history analyses. Asymmetric structures with different configurations of mass, stiffness, and strength centers, in combination with a wide range of diaphragm flexibility, were evaluated. The behavior of structures was studied by considering three aspects: (1) effect of structural asymmetry on diaphragms deformation; (2) effect of diaphragm flexibility on demands of the lateral load-resisting elements; (3) optimum configuration of mass, stiffness, and strength centers to limit important engineering demand parameters in asymmetric structures with a flexible diaphragm. The results showed that the shear-dominant deformation of diaphragms is sensitive to both structure asymmetry specifications and the degree of diaphragm flexibility; therefore, it can be used for the qualitative classification of the seismic behavior of structures. Also, the center of strength in structures with flexible diaphragm is more important relative to the stiffness center and has a significant effect on engineering demands at all levels of diaphragm flexibility. Moreover, it was found that a suitable configuration of centers in torsionally stiff structures depends on the degree of diaphragm flexibility, in addition to the intensity of earthquakes (structure yield level) and selected engineering demand parameter.

## 1. Introduction

In some structures, the assumption of a fully rigid seismic diaphragm is far from reality and can lead to a significant difference in the actual responses of structure and the results of analysis [1–3]. The type of floor system is an important factor in the degree of diaphragm flexibility. Many types of reinforced concrete floors such as prestressed beam and block [4], RC waffle slabs [5], ribbed RC slabs [6], and the traditional beam and block floor systems [7] can be considered as flexible diaphragms under certain conditions. Based on previous studies, diaphragm flexibility depends not only on the floor type, but also on other parameters such as the diaphragm aspect ratio and ratio of diaphragm stiffness to adjoining lateral elements stiffness [6].

Previous studies suggest that plan-asymmetric structures have more potential for diaphragm flexibility [2, 8, 9]. In plan-asymmetric structures, the degree of diaphragm flexibility and distribution of structure stiffness and strength are key

parameters that affect the distribution of forces between the lateral load-resisting elements (LLREs) simultaneously. On the other hand, LLREs forces and deformations affect the response of diaphragms and their components. Therefore, there is a close relationship between diaphragm flexibility and structural asymmetry. Most previous studies have examined extreme cases of this relationship. For example, when the diaphragm is quite rigid, the distribution of stiffness and strength in the structure plan has the greatest effects on the seismic response of plan-asymmetric structures. However, for absolutely flexible diaphragms, the distribution of force between the LLREs is only based on their tributary area.

While past earthquakes observations [10, 11] clearly showed that the diaphragm of many structures has a semiflexible performance, the behavior of plan-asymmetric structures with a semiflexible diaphragm has received less attention in previous studies and some issues remain unresolved. These issues include (1) the effect of stiffness and strength eccentricity parameters on the deformation demands of

flexible diaphragms, (2) the effect of diaphragm flexibility on the response of LLREs of asymmetric structures, especially in the field of nonlinear behavior, and (3) proper configuration of centers with the aim of limiting engineering demand parameters (EDPs) in plan-asymmetric structures with a flexible diaphragm.

In the current study, a parametric study was conducted to address these issues. Simple numerical models were used to determine the general characteristics of the seismic response of plan-asymmetric structures with flexible diaphragms. A wide range of diaphragm flexibility was considered for eight single-story structures with different and realistic configurations of stiffness, strength, and mass centers. Models were exposed to a suite of unidirectional earthquake records with two different intensities (DBE and MCE). The mean maximum displacements and ductility demands of LLREs and deformation components of diaphragms were evaluated using an inelastic dynamic time-history analyses. In order to compare the results, elastic analysis of the structures was performed.

## 2. A Review of Previous Studies on Flexibility of Seismic Diaphragm

Several studies have been conducted on the effects of diaphragm flexibility on structures with different dimensions, lateral load-resisting systems, stories height, and numbers. The results indicated that diaphragm flexibility is more important in structures with stiffer LLREs such as shear walls [2, 12], lower story height [12], less number of stories [1, 12–14], less number of structure spans [1, 13], and larger aspect ratios [12–14].

Diaphragm flexibility affects the dynamic characteristics of structures. For example, it increases the natural vibrational periods of structures [1, 3], and also the participation of higher modes in structural response [14, 15]. An increase in the period, depending on the natural period of the initial structure with rigid diaphragm and the soil type, can cause an increase in the spectral acceleration (ascending branch), decrease in spectral acceleration (descending branch), or no change in the spectral acceleration (fixed branch) in structures with diaphragm flexibility [6]. Also, diaphragm flexibility can lead to the modification of mode shapes and cause a phenomenon called “mode shift” in which some modes of the structure with rigid diaphragm appear in higher modes of similar structures with a flexible diaphragm [13].

Diaphragm flexibility causes changes in the distribution of forces in the LLREs. For example, while in symmetric structures with rigid diaphragm all elements experience the same deformation and accordingly, the stiffer elements absorb more lateral forces in those with absolutely flexible diaphragms; as previously mentioned, the distribution of force between the LLREs is only based on their tributary area [3].

One of the other important issues addressed in flexible diaphragm studies is the local failures of the diaphragms connections with LLREs, especially in the unreinforced masonry

structures (URM) that can lead to out of plane failures of walls [10, 11, 16, 17].

Fewer studies have addressed diaphragm flexibility in plan-asymmetric structures, in comparison with symmetric structures. Studies have shown that, with increase in flexibility, the effects of stiffness eccentricity and consequently the torsional response of the structures reduce significantly [8]. This performance has been introduced as one of the noticeable advantages of diaphragm flexibility [6].

De-La-Colina [8] examined the seismic response of one-span, single-story plan-asymmetric structures with a flexible diaphragm. The investigated structures had stiffness eccentricity and it was assumed that the strength of elements is independent of their stiffness, and, consequently, the strength of structure was distributed among the LLREs according to their stiffness. It was concluded that, by increasing the initial natural period of the structure and the level of elements yield (increase in force reduction factor), the flexibility effects are reduced.

In a parametric study, Kim and White [18] evaluated the structural behavior of one-story reinforcement masonry buildings with timber diaphragm in the inelastic range. They found that the maximum wall displacement occurs when the diaphragm has a semirigid behavior.

Nakamura et al. [19] investigated the impacts of diaphragm flexibility on masonry structures. In asymmetric structures, it was assumed that the strength center coincided with the stiffness center. They concluded that the diaphragm flexibility, depending on the degree of eccentricity, can have different effects on the responses of LLREs. Their study also showed that the stiffness and strength of orthogonal side elements, except in structures with very stiff diaphragms, do not have much impact on responses.

While the experiences of past earthquakes clearly show that the diaphragms of many structures have a semiflexible behavior, the likely change in response of plan-asymmetric structures for different levels of diaphragm flexibility is unknown and less addressed in previous studies. Therefore, the identification of asymmetric structures behavior with a flexible diaphragm is one of the main objectives of the present study.

## 3. Configuration of Stiffness and Strength Centers in Plan-Asymmetric Buildings

In seismic design, the lateral elements nonlinear moment-curvature can be considered satisfactory as an ideal bilinear relationship [20]. Also, the researches conducted on the concrete columns and shear walls [21, 22] showed that yield displacement of LLREs (D-type elements [23]) is only dependent on the material properties and geometric dimensions of elements and is independent of its axial force and strength (reinforcement ratio). Based on these assumptions, the yield displacement for a cantilever shear wall with different conditions of loading ( $\Delta_y$ ) can be calculated from [24]

$$\Delta_y = \frac{C\varepsilon_y h^2}{l_w}, \quad (1)$$

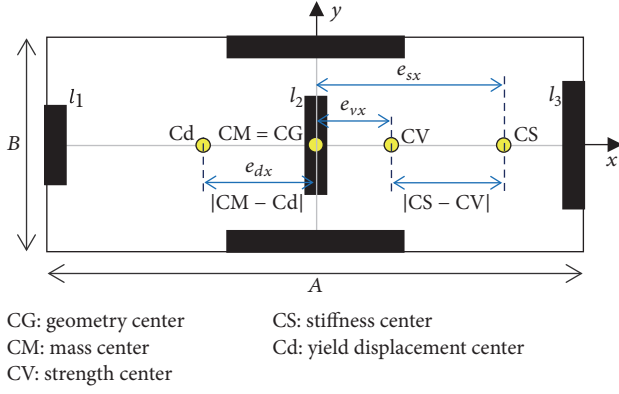


FIGURE 1: Centers of structural model and their eccentricities.

where  $l_w$  and  $h$  are, respectively, the length and height of the shear wall,  $\epsilon_y$  is the yield strain of longitudinal reinforcements, and  $C$  is a coefficient related to the shape of lateral force distribution and element section. For example, for a cantilever shear wall with lateral load acting on the top of the wall (as in a single-story building), the value of  $C$  is equal to 0.66.

Unlike the traditional assumption, element stiffness depends on its nominal strength and is not a constant property. Therefore, the stiffness of the lateral load-resisting element ( $K_i$ ) can be calculated according to (2) using the nominal base shear strength of the wall and its yield displacement (see (1)) [24]:

$$K_i = \frac{V_{ni}}{\Delta_{yi}}, \quad (2)$$

where  $V_{ni}$  and  $\Delta_{yi}$  are the nominal strength and yield displacement of the element, respectively.  $\Delta_{yi}$  for a cantilever shear wall is given by (1).

Therefore, in buildings consisting of D-type elements, the location of the stiffness center is a function of their strength and yield displacement. In a study, Tso and Myslimaj [25] showed that even in the case of using different methods to assign strength to LLREs, the distance between the centers of strength and stiffness will be almost equal to the distance between the centers of mass and yield displacement.

The models considered in this study had three shear walls in the direction of the applied seismic load (unidirectional excitations applied in the  $y$  direction) (Figure 1).

In this figure, CM, CS, CV, and Cd are, respectively, mass, stiffness, strength, and yield displacement centers of structures. The lengths of walls from left to right are  $l_1$ ,  $l_2$ , and  $l_3$  and their distances from the geometric center of the diaphragm are equal to  $-A/2$ ,  $0$  and  $A/2$ , respectively. As shown in Figure 1, the center of mass (CM) coincides with the geometric centroid (CG). Uniaxial stiffness eccentricity ( $e_{sx}$ , defined as the distance between CM and the center of stiffness, CR) and strength eccentricity ( $e_{vx}$ , defined as the distance between the CM and the center of strength, CV) are introduced by change in edge walls strength and length. Stiffness, strength, and yield displacement of the  $i$ th wall

oriented in the  $y$  direction are defined by  $K_{yi}$ ,  $V_{yi}$ , and  $\Delta_{yi}$ , respectively, and the wall located at a distance  $x_i$  from the CM. The configuration of the analytical models is defined by the following parameters:

(a) The yield displacement eccentricity is expressed as normalized to the dimension of the diaphragm perpendicular to the direction of excitation ( $\epsilon_{dx}$ ).

$$\epsilon_{dx} = \frac{e_{dx}}{A} = \frac{1}{A} \frac{\sum_{i=1}^3 \Delta_{yi} x_i}{\sum_{i=1}^3 \Delta_{yi}} = \frac{(l_2 l_1 - l_3 l_2)}{2(l_2 l_3 + l_1 l_3 + l_1 l_2)}. \quad (3)$$

It is notable that since in the model shown in Figure 1, the height, material properties, and coefficient  $C$  of all LLREs are considered the same, therefore, their yield displacement is inversely proportional to the length of the elements ( $\Delta_{yi} \propto 1/l_i$ ).

(b) The stiffness eccentricity is expressed as normalized to the dimension of the diaphragm perpendicular to the direction of excitation ( $\epsilon_{sx}$ ).

$$\epsilon_{sx} = \frac{e_{sx}}{A} = \frac{1}{A} \frac{\sum_{i=1}^3 k_i x_i}{\sum_{i=1}^3 k_i} = \frac{(V_3 l_3 - V_1 l_1)}{2(V_1 l_1 + V_2 l_2 + V_3 l_3)}. \quad (4)$$

(c) The strength eccentricity is expressed as normalized to the dimension of the diaphragm perpendicular to the direction of excitation ( $\epsilon_{vx}$ ).

$$\epsilon_{vx} = \frac{e_{vx}}{A} = \frac{1}{A} \frac{\sum_{i=1}^3 V_i x_i}{\sum_{i=1}^3 V_i} = \frac{(V_3 - V_1)}{2(V_1 + V_2 + V_3)}. \quad (5)$$

Aziminejad and Moghadam [26] showed that, in this model, for eccentricities of yield displacement and strength in the range of  $-15$  to  $15\%$ , the distance between centers of strength and stiffness can be assumed to be equal to yield displacement eccentricity with an acceptable approximation.

Although these eccentricities are typically used to explain the asymmetry in structures with rigid diaphragm, in some researches conducted on asymmetric structures with flexible diaphragm, the same indices in similar structures to rigid diaphragm were used as convenient definitions [8, 19]. Accordingly, in this study, the eccentricities in structures with flexible diaphragms mean the same values in similar structures with rigid diaphragms.

#### 4. Studied Models

In order to study the combined effects of asymmetry and flexibility in structures, different configurations of the mass, stiffness, and strength centers were considered in the evaluated models. A one-story ideal model with a rectangular plan (diaphragm) and dimensions of  $30 \text{ m} \times 12 \text{ m}$  and shear wall system was considered. The height of the model was equal to  $3.2 \text{ m}$  and the floor masses ( $850 \text{ kg/m}^2$ ) were distributed across the diaphragm uniformly. The base model has two shear walls in the  $x$  direction and three shear walls in the  $y$  direction, respectively. Building asymmetry was only relative to the  $y$ -axis (Figure 2).

TABLE 1: Strength and stiffness of LLREs in analytical models.

Model	Description	Length (cm)			Strength (Ton)			Stiffness (ton/cm)		
		Wall 1	Wall 2	Wall 3	Wall 1	Wall 2	Wall 3	Wall 1	Wall 2	Wall 3
1	Symmetric	200	200	200	17.85	17.85	17.85	36.99	36.99	36.99
2	Stiffness symmetric	260	200	140	12.50	17.85	23.21	33.66	36.99	33.66
3	Balance (0.75 CV-CS)	260	200	140	13.83	17.85	21.87	37.26	36.99	31.71
4	Balance (0.5 CV-CS)	260	200	140	15.17	17.85	20.53	40.87	36.99	29.77
5	Balance (0.25 CV-CS)	260	200	140	16.51	17.85	19.19	44.47	36.99	27.83
6	Strength symmetric	260	200	140	17.85	17.85	17.85	48.08	36.99	25.89
7	De Stefano (0.25 CM-CS)	260	200	140	19.63	17.85	16.07	52.88	36.99	23.30
8	De Stefano (0.5 CM-CS)	260	200	140	23.21	17.85	12.50	62.51	36.99	18.12

TABLE 2: Eccentricity of asymmetric buildings.

Model	Description	Eccentricity (%)			$e_v/e_d$
		Yield displacement	Strength	Stiffness	
1	Symmetric	0	0	0	0
2	Stiffness symmetric	10	10	0	1
3	Balance (0.75 CV-CS)	10	7.5	-2.5	0.75
4	Balance (0.5 CV-CS)	10	5.0	-5	0.5
5	Balance (0.25 CV-CS)	10	2.5	-7.5	0.25
6	Strength symmetric	10	0	-10	0
7	De Stefano (0.25 CM-CS)	10	-3.33	-13.33	-0.33
8	De Stefano (0.5 CM-CS)	10	-10	-20	-1

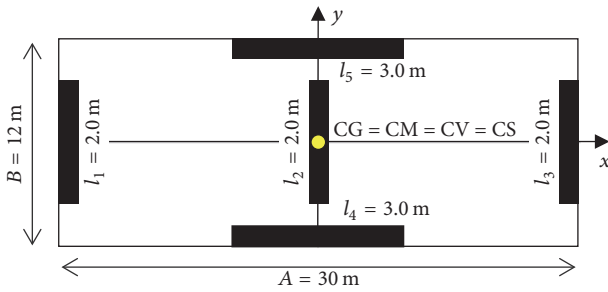


FIGURE 2: Plan view of the base symmetric model.

It was assumed that gravity loads are transferred by a simple frame system. The analysis and design of LLREs were carried out based on the characteristics of the base symmetric model and assuming full rigidity of the seismic diaphragm. Gravity design loads of structures were determined based on the sixth part of the National Building Code of Iran [27]. Seismic design loads were calculated based on seismic provisions of Standard 2800 of Iran [28]. The structure force reduction factor was considered to be equal to 5.0 based on the Standard 2800. The total base shear of the symmetric structure was calculated as 53.55 tons (535.5 KN). To create asymmetric models, the length of the left and right walls of the structure changed in such a way that the yield displacement eccentricity of the structure was equal to 10% of the plan length. Therefore, the wall lengths were similar in all the asymmetric models. The lengths of left, central, and right walls were considered as 260, 200, and 140 cm, respectively

TABLE 3: Natural period and torsional to lateral frequency ratios ( $\Omega$ ) of models with rigid diaphragm assumption.

Model	Mode x (sec)	Mode y (sec)	Mode $\theta$ (sec)	$\Omega_x$	$\Omega_y$
1	0.381	0.330	0.231	1.649	1.429
2	0.381	0.330	0.231	1.649	1.429
3	0.381	0.339	0.238	1.601	1.424
4	0.381	0.339	0.234	1.628	1.449
5	0.381	0.342	0.230	1.656	1.487
6	0.381	0.346	0.226	1.685	1.531
7	0.381	0.354	0.221	1.723	1.602
8	0.381	0.376	0.209	1.823	1.799

(Table 1). The length of the two orthogonal side walls (in  $x$  direction) was considered the same in all models and equal to 300 cm. The width of all the walls was considered the same and equal to 30 cm. To create different degrees of the strength eccentricity, the strength of the left wall increased, while the strength of the right wall decreased, such that the overall strength of the structure was assumed to be fixed and the same strength of the base symmetric model. Revealing the initial yield displacement of any structural elements from (1) and their initial strength (Table 1), the initial stiffness of elements can be determined using (2).

Also, the eccentricities of structure models can be calculated from (3) to (5) (Table 2). Natural periods and also the torsional to lateral frequency ratio of analytical models assuming the full rigidity of the diaphragm are presented in Table 3.

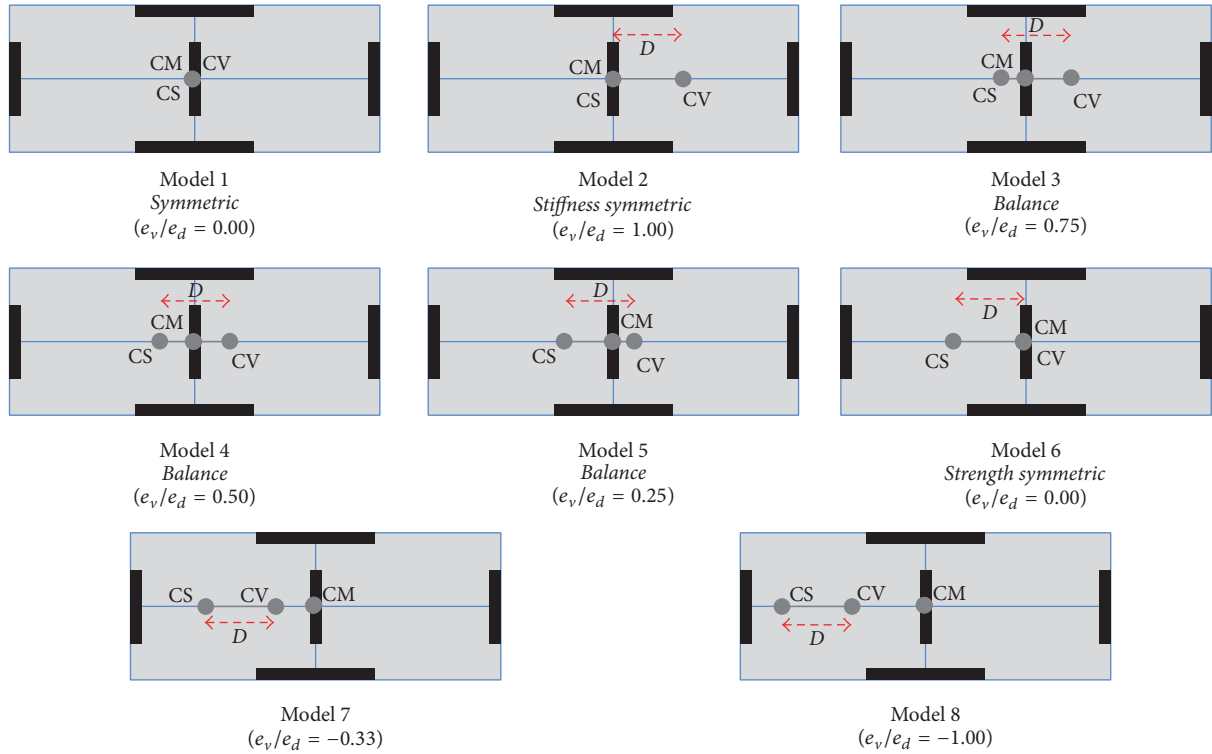


FIGURE 3: Schematic view of centers configuration in models (distance is not in scale).

Given that the torsional to lateral frequency ratio is larger than one in all the models, all the primary models are considered torsionally stiff and their responses are predominantly in transitional mode. The mentioned models are similar to models used in previous studies and as a representative of a wide range of asymmetric buildings [29].

The configuration of centers of the symmetric model and seven plan-asymmetric models are depicted in Figure 3.

These models have been briefly described as follows. Model 1 is the base symmetric model with a regular geometric shape and uniform distribution of mass, stiffness, and strength in its plan. In model 2, the stiffness center coincided with the center of mass. Models 3 to 5 which were presented by Myslimaj and Tso [30, 31] are called “balance configuration” models. The center of the mass is located between the stiffness and strength centers in these three models. In model 3, the distance between the center of mass and the center of strength is about 0.75 of the distance between the stiffness center and the strength center. The distance between the center of mass and the center of strength in models 4 and 5 is, respectively, 0.5 and 0.25 of the distance between the center of stiffness and the center of strength. Model 6 is a model with uniform strength distribution and stiffness eccentricity. Models 7 and 8 are known as “optimum configuration” models according to the study of De Stefano et al. [32]. In model 7, the distance between the mass center and strength center is 0.25 of the distance between the mass center and the stiffness center, while in model 8, the strength center is between the mass and stiffness centers and in an equal distance from each of them.

After determining the configuration of centers in eight structures with rigid diaphragms, different degrees of flexibility were considered for the diaphragm and the responses of the structures were determined using finite element modeling and inelastic dynamic time-history analyses.

Although the most powerful method of identifying all failure mechanisms in structures is nonlinear modeling by considering the details of diaphragms and their connections, this method is complicated and very time consuming. With the increasing complexity of the model and lack of detailed information, sources of error in the model are likely to increase. Since the main objective of this research was to investigate the overall characteristics of the dynamic responses of asymmetric structures with flexible diaphragm, and the relatively simple models are able to estimate the overall response of the structure, the simplifying assumptions were considered in the ideal model. Some of the most important assumptions and details considered in the design and analysis of selected models include the following:

(1) Based on the principles of many seismic design codes [28, 33], seismic diaphragms must be designed in such a way that they behave in the elastic range; in this study, the elastic behavior was proposed for the diaphragms. As pointed out by Tena-Colunga et al. [6], the stiffness properties of some concrete diaphragms such as two-way concrete slabs, ribbed RC slabs, and RC waffle flat slabs in two main directions are the same and therefore an isotropic material modeling can be used to model their stiffness properties in the elastic range. In modeling, the overall diaphragm stiffness was considered

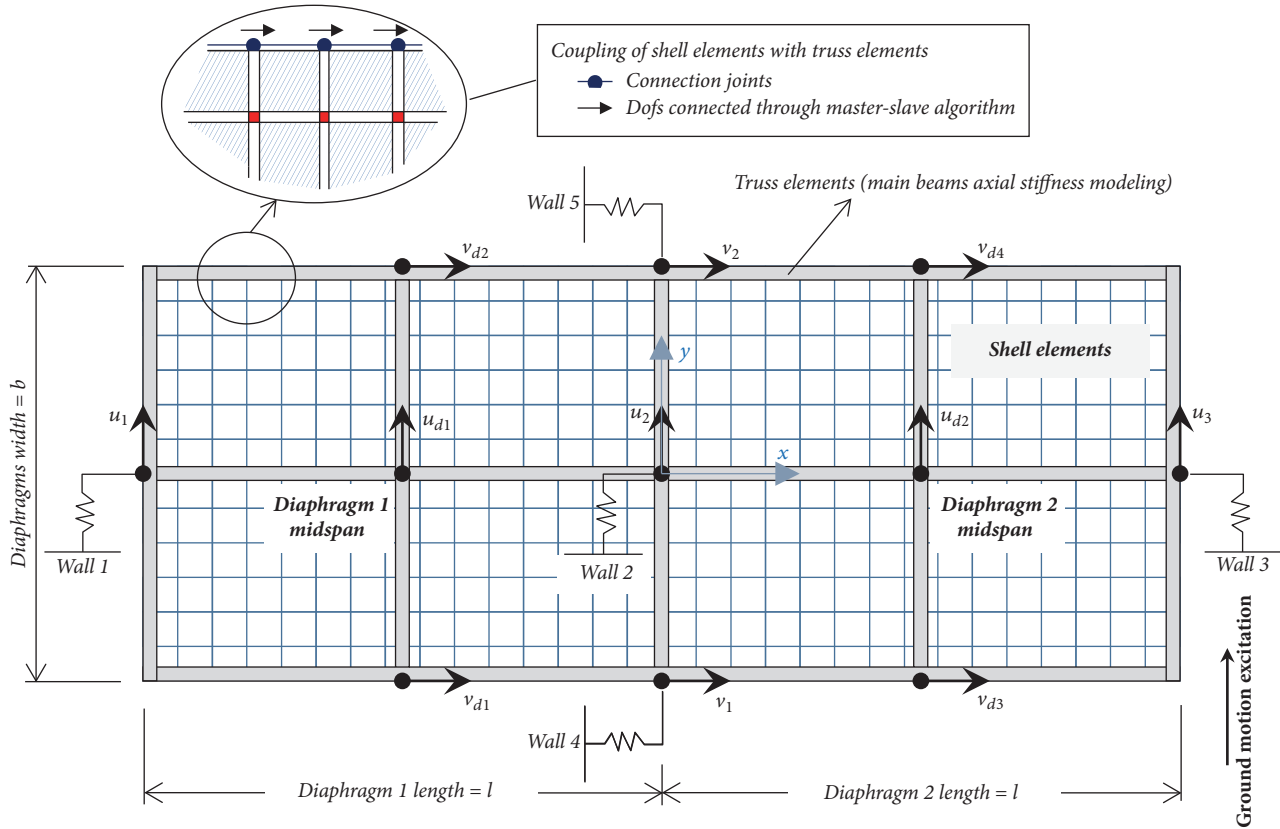


FIGURE 4: Finite element model of structures and main displacement recorders.

and the flexural stiffness of the diaphragm beams was not considered explicitly.

Based on given descriptions for diaphragms modeling, 384 shell elements with isotropic elastic behavior were used. The diaphragm modeling was performed in OpenSees [34] using the Elastic Membrane Plate Section commands for the diaphragm cross section and the ShellMITC4 command for the diaphragm element type. A complete description of the material, element type models, and their parameters is given in the OpenSees Manual [35]. The ideal analytical model and main recorders of wall displacements and structure diaphragms are shown in Figure 4.

Also, the mesh sensitivity analysis was performed and approved. In another simplification, it was assumed that the diaphragm is completely and continuously connected to the LLREs. Also, the connection of diaphragms to the walls in all seismic levels was considered perfect and without any imperfections.

Since the shear walls of the structure modeled using spring models are connected to the diaphragm at a point, to make the results more realistic and prevent strain concentration at the connection point, especially in very flexible diaphragms, as depicted in Figure 4, the axial stiffness of the main beams was added to the analytical model using one-dimensional truss elements. The axial stiffness of these elements was calculated based on the initial design (under gravity and seismic loads).

(2) In each model, the material properties of the two structure diaphragms were considered identical, and the fundamental natural period of the individual diaphragm with fixed ends ( $T_d$ ) was used to express the degree of flexibility.

Different values of the diaphragms period considered in this study are presented in Table 4. Diaphragm thickness was considered a realistic value (0.15 m). Also as previously mentioned, structure plan dimensions were considered constant for all analytical models (12 m  $\times$  30 m). The flexible diaphragm modulus of elasticity ( $E_d$ ) was calculated using error and trial method so that the structure diaphragm period converges to the target values in Table 4.

In order to better understand this parameter, the corresponding amounts of diaphragm flexibility ratio ( $\gamma_s$ ) in the symmetric structure are given in the table in accordance with the common definition of diaphragm flexibility ratio in seismic codes [33]. Diaphragm flexibility ratio ( $\gamma_s$ ) is quantified as the ratio of the maximum diaphragm deflection to average drift of adjoining lateral load-resisting system, under uniform distributed lateral load along the diaphragm. This study considered a relatively wide range of different degrees of diaphragm flexibility.

(3) The structures were exposed to unidirectional ( $y$  direction) earthquake excitations. Models have different degrees of stiffness and strength eccentricity only in the perpendicular direction ( $x$  direction) to seismic loading. However, according to the description of the previous sections, the

TABLE 4: Natural periods of individual diaphragms and corresponding values of flexibility in base symmetric structure.

Number	$T_d$ (sec)	$\gamma_s$
(1)	0.000	0.000
(2)	0.027	0.031
(3)	0.038	0.062
(4)	0.056	0.125
(5)	0.089	0.250
(6)	0.142	0.500
(7)	0.191	0.750
(8)	0.235	1.000
(9)	0.276	1.250
(10)	0.314	1.50
(11)	0.382	2.00
(12)	0.441	2.50
(13)	0.494	3.00
(14)	0.587	4.00
(15)	0.667	5.00
(16)	0.740	6.00
(17)	0.806	7.00
(18)	0.867	8.00

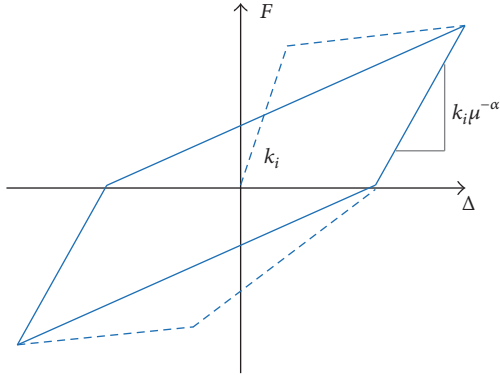


FIGURE 5: Takeda thin hysteresis rule [36].

distance between the centers of stiffness and strength in all asymmetric models were considered the same. The mass of walls was neglected as compared to the diaphragm mass, and the diaphragm mass is uniformly distributed on its surface. Therefore, in all the models, the mass center matches the geometric center of the diaphragm.

(4) The out of plane stiffness and strength of the walls were neglected. The local and out of plane failures of the walls were avoided. The dependence of the strength of the walls to the axial force was neglected. The force-displacement relationship of concrete shear walls was modeled using the thin Takeda hysteresis model (Figure 5).

This model is commonly used to simulate the seismic behavior of reinforced concrete shear walls and columns [36]. The postyield stiffness was considered zero on all walls. It is notable that, in this study, the collapse potential of resisting elements was not considered in analytical modeling. A 5%

damping ratio proportional to the mass was included in the analyses.

Analytical modeling and nonlinear inelastic dynamic time-history analyses were performed using the OpenSees software package [34]. Due to the long period of time needed to analyze each of the models, the facilities of DesignSafe [37] were used.

After the finite elements modeling, the structures were subjected to seven unidirectional records of far-field earthquakes. The earthquake records considered were related to the same soil conditions with a minimum magnitude of 6 and a minimum PGA of 0.15 g (Table 5). The displacement and pseudo-acceleration spectra of the used records are presented in Figure 6. In dynamic time-history analyses, each record was scaled for two different earthquake intensities with PGA = 0.35 g for Design Basis Earthquake (DBE) and PGA = 0.70 g for Maximum Considered Earthquake (MCE).

## 5. Results of Analyses

5.1. *The Effect of Structure Asymmetry on the Deformations of Flexible Diaphragms.* According to the dimensions of the diaphragms and modeling of the axial stiffness of the primary beams, and also applying the unidirectional seismic loading in this study, the investigations showed that one can decompose the deformation of each diaphragm into four components with a very accurate approximation: (1) the translation of the diaphragm as a rigid mode ( $\delta_t$ ), (2) the rotation of the diaphragm as a rigid mode ( $\delta_r$ ), and (3) shear-dominant deformation ( $\delta_s$ ) and bending-dominant deformation ( $\delta_d$ ) (Figure 7). It should be noted that shear-dominant and bending-dominant deformations are the overall deformation shapes of the diaphragm and is not related to the components of the deformation of a Timoshenko beam.

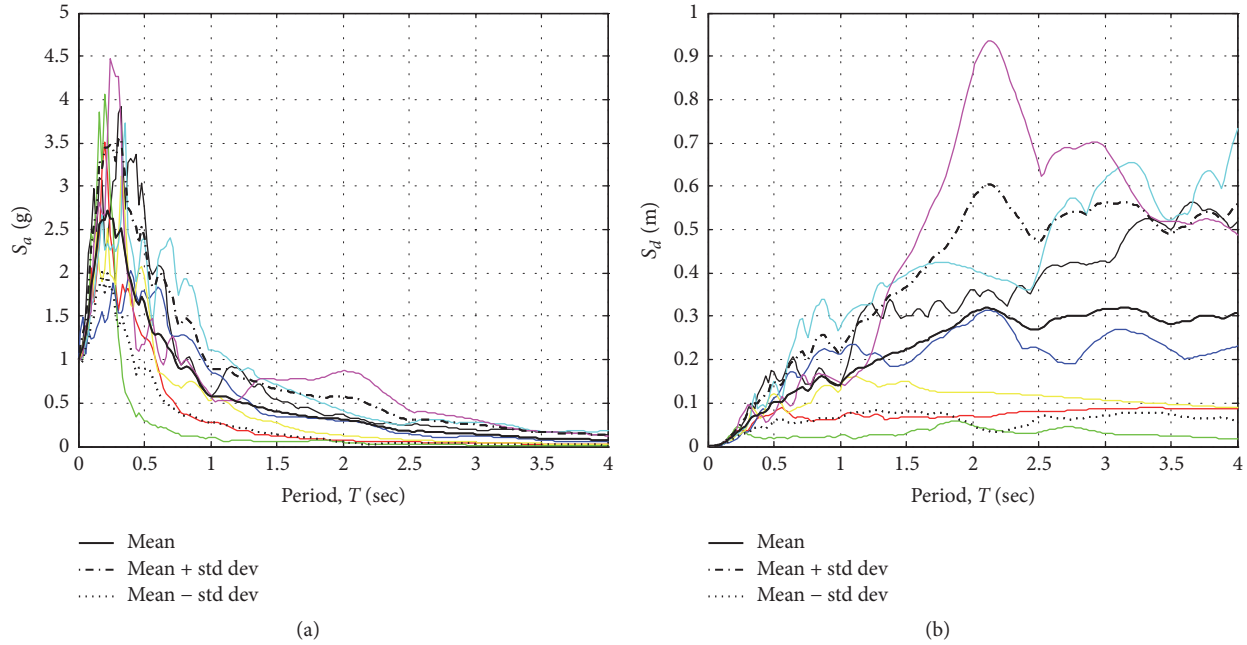
Majority of these deformations can be calculated using the displacement recorders considered in the analytical models (Figure 4) for each of the diaphragms (DPH):

$$\begin{aligned}
 \text{DPH 1: } \delta_t &= 0.5(u_1 + u_2) \\
 \delta_r &= \frac{l(vd_1 - vd_2)}{b} \\
 \delta_s &= (u_2 - u_1) - \delta_r \\
 \delta_d &= u_{d1} - \delta_t \\
 \text{DPH 2: } \delta_t &= 0.5(u_2 + u_3) \\
 \delta_r &= \frac{l(vd_3 - vd_4)}{b} \\
 \delta_s &= (u_3 - u_2) - \delta_r \\
 \delta_d &= u_{d2} - \delta_t.
 \end{aligned} \tag{6}$$

In Figure 8, the mean of maximum values of  $\delta_t$ ,  $\delta_r$ ,  $\delta_s$ , and  $\delta_d$  for diaphragms of model 6 (which has only stiffness eccentricity) for DBE earthquakes is shown: (a) elastic response and (b) inelastic response. For comparison, the results of the

TABLE 5: Earthquake records used in dynamic time-history analysis.

Event	Year	Station	$M_w$	Mechanism	Closest distance (m)	$V_{s30}$ (m/s)	PGA (g)	Duration (sec)
Imperial Valley-06	1979	Cerro Prieto	6.53	Strike slip	15.19	471.53	0.168	36.27
N. Palm Springs	1986	San Jacinto, Soboba	6.06	Reverse oblique	22.96	447.22	0.254	20.09
Cape Mendocino	1992	Shelter Cove Airport	7.01	Reverse	26.51	518.98	0.228	30.5
Chi-Chi, Taiwan	1999	TCU045	7.62	Reverse oblique	26	704.64	0.507	35.095
San Fernando	1971	Castaic, Old Ridge Route	6.61	Reverse	19.33	450.28	0.320	20.27
Kern County	1952	Taft Lincoln School	7.36	Reverse	38.42	385.43	0.159	47.64
Manjil, Iran	1990	Qazvin	7.37	Strike slip	49.97	302.64	0.184	35.99

FIGURE 6: The response spectra of records ( $\xi = 0.05$ ): (a) pseudo-acceleration and (b) displacement. Thin curves are the response spectra of earthquake records in Table 5.

corresponding deformations in the symmetric structures are also drawn as a continuous line.

As shown, the diaphragms deformations of the asymmetric structure, especially in the inelastic analysis, are very similar to those of the symmetric structure. The only major difference is the lack of rotational deformation of the diaphragms in the symmetric structure. Another significant point is the importance of the shear deformation and its growth for the inelastic range, and even for the symmetric structure. This can be due to the fact that, with increase in the flexibility, the central wall of the structure with a greater tributary area than the two side walls absorbs more seismic load and thus experiences more deformations than the lateral elements, and this increases the shear deformation of the diaphragms.

Reducing the translational and rotational rigid modes and, in contrast, the increase in bending and shear deformations of the diaphragm which occurs with increase in diaphragm flexibility clearly reflect a change in the seismic behavior of the structure. Although this change in behavior

(changing the mode from the rigid modes to the deformational modes) can lead to a reduction in engineering demands in some LLREs, another issue that needs to be fully addressed is the growth of the demand for deformational modes in the diaphragms, which usually has no capability for large deformations.

The mean of maximum values of the deformations for the diaphragms of model 2 (which has only strength eccentricity), at inelastic range and for DBE earthquakes, is depicted in Figure 9. For comparison, the results of the corresponding deformations in the symmetric structure are also drawn in the form of a dashed line.

As shown, the modes of rotational motion and bending deformation of the two diaphragms of the asymmetric structures are very similar. Also, the bending deformation of the diaphragms corresponds to their values in a symmetric structure. The major difference in the deformation of the neighbor diaphragms is the translation and shear deformations modes. It can be clearly seen that the values of shear deformation for the weak side diaphragm (DPH1) of the asymmetric structure

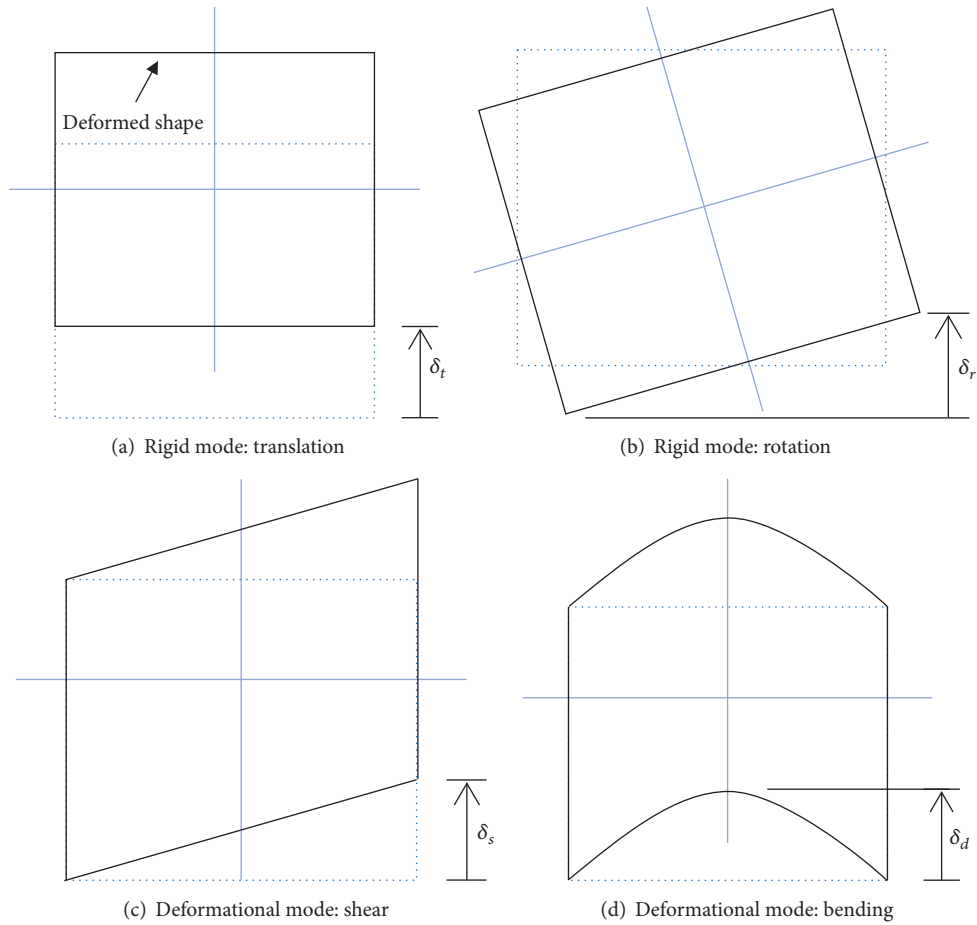


FIGURE 7: Deformation components of the diaphragm.

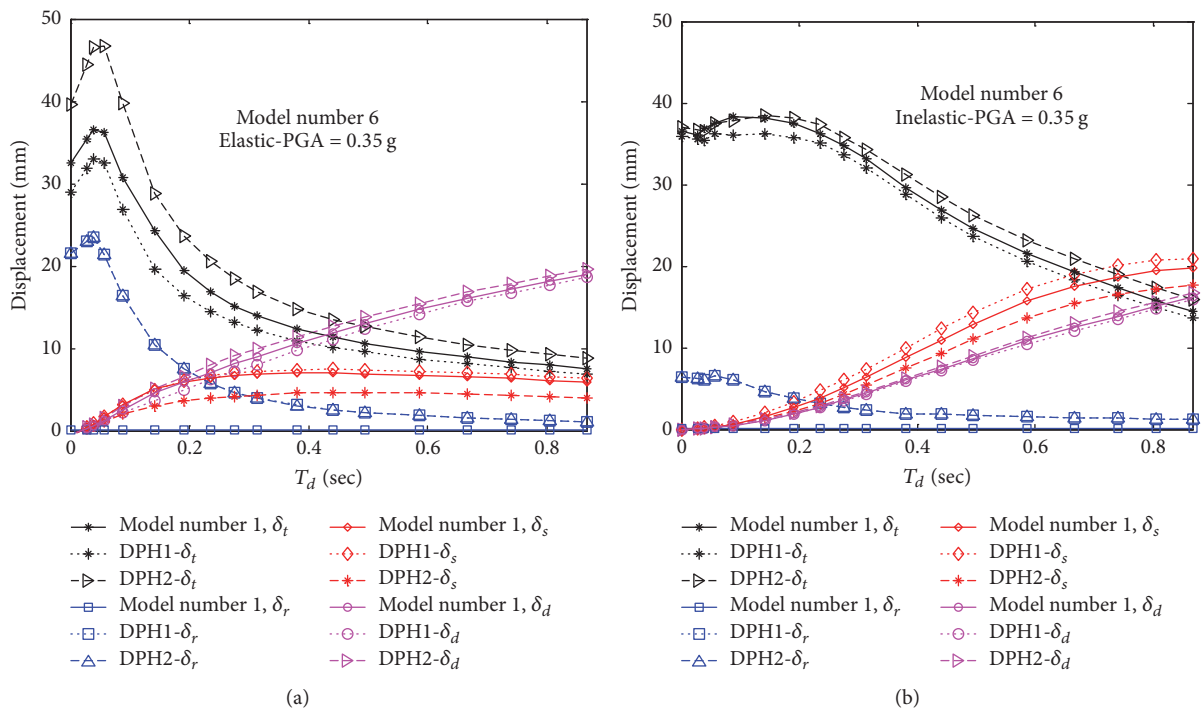


FIGURE 8: Deformation components of diaphragms for model 6 in DBE earthquakes: (a) elastic and (b) inelastic.

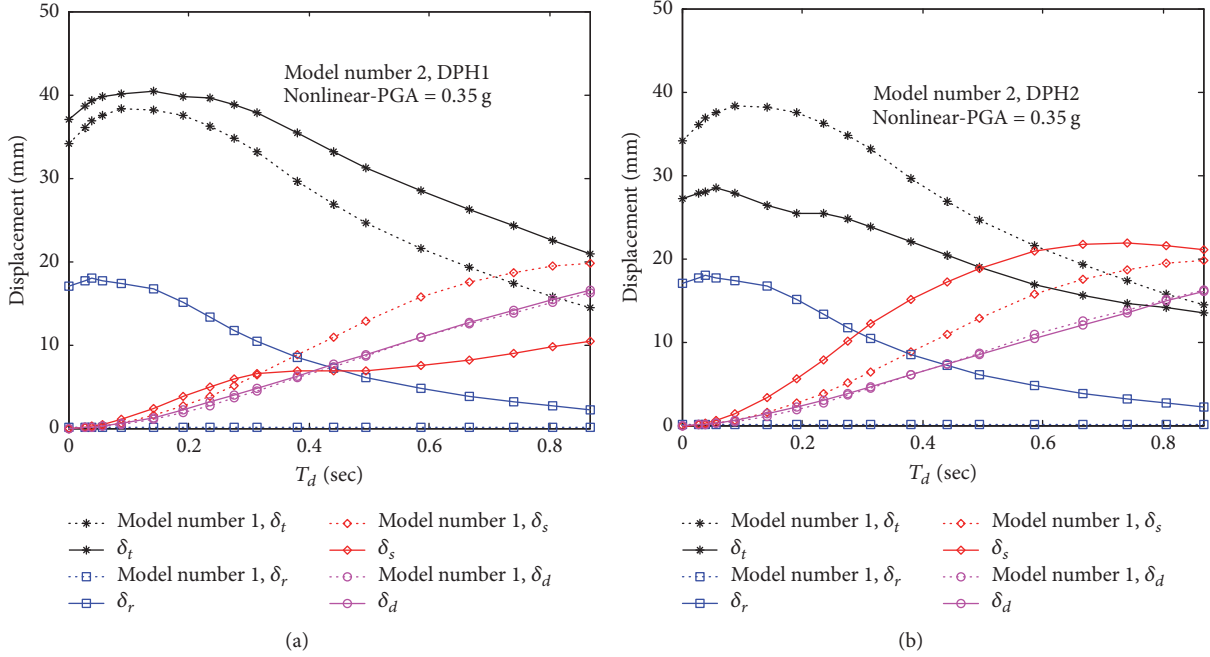


FIGURE 9: Deformation components of diaphragms for model 2 in DBE earthquakes: (a) DPH1 and (b) DPH2.

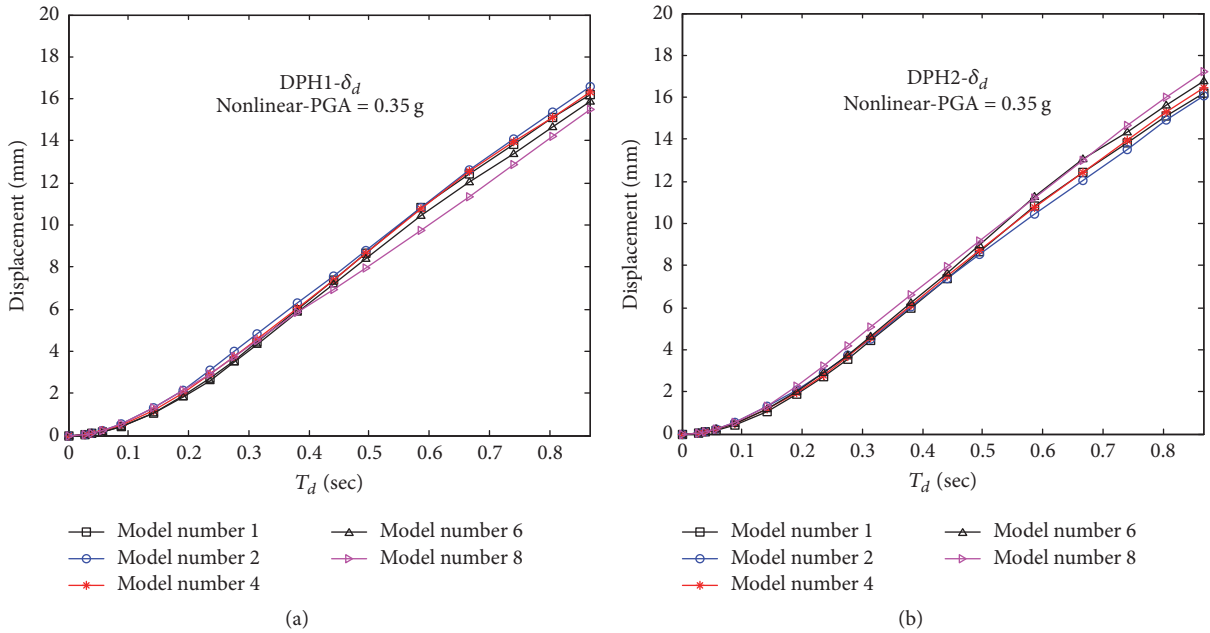


FIGURE 10: Bending-dominant deformation of diaphragms in DBE earthquakes: (a) DPH1 and (b) DPH2.

are lesser than that of the strong side diaphragm (DPH2). This phenomenon can be interpreted as the concentration of shear-dominant deformations in the strong side diaphragm of the structure which is accompanied by the concentration of the translational motion (rigid mode) on the weak side diaphragm of the structure.

Therefore, it can be concluded that, by increasing the diaphragm flexibility, the rigid modes of the translational

and rotational motions of the diaphragm are reduced and the diaphragm shear and bending deformations grow. The growth of the diaphragm shear deformation approximately stops after a certain degree of flexibility, but the growth of the bending deformation of the diaphragm is continuous. The bending deformation of adjacent diaphragms in different asymmetric structures is very close to each other and similar to that in the symmetric structure (Figure 10),

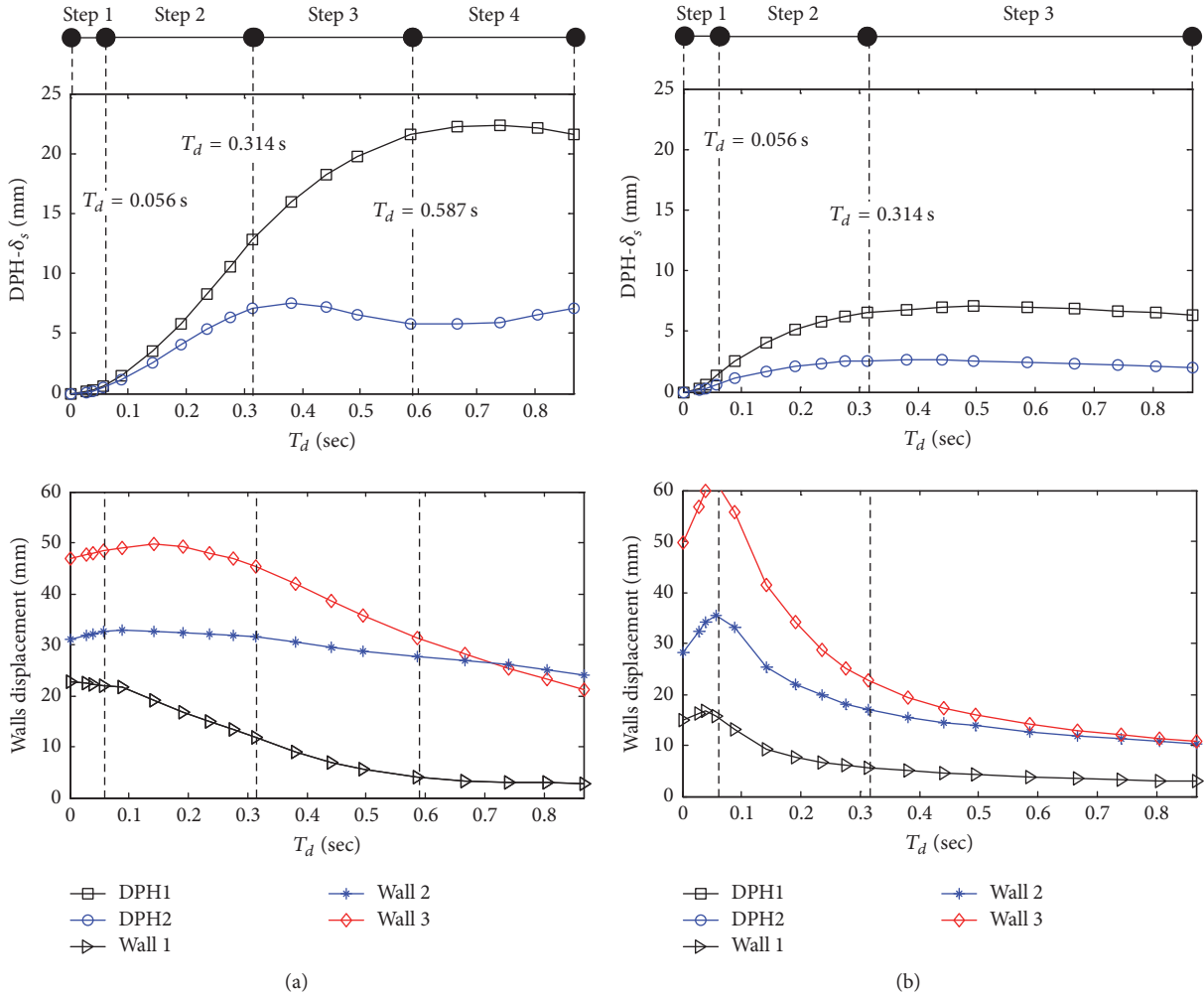


FIGURE 11: Qualitative classification of the asymmetric structures behavior for model 8 in DBE earthquakes: (a) inelastic and (b) elastic.

while the shear deformation of adjacent diaphragms of asymmetric structures is very different and the concentration of shear deformations in one of the diaphragms is observed.

**5.2. Qualitative Classification of the Asymmetric Structures Behavior Based on Degree of Diaphragm Flexibility.** As a result of the shear deformation sensitivity of the diaphragms to structure asymmetry and the degree of flexibility, the shear deformation can be a better criterion for measuring the performance of structure diaphragms. The shear deformations of diaphragms and displacement of walls for model 8 are depicted in Figure 11: (a) elastic and (b) inelastic. In accordance with Figure 11(a), for the inelastic range, the behavior of the considered asymmetric structures can be categorized qualitatively into four steps based on their degree of diaphragm flexibility.

**Step 1 (rigid diaphragms).** The diaphragm's shear deformation is negligible in comparison with the rotational and translational motions.

**Step 2 (semirigid diaphragms).** In this step, by increasing the diaphragm flexibility, the shear deformation of both structure diaphragms continuously grows at a fast rate.

**Step 3 (fixed shear-dominant response in the weak side diaphragm (DPH2)).** Starting the third step, with increase in diaphragm flexibility, the shear deformation of the weak side diaphragm remains almost constant, while the shear deformation of the strong side diaphragm continues to grow. In this step, the displacement of the central wall has almost a constant trend.

**Step 4 (fixed shear-dominant response on both diaphragms of the structure).** In this step, the shear deformation growth of the strong side diaphragm will stop and will have a constant trend. In this step, displacement of the strong wall has an approximately constant trend.

In elastic structures, given that the elements response is only in the elastic range, only three steps of behavior can be identified. (1) rigid diaphragm, (2) semirigid diaphragms, and (3) fixed shear-dominant response on both

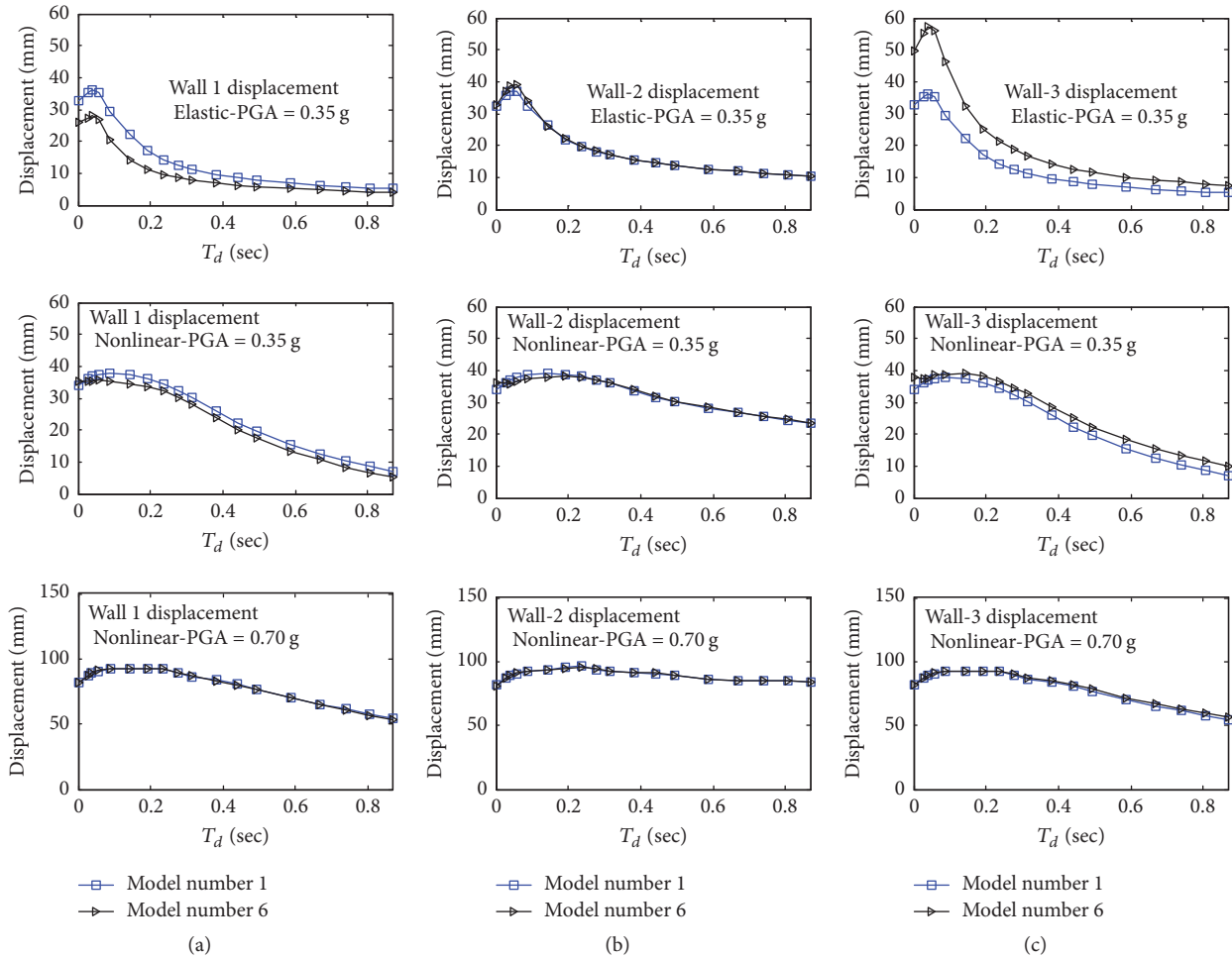


FIGURE 12: Walls displacements of model 6 in DBE and MCE earthquakes: (a) wall 1 (left side, stiff), (b) wall 2 (central), and (c) wall 3 (right side, flexible).

diaphragms of the structure. It should be noted that, in the third step of elastic structures, the convergence of the weak wall displacement to the central wall displacement is mainly due to decrease in the rotational deformation of the weak side diaphragm. From this discussion, it can be concluded that, first, the behavior of the structure diaphragms is not only a function of the diaphragm flexibility, but the overall configuration of the structure and configuration of the centers. It should be noted that the center of strength has the most significant effect on the behavior of diaphragms. Second, while the bending deformation of the diaphragms in all structures is almost identical, the shear-dominant deformation gives clearer criteria of diaphragm performance.

**5.3. Effect of Diaphragm Flexibility on LLREs of Asymmetric Structures.** In Figures 12(a), 12(b), and 12(c), respectively, the mean of maximum displacement of walls 1 (stiff side), 2 (central), and 3 (flexible side), which are the main walls in the direction of seismic loading, for model 6 (which has stiffness eccentricity and strength symmetry) is shown for

different degrees of diaphragm flexibility ( $T_d$ ). The first row corresponds to the elastic structure response under DBE earthquakes, while the second and third rows, respectively, represent the results of nonlinear analyses in DBE and MCE earthquakes. In all the diagrams, the displacements of the corresponding walls in the symmetric structure (model 1) are also presented for comparison.

In general, by increasing the diaphragm flexibility, the displacement of the LLREs decreases in both symmetric and asymmetric structures. According to the acceleration response spectra of earthquakes records, rigid diaphragm models fall into a resonance region, while their flexible diaphragm structures fall into the descending branch of the spectra; this explains why those demands are considerably reduced. It is notable that an increase in flexibility result in a higher participation of the tributary area in lateral forces distribution and, consequently, less reduction in demands can be seen for the central walls.

As shown, the overall asymmetric structure response is similar to the symmetric structure response and the asymmetry has little effect on the displacements of the walls.

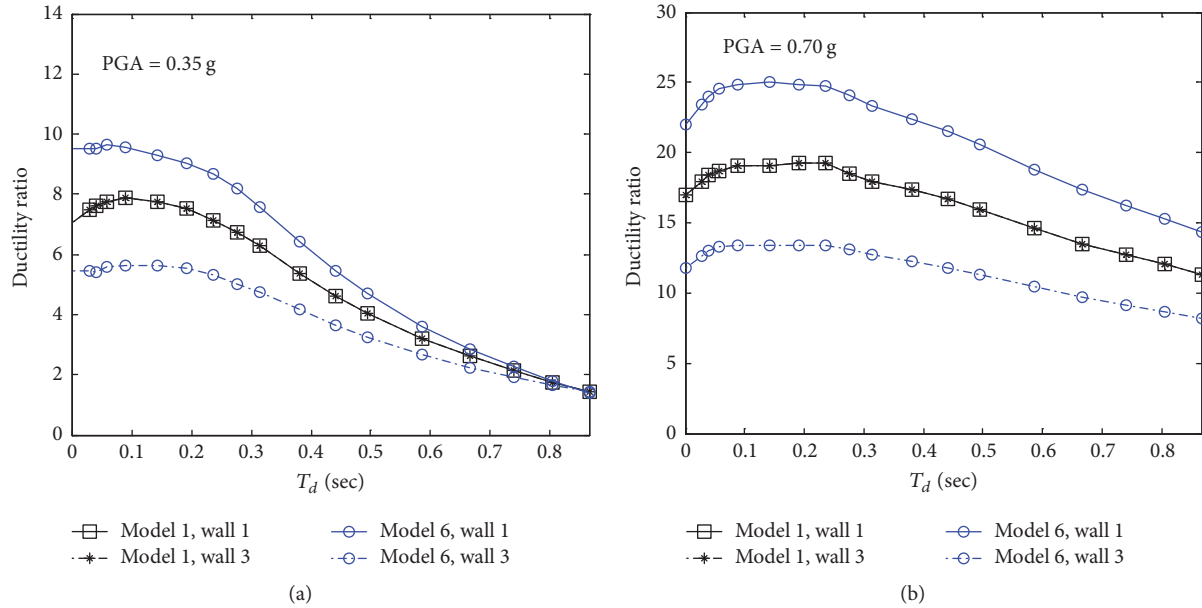


FIGURE 13: Ductility demands of stiff (wall 1) and flexible (wall 3) walls of the model 6: (a) DBE earthquakes (0.35 g) and (b) MCE earthquakes (0.70 g).

In the elastic asymmetric structure, the flexible side wall shows more displacement compared to the same wall in the symmetric structure, and the opposite is true in the stiff side wall. In general, it can be said that the stiffness eccentricity only in elastic analyses and in low flexibilities (rigid and semirigid diaphragms) increases displacement of the flexible side wall relative to the similar symmetric structure. With increase in the diaphragm flexibility or the intensity of the earthquake (yield level of elements), the effect of the stiffness eccentricity on structure displacements quickly decreases. Similar conclusions were provided in previous studies [6].

The mean of maximum ductility demands for end walls of model 6 in DBE and MCE earthquakes for various degrees of flexibility ( $T_d$ ) is shown in Figures 13(a) and 13(b), respectively. The results of the corresponding walls in the symmetric structure (model 1) are presented for comparison.

As shown, in contrast to the displacement responses, the stiff side wall of the asymmetric structure (wall 1) experiences more ductility demands than that of the symmetric structures, while the opposite is true for the flexible side wall (wall 3). Higher ductility demand values can be observed in semirigid diaphragm structures and by increasing the flexibility, the ductility demands converge to its values in symmetric structures. This phenomenon actually represents a more uniform distribution of damage in the asymmetric structure walls by increasing the flexibility. As the intensity of the earthquake increases, variation in the ductility demands of the asymmetric structure walls becomes closer to that of the symmetric structure. In general, the stiffness eccentricity, in contrast to the displacement response of walls, affects the ductility demand of asymmetric structure walls and

increases the ductility demands in stiff structural elements. By increasing the diaphragm flexibility, the ductility demands of the LLREs are also reduced.

In Figures 14(a), 14(b), and 14(c), respectively, the mean of maximum displacement of walls 1 (weak side), 2 (central), and 3 (strong side) for model 2 (which has strength eccentricity and stiffness symmetry) is shown for different degrees of flexibility ( $T_d$ ). The first and second rows respectively represent the results of nonlinear analyses in the DBE and MCE earthquakes. In all the diagrams, displacements of the corresponding walls in the symmetric structure (model 1) are also presented for comparison.

As shown, the overall responses of asymmetric structures are similar to the responses of symmetric structures. In contrast to structures with stiffness eccentricity, in this group of structures, flexibility has a significant effect on the displacement of the end walls. In this model, the weak side wall shows more displacements than similar symmetric structure, and the opposite is true for the strong side wall. Also, by increasing the diaphragm flexibility or the intensity of the earthquake (the yield level of elements), the effect of strength eccentricity will not be diminished on the displacement of structure walls, so that, in structures with a very flexible diaphragm, the effect of the strength eccentricity on the displacement of the walls is quite significant.

The mean of maximum ductility demand for end walls of model 2 (which has strength eccentricity and stiffness symmetry) in DBE and MCE for different degrees of flexibility ( $T_d$ ) is shown in Figures 15(a) and 15(b), respectively.

Generally, by increasing the diaphragm flexibility, the ductility demands of the walls in the asymmetric structure decrease. As shown, the weak side wall of the asymmetric structure (wall 1) experiences more ductility demands than

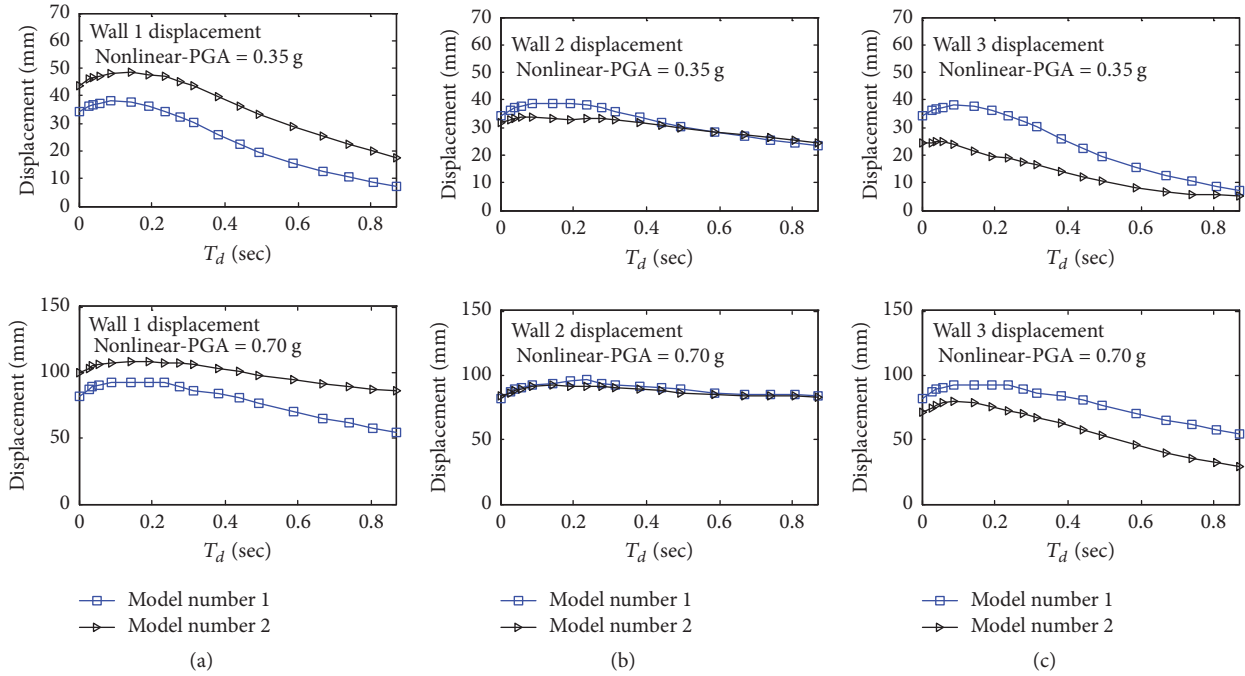


FIGURE 14: Walls displacements of model 2 in DBE and MCE earthquakes: (a) wall 1 (left side, weak), (b) wall 2 (central), and (c) wall 3 (right side, strong).

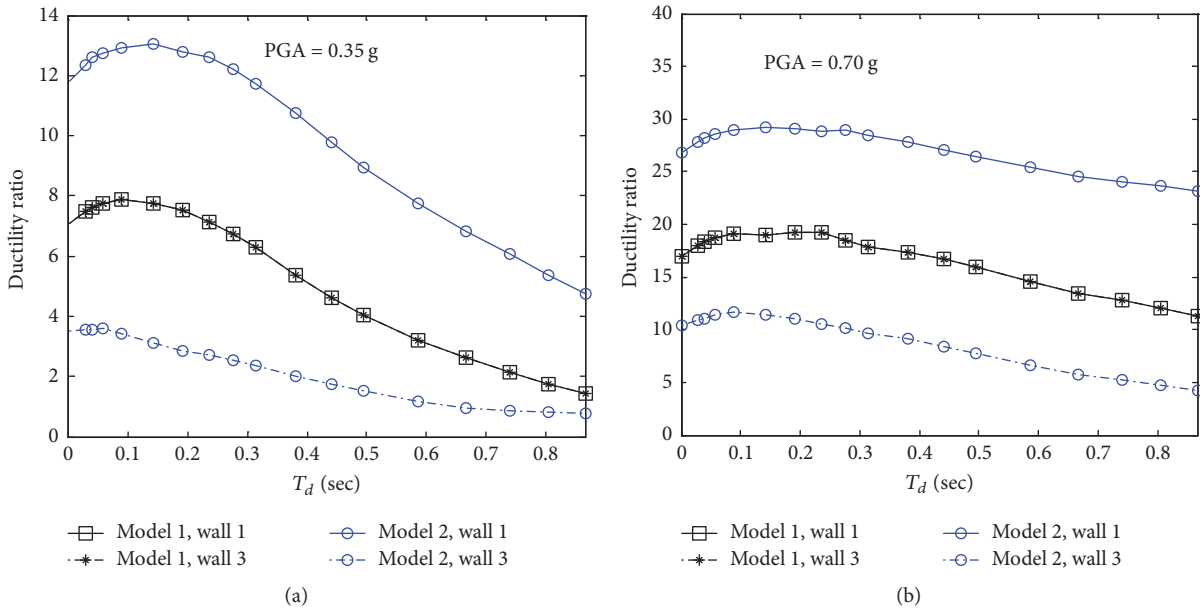


FIGURE 15: Ductility demands of weak (wall 1) and strong (wall 3) walls of model 2: (a) DBE earthquake (0.35 g) and (b) MCE earthquake (0.70 g).

symmetric structures, while the ductility demands in the strong side wall (wall 3) are less than that in the symmetric structure. A comparison of Figures 13 and 15 clearly shows that the influence of the strength eccentricity is much greater than that of the stiffness eccentricity on the displacement of walls in structures with flexible diaphragms. In structures

with a very flexible diaphragm, the influence of strength eccentricity in the ductility demands of walls is clearly significant. As the intensity of the earthquake increases, the variation in the ductility demand of the asymmetric structure walls becomes closer to that of the symmetric structure. Contrary to the structures with stiffness eccentricity,

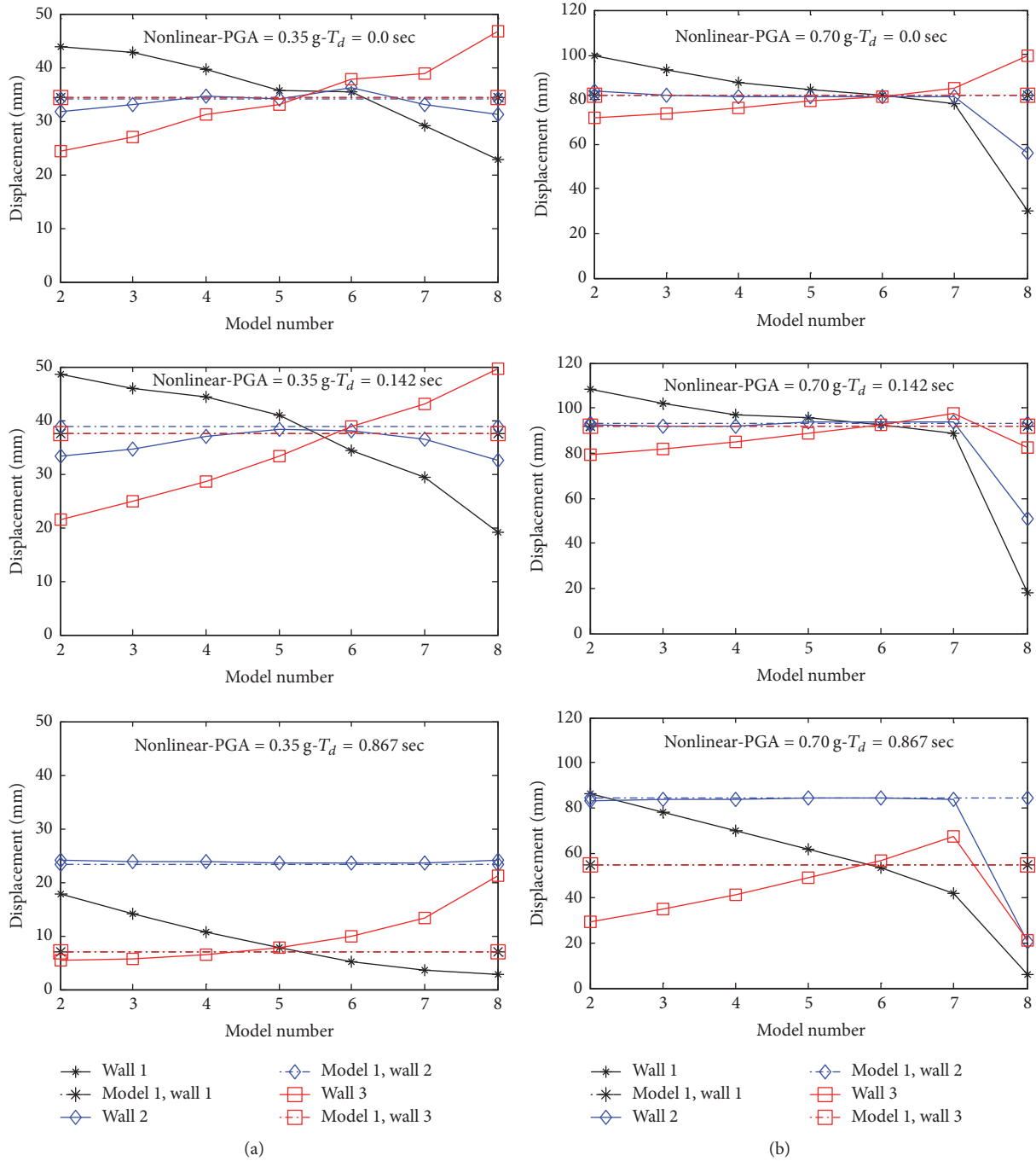


FIGURE 16: The mean of maximum displacements of walls in asymmetric structures: (a) DBE earthquakes (0.35 g) and (b) MCE earthquakes (0.70 g).

in structures with strength eccentricity, ductility demands converge less by increasing the flexibility, indicating a greater concentration of damage in the weak wall of the asymmetric structure.

5.4. Proper Configuration of Stiffness and Strength Centers in Structures with Flexible Diaphragm. The mean of the maximum displacement for walls of asymmetric models in DBE

and MCE earthquakes is shown in Figures 16(a) and 16(b), respectively. The first row graphs refer to a completely rigid diaphragm structures ( $T_d = 0.0$  sec), the second row belongs to a semirigid diaphragm structure ( $T_d = 0.142$  sec), and the third row is for structures with quite a flexible diaphragm ( $T_d = 0.867$  sec). The displacement of the corresponding walls in the symmetric structures (model 1) is presented in the form of a dashed line and for comparison. The horizontal axis

represents the number of structure models and displacements are presented only for the main walls that are exposed to seismic loads.

As shown in Figure 16(a), for DBE earthquakes in structures with a rigid diaphragm, the optimal configuration for reducing the mean displacement of all walls is related to model 5. This model has a balance configuration in which the center of the mass is located between stiffness and strength centers and the strength eccentricity is equal to one-quarter yield eccentricity. This conclusion is consistent with the findings of Aziminejad and Moghadam [26]. Considering other diagrams of Figure 16(a), which is related to structures with flexible diaphragms, it was observed that the degree of flexibility affects the optimal configuration. By increasing the flexibility from  $T_d = 0.0$  sec to  $T_d = 0.142$  sec, the best configuration of the centers moves from models 5 to 6, and then with increasing flexibility from  $T_d = 0.142$  sec to  $T_d = 0.867$  sec, the optimal configuration continuously returns to model 5. As seen in the structure with quite flexible diaphragm ( $T_d = 0.867$  sec), model 5 is the best configuration for minimizing the displacement of walls.

Another important point is that, in structures with a flexible diaphragm, the presence of only balance configuration cannot reduce the displacement of walls. Models 3 and 4, despite the presence of balance configuration, showed almost the same responses or even worse than the responses of model 7, which has no balance condition.

In MCE earthquakes, the optimal configuration of the centers is somewhat different for displacement of the walls. As shown in Figure 16(b), in structures with a rigid diaphragm, model 6 (which has strength symmetry) is considered as the optimal model. The displacement of walls in this model is consistent with that of the symmetric structure. This result is in accordance with the findings of Aziminejad and Moghadam [26]. With increase in the flexibility, while the responses of model 6 have a major similarity to symmetric structures in almost all the degrees of flexibility, in the flexibility of  $T_d = 0.142$  sec and higher values, model 8 offers displacements even less than that of the symmetric model. Therefore, this configuration can be considered as optimal configuration for the displacement of walls.

The mean of maximum ductility demand for walls of the asymmetric model in DBE and MCE earthquakes is shown in Figures 17(a) and 17(b), respectively.

As shown, in DBE earthquakes for a structure with a rigid diaphragm, the best configuration to reduce the ductility demand is the configuration of centers in model 8. By increasing the flexibility, the optimal configuration moves towards model 6, so that in structures having quite a flexible diaphragm with  $T_d = 0.867$  sec, model 6 is the best configuration of centers. The conditions in the MCE earthquakes vary slightly. In structures with a rigid diaphragm, the best configuration is between models 7 and 8, while by increasing the flexibility, the optimum configuration moves to model 8. For flexibilities more than  $T_d = 0.142$  sec, model 8 is considered as the best configuration for minimizing the walls ductility demands.

## 6. Conclusion

In this article, the effects of diaphragm flexibility on plan-asymmetric structures subjected to far-field ground motions are studied. A wide range of diaphragm flexibility in single-story models with different configurations of mass, stiffness, and strength centers were considered. The analytical study resulted in the following major conclusions:

(1) By increasing the diaphragm flexibility, the intensities of rigid modes of diaphragms deformation are reduced, and bending and, especially, shear-dominant deformations grow. This clearly demonstrates changes in the mechanism of seismic forces absorption by asymmetric structure with a flexible diaphragm. Moreover, the concentration of shear-dominant deformations in some diaphragms of the plan-asymmetric structures is one of the most important weaknesses of these structures.

(2) Based on the shear deformation of the structure diaphragms, it is possible to qualitatively classify the behavior of asymmetric structures with various degrees of flexibility. This classification actually represents the single or coordinated function of the structural elements at various levels of diaphragm flexibility.

(3) Generally, increasing the diaphragm flexibility reduces the displacement and ductility demands of the LLREs in both symmetric and asymmetric structures. The changes observed in structural demands with diaphragm flexibility are strongly related to the considered ground motions. According to the acceleration response spectra of earthquakes records, rigid diaphragm models are put into the resonance region and, in contrast, their very flexible diaphragm structures fall in the descending branch of the spectra; this explains why those demands are considerably reduced.

(4) The effect of strength eccentricity on the demands of lateral walls is much greater than that of the stiffness eccentricity. High ductility demands in weak walls of structures with strength eccentricity indicate the concentration of more damage in these elements even in structures with quite flexible diaphragms.

(5) The proper configuration of centers in asymmetric structures with flexible diaphragm depends on three factors: degree of diaphragm flexibility, yield level of elements (earthquake intensity), and selected engineering demand parameter. In general, the proper configuration of centers in structures with flexible diaphragm is very similar to that in structures with a rigid diaphragm.

While this study focused on structures with concrete shear walls, the results can be used for other types of structures with different degrees of diaphragm flexibility. Also, it is expected that the general results of this study can be applicable in low-rise buildings because it is possible to ignore the participation of higher modes in these structures [19].

## Conflicts of Interest

The authors declare that they have no conflicts of interest.

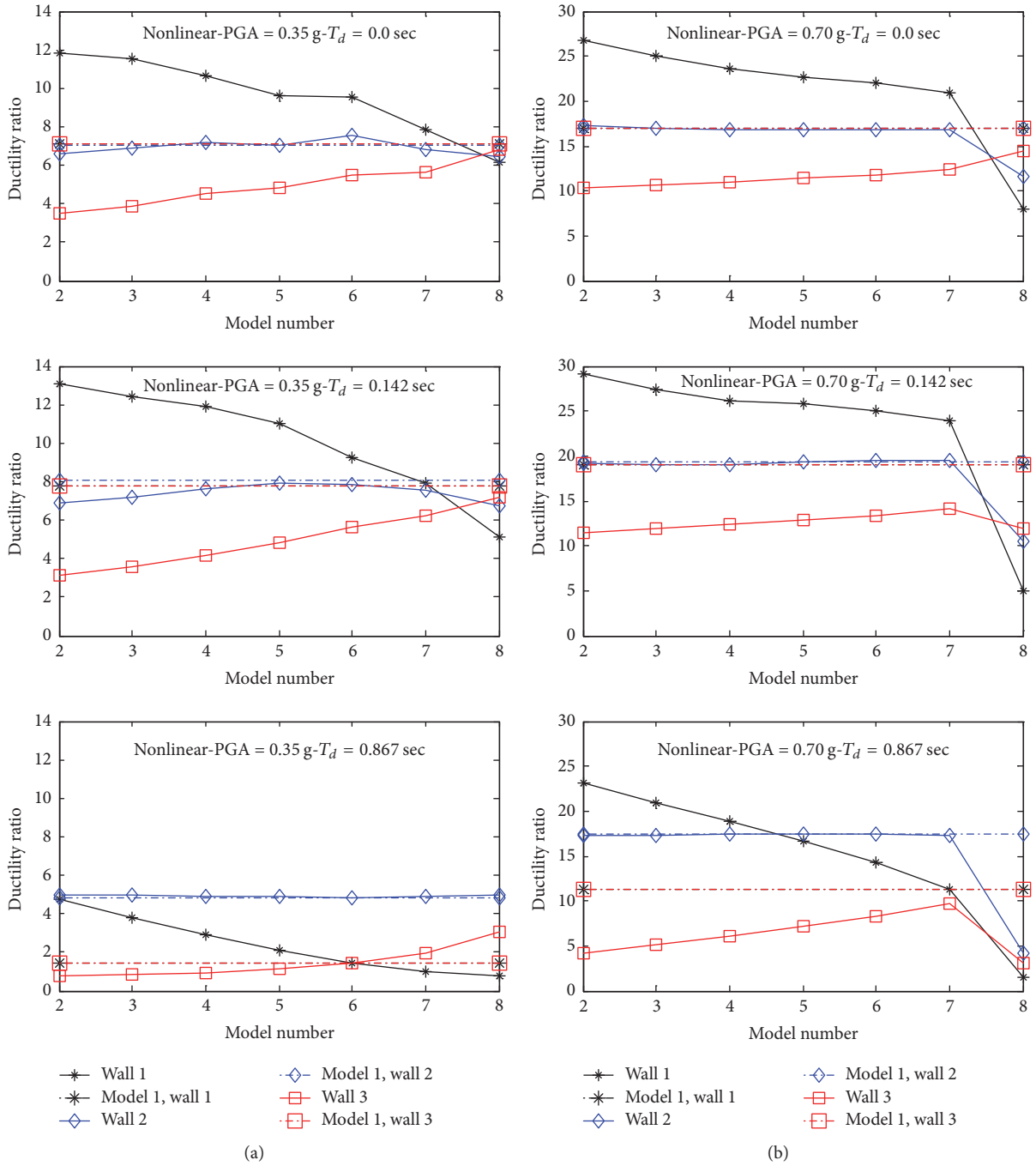


FIGURE 17: The mean of maximum ductility demands of walls in asymmetric structures: (a) DBE earthquake (0.35 g) and (b) MCE earthquake (0.70 g).

**References**

[1] S. K. Kunnath, N. Panahshahi, and A. M. Reinhorn, "Seismic response of RC buildings with inelastic floor diaphragms," *Journal of Structural Engineering (United States)*, vol. 117, no. 4, pp. 1218–1237, 1991.

[2] S. H. Ju and M. C. Lin, "Comparison of building analyses assuming rigid or flexible floors," *Journal of Structural Engineering*, vol. 125, no. 1, pp. 25–31, 1999.

[3] V. K. Sadashiva, G. A. Macrae, B. L. Deam, and M. S. Spooner, "Quantifying the seismic response of structures with flexible diaphragms," *Earthquake Engineering & Structural Dynamics*, vol. 41, no. 10, pp. 1365–1389, 2012.

[4] A. K. L. Damian, C. T. Bia, O. Gosa, H. Maniu, and C. S. Dico, "Diaphragm behaviour of the floor with prestressed beam and filler blocks," in *Proceedings of the 12th World Conference on Earthquake Engineering (WCEE 12)*, Paper No. 0696, Auckland, New Zealand, February 2000.

- [5] E. R. Mario, S. Santiago, and R. Meli, "Seismic load tests on two-story waffle-flat-plate structure," *Journal of Structural Engineering (United States)*, vol. 121, no. 9, pp. 1287–1293, 1995.
- [6] A. Tena-Colunga, K. L. Chinchilla-Portillo, and G. Juárez-Luna, "Assessment of the diaphragm condition for floor systems used in urban buildings," *Engineering Structures*, vol. 93, pp. 70–84, 2015.
- [7] M. A. Hadianfard and S. Sedaghat, "Investigation of joist floor diaphragm flexibility on inelastic behavior of steel braced structures," *Scientia Iranica*, vol. 20, no. 3, pp. 445–453, 2003.
- [8] J. De-La-Colina, "In-plane floor flexibility effects on torsionally unbalanced systems," *Earthquake Engineering & Structural Dynamics*, vol. 28, no. 12, pp. 1705–1715, 1999.
- [9] O. A. López and E. Raven, "An Overall Evaluation of Irregular-Floor-Plan—Shaped Buildings Located in Seismic Areas," *Earthquake Spectra*, vol. 15, no. 1, pp. 105–120, 1999.
- [10] P. Somers, D. Campi, W. Holmes, B. E. Kehoe et al., "Unreinforced masonry buildings," *Earthquake Spectra*, vol. 12, no. S1, pp. 195–217, 1996.
- [11] R. Shepherd, W. T. Holmes, B. Lizundia et al., "Buildings," *Earthquake Spectra*, vol. 6, no. S1, pp. 127–149, 1990.
- [12] H. S. Saffarini and M. M. Qudaimat, "In-plane floor deformations in RC structures," *Journal of Structural Engineering (United States)*, vol. 118, no. 11, pp. 3089–3102, 1992.
- [13] S.-K. Moon and D.-G. Lee, "Effects of inplane floor slab flexibility on the seismic behaviour of building structures," *Engineering Structures*, vol. 16, no. 2, pp. 129–144, 1994.
- [14] H. J. Lee, M. A. Aschheim, and D. Kuchma, "Interstory drift estimates for low-rise flexible diaphragm structures," *Engineering Structures*, vol. 29, no. 7, pp. 1375–1397, 2007.
- [15] R. B. Fleischman and K. T. Farrow, "Dynamic behavior of perimeter lateral-system structures with flexible diaphragms," *Earthquake Engineering & Structural Dynamics*, vol. 30, no. 5, pp. 745–763, 2001.
- [16] G. Magenes, A. Penna, I. E. Senaldi, M. Rota, and A. Galasco, "Shaking table test of a strengthened full-scale stone masonry building with flexible diaphragms," *International Journal of Architectural Heritage*, vol. 8, no. 3, pp. 349–375, 2014.
- [17] I. Senaldi, G. Magenes, A. Penna, A. Galasco, and M. Rota, "The effect of stiffened floor and roof diaphragms on the experimental seismic response of a full-scale unreinforced stone masonry building," *Journal of Earthquake Engineering*, vol. 18, no. 3, pp. 407–443, 2014.
- [18] S.-C. Kim and D. W. White, "Nonlinear analysis of a one-story low-rise masonry building with a flexible diaphragm subjected to seismic excitation," *Engineering Structures*, vol. 26, no. 14, pp. 2053–2067, 2004.
- [19] Y. Nakamura, H. Derakhshan, G. Magenes, and M. C. Griffith, "Influence of Diaphragm Flexibility on Seismic Response of Unreinforced Masonry Buildings," *Journal of Earthquake Engineering*, vol. 21, no. 6, pp. 935–960, 2017.
- [20] T. Paulay, "Seismic response of structural walls: Recent developments," *Canadian Journal of Civil Engineering*, vol. 28, no. 6, pp. 922–937, 2001.
- [21] M. J. N. Priestley and M. J. Kowalsky, "Aspects of drift and ductility capacity of rectangular cantilever structural walls," *Bulletin of the New Zealand National Society for Earthquake Engineering and Structural Dynamics*, vol. 31, no. 2, pp. 73–85, 1998.
- [22] T. Paulay, "Seismic torsional effects on ductile structural wall systems," *Journal of Earthquake Engineering*, vol. 1, no. 4, pp. 721–745, 1997.
- [23] W. K. Tso and R. S. H. Smith, "Re-evaluation of seismic torsional provisions," *Earthquake Engineering & Structural Dynamics*, vol. 28, no. 7–8, pp. 899–917, 1999.
- [24] T. Paulay, "Some design principles relevant to torsional phenomena in ductile buildings," *Journal of Earthquake Engineering*, vol. 5, no. 3, pp. 273–308, 2001.
- [25] W. K. Tso and B. Myslimaj, "Effect of strength distribution on the inelastic torsional response of asymmetric structural systems," in *Proceedings of the 12th European Conference on Earthquake Engineering*, Paper No. 081, London, UK, September 2002.
- [26] A. Aziminejad and A. S. Moghadam, "Fragility-based performance evaluation of asymmetric single-story buildings in near field and far field earthquakes," *Journal of Earthquake Engineering*, vol. 14, no. 6, pp. 789–816, 2010.
- [27] Iranian national building code, *Part 6. Design Loads for Buildings*, Building and Housing Research Center, Tehran, Iran, 2013.
- [28] Standard No. 2800, *Iranian Code of Practice for Seismic Resistant Design of Buildings*, Building and Housing Research Center, Tehran, Iran, 2014.
- [29] A. Rutenberg, "EAEE task group 8: Behaviour of irregular and complex structures: progress since 1998," in *Proceedings of the 12th European Conference on Earthquake Engineering*, Paper No. 832, London, UK, September 2002.
- [30] B. Myslimaj and W. K. Tso, "A strength distribution criterion for minimizing torsional response of asymmetric wall-type systems," *Earthquake Engineering & Structural Dynamics*, vol. 31, no. 1, pp. 99–120, 2002.
- [31] B. Myslimaj and W. K. Tso, "A design-oriented approach to strength distribution in single-story asymmetric systems with elements having strength-dependent stiffness," *Earthquake Spectra*, vol. 21, no. 1, pp. 197–212, 2005.
- [32] M. De Stefano, G. Faella, and R. Ramasco, "Inelastic response and design criteria of plan-wise asymmetric systems," *Earthquake Engineering & Structural Dynamics*, vol. 22, no. 3, pp. 245–259, 1993.
- [33] ASCE/SEI 7-10, *Minimum Design Loads for Buildings and Other Structures*, American Society of Civil Engineers, Reston, Va, US, 2010.
- [34] M. Silvia, M. Frank, and H. Michael, *Open System for Earthquake Engineering Simulation User Manual*, Pacific Earthquake Engineering Research Center, University of California, Berkeley, Calif, USA, 2005.
- [35] S. Mazzoni, F. McKenna, and G. L. Fenves, *OpenSees Command Language Manual*, Pacific Earthquake Engineering Center, University of California, Berkeley, Calif, USA, 2005.
- [36] M. J. N. Priestley, G. M. Calvi, and M. J. Kowalsky, *Displacement-Based Seismic Design of Structures*, IUSS Press, Pavia, Italy, 2007.
- [37] E. M. Rathje, C. Dawson, J. E. Padgett et al., "DesignSafe: new cyberinfrastructure for natural hazards engineering," *Natural Hazards Review*, vol. 18, no. 3, 2017.

## Research Article

# Lateral Torsional Buckling of Steel Beams under Transverse Impact Loading

Wenna Zhang <sup>1,2</sup>, Feng Liu,<sup>3</sup> and Feng Xi <sup>2</sup>

<sup>1</sup>Research Institute of Structural Engineering and Disaster Reduction, Tongji University, Shanghai 200092, China

<sup>2</sup>School of Civil Engineering, Shandong Jianzhu University, Jinan 250101, China

<sup>3</sup>Shandong University of Science and Technology,

Shandong Provincial Key Laboratory of Civil Engineering Disaster Prevention and Mitigation, Qingdao 266590, China

Correspondence should be addressed to Feng Xi; [xifeng@sdjzu.edu.cn](mailto:xifeng@sdjzu.edu.cn)

Received 12 July 2017; Revised 8 November 2017; Accepted 6 December 2017; Published 3 January 2018

Academic Editor: Hugo Rodrigues

Copyright © 2018 Wenna Zhang et al. This is an open access article distributed under the Creative Commons Attribution License, which permits unrestricted use, distribution, and reproduction in any medium, provided the original work is properly cited.

This study employs experiments and numerical simulation to analyze the dynamic response of steel beams under huge-mass impact. Results show that lateral torsional buckling (LTB) occurs for a narrow rectangular cross-section steel beam under transverse impact. The experiments were simulated using LS-DYNA. The numerical simulation is in good agreement with experimental results, thus indicating that the LTB phenomenon is the real tendency of steel beams under impact. Meanwhile, the study shows that LS-DYNA can readily predict the LTB of steel beams. A numerical simulation on the dynamic response of H-shaped cross-section steel beams under huge-mass impact is conducted to determine the LTB behavior. The phenomenon of dynamic LTB is illustrated by displacement, strain, and deformation of H-shaped steel beams. Thereafter, a parametric study is conducted to investigate the effects of initial impact velocity and momentum on LTB. The LTB of H-shaped cross-section steel beams under transverse impact is primarily dependent on the level of impact kinetic energy, whereas impact momentum has a minor effect on LTB mode.

## 1. Introduction

Beams and columns of special steel frame structures should withstand not only normal design load but also explosion, impact, collision, fire, and other extreme loads during the period of service. Hence, the dynamic response and failure behavior of steel members under these extreme loads need to be studied. In fact, explosion and shock have often been associated with fire. Therefore, the effect of the interaction between the structure under impact load and fire needs to be investigated.

Stability is a potent issue in the design of steel structures. Bad stability of steel components may cause serious structural failure. Lateral torsional buckling of a component is a very common type of instability that needs further investigation [1]. Lateral torsional buckling (overall instability) of steel beams under static loads can be described as follows [2]: when steel beams, without lateral support in the net span, are subjected to a certain value of transverse load or moment about the major-axis, a large lateral displacement  $u$  and

twist angle  $\theta$  occur as shown in Figure 1. Then, the beam loses its carrying capacity. Obviously, out-of-plane buckling analysis is more difficult than analysis of in-plane bending buckling. However, a number of studies have been conducted based on elastic buckling theory, particularly experimental studies and theoretical analysis [3] on lateral torsional buckling of steel beams under static load. Yang et al. carried out experimental tests and numerical simulations on lateral torsional buckling behavior of singly symmetric I-beams fabricated from Q460GJ steel [4, 5]. Their results showed that steel beams developed lateral torsional buckling under concentrated point loads at the mid-span. Hence, local buckling was not observed. Karmazínová et al. [6] studied the lateral flexural-torsional buckling of steel sigma-cross-section beams with web holes. Their study conclusions became the background of the supplements to specified provisions for the design of steel structures. Kala and Valeš [7] examined a hot-rolled steel I-beam subjected to lateral torsional buckling (LTB) due to bending moment and obtained the stochastic effects of initial imperfection and residual

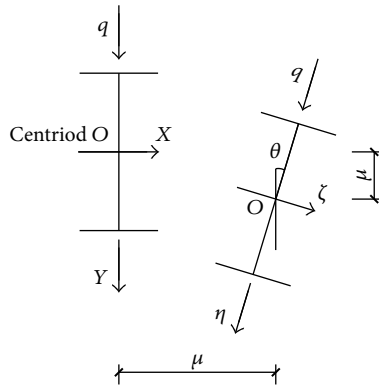


FIGURE 1: LTB of H-shaped steel beams.

stress on the resistance of the investigated steel beam. The development of numerical methods, such as finite element (FE), has facilitated research on lateral torsional buckling of steel beams from experimental studies to numerical analysis [8–10]. Moreover, research on the fire resistance of steel structures has made great progress [11]. Lateral torsional buckling problem of steel beams under fire has been given considerable attention [12–14]. This problem is due to the substantial number of the torsional buckling modes of steel beam during fire accidents. A steel structure can endure fire for a very long time. Hence, analysis of structures under fire can be regarded as a static problem. When structures are subjected to fire, elevated temperature causes degradation of material properties and triggers plastic deformation of the structure. Thus, elastic buckling theory is not suitable anymore. Therefore, numerical simulation is an effective research method to deal with inelastic buckling problems. For example, Vila Real et al. [15, 16] performed a numerical study and proposed a design curve for the LTB of steel beams. Yin and Wang [17] have numerically investigated the effects of several design factors on lateral torsional buckling bending moment resistance of steel I-beams submitted to nonuniform temperature distribution. Couto et al. [18] studied the lateral torsional buckling of beams with slender cross-sections in the case of fire using a numerical method.

Whether LTB behavior occurs when steel beam is subjected to the combined action of impact and fire loading is difficult to determine because of the complexity of two-load interaction effects. In addition, LTB occurrence on the steel beam when it is only subjected to impact is difficult to investigate because impact load affects the plastic buckling of beams whereas the inertial effect may delay or avoid plastic buckling. On one hand, steel is a rate sensitive material meaning that the yield strength of steel can be improved because of the strain rate effect. Hence, the strain rate effect of steel may lead to the occurrence of elastic LTB. These complex factors hinder the full understanding of LTB behavior of steel beams under impact. In recent years, several studies were conducted on the dynamic response of steel members under impact. The drop weight impact test of clamped steel beams struck transversely at the center by a mass with a rectangular indenter was conducted by Villavicencio and Guedes Soares [19] to define

the proper boundary conditions of impacted beams. Wang et al. [20] studied the dynamic behavior of steel beams with fin-plate connections subjected to falling floor impact loads. The results show that steel beams show dynamic behaviors under a certain impact energy with varying impact masses and velocities. A higher impact velocity can slightly improve the energy dissipation rate. Steel beams develop different impact resistances while impact loads are applied at various locations. Al-Thairy and Wang [21] examined the behavior and failure modes of axially compressed steel columns subject to transverse impact by a rigid mass at varying impact speeds and locations. Ning and Zhao [22, 23] completed the experimental study on the stability of aluminum alloy cantilever high beams under cylinder head impact. However, studies on LTB of steel beams under impact load are lacking.

Above all, systemic research on LTB of steel beams under impact load is necessary. This article is a preliminary attempt of related studies. This paper presents the experimental results of the LTB of rectangular section steel beams under drop hammer impact. Afterwards, the LTB behavior of rectangular section and H-shaped steel beams under impact is discussed.

## 2. Experimental Test Introduction

The drop weight test of steel beams was carried out by setting up a DHR9401 drop hammer test machine. The overall height of the DHR9401 drop hammer test machine is about 13.47 m above the floor and its impact velocity is up to 15.70 m/s. Figure 2 shows the components of the drop hammer test machine. The impact hammer comprises several main components. The first piece is a toughened flat head which is 80 mm long and 30 mm thick and made from high-strength chromium 15 (64HRC) as shown in Figure 3. The second component of the striker is the weight element. This component contains the main mass of the striker and delivers a variety of striker weights from 2 to 250 kg. The third part of the striker is load cells. The overall weight of the impact hammer is 57.8 kg and can be raised to the required height to produce varied impact velocities (up to 15.7 m/s) and energies [24].

Rolled steel plates (Q235) were selected to make the specimens. The specimens were classified according to the thickness of the beam: #A:  $5 \times 50 \times 1250 \text{ mm}^3$ , #B:  $5 \times 70 \times 1250 \text{ mm}^3$ , and #C:  $5 \times 100 \times 1250 \text{ mm}^3$ . The effective spans of steel beams were 500, 750, and 1000 mm, as shown in Figure 4.

Table 1 shows the dimensions of steel beams. The constraints of steel beams were implemented by the length of the reserved. Two supports were fixed on both ends of the experimental platforms. Bolts flank the support side to implement lateral fixation. The rotation constraint was fixed by a steel cover plate as shown in Figure 5. The material properties of the specimens are determined from standard static tensile coupon tests which have been carried out by a CM5105A computer-controlled electronic omnipotence test machine. The experiment was repeated 3 times and the data averaged. Figure 6 shows the stress-strain curve of the steel.

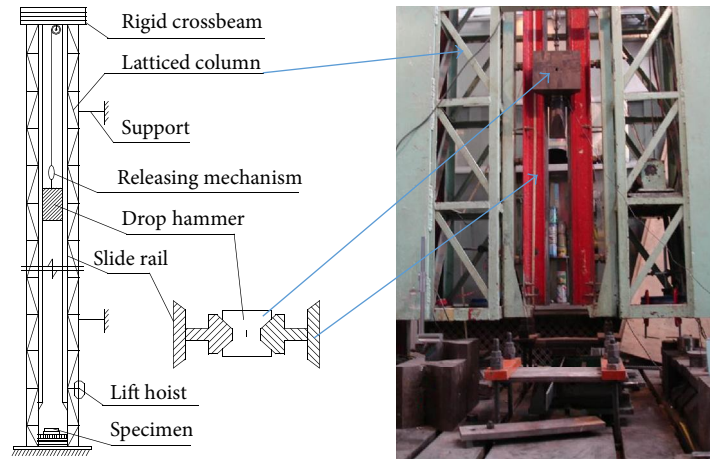


FIGURE 2: DHR9401 drop hammer test machine.

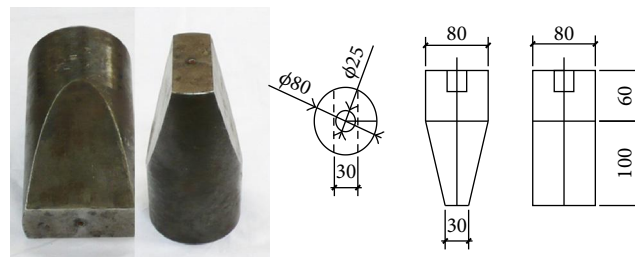


FIGURE 3: Shape and size of drop hammer.

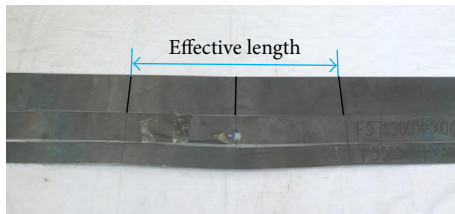


FIGURE 4: Test specimens.

The modulus of elasticity and yield stress of the steel beams are 185 GPa and 315 MPa, respectively.

### 3. Experimental Test Results

**3.1. General Results.** In these tests, the ultimate deformation modes and lateral and vertical deflections on mid-span of beams were recorded. Then, the influence of section properties, height–width ratio, length–height ratio, and impact velocity on the ultimate deformation modes was studied. Table 2 shows the results of the test specimens, where  $H_I$  is the impact height,  $D_V$  is the vertical displacement,  $D_L$  is the lateral displacement, and  $V_0$  is the initial impact velocity.

In Table 2, it is noticed that the lateral and vertical deflections increase with the increase in impact velocity. It is also observed that the deformation of beams is influenced by

the height–width and length–height ratio. The length–height ratio varied at a range of 10 and 20 of specimens A1-3 and A3-1, while the impact velocity is 3.13 m/s and height–width ratio is 10. The lateral displacements of specimens A1-3 and A3-1 are 0.9 and 21.78 mm, respectively. The vertical displacements of specimens A1-3 and A3-1 are 9.82 and 20.4 mm. Thus, the deformation of the beams is proportional to the length–height ratio. The height–width ratio varies at a range of 10, 14, and 20 of specimens A3-3, B3-2, and C3-2 whereas the impact velocity is 5.42 m/s and length–height ratio is 20. The lateral displacements of specimens A3-3, B3-2, and C3-2 are 75.1, 51.3, and 17.6 mm, respectively. The vertical displacements of specimens A3-3, B3-2, and C3-2 are 94.4, 46.36, and 18.14 mm, respectively. Thus, the deformation of the beams is inversely proportional to the height–width ratio. Moreover, the ultimate deformation modes of beams are influenced by section properties, height–width and length–height ratios, and impact velocity.

**3.2. Ultimate Deformation Modes.** Figure 7 shows the ultimate deformation modes of specimen #A1 for various velocities. Specimen A1-1 has noticeable in-plane deformation without the lateral displacements on twists. The local deformation of specimens A1-2 and A1-3 has been found without the LTB. When impact velocity reaches 4.43 m/s, in specimens A1-4 and A1-5, the LTB occurs. At the same time, specimen A1-5 has a risen deformation. The experimental

TABLE 1: Specifications of test specimens.

Specimen number	Geometry size ( $B \times H \times L$ ) ( $\text{mm}^3$ )	Height-width ratio $\alpha = H/B$	Length-height ratio $\beta = L/H$
#A1	$5 \times 50 \times 500$	10	10
#A2	$5 \times 50 \times 750$	10	15
#A3	$5 \times 50 \times 1000$	10	20
#B1	$5 \times 70 \times 500$	14	10
#B3	$5 \times 70 \times 1000$	14	20
#C1	$5 \times 100 \times 500$	20	10
#C2	$5 \times 100 \times 750$	20	15
#C3	$5 \times 100 \times 1000$	20	20

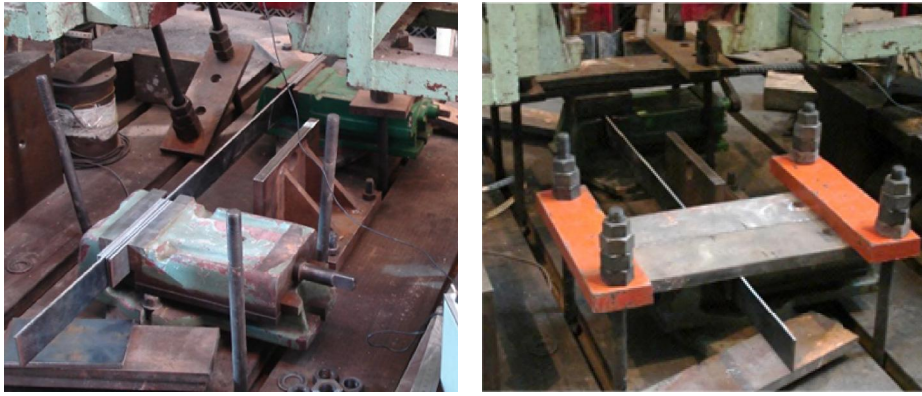


FIGURE 5: Boundary conditions of the experiment.

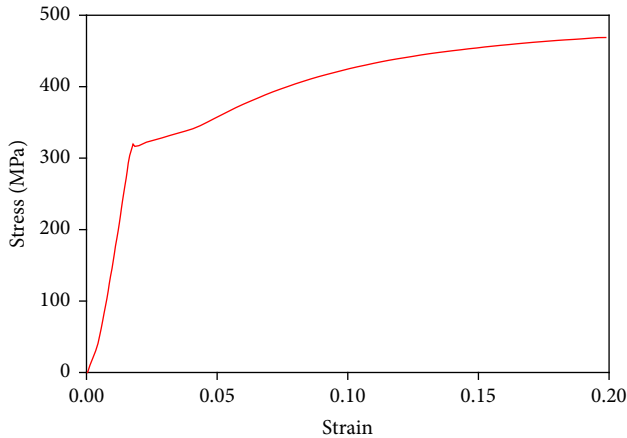


FIGURE 6: Stress-strain curve.

results show that LTB occurs for rectangular section steel beams under transverse impact. This LTB phenomenon is mainly influenced by the impact velocity. It can be seen that the LTB critical velocity of A1 must be between 3.13 and 4.43 m/s.

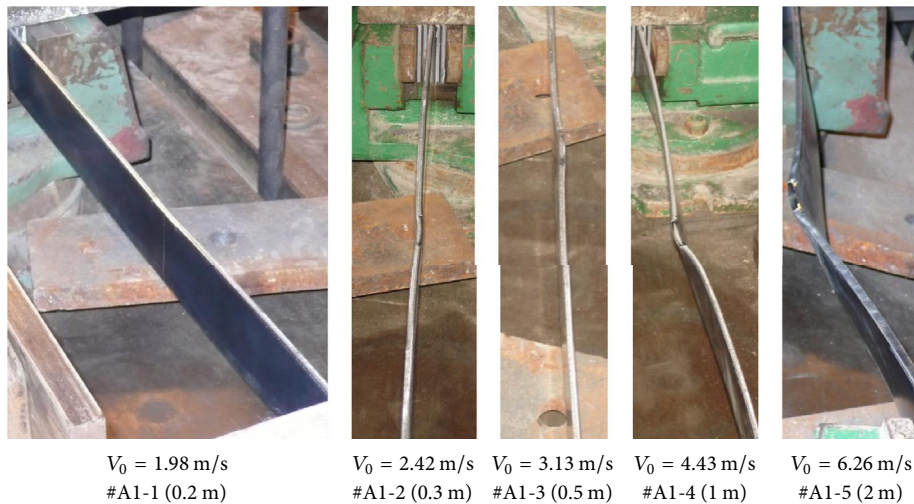
Figure 8 shows the ultimate deformation modes of specimen #A2 with different velocities of 4.43, 5.42, and 6.26 m/s. Specimens A2-1, A2-2, and A2-3 all show LTB behavior. In

the meantime, the deformation of #A2 increases with the increase of the impact velocity. Figure 9 shows the ultimate deformation modes of specimen #A3. Specimen #A3 also has the LTB behavior. The LTB deformation of #A3-1 is mainly the out-of-plane bending deformation. The torsion deformation of #A3-1 is relatively small. From the ultimate deformation modes of A1-4, A2-1, and A3-2, it can be observed that the length-height ratio has a considerable influence on LTB modes.

Figure 10 shows the ultimate deformation modes of specimen #B1 for various velocities. When the impact velocity is 3.13 m/s, specimen B1-1 has an in-plane deformation without the lateral displacements on twists. Specimen B1-2 has an out-plane deformation with an impact velocity of 4.43 m/s. When the impact velocity reaches 5.42 and 6.26 m/s, specimens B1-3 and B1-4 have the behavior of LTB with flexural buckling as the main deformation. When the impact velocity reaches 7 and 7.67 m/s, specimens B1-5 and B1-6, respectively, have different LTB modes with torsional deformation. Once again, it can be observed that the impact velocity has a considerable influence on the deformation of beams. Figure 11 shows the ultimate deformation modes of specimen #B3 with different velocities. It can be seen that specimen B3-1 presents the flexural-torsional buckling behavior with flexural buckling as the main deformation. When the impact velocity reaches 5.42 and 6.26 m/s, the beam presents various LTB modes.

TABLE 2: Numbers and test results of specimens.

Specimen number	$H_I$ (m)	$\alpha$	$\beta$	$V_0$ (m/s)	$D_V$ (mm)	$D_L$ (mm)	Deformation mode
#A1-1	0.2	10	10	1.98	4.10	0.98	In-plane bending
#A1-2	0.3	10	10	2.42	5.86	0.80	Local deformation
#A1-3	0.5	10	10	3.13	9.82	0.90	Local deformation
#A1-4	1.0	10	10	4.43	21.74	9.50	LTB
#A1-5	2.0	10	10	6.26	46.10	20.88	LTB
#A2-1	1.0	10	15	4.43	45.46	47.56	LTB
#A2-2	1.5	10	15	5.42	84.03	61.60	LTB
#A2-3	2.0	10	15	6.26	117.8	59.40	LTB
#A3-1	0.5	10	20	3.13	20.40	21.78	LTB
#A3-2	1.0	10	20	4.43	42.48	36.10	LTB
#A3-3	1.5	10	20	5.42	94.40	75.10	LTB
#B1-1	0.5	14	10	3.13	5.36	–	In-plane bending
#B1-2	1.0	14	10	4.43	5.52	0.80	Local deformation
#B1-3	1.5	14	10	5.42	9.72	0.80	LTB
#B1-4	2.0	14	10	6.26	22.16	6.66	LTB
#B1-5	2.5	14	10	7.00	33.60	–	LTB
#B1-6	3.0	14	10	7.76	41.60	–	LTB
#B3-1	1.0	14	20	4.43	24.20	21.30	LTB
#B3-2	1.5	14	20	5.42	46.36	51.30	LTB
#B3-3	2.0	14	20	6.26	80.10	67.70	LTB
#C1-1	0.5	20	10	3.13	3.22	–	LTB
#C1-2	1.0	20	10	4.43	4.97	–	LTB
#C1-3	2.0	20	10	6.26	10.26	–	LTB
#C1-4	2.5	20	10	7.00	11.92	1.60	LTB
#C2-1	1.0	20	15	4.43	7.10	3.40	LTB
#C2-2	1.5	20	15	5.42	10.94	3.40	LTB
#C2-3	2.0	20	15	6.26	16.56	2.06	LTB
#C3-1	1.0	20	20	4.43	10.44	9.72	LTB
#C3-2	1.5	20	20	5.42	18.14	17.60	LTB
#C3-3	2.0	20	20	6.26	26.14	4.90	LTB

FIGURE 7: Deformation modes of #A1 ( $\alpha = 10, \beta = 10$ ).



$V_0 = 4.43 \text{ m/s}$     $V_0 = 5.42 \text{ m/s}$     $V_0 = 6.26 \text{ m/s}$   
 #A2-1 (1 m)   #A2-2 (1.5 m)   #A2-3 (2 m)

FIGURE 8: Deformation modes of #A2 ( $\alpha = 10, \beta = 15$ ).



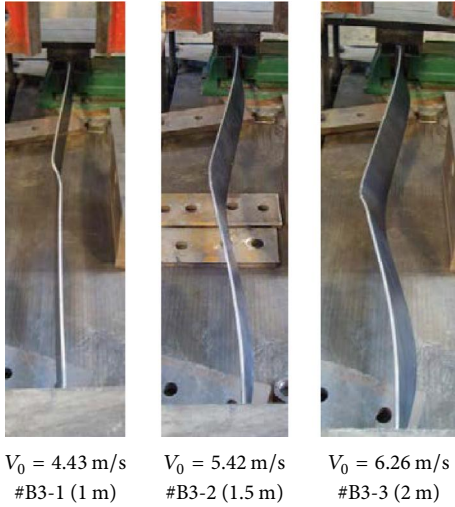
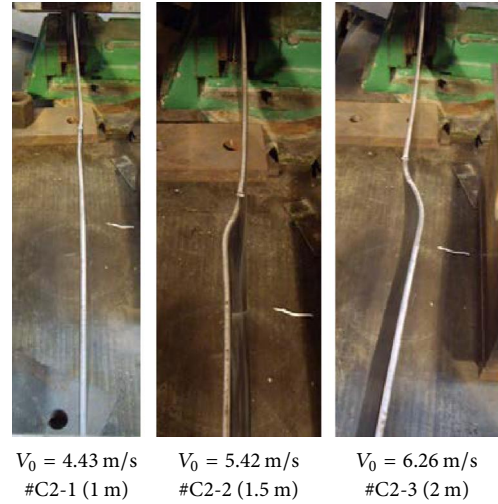
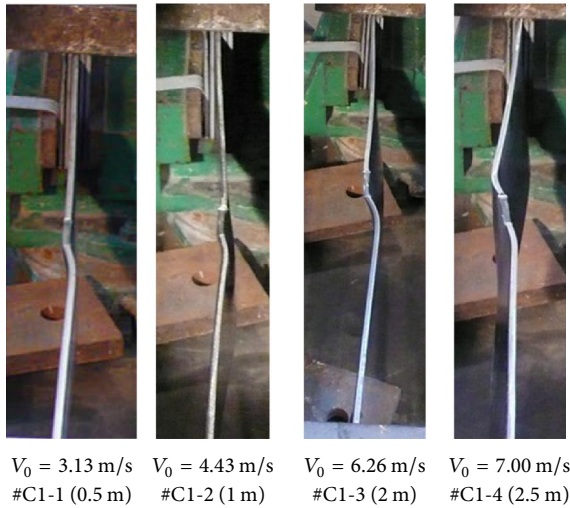
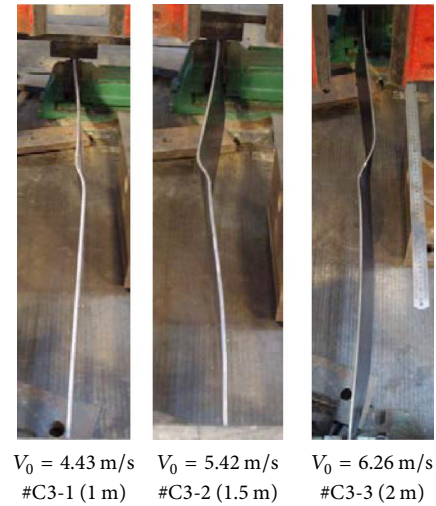
$V_0 = 3.13 \text{ m/s}$     $V_0 = 4.43 \text{ m/s}$     $V_0 = 5.42 \text{ m/s}$   
 #A3-1 (0.5 m)   #A3-2 (1 m)   #A3-3 (1.5 m)

FIGURE 9: Deformation modes of #A3 ( $\alpha = 10, \beta = 20$ ).



$V_0 = 3.13 \text{ m/s}$     $V_0 = 4.43 \text{ m/s}$     $V_0 = 5.42 \text{ m/s}$     $V_0 = 6.26 \text{ m/s}$     $V_0 = 7 \text{ m/s}$     $V_0 = 7.76 \text{ m/s}$   
 #B1-1 (0.5 m)   #B1-2 (1 m)   #B1-3 (1.5 m)   #B1-4 (2 m)   #B1-5 (2.5 m)   #B1-6 (3 m)

FIGURE 10: Deformation modes of #B1 ( $\alpha = 14, \beta = 10$ ).

FIGURE 11: Deformation modes of #B3 ( $\alpha = 14, \beta = 20$ ).FIGURE 13: Deformation modes of #C2 ( $\alpha = 20, \beta = 15$ ).FIGURE 12: Deformation modes of #C1 ( $\alpha = 20, \beta = 10$ ).FIGURE 14: Deformation modes of #C3 ( $\alpha = 20, \beta = 20$ ).

Figures 12, 13, and 14 show the ultimate deformation modes of specimens #C1, #C2, and #C3 with different velocities. Flexural-torsional buckling noticeably occurs for specimens #C1, #C2, and #C3 at different impact velocities. At the same impact kinetic energy, specimens B3 and C3 have different LTB modes. This difference is caused by the variation of section heights between B3 and C3. The LTB of the steel beams with smaller section height is similar to the first-order static buckling mode. With the increase of the section height, the torsional stiffness of the steel beam increases and the possibility of first-order static buckling-like LTB mode decreases. As a result, the steel beams with larger section height are more likely to behave the second-order buckling mode.

The abovementioned results show that rectangular section steel beams under transverse impact can lead to LTB behavior. The LTB mode of rectangular section steel beams

under impact is not a single pattern and depends on the geometry of the specimen.

## 4. Numerical Simulation

**4.1. Finite Element Model.** Numerical simulation is carried out by finite element code LS-DYNA and element SOLID164 was used to simulate the solid beam and drop hammer. SOLID164 [25] is used for the 3D modeling of solid structures. The element is defined by eight nodes having the following degrees of freedom at each node: translations, velocities, and accelerations in the nodal  $x$ ,  $y$ , and  $z$  directions. This element is used in explicit dynamic analyses. In this paper, the elastic-perfectly plastic model is adopted for the numerical analysis using the Material Type 3 [26] of LS-DYNA. This model is suited for modeling isotropic and kinematic hardening plasticity with the option of including rate effects. As a type of strain rate sensitive material, steel

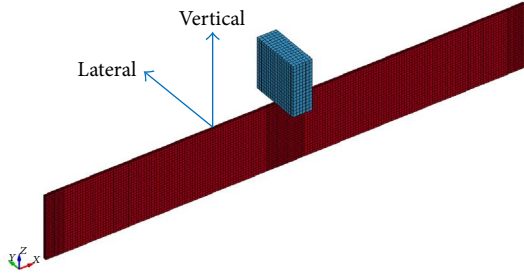


FIGURE 15: Finite element model.

has a considerably high yield stress under high strain rates. When structures are subjected to impact loads, strain rate effect has a considerable influence on the dynamic behavior and damage [20]. The strain rate effects are described by employing the Cowper–Symonds [27] equation with material parameters of  $\dot{\epsilon}_p = 40 \text{ s}^{-1}$ ,  $n = 5$ . The relationship between yield stress and strain rate is expressed in the following equation:

$$\sigma_y = \sigma_0 \left[ 1 + \left( \frac{\dot{\epsilon}_p}{D} \right)^{1/n} \right], \quad (1)$$

where  $\sigma_y$  and  $\sigma_0$  are the dynamic and static yield stress of the material, respectively, and  $\dot{\epsilon}_p$  is the equivalent plastic strain rate. The values for  $E$  and  $\sigma_0$  have been chosen to be consistent with those given in the previous section. The density of steel is  $7,850 \text{ kg/m}^3$  while the Poisson ratio is 0.3. The values of elastic modulus, yield strength, and tangent modulus are similar to those in Figure 3 which features the stress–strain curve. Since the current study aims to investigate the behavior of steel beams under transverse impact load, the emphasis is on the beam rather than the drop hammer. Therefore, only a brief description is given on the drop hammer which is assumed to be a rigid cuboid with dimensions of  $30 \times 80 \times 80 \text{ mm}^3$ . To increase the calculation precision and efficiency, the impact location and nearby supports are simulated in a fine mesh whereas a coarse mesh is used elsewhere. The drop hammer is modeled as a nondeformable solid object. The number of elements has no effect on the calculation precision. Hence, the drop hammer is simulated in a coarse mesh and divided into 1,536 eight-node hexahedrons. A steel beam is divided into 8,216 eight-node hexahedrons. The maximum mesh size of the solid elements is 15 mm as shown in Figure 15. An initial imperfection is generally applied to a structure model in buckling analysis. The buckling mode under impact load should be the superposition of static buckling modes whereas the percentage of the low order buckling mode is comparatively high. For the low-speed impact problem in this paper, buckling should be close to the first-order mode. Therefore, in the analysis, the initial imperfection has the same shape as the first-order mode for bending vibration with amplitude of  $L/1000$ , where  $L$  is the beam span.

In this paper, the boundary conditions of beam are simulated by restraining the  $x$ ,  $y$ , and  $z$  direction node displacement in both ends of the steel beam constrained area. The impact hammer moves only in the vertical direction while other displacement and angle directions are restrained.

In the numerical simulation analysis, the impact energies are given by setting the different initial velocities of the drop hammer. During the impact experiment, the contact interface is formed using the impact hammer and steel surface. When two solid bodies touch, contact stresses are transmitted across their common interface. This contact interface is able to pass the force but is not allowed to penetrate. To model the contact behavior between the front surface of the impact hammer and top surface of beams, the automatic surface-to-surface constraint algorithm with friction is used, where the friction coefficients are introduced to simulate the friction forces transmitted across the contact interface.

**4.2. Comparison of Simulation and Experiment Results.** The numerical simulation on the experiment of steel beams #A1, #B3, and #C2 under the drop hammer was carried out using the previously mentioned FE technique. Then, the simulation and experiment results are compared. Figure 16 shows both results of deformation mode of #A1. It is noticed that, under different impact velocities, the deformation behavior of the steel beams is different. When  $V_0 = 1.98 \text{ m/s}$ , the experimental and numerical results show that the beams do not produce LTB, but only the in-plane bending deformation. When  $V_0 = 3.13 \text{ m/s}$ , local deformation occurs in the mid-span and the steel beams do not produce overall buckling yet. However, at the initial impact velocity of  $4.43 \text{ m/s}$ , the experiment and numerical results all show that the beam produces out-of-plane buckling and mainly lateral bending deformation. When impact velocity is up to  $6.26 \text{ m/s}$ , the LTB behavior of beams is presented by experimental and numerical results and mainly torsional deformation. Figures 17 and 18 show the experimental and numerical results of the deformation mode of #B3 and #C2, respectively. It is noticed that the numerical simulation results are basically consistent with the experiment results under varied impact velocities. Table 3 shows the lateral and vertical deflections at mid-span of beams under different impact velocities. It is noticed that the results of the numerical simulation are in good agreement with the experimental results. Thus, the validity and reliability of the simulation method used in the paper are verified. At the same time, it is observed that the numerical simulation method can predict the LTB of steel beams.

## 5. Numerical Simulation on the LTB of H-Shaped Steel Beams under Transverse Impact

Nowadays, H-shaped steel beams are commonly used as important bearing component of steel structures. Steel beams and columns may fail under a lateral torsional buckling mode under impact and lead to the collapse of the structure. Therefore, studying the buckling tendency of H-shaped steel members under impact is increasingly important [28]. In this section, the numerical simulation analysis on the dynamic response of H-shaped steel beams is carried out using the numerical simulation method which has been verified. The LTB behavior of H-shaped steel beams is studied based on the characteristics of lateral displacement and strain. In

TABLE 3: Comparisons of deflection on mid-span from tests and numerical simulations.

Specimen number	Constraint	$V_0$ (m/s)	$D_L$ (mm)		$D_V$ (mm)	
			Experiment	Simulation	Experiment	Simulation
#A1-1	Fixed-fixed	1.98	0.90	0.98	4.10	3.10
#A1-3	Fixed-fixed	3.13	0.90	0.88	9.80	8.40
#A1-4	Fixed-fixed	4.43	9.80	9.80	21.70	16.80
#A1-5	Fixed-fixed	6.26	20.90	26.90	46.10	45.20
#B3-1	Fixed-fixed	4.43	24.20	18.20	21.30	19.50
#B3-2	Fixed-fixed	5.42	46.36	31.70	51.30	35.30
#B3-3	Fixed-fixed	6.26	80.10	43.70	67.70	44.40
#C2-1	Fixed-fixed	4.43	7.10	5.09	3.40	4.08
#C2-2	Fixed-fixed	5.42	10.94	9.53	3.40	3.00
#C2-3	Fixed-fixed	6.26	16.56	12.60	2.06	1.53

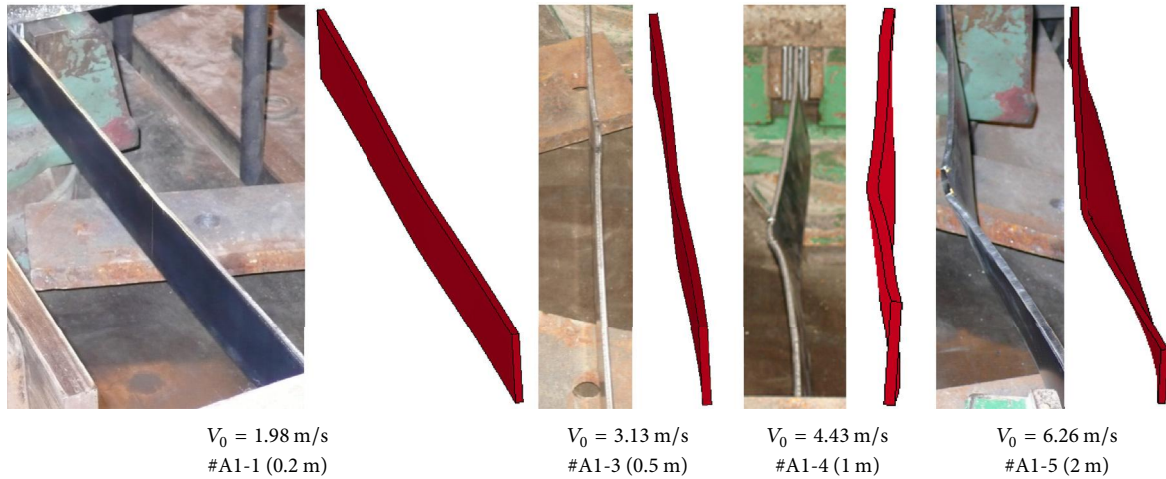


FIGURE 16: Comparison with #A1.

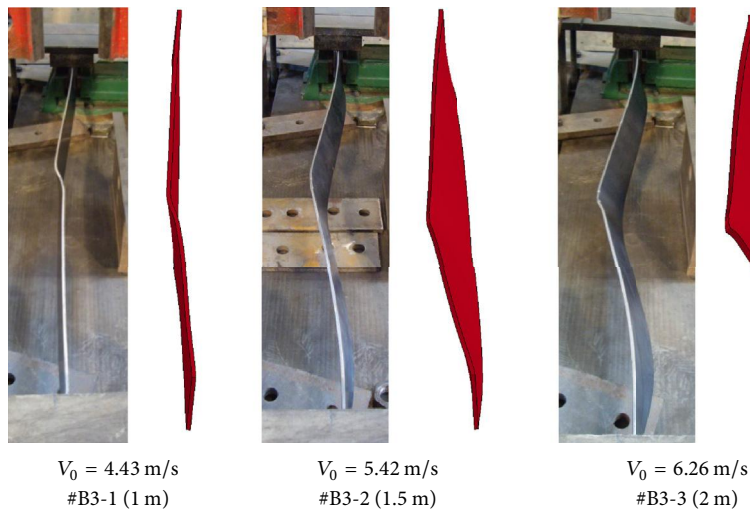


FIGURE 17: Comparison with #B3.

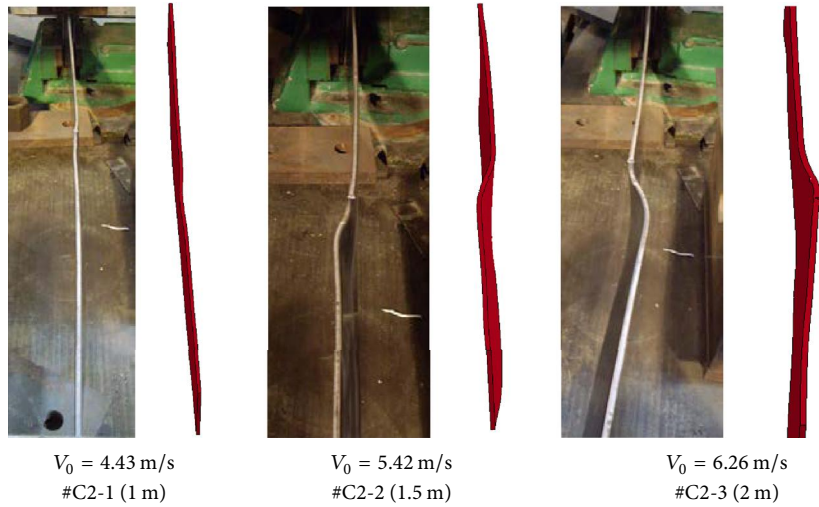


FIGURE 18: Comparison with #C2.

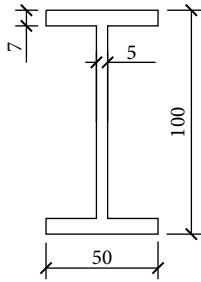


FIGURE 19: Cross-section of a beam.

this research, the following important parameters have been identified for parametric study: impact velocity and impact momentum.

**5.1. Numerical Model.** Figure 19 shows the dimension of an H-shaped cross-section; the span of the beam is 1.5 m. The beam is fixed on both ends. Steel is assumed to be grade Q235 while the steel modulus of elasticity and yield strength are assumed to be 206 GPa and 235 MPa, respectively. The impact energies are given by setting different impact heights. The mass of the drop hammer is assumed to be 200 kg in this research.

Explicit dynamical analysis is used to simulate the dynamic response of the beams under impact. The simulation model comprises the following mesh and material properties.

Strain rate effect: Cowper–Symonds equation with  $D = 40.4 \text{ s}^{-1}$ ,  $n = 5$ , and mesh: steel beam is divided into 22,716 eight-node hexahedrons (SOLID164) and the maximum mesh size of the solid elements is 15 mm as shown in Figure 20. Since the current study aims to investigate the behavior and failure modes of H-shaped steel beams under transverse impact load, the emphasis is on the beam rather than the drop hammer. Hence, only one drop hammer geometry with a dimension of  $30 \times 80 \times 120 \text{ mm}^3$  is considered. In the numerical simulation analysis, the density of the drop

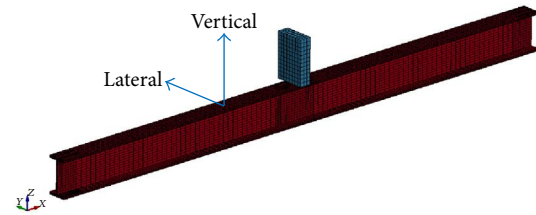


FIGURE 20: Finite element model.

hammer is adjusted to obtain the required mass. The drop hammer is divided into 1,536 eight-node hexahedrons. The initial distance between the striking tip of the drop hammer and top surface of H-shaped steel beam is set at 5 mm. In this section, the initial imperfection has the same shape as the first mode for bending vibration with an amplitude of  $L/1000$ , where  $L$  is the beam span.

**5.2. Numerical Results.** In the current section, the numerical results of the H-shaped steel beam under transverse impact, such as the entire process of the impact, residual deformation of beam, and time history curves of strain, will be discussed. Output data curves of displacement during the simulation are at a 3,750 Hz sampling rate.

**5.2.1. Plastic Deformation of Beam.** Figure 21 shows the residual deformation of the H-shaped steel beam under transverse impact when the initial impact velocity is 6 m/s. It is noticed from Figure 21 that an LTB behavior is observed while the maximum of the lateral deformation is produced mid-span. At the same time, a local deformation of the beam flange is observed at the location of the steel beam top flange in contact with the impact hammer.

**5.2.2. Impact Process.** Figure 22 illustrates the whole dynamic response of H-shaped steel beams under transverse impact. It is observed that the lateral displacement of the beam increases

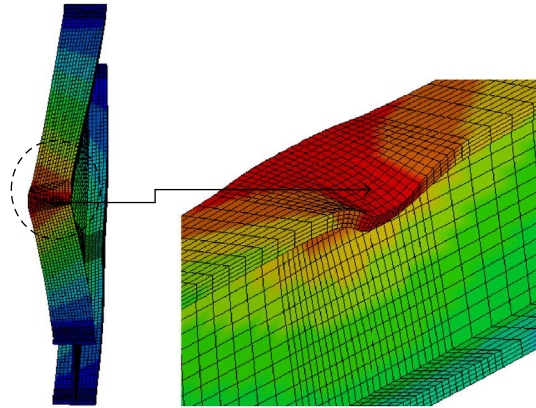


FIGURE 21: Plastic deformation of beam.

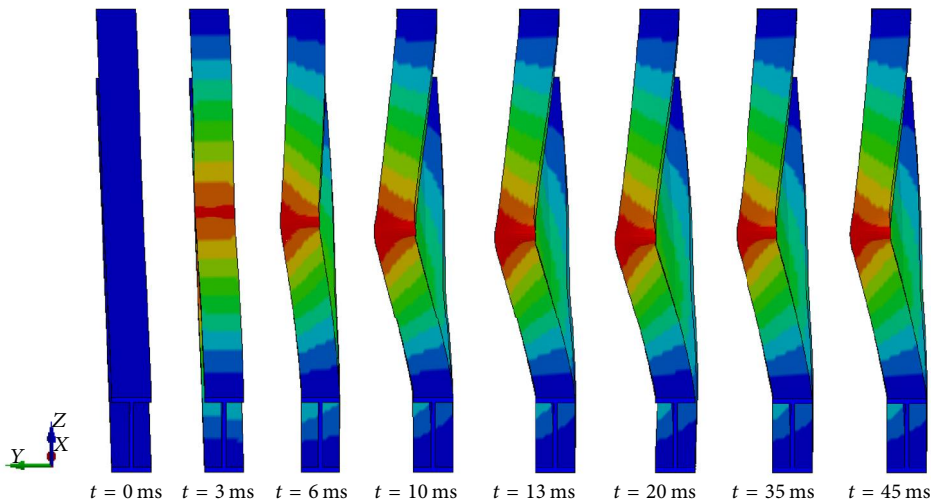


FIGURE 22: Impact process.

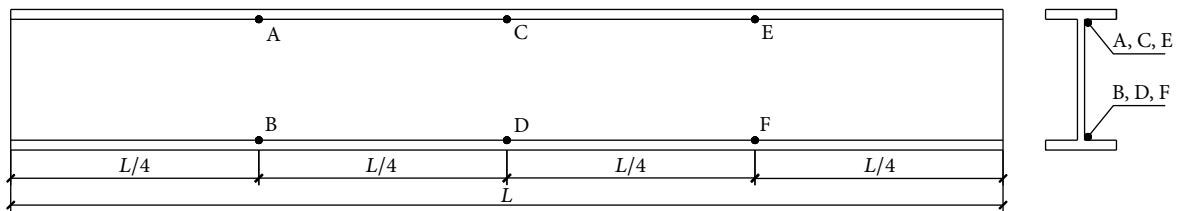


FIGURE 23: Location of nodes.

with the increase in contact time of the drop hammer and beam. The maximum lateral displacement occurs at an impact time of 13 ms, which includes elastic and plastic deformation. With the movement of the drop hammer and beam, the elastic deformation of beam gradually recovers and the whole displacement of the beam is reduced until the elastic deformation of beam fully recovers. The plastic deformation of the H-shaped steel beam occurs at 35 ms.

*5.2.3. Plastic Deformation of Beam.* In the current section, the lateral and vertical displacements–time history curves at

different nodes of the steel beam are studied. Figure 23 shows the location of the nodes and all points belong to the beam web.

The lateral displacement–time history curves at different nodes of the steel beam are given as shown in Figure 24. It is observed that the lateral displacement of nodes from various locations of beam is different. The residual lateral displacements of nodes A and E are 15.4 mm whereas node C is at 36.7 mm. The difference of the residual lateral displacements on nodes A and C indicates that the beam produces lateral bending deformation. The residual lateral displacements of

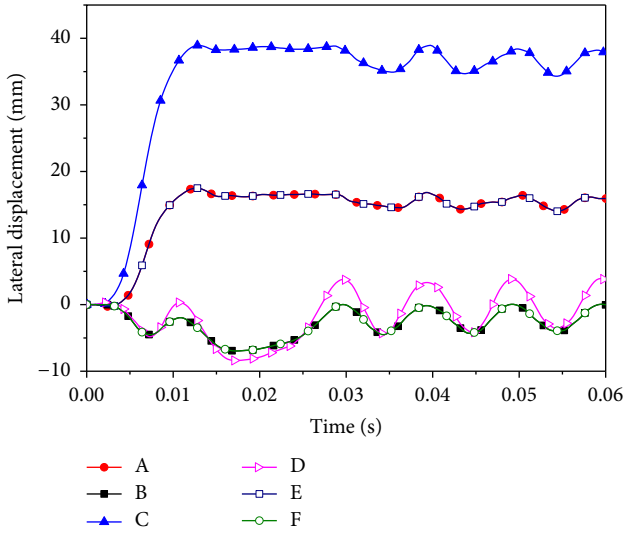


FIGURE 24: Lateral displacement–time history curve.

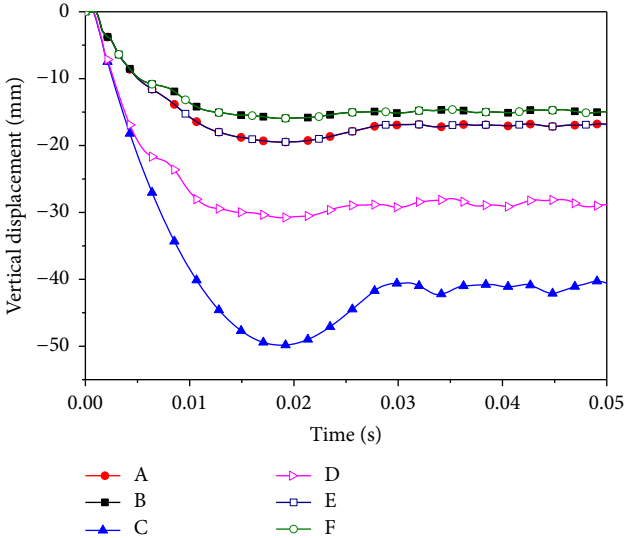


FIGURE 25: Vertical displacement–time history curve.

nodes A, C, and E are greater than zero and corresponding displacements of nodes B, D, and F are less than zero. This shows that the out-of-plane torsion deformation of the steel beam is produced during movement. From the abovementioned discussion, the H-shaped steel beam under transverse impact produces the LTB phenomenon.

Figure 25 shows that the residual vertical displacements of nodes C and D are 41.2 and 28.3 mm, respectively. From the difference of the residual vertical displacement, it can be seen that the H-shaped steel beam under transverse impact occurs in not only in-plane bending deformation but torsional deformation. Figure 25 also demonstrates that the residual vertical displacements of nodes A and B agree with nodes E and F, respectively. This agreement is brought by the constraint and symmetrical load of specimen. Hence,

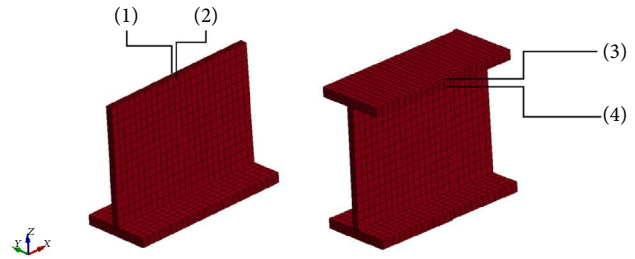


FIGURE 26: Symmetrical elements of web and flange.

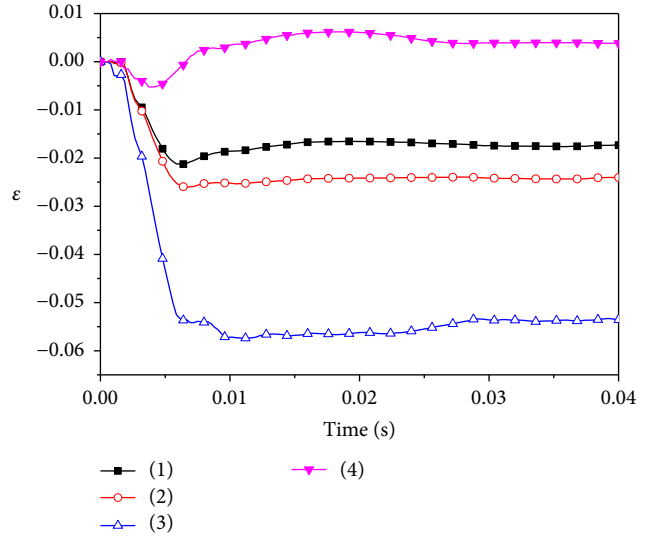


FIGURE 27: Strain–time history curves.

the residual vertical displacement–time history curves of the beam are also symmetrical.

**5.2.4. Strain–Time History Curves.** Figure 27 presents the strain–time history curves for the two groups of symmetrical elements from the mid-span of the H-shaped steel beam web and flange, respectively. Figure 26 shows the locations of symmetrical elements. Figure 27 shows that the strain of the two symmetrical elements of the beam web is coincident during 0 to 4 ms. This behavior indicates that the H-shaped steel beam web moves in a plane at the beginning and then produces an out-of-plane movement. Figure 27 also shows that the strain–time curves of the two symmetrical elements on the beam flange are different at the beginning of the movement. This result indicates that the H-shaped steel beam flange produces out-of-plane movement first. This is because the drop hammer comes into contact with the beam flange directly and leads the top flange to produce the buckling first.

Based on the above discussion, it can be found that the H-shaped steel beams under transverse impact can cause the LTB behavior.

**5.3. Effects of Different Drop Hammers.** In this research, the following two important parameters have been identified for parametric study: impact velocity and impact momentum.

TABLE 4: Analytical results of momentum effects.

Case	Mass (kg)	$K_I$ (J)	$M_I$ (Ns)	$V_0$ (m/s)	$D_V$ (mm)	$T_C$ (ms)	Deformation mode
1	100	3600	850	8.5	39.2	19.3	LTB
2	200	3600	1200	6.0	40.8	28.8	LTB
3	300	3600	1470	4.9	42.4	35.8	LTB

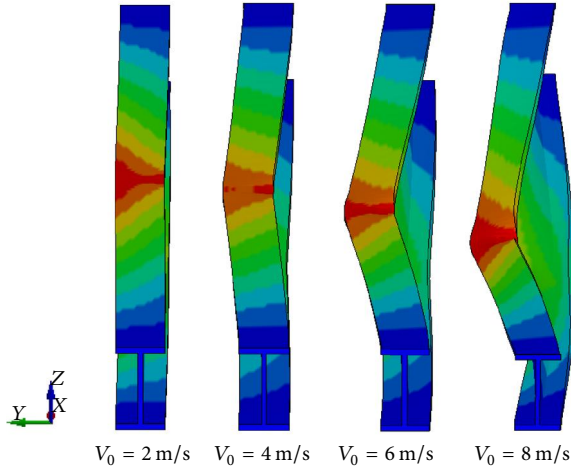


FIGURE 28: Plastic deformation of beam under different impact velocities.

This section will present numerical simulation results to help understand the effects of these design parameters.

**5.3.1. Effects of Impact Velocity.** In this section, the dynamic responses of H-shaped steel beams are studied at different impact velocities where the initial impact velocity  $V_0$  is 2, 4, 6, and 8 m/s.

Figure 28 presents the plastic deformation of the H-shaped steel beam under different impact velocities. When  $V_0 = 2$  m/s, the H-shaped steel beam only occurs in in-plane bending deformation whereas LTB behavior is not observed. When  $V_0 = 4, 6,$  and  $8$  m/s, it is observed that the H-shaped steel beam produces the LTB accompanied by the local deformation of the beam flange. Figure 29 shows the impact response for the lateral displacement of mid-span of the H-shaped steel beam under different impact velocities. It can be seen that the plastic deformation of H-shaped steel beam increases with the increase of initial impact velocity. Hence, with the increase in initial impact velocity, the H-shaped steel beams are more sensitive to the LTB.

**5.3.2. Impact Momentum Effects on the LTB of H-Shaped Steel Beams.** In this section, the dynamic response analyses on H-shaped steel beam subjected to transverse impact are carried out using three cases. The three cases have different masses of drop hammer, impact velocities, and same kinetic energy of 3600 J. Table 4 shows the three sets of conditions and impact momentum effects on the LTB of H-shaped steel beams, where  $K_I$  is the impact kinetic energy of the drop hammer,  $M_I$  is the impact momentum of the drop hammer, and  $T_C$  is the contact time.

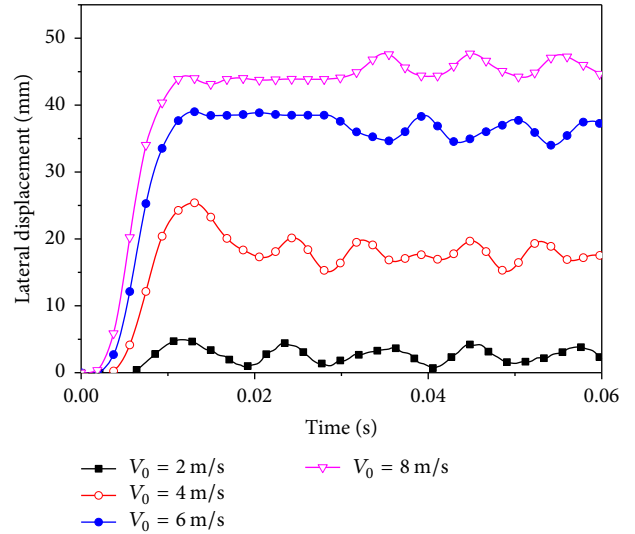


FIGURE 29: Lateral displacement of mid-span of beam under different impact velocities.

Table 4 shows that if the impact kinetic energy remains constant, then the residual vertical deformation of the H-shaped steel beam and contact time decrease with the decrease in impact momentum. The transfer energy is proportional to the mass ratio whereas the mass ratio decreases with the decrease in impact momentum. Thus, the residual vertical deformation of the H-shaped steel beam is small under low impact momentum. Figure 30 also shows that the change of the impact momentum has negligible effect in the LTB forms of the H-shaped steel beam. Figure 31 presents the time history curves of the lateral displacement on the beam mid-span. It can be seen that the lateral displacement decreases with the decrease in impact momentum. Under constant impact kinetic energy and varying impact momentum, the maximum vertical displacement difference is only 1.6 mm but the maximum lateral displacement difference is 7.7 mm as shown in Table 4 and Figure 31. This is because the LTB deformation is governed by the lateral displacement compared to vertical displacements. Based on the discussion above, it is conducted that the impact momentum is not a deciding factor for the LTB of the H-shaped steel beam under transverse impact.

## 6. Conclusion

Through drop weight impact test, it is found that the narrow rectangular cross-section steel beam under transverse impact leads to LTB. The numerical simulation results are consistent with experimental results, which means that the

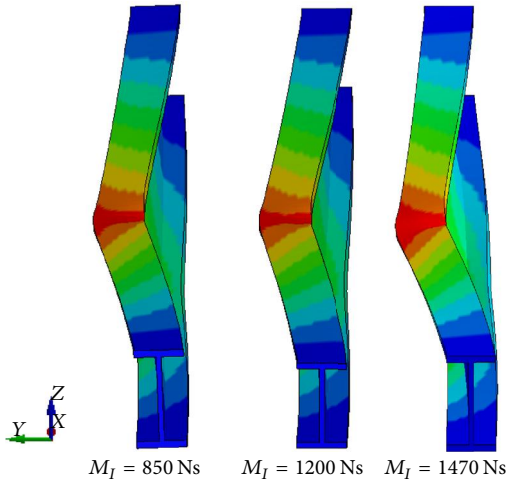


FIGURE 30: Plastic deformation of beam under different impact momentums.

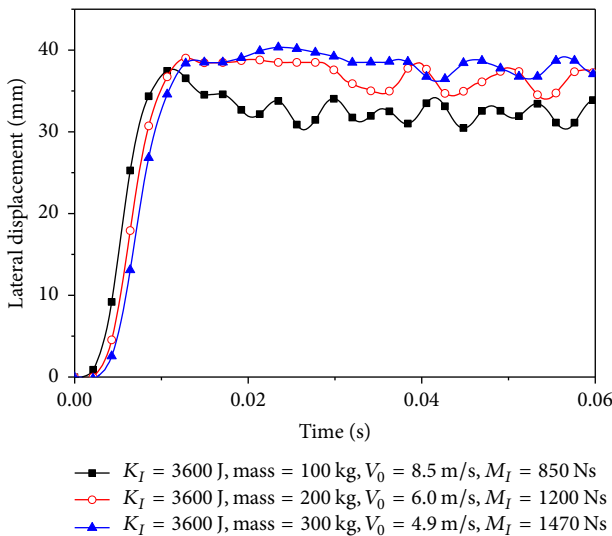


FIGURE 31: Lateral displacement-time history curve of mid-span of beam.

LTB behavior from the experimental test is not an accidental consequence due to structure or material defects, but the real response mode of the structure. The consistency of the numerical simulation and experiment results also shows that the FE code ANSYS/LS-DYNA can effectively simulate LTB with material and geometrical nonlinearities. On this basis, the abovementioned numerical method is used to conduct a study on LTB of H-shaped steel beams subject to transverse impact. From the results, the following conclusions are drawn:

- (1) After studying the impact process, the deformation modes, lateral displacement, and strain of the H-shaped steel beam, it can be seen that not only can the rectangular section beam under transverse impact lead to LTB, but the H-shaped steel beam under

transverse impact also easily causes LTB accompanied by the local deformation of the top flange.

- (2) The LTB of the H-shaped steel beam under transverse impact is primarily dependent on the level of impact kinetic energy. With the increase in impact kinetic energy, the H-shaped steel beam subject to transverse impact is more prone to LTB and local deformation.
- (3) If the impact kinetic energy remains constant, then the plastic deformation of the H-shaped steel beam and contact time increase with the increase in impact momentum whereas different impact momentum has a minor effect on LTB of the H-shaped steel beam under transverse impact.

## Conflicts of Interest

The authors declare that they have no conflicts of interest.

## Acknowledgments

This work is supported by the National Natural Science Foundation of China (Grant nos. 10872117, 11272189, 11672165, and 51208289).

## References

- [1] J. Chen, *Stability of Steel Structures Theory and Design*, Science Press, Beijing, China, 2014.
- [2] Z. B. Xia, "The theory, experiment and calculation method on the lateral torsional buckling of Steel beam," *Industrial Constructio*, vol. no. 1, pp. 23–29, 1983.
- [3] N. S. Trahair, *Flexural-Torsional Buckling of Structures*, CRC Press, London, UK, 2000.
- [4] B. Yang, G. Xiong, K. Ding et al., "Experimental and numerical studies on lateral-torsional buckling of GJ structural steel beams under a concentrated loading condition," *International Journal of Structural Stability & Dynamics*, vol. 16, no. 1, pp. 19–24, 2016.
- [5] B. Yang, S.-B. Kang, G. Xiong et al., "Experimental and numerical study on lateral-torsional buckling of singly symmetric Q460GJ steel I-shaped beams," *Thin-Walled Structures*, vol. 113, pp. 205–216, 2017.
- [6] M. Karmazínová, J. Melcher, and M. Horáček, "Thin-walled cold-formed steel beams with holes in lateral flexural-torsional buckling," *Advanced Materials Research*, vol. 743, pp. 170–175, 2013.
- [7] Z. Kala and J. Valeš, "Global sensitivity analysis of lateral-torsional buckling resistance based on finite element simulations," *Engineering Structures*, vol. 134, pp. 37–47, 2017.
- [8] M. Vild, J. Piják, J. Barnat, M. Bajer, J. Melcher, and M. Karmazínová, "Comparison of analytical and numerical methods applied to lateral torsional buckling of beams," *Procedia Engineering*, vol. 195, pp. 48–55, 2017.
- [9] S. Kwani and P. K. Wijaya, "Lateral torsional buckling of castellated beams analyzed using the collapse analysis ?" *Procedia Engineering*, vol. 171, pp. 813–820, 2017.
- [10] A. Mohebkhah and M. G. Azandariani, "Lateral-torsional buckling resistance of unstiffened slender-web plate girders under moment gradient," *Thin-Walled Structures*, vol. 102, pp. 215–221, 2016.

- [11] European Committee For Standardisation, "ENV 1993-1-2, Eurocode 3: Design of steel structures. Part 1-2: General rules. Structural fire design," Ed., Brussels, Belgium, 1995.
- [12] P. M. M. Vila Real, P. A. G. Piloto, and J.-M. Franssen, "A new proposal of a simple model for the lateral-torsional buckling of unrestrained steel I-beams in case of fire: Experimental and numerical validation," *Journal of Constructional Steel Research*, vol. 59, no. 2, pp. 179–199, 2003.
- [13] Y. Gao and F. Xi, "The lateral torsional buckling of mono-symmetric cross-section steel beams under fire conditions," *Chinese Journal of Applied Mechanics*, vol. 30, no. 1, pp. 130–135, 2013.
- [14] C. Zhang, J. L. Gross, and T. P. McAllister, "Lateral torsional buckling of steel W-beams subjected to localized fires," *Journal of Constructional Steel Research*, vol. 88, pp. 330–338, 2013.
- [15] P. M. M. Vila Real, N. Lopes, L. Simões da Silva, and J.-M. Franssen, "Lateral-torsional buckling of unrestrained steel beams under fire conditions: Improvement of EC3 proposal," *Computers & Structures*, vol. 82, no. 20-21, pp. 1737–1744, 2004.
- [16] N. Lopes and P. M. M. Vila Real, "Class 4 stainless steel i beams subjected to fire," *Thin-Walled Structures*, vol. 83, pp. 137–146, 2014.
- [17] Y. Z. Yin and Y. C. Wang, "Numerical simulations of the effects of non-uniform temperature distributions on lateral torsional buckling resistance of steel I-beams," *Journal of Constructional Steel Research*, vol. 59, no. 8, pp. 1009–1033, 2003.
- [18] C. Couto, P. Vila Real, N. Lopes, and B. Zhao, "Numerical investigation of the lateral-torsional buckling of beams with slender cross sections for the case of fire," *Engineering Structures*, vol. 106, pp. 410–421, 2016.
- [19] R. Villavicencio and C. Guedes Soares, "Numerical modelling of the boundary conditions on beams struck transversely by a mass," *International Journal of Impact Engineering*, vol. 38, no. 5, pp. 384–396, 2011.
- [20] H. Wang, B. Yang, X.-H. Zhou, and S.-B. Kang, "Numerical analyses on steel beams with fin-plate connections subjected to impact loads," *Journal of Constructional Steel Research*, vol. 124, pp. 101–112, 2016.
- [21] H. Al-Thairy and Y. C. Wang, "A numerical study of the behaviour and failure modes of axially compressed steel columns subjected to transverse impact," *International Journal of Impact Engineering*, vol. 38, no. 8-9, pp. 732–744, 2011.
- [22] J. G. Ning, "The experimental investigation on the lateral unitability of cantilever high beams under impact loading," *Mechanics and Practice*, vol. 18, no. 3, pp. 34–36, 1996.
- [23] J. G. Ning and Y. G. Zhao, "The experimental investigation on the lateral unitability of cantilever highbeams under impact loading," *Journal of Taiyuan University of Technology*, vol. 30, no. 1, pp. 11–14, 1999.
- [24] W. Zhang, *Numerical simulation analysis on the lateral torsional buckling behavior of steel beams under transverse impact*, Shandong Jianzhu University, China, 2013.
- [25] LS-DYNA, "Keyword User's Manual," Livermore Software Technology Corporation(LSTC), 2014.
- [26] LS-DYNA, "Keyword User's Manual, Material models, II," Livermore Software Technology Corporation(LSTC), 2014.
- [27] G. R. Cowper and P. S. Symonds, "Strain hardening and strain-rate effect in the impact loading of cantilever beams," Tech. Rep. 28, Brown University Division of Applied Mathematics, Providence, RI, USA, 1957.
- [28] R. Wang and C. Pei, "Parametric analysis of dynamic response of hot-rolled h-shaped steel beam under lateral impact load," *Engineering Mechanics*, vol. 30, no. s1, pp. 258–262, 2013.

## Research Article

# Influence of Wheel Eccentricity on Vertical Vibration of Suspended Monorail Vehicle: Experiment and Simulation

**Kaikai Lv, Kaiyun Wang, Zhihui Chen, Chengbiao Cai, and Lirong Guo**

*State Key Laboratory of Traction Power, Southwest Jiaotong University, Chengdu 610031, China*

Correspondence should be addressed to Kaiyun Wang; [kywang@swjtu.edu.cn](mailto:kywang@swjtu.edu.cn)

Received 28 July 2017; Revised 8 November 2017; Accepted 3 December 2017; Published 20 December 2017

Academic Editor: Abdul Qadir Bhatti

Copyright © 2017 Kaikai Lv et al. This is an open access article distributed under the Creative Commons Attribution License, which permits unrestricted use, distribution, and reproduction in any medium, provided the original work is properly cited.

This paper investigates the influence of wheel eccentricity on vertical vibration of suspended monorail vehicle based on experiment and simulation. Two sets of tests are conducted in the first Chinese suspended monorail, and the tested acceleration is analyzed and exhibited. A multibody dynamic model of the suspended monorail vehicle is established to simulate the vertical vibration of car body excited by wheel eccentricity. The results show that there are three factors which may cause an abnormal vibration considering the track and the vehicle system. The influence of wheel eccentricity on the car body vibration was firstly analyzed. Simulated acceleration of car body has a great accordance with test. The wheel eccentricity could excite the resonance of car body at the speed of 21 km/h, and the vertical acceleration would increase considerably. Decreasing the secondary stiffness can effectively reduce the vertical vibration caused by wheel eccentricity, especially at the resonant speed. In the secondary test, the peak of car body acceleration at speed of 20 km/h is not appearing when only renewing the wheels, and the acceleration is decreasing obviously at the domain frequency. It is further determined that the abnormal vibration is mainly caused by the wheel eccentricity.

## 1. Introduction

Nowadays, most Chinese cities are facing the pressure of traffic jam. As to solve the problem, a large number of short-distance transportation systems are built, such as subways, light rail transit, bus rapid transit (BRT), maglev transit, and straddle monorail [1]. And now, another new transportation is developed, suspended monorail. This new form of transportation is researched and developed, and the experimental stage has been finished. Several problems of vehicle and monorail track were found and solved at the experimental stage, such as the wheel eccentricity.

Wheel eccentricity is mainly caused by misalignment in the fixation of the wheel during manufacturing or maintenance and is a special classification of wheel out-of-roundness (OOR) [2]. The wheel OOR is a common phenomenon in railway vehicles, which could cause high-frequency forces between wheel and rail with the increasing of the running speed [3–5]. In addition, under the certain periodic excitation, the running comfort of the vehicle is severely threatened [6, 7]. A number of scholars have been devoted to investigate

the mechanism and the influence of wheel OOR in railway. Jin et al. [8] investigated the mechanism of the polygonal wear of metro train wheels based on experiment and structure model test, and the average passing frequency of a polygonal wheel is approximately close to the first bending resonant frequency of the wheelset, which is the main reason of the polygonal wear. More than 2000 wheels of seven types of locomotives widely used in China have been measured [9], two types of freight locomotives suffer serious polygonal wear problem, and the other types exhibited more or less wheel eccentricity. Johansson and Andersson [10, 11] analyzed and summarized the extensive wheel measurement campaign performed in Sweden, the wheel roughness and the rail roughness were also been compared, and a tool was developed for investigation of wheel tread polygonal wear. The mechanism of the wheel OOR was explained by a simple model proposed by Brommundt [12]. Badger et al. [13] studied the evident degradation of the grinding force, wheel wear, and vibration caused by the wheel eccentricity, and some recommendations are given for detecting and determining the wheel eccentricity. Wu et al. [14] studied the dynamic stresses of the wheel set

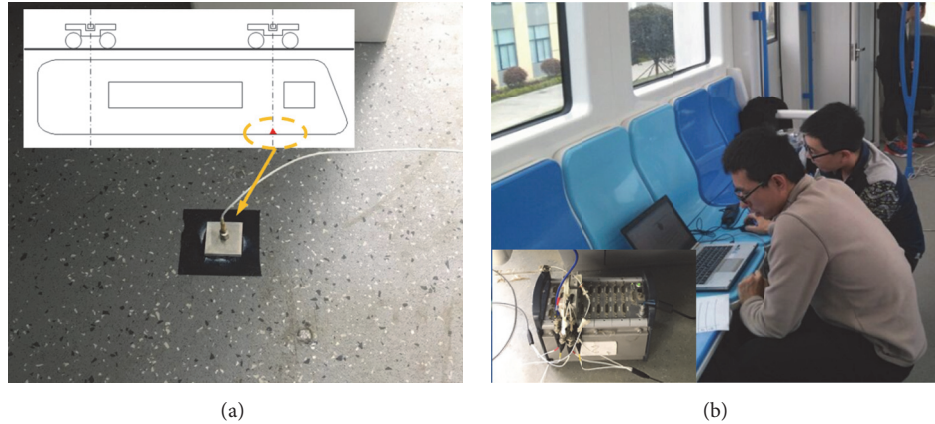


FIGURE 1: Acceleration measurement of the car body: (a) sensor position and (b) data acquisition.

axle based on a coupled vehicle/track dynamic model with the flexible wheelset; the results show that the resonance of wheel set axle could be excited by polygonal wear, which would increase the dynamic stress for the wheel set axle. The growth mechanism of wheel polygonal of railway vehicle and its damage for the track and components were overviewed in detail [2, 15, 16]. Although a great number of researches have been carried out by scholars all over the world, the OOR of the railway wheels has not been completely explained and solved [14].

For the first suspended monorail vehicle in China, an abnormal vertical vibration of car body was found in the experimental stage, which seriously affects the ride comfort. The objective of this paper is to validate the wheel eccentricity which is the root cause for this abnormal vibration of car body based on experiment and simulation. And the influence mechanism of the wheel eccentricity on the car body acceleration is also analyzed.

## 2. Investigation on the Vertical Vibration of Car Body by First Test

On the trial running stage of the first suspended monorail vehicle in China, the vertical vibration of the car body exhibited an abnormal phenomenon. The obvious feature of the vibration is that it shows a clear resonance characteristic, and the amplitude of vibration was particularly violent at the speed of about 20 km/h. The ride comfort is extremely influenced by the abnormal vibration, and the maximum speed of the vehicle is therefore limited. As to explore the root reason of this special vibration, the first test was conducted.

**2.1. Description of the First Test.** The test was conducted in the first suspended monorail line of China, aiming to find the main reason of the abnormal vibration. This test mainly measured the vertical acceleration of the car body, the acceleration sensors were mounted on the floor of car body, as shown in Figure 1(a), and Figure 1(b) shows the data acquisition.

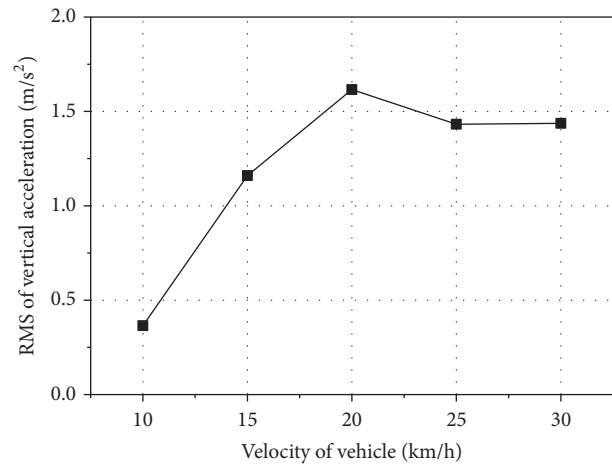


FIGURE 2: Measured acceleration of car body at different velocity.

In this test, the velocity of the vehicle was set to 10~30 km/h and the interval was 5 km/h. Due to the fact that the cause of the abnormal vibration is not clear, the maximum speed of 30 km/h was mainly to ensure the running safety.

**2.2. Results and Discussion of the First Test.** Analyzing the measured data was the key means to find the cause of vibration. Firstly, the RMS of the acceleration was counted to represent the level of the vertical vibration, and its variation trend with speeds is illustrated in Figure 2. It can be seen that, at the speed of 20 km/h, the maximum amplitude of the acceleration for the car body increases considerably and reaches a peak of 1.62 m/s<sup>2</sup>. The test results show a very uniformity with the travel experience.

In order to further analyze the measured data, the frequency spectrum of the measured acceleration is shown in Figure 3. It can be clearly found that each acceleration has a certain domain frequency. With the increase of running speed, the domain frequency increased accordingly.

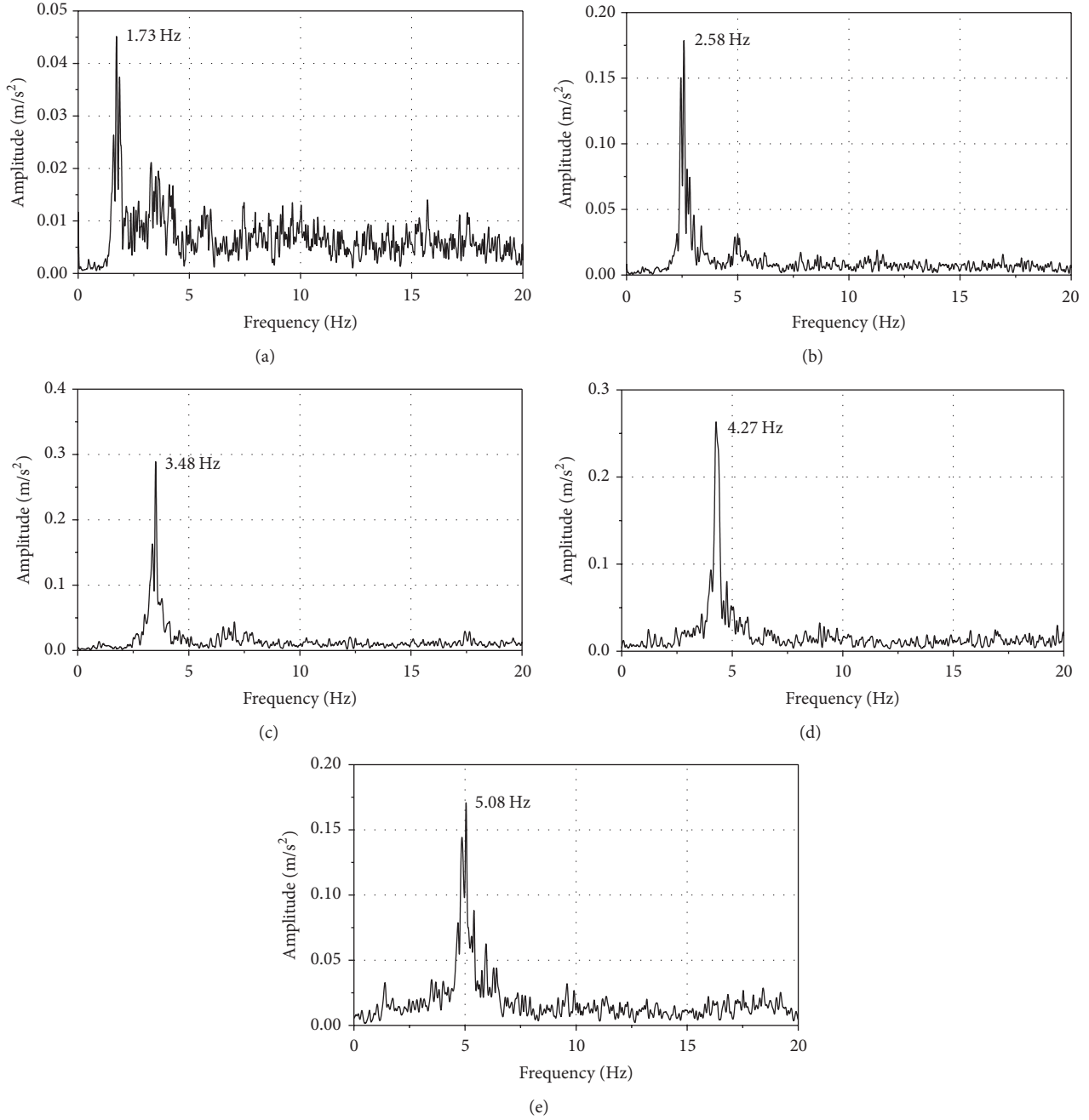


FIGURE 3: The frequency spectrum of the measured acceleration at different speeds: (a) 10 km/h, (b) 15 km/h, (c) 20 km/h, (d) 25 km/h, and (e) 30 km/h.

It is known that vibration is caused by the excitation, and excitation is mainly generated from the vehicle itself and the track. The relationship among domain frequency of measured acceleration, wavelength of the excitation, and the velocity is as follows:

$$\lambda = \frac{v}{f}, \quad (1)$$

where  $\lambda$  denotes the wavelength of excitation,  $v$  is the running velocity, and  $f$  is the domain frequency of vibration.

TABLE 1: Calculated wavelength of excitation.

Velocity (km/h)	10	15	20	25	30
Domain frequency (Hz)	1.73	2.58	3.48	4.27	5.08
Calculated wavelength (m)	1.61	1.61	1.60	1.63	1.64

According to formula (1), the excited wavelength at each speed can be calculated, as listed in Table 1.

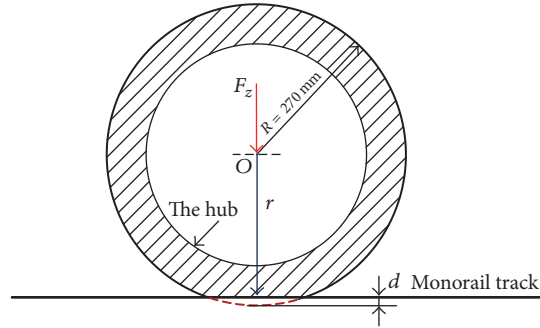


FIGURE 4: Schematic diagram of compressed wheel.

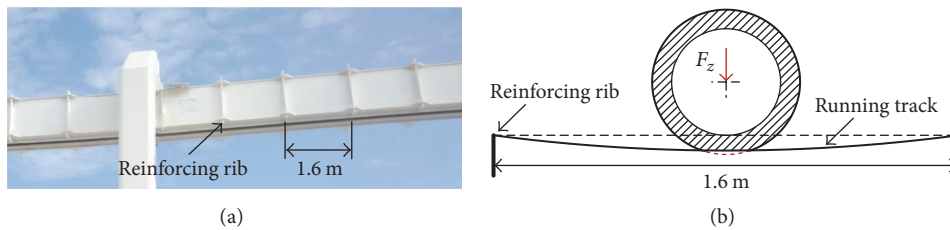


FIGURE 5: The monorail track: (a) the reinforcing rib and (b) the compressed deformation of track.

The calculated wavelengths in Table 1 are 1.60~1.64 m, which can conclude that the main wavelength of the excitation is 1.60~1.64 m, and this is the main reason for the abnormal vibration.

**2.3. The Possibilities for the Excitation.** According to the measured car body acceleration, the existence of the excitation with 1.6~1.64 m wavelength is the cause for abnormal vibration. For this type of excitation, there have three possibilities considering the track and vehicle system.

(1) *The Wheel Eccentricity.* The radius of the wheel is 0.27 m, and the wheel circumference is 1.70 m. But it is noted that the wheel of suspended monorail vehicle is solid tire and the compressed deformation cannot be ignored during running, as shown in Figure 4. The axle load of the vehicle is  $4t$ , the static vertical force  $F_z$  is about 20 kN, and the compressed deformation  $d$  is about 6.7 mm. In this condition, the rolling radius  $r$  decreased to 0.263 m, the rolling circumference decreased to about 1.65 m, and this is in great accordance with the domain wavelength of the excitation.

(2) *The Inherent Characteristics of the Monorail Track.* Figure 5(a) shows the monorail track, and in order to ensure the running safe, the reinforcing rib is used to promote the reliability of the running track. When the vehicle passes, the unevenness of the track stiffness will cause the vibration [17, 18], as shown in Figure 5(b). The designed interval of the rib is 1.6 m, which is also in great accordance with the domain wavelength of the excitation.

(3) *The Track Irregularity.* If the wavelength of irregularity is concentrated at about 1.6 m, the excited vibration of car body will show the measured characteristic.

As the above analysis, there are three factors which may cause the abnormal vibration considering the track and the vehicle system. To improve the ride comfort, the effective strategy for the three factors is introduced. For the reinforcing rib, it is the inherent characteristic of the track to ensure running safety. The influence of rib on the car body vibration is inevitable but could effectively reduce by matching the vehicle parameters. As to the track irregularity, grinding the track surface could smooth the track and improve the ride comfort. In general, the irregularity is random, so the abnormal vibration is not likely caused by the irregularity. For wheel eccentricity, controlling the errors of manufacture and installation could reduce its influence on the ride comfort significantly.

Modifying the reinforcing rib and track irregularity is difficult operation, especially on the line that has been built. But the detection and elimination of wheel eccentricity are easy. So, the influence of the wheel eccentricity on the vertical vibration of the car body is firstly analyzed.

### 3. Multibody Dynamic Simulation

In this section, numerical simulations are conducted to give an insight into the consequent influence of the wheel eccentricity on the vehicle vibration. Only the wheel eccentricity is considered in the simulation. The results are compared with the test data, which can provide the evidence for the causes of the abnormal vibration.

**3.1. Dynamic Model of Suspended Monorail Vehicle.** In order to analyze the influence of the wheel eccentricity on the car body vibration, a detailed simulation model has been established using the multibody dynamic software of SIMPACK, as

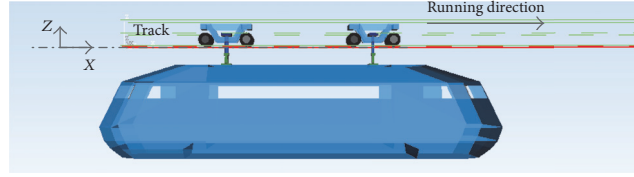


FIGURE 6: The simulation models for suspended monorail vehicle.

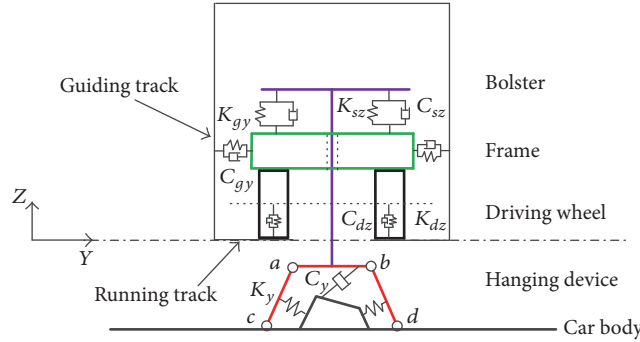


FIGURE 7: The simulation models of bogie.

illustrated in Figure 6. In this model, the vehicle was treated as a full rigid multibody dynamic model, and the flexibility of the monorail track is not considered. The monorail track is box-sectioned beams with bottom opening, as shown in Figure 5(a). The bogie is placed inside the box beams, which could avoid the influence of the weather. The car body is suspended under the bogie; thus it can be running in the sky.

The suspended monorail vehicle consists of two bogies, and each bogie is mainly made up of one frame, one bolster, four driving wheels, four guiding wheels, a hanging device, and suspension systems. The structure of the bogie can be clearly seen in Figure 7.

The driving wheel (solid rubber tire) is running on the running track, acting as the primary suspension. Each driving wheel can be rotated around the bogie, independently. In the dynamic model, the tire model of Pacejka Magic Formula was referenced to calculate the interaction between the driving wheel and the track, and  $C_{dz}$  and  $K_{dz}$  are representing the vertical damping and stiffness of the driving tire.

Not like the self-steering performance of the railway vehicle, the guiding wheels are needed to provide the steering force when the suspended monorail vehicle passes curve. The guiding wheels are also solid rubber tire, and they are running along the guiding track. In order to ensure the curving passing performance of the vehicle, the guiding wheels have an initial compression to provide an initial lateral force. In the dynamic model, the linear force element was used to simulate the guiding force, and  $C_{gy}$  and  $K_{gy}$  are representing the damping and stiffness of the guiding wheel.

The connection between the car body and the bolster is the hanging device, and the points  $a$ ,  $b$ ,  $c$ , and  $d$  are four rotated joints, which can rotate around the  $x$ -axis. There has one damper between the car body and the hanging device,

which is used to reduce the lateral vibration of the car body, and  $C_y$  represents its damping. The lateral stopper between car body and hanging device limits the large lateral rotation angle of the car body, and  $K_y$  represents the stiffness of the stopper.

Two sets of spring-damper systems are installed between the bolster and the frame, where  $C_{sz}$  and  $K_{sz}$  are representing the damping and stiffness.

**3.2. Eccentricity Model of Monorail Wheel.** The wheel OOR is a very common phenomenon in the railway vehicle, and a lot of investigations have been done aiming at this uneven problem. As to the wheel OOR model, two main methods are used to describe the polygonal wear in the wear circumferential direction in railway, as shown in Figure 8.

The first method is transforming the wheel OOR into the track irregularity, and the wheel surface is kept constant. The second method is using the harmonic deviation of the wheel radius to describe the wheel OOR. The formulas of the harmonic deviation are given as follows [19]:

$$\begin{aligned} \Delta r &= A \cdot \sin(n \cdot \theta) \\ r &= R - \Delta r, \end{aligned} \quad (2)$$

where  $A$  denotes the amplitude of the polygonal wear,  $R$  is the radius of the wheel,  $n$  is the order of polygon wear,  $\theta$  is the wheel rotation angle, and  $r$  is the actual radius of the wheel from the central axis, which is related to  $\theta$ .

In the monorail vehicle, the compressed deformation of tire cannot be ignored which is caused by vertical forces. Therefore, the second method was chosen to investigate the influence of the wheel eccentricity on the vertical vibration of monorail vehicle.

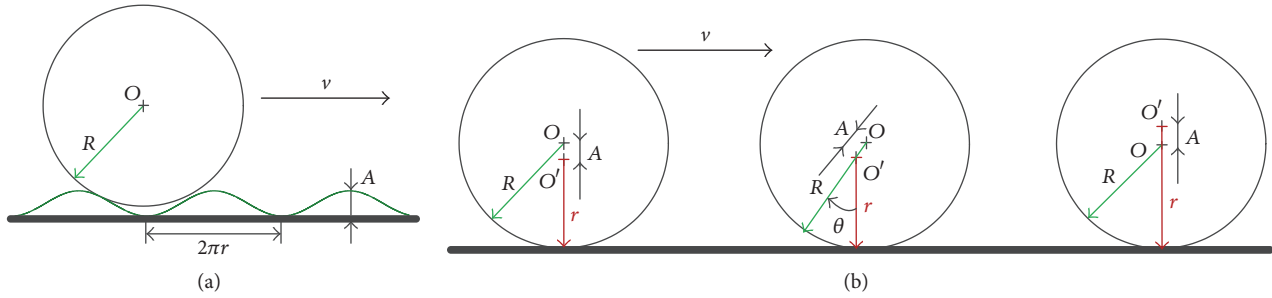


FIGURE 8: Methods to describe the wheel OOR: (a) transforming into track irregularity and (b) the harmonic deviation.

TABLE 2: Main parameters of the vehicle.

Parameters	Value	Units
Axle load	4000	kg
Bogie distance	5900	mm
Driving wheel base	1500	mm
Guiding wheel base	2900	mm
Driving wheel radius	270	mm
Mass of car body	7500	kg
Mass of bogie	1000	kg
Vertical stiffness of driving wheel	3.0	MN/m
Vertical stiffness of guiding wheel	1.8	MN/m
Secondary stiffness z-axis (one side)	1.0	MN/m
Secondary damper z-axis (one side)	30	kN·s/m
lateral damper ( $C_y$ )	30	kN·s/m

**3.3. Dynamic Vibration of Car Body with Wheel Eccentricity at Different Speeds.** In the simulation, only the excitation of wheel eccentricity is considered. All the driving wheels are equipped with wheel eccentricity and no phase difference exists. The vehicle was running on the tangent track. The main parameters of the suspended monorail vehicle used in the simulation are listed in Table 2.

The effects of the wheel eccentricity and its amplitude on the vertical acceleration of car body are illustrated in Figure 9. It can be observed that, with the increase of the eccentricity amplitude, the vertical acceleration of car body is increasing correspondingly. But the variation trend of the vertical acceleration of car body with the speed is not influenced by the amplitude of the wheel eccentricity. In the speed range ( $v < 21$  km/h), the acceleration of car body is obviously increased with the speed rising. Nevertheless, when the speed is in the range of  $21$  km/h  $< v < 35$  km/h, the car body acceleration decreases gradually. With the continuous increasing in the velocity, the acceleration of car body induced by the wheel eccentricity rises gradually. There is a peak at the speed of  $21$  km/h, which means that the vertical vibration of the car body is more obvious, and this is fully coincided with the experiment.

To understand the effects of the wheel eccentricity on the vibration of the car body, the time history of the vertical acceleration of the car body at the speed of  $21$  km/h is shown in Figure 10. The amplitude of wheel eccentricity is set to

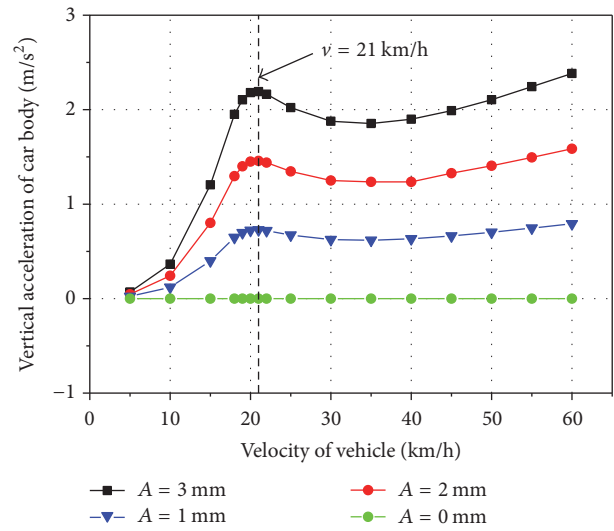


FIGURE 9: Vertical acceleration of car body at different speeds.

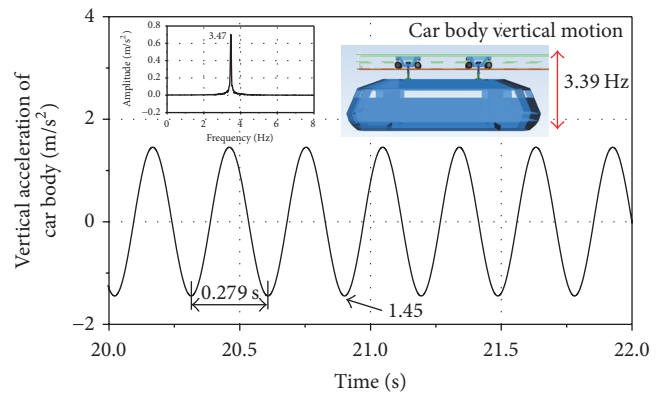


FIGURE 10: Vertical acceleration of car body at the speed of  $21$  km/h.

$2$  mm. For the case of wheel with eccentricity, the maximum vertical acceleration of car body is about  $1.45$  m/s<sup>2</sup>. The period of the oscillation of the acceleration is about  $0.279$  s. According to the calculated results, the excitation frequency of wheel eccentricity for the car body acceleration at the speed of  $21$  km/h is  $3.47$  Hz approximately, which gets close to the resonant frequency of the car body vertical motion  $3.39$  Hz. Therefore, the wheel eccentricity attributes to the vertical

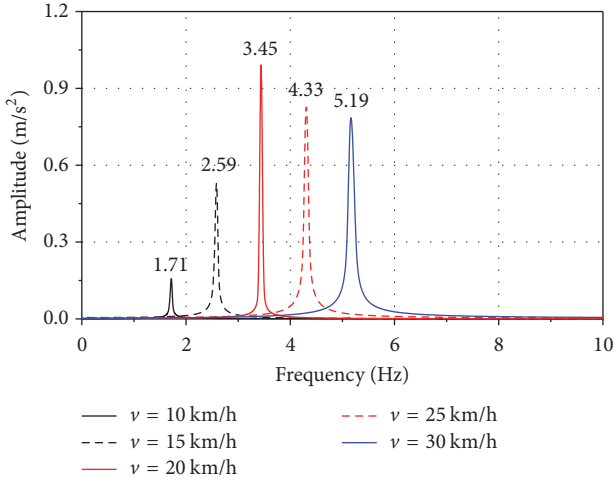


FIGURE 11: The frequency spectrum of the simulated acceleration at different speeds.

TABLE 3: Simulated dominant frequency of car body acceleration.

Velocity/(km/h)	10	15	20	25	30
Simulated/Hz	1.71	2.59	3.45	4.33	5.19
Experiment/Hz	1.73	2.58	3.48	4.27	5.08

resonance of car body at the speed of 21 km/h, so that the vertical vibration of car body is rising considerably.

Figure 11 shows the frequency spectrum of the vertical acceleration of car body at different speeds. It can be seen that there is a major frequency existing in the frequency domain, which is induced by the wheel eccentricity.

The comparison of simulated and experiment results in the dominant frequency of the car body acceleration which is showed in Table 3. It can be clear seen that the calculated domain frequency of car body acceleration with wheel eccentricity shows well accordance with the experiment. This comparison further verifies that the wheel eccentricity may cause the abnormal vibration of car body.

**3.4. Influence of the Secondary Suspension on the Vibration of Car Body with Wheel Eccentricity.** The vibration induced by wheel eccentricity transfers to the car body, which will seriously affect the ride comfort. For the suspended monorail vehicle, the secondary suspension is the most important component to attenuate the car body vibration, so its effect on the car body acceleration is calculated in the excitation of wheel eccentricity, which is hoped to reduce the influence of wheel eccentricity on ride comfort. The cases of vertical acceleration of car body with different secondary stiffness and damping are compared, as shown in Figure 12. The amplitude of wheel eccentricity is also set to 2 mm in the simulation.

Figure 12(a) indicates that, with the decrease of the secondary stiffness, the vertical acceleration of car body decrease significantly. When the stiffness decreased to 0.3 MN/m, the abnormal vibration is not appearing at low speed (<20 km/h). When the stiffness increased to 1.5 MN/m, the peak of vertical

acceleration is appearing at the speed of 23 km/h, which is a little higher than the stiffness of 1.0 MN/m.

The comparison analysis for the effect of the secondary damping on the vertical acceleration of car body with wheel eccentricity is demonstrated in Figure 12(b). When the speed is lower than 25 km/h, increasing the secondary damping can effectively reduce the car body acceleration caused by the wheel eccentricity. However, when the speed is higher than 25 km/h, the index of car body acceleration is rising with the increasing of the secondary damping.

## 4. Investigation on the Vertical Vibration of Car Body by Second Test

From the above analysis, the calculated result with wheel eccentricity shows a great accordance with the experiment. But the reinforcing rib and the track irregularity were not considered in the simulation. In order to verify that the abnormal vibration was induced by the wheel eccentricity, the secondary test is conducted. New wheel without eccentricity was installed on the vehicle and the monorail track was as same as the first test, so as the sensor position and test methods.

Figure 13 gives the comparison of the two test results of car body vertical acceleration. It should be noted that the maximum speed in the second test is set to 60 km/h.

It can be observed that the overall trend of the vertical acceleration of the car body increases as the vehicle velocity rising in the second test. Compared to the first test, the peak of car body acceleration at speed of 20 km/h is not appearing, which states that the vertical resonance of car body disappeared when renewing the wheel without eccentricity.

Figure 14 gives the comparison of the frequency spectrum of the two test results at different speeds. In the case of the second test, the car body acceleration is decreasing obviously at the domain frequency. Therefore, it can be deduced that the main reason of the abnormal vibration in the first test is wheel eccentricity.

From the comparison of the two tests, the abnormal vertical vibration of car body was disappearing when only eliminate the wheel eccentricity. Because the track is the same in the two tests, it could confirm that the wheel eccentricity is the main reason of the abnormal vibration. Meanwhile, the domain frequency also can be seen at low frequency, this may mainly cause the irregularity and the reinforcing rib existing on the monorail track, and its influence and optimization will be carried out in the future work.

## 5. Conclusions

In this study, the influence of the wheel eccentricity on the vertical vibration of suspension monorail vehicle is investigated and validated, based on extensive experiments and simulation. The main conclusions can be drawn as follows:

- (1) Based on the amplitude-frequency characteristic of the vertical acceleration in the first test, three possible reasons are proposed, which may cause the abnormal vibration of car body.

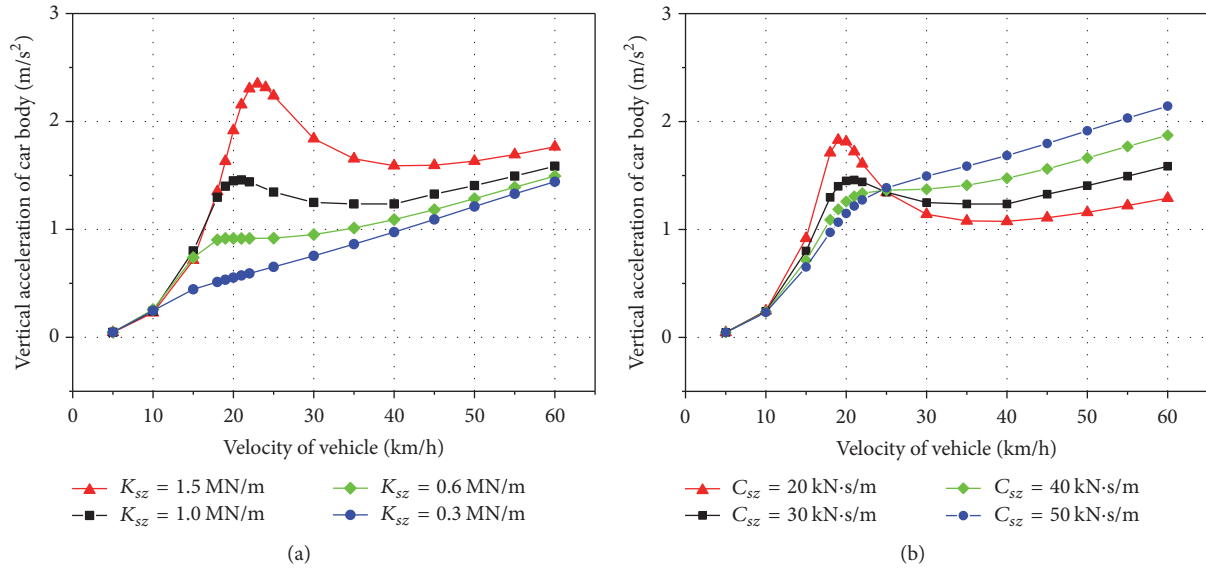


FIGURE 12: The effect of secondary suspension on the vibration of car body with wheel eccentricity: (a) stiffness and (b) damping.

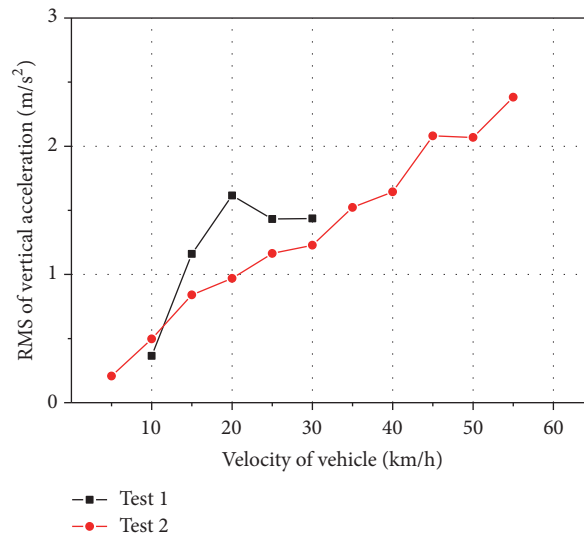


FIGURE 13: The comparison of the two test results.

- (2) The simulated acceleration excited only by wheel eccentricity shows great accordance with the first tested results. The variation trend of the acceleration is not influenced by the amplitude of wheel eccentricity. The vertical vibration induced by the wheel eccentricity could excite the resonance of car body at the speed of 21 km/h.
- (3) Decreasing the secondary stiffness can significantly reduce the vertical vibration of the car body caused by wheel eccentricity, especially at the resonant speed. As to the secondary damping, increasing the secondary damping can effectively reduce the car body acceleration caused by the wheel eccentricity at low speed

(<25 km/h). However, the index of car body acceleration is rising with the increasing of the secondary damping as the speed is higher.

- (4) In the case of the second test with new wheel, the peak of car body acceleration at speed of 21 km/h is not appearing, and the car body acceleration is decreasing obviously at the domain frequency. It is further determined that the abnormal vibration is mainly caused by the wheel eccentricity.

It should be noted that the flexibility of the monorail track is not considered in this study. However, in the real condition the track is not rigid; thus, it is necessary to take

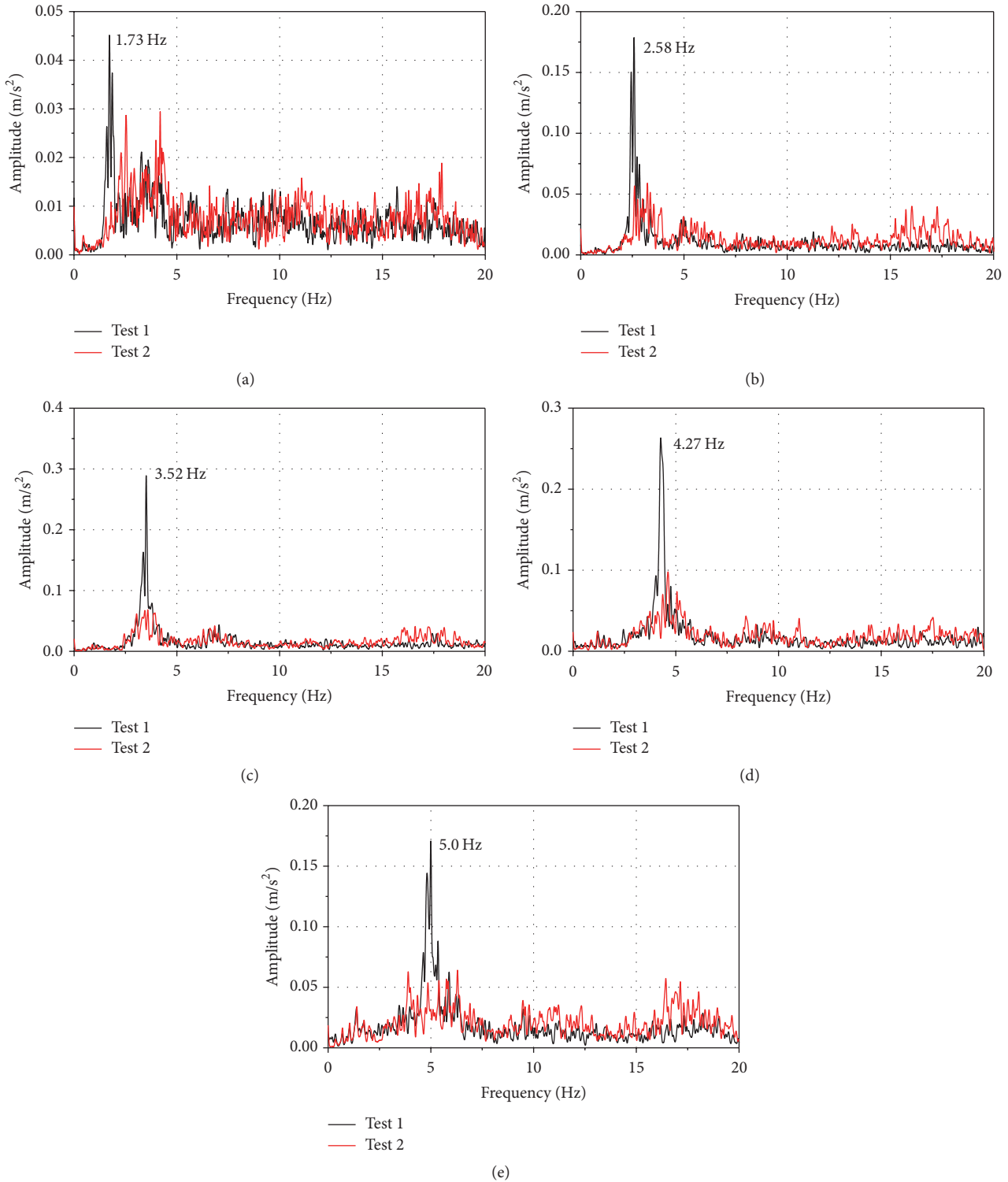


FIGURE 14: The comparison of frequency spectrum: (a) 10 km/h, (b) 15 km/h, (c) 20 km/h, (d) 25 km/h, and (e) 30 km/h.

the effects of the track flexibility into account in future work. Meanwhile, the curve passing performance of vehicle with wheel eccentricity should be investigated in future work.

**Conflicts of Interest**

The authors declare that they have no conflicts of interest.

## Acknowledgments

The authors wish to express their gratitude to State Key Laboratory of Traction Power for providing equipment and materials to this project and the China Sky Train Co., Ltd., for the cooperation and support. The authors are grateful for the financial support provided by the National Natural Science Key Foundation of China under Contract (Grant no. 51735012) and the Science and Technology Project of Sichuan Province (Grant no. 2017GZ0082).

## References

- [1] W. Zhai and C. Zhao, "Frontiers and challenges of sciences and technologies in modern railway engineering," *Xinan Jiaotong Daxue Xuebao/Journal of Southwest Jiaotong University*, vol. 51, no. 2, pp. 209–226, 2016.
- [2] J. C. O. Nielsen and A. Johansson, "Out-of-round railway wheels—a literature survey," *Proceedings of the Institution of Mechanical Engineers, Part F: Journal of Rail and Rapid Transit*, vol. 214, no. 2, pp. 79–91, 2000.
- [3] W. Zhai, *Vehicle-Track Coupled Dynamics [M]*, Science Press, 4th edition, 2015.
- [4] S. Iwnicki, *Handbook of Railway Vehicle Dynamics [M]*, CRC Press, 2006.
- [5] B. Morys, "Enlargement of out-of-round wheel profiles on high speed trains," *Journal of Sound and Vibration*, vol. 227, no. 5, pp. 965–978, 1999.
- [6] K. Wang, W. Zhai, K. Lv, and Z. Chen, "Numerical investigation on wheel-rail dynamic vibration excited by rail spalling in high-speed railway," *Shock and Vibration*, vol. 2016, Article ID 9108780, 11 pages, 2016.
- [7] K. Y. Wang, P. F. Liu, W. M. Zhai, C. Huang, Z. G. Chen, and J. M. Gao, "Wheel/rail dynamic interaction due to excitation of rail corrugation in high-speed railway," *Science China Technological Sciences*, vol. 58, no. 2, pp. 226–235, 2014.
- [8] X. Jin, L. Wu, J. Fang, S. Zhong, and L. Ling, "An investigation into the mechanism of the polygonal wear of metro train wheels and its effect on the dynamic behaviour of a wheel/rail system," *Vehicle System Dynamics*, vol. 50, no. 12, pp. 1817–1834, 2012.
- [9] G. Tao, L. Wang, Z. Wen, Q. Guan, and X. Jin, "Measurement and assessment of out-of-round electric locomotive wheels," *Proceedings of the Institution of Mechanical Engineers, Part F: Journal of Rail and Rapid Transit*.
- [10] A. Johansson, "Out-of-round railway wheels—assessment of wheel tread irregularities in train traffic," *Journal of Sound and Vibration*, vol. 293, no. 3-5, pp. 795–806, 2006.
- [11] A. Johansson and C. Andersson, "Out-of-round railway wheels—a study of wheel polygonalization through simulation of three-dimensional wheel-rail interaction and wear," *Vehicle System Dynamics*, vol. 43, no. 8, pp. 539–559, 2005.
- [12] E. Brommundt, "A simple mechanism for the polygonalization of railway wheels by wear," *Mechanics Research Communications*, vol. 24, no. 4, pp. 435–442, 1997.
- [13] J. Badger, S. Murphy, and G. Odonnell, "The effect of wheel eccentricity and run-out on grinding forces, waviness, wheel wear and chatter," *The International Journal of Machine Tools and Manufacture*, vol. 51, no. 10-11, pp. 766–774, 2011.
- [14] X. Wu, M. Chi, and P. Wu, "Influence of polygonal wear of railway wheels on the wheel set axle stress," *Vehicle System Dynamics*, vol. 53, no. 11, pp. 1535–1554, 2015.
- [15] D. W. Barke and W. K. Chiu, "A review of the effects of out-of-round wheels on track and vehicle components," *Proceedings of the Institution of Mechanical Engineers, Part F: Journal of Rail and Rapid Transit*, vol. 219, no. 3, pp. 151–175, 2005.
- [16] K. L. Knothe and S. L. Grassie, "Modelling of railway track and vehicle/track interaction at high frequencies," *Vehicle System Dynamics*, vol. 22, no. 3-4, pp. 209–262, 1993.
- [17] W. Zhai, H. Xia, C. Cai et al., "High-speed train–track–bridge dynamic interactions—part I: theoretical model and numerical simulation," *International Journal of Rail Transportation*, vol. 1, no. 1-2, pp. 3–24, 2013.
- [18] W. Zhai, S. Wang, N. Zhang et al., "High-speed train–track–bridge dynamic interactions—part II: experimental validation and engineering application," *International Journal of Rail Transportation*, vol. 1, no. 1-2, pp. 25–41, 2013.
- [19] R. Luo, J. Zeng, P.-B. Wu, and H.-Y. Dai, "Simulation and analysis of wheel out-of-roundness wear of high-speed train," *Tiedao Xuebao/Journal of the China Railway Society*, vol. 32, no. 5, pp. 30–35, 2010.

## Review Article

# Review of Blast Loading Models, Masonry Response, and Mitigation

Eid Badshah,<sup>1</sup> Amjad Naseer,<sup>1</sup> Muhammad Ashraf,<sup>1</sup> Feroz Shah,<sup>2</sup> and Kareem Akhtar<sup>2</sup>

<sup>1</sup>Department of Civil Engineering, UET Peshawar, Peshawar, Pakistan

<sup>2</sup>Department of Mechanical Engineering, UET Peshawar, Peshawar, Pakistan

Correspondence should be addressed to Amjad Naseer; amjad\_naseer@yahoo.com

Received 12 April 2017; Revised 3 July 2017; Accepted 3 August 2017; Published 29 November 2017

Academic Editor: Abdul Qadir Bhatti

Copyright © 2017 Eid Badshah et al. This is an open access article distributed under the Creative Commons Attribution License, which permits unrestricted use, distribution, and reproduction in any medium, provided the original work is properly cited.

Different models for prediction of blast loading, response of masonry structure against blast load, and various mitigation strategies are discussed. Variation of peak positive incident pressure with scale distance in free field spherical burst and surface burst scenarios, proposed by different researchers, is presented and compared. The variation is found significant in the region of small scaled distances. Blast wave parameters in urban environment have been found different from the free field scenario. Effects of geometry, boundary conditions, and material properties on response of masonry buildings were found significant. Different mitigation strategies such as blast wall, landscaping, architecture, and retrofitting techniques are presented.

## 1. Introduction

Terrorism has played havoc with civilian and public infrastructure by use of explosive materials for the last several decades. Bird's eye view on the incidents of terrorism speaks volumes for vulnerability of public buildings along with security installations to blast loading. The situation is becoming increasingly alarming due to simple techniques required for synthesis of explosive material from urea and fuel oil freely available in open market. The situation has been complicated further as the available literature for prediction of blast loads and response of structure is limited and qualitative in nature. Most of quantitative research and design guidelines developed since World War I are classified and limited to military establishments. However, several researchers have developed models, tables, and charts for predicting shock wave parameters on the basis of scaled distance ( $Z = R/W^{1/3}$ ). The results are largely scattered in the region of small scaled distances.

Blast results in extreme loading conditions against the nearby structures resulting in damage, shrapnel, and complete collapse. Percentage of injuries and deaths is greater due to impinging high velocity projectiles discharged from the structural elements than the direct shock waves in terrorist

bombing and accidental explosion. Furthermore, response of structure is dependent on relative position of point of detonation with respect to structure as well as ground surface, type and quantity of explosive used, natural time period, geometry, boundary conditions, and material properties of target structure.

A structure cannot be made safe completely against a defined threat level; however, the damages can be controlled by using different techniques. Various mitigation strategies can be used. These include strict surveillance of intelligence and security agencies, increasing stand-off distance between the centre of explosion and target structure using physical barriers, fabricating blast walls for attenuation of shock wave parameters before reaching the target structure, proper landscaping of site, optimizing orientation and architecture of structure, redetailing of structural elements, using energy absorbing materials, and hardening the structures by retrofitting techniques.

## 2. Pressure-Time History and Pressure Models

Blast load is an extreme and complex event characterized by abrupt increase to peak value of pressure and decaying

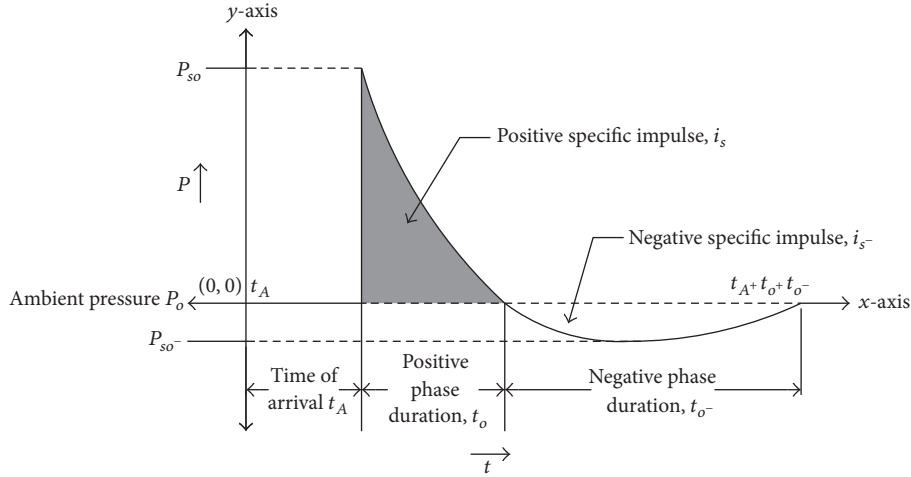


FIGURE 1: Pressure-time history (reproduced from UFC 3-340-02 [1]).

to atmospheric pressure, in microseconds. Simplified and typical pressure-time history is shown in Figure 1.

Pressure ( $P$ ) is shown on  $y$ -axis and time ( $t$ ) on  $x$ -axis. The ambient pressure  $P_o$  is shown as reference or zero pressure for the positive and negative pressure values. After explosion, the blast wave front reaches a target point in time  $t_A$  and in no time reaches peak incident pressure  $P_{so}$  which is the maximum positive pressure and then promptly decays to atmospheric pressure  $P_o$ . The trend continues in the negative direction and reaches peak negative pressure  $P_{so}^-$ . It is followed by further pulsations which are considered insignificant. Incident peak overpressure ( $P_{so}$ ) is important parameters for finding the response and design of structure against blast loading.

Researchers have developed models for peak positive incident pressure ( $P_{so}$ ) along with other parameters of shock wave for free air burst and surface burst scenarios. For surface burst, the TNT equivalent weight in free air burst shall be increased by 70–80% to account for earth surface reflection and consequent reinforcement (Karlos et al. [2]). Surface reflection and reinforcement is mainly dependent on the nature of base materials. Ullah et al. [3] reported reflection factors for commonly used base materials. Similarly, shape of explosive and its point of ignition affect positive overpressure. Badshah [4] found attenuated reflection of blast waves from ground surface for cylindrical shaped explosives when ignited at top flat face.

2.1. Free Air Burst Models. Brode model [5] is

$$P_{so} = \frac{0.67}{Z^3} + 0.1, \quad (P_{so} > 1),$$

$$P_{so} = \frac{0.0975}{Z} + \frac{0.1455}{Z^2} + \frac{0.585}{Z^3} - 0.0019, \quad (0.01 < P_{so} < 1).$$
(1)

Henrych and Major model [6] is

$$P_{pos} = \frac{1.4072}{Z} + \frac{0.5540}{Z^2} - \frac{0.0357}{Z^3} + \frac{0.000625}{Z^4},$$

(0.05 < Z < 0.3),

$$P_{pos} = \frac{0.6194}{Z} - \frac{0.0326}{Z^2} + \frac{0.2132}{Z^3}, \quad (0.3 \leq Z \leq 1),$$

$$P_{pos} = \frac{0.0662}{Z} + \frac{0.405}{Z^2} + \frac{0.3228}{Z^3}, \quad (1 \leq Z < 10).$$

(2)

Held model [7] is

$$P_{pos} = 2 \frac{W^{2/3}}{R^2}. \quad (3)$$

Kinny and Graham model [8] is

$$P_{pos} = P_o \cdot \frac{80.8 [1 + (Z/4.5)^2]}{\sqrt{[1 + (Z/0.048)^2]} X \sqrt{[1 + (Z/0.32)^2]} X \sqrt{[1 + (Z/1.35)^2]}}. \quad (4)$$

Mills model [9] is

$$P_{pos} = \frac{1.772}{Z^3} - \frac{0.114}{Z^2} + \frac{0.108}{Z}. \quad (5)$$

Sadovskiy model [10] is

$$P_{pos} = 0.085 \frac{W^{1/3}}{R} + 0.3 \left[ \frac{W^{1/3}}{R} \right]^2 + 0.8 \left[ \frac{W^{1/3}}{R} \right]^3. \quad (6)$$

Bajic model [11] is

$$P_{pos} = 0.102 \frac{W^{1/3}}{R} + 0.436 \frac{W^{1/3}}{R^2} + 1.4 \frac{W}{R^3}. \quad (7)$$

TM5-855-1 model [12] is

$$P_{pos} = \frac{4120}{Z^3} - \frac{105}{Z^2} + \frac{39.5}{Z},$$

for ( $2 < P_{so} < 160$ ), ( $3 < Z < 20$ ).

(8)

2.2. *Surface Burst Models.* Newmark and Hansen model [13] is

$$P_{so} = 0.6784 \frac{W}{R^3} + 0.294 \frac{W^{1/2}}{R^{3/2}}. \quad (9)$$

Swisdak model [14] is

$$P_{pos} = \left( \exp A + B \times \ln(Z) + C \times (\ln(Z))^2 + D \times (\ln(Z))^3 + E \times (\ln(Z))^4 + F \times (\ln(Z))^5 + G \times (\ln(Z))^6 \right) \times 10^{-3}. \quad (10)$$

Wu and Hao model [15] is

$$P_{pos} = 1.059 \left[ \frac{R}{W^{1/3}} \right]^{-2.56} - 0.051, \quad \text{for } \left( 0.1 \leq \frac{R}{W^{1/3}} \leq 1 \right), \quad (11)$$

$$P_{pos} = 1.008 \left[ \frac{R}{W^{1/3}} \right]^{-2.01}, \quad \text{for } \left( 1 < \frac{R}{W^{1/3}} \leq 10 \right).$$

Siddiqui and Ahmad model [16] is

$$P_{pos} = 1.017 \left[ \frac{R}{W^{1/3}} \right]^{-1.91}, \quad \text{for } \left( 1 \leq \frac{R}{W^{1/3}} \leq 12 \right). \quad (12)$$

Ahmad et al. model [17] is

$$P_{pos} = 2.46 \left[ \frac{R}{W^{1/3}} \right]^{-2.67}. \quad (13)$$

Iqbal and Ahmad model [18] is

$$P_{pos} = 1.026 \left[ \frac{R}{W^{1/3}} \right]^{-1.96}, \quad \text{for } \left( 1 \leq \frac{R}{W^{1/3}} \leq 12 \right). \quad (14)$$

Badshah model [4] is

$$P_r = 4.34 \times Z^{-2.84}, \quad (15)$$

where “ $W$ ” is TNT equivalent weight (kg), “ $R$ ” is stand-off distance (m), and “ $Z$ ” is the scaled distance defined below:

$$Z = \frac{R}{W^{1/3}} \quad (\text{m/kg}^{1/3}). \quad (16)$$

All the above models for peak positive reflected overpressure are plotted in Figure 2.

Held model [7] and Brode model [5] predict the highest and lowest values, respectively, among all the investigated free air burst and surface burst models for the selected range of scaled distance  $Z$  (4.353–1.830 m/kg<sup>1/3</sup>) in this study. The behavior of Held [7], Sadoyskiy [10], and Bajić [11] models is strange enough as it gives even higher values than all the surface burst models. Iqbal and Ahmad model [18] and Siddiqui and Ahmad model [16] give almost same values and are placed at the centre of all plots. Similarly, Badshah [4] and Kinney and Graham model [8] demonstrate nearly the same values in the region of large scaled distances. The results for both free air burst and surface burst are scattered largely in the region of small scaled distance. Furthermore, the results of surface burst models are less scattered as compared to free air burst models. Scattering of models indicate poor investigation of blast loads in near field and variability of behavior of blast load models from near to far field scenarios.

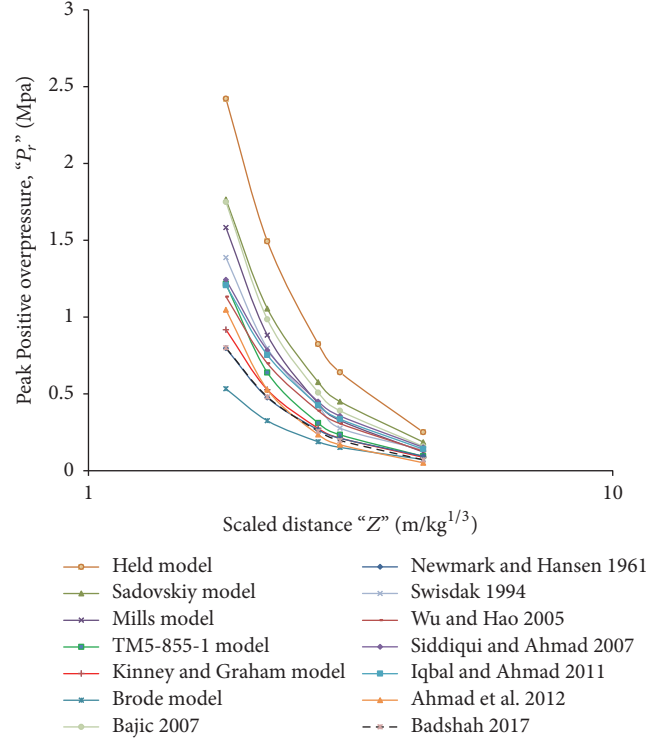


FIGURE 2: Comparison of blast models.

2.3. *Effect of Adjacent Structures.* Shock wave parameters are different in free field than urban environment for the same TNT equivalent charge weight and stand-off distance. Smith and Rose [19] reported, “regions of high and low loading do not necessarily occur where they might intuitively be expected; ‘hot spots’ occur where a building surface might be expected to be shielded and relatively low loads are evident where a direct line from charge to ‘target’ might be expected to produce a higher load.” The author found that Feng followed by Whalen was among the earliest investigators who found enhanced blast wave parameters in simple straight and model city streets configurations, respectively.

Birnbaum et al. [20] used three-dimensional Eulerian FCT techniques to study the channeling effect on the blast wave parameters on the target office block near the ground, in the scenario of partial confinement of blast wave in city street as shown in Figure 3.

Blast wave parameters at the base of office block were found reinforced by the channeling effect due to the presence of other buildings and comparison with free field scenario is shown in Figure 4. Channeling effect increased peak over pressure and maximum impulse by 153% and 340%, respectively, when compared with free field results using analytical model.

Johansson et al. [21] studied the effect of urban environment on the blast wave parameters. Semiempirical model AUTODYN™ [19] based on computational fluid dynamics (CFD) was used for numerical studies. For simulating the urban environment, experimental test was carried in simple intersection comprising four concrete blocks with reduced

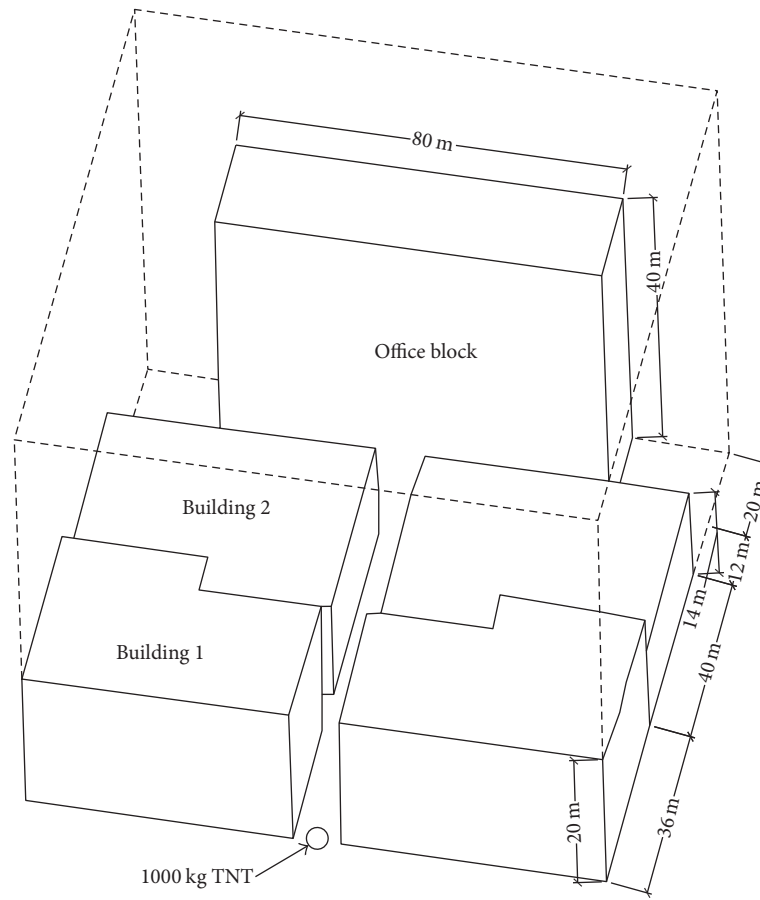


FIGURE 3: Detail of explosive placement, street, and target office block.

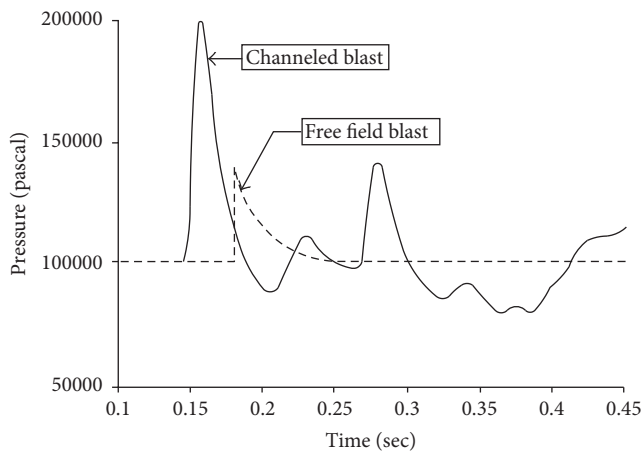


FIGURE 4: Comparison of free air field and street channeled blast pressure-time history.

scale of 1:5. Complex urban scenario changed blast wave parameters as a result of diffractions and reflections at various points in comparison to free field. Sixty-five percent (65%) pressure-time histories of experimental and AUTODYN results showed good match and reached  $\text{Coh} \geq 0.5$ . Furthermore, author has shown that superposition theorem with

adjustment for diffraction of pressure waves where needed can be used as raw technique for estimating pressure from incident pressures and consequent load generated in complex environment. By using this technique results obtained were deviating only 20% from the experimental data.

Reminnikov [22] studied the increasing or decreasing effect on blast loads on building due to the presence of adjacent structures. Air3D program was used for numerical simulation. Blast event targeted medium sized shopping mall at the end of T-junction in a portion of straight city street. City street was 100-meter long passing through buildings of different heights 10 m, 20 m, and 30 m to 40 m. The blast environment was generated by use of 1000 kg TNT equivalent explosive placed on the ground surface in the middle of the street. The stand-off distance for the nearest building was 5 m. It was observed that peak over pressure as well as positive impulse increased along the street due to multiple reflections from the adjacent structures when compared with free field surface burst explosion scenario. It was shown that all buildings with scaled height ( $h/W^{1/3}$ ) greater than  $1.0 \text{ m/kg}^{1/3}$  provided same level confinement to the peak pressure. Similarly, all buildings with scaled height greater than  $3.0 \text{ m/kg}^{1/3}$  have equal effect on positive impulse at ground level. Enhancement Design Factors (ratio of numerical and empirical values) as a function of distance for pressures and

impulses were derived along the street. The peak reflected pressure on the target building at the T-junction was found 300% greater than empirically (free field) measured pressure. Enhancement Factors for reflected pressure and reflected impulse remained constant on the front wall of the target building along vertical line but decreased near the top of the building due to diffraction of pressure waves over the roof.

Rose and Smith [23] studied the effect on the profile of impulse from a blast event occurring in city street bordered by representative height of buildings. Numerical study using three-dimensional Air3D program was compared to the results of reduced scale (1/40) experiments. Peak positive and negative impulses on front of buildings near the ground level were plotted against the scaled distance along the street. It was observed that street width scaled distance greater than  $4.8 \text{ m/kg}^{1/3}$  does not affect the positive impulse on the near side. Similarly, buildings with scaled height more than  $3.2 \text{ m/kg}^{1/3}$  do not increase positive impulse significantly. Negative impulse is maximum when scaled building height reaches  $12.8 \text{ m/kg}^{1/3}$ . Negative phase impulse is more than positive impulse pertaining to street centre line scaled distance of  $2.0 \text{ m/kg}^{1/3}$  for all widths of streets and height of buildings.

Mays and Smith [24] discussed the funneling effect of shock waves in urban environment. Authors reported that hemispherical flow of blast wave is restrained in city streets due to the reflection, refraction, and diffraction from the adjacent structures. Consequently, pressure drop with distance is more slowly which endanger relatively far off located buildings.

Effects of terrorist activities in urban centre are neither limited to target structure nor equivalent to free field environment. The effects may be devastating for structure due to channeling/funneling effect of the adjacent structures. Sophisticated numerical methods or software based on computational fluid dynamics (CFD) such as AUTODYN and Air3D may be used for accurate analysis of the structure under blast loading in complex urban environment.

### 3. Structural Response

Response of structure is dependent on blast wave parameters, natural time period, geometry, boundary conditions, and material properties of target structure.

**3.1. Effect of Stand-Off Distance.** Response of structure varies between local failure of structural elements and global failure of the structure depending mainly on the stand-off distance. TEK 14-2A Structural [25] reported that close-in and far-away blasts initiate local punching and flexure failure, respectively. Localized shear failure is initiated in structural element in the shape of punching, spalling producing low and high velocity debris when centre of blast is in close proximity or contact (Ngo et al. [26]). Shi et al. [27] experimentally studied local damage and fragments characterization discharging from unreinforced masonry wall subjected to near field blast scenario. Two (02) unreinforced masonry walls fabricated in RC frames were subjected separately to blast loads 1 kg and 6 kg TNT equivalent weight at a constant stand-off distance

of 0.4 m. For 1 kg TNT weight blasts, no wall local damage was observed while, for 6 kg TNT weight blast scenario, hole was punched in the masonry wall. Thus close range blast scenario, resulted in local damage in the shape of punching or spalling instead of flexural or shear failure of wall. Furthermore, smaller fragments scattered at larger distance and larger fragments fell in the nearby area.

Failure pattern changes into global domain as the distance between centre of explosion and structure is increased. When structure is exposed to long duration out-of-plan loading, global response in the shape of bending or shear failure is initiated (Ngo et al. [26]). Keys and Clubley [28] investigated masonry debris distribution and failure patterns of masonry when subjected to blast pressure with more than 100 ms positive phase duration. A total of ten (10) masonry walls of different geometries were subjected to blast test events with 200 ms and 150 ms positive phase durations corresponding to peak over pressures of 55 kpa and 110 kpa, respectively. All ten (10) samples exhibited structural failure and it was observed that failure pattern, debris distribution, and initial fragmentation were affected by geometry of walls, overpressure, and impulse of blast loads.

Blast close in contact with structure impinges the structural element such as wall or column before encompassing the whole structure. Local failure changes to global failure due to progressive collapse for poorly designed structural systems.

**3.2. Effect of Structural Element Geometries.** Structural element length, height, and thickness affect response of the structure to a given blast scenario. Increasing thickness of structural elements improves the performance if other parameters are kept constant. Pandey and Bisht [29] and Pereira et al. [30] reported enhanced dynamic performance with increasing thickness of brick masonry wall against blast loading. Wei and Stewart [31], using LS-DYNA, reported that increasing masonry wall thickness decreases damage level. Increasing aspect ratio (height/thickness) of masonry wall decreases its resistance against blast loading. Parisi et al. [32] reported 116% increase in resistance against blast loading of tough stone masonry (TSM) when transverse aspect ratio was decreased from 10 to 5.

**3.3. Effect of Material Properties.** Response of structure against blast loading varies among structures fabricated from different materials. Wei and Stewart [31], using LS-DYNA, found that increase in strength of mortar and masonry unit results in decrease of maximum deflection in masonry and rotation at support under small blast loading. Pereira et al. [30] studied behavior of  $1.7 \text{ m} \times 3.5 \text{ m}$  masonry infill wall on scaled model of 1:1.5, subjected to out-of-plane loading using newly developed technique of confined underwater blast wave generators (WBWG) with experimental set-up shown in Figure 5. Parametric study regarding the effect of geometrical and material properties of infill masonry on the performance of masonry was carried out. Increasing compressive and tensile strengths and, modulus of rigidity  $G$  of infill masonry up to certain level decreased maximum deflection in the masonry in the region of small scaled

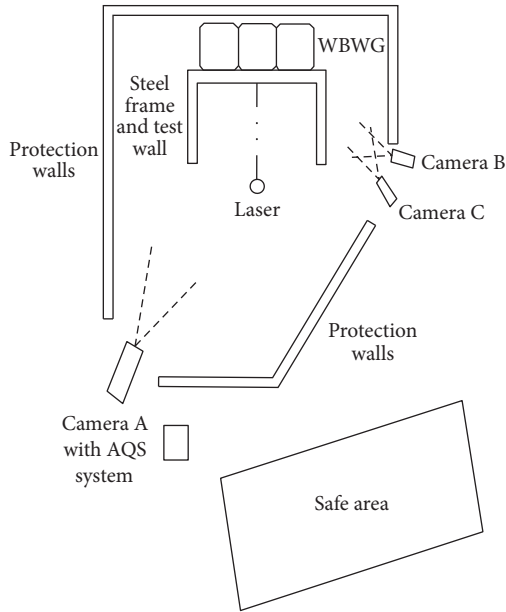


FIGURE 5: Detail of experimental set-up.

distances. Increasing Young's Modulus  $E$  decreased maximum deflection at all scaled distances.

Pandey and Bisht [29] reported that increasing coefficient of friction and richness of mortar used in masonry resulted in decreasing max deflection at the centre as well as at masonry and frame interface against blast loading. Parisi et al. [32] reported significant influence of material strength on resistance of tough tile masonry (TSM) against impulsive and dynamic loading.

**3.4. Boundary Conditions and Precompression Ratio.** Boundary condition of structural or nonstructural elements plays an important role in structural response and damage level against blast loading. Wei and Stewart [31], using LS-DYNA, studied response of masonry walls with different boundary conditions as shown in Figure 6. Maximum deflection and damage level decreased with inducing increased number of fixed ended conditions. All walls predicted to collapse under larger blast loads when scaled distance is less than or equal to  $4.0 \text{ m/kg}^{1/3}$ . El-Domiatty et al. [33] reported that changing boundary conditions changes response of brick masonry appreciably; however, modifying boundary conditions especially in infill masonry has its limitations.

Hao and Wu [34] and Wu and Hao [35] found different scaled distances  $4.50 \text{ m/kg}^{1/3}$  and  $4.22 \text{ m/kg}^{1/3}$ , respectively, for the same damage level (nonexcessive damage) in infill masonry with same material model but with different material models of RC frames. Ahmad et al. [36] reported no damage at scaled distance of  $2.28 \text{ m/kg}^{1/3}$  of solid clay brick masonry cantilever wall in experimental study but Wu and Hao [35] found collapse of infilled CMU masonry in RC frame at a higher scaled distance of  $2.37 \text{ m/kg}^{1/3}$  in numerical study. Badshah [4] found minor damage and no damage in unconfined and confined clay brick masonry, respectively, for

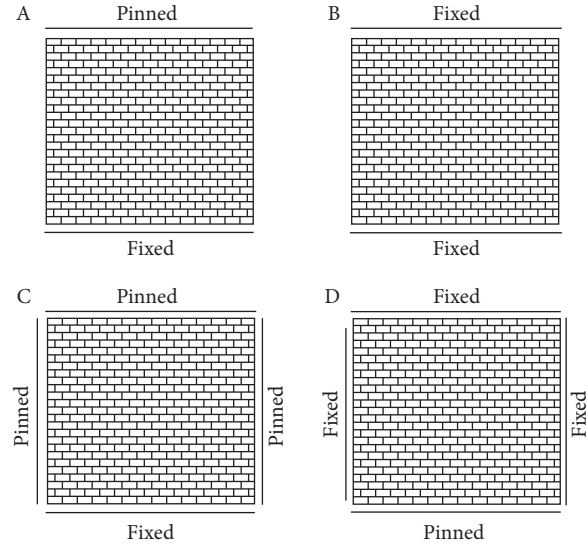


FIGURE 6: Detail of boundary conditions.

the same scaled distance  $4.5 \text{ m/kg}^{1/3}$  as shown in Figure 7. Similarly, for scaled distance  $1.89 \text{ m/kg}^{1/3}$ , unreinforced wall collapsed completely and confined masonry wall, though damaged, remained intact as shown in Figure 8.

Precompression in load bearing masonry significantly changes response against blast loading. Parisi et al. [32] found an enhanced performance against blast loading of tough tile masonry (TSM) with increasing precompression ratio.

## 4. Mitigation

No single remedy exists against blast loading but combination of the following active and passive techniques shall be employed for effective mitigation:

- (i) Initial layer of mitigation against terrorist bombing is the efficient use of intelligence and security agencies for intercepting the suicide bombers and other criminals laden with explosive devices before reaching specified public or private commercial building.
- (ii) It is followed by increasing the stand-off distance between point of explosion and targeted buildings by providing physical barriers. Physical barriers in the shape of blast walls attenuate blast wave parameters behind the wall.
- (iii) Proper landscape, building orientation, and architectural design with respect to specific blast threat play important attenuating role.
- (iv) Building redetailing, capacity design, designed for continuity and use of ductile and energy absorbing yet high strength materials in structure fabrication, and proper retrofitting techniques strengthen the structure when all other techniques fail against blast loading.

Goel et al. [37] reviewed mitigation strategies for mitigation of blast load against buildings. Different blast mitigation



FIGURE 7: For scaled distance  $4.5 \text{ m/kg}^{1/3}$  postblast scenario, (a) unreinforced masonry and (b) confined masonry.



FIGURE 8: For scaled distance  $1.89 \text{ m/kg}^{1/3}$  postblast scenario, (a) unreinforced masonry and (b) confined masonry.

strategies include increasing stand-off distance by construction of barriers, redistribution of mass of structure, shaping building in such way to avoid square-edge, rectangular long-edge sections in the path of direct shock waves, using light weight energy absorbing materials (metal and polymeric foams) in fabrication of buildings, and provision of properly designed sacrificial blast walls. Design of blast wall shall result in nonformation of Mach stem behind it.

**4.1. Blast Wall.** It is a physical barrier used to protect vulnerable buildings and structures along with people inside from the devastating effects of a nearby explosion. Smith and Rose [38] defined blast wall as “a physical barrier separating a valuable asset from explosive threat that produces a blast capable of damaging asset; the wall mitigates the level of blast loading that impinges on the asset being protected.”

Beyer [39] visualized the path of the incident wave diffracting over the blast wall as shown in Figure 9 and reported attenuated positive peak overpressure behind the wall.

Chapman et al. [40] incorporated geometrical parameters in finding protection factor as a function of scaled distance in small scale experimental study. Efficiency of blast wall was found dependent on its height, height of explosive above ground surface, height of target, and horizontal stand-off distances from blast wall to target structure and from blast wall to the charge.

Rose et al. [41], developed design charts, incorporating effect of distance from the wall to the target point behind the wall, distance of wall from the charge, and height of blast wall.

Author reported that, in case of rigid wall, the effect of canopy or shape of the canopy as compared to the plan wall on the pressure behind the wall was found insignificant. It was also found that the wall should be close to the point of blast for an early interaction and consequently more attenuation effect.

Zhou and Hao [42] carried out numerical study using AUTODYN3D to estimate surface blast loads on a structure behind the protective barrier or blast wall. The weight of equivalent TNT “ $W$ ,” height of building “ $H_B$ ,” distance between the charge and building “ $D$ ,” the height of the blast wall “ $H_1$ ,” the ratio of distance between the blast wall and explosion to that between the building and the explosion “ $L_1/D$ ,” and thickness of blast wall were varied between 10 kg to 1000 kg, 3 m to 40 m, 0.2 to 0.8, 1 m to 40 m, and 150 mm to 300 mm, respectively, as shown in Figure 10.

Numerical study showed insignificant effects on the pressure parameters behind the protective barrier with the changing of barrier thickness in the range 150 mm to 300 mm. Therefore, wall thickness was fixed at 250 mm in each case. Provision of barrier between building and point of explosion decreased positive peak reflected pressure and impulse on the building and arrival time of shock wave was increased. Effects on negative wave parameters were found insignificant. The efficiency of protective wall was found dependent on barrier height, separation of point of explosion and barrier, and distance between the building and barrier structure and height of the structure. Based on the numerical results, models were derived for estimating reflected pressure-time history parameters behind the barrier structure.

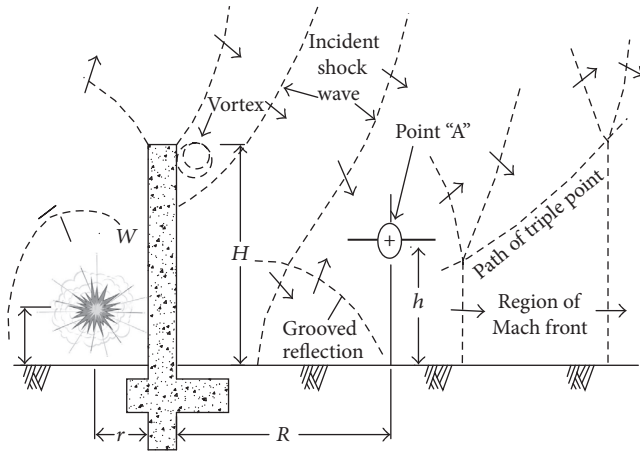


FIGURE 9: Experimental arrangement and visualization pressure waves trajectories diffracting over the blast wall.

Hajek et al. [43] experimentally studied the effect of shape of surface and type of material on performance of barrier wall using 40% scaled down ratio for the blast wall. Deformable material performance was compared with Ultra High Performance Fiber-Reinforced Self Compacting Concrete (UHPRSCC). Small rough surface wall produced results comparable with the results attainable by larger smooth surface walls, thereby inducing an added advantage to the former in congested environment. Sheeting with an uneven surface can also be used in structural walls, ceiling, and so forth for reducing the reflected over pressure. The deformable wall showed an increased mitigation in comparison to the rigid wall. UHPRSCC wall performance was found excellent and recommended its use for internal as well as external applications.

Philip [44] experimentally worked out reduction factors for pressure and impulse behind the barrier wall. These factors were based on slant ranges from top of wall to the top of building and from top of wall to the charge. Research in this field was accelerated in the back drop of terrorist activities in 1970.

Jones et al. [45] used 1/10th scaled model of blast wall and suitable scaled charge of vehicle born improvised explosive device (VBIED), exploded at varying stand-off distances from embassy building to evaluate its potential against blast loading. Models were developed for overpressure and reflected overpressure impulse with and without perimeter wall (blast wall) shown in equations (17)-(18).

Reflected overpressure and reflected overpressure impulse without perimeter wall (blast wall) are as follows:

$$\begin{aligned} P_w &= 287.0 * Z^{-1.57}, \\ I_w &= 30.9 * Z^{-0.822} * W^{1/3}. \end{aligned} \quad (17)$$

Reflected overpressure and reflected overpressure impulse with perimeter wall (blast wall) are as follows:

$$\begin{aligned} P_{wo} &= 1433.0 * Z^{-2.21}, \\ I_{wo} &= 70.9 * Z^{-0.977} * W^{1/3}. \end{aligned} \quad (18)$$

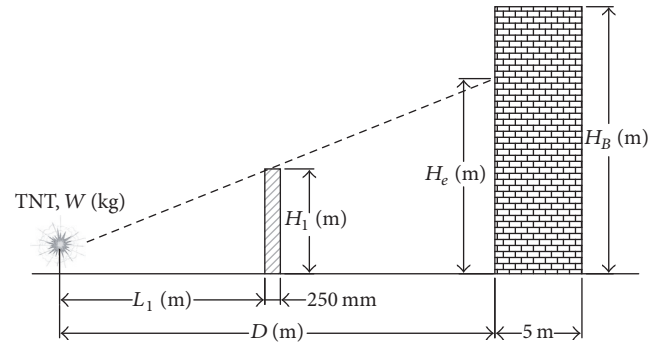


FIGURE 10: Detail of explosive placement, barrier wall, and target building.

Comparison of both scenarios indicates the mitigation capacity of blast wall against blast loading.

Rose et al. [46] used 1/10th scaled model of 3 m plan tall wall fabricated from steel for affecting the blast on selected points behind the wall. The results with and without barrier wall shown in contour maps indicating reduction in zone of highest pressure are shown in Figure 11.

This study showed that rigid, plane, and robust wall mitigated pressure and impulse significantly up to six times of wall height behind the wall.

Rose et al. [47] studied effect of mass and strength of blast wall on attenuating peak pressure behind the wall. Thick sand wall showed better performance against rigid plan wall as well as walls made of wood, polymer sheets, and ice, as shown in Figure 12.

Bogosian and Piepenburg [48] reported that frangible walls fabricated from light weight concrete masonry unit (CMU), water wall, or thin precast concrete panels reduce the blast effects significantly as shown in Figure 13.

Figure 13 shows that less expensive frangible material walls exhibiting mitigation effects are almost at par with rigid wall.

Mayor and Flanders [49] developed computer software incorporating the models developed by Jones et al. [45] for assessing the effects of vehicle born improvised explosive device (VBIED) on the structure and personnel of US embassies.

Smith and Rose [38] presented research work dealing with blast wall performance in protection against blast loading. Furthermore, different types of blast wall in use were presented.

Properly designed blast walls attenuate blast wave parameters significantly. Consequently, damage to built environment and life is minimized. Choice of particular type of blast is governed by ease of fabrication, transportation, space constraints, economy, and vitality and importance of property to be protected.

**4.2. Architectural and Geometrical Aspects of Buildings.** Buildings shapes, space, and orientation are usually decided based on environmental consideration, aesthetics, and functionality coupled with available land space and resources. This general practice may not be in consonance with specific

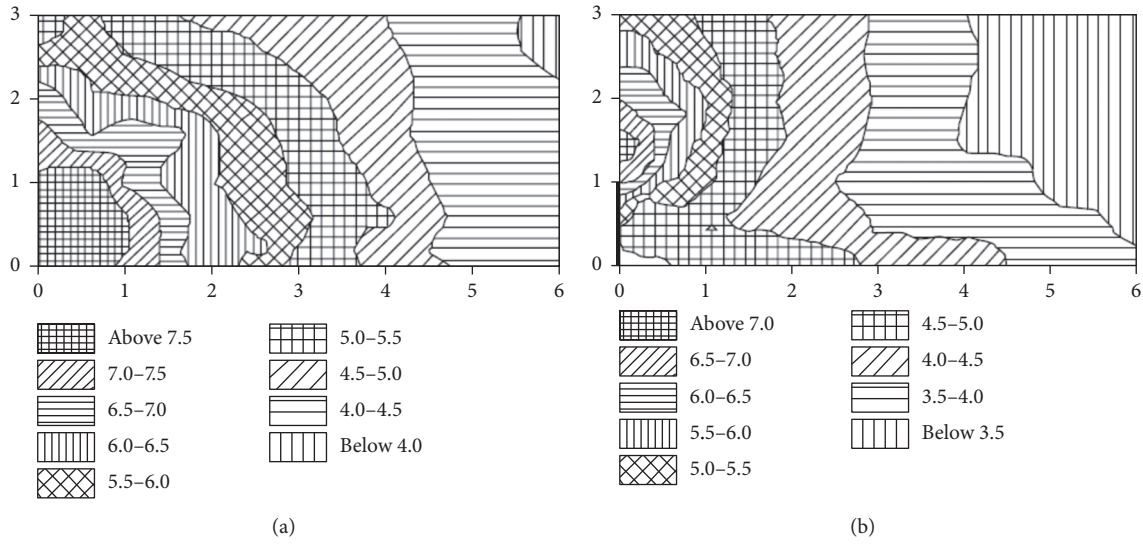


FIGURE 11: (a) Pressure contour map without wall; (b) pressure contour map with wall.

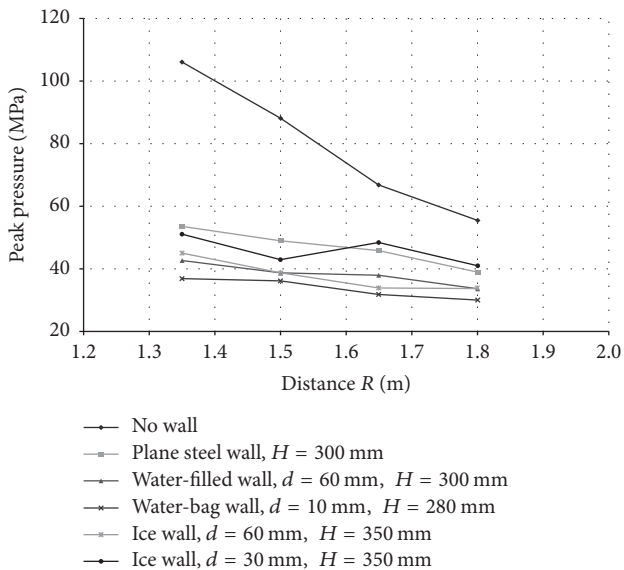


FIGURE 12: Peak pressure attenuation with different blast wall.

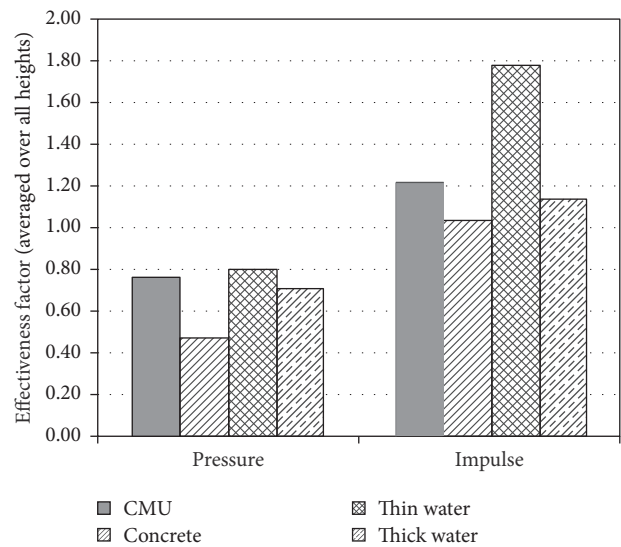


FIGURE 13: Peak pressure and impulse variation with blast wall fabricated from different materials.

requirements of blast loading. Various researchers investigated blast efficient architectural design of buildings. Koccz et al. [50] studied incorporation of blast resistant design aspects in both architectural and structural design stages of buildings. Author has reported as much stand-off distance by erection of barriers between external bomb and newly planned and existing buildings as possible and minimum stand-off distance from building shall be 30 meters as shown in Figure 14.

Arches and domes shapes attenuate the effect of blast pressure when compared with cubicle or rectangular shapes. Similarly, complex shape geometry of building causing multiple reflections experiences much loads. Single-storey building and partially or fully embedded building response

are well against blast loading. Sensitive or high value assets in building shall be separated as far as possible from the highest possible threat. Entry points to building shall be separated and strictly controlled. Underground car parking or passage poses risk unless properly checked and controlled. Properly designed shelter areas shall be provided in case of any incident. Building shall be designed to tolerate reversal of loads and avoid progressive collapse. Beam-column joint shall be properly designed against blast induced forces. Barakat and Hetherington [51] found the effects on blast waves and fragments due to landscape. Author mentioned that ground profile technique, as shown in Figure 15, provided shielding effect to the building.

Barakat and Hetherington [52] introduced blast efficient architectural forms after evaluating efficiency of various

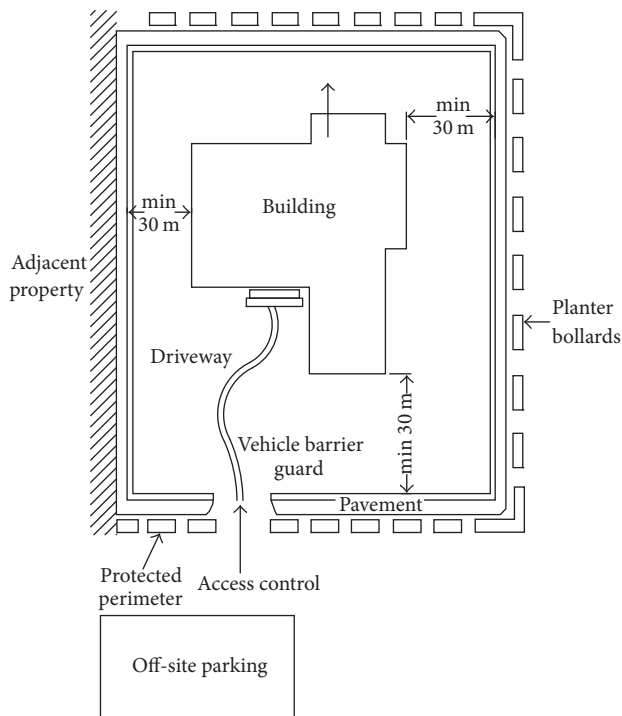


FIGURE 14: Layout of building for blast protection.

structural shapes subjected to car bomb threat scenario at 15 m stand-off distance by using simulations in AUTODYN. Decrease in impulse with height was found more when the corner or apex of the plan structure was positioned towards the explosion. In wing-form-plan structure with obtuse angle between the two wings more decrease in impulse with height was found. Significant decrease in impulse in hemispherical structure was observed. Similarly, stepped form architecture and introvert design manifested relief in the impulse. Gebbeken and Döge [53] discussed different strategies for protecting buildings in urban environment against blast loadings. Properly designed nonconvex shape, planting hedges in landscape, use of soft and energy absorbing material in facades, selecting circular sections for structural elements, and increasing stand-off distance attenuate the blast wave parameters. Gunaratan, [54] narrated that truck loaded explosive caused enormous devastation in Mariot Hotel Islamabad Pakistan despite greater stand-off distance of 40.23 m against standard practice distance of 30.50 m between the gate and main building. Kulkarni and Sambireddy [55] reported that maximum storey drift in regular frame was found less than the irregular frame for the same loading scenario. Infill frame performed well in storey drift against lateral blast loading. Consequently, regular infill frame was found most efficient in blast loading.

**4.3. Retrofitting Techniques.** Building may be strengthened against blast loading by using different retrofitting techniques. Knox et al. [56] and El-Domiatiy et al. [33] reported different techniques for enhancing response of unreinforced brick masonry against blast loading such as increasing

wall thickness, changing boundary conditions, replacement of weak elements, and incorporating steel reinforcement. All these techniques are expensive, impractical, and time-consuming in most of the situations. Therefore, new techniques which are easier, light weight, and less expensive such as FRP (CFRP, GFRP, and AFRP), polyurea, polyurethane, aluminum foam, engineered cementitious composites, and ferrocement are used. These techniques are used for increasing ductility as well as arresting dangerous high velocity debris discharging from the target structure or building during blast loading.

**4.3.1. FRP.** Fiber reinforced polymers (FRP) are unidirectional fabric composites in matrix which are attached to masonry surface by using proper resin or epoxy. FRP strengthened masonry has been extensively investigated (Lantz et al. [57]).

Urgessa and Maji [58] studied, experimentally, the Dynamic Response of Masonry Walls reinforced with carbon fibers using two different matrices against blast loading. Eight masonry walls  $101.5 \text{ cm} \times 304.8 \text{ cm} \times 20.4 \text{ cm}$  were fabricated in a circular arrangement inside reinforced concrete containment structure. These walls were retrofitted with unidirectional two layered and four layered FRP by using inorganic matrix geopolymer and organic matrix thixotropic epoxy resin coupled with 2 : 1 hardener separately to four walls each. The FRPs were fastened to the boundaries by use of suitable angle irons. The walls were subjected to blast wave parameters generated from explosive of 0.64 kg TNT equivalent weight suspended from the roof of test structure in the geometrical centre of experimental arrangement of walls. The displacement response of two layered FRPs walls had little correlation with the type of matrix used. The carbon fibers in four layered walls were able to contain the fragmentation. Retrofit Design procedure was proposed for analysis and design of masonry walls strengthened with FRPs against blast loading. Numerical algorithm of nonlinear SDOF was run for the masonry walls with assumed number of retrofits of FRPs with known tensile strength, modulus of elasticity, and percent elongation. If the peak deflection value taken from displacement time history of the numerical model exceeds the displacement limit, the number of layers of FRPs is reconsidered.

El-Domiatiy et al. [33] carried out experimental and numerical studies for assessing the feasibility of Fiber Reinforced Polymers (FRP) as reinforcing technique for unreinforced brick masonry against blast loading. The damage levels in these were coupled with charge weight and stand-off distance. Pressure transducers and accelerometers were installed on the test specimen for recording pressure and acceleration time histories.

The response of different walls demonstrated enhanced capacity of FRP retrofitted walls against more threat levels. FRP strengthened walls failed in safe manner avoiding dangerous scattering of fragments while the unreinforced masonry wall failed in abrupt flexure mode splashing debris. Single Degree of Freedom System Analysis was successfully used for predicting the response of FRP reinforced masonry wall. Similarly, comparing the test results with TM 5-1300 Code etc requirements, support rotations and ductility ratio

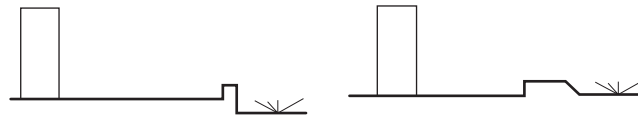


FIGURE 15: Landscape design for attenuating blast effect.

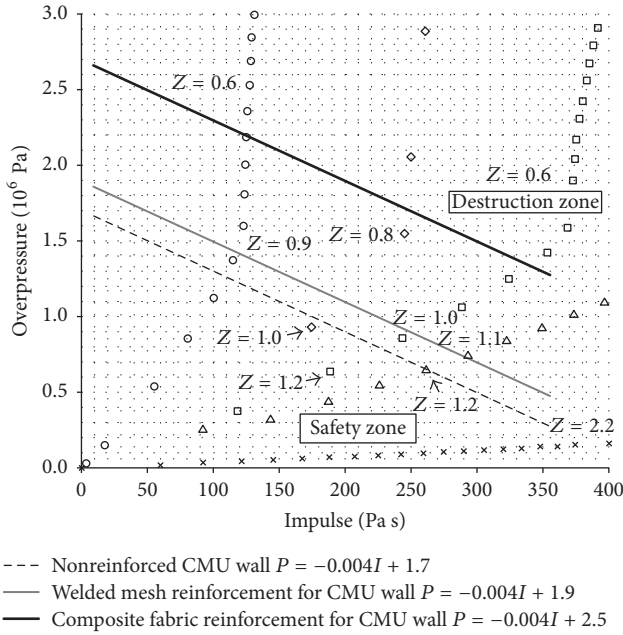


FIGURE 16: Resistance of CMU for different system of reinforcement.

guidelines were suggested for retrofitting of masonry with RFP.

Sielicki [59], in Ph.D. thesis, elaborated the failure of masonry subjected to impulse loading. The researcher obtained the highest safety threshold by application of composite fabric reinforcement to concrete masonry wall as shown in  $P$ - $I$  curves in Figure 16.

Similarly, Tan and Patoary [60], Baylot et al. [61], Stanley et al. [62], Stratford et al. [63], Alsayed et al. [64], Bui and Limam [65], Chen et al. [66], Hamed and Rabinovitch [67], Hamed and Rabinovitch [68], and Haderi et al. [69] investigated and reported increased performance of FRP strengthened masonry walls.

According to Buchan and Chen [70], extensive experimental and numerical studies have shown benefits of FRP and Polymer retrofitting in increasing structural strength and ductility of structure along with reducing the danger of shrapnel. Blast loading and response problems is complex in nature, involving so many variables, lacking vital information regarding exact charge weight and stand-off distances and designs guidelines for practical applications cannot be established on the basis of experiments only. Consequently, studies conducted so far are not quantitative in nature and explicit guidelines for application of FRP to large structures are still wanting.

4.3.2. *Polyurea*. It is cross-linked amorphous monomer or polyamine and prepolymer, essentially containing at least 80% polyamine (Tekalur et al. [71]). Water, chemical, and abrasion resistant elastomeric material used in retrofitting of masonry structures.

Knox et al. [56] reported successful arresting of fragments when elastomeric polymer (polyurea) coated with concrete block walls was subjected to 0.55 MPa blast pressure. Wang et al. [72] experimentally studied failure mechanism, modes, and peak pressure for damage of clay brick masonry and aerated concrete block walls strengthened with polyurea with different boundary conditions subjected to blast loading. The damage in clay brick masonry wall started at the joints and extended from top to bottom at the centre of wall and deformation is less pronounced. In aerated concrete block walls, greater cracks were found in mortar and deformation observed were significant. Polyurea-sprayed walls exhibited enhanced performance against blast loading and flexural strength was improved and mortar joint damage was localized. The performance of clay brick masonry wall exceeded the aerated concrete block masonry wall in both unreinforced and reinforced scenario. The structural collapse of walls was avoided and fatal fragments were arrested. After application of polyurea, the ultimate blast resistance of clay brick masonry and aerated concrete block masonry was increased by factors 4.5-11 and 15, respectively.

Similarly, Johnson et al. [73], Davidson et al. [74], Davidson et al. [75], Baylot et al. [61], Irshidat et al. [76], Haderi et al. [69], and Aghdamy et al. [77] reported enhanced performance of polyurea treated masonry against blast loading.

4.3.3. *Aluminium Foam*. An early start of plastic deformation, high strength, and corrosion resistance of aluminum foam makes it suitable for retrofitting masonry structures (Lantz et al. [57]). Su et al. [78] and Aghdamy et al. [77] investigated performance of aluminium foam by conducting FEA-analysis using LS-DYNA and found its potentiality to be used as retrofitting material.

4.3.4. *Engineered Cementitious Composites*. It is micromechanically designed material, molded mortar-based composite reinforced with specially selected short random fibers, usually polymer fibers, and was invented in early 90s (Li [79]). Maalej et al. [80] reported increased resistance of engineered cementitious composites and recommended its use for increasing masonry wall resistance against blast loading.

4.3.5. *Ferrocement*. It has been widely used in masonry structures for mitigation against seismic loading. Badshah [4],



FIGURE 17: (a) Major shear and flexural cracks in unreinforced masonry wall and (b) no damage ferrocement wall.



FIGURE 18: (a) Collapse of unreinforced masonry wall and (b) partially damaged but intact ferrocement wall.

in his Ph.D. experimental work, found an enhanced performance of ferrocement clay brick masonry in comparison to unreinforced masonry wall against blast loading. Geometrical and material models of both walls were kept constant. Unreinforced wall showed major diagonal (shear) and central (flexural) cracks at measured peak reflected pressure of 0.205 MPa while ferrocement wall experienced no damage as shown in Figure 17. Similarly, unreinforced masonry wall collapsed and ferrocement wall, though partially damaged, remained intact when subjected to same peak positive reflected pressure of magnitude 1.01 MPa as shown in Figure 18. This technique is relatively simple, is less costly, and requires no special skill during fabrication.

All the above techniques incorporate ductility and strength to the masonry walls. Furthermore, high velocity debris ejected are confined and injuries are minimized.

## 5. Conclusions

(1) Most of blast load empirical models are either for free air burst or surface burst. Free air burst and surface burst empirical models proposed by different researchers for peak over pressure show large variation especially in the region of small scaled distance. Further research is required for predicting accurate shock wave parameters in the region very close to the centre of explosion.

(2) Ground conditions (sandy, clayey, gravel, loose, compacted, consolidated, rock, concrete, and RCC pavement)

shall be incorporated in the prediction models. Similarly, empirical models are oversimplified and do not take the complex interaction of shock waves with the target structure and surrounding built environment. Therefore, numerical methods based on computational fluid dynamics (CFD) may be used for finding more accurate blast wave parameters and evaluating response of structure in urban environment.

(3) Different researchers have studied individual structural elements such as reduced scale wall, column, and slab. The response of complete masonry building shall be studied. Most of the research work has been devoted to concrete block masonry. Clay brick masonry is a major structural and infill material in many regions. Therefore, response of clay brick masonry against blast loading shall be studied.

(4) Damage to structure can be confined to certain level either by attenuating blast load parameters before reaching the target or redetailing and retrofitting of structural elements, proper landscaping, and incorporating blast load efficient architecture. In important buildings where space is not expensive, proper landscaping and blast efficient architectural design can play important role in blast mitigation.

(5) Retrofitting techniques using FRP and polyurea have been proved efficient in blast mitigation. Retrofitting techniques to masonry have been applied and investigated in the preblast scenario. Efficiency of retrofitting techniques in the damaged masonry buildings in the postblast scenario shall be investigated and evaluated. FRP retrofitting techniques are quite efficient in increasing the ductility of structure

and arresting the flying debris but fail in debonding usually at the supports and need further investigation and design guidelines.

(6) Low cost techniques such as ferrocement have been proven efficient against earthquake loads and also manifested its potential against blast loads. Ferrocement gives smooth plastered surface and further surface treatment and ensuing cost can be avoided. Furthermore, main constituents of ferrocement are mortar and steel mesh, screw, and rowel plug which are indigenously available in most of the blast prone regions. Therefore, it requires further investigation as strengthening technique in pre- and postblast scenarios.

## Notations

TNT:	Trinitrotoluene
$Z$ :	Scaled distance, $\text{m/kg}^{1/3}$
$W$ :	TNT equivalent weight, Kg
$R$ :	Scaled distance, M
$P_o$ :	Standard atmospheric pressure, Pa
$P_{\text{pos}}$ :	Peak positive incident overpressure, Pa
$P_r$ :	Peak positive reflected pressure, Pa
$P_{\text{so}}^-$ :	Peak negative pressure, Pa
$t_A$ :	Time of arrival of shock waves, S
$t_o^+$ :	Positive phase duration, S
$t_o^-$ :	Negative phase duration, S
$i_s^+$ :	Positive specific impulse, s·Pa
$i_s^-$ :	Negative specific impulse, s·Pa.

## Conflicts of Interest

The authors declare that there are no conflicts of interest regarding the publication of this paper.

## References

- [1] Unified Facilities Criteria (UFC) 3-340-02, *Structures to Resist the Effects of Accidental Explosions*, Department of Defense, Washington, DC, USA, 2008.
- [2] V. Karlos, G. Solomos, and M. Larcher, "Analysis of the blast wave decay coefficient using the Kingery–Bulmash data," *International Journal of Protective Structures*, vol. 7, no. 3, pp. 409–429, 2016.
- [3] A. Ullah, F. Ahmad, H.-W. Jang, S.-W. Kim, and J.-W. Hong, "Review of analytical and empirical estimations for incident blast pressure," *KSCE Journal of Civil Engineering*, pp. 1–15, 2016.
- [4] E. Badshah, *Performance evaluation of clay brick masonry against blast loading [Ph.D. thesis]*, University of Engineering Technology (UET) Peshawar Pakistan, 2017.
- [5] H. L. Brode, "Numerical solutions of spherical blast waves," *Journal of Applied Physics*, vol. 26, no. 6, pp. 766–775, 1955.
- [6] J. Henrych and R. Major, *The Dynamics of Explosion and its Use*, Elsevier Scientific, Amsterdam, Netherlands, 1979.
- [7] M. Held, "Blast waves in free air," *Propellants, Explosives, Pyrotechnics*, vol. 8, no. 1, pp. 1–7, 1983.
- [8] G. F. Kinney and K. J. Graham, *Explosive Shocks in Air*, Springer Science & Business Media, 2013.
- [9] C. A. Mills, "The design of concrete structure to resist explosions and weapon effects," in *Proceedings of the 1st International Conference on concrete for hazard protections*, pp. 61–73, September 1987.
- [10] M. A. Sadovskiy, "Mechanical effects of air shockwaves from explosions according to experiments," in *Sadovskiy MA Selected Works: Geophysics and Physics of Explosion*, Nauka Press, Moscow, Russia, 2004.
- [11] Z. Bajić, *Determination of TNT equivalent for various explosives [M.S. thesis]*, University of Belgrade, Belgrade, Serbia, 2007.
- [12] US Army, *Fundamentals of Protective Design (Non-Nuclear)*, Department of Army Technical Manual, TM5-855-1, US Army, Washington, DC, USA, 1965.
- [13] N. M. Newmark and R. J. Hansen, "Design of blast resistant structures," in *Shock and vibration handbook 3*, 1961.
- [14] M. M. Swisdak Jr., *Simplified Kingery Airblast Calculations*, Naval Surface Warfare Center, Indian Head, Md, USA, 1994.
- [15] C. Wu and H. Hao, "Modeling of simultaneous ground shock and airblast pressure on nearby structures from surface explosions," *International Journal of Impact Engineering*, vol. 31, no. 6, pp. 699–717, 2005.
- [16] J. I. Siddiqui and S. Ahmad, "Impulsive loading on a concrete structure," *Proceedings of the Institution of Civil Engineers: Structures and Buildings*, vol. 160, no. 4, pp. 231–241, 2007.
- [17] S. Ahmad, A. Elahi, J. Iqbal, M. A. Keyani, and A. G. A. Rahman, "Impulsive loading on reinforced concrete wall," *Proceedings of the Institution of Civil Engineers: Structures and Buildings*, vol. 166, no. 3, pp. 153–162, 2013.
- [18] J. Iqbal and S. Ahmad, "Improving safety provisions of structural design of containment against external explosion," in *Proceedings of International conference on opportunities and challenges for water cooled reactors in the 21st century*, International Atomic Energy Agency (IAEA), 2011.
- [19] P. D. Smith and T. A. Rose, "Blast wave propagation in city streets—an overview," *Progress in Structural Engineering and Materials*, vol. 8, no. 1, pp. 16–28, 2006.
- [20] Birnbaum, K. Naury, A. Richard, E. F. Gerg, J. H. Colin, and J. F. Nigel, "Analysis of blast loads on buildings," in *Preprint from Structures under Extreme Loading Conditions*, 1996.
- [21] M. Johansson, O. P. Larsen, L. Laine, and REINERTSEN Sverige AB, "Explosion at an intersection in an Urban Environment—Experiments and analyses," in *Proceedings of the 78th Shock and Vibration Symposium*, Philadelphia, PA, USA, 2007.
- [22] A. M. Remennikov, "Evaluation of blast loads on buildings in urban environment," *WIT Transactions on The Built Environment*, vol. 73, 2004.
- [23] T. A. Rose and P. D. Smith, "Influence of the principal geometrical parameters of straight city streets on positive and negative phase blast wave impulses," *International Journal of Impact Engineering*, vol. 27, no. 4, pp. 359–376, 2002.
- [24] G. C. Mays and P. D. Smith, *Blast Effects on Buildings: Design of Buildings to Optimize Resistance to Blast Loading*, Thomas Telford, 1995.
- [25] Design of Concrete Masonry Walls for Blast loading, TEK 14-21A. National Concrete Masonry Association, 2014.
- [26] T. Ngo, P. Mendis, A. Gupta, and J. Ramsay, "Blast loading and blast effects on structures – an overview," *Electronic Journal of Structural Engineering*, vol. 3, article 5, 2007.
- [27] Y. Shi, W. Xiong, Z.-X. Li, and Q. Xu, "Experimental studies on the local damage and fragments of unreinforced masonry walls under close-in explosions," *International Journal of Impact Engineering*, vol. 90, pp. 122–131, 2016.
- [28] R. A. Keys and S. K. Clubley, "Experimental analysis of debris distribution of masonry panels subjected to long duration blast loading," *Engineering Structures*, vol. 130, pp. 229–241, 2017.

- [29] A. Pandey and R. Bisht, "Numerical modelling of infilled clay brick masonry under blast loading," *Advances in Structural Engineering*, vol. 17, no. 4, pp. 591–606, 2014.
- [30] J. M. Pereira, J. Campos, and P. B. Lourenço, "Experimental study on masonry infill walls under blast loading," in *Proceedings of the 9th International Masonry Conference*, pp. 1–9, 2014.
- [31] X. Wei and M. G. Stewart, "Model validation and parametric study on the blast response of unreinforced brick masonry walls," *International Journal of Impact Engineering*, vol. 37, no. 11, pp. 1150–1159, 2010.
- [32] F. Parisi, C. Balestrieri, and D. Asprone, "Blast resistance of tuff stone masonry walls," *Engineering Structures*, vol. 113, pp. 233–244, 2016.
- [33] K. A. El-Domiati, J. J. Myers, and A. Belarbi, "Blast Resistance of UnReinforced Masonry Walls Retrofitted with Fiber Reinforced Polymers," Center for Infrastructure Engineering Studies Report 02-28, University of Missouri, Rolla, Missouri, 2002.
- [34] H. Hao and C. Wu, "Numerical simulation of damage of low-rise RC frame structures with infilled masonry walls to explosive loads," *Australian Journal of Structural Engineering*, vol. 7, no. 1, pp. 13–22, 2006.
- [35] C. Wu and H. Hao, "Safe scaled distance for masonry infilled RC frame structures subjected to airblast loads," *Journal of Performance of Constructed Facilities*, vol. 21, no. 6, pp. 422–431, 2007.
- [36] S. Ahmad, A. Elahi, H. Pervaiz, A. G. A. Rahman, and S. Barbhuiya, "Experimental study of masonry wall exposed to blast loading," *Materiales de Construcción*, vol. 64, no. 313, 2014.
- [37] M. D. Goel, V. A. Matsagar, A. K. Gupta, and S. Marburg, "An abridged review of blast wave parameters," *Defence Science Journal*, vol. 62, no. 5, pp. 300–306, 2012.
- [38] P. D. Smith and T. A. Rose, "Blast wave propagation in city streets - an overview," *Progress in Structural Engineering and Materials*, vol. 8, no. 1, pp. 16–28, 2006.
- [39] M. E. Beyer, *Blast Loads behind Vertical Walls*, Naval civil engineering lab port hueneme, Port Hueneme, CA, USA, 1986.
- [40] T. C. Chapman, T. A. Rose, and P. D. Smith, "Reflected blast wave resultants behind cantilever walls: a new prediction technique," *International Journal of Impact Engineering*, vol. 16, no. 3, pp. 397–403, 1995.
- [41] T. A. Rose, P. D. Smith, and G. C. Mays, "Design charts relating to protection of structures against air blast from high explosives," *Proceedings of the Institution of Civil Engineers - Structures and Buildings*, vol. 122, no. 2, pp. 186–192.
- [42] X. Q. Zhou and H. Hao, "Prediction of airblast loads on structures behind a protective barrier," *International Journal of Impact Engineering*, vol. 35, no. 5, pp. 363–375, 2008.
- [43] R. Hajek, M. Foglar, and J. Fladr, "Influence of barrier material and barrier shape on blast wave mitigation," *Construction and Building Materials*, vol. 120, pp. 54–64, 2016.
- [44] E. B. Philip, *The Passage of a Blast over a Wall*, Ministry of Home Security, 1942.
- [45] P. S. Jones, K. P. Vitaya-Udom, and J. M. Watt Jr., "Design of Structures to resist terrorist attack; 1/10th scale model perimeter wall tests," Tech. Rep. SL-87-13, US Army Waterways Experiment Station, Structures Laboratory, Vicksburg, MS, USA, 1987.
- [46] T. A. Rose, P. D. Smith, and G. C. Mays, "Effectiveness of walls designed for the protection of structures against airblast from high explosives," *Proceedings of the Institution of Civil Engineers: Structures and Buildings*, vol. 110, no. 1, pp. 78–85, 1995.
- [47] T. A. Rose, P. D. Smith, and G. C. Mays, "Protection of structures against airblast using barriers of limited robustness," *Proceedings of the Institution of Civil Engineers. Structures and Buildings*, vol. 128, no. 2, pp. 167–176, 1998.
- [48] D. Bogosian and D. Piepenburg, "Effectiveness of frangible barriers for blast shielding," in *Proceedings of the 17th International Symposium on the Military Aspects of Blast and Shock*, pp. 1–11, 2002.
- [49] R. P. Mayor and R. Flanders, *Technical Manual-Simplified computer model of air blast effects on building walls*, Dept of Transportation, Research and Special Programs Administration, Transportation System Center, Vehicle Crashworthiness Division, Safety and Security System Division, Kendall Square, Cambridge, MA, USA, 1990.
- [50] Z. Koccaz, F. Sutcu, and N. Torunbalci, "Architectural and Structural Design for Blast Resistant Buildings," in *Proceedings of the 14th World Conference on Earthquake Engineering*, Beijing, China, October 2008.
- [51] M. Barakat and J. G. Hetherington, "New architectural forms to reduce the effects of blast waves and fragments on structures," in *WIT Transactions on The Built Environment*, vol. 35, 1970.
- [52] M. A. Barakat and J. G. Hetherington, "Architectural approach to reducing blast effects on structures," *Proceedings of the Institution of Civil Engineers: Structures and Buildings*, vol. 134, no. 4, pp. 333–343, 1999.
- [53] N. Gebbeken and T. Döge, "Explosion protection - Architectural design, urban planning and landscape planning," *International Journal of Protective Structures*, vol. 1, no. 1, pp. 1–22, 2010.
- [54] R. Gunaratan, *Case Study: The Islamabad Marriott in Flames: Attack on the World's Most Protected Hotel*, International Centre for Political Violence and Terrorism Research (ICPVTR), 2008.
- [55] A. V. Kulkarni and G. Sambireddy, "Analysis of Blast Loading Effect on High Rise Buildings," *Civil and Environmental Research*, vol. 6, no. 10, 2014.
- [56] K. J. Knox, M. I. Hammons, T. T. Lewis, and J. R. Porter, *Polymer Materials for Structural Retrofit*, Force Protection Branch, Air Expeditionary Forces Technology Division, Air Force Research Laboratory, Tyndall AFB, Panama, Fla, USA, 2000.
- [57] L. Lantz, J. Maynez, W. Cook, and C. M. D. Wilson, "Blast protection of unreinforced masonry walls: a state-of-the-art review," *Advances in Civil Engineering*, vol. 2016, Article ID 8958429, 11 pages, 2016.
- [58] G. S. Urgessa and A. K. Maji, "Dynamic response of retrofitted masonry walls for blast loading," *Journal of Engineering Mechanics*, vol. 136, no. 7, Article ID 008007QEM, pp. 858–864, 2010.
- [59] P. W. Sielicki, "Masonry failure under unusual impulse loading," *Wydawnictwo Politechniki Poznań, skiej*, 2013.
- [60] K. H. Tan and M. K. H. Patoary, "Blast resistance of FRP-strengthened masonry walls. I: approximate analysis and field explosion tests," *Journal of Composites for Construction*, vol. 13, no. 5, pp. 422–430, 2009.
- [61] J. T. Baylot, B. Bullock, T. R. Slawson, and S. C. Woodson, "Blast response of lightly attached concrete masonry unit walls," *Journal of Structural Engineering*, vol. 131, no. 8, pp. 1186–1193, 2005.
- [62] M. Stanley, J. Metzger, R. Martinez, and J. Koenig, *UL-like testing of commercial off-the-shelf products that enhance the blast and ballistic resistance of structures, quick look Report 2*, New Mexico Tech, Energetic Materials Research and Testing Center, Karagozian & Case, Burbank, CA, USA, 2005.

- [63] T. Stratford, G. Pascale, O. Manfroni, and B. Bonfiglioli, "Shear strengthening masonry panels with sheet glass-fiber reinforced polymer," *Journal of Composites for Construction*, vol. 8, no. 5, pp. 434–443, 2004.
- [64] S. H. Alsayed, H. M. Elsanadedy, Z. M. Al-Zaheri, Y. A. Al-Salloum, and H. Abbas, "Blast response of GFRP-strengthened infill masonry walls," *Construction and Building Materials*, vol. 115, pp. 438–451, 2016.
- [65] T. T. Bui and A. Limam, "Out-of-plane behaviour of hollow concrete block masonry walls unstrengthened and strengthened with CFRP composite," *Composites Part B: Engineering*, vol. 67, pp. 527–542, 2014.
- [66] L. Chen, Q. Fang, J. Fan, Y. Zhang, H. Hao, and J. Liu, "Responses of masonry infill walls retrofitted with CFRP, steel wire mesh and laminated bars to blast loadings," *Advances in Structural Engineering*, vol. 17, no. 6, pp. 817–836, 2014.
- [67] E. Hamed and O. Rabinovitch, "Failure characteristics of FRP-strengthened masonry walls under out-of-plane loads," *Engineering Structures*, vol. 32, no. 8, pp. 2134–2145, 2010.
- [68] E. Hamed and O. Rabinovitch, "Out-of-plane behavior of unreinforced masonry walls strengthened with FRP strips," *Composites Science and Technology*, vol. 67, no. 3-4, pp. 489–500, 2007.
- [69] M. Haderi, V. A. Maleki, and K. Andalibi, "Retrofitting of unreinforced masonry walls under blast loading by FRP and spray on polyurea," *Cumhuriyet Science Journal*, vol. 36, no. 4, pp. 462–477, 2015.
- [70] P. A. Buchan and J. F. Chen, "Blast resistance of FRP composites and polymer strengthened concrete and masonry structures—a state-of-the-art review," *Composites Part B: Engineering*, vol. 38, no. 5-6, pp. 509–522, 2007.
- [71] S. A. Tekalur, A. Shukla, and K. Shivakumar, "Blast resistance of polyurea based layered composite materials," *Composite Structures*, vol. 84, no. 3, pp. 271–281, 2008.
- [72] J. Wang, H. Ren, X. Wu, and C. Cai, "Blast response of polymer-retrofitted masonry unit walls," *Composites Part B: Engineering*, 2016.
- [73] C. F. Johnson, T. R. Slawson, T. K. Cummins, and J. L. Davis, *Concrete Masonry Unit Walls Retrofitted with Elastomeric Systems for Blast Loads*, Engineer Research And Development Center Vicksburg Ms, 2004.
- [74] J. S. Davidson, J. R. Porter, R. J. Dinan, M. I. Hammons, and J. D. Connell, "Explosive testing of polymer retrofit masonry walls," *Journal of Performance of Constructed Facilities*, vol. 18, no. 2, pp. 100–106, 2004.
- [75] J. S. Davidson, J. W. Fisher, M. I. Mammons, J. R. Porter, and R. J. Dinan, "Failure mechanisms of polymer-reinforced concrete masonry walls subjected to blast," *Journal of Structural Engineering*, vol. 131, no. 8, pp. 1194–1205, 2005.
- [76] M. Irshidat, A. Al-Ostaz, A. H.-D. Cheng, and C. Mullen, "Nanoparticle reinforced polymer for blast protection of unreinforced masonry wall: laboratory blast load simulation and design models," *Journal of Structural Engineering*, vol. 137, no. 10, pp. 1193–1204, 2011.
- [77] S. Aghdamy, C. Wu, and M. Griffith, "Simulation of retrofitted unreinforced concrete masonry unit walls under blast loading," *International Journal of Protective Structures*, vol. 4, no. 1, pp. 21–44, 2013.
- [78] Y. Su, C. Wu, and M. Griffith, "Mitigation of blast effects on aluminum foam protected masonry walls," *Transactions of Tianjin University*, vol. 14, no. 1, pp. 558–562, 2008.
- [79] V. C. Li, "On engineered cementitious composites (ECC)," *Journal of Advanced Concrete Technology*, vol. 1, no. 3, pp. 215–230, 2003.
- [80] M. Maalej, V. W. J. Lin, M. P. Nguyen, and S. T. Quek, "Engineered cementitious composites for effective strengthening of unreinforced masonry walls," *Engineering Structures*, vol. 32, no. 8, pp. 2432–2439, 2010.

## Research Article

# Dropping Shock Characteristics of the Suspension Cushioning System with Critical Components

Hui Li,<sup>1</sup> Anjun Chen,<sup>1,2</sup> and Ningning Duan<sup>1</sup>

<sup>1</sup>Department of Packaging Engineering, Jiangnan University, Wuxi, Jiangsu 214122, China

<sup>2</sup>Jiangsu Province Key Laboratory of Advanced Food Manufacturing Equipment and Technology, Wuxi, Jiangsu 214122, China

Correspondence should be addressed to Anjun Chen; [caj62@jiangnan.edu.cn](mailto:caj62@jiangnan.edu.cn)

Received 22 July 2017; Accepted 29 August 2017; Published 13 November 2017

Academic Editor: Hugo Rodrigues

Copyright © 2017 Hui Li et al. This is an open access article distributed under the Creative Commons Attribution License, which permits unrestricted use, distribution, and reproduction in any medium, provided the original work is properly cited.

Dimensionless dropping shock dynamic equations of suspension nonlinear packaging system with critical components were obtained. The numerical results of shock response were gained using Runge-Kutta method. To evaluate the dropping shock characteristics of critical components, the dropping damage boundary curve was established, where the system parameter and the dimensionless shock velocity were selected as two coordinate parameters. Then, the frequency ratio and the system damping ratio were taken as third basic parameters of the dropping damage boundary surface, respectively. To study dynamic properties of the suspension system with critical components, the shock response acceleration, shock response displacements, and dropping damage boundary were analyzed. Based on the numerical results, the effects of the relevant parameters on dropping shock response and damage boundary of critical component were investigated. It is demonstrated that both a higher frequency ratio and a system damping ratio in the specific range can exert a positive effect on the product protection and should be selected in design process of the suspension system. Furthermore, with the decrease of suspension angle, the acceleration response peak decreases, the displacement response peak increases, and the safety zone enlarges.

## 1. Introduction

The concept of the product fragility is the foundation for dynamics of packaging cushioning [1]. But the value of the fragility cannot be obtained exactly and a valid damage evaluation method needs to be found. According to extensive investigation, both shock and vibration are main dynamic factors of damage for the product in the transportation. For evaluating the damage potential of impacts to a product, the two-dimensional damage boundary concept was suggested [2]. However, this concept was assumed that the cushion pad was not only linear elastic material but also thick enough; furthermore, only when the maximum acceleration response value exceeded the product fragility can the product be damaged. Thus, this theory may be limited in the practical application. Then, some researchers presented the subsequent improved damage evaluation methods, that is, fatigue damage boundary concept [3, 4] and displacement damage boundary concept [5]. Because dropping shock is one of the

main factors that cause the mechanical damage of most packaged products potentially in the transportation, the numerical results of a nonlinear cushioning system were derived by applying Runge-Kutta method and the dropping damage boundary concept of the packaged article was proposed [6], but no research has been conducted on whether the drop equivalent test is still suitable for nonlinear system. Then, some researchers improved the accuracy of a nonlinear system drop test [7, 8]. For taking into consideration the damage of cumulative fatigue, the repetitive-shock-induced damage of the product was analyzed by conducting drop tests [9].

For the Runge-Kutta method that is used to solve nonlinear system problem, one advantage of this Runge-Kutta method is high calculation accuracy, but this numerical approach cannot present this relationship of relevant parameters clearly. To make the relationship clear in the relevant expressions of nonlinear dynamic models, variational iteration method (VIM) was used to obtain the dropping shock properties of nonlinear packaging systems [10–12].

Note that the research objects that were mentioned above were treated as a single degree of freedom system. In fact, the products include many critical parts and should be regarded as multidegree of freedom system and nonlinear system by nature. Therefore, some researchers investigated the dropping damage evaluation of the typical material nonlinear packaging system with two degrees of freedom [13–16], which enriches the dropping damage boundary theory of products. Note that the aforesaid material nonlinear packaging system is just one of the cushioning packaging systems, and geometric nonlinear systems are also indispensable in product protection. Furthermore, the geometric nonlinear systems show excellent cushioning properties and should be further researched. Thus, some authors researched the shock characteristics of titled support spring geometric nonlinear system with critical components [17, 18].

The suspension system usually shows distinguished properties against shock and vibration and was devoted to protecting electronic product by some authors [19]. However, the fragile components were connected to the base through a spring. To further study the suspension system, the model of suspension system with eight springs as cushioning components was established, and the dynamic properties of the suspension system have been given insights into by some researchers, such as nature vibration [20], the shock response, and damage evaluation properties under classical pulse excitation [21, 22]. To show the relationship of correlation parameters of the suspension system clearly, several authors obtained the first-order approximate solution of system by applying the VIM and analyzed the effects of the relevant system parameters on the dropping damage boundary of suspension system [23, 24]. However, those aforementioned studies mainly focus on one-degree-of-freedom suspension system, and it has no research on the dynamic characteristics of two-degree-of-freedom suspension systems with critical components, especially on the dropping shock characteristics of the system.

In this paper, the dimensionless nonlinear dynamic equations of two-degree-of-freedom suspension system with critical components were established. The numerical results of this dimensionless dynamic equations were derived by applying the fourth-order Runge-Kutta method. To evaluate the dropping shock response and potential damage of critical components, the effects of the suspension angle, the frequency ratio, and the damping ratios on shock response and dropping damage boundary of critical components were discussed.

## 2. Modeling and Dimensionless Equations

The two-degree-of-freedom model of the suspension system is derived in Figure 1(a). The main body of the product is suspended in the center of container ADGH-A'D'G'H' by eight springs, that is, four springs on the top and the rest on the bottom.  $m_1$  and  $m_2$  denote the mass of critical components and main body;  $k_1$  and  $k$  denote stiffness coefficient of the junction linking critical components to main part and the suspension system;  $c_1$  and  $c_2$  are the damping coefficient of the junction linking critical components to main part and

the suspension system;  $\phi_0$  is the suspension angle;  $l_0$  is the original length of suspension spring, respectively.

To evaluate the dropping shock dynamic characteristics of critical components, it is assumed that the system falls from the height  $H$ . The static equilibrium positions of main part and critical components are selected as the origins, and the downward direction is defined as plus direction. The stress analysis diagram of critical components and the main part can be derived from Figure 1(b), where  $F$  is the force of suspension springs acting on main body in vertical direction. The motion of critical components can be obtained as

$$m_1 \ddot{x}_1 + k_1 (x_1 - x_2) + c_1 (\dot{x}_1 - \dot{x}_2) = 0. \quad (1)$$

Based on the equations of suspension system with one degree of freedom [21–24], the expression of the force  $F$  can be expressed as follows:

$$F = 8k \left[ \sin^2 \phi_0 x_2 + \frac{1}{2l_0^2} (1 - 6 \sin^2 \phi_0 + 5 \sin^4 \phi_0) x_2^3 \right]. \quad (2)$$

According to the stress analysis diagram of main body (see Figure 1(b)) and expression (2), the equation of main body can be shown as follows:

$$m_2 \ddot{x}_2 + c_2 \dot{x}_2 + 8k \left[ a_0 x_2 + \left( \frac{b_0}{l_0^2} \right) x_2^3 \right] - k_1 (x_1 - x_2) - c_1 (\dot{x}_1 - \dot{x}_2) = 0, \quad (3)$$

where  $a_0 = \sin^2 \phi_0$ ,  $b_0 = (1 - 6 \sin^2 \phi_0 + 5 \sin^4 \phi_0)/2$ . Integrating (1) with (3), the motion of the suspension system with critical components can be governed by

$$\begin{aligned} m_1 \ddot{x}_1 + k_1 (x_1 - x_2) + c_1 (\dot{x}_1 - \dot{x}_2) &= 0 \\ m_2 \ddot{x}_2 + c_2 \dot{x}_2 + 8k \left[ a_0 x_2 + \left( \frac{b_0}{l_0^2} \right) x_2^3 \right] - k_1 (x_1 - x_2) &= 0 \\ -c_1 (\dot{x}_1 - \dot{x}_2) &= 0. \end{aligned} \quad (4)$$

Let the initial conditions of the displacements and the velocity be

$$\begin{aligned} x_{1,2}(0) &= 0 \\ \dot{x}_{1,2}(0) &= \sqrt{2gH}. \end{aligned} \quad (5)$$

To simplify these equations, dimensionless variables can be introduced as follows: the dimensionless displacements of critical components and main part are  $y_1 = x_1/l_0$  and  $y_2 = x_2/l_0$ , respectively; the dimensionless time is  $\tau = t/T$ ; the frequency parameters of critical components and main part are  $\omega_1 = \sqrt{k_1/m_1}$  and  $\omega_2 = \sqrt{8k/m_2}$  separately; the period parameter of main part is  $T = 1/\omega_2$ . The dimensionless

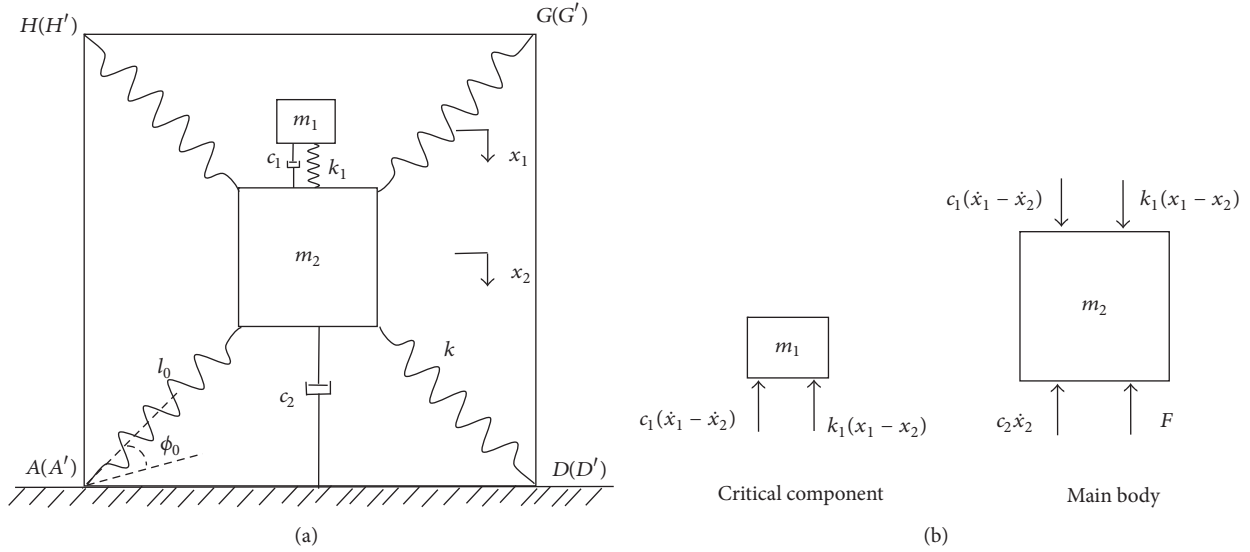


FIGURE 1: The model and stress analysis diagram of the suspension system with critical components: (a) the model of the suspension system with critical; (b) the stress analysis diagram of the system.

dropping shock dynamic equations for the suspension system can be got as follows:

$$\begin{aligned} y_1'' + \lambda_2^2 (y_1 - y_2) + 2\zeta_1 \lambda_2 (y_1' - y_2') &= 0 \\ y_2'' + 2\zeta_2 y_2' + a_0 y_2 + b_0 y_2^3 - \lambda_1 \lambda_2^2 (y_1 - y_2) & \quad (6) \\ - 2\zeta_1 \lambda_1 \lambda_2 (y_1' - y_2') &= 0. \end{aligned}$$

And the initial conditions for dynamic equations may be expressed as

$$\begin{aligned} y_{1,2}(0) &= 0 \\ y_{1,2}'(0) &= V = \sqrt{\frac{2gm_2 H}{8kl_0^2}}, \quad (7) \end{aligned}$$

where  $y_1' = dy_1/d\tau$  and  $y_2' = dy_2/d\tau$  are the dimensionless response velocities of critical components and main part, respectively;  $y_1'' = d^2y_1/d\tau^2$  and  $y_2'' = d^2y_2/d\tau^2$  are the dimensionless response acceleration of critical components and main part;  $\zeta_1 = c_1/2\sqrt{k_1 m_1}$  is the damping ratio between critical components and main part;  $\zeta_2 = c_2/2\sqrt{8km_2}$  is the damping ratio of the suspension system;  $\lambda_1 = m_1/m_2$  is the system mass ratio;  $\lambda_2 = \omega_1/\omega_2$  is the suspension system frequency ratio, separately.

### 3. Dimensionless Displacement Response

According to (6), the numerical analysis was obtained by using the fourth-order Runge-Kutta method, and the dropping shock response characteristics of critical components were studied.

**3.1. The Influence of Frequency Ratio.** Figure 2(a) depicts the displacement response of critical components with different

frequency ratios, when the suspension angle  $\phi_0 = 60^\circ$ , the mass ratio  $\lambda_1 = 0.05$ , the damping ratios  $\zeta_1 = \zeta_2 = 0.1$ , and dimensionless shock velocity  $V = 0.3$ .

**3.2. The Influence of System Damping Ratio.** Figure 2(b) shows the displacement response of critical components with different damping ratios  $\zeta_2$ , based on the suspension angle  $\phi_0 = 60^\circ$ , the mass ratio  $\lambda_1 = 0.05$ , the damping ratio  $\zeta_1 = 0.1$ , the frequency ratio  $\lambda_2 = 5$ , and dimensionless shock velocity  $V = 0.3$ .

**3.3. The Influence of Damping Ratio between the Critical Components and the Body.** The displacement response of critical components with different damping ratios  $\zeta_1$  is revealed in Figure 2(c), when the suspension angle  $\phi_0 = 60^\circ$ , the mass ratio  $\lambda_1 = 0.05$ , the damping ratio  $\zeta_2 = 0.1$ , the frequency ratio  $\lambda_2 = 5$ , and dimensionless shock velocity  $V = 0.3$ .

**3.4. The Influence of Suspension Angle.** Figure 2(d) illustrates the displacement response of critical components with different suspension angles, when the mass ratio  $\lambda_1 = 0.05$ , the damping ratio  $\zeta_1 = \zeta_2 = 0.1$ , the frequency ratio  $\lambda_2 = 5$ , and dimensionless shock velocity  $V = 0.3$ .

**3.5. The Influence of Dimensionless Shock Velocity.** Figure 2(e) illustrates the displacement response of critical components with different dimensionless shock velocities, when the suspension angle  $\phi_0 = 60^\circ$ , the damping ratio  $\zeta_1 = \zeta_2 = 0.1$ , the mass ratio  $\lambda_1 = 0.05$ , and the frequency ratio  $\lambda_2 = 5$ .

### 4. Dimensionless Acceleration Response

**4.1. The Influence of Frequency Ratio.** Figure 3(a) depicts the acceleration response of critical components with different frequency ratios, to get the results; let the suspension angle  $\phi_0 = 60^\circ$ , the mass ratio  $\lambda_1 = 0.05$ , the damping ratio  $\zeta_1 = \zeta_2 = 0.1$ , and dimensionless shock velocity  $V = 0.3$ .

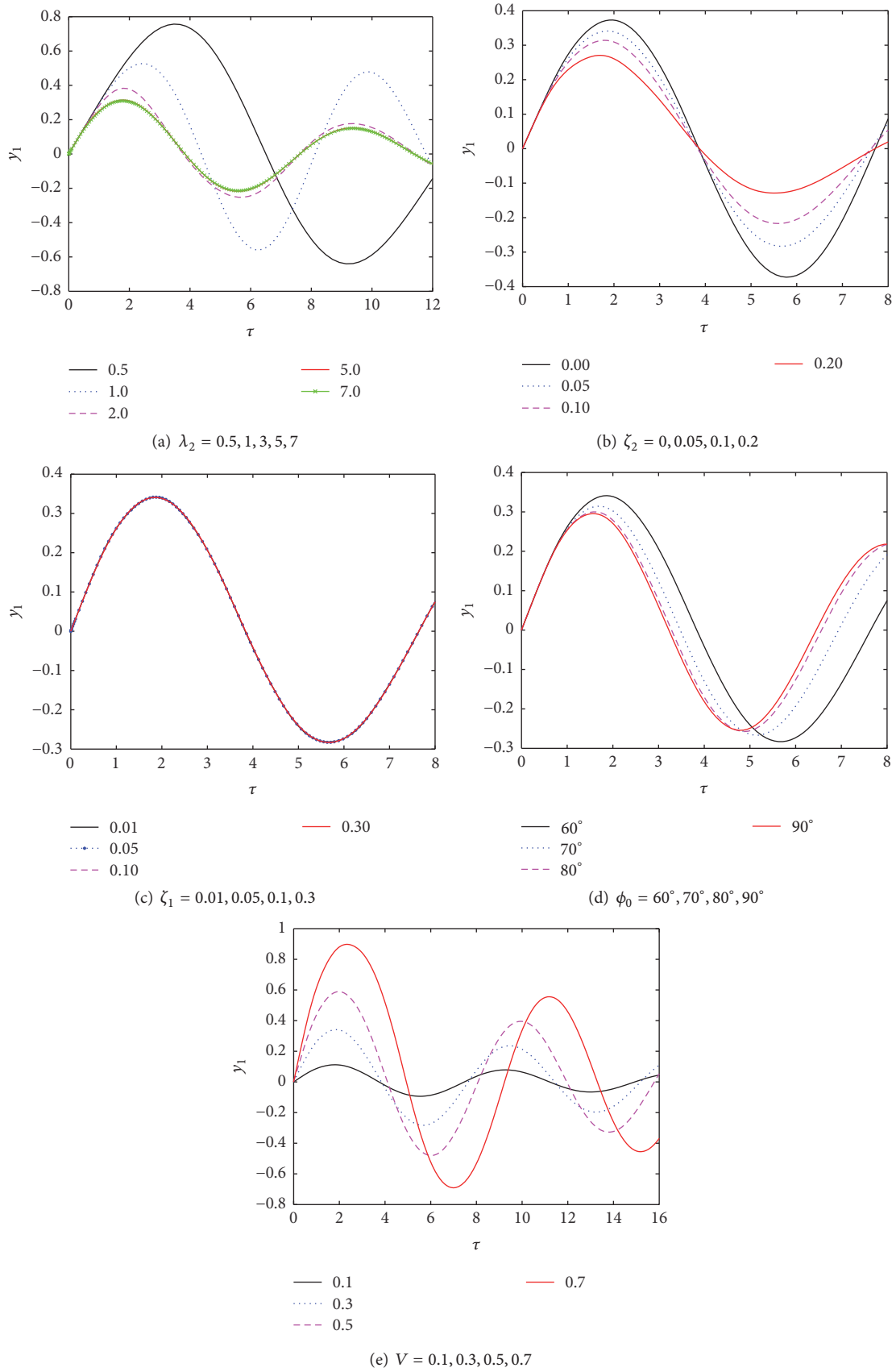


FIGURE 2: The displacement response for different parameters.

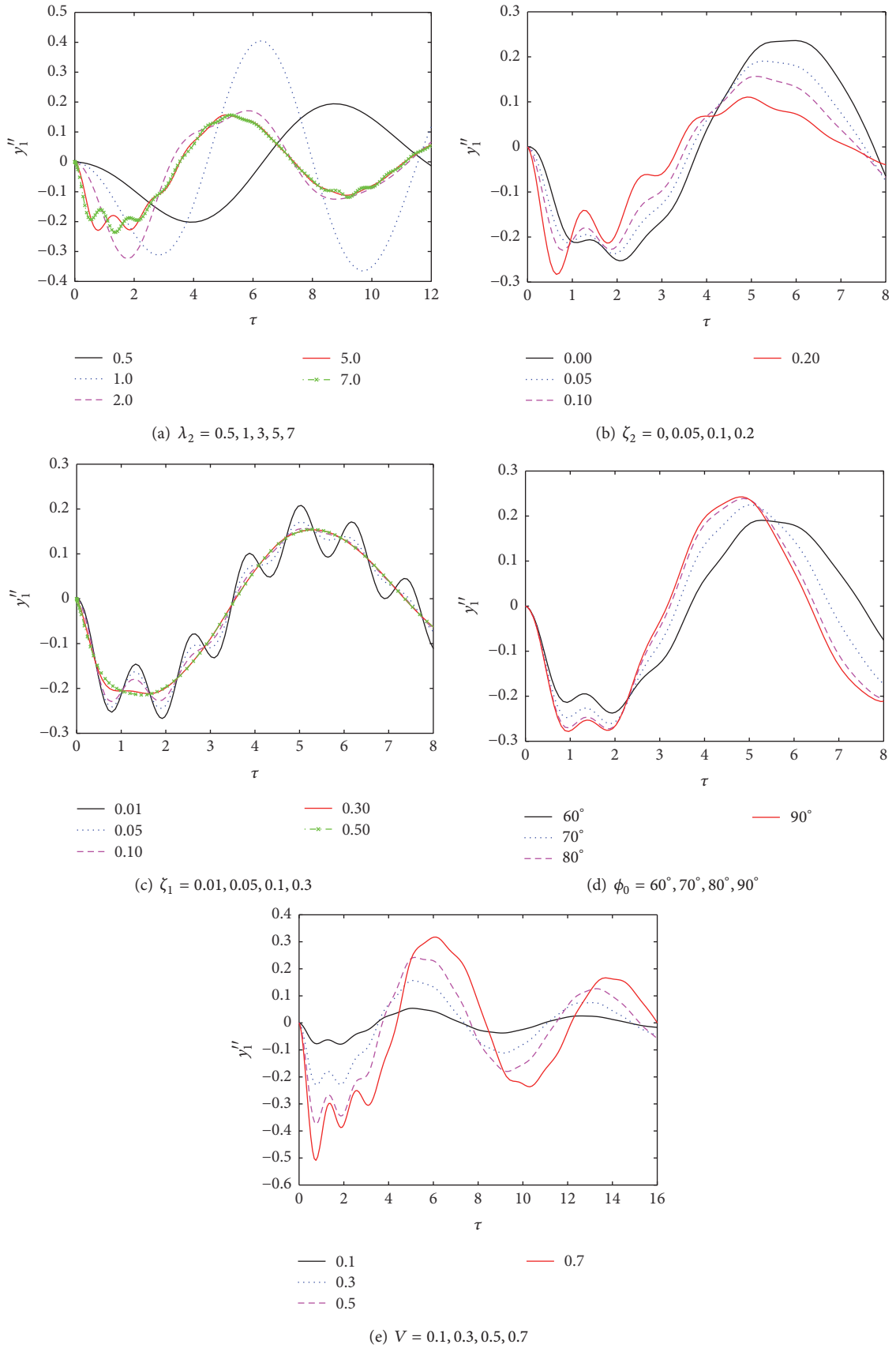


FIGURE 3: The acceleration response for different parameters.

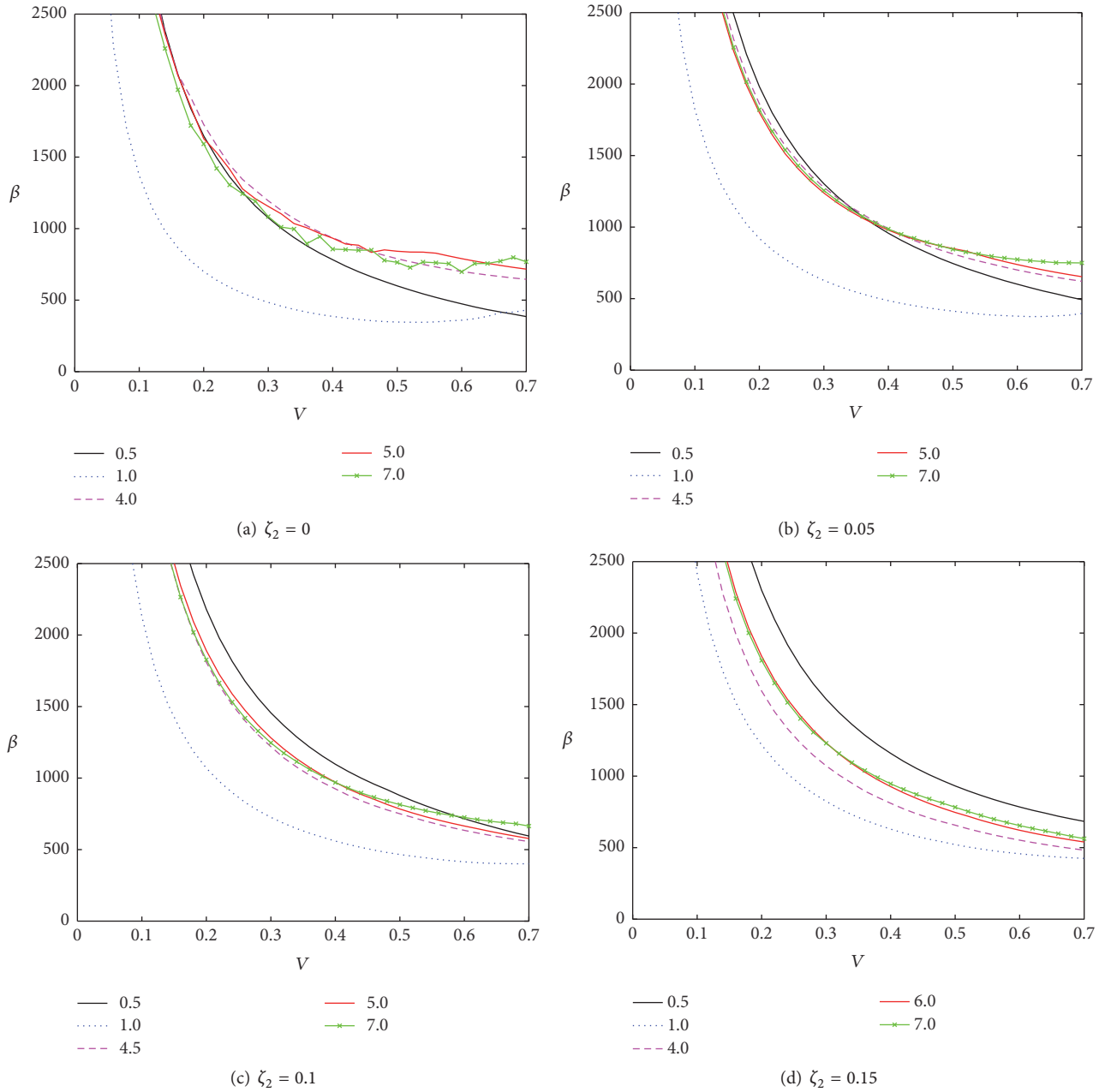


FIGURE 4: Dropping damage boundary curves for different damping ratio  $\zeta_2$ . Here,  $\lambda_1 = 0.05$ ,  $\zeta_1 = 0.1$ ,  $\phi_0 = 60^\circ$ ,  $A_c = 30$ .

**4.2. The Influence of System Damping Ratio.** Figure 3(b) shows the acceleration response of critical components with different damping ratios  $\zeta_2$ , when we set the suspension angle  $\phi_0 = 60^\circ$ , the mass ratio  $\lambda_1 = 0.05$ , the damping ratio  $\zeta_1 = 0.1$ , the frequency ratio  $\lambda_2 = 5$  and dimensionless shock velocity  $V = 0.3$ .

**4.3. The Influence of Damping Ratio between the Critical Components and the Body.** Figure 3(c) conveys the acceleration response of critical components with different damping ratios  $\zeta_1$ , when we choose the suspension angle  $\phi_0 = 60^\circ$ , the mass ratio  $\lambda_1 = 0.05$ , the damping ratio  $\zeta_2 = 0.05$ , the frequency ratio  $\lambda_2 = 5$ , and dimensionless shock velocity  $V = 0.3$ .

**4.4. The Influence of Suspension Angle.** Figure 3(d) illustrates the acceleration response of critical components with different suspension angles, based on the mass ratio  $\lambda_1 = 0.05$ , the damping ratio  $\zeta_1 = \zeta_2 = 0.1$ , the frequency ratio  $\lambda_2 = 5$ , and dimensionless shock velocity  $V = 0.3$ .

**4.5. The Influence of Dimensionless Shock Velocity.** Figure 3(e) performs the acceleration response of critical components with different dimensionless shock velocities, under the conditions of the suspension angle  $\phi_0 = 60^\circ$ , the mass ratio  $\lambda_1 = 0.05$ , the damping ratio  $\zeta_1 = \zeta_2 = 0.1$ , and frequency ratio  $\lambda_2 = 5$ .

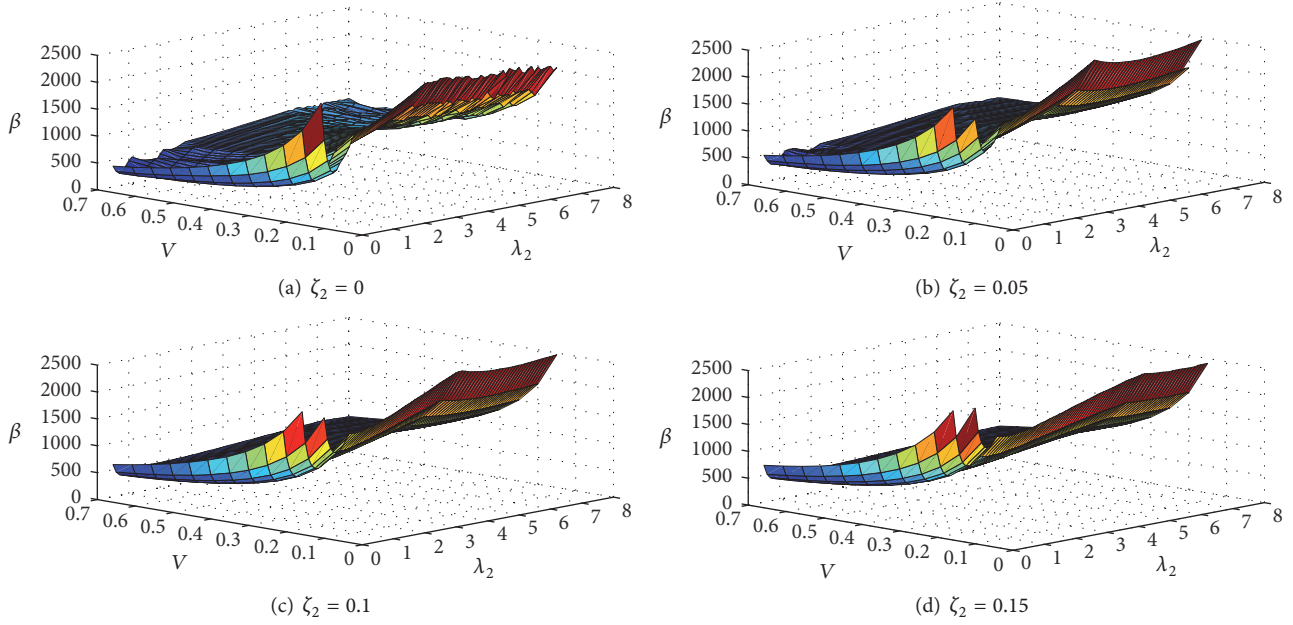


FIGURE 5: Dropping damage boundary surfaces for different damping ratio  $\zeta_2$ . Here,  $\lambda_1 = 0.05$ ,  $\zeta_1 = 0.1$ ,  $\phi_0 = 60^\circ$ ,  $A_c = 30$ .

## 5. Dropping Damage Evaluation

The concept of dropping damage boundary curve was presented [6], based on which the dropping damage boundary curve of the suspension system with two degrees of freedom can be derived.

The Runge-Kutta method can be used to solve the nonlinear equations (6); then the dimensionless maximum acceleration  $y''_{1m}$  can be derived. Set  $A_c$  as the fragility of the critical components, and the critical components are destroyed, if the maximum response acceleration meets the requirements:

$$\ddot{x}_{1m} = \left( \frac{d^2 x_1}{dt^2} \right)_m > A_c g, \quad (8)$$

where  $g$  is gravity acceleration. Let

$$\left( \frac{d^2 x_1}{dt^2} \right)_m = \beta \left( \frac{d^2 y_1}{d\tau^2} \right)_m = A_c g, \quad (9)$$

where the system parameter  $\beta = l_0/T^2 = 8kl_0/m_2$ . The relational expression can be also written as

$$\beta = \frac{A_c g}{y''_{1m}}. \quad (10)$$

According to (6), the dimensionless maximum acceleration  $y''_{1m}$  is related to the suspension angle, the frequency ratio, the damping ratios  $\zeta_1$  and  $\zeta_2$ , and the dimensionless shock velocity. Integrating the dimensionless maximum acceleration  $y''_{1m}$  with (10), the dropping damage boundary curves were established, the two coordinate parameters of which are composed of the dimensionless dropping shock velocity  $V$  and the system parameter  $\beta$ .

**5.1. The Influence of Frequency Ratio.** The dropping damage boundary curves of critical components are shown in Figure 4. Next, the frequency ratio  $\lambda_2$  is set as third coordinate parameter; the dropping damage boundary surfaces of critical components are derived in Figure 5.

**5.2. The Influence of System Damping Ratio.** The dropping damage boundary curves of critical components are shown in Figure 6. Then, we choose the damping ratio  $\zeta_2$  as third coordinate parameter, and the dropping damage boundary surfaces of critical components are derived in Figure 7.

**5.3. The Influence of Damping Ratio between the Critical Components and the Main Body.** To discuss the influence of damping ratio between the critical components and the main body, the dropping damage boundary curves of critical components are shown in Figure 8. Selecting the frequency ratio as third coordinate parameter, and the dropping damage boundary surfaces of critical components are graphed in Figure 9.

**5.4. The Influence of Suspension Angle.** The dropping damage boundary curves of critical components are shown in Figure 10. Consider the frequency ratio as third coordinate parameter, and the dropping damage boundary surfaces of critical components are presented in Figure 11.

## 6. Discussion

**6.1. The Influences of the Frequency Ratio.** Figures 2(a), 3(a), 4, and 5 show that the dynamic characteristics of critical components are sensitive to the frequency ratio, and increasing the frequency ratio can decrease the displacement response peak (Figure 2(a)). Furthermore, a small value of frequency ratio ( $\lambda_2 < 5$ ) can generate fluctuation of the maximum

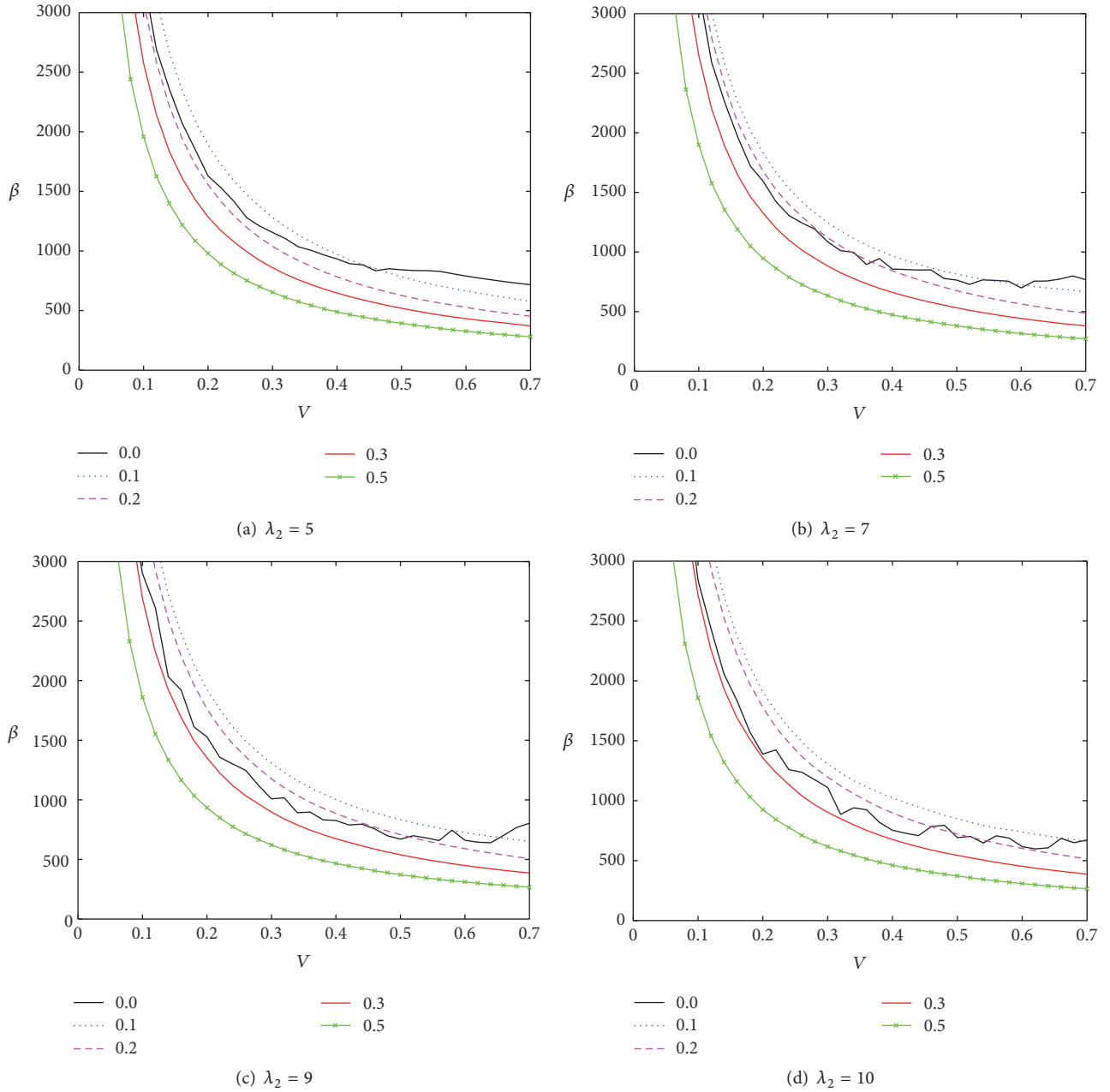


FIGURE 6: Dropping damage boundary curves for different frequency ratio  $\lambda_2$ . Here,  $\lambda_1 = 0.05$ ,  $\zeta_1 = 0.1$ ,  $\phi_0 = 60^\circ$ ,  $A_c = 30$ .

acceleration response values and the safety zone, where the critical components is more easily damaged. Correspondingly, a high frequency ratio value ( $\lambda_2 > 5$ ) can reduce the maximum acceleration response values and enlarge safety zone obviously (Figures 3(a), 4, and 5). In summary, the high frequency ratio value ( $\lambda_2 > 5$ ) can improve the protection performance of the product.

**6.2. The Influences of the System Damping Ratio  $\zeta_2$ .** According to Figures 2(b), 3(b), 6, and 7, we observed that the suspension system damping ratio is another sensitive parameter of dynamic characteristics for critical components, and the

displacement response peak decreases along with the increase of system damping ratio (Figure 2(b)). For the acceleration response peak and the safety zone of critical components, there exists the best damping ratio ( $\zeta_2 = 0.1$ ). That is, when the system damping ratio  $\zeta_2 = 0.1$ , the acceleration response peak reaches the minimum value (Figure 3(b)) and the safety zone reaches the maximum value (Figure 6). Further research showed that the precise value of the best damping ratio varies depending on the frequency ratio (Figure 7). Thus, when the values of relevant parameters are uncertain, we cannot get the exact value of the best damping ratio. To summarize, it is not a wise choice to increase the system damping ratio value as far

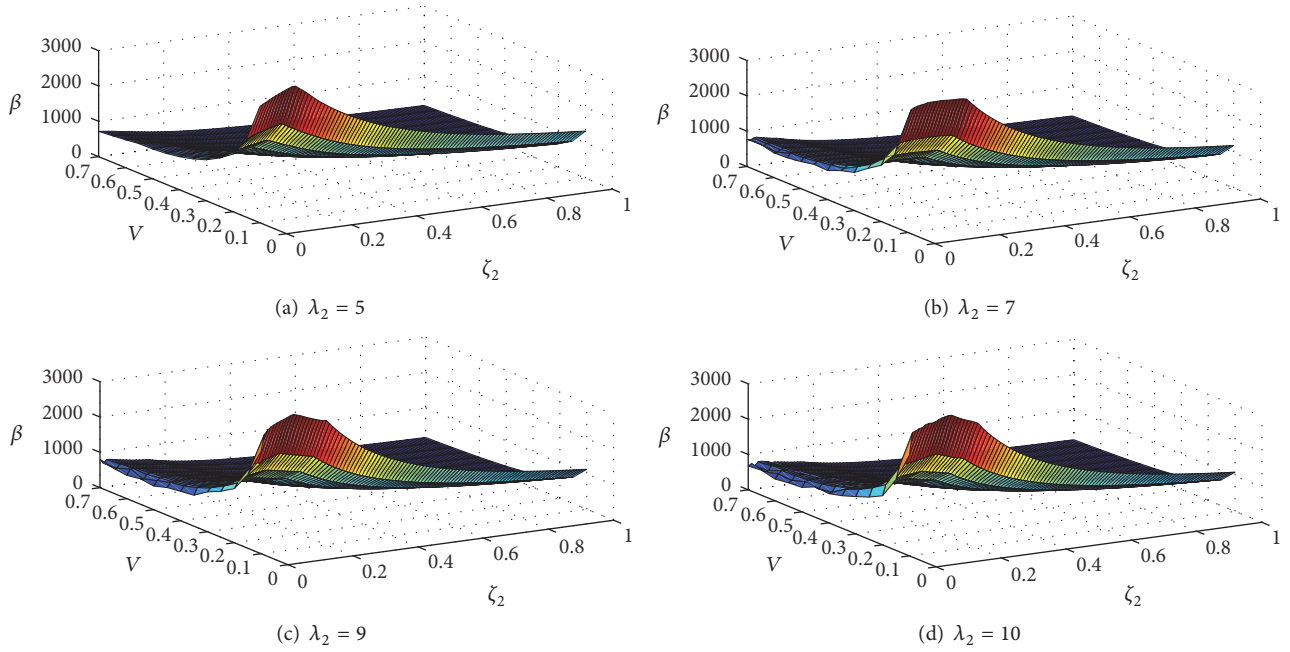


FIGURE 7: Dropping damage boundary surfaces for different frequency ratio  $\lambda_2$ . Here,  $\lambda_1 = 0.05$ ,  $\zeta_1 = 0.1$ ,  $\phi_0 = 60^\circ$ ,  $A_c = 30$ .

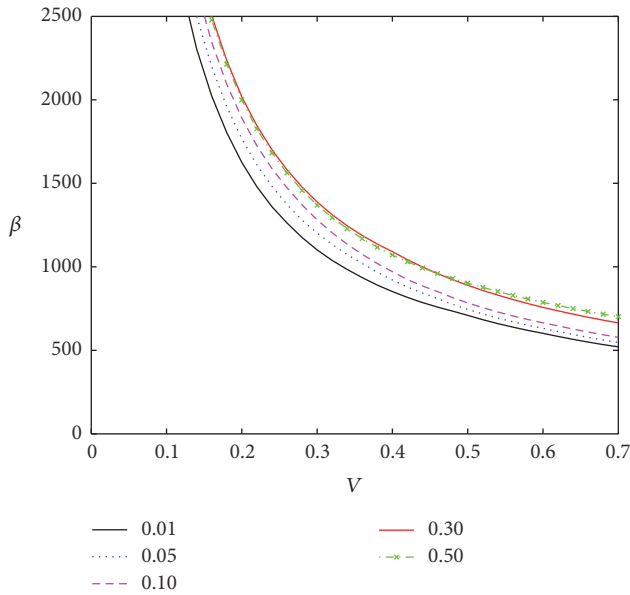


FIGURE 8: Dropping damage boundary curves with different damping ratio  $\zeta_1$ . Here,  $\lambda_1 = 0.05$ ,  $\zeta_2 = 0.1$ ,  $\phi_0 = 60^\circ$ ,  $\lambda_2 = 5$ ,  $A_c = 30$ .

as possible in the design procedure of cushioning packaging, and the system damping ratios in the specific range can exert a positive effect on the product protection.

**6.3. The Influences of the Damping Ratio  $\zeta_1$  between Critical Components and Main Body.** From Figures 2(c), 3(c), 8, and 9, we found that the influence of damping ratio  $\zeta_1$  on the response peak of displacement is not noticeable (Figure 2(c)). On the contrary, it is obvious that increasing the damping

ratio can decrease the response peak of acceleration and enlarge safety zone. However, when damping ratio  $\zeta_1 > 0.3$ , the change of acceleration response peak is not significant with the damping ratio  $\zeta_1$  increasing (Figures 3(c), 8, and 9). Hence, the protection performance of the suspension system should be improved by increasing the damping ratio  $\zeta_1$  suitably.

**6.4. The Influences of the Suspension Angle.** On the basis of the numerical results of Figures 2(d), 3(d), 10, and 11, it is demonstrated that decreasing suspension angle can reduce the acceleration response peak and enlarge the safety area (Figures 3(c), 10, and 11). However, note that decreasing the suspension angle can also increase the displacement response peak and expend the response period (Figure 2(d)), and the increase of displacement response peak may exceed the maximum deformation of the suspension spring. In summary, within the maximum compression range of the suspension springs, the decrease in the suspension angle can benefit the product protection. The results indicate that the geometrical nonlinearity system performs better than the linear system ( $\phi_0 = 90^\circ$ ) on buffering performance.

**6.5. The Influences of the Dimensionless Shock Velocity.** It is shown in Figures 2(e) and 3(e) that the system acceleration and displacement responses increase and the period is expended closely along with an augment of dimensionless velocity. Surprisingly, we found that (7) can reveal the relationship between the dimensionless shock velocity and relevant parameters clearly. By the analysis of the equation  $V = \sqrt{2m_2gH/8kl_0^2}$ , we can decrease the dimensionless response velocity through increasing the original length of the suspension springs, increasing the stiffness coefficient of the

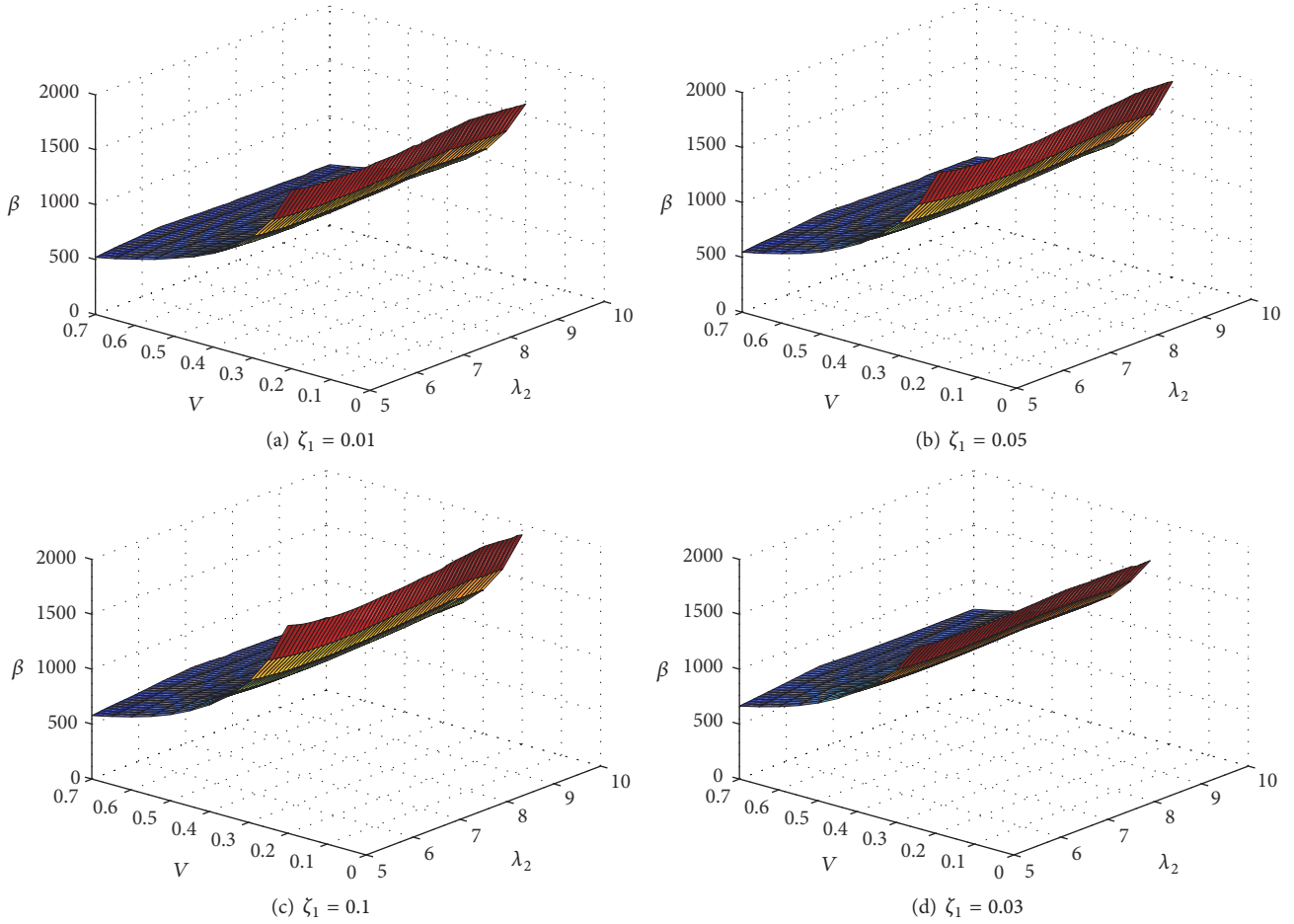


FIGURE 9: Dropping damage boundary surfaces for different damping ratio  $\zeta_1$ . Here,  $\lambda_1 = 0.05$ ,  $\zeta_2 = 0.1$ ,  $\phi_0 = 60^\circ$ ,  $A_c = 30$ .

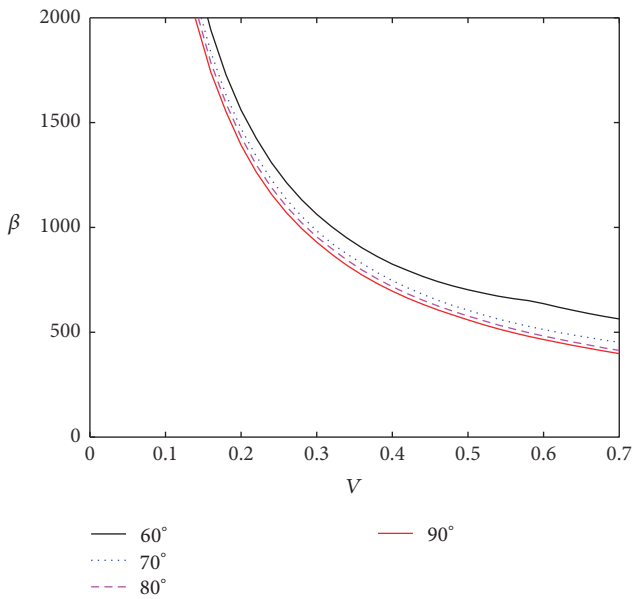


FIGURE 10: Dropping damage boundary curves with different suspension angle  $\phi_0$ . Here,  $\lambda_1 = 0.05$ ,  $\zeta_1 = \zeta_2 = 0.1$ ,  $\lambda_2 = 5$ ,  $A_c = 30$ .

suspension springs and/or decreasing the dropping height. The results indicate that the dropping shock velocity should be reduced as much as possible by changing the value of relevant parameters in the product protection.

For the real suspension packaging system, the simplified models were established by some authors [20–24]. To improve the present models, this paper took the critical component into account and derived the two-degree-of-freedom system. The new models of suspension system contain eight inclined linear springs, and (2) reveals that the relation between the resilience and the distortion presents nonlinear property, that is, geometric nonlinearity. However, the models of suspension packaging system will be more realistic to include nonlinear constitutive relations for the spring and damper and need to be further studied. Even so, the results provide us with a good reference to design the real suspension packaging system.

### 7. Conclusion

The aim of this paper is to derive the governing equations of two-degree-of-freedom suspension system and discuss the

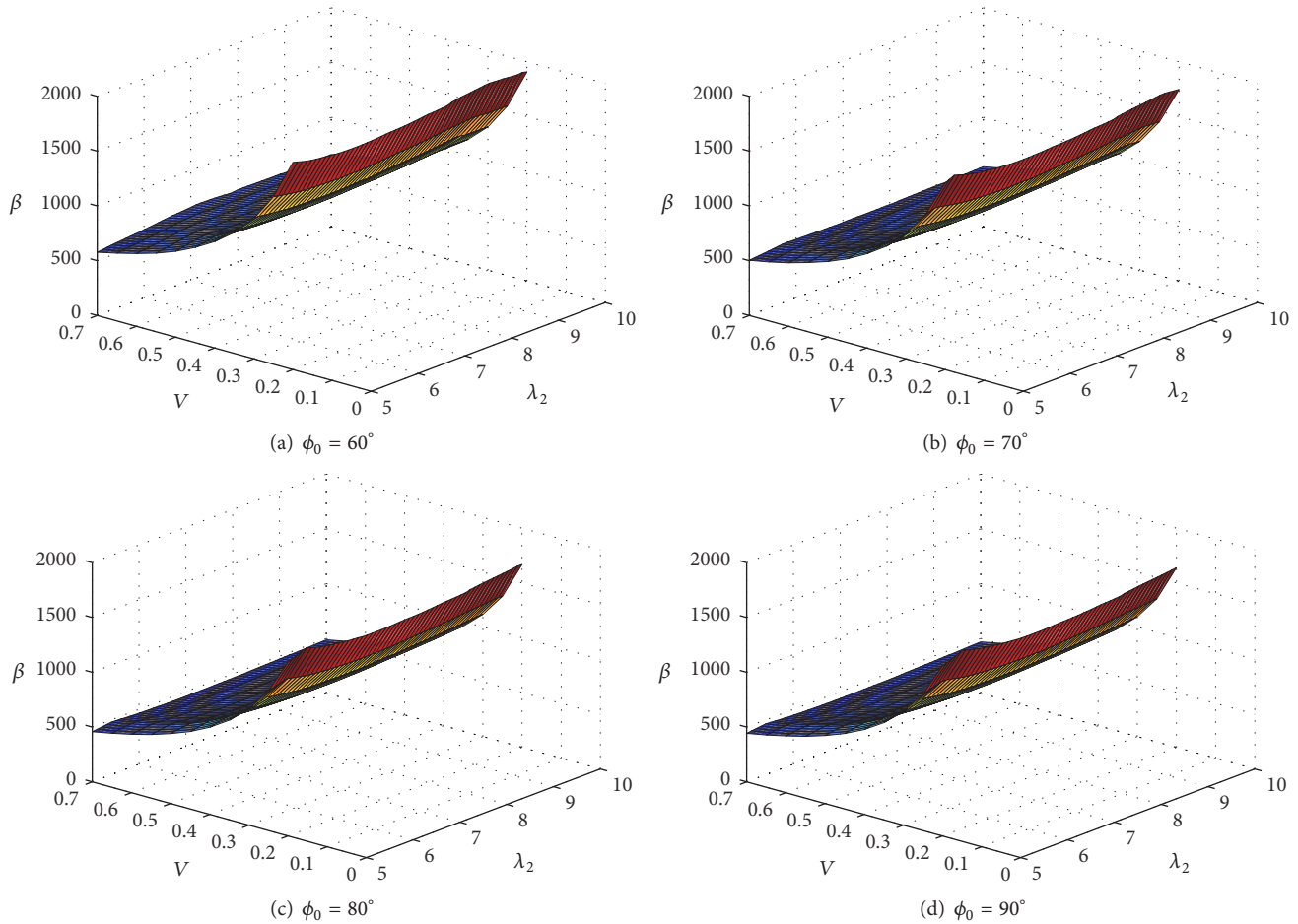


FIGURE 11: The dropping damage boundary surfaces for different suspension angle  $\phi_0$ . Here,  $\lambda_1 = 0.05$ ,  $\zeta_1 = \zeta_2 = 0.1$ ,  $A_c = 30$ .

influences of the frequency ratio, the system damping ratio, the suspension angle, and the damping ratio between critical components and the product on dynamic characteristics of this system. Summing up the results, it is shown that the dynamic characteristics of the suspension system are sensitive to the frequency ratio, the system damping ratio, and the suspension angle. First, when the values of frequency ratio are more than five, the maximum shock response value can reduce and the safety zone can enlarge obviously. Next, it is shown that when a system damping ratio value falls in a specific range, the performance in the product protection can be improved remarkably. Furthermore, compared with linear system, a low suspension angle can benefit the product protection relatively. The results can provide a guideline for the design process of the suspension packaging system.

### Conflicts of Interest

The authors declare that there are no conflicts of interest regarding the publication of this paper.

### References

- [1] R. D. Mindlin, "Dynamics of Package Cushioning," *Bell System Technical Journal*, vol. 24, no. 3, pp. 353–461, 1945.
- [2] R. E. Newton, *Fragility Assessment Theory and Practice*, Monterey Research Laboratory, Monterey, Calif, USA, 1968.
- [3] G. J. Burgess, "Product fragility and damage boundary theory," *Packaging Technology and Science*, vol. 1, no. 1, pp. 5–10, 1988.
- [4] G. J. Burgess, "Effects of fatigue on fragility testing and the damage boundary curve," *Journal of Testing and Evaluation*, vol. 24, no. 6, pp. 419–426, 1996.
- [5] Z. Wang, C. Wu, and D. Xi, "Damage boundary of a packaging system under rectangular pulse excitation," *Packaging Technology and Science*, vol. 11, no. 4, pp. 189–202, 1998.
- [6] Z. Wang, "On evaluation of product dropping damage," *Packaging Technology and Science*, vol. 15, no. 3, pp. 115–120, 2002.
- [7] C. Zhong, K. Saito, and K. Kawaguchi, "Improvement of equivalent drop theory for transport packaging," *Packaging Technology and Science*, vol. 26, no. 2, pp. 67–81, 2013.
- [8] C. Zhong, K. Saito, K. Kawaguchi, and H. Setoue, "The hybrid drop test," *Packaging Technology and Science*, vol. 27, no. 7, pp. 509–520, 2014.
- [9] H. Kitazawa, K. Saito, and Y. Ishikawa, "Effect of difference in acceleration and velocity change on product damage due to repetitive shock," *Packaging Technology and Science*, vol. 27, no. 3, pp. 221–230, 2014.
- [10] A.-J. Chen, "Application of variational iteration method with energy method for nonlinear equation arisen from packaging

- system,” *Mathematical Problems in Engineering*, vol. 2013, Article ID 326239, 5 pages, 2013.
- [11] A.-J. Chen, “Ren-He’s method for solving dropping shock response of nonlinear packaging system,” *Advances in Difference Equations*, vol. 2016, no. 1, article no. 279, 2016.
- [12] A.-J. Chen, “Resonance analysis for tilted support spring coupled nonlinear packaging system applying variational iteration method,” *Mathematical Problems in Engineering*, vol. 2013, Article ID 384251, 4 pages, 2013.
- [13] J. Wang, J. Jiang, L. Lu, and Z. Wang, “Dropping damage evaluation for a tangent nonlinear system with a critical component,” *Computers & Mathematics with Applications*, vol. 61, no. 8, pp. 1979–1982, 2011.
- [14] Z.-W. Wang and J.-H. Jiang, “Evaluation of product dropping damage based on key component,” *Packaging Technology and Science*, vol. 23, no. 4, pp. 227–238, 2010.
- [15] J.-H. Jiang and Z.-W. Wang, “Dropping damage boundary curves for cubic and hyperbolic tangent packaging systems based on key component,” *Packaging Technology and Science*, vol. 25, no. 7, pp. 397–411, 2012.
- [16] J. Wang, F. Duan, J. Jiang, L. Lu, and Z. Wang, “Dropping damage evaluation for a hyperbolic tangent cushioning system with a critical component,” *Journal of Vibration and Control*, vol. 18, no. 10, pp. 1417–1421, 2012.
- [17] A.-J. Chen, “The shock characteristics of tilted support spring packaging system with critical components,” *Shock and Vibration*, vol. 2014, Article ID 496035, 8 pages, 2014.
- [18] N. Duan, M. Hao, and A. Chen, “Damage evaluation of critical components of tilted support spring nonlinear system under a rectangular pulse,” *Mathematical Problems in Engineering*, vol. 2015, Article ID 910143, 9 pages, 2015.
- [19] S. Goyal, E. K. Buratynski, and G. W. Elko, “Role of shock response spectrum in electronic product suspension design,” *The International Journal of Microcircuits and Electronic Packaging*, vol. 23, no. 2, pp. 182–190, 2000.
- [20] X. Wu and L. J. Yang, “Natural vibration characteristics of suspension spring geometric nonlinear damping system,” *Journal of Vibration and Shock*, vol. 27, no. 11, pp. 71–72, 2008.
- [21] L. Wang and A. Chen, “The damage boundary curve of the suspension packaging system under rectangular pulse,” *Applied Mechanics and Materials*, vol. 105–107, pp. 70–73, 2012.
- [22] L. Wang and A. J. Chen, “The Shock response spectra of the suspension packaging system under rectangular pulse,” *The Journal of Applied Packaging Research*, vol. 5, no. 4, pp. 237–246, 2012.
- [23] S. Song and A.-J. Chen, “Variational iteration method of dropping shock response for the suspension spring packaging system,” *Shock and Vibration*, vol. 2015, Article ID 408674, 6 pages, 2015.
- [24] S. Song, N.-N. Duan, and A.-J. Chen, “Application of variational iteration method for dropping damage evaluation of the suspension spring packaging system,” *Abstract and Applied Analysis*, vol. 2014, Article ID 385404, 7 pages, 2014.

## Research Article

# A Numerical Approach to the Dynamic Response of the Deployment System during a Circular Cylinder Crossing through the Wave Zone

Xiaozhou Hu, Daojun Cai, and Yiyao Jiang

*School of Mechanical and Electrical Engineering, Central South University, Changsha 410083, China*

Correspondence should be addressed to Xiaozhou Hu; [smallboathu@163.com](mailto:smallboathu@163.com)

Received 22 April 2017; Accepted 14 September 2017; Published 18 October 2017

Academic Editor: Abdul Qadir Bhatti

Copyright © 2017 Xiaozhou Hu et al. This is an open access article distributed under the Creative Commons Attribution License, which permits unrestricted use, distribution, and reproduction in any medium, provided the original work is properly cited.

The dynamic response of the deployment system while deploying a circular cylinder crossing wave surface and the following submerging process are investigated numerically. The present numerical approach is based on the combination of solution methods of cable dynamics and computational fluid dynamics (CFD). For the implementation of the numerical approach, a cosimulation platform based on a CFD code and MATLAB is developed to study the fluid-solid interaction problem in the process. To generate regular waves, a numerical wave tank is built based on a piston-type wave generation method and a wave damping method applying porous media. Numerical simulations are performed based on the cosimulation platform. The sensitivities of cable tension, velocity, and acceleration of deployed body to different input parameters are investigated, including phase angles, wave heights, and periods of regular waves and deploying velocities, and the effects of those input parameters on dynamic responses of the deployment system are also discussed.

## 1. Introduction

In recent years, subsea working systems are widely used in such applications as marine resource development and utilization, maritime exploration, and survey [1–3]. To ensure the proper functioning of subsea working systems, the safe deployment or installation of them is one of the primary issues for marine and ocean engineers. When an offshore structure is deployed or launched into water, slamming occurs. Impulsive slamming loads lead to a nonlinear vibration of the deployment system, and the nonlinear effect which is enhanced because of the influence of waves would cause some problems, such as the slack cable phenomenon. If the operation of deploying cables is in frequently alternating taut-slack state, an exceptionally high tension in the cable will occur, which is also named as snap load because of its impact effect. In hostile ocean conditions, snap load would greatly increase the probability of missing of subsea structures. Moreover, the process of an offshore structure lowering through splash zone accompanies the interaction between the air, wave, and the rigid body, which is a complicated

fluid-solid problem, involving comprehensive consideration of time-varying hydrodynamic forces (slamming, drag, and inertia), buoyancy, vessel motion, waves, and possible snap loads in deploying cables. Therefore, to ensure a safe deployment of subsea working systems when they are lowered through the wave zone, it is essential to study the dynamic response of the deployment system with wave-solid interaction considered.

This paper mainly pays attention to the dynamic response of a deployment system while deploying a horizontal circular cylinder through wave zone for different deploying velocities and ocean conditions. In the wave impact and water entry process, offshore structures firstly impact on the wave surface, and then are gradually lifted from a dry state (in air) to partially immersed state and, eventually, to a wet state (fully immersed in water), which can be seen in Figure 1.

Hydrodynamic impact problems when solid bodies enter water have been investigated for nearly a century.

Pioneering researches performed by Karman [4], Wagner [5], Faltinsen [6], and others provided widely accepted theoretical basis. In the recent decade, researchers applied various

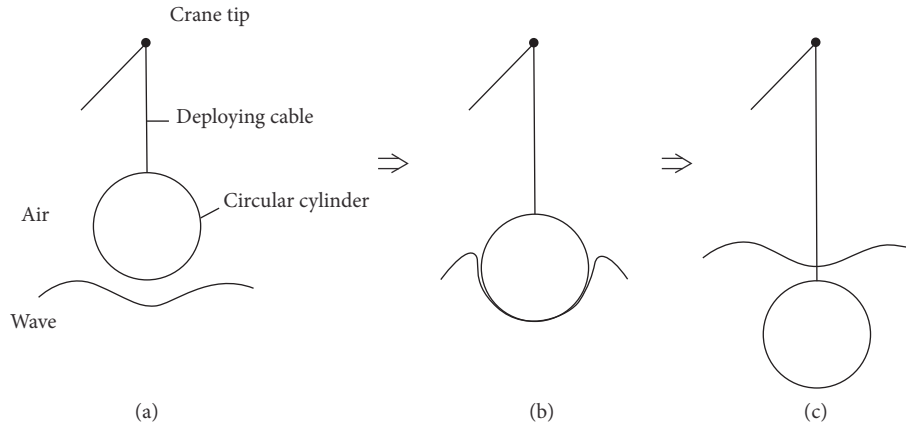


FIGURE 1: A circular cylinder lowering through the wave zone: (a) dry state; (b) partially immersed state; (c) fully immersed state.

theoretical or numerical methods for studying water entry of a circular cylinder, such as Sun and Faltinsen [7], Mnasri and Hafsia [8], Ghadimi et al. [9], Tassin et al. [10] and Iranmanesh and Passandideh-Fard [11]. However, as far as researches of deploying operation are concerned, these researchers were mainly devoted to investigating impact loads on rigid bodies and the deformation of water surface, with little attention paid to dynamic responses of the deployment or lifting system.

In recent years, remarkable progress in computer hardware and software technology and computational fluid dynamics (CFD) has greatly promoted researches in this field. For example, Buckner et al. [12], Bunnik and Buchner [13], and Bunnik et al. [14] applied an improved Volume of Fluid method to numerically predict wave loads during offshore structures in the splash zone. Zhang et al. [15] analyzed dynamic characteristics of the deployment system before and after water entry by using multibody dynamics (MBD) code Adams and CFD code Fluent, respectively; however, the dynamic response of deployment system during water entry process was not considered because MBD and CFD analysis were not integrated. W.-H. Wang and Y.-Y. Wang [16] simulated the physical process of a circular cylinder impacting on waves, and the response of lifting cable was obtained. Ryzhakov et al. [17] used a Particle Finite Element Method (PFEM) for simulations of the sea-landing of an unmanned aerial vehicle (UAV). Zhang et al. [18] investigated impact force acting on autonomous underwater vehicles when they contact with docks adopting commercial code Adams in conjunction with CFD software Fluent. Wen and Qiu [19] solved water entry problem by a constrained interpolation profile (CIP) method.

As mentioned above, the prediction of snap load which would result in highly nonlinear tension in deploying cables is very important; in this research field, Niedzwecki and Thampi [20], Thurston and Swanson [21], Lu [22], and others had made great contributions.

Many researchers utilized commercial software for ocean engineering to implement dynamic analysis of the deployment system, such as Orcaflex, SIMO, and SIMA. Selvåg [23]

applied SIMO and Orcaflex to calculate wave impact forces on complex compression module in the splash crossing process, and comparisons between results obtained from numerical estimations and from model tests were made. Wu [24] carry out researches on the dynamic response of a template during the lifting operation through wave zone by SIMA program. Valen [25] modeled the lifting operation of ROV in the launching and recovery process, and results were compared with analysis based on DNV Recommended Practices. Gordon et al. [26] simulated the splash zone crossing process of suction pile using SIMO, and the sensitivity of cable tension to key parameters was presented. Jacobsen and Leira [27] developed a 1-degree-of-freedom dynamic system to estimate the tension acting in the lifting wire, and comparisons were made with the results obtained by SIMO. Li et al. [28, 29] simulated the lifting process of a monopole by the combination of an external Dynamic Link Library and SIMO program. Simulations performed by ocean engineering codes provided useful results; however, these commercial software programs are not based on CFD methods, and their failure to solve fluid-solid coupling problems during bodies lowering through wave zone results in the inability to consider the interaction between waves and deployed bodies; therefore hydrodynamic force on bodies and tension in deploying cables may be not well estimated.

This work is devoted to studying the dynamics of a cable-rigid body system during a circular cylinder lifting through wave zone with different deploying velocities and regular waves with different phase angles and wave heights and periods. Because vertical motion is much more important than motions of other directions for the deploying operation, the cable-rigid body system can be simplified as a 1-degree-of-freedom (1-DOF) mass spring system. For implementation, a cosimulation platform based on CFD codes Fluent and MATLAB is established [30], and calculations of 1-DOF system are performed by MATLAB, while wave related loads on bodies are estimated in a numerical wave tank generated by Fluent. Furthermore, sensitivities of cable tension and motion parameters of deployed body to regular waves and deploying velocities are also investigated.

The CFD numerical approaches will be firstly outlined, including governing equations, boundary conditions, wave generation, and absorption methods. Then, a number of numerical tests involving different deploying velocities and different waves are presented, and simulation results are discussed. Finally, conclusions are drawn in Section 5.

## 2. Numerical Methods

**2.1. Governing Equations.** For the motion of homogeneous and incompressible fluid, the continuity equation and Navier-Stokes equations are governing equations. Applying the Reynolds decomposition in N-S equations and averaging, the Reynolds-Averaged Navier-Stokes (RANS) equations can be derived:

$$\begin{aligned} \frac{\partial \rho}{\partial t} + \frac{\partial(\rho \bar{u}_i)}{\partial x_i} &= 0 \quad (i = 1, 2) \\ \frac{\partial(\rho \bar{u}_i)}{\partial t} + \frac{\partial(\rho \bar{u}_i \bar{u}_j)}{\partial x_j} &= -\frac{\partial \bar{p}}{\partial x_i} \\ &+ \frac{\partial}{\partial x_j} \left[ \mu \left( \frac{\partial \bar{u}_i}{\partial x_j} + \frac{\partial \bar{u}_j}{\partial x_i} \right) \right] \\ &+ \frac{\partial}{\partial x_j} \left( -\rho \overline{u'_i u'_j} \right) + \rho \bar{f}_i, \end{aligned} \quad (1)$$

where superscripts “ $\bar{\phantom{x}}$ ” stand for ensemble average of physical variables,  $u_i$  is the  $i$ th component of the velocity vector,  $\rho$  is the density of fluid,  $p$  is the pressure,  $\mu$  is the dynamic viscous coefficient,  $f_i$  is body forces, and  $-\rho \overline{u'_i u'_j}$  is the Reynolds stress tensor.

To fulfill turbulence closures for RANS equations, the standard  $k$ - $\varepsilon$  turbulence model is applied in this work. Governing equations for the standard  $k$ - $\varepsilon$  model are given by

$$\begin{aligned} \frac{\partial(\rho k)}{\partial t} + \frac{\partial(\rho k \bar{u}_j)}{\partial x_j} &= \frac{\partial}{\partial x_j} \left[ \left( \mu + \frac{\mu_t}{\sigma_k} \right) \frac{\partial k}{\partial x_j} \right] + \rho G_k \\ &- \rho \varepsilon \\ \frac{\partial(\rho \varepsilon)}{\partial t} + \frac{\partial(\rho \varepsilon \bar{u}_j)}{\partial x_j} &= \frac{\partial}{\partial x_j} \left[ \left( \mu + \frac{\mu_t}{\sigma_\varepsilon} \right) \frac{\partial \varepsilon}{\partial x_j} \right] \\ &+ \frac{\varepsilon}{k} (C_{\varepsilon 1} \rho G_k - C_{\varepsilon 2} \rho \varepsilon) \\ \mu_t &= \frac{C_\mu \rho k^2}{\varepsilon} \\ G_k &= \frac{\mu_t}{\rho} \left( \frac{\partial \bar{u}_i}{\partial x_j} + \frac{\partial \bar{u}_j}{\partial x_i} \right) \frac{\partial \bar{u}_i}{\partial x_j}, \end{aligned} \quad (2)$$

where  $k$  is the turbulence kinetic energy (TKE),  $\varepsilon$  is the dissipation rate of TKE,  $\mu_t$  is the eddy viscosity, and  $G_k$  is the production rate of TKE.

Referring to Launder et al.'s work [31], the empirical coefficients in (2) can be given as follows:

$$\begin{aligned} C_\mu &= 0.09, \\ C_{\varepsilon 1} &= 1.44, \\ C_{\varepsilon 2} &= 1.92, \\ \sigma_k &= 1.0, \\ \sigma_\varepsilon &= 1.3. \end{aligned} \quad (3)$$

To track the wave surface, the Volume of Fluid (VOF) method is employed. If the volume fraction of water and air in each cell is  $a_w$  and  $a_a$ , respectively, the capturing of the interface between different phases is achieved by the solution of a continuity equation for the volume fraction of liquid. This equation of  $a_w$  has the following form:

$$\frac{\partial a_w}{\partial t} + u_i \frac{\partial (a_w)}{\partial x_i} = 0 \quad (4)$$

$$a_w + a_a = 1. \quad (5)$$

For (5),  $a_w = 0$  means gas phase, and  $a_a = 0$  means liquid phase, while  $a_a = 0 \sim 1$  means the mixture phase or interface between gas and liquid water.

For the solution of governing equations, appropriate boundary conditions at all boundaries of the domain should be defined. The boundary conditions which need to be satisfied are as follows: (1) the kinematic and dynamic free surface boundary conditions at the free surface; (2) the normal-flux boundary condition at the bottom of domain and the rigid body. Besides, for generating waves for studying dynamic problems described in this work, a numerical wave-maker and an artificial damping zone are put on the left and right wall boundary, respectively.

**2.2. Wave Generation and Damping Methods.** In this work, the wave generation is performed by a piston-type wave-maker. The schematic of a numerical wave tank with a piston wave-maker at the left wall boundary is given in Figure 2.

A paddle moves sinusoidally with the function:

$$X(t) = \frac{X_0}{2} \sin \omega t, \quad (6)$$

where  $X_0$  is the maximum horizontal displacement of the paddle and  $\omega$  is the angular frequency. The motion of the paddle generates a propagating wave which is composed of a regular incoming wave with wave number  $k$  and angular frequency  $\omega$  and attenuating incident waves. With the attenuating components eliminated, surface elevation can be given by

$$\begin{aligned} \eta(x, t) &= \frac{X_0}{2} \frac{4 \sinh^2 kd}{2kd + \sinh 2kd} \cos(kx - \omega t) \\ &= \frac{H}{2} \cos(kx - \omega t), \end{aligned} \quad (7)$$

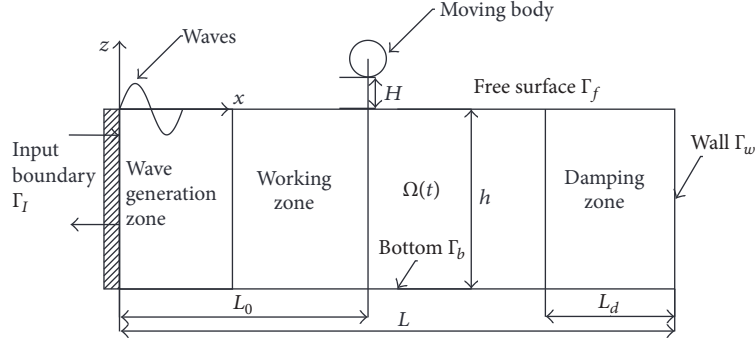


FIGURE 2: Numerical wave tank and a moving body.

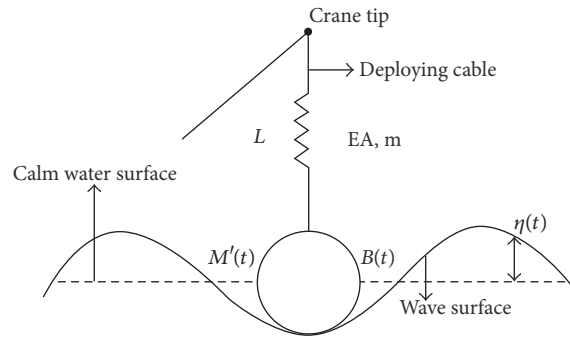


FIGURE 3: The cable-rigid body system.

where  $d$  is the water depth,  $k$  is wave number, and wave height  $H$  can be obtained by

$$H = \frac{4\sinh^2(kd)}{2kd + \sinh(2kd)} X_0. \quad (8)$$

It is necessary to absorb the attenuating incident wave so as to avoid the wave surface of the working zone being disturbed. In this work, at the right part of the flow domain, porous media are used to form an artificial damping zone so that reflected waves are gradually vanished along the direction of wave propagation. Porous media are modeled by the addition of a momentum source term to the standard fluid flow equations, which can be given by

$$S_i = -\left(\frac{\mu}{\alpha} v_i + C_2 \frac{1}{2} \rho |v_i| v_i\right), \quad (9)$$

where  $S_i$  is the source term for the  $i$ th ( $x$ ,  $y$  or  $z$ ) momentum equation,  $|v_i|$  is the magnitude of the velocity,  $\mu$  is the viscosity of the fluid,  $C_2$  is the inertial resistance factor, and  $\alpha$  is the permeability of porous media.

### 3. Simplified Analytical Model

Although the motion of a deployed body has six degrees of freedom of a rigid body, the predominant motion is vertical direction. Compared with accurate but time-consuming

multibody dynamics approaches, the 1-DOF dynamic system is more suitable for the present research. Therefore, it is fairly reasonable to assume that the cable-rigid body (circular cylinder) system can be simplified as a 1-DOF system, as shown in Figure 3.

Hu et al. [30] developed an analytical model to investigate the dynamic responses of deployment system during bodies impacting on initially calm water. In this paper, based on Hu et al. [30], an improved approach is presented so as to consider the influence of waves, which is briefly described as follows.

For the 1-DOF cable-rigid body system, if the deployed body has a vertical motion  $z$  relative to coordinate system fixed with space, the following equation can be obtained:

$$\begin{aligned} M'(t) \left( \frac{d^2 z}{dt^2} - \frac{d\eta}{dt} \right) \\ = Mg - B(t) - \rho V(t) \frac{d\eta}{dt} - T(t) \\ - 0.5\rho C_D A \left( \frac{dz}{dt} - \eta \right) \left| \frac{dz}{dt} - \eta \right| - F_s \end{aligned} \quad (10)$$

and  $M'(t) = M + A_{33}$ ,  $B(t) = \rho V(t)g$ ,  $\eta = \omega(H/2) \cos(kx - \omega t)$ , and  $F_s = (d/dt)[A_{33}(dz/dt - \eta)]$ , where  $M$  is the mass of the deployed body in air,  $A_{33}$  is the time-varying heave added

mass of the deployed body,  $g$  is gravitational acceleration,  $B(t)$  is the buoyancy force,  $\rho$  is density of water,  $V(t)$  is the submerged volume of the deployed body,  $H$  and  $\omega$  are wave height and frequency of regular waves, respectively,  $T(t)$  is the tension that the cable acts on the deployed body,  $C_D$  is the drag coefficient,  $A$  is vertical projected area, and  $F_s$  is the slamming force.

Equation (10) can be rewritten as

$$M \frac{d^2 z}{dt^2} = Mg - T(t) - F_{\text{hyd}}, \quad (11)$$

where  $F_{\text{hyd}}$  is hydrodynamic forces which can be obtained by

$$F_{\text{hyd}} = A_{33} \left( \frac{d^2 z}{dt^2} - \frac{d\eta}{dt} \right) + \rho V(t) \left( g + \frac{d\eta}{dt} \right) + 0.5 \rho C_D A \left( \frac{dz}{dt} - \eta \right) \left| \frac{dz}{dt} - \eta \right| + F_s. \quad (12)$$

Hydrodynamic forces  $F_{\text{hyd}}$  can be calculated by CFD codes. It is worth noting that both the time-varying buoyancy and drag force on the deployed body during water entry are included in hydrodynamic forces.

In the 1-DOF cable-rigid body system, the cable can be modeled as a linear spring; if the position of line end of the cable can be obtained, the elongation and thereby the tension on the cable can be determined. For more details, one can refer to the paper by Hu et al. [30].

The dynamic response of deployment system during a rigid body crossing wave zone is a complex fluid-structure interaction problem, which involves fluid dynamics, mechanical dynamics, and the coupling between them, and thus single solution methods have incapacity to deal with this problem. Therefore, a cosimulation platform is developed based on the CFD software Fluent and MATLAB, and this can also be referred to Hu et al. [30].

## 4. Dynamic Simulation and Analysis

**4.1. Verification of Numerical Wave Tank.** To verify the effectiveness and accuracy of numerical wave generation and dissipation approaches presented in Section 2, a regular wave with wave height 2.5 m and period of 6 s is applied as the target wave. The permeability of porous media of the damping zone is given by

$$\frac{1}{\alpha(x)} = \alpha_0 \left( \frac{x - x_s}{x_e - x_s} \right), \quad (13)$$

where  $\alpha_0$  is a constant permeability and  $x_s$  and  $x_e$  are the starting point coordinate and the ending point coordinate of the damping zone, respectively. Parameters used in simulations are as follows:  $\alpha_0 = 1 \times 10^{-6}$ ,  $x_e = 300$  m,  $x_s = 150$  m, and calm water depth ( $d$ ) = 30 m. Parameters of the numerical wave tank and locations of wave gauges are shown in Figure 4.

Wave surface elevations are probed at four locations ( $x = 50$  m, 100 m, 200 m, and 300 m, as shown in Figure 4) of the numerical wave tank, and time histories of numerical wave

surface elevations are compared with those of the target wave, which are shown in Figure 5. In working zone of wave tank ( $x = 50$  m, 100 m), a good agreement can be observed between simulation results and those of the target wave, while wave elevations in the damping zone ( $x = 200$  m, 300 m) are close to zero, which means satisfactory wave energy-dissipation capacity is achieved. Therefore, it can be concluded that the wave generation and damping performance of the numerical wave tank is good and can meet demands of investigating the dynamic response of deployment system during a circular cylinder lowering through splash zone numerically.

**4.2. Parameters of Dynamic Simulations.** A circular cylinder with neutral buoyancy is selected as the rigid body which is to be deployed by the deployment system, parameters of which are as follows: length  $L = 10$  m, diameter  $D = 2$  m, and thus mass  $M = 31416$  kg. The unstretched length  $L_0$  and initial stiffness  $K$  of the deploying cable are 10 m and 2000 kN/m, respectively.

To investigate the sensitivity of cable tension and motion parameters of the circular cylinder to regular waves and deploying velocities, different parameters are considered in simulations:

- (1) Phase angle =  $\{0^\circ, 90^\circ, 180^\circ, 270^\circ\}$ .
- (2) Wave height  $H = \{1, 2, 2.5, 4\}$  (m).
- (3) Wave period  $T = \{2, 4, 6, 8\}$  (s).
- (4) Deploying velocity  $V_d = \{0.5, 1, 2, 4\}$  (m/s).

**4.3. A Simulation Example of Water Entry Process of a Circular Cylinder.** A simulation example is used to reveal the whole process of water entry of the circular cylinder with considering the influence of waves. Main setups of this example are as follows: the radius of the circular cylinder  $R$  is 1 m, the target wave is a regular wave with wave height  $H = 2.5$  m, and period  $T = 6$  s; the deploying velocity  $V_d$  is 2.5 m/s; a dimensionless parameter  $V_d t/R$  is defined, and  $t = 0$  when the cylinder initially touches wave surface. Wave surface profiles at  $V_d t/R = 0, 0.5, 1,$  and  $2$  are shown in Figure 6. Figures can demonstrate the water entry process of the circular cylinder in waves, and time-varying free surface deformation can be clearly observed.

**4.4. Influence of Wave Impact Phase Angles.** Wave impact phase angles can reflect the relative position between the rigid body and wave surface when impact occurs. Figure 7 shows different wave impact phase angles: positions marked 1, 2, 3, and 4 correspond to phase angles of  $0^\circ, 90^\circ, 180^\circ,$  and  $270^\circ$ , respectively. The regular wave on which the rigid body impacts is determined as wave with  $H = 2.5$  m and  $T = 6$  s. Besides, the case of the body lifting through initially calm water surface is also considered.

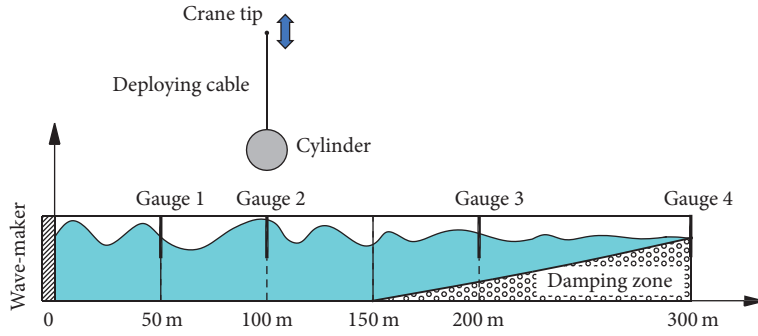


FIGURE 4: A schematic of numerical wave tank.

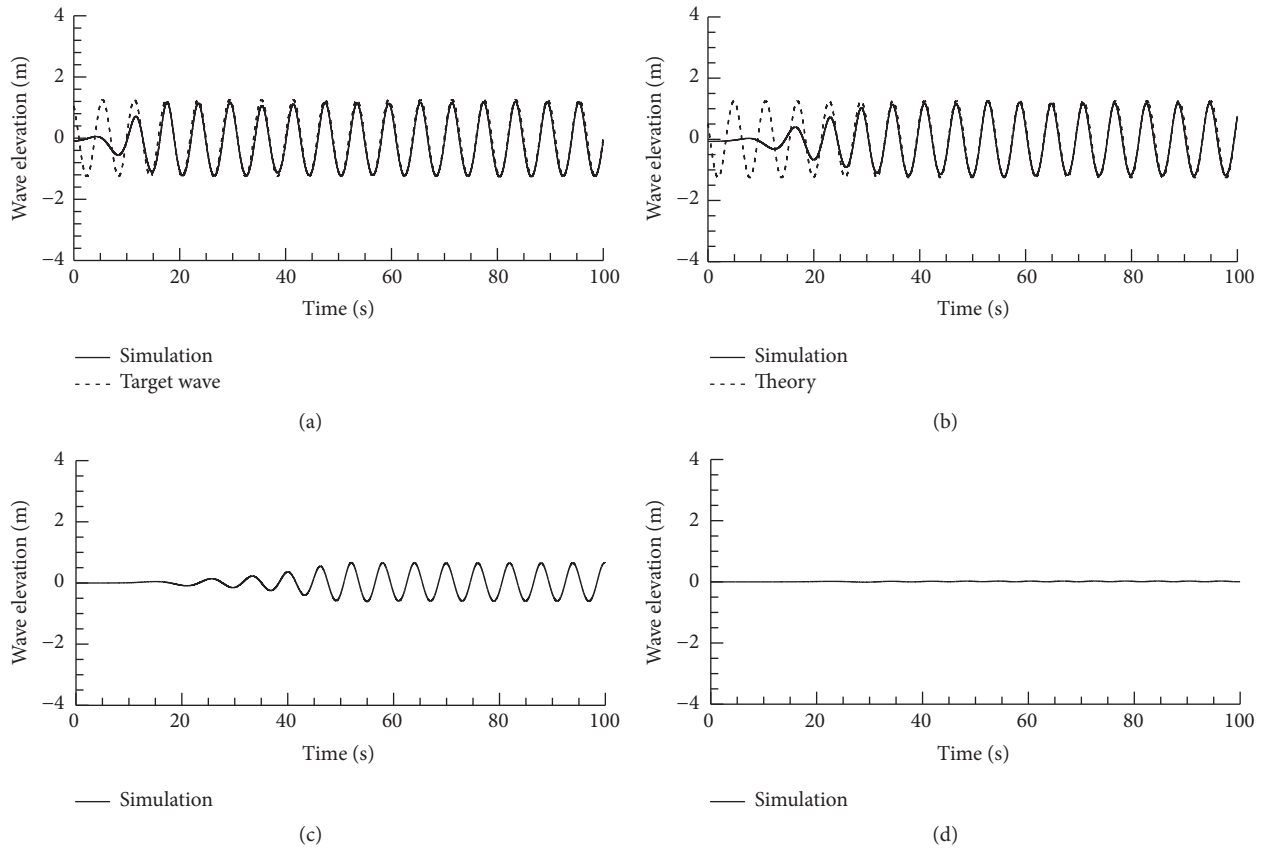


FIGURE 5: Wave elevation at four different locations: (a)  $x = 50$  m; (b)  $x = 100$  m; (c)  $x = 200$  m; (d)  $x = 300$  m.

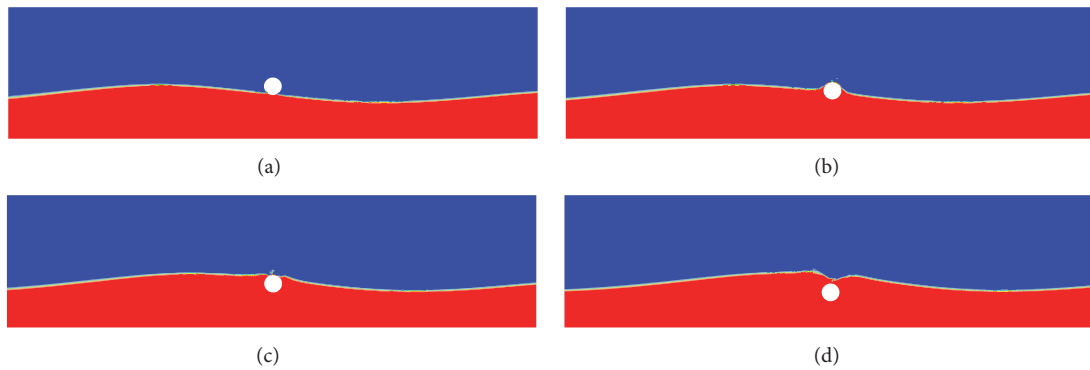


FIGURE 6: Water entry process of a circular cylinder: (a)  $V_d t/R = 0$ ; (b)  $V_d t/R = 0.5$ ; (c)  $V_d t/R = 1$ ; (d)  $V_d t/R = 2$ .

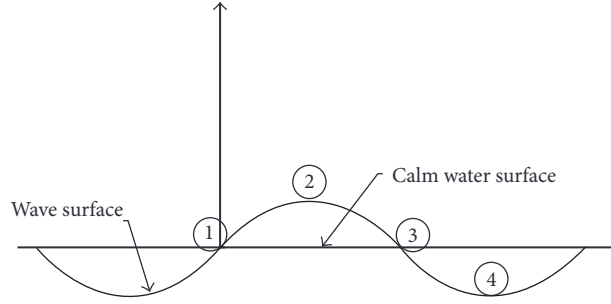


FIGURE 7: Wave impact positions.

From Figures 6(a)–6(c), 9(a)–9(c) and 10(a)–10(c), it can be seen that most of time history curves of velocity, acceleration of the body, and tension acting on the body have the characteristic of periodic but not harmonic oscillations. Applying  $M = 31416$  kg and  $K = 2000$  kN/m, the natural period of the cable-rigid body system can be calculated by

$$T_0 = 2\pi\sqrt{\frac{M}{K}} = 0.787 \text{ s.} \quad (14)$$

It can be seen that oscillating periods of cases are nearly approximate but bigger than the natural period, which is mainly due to the complex body-wave interaction.

From curves of tension, it is worth noting that some points or parts of curves are equal to zero; that is to say, cables of these cases are in a slack state, and the occurrence of this phenomenon is because the deploying cable is highly resistible to tension while could hardly bear compression. When the slack state appears, the cable exerts no influence on the motion of the deployed body, and this is a dangerous condition because control methods which play a role by means of the cable cannot make a difference in hostile ocean conditions. It can also be observed that an alternating slack-taut condition of the deploying cable emerges in some cases, including  $V_d = 0.5$  m/s with  $0^\circ$  and  $V_d = 1$  m/s with  $180^\circ$ , and if the transition rate at which the cable becomes taut from slack state is big enough, it may cause snap force which is preferably avoided. Although smaller deploying velocity means smaller slamming load, the idea that smaller deploying velocities are much safer than bigger ones is not absolutely correct; for example, the dangerous alternating slack-taut condition occurs when  $V_d = 0.5$  m/s and  $V_d = 1$  m/s, while it does not occur when  $V_d = 2$  m/s.

Figures 8–10 also clearly illustrate that wave phase angles play an important role in determining the dynamic response of the cable-rigid body system: for all cases, the maximum upward acceleration appears at the moment just after wave impact occurs, and, compared with other phase angles, cases with  $0^\circ$  have the biggest acceleration, while cases with  $270^\circ$  have the smallest one. This phenomenon is mainly due to

the effect of wave slamming load. At the moment when wave impact occurs, buoyancy, drag force, and added mass are zero, and  $T = Mg$ , (10) can be rewritten as:

$$\frac{d^2z}{dt^2} = -\frac{F_s}{M}. \quad (15)$$

According to previous researches, the slamming force  $F_s$  on an object is mainly dependent on the relative velocity between it and wave surface; from this point of view, the cases with  $0^\circ$  have the biggest relative velocities while cases with  $270^\circ$  have the smallest one. Besides, curves of tension and velocity have the tendency similar to those of acceleration.

From the case of  $V_d = 0.5$  m/s with phase angle =  $270^\circ$ , a special phenomenon can be seen: curves of tension, velocity, and acceleration are parallel to  $x$ -axis at the beginning, and it is because of the fact that the wave is receding faster than the body is being lowered and thus no slamming occurs.

**4.5. Influence of Wave Height.** Cases with four wave heights of regular waves—1 m, 2 m, 2.5 m, and 4 m—are considered, while periods of regular waves and deploying velocity are determined as 6 s and 1 m/s, respectively.

Figure 11 shows time histories of tension, velocity, and acceleration of the circular cylinder subjected to waves with different heights. On one hand, as a whole, with wave height increasing, the amplitude of variation of curves becomes much bigger. On the other hand, curves with smaller wave height are stable and nearly harmonic; with the wave height increasing, the curves are no longer harmonic but still are periodic. When wave height is 4 m, the minimum tension reaches zero, which means the deploying cable becomes slack; after a short period of time, the tension is larger than zero again, which means deploying cable becomes taut, and therefore the alternating slack-taut condition occurs, as mentioned in Section 4.4.

**4.6. Influence of Wave Period.** Cases with four periods of regular waves—2 s, 4 s, 6 s, and 8 s—are considered, while wave heights of regular waves and deploying velocity are determined as 2.5 m and 1 m/s, respectively.

Figure 12 shows time histories of tension, velocity, and acceleration subjected to waves with different periods. With

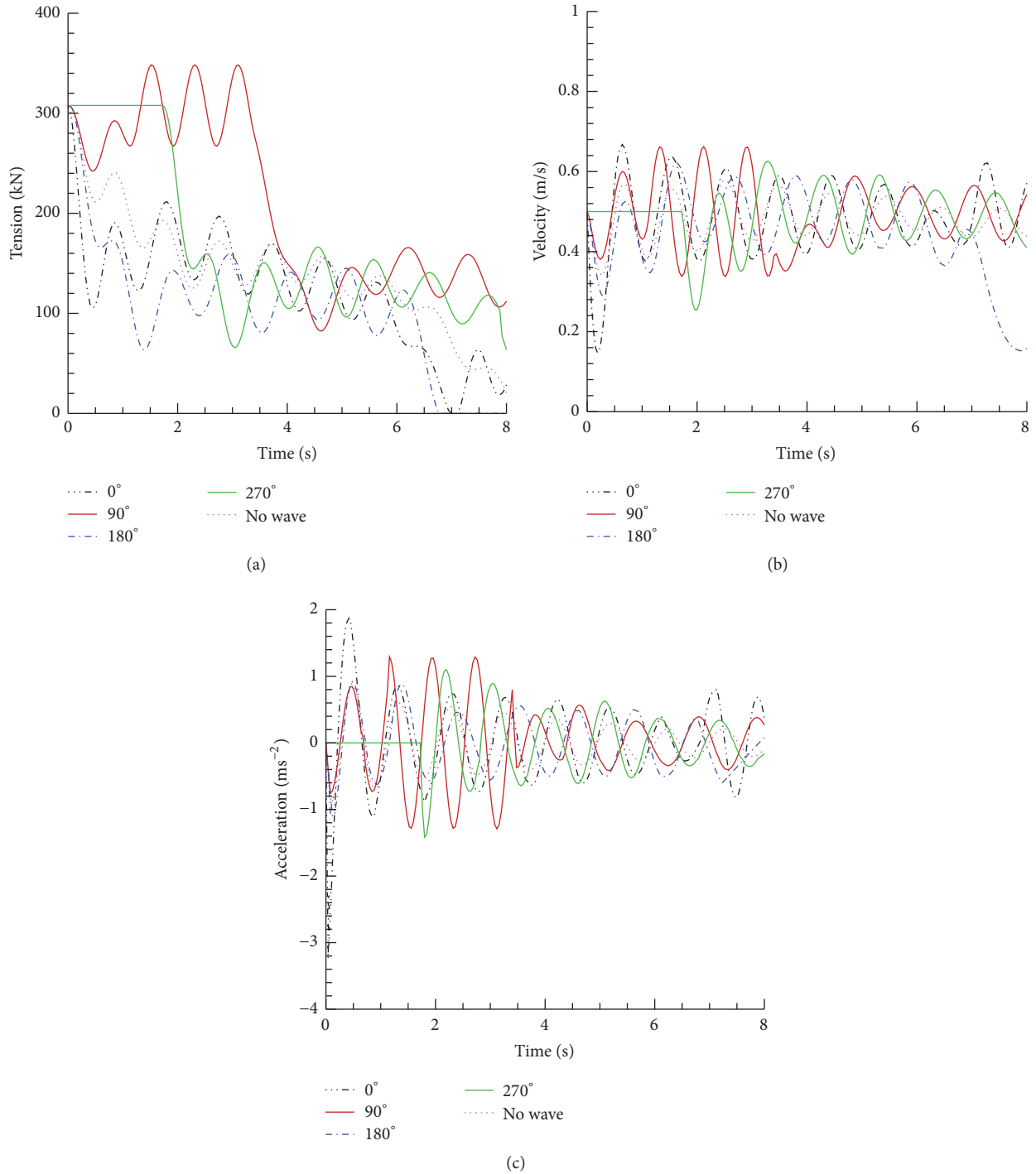


FIGURE 8: Influence of wave impact phase angles ( $V_d = 0.5$  m/s): (a) tension acting on the cylinder; (b) velocity of the cylinder; (c) acceleration of the cylinder.

wave period increasing, the amplitude of variation of curves becomes much smaller. When wave period is 6 s and 8 s, curves are stable and nearly harmonic, and no slack condition can be seen. When wave period is 2 s or 4 s, the situation is different; for the case with  $T = 2$  s, the alternating slack-taut

condition occurs three times, and there are two local peak values of tension, and the first and the second one are 1.4 and 2.1 times bigger than the gravitational force of the deployed circular cylinder, respectively, which is a rather dangerous condition.

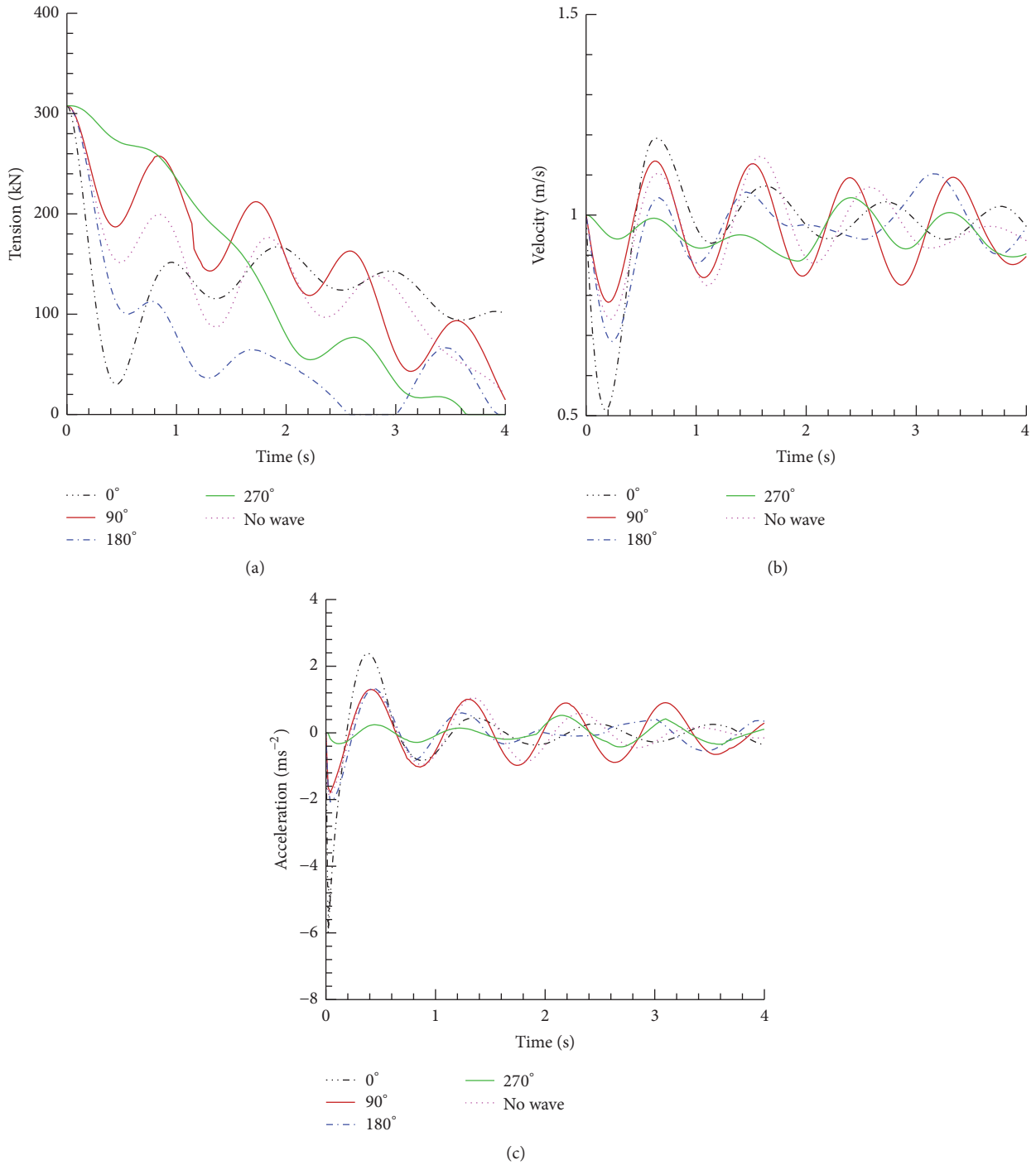


FIGURE 9: Influence of wave impact phase angles ( $V_d = 1$  m/s): (a) tension acting on the cylinder; (b) velocity of the cylinder; (c) acceleration of the cylinder.

condition occurs once; however, the maximum tension is smaller than the gravitational force of the circular cylinder. Considering that the natural period of the cable-deployed body system  $T_0$  is 0.787 s, it is reasonable to conclude that the alternating slack-taut condition is more likely to occur when wave period is closer to the natural period of the cable-rigid body system.

### 5. Conclusion

In this paper, the dynamic response of a deployment system during a circular cylinder lowering through wave zone is investigated numerically. A 1-DOF approach is applied to represent the dynamic cable-rigid body (circular cylinder) system. Numerical simulations are performed on

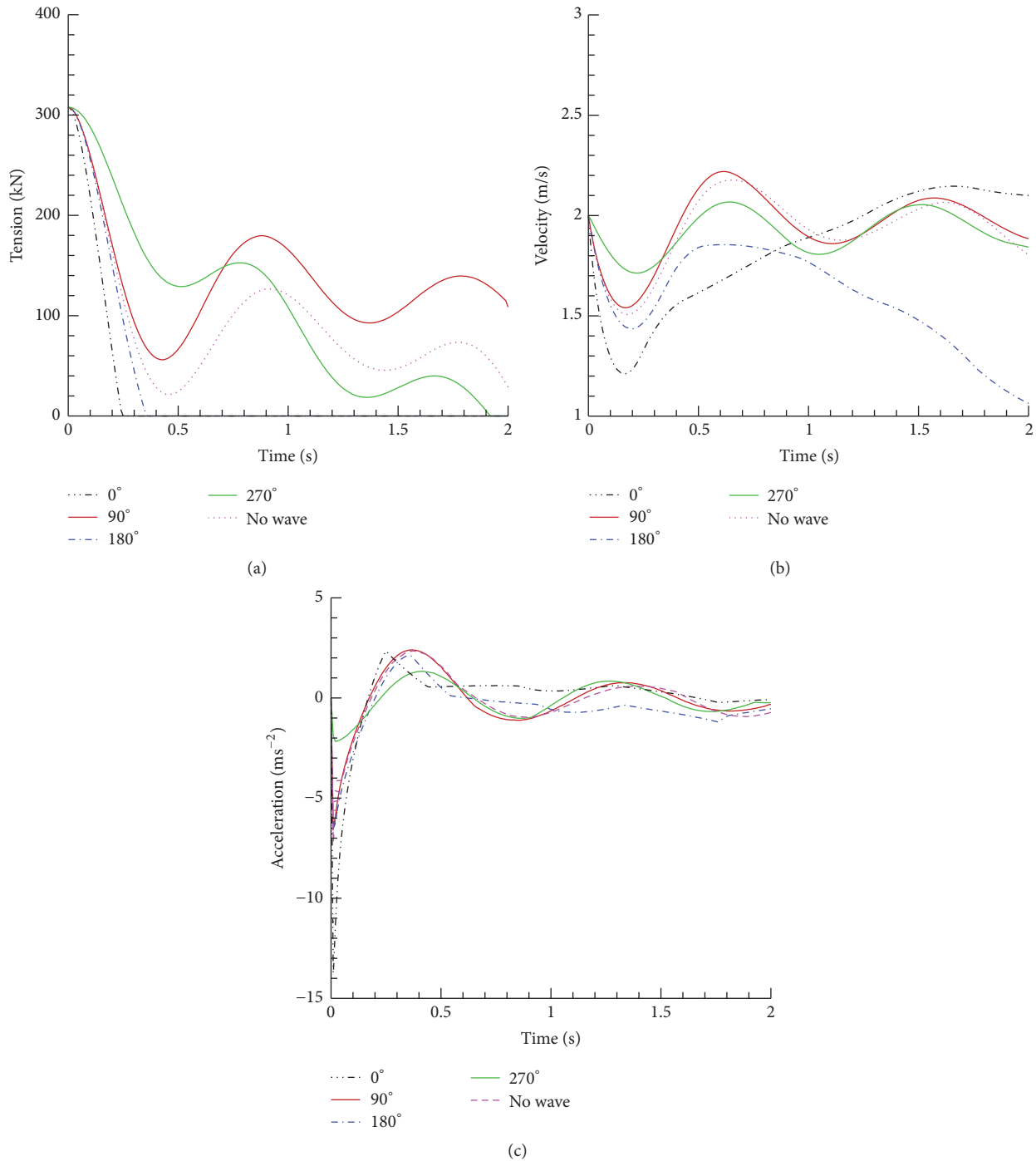


FIGURE 10: Influence of wave impact phase angles ( $V_d = 2$  m/s): (a) tension acting on the cylinder; (b) velocity of the cylinder; (c) acceleration of the cylinder.

a cosimulation platform based on CFD code and MATLAB, which can generate regular waves and deal with fluid-solid coupling problems.

The following conclusions can be given, based on analysis of simulation results:

- (1) A piston-type wave generation and porous media wave absorption methods are applied to generate

regular waves and verified by the comparison with the target wave.

- (2) Cases with wave phase angle  $0^\circ$  have the largest amplitude of variation of curves and the biggest maximum acceleration, which is due to the largest relative velocity between body and wave. At some time points, the cable become slack, and an alternating slack-taut

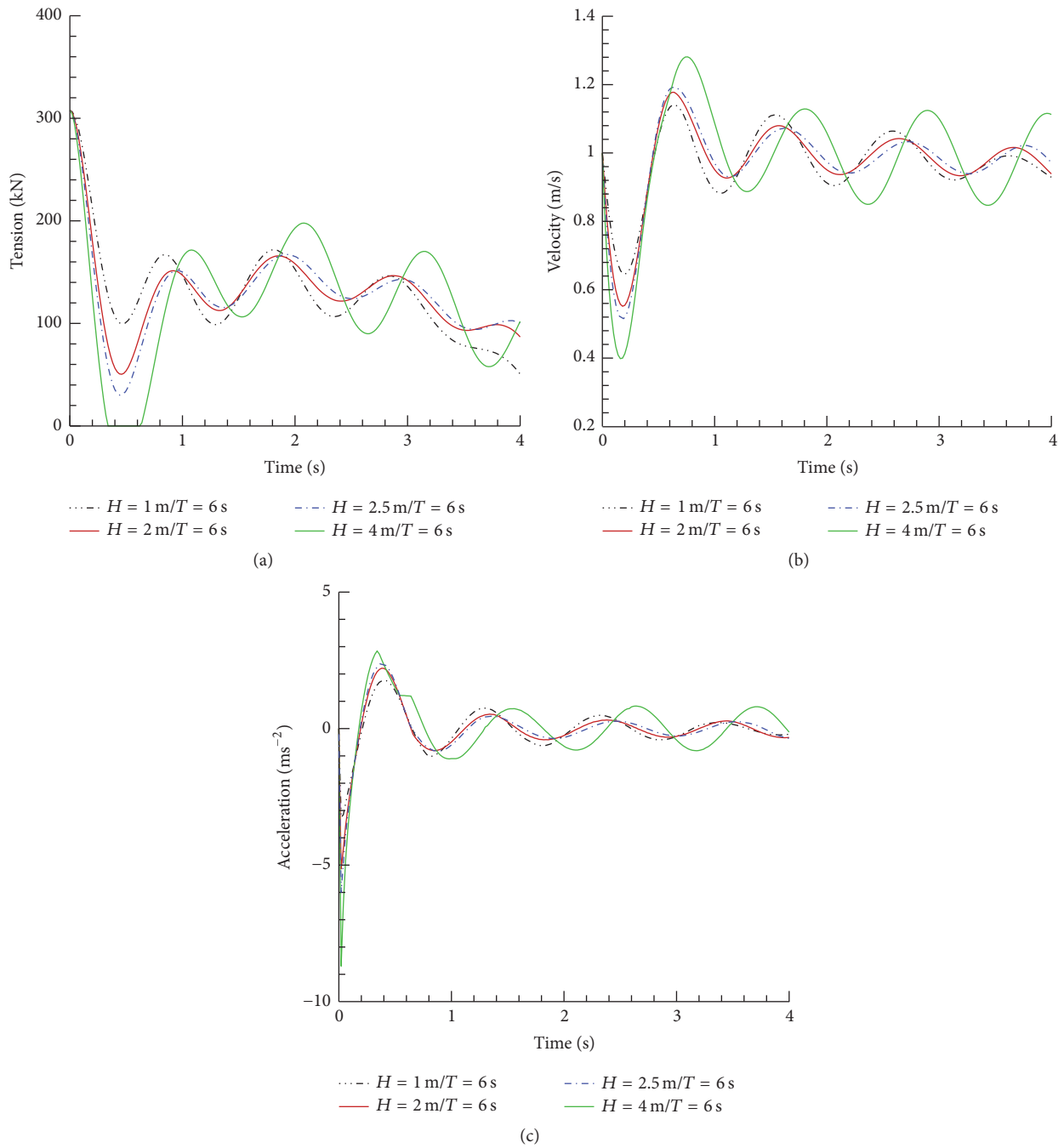


FIGURE 11: Influence of wave heights: (a) tension acting on the cylinder; (b) velocity of the cylinder; (c) acceleration of the cylinder.

condition of the deploying cable can be observed, which is preferably avoided.

- (3) Except for some extreme situations, curves of velocity, acceleration, and tension of the circular cylinder oscillate periodically. With wave height increasing and wave period decreasing, the amplitude of variation of curves becomes bigger, and the alternating slack-taut condition occurs when wave height is large enough or wave period is close to the natural period of the dynamic system.

### Conflicts of Interest

The authors declare that there are no conflicts of interest regarding the publication of this paper.

### Acknowledgments

The authors gratefully acknowledge the support of National Natural Science Foundation of China (Grant no. 51305463), Natural Science Foundation of Hunan Province of China

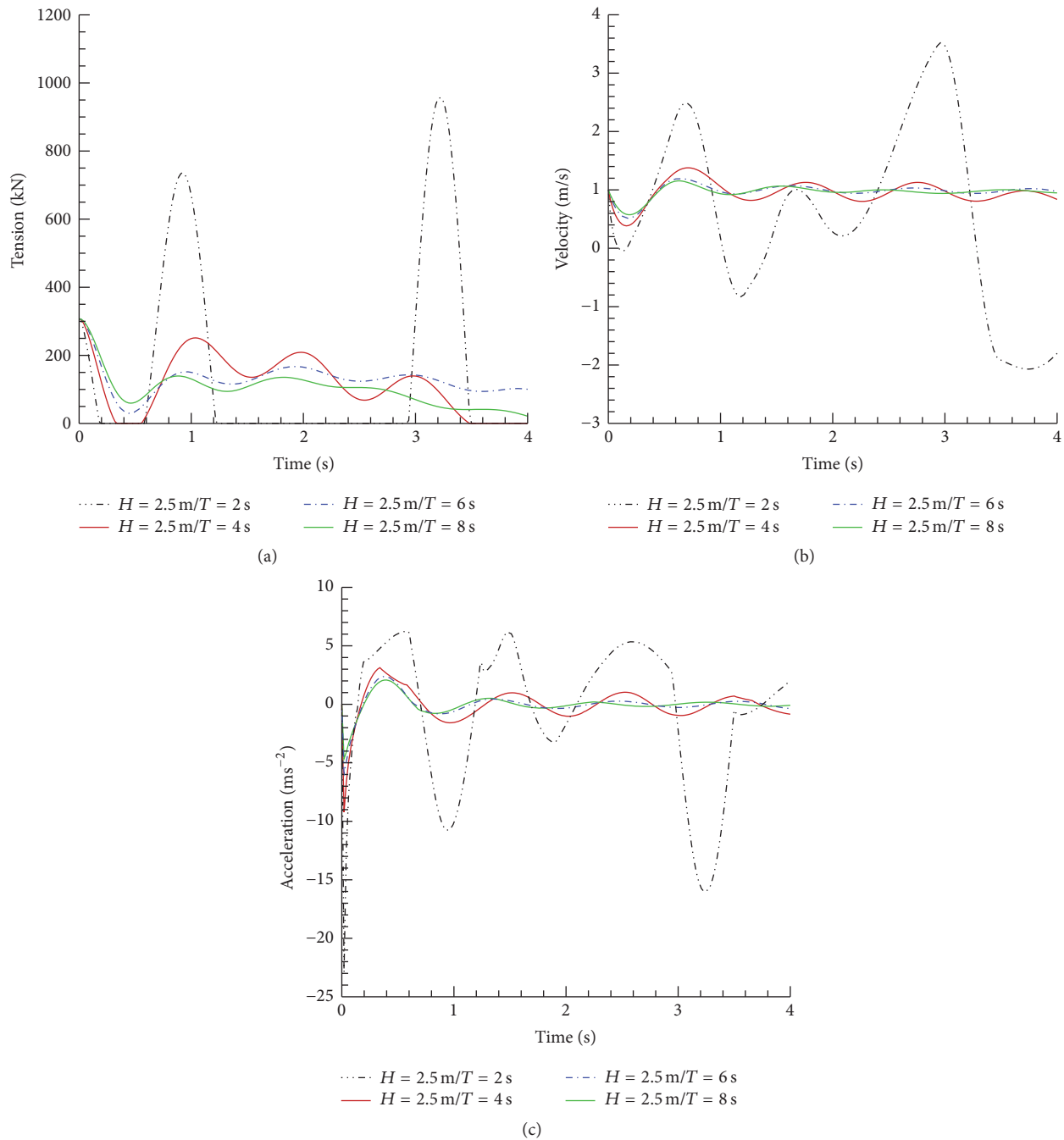


FIGURE 12: Influence of wave periods: (a) tension acting on the cylinder; (b) velocity of the cylinder; (c) acceleration of the cylinder.

(Grant no. 2017JJ3393), and National Key Research and Development Plan of China (Grant no. 2016YFC0304103).

## References

- [1] X. Li, C. Ye, C. Wang, C. Tao, and X. Xiao, "Chinese manned submersible JIAOLONG's scientific cruise in 2014-2015," in *Proceedings of the MTS/IEEE Washington, OCEANS 2015*, October 2015.
- [2] T. Shimizu, Y. Yamamoto, N. Tenma, and H. Narita, "Electric-submersible-pump performance under methane/water/methane-hydrate pipe flows," in *Proceedings of the 25th International Ocean and Polar Engineering Conference, ISOPE 2015*, pp. 132–138, USA, June 2015.
- [3] D.-J. Li, Y.-H. Chen, J.-G. Shi, and C.-J. Yang, "Autonomous underwater vehicle docking system for cabled ocean observatory network," *Ocean Engineering*, vol. 109, pp. 127–134, 2015.
- [4] V. Karman, The impact of seaplane floats during landing. National Advisory Committee for Aeronautics, TN 321, pp.1-8, 1929.

- [5] H. Wanger, "Trans phenomena associated with impacts and sliding on liquid surfaces," *Math Mechanics*, vol. 12, no. 4, pp. 193–215, 1932.
- [6] O. M. Faltinsen, *Sea Loads on Ships and Offshore Structure*, Cambridge university press, 1993.
- [7] H. Sun and O. M. Faltinsen, "Water impact of horizontal circular cylinders and cylindrical shells," *Applied Ocean Research*, vol. 28, no. 5, pp. 299–311, 2006.
- [8] C. Mnasri, Z. Hafsia, M. Omri, and K. Maalel, "A moving grid model for simulation of free surface behavior induced by horizontal cylinders exit and entry," *Engineering Applications of Computational Fluid Mechanics*, vol. 4, no. 2, pp. 260–275, 2014.
- [9] P. Ghadimi, A. Dashtimanesh, and S. R. Djeddi, "Study of water entry of circular cylinder by using analytical and numerical solutions," *Journal of the Brazilian Society of Mechanical Sciences & Engineering*, vol. 34, no. 3, pp. 225–232, 2012.
- [10] A. Tassin, D. J. Piro, A. A. Korobkin, K. J. Maki, and M. J. Cooker, "Two-dimensional water entry and exit of a body whose shape varies in time," *Journal of Fluids and Structures*, vol. 40, pp. 317–336, 2013.
- [11] A. Iranmanesh and M. Passandideh-Fard, "A three-dimensional numerical approach on water entry of a horizontal circular cylinder using the volume of fluid technique," *Ocean Engineering*, vol. 130, pp. 557–566, 2017.
- [12] B. Bas, T. Bunnik, D. Honig, and G. Meskers, "A new simulation method for installation of subsea structures from the splash zone to the ultra deep," in *Proceedings of the DOT Conference*, New Orleans, La, USA, 2004.
- [13] T. Bunnik and B. Buchner, "Numerical prediction of wave loads on subsea structures in the splash zone," in *Proceedings of the 14th International Offshore and Polar Engineering Conference (ISOPE)*, pp. 284–290, Toulon, France, May 2004.
- [14] T. Bunnik, B. Buchner, and A. Veldman, "The use of a Volume of Fluid (VOF) method coupled to a time domain motion simulation to calculate the motions of a subsea structure lifted through the splash zone," in *Proceedings of the 25TH International Conference on Offshore Mechanics and Arctic Engineering, OMAE 2006*, Hamburg, Germany, June 2006.
- [15] J. Y. Zhang, D. J. Li, X. Y. Gao, Q. C. Meng, C. J. Yang, and Y. Chen, "Simulation analysis of deployment and retrieval of junction box used in cabled seafloor observatory," *Ship Engineering*, vol. 32, no. 6, pp. 53–59, 2010 (Chinese).
- [16] W.-H. Wang and Y.-Y. Wang, "An essential solution of water entry problems and its engineering applications," *Journal of Marine Science and Application*, vol. 9, no. 3, pp. 268–273, 2010.
- [17] P. Ryzhakov, R. Rossi, A. Viña, and E. Oñate, "Modelling and simulation of the sea-landing of aerial vehicles using the Particle Finite Element Method," *Ocean Engineering*, vol. 66, pp. 92–100, 2013.
- [18] P. Wen and W. Qiu, "Solving 2-D water entry problems with a CIP method and a parallel computing algorithm," *Marine Systems Ocean Technology*, vol. 11, no. 1-2, p. 1, 2016.
- [19] T. Zhang, D. Li, and C. Yang, "Study on impact process of AUV underwater docking with a cone-shaped dock," *Ocean Engineering*, vol. 130, pp. 176–187, 2017.
- [20] J. M. Niedzwecki and S. K. Thampi, "Snap loading of marine cable systems," *Applied Ocean Research*, vol. 13, no. 1, pp. 2–11, 1991.
- [21] K. W. Thurston, R. C. Swanson, and F. Kopp, "Statistical characterization of slacking and snap loading during offshore lifting and lowering in a wave environment," in *Proceedings of the ASME 2011 30th International Conference on Ocean, Offshore and Arctic Engineering, OMAE2011*, pp. 269–277, nld, June 2011.
- [22] W. Lu, F. Ge, L. Wang, X. Wu, and Y. Hong, "On the slack phenomena and snap force in tethers of submerged floating tunnels under wave conditions," *Marine Structures*, vol. 24, no. 4, pp. 358–376, 2011.
- [23] A. Selvåg, Wave impact forces on complex structures during lowering through the splash zone, Master's Thesis, Norw. Univ. Sci. Technol., Trondheim, 2013.
- [24] M. Wu, Dynamic analysis of a subsea module during splash-zone transit, Master's Thesis, Norw. Univ. Sci. Technol., Trondheim, 2013.
- [25] M. Valen, Launch and recovery of ROV: Investigation of operational limit from DNV Recommended Practices and time domain simulations in SIMO, Master's Thesis, Norwegian Norw. Univ. Sci. Technol., Trondheim, 2010.
- [26] R. B. Gordon, G. Grytøy, and M. Dhaigude, "Modeling suction pile lowering through the splash zone," in *Proceedings of the ASME 32nd International Conference on Ocean, Offshore and Arctic Engineering, OMAE 2013*, Nantes, France, June 2013.
- [27] T. Jacobsen and B. J. Leira, "Numerical and experimental studies of submerged towing of a subsea template," *Ocean Engineering*, vol. 42, pp. 147–154, 2012.
- [28] L. Li, Z. Gao, T. Moan, and H. Ormberg, "Analysis of lifting operation of a monopile for an offshore wind turbine considering vessel shielding effects," *Marine Structures*, vol. 39, pp. 287–314, 2014.
- [29] L. Li, Z. Gao, and T. Moan, "Comparative study of lifting operations of offshore wind turbine monopile and jacket substructures considering vessel shielding effects," in *Proceedings of the Twenty-fifth International Ocean and Polar Engineering Conference*, pp. 1290–1298, USA, 2015.
- [30] H. Xiaozhou and L. Shaojun, "Numerical investigation of dynamic response of deploying system during a circular cylinder lowering through air-water interface," *International Journal of Fluid Mechanics Research*, vol. 42, no. 3, pp. 191–205, 2015.
- [31] B. E. Launder and D. B. Spalding, *Lectures in Mathematical Models of Turbulence*, Academic Press, London, England, 1972.

## Research Article

# Investigation of Axial Strengthened Reinforced Concrete Columns under Lateral Blast Loading

**Mohammad Esmailnia Omran and Somayeh Mollaei**

*Department of Civil Engineering, University of Kurdistan, Sanandaj, Iran*

Correspondence should be addressed to Somayeh Mollaei; [s.mollaei@eng.uok.ac.ir](mailto:s.mollaei@eng.uok.ac.ir)

Received 26 May 2017; Revised 25 August 2017; Accepted 6 September 2017; Published 16 October 2017

Academic Editor: Abdul Qadir Bhatti

Copyright © 2017 Mohammad Esmailnia Omran and Somayeh Mollaei. This is an open access article distributed under the Creative Commons Attribution License, which permits unrestricted use, distribution, and reproduction in any medium, provided the original work is properly cited.

Different factors can affect blast response of structural components. Hence, experimental tests could be the best method for evaluating structures under blast loading. Therefore, an experimental explosion loading has been done on RC members by the authors. Four RC components, with identical geometry and material, with and without axial load were imposed to air blast. Observed data of the members' response under blast loading was used for validation of finite element modeling process using ABAQUS software. With respect to complexity, limitations, and high costs of experimental tests, analytical studies and software modeling can be good alternatives. Accordingly, in this paper, the behavior of 6 different models of normal and strengthened RC columns under blast loading was evaluated using ABAQUS. Strengthening configurations considered here were designed for enhancing axial capacity of RC columns. Therefore, we can investigate the effectiveness of axial strengthening of column on its blast resistance capacity and residual axial strength. The considered strengthening methods were different steel jacket configurations including steel angle, channel, and plate sections. The results showed that retrofitting significantly improves blast performance of the columns. Moreover, residual strength capacity of the columns strengthened with steel channel is higher than the other models.

## 1. Introduction

A wide range of engineering structures such as high-rise buildings, bridges, tunnels, dams, platforms, and military and security shelters are constructed by reinforced concrete materials. There has been much attention to reinforced concrete (RC) structures performance under static and seismic loads but evaluation of RC structures' behavior under blast loading and identification of their dynamic characteristics are important for valid design of concrete structures given that many structures may face extreme dynamic loading such as explosion in their lifetime. Columns are the key load bearing elements in building structures and in case of an explosion event near the building, columns are mostly the first structural elements which are affected by lateral loading caused by explosion. Studying the explosion of explosives has been considered by scientists and researchers and the efforts of scientists and researchers in the field of shock wave physics became important since the 20th century [1]. One of the pioneers in this field is Hopkinson (1915) who conducted

extensive research and tests and formed the Hopkinson-Cranz scaling law [1, 2].

Recently, many different studies have been conducted on different types of concrete structures such as columns under explosion loads [3–7]. With respect to complexity, limitations, and high cost of laboratory researches in this field, analytical studies and software modeling can be a good alternative to laboratory and experimental methods. Finite element analysis method is a powerful and useful tool for researchers and structural designers to have an accurate estimation of behavior of structures under blast loading without requiring high costs and great difficulty. Shi et al. (2008) defined a failure criterion based on residual axial capacity for reinforced concrete columns and drew  $P-I$  (pressure-impulse) diagrams for columns based on this failure criterion using numerical modeling by LS-DYNA software [8]. Bao and Li (2010) conducted parametric studies on RC columns using numerical modeling in LS-DYNA [3]. In line with the most important results, reinforced concrete columns must be designed in such a way that their moment

capacity should be less than shear capacity. On the other hand, lateral deformation of column must be controlled in order to prevent instability caused by secondary moments. In this study, standoff distance has been considered to be constant and explosion has been considered to occur at a close distance. A similar study has been carried out by Wu et al. (2011) using arbitrary Euler–Lagrange analysis in LS-DYNA software for analysis of columns' response under contact explosion [9]. The results obtained have been used for evaluation of residual axial capacity of columns and the effect of different parameters on this capacity has been evaluated. ABAQUS/Explicit software has been used in finite element modeling by Arlery et al. (2013) on effects of close explosion on reinforced concrete columns [10]. In line with the results, depth of column section and distance to the center of the explosion had the greatest effects in reducing the amount of damage in the column and height and width of section and concrete compressive strength are less effective [10]. Center of the explosion is extremely close to the structure in this study and the response of structure in this case is usually local and in form of erosion of section. A numerical study was carried out by Kyei and Braimah (2017) to investigate the effects of transverse reinforcement spacing on the blast resistance of RC columns using LS-DYNA code. The study revealed that the effect of transverse reinforcement spacing and axial loading significantly affects RC column behavior under blast loading at low scaled distances. At higher scaled distances, however, the effects were insignificant [11].

Some researchers have studied the retrofitting and strengthening of RC columns under the blast loading. Crawford (2013) reported some of the methods of using FRP for strengthening RC columns in order to increase the strength of RC columns under the simultaneous effect of blast loading and axial force [6]. According to the main results, FRP coating increases the ductility and shear strength of the column. The focus in these studies was based on FRP material and other methods for retrofitting RC columns were not considered. Carriere et al. (2009) have introduced SRP covers as a perfect replacement for CFRP for retrofitting RC elements against explosion [12]. The effect of retrofitting reinforced concrete beams and columns using SRP coating has been evaluated using explosion tests and numerical modeling by AUTODYN. Based on the obtained results, SRP coatings have lower cost and easier installation process in comparison to CFRP covers. Also, SRP increases ductility of RC columns under blast loading and prevents brittle collapse of RC columns. Nevertheless, there has been no reference to displacements or strains in the considered samples and also the scales of studied samples are small. Xu et al. (2016) discussed the blast resistance of UHPC (ultra-high performance concrete) columns by conducting a series of field tests. It was reported that UHPC materials provide sufficient strength, ductility, and energy absorption and crack controlling capacities compared to conventional normal strength concrete [13]. Zhang et al. (2016) reported an experimental investigation on Concrete-filled double-skin tubes (CFDST) columns subjected to blast loading. Based on the results, it was obvious that CFDST column

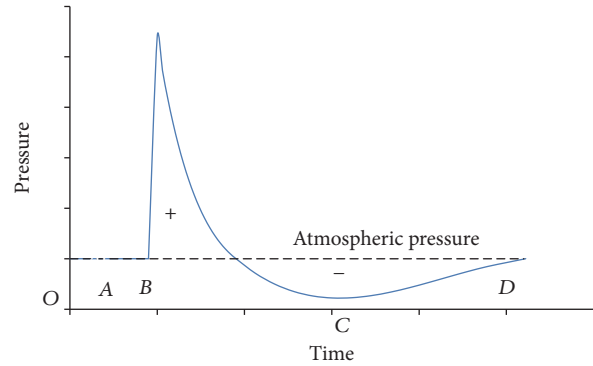


FIGURE 1: Pressure-time diagram of blast wave.

has excellent blast resistance and it can prevent concrete crushing and steel buckling and thus has an overall global flexural response as opposed to localized structural failure [14].

By reviewing literature, it can be observed that retrofitting effects have been considered in minor studies. Moreover, most studies about blast retrofitting of RC columns have been considered using polymer sheets. On the other hand, the need for further studies in this field still remains due to uncertainties in the phenomenon of explosion and complexity of the behavior of RC sections under lateral blast loading. Thus, in this paper, 6 models of retrofitted RC columns have been evaluated under blast loading. The effects of different configuration of steel jackets have been investigated using ABAQUS 6.13 software [15]. All of the strengthening configurations considered here were designed with the purpose of enhancing the axial load bearing capacity of the RC columns. Therefore, we can investigate the effectiveness of axial strengthening of the RC columns by steel jackets on their blast resistance capacity.

## 2. Blast Loading

Explosion is an instantaneous phenomenon which creates large amounts of light, heat, sound, and pressure resulting from blast wave due to sudden release of large amounts of energy. The real source of this energy can be gunpowder, steam compressed in the boiler, or uncontrolled nuclear developments. However, release of energy should be sudden and a high-energy environment should be formed around it. A part of this energy is released through heat radiations and a part of it enters into the air (air blast) and ground (ground shock) through radial waves [18]. An approximate pressure-time diagram at a certain distance from the center of the explosion is drawn in Figure 1. As can be seen in the figure, Section A corresponds to time before the arrival of the wave front and B is after incident shock impact and shows the sudden increase of pressure. Positive pressure has ended at C and negative phase of pressure (suction) can be felt in the environment. This is alongside the blast wind in the opposite direction to the direction of incident shock impact and D corresponds to the disappearance of blast wave effects and return of pressure to atmospheric pressure [19].

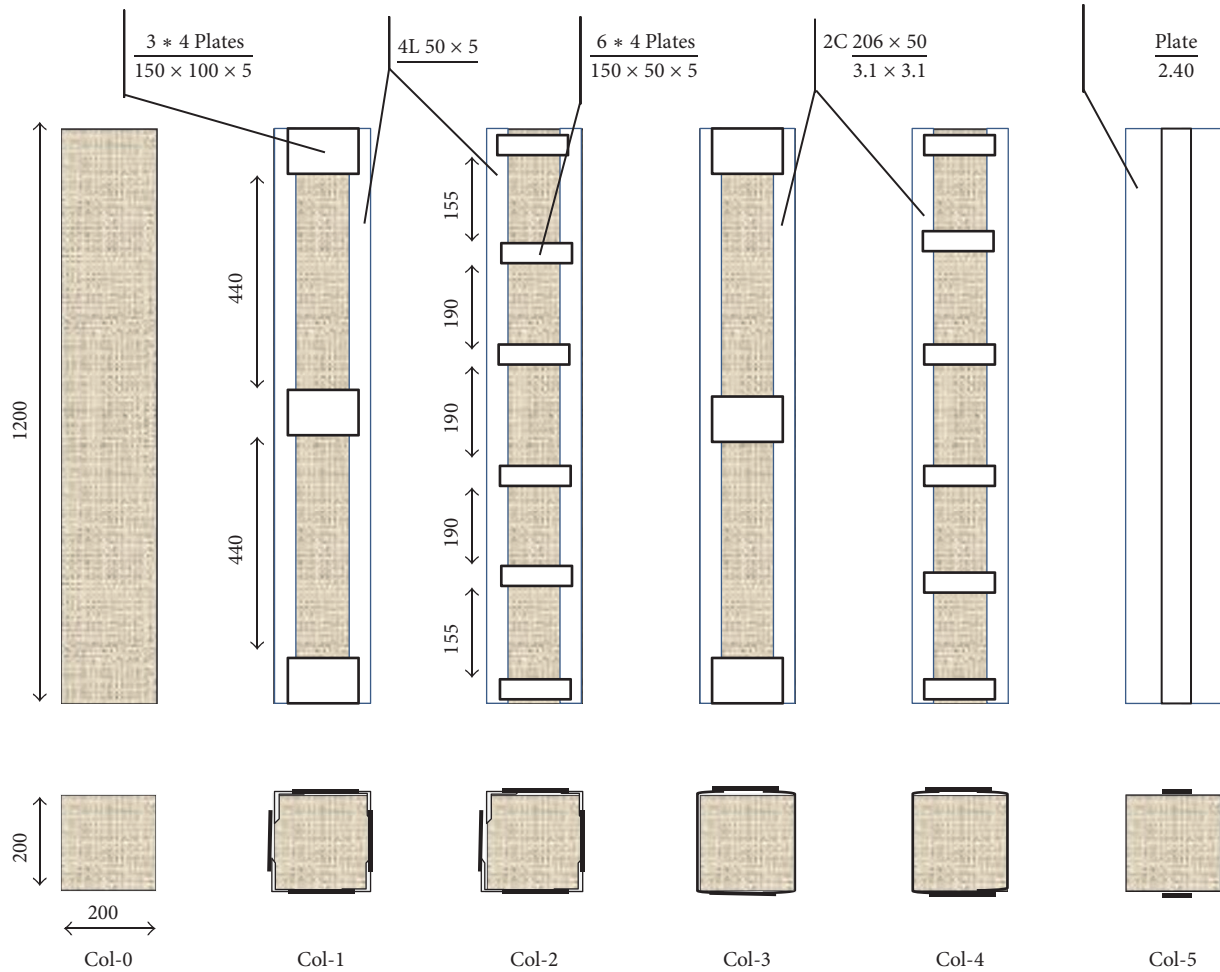


FIGURE 2: Details of dimensions and retrofitting configuration of columns [16].

Methods for estimation of pressure diagram for an explosion and its distribution on structural face have been presented in many different references [18–21].

### 3. Details of the Studied Models

Here, RC columns with the specifications provided in [16] by Belal et al. (2015) have been used. Six models of RC columns were considered; one of them is simple (not retrofitted) while others are retrofitted using different configuration of steel jackets. Characteristics of the section and details of retrofitting methods for all samples are summarized in Figure 2 and Table 1. Columns have rectangular symmetric section with dimensions of 200 mm and height of 1200 mm which retrofitting offered in order to increase their axial bearing capacity. Steel elements used in strengthening of samples have been used in such a way that they all have equal horizontal cross-sectional area [16].

Concrete compressive strength used in samples is 34 MPa which is the same for all samples. Specifications of steel materials have been mentioned in Table 2 and failure strain here is the strain which corresponds to ultimate tensile stress of steel material.

### 4. Finite Element Modeling

Here, finite element models of columns and steel jackets have been initially developed and then these models have been analyzed under lateral blast loading. Proper modeling and meshing of reinforced concrete and steel as well as the interaction between them are important factors in development of accurate models. Details of modeling process are explained in this section.

**4.1. Modeling of Concrete Material.** Concrete damage plasticity (CDP) model has been used in this study for modeling of concrete's behavior which was presented by Lubliner et al. (1989) [22] and was later completed by other researchers [23, 24]. Two main failure mechanisms including tensile cracking and compressive crushing are assumed for concrete in this model. Nonlinear behavior of concrete is described using isotropic damage elasticity and tensile and compressive plastic concepts. Figure 3 shows stress-strain curves for concrete material in uniaxial tension and compression.

In Figure 3,  $E_0$  is the modulus of elasticity,  $\sigma_t$  is tensile stress,  $\sigma_c$  is compressive stress,  $\epsilon_t^{\sim ck}$  is cracking strain,  $\epsilon_t^{\sim in}$  is inelastic strain associated with existing stress, and  $d_t$

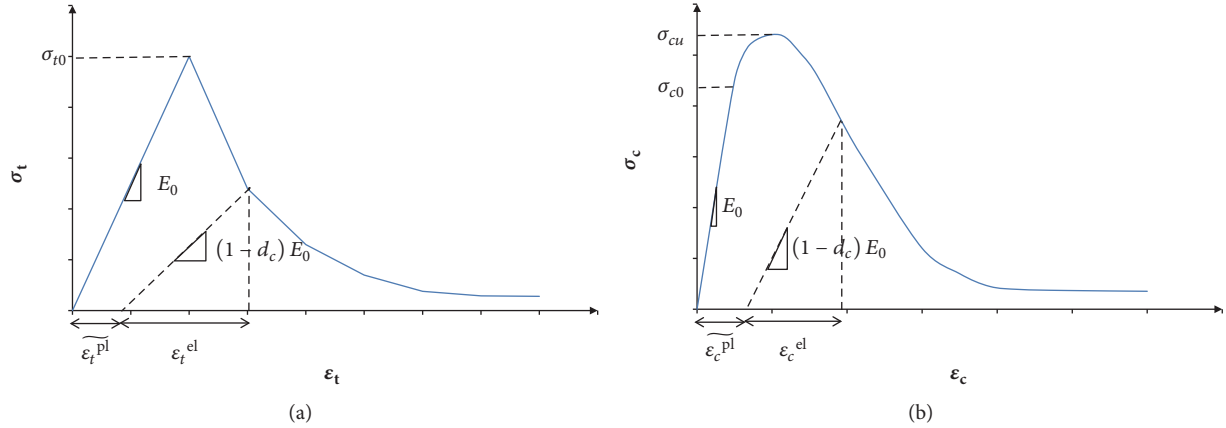


FIGURE 3: Uniaxial behavior of concrete; (a) tension; (b) compression [15].

TABLE 1: Specifications of models (dimensions: mm).

Model	Strengthening configuration	Longitudinal and transverse reinforcement	Dimensions
Col-0	Without strengthening	4 $\phi$ 12 - $\phi$ 8 @ 100	200 $\times$ 200 $\times$ 1200
Col-1	Steel angles 4 L 50 $\times$ 50 $\times$ 5 + 3 $\times$ 4 plates 150 $\times$ 100 $\times$ 2	4 $\phi$ 12 - $\phi$ 8 @ 100	200 $\times$ 200 $\times$ 1200
Col-2	Steel angles 4 L 50 $\times$ 50 $\times$ 5 + 3 $\times$ 4 plates 150 $\times$ 50 $\times$ 2	4 $\phi$ 12 - $\phi$ 8 @ 100	200 $\times$ 200 $\times$ 1200
Col-3	Steel channels 2C (206 $\times$ 50)/(3.1 $\times$ 3.1) + 3 $\times$ 4 plates 150 $\times$ 100 $\times$ 2	4 $\phi$ 12 - $\phi$ 8 @ 100	200 $\times$ 200 $\times$ 1200
Col-4	Steel channels 2C (206 $\times$ 50)/(3.1 $\times$ 3.1) + 3 $\times$ 4 plates 150 $\times$ 50 $\times$ 2	4 $\phi$ 12 - $\phi$ 8 @ 100	200 $\times$ 200 $\times$ 1200
Col-5	Complete steel jacket (steel plates) 4 $\times$ 4 plates 200 $\times$ 2.4	4 $\phi$ 12 - $\phi$ 8 @ 100	200 $\times$ 200 $\times$ 1200

TABLE 2: Specifications of steel material.

Material	Nominal diameter (mm)	Modulus of elasticity (MPa)	Yield strength (MPa)	Ultimate stress (MPa)	Failure strain
Longitudinal bars	12	210000	360	463	11
Stirrups	8	210000	240	340	14

and  $d_c$  are damage parameters in tension and compression, respectively. Completion of failure surface is controlled using hardening variables of  $\varepsilon_c^{pl}$  and  $\varepsilon_t^{pl}$  which are, respectively, related to failure mechanisms under compressive and tensile loading [15]. In fact,  $\varepsilon_c^{pl}$  and  $\varepsilon_t^{pl}$  are equivalent plastic strains. Stress-strain curve changes linearly until the failure stress point  $\sigma_{t0}$  due to uniaxial tensile of stress-strain curve and these stresses are along with onset and extension of small cracks in concrete. Damage will be visible in form of cracks after passing the mentioned point which is shown in form of softening regime in stress-strain space. Response in uniaxial compressive will be elastic until reaching  $\sigma_{c0}$  yielding point and behavior in plastic zone is generally expressed in form of hardening regime and curves will change to softening curves in the end by reaching the point of ultimate tension  $\sigma_{cu}$  [15].

**4.1.1. Failure Criterion.** William-Warnke failure criterion and Hillborg failure energy model (1976) are used to describe the failure and crack propagation in CDP model. The general

form of William-Warnke failure criterion is in the form of

$$F(I_1, I_2, I_3) = 0, \quad (1)$$

where  $I_1$ ,  $I_2$ , and  $I_3$  are the first, second, and third stress tensor invariants, respectively. This failure surface is a cone-like shape in the stress space. Each form of stress corresponds to one point in stress space. If this point is out of space defined in the above equation, it shows the failure of material [15]. The brittle behavior of concrete in Hillborg failure energy model is more determined by stress-displacement response than by stress-strain response under the tension. Crack failure energy model can be achieved using the expression of tensions after failure as a function of crack's width [15].

In the CDP model used here, values for dilation angle, eccentricity,  $f_{b0}/f_{c0}$  ratio (compression biaxial yield stress to uniaxial yield stress),  $k$  yield level parameter, and viscosity parameter ( $\mu$ ) have been considered to be equal to 40, 0.1, 1.16, 0.6667, and 0.001, respectively.

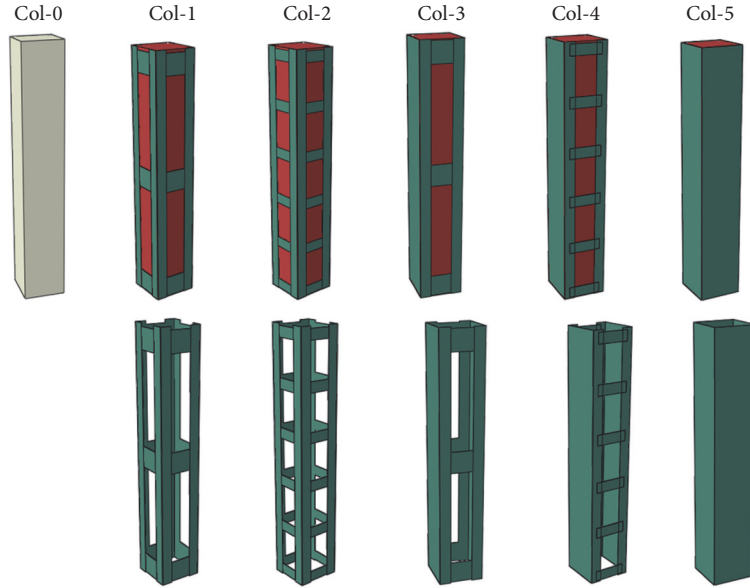


FIGURE 4: Finite element models of studied RC columns.

**4.2. Modeling of Steel Material.** In this study, steel reinforcing bars have been modeled separately and with dimensions similar to those used in real samples. Steel material behavior has been assumed to be linear elastic-perfectly plastic. It should be noted that the behavior of steel has been considered to be isotropic. In all stages, Von-Mises surface model is used here for steel. In this model, yielding has been considered to be isotropic and it has been assumed to be a function of main stresses and when deviatoric stress reaches a critical value in the main stresses space, yielding occurs. This model is defined in the form of the following equation:

$$\Phi = \frac{1}{2} [(\sigma_1 - \sigma_3)^2 + (\sigma_1 - \sigma_2)^2 + (\sigma_2 - \sigma_3)^2] - F_y^2. \quad (2)$$

In this equation,  $\sigma_1$ ,  $\sigma_2$ , and  $\sigma_3$  describe the main stresses and  $F_y$  is the yield stress of material. In fact, the above equation describes a three-dimensional space in which each mode of stress corresponds to one point in the stress space. If this point is out of three-dimensional cylinder defined by the above equation, it shows the yielding of material. At this model, effect of hardening is not considered [15].

**4.3. Concrete and Reinforcement Interaction.** The interaction between concrete and steel reinforcing bars is a very important parameter in modeling of RC structures. This interaction as a factor causes continuity between steel and concrete materials and thus makes it possible to use the whole capacity of materials including concrete compressive strength and tensile strength of steel bars. Embedded element model has been used in this study for modeling of interaction between concrete and steel elements. In this technique, if a node of steel elements is placed in concrete elements, degrees of freedom for that node are removed and node becomes a buried node. Thus, the degrees of freedom for buried node are calculated using the degrees of freedom of concrete elements adjacent to this node. Therefore, degrees of freedom

of each buried node depend on degree of freedom of concrete element node adjacent to it [15].

**4.4. Meshing and Elements.** C3D8R solid element has been used for three-dimensional modeling of concrete. This element is a three-dimensional cube with 8 nodes which uses reduced integration method. T3D2 truss element has been used for modeling of steel bars which is a three-dimensional truss element with 2 nodes. This element has been selected because axial force plays a key role in the analysis of bars and there is no need for elements with several nodes. Thus, volume and time of computation will be significantly reduced. S4R shell element has also been used for modeling of steel jacket which is three-dimensional shell element with 4 nodes and 6 degrees of freedom [15].

Figure 4 shows finite element models of RC columns with different types of steel jacket retrofitting configuration. In the next section, these columns will be evaluated under the effect of blast loading.

**4.5. Loading and Boundary Conditions.** Blast loading applied on columns has been done based on the methodology proposed in UFC 3-340-02 [19]. Determined pressure has been applied to lateral surface of the column. Figure 5 shows pressure-time curve and applied pressure for blast loading of the retrofitted columns model.

## 5. Experimental Program

In the present study, a field test was conducted to investigate the behavior of conventional columns subjected to blast loading. In total, four  $0.35 \text{ m} \times 0.35 \text{ m}$  RC members with the same reinforcement and span length of 3 m were tested under an explosion loading at a standoff distance of 3 m. Blast test was performed on two reinforced concrete columns with initial axial force and two columns without

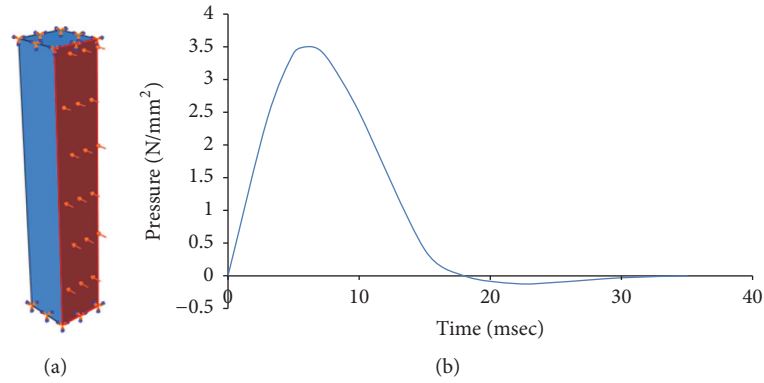


FIGURE 5: Blast pressure-time history (b) and applied blast load (a).

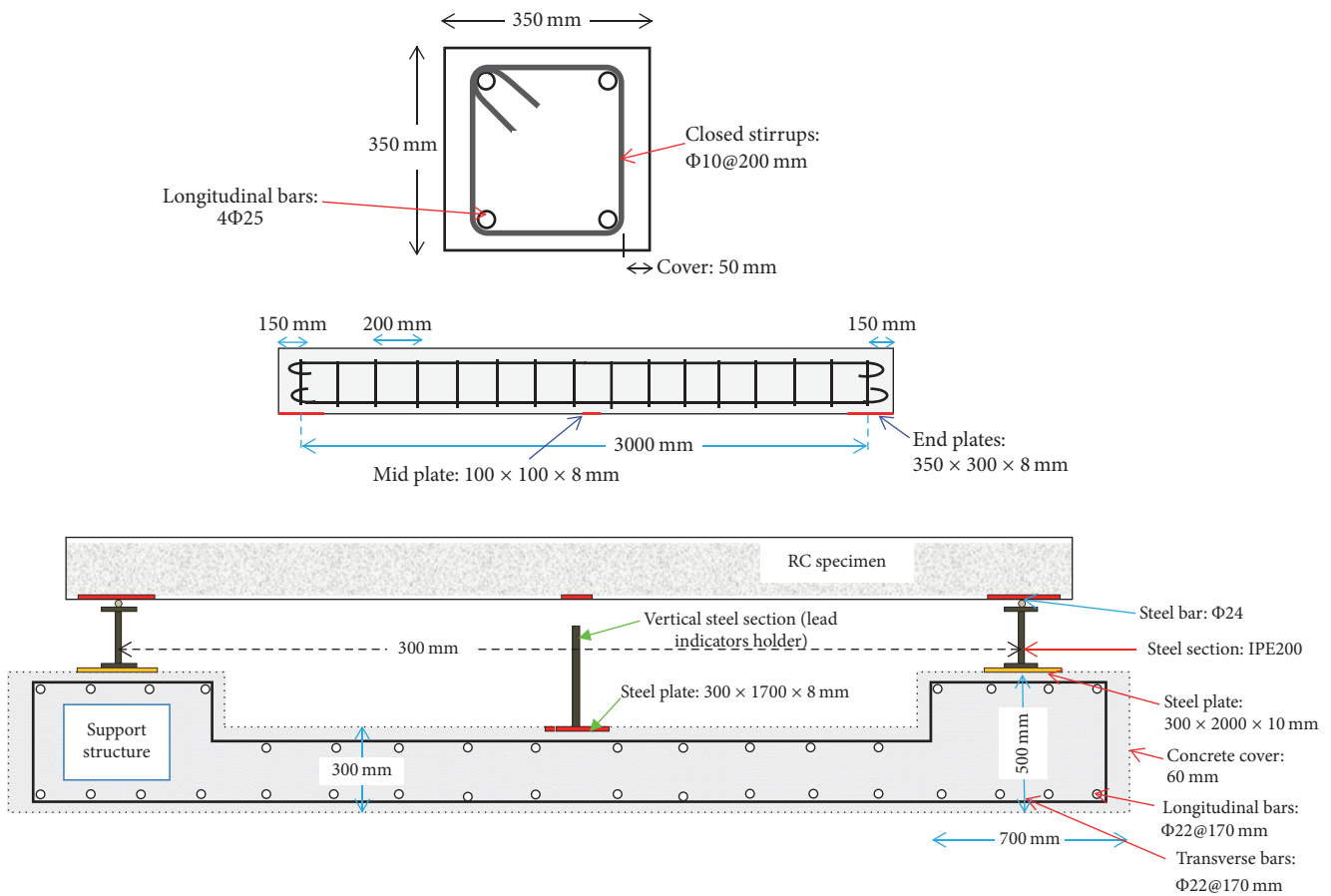


FIGURE 6: Cross section and reinforcement details of the specimen and support condition.

axial force to evaluate their behavior under the same loading conditions. RC components not forming part of the seismic force resisting system were detailed according to ACI 318-14 [25]. The data collected from each specimen included maximum transverse displacement (deflections at center), axial strain of longitudinal bars, and postblast crack patterns. Recorded data from this test were used in order to validate FEM modeling and analysis process. Charge weight including 20 kg of cartridge emulsion explosive with

density of 1.165 g/cm<sup>3</sup> and velocity of detonation of 5800 m/s (27 mm diameter) is used such that TNT equivalent factor is about 0.90 ( $W = 18 \text{ kg-TNT}$ ). Dimensions and reinforcement details of the samples are shown in Figure 6. All the samples were placed horizontally simply on the support structure so that there were pinned support conditions at both ends of the samples. Characteristic compressive strength of the concrete, used for construction of the samples, was determined by laboratory tests and its average value was



FIGURE 7: Test setup for blast loading of the specimen (a) and aerial photos of the explosion event (b).

30 MPa. AIII steel bars with yield strength of 400 MPa and ultimate strength of 600 MPa were used as longitudinal and transverse reinforcement as well as posttensioning system.

In order to impose constant axial compressive load on the samples, 6 posttensioned steel bars were used and each bar had been initially tensioned using click-type torque wrench (Britool Expert HVT7200 (200–810 N·m)). In each case, the bars were anchored to a 50 mm thick steel plate at two ends of the columns. Constant axial stress in each steel bar was 100 kN and there were six posttensioning bars in every column. Hence, there is an axial force of 600 kN in two posttensioned columns (equal to 16% of the static axial load capacity of the column). In Figure 7, the test setup and aerial photos of the explosion event are shown.

Axial strain gauges (FLA-3-350-11, 350  $\Omega$  (Tokyo Sokki Kenkyujo Co. Ltd.)) were installed on the longitudinal bars at half-length of the samples. The data transferred from strain gauges during the blast loading are recorded using digital data acquisition card DAQ- NI USB-6009 (National Instruments Corporation). Lead rods were installed under the samples as maximum displacement indicators at mid length. There were two lead rods under each sample and comparing their length before and after blast loading could show the maximum displacement of the column at mid length. Figure 8 shows the shape of the indicator rods before and after blast loading. Based on the results, average amount of lateral displacement

of the columns with and without axial load under blast loading is 3.5 and 8 mm, respectively.

FE modeling and analysis of the columns were done using the process described in Section 4. For imposing axial load, a rigid part was modeled at one end of the column. Deformed shape and main crack pattern of the column models under blast loading are shown in Figure 9. Maximum transverse displacement of a nod at mid length of the models with and without axial loading is calculated to be 3.04 and 7.23 mm, respectively. These estimations are in a good agreement with experimental test results.

Axial strain curves of the steel bars at mid length of the column resulting from strain gauges in the laboratory specimen are drawn in Figure 10 in comparison with FEM results. The strain curves are for front face (up-side) and back face (beneath) of the columns. It was observed that FE analysis can have an appropriate prediction of strain changes during the blast loading. Some discrepancy of the results could occur probably because of unintended noises during the blast event that can affect recorded data.

In the next step of validation of the FE analysis, maximum blast response of the equivalent single-degree-of-freedom (SDOF) system of the considered RC beam (without axial force) was calculated using UFC-3-340-02 [19] methodology (Chapters 3 and 4). For the charge weight of 18 kg-TNT with standoff distance of 3 m, the scaled distance of the blast loading is  $Z = 1.14 \text{ m/kg}^{1/3}$ . At such scaled distance, one can



FIGURE 8: Lead rods installed under the specimen.

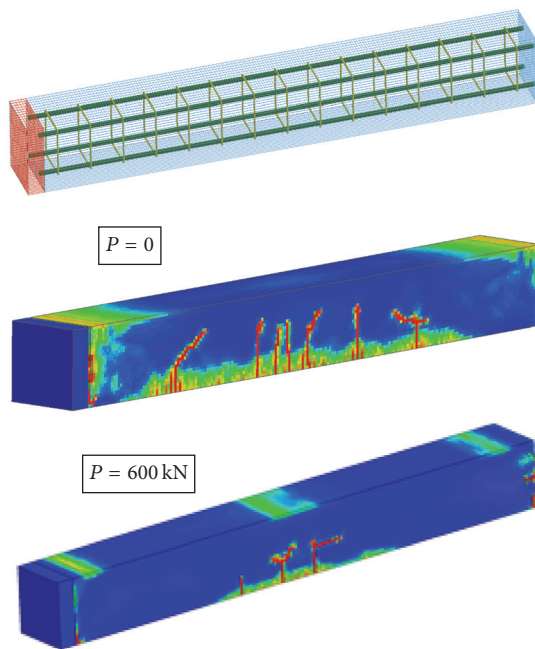


FIGURE 9: FE modeling and analysis of the columns.

assume uniformly pressure distribution on the structural face [19, 21]. Based on empirical equations proposed by UFC 3-340-02 [19], over-peak pressure ( $P_{s0} = 0.72$  MPa) and positive phase duration ( $t_0 = 5.1$  msec) of the blast wave could be estimated. Dynamic Increase Factor (DIF) for RC members in bending for concrete and reinforcement is 1.05 and 1.17, respectively. Using the methodology introduced in UFC-3-340-02, estimated maximum response of elastoplastic SDOF system under ideal bilinear-triangular pulse is  $X_m = 9.18$  mm. Experimental result of maximum transverse displacement of the specimen without axial load was about 8 mm. It should be noted that generally this method produces a conservative estimate of the blast response of the structure for design purpose [19].

Selected sample for validation axial loading process in FE software is a real column which has been considered as 0C0 in

[17] by Hadi and Widiarsa (2012). Geometric characteristics and reinforcing details in this sample are very similar to our own sample. Specifications of this model and its axial test process are shown in Figure 11. Compressive strength of concrete in this sample is equal to 79.5 MPa and yield strength of longitudinal and transverse reinforcement is 564 and 516, respectively [17].

Sample 0C0 is tested under static axial loading and axial load-displacement diagram is drawn for it. Axial load-displacement curves obtained from the experiments are shown in Figure 12(a) [17] in which dashed curve (---) is related to 0C0 sample column. Diagrams obtained from FE modeling and experimental testing have been drawn together for better comparison in Figure 12(b). It is evident from Figure 12 that the result of FEM here matches with the experimental results with a good accuracy. Thus, finite element method in this research can be used to continue analysis.

## 6. Results of Analysis under Blast Loading

Curves in Figure 13 show the results of shear strength-lateral displacement (at the middle height) of the columns. It is evident from Figure 13 that the Col-0 which has not been retrofitted has the lowest shear strength compared to other columns. In this model, the shear strength initially reaches the maximum amount of 300 kN and then slightly increases with slight ups and downs. The initial resistance is greater in other columns compared to Col-0 column. Moreover, the greatest displacement of column's mid height corresponds to unretrofitted column.

Curves in Figure 14 show horizontal displacement history at the columns mid height. For better understanding of the details, results are shown once without Col-0 curve. It is clear that Col-0 has the highest lateral deformation. In addition, the lowest horizontal displacement in the middle height of the columns is observed for Col-3 and Col-4 (maximum amount of about 4 mm). These columns have been strengthened by two steel channels and have shown a high resistance against lateral blast loading. Moreover, Col-5 which is completely covered with steel plates has shown a low deformation (maximum 10 mm). Afterwards, there is Col-2 and Col-1 that

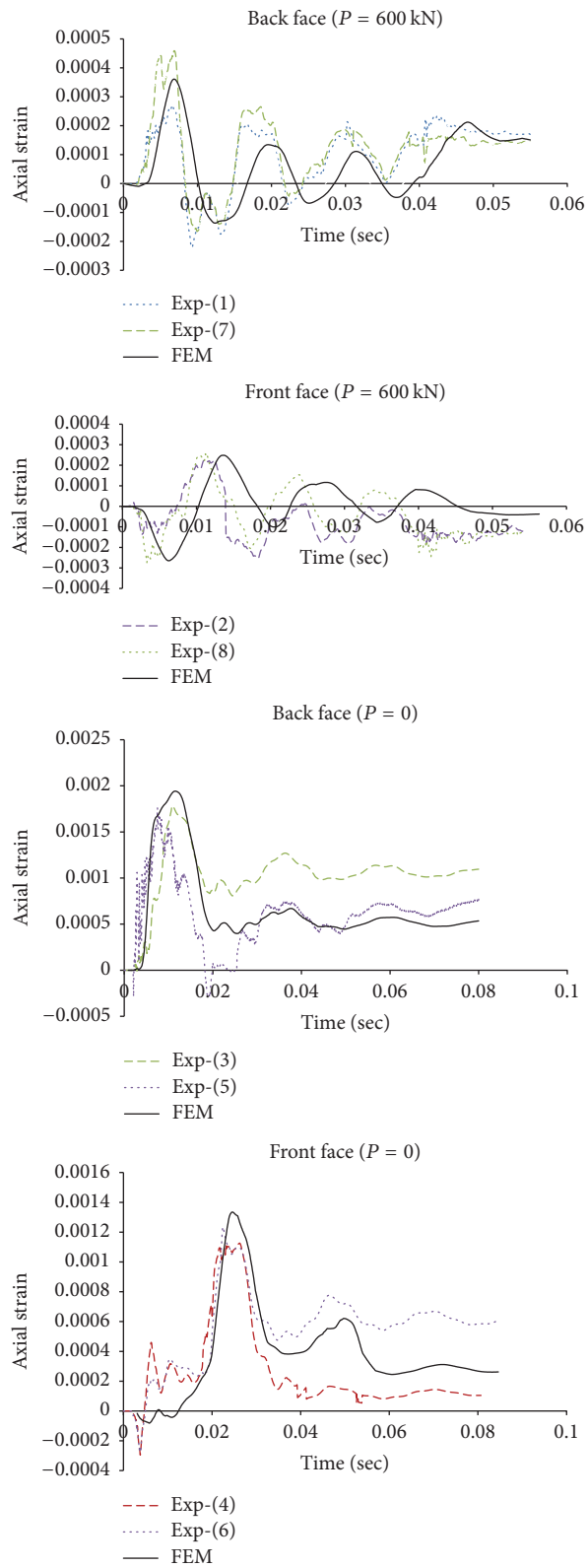


FIGURE 10: Axial strain-time curves for the longitudinal reinforcement resulting from experimental test and FEM.

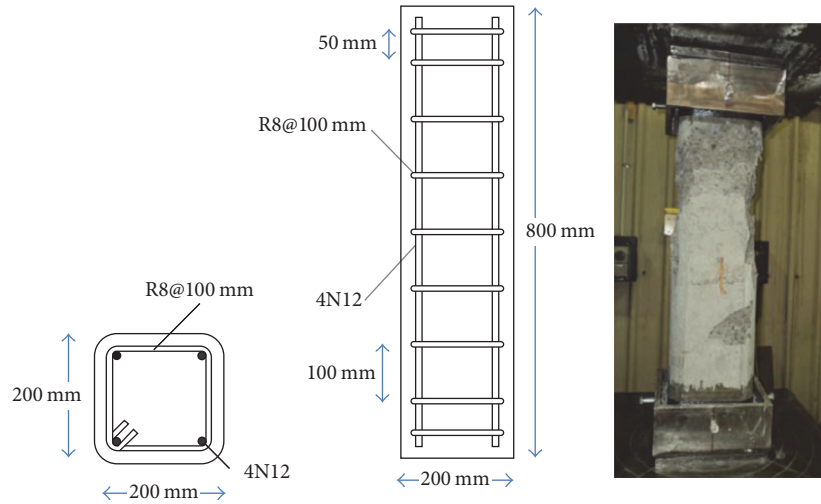


FIGURE 11: Column sample selected for validation [17].

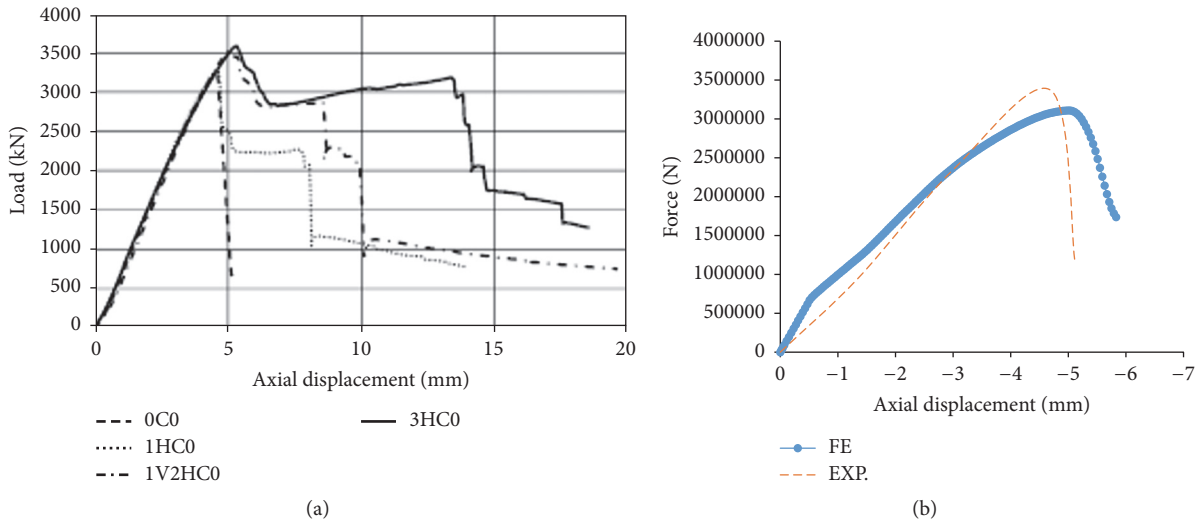


FIGURE 12: Result of finite element analysis (b) and experimental results [17] (a).

have four steel angles and their maximum displacement is about 16 and 23 mm, respectively.

Based on Figure 14(a), failure mode of RC column without retrofitting (Col-0) is brittle and the column's lateral displacement increases dramatically. However, all strengthened RC columns with steel jackets have more ductile behavior. Belal et al. (2015) demonstrated that specimen strengthened with angles or channel sections (Col-1, 2, 3, and 4) recorded a higher axial strength than that strengthened with plates (Col-5). Moreover, strengthening strategy of Col-4 and Col-1 is more effective than the other methods [16]. Here, we showed that Col-3 and Col-4 have the highest blast capacity than the other columns.

Deformations of reinforcing bars for three column models are shown in Figure 15 for better understanding of the condition of these columns under the effect of blast loading. Figures 15(a) shows the ultimate moments for Col-0 (without retrofitting) under blast loading. Also, Figures 15(b) and

15(c) show the condition of steel bars in Col-3 and Col-5, respectively. It is clear that steel reinforcement in Col-3 does not have considerable deformations and this leads to high resistance of column under the blast loading. On the other hand, there are some plastic deformations in bar grids in Col-5.

Figures 16–21 show the graphical stress contours for 6 columns. Figure 16 shows bending stress in the column without retrofitting (Col-0). Failure conditions can be clearly observed in this figure. In Figures 17–21, bending stress contours (left) and Von-Mises stress in steel jackets (middle) and in the column itself (right) have been shown for 5 retrofitted columns. It is clear that Col-1 (with 3 connecting plates) has a lower resistance and has deformed greater than Col-2 (with 6 connecting plates). Given the fact that columns are fixed at both ends, upper and lower parts of the columns have more critical conditions. Other critical conditions have occurred in connecting plates in

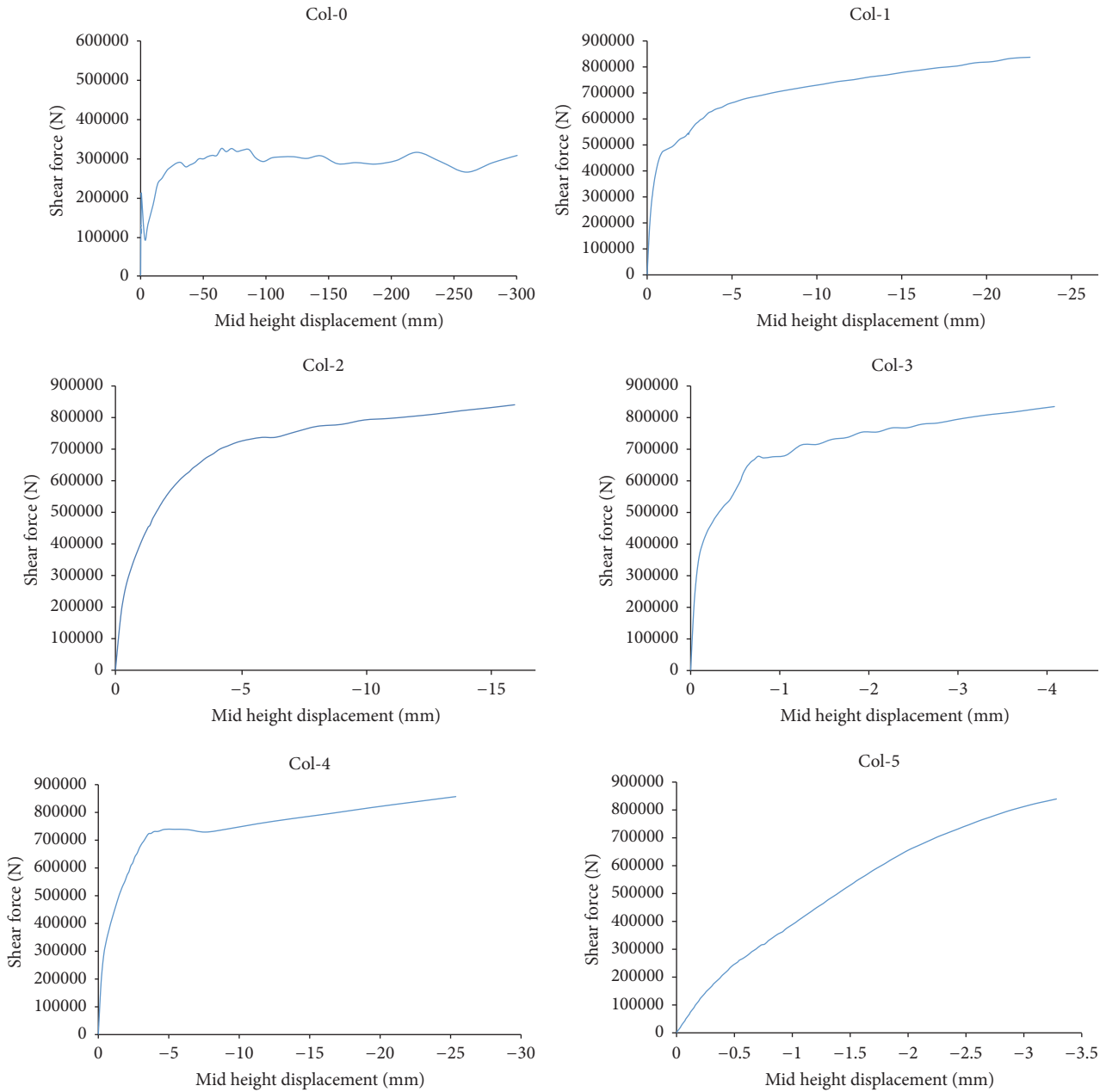


FIGURE 13: Results of shear strength of columns.

columns with perforated retrofitting. For instance, the middle plate in Col-2 and Col-3 has experienced less von-Mises stress, while other two plates have critical state of stress.

### 7. Residual Axial Strength

Axial capacity of columns before and after blast loading can define residual axial strength of the column. Residual axial strength is a very important parameter for estimating the overall behavior and progressive collapse of the buildings under the blast loads. Given that residual axial strength is independent of the mode of behavior of the structure, it could be the best criterion for defining damage level of

the columns after blast loading [3, 10, 26]. In this paper, after analysis of FE models under lateral blast loading, a compressive uniform axial pressure was applied on one end of the column and failure of the column, ultimate axial load, and its deformation were investigated. In Table 3,  $P_{u0}$  axial strength of undamaged RC column (before blast loading) and  $P_{u1}$  axial strength of damaged column are summarized. Here, axial strength is assumed to be an axial load level in which by 1% increase in load, displacement increases more than 10%.

According to Table 3, Col-4 and Col-1 undamaged column models have the highest axial capacity. Then, there are Col-2 and Col-3 and the lowest undamaged axial capacity is observed in Col-5 model. After applying blast load, Col-0,

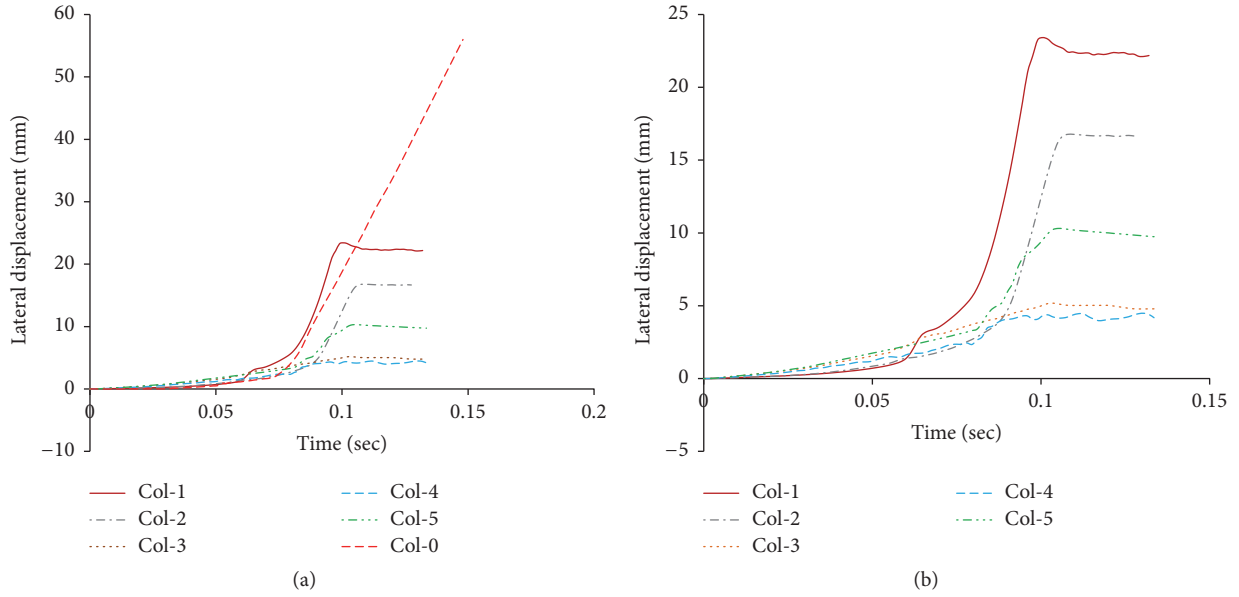


FIGURE 14: Lateral displacement of column's middle height.

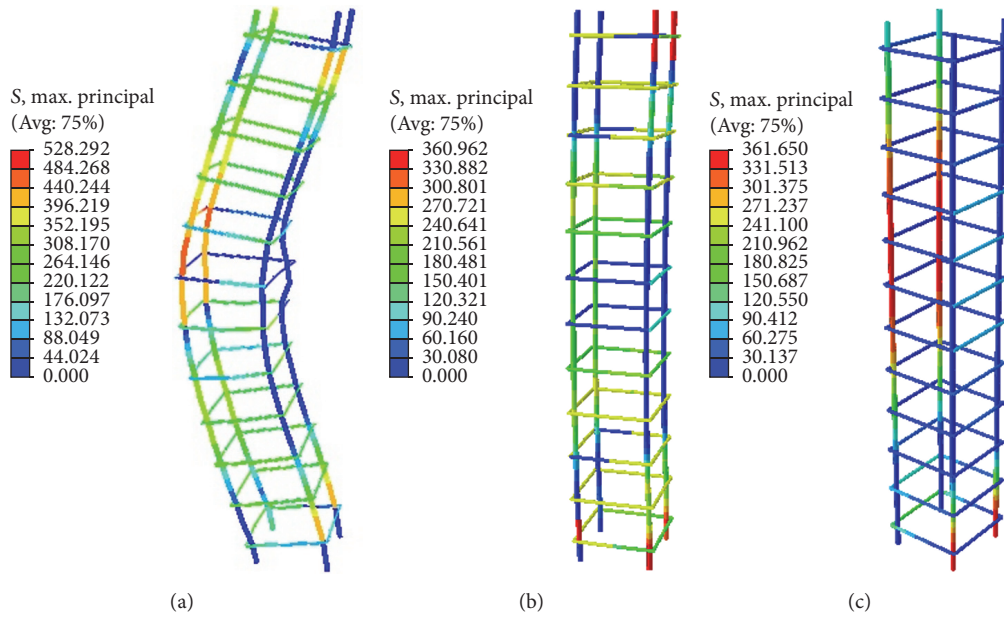


FIGURE 15: Deformations of steel bars in (a) Col-0, (b) Col-3, and (c) Col-5.

TABLE 3: Failure loads of the columns.

Model	$P_{u0}$ (kN)	$P_{u1}$ (kN)	$P_{u1}/P_{u0}$
Col-0	1231	—	—
Col-1	1897	380	0.2
Col-2	1684	791	0.47
Col-3	1627	1506	0.92
Col-4	1873	1762	0.94
Col-5	1524	990	0.65

which is unstrengthened, has lost its whole capacity. The least decrease in axial capacity was observed for Col-4 and Col-3 (6

and 8%, resp.). Axial strength of Col-1 and Col-2 has intensely decreased (80 and 53%, resp.). Buckling of the steel angles could be the reason for this phenomenon.

In Figure 22, deformation shapes of the blast damaged columns under axial load, near the failure state, are shown. According to Figure 22, failure mode in Col-1, 2, 3, 4, and 5 is close to the column's head. However, in Col-0 (without retrofitting), failure occurs through the whole height of the column.

In Figure 23, axial load-displacement curves, after and before blast loading, are drawn. According to Figure 23, residual axial strengths for Col-1 and Col-2 are  $P_{u1} = 380$  and 791 kN and corresponding axial displacements are

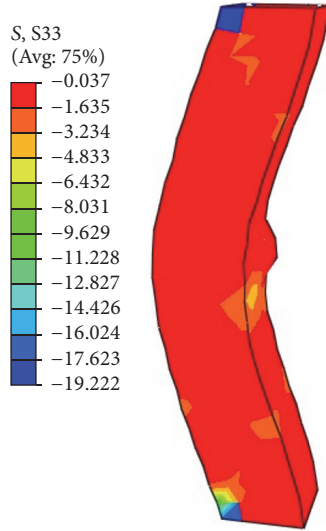


FIGURE 16: Bending stress in Col-0.

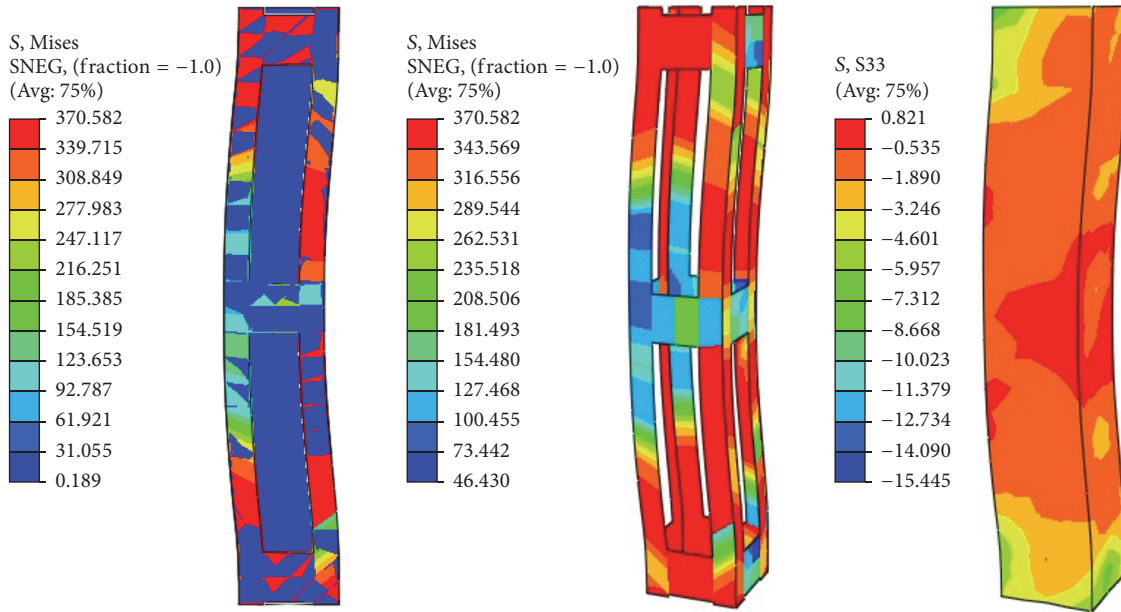


FIGURE 17: Stress contours in Col-1.

$\delta_{u1} = 3.2$  and  $4.79$  mm, respectively. It should be noted that deformation of Col-1 is increasing rapidly. In contrast, these values for the undamaged models are  $P_{u0} = 1897$  kN,  $\delta_{u0} = 1.18$  mm and  $P_{u0} = 1684$  kN,  $\delta_{u0} = 2.04$  mm, respectively. Hence, dramatic decrease in axial capacity and increase in deformation in Col-1 and Col-2 are obvious. In Col-3 and Col-4, which are strengthened by steel channels, maximum axial loads and corresponding deformations, after blast loading, are  $P_{u1} = 1506$  kN,  $\delta_{u1} = 2.01$  mm and  $P_{u1} = 1762$  kN,  $\delta_{u1} = 1.27$  mm, respectively. For undamaged column models Col-3 and Col-4, maximum axial loads and corresponding deformations are  $P_{u0} = 1627$  kN,  $\delta_{u0} = 1.84$  mm and  $P_{u0} = 1873$  kN,  $\delta_{u0} = 1.37$  mm, respectively. For Col-5, the difference between the axial capacity and corresponding displacement,

before and after blast loading, is more than Col-3 and Col-4 models ( $P_{u1} = 990$  kN,  $\delta_{u1} = 3.65$  mm and  $P_{u0} = 1524$  kN,  $\delta_{u0} = 2.11$  mm).

### 8. Conclusion

In this study, the performance of simple and steel jacket strengthened reinforced concrete columns has been evaluated under the effect of blast transverse loading. It should be noted that all of the strengthening configurations originally are used for enhancing the axial capacity of RC columns under pure axial loading. Here, the effectiveness of those strengthening methods on explosion capacity of the RC columns was investigated. Finite element method (FEM) was

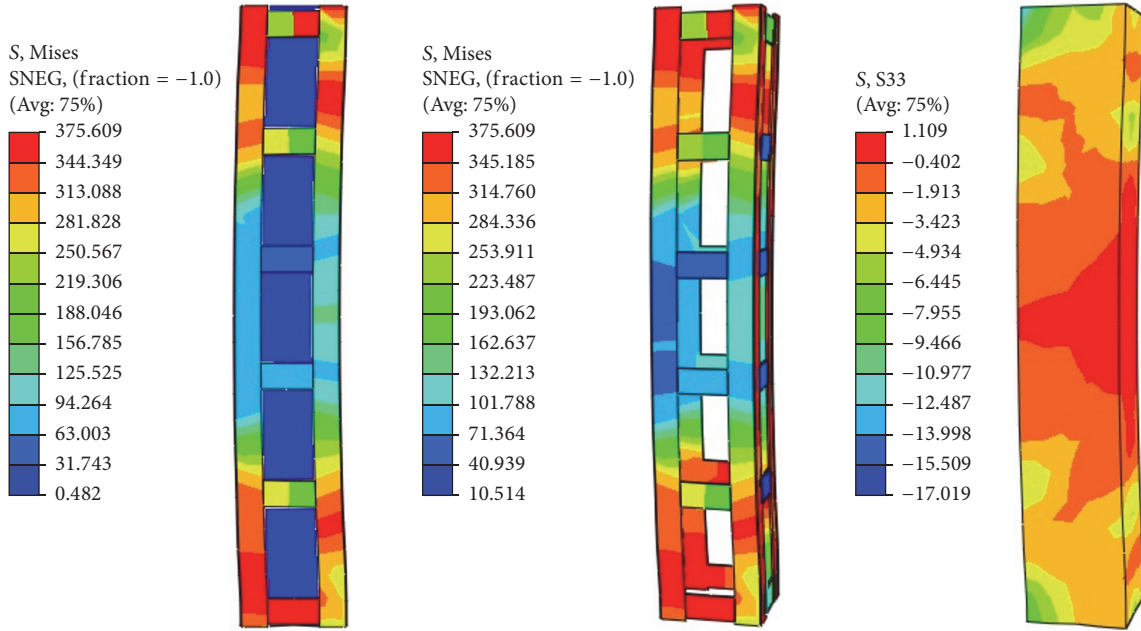


FIGURE 18: Stress contours in Col-2.

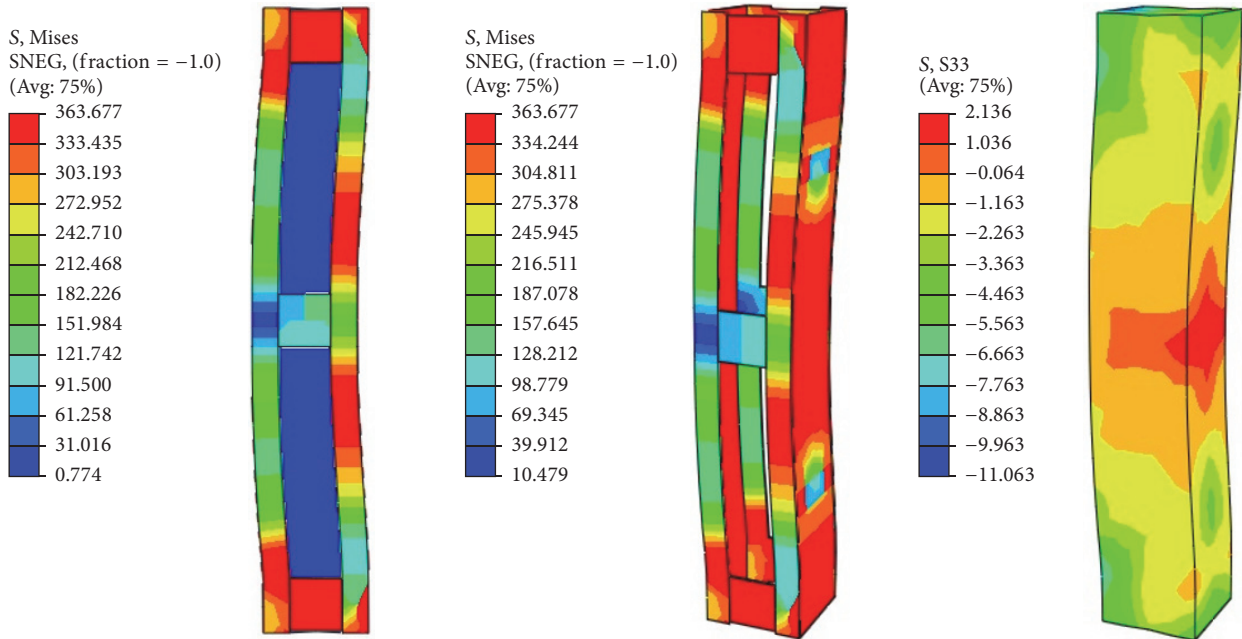


FIGURE 19: Stress contours in Col-3.

presented for analysis of models using ABAQUS software package. A real scale blast loading test was done by the authors and its results are used for validating FE modeling and analysis process. The test included four RC members with the same geometry and reinforcement details where two samples have initial axial force and two other samples have no axial force. FE modeling of the samples under blast loading showed a good agreement with experimental observations. Afterward, FE modeling process was used for analysis of steel jacket retrofitted columns under lateral blast

loading and postblast condition. According to the obtained results, simple column without retrofitting has much less blast resistance compared to retrofitted columns. Thus, retrofitting columns with steel jacket can greatly improve the resistance of columns against explosion loads and extremely enhance residual axial capacity of the RC columns after blast loading.

Retrofitting method with steel channels and connecting plates (Col-4) can be used as an effective way to simultaneously enhance axial and lateral blast resistance of the RC

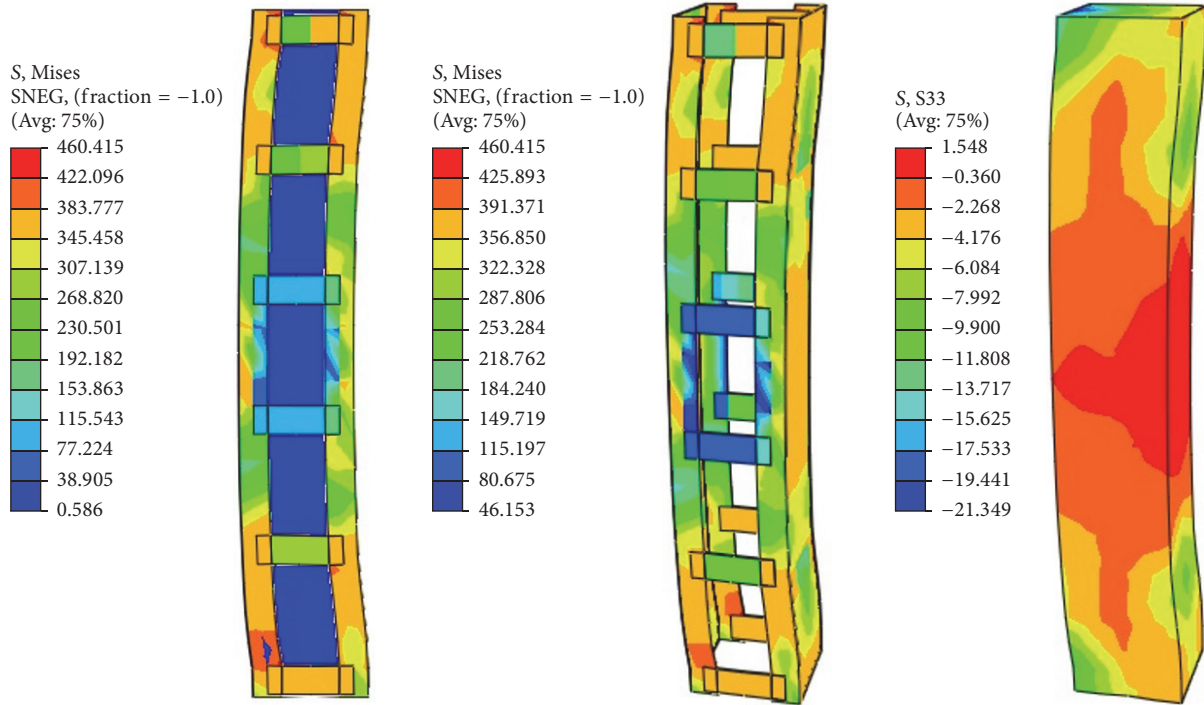


FIGURE 20: Stress contours in Col-4.

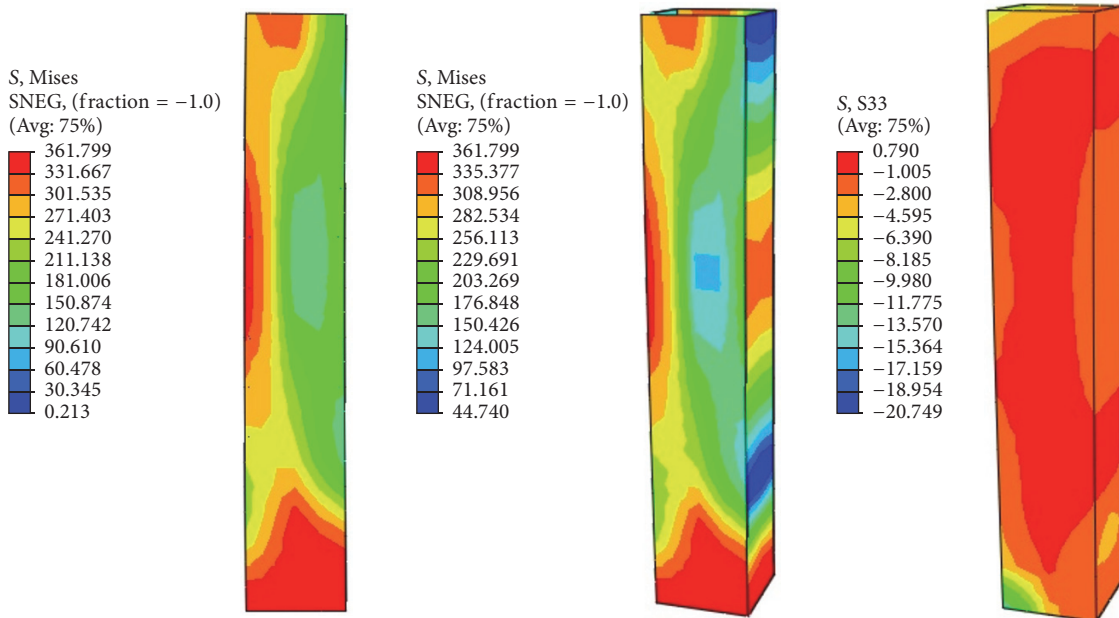


FIGURE 21: Stress contours in Col-5.

columns. Although strengthening with steel angles (Col-1 and Col-2) has enhancing effects on axial capacity, they are the least effective ways for enhancing blast resistance of the columns. Hence, we can say that deformations of the RC columns under blast loading have the lowest level

in retrofitting with steel channel sections compared to steel angles. This fact leads to higher residual strength capacity of the columns strengthened with steel channel sections. However, buckling of the angles under axial load decreases the axial strength of the column. Given the fact that both

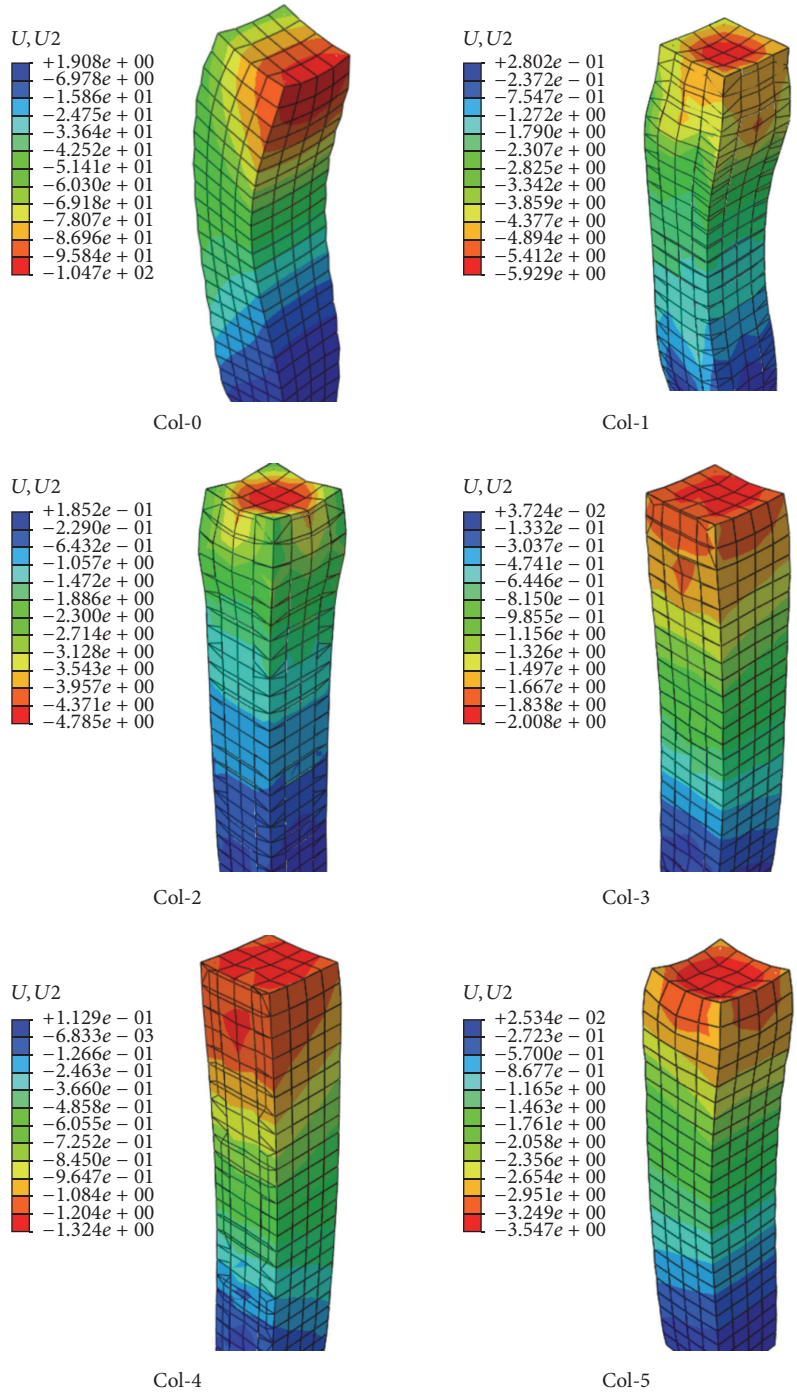


FIGURE 22: Deformation of damaged columns at failure load.

ends of columns have been assumed to be clamped, the most critical points are located in those areas under blast loading. This critical condition was observed in Col-1 (strengthening with steel angles) and Col-3 (strengthening with steel channels) which have 3 connecting plates in two upper and lower plates.

Generally, it can be said that the results obtained from FEM have been very useful and can have acceptable

precision in comparison with experimental test data. Possible differences between finite element analysis results and experimental observations are due to laboratory errors and equipment failure under blast pressure, assumptions of homogeneity of materials, lack of accurate estimation of explosion loads on the structures, and the difference between the actual mechanism of interaction between steel reinforcing bars and concrete. In general, retrofitting with the steel jackets

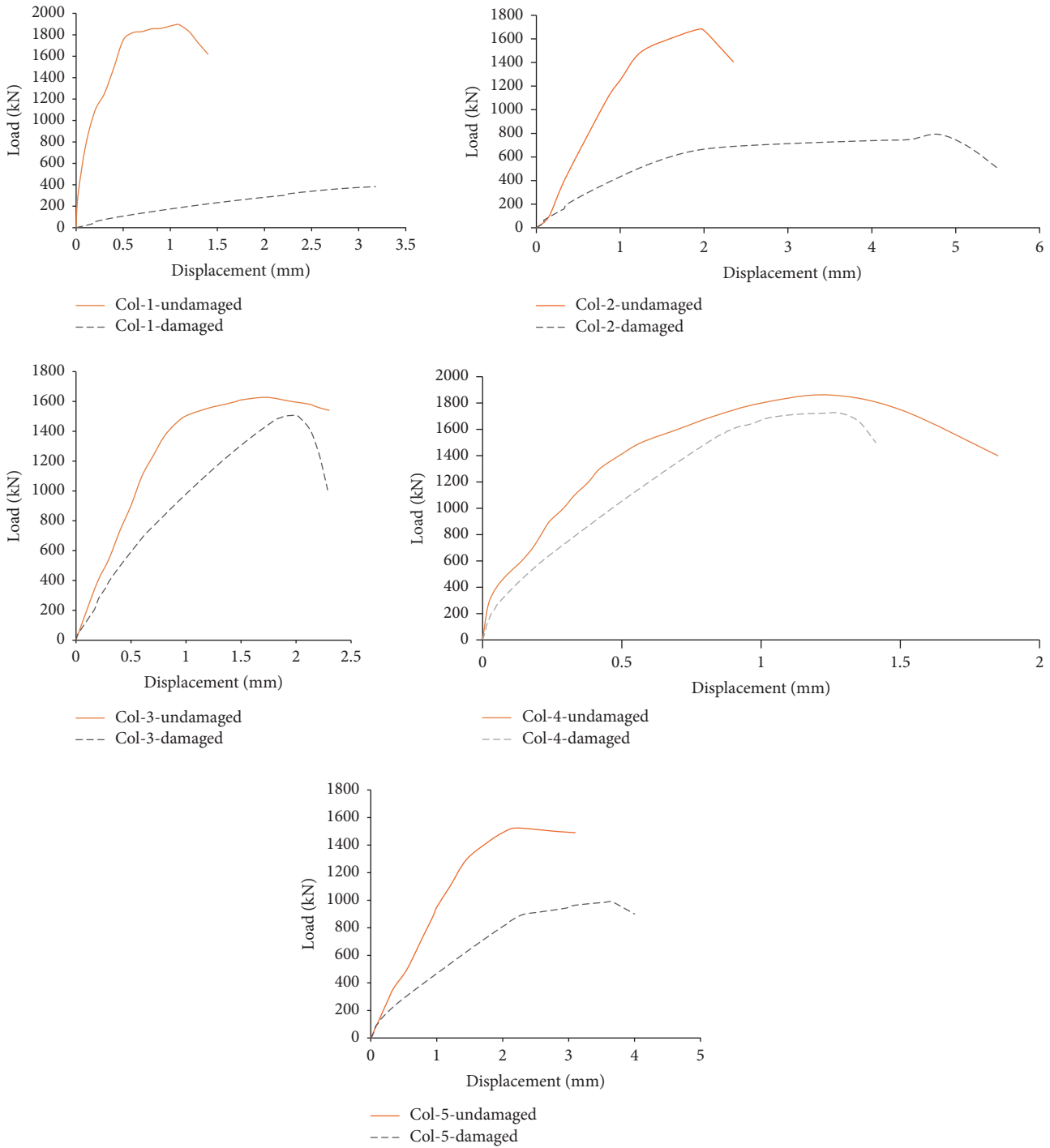


FIGURE 23: Axial load-displacement curves for the columns before and after blast loading.

would cause a large improvement in the performance of RC columns under the blast loading and their residual axial capacity after blast event.

**Conflicts of Interest**

The authors declare that there are no conflicts of interest regarding the publication of this paper.

**References**

- [1] P. W. Cooper, *Explosives Engineering*, Wiley-VCH Inc., New York, NY, USA, 1996.
- [2] B. Hopkinson, *British Ordnance Minutes; Report No. 13563*, British Ordnance Office, 1915.
- [3] X. Bao and B. Li, "Residual strength of blast damaged reinforced concrete columns," *International Journal of Impact Engineering*, vol. 37, no. 3, pp. 295–308, 2010.

- [4] T. Rodriguez-Nikl, C.-S. Lee, G. A. Hegemier, and F. Seible, "Experimental performance of concrete columns with composite jackets under blast loading," *Journal of Structural Engineering (United States)*, vol. 138, no. 1, pp. 81–89, 2012.
- [5] K. Fujikake and P. Aemlaor, "Damage of reinforced concrete columns under demolition blasting," *Engineering Structures*, vol. 55, pp. 116–125, 2013.
- [6] J. E. Crawford, "State of the art for enhancing the blast resistance of reinforced concrete columns with fiber-reinforced plastic," *Canadian Journal of Civil Engineering*, vol. 40, no. 11, pp. 1023–1033, 2013.
- [7] J. I. Siddiqui and S. Ahmad, "Impulsive loading on a concrete structure," *Proceedings of the Institution of Civil Engineers: Structures and Buildings*, vol. 160, no. 4, pp. 231–241, 2007.
- [8] Y. Shi, H. Hao, and Z. Li, "Numerical derivation of pressure-impulse diagrams for prediction of RC column damage to blast loads," *International Journal of Impact Engineering*, vol. 35, no. 11, pp. 1213–1227, 2008.
- [9] K.-C. Wu, B. Li, and K.-C. Tsai, "The effects of explosive mass ratio on residual compressive capacity of contact blast damaged composite columns," *Journal of Constructional Steel Research*, vol. 67, no. 4, pp. 602–612, 2011.
- [10] M. Arlery, A. Rouquand, and S. Chhim, "Numerical dynamic simulations for the prediction of damage and loss of capacity of RC column subjected to contact detonations," in *Proceedings of the 8th International Conference on Fracture Mechanics of Concrete and Concrete Structures, FraMCoS 2013*, pp. 1625–1634, Toledo, Spain, March 2013.
- [11] C. Kyei and A. Braimah, "Effects of transverse reinforcement spacing on the response of reinforced concrete columns subjected to blast loading," *Engineering Structures*, vol. 142, pp. 148–164, 2017.
- [12] M. Carriere, P. J. Heffernan, R. G. Wight, and A. Braimah, "Behaviour of steel reinforced polymer (SRP) strengthened RC members under blast load," *Canadian Journal of Civil Engineering*, vol. 36, no. 8, pp. 1356–1365, 2009.
- [13] J. Xu, C. Wu, H. Xiang et al., "Behaviour of ultra high performance fibre reinforced concrete columns subjected to blast loading," *Engineering Structures*, vol. 118, pp. 97–107, 2016.
- [14] F. Zhang, C. Wu, X.-L. Zhao, A. Heidarpour, and Z. Li, "Experimental and numerical study of blast resistance of square CFDST columns with steel-fibre reinforced concrete," *Engineering Structures*, 2016.
- [15] "Abaqus 6.13 documentation," 2013, [https://things.maths.cam.ac.uk/computing/software/abaqus\\_docs/docs/v6.12/books/usb/default.htm](https://things.maths.cam.ac.uk/computing/software/abaqus_docs/docs/v6.12/books/usb/default.htm).
- [16] M. F. Belal, H. M. Mohamed, and S. A. Morad, "Behavior of reinforced concrete columns strengthened by steel jacket," *HBRC Journal*, vol. 11, no. 2, pp. 201–212, 2015.
- [17] M. N. S. Hadi and I. B. R. Widiarsa, "Axial and flexural performance of square RC columns wrapped with CFRP under eccentric loading," *Journal of Composites for Construction*, vol. 16, no. 6, pp. 640–649, 2012.
- [18] FEMA (Federal Emergency Management Association), *Designer's Notebook—Blast Consideration*, FEMA Press, 2006.
- [19] US Department of Defense (DOD), *Structures to Resist the Effects of Accidental Explosions. UFC 3-340-02*, Wash, USA, 2008.
- [20] J. A. Zukas and W. P. Walters, *Explosive Effect and Applications*, Springer, New York, NY, USA, 2002.
- [21] "The Design of Structures to Resist the Effects of Accidental Explosions," US Department of Army, Navy and Air Force TM 5-1300, Wash, USA, 1990.
- [22] J. Lubliner, J. Oliver, S. Oller, and E. Oñate, "A plastic-damage model for concrete," *International Journal of Solids and Structures*, vol. 25, no. 3, pp. 299–326, 1989.
- [23] J. Lee and G. L. Fenves, "Plastic-damage model for cyclic loading of concrete structures," *Journal of Engineering Mechanics*, vol. 124, no. 8, pp. 892–900, 1998.
- [24] T. Yu, J. G. Teng, Y. L. Wong, and S. L. Dong, "Finite element modeling of confined concrete-II: Plastic-damage model," *Engineering Structures*, vol. 32, no. 3, pp. 680–691, 2010.
- [25] ACI Committee, *Building Code Requirements for Structural Concrete and Commentary (ACI 318-14)*, American Concrete Institute, Farmington Hills, Mich, USA, 2014.
- [26] K. Wu, B. Li, and K. Tsai, "Residual axial compression capacity of localized blast-damaged RC columns," *International Journal of Impact Engineering*, vol. 38, no. 1, pp. 29–40, 2011.

## Research Article

# Dynamic Response Analysis of Cable of Submerged Floating Tunnel under Hydrodynamic Force and Earthquake

**Zhiwen Wu and Guoxiong Mei**

*Key Laboratory of Disaster Prevention and Structural Safety of Ministry of Education,  
Guangxi Key Laboratory of Disaster Prevention and Structural Safety, College of Civil Engineering and Architecture,  
Guangxi University, Nanning 530004, China*

Correspondence should be addressed to Guoxiong Mei; meiguox@163.com

Received 21 June 2017; Accepted 28 August 2017; Published 9 October 2017

Academic Editor: Hugo Rodrigues

Copyright © 2017 Zhiwen Wu and Guoxiong Mei. This is an open access article distributed under the Creative Commons Attribution License, which permits unrestricted use, distribution, and reproduction in any medium, provided the original work is properly cited.

A simplified analysis model of cable for submerged floating tunnel subjected to parametrically excited vibrations in the ocean environment is proposed in this investigation. The equation of motion of the cable is obtained by a mathematical method utilizing the Euler beam theory and the Galerkin method. The hydrodynamic force induced by earthquake excitations is formulated to simulate real seaquake conditions. The random earthquake excitation in the time domain is formulated by the stochastic phase spectrum method. An analytical model for analyzing the cable for submerged floating tunnel subjected to combined hydrodynamic forces and earthquake excitations is then developed. The sensitivity of key parameters including the hydrodynamic, earthquake, and structural parameters on the dynamic response of the cable is investigated and discussed. The present model enables a preliminary examination of the hydrodynamic and seismic behavior of cable for submerged floating tunnel and can provide valuable recommendations for use in design and operation of anchor systems for submerged floating tunnel.

## 1. Introduction

Submerged floating tunnel is an innovative underwater transportation system to avoid water traffic and weather at a depth of usually 20–50 m. The tunnel floats in water and its position is restrained at a certain distance from the sea bed by means of suitable anchoring systems, such as cables or bars. Cables for submerged floating tunnel are lightweight, very flexible, and lightly damped, the features of which make them particularly prone to vibration. Frequent vibration may lead to fatigue damage of cable, where fatigue cracks could be formed on the cable surface to destroy the anticorrosion system. Eventually the bearing capacity of cable will be lost completely with the propagation of fatigue cracks. The cable for submerged floating tunnel experiences complex dynamic forces under various ocean conditions, which is the key to the safe operation.

Many attentions have been received to the vibration of submerged floating tunnel cables. Sun et al. [1] analyzed the

nonlinear response of cables subjected to parametric excitations. Sun and Su [2] investigated the parametric vibration of submerged floating tunnel cable under random excitations. Lu et al. [3] studied the slack phenomenon and the snap force in the cable for submerged floating tunnels under wave conditions. Seo et al. [4] conducted a series of simplified analyses to estimate the behavior of submerged floating tunnel cables in waves and compared their calculations with experimental measurements. Cifuentes et al. [5] implemented a numerical model to analyze the coupled dynamic response of a submerged floating tunnel with mooring lines in regular waves.

It is noted by Duan et al. [6] that 85% of the total amount of earthquakes occurs in the ocean. The Bohai Strait, the Qiongzhou Strait, and the Taiwan Strait in China are three potential areas to build submerged floating tunnels, which are also in the Circum-Pacific seismic belt. Hence, the performance of subsea cables in seismic zones becomes one of the significant academic and engineering attractions

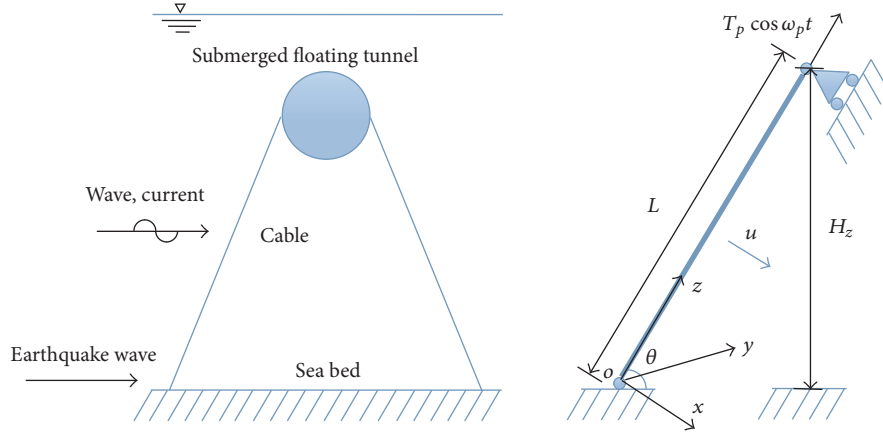


FIGURE 1: Definition sketch of the submerged floating tunnel model and its cable coordinate system.

in offshore engineering. In addition, the effect of seaquake is much more complex, which can induce hydrodynamic pressures acting on the cable [7, 8]. The combined fluid and seismic motion induced by ocean hydrodynamic forces must be considered rigorously in the analysis of cables for submerged floating tunnel during earthquakes. Therefore, it is of significance to evaluate how parametrically excited vibrations influence the behavior of cable for submerged floating tunnel under combined hydrodynamic force and earthquake.

Although earthquakes have significant effect on the performance of cables for submerged floating tunnel, few studies have been reported to assess the seismic response of cables except those from [9–11]. In these previous studies, the effects of earthquake on the development of hydrodynamic force were usually neglected, and the seismic design spectrum was taken from design guidelines for buildings (e.g., the Chinese code for seismic design of buildings (GB 50011-2010) [12] directly). However, the seismic design spectrum for buildings is not always suitable for marine structures, the distinctiveness of marine site classifications of offshore structures in marine environment cannot be considered, and the correctness of this approach becomes questionable.

The present study aims to establish a mathematical method to explore the dynamic response of cable for submerged floating tunnel under simultaneous hydrodynamic forces and earthquake excitations. A simplified analysis model to estimate the behavior of cable for submerged floating tunnel under the ocean environmental excitation is proposed. The equation of motion of the cable is obtained by a mathematical method utilizing the Euler beam theory and the Galerkin method. The hydrodynamic force induced by earthquake excitations is formulated to simulate real seaquake conditions. The random earthquake force in the time domain is calculated by the stochastic phase spectrum method. An analytical model for analyzing the cable for submerged floating tunnel subjected to combined hydrodynamic forces and earthquake excitations is then developed. The sensitivity of key parameters including the hydrodynamic, earthquake,

and structural parameters on the dynamic response of the cable is investigated and discussed.

## 2. Method

**2.1. Equation of Motion for the Cable.** Following previous studies [1, 3, 11, 13], a simplified analysis model is proposed to evaluate the motion of cables for submerged floating tunnel subjected to ocean environmental excitations. For simplification, the cable for submerged floating tunnel is modeled as a Bernoulli-Euler beam, which only allows the in-plane motion of the cable. Furthermore, a conservative assumption is adopted that the response of the cable under combined effects of hydrodynamic forces and earthquake excitations is maximized when the two actions are in the same direction. A submerged floating tunnel and the direction of earthquake wave and wave/current force are schematically shown in Figure 1, where the cable is allowed to move only in the in-line direction. It should be emphasized that the horizontal earthquake excitation is acting on the anchoring point of the cable.

Figure 1 shows the schematic illustration of a submerged floating tunnel and cable. In this simplified analysis model, the three-dimensional behavior is not taken into consideration. Although this assumption simplifies the physical phenomenon, the two-dimensional model enables a preliminary examination of the hydrodynamic and seismic behavior of cables. The origin of the coordinate system is set at the anchored point of the cable on the sea bed. The parameter  $L$  is the undeformed length of the cable,  $H_z$  shows the vertical height above the sea bed,  $u$  represents the dynamic displacement at the mid-span of the cable, and  $\theta$  denotes the inclination angle of the cable with respect to the sea bed.

The effect of the tunnel tube on the cable is simplified as a parametric excitation  $T_p \cos \omega_p t$ , and the ends of the cable are hinged [2, 14], where  $T_p$  is the dynamic tension acting on the cable induced by the motion of the tube, and  $\omega_p$  is the parametric excitation frequency. For simplicity, the initial tension, geometry, stiffness, and material property of the cable are assumed to be constant along the cable length.

Thus, the governing equation of the motion of the cable can be written as [2, 3, 11, 13]

$$E_{\text{eq}} I \frac{\partial^4 u(z, t)}{\partial z^4} - \frac{\partial}{\partial z} (T_0 + T_p \cos \omega_p t) \frac{\partial u(z, t)}{\partial z} + m \frac{\partial^2 u(z, t)}{\partial t^2} + C_s \frac{\partial u(z, t)}{\partial t} = F_L - F_D - Q_s \sin \theta, \quad (1)$$

where  $u(z, t)$  is the dynamics lateral displacement of cable,  $T_0$ ,  $m$ ,  $E_{\text{eq}}$ , and  $I$  are the initial tension, mass per unit length, the equivalent modulus of elasticity, and the cross-sectional moment of inertia of the cable, respectively,  $C_s$  is the viscous damping coefficient,  $F_L$  is the vortex-induced lift force,  $F_D$  is the acting drag force applied by water per unit length when the cable oscillates, and  $Q_s$  is the earthquake excitation force.

While considering the cable sag effect, the equivalent elastic modulus of cable can be obtained by the following equivalent method [11]:

$$E_{\text{eq}} = \frac{E}{(1 + E/E_f)}, \quad E_f = \frac{12\sigma^3}{[\gamma_1^2 (L \cos \theta)^2]}, \quad \sigma = \frac{T_0}{A_c}, \quad (2)$$

where  $E$  is the modulus of elasticity of cable,  $E_f$  is the modulus of elasticity induced by sag of cable,  $\gamma_1$  is the buoyant unit weight of the cable,  $\sigma$  is the stress of cable, and  $A_c$  is the cross-sectional area of cable.

**2.2. Earthquake Excitation in the Time Domain.** The earthquake excitation in the time domain can be expressed as

$$Q_s = m \ddot{x}_g, \quad (3)$$

where  $\ddot{x}_g$  is the acceleration of the input ground motion, which can be derived from the earthquake records obtained from seismic stations at a given location or from an artificial stochastic process using the trigonometric series method.

Since the random excitation of earthquakes is transient, the nonstationary characteristics of random excitation should be considered. Using the evolutionary theory of power spectrum density [15], the nonstationary random process can usually be written as the product of a stationary random process and a deterministic slowly varying modulation function

$$\ddot{x}_g = a(t) w(t), \quad (4)$$

where  $a(t)$  is a stationary process and  $w(t)$  is the deterministic envelope function with a maximum value of 1.0.

The deterministic envelope function  $w(t)$  is written as [10]

$$w(t) = \begin{cases} \left(\frac{t}{t_0}\right)^2 & 0 < t < t_0 \\ 1 & t_0 < t < t_n \\ \exp[-c(t - t_n)] & t_0 < t, \end{cases} \quad (5)$$

where  $t_0$  and  $t_n$  are the initial time and the  $n$ th time, respectively,  $t_0 - t_n$  is the significant duration of the accelerogram, and  $c$  is the nonuniformly modulated coefficient. A typical value of  $c$  is adopted as 0.2.

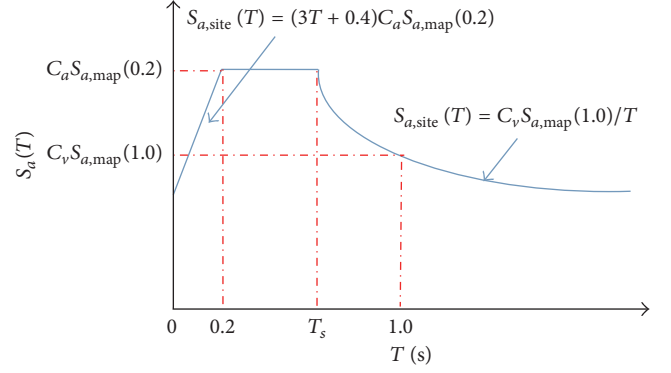


FIGURE 2: ISO seismic design spectrum.

A possible approach to define  $a(t)$  is by assuming that the motion induced by earthquakes is a realization of a stationary stochastic process. The time history of a stationary earthquake excitation can be readily generated based on the spectral density as follows:

$$a(t) = \sum_{k=1}^n \sqrt{(4 \cdot \Delta\omega \cdot S(\omega_k))} \cos(\omega_k t + \varepsilon_k), \quad (6)$$

where  $\Delta\omega$  is the constant difference between successive frequencies,  $\omega_k = k \cdot \Delta\omega$  is the  $k$ th wave frequency,  $S(\omega_k)$  is the power spectrum of  $\omega_k$ ,  $n$  is the total number of frequency points considered in the calculation, and  $\varepsilon_k$  is the random phase angle varying between 0 and  $2\pi$ .

In engineering practice [15], the design target response spectrum at a given site is more commonly available than the ground motion power spectrum density function. Therefore, it will be very useful to generate time histories of ground motion that are compatible to a given design target response spectrum.

The design target acceleration response spectrum  $S_a^T(\omega)$  can be obtained in seismic design guidelines, which cannot be directly used by (6). Thus, a conversion formula is needed to obtain the corresponding ground motion power spectrum  $S(\omega)$ .

For a given design target acceleration response spectrum  $S_a^T(\omega)$ , the corresponding ground motion power spectrum  $S(\omega)$  can be estimated by [15]

$$S(\omega) = \frac{\zeta}{\pi\omega} [S_a^T(\omega)]^2 \frac{1}{\ln[-(\pi/\omega T_d) \ln(1 - P)]}, \quad (7)$$

where  $T_d$  is the time duration of earthquake,  $\zeta$  is the damping ratio, and  $P$  is the exceeding probability. In the present study, the value of the parameter  $P$  is taken as 0.9.

The design target acceleration response spectrum is normally determined by basic parameters of seismic intensity, site classification, peak acceleration, and damping ratio. The seismic design spectrum curve as shown in Figure 2 can be found in the ISO design guidelines (ISO, 2006) [16]. In the figure,  $S_a$  is the spectral acceleration,  $S_{a,site}(T)$  is the site spectral acceleration, and  $S_{a,map}$  is the bedrock spectral acceleration. When the fundamental period of a structure is

equal to 0.2 or 1.0 s, the bedrock spectral acceleration can be calculated by  $S_{a,\text{map}}(0.2) = 0.5g$  or  $S_{a,\text{map}}(1.0) = 0.2g$ . The parameter  $T$  is the fundamental period of the structure, and  $T_s$  is the site characteristic period and can be calculated as follows:

$$T_s = \frac{C_v S_{a,\text{map}}(1.0)}{C_a S_{a,\text{map}}(0.2)}, \quad (8)$$

where  $C_a$  and  $C_v$  are the site coefficients and can be obtained from the design tables in ISO (2006) [16].

Assuming that the submerged floating tunnel investigated in this paper is located in the Bohai Sea of China with anchoring systems on a shallow foundation, the site class of the foundation is categorized as A. For a site class A/B and a shallow foundation, the parameters  $C_a$  and  $C_v$  are both assigned as 1.0.

Using the above approach, the generated time histories of ground motion usually match well with the design target response spectrum. Iterations should be carried out to adjust the power spectrum density function if the two spectra do not match satisfactorily [15].

**2.3. Formulation of Hydrodynamic Force in Time Domain.** The vortex-induced lift force can be expressed as [17]

$$F_L = \frac{1}{2} \rho_w D C_L (v_L \sin \theta)^2 \sin(\omega_v t), \quad (9)$$

where  $\rho_w$  is the water density,  $D$  is the outer diameter of the cable,  $\omega_v$  is the vortex shedding frequency,  $C_L$  is the vortex-induced lift coefficient, and  $v_L$  is the vortex flow velocity and its typical value is taken as 1.0 m/s.

The hydrodynamic force  $F_D$  can be expressed by Morison's equation [14] as follows:

$$F_D = \frac{1}{2} \rho_w D C_D \left( v - \frac{\partial u}{\partial t} \right) \left| v - \frac{\partial u}{\partial t} \right| + C_M \frac{\pi}{4} \rho_w D^2 \frac{\partial v}{\partial t} - (C_M - 1) \frac{\pi}{4} \rho_w D^2 \frac{\partial^2 u}{\partial t^2}, \quad (10)$$

where  $C_D$  is the drag coefficient,  $C_M$  is the inertia coefficient,  $u$  is the displacement of the cable, and  $v$  is the instantaneous current velocity.

The hydrodynamic force induced by earthquake excitation is formulated following four assumptions [7, 18, 19].

(1) As the earthquake excitation process is in a short time duration, the current velocity around the cable during earthquakes is assumed to be negligible.

(2) When the ground motion is horizontal, the current velocity is set as zero; when the ground motion is vertical, the current velocity is equal to the ground velocity.

(3) The wave force is neglected as the cable is located in deep water.

(4) The coupled effect between the motions in different directions is neglected.

Thus, the hydrodynamic force under earthquake excitation can be expressed by [7, 18, 19]

$$F_D = \frac{1}{2} \rho_w D C_D \left( \dot{x}_g - \frac{\partial u}{\partial t} \right) \left| \dot{x}_g - \frac{\partial u}{\partial t} \right| + C_M \frac{\pi}{4} \rho_w D^2 \ddot{x}_g - (C_M - 1) \frac{\pi}{4} \rho_w D^2 \frac{\partial^2 u}{\partial t^2}. \quad (11)$$

**2.4. Solution of the Equation.** Suppose that the oscillation mode of the cable is that of standard chord

$$u(z, t) = \sum_{n=1}^{\infty} \sin \frac{n\pi z}{L} u_n(t). \quad (12)$$

To obtain an approximate solution of (1), Galerkin method is applied to transform the partial differential equation into a set of ordinary ones.

Substituting (12) into (1), multiplying each term by  $\sin(n\pi z/L)$ , integrating over  $z \in (0, L)$ , and invoking the orthogonality property of the normal modes give

$$\ddot{u}_n + \left[ \omega_{Mn}^2 + \omega_{An}^2 (1 + \varepsilon \cos \omega_p t) \right] u_n + \frac{C_{sn}}{m} \dot{u}_n - \int_0^L \frac{2(F_L - F_D - Q_s \sin \theta)}{mL} \sin \frac{n\pi z}{L} dz = 0 \quad (13)$$

with

$$\omega_{Mn}^2 = \left( \frac{n\pi}{L} \right)^4 \frac{E_{\text{eq}} I}{m}, \quad (14)$$

$$\omega_{An}^2 = \left( \frac{n\pi}{L} \right)^2 \frac{T_0}{m}, \quad (15)$$

$$\omega_n = \sqrt{\omega_{Mn}^2 + \omega_{An}^2}, \quad (16)$$

$$C_{sn} = 2m\omega_n \zeta, \quad (17)$$

where  $\zeta$  is the damping ratio of the cable,  $\omega_{Mn}$ ,  $\omega_{An}$  are the  $n$ th order natural frequency of the system of bending vibration and axial vibration, respectively,  $\omega_n$  is the total  $n$ th order natural frequency of the system, and  $\varepsilon$  is the ratio of dynamic tension to static tension.

The fourth-order Runge-Kutta method is used to solve the differential equation (13); each mode response of the cable under excitation may be obtained. By substituting the mode response into (12), the displacement response of the cable may be obtained.

### 3. Numerical Results and Discussion

The cable of a submerged floating tunnel is analyzed in the present study as an illustrative example to show the efficacy of the proposed analytical solution that is programmed in MATLAB. The physical and geometric parameters are listed in Table 1 following the work of Sun and Su [2]. If the same values of  $C_M = 1.0$  and  $C_D = 0.7$  provided by Sun and Su [2] are used, it can result in the loss of hydrodynamic added

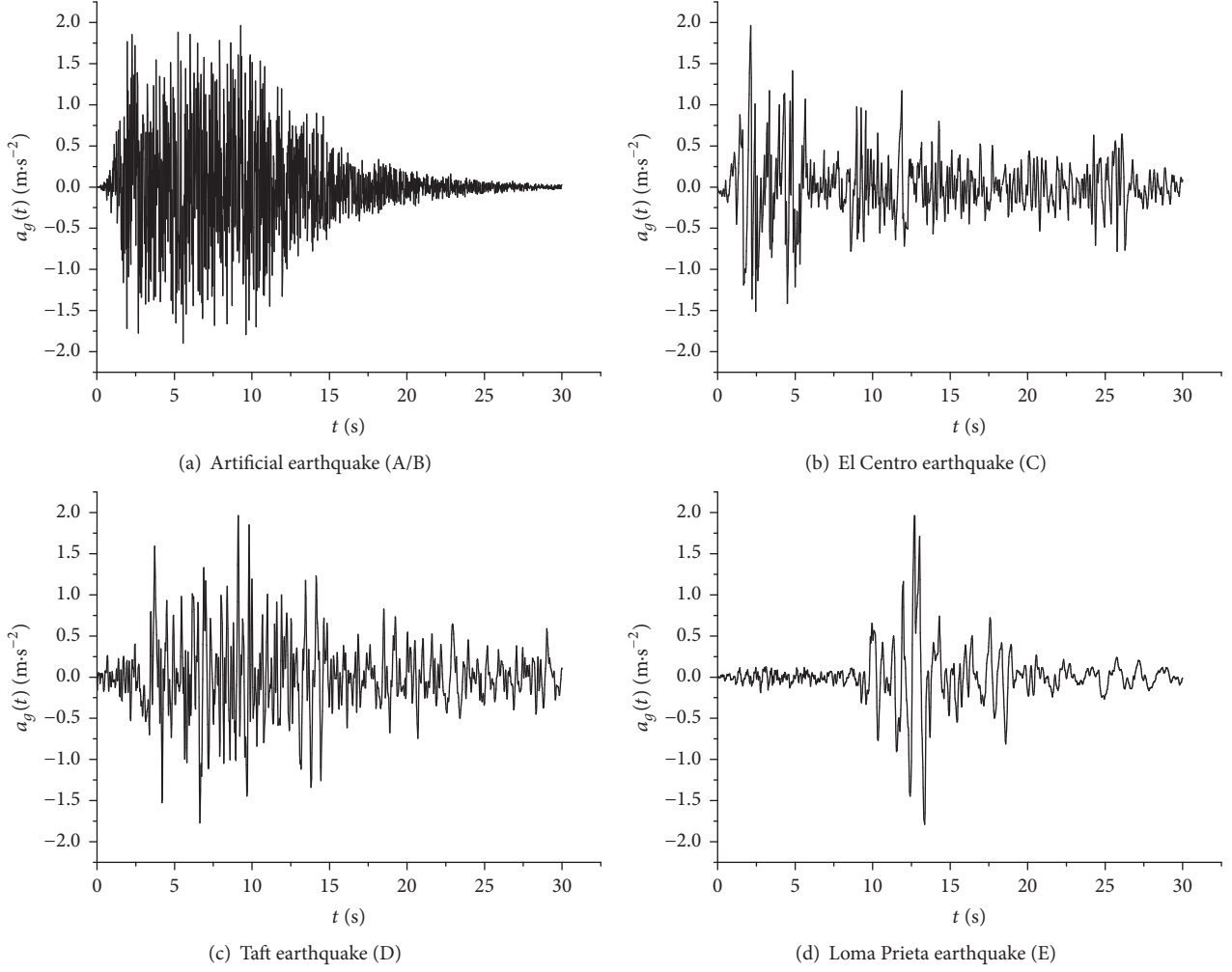


FIGURE 3: Time histories of four selected earthquake records.

TABLE 1: Basic characteristics of the analysis case.

Parameters	Values
Density of water $\rho_w$ ( $\text{kg/m}^3$ )	1028
Depth of water $d$ (m)	170
Vertical height $H_z$ (m)	140
Unstretched length of cable $L$ (m)	161.66
Outside diameter of cable $D$ (m)	0.489
Density of cable $\rho_s$ ( $\text{kg/m}^3$ )	7850
Modulus of elasticity of cable $E$ (Pa)	2.10E11
Initial tension of cable $T_0$ (N)	2.572E7
Mass per unit length of cable $m$ (kg/m)	1474.23
Damping ratio $\zeta$	0.0018
Inertia coefficient $C_M$	2.0
Drag coefficient $C_D$	1.0
Inclination angle $\theta$ ( $^\circ$ )	60

mass. Thus, the values of  $C_M$  and  $C_D$  are taken as 2.0 and 1.0, respectively, following the work of Martire et al. [20].

In the present study, four earthquake records in different representative sites are selected. For comparison, the peak acceleration of these accelerograms is adjusted to  $0.2g$ , corresponding to earthquakes with an intensity factor of 8 as shown in Figure 3 and Table 2 [16, 21].

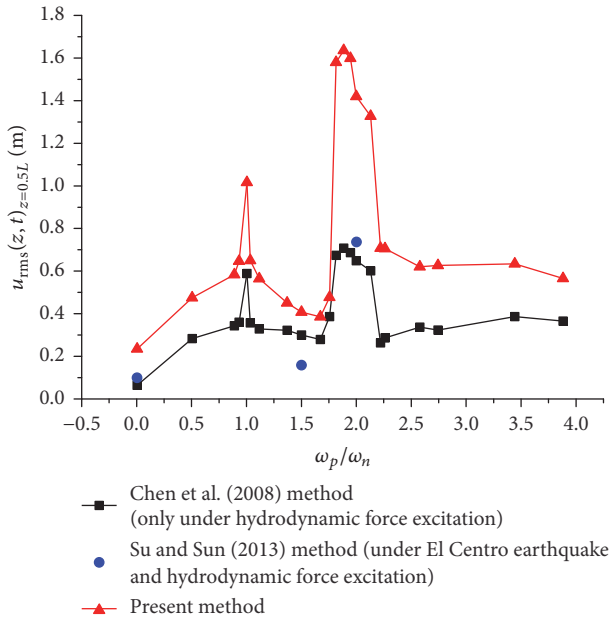
The artificial earthquake is generated by using the aforementioned theory in Section 2.2, and the other three earthquakes are the classical earthquake records obtained from corresponding site classifications. The time histories in time domain, the amplitude, and energy in frequency domain of four earthquakes are different, matching different site classifications.

A sensitivity analysis is conducted to evaluate the influence of key parameters to provide recommendations for use in design and construction of the anchor system for a submerged floating tunnel under hydrodynamic force and earthquake. The effects of key environmental and structural



TABLE 2: Site classifications of earthquake records used for this study.

Ground motion	Site classifications	Site condition	Time duration (s)	Time interval (s)
Artificial earthquake	A/B	Rock	30	0.02
El Centro earthquake in the EW direction	C	Very dense hard soil and soft rock	30	0.02
Taft Kern County (Taft for short) earthquake in the N21E direction	D	Stiff to very stiff soil	30	0.02
Loma Prieta Oakland outer wharf (Loma for short) earthquake	E	Soft soil	30	0.02

FIGURE 5: Variations of RMS of mid-span displacement of the cable with  $\omega_p/\omega_n$  calculated using different methods.

incorporated in the present approach, while this coupled effect and the hydrodynamic added mass are neglected in other strategies. Similar results of underestimation by the existing analytical models [11, 22] compared to experimental measurements and numerical simulations were reported [8, 19].

**3.2. Dynamic Response of the Cable under Only Vortex Excitation.** Vortex-induced vibration of cables is caused by complex interactions between cylindrical structures and the correlated wake vortex, and it is an important source of fatigue damage to the cables. Figure 6 shows the dynamic response of the cable under only vortex excitation. Two cases are investigated in which no oscillation was excited by vortex-shedding in type of  $\omega_v = 0.1\omega_1$  and vortex-induced vibration in type of  $\omega_v = \omega_1$ , which are showed in Figures 6(a) and 6(b) respectively. In Figure 6(a), the dynamic response of the cable shapes as a sinusoidal curve and its amplitude is small. And, in Figure 6(b), the action of exciting system to vibrate will happen as the lift force falls into the lock-in range;

that is, beat phenomenon obviously occurs. Besides, due to the self-limitation of damping, the time history of vortex-induced vibration shown in Figure 6(b) decreases rapidly in the first 200 s, but the decreasing pattern is roughly linear and reaches a steady-state response quickly. And it can be observed that the amplitude of dynamic responses of the cable in the condition of lock-in case  $\omega_v = \omega_1$  is signally larger than the other case of  $\omega_v \neq \omega_1$ . Figure 6(c) shows similar results; the largest dynamic response occurs when vortex-induced frequency is consistent with the structural natural frequency; that is,  $\omega_v = \omega_1$ . Besides, the value of dynamic response of the cable in the other frequency is relatively small.

**3.3. Dynamic Response of the Cable under Combinations of Vortex Excitation and Parametric Excitation.** In practice, for the cable of submerged floating tunnel suffering both parametric excitation and vortex excitation, its structural configuration is more complex rather than merely an Euler beam alone. Moreover, it is more complicated if two excitation frequencies of both top-end tube and vortex-induced lift force are involved.

Figures 7(a)–7(d) show four typical examples of the cable under combinations of vortex excitation and parametric excitation, and these dynamic responses exhibit interesting and different features of the pattern and shape of the time history. In Figure 7(c), a combined resonance occurs owing to both parametric excitation and vortex-shedding excitation, where both excitations satisfy the condition that can excite resonance of a system under only parametric or vortex shedding excitation, and its motion amplitude is obviously larger and more unstable than those of the other cases in Figures 7(a), 7(b), and 7(c). Figure 7(a) shows the time history of the cable when in case of  $\omega_v = \omega_1$  and  $\omega_p = 0.1\omega_1$ , as vortex excitation dominates parametric excitation, beat phenomenon still occurs in this case and has the smallest motion amplitude. In Figures 7(b) and 7(d), as parametric excitation dominates vortex excitation, beat phenomenon is broken in those cases, the pattern of each time history is a kind of “standing wave,” where each has a repeating wave-unit but with mutually different profiles, and the number of wave-units is approximately ranging from 2.5 to 3.5 and the profiles become more irregular. Therefore, it can be concluded that the dynamic response of the cable under combinations of vortex excitation and parametric excitation became more complicated, especially in combined resonance condition.

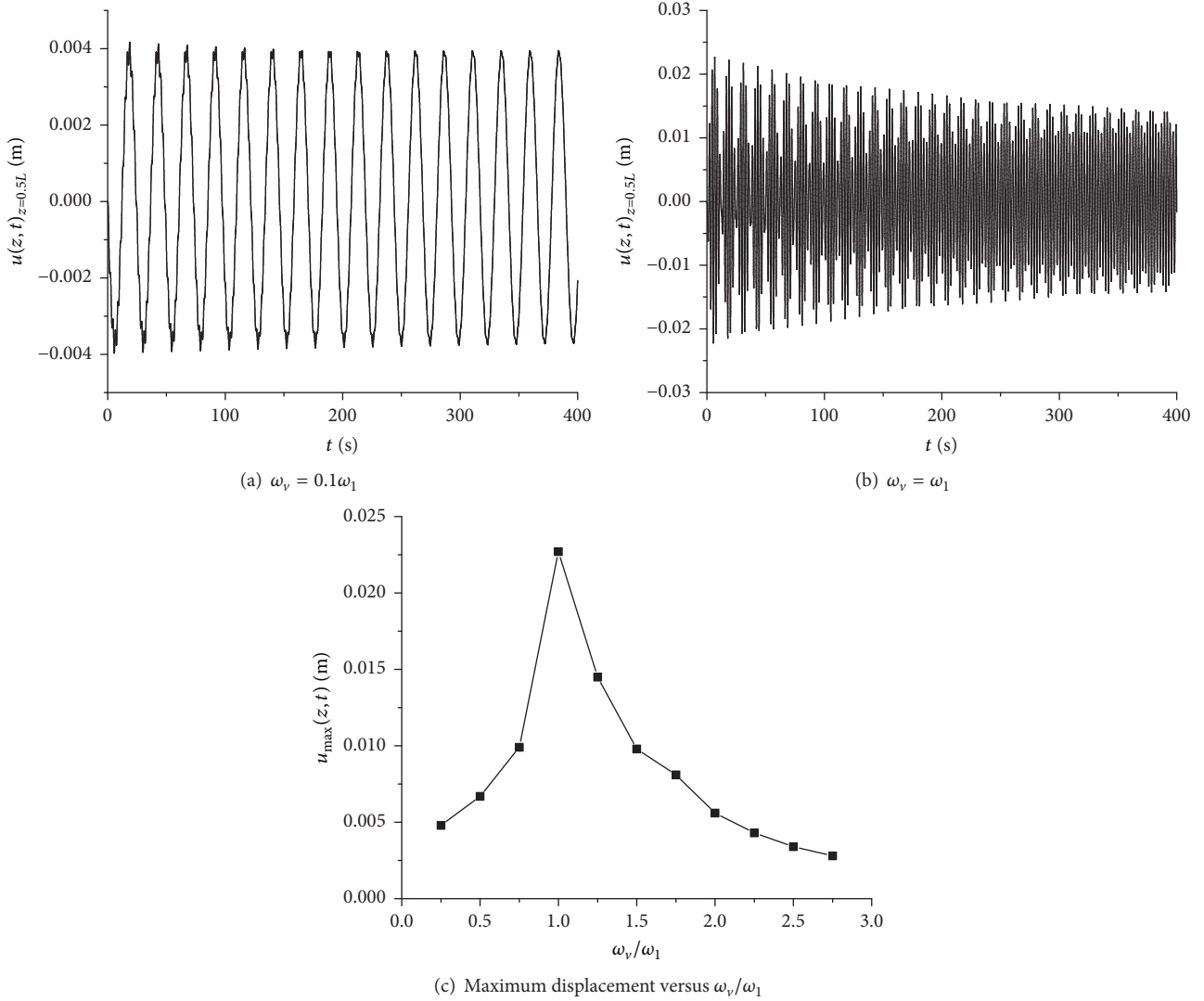
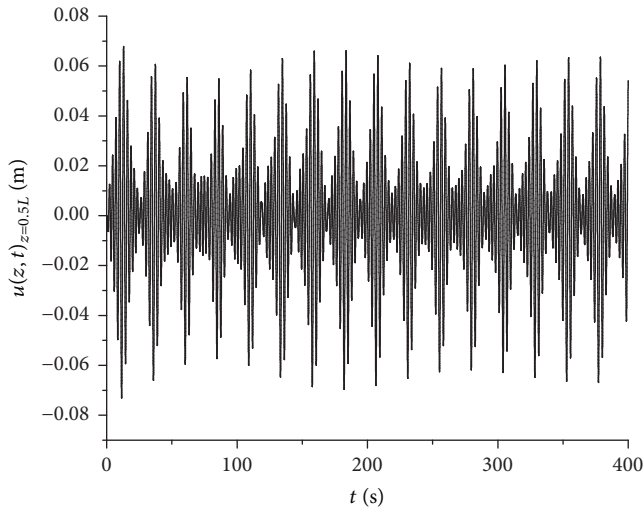


FIGURE 6: Dynamic response of the cable under only vortex excitation.

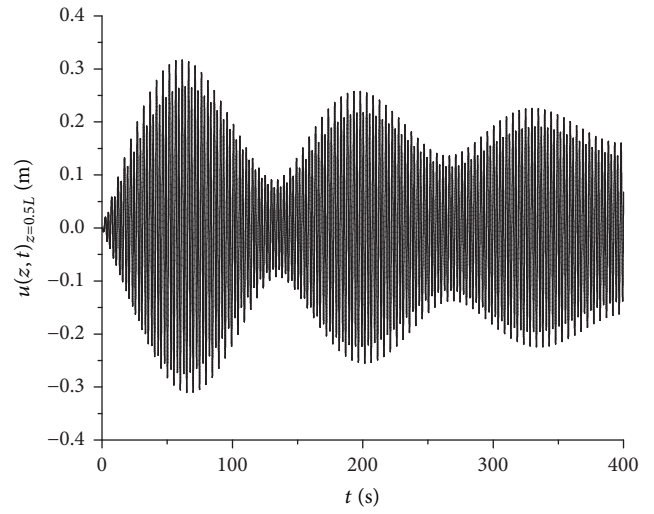
Figure 7(e) indicates that three largest amplitudes of dynamic response are, respectively, at the ratio of parametric frequency to natural frequency of  $\omega_p/\omega_1 = 1, 2,$  and  $3,$  and the peak values of the mid-span displacement of the cable under above cases are  $0.4013$  m,  $0.8914$  m, and  $0.2891$  m, respectively. Particularly, the largest response amplitude occurs at frequency  $\omega_p/\omega_1 = 2.$  Or, we may say, for mode 1, the largest dynamic response might occur when top-end tube parametric frequency is twice as much as the natural frequency; that is,  $\omega_p = 2\omega_1$  when parametric excitation satisfies the condition which can excite parametric resonance of a system under parametric excitation. Besides, the value of dynamic response of the cable in the other frequency case is relatively small. The results suggest that parametric excitation has a strong effect on the dynamic response of the cable, especially combined with vortex shedding frequency consistent with the structural natural frequency; that is,  $\omega_v = \omega_1.$

Thus, the fundamental frequency of cable of submerged floating tunnel located in complicated marine environment should be thought over carefully to avoid parametric resonance. Based on (14)–(16), the key parameters for deciding the fundamental frequency of the cable are  $m, E_{eq}, I, T_0,$  and  $L,$  while the parametric excitation frequency  $\omega_p$  mainly depends on ocean environmental conditions acting on the tube.

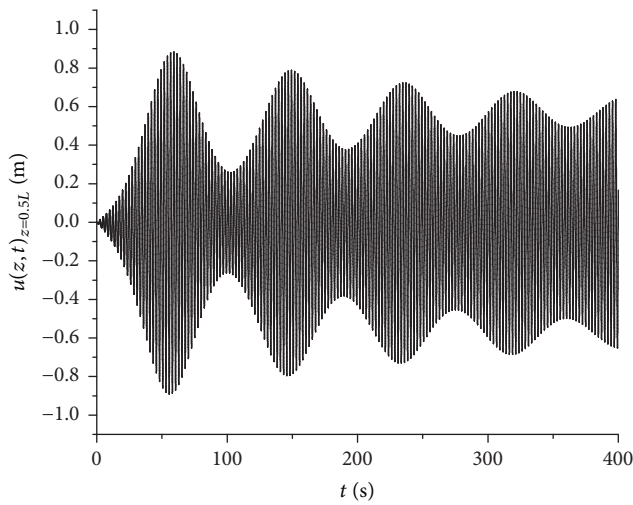
**3.4. Effect of Motion of Top-End Tube.** The comparison of modal dynamic responses between the cases with top-end tube moving and without top-end tube moving is presented in Figure 8. The dynamic responses of the cable are numerically simulated, while the top-end tube is moving at the cable's natural frequencies of modes ranging from mode 1 to mode 12, and the most dangerous cases are taken into account; that is,  $\omega_v = \omega_j$  and  $\omega_p = 2\omega_j;$  here,  $\omega_j$  is the  $j$  model natural frequency. In Figure 8, as modal number increases, the cable's



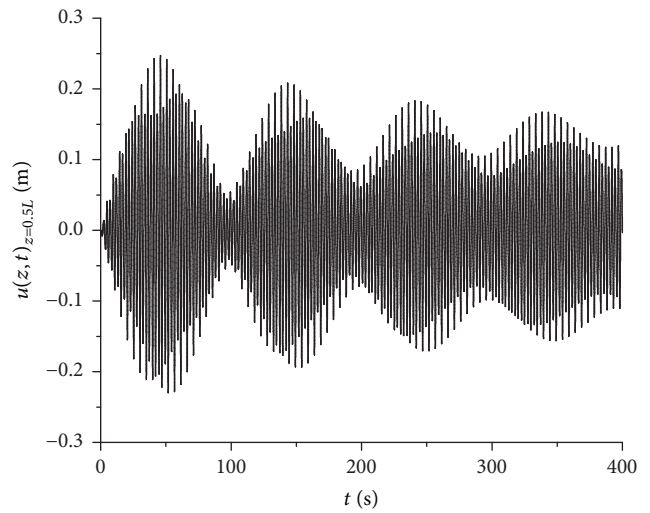
(a)  $\omega_v = \omega_1$  and  $\omega_p = 0.1\omega_1$



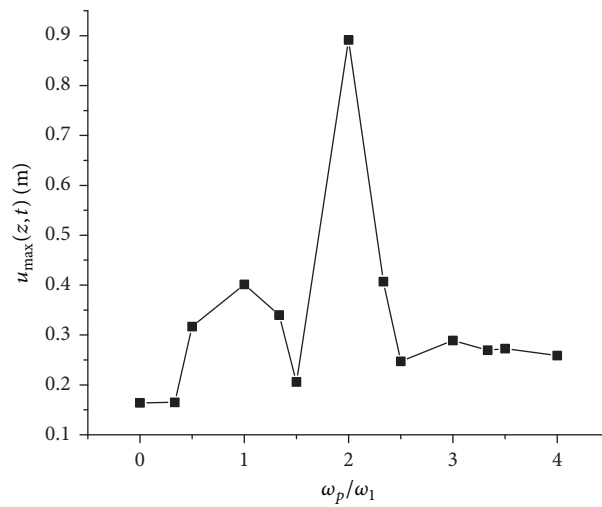
(b)  $\omega_v = \omega_1$  and  $\omega_p = 0.5\omega_1$



(c)  $\omega_v = \omega_1$  and  $\omega_p = 2\omega_1$



(d)  $\omega_v = \omega_1$  and  $\omega_p = 2.5\omega_1$



(e) Maximum displacement versus  $\omega_p/\omega_1$

FIGURE 7: Dynamic response of the cable under combinations of vortex excitation and parametric excitation.

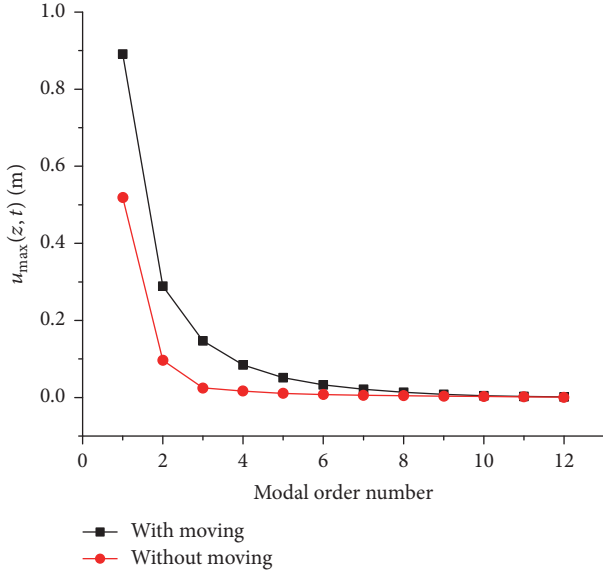


FIGURE 8: Comparison of modal dynamic responses between the cases with top-end tube moving and without top-end tube moving.

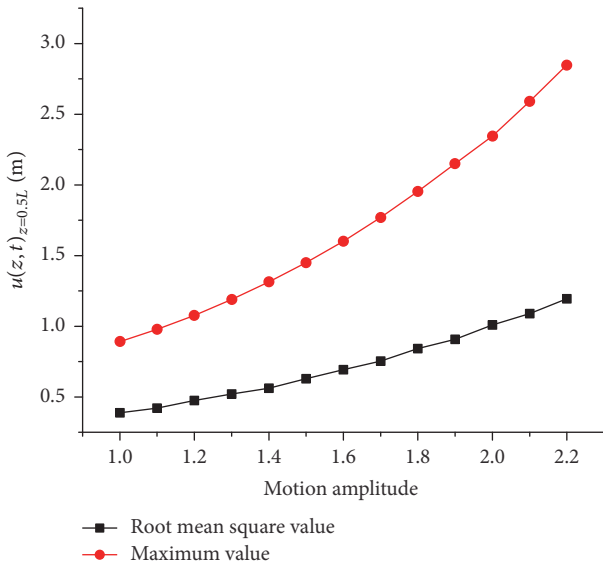
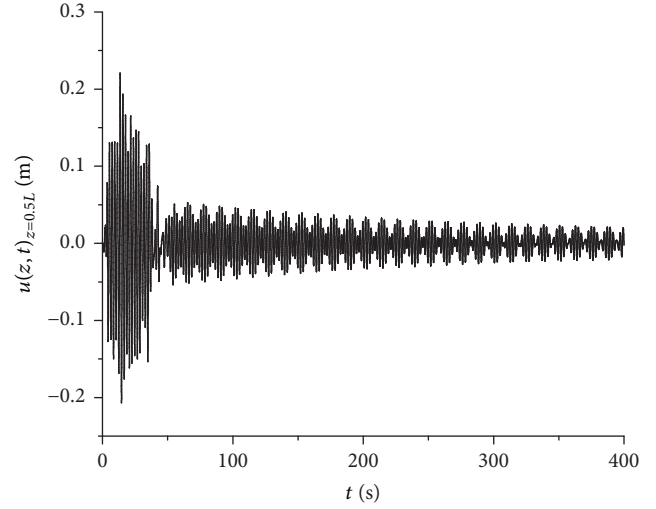


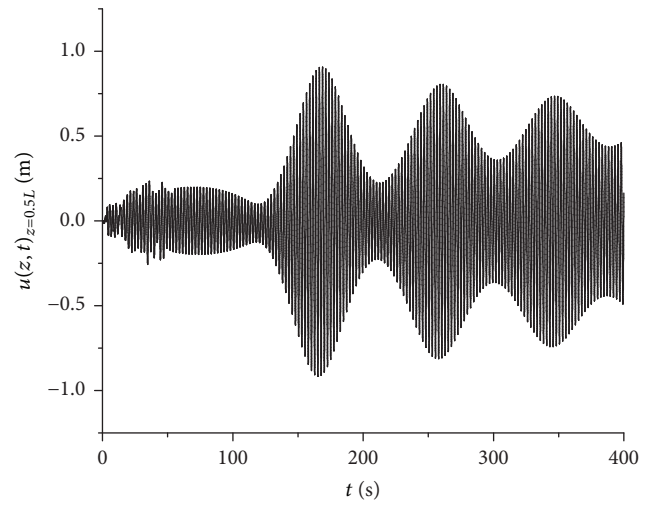
FIGURE 9: The effect of motion amplitude of top-end tube on the dynamic response of the cable.

vibration either with top-end tube moving or without top-end tube moving attenuates rapidly to small value, even zero. It is noted that the first third-order mode responses are mostly dominated, and they take up more than 80% of the whole mode response. Also, it is shown that the maximum amplitudes of the cable with top-end tube moving are larger than the cases without top-end tube moving, and taking mode 1 as an example, its maximum amplitude is about twice larger than the case without top-end tube moving.

Figure 9 shows the curves of the maximum value and root mean square value of the dynamic response of the cable as the motion amplitude of top-end tube varies from 1.0 to



(a)  $\omega_v = \omega_1, \omega_p = 0.0\omega_1$  and under Taft earthquake



(b)  $\omega_v = \omega_1, \omega_p = 1.0\omega_1$  and under Taft earthquake

FIGURE 10: The effect of earthquake on the dynamic response of the cable.

2.2, where motion amplitude is expressed by the ratio of dynamic tension to static tension  $\varepsilon$ . In both the two cases, the variational laws of curves are similar, and the maximum value of the displacement increases with the increase of motion amplitude, which is very dangerous for the cable system. And, the root mean square value of the dynamic response of the cable rises almost linearly with the increase of motion amplitude. Thus, motion amplitude of top-end tube is the most important parameter in determining the dynamic response of the cable which necessitates careful consideration during the early stage of design.

3.5. *Effect of Earthquake.* Figure 10 shows the dynamic response time history of the cable when in combinations of vortex excitation and parametric excitation under Taft earthquake. When the cable is subjected to the earthquake, the maximum value and the mean value in this case are signally

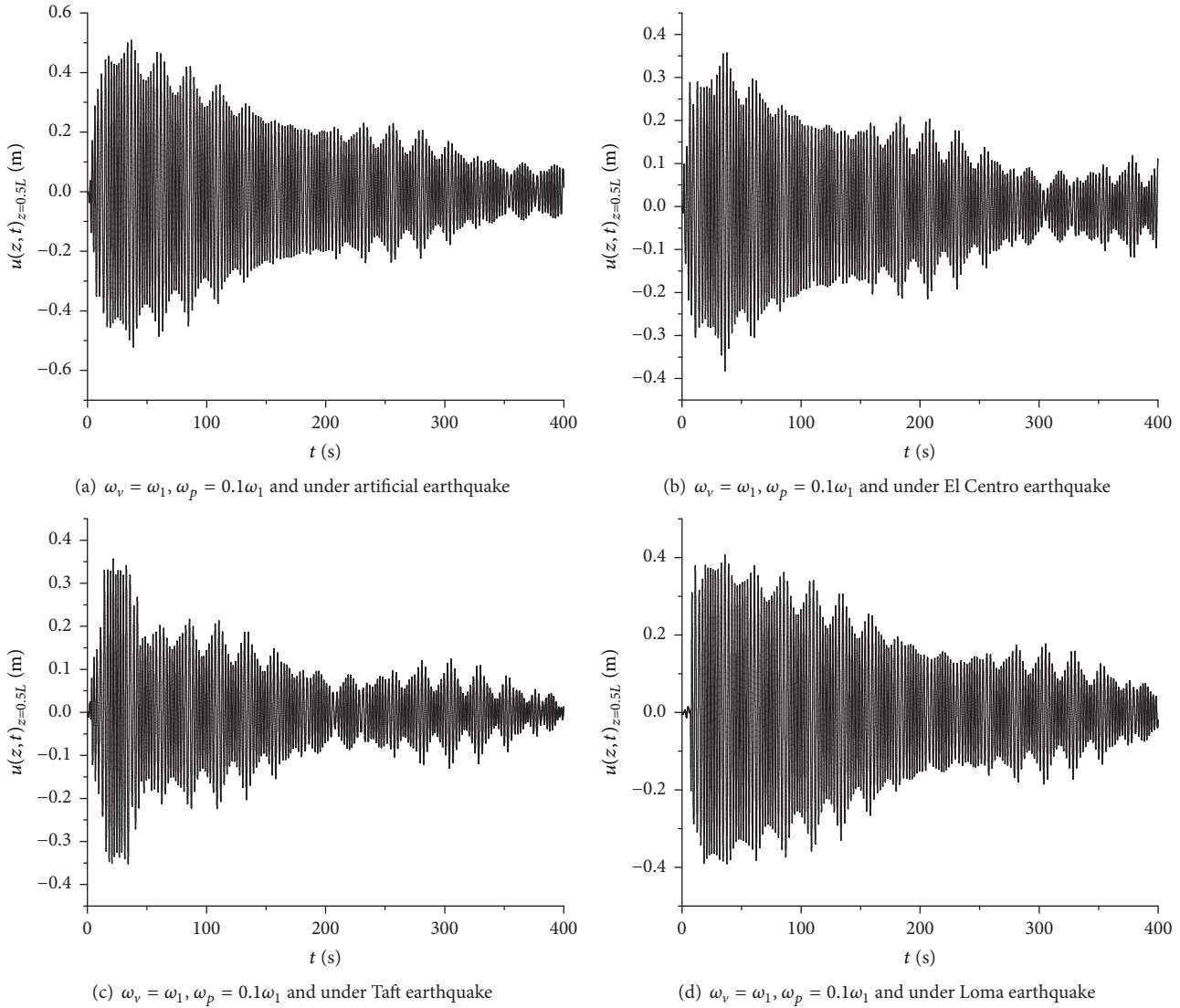


FIGURE 11: Comparison of dynamic responses of the cable between the cases of four site classifications earthquakes.

larger than the other two cases with only combinations of vortex excitation and parametric excitation. Besides, due to the randomness of the earthquake, the curves of dynamic response of the cable become more irregular. Compared with Figure 6(b), due to the effect of earthquake, the maximum value appears at the time of 0~50 s, that is, the time duration of earthquake; after that the motion amplitude attenuates, and the maximum values of dynamic response in Figure 10(a) add from 0.0223 m to 0.221 m. When compared with Figure 7(c), the maximum values of dynamic response in Figure 10(b) add from 0.883 m to 0.916 m, and the maximum value of motion response of the cable appears around from the time point of 50 s to 160 s. It is noted that the earthquake can significantly affect the motion amplitude and time points reach the maximum value of the cable. Therefore, dynamic analysis under combined vortex, parametric, and earthquake excitations is necessary.

From Figures 11(a) to 11(d), it can be seen that site class of earthquake wave affects the vibration response of cable largely, and the pattern and motion amplitude of time history of the cable are invariant. The maximum value appears at the time of 0~50 s, that is, the time duration of earthquake; after that the motion amplitude attenuates. In other words, the energy of the dynamic response of the cable is focused on the time duration of earthquake. The difference of seismic wave spectrum characteristics results in the difference of maximum mid-span displacements of the cable. The peak values of the dynamic response of the cable under artificial earthquake, El Centro earthquake, Taft earthquake, and Loma earthquake are 0.522 m, 0.383 m, 0.356 m, and 0.406 m, respectively, and occur at the time that the earthquake wave reaches its energy-intensive zone. Similarly, the root mean square values of the dynamic response of the cable under the above earthquake waves are 0.236 m, 0.156 m, 0.131 m, and 0.202 m, respectively.

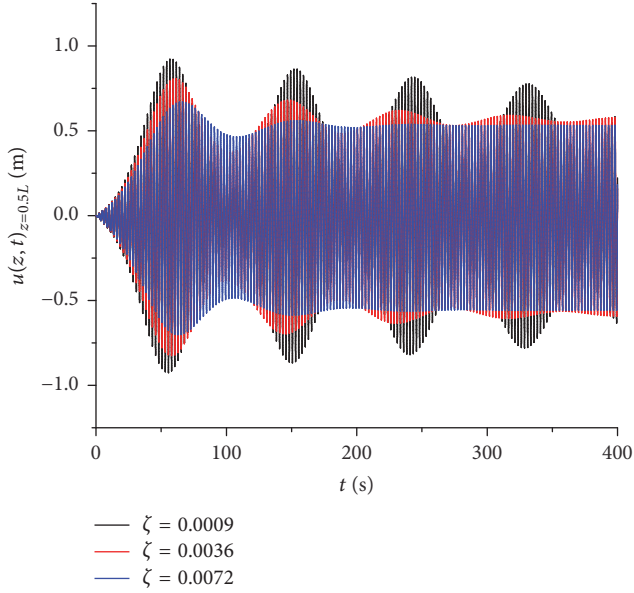


FIGURE 12: The effect of damping ratio on the dynamic response of the cable ( $\omega_v = \omega_1$  and  $\omega_p = 2\omega_1$ ).

It is concluded that dynamic response of the cable under artificial earthquake which is suited to rock foundation is the largest. Oppositely, the Taft earthquake which is suited to medium soil foundation induces the smallest dynamic response values of the cable.

**3.6. Effect of Damping Ratio.** The influence of damping ratio on the dynamic response of the cable is also investigated, and three alternative levels of damping ratio  $\zeta = 0.0009, 0.0036, 0.0072$  are adopted. As shown in Figure 12, the motion amplitude and energy of the dynamic response of the cable are decreased as the modal damping ratio is increased. As the damping ratio increases to 0.0072, the wave crests induced by combinations of vortex excitation and parametric excitation are smoothed after the time of 150 s. The rate of descent of the maximum values between  $\zeta = 0.0009$  and  $\zeta = 0.0072$  is reached up to 72.82%. This is an expected result because damping plays an important role in energy dissipation and makes the cable system more stable [23, 24]. In preliminary design of the cable system, it is recommended that the damping of cable should be increased to reduce the dynamic responses of the system, and large-amplitude vibration of cable may be avoided by locating dampers on the cable or the tube.

**3.7. Effect of Lift Coefficient.** Based on the work conducted by Chen et al., 2015, the lift coefficient is adopted as a constant value ranging usually from 0.8 to 1.2. As shown in Figure 13, four cases of the cable system under combined excitation are explored to determine the influence of the lift coefficient on the dynamic response, and the three different lift coefficients are  $C_L = 0.8, 1.0, 1.2$ . When the lift coefficient is ranged from 0.8 to 1.2, the lift coefficient is an important part of the

correlated lift force due to vortex shedding; as a consequence, larger lift coefficient can cause larger dynamic response. Thus, the dynamic response of the cable in case of lift coefficient in 0.8 is the smallest while comparing with the case of other constant lift coefficients. As a consequence, larger lift coefficient can cause more unstable dynamic response. In the meanwhile, the inclusion of parametric excitation can strengthen the instability, when it satisfies the special condition which can cause parametric resonance of a cable system. As the effect of self-excitation of nonlinear vortex-induced lift terms, the excitation of resonance becomes weaker, while the lift coefficient is getting lower. In Figure 13(b), the mid-span displacement of the cable is largest, when along axial location, and the maximum amplitude in the case of lift coefficient in 1.2 is more than twice larger than the case of lift coefficient in 0.8.

## 4. Conclusions

The parametrically excited vibrations of cable of submerged floating tunnel under hydrodynamic and earthquake excitation are studied in this paper. The dynamics motion of the cable is built by Euler beam theory and Galerkin method. Random earthquake excitation in time domain is formulated by trigonometric series method. The hydrodynamic force induced by earthquake excitations is formulated to represent real seaquake conditions. An analytical model is proposed to analyze the cable system for submerged floating tunnel model subjected to combined hydrodynamic force and earthquake excitations. The effects of the hydrodynamic and earthquake parameters and structural parameters on the resulting dynamics response of the system are explored and discussed. The sensitivity of key parameters on the anchor system for submerged floating tunnel is investigated to enable a preliminary examination of the hydrodynamic and seismic behavior of the cable and provide guidance for design and operation of the anchor system for submerged floating tunnel.

The following conclusions can be drawn:

(1) The overall trends of the results obtained by the present method generally agree with the evaluations calculated from the other methods. Due to the seismic design spectrum for offshore structure and the coupled effect of hydrodynamic force and earthquake excitation considered in the present approach, the dynamic responses of the cable are greatly amplified and FFT amplitude component obtained by the present method has more abundant high-frequency contents and excites wider peak frequency region.

(2) The dynamic response of the cable under combinations of vortex excitation and parametric excitation become more complicated, especially in combined resonance condition. Thus, the fundamental frequency of cable of submerged floating tunnel located in complicated marine environment should be thought over carefully to avoid parametric resonance.

(3) Dynamic response of the cable under artificial earthquake which is suited to rock foundation is the largest. Oppositely, the Taft earthquake which is suited to medium soil foundation induces the smallest dynamic response values of the cable.

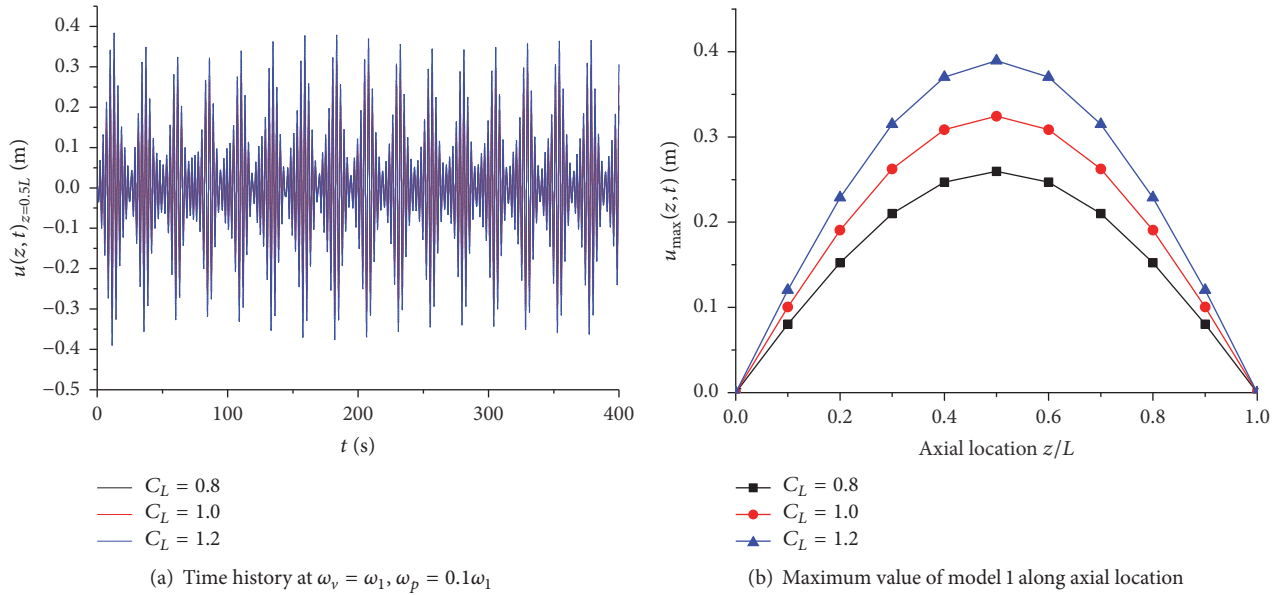


FIGURE 13: The effect of lift coefficient on the dynamic response of the cable.

(4) Damping plays an important role in energy dissipation and makes the cable system more stable. In preliminary design of the cable system, it is recommended that the damping of cable should be increased to reduce the dynamic responses of the system, and large-amplitude vibration of cable may be avoided by locating dampers on the cable or the tube.

### Conflicts of Interest

The authors declared no potential conflicts of interest with respect to the research, authorship, and/or publication of this article.

### Acknowledgments

This work had been supported by the National Natural Science Foundation of China (Grants nos. 51578164 and 41672296), the China Postdoctoral Science Foundation (Grant no. 2017M610578), the Systematic Project of Guangxi Key Laboratory of Disaster Prevention and Structural Safety (Grant no. 2016ZDX008), and the Innovative Research Team Program of Guangxi Natural Science Foundation (Grant no. 2016GXNSFGA380008).

### References

- [1] S.-N. Sun, J.-Y. Chen, and J. Li, "Non-linear response of tethers subjected to parametric excitation in submerged floating tunnels," *China Ocean Engineering*, vol. 23, no. 1, pp. 167–174, 2009.
- [2] S.-N. Sun and Z.-B. Su, "Parametric vibration of submerged floating tunnel tether under random excitation," *China Ocean Engineering*, vol. 25, no. 2, pp. 349–356, 2011.
- [3] W. Lu, F. Ge, L. Wang, X. Wu, and Y. Hong, "On the slack phenomena and snap force in tethers of submerged floating tunnels under wave conditions," *Marine Structures*, vol. 24, no. 4, pp. 358–376, 2011.
- [4] S.-I. Seo, H.-S. Mun, J.-H. Lee, and J.-H. Kim, "Simplified analysis for estimation of the behavior of a submerged floating tunnel in waves and experimental verification," *Marine Structures*, vol. 44, pp. 142–158, 2015.
- [5] C. Cifuentes, S. Kim, M. Kim, and W. Park, "Numerical simulation of the coupled dynamic response of a submerged floating tunnel with mooring lines in regular waves," *Ocean Systems Engineering*, vol. 5, no. 2, pp. 109–123, 2015.
- [6] M. Duan, Y. Wang, Z. Yue, S. Estefen, and X. Yang, "Dynamics of risers for earthquake resistant designs," *Petroleum Science*, vol. 7, no. 2, pp. 273–282, 2010.
- [7] R. Dong, X. Li, Q. Jin, and J. Zhou, "Nonlinear parametric analysis of free spanning submarine pipelines under spatially varying earthquake ground motions," *China Civil Engineering Journal*, vol. 41, no. 7, pp. 103–109, 2008.
- [8] J. H. Lee, S. I. Seo, and H. S. Mun, "Seismic behaviors of a floating submerged tunnel with a rectangular cross-section," *Ocean Engineering*, vol. 127, pp. 32–47, 2016.
- [9] M. Di Pilato, F. Perotti, and P. Fogazzi, "3D dynamic response of submerged floating tunnels under seismic and hydrodynamic excitation," *Engineering Structures*, vol. 30, no. 1, pp. 268–281, 2008.
- [10] L. Martinelli, G. Barbella, and A. Feriani, "A numerical procedure for simulating the multi-support seismic response of submerged floating tunnels anchored by cables," *Engineering Structures*, vol. 33, no. 10, pp. 2850–2860, 2011.
- [11] Z.-B. Su and S.-N. Sun, "Seismic response of submerged floating tunnel tether," *China Ocean Engineering*, vol. 27, no. 1, pp. 43–50, 2013.
- [12] Ministry of Construction, "Code for seismic design of buildings," GB 50011-2010, Ministry of Construction, Beijing, China, 2010.

- [13] Z. Su and S. Sun, "Stability of submerged floating tunnel tether subjected to parametric excitation," *Journal of Central South University*, vol. 44, no. 6, pp. 2549–2553, 2013.
- [14] S. Lei, W.-S. Zhang, J.-H. Lin, Q.-J. Yue, D. Kennedy, and F. W. Williams, "Frequency domain response of a parametrically excited riser under random wave forces," *Journal of Sound and Vibration*, vol. 333, no. 2, pp. 485–498, 2014.
- [15] K. Bi and H. Hao, "Modelling and simulation of spatially varying earthquake ground motions at sites with varying conditions," *Probabilistic Engineering Mechanics*, vol. 29, pp. 92–104, 2012.
- [16] International Organization for Standardization (ISO), 2006, Petroleum and Natural Gas Industries-specific Requirements for Offshore Structures-Part 2. Seismic design procedures and criteria, Switzerland.
- [17] K. Wang, W. Tang, and H. Xue, "Time domain approach for coupled cross-flow and in-line VIV induced fatigue damage of steel catenary riser at touchdown zone," *Marine Structures*, vol. 41, pp. 267–287, 2015.
- [18] T. K. Datta and E. A. Mashaly, "Seismic response of buried submarine pipelines," *Journal of Energy Resources Technology*, vol. 110, no. 4, pp. 208–218, 1988.
- [19] J. H. Lee and J. K. Kim, "Dynamic response analysis of a floating offshore structure subjected to the hydrodynamic pressures induced from seaquakes," *Ocean Engineering*, vol. 101, pp. 25–39, 2015.
- [20] G. Martire, B. Faggiano, F. M. Mazzolani, A. Zollo, and T. A. Stabile, "Seismic analysis of a SFT solution for the Messina Strait crossing," *Procedia Engineering*, vol. 4, pp. 303–310, 2010.
- [21] Z. W. Wu, J. K. Liu, Z. Q. Liu, and Z. R. Lu, "Parametrically excited vibrations of marine riser under random wave forces and earthquake," *Advances in Structural Engineering*, vol. 19, no. 3, pp. 449–462, 2016.
- [22] J. Chen, S. Sun, and B. Wang, "Dynamic analysis for the tether of submerged floating tunnel," *Chinese Journal of Computational Mechanics*, vol. 25, no. 4, pp. 487–493, 2008 (Chinese).
- [23] W. B. Wu, H. Liu, M. H. El Naggar, G. X. Mei, and G. S. Jiang, "Torsional dynamic response of a pile embedded in layered soil based on the fictitious soil pile model," *Computers and Geotechnics*, vol. 80, pp. 190–198, 2016.
- [24] W. Wu, G. Jiang, S. Huang, and C. J. Leo, "Vertical dynamic response of pile embedded in layered transversely isotropic soil," *Mathematical Problems in Engineering*, vol. 2014, Article ID 126916, 12 pages, 2014.

## Research Article

# Normalized Study of Three-Parameter System in the Time Domain and Frequency Domain

**Xiao-Lei Jiao, Yang Zhao, and Wen-Lai Ma**

*School of Astronautics, Harbin Institute of Technology, Harbin 150001, China*

Correspondence should be addressed to Yang Zhao; yangzhao@hit.edu.cn

Received 12 April 2017; Revised 26 July 2017; Accepted 16 August 2017; Published 1 October 2017

Academic Editor: Naveed Ahmad

Copyright © 2017 Xiao-Lei Jiao et al. This is an open access article distributed under the Creative Commons Attribution License, which permits unrestricted use, distribution, and reproduction in any medium, provided the original work is properly cited.

Three-parameter isolation system can be used to isolate microvibration for control moment gyroscopes. Normalized analytical model for three-parameter system in the time domain and frequency domain is proposed by using analytical method. Dynamic behavior of three-parameter system in the time domain and frequency domain is studied. Response in the time domain under different types of excitations is analyzed. In this paper, a regulatory factor is defined in order to analyze dynamic behavior in the frequency domain. For harmonic excitation, a comparison study is made on isolation performance between the case when the system has optimal damping and the case when regulatory factor is 1. Besides, phase margin of three-parameter system is obtained. Results show that dynamic behavior in the time domain and frequency domain changes with regulatory factor. Phase margin has the largest value when the value of regulatory factor is 1. System under impulse excitation and step excitation has the shortest settling time for the response in the time domain when the value of regulatory factor is 1. When stiffness ratio is small, isolation performances of two cases are nearly the same; when system has a large stiffness ratio, isolation performance of the first case is better.

## 1. Introduction

The classic mass-spring-damper system includes spring and parallel viscous damper; it is two-parameter isolation system. Three-parameter system includes spring and an elastically supported damper. The system can be tuned by selecting parameter values that provide maximum damping at the fundamental frequency and reduced damping at higher frequencies [1]. Isolator based on three-parameter system is widely used in order to isolate microvibration in the aircraft. Microvibration is produced by control moment gyroscopes and reaction wheel assemblies with a frequency range of 0.1–300 Hz. Microvibration in a satellite can take a long time to attenuate because of special space environment. It is necessary to protect high precision payloads from the influence of microvibration [2–12]. Isolator based on three-parameter system can be used to tackle this problem.

Early studies focused on two-parameter isolation system. References [13, 14] had a simple study on three-parameter system. They showed that the system had considerable advantages to prevent impact. Honeywell Inc. developed a series of isolators based on three-parameter system [1, 15–17]. The

isolator had a pair of bellows which can be used to provide main stiffness; additional stiffness was volume stiffness produced by silicone oil. It was installed as a part of the complete reaction wheel isolation system; after being tested in Hubble Space Telescope, isolation performance was very good, with the maximum reduction in vibration, occurring at frequency as low as 50 Hz, and the maximum attenuation rate was approximately 60 dB. These isolators were assembled into isolation platform in order to prevent microvibration in all directions [18, 19]. Then, a lot of isolators based on three-parameter system were developed [20–27]; isolation performance became better. Dynamic behavior of three-parameter system was studied by Brennan [28]; he pointed out that the system had critical damping if additional stiffness was at least eight times that of the main stiffness; the isolator afforded no advantages if the system was excited by white noise. Liu et al. [29] developed a fluid viscous damper based on three-parameter system; it was used to isolate vibration of the whole satellite; the performance was better than traditional isolator. Zhang et al. [30, 31] had a research on the performance of isolation platform based on three-parameter system. If parameters were selected reasonably, the system

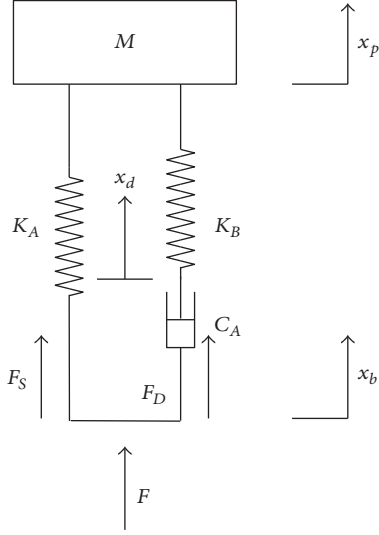


FIGURE 1: Three-parameter system (Zener model).

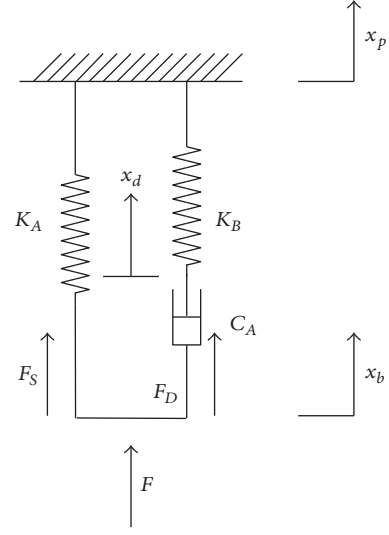


FIGURE 2: Mechanical impedance model.

not only satisfied the requirement for vibration isolation but also guaranteed the stability of closed-loop attitude control system. Wang et al. [32, 33] proposed a method to test stiffness and damping of the isolator based on three-parameter system; an equivalent two-parameter physical system was obtained based on mechanical impedance theory. Wang et al. [34] proposed a method to design isolator based on three-parameter system; optimal damping of the isolator was obtained. Wang et al. [35] had a research on nonlinear three-parameter system. An optimization method called the generalized pattern search (GPS) algorithm was proposed and applied to identify the nonlinear model parameters. Wang et al. [36] pointed out that the usage of nonlinear secondary spring had improved high frequency isolation performance and meanwhile maintained or even reduced its already low resonance amplitude. Shi et al. [37] developed a fluid viscous damper based on three-parameter system; they proposed equivalent stiffness and equivalent damping.

This study is concerned with dynamic behavior of three-parameter system in the time domain and frequency domain. By defining normalized parameters  $\alpha$  and  $\beta$ , analytical normalized model of three-parameter system in the time domain and frequency domain is derived. After that, dynamic behavior in the frequency domain is obtained. System's response in the time domain under different types of excitation is analyzed. Then, we make a comparison research on isolation performance between the case when system has optimal damping and the case when the value of regulatory factor is 1. The results reveal that the second case has better isolation performance; this is a correction of previous studies.

## 2. Normalized Model of Three-Parameter System

**2.1. Modeling of Three-Parameter System.** Three-parameter system is shown in Figure 1.  $M$  is mass of payload.  $K_A$  is main stiffness of the system.  $K_B$  is additional stiffness.  $C_A$

is damping of the system. Figure 2 describes the mechanical impedance model of three-parameter system.  $F$  is total force.  $x_p$  is displacement of the payload.  $x_b$  is displacement of the base.  $x_d$  is displacement of damper node.  $\dot{x}_p$  is velocity of the payload.  $\dot{x}_b$  is velocity of the base.  $\dot{x}_d$  is velocity of damper node.

The equations of motion for this system are

$$\begin{aligned} M\ddot{x}_p + K_A(x_p - x_b) + K_B(x_p - x_d) &= 0, \\ K_B(x_d - x_p) + C_A(\dot{x}_d - \dot{x}_b) &= 0. \end{aligned} \quad (1)$$

Taking the Laplace transform and rearranging,

$$\begin{bmatrix} (Ms^2 + K_A + K_B) & -K_B \\ -K_B & (K_B + C_A s) \end{bmatrix} \begin{bmatrix} x_p \\ x_d \end{bmatrix} = \begin{bmatrix} K_A \\ C_A s \end{bmatrix} x_b. \quad (2)$$

$\delta$  is the stroke,  $\delta = x_b - x_p$ ,  $F_S$  is the static force,  $F_S = K_A \delta$ ,  $F_D$  is the dynamic force,  $F_D = K_B(x_d - x_p)$ , and  $F$  is the total force,  $F = F_S + F_D$ .

**2.2. Complex Mechanical Impedance.** Figure 2 is schematic diagram of mechanical impedance model, one end of the model connected to the ground; therefore  $x_p = 0$ .

The equations of motion for this system can be written as

$$\begin{aligned} K_A x_b + C_A(\dot{x}_b - \dot{x}_d) &= F, \\ C_A(\dot{x}_b - \dot{x}_d) - K_B x_d &= 0. \end{aligned} \quad (3)$$

Taking the Laplace transform and rearranging,

$$\begin{bmatrix} (K_A + C_A s) & -C_A s \\ -C_A s & (K_B + C_A s) \end{bmatrix} \begin{bmatrix} x_b \\ x_d \end{bmatrix} = \begin{bmatrix} 1 \\ 0 \end{bmatrix} F. \quad (4)$$

The complex mechanical impedance  $Z(s)$  can be written as

$$Z(s) = \frac{K_A K_B + (K_A + K_B) C_A s}{K_B + C_A s}. \quad (5)$$

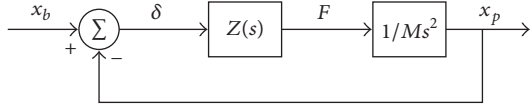


FIGURE 3: General isolator block diagram.

$\omega_1$  is zero (lead) frequency in impedance,  $\omega_1 = K_A K_B / (K_A + K_B) C_A$ .  $\omega_2$  is pole (lag) frequency in impedance,  $\omega_2 = K_B / C_A$ .

Equation (5) becomes

$$Z(s) = K_A \frac{(s/\omega_1 + 1)}{(s/\omega_2 + 1)}. \quad (6)$$

For sinusoidal excitation, the complex mechanical impedance can be written as

$$Z(\omega) = K_A \left[ \frac{1 + \omega^2/\omega_1\omega_2}{1 + \omega^2/\omega_2^2} + \frac{\omega/\omega_1 - \omega/\omega_2}{1 + \omega^2/\omega_2^2} \right]. \quad (7)$$

$\omega_0$  is maximum phase frequency,  $\omega_0 = \sqrt{\omega_1\omega_2}$ ,  $\alpha$  is lead/lag separation ratio,  $\alpha = \sqrt{\omega_2/\omega_1}$ ,  $\Omega$  is normalized frequency,  $\Omega = \omega/\omega_0$ , transformation between  $K_A$ ,  $K_B$ ,  $C_A$  and  $K_A$ ,  $\alpha$ ,  $\omega_0$  can be written as

$$\begin{aligned} \alpha &= \sqrt{1 + \frac{K_B}{K_A}}, \\ \omega_0 &= \frac{K_B}{C_A} \sqrt{\frac{K_A}{K_A + K_B}}, \\ K_B &= K_A (1 - \alpha^2), \\ C_A &= K_A \frac{\alpha^2 - 1}{\alpha\omega_0}. \end{aligned} \quad (8)$$

**2.3. Normalized Open-Loop Transfer Function.** Figure 3 is general isolator block diagram for three-parameter system; the open-loop transfer function can be written as

$$G_{ol}(s) = \frac{K_A}{Ms^2} \frac{1 + s/\omega_1}{1 + s/\omega_2}. \quad (9)$$

$G_{ol}(s)$  is open-loop transfer function.

Figure 4 is Bode plot of the open-loop transfer function. Asymptotic gain is  $K_A/Ms^2$ ; the asymptote intersects with the lateral axis at frequency  $\omega_s$ ,  $\omega_s = \sqrt{K_A/M}$ ; (9) can be written as

$$G_{ol}(s) = \frac{\omega_s^2}{s^2} \frac{(1 + \alpha(s/\omega_0))}{(1 + (1/\alpha)(s/\omega_0))}. \quad (10)$$

$\omega_s^2 = (\omega_0/\alpha)\omega_{c0}$ ,  $\omega_{c0}$  is cross frequency in Bode plot of the open-loop transfer function, and it is marked in Figure 4.  $\beta$  is regulatory factor,  $\beta = \omega_{c0}/\omega_0$ .  $\omega_s$  can be written as  $\omega_s = \omega_0 \sqrt{\beta/\alpha}$ ;  $G_{ol}(s)$  can be written as

$$G_{ol}(s) = \frac{\beta \omega_0^2}{\alpha s^2} \frac{(1 + \alpha(s/\omega_0))}{(1 + (1/\alpha)(s/\omega_0))}. \quad (11)$$

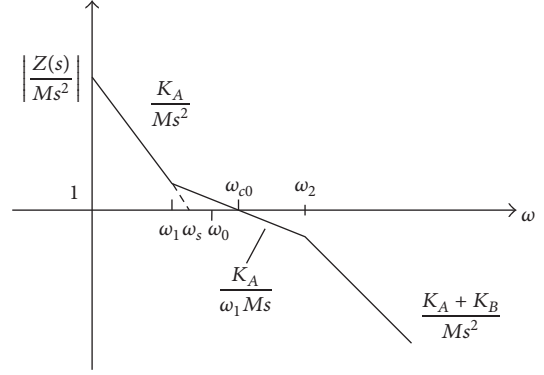


FIGURE 4: Bode plot of open-loop transfer function.

$\omega_0$ ,  $\alpha$ ,  $\beta$  can be written as

$$\begin{aligned} \omega_0 &= \sqrt{\frac{K_A K_B^2}{(K_A + K_B) C_A^2}}, \\ \alpha &= \sqrt{\frac{K_A + K_B}{K_A}}, \\ \beta &= \frac{(K_A + K_B) C_A^2}{M K_B^2} \sqrt{\frac{K_A + K_B}{K_A}}. \end{aligned} \quad (12)$$

$K_A$ ,  $K_B$ ,  $C_A$  can be written as

$$\begin{aligned} K_A &= M\omega_0^2 \frac{\beta}{\alpha}, \\ K_B &= M\omega_0^2 (\alpha^2 - 1) \frac{\beta}{\alpha}, \\ C_A &= M\omega_0 (\alpha^2 - 1) \frac{\beta}{\alpha^2}. \end{aligned} \quad (13)$$

When  $\beta = 1$ ,  $K_A$ ,  $K_B$ ,  $C_A$  can be written as

$$\begin{aligned} K_A &= \frac{M\omega_0^2}{\alpha}, \\ K_B &= M\omega_0^2 \frac{(\alpha^2 - 1)}{\alpha}, \\ C_A &= \frac{M\omega_0 (\alpha^2 - 1)}{\alpha^2}. \end{aligned} \quad (14)$$

If parameters of physical model ( $K_A$ ,  $K_B$ ,  $C_A$ ) or normalized parameters ( $\alpha$ ,  $\beta$ ) are known, transmissibility curve can be obtained; it is convenient to design three-parameter system if we use normalized model.

**2.4. Normalized Close-Loop Transfer Function.** According to block diagram of open-loop transfer function, isolation transfer function can be written as

$$G_{xp-xb}(s) = \frac{x_p(s)}{x_b(s)}. \quad (15)$$

$G_{xp\_xb}(s)$  is open-loop transfer function. Equation (15) can be written as

$$G_{xp\_xb}(s) = \frac{G_{ol}(s)}{1 + G_{ol}(s)}. \quad (16)$$

Defining  $\psi = s/\omega_0$ , (16) can be written as

$$G_{xp\_xb}(\psi) = \frac{C(\psi)}{R(\psi)} = \frac{1 + \alpha\sqrt{\beta}\psi}{1 + \alpha\sqrt{\beta}\psi + \alpha\psi^2 + \sqrt{\beta}\psi^3}. \quad (17)$$

$C(\psi)$  is numerator,  $C(\psi) = 1 + \alpha\sqrt{\beta}\psi$ , and  $R(\psi)$  is denominator,  $R(\psi) = 1 + \alpha\sqrt{\beta}\psi + \alpha\psi^2 + \sqrt{\beta}\psi^3$ .

Equation (17) can be written as

$$G_{xp\_xb}(s) = \frac{1 + (\alpha\sqrt{\beta}/\omega_0)s}{1 + (\alpha\sqrt{\beta}/\omega_0)s + (\alpha/\omega_0^2)s^2 + (\sqrt{\beta}/\omega_0^3)s^3}. \quad (18)$$

When  $\beta = 1$ , (17) can be written as

$$G_{xp\_xb}(\psi) = \frac{C(\psi)}{R(\psi)} = \frac{1 + \alpha\psi}{1 + \alpha\psi + \alpha\psi^2 + \psi^3}. \quad (19)$$

### 3. Dynamic Behavior in the Frequency Domain

3.1. *Root Locus.* According to (17), characteristic equation can be written as

$$1 + \alpha\sqrt{\beta}\psi + \alpha\psi^2 + \sqrt{\beta}\psi^3 = 0, \quad (20)$$

$$\left( \alpha = \sqrt{\frac{K_A + K_B}{K_A}} > 1 \right).$$

The shape of root locus will be diverse because of different values of  $\alpha$ .

Equation (20) can be written as

$$\frac{1}{\sqrt{\beta}} \frac{1 + \alpha\psi^2}{\psi^3 + \alpha\psi} = -1. \quad (21)$$

Figure 5 is root locus for  $\alpha < 3$ . Figure 6 is root locus for  $\alpha = 3$ . Figure 7 is root locus for  $\alpha > 3$ . Root locus is located on the left side of lateral axis; it means that the system is stable. Each root locus has three branches corresponding to three characteristic roots.

(1) If  $\alpha < 3$ , the system has real poles and conjugate poles. When the system has real poles, it means that the system has critical damping. Free vibration mode of the system is shown in Figure 8 (red line), which has obvious oscillation.

(2) If  $\alpha = 3$ , root locus intersects with lateral axis at point  $(-1, 0)$ . Real poles mean that the system has critical damping. Free vibration mode is shown in Figure 8 (green line); the oscillation is not obvious.

(3) If  $\alpha > 3$ , the system has real poles and conjugate poles. Real poles mean that the system has critical damping. Free

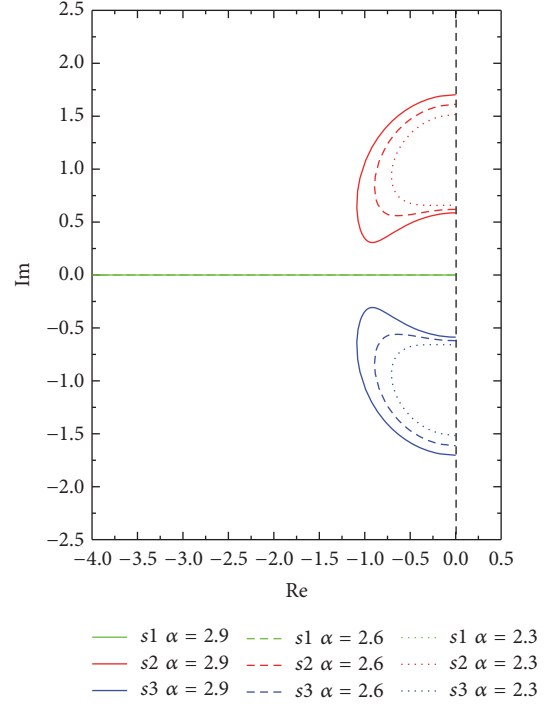


FIGURE 5: Root locus ( $\alpha < 3$ ).

vibration mode of the system is shown in Figure 8 (blue line); oscillation decays with time quickly.

When  $\beta = 1$ , denominator of close-loop transfer function can be written as

$$R(\psi) = \psi^3 + \alpha\psi^2 + \alpha\psi + 1. \quad (22)$$

Equation (22) can be written as

$$R(\psi) = (\psi + 1) [\psi^2 + \psi(\alpha - 1) + 1]. \quad (23)$$

For  $\beta = 1$ , free vibration mode of the system will be analyzed for different values of  $\alpha$ .

(1) If  $\alpha > 3$ ,  $\Delta > 0$ , and  $\Delta = (\alpha - 1)^2 - 4$ , there are three different real poles

$$r_1 = -1,$$

$$r_2 = \frac{-(\alpha - 1) + \sqrt{(\alpha - 1)^2 - 4}}{2}, \quad (24)$$

$$r_3 = \frac{-(\alpha - 1) - \sqrt{(\alpha - 1)^2 - 4}}{2}.$$

These three real poles mean that the system has three different free vibration modes

$$c_1(t) = e^{-t},$$

$$c_2(t) = e^{((- \alpha - 1) + \sqrt{(\alpha - 1)^2 - 4})/2 t}, \quad (25)$$

$$c_3(t) = e^{((- \alpha - 1) - \sqrt{(\alpha - 1)^2 - 4})/2 t}.$$

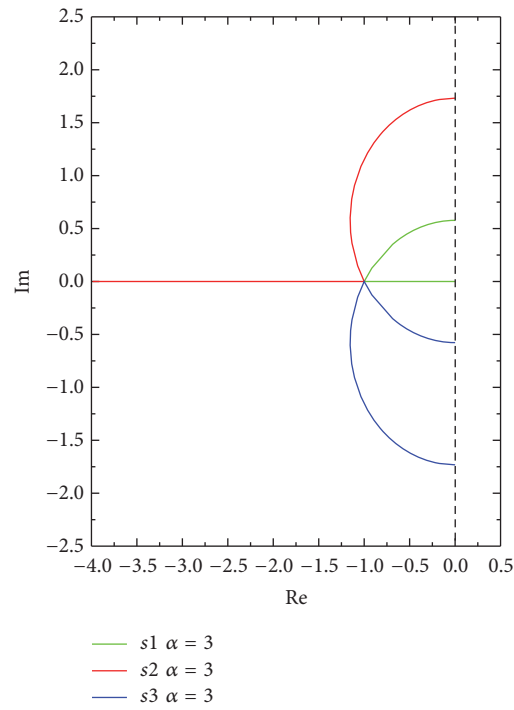


FIGURE 6: Root locus ( $\alpha = 3$ ).

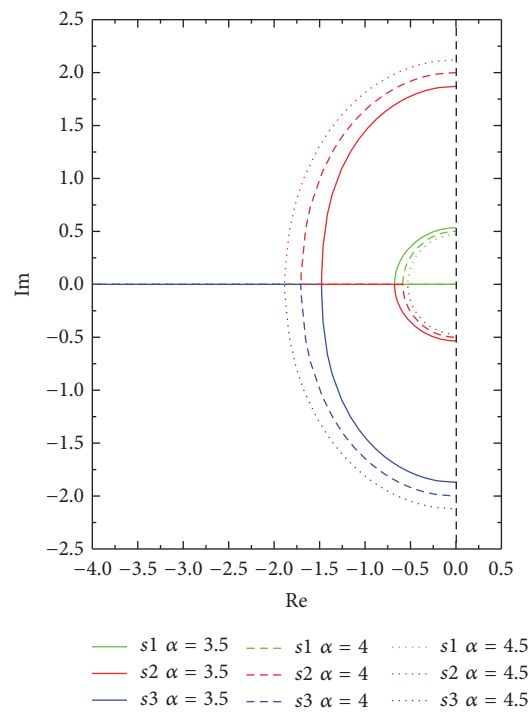


FIGURE 7: Root locus ( $\alpha > 3$ ).

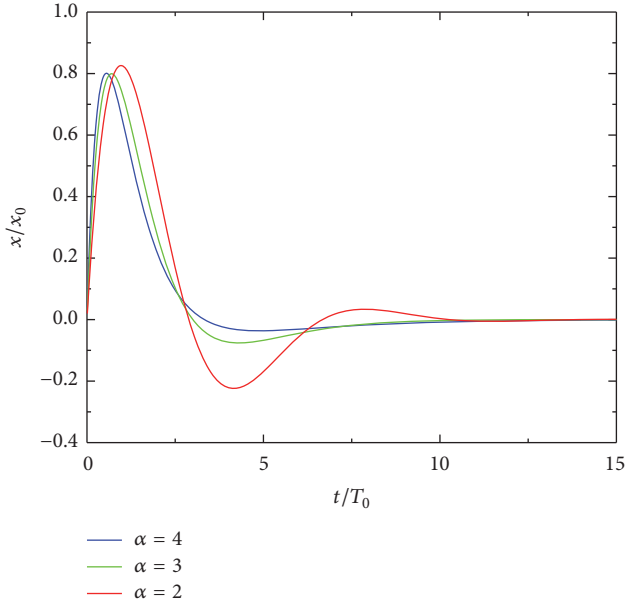


FIGURE 8: Free motion modes for different values of  $\alpha$ .

For unit pulse excitation, response in the time domain can be written as

$$c(t) = \alpha \left[ \frac{1/\alpha + r_1}{(r_1 - r_2)(r_1 - r_3)} e^{r_1 t} + \frac{1/\alpha + r_2}{(r_2 - r_1)(r_2 - r_3)} e^{r_2 t} + \frac{1/\alpha + r_3}{(r_3 - r_1)(r_3 - r_2)} e^{r_3 t} \right]. \quad (26)$$

(2) If  $\alpha = 3$  and  $\Delta = 0$ , there is a single real pole

$$r = -1. \quad (27)$$

$$c(t) = \alpha \left\{ \frac{1/\alpha - 1}{((\alpha - 1)/2 - 1)^2 + 1 - ((\alpha - 1)/2)^2} e^{-t} + \frac{1}{\sqrt{1 - ((\alpha - 1)/2)^2}} \left[ \frac{(1/\alpha - (\alpha - 1)/2)^2 + 1 - ((\alpha - 1)/2)^2}{(1 - (\alpha - 1)/2)^2 + 1 - ((\alpha - 1)/2)^2} \right]^{1/2} e^{-(\alpha-1)/2 t} \sin \left[ \sqrt{1 - \left( \frac{\alpha - 1}{2} \right)^2} t + \varphi \right] \right\}. \quad (31)$$

$\varphi$  is phase angle.

According to (23), zero-pole plots for different values of  $\alpha$  can be obtained.

Figures 9, 10, and 11 are zero-pole plots for different values of  $\alpha$ .

If  $\alpha = 2$ , there is a real pole and a pair of conjugate poles. The real pole means that the system has critical damping. It can be seen from Figure 9 that the system has dominant poles; it means that free vibration modes corresponding to conjugate poles are main modes. If  $\alpha = 3$ , there is a real pole and a pair of conjugate poles; it can be seen from Figure 10

It means that the system has a single free vibration mode; for unit pulse excitation, response in the time domain can be written as

$$c(t) = \alpha \left[ \frac{1 - \alpha}{2} t^2 + \alpha t \right] e^{-t}. \quad (28)$$

(3) If  $1 < \alpha < 3$  and  $\Delta < 0$ , there is a real pole and a pair of conjugate poles

$$r_1 = -1, \\ r_2 = \frac{-(\alpha - 1) + j\sqrt{4 - (\alpha - 1)^2}}{2}, \\ r_3 = \frac{-(\alpha - 1) - j\sqrt{4 - (\alpha - 1)^2}}{2}. \quad (29)$$

Free vibration modes can be written as

$$c_1(t) = e^{-t}, \\ c_2(t) = e^{-(\alpha-1)/2 t} \left( \cos \frac{\sqrt{(\alpha-1)^2 - 4}}{2} t + \sin \frac{\sqrt{(\alpha-1)^2 - 4}}{2} t \right). \quad (30)$$

For unit pulse excitation, response in the time domain can be written as

that imaginary part of conjugate poles is very small. If  $\alpha = 4$ , there are three different real poles which means the system has critical damping.

3.2. *Nyquist Diagram.* Open-loop transfer function can be written as

$$G_{ol}(\psi) = \frac{1 + \alpha\sqrt{\beta}\psi}{\sqrt{\beta}\psi^3 + \alpha\psi^2}. \quad (32)$$

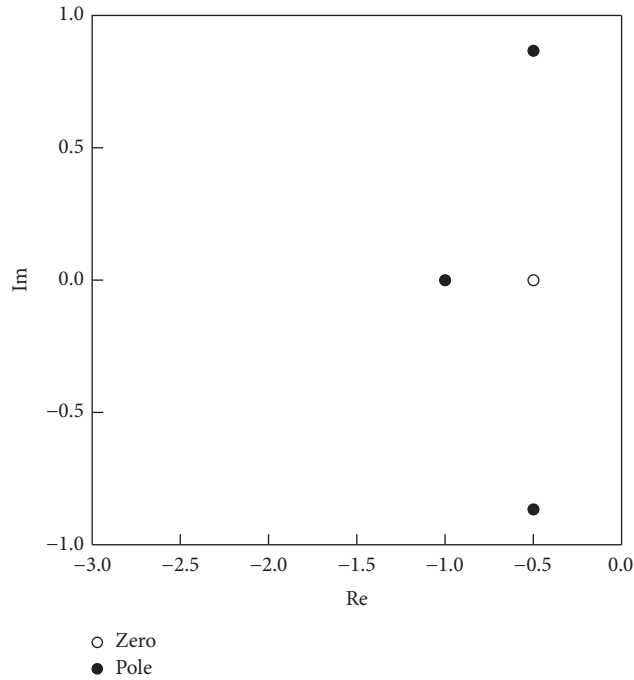


FIGURE 9: Zero-pole plot ( $\alpha = 2, \beta = 1$ ).

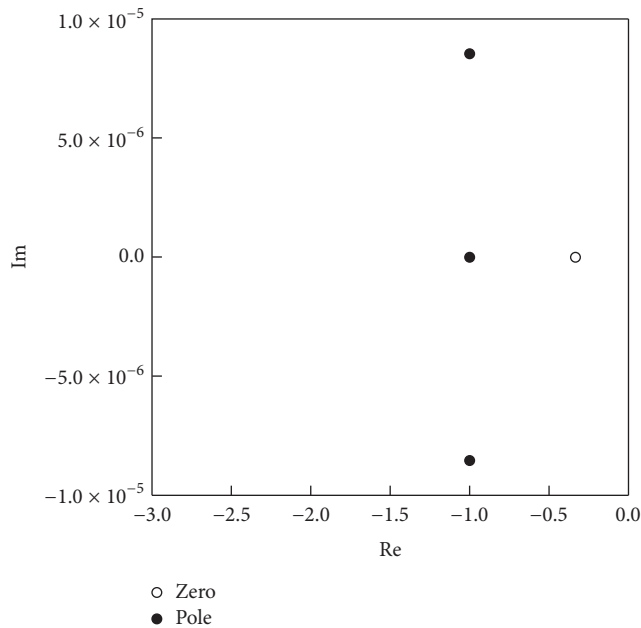


FIGURE 10: Zero-pole plot ( $\alpha = 3, \beta = 1$ ).

Nyquist diagram can be obtained according to the open-loop transfer function.

Figures 12, 13, 14, and 15 are the Nyquist diagrams for different values of  $\alpha$ . It can be concluded from Nyquist diagram that phase margin has the maximum value when  $\beta = 1$ ; phase margin increases with the value of  $\alpha$ , which means that stability of system increases too.

*3.3. Amplitude-Frequency Characteristic and Phase-Frequency Characteristic.* Transmissibility is an important index for isolation performance of the isolator. In this section, amplitude-frequency characteristic and phase-frequency characteristic of three-parameter system will be analyzed.

Figures 16–19 have described three-parameter system’s amplitude-frequency characteristic and phase-frequency

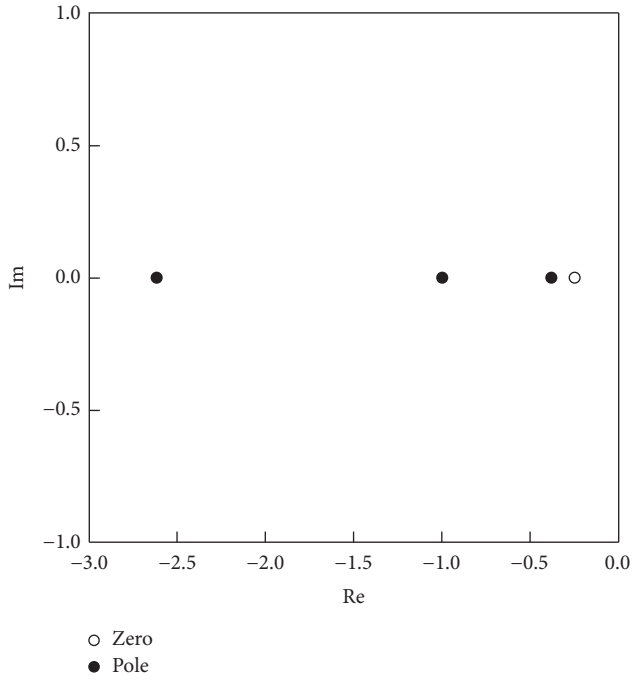


FIGURE 11: Zero-pole plot ( $\alpha = 4, \beta = 1$ ).

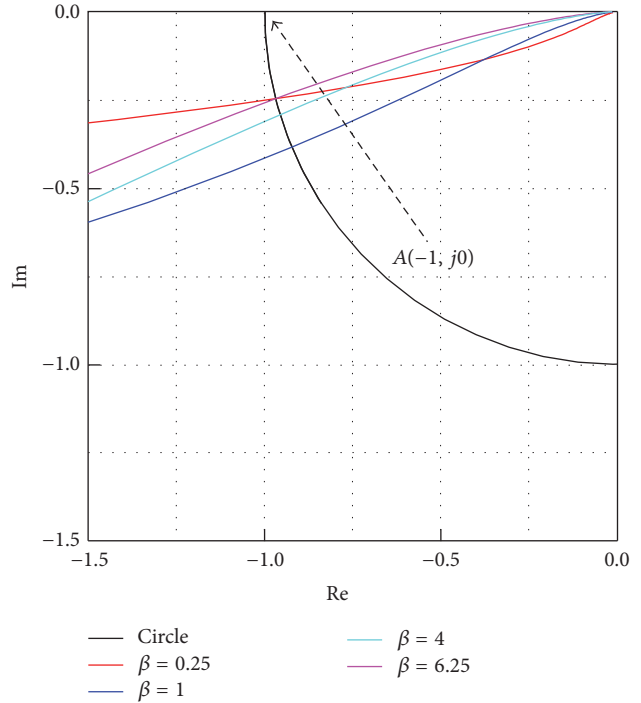


FIGURE 13: Nyquist diagram ( $\alpha = 1.5$ ).

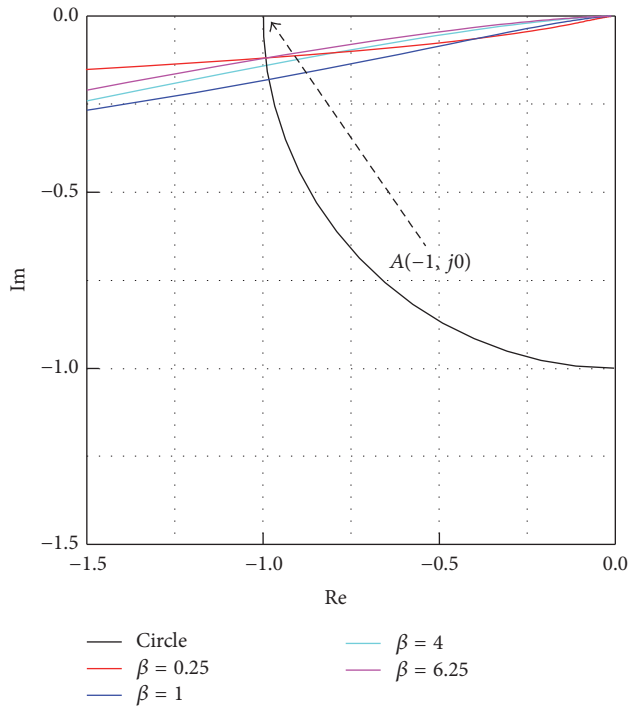


FIGURE 12: Nyquist diagram ( $\alpha = 1.2$ ).

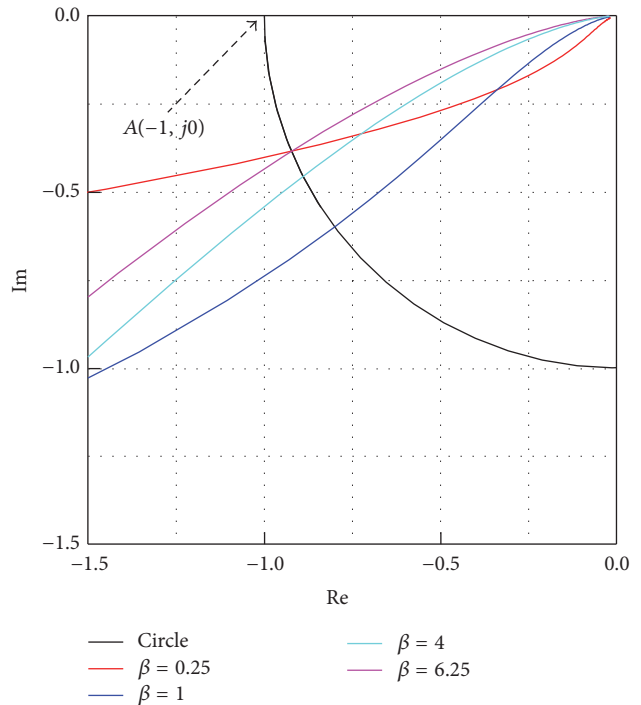
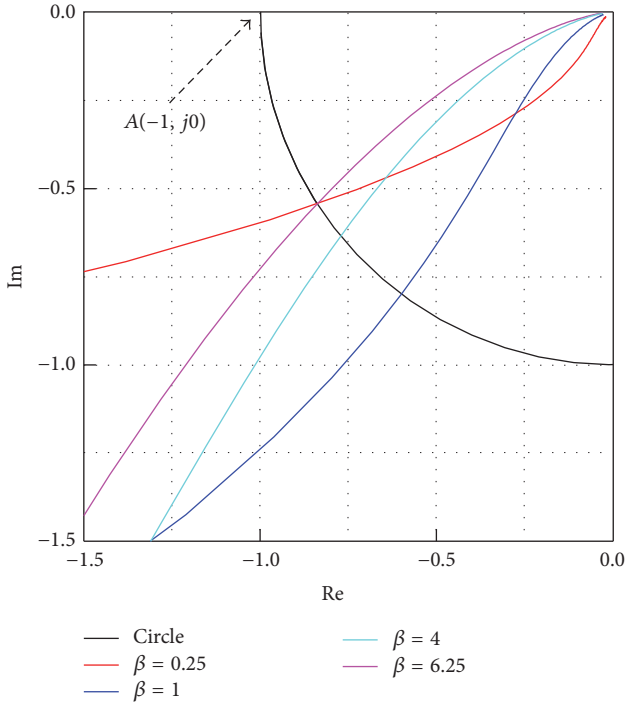
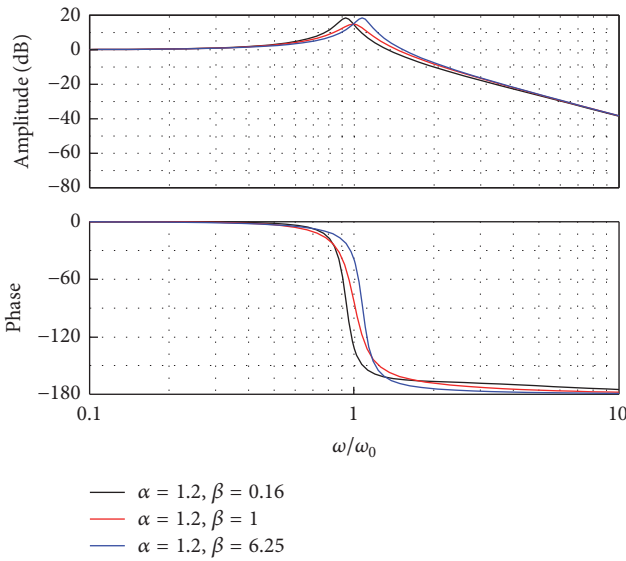


FIGURE 14: Nyquist diagram ( $\alpha = 2$ ).

characteristic for different values of  $\alpha$  and  $\beta$ . It can be concluded that when  $\beta = 1$ , system has a minimum resonance peak compared with the case when  $\beta < 1$  and  $\beta > 1$ ; resonance peak decreases with the value of  $\alpha$ . The case when  $\beta = 1$  is very important; it can be used to design an isolator which has minimum resonance peak.

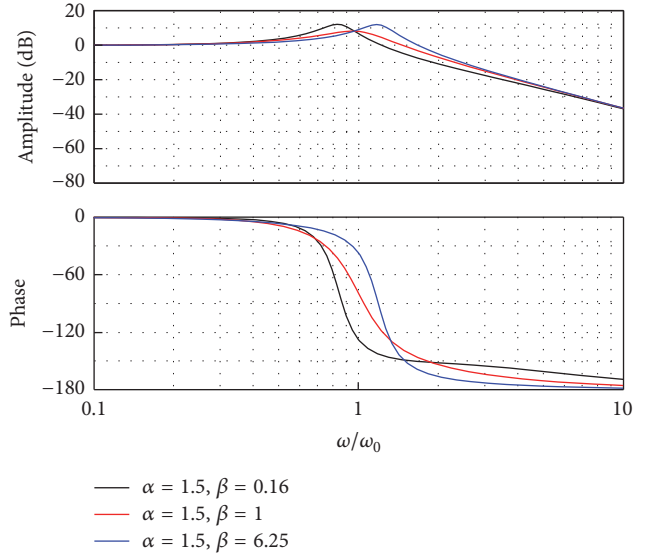
#### 4. Dynamic Behavior in the Time Domain

4.1. Response in the Time Domain under Different Types of Excitations. When system is applied to different types of excitation, response in the time domain will be different. In

FIGURE 15: Nyquist diagram ( $\alpha = 3$ ).FIGURE 16: Amplitude-frequency characteristic and phase-frequency characteristic ( $\alpha = 1.2$ ,  $\beta = 0.16, 1, 6.25$ ).

this section, response in the time domain for different types of excitation will be analyzed.

(1) *Step Excitation.* As has been analyzed in Section 3.1, characteristic root has relationship with the value of  $\Delta$ . In this section, only the case when system has a real root and conjugate roots will be analyzed.

FIGURE 17: Amplitude-frequency characteristic and phase-frequency characteristic ( $\alpha = 1.5$ ,  $\beta = 0.16, 1, 6.25$ ).

For step excitation, output function can be written as

$$C(\psi) = \frac{1}{\sqrt{\beta}} \frac{\alpha\sqrt{\beta}\psi + 1}{\psi(\psi - \psi_1)(\psi - \psi_2)(\psi - \psi_3)}, \quad (33)$$

$$\left(\psi = \frac{s}{\omega_0}\right).$$

Equation (33) has three characteristic roots  $\psi_1, \psi_2, \psi_3$  which can be written as

$$\begin{aligned} \psi_1 &= c, \\ \psi_2 &= a + bi, \\ \psi_3 &= a - bi. \end{aligned} \quad (34)$$

$c$  is real root,  $a$  is real part of complex root, and  $b$  is the imaginary part of complex root. Response in the time domain can be derived by using inverse Laplace transform method; it can be written as

$$c(t) = \frac{1}{\sqrt{\beta}} \left( A_0 + A_1 e^{ct} + 2Ue^{at} \cos bt - 2Ve^{at} \sin bt \right),$$

$$A_0 = -\frac{1}{c(a^2 + b^2)},$$

$$A_1 = \frac{1/c + \alpha\sqrt{\beta}}{(c^2 - a^2) + b^2},$$

$$U = \frac{p_1 p_3 + p_2 p_4}{p_3^2 + p_4^2},$$

$$V = \frac{p_1 p_4 - p_2 p_3}{p_3^2 + p_4^2},$$

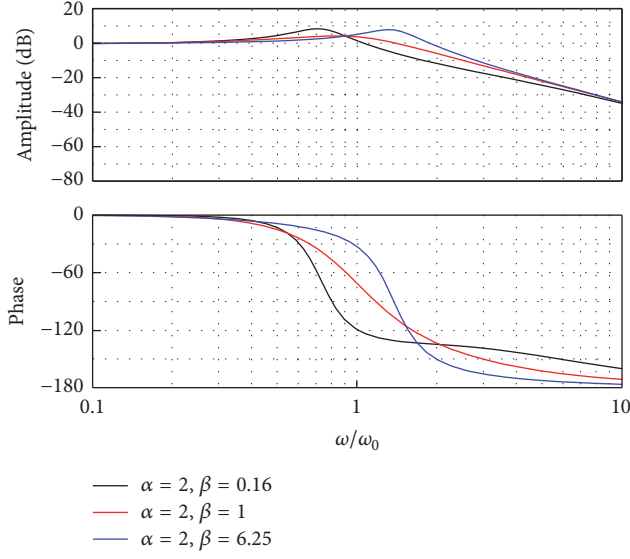


FIGURE 18: Amplitude-frequency characteristic and phase-frequency characteristic ( $\alpha = 2, \beta = 0.16, 1, 6.25$ ).

$$\begin{aligned}
 p_1 &= ma + 1, \\
 p_2 &= mb, \\
 p_3 &= -4ab^2 + 2cb^2, \\
 p_4 &= 2ab(a - c) - 2b^3, \\
 m &= \alpha\sqrt{\beta}.
 \end{aligned} \tag{35}$$

(2) *Slope Excitation*. For slope excitation, output function can be written as

$$C(\psi) = \frac{1}{\sqrt{\beta}} \frac{\alpha\sqrt{\beta}\psi + 1}{\psi^2(\psi - \psi_1)(\psi - \psi_2)(\psi - \psi_3)}. \tag{36}$$

Three characteristic roots are  $\psi_1, \psi_2, \psi_3$ , which can be written as

$$\begin{aligned}
 \psi_1 &= c, \\
 \psi_2 &= a + bi, \\
 \psi_3 &= a - bi.
 \end{aligned} \tag{37}$$

$c$  is real root,  $a$  is real part of complex root, and  $b$  is the imaginary part of complex root. Response in the time domain can be derived by using inverse Laplace transform method; it can be written as

$$\begin{aligned}
 c(t) &= \frac{1}{\sqrt{\beta}} \left\{ A_0 t + A_1 + A_2 e^{-ct} \right. \\
 &\quad \left. + 2e^{at} (-F \sin bt + E \cos bt) \right\}, \\
 A_0 &= -\frac{1}{c(a^2 + b^2)},
 \end{aligned}$$

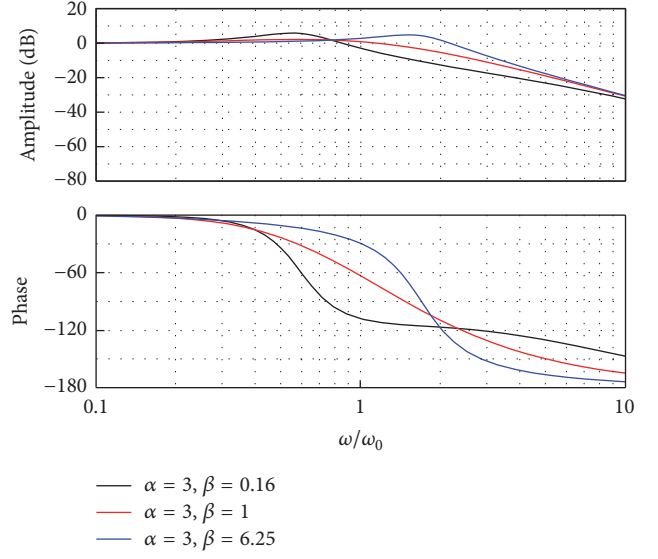


FIGURE 19: Amplitude-frequency characteristic and phase-frequency characteristic ( $\alpha = 3, \beta = 0.16, 1, 6.25$ ).

$$A_1 = \frac{-mc(a^2 + b^2) - (a^2 + b^2 + 2ac)}{c^2(a^2 + b^2)^2},$$

$$A_2 = \frac{mc + 1}{c^2[(c - a)^2 + b^2]},$$

$$p_1 = ma + 1,$$

$$p_2 = mb,$$

$$p_3 = -2b^2(a^2 - b^2) - 4ab^2(a - c),$$

$$p_4 = 2b(a^2 - b^2)(a - c) - 4ab^3,$$

$$E = \frac{p_1 p_3 + p_2 p_4}{p_3^2 + p_4^2},$$

$$F = \frac{p_2 p_3 - p_1 p_4}{p_3^2 + p_4^2},$$

$$m = \alpha\sqrt{\beta}.$$

(38)

(3) *Acceleration Excitation*. For acceleration excitation, output function can be written as

$$C(\psi) = \frac{1}{\sqrt{\beta}} \frac{\alpha\sqrt{\beta}\psi + 1}{\psi^3(\psi - \psi_1)(\psi - \psi_2)(\psi - \psi_3)}. \tag{39}$$

Three characteristic roots are  $\psi_1, \psi_2, \psi_3$ , which can be written as

$$\begin{aligned}
 \psi_1 &= c, \\
 \psi_2 &= a + bi, \\
 \psi_3 &= a - bi.
 \end{aligned} \tag{40}$$

$c$  is real root,  $a$  is real part of complex root, and  $b$  is the imaginary part of complex root.

Response in the time domain can be derived by using inverse Laplace transform method; it can be written as

$$\begin{aligned}
 c(t) &= \frac{1}{\sqrt{\beta}} \left[ \frac{1}{2} A_0 t^2 + A_1 t + A_2 + A_3 e^{ct} + 2e^{at} (-F \sin bt + E \cos bt) \right], \\
 A_0 &= -\frac{1}{c(a^2 + b^2)}, \\
 A_1 &= \frac{-mc(a^2 + b^2) - (a^2 + b^2 + 2ac)}{c^2(a^2 + b^2)^2}, \\
 A_2 &= \frac{(c + 2a)[-c(a^2 + b^2)] - (a^2 + b^2 + 2ac) \{m[-c(a^2 + b^2)] - (a^2 + b^2 + 2ac)\}}{[-c(a^2 + b^2)]^3}, \\
 E &= \frac{p_1 p_3 + p_2 p_4}{p_3^2 + p_4^2}, \\
 F &= \frac{p_2 p_3 - p_1 p_4}{p_3^2 + p_4^2}, \\
 p_1 &= -\frac{ma + 1}{2b}, \\
 p_2 &= -\frac{m}{2}, \\
 p_3 &= b(a - c)(3a^2 - b^2) - ab(3b^2 - a^2), \\
 p_4 &= b^2(3a^2 - b^2) + a(a - c)(3b^2 - a^2), \\
 m &= \alpha\sqrt{\beta}.
 \end{aligned} \tag{41}$$

(4) *Impulse Excitation.* For impulse excitation, output function can be written as

$$C(\psi) = \frac{1}{\sqrt{\beta}} \frac{\alpha\sqrt{\beta}\psi + 1}{(\psi - \psi_1)(\psi - \psi_2)(\psi - \psi_3)}. \tag{42}$$

Three characteristic roots are  $\psi_1, \psi_2, \psi_3$ , which can be written as

$$\begin{aligned}
 \psi_1 &= c, \\
 \psi_2 &= a + bi, \\
 \psi_3 &= a - bi.
 \end{aligned} \tag{43}$$

$c$  is real root,  $a$  is real part of complex root, and  $b$  is the imaginary part of complex root. Response in the time domain can be derived by using inverse Laplace transform method; it

can be written as

$$\begin{aligned}
 c(t) &= \frac{1}{\sqrt{\beta}} \{-2Ee^{ct} + 2e^{at} (-F \sin bt + E \cos bt)\}, \\
 p_1 &= -a + c, \\
 p_2 &= b, \\
 p_3 &= -a^2 - b^2 + ac, \\
 p_4 &= bc, \\
 E &= \frac{mp_4 - p_2}{2(p_1 p_4 - p_2 p_3)}, \\
 F &= \frac{mp_3 - p_1}{2(p_1 p_4 - p_2 p_3)}, \\
 m &= \alpha\sqrt{\beta}.
 \end{aligned} \tag{44}$$

(5) *Harmonic Excitation.* For harmonic excitation, output function can be written as

$$C(\psi) = \frac{1}{\sqrt{\beta}} \frac{\alpha\sqrt{\beta}\psi + 1}{(\psi^2 + \omega^2)(\psi - \psi_1)(\psi - \psi_2)(\psi - \psi_3)}. \quad (45)$$

Three characteristic roots are  $\psi_1, \psi_2, \psi_3$ , which can be written as

$$\begin{aligned} \psi_1 &= c, \\ \psi_2 &= a + bi, \\ \psi_3 &= a - bi. \end{aligned} \quad (46)$$

$c$  is real root,  $a$  is real part of complex root, and  $b$  is the imaginary part of complex root. Response in the time domain can be derived by using inverse Laplace transform method; it can be written as

$$\begin{aligned} c(t) &= \frac{A\omega}{\sqrt{\beta}} \left[ \frac{mc + 1}{[(c - a)^2 + b^2](c^2 + \omega^2)} e^{ct} \right. \\ &\quad + 2e^{at} (-F \sin bt + E \cos bt) \\ &\quad \left. + 2(N \sin \omega t + M \cos \omega t) \right], \\ E &= \frac{p_1 p_3 + p_2 p_4}{p_3^2 + p_4^2}, \\ F &= \frac{p_2 p_3 - p_1 p_4}{p_3^2 + p_4^2}, \\ M &= \frac{p_5 p_7 + p_6 p_8}{p_7^2 + p_8^2}, \\ N &= \frac{p_6 p_7 - p_5 p_8}{p_7^2 + p_8^2}, \\ p_1 &= ma + 1, \\ p_2 &= mb, \\ p_3 &= -2b^2(a^2 - b^2 + \omega^2), \\ p_4 &= -4ab^3 + 2b(a - c)(a^2 - b^2 + \omega^2), \\ p_5 &= 1, \\ p_6 &= -m\omega, \\ p_7 &= -2\omega^2(a^2 + b^2 - \omega^2) - 4ac\omega^2, \\ p_8 &= -4a\omega^3 + 2\omega c(a^2 + b^2 - \omega^2), \\ m &= \alpha\sqrt{\beta}. \end{aligned} \quad (47)$$

#### 4.2. Simulation Results

(1) *Step Excitation.* Figures 20–23 are responses in the time domain for step excitation. Lateral axis represents normalized

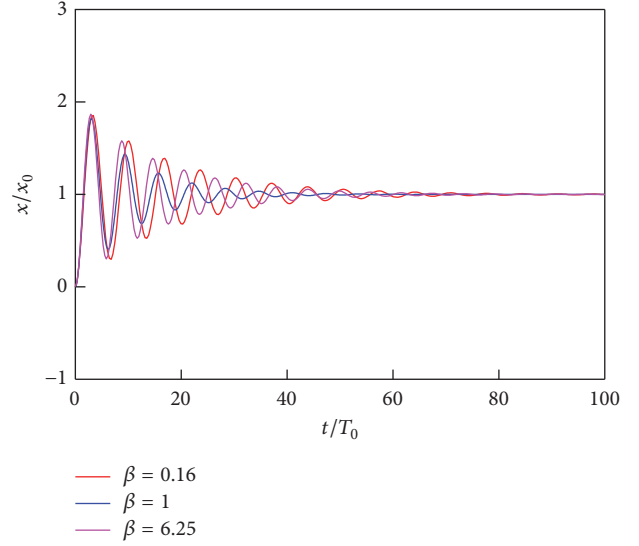


FIGURE 20: Response in the time domain ( $\alpha = 1.2$ ,  $\beta = 0.16, 1, 6.25$ ).

time. It can be concluded that the system has the shortest settling time when  $\beta = 1$  compared with other values of  $\beta$ . Settling time decreases with the value of  $\alpha$ .

(2) *Slop Excitation.* Figures 24–27 are the responses in the time domain for slop excitation; lateral axis represents normalized time. It can be seen from these figures that response in the time domain has a oscillation at the beginning. Duration of oscillation decreases with the value of  $\alpha$ ; then, response is consistent with the input function.

(3) *Acceleration Excitation.* Figures 28–31 are the responses in the time domain for acceleration excitation. Lateral axis represents normalized time. It can be seen from these figures that response in the time domain is consistent with the input function; this trend has no relationship with the values of  $\alpha$  and  $\beta$ .

(4) *Impulse Excitation.* Figures 32–35 are the responses in the time domain for impulse excitation. Lateral axis represents normalized time. When the value of  $\alpha$  is small, response in the time domain has an obvious oscillation. Oscillation decays with the value of  $\alpha$ . The system has the shortest settling time when  $\beta = 1$  compared with the case when  $\beta < 1$  and  $\beta > 1$ .

4.3. *A Comparison Study on the Case When the System Has Optimal Damping and the Case When  $\beta = 1$ .* The system has minimum resonance peak when system has optimal damping. It can be proved that all the transmissibility curves will intersect at one point; this point is resonance peak when the system has optimal damping. In this section, a comparison study on the responses in the time domain at two frequencies ( $\omega/\omega_0 = 2$  and the resonance peak frequency) is made. According to (17), transmissibility can be written as

$$|G(j\Omega)| = \sqrt{\frac{1 + \alpha^2 \beta \Omega^2}{(1 - \alpha \Omega^2)^2 + \beta \Omega^2 (\alpha - \Omega^2)^2}}. \quad (48)$$

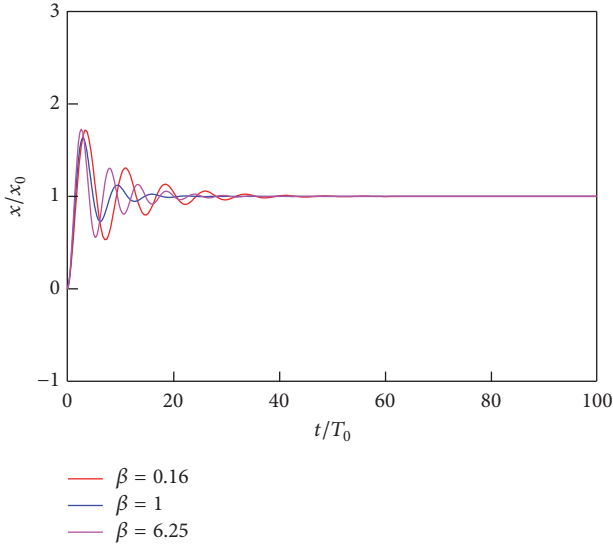


FIGURE 21: Response in the time domain ( $\alpha = 1.5$ ,  $\beta = 0.16, 1, 6.25$ ).

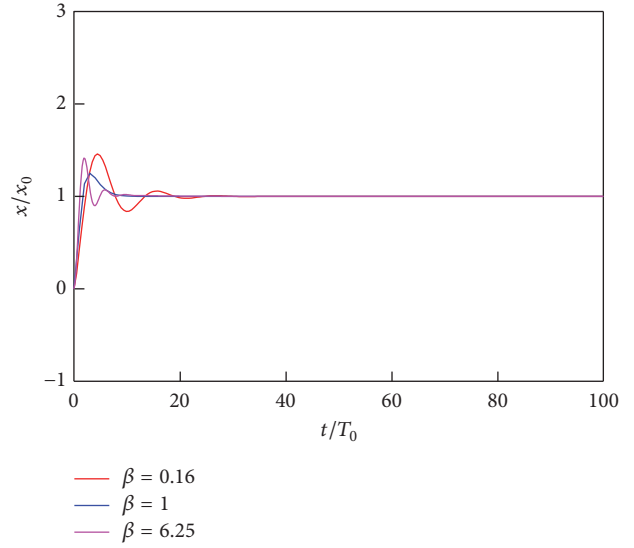


FIGURE 23: Response in the time domain ( $\alpha = 3$ ,  $\beta = 0.16, 1, 6.25$ ).

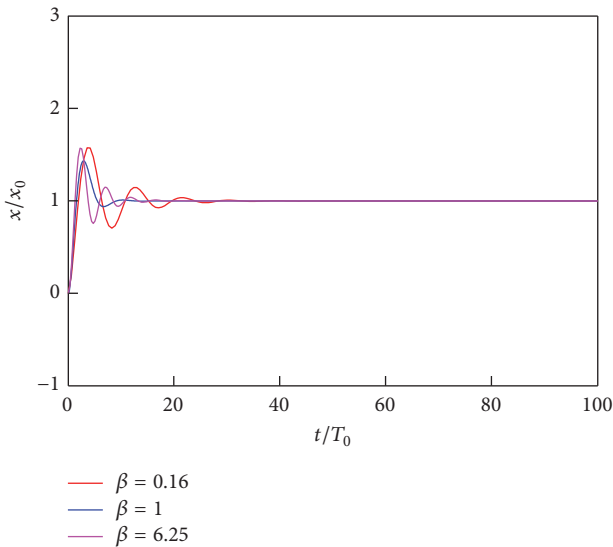


FIGURE 22: Response in the time domain ( $\alpha = 2$ ,  $\beta = 0.16, 1, 6.25$ ).

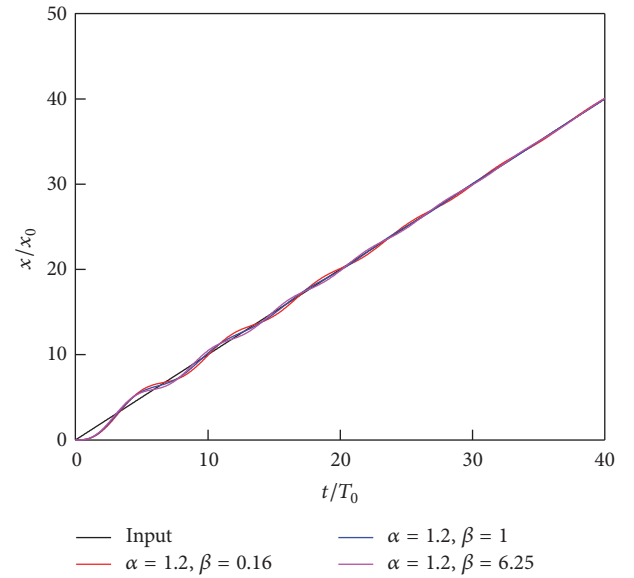


FIGURE 24: Response in the time domain ( $\alpha = 1.2$ ,  $\beta = 0.16, 1, 6.25$ ).

$\psi = s/\omega_0$ ,  $s = j\omega$ , and, defining  $\Omega = \omega/\omega_0$ ,  $\Omega$  is normalized frequency.

$|G(j\Omega_1)| = |G(j\Omega_2)|$ . Resonance frequency when system has optimal damping can be obtained

$$\Omega_0 = \sqrt{\frac{2\alpha}{1 + \alpha^2}}. \quad (49)$$

Taking the derivative of (48) and taking result into (49), the value of  $\beta$  can be obtained.

$$\beta = \frac{1 + \alpha^2}{2\alpha}. \quad (50)$$

Figures 38–41 are the responses in the time domain for sinusoidal excitation. Two cases are analyzed; the first case is when  $\beta = 1$  and the second case is when system has optimal damping.

Figure 36 is response in the time domain when  $\omega/\omega_0 = 2$  and  $\alpha = 2$ ; there are three curves; the black line represents input function, red line represents response in the time domain when  $\beta = 1$ , and blue line represents response in the time domain when system has optimal damping. According to (50),  $\beta = 1.25$ . Longitudinal axis represents displacement transmissibility. It can be seen from the figure that transmissibility when  $\beta = 1$  is nearly the same as the case when  $\beta = 1.25$ . Figure 37 is response at resonance frequency.

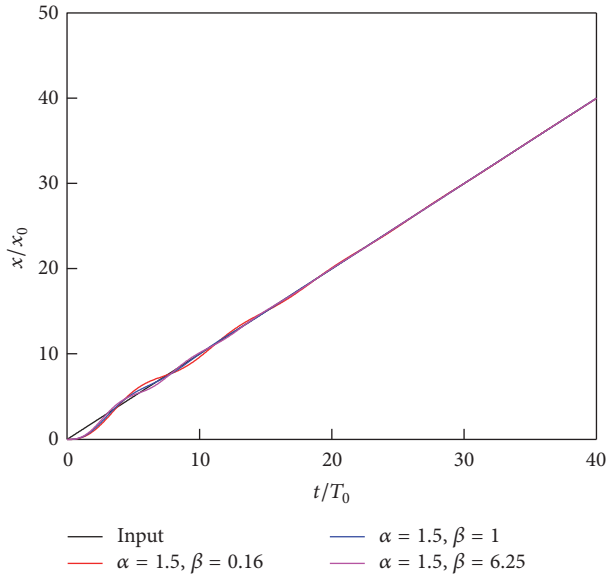


FIGURE 25: Response in the time domain ( $\alpha = 1.5, \beta = 0.16, 1, 6.25$ ).

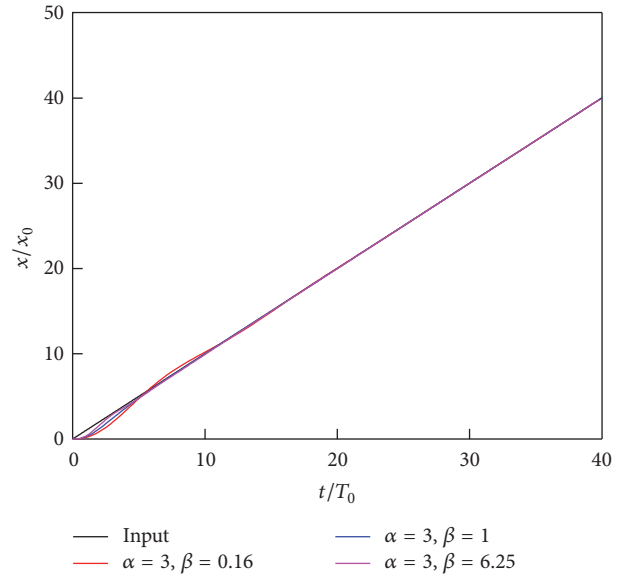


FIGURE 27: Response in the time domain ( $\alpha = 3, \beta = 0.16, 1, 6.25$ ).

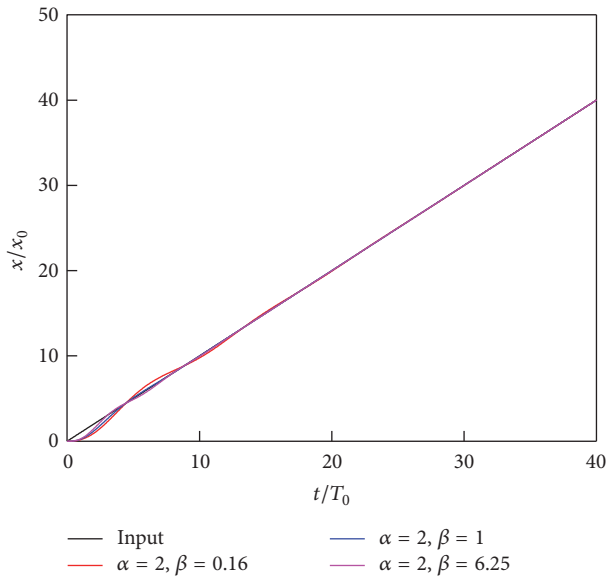


FIGURE 26: Response in the time domain ( $\alpha = 2, \beta = 0.16, 1, 6.25$ ).

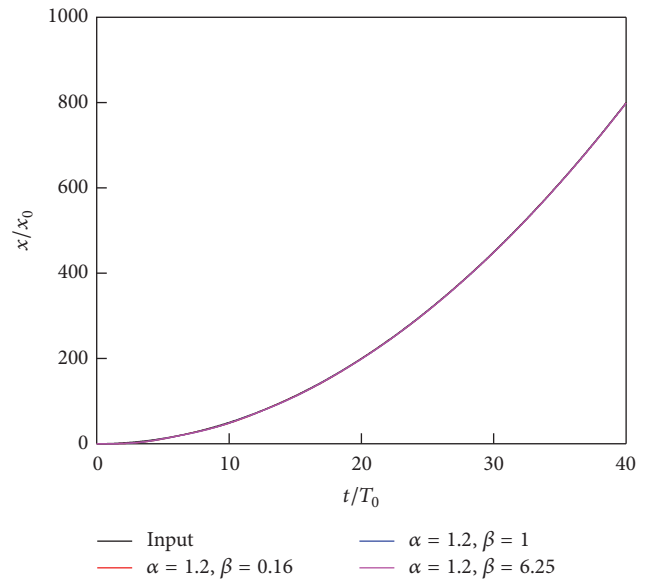


FIGURE 28: Response in the time domain ( $\alpha = 1.2, \beta = 0.16, 1, 6.25$ ).

It can be seen from the figure that the two cases ( $\beta = 1$  and  $\beta = 1.25$ ) nearly have the same transmissibility.

Figure 38 is response in the time domain when  $\omega/\omega_0 = 2$  and  $\alpha = 3$ . According to (50),  $\beta = 1.6667$ . It can be seen from the figure that the system has better isolation performance when  $\beta = 1$  than the case when  $\beta = 1.6667$ . Figure 39 is response at resonance frequency. It can be seen from the figure that the two cases ( $\beta = 1$  and  $\beta = 1.6667$ ) nearly have the same transmissibility.

Figure 40 is response in the time domain when  $\omega/\omega_0 = 2$  and  $\alpha = 4$ . According to (50),  $\beta = 2.215$ . It can be seen from the figure that the system has better isolation performance

when  $\beta = 1$  than the case when  $\beta = 2.215$ . Figure 41 is response at resonance frequency. It can be seen from the figure that the two cases ( $\beta = 1$  and  $\beta = 2.215$ ) nearly have the same transmissibility.

With the increasing values of  $\alpha$ , isolation performance at  $\omega/\omega_0 = 2$  becomes better, while the two cases (the case when  $\beta = 1$  and the case when the system has the optimal damping) nearly have the same transmissibility at resonance frequency.

### 5. Transmissibility of Three-Parameter System

Transmissibility is an important index for isolation performance. In this section, transmissibility of three-parameter

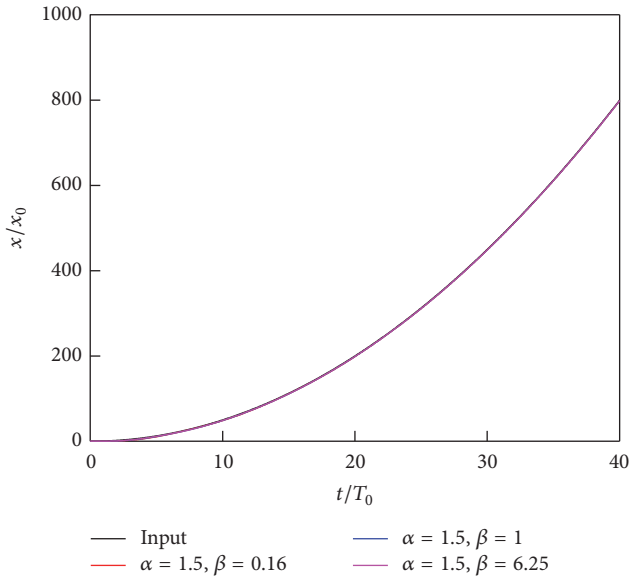


FIGURE 29: Response in the time domain ( $\alpha = 1.5, \beta = 0.16, 1, 6.25$ ).

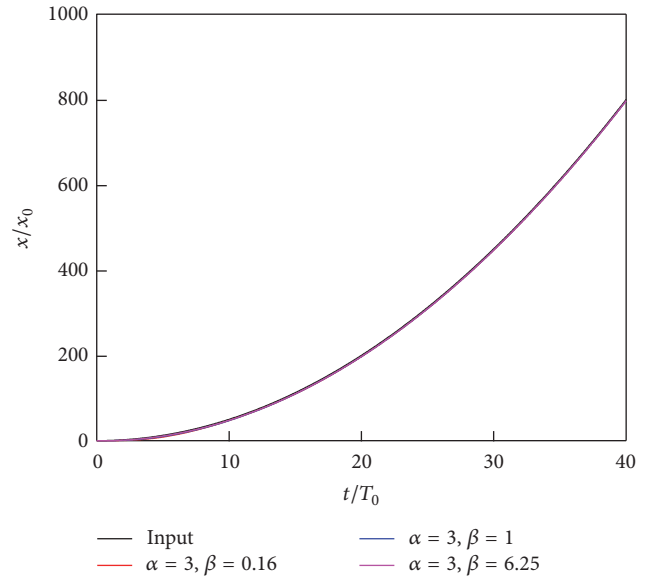


FIGURE 31: Response in the time domain ( $\alpha = 3, \beta = 0.16, 1, 6.25$ ).

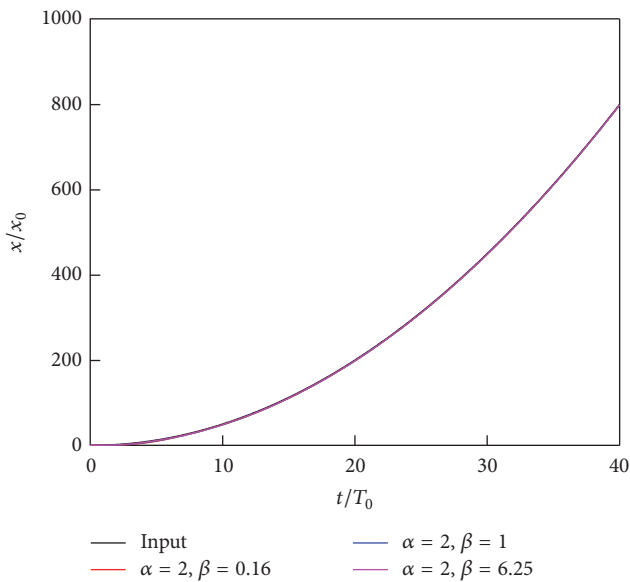


FIGURE 30: Response in the time domain ( $\alpha = 2, \beta = 0.16, 1, 6.25$ ).

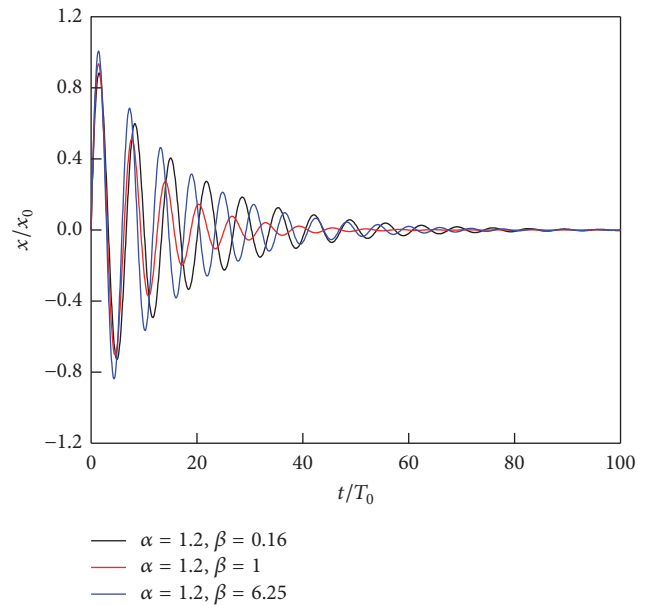


FIGURE 32: Response in the time domain ( $\alpha = 1.2, \beta = 0.16, 1, 6.25$ ).

system will be discussed. Two cases are analyzed; the first case is when  $\beta = 1$ ; the second case is when the system has optimal damping.

Figure 42 is transmissibility of three-parameter system ( $\alpha = 2$ ). Lateral axis represents normalized frequency. Black line is transmissibility for the case when  $\beta = 1$ , resonance frequency is 0.83, and amplification factor of resonance peak is 1.6823. Red line is transmissibility for the case when system has optimal damping, resonance frequency is 0.89, and amplification factor of resonance peak is 1.6667. It is shown that amplification factors of two cases are nearly the

same (1.6823 and 1.6667). Besides, the two cases nearly have the same transmissibility in the high frequency domain.

Figure 43 is transmissibility of three-parameter system ( $\alpha = 3$ ). Lateral axis represents normalized frequency. Black line is transmissibility for the case when  $\beta = 1$ , resonance frequency is 0.58, and amplification factor of resonance peak is 1.299. Red line is transmissibility for the case when system has optimal damping, resonance frequency is 0.77, and amplification factor of resonance peak is 1.25. It is shown that amplification factors of two cases are nearly the same (1.299 and 1.25), while transmissibility characteristics of two

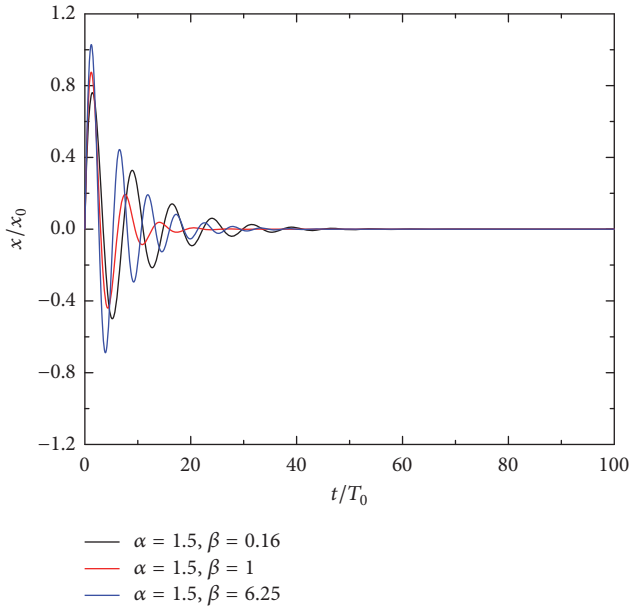


FIGURE 33: Response in the time domain ( $\alpha = 1.5$ ,  $\beta = 0.16, 1, 6.25$ ).

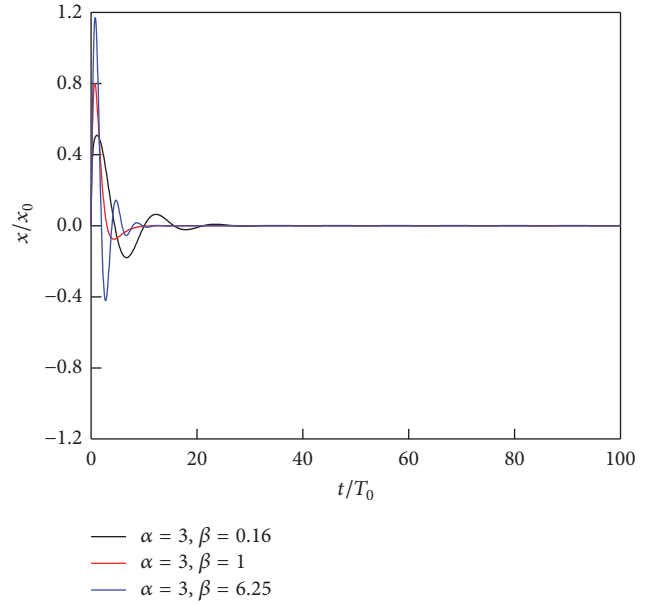


FIGURE 35: Response in the time domain ( $\alpha = 3$ ,  $\beta = 0.16, 1, 6.25$ ).

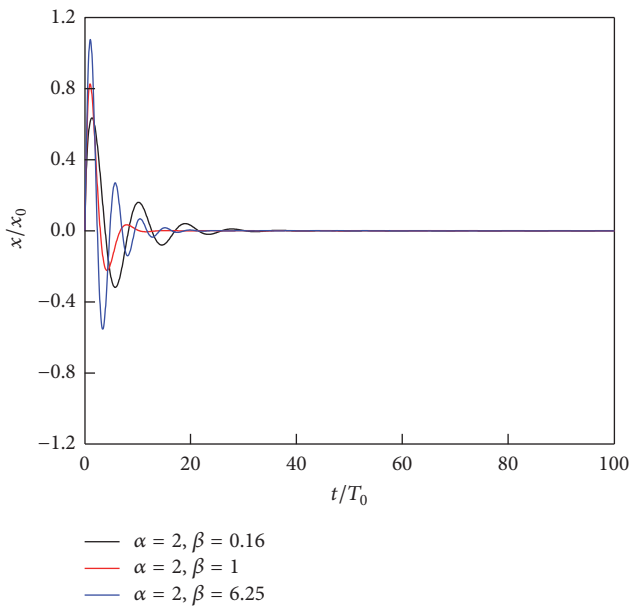


FIGURE 34: Response in the time domain ( $\alpha = 2$ ,  $\beta = 0.16, 1, 6.25$ ).

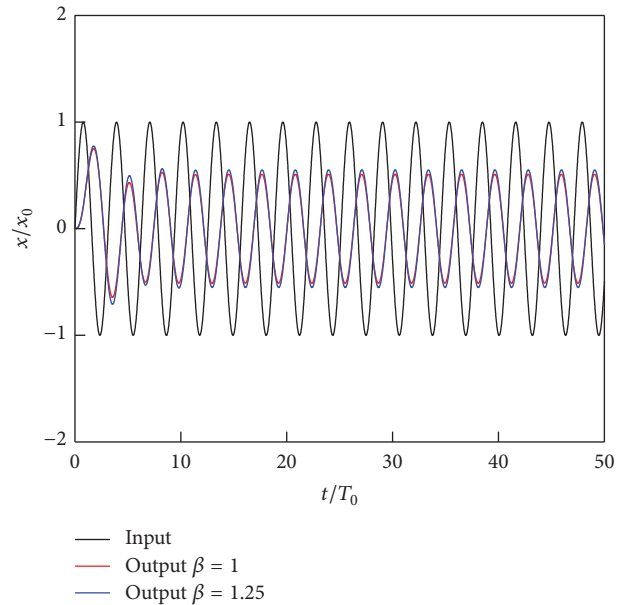


FIGURE 36: Response in the time domain ( $\alpha = 2$ ,  $\beta = 1, 1.25$ ,  $\omega/\omega_0 = 2$ ).

cases are different in the high frequency domain. Isolation performance when  $\beta = 1$  is better than the case when system has optimal damping.

Figure 44 is transmissibility of three-parameter system ( $\alpha = 4$ ). Lateral axis represents normalized frequency. Black line is transmissibility for the case when  $\beta = 1$ , resonance frequency is 0.44, and amplification factor of resonance peak is 1.1978. Red line is transmissibility for the case when system has optimal damping, resonance frequency is 0.69, and amplification factor of resonance peak is 1.3333. It is

shown that amplification factors of two cases are nearly the same (1.1978 and 1.3333), while transmissibility characteristics of two cases are different in the high frequency domain. Isolation performance when  $\beta = 1$  is better than the case when system has optimal damping.

It can be concluded that the case when  $\beta = 1$  has better isolation performance in the high frequency domain, but amplification factors of two cases are nearly the same.

Figure 45 is a comparison of resonance factors between the case when  $\beta = 1$  and the case when system has optimal

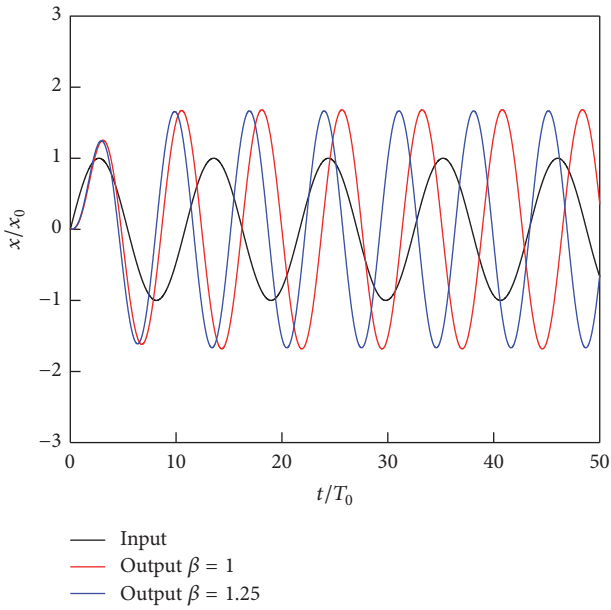


FIGURE 37: Response in the time domain ( $\alpha = 2$ ,  $\beta = 1, 1.25$ , at resonance frequency).

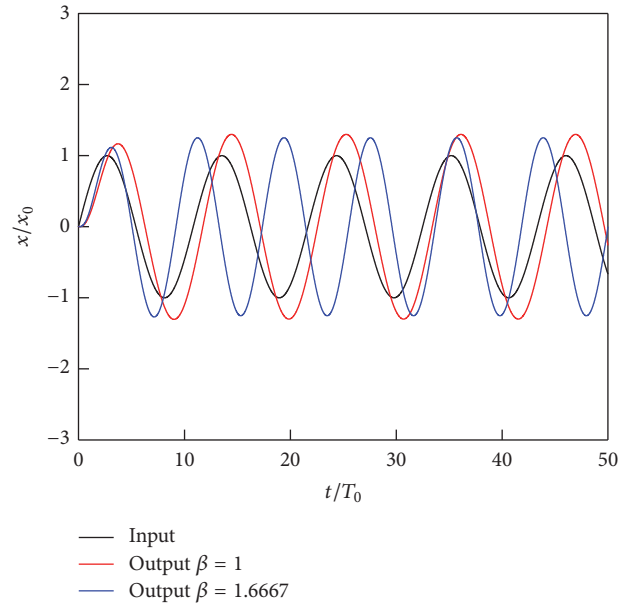


FIGURE 39: Response in the time domain ( $\alpha = 3$ ,  $\beta = 1, 1.6667$ , at resonance frequency).

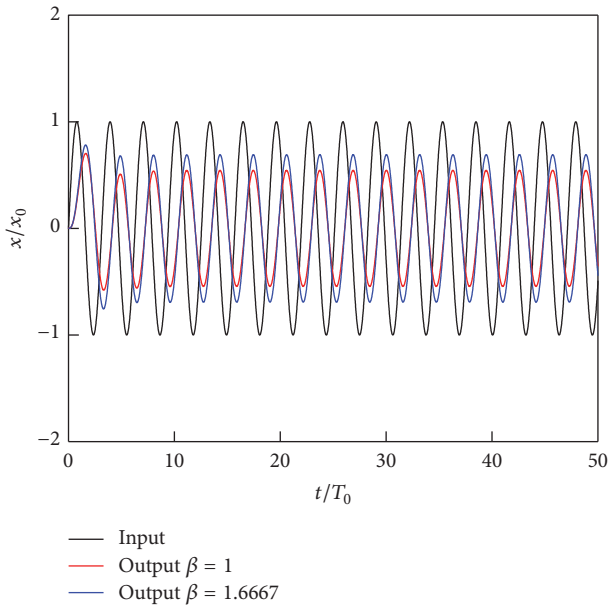


FIGURE 38: Response in the time domain ( $\alpha = 3$ ,  $\beta = 1, 1.6667$ ,  $\omega/\omega_0 = 2$ ).

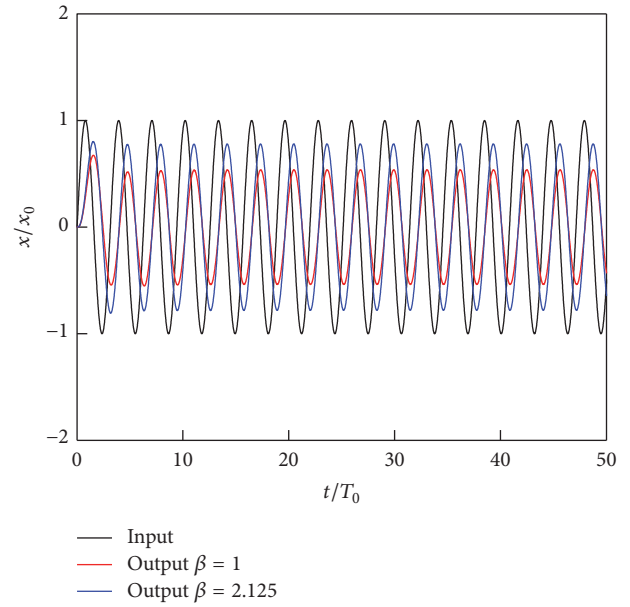


FIGURE 40: Response in the time domain ( $\alpha = 4$ ,  $\beta = 1, 2.125$ ,  $\omega/\omega_0 = 2$ ).

damping. Lateral axis represents the value of  $\alpha$ . If the value of  $\alpha$  is small, there is no difference between these two cases. If the value of  $\alpha$  is large, difference between two cases is obvious; the second case has smaller resonance factor than the first case.

Figures 46–50 are the transmissibility surfaces for different values of  $\alpha$  and  $\beta$ . The first axis represents normalized frequency ( $\omega/\omega_0$ ), the second axis represents the value of  $\alpha$ , and the third axis represents transmissibility. Figure 46 is transmissibility surface when  $\beta = 1$ . It can be seen from the

figure that the largest amplification factor is less than 10, and amplification factor decreases with the value of  $\alpha$ . Figure 47 is transmissibility surface when  $\alpha = 1.2$ . It can be seen from the figure that the largest amplification factor is less than 10; with the increasing values of  $\beta$ , amplification factor decreases, but this trend is not obvious. Figure 48 is transmissibility surface when  $\alpha = 1.5$ . It can be seen from the figure that the largest amplification factor is less than 4; amplification factor decreases obviously compared with the case when  $\alpha = 1.2$ .

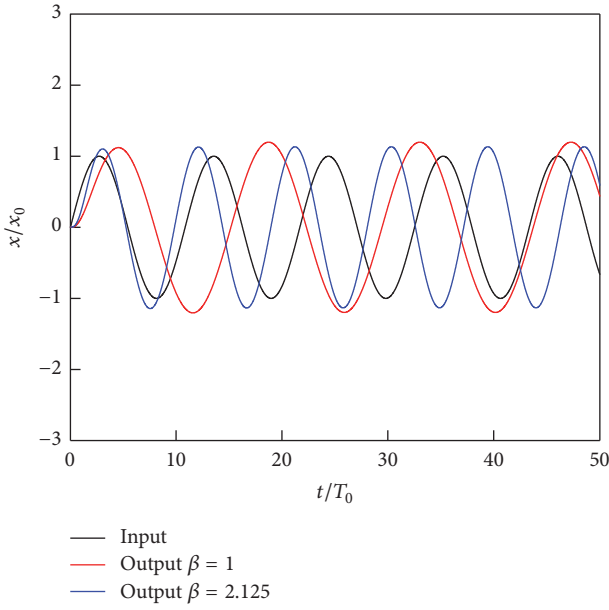


FIGURE 41: Response in the time domain ( $\alpha = 4$ ,  $\beta = 1, 2.125$ , at resonance frequency).

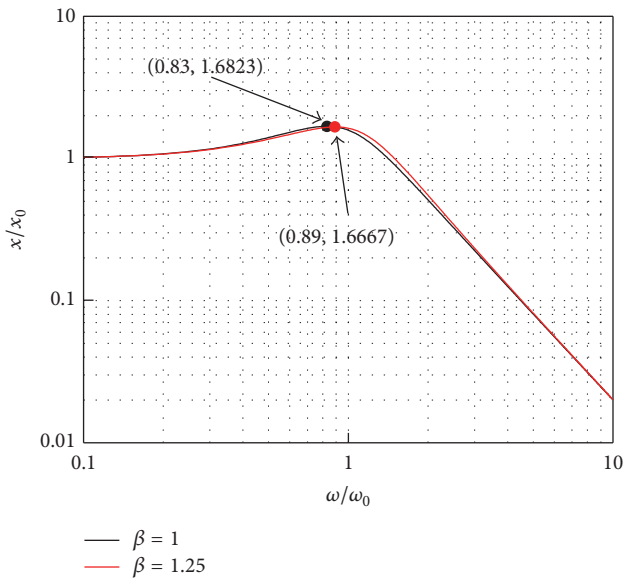


FIGURE 42: Transmissibility ( $\alpha = 2$ ,  $\beta = 1, 1.25$ ).

Figure 49 is transmissibility surface when  $\alpha = 2$ . It can be seen from the figure that the largest amplification factor is less than 3; amplification factor decreases obviously compared with the case when  $\alpha = 1.5$ . Figure 50 is transmissibility surface when  $\alpha = 3$ . It can be seen from the figure that the largest amplification factor is less than 3; amplification factor decreases obviously compared with the case when  $\alpha = 2$ . It can be concluded that amplification factor decreases with the value of  $\alpha$ .

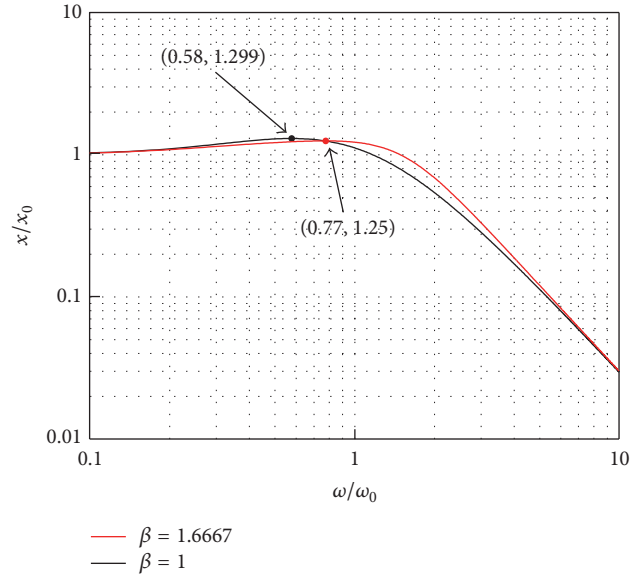


FIGURE 43: Transmissibility ( $\alpha = 3$ ,  $\beta = 1, 1.6667$ ).

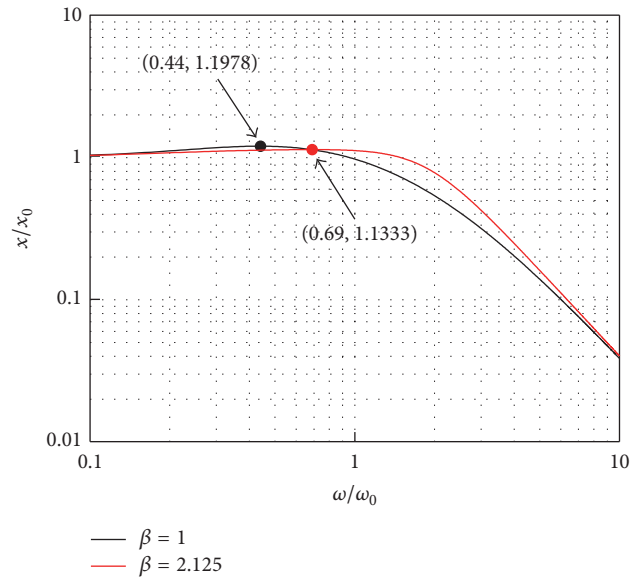


FIGURE 44: Transmissibility ( $\alpha = 4$ ,  $\beta = 1, 2.215$ ).

## 6. Conclusion

In this paper, dynamic behavior of three-parameter system has been studied by using normalized model. Different types of excitation have been considered in order to analyze response in the time domain. In order to analyze dynamic behavior in the frequency domain, root locus and phase margin of the system have been analyzed. The results reveal the following:

- (1) System under impulse excitation and step excitation has the shortest settling time for the response in the time domain when the value of regulatory factor is 1; meanwhile, the system has the largest phase margin.

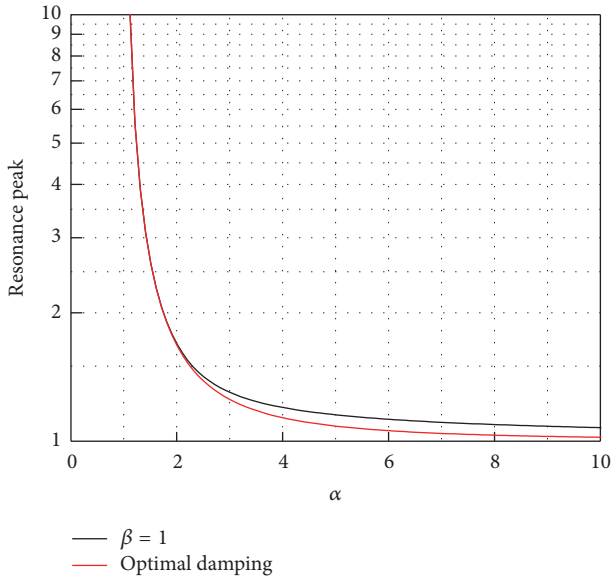


FIGURE 45: Comparison of resonance peaks.

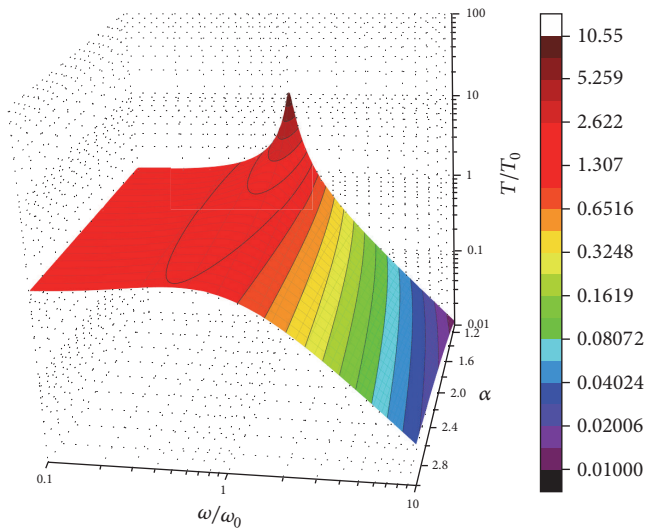


FIGURE 46: Transmissibility surface ( $\beta = 1$ ).

- (2) A comparison study for isolation performance at resonance frequency is made between the case when system has optimal damping and the case when  $\beta = 1$ . If stiffness ratio is small, isolation performances of two cases are nearly the same; if stiffness ratio is large, isolation performance of the first case is much better. Previous researches showed that isolation performance of the second case was much better.
- (3) Amplification factor decreases with the value of  $\alpha$ . Because parameter  $\alpha$  is the function of stiffness ratio, it means that the system has small amplification factor when stiffness ratio is large.

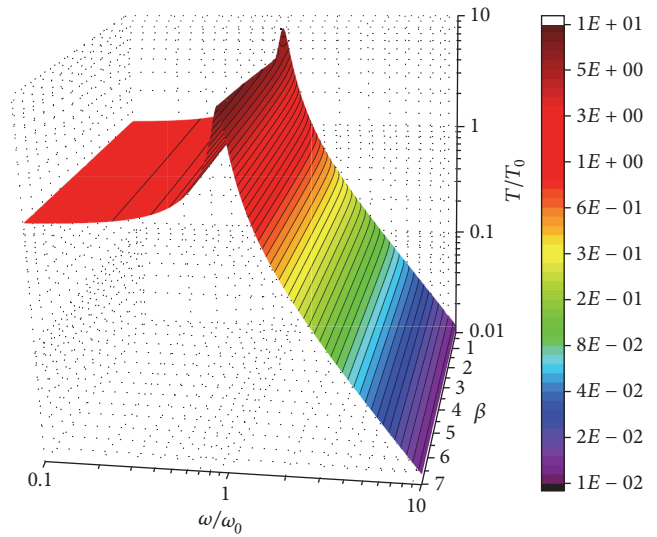


FIGURE 47: Transmissibility surface ( $\alpha = 1.2, \beta = 0.2-7$ ).

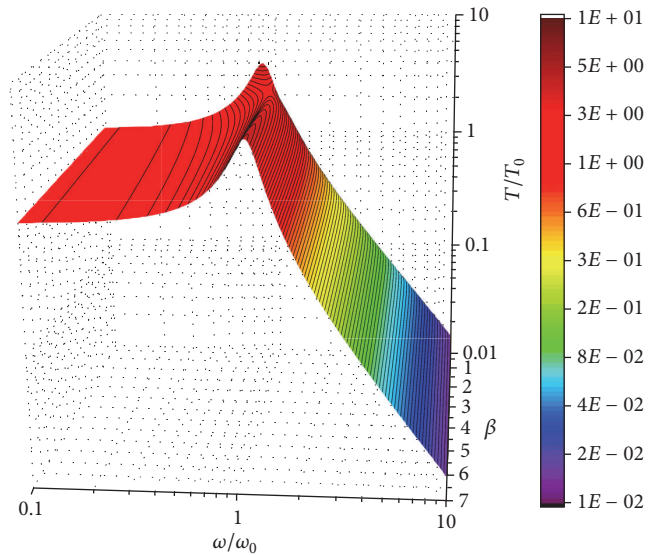


FIGURE 48: Transmissibility surface ( $\alpha = 1.5, \beta = 0.2-7$ ).

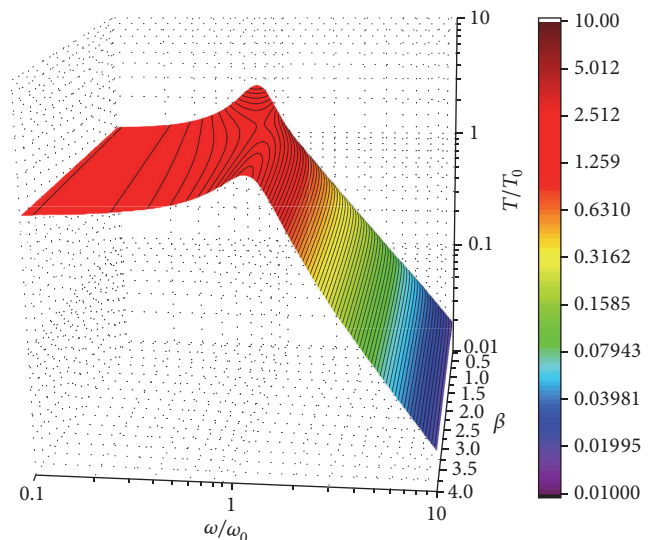


FIGURE 49: Transmissibility surface ( $\alpha = 2, \beta = 0.2-7$ ).

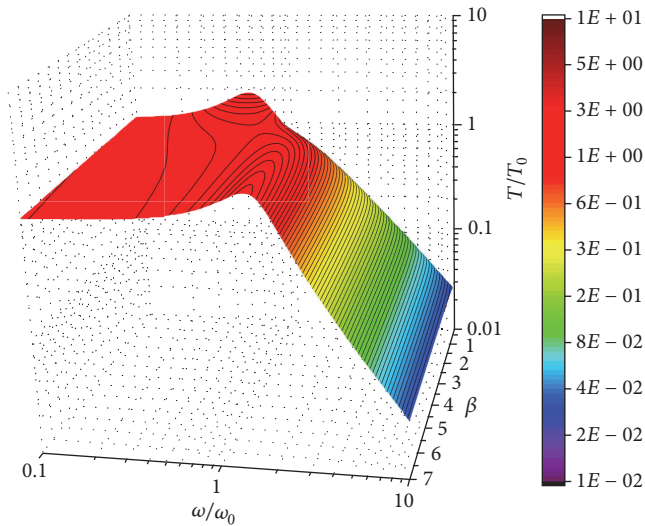


FIGURE 50: Transmissibility surface ( $\alpha = 3$ ,  $\beta = 0.2-7$ ).

- (4) The normalized model has two dimensionless parameters  $\alpha$  and  $\beta$ ; it can make the dynamic model of three-parameter system more concise than the physical parameter model; therefore, dynamic behavior can be analyzed easily.

## Conflicts of Interest

The authors declare that there are no conflicts of interest regarding the publication of this paper.

## Acknowledgments

This work is supported by the National Basic Research Program of China (Grant no. 2013CB733004) and National Defense Basic Research Plan of China (no. A0320110016).

## References

- [1] P. Davis, D. Cunningham, and J. Harrell, "Advanced 1.5Hz passive viscous isolation system," *Structures, Structural Dynamics, and Materials Conference*, vol. 5, pp. 2655–2665, 1994.
- [2] B. J. Kawak, "Development of a low-cost, low micro-vibration CMG for small agile satellite applications," *Acta Astronautica*, vol. 131, pp. 113–122, 2017.
- [3] A. Stabile, G. S. Aglietti, G. Richardson, and G. Smet, "A 2-collinear-DoF strut with embedded negative-resistance electromagnetic shunt dampers for spacecraft micro-vibration," *Smart Materials and Structures*, vol. 26, no. 4, Article ID 045031, 2017.
- [4] A. Stabile, G. S. Aglietti, G. Richardson, and G. Smet, "Design and verification of a negative resistance electromagnetic shunt damper for spacecraft micro-vibration," *Journal of Sound and Vibration*, vol. 386, pp. 38–49, 2017.
- [5] A. J. Bronowicki, "Vibration isolator for large space telescopes," *Journal of Spacecraft and Rockets*, vol. 43, no. 1, pp. 45–53, 2006.
- [6] J. F. Yang, Z.-B. Xu, Q.-W. Wu, Z.-S. Wang, H. Li, and S. He, "Design of a vibration isolation system for the space telescope," *Journal of Guidance, Control, and Dynamics*, vol. 38, no. 12, pp. 2441–2448, 2015.
- [7] R. E. Erwin, V. Babuska, and L. Sullivan, "On-orbit active vibration isolation: the Satellite Ultraquiet Isolation Technologies Experiment (SUITE)," *AIAA Space Conference and Exposition*, vol. 13, no. 3, 10 pages, 2003.
- [8] Z.-J. Wei, D.-X. Li, Q. Luo, and J.-P. Jiang, "Modeling and analysis of a flywheel microvibration isolation system for spacecrafts," *Advances in Space Research*, vol. 55, no. 2, pp. 761–777, 2015.
- [9] V. Preda, J. Cieslak, D. Henry, S. Bennani, and A. Falcoz, "Microvibration attenuation based on H $\infty$ /LPV theory for high stability space missions," *Journal of Physics: Conference Series*, vol. 659, no. 1, Article ID 012026, 2015.
- [10] D. Kamesh, R. Pandiyan, and A. Ghosal, "Modeling, design and analysis of low frequency platform for attenuating microvibration in spacecraft," *Journal of Sound and Vibration*, vol. 329, no. 17, pp. 3431–3450, 2010.
- [11] M. Remedia, G. S. Aglietti, G. Richardson, and M. Sweeting, "Integrated semiempirical methodology for microvibration prediction," *AIAA Journal*, vol. 53, no. 5, pp. 1236–1250, 2015.
- [12] Y. Zhang, M. Li, Z.-Y. Song, J.-J. Shan, X. Guan, and L. Tang, "Design and analysis of a moment control unit for agile satellite with high attitude stability requirement," *Acta Astronautica*, vol. 122, pp. 90–105, 2016.
- [13] J. E. Ruzicka and T. F. Derby, "Influence of damping in vibration isolation," *Shock and Vibration Information Center*, 1971.
- [14] I. Yamakawa, "Free and transient vibration of an elastically supported damper system," 1961.
- [15] L. P. Davis, D. Cunningham, A. S. Bicos, M. Enright, and C. D. Johnson, "Adaptable passive viscous damper: an adaptable D-StrutTM," *Smart Structures and Materials 1994: Passive Damping*, vol. 2193, pp. 47–58, 1994.
- [16] L. P. Davis, D. R. Carter, T. T. Hyde, and C. D. Johnson, "Second-generation hybrid D-strut," in *Proceedings of the Smart Structures & Materials '95*, pp. 161–175, San Diego, CA.
- [17] L. P. Davis, D. C. Cunningham, and D. H. Duncan, "Three parameter viscous damper and isolator," *United States Patent*, 1994.
- [18] D. Cunningham and P. Davis, "A multi axis passive isolation system for a magnetic bearing reaction wheel," *Advances in the Astronautical Sciences*, vol. 95, no. Article ID 80426, 1993.
- [19] J. J. Rodden, H. J. Dougherty, and L. F. Reschke, "Ine of sight performance improvement with reaction-wheel isolation," *Spacecraft Design, Testing and Performance*, Article ID 19870045457, 1987.
- [20] J. Tosovsky, V. Janulik, and D. T. Ruebsamen, "Adaptive three parameter isolator assemblies including external magnetorheological valves," *European Patent*, 2016.
- [21] R. Goold and Z. Rogers, "Low profile three parameter isolators and isolation systems employing the same," *United States Patent*, 2016.
- [22] D. W. Smith and S. Hadden, *Thermally-conductive vibration isolators and spacecraft isolation systems employing the same*, United States Patent, 2014.
- [23] W. L. Meacham, E. Bridges, and A. Margolis, *Three parameter damper anisotropic vibration isolation mounting assembly*, United States Patent, 2016.
- [24] D. T. Ruebsamen, J. H. Boyd, and T. S. Davis, *Vibration isolation apparatus and methods of manufacture*, United States Patent, 2011.

- [25] D. Martinez, J. Pagan, and R. Goold, *Isolators including damper assemblies having variable annuli and spacecraft isolation systems employing the same*, United States Patent, 2014.
- [26] D. C. Cunningham, *Isolators including damper assemblies having variable annuli and spacecraft isolation systems employing the same*, European Patent, 1994.
- [27] S. Hadden and D. T. Ruebsamen, *Three parameter, multi-axis isolators, isolation systems employing the same, and methods for producing the same*, European Patent, and methods for producing the same, 2012.
- [28] M. J. Brennan, A. Carrella, T. P. Waters, and V. Lopes Jr., "On the dynamic behaviour of a mass supported by a parallel combination of a spring and an elastically connected damper," *Journal of Sound and Vibration*, vol. 309, no. 3–5, pp. 823–837, 2008.
- [29] L.-K. Liu, G.-T. Zheng, and W.-H. Huang, "Study of liquid viscosity dampers in octo-strut platform for whole-spacecraft vibration isolation," *Acta Astronautica*, vol. 58, no. 10, pp. 515–522, 2006.
- [30] Y. Zhang, J.-R. Zhang, and S.-J. Xu, "Parameters design of vibration isolation platform for control moment gyroscopes," *Acta Astronautica*, vol. 81, no. 2, pp. 645–659, 2012.
- [31] Y. Zhang and J.-R. Zhang, "Analysis of influence of vibration isolation platform on attitude control system and its parameter selection," *Yuhang Xuebao/Journal of Astronautics*, vol. 34, no. 5, pp. 657–664, 2013.
- [32] J. Wang and S. G. Zhao, "A test method of dynamic parameters of vibration isolators," *Journal of Vibration Engineering*, vol. 27, no. 6, pp. 885–892, 2014.
- [33] J. Wang, S.-G. Zhao, D.-F. Wu, and M. Luo, "A test method of dynamic damping coefficient of micro-vibration isolators," *Hangkong Xuebao/Acta Aeronautica et Astronautica Sinica*, vol. 35, no. 2, pp. 454–460, 2014.
- [34] C.-X. Wang, J.-Y. Sun, Z.-Y. Zhang, and H.-X. Hua, "Design and experiment of a three-parameter isolation system with optimal damping," *Jixie Gongcheng Xuebao/Journal of Mechanical Engineering*, vol. 51, no. 15, pp. 90–96, 2015.
- [35] J. Wang, S.-G. Zhao, and D.-F. Wu, "Performance of a type of nonlinear fluid microvibration isolators," *Journal of Aerospace Engineering*, vol. 28, no. 6, p. 04015002, 2015.
- [36] X. Wang, H.-X. Yao, and G.-T. Zheng, "Enhancing the isolation performance by a nonlinear secondary spring in the Zener model," *Nonlinear Dynamics*, vol. 87, no. 4, pp. 2483–2495, 2017.
- [37] W.-K. Shi, C. Qian, Z.-Y. Chen, Y. Cao, and H.-H. Zhang, "Modeling and Dynamic Properties of a Four-Parameter Zener Model Vibration Isolator," *Shock and Vibration*, vol. 2016, Article ID 5081812, 2016.

## Research Article

# Experimental Investigation of Seismic-Induced Hydrodynamic Pressures on a Vertical Wall under Conditions of Wave Resonance

YiLiang Zhou,<sup>1</sup> LingKan Yao,<sup>1,2,3</sup> MingYuan Gao,<sup>1</sup> and Hongzhou Ai<sup>1</sup>

<sup>1</sup>School of Civil Engineering, Southwest Jiaotong University, Chengdu, Sichuan 610031, China

<sup>2</sup>MOE Key Laboratory of High-Speed Railway Engineering, Southwest Jiaotong University, Chengdu, Sichuan 610031, China

<sup>3</sup>National Engineering Laboratory for Technology of Geological Disaster Prevention in Land Transportation, Chengdu 610031, China

Correspondence should be addressed to LingKan Yao; yaolk@swjtu.edu.cn

Received 20 April 2017; Revised 18 July 2017; Accepted 31 July 2017; Published 6 September 2017

Academic Editor: Hugo Rodrigues

Copyright © 2017 YiLiang Zhou et al. This is an open access article distributed under the Creative Commons Attribution License, which permits unrestricted use, distribution, and reproduction in any medium, provided the original work is properly cited.

The distribution of hydrodynamic pressure acting on the structural face of a dam significantly influences the stability of the dam. The present study investigates the development of the hydrodynamic pressure acting on the surface of a dam at different heights with respect to time during earthquakes with different dominant frequencies using a shaking table. The results demonstrate that the variation in the hydrodynamic pressure significantly follows the seismically accelerated wave motion in the absence of resonance. However, under conditions of resonance, the fluctuations in the hydrodynamic pressure exhibit similarities with a sine wave, and the positive peak values present some hysteresis. The experimental pressure values in the absence of resonance present parabolic distributions with respect to the water height that are in good agreement with the corresponding hydrodynamic pressures determined by Westergaard's equation, while conditions of wave resonance produce a uniform distribution of hydrodynamic pressures with greater values and much longer periods of increased hydrodynamic pressure than the case of nonresonance. In addition, the seismic frequency, fundamental frequency of the reservoir, maximum peak seismic acceleration, and initial water depth are treated as variables. An empirical equation is derived to predict the maximum hydrodynamic pressure in conjunction with wave resonance conditions.

## 1. Introduction

The motion of seismic-induced hydraulic structures can generate considerable hydrodynamic pressure on the structural face of a dam, which can significantly affect its stability. Westergaard [1] first derived an expression for the hydrodynamic pressure exerted on the vertical upstream face of a concrete dam subjected to a single harmonic excitation. In fact, many current engineering designs have continued to employ a simplified form of this formula to account for hydrodynamic pressure loads [2–4]. In 1953, Zangar [5] developed an experimental solution for the same problem using an electrical analogue and reported extensive results for a variety of nonvertical upstream faces. Chwang and Housner [6, 7] solved the hydrodynamic pressure problem for a more general dam configuration using the momentum method and two-dimensional (2D) potential flow theory, respectively.

Wang et al. [8] modified Westergaard's equation by considering the influence of dam height, elasticity, and reservoir bottom condition. The results generated by these works were more or less equivalent to the results of Westergaard.

Numerous researchers have studied hydrodynamic pressure under seismic excitation using a variety of other methods to consider the effects of different parameters. Saini et al. [9] employed the finite element method to analyze the 2D response of a reservoir-dam system subjected to horizontal ground motion. When the water was assumed to be incompressible, its effect on the dam was found to be equivalent to that of an added mass. When the water was assumed to be compressible, its effect was found to be equivalent to that of an added mass in conjunction with added damping. Moreover, the coupled response of the system was significantly increased relative to the uncoupled response at the fundamental natural frequency of the system. Zingales [10]

analyzed the hydrodynamic pressure in a dam-reservoir system with an infinite reservoir composed of a compressible fluid and modeled seismic acceleration as a normal zero-mean stochastic process. Based on the results, the close relationship between the frequency content of the seismic vibrations and the seismic-induced hydrodynamic pressure was outlined. Bouaanani et al. [11] considered water compressibility and wave absorption at the reservoir bottom to establish closed-form formulas for solving the fluid-dam interaction problem. Gogoi and Maity [12] conducted seismic excitation analysis based on the short-time Fourier transform to evaluate hydrodynamic pressures along the upstream face of a dam-reservoir system. Chen and Malenica [13] examined the distributions of hydrodynamic pressure on the surface of a ship hull for a large range of encounter frequencies. Saleh and Madabhushi [14, 15] investigated the effect of dam-foundation interaction on the hydrodynamic pressure response on a dam face under different seismic excitations using the dynamic centrifuge modeling technique. This work proposed an experimental method for examining hydrodynamic pressure. Pelecanos et al. [16, 17] employed numerical modeling to investigate the hydrodynamic pressures of stiff and flexible dams with vertical and sloped upstream faces under ramp, harmonic, and random acceleration loads and further examined the elastic dynamic response of dams. Xu et al. [18] employed a semianalytical scaled boundary finite element method (SBFEM) to investigate the hydrodynamic pressure acting on the concrete face slabs of rockfill dams. In addition, Chen and Yuan [19] studied nonlinear hydrodynamic pressures with consideration for the influence of vertical seismic waves.

As can be seen from the above discussion, considerable efforts have been made to investigate seismic-induced hydrodynamic pressure on dam faces. However, thus far, few experimental studies have examined the development of seismic-induced hydrodynamic pressures with respect to time in conjunction with wave resonance. Therefore, the present study simulated actual seismic waves using a shaking table, and experiments were accordingly conducted to investigate the characteristics of the seismic hydrodynamic pressure acting on the wall. Use of the shaking table allowed the acceleration amplitude and frequency of waves to be finely controlled. In each experimental test, the pressures exerted by the water were recorded by sensors attached to the wall at various water heights. Here, the additional seismic-induced water pressure acting on the wall is regarded as the seismic hydrodynamic pressure. Then, the effects of main parameters such as seismic frequency, maximum peak seismic acceleration, the fundamental frequency of the reservoir, and initial water depth are considered in the analysis of the results. An empirical equation is established for evaluating seismic hydrodynamic pressure in conjunction with wave resonance.

## 2. Shaking Table Experiments

*2.1. Experimental Setup.* The present experimental setup consists of six components: a shaking platform, vibrator, hydraulic pumps, control system, water tank, and water

pressure acquisition system, as illustrated in Figure 1. The platform was 4 m × 2 m and accommodated a maximum payload of 25 t. The water tank was installed on the platform and had a length of 3.76 m, a width of 1.76 m, and a height of 1.50 m. The water body (i.e., the actual reservoir within the water tank) had a length of 2.73 m, a width of 1.76 m, and a depth of 0.35 m. To simulate the excitation of an earthquake during tests, the water body was subjected to movement in a single direction along its length using hydraulic pumps. The motion induced after which the vibrator received the signal and the hydraulic pumps caused the platform and water tank to shake. The frequency of the shaking table ranged from 0.4 Hz to 15 Hz, with a corresponding maximum amplitude of 100 mm and a maximum acceleration of 1.2 g, where g is the acceleration due to gravity. Prior to each experimental test, the input accelerated wave motion was calibrated to ensure accurate experimental measurements. The input accelerated seismic wave was firstly designed using a digital control system, and then the actual shaking table waveform obtained by the vibrator based on the designed waveform was compared with the designed waveform for feedback correction and iterative optimization to ensure a good match. The final optimized signal obtained was then applied for driving the shaking table during experiments. Six pulsating water pressure sensors were attached to the vertical wall for measuring the hydrodynamic pressures at a frequency of 500 Hz. The pulsating water pressure sensors employed have a range of −100 kPa to 100 kPa and an accuracy of 0.1%. The sensors were numbered as P1 to P6, with corresponding heights from the reservoir bottom of 2 cm, 8 cm, 14 cm, 20.5 cm, 27.5 cm, and 31.5 cm, respectively. A detailed illustration of the sensor positions is presented in Figure 2.

*2.2. Experimental Design.* To analyze the seismic-induced hydrodynamic pressure in conjunction with wave resonance, we firstly obtained the resonant frequency of the water body. According to the study of Saini et al., the hydrodynamic pressure response is significantly reduced at resonant frequencies higher than the fundamental resonant frequency [9]. Therefore, the present study considered only the fundamental natural frequency of the water body (i.e., the reservoir). The analytical formula generally employed for defining the natural angular frequencies of a reservoir in a single direction is expressed as follows [20–22]:

$$\omega_n^2 = \frac{ng\pi}{L} \tanh\left(\frac{n\pi h}{L}\right) \quad n = (1, 3, 5, \dots), \quad (1)$$

where  $L$  is the length of the reservoir and  $h$  is the depth of the reservoir. The fundamental natural frequency in the single direction  $L$  of the reservoir employed for testing is then

$$\begin{aligned} f_1 &= \frac{\omega_1}{2\pi} \\ &= \frac{\sqrt{((9.8 \times 3.14) / 2.73) \times \tanh((3.14 \times 0.35) / 2.73)}}{(2 \times 3.14)} \quad (2) \\ &= 0.33 \text{ Hz.} \end{aligned}$$

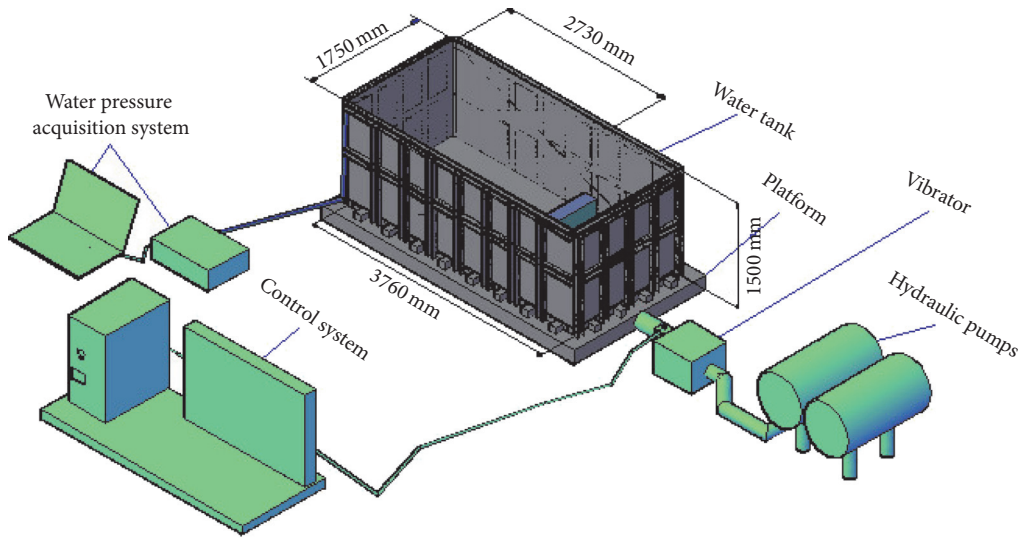


FIGURE 1: A typical illustration of the experimental setup design.

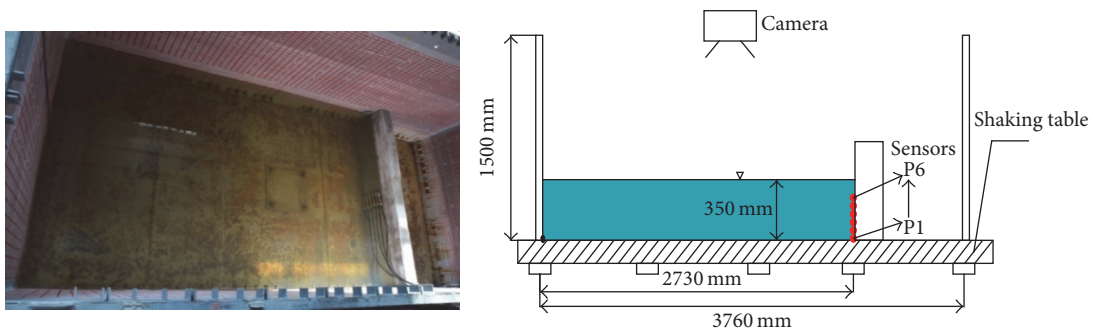


FIGURE 2: Image and schematic diagram of the pulsating water pressure sensor positions.

White noise was then employed as the signal source to test the resonant frequency of the reservoir. A fast Fourier transform (FFT) analysis of the measured water pressure caused by the white noise signal is presented in Figure 3, which shows that the measured fundamental natural frequency was 0.3325 Hz, which is in good agreement with the theoretical prediction. The presented formula therefore provides an effective method for calculating the fundamental natural frequency of a reservoir in the absence of actual measured data.

Two different seismic waves were utilized to compare the development of the hydrodynamic pressure at various heights with respect to time for conditions both with and without wave resonance. One seismic waveform was modeled according to the Wenchuan Ms 8.0 earthquake that transpired on May 12, 2008, in Wolong, China, which exhibited a dominant frequency of 2.35 Hz (denoted herein as EQ1). The second seismic waveform was modeled according to the Mexicali-California Ms 7.2 earthquake that transpired on April 4, 2010, which exhibited a dominant frequency of 0.38 Hz (denoted herein as EQ2). These seismic waveforms are presented in Figures 4 and 5, respectively. Here, we note that the dominant

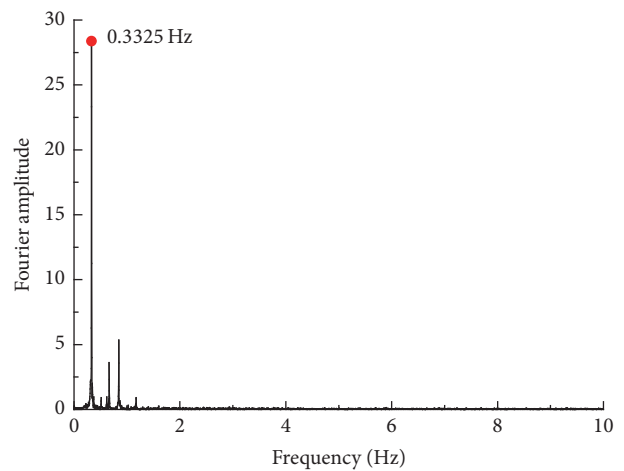


FIGURE 3: Fourier amplitude spectrum of the hydrodynamic pressure of the reservoir employed in the tests due to white noise excitation.

frequency of EQ2 is close to the fundamental natural frequency of the water body, whereas the dominant frequency of

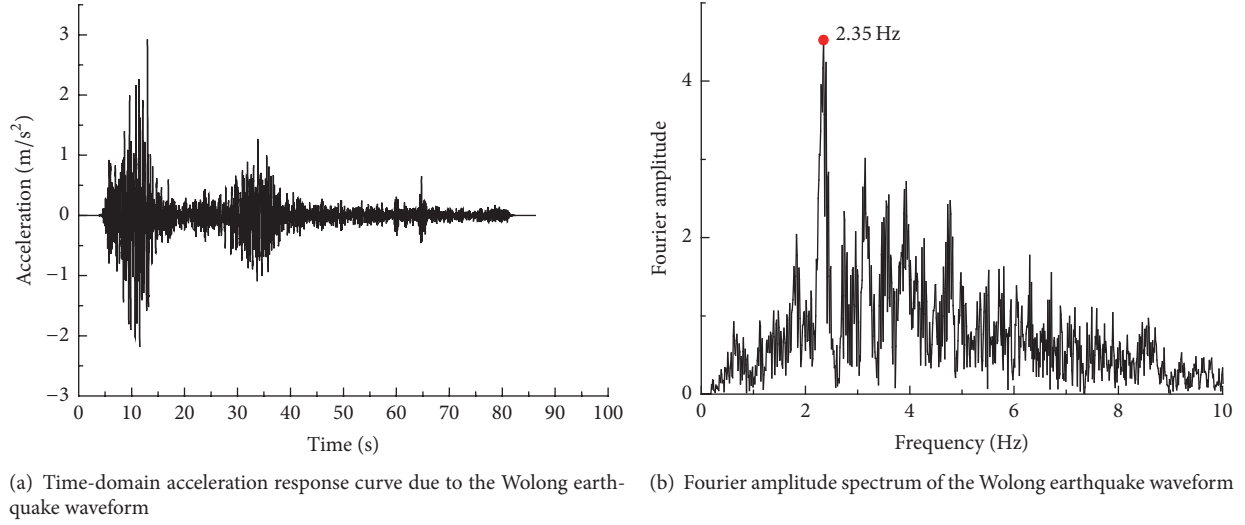


FIGURE 4: Seismic parameters of the Wolong earthquake waveform (EQ1).

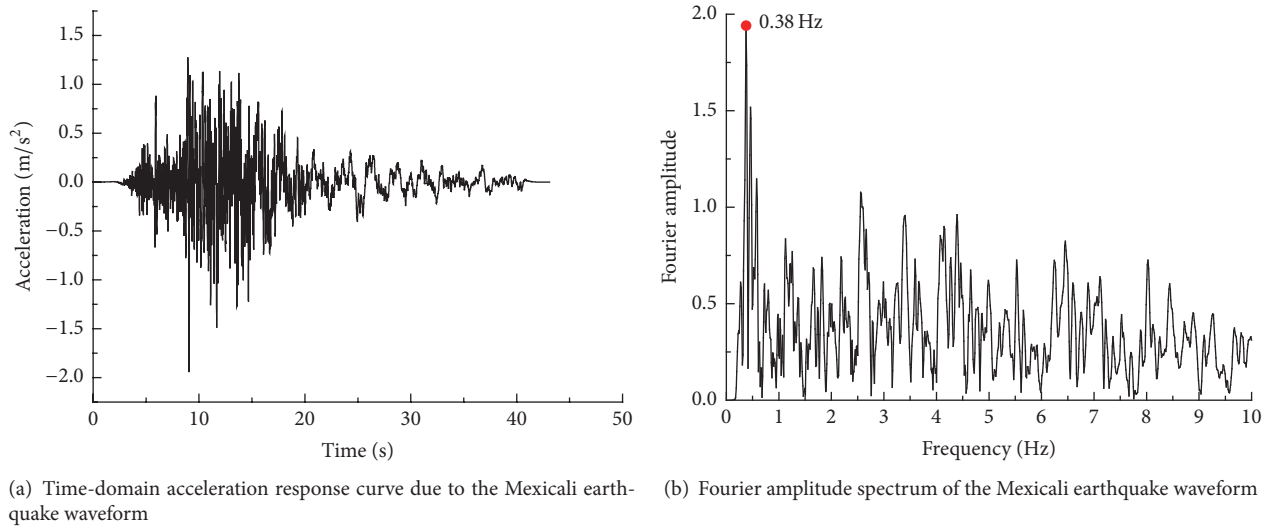


FIGURE 5: Seismic parameters of the Mexicali earthquake waveform (EQ2).

EQ1 is much greater than the fundamental natural frequency. The details of the experimental seismic waves and the corresponding peak ground acceleration (PGA) are presented in Table 1. In each test, the modeled seismic waveform was applied to the shaking table, and the hydrodynamic pressures at the corresponding heights were recorded by the water pressure acquisition system with respect to time. Following the completion of the seismic waveform, the acquisition system continued operation until the entire water body had achieved a calm state. The water pressure values obtained for the individual sensors prior to testing were subtracted from the hydrodynamic pressures obtained during earthquake simulation at the corresponding heights. Therefore, both the pressure caused by seismic-induced free surface waves and the pressure caused by dynamic interaction between the

TABLE 1: Seismic waveforms employed in testing and their peak ground acceleration (PGA).

Seismic waveform	Seismic peak ground acceleration ( $m/s^2$ )					
	0.05 g	0.1 g	0.15 g	0.2 g	0.25 g	0.3 g
Wolong wave (EQ1)	0.05 g	0.1 g	0.15 g	0.2 g	0.25 g	0.3 g
Mexicali wave (EQ2)	0.05 g	0.1 g	0.15 g	0.2 g	0.25 g	0.3 g

water body and the sidewall during earthquake simulation may be included in the recorded hydrodynamic pressures. We did not fractionize the components of the seismic-induced water pressure.

### 3. Experimental Results and Discussion

**3.1. Hydrodynamic Pressure in the Absence of Wave Resonance.** Figure 6 presents the hydrodynamic pressures recorded by sensors P1–P6 (i.e., from the bottom to the top of the water body) during simulation of the EQ1 waveform. In addition, the 0.25 g acceleration results are also presented.

Generally, the synchronized hydrodynamic pressures obtained at  $P_i$ , where  $i = 1, 2, 3, 4, 5, 6$ , in Figure 6 yield similar values. However, the variation in the hydrodynamic pressure with respect to time measured near the surface by P6 differed somewhat from the pressures measured by the other sensors because the pressure at P6 was also strongly affected by the surface wave. Therefore, the hydrodynamic pressures measured near the bottom by P1 were selected for analyzing the variation in the hydrodynamic pressure acting on the wall with respect to time. The development of the hydrodynamic pressures at various water heights with respect to time can be divided into two main stages based on the red broken vertical line shown in Figure 6 for P1. For  $0 < t < 83$  s, (a) the hydrodynamic pressures vary significantly following the seismically accelerated wave motion. For  $t > 83$  s, (b) the hydrodynamic pressure returns to zero after the completion of seismic excitation. We note that the employment of an excitation frequency far from the fundamental frequency of the water body resulted in the synchronization between the seismic acceleration wave response and the hydrodynamic pressure response, such that the hydrodynamic pressure was mainly affected by the amplitude of the seismic acceleration.

A comparison between the maximum experimental hydrodynamic pressures on the wall and the values theoretically determined by the Westergaard formula is presented in Figure 7. The sensor heights  $y$  have been normalized with respect to the reservoir depth  $h$  and the maximum hydrodynamic pressures  $P_{\max}(y)$  have been normalized with respect to the total hydrostatic pressure  $\rho gh$ , where  $\rho$  is the unit density of water ( $1.0 \text{ t/m}^3$ ). Generally, the formulas developed by Westergaard and others were derived based on a simple harmonic wave, which differs from actual seismic waves that consist of a continuum of harmonic waves. However, the results presented in Figure 6 indicate that the variation in the hydrodynamic pressure significantly follows the seismically accelerated wave motion well, and, clearly, the peak acceleration of the seismic excitation corresponds with the maximum hydrodynamic pressure. Therefore, the maximum hydrodynamic pressures generated by EQ1 can be calculated by Westergaard's formula using the corresponding seismic peak acceleration. And according to Figure 7, the maximum hydrodynamic pressure increases monotonically with respect to the seismic acceleration, and the measured values match well with the hydrodynamic pressure calculated by Westergaard's formula. It is evident that Westergaard's approximate formula appropriately predicts the hydrodynamic pressures in the absence of wave resonance.

**3.2. Hydrodynamic Pressure with Wave Resonance.** As was found for EQ1, the hydrodynamic pressures obtained at different heights along the wall during the simulated Mexicali earthquake waveform (EQ2) exhibited similar values with

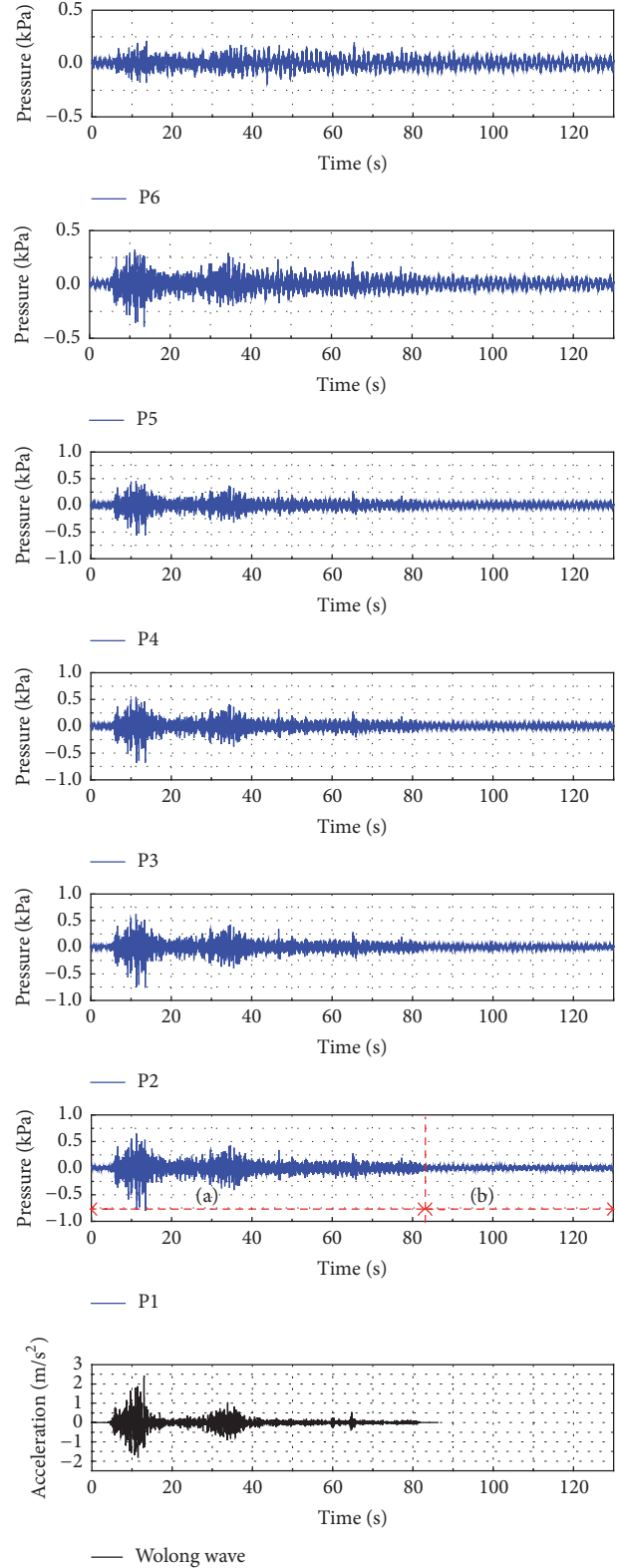


FIGURE 6: Fluctuations in the hydrodynamic pressures at sensors P1–P6 and the 0.25 g acceleration results with respect to time due to the Wolong earthquake waveform (EQ1).

respect to time. As discussed earlier, the pressure recorded at P6 was also affected between the sensor and the surface wave.

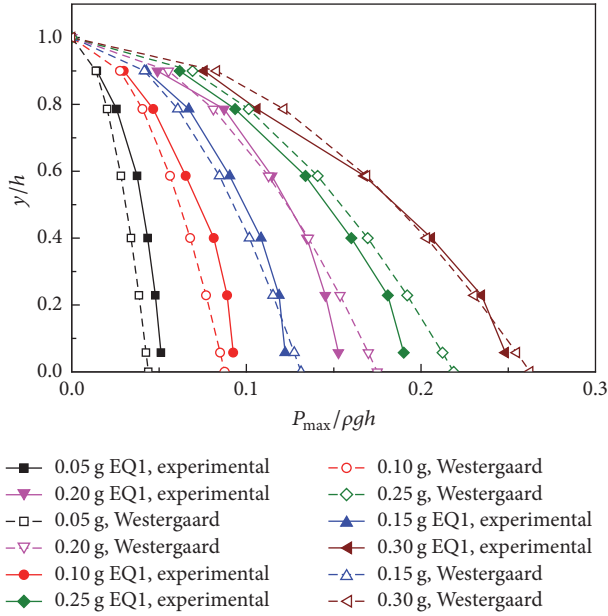


FIGURE 7: Comparison of the maximum hydrodynamic pressures acting on the wall at the vertical face due to the Wolong earthquake waveform (EQ1): experimental results and Westergaard's formula.

Therefore, Figure 8 presents the hydrodynamic pressures recorded by sensors  $P_i$  ( $i = 1, 2, 3, 4, 5$ ) with respect to time for EQ2 along with the 0.15 g acceleration data.

The results presented in Figure 8 indicate that the hydrodynamic pressure variations of EQ2 did not closely follow the seismic acceleration wave motion. The positive peak seismic acceleration was generated at 9 s–13 s while the corresponding positive peak hydrodynamic pressures were observed at 19 s–30 s for all sensors and exhibited some hysteresis. The development of the hydrodynamic pressure at sensor P1 with respect to time is examined over shorter time periods in Figure 9, indicating that the process can be divided into three stages. For  $0 < t < 15$  s in the segment denoted as (a), the fluctuations in the hydrodynamic pressure are initially similar to those of the seismic wave, and the amplitude increased with increasing time. For  $15 < t < 30$  s in the segment denoted as (b), the hydrodynamic pressure developed into a sine wave variation and maintained a fairly constant amplitude and steady period. For  $t > 30$  s in the segment denoted as (c), the amplitude of the sine wave variation in the hydrodynamic pressure diminished because of the significant reduction in the excitation amplitude while approaching the completion of the EQ2 waveform. However, the amplitude required considerable time to decrease to zero after completion of the EQ2 waveform and did not attain a value of zero even after 250 s of monitoring, which is greater than five times the duration of the EQ2 waveform. Clearly, an excitation frequency close to the fundamental frequency of the water body resulted in a resonance phenomenon. In addition, the hydrodynamic pressure under conditions of resonance was significantly greater and the fluctuations far more stable than what was obtained from EQ1. The experimental data

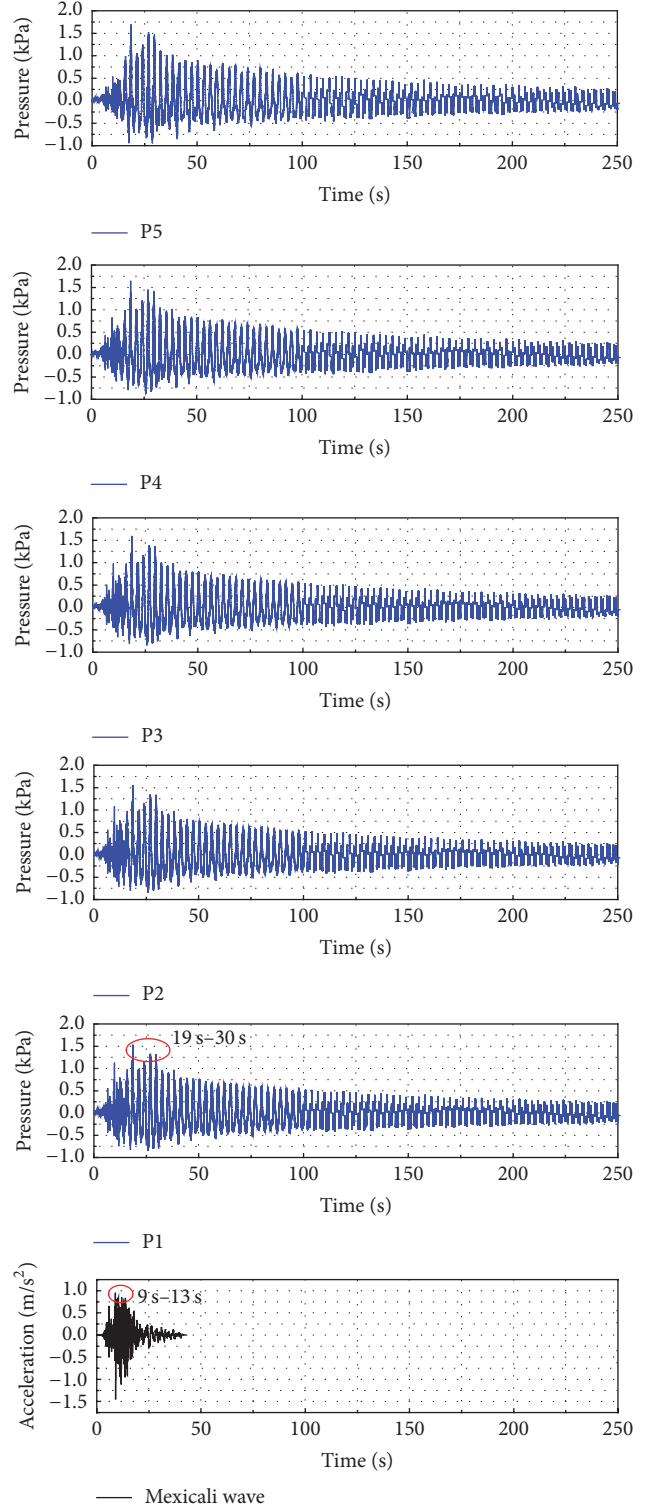


FIGURE 8: Fluctuations in the hydrodynamic pressures at sensors P1–P5 and the 0.15 g acceleration results with respect to time due to the Mexicali earthquake waveform (EQ2).

for the maximum hydrodynamic pressures obtained at the corresponding heights are listed in Table 2.

Figure 10 indicates that the distributions of the maximum hydrodynamic pressures with respect to the water height

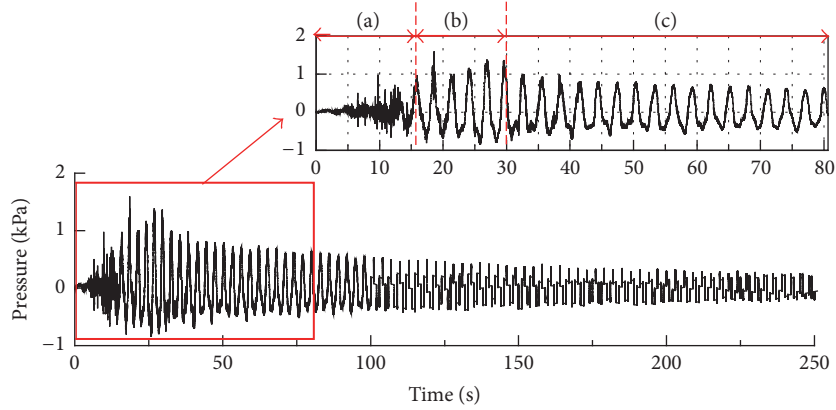


FIGURE 9: Hydrodynamic pressure variations at P1 due to EQ2.

TABLE 2: Maximum values of the hydrodynamic pressure due to the Mexicali earthquake waveform (EQ2).

Number	Height (cm)	PGA (g)					
		0.05	0.10	0.15	0.20	0.25	0.30
P1	2	0.231	0.453	0.831	1.296	1.543	1.799
P2	8	0.223	0.452	0.83	1.303	1.562	1.8
P3	14	0.207	0.448	0.83	1.329	1.599	1.83
P4	20.5	0.182	0.44	0.845	1.372	1.653	1.867
P5	27.5	0.152	0.413	0.792	1.394	1.702	1.905

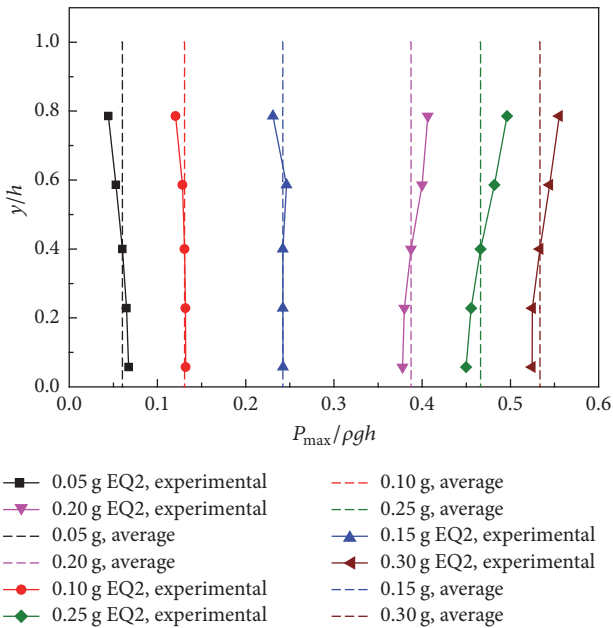


FIGURE 10: Distributions of the maximum hydrodynamic pressures acting on the wall at the vertical face due to the Mexicali earthquake waveform (EQ2).

at equivalent PGA presented a uniform distribution under conditions of resonance. The uniform distributions obtained for EQ2 indicates equal impacting forces at each horizontal layer of the water body. The dashed lines represent the average

values of the hydrodynamic pressures under different PGA, which were in particularly good agreement with the values measured by P3. Therefore, the measured pressures at P3 under different PGA were selected for further analysis of the hydrodynamic pressures and later employed to develop an empirical equation for hydrodynamic pressure under wave resonance conditions.

3.3. Comparison. For comparison, the hydrodynamic pressures obtained at different heights along the wall during excitation by EQ1 and EQ2 are presented in Figure 11 for PGA of 0.1 g, 0.2 g, and 0.3 g. Here, we note that the hydrodynamic pressures induced by EQ1 were significantly less than those induced by EQ2 at equivalent PGA owing to the larger hydrodynamic pressures induced under the wave resonance conditions of EQ2. And the distributions of the maximum hydrodynamic pressures with respect to the water height at equivalent PGA transformed from a parabolic distribution for EQ1 without resonance to a uniform distribution for EQ2 under conditions of resonance. Clearly, the Westergaard formula is not appropriate for estimating the maximum hydrodynamic pressure with wave resonance, which yield entirely different distributions of maximum hydrodynamic pressures.

Here, we would like to briefly discuss the effect of boundary interactions on the hydrodynamic pressure. For a nonresonant response, the works of Saini et al. [9], Aviles and Sanchez-Sesma [23], and Pelecanos et al. [16] indicated that the influence of finite reservoir dimensions is negligible for  $L/h > 5$ . For the reservoir employed in the present experiments,  $L/h = 7.8$ , which represents a semi-infinite

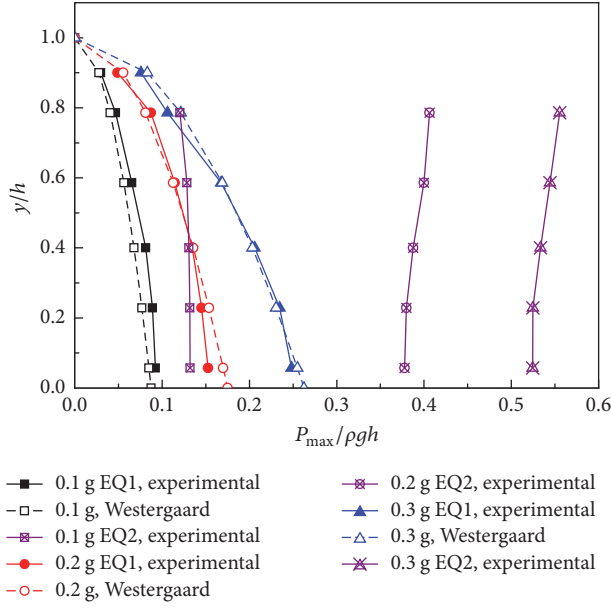


FIGURE 11: Comparison of the maximum hydrodynamic pressures on the wall at the vertical face due to waveforms EQ1 and EQ2: experimental and theoretical.

reservoir and is therefore not subject to the influence of reflection waves. During the resonant process, the influence of the reservoir dimensions was mainly reflected in the fundamental frequency of the reservoir, as demonstrated by (1). When the excitation frequency was close to the fundamental frequency of the water body, the water body presented regular wave motion of constant amplitude and tended to move as a whole. This suggests that the hydrodynamic pressures on the wall were not subject to downstream end effects under conditions of resonance.

**3.4. Empirical Equation for Hydrodynamic Pressure with Wave Resonance.** Without wave resonance, the hydrodynamic pressure coefficient  $C_p$  is obtained from the following relationships [1, 6]:

$$P_{\max} = C_p \rho a_{\max} h = C_p \rho k_h g h, \quad (3)$$

where  $a_{\max}$  is the PGA,  $a_{\max} = k_h g$ , and  $k_h$  is the seismic acceleration coefficient in the horizontal direction. Based on the study of Westergaard, the hydrodynamic pressure loads exerted on the face of the dam can be represented as inertial forces like a certain part of the water as moving with the dam, of which that part was characterized as added mass [1], to define

$$\int_0^h C_p \rho a_{\max} h dy = M a_{\max}, \quad (4)$$

where  $M$  denotes the added mass. In this paper, following a consideration of the seismic frequency and water fundamental frequency by using a mass-spring model and assuming

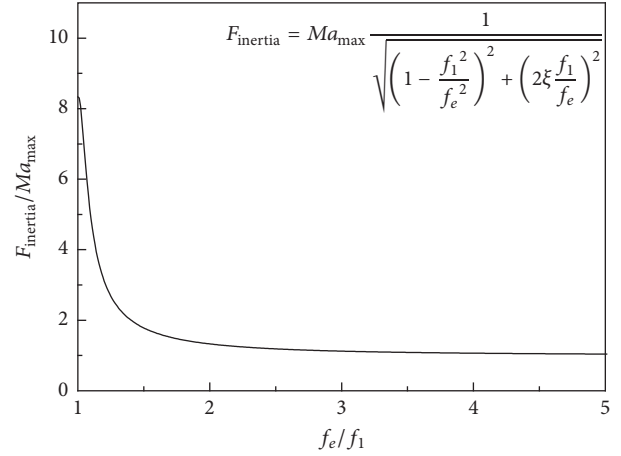


FIGURE 12: Relation between the ratio of the inertial force of the water  $F_{\text{inertia}}$  and product of the added mass  $M$  and maximum seismic acceleration  $a_{\max}$  and the ratio of the seismic excitation frequency  $f_e$  and fundamental frequency of the water body  $f_1$ .

equality between the maximum hydrodynamic pressure loads and the inertial force, the following equation is generated:

$$\begin{aligned} & \int_0^h C_p \rho a_{\max} h dy \\ &= M a_{\max} \frac{1}{\sqrt{\left(1 - f_1^2/f_e^2\right)^2 + \left(2\xi (f_1/f_e)\right)^2}} \quad (5) \\ &= M a_{\max} \beta, \end{aligned}$$

where  $f_1$  is the fundamental frequency of the water body,  $f_e$  is the seismic excitation frequency,  $\beta$  is the acceleration amplification coefficient, and  $\xi$  is the damping ratio of this equivalent single degree of freedom (SDOF) system. An increase in the value of  $\beta$  generates a stronger inertial force on the wall. The close relationship between the seismic excitation frequency and the hydrodynamic pressure is also outlined.

Figure 12 presents a plot of (5) presented above, where  $F_{\text{inertia}}$  represents the inertial force of the water body on the wall. The work of Chopra has provided a simplified analysis method for determining the value of  $\xi$  for a reservoir with rigid walls and foundation, which demonstrated that reservoir depth to wall height ratios ( $h/H$ ) from 0 to 1.0 provided a value of  $\xi$  between 0.05 to 0.07 [24]. The present experiments employed  $h/H = 0.7$ , such that Chopra's method generated a reasonable value of  $\xi = 0.06$ . In general, a reservoir that is not completely empty or full will have a value of  $\xi$  that can be approximated as 0.06. For  $f_e$  much greater than  $f_1$ , that is,  $f_1^2/f_e^2 \approx 0$ , the water body exhibited steady-state movement that was synchronized to the seismic wave, such that  $F_{\text{inertia}}$  was approximately equal to  $Ma_{\max}$ . The water body exhibited a small corresponding vibration amplitude, and the pressure amplitude exhibited enhanced attenuation. For  $f_e \approx f_1$ , that is,  $f_1^2/f_e^2 \approx 1$ , the water body exhibited an increase in the corresponding vibration amplitude, which thereby resulted in an increased  $F_{\text{inertia}}$  on the wall. Therefore,

the effect of frequency is taken into consideration by the hydrodynamic pressure coefficient ( $C'_p$ ), which is defined as

$$\begin{aligned} C'_p &= C_p \beta, \\ \frac{P_{\max}}{\rho g h} &= C'_p k_h = C_p \beta k_h. \end{aligned} \quad (6)$$

Westergaard [1] and Chwang and Housner [6] observed minimal effects on hydrodynamic pressures following changes in the frequency. Namely, the value  $\beta \approx 1$  generates the following:

$$\begin{aligned} \text{Westergaard's formula: } C'_p &= \frac{7}{8} \beta \sqrt{1 - \frac{y}{h}} \approx \frac{7}{8} \sqrt{1 - \frac{y}{h}} \\ &= C_p; \end{aligned}$$

$$\begin{aligned} \text{Chwang's formula: } C'_p &= \frac{1}{\sqrt{2}} \beta \sqrt{1 - \left(\frac{y}{h}\right)^2} \\ &\approx \frac{1}{\sqrt{2}} \sqrt{1 - \left(\frac{y}{h}\right)^2} = C_p. \end{aligned} \quad (7)$$

With wave resonance, the horizontal components of the inertial force of the water body were equivalent at each layer (Figure 10), which indicates that  $C'_p$  does not depend on the vertical location ( $y/h$ ). Therefore, the hydrodynamic pressure coefficient with wave resonance (denoted herein as  $C_{p\text{-res}}$ ) can be expressed as

$$C_{p\text{-res}} = C\beta, \quad (8)$$

$$\frac{P_{\max}}{\rho g h} = C\beta k_h = \frac{Ck_h}{\sqrt{(1 - f_1^2/f_e^2)^2 + (0.12(f_1/f_e))^2}}, \quad (9)$$

where  $C$  is a constant.

An empirical equation was developed according to (9) for the maximum hydrodynamic pressure with respect to the PGA under conditions of wave resonance based on the measured data at P3 generated by EQ2. In this paper,  $f_1 = 0.33$  Hz and  $f_e = 0.38$  Hz, such that a linear fitting of the data of  $P_{\max}/\rho g h$  versus  $k_h$  for P3 yields a value of 0.466 for  $C$  in (9) with a degree of fit indicated by  $R^2 = 0.9573$ . The resulting empirical expression is given as follows:

$$\begin{aligned} \frac{P_{\max}}{\rho g h} &= \frac{0.466k_h}{\sqrt{(1 - f_1^2/f_e^2)^2 + (0.12(f_1/f_e))^2}} \\ R^2 &= 0.9573. \end{aligned} \quad (10)$$

The results shown in Figure 13 indicate that the maximum error is about 35% while most errors were less than 10%. In the absence of good experimental data, the empirical equation given by (10) can be employed to estimate the maximum hydrodynamic pressure under conditions of wave resonance.

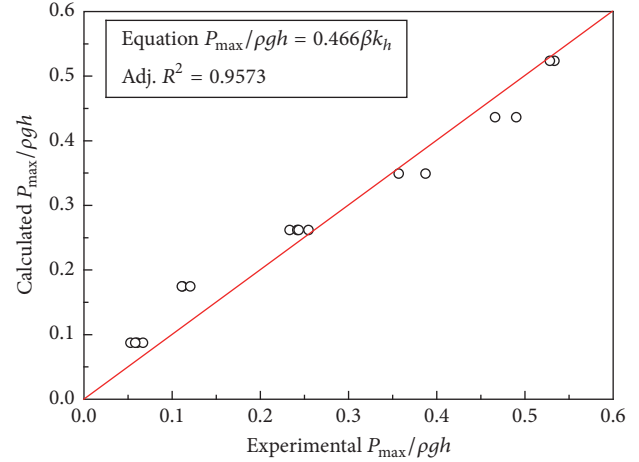


FIGURE 13: A comparison of the calculated values obtained from a linear fit of the experimental hydrodynamic pressure data at P3 for EQ2.

**3.5. Discussion.** In the present study, the experiments only considered the distribution of hydrodynamic pressures on a rigid wall with a vertical face. In reality, the upstream face of a natural dam is irregular. Therefore, the variations in the hydrodynamic pressures under conditions of resonance will be more complex. Additionally, the present study only considered the homodromous movement of seismic waves. Different seismic wave directions must be considered in future studies to understand the failure mechanisms of moraine dams.

## 4. Conclusions

The characteristics of seismic-induced hydrodynamic pressures acting on a vertical wall face were experimentally investigated using a shaking table. Two seismic waveforms, EQ1 and EQ2, were utilized to obtain different hydrodynamic pressures under equivalent conditions, where the dominant frequency of EQ1 was much greater than the fundamental frequency of the water body employed in the experiments (i.e., no resonance) and that of EQ2 was nearly equivalent to the fundamental frequency (i.e., with resonance). The experimental results were employed to develop an empirical equation to predict the maximum hydrodynamic pressure under conditions of wave resonance. The following conclusions were generated.

(1) In the case of nonresonance, the hydrodynamic pressure variation significantly followed the seismically accelerated wave motion, and the experimental pressure values were in good agreement with corresponding hydrodynamic pressures determined by Westergaard's equation. However, the fluctuations in the hydrodynamic pressure observed under conditions of resonance were similar to the variations of a sine wave, and the positive peak values exhibited some hysteresis. Conditions of wave resonance produced larger hydrodynamic pressure values and much longer periods of increased hydrodynamic pressure than the case of nonresonance, which obviously poses a greater threat to the stability of dams.

(2) The effect of the seismic excitation frequency and the fundamental frequency of the reservoir on the maximum hydrodynamic pressure was analyzed from the standpoint of a mass-spring model. The maximum hydrodynamic pressures on the vertical wall under conditions of resonance exhibited a uniform distribution rather than the parabolic distribution obtained without resonance. The experimentally obtained maximum hydrodynamic pressures under conditions of resonance were linearly fitted to an analytically derived expression to obtain an empirical equation for predicting the maximum hydrodynamic pressure with wave resonance. An  $R^2$  value of 0.9573 was obtained, which, to the best of our knowledge, represents a reasonable degree of accuracy for estimating the maximum pressure.

(3) Based a theoretical formula calculation [22], a small reservoir range, which had a length less than 100 m and a depth less than 20 m, exhibited a fundamental frequency between 0.1 Hz and 1 Hz. However, the seismic wave spectrum exhibited a wider range than the small reservoir spectrum. Hence, an assessment of the outburst risk of such a small lake in seismic zones must consider the wave resonance caused by earthquakes as a security practice, particularly in far-field earthquake regions where the seismic amplitudes are reduced. However, these spectrums are mainly composed of low frequencies. Ultimately, the effect of wave resonance must not be neglected.

(4) The issue of seismic-induced wave resonance was mainly characterized by relatively large hydrodynamic pressure. During the propagation of the seismic surge wave, the surge wave lashed against the wall of the reservoir such that the run-up wave height became a key parameter. The wave continued to propagate and erode, thereby forming an outflow channel. The surge wave also affected the stability of the dam and could significantly impact the lives and property of residents along the shore. Therefore, quantification of the seismic surge wave height is a further issue that requires rigorous characterization and further investigation.

## Conflicts of Interest

The authors declare that there are no conflicts of interest regarding the publication of this paper.

## Acknowledgments

This work is financially supported by the Natural Science Foundation of China under Contract no. 41571004; Scientific and Technological Research and Development Plan of China Railway Corporation (no. 2015G002-N); and Natural Science Foundation of China (no. 41172321). The authors express their gratitude to these foundations. The authors acknowledge LetPub for their linguistic assistance during the preparation of this manuscript.

## References

- [1] H. M. Westergaard, "Water pressures on dams during earthquakes," *Transactions of the American Society of Civil Engineers*, vol. 98, no. 3, pp. 418–433, 1933.
- [2] D. Zou, Y. Zhou, H. I. Ling, X. Kong, and B. Xu, "Dislocation of face-slabs of Zipingpu concrete face rockfill dam during Wenchuan earthquake," *Journal of Earthquake and Tsunami*, vol. 6, no. 2, Article ID 1250007, 2012.
- [3] D. Chakraborty and D. Choudhury, "Sliding stability of non-vertical waterfront retaining wall supporting inclined backfill subjected to pseudo-dynamic earthquake forces," *Applied Ocean Research*, vol. 47, pp. 174–182, 2014.
- [4] D. Chakraborty and D. Choudhury, "Stability of non-vertical waterfront retaining wall supporting inclined backfill under earthquake and tsunami," *Ocean Engineering*, vol. 78, pp. 1–10, 2014.
- [5] C. N. Zangar, "Hydrodynamic pressures on dams due to horizontal earthquakes," *Proceedings of the Society for Experimental Stress Analysis*, vol. 10, pp. 93–102, 1953.
- [6] A. T. Chwang and G. W. Housner, "Hydrodynamic pressures on sloping dams during earthquakes. Part 1. Momentum method," *Journal of Fluid Mechanics*, vol. 87, no. 2, pp. 335–341, 1978.
- [7] A. T. Chwang, "Hydrodynamic pressures on sloping dams during earthquakes. Part 2. Exact theory," *Journal of Fluid Mechanics*, vol. 87, no. 2, pp. 343–348, 1978.
- [8] M. M. Wang, J. Y. Chen, and Q. Xu, "Study on different height gravity hydrodynamic pressure and westergaard correction formula," *Engineering Mechanics*, vol. 30, no. 12, pp. 65–70, 2013.
- [9] S. S. Saini, P. Bettess, and O. C. Zienkiewicz, "Coupled hydrodynamic response of concrete gravity dams using finite and infinite elements," *Earthquake Engineering & Structural Dynamics*, vol. 6, no. 4, pp. 363–374, 1978.
- [10] M. Zingales, "Seismically induced, non-stationary hydrodynamic pressure in a dam-reservoir system," *Probabilistic Engineering Mechanics*, vol. 18, no. 2, pp. 151–163, 2003.
- [11] N. Bouaanani, P. Paultre, and J. Proulx, "A closed-form formulation for earthquake-induced hydrodynamic pressure on gravity dams," *Journal of Sound and Vibration*, vol. 261, no. 3, pp. 573–582, 2003.
- [12] I. Gogoi and D. Maity, "A novel procedure for determination of hydrodynamic pressure along upstream face of dams due to earthquakes," *Computers and Structures*, vol. 88, no. 9–10, pp. 539–548, 2010.
- [13] X. B. Chen and S. Malenica, "Hydrodynamic pressure distribution on ship hull at very high encounter frequencies," *Journal of Hydrodynamics*, vol. 22, no. 5, pp. 515–520, 2010.
- [14] S. Saleh and S. P. G. Madabhushi, "An investigation into the seismic behaviour of dams using dynamic centrifuge modelling," *Bulletin of Earthquake Engineering*, vol. 8, no. 6, pp. 1479–1495, 2010.
- [15] S. Saleh and S. P. G. Madabhushi, "Response of concrete dams on rigid and soil foundations under earthquake loading," *Journal of Earthquake and Tsunami*, vol. 4, no. 3, pp. 251–268, 2010.
- [16] L. Pelecanos, S. Kontoe, and L. Zdravković, "Numerical modelling of hydrodynamic pressures on dams," *Computers and Geotechnics*, vol. 53, pp. 68–82, 2013.
- [17] L. Pelecanos, S. Kontoe, and L. Zdravković, "Dam-reservoir interaction effects on the elastic dynamic response of concrete and earth dams," *Soil Dynamics and Earthquake Engineering*, vol. 82, pp. 138–141, 2016.
- [18] H. Xu, D. Zou, X. Kong, and Z. Hu, "Study on the effects of hydrodynamic pressure on the dynamic stresses in slabs of high CFRD based on the scaled boundary finite-element method," *Soil Dynamics and Earthquake Engineering*, vol. 88, pp. 223–236, 2016.

- [19] B.-F. Chen and Y.-S. Yuan, "Hydrodynamic Pressures on Arch Dam during Earthquakes," *Journal of Hydraulic Engineering*, vol. 137, no. 1, pp. 34–44, 2011.
- [20] E. W. Graham and A. M. Rodriguez, "The characteristics of fuel motion which affect airplane dynamics," *Journal of applied mechanics*, vol. 19, no. 03, pp. 381–388, 1952.
- [21] G. W. Housner, "Earthquake Pressures on Fluid Containers," Eight Technical Report under Office of Naval Research, California Institute of Technology, Pasadena, CA, USA, 1954.
- [22] G. X. Wu, Q. W. Ma, and R. Eatock Taylor, "Numerical simulation of sloshing waves in a 3D tank based on a finite element method," *Applied Ocean Research*, vol. 20, no. 6, pp. 337–355, 1998.
- [23] J. Aviles and F. J. Sanchez-Sesma, "Water pressures on rigid gravity dams with finite reservoir during earthquakes," *Earthquake Engineering & Structural Dynamics*, vol. 18, no. 4, pp. 527–537, 1989.
- [24] G. Fenves and A. K. Chopra, "Simplified earthquake analysis of concrete gravity dams," *Journal of Structural Engineering (United States)*, vol. 113, no. 8, pp. 1688–1708, 1987.

## Research Article

# Modal and Vibration Analysis of Filter System in Petrochemical Plant

Zhongchi Liu,<sup>1</sup> Ji Wang,<sup>2,3</sup> Wie Min Gho,<sup>4</sup> Xiao Liu,<sup>3</sup> and Xuebing Yu<sup>1</sup>

<sup>1</sup>*Institute of Internal Combustion Engine, Dalian University of Technology, Dalian, China*

<sup>2</sup>*Collaborative Innovation Center for Advanced Ship and Deep-Sea Exploration, Dalian, China*

<sup>3</sup>*School of Naval Architecture & Ocean Engineering, Dalian University of Technology, Dalian, China*

<sup>4</sup>*Maritime Research Centre and School of Civil and Environmental Engineering, Nanyang Technological University, Singapore*

Correspondence should be addressed to Ji Wang; wangji@dlut.edu.cn

Received 17 March 2017; Revised 22 June 2017; Accepted 13 July 2017; Published 22 August 2017

Academic Editor: Hugo Rodrigues

Copyright © 2017 Zhongchi Liu et al. This is an open access article distributed under the Creative Commons Attribution License, which permits unrestricted use, distribution, and reproduction in any medium, provided the original work is properly cited.

Filter systems are widely used in petrochemical plants for removing solid impurities from hydrocarbon oils. The backwash is the cleaning process used to remove the impurities on the sieves of the filters without a need to interrupt the operation of the entire system. This paper presents a case study based on the actual project of a filter system in a petrochemical plant, to demonstrate the significant effect of vibration on the structural integrity of piping. The induced vibration had led to the structural fatigue failure of the pipes connecting the filter system. A preliminary assessment suggested that the vibrations are caused by the operation of backwashing of the filter system. A process for solving the vibration problem based on the modal analysis of the filter system using the commercial finite element software for simulation is therefore proposed. The computed natural frequencies of the system and the vibration data measured on site are assessed based on the resonance effect of the complete system including the piping connected to the filters. Several approaches are proposed to adjust the natural frequencies of the system in such a way that an optimal and a reasonable solution for solving the vibration problem is obtained.

## 1. Introduction

A filter system plays an important role in petrochemical plant for removing solid particles and impurities from hydrocarbon oils. In the system, the pipes of various geometrical properties are connected to pumps and filters to transport oil and oil products for treatment [1, 2]. The temperature of the oil and the oil products in the system can be as high as 200°C. As the flow and collision of oils in the pipes cause severe vibrations, this led to fatigue and fracture of structural pipe members and connections after being subject to a number of load cycles [3]. As a result, there is a need to examine carefully the most appropriate approach to reducing the unexpected vibrations to prevent the oil leakages and structural member failure in the system.

One of the earliest studies of vibration problems in pipes was conducted by Ashley and Haviland [4]. They used a beam model to establish differential equations for analyzing the pipe motion. On the other hand, Niordson [5] built a shell

model to derive differential equations for solving pipe vibration, where the results were found to be comparable to that of Ashley and Haviland [4]. A more complicated study of pipe vibration due to the effect of fluid-structure interaction was carried out based on travelling-wave method by Païdoussis and Denise [6]. Lavooij and Tusseling [7] however derived differential equations using the method of characteristics for solving pipe vibration. For the past 2 decades, the research of pipe vibration has been directed towards the nonlinear analysis, Gorman et al. [8] studied the nonlinear vibration of pipeline system based on a series of simple models comprising pipes of various geometrical properties.

In a petrochemical plant, the filter system is used to filter solid particles and impurities from hydrocarbon oils. The solid particles will clog the sieves after some period of time of operation and thus will affect the flow of oils in pipes. However, it is impossible to replace the sieves or to remove the filter for cleaning while the filter system is in operation. Therefore, a backwashing process is used to clean the sieves of

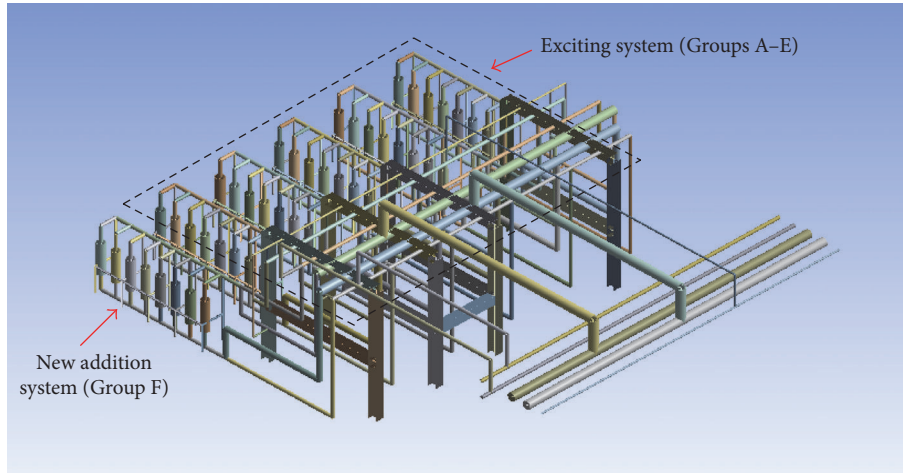


FIGURE 1: The exciting and addition filter system.

the filters. With full particles clogging the sieves and reduced speed of oil flows, a pressure difference between inlet and outlet of the filter system will be generated. The backwashing process will then be activated due to the difference of these working pressures. The backwashing process uses the product oil as a backwashing liquid to flush the filter nets at high pressure so that the solid particles on the sieves could be removed. Once the backwashing liquid hits the filter nets and pipes after it passes through the filters, it causes the filter and the piping system to vibrate. In general, the magnitude of vibration is insignificant and cannot be observed. However, with the increasing production of oil products to meet the demand, the petrochemical company redesigned the system with one additional filter system (Group F) installed next to the existing filters (Groups A to E) as shown in Figure 1. Despite the magnitude of vibration being considered small during the process of backwashing, the oil leakages on pipes and connections however appear after a few years of operation.

An internal stress analysis of the pipes was thereafter performed to rectify the unexpected vibration problem that resulted in fatigue cracking on pipes. The internal stress analysis is a conventional approach commonly adopted for analyzing pipe abnormality under various load conditions based on structural mechanics [9, 10]. In recent years, Wu et al. [11] carried out a stress analysis model of tunnel pipes under various load combinations. Huang et al. [12] conducted a stress analysis model of elastic laying pipelines in mountainous areas. There is a need to note that the exciting forces of these cases could not easily be determined and measured. On the other hand, the internal forces of the pipelines were typically small that would not result in structural ultimate failure. Most of the structural failures of these pipelines occurring within the elastic limit of materials were actually due to fatigue under load cycles which applied for a period of time. Thus, the stress analysis in this case was not suitable to assess the failure behavior of the filter system. The objective of the current study is to determine a suitable solution with the adjustment of period of vibration to reduce the amplitude of vibration of the system.

In the current study, the filter and the piping system were connected and modelled as a complete system. A modal analysis is conducted to determine the natural frequencies of the system. The exciting forces of the vibration include the pulses of the oil in the pipes and the interaction effect among the oil, the pipes, and the filter system. The response vibration of the complete system due to backwash was measured and presented in a form of time spectrum. The time spectrum was then transformed into the frequency domain by means of fast Fourier transformation (FFT). The FFT spectrum allowed the response frequencies that contributed to vibration to be determined. The peaks of the spectrums presented the frequencies to the natural frequencies of the complete system, where the unexpected vibration is due to the effect of resonance. With the comparison of the FFT spectrums of response vibration to the natural frequencies of the complete system, the region of resonance could be identified [13]. The natural frequencies that cause the resonance and the locations of resonance vibrations could therefore be obtained. As a result, the filter and the piping system could be designed with a specific natural frequency to reduce resonance vibration. Apart from the design of the system to the required natural frequency, the construction time to integrate the new and the existing filter and piping system based on the actual site conditions could also be optimized. In this paper, a method for solving the vibration problem of the complete system with a certain amount of exciting force is summarized and presented.

## 2. Modal Analysis

*2.1. Modelling of Filter and the Piping System.* The filter and the piping system are modelled using commercial software SolidWorks and ANSYS, as shown in Figure 2, with the modal analysis conducted based on ANSYS.

There are 6 groups of filter and piping system. Each group comprises 8 filter elements. The detail of each filter system is shown in Figure 3. The oil flows through the filter from the bottom of the system from Pipe 1 (inlet) to Pipe 2 (outlet). After the sieves are clogged with solid particles, the backwash

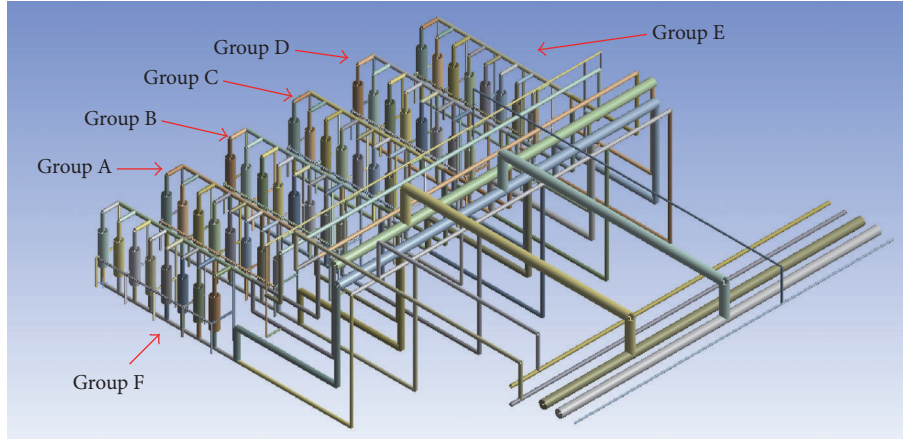


FIGURE 2: A filter and piping system model.

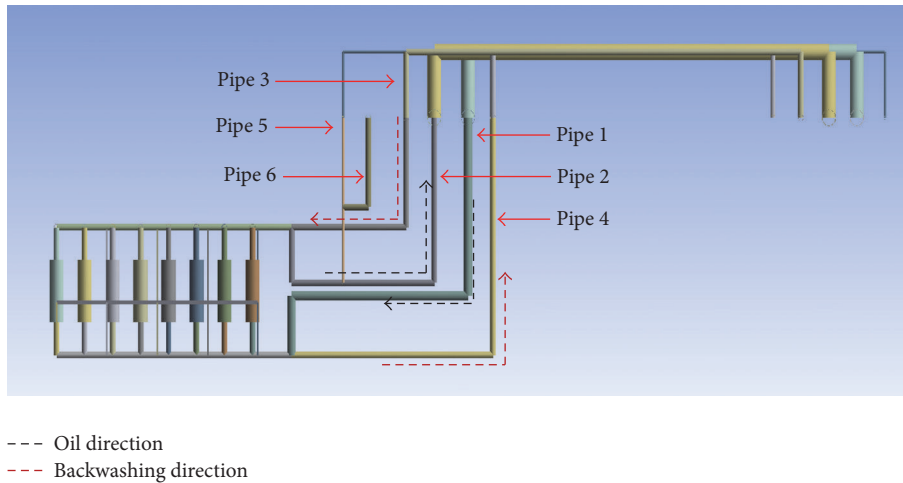


FIGURE 3: Details of each filter system.

operation was activated at a pressure difference between the top and bottom of the filters at  $10 \text{ N/cm}^2$ . The backwashing oil enters the system from Pipe 3 to Pipe 4. Pipes 5 and 6 are gas pipes for gas backwashing after the filter nets could not be cleaned using the backwash liquid. These two pipes were usually empty. The 5 pipes were fixed onto a large bracket, which was connected to other brackets on the floor. In the modelling, the brackets were considered fixed on the ground.

The filters were made of stainless steel. Each single filter comprised 28 filter elements with diameter 25 mm and length 814 mm. The filter elements were threaded into a common flange. The pipes are made of mild steels with geometrical properties as shown in Table 1. Apart from the filters and the pipes, the brackets representing the locations of the constraints would have a significant effect on the natural frequencies of the complete system. These brackets are made of mild steels with cross-sectional properties presented in Figure 4. The complete filter and piping system and their support brackets can be seen in Figure 5.

**2.2. Modal Analysis.** The modal analysis was carried out to determine the natural frequencies of the complete system. In

TABLE 1: Outer diameter and thickness of pipes.

Pipe number	Outer diameter (mm)	Thickness (mm)
(1)	150	7
(2)	100	7
(3)	100	7
(4)	100	7
(5)	100	7
(6)	50	4

the analysis, there were  $N$  nodes in the entire system. Each node contained six (6) degrees of freedom with 3 translations and 3 rotations in  $x$ -,  $y$ -, and  $z$ -axis direction [14–16]. A total of  $6N$  degrees of freedom were considered in this case. For the complete filter and piping system, it would have  $6N$  natural frequencies. The equations of motion can be expressed as follows [14–17]:

$$[M_x] x'' + [C_x] x' + [K_x] x = \{F_x\},$$

$$[M_y] y'' + [C_y] y' + [K_y] y = \{F_y\},$$





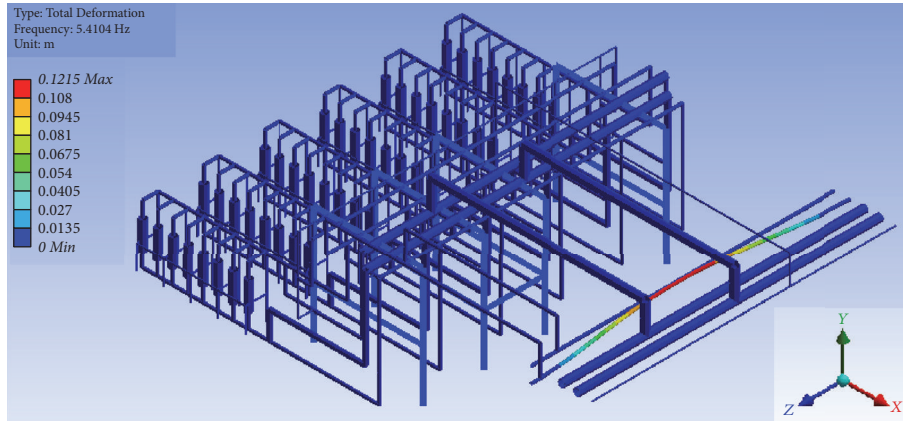


FIGURE 6: Vibration mode of the 1st modal order.

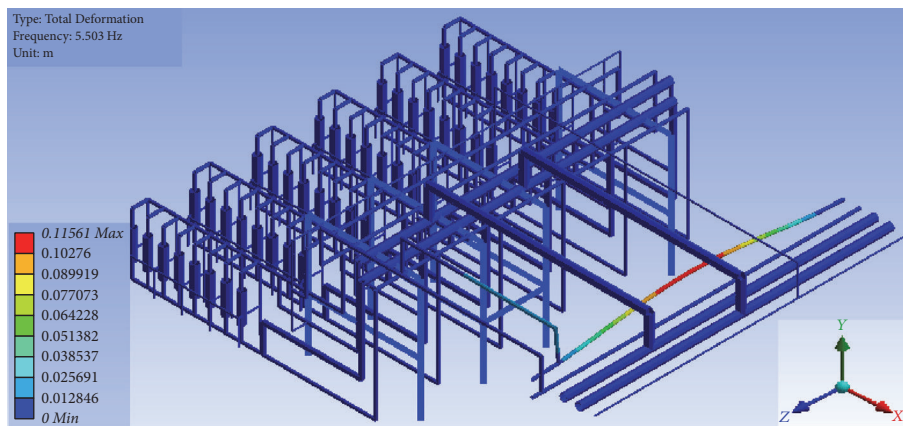


FIGURE 7: Vibration mode of the 2nd modal order.

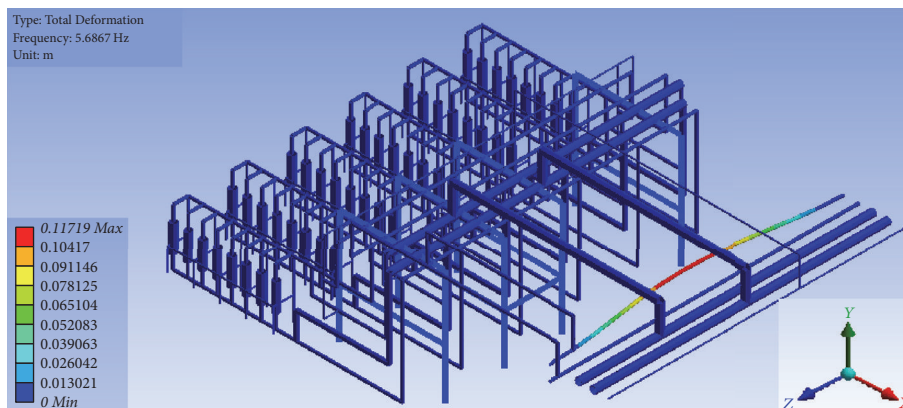


FIGURE 8: Vibration mode of the 3rd modal order.

problem in this case was to propose a suitable method based on the natural frequency of the system.

#### 4. Solutions

From the modal analysis and the vibration measurement, the natural frequencies of the system should be increased

above 10 Hz to avoid the effect of resonance. From the observation of the system performance on site, it can be seen that the vibration actually occurred on free span long pipes without any supports. These pipes were located in the critical vibration of the system. Thus, adding adequate constraints to stiffen these pipes was the first approach to solving the vibration problem.

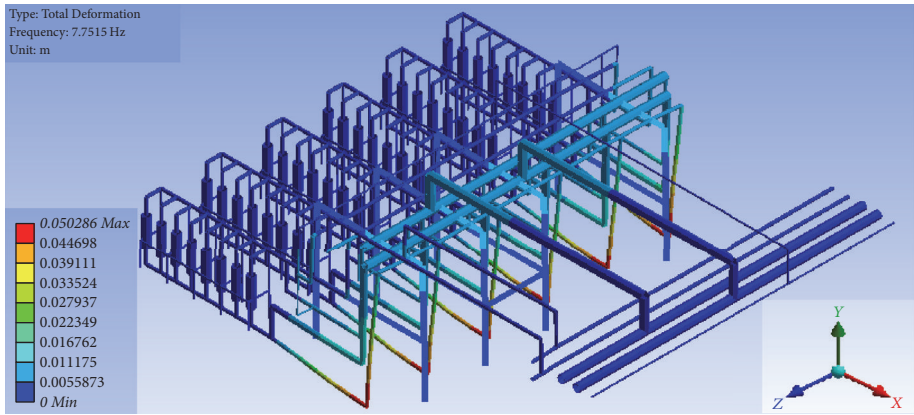


FIGURE 9: Vibration mode of the 4th modal order.

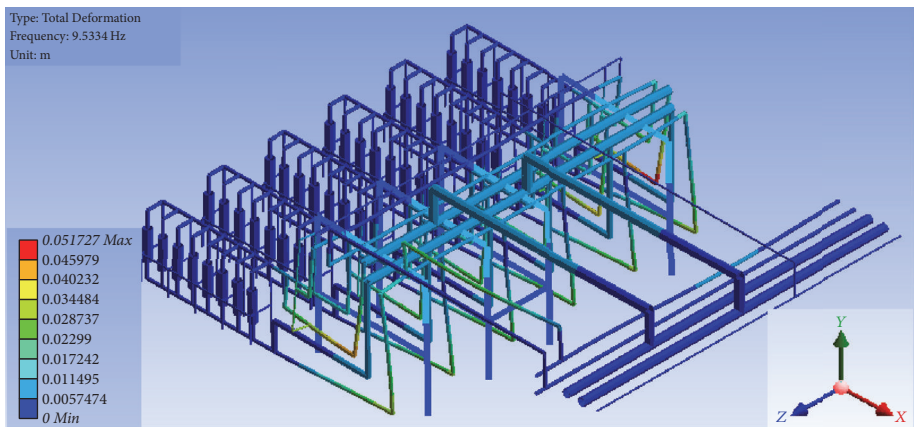


FIGURE 10: Vibration mode of the 5th modal order.

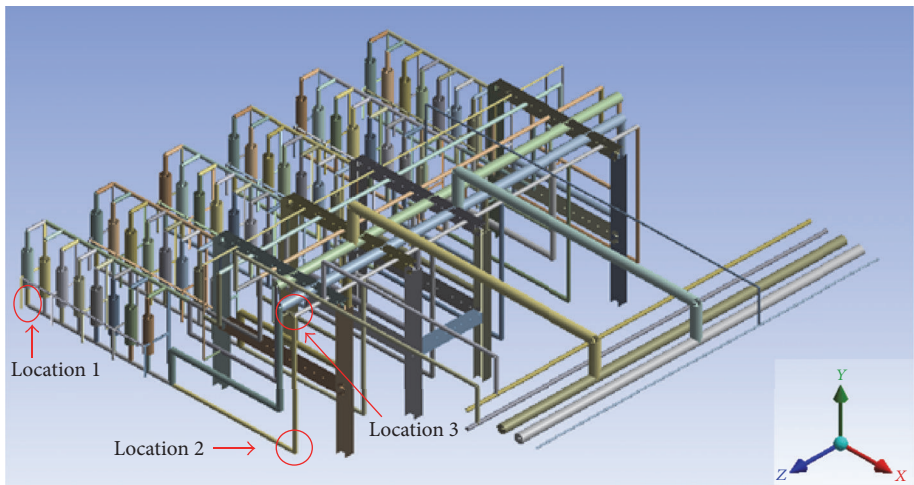


FIGURE 11: Locations of vibration measurement.

4.1. *Solution 1.* The first approach is to add adequate constraints by connecting the pipes together. This was carried out by connecting the long pipes (Location 4) using 50 mm diameter pipes. After the pipes are connected, the natural frequencies of the system slightly increase, as shown in Table 3.

However, the vibration of the modal orders with natural frequencies below 10 Hz no longer occurred at Location 4. As shown in Figures 16 and 17, the first 2 modes of vibration showed that the vibration locations of the long pipes in the first few modal orders had been shifted.

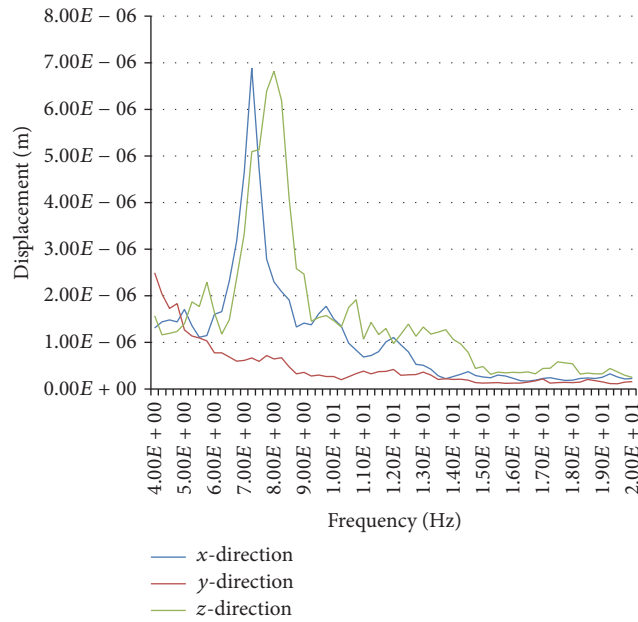


FIGURE 12: The FFT spectrums of Location 1.

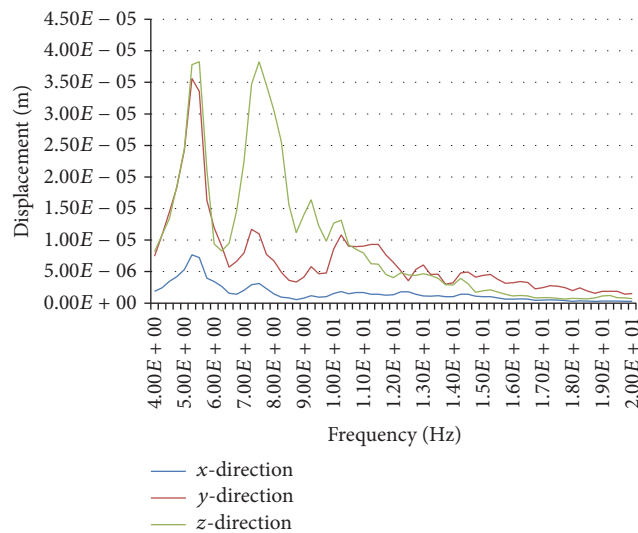


FIGURE 13: The FFT spectrums of Location 2.

The second approach is to connect the long pipes above the passage with 2 additional supports at both sides, as shown in Figure 18. With this arrangement, the natural frequencies of the system are found to increase as shown in Table 4. The vibration locations of the first several modal orders were located along the long pipes in Location 5.

The 3rd approach is to add additional constraints at Location 1 by connecting the long pipes with 50 mm diameter pipes, as shown in Figure 19. With the additional constraints, all the natural frequencies of the system are found higher than 10 Hz, which is outside the range of resonance (Table 5).

**4.2. Solution 2.** The process of Solution 2 was identical to that of Solution 1. The locations of additional constraints are similar to those in Solution 1, as shown in Figure 20. The

difference between the 2 solutions was that the constraints of the long pipes in Solution 2 were supported on the floor and other parts of the entire structure system. The natural frequencies of Solution 2 are higher than 10 Hz (Table 6). The purpose of proposing Solution 2 is to provide an alternative taking into the consideration of construction process of the existing additional filter and piping system.

**4.3. Solution 3.** For Solution 3, the pipes were connected using spring bumpers to control the increasing stress of the structure system with reduced vibration. The bumpers also absorbed part of the vibration energy. However, the spring bumpers did not increase the natural frequencies of the system effectively. The natural frequencies of the new structure with additional filter and piping system are

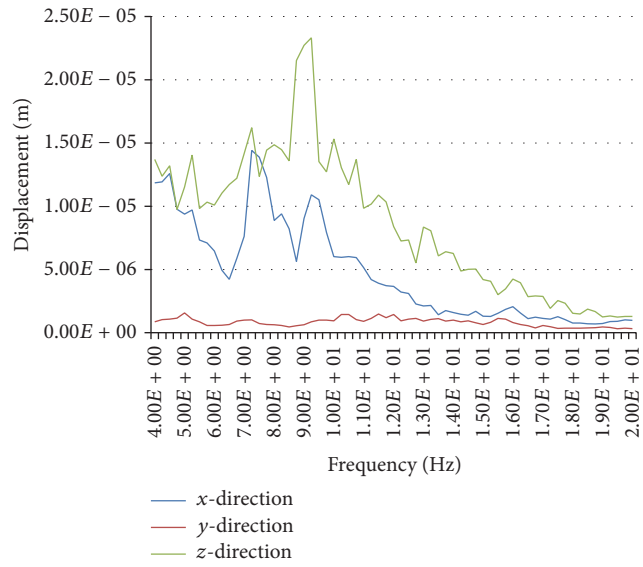


FIGURE 14: The FFT spectrums of Location 3.

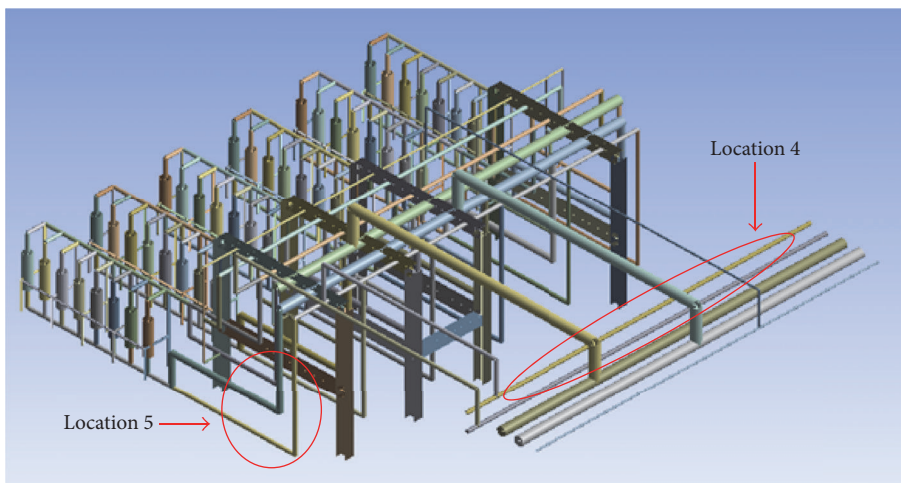


FIGURE 15: Critical locations of vibration.

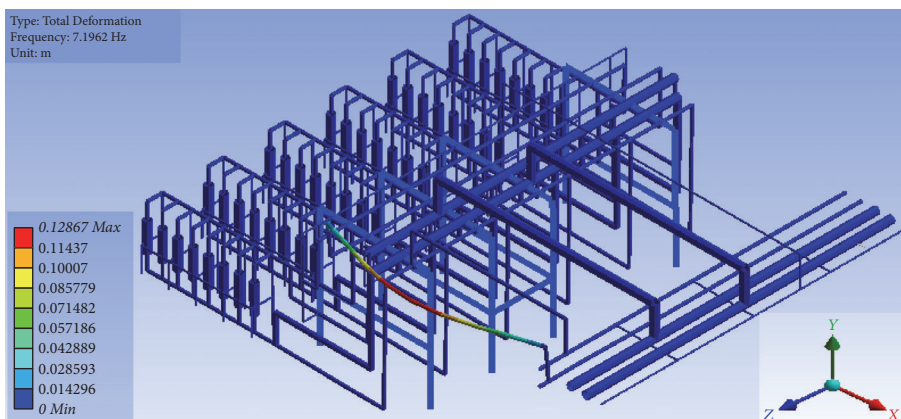


FIGURE 16: Vibration mode of 1st modal order.

TABLE 3: Natural frequencies of the system (1st approach).

Modal order	Natural frequency
(1)	7.1962
(2)	7.5748
(3)	9.3668
(4)	10.426
(5)	10.643
(6)	10.918
(7)	11.347
(8)	11.413
(9)	11.72
(10)	12.312
(11)	12.822
(12)	13.144
(13)	13.517
(14)	14.292
(15)	14.715
(16)	14.751

TABLE 4: Natural frequencies of the system (2nd approach).

Modal order	Natural frequency
(1)	7.6771
(2)	9.7916
(3)	10.425
(4)	10.558
(5)	10.759
(6)	10.918
(7)	11.349
(8)	11.414
(9)	12.327
(10)	12.834
(11)	13.139
(12)	13.261
(13)	13.551
(14)	14.308
(15)	14.401
(16)	14.715

TABLE 5: Natural frequencies of the system (3rd approach).

Modal order	Natural frequency
(1)	10.558
(2)	11.323
(3)	13.261
(4)	19.462
(5)	19.984
(6)	20.137
(7)	20.491
(8)	20.534
(9)	20.678
(10)	20.928

TABLE 6: Natural frequencies of the new system.

Modal order	Natural frequency
(1)	12.156
(2)	16.414
(3)	17.301
(4)	18.083
(5)	18.367
(6)	18.444
(7)	18.541
(8)	18.636
(9)	19.723
(10)	20.321

TABLE 7: Natural frequencies of the new structure.

Modal order	Natural frequency
(1)	5.6967
(2)	7.3319
(3)	8.6949
(4)	10.512
(5)	10.534
(6)	11.01
(7)	11.048
(8)	11.428
(9)	11.488
(10)	12.241

TABLE 8: Natural frequencies of original and new system.

Modal order	Original	Solution 1	Solution 2	Solution 3
(1)	5.4104	10.558	12.156	5.6967
(2)	5.503	11.323	16.414	7.3319
(3)	5.6867	13.261	17.301	8.6949
(4)	7.7515	19.462	18.083	10.512
(5)	9.5334	19.984	18.367	10.534
(6)	10.436	20.137	18.444	11.01
(7)	10.64	20.491	18.541	11.048
(8)	10.918	20.534	18.636	11.428
(9)	11.337	20.678	19.723	11.488
(10)	11.37	20.928	20.321	12.241

listed in Table 7. As each spring bumper is only effective in one direction, more constraints would be needed in this solution, which led to a longer construction time and a more complicated construction process.

*4.4. Optimal Solution.* The natural frequencies of Solutions 1, 2, and 3 are summarized in Table 8. Unlike Solution 3, both Solutions 1 and 2 increase the natural frequencies to a level higher than 10 Hz. Solution 3 could not achieve the same effect even with additional constraints. It can therefore be concluded that a fixed constraint would perform better in changing the natural frequencies than an elastic restraint.

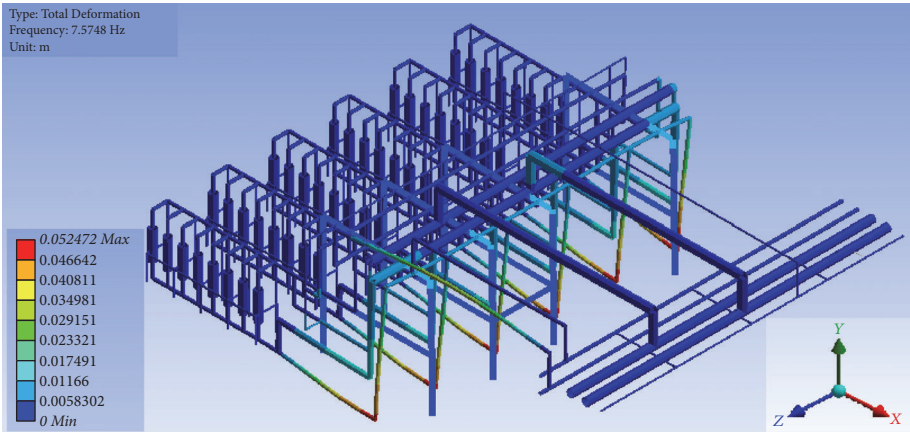


FIGURE 17: Vibration mode of 2nd modal order.

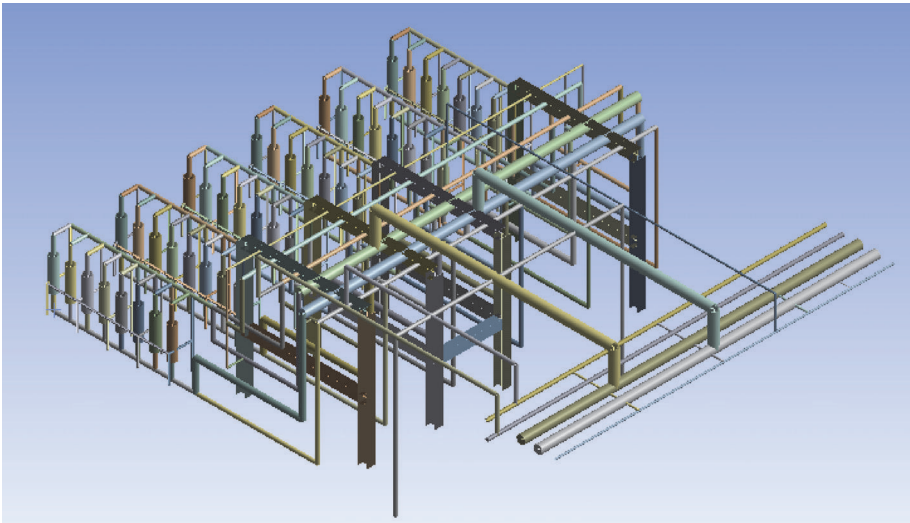


FIGURE 18: Additional constraints (2nd approach).

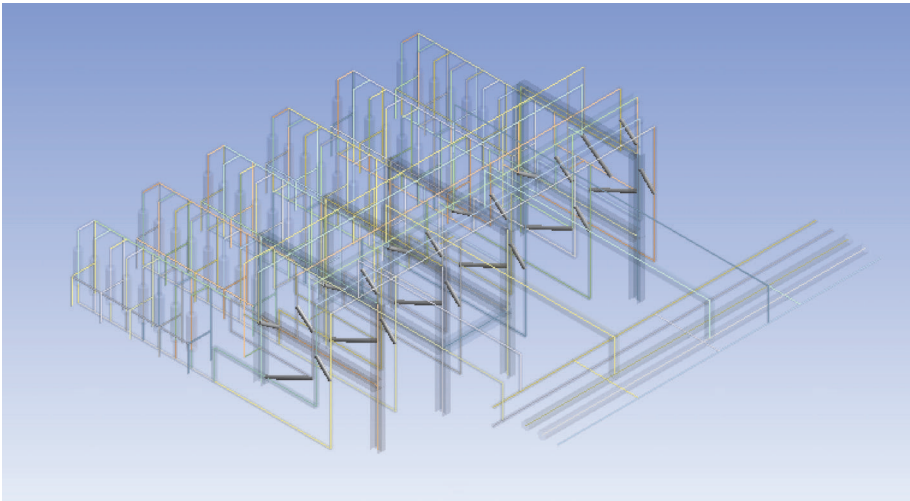


FIGURE 19: Additional constraints (3rd approach).

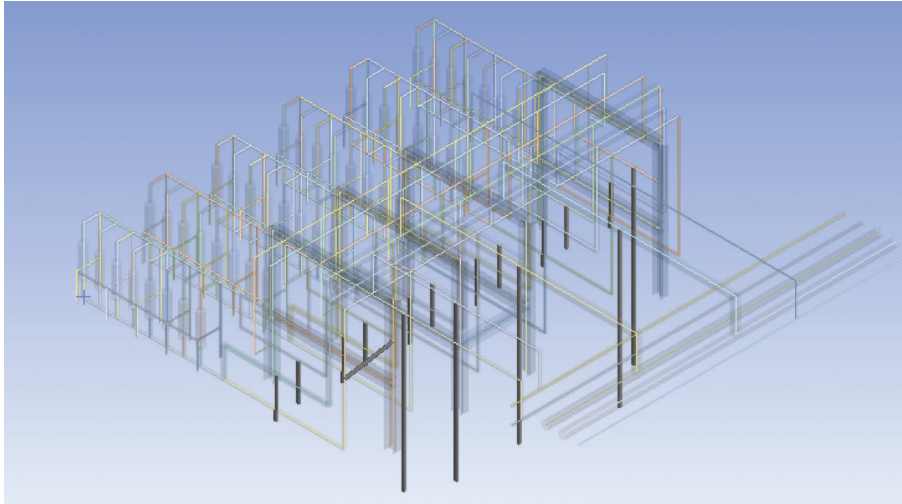


FIGURE 20: Additional constraints in Solution 2.

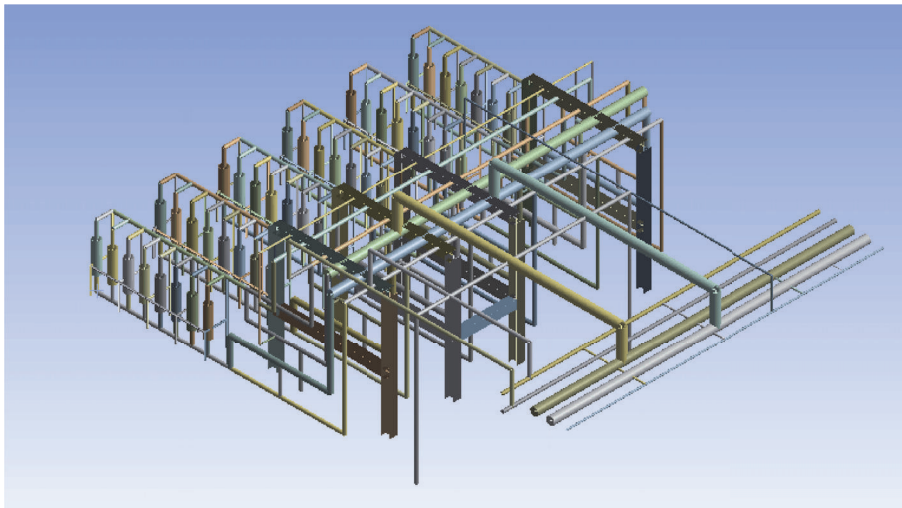


FIGURE 21: Structural modification.

Further, an elastic restraint such as a spring bumper was only effective in one direction, which requires a more complex construction and a longer construction time. Based on the simulation results, Solution 1 or 2 should be chosen as the optimal solution. The choice of a suitable solution would depend on the kind of constraints and the requirement on site.

**4.5. Structural Modification.** The structural modification combined Solutions 1 and 2 based on site condition. The long pipes in Location 4 in Solution 1 were connected with each other. The pipes above were supported and fixed onto a large bracket. As the pipes in Location 5 were very close to the foundation of the system, they were fixed to the short brackets on the floor (Figure 21). A vibration measurement of Location 2 was carried out to inspect the effect of the modification of the system. The FFT spectrums are plotted as shown in Figure 22. The peaks of the spectrums did not exist and the displacement of vibrations was reduced. Thus by changing

the natural frequencies, the system could be made outside the region of resonance.

## 5. Conclusion

The current study provides three (3) solutions to reduce the unexpected vibration of a backwashing system of a petrochemical plant. The comparison of the results between the site measurement and the modal analysis suggested that the cause of vibration of the system can be speculated as being resonance.

All the 3 proposed solutions will result in the increment of natural frequencies of the system. However, from the simulation, it can be seen that the fixed constraint is more effective than the elastic restraint in changing the natural frequencies to reduce the vibration of the structure system. The proposed Solution 3, with spring bumpers to constrain the pipes, has a longer construction time and is less effective in increasing the natural frequencies. With the consideration

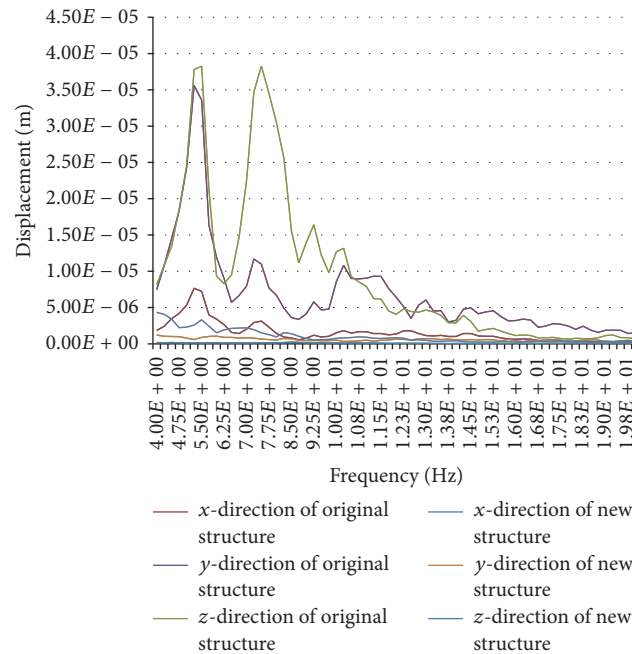


FIGURE 22: The FFT spectrums of original and new structure at Location 2.

of analysis results and the site conditions, Solutions 1 and 2 are the optimal solutions for solving the resonance problem of backwashing system. The combined Solutions 1 and 2 provide the best solution based on the site situation.

## Conflicts of Interest

The authors declare that they have no conflicts of interest.

## References

- [1] J. Tian, C. Yuan, L. Yang, C. Wu, G. Liu, and Z. Yang, "The vibration analysis model of pipeline under the action of gas pressure pulsation coupling," *Engineering Failure Analysis*, vol. 66, pp. 328–340, 2016.
- [2] H. Lu, K. Huang, and S. Wu, "Vibration and stress analyses of positive displacement pump pipeline systems in oil transportation stations," *Journal of Pipeline Systems Engineering and Practice*, vol. 7, no. 1, Article ID 05015002, 2016.
- [3] J. C. Wachel, F. R. Szenasi, and S. C. Denison, "Analysis of vibration and failure problems in reciprocating triplex pumps for oil pipelines," in *Proceedings of the Proc., Energy-Sources and Technology Conf. and Exhibition*, pp. 1–8, Dallas, TX, USA, 1985.
- [4] H. Ashley and G. Haviland, "Bending vibrations of a pipe line containing flowing fluid," *Journal of Applied Mechanics*, vol. 17, no. 3, pp. 229–232, 1950.
- [5] F. I. Niordson, *Vibrations of a Cylindrical Tube Containing Flowing Fluid*, Transactions of the Royal Institute of Technology, Stockholm, Sweden, Elanders Boktr, Stockholm, Sweden, 1953.
- [6] M. P. Paidoussis and J.-P. Denise, "Flutter of cylindrical shells conveying fluid," *Journal of Sound and Vibration*, vol. 16, no. 3, pp. 459–461, 1971.
- [7] C. S. W. Lavooij and A. S. Tusseling, "Fluid-structure interaction in liquid-filled piping systems," *Journal of Fluids and Structures*, vol. 5, no. 5, pp. 573–595, 1991.
- [8] D. G. Gorman, J. M. Reese, and Y. L. Zhang, "Vibration of a flexible pipe conveying viscous pulsating fluid flow," *Journal of Sound and Vibration*, vol. 230, no. 2, pp. 379–392, 2000.
- [9] R. K. Watkins and L. R. Anderson, *Structural Mechanics of Buried Pipes*, CRC Press, London, UK, 1999.
- [10] G. Q. Yu and Z. H. Lv, "Load calculation and analysis of heating-pipeline based on elastic center method," *GasHeat*, vol. 28, no. 12, pp. 20–24, 2008.
- [11] X. N. Wu, Y. Xian, K. Huang, M. L. Hu, and B. J. Shang, "Therstress analysis of tunnel gas pipeline underoperating situation," *Oil GasStorage Trans*, vol. 31, no. 12, pp. 927–930, 2012.
- [12] K. Huang, S. J. Wu, H. F. Lu, Y. Xian, and Q. W. Su, "Stressanalysis of the pipeline laid along the slope," *Natural Gas Oil*, vol. 30, no. 4, pp. 1–4, 2012.
- [13] Z. J. Wang and Y. Zhou, "Vortex-induced vibration characteristics of an elastic square cylinder on fixed supports," *Journal of Fluids Engineering, Transactions of the ASME*, vol. 127, no. 2, pp. 241–249, 2005.
- [14] W. T. Thomson, *Free Vibration. Theory of Vibration with Applications*, Allen Unwin, London, UK, 2nd edition, 1981.
- [15] W. T. Thomson, *Two Degrees of Freedom. Theory of Vibration with Applications*, Allen Unwin, London, UK, 2nd edition, 1981.
- [16] W. T. Thomson, *Properties of Vibration Systems. Theory of Vibration with Applications*, Allen Unwin, London, UK, 2nd edition, 1981.
- [17] S. Gao, L. Wen, and W. Liao, "Application of dynamic characteristic analysis technology for stator end-winding of large capacity turbo-generator," in *Proceedings of the 3rd International Symposium on Intelligent Information Technology Application, (IITA '09)*, pp. 669–671, November 2009.
- [18] M. R. Kruntcheva, "Acoustic-structural resonances of thin-walled structure - Gas systems," *Journal of Vibration and Acoustics, Transactions of the ASME*, vol. 128, no. 6, pp. 722–731, 2006.

## Research Article

# Shock Mechanism Analysis and Simulation of High-Power Hydraulic Shock Wave Simulator

Xiaoqiu Xu,<sup>1,2</sup> Han Tao,<sup>1</sup> and Junwei Han<sup>1</sup>

<sup>1</sup>*School of Mechatronic Engineering, Harbin Institute of Technology, Harbin 150000, China*

<sup>2</sup>*Department of Mechanics, Harbin University of Science and Technology, Rongcheng Campus, Rongcheng 264300, China*

Correspondence should be addressed to Xiaoqiu Xu; 13b908020@hit.edu.cn

Received 10 May 2017; Accepted 21 June 2017; Published 2 August 2017

Academic Editor: Abdul Qadir Bhatti

Copyright © 2017 Xiaoqiu Xu et al. This is an open access article distributed under the Creative Commons Attribution License, which permits unrestricted use, distribution, and reproduction in any medium, provided the original work is properly cited.

The simulation of regular shock wave (e.g., half-sine) can be achieved by the traditional rubber shock simulator, but the practical high-power shock wave characterized by steep prepeak and gentle postpeak is hard to be realized by the same. To tackle this disadvantage, a novel high-power hydraulic shock wave simulator based on the live firing muzzle shock principle was proposed in the current work. The influence of the typical shock characteristic parameters on the shock force wave was investigated via both theoretical deduction and software simulation. According to the obtained data compared with the results, in fact, it can be concluded that the developed hydraulic shock wave simulator can be applied to simulate the real condition of the shocking system. Further, the similarity evaluation of shock wave simulation was achieved based on the curvature distance, and the results stated that the simulation method was reasonable and the structural optimization based on software simulation is also beneficial to the increase of efficiency. Finally, the combination of theoretical analysis and simulation for the development of artillery recoil tester is a comprehensive approach in the design and structure optimization of the recoil system.

## 1. Introduction

In modern shooting range construction process, the consumption was significantly increased due to the real firing practice. Four sorts of capability, that is, reliability, security, testability, and supportability, were the critical aims for the examinations [1]. Increasing development quality, shortening test cycle, and saving full-life research cost had been defined as important objectives of improving operational effectiveness of artillery equipment [2]. Since the 1950s, equivalent reliable artillery simulation test method had been initially explored at home and abroad. For example, an artillery fire shock simulation tester equipped with a hydraulic shock cylinder was developed by US researchers [3, 4]. According to the reports, this simulator was characterized by high accuracy, promoted safety performance, and pertinence, which successfully avoided the shortages as mentioned above.

With the fast development of hardware and software resource, computational simulation is gradually introduced in the design of fire shock simulation tester. Yangwu

innovatively reported the build of a numerical simulation model of artillery recoil system simulator with applying the classical internal ballistics and systematic dynamic related theories [5].

A further optimization of the simulation model was proposed by Hang and Zhang which considered the load conditions and structure parameters of DS-II artillery recoil system [6]. Changchun et al. developed a virtual recoil tester in MSC in the ADAMS software for investigating a stereotype of ground artillery tester. The simulation of dynamic recoil process was achieved via applying homogeneous experiment design and influence study of shock parameters using Matlab [7, 8]. Yuliang et al. carried out finite element simulations and test researches of constitutive models of the rubber wave simulators and conducted optimization design of rubber wave simulators [9–13]. Jiao et al. analyzed shock wave characteristics of a hydraulic damper for shock test machine and achieved the influence of the annular gap, the diameter of the orifice pore, and the shock wave under different velocities [14]. Duym et al. carried out evaluation of shock absorber

models and presented a nonexhaustive overview of shock absorber models [15]. Shams et al. analyzed hydraulic shock absorber valve behavior using CFD-FEA [16]. JiuHong et al. presented a design method for fluid viscous dampers, derived mathematical model of viscous dampers, and carried out the shock test [17]. Hou et al. proposed a new model for nonlinear viscous fluid dampers with a simple annular orifice and analyzed its fluid dynamics behavior and shear-thinning effects [18–20]. In conclusion, the method where mass block with high velocity impacted artillery muzzle to simulate artillery firing process was proven as a feasible recoil simulation test method [21, 22], and the effects of structure parameters and shock parameters on dynamics and behavior had drawn attentions for hydraulic shock absorber as well as viscous fluid dampers. In order to verify the effectiveness of the simulation method, the similarity of time consequence was an important evaluation method; whatever the test data or the simulation data, both were seen as time consequence. The similarity measuring algorithm included time bend distance [23], slope distance [24], curvature distance [25], and radian distance [26]. Time bend distance was hard to calculate and slope distance and radian distance reflected the relationship within the adjacent time and were short of the adjacent time relevance. The curvature distance algorithm not only reflected the relationship but also expressed the relevance of the adjacent time. Wang et al. carried out credibility evaluation for guidance system dynamic simulation with curvature distance [27]. Yuliang et al. calculated accuracy evaluation of cannon dynamic recoil simulation based on the numerical and shape similarity and verified that rubber shock wave simulator could realize the cannon dynamic recoil motion [28].

In shock simulation tests, the shock wave simulator played an important role in energy transferring and conversion. In addition, it could also achieve the recoil simulation of various cannons under various loading conditions with adjusting the structure parameters. For a regular wave test, a rubber shock wave simulator was usually used. However, practical shock wave was a complex shock curve; traditional rubber shock wave simulator was not fit for practical shock wave.

Therefore, in the current work, a novel high-power hydraulic shock wave simulator was proposed to simulate the real shock wave. In the paper, the shock process and working principle were described and optimization design analysis of reasonable shock's characteristic parameters was achieved. Finally, the similarity evaluation of shock wave simulation was achieved for evaluating the simulation method based on the curvature. The analysis results indicated that the novel high-power hydraulic shock wave simulator could solve the reappearance problem of practical high-power shock wave, which replaced a traditional rubber wave simulator, and also supplied theoretical references for designs of artillery fire shock simulation test.

## 2. Structure and Working Principle

*2.1. Principle of the Live Firing Muzzle Shock Test.* Breech resultant force  $F_{pt}$  that acted on breech axis direction in live firing was an active force that drives artillery recoil motion,

which reaches  $10^7$  N, and the whole process just requires 5–11 ms; this process belongs to instant strong shock.

$$m_h = \frac{d^2x}{dt^2} = F_{pt} - F_R, \quad (1)$$

where  $m_h$  was the mass of recoil parts;  $x$  was recoil displacement;  $t$  was recoil time;  $F_{pt}$  was breech resultant force;  $F_R$  was recoil resistance. Breech resultant force  $F_{pt}$  was expressed as formula (2), when the projectile moves in the bore [29].

$$F_{pt} = \frac{1}{\varphi} \left( 1 + \frac{1}{2} \frac{m_\omega}{m_q} \right) sp, \quad (2)$$

where  $\varphi$  was secondary work calculation coefficient,  $m_\omega$  was explosive payload,  $m_q$  was projectile mass,  $s$  was cross-sectional area of line chamber, and  $p$  was powder gas pressure, which changes with time and projectile trip. Shock of the projectile on the bore disappeared at the moment when projectile rushed out of the artillery muzzle, which led to a sudden increase of breech resultant force, a phenomenon where transient muzzle-exit  $F_{ptg}$  jumped to  $F_g$  was formed at the beginning of after-effect period.

$$F_{ptg} = \frac{1}{\varphi} \left( 1 + \frac{1}{2} \frac{m_\omega}{m_q} \right) sp_R, \quad (3)$$

$$F_g = \frac{1}{\varphi} \left( \varphi_1 + \frac{1}{2} \frac{m_\omega}{m_q} \right) sp_g,$$

where  $p_g$  was explosive gas's average pressure in artillery bore at the moment of projectile out from the artillery muzzle and  $\varphi_1$  was secondary coefficient considering projectile rotation and friction. At explosive gas's after-effect period, breech resultant force involves a complex phenomenon of explosive gas flowing out from an artillery muzzle. For convenient calculation,  $F_{pt}$  was expressed as formula (4) with exponential empirical formula.

$$F_{pt} = F_g e^{-1/h}, \quad (4)$$

where  $h$  was time constant of breech resultant force damping speed at after-effect period and  $t$  was after-effect time at the beginning of after-effect period. In simulation test, an active force that drives artillery recoil motion was  $F_C$ , generated by mass block with high velocity impacting an artillery muzzle.

$$m_h = \frac{d^2X}{dt^2} = F_C - F_R. \quad (5)$$

An alternative model of breech resultant force, where shock force  $F_C$  replaced breech resultant force  $F_{pt}$ , played a similar explosive and promoting role for propellant burning. To be certain that shock simulation test possessed higher precision, we need to design right shock parameters and wave simulator structure forms to ensure the equivalence between shock force and breech resultant force. Therefore, for making sure that dynamic behavior of artillery fire shock simulation test was similar to live firing, similar simulation method was chosen, which could generate instant strong shock effect.

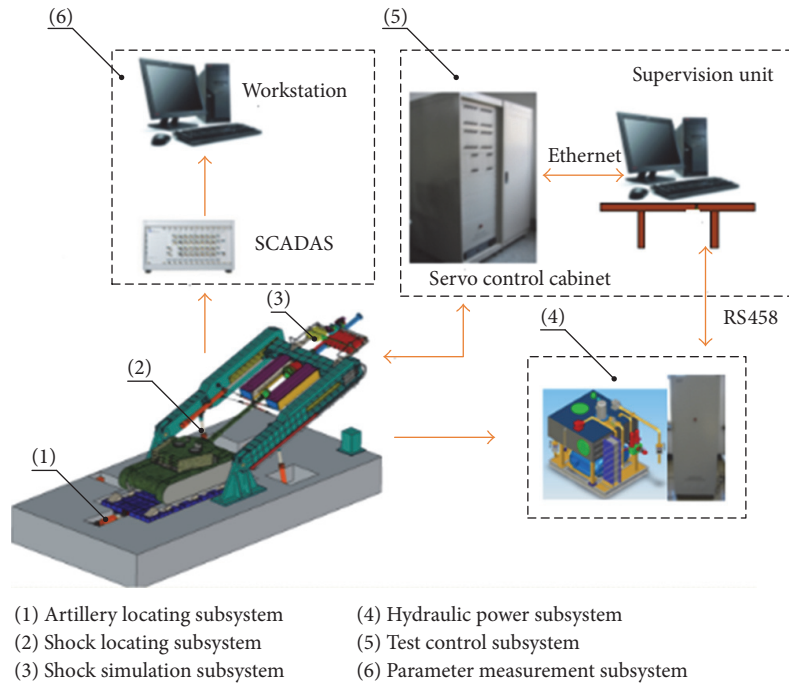


FIGURE 1: Firing shock simulation test system.

2.2. *Shock Simulation Tester Description.* Firing shock simulation test system (shown in Figure 1) was a distributing measurement and control system based on industrial Ethernet and fieldbus technology, and the system was composed of six subsystems which were artillery locating subsystem, shock simulation subsystem, test control subsystem, shock locating subsystem, parameter measurement subsystem, and hydraulic power subsystem. In the shock simulation subsystem, shock simulation tester was the key component.

The shock simulation tester used in the firing shock simulation test system was shown in Figure 2 for artillery firing process simulation by computer control. The tester took liquid as storage medium to simulate the shock wave based on controlled hydraulic technology. In the past shock test, the rubber shock simulator was used for simulating the shock wave, and the rubber shock simulator is composed by several rubber blankets with certain stiffness that was calculated for meeting shock wave requirements, and these rubber blankets were installed on subpanel.

Controlling firing rate, firing angle and shock load simulation were realized, which were used to test reliability and durability of the big bore ground and self-propelled and tank artillery. Hydraulic subsystem drove big mass block with shock wave simulator; then the high-velocity big mass block impacted artillery muzzle and simulated the deflagration effect. The simulations made artillery shock test system generate similar recoil motion with artillery live firing.

Shock and restoration processes were shown in Figure 3. Shock wave simulator was accelerated by velocity generator and then impacted muzzle to simulate the required shock wave; after a shock was finished, the shock wave simulator was restated. After the above steps, a shock test was finished, repeating the above process to carry out many experiments.

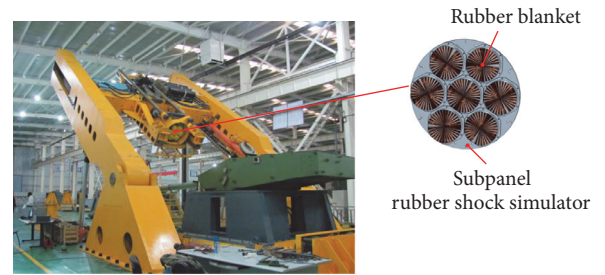


FIGURE 2: Shock simulation tester with rubber shock simulator.

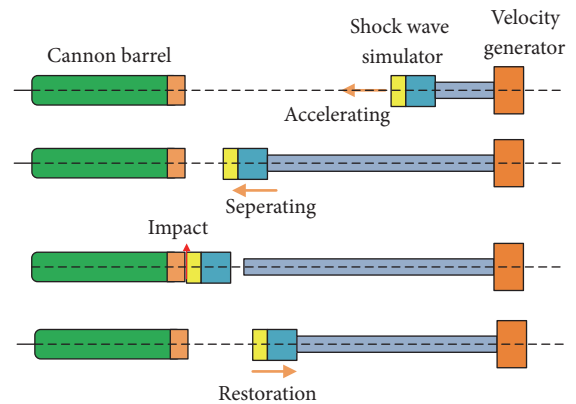


FIGURE 3: Shock and restoration process.

In shock simulation tests, the shock wave simulator was a key component which played an important role in transfer and conversion of shock energy.

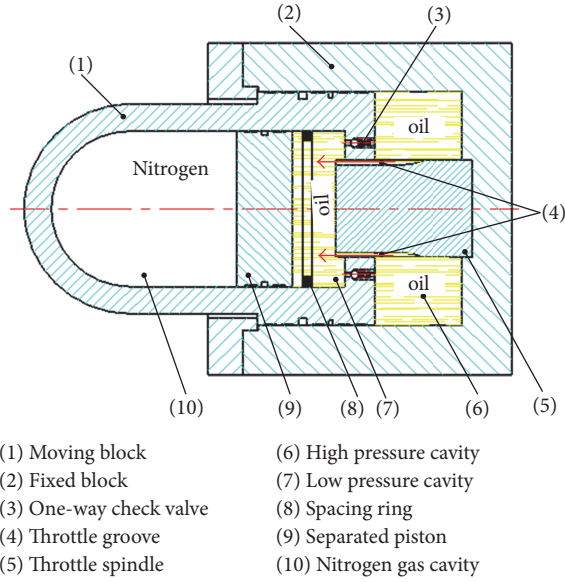


FIGURE 4: Structure stretch of the high-power hydraulic shock wave simulator.

The rubber shock simulator was usually used for the regular shock wave reappearance such as a half-sine shock wave. Additionally, practical shock force wave simulating the breech force had the characteristic of steep prepeak and gentle postpeak relatively (dotted line in Figure 10); the traditional rubber wave simulator was not fit for the simulation. Therefore, for simulating the practical shock force wave and solving the distortion problem, a new idea about high-power hydraulic shock wave simulator was proposed based on hydraulic buffering technology.

**2.3. Structure and Principle of the High-Power Hydraulic Shock Wave Simulator.** Shock simulation system adopted the principle of the momentum transfer; that is, a shock wave simulator with a certain velocity transferred momentum into cannon barrel during the shock, and the large shock force and the shock acceleration were formed on cannon barrel, and the shock wave could be adjusted by the damping and rigidity of the shock wave simulator. Structure sketch of the high-power hydraulic shock wave simulator was shown in Figure 4.

The inner diameter of the fixed block was 440 mm, and its initial length was 100 mm. The inner diameter of the moving block was 310 mm, and its initial length was 80 mm; there were two throttle holes in the throttle spindle. The piston chambers were fully filled with silicone oil.

The shock wave simulator was accelerated to certain velocity before shock, and then shocking the cannon barrel through the high-power hydraulic shock wave simulator produced instantaneous shock force. During the shock, the moving block moved to the right relative to the fixed block, which led to the oil pressure rise; silicone oil was squeezed to the left side of moving cylinder block through orifice plunger; then isolating piston was pushed to compress Nitrogen for the energy storage. The damping force varied with oil cavity pressure changes.

When an external shock force was applied to the left of the shock wave simulator, the moving block moved toward the right. The oil in the right fixed block chamber was compressed and flew through the throttle gap into the left chamber (as the red arrow shown in Figure 4). In this process, damping force was raised to balance the external shock force.

### 3. Coupling Model Building of a High-Power Shock Wave Simulation Test System

In the high-power shock simulation test, the whole simulation process could be divided into two stages. The sketch of the whole model is shown in Figure 5. In the figure, the model can be considered as two coupling systems: the left one is the recoil system and the right one is the damping system including a damper.

The shock was the first stage; in this process, the rubber pad located on the pounding head of a high-power hydraulic shock wave simulator collides with the canon muzzle and supplies velocity to the cannon barrel and accelerates the canon barrel including recoil buffer device and the canon suffered shock force from the shock system and the resistance from the recoil system. In the second process, the moving block part will be braked by the damper part of the high-power hydraulic shock wave simulator.

**3.1. Model of the Recoil System.**  $m_1$  represents the canon muzzle and it suffers the shock force  $F_C$  and recoil resistance  $R$  in the axis direction; recoil resistance  $R$  includes recuperator force  $F_{FJ}$ , recoil brake force  $F_{ZT}$ , and constant friction  $F_\phi$ .

$$R = F_{FJ} + F_{ZT} + F_\phi. \quad (6)$$

Recuperator force could be expressed as follows in a recoil process:

$$F_{FJ} = 50000 \times \left( \frac{2.15}{2.15 - x_1} \right)^{1.3}, \quad (7)$$

where  $x_1$  is the displacement of  $m_1$ . Recuperator force is a function related to canon recoil displacement. Recuperator force could be expressed as follows in recoil process.

$$F_{ZT} = \left( 1800 \times \frac{150 + a_x}{a_x^2} + 130 \right) \left( \frac{dx_1}{dt} \right)^2, \quad (8)$$

where  $a_x$  is equivalent area of recoil brake ventage and  $dx_1/dt$  is canon recoil velocity.

$$a_x = \left( 23 - \frac{\pi}{4} d_x^2 \right), \quad (9)$$

where  $d_x$  is throttling bar diameter.

Although the corresponding throttling bar diameters under different recoil displacement are different, throttling bar diameter remains constant.

$$F_{ZT} = 1580 \frac{dx_1}{dt}. \quad (10)$$

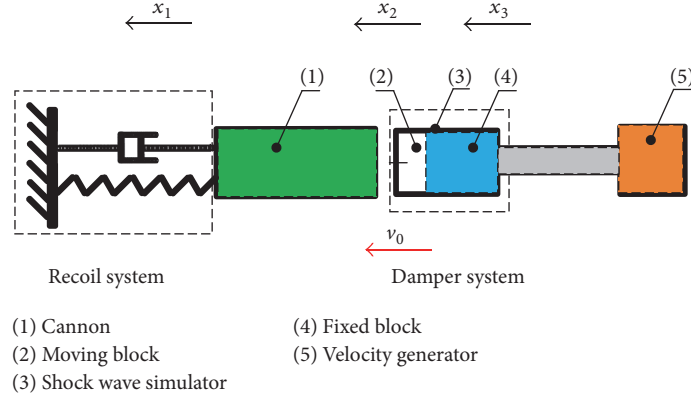


FIGURE 5: Coupling model for the high-power shock simulation test.

Recoil brake force is a function related to canon recoil velocity. Constant friction  $F_\varphi$  could be expressed as follows:

$$F_\varphi = f_1 mg \cos \varphi - mg \sin \varphi + F_0. \quad (11)$$

where  $f_1$  is the friction coefficient between canon recoil and cradle,  $\varphi$  is canon firing angle, and  $F_0$  is the friction generated by plug component of counter-recoil mechanism, which is composed by two parts.

$$F_0 = F_{01} + F_{02}, \quad (12)$$

where  $F_{01}$  is the friction generated by plug component in recuperator and  $F_{02}$  is the friction generated by plug component in the recoil brake. When canon firing angle remains constant, constant friction could be seen as constant value.  $F_\varphi = 10500$  N when canon firing angle  $\varphi$  equals  $0^\circ$ .

In conclusion, the force balance equation of the shocked cannon is expressed as follows when firing angle is  $0^\circ$ :

$$\begin{aligned} m_1 \frac{d^2 x_1}{dt^2} &= F_C - F_{FJ} - F_{ZT} - F_\varphi \\ &= F_C - 50000 \times \left( \frac{2.15}{2.15 - x_1} \right)^{1.3} - 1580 \frac{dx_1}{dt} \\ &\quad - 10500, \end{aligned} \quad (13)$$

where  $F_C$  is the shock force acting on the canon muzzle and  $d^2 x_1 / dt^2$  is recoil acceleration.

**3.2. Model of the Damper System.** For the shock wave simulator, considering oil compressibility, formula (14) is expressed according to flow continuity function in the damper system.

$$Q_{jl} + Q_{ys} + Q_{xl} = Q_z, \quad (14)$$

where  $Q_{jl}$  is the throttled flow,  $Q_{ys}$  is the compressed flow,  $Q_{xl}$  is the leakage flow, and  $Q_z$  is the total flow.

$$Q_{ys} = \frac{A_1 L - A_1 (x_2 - x_3)}{\beta} \frac{dP_1}{dt}, \quad (15)$$

where  $L$  is the original length,  $\beta$  is the bulk elastic modulus of oil,  $x_2$  is the displacement of the moving block,  $x_3$  is the displacement of the fixed block,  $A_1$  is the area of the right end surface of the moving block, and  $P_1$  is the pressure imposed on the left end surface.

$$Q_z = \left( \frac{dx_2}{dt} - \frac{dx_3}{dt} \right) A_1, \quad (16)$$

where  $dx_2/dt$  is the velocity of the moving block and  $dx_3/dt$  is the velocity of the fixed block.

Throttling groove adopts slender hole; flow state is laminar flow because the flow is not free when viscous fluid flows through the throttling groove. The flow of slender hole is related to the viscosity of the fluid. The viscosity of oil changes with its temperature.

When the area  $A$  of throttling hole is  $\pi d^2/4$ , the throttling flow could be expressed as follows:

$$Q_{jl} = \frac{d^2}{(32\mu l)} A \Delta P = \frac{\pi d^4 \Delta P}{(128\mu l)} = \frac{\pi d^4 (P_1 - P_2)}{(128\mu l)}, \quad (17)$$

where  $\mu$  is the dynamic viscous,  $l$  is the through-flow length, and  $d$  is the hole diameter. Formula (18) is achieved by plugging formulas (15), (16), and (17) into formula (14).

$$\begin{aligned} \frac{\pi d^4 (P_1 - P_2)}{(128\mu l)} + \frac{A_1 Y_{\max} - A_1 (x_2 - x_3)}{\beta} \frac{dP_1}{dt} \\ = \left( \frac{dx_2}{dt} - \frac{dx_3}{dt} \right) A_1. \end{aligned} \quad (18)$$

The ideal gas adiabatic compression equation is as follows:

$$\frac{P_2}{P_0} = \left( \frac{V_0}{V_0 - x_2 A_0} \right)^k, \quad (19)$$

where  $P_0$  is the initial pressure in nitrogen gas cavity,  $V_0$  is the initial volume in nitrogen gas cavity,  $A_0$  is the inertial effective working area in the nitrogen gas cavity, and  $k$  is the adiabatic coefficient.

#### 4. Numerical Simulation and Result Analysis

Using Matlab/Simulink software, firstly, import into the characteristic parameters  $\rho, \mu, \beta, k, f_{mc}$  the test parameters  $M, m, P_0, V_0, L$  and the controlled parameters  $l, d$  as well as the initial velocity  $v_0$ ; then solve the above motion functions according to the fourth-order Runge-Kutta method adopting variable step arithmetic. Shock force curve, acceleration curve, velocity curve, and displacement were received in the high pressure cavity. Finally, model accuracy was verified by the comparison of simulation test and live firing test, and parameters were optimized and corrected. The optimized model could use debugged shock wave simulator for simulating various shock force waves. The specific method was that practical shock force curve was imported as a known condition, throttling area curve was deduced, and required shock force curve was simulated by adjusting the throttling area.

From the building process of mechanical model, the factors affecting shock wave characteristics were mainly divided into three classes: the first class was test parameters including  $\rho, \mu, \beta, k$ , and  $f_{mc}$ ; the second class was characteristic parameters including  $M, m, P_0, V_0$ , and  $L$ , and the third class was controlled parameters including  $d$  and  $v_0$ .

The influences of typical parameters on the shock force wave were analyzed, and these typical parameters included initial velocity  $v_0$ , dynamic viscosity  $\mu$ , the bulk elastic modulus  $\beta$  of oil, and the diameter  $d$  of the throttling hole.

**4.1. The Influence of Initial Velocity  $v_0$  on the Shock Behavior.** The influence of initial velocity  $v_0$  on the shock behavior in controlled parameters could be inferred in that the increase of initial velocity would increase the total flow  $Q_z$  and then affect the shock force according to (17) and (6); the shock force waves were shown in Figure 6 under different initial velocities. In comparison, it was obvious that the shape trend of shock force wave had similar values under different initial velocity  $v_0$ , and the peak value increased with the initial velocity increase, which accorded with the theory analysis as well as the mechanical performances of the shock wave simulator.

**4.2. The Influence of Dynamic Viscosity  $\mu$  on the Shock Behavior.** In characteristic parameters, the dynamic viscosity  $\mu$  affected the throttled flow  $Q_{j1}$  and the throttled flow  $Q_{j1}$  increased with  $\mu$  declining according to function (18). Hence, shock force wave was simulated under various dynamic viscosities  $\mu$  for describing the influence of the dynamic viscosity  $\mu$  on the shock behavior. The curves were shown in Figure 8, and it was obvious that the shape of shock force wave curves changed obviously in the postpeak period under different dynamic viscosity  $\mu$  in Figure 7; the shock force decreased seriously with dynamic viscosity  $\mu$  declining and the curve's shape fluctuated seriously with dynamic viscosity  $\mu$  declining.

**4.3. The Influence of the Bulk Elastic Modulus  $\beta$  of Oil on the Shock Behavior.** According to the building process of mechanical model, the bulk elastic modulus  $\beta$  of oil in characteristic parameters affected the compressed flow  $Q_{ys}$ , and the compressed flow  $Q_{ys}$  increased with  $\beta$  declining according to function (16). Hence, shock force wave was

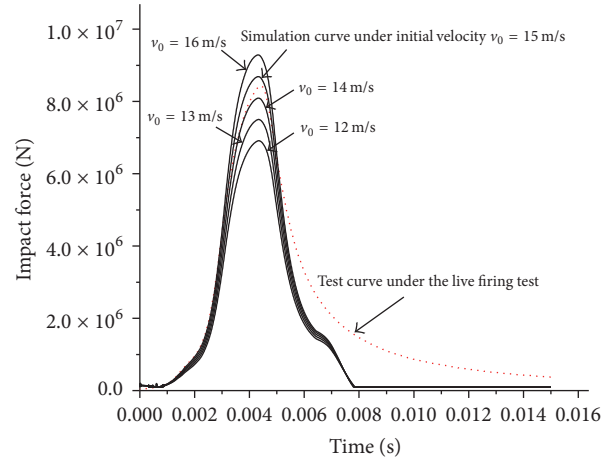


FIGURE 6: Shock force curve of the high-power hydraulic shock wave simulator under various initial velocity  $v_0$ .

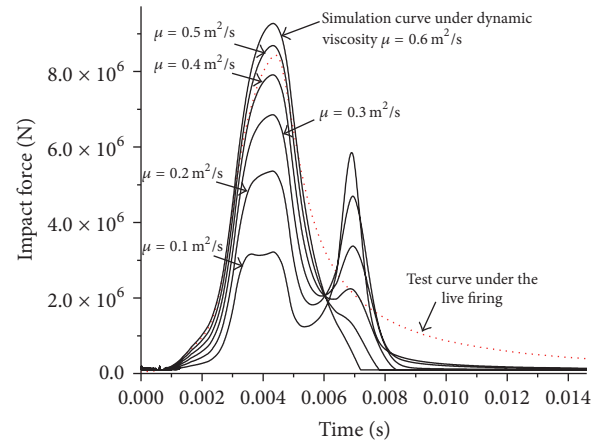


FIGURE 7: Shock force curve of the high-power hydraulic shock wave simulator under various dynamic viscosity  $\mu$ .

simulated under bulk elastic modulus  $\beta$  of oil for describing the influence of the bulk elastic modulus  $\beta$  of oil on shock behavior. The comparison curves were shown in Figure 8, and it was obvious that the shape of shock force wave curves changed gently under bulk elastic modulus  $\beta$  of oil, the shock force decreased, and the impulse increased with the decline of bulk elastic modulus  $\beta$  of oil in Figure 8.

**4.4. The Influence of the Diameter  $d$  of the Throttling Hole on the Shock Behavior.** In controlled parameters, the diameter  $d$  of the throttling hole directly affected the throttled flow  $Q_{j1}$  and the throttled flow  $Q_{j1}$  increased with the increase of the diameter  $d$  of the throttling hole according to function (18). For describing the influence of the diameter  $d$  of the throttling hole on the shock behavior, the shock force wave was simulated under varying diameter  $d$  of the throttling hole. The curves were shown in Figure 9, and it was obvious that the shape of shock force wave curves changed obviously in the postpeak period, the shock force decreased seriously

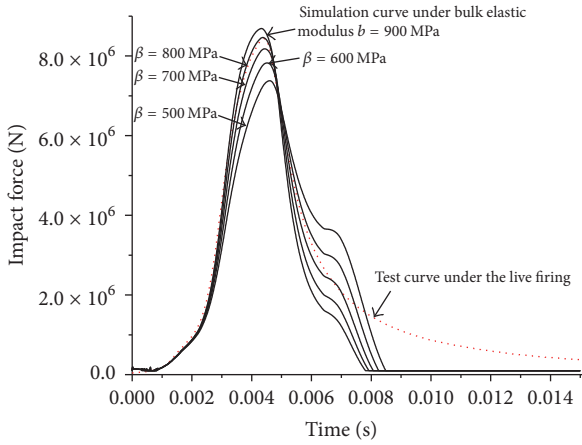


FIGURE 8: Shock force curve of the high-power hydraulic shock wave simulator under various bulk elastic modulus  $\beta$  of oil.

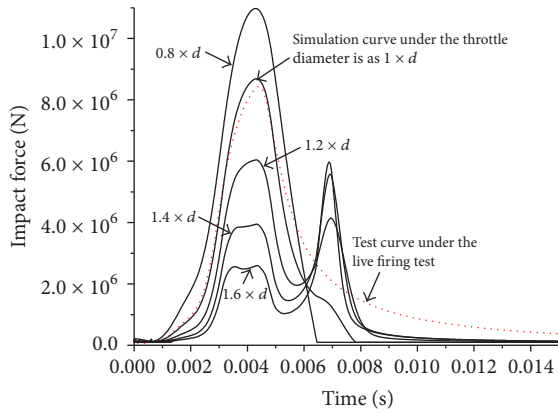


FIGURE 9: Shock force curve of the high-power hydraulic shock wave simulator under varying throttle diameter  $d$ .

with the increase of the diameter  $d$  of the throttling hole, and the wave's shape fluctuated seriously.

By the optimization design analysis of typical shock parameters, a set of reasonable shock parameters were received as shown in Table 1.

The throttle diameter  $d$  curve of the optimized model was debugged shock wave simulator for simulating various shock force waves. The specific method was that practical shock force curve was imported as a known condition, throttling diameter  $d$  curve was deduced, and the curve required subsection discretization in practical engineering design. Required shock force curve was simulated by the optimization of throttling diameter  $d$  curve.

The shock force wave was simulated adopting the optimized shock parameters in Figure 10.

The simulation curve was similar to the test curve under the live firing. It was indicated that the above mathematical model had good precision by optimization and correction of numerical simulation tests under various working conditions, and the high-power hydraulic shock wave simulator adopting the optimized shock parameters realized the shock

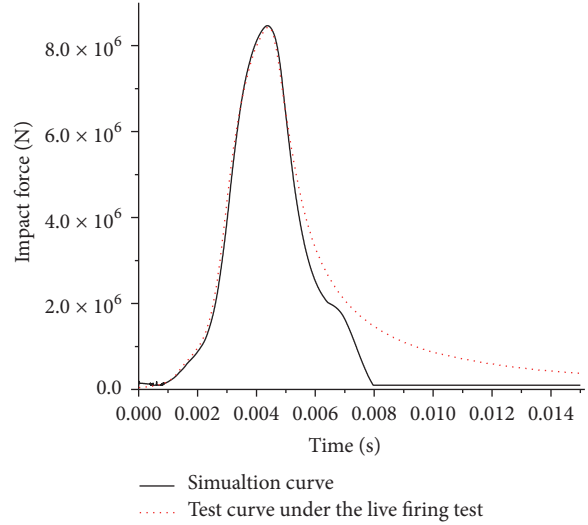


FIGURE 10: Shock force curve comparison generated by the high-power hydraulic shock wave simulator and live firing test, respectively.

wave reappearance of the shock force on artillery muzzle in the live firing test.

## 5. Similarity Evaluation

Using the above data, similarity evaluation was carried out for the simulation method based on the numerical similarity and shape similarity.

**5.1. Numerical Similarity.** Assume that the test data consequence was  $DT = (dt(1), dt(2), \dots, dt(n))$  and the simulation consequence was  $DS = (ds(1), ds(2), \dots, ds(n))$ . Weighted mean of the relative error in the two time sequences was used for expressing numerical similarity. The calculation method was as follows.

When  $dt(i)$  and  $ds(i)$  ( $i = 1, 2, \dots, n$ ) were both not zero, numerical similarity of each point  $s_1(i)$  was expressed as follows:

$$s_1(i) = \begin{cases} 1 - \frac{|dt(i) - ds(i)|}{\max(|dt(i)|, |ds(i)|)} & dt(i) ds(i) > 0 \\ 0 & dt(i) ds(i) < 0. \end{cases} \quad (20)$$

When at least one parameter was zero in  $dt(i)$  and  $ds(i)$ , numerical similarity of each point  $s_1(i)$  was as follows:

$$s_1(i) = \begin{cases} 0 & dt(i) = 0 \text{ or } ds(i) = 0 \\ 1 & dt(i) = 0, ds(i) = 0. \end{cases} \quad (21)$$

Take the ratio of each point's amplitude and all sample points' sum as the weight  $\gamma_i$  of the point.

$$\gamma_i = \frac{|dt(i)|}{\sum_{i=1}^n |dt(i)|}. \quad (22)$$

TABLE 1: Main shock parameter list.

Main shock parameter	$M$ (kg)	$m$ (kg)	$v_0$ (m/s)	$\mu$ (m <sup>2</sup> /s)	$\beta$ (MPa)	$l$ (m)	$L$ (m)
Value	3000	2540	15	0.5	800	0.08	0.27

The total numerical similarity  $S_1$  of the two time sequences was shown as follows:

$$S_1 = \sum_{i=1}^n s_1(i) \gamma_i, \quad (i = 1, 2, \dots, n). \quad (23)$$

**5.2. Shape Similarity.** The shape similarity was calculated according to the curvature distance between the two time sequences [27]; the calculating process was as follows.

Firstly, primitive sequence  $X^{(0)} = [x^{(0)}(1), x^{(0)}(2), \dots, x^{(0)}(n)]$  was translated into nonnegative sequence  $X^{(1)}$ , and make sure that the sequence shape was constant.

$$x^{(1)}(i) = \begin{cases} x^{(0)}(i) & \min X^{(0)} \geq 0 \\ x^{(0)}(i) - \min X^{(0)} & \min X^{(0)} < 0. \end{cases} \quad (24)$$

For improving the precision and decreasing the calculation amount, the time sequence needs sector-by-sector solution.

$X^{(1)} = [X_1(1), X_2(2), \dots, X_m(1)]$  and  $X_j^{(1)} = [x_j^{(1)}(1), x_j^{(1)}(2), \dots, x_j^{(1)}(l_j)]$ , where  $X_j^{(1)}$  was the  $j$ th nonnegative subsequence ( $j = 1, 2, \dots, m$ ),  $m$  was the number of the subsequences, and  $l_j$  was the length of  $j$ th subsequence.

Nonnegative subsequence was generated according to AGO (Accumulated Generating Operation), and the consequence presents approximate exponential increase law, which decreased the randomness, possessed statistical significance, and kept the relevance of primitive consequence. Nonnegative subsequence  $X^{(1)}$  carried out accumulation calculation, generating the consequence  $X^{(2)} = [X_1^{(2)}, X_2^{(2)}, \dots, X_m^{(2)}]$ . Take subsequence  $X_j^{(2)}$  as example.

$$x_j^{(2)}(p) = \sum_{a=1}^p x_j^{(1)}(a), \quad (j = 1, 2, \dots, m), \quad (25)$$

where  $x_j^{(2)}(p)$  was the  $p$ th data in  $j$ th generated subsequence.

We can get  $x_j^{(2)}(1) = x_j^{(1)}(1)$ . Time consequence  $X^{(2)}$  carried out subtraction calculation; original nonnegative subsequence  $X^{(1)}$  could be achieved as follows:

$$x_j^{(1)}(p) = x_j^{(2)}(p) - x_j^{(2)}(p-1) \quad (p = 1, 2, \dots, l_j). \quad (26)$$

Consequences  $X^{(1)}$  and  $X^{(2)}$  could be converted into one another, and  $X^{(2)}$  reflected change law in consequence  $X^{(1)}$ , so we can build the model of  $X^{(2)}$  to analyze  $X^{(1)}$ .

For increasing the fitting model accuracy of time consequence, the subsequence  $X_j^{(2)}$  model was built.

$$x_j^{(2)}(\lambda) = c_1 e^{\gamma \lambda} + c_2 \lambda^3 + c_3 \lambda^2 + c_4 \lambda + c_5, \quad (27)$$

where  $c_i$  ( $i = 1, 2, \dots, 5$ ) and  $\gamma$  were model parameters;  $\lambda = 1, 2, \dots, l_j$ . The fitting model could represent the exponent, the parabola, and the third power curve according to the value of model parameters  $c_i$  ( $i = 1, 2, \dots, 5$ ) and  $\gamma$ , which is the precise expression of the consequence.

Assume that the curvature of each section in time consequence was  $K = [K_1, K_2, \dots, K_m]$ ; the curvature was  $K_j = [k_j(1), k_j(2), \dots, k_j(l_j)]$  of each subsequence.

$$k_j(\lambda) = \frac{|x_j^{(2)'''}(\lambda)|}{[1 + (x_j^{(2)'}(\lambda))^2]^{3/2}} \quad (\lambda = 1, 2, \dots, l_j). \quad (28)$$

Assume that the curvatures of the two time consequence were  $K = [K_1, K_2, \dots, K_m]$  and  $\bar{K} = [\bar{K}_1, \bar{K}_2, \dots, \bar{K}_m]$ ; taking subsequences  $K_j$  and  $\bar{K}_j$  as example, the shape similarity was calculated:  $K_j = [k_j(1), k_j(2), \dots, k_j(l_j)]$  and  $\bar{K}_j = [\bar{k}_j(1), \bar{k}_j(2), \dots, \bar{k}_j(l_j)]$ .

The curvature distance of subsequences  $K_j$  and  $\bar{K}_j$  was as follows:

$$d_j = \frac{1}{l_j} \sum_{p=1}^{l_j} |k_j(p) - \bar{k}_j(p)|. \quad (29)$$

Assume that curvature distance threshold value of the two subsequences is  $th_{DC}$ . When the curvature distance was less than threshold value, the two subsequences were similar, while when the curvature distance was greater than threshold value  $th_{DC}$ , the two subsequences were not similar, where threshold value  $th_{DC}$  was related to curvature of each point in each subsequence. Use the ratio of all the similar subsequences' length and the consequence total length as measurement of shape similarity of consequence.

$$S_2 = \frac{\sum_{j=1}^n L(j)}{L(X)}, \quad (30)$$

where  $S_2$  was the shape similarity of time consequences  $X$  and  $Y$ ,  $L(X)$  was the total length of time consequence  $X$ ,  $L(j)$  was the  $j$ th similar subsequence of  $X$  and  $Y$ , and  $n$  was the number of similar subsequences of  $X$  and  $Y$ .

**5.3. Integrated Similarity of Time Consequence.** Numerical similarity and shape similarity were, respectively, calculated based on the two time consequences. Based on the multi-attribute integrated evaluation theory, we use multiplication relationship to obtain comprehensive similarity.

So the comprehensive similarity of  $S$  was as follows between live firing and simulation firing.

$$S = \sqrt{S_1 S_2}, \quad (31)$$

where  $S_1$  and  $S_2$  were, respectively, numerical similarity and shape similarity.

TABLE 2: Similarity of shock wave simulation.

	Subsequence 1	Subsequence 2	Total consequence
Numerical similarity	0.95	0.78	0.894
Shape similarity	0.92	0.73	0.857

**5.4. Shock Wave Simulation Evaluation.** In cannon recoil motion process, recoil time consequence was divided into recoil section and counter-recoil section. Recoil section was from original point to displacement peak point; counter-recoil section was from displacement peak point to the end point. In recoil section, cannon motion velocity was high and had serious vibration and the maximum velocity existed in the section; cannon motion velocity was low and had small vibration. The weights of recoil section and counter-recoil section were, respectively, 0.67 and 0.33.

The two long subsequences were divided into multiple short subsequences. The length of each short subsequence was 8; numerical similarity and shape similarity of each short subsequence were calculated by the above method; then the numerical similarity and shape similarity of each long subsequence and the total consequence were calculated. Using the data in simulation, the integrated similarity of the shock wave was calculated as in Table 2.

The evaluation result indicated that the high-power hydraulic shock wave could simulate the dynamic process of live firing accurately. Therefore, the optimization of shock characteristic parameters could improve the simulation accuracy.

## 6. Conclusions

Theoretical analysis and numerical simulation result analysis demonstrated that the high-power hydraulic shock wave simulator could be adopted for simulating the shock force generated on the artillery muzzle; the similarity evaluation of shock wave simulation indicated that high similarity existed between the shock force in simulation test and the practical shock force in live firing test. In other words, the simulation method was reasonable. Finally, the analysis supplied references for the utility of artillery fire simulation technology. The novel high-power hydraulic shock wave simulator replaced a traditional rubber wave simulator to realize practical high-power shock wave reappearance, which also supplied references for the artillery dynamic recoil simulation test.

## Conflicts of Interest

The authors declare that there are no conflicts of interest regarding the publication of this paper.

## References

- [1] Z. Fusan, *Theory and Practice in Artillery Type Test*, National Defence Industry Press, Beijing, China, 2000.
- [2] G. Ting, *Simulation and Experimental Research on Artillery Firing Shock Simulation Wave form Generator*, Harbin Institute of Technology, Heilongjiang Sheng, China, 2014.
- [3] M. Cast, "Army test move to 'virtual proving ground,'" *National Defence*, vol. 11, pp. 62–64, 2001.
- [4] D. Brown, "Simulating firing loads provides flexibility and test repeatability," ADA323489, 1997.
- [5] Y. Yangwu, "Numerical simulations of test system and dynamics of the gun recoil," *Journal of China Ordnance*, vol. 22, no. 2, pp. 152–155, 2001.
- [6] X. Hang and Z.-j. Zhang, "Study on dynamic simulation experiments in a artillery dynamic recoil test," *Journal of Ballistic*, vol. 7, no. 1, pp. 29–33, 1995.
- [7] D. Changchun, Y. Yuliang, Q. Yuliang, and C. Kaibo, "Research on the effect of shock parameters in a artillery dynamic recoil test device," *Journal of Artillery Launch and Control*, vol. 2, pp. 25–28, 2012.
- [8] D. Changchun, L. Lin, Z. Jian, and C. Yongcai, "Numerical analysis of artillery dynamic recoil simulation test based on the principle of artillery muzzle shock," *Explosion and Shock Waves*, vol. 32, no. 3, pp. 323–327, 2012.
- [9] Y. Yuliang, Q. Junqi, D. Changchun, and D. Huiyong, "Finite element simulation and test study of the material constitutive model of rubber wave generator," *Mechanical Design*, vol. 30, no. 9, pp. 86–89, 2013.
- [10] Y. Yuliang, Q. Junqi, D. Changchun, S. Yezun, and L. Xiaowei, "Accuracy evaluation of artillery dynamic recoil simulation based on numerical and shape similarity," *Journal of Vibration and Shock*, vol. 34, no. 10, pp. 157–160, 2015.
- [11] Y. Yuliang, Q. Junqi, D. Changchun et al., "Optimization design of artillery dynamic recoil tester," *Journal of Vibration and Shock*, vol. 33, no. 2, pp. 47–51, 2014.
- [12] Y. Yang, C. Di, D. Wu, and C. Liu, "Design on the Theoretical Breechblock Operating Force of Shock Test Bed for artillery Breechblock System," in *Proceedings of the 5th International Conference on Information Engineering for Mechanics and Materials (ICIMM '15)*, Atlantis Press, Huhhot, Inner Mongolia, China, July 2015.
- [13] Y. Yang, J. Zheng, C. Di, and J. Chen, "Model and simulation on a shock test bed for gun breechblock system," in *Proceedings of the First International Conference on Information Sciences, Machinery, Materials and Energy (ICISMME '15)*, Atlantis Press, Chongqing, China, April 2015.
- [14] S. Jiao, Y. Wang, L. Zhang, and H. Hua, "Shock wave characteristics of a hydraulic damper for shock test machine," *Mechanical Systems and Signal Processing*, vol. 24, no. 5, pp. 1570–1578, 2010.
- [15] S. Duym, R. Stiens, and K. Reybrouck, "Evaluation of shock absorber models," *Vehicle System Dynamics*, vol. 27, no. 2, pp. 109–127, 1997.
- [16] M. Shams, R. Ebrahimi, A. Raouh, and B. J. Jafari, "CFD-FEA analysis of hydraulic shock absorber valve behavior," *International Journal of Automotive Technology*, vol. 8, no. 5, pp. 615–622, 2007.
- [17] J. Jiahong, D. Jianye, W. Yu, and H. Hongxing, "Design method for fluid viscous dampers," *Archive of Applied Mechanics*, vol. 78, no. 9, pp. 737–746, 2008.
- [18] C.-Y. Hou, "Fluid dynamics and behavior of nonlinear viscous fluid dampers," *Journal of Structural Engineering*, vol. 134, no. 1, pp. 56–63, 2008.

- [19] C.-Y. Hou, "Behavior explanation and a new model for nonlinear viscous fluid dampers with a simple annular orifice," *Archive of Applied Mechanics*, vol. 82, no. 1, pp. 1–12, 2012.
- [20] C.-Y. Hou, D.-S. Hsu, Y.-F. Lee, H.-Y. Chen, and J.-D. Lee, "Shear-thinning effects in annular-orifice viscous fluid dampers," *Journal of the Chinese Institute of Engineers*, vol. 30, no. 2, pp. 275–287, 2007.
- [21] M. Cast, "Army test moves to virtual proving ground," *National Defense*, vol. 11, pp. 62–64, 2001.
- [22] L. Lin, D. Changchun, P. Baoqing, and Y. Jiajun, "Test design and optimization of artillery simulation firing test," *Journal of Artillery Launch and Control*, no. 3, pp. 99–102, 2010.
- [23] H. Xiao and Y. Hu, "Data mining based on segmented time warping distance in time series database," *Journal of Computer Research and Development*, vol. 42, no. 1, pp. 72–78, 2005.
- [24] L. Jianhai, Z. Jianye, Y. Feng, and P. Quan, "Study of distance-measuring method in time series based on slope departure," *Computer Engineering and Applications*, vol. 45, no. 22, pp. 4–6, 2009.
- [25] B.-N. Liu, J.-Y. Zhang, P. Zhang, and Z.-L. Wang, "Similarity search method in time series based on curvature distance," *Journal of Electronics and Information Technology*, vol. 34, no. 9, pp. 2200–2207, 2012.
- [26] Y.-W. Ding, X.-H. Yang, G.-C. Chen, and A. J. Kavs, "Radian-distance based time series similarity measurement," *Journal of Electronics and Information Technology*, vol. 33, no. 1, pp. 122–128, 2011.
- [27] F. Wang, X.-G. Liang, Y.-K. Wang, and Q. Zheng, "Credibility evaluation for guidance system dynamic simulation with curvature distance," *Journal of System Simulation*, vol. 25, no. 8, pp. 1896–1900, 2013.
- [28] Y. Yuliang, Q. Junqi, D. Changchun, D. Huiyong, and Z. Xiaoga, "Modeling and firing simulation accuracy assessment of a gun-power-recoil test table," *Journal of Vibration and Shock*, vol. 33, no. 10, pp. 127–130, 2014.
- [29] Z. Xiangyan, Z. Jianguo, and Y. Junrong, *Cannon Design Principle*, Beijing Institute of Technology Press, Beijing, China, 2005.

## Research Article

# Modeling and Analysis of a Multi-Degree-of-Freedom Micro-Vibration Simulator

Xiaoming Wang,<sup>1,2</sup> Zhenbang Xu,<sup>1</sup> Shuai He,<sup>1</sup> Qingwen Wu,<sup>1</sup> Hang Li,<sup>1</sup>  
Yaping Zhao,<sup>1,2</sup> and Lei He<sup>1,2</sup>

<sup>1</sup>Innovation Lab of Space Robot System, Space Robotics Engineering Center, Changchun Institute of Optics, Fine Mechanics and Physics, Chinese Academy of Sciences, No. 3888 Dong Nanhu Road, Changchun 130033, China

<sup>2</sup>University of Chinese Academy of Sciences, No. 19A Yuquan Road, Beijing 100049, China

Correspondence should be addressed to Zhenbang Xu; xuzhenbang@gmail.com

Received 15 March 2017; Accepted 30 May 2017; Published 2 August 2017

Academic Editor: Naveed Ahmad

Copyright © 2017 Xiaoming Wang et al. This is an open access article distributed under the Creative Commons Attribution License, which permits unrestricted use, distribution, and reproduction in any medium, provided the original work is properly cited.

To reproduce the disturbance forces and moments generated by the reaction/momentum wheel assembly, a multi-degree-of-freedom micro-vibration simulator is proposed. This can be used in the ground vibration experiments of an optical payload replacing the real action/momentum wheel assembly. First, the detailed structure of the micro-vibration simulator is introduced. Then, the complete system kinematic and dynamic models of the micro-vibration simulator are derived. In addition, the disturbance forces and moments produced by the micro-vibration simulator are calculated. Finally, the normal mode analysis and a cosimulation are adopted to verify the validity of this method. The analysis and simulation results show that the micro-vibration simulator can exactly reproduce the disturbance forces and moments with different amplitudes and different frequency ranges.

## 1. Introduction

With the development of space technology, space optical remote sensors with large aperture and high-resolution imaging are playing an increasing role in many fields of military, science, astronomy, and civil use. However, micro-vibrations produced by the operation of on-board equipment, such as reaction/momentum wheel assemblies (R/MWAs), thrusters, electric motors, and cryogenic coolers, can cause significant effects in the image quality degradation [1].

Among the various micro-vibration disturbance sources, that produced by R/MWAs is generally regarded as the largest [2–4]. There have been numerous studies on R/MWA disturbance modeling, as well as the characteristics of micro-vibration caused by R/MWAs [2, 3, 5]. The general approach to reducing the disturbance effect on the image quality of an optical payload is to insert one or several isolators in the transmission path between the disturbance source and the payload [6]. To develop the appropriate isolators and ensure mission success, a significant amount of analysis and ground experiments needs to be devoted to validating the isolation

effect of the isolators and the image performance of optical payload before launch. During the ground experiments, the effects of R/MWA induced disturbance on the optical payload are of prime concern. Zhou et al. [7, 8] and Kamesh et al. [9, 10] all used a real momentum wheel assembly (MWA) to measure the micro-vibrations produced by the MWA with and without the proposed soft suspension system. However, it is not usual to employ all the flight R/MWAs to conduct the ground validating experiments because of scheduling issues or product assurance activities. Therefore, developing a micro-vibration simulator, which can replace the real flight R/MWAs, is considered to be an important adjunct to the development processes for space missions.

Hostens et al. [11, 12] have proposed a six-degree-of-freedom (DOF) vibration simulator driven by hydraulic, which can be used to test the vibration of mobile machinery. The vibration simulator adopted Gough-Stewart platform, which greatly improved the structural stability. Parallel manipulator such as the Gough-Stewart platform (GSP) has been widely used in many different application fields

for its remarkable performance (e.g., high maneuverability, precision, and high load/weight capacity). Dynamic analysis of the parallel manipulator plays a vital role in the design and control of such manipulators. Over the past decades, numerous research results have been reported on the kinematics of the GSP and relatively fewer results on the dynamic of GSP [13]. Oftadeh et al. [14] presented the explicit dynamics formulation for the GSP and utilized the Lagrange method to verify the resulting dynamics equations. Dasgupta and Mruthyunjaya [15] derived an inverse dynamic formulation by the Newton-Euler approach for the GSP, with the frictional forces occurring in the joints; meanwhile the mass of inertia of the pods was taken into consideration in their study. Pedrammehr et al. [16] produced the improved dynamic equations of the GSP, which took into account the rotational degree of the pods around the axial direction. Similar efforts can be found in [17–20]. Generally in the literature, many researches focused on the influence of the inertia forces, Coriolis forces, and the frictional forces on the dynamics control of the GSP. However, researches on the disturbance forces and moments acting on the mounting surface of the GSP are still rare. Moreover, the calculation of disturbance forces and moments is critical for the GSP based micro-vibration simulator.

There are two kinds of simulation methods of micro-vibration. One is outputting micro-vibration through the moving platform. The first method has been studied by many scholars. For example, Hostens et al. [11, 12] designed a vibration simulator which can simulate 6-dimensional vibrations. The other is outputting disturbance forces and moments through the base platform. A few scholars have studied this method. Park et al. [21] developed a micro-vibration emulator to test the jitter in spacecraft. However, this emulator can only produce three disturbance forces which are mutually perpendicular. Therefore, developing a micro-vibration simulator which can reproduce 6-dimensional disturbance forces and moments is novel.

In this study, a multi-degree-of-freedom micro-vibration simulator (MMVS) based on the GSP, which can exactly reproduce the 6-dimensional disturbance forces and moments, is presented. The dynamic models of the MMVS, which consider the effects of actuator inertia and eccentric load, are derived using the Newton-Euler method and Lagrange approach. The formulation incorporates all the elastic, inertia, Coriolis, centrifugal, and external forces; furthermore, the disturbance forces and moments produced by the MMVS are also analyzed. Based on the derived dynamic models, a disturbance planning method is proposed to obtain the target disturbance forces and moments. The cosimulation using ADAMS and MATLAB®/Simulink is adopted to verify the validity of the dynamic models and the feasibility of MMVS.

This paper is organized as follows: in Section 2, we describe the structure of the MMVS. Section 3 presents the dynamics model including details of the calculation of actuator forces and planning method of the disturbance forces and moments. Section 4 presents the normal mode analysis and cosimulation verification. Concluding remarks on the micro-vibration simulator are presented in Section 5.

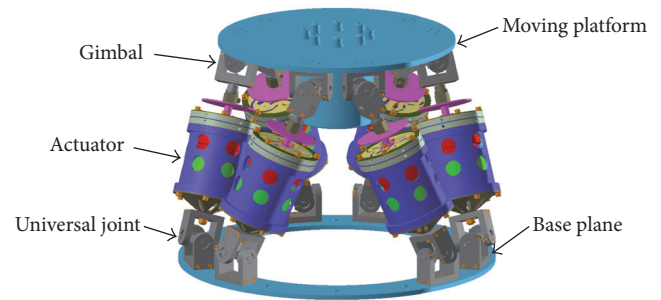


FIGURE 1: Virtual prototype of the vibration simulator.

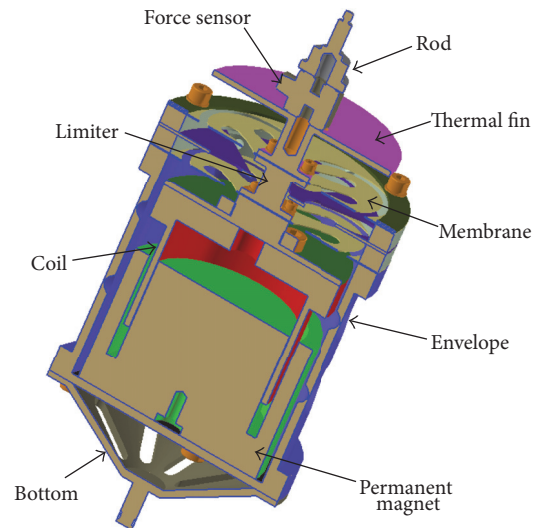


FIGURE 2: Cross-sectional view of actuator.

## 2. Micro-Vibration Simulator Description

The detailed structure of the MMVS is depicted in Figure 1. It consists of a moving platform, base plane, and six actuators. Each actuator, driven by a voice coil motor, is connected to the base plane by a universal joint at one end and the moving platform by a gimbal, which has three degrees-of-freedom, at the other end. Figure 2 shows a cross-sectional view of the actuator with a permanent magnet attached to the envelope. The two membranes perform the function of spring only for axial compliance. A connecting rod attached to the central point of the upper membrane connects the lower membrane and the voice coil. The one active degree-of-freedom (DOF) on the actuator is the axial movement of the coil.

The working principle of this proposed MMVS is as follows: the control signal produced by the upper computer is amplified by the power amplifier to drive the voice coil motors. The reciprocating motion of the actuators causes the moving platform to move together. As a result, the inertial forces are generated. According to Newton's Third Law, the inertial forces produced by the moving parts will be transmitted to the mounting surface through the universal joints, which leads to the generation of disturbance forces and

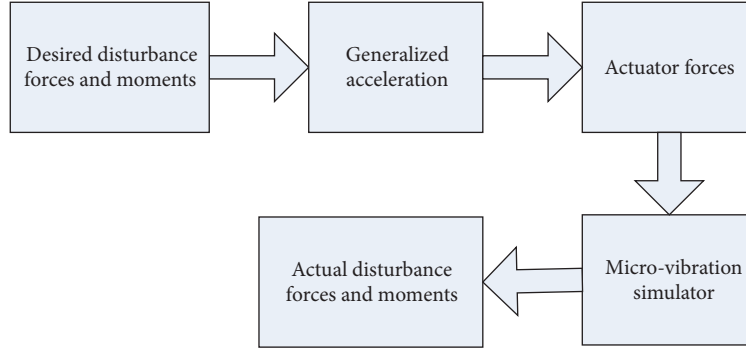


FIGURE 3: Block diagram of the planning method of disturbance forces and moments.

moments. The object of this study is to calculate the actuator forces, which are used to generate the target disturbance forces and moments.

### 3. Dynamics Model

The object of this study is to develop a MMVS which can reproduce the desired disturbance forces and moments. So we need to calculate the actuator forces which can be used to derive the MMVS to obtain the desired disturbance forces and moments. First, the dynamic relations between the actuator forces and the generalized acceleration, velocities, and displacements are derived. It is noted that the assumption is adopted that the generalized velocities and generalized displacements of the moving platform are the time integral and time double integral of the generalized acceleration, respectively. Then we calculate the disturbance forces and moments of the MMVS acting on the mounting surface when the generalized acceleration of the moving platform is given. Finally the dynamic relations between the actuator forces and the desired disturbance forces and moments are carried out. The planning method of disturbance forces and moments is depicted in Figure 3.

**3.1. Kinematics.** The scheme of the vibration simulator is shown in Figure 4, in which the coordinate system  $\{P\}$  is the body frame fixed to the geometric center of the joints of the

moving platform, while the  $\{B\}$  coordinate system is the base frame attached to the geometric center of the joints of the base plane. The  $\{g\}$  coordinate system is the inertial frame fixed to the geometric center of the bottom of the base plane, and its orientation is identical with frame  $\{B\}$ . The linear motions are denoted as surge ( $x$ ), sway ( $y$ ), and heave ( $z$ ) along the  $X_B - Y_B - Z_B$  axes of the base frame, and the angular motions roll ( $\gamma$ ), pitch ( $\beta$ ), and yaw ( $\alpha$ ) are  $X-Y-Z$  fixed angles. The upper joint points and the lower joint points are denoted with  ${}^P\mathbf{p}_i$  in frame  $\{P\}$  and  ${}^B\mathbf{p}_i$  in frame  $\{B\}$ , respectively.  $R_p$  and  $R_B$  describe the radii of the payload and base platforms. The angle between  $P_6$  and  $P_1$  is denoted by  $\varphi$ . The angle between  $B_6$  and  $B_1$  is denoted by  $\theta$ , which is illustrated in Figure 4(b).

**3.1.1. Velocity Analysis.** In the base frame, the kinematic equations of the  $i$ th actuator can be described by

$${}^B\mathbf{l}_i = {}^B\mathbf{t} + {}^B\mathbf{p}_i - {}^B\mathbf{b}_i = {}^B\mathbf{t} + {}^B\mathbf{R} \cdot {}^P\mathbf{p}_i - {}^B\mathbf{b}_i, \quad (1)$$

where the variable  $i$  defines the  $i$ th actuator variables, indicating that in general the equations are applicable to any actuator.  ${}^B\mathbf{l}_i$  is the length vector of the actuator with respect to the base frame  $\{B\}$ ,  ${}^B\mathbf{t}$  is the position vector of the body frame,  ${}^B\mathbf{t} = [x \ y \ z]^T$ , and  ${}^B\mathbf{R}$  is the rotation matrix of the transformation from the body frame  $\{P\}$  to base frame  $\{B\}$ . The rotation matrix is given by

$${}^B\mathbf{R} = \begin{bmatrix} \cos \alpha \cos \beta & \cos \alpha \sin \beta \sin \gamma - \sin \alpha \cos \gamma & \cos \alpha \sin \beta \cos \gamma + \sin \alpha \sin \gamma \\ \sin \alpha \cos \beta & \sin \alpha \sin \beta \sin \gamma + \cos \alpha \cos \gamma & \cos \alpha \sin \beta \cos \gamma - \cos \alpha \sin \gamma \\ -\sin \beta & \cos \beta \sin \gamma & \cos \beta \cos \gamma \end{bmatrix}. \quad (2)$$

Taking the derivative of (1) with respect to time, the velocity mapping function can be obtained and is given by

$$\dot{\mathbf{q}}_{pi} = {}^B\dot{\mathbf{l}}_i = {}^B\dot{\mathbf{t}} + \boldsymbol{\omega} \times {}^B\mathbf{R} \cdot {}^P\mathbf{p}_i = \left[ \mathbf{E}_3 \quad {}^B\mathbf{R} \left( {}^P\tilde{\mathbf{p}}_i \right)^T \right] \dot{\mathbf{q}}, \quad (3)$$

where  $\dot{\mathbf{q}}_{pi}$  is the velocity of the joint  $P_i$ ,  ${}^B\dot{\mathbf{t}}$  and  $\boldsymbol{\omega}$  are the translational velocity and angular velocity of the moving platform, respectively,  ${}^B\dot{\mathbf{t}} = [\dot{x} \ \dot{y} \ \dot{z}]^T$ , and  $\boldsymbol{\omega} = [\dot{\gamma} \ \dot{\beta} \ \dot{\alpha}]^T$ ,

$\mathbf{E}_3$  is a unit  $3 \times 3$  matrix,  ${}^P\tilde{\mathbf{p}}_i$  is the skew symmetry matrix of  ${}^P\mathbf{p}_i$ ,  $\dot{\mathbf{q}}$  is the general velocity of the moving platform, and  $\dot{\mathbf{q}} = [{}^B\dot{\mathbf{t}}^T \ \boldsymbol{\omega}^T]^T$ .

Letting  ${}^{pi}\mathbf{J}_q = \left[ \mathbf{E}_3 \quad {}^B\mathbf{R} \left( {}^P\tilde{\mathbf{p}}_i \right)^T \right]$ , (3) can be rewritten as

$$\dot{\mathbf{q}}_{pi} = {}^{pi}\mathbf{J}_q \cdot \dot{\mathbf{q}}, \quad (4)$$

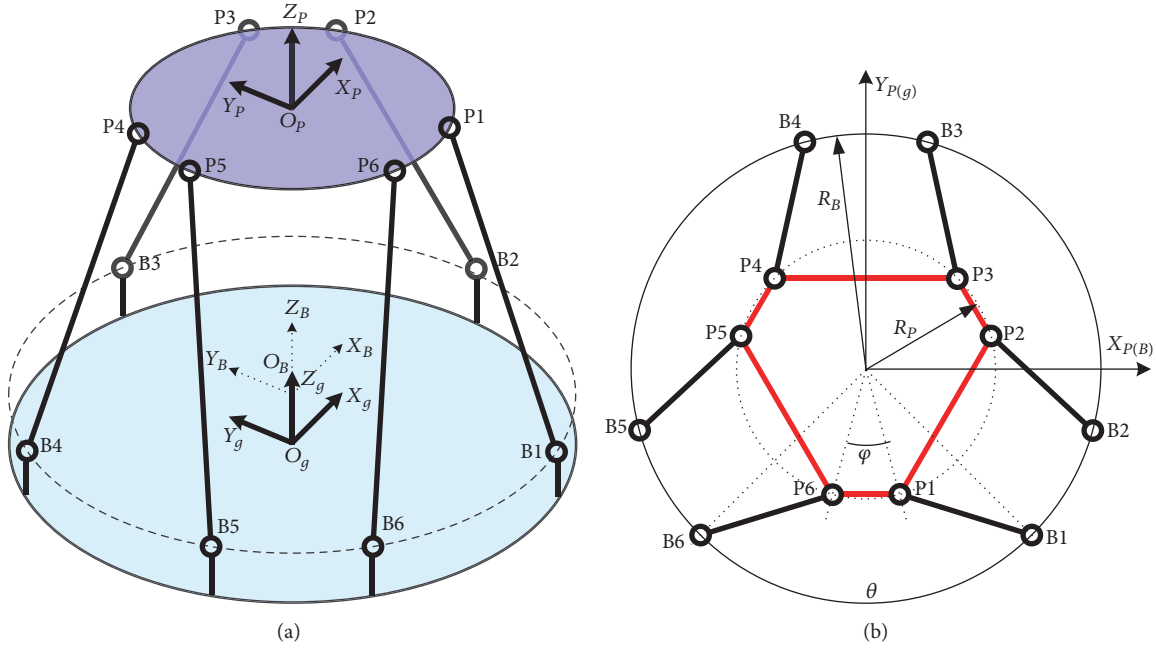


FIGURE 4: A schematic view of the vibration simulator: (a) isometric view and (b) vertical view.

where  ${}^P J_q$  denotes the Jacobian matrix relating the general velocity to the velocity of the upper joint  $\mathbf{p}_i$ .

The length of actuator can be described as

$$l_i = \sqrt{{}^B \mathbf{l}_i^T \cdot {}^B \mathbf{l}_i}. \quad (5)$$

Taking the time derivative of (5), the sliding velocity of the actuator can be obtained:

$$\dot{l}_i = {}^B \mathbf{l}_{ni}^T \cdot {}^B \dot{\mathbf{t}} + {}^B \mathbf{l}_{ni}^T \cdot (\boldsymbol{\omega} \times {}^P \mathbf{R} \cdot {}^P \mathbf{p}_i), \quad (6)$$

where  ${}^B \mathbf{l}_{ni}$  is the unit vector of  ${}^B \mathbf{l}_i$ .

Equation (6) can be rewritten as

$$\dot{l}_i = \left[ {}^B \mathbf{l}_{ni}^T, ({}^P \mathbf{R} \cdot {}^P \mathbf{p}_i \times {}^B \mathbf{l}_{ni})^T \right] \cdot \begin{bmatrix} {}^B \dot{\mathbf{t}} \\ \boldsymbol{\omega} \end{bmatrix}. \quad (7)$$

Thus (8) may be obtained as

$$\dot{\mathbf{L}} = \mathbf{J} \cdot \dot{\mathbf{q}}, \quad (8)$$

where  $\dot{\mathbf{L}}$  denotes actuator sliding velocities,  $\dot{\mathbf{L}} = [\dot{l}_1, \dot{l}_2, \dot{l}_3, \dot{l}_4, \dot{l}_5, \dot{l}_6]^T$ , and  $\mathbf{J}$  is the actuator Jacobian matrix expressing mappings from the general velocity to the actuator sliding velocities, which is given by

$$\mathbf{J} = \begin{bmatrix} {}^B \mathbf{l}_{n1}^T, ({}^P \mathbf{R} \cdot {}^P \mathbf{p}_1 \times {}^B \mathbf{l}_{n1})^T \\ {}^B \mathbf{l}_{n2}^T, ({}^P \mathbf{R} \cdot {}^P \mathbf{p}_2 \times {}^B \mathbf{l}_{n2})^T \\ {}^B \mathbf{l}_{n3}^T, ({}^P \mathbf{R} \cdot {}^P \mathbf{p}_3 \times {}^B \mathbf{l}_{n3})^T \\ {}^B \mathbf{l}_{n4}^T, ({}^P \mathbf{R} \cdot {}^P \mathbf{p}_4 \times {}^B \mathbf{l}_{n4})^T \\ {}^B \mathbf{l}_{n5}^T, ({}^P \mathbf{R} \cdot {}^P \mathbf{p}_5 \times {}^B \mathbf{l}_{n5})^T \\ {}^B \mathbf{l}_{n6}^T, ({}^P \mathbf{R} \cdot {}^P \mathbf{p}_6 \times {}^B \mathbf{l}_{n6})^T \end{bmatrix}. \quad (9)$$

According to their physical meaning, the velocities of the actuator can also be described in terms of the sliding and angular velocities of the actuator underframe  $\{\mathbf{B}\}$  as

$${}^B \dot{\mathbf{t}}_i = \dot{l}_i \cdot {}^B \mathbf{l}_{ni} + \boldsymbol{\omega}_{ai} \times {}^B \mathbf{l}_i, \quad (10)$$

where  $\boldsymbol{\omega}_{ai}$  is the angular velocity of the actuator.

Taking the cross product of the above equation with  ${}^B \mathbf{l}_{ni}$  and considering the assumption that no rotation is allowed about the actuator axis (i.e.,  $\boldsymbol{\omega}_{ai}^T \cdot {}^B \mathbf{l}_i = 0$ ) yield

$$\boldsymbol{\omega}_{ai} = \frac{({}^B \mathbf{l}_{ni} \times {}^B \dot{\mathbf{t}}_i)}{l_i} = \frac{({}^B \mathbf{l}_{ni} \times \dot{\mathbf{q}}_{pi})}{l_i}. \quad (11)$$

**3.1.2. Acceleration Analysis.** For convenience of analysis, the actuator is derived into two parts: the upper leg and the lower leg as shown in Figure 5.

Taking the derivative of both sides of (11) with respect to time and taking into account the fact that  $\boldsymbol{\omega}_{ai}^T \cdot {}^B \mathbf{l}_{ni} = 0$  and  $\boldsymbol{\varepsilon}_{ai}^T \cdot {}^B \mathbf{l}_{ni} = 0$ , the angular acceleration of the actuator can be obtained as

$$\boldsymbol{\varepsilon}_{ai} = \frac{({}^B \mathbf{l}_{ni} \times \ddot{\mathbf{q}}_{pi} - 2\boldsymbol{\omega}_{ai} \cdot \dot{l}_i)}{l_i}. \quad (12)$$

The translational acceleration of the upper joint  $P_i$  can be obtained by taking the derivative of (3) with respect to time as described by

$$\ddot{\mathbf{q}}_{pi} = {}^B \ddot{\mathbf{t}} + \dot{\boldsymbol{\omega}} \times {}^P \mathbf{R} \cdot {}^P \mathbf{p}_i + \boldsymbol{\omega} \times (\boldsymbol{\omega} \times ({}^P \mathbf{R} \cdot {}^P \mathbf{p}_i)). \quad (13)$$

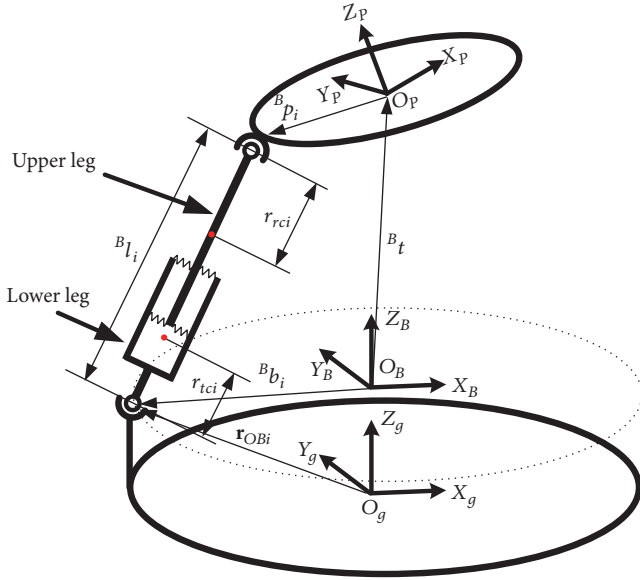


FIGURE 5: Diagram of the actuator.

According to their physical meaning, the velocities of the upper joint  $P_i$  can be described in terms of the velocity of the center of mass of the upper leg of the underframe  $\{B\}$  as

$$\dot{\mathbf{q}}_{pi} = {}^B\mathbf{v}_{rci} + \boldsymbol{\omega}_{ai} \times (r_{rci} \cdot {}^B\mathbf{l}_{ni}). \quad (14)$$

Rearranging (14) yields

$${}^B\mathbf{v}_{rci} = \dot{\mathbf{q}}_{pi} - \boldsymbol{\omega}_{ai} \times (r_{rci} \cdot {}^B\mathbf{l}_{ni}). \quad (15)$$

Substituting (11) into (15), the velocity of the upper leg centroid is given by

$${}^B\mathbf{v}_{rci} = \dot{\mathbf{q}}_{pi} + \frac{({}^B\mathbf{l}_{ni} \times ({}^B\mathbf{l}_{ni} \times \dot{\mathbf{q}}_{pi})) r_{rci}}{l_i}. \quad (16)$$

Let  ${}^{rci}\mathbf{J}_{pi} = \mathbf{E}_3 + r_{rci}/l_i \cdot {}^{B\tilde{}}\mathbf{l}_{ni}^2$ , and (16) can be rewritten as

$${}^B\mathbf{v}_{rci} = {}^{rci}\mathbf{J}_{pi} \dot{\mathbf{q}}_{pi}, \quad (17)$$

where  ${}^{rci}\mathbf{J}_{pi}$  denotes the Jacobian matrix relating the velocity of the upper joint  $\mathbf{p}_i$  to the velocity of the upper leg centroid.

In the following section, to obtain the acceleration of the upper leg centroid, (18) can be used, which is given by

$$\frac{d({}^{B\tilde{}}\mathbf{l}_{ni}^T \cdot {}^B\mathbf{l}_{ni})}{dt} = - \frac{({}^{B\tilde{}}\mathbf{l}_{ni}^T {}^{B\tilde{}}\mathbf{l}_{ni} \dot{\mathbf{q}}_{pi} {}^B\mathbf{l}_{ni}^T + {}^B\mathbf{l}_{ni} \dot{\mathbf{q}}_{pi}^T {}^{B\tilde{}}\mathbf{l}_{ni}^T {}^{B\tilde{}}\mathbf{l}_{ni})}{l_i}. \quad (18)$$

Taking the derivative with respect to time, of (17), and considering (18), the acceleration of the upper leg centroid is given by

$$\begin{aligned} {}^B\mathbf{a}_{rci} &= {}^{rci}\mathbf{J}_{pi} \cdot \ddot{\mathbf{q}}_{pi} \\ &+ \frac{(2{}^{B\tilde{}}\mathbf{l}_{ni}^T {}^{B\tilde{}}\mathbf{l}_{ni} \dot{\mathbf{q}}_{pi} {}^B\mathbf{l}_{ni}^T + {}^B\mathbf{l}_{ni} \dot{\mathbf{q}}_{pi}^T {}^{B\tilde{}}\mathbf{l}_{ni}^T {}^{B\tilde{}}\mathbf{l}_{ni} \dot{\mathbf{q}}_{pi}) r_{rci}}{l_i^2}. \end{aligned} \quad (19)$$

The same procedure may be easily adopted to obtain the velocity and acceleration of the lower leg, which are given by

$${}^B\mathbf{v}_{tci} = r_{tci} \cdot \boldsymbol{\omega}_{ai} \times {}^B\mathbf{l}_{ni} = {}^{tci}\mathbf{J}_{pi} \cdot \dot{\mathbf{q}}_{pi}, \quad (20)$$

$$\begin{aligned} {}^B\mathbf{a}_{tci} &= {}^{tci}\mathbf{J}_{pi} \cdot \ddot{\mathbf{q}}_{pi} \\ &- \frac{(2{}^{B\tilde{}}\mathbf{l}_{ni}^T {}^{B\tilde{}}\mathbf{l}_{ni} \dot{\mathbf{q}}_{pi} {}^B\mathbf{l}_{ni}^T + {}^B\mathbf{l}_{ni} \dot{\mathbf{q}}_{pi}^T {}^{B\tilde{}}\mathbf{l}_{ni}^T {}^{B\tilde{}}\mathbf{l}_{ni} \dot{\mathbf{q}}_{pi}) r_{tci}}{l_i^2}, \end{aligned} \quad (21)$$

where  ${}^{tci}\mathbf{J}_{pi}$  denotes the Jacobian matrix relating the velocity of the upper joint  $\mathbf{p}_i$  to the velocity of the lower leg centroid,  ${}^{tci}\mathbf{J}_{pi} = {}^{B\tilde{}}\mathbf{l}_{ni}^T {}^{B\tilde{}}\mathbf{l}_{ni} r_{tci}/l_i$ .

When the center of mass of the moving platform does not coincide with the origin of the frame  $\{P\}$ , the centrifugal and Coriolis forces will manifest themselves. Therefore the centrifugal and Coriolis terms cannot be ignored when we derive explicit equations for the dynamics of the moving platform. Let  ${}^P\mathbf{p}_c$  denote the position vector of the centroid of the moving platform under body frame  $\{P\}$ , which can be shown by

$${}^B\mathbf{p}_c = {}^B\mathbf{t} + {}^B\mathbf{R} \cdot {}^P\mathbf{p}_c. \quad (22)$$

Taking the derivative of both sides of (22) with respect to time, the acceleration of the centroid of the moving platform is given by

$${}^B\ddot{\mathbf{p}}_c = {}^B\dot{\mathbf{t}} + {}^B\mathbf{R} \cdot {}^P\ddot{\mathbf{p}}_c + {}^B\mathbf{R}^T \cdot {}^B\mathbf{R} \cdot \dot{\boldsymbol{\omega}} + \dot{\boldsymbol{\omega}}^2 \cdot ({}^B\mathbf{R} \cdot {}^P\mathbf{p}_c). \quad (23)$$

So far, all the kinematic parameters required for the inverse dynamics are derived. In the next section, attention will be paid to the deduction of dynamic equations of the MMVS.

**3.2. Actuator Forces.** In this subsection, the Lagrange approach and Newton-Euler method are adopted to develop the dynamic equations of the MMVS. Because of the function of the membrane of the actuators, the effect of gravity on the moving platform and the actuators can be compensated by the elastic forces of the membrane; that is, the moving platform will move to a new equilibrium position; therefore the effect of gravity on the micro-vibration simulator may be ignored.

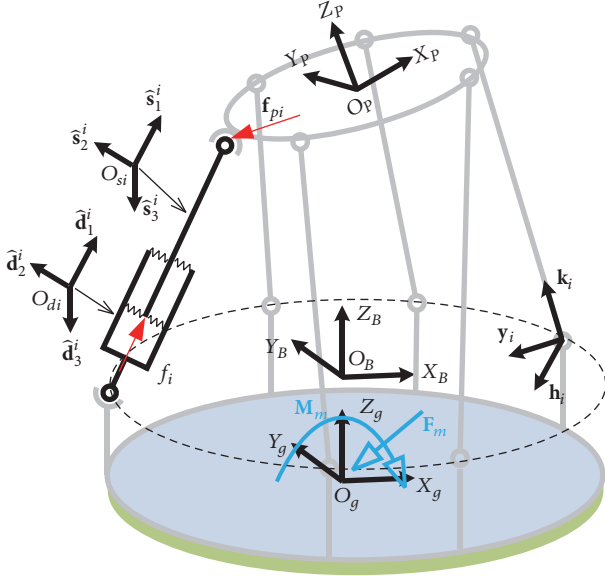


FIGURE 6: Schematic of the actuator.

**3.2.1. Analysis of a Single Actuator.** For the dynamic modeling of the actuator, only the actuator forces  $f_i$  and the interaction forces  $f_{pi}$  between the upper joints are covered in this subsection. Figure 6 shows a schematic of the actuator. As shown in Figure 6, frame  $\hat{s}^i$  is the body frame of the upper leg which is attached to the center of mass of upper leg with  $\hat{s}_1^i$  along the  $i$ th actuator. Here the over hat indicates a unit of length. The  $\hat{d}^i$  coordinate system is located to the  $i$ th actuator at the mass center of the lower leg with  $\hat{d}_1^i$  along the  $i$ th leg.

The Lagrange equation of the actuator can be written as in

$$\frac{d(\partial T_i / \partial \dot{\mathbf{q}}_{pi})}{dt} - \frac{\partial T_i}{\partial \mathbf{q}_{pi}} = \mathbf{Q}_i, \quad (24)$$

where  $\mathbf{Q}_i$  is the generalized force component associated with the generalized coordinate  $\mathbf{q}_{pi}$  and  $T$  is the kinematic energy of the  $i$ th actuator, given by

$$T_i = \frac{\mathbf{V}_{rci}^T m_{rci} \mathbf{V}_{rci} + \mathbf{V}_{tci}^T m_{tci} \mathbf{V}_{tci}}{2} + \frac{\boldsymbol{\omega}_{ai}^T (\mathbf{I}_{rci} + \mathbf{I}_{tci}) \boldsymbol{\omega}_{ai}}{2}, \quad (25)$$

where  $\mathbf{I}_{rci}$  and  $\mathbf{I}_{tci}$  are the moments of inertia of the upper leg and lower leg with respect to frame  $\{B\}$ , respectively.

The moments of inertia  $\mathbf{I}_{rci}$  and  $\mathbf{I}_{tci}$  are discussed in what follows. Assuming that the actuator is axisymmetric and the principal axes of inertia of the upper leg are consistent with the corresponding axes of frame  $\hat{s}^i$ , the principal

moments of inertia are denoted by  $I_{\hat{s}_1^i}$ ,  $I_{\hat{s}_2^i}$ , and  $I_{\hat{s}_3^i}$ , and the following expression can be obtained:

$$\begin{aligned} \mathbf{I}_{rci}^B &= \mathbf{R}_{\hat{s}^i}^B \hat{\mathbf{I}}_{rci} \mathbf{R}_{\hat{s}^i}^B{}^T \\ &= \mathbf{R}_{\hat{s}^i}^B \cdot \text{diag} [I_{\hat{s}_1^i}^i, I_{\hat{s}_2^i}^i, I_{\hat{s}_3^i}^i] \cdot \mathbf{R}_{\hat{s}^i}^B{}^T \\ &= I_{\hat{s}_1^i}^i \hat{\mathbf{s}}_1^i \hat{\mathbf{s}}_1^{iT} + I_{\hat{s}_2^i}^i \hat{\mathbf{s}}_2^i \hat{\mathbf{s}}_2^{iT} + I_{\hat{s}_3^i}^i \hat{\mathbf{s}}_3^i \hat{\mathbf{s}}_3^{iT}, \end{aligned} \quad (26)$$

where  $\mathbf{R}_{\hat{s}^i}^B$  is the rotation matrix of the transformation from frame  $\hat{s}^i$  to base frame  $\{B\}$ , given by

$$\mathbf{R}_{\hat{s}^i}^B = \begin{bmatrix} \hat{\mathbf{s}}_1^{iT} \cdot \hat{\mathbf{i}} & \hat{\mathbf{s}}_2^{iT} \cdot \hat{\mathbf{i}} & \hat{\mathbf{s}}_3^{iT} \cdot \hat{\mathbf{i}} \\ \hat{\mathbf{s}}_1^{iT} \cdot \hat{\mathbf{j}} & \hat{\mathbf{s}}_2^{iT} \cdot \hat{\mathbf{j}} & \hat{\mathbf{s}}_3^{iT} \cdot \hat{\mathbf{j}} \\ \hat{\mathbf{s}}_1^{iT} \cdot \hat{\mathbf{k}} & \hat{\mathbf{s}}_2^{iT} \cdot \hat{\mathbf{k}} & \hat{\mathbf{s}}_3^{iT} \cdot \hat{\mathbf{k}} \end{bmatrix}, \quad (27)$$

where  $\hat{\mathbf{i}} = [1 \ 0 \ 0]^T$ ,  $\hat{\mathbf{j}} = [0 \ 1 \ 0]^T$ , and  $\hat{\mathbf{k}} = [0 \ 0 \ 1]^T$  are three unit vectors, which are used to present the base frame  $\{B\}$ .

Because the actuator is axisymmetric, the principal moment of inertia  $I_{\hat{s}_2^i}^i$  is equal to  $I_{\hat{s}_3^i}^i$ . Letting  $I_r^i$  denote  $I_{\hat{s}_2^i}^i$ , (26) can be rewritten by

$$\mathbf{I}_{rci}^B = I_{\hat{s}_1^i}^i \hat{\mathbf{s}}_1^i \hat{\mathbf{s}}_1^{iT} + I_r^i (\mathbf{E}_3 - \hat{\mathbf{s}}_1^i \hat{\mathbf{s}}_1^{iT}). \quad (28)$$

Similarly, the moment of inertia  $\mathbf{I}_{tci}^B$  can be described by

$$\mathbf{I}_{tci}^B = I_{\hat{d}_1^i}^i \hat{\mathbf{d}}_1^i \hat{\mathbf{d}}_1^{iT} + I_t^i (\mathbf{E}_3 - \hat{\mathbf{d}}_1^i \hat{\mathbf{d}}_1^{iT}), \quad (29)$$

where  $I_{\hat{d}_1^i}^i$  is the principal moment of inertia of the lower leg with respect to the axis  $\hat{\mathbf{d}}_1^i$  of frame  $\hat{d}^i$  and  $I_t^i$  presents the principal moment of inertia of the lower leg with respect to the axis  $\hat{\mathbf{d}}_2^i$  (or the axis  $\hat{\mathbf{d}}_3^i$ ) of frame  $\hat{d}^i$ .

Substituting (17), (20), (28), and (29) into (25) yields

$$\begin{aligned} T_i &= \frac{1}{2} \dot{\mathbf{q}}_{pi}^T [\text{}^{rci} \mathbf{J}_{pi} m_{rci} + \text{}^{tci} \mathbf{J}_{pi} m_{tci}] \dot{\mathbf{q}}_{pi} + \frac{1}{2} \\ &\quad \cdot \boldsymbol{\omega}_{ai}^T \left[ I_{\hat{s}_1^i}^i \hat{\mathbf{s}}_1^i \hat{\mathbf{s}}_1^{iT} + I_r^i (\mathbf{E}_3 - \hat{\mathbf{s}}_1^i \hat{\mathbf{s}}_1^{iT}) + I_{\hat{d}_1^i}^i \hat{\mathbf{d}}_1^i \hat{\mathbf{d}}_1^{iT} \right. \\ &\quad \left. + I_t^i (\mathbf{E}_3 - \hat{\mathbf{d}}_1^i \hat{\mathbf{d}}_1^{iT}) \right] \boldsymbol{\omega}_{ai}. \end{aligned} \quad (30)$$

From Figure 6, it can be known that  $\hat{\mathbf{s}}_1^i$ ,  $\hat{\mathbf{d}}_1^i$ , and  $\mathbf{l}_{ni}$  are equal to each other. Thus, (30) can be rewritten as

$$\begin{aligned} T_i &= \frac{1}{2} \dot{\mathbf{q}}_{pi}^T [\text{}^{rci} \mathbf{J}_{pi} m_{rci} + \text{}^{tci} \mathbf{J}_{pi} m_{tci}] \dot{\mathbf{q}}_{pi} \\ &\quad + \frac{1}{2} \left[ (I_{\hat{s}_1^i}^i + I_{\hat{d}_1^i}^i - I_r^i - I_t^i) (\boldsymbol{\omega}_{ai}^T \cdot \mathbf{l}_{ni})^2 \right. \\ &\quad \left. + (I_r^i + I_t^i) \boldsymbol{\omega}_{ai}^T \cdot \boldsymbol{\omega}_{ai} \right]. \end{aligned} \quad (31)$$

Considering the assumption that no rotation is allowed about the actuator axis (i.e.,  $\boldsymbol{\omega}_{ai}^T \cdot {}^B\mathbf{l}_{ni} = 0$ ) and substituting (11) into (31), the following expression can be obtained:

$$T_i = \frac{1}{2} \dot{\mathbf{q}}_{pi}^T \left[ {}^{rci}\mathbf{J}_{pi} m_{rci} + {}^{tci}\mathbf{J}_{pi} m_{tci} \right] \dot{\mathbf{q}}_{pi} + \frac{1}{2} (I_r^i + I_t^i) \boldsymbol{\omega}_{ai}^T \cdot \boldsymbol{\omega}_{ai} = \frac{1}{2}$$

$$\cdot \dot{\mathbf{q}}_{pi}^T \left[ {}^{rci}\mathbf{J}_{pi} m_{rci} + {}^{tci}\mathbf{J}_{pi} m_{tci} + {}^{B\bar{\mathbf{l}}}_{ni} \cdot \frac{{}^{B\bar{\mathbf{l}}}_{ni} (I_r^i + I_t^i)}{l_i^2} \right] \cdot \dot{\mathbf{q}}_{pi} = \frac{1}{2} \dot{\mathbf{q}}_{pi}^T \mathbf{M}_{leg}^i \dot{\mathbf{q}}_{pi}, \quad (32)$$

where  $M_{leg}^i = {}^{rci}\mathbf{J}_{pi} m_{rci} + {}^{tci}\mathbf{J}_{pi} m_{tci} + {}^{B\bar{\mathbf{l}}}_{ni} \cdot {}^{B\bar{\mathbf{l}}}_{ni} (I_r^i + I_t^i) / l_i^2$ . The first and second terms in (24) can be written as

$$\begin{aligned} \frac{d(\partial T / \partial \dot{\mathbf{q}}_{pi})}{dt} &= \mathbf{M}_{leg}^i \ddot{\mathbf{q}}_{pi} + \dot{\mathbf{q}}_{pi} \left( \frac{2 \left( {}^B\mathbf{l}_{ni} \dot{\mathbf{q}}_{pi}^T {}^{B\bar{\mathbf{l}}}_{ni} {}^{B\bar{\mathbf{l}}}_{ni} \right) m_{rci} r_{rci}}{l_i^2} + {}^B\mathbf{l}_{ni}^T \dot{\mathbf{q}}_{pi} {}^{B\bar{\mathbf{l}}}_{ni} {}^{B\bar{\mathbf{l}}}_{ni} + {}^{B\bar{\mathbf{l}}}_{ni} {}^{B\bar{\mathbf{l}}}_{ni} \dot{\mathbf{q}}_{pi} {}^B\mathbf{l}_{ni}^T \right. \\ &\quad \left. - \frac{\left( 2 {}^B\mathbf{l}_{ni}^T \dot{\mathbf{q}}_{pi} {}^{B\bar{\mathbf{l}}}_{ni} {}^{B\bar{\mathbf{l}}}_{ni} + {}^B\mathbf{l}_{ni} \dot{\mathbf{q}}_{pi}^T {}^{B\bar{\mathbf{l}}}_{ni} {}^{B\bar{\mathbf{l}}}_{ni} + {}^{B\bar{\mathbf{l}}}_{ni} {}^{B\bar{\mathbf{l}}}_{ni} \dot{\mathbf{q}}_{pi} {}^B\mathbf{l}_{ni}^T \right) \left( m_{rci} r_{rci}^2 + m_{tci} r_{tci}^2 + I_r^i + I_t^i \right)}{l_i^3} \right), \quad (33) \\ \frac{\partial T}{\partial \mathbf{q}_{pi}} &= \frac{\left( {}^B\mathbf{l}_{ni} \dot{\mathbf{q}}_{pi}^T \dot{\mathbf{q}}_{pi} + 2 {}^B\mathbf{l}_{ni}^T \dot{\mathbf{q}}_{pi} \dot{\mathbf{q}}_{pi} - 3 {}^B\mathbf{l}_{ni} \dot{\mathbf{q}}_{pi}^T {}^B\mathbf{l}_{ni} {}^B\mathbf{l}_{ni}^T \dot{\mathbf{q}}_{pi} \right) m_{rci} r_{rci}}{l_i^2} \\ &\quad - \frac{\left( {}^B\mathbf{l}_{ni} \dot{\mathbf{q}}_{pi}^T \dot{\mathbf{q}}_{pi} + \dot{\mathbf{q}}_{pi} \dot{\mathbf{q}}_{pi}^T {}^B\mathbf{l}_{ni} - 2 {}^B\mathbf{l}_{ni} {}^B\mathbf{l}_{ni}^T \dot{\mathbf{q}}_{pi} \dot{\mathbf{q}}_{pi} {}^B\mathbf{l}_{ni} \right) \left( m_{rci} r_{rci}^2 + m_{tci} r_{tci}^2 + I_r^i + I_t^i \right)}{l_i^3}. \end{aligned}$$

The right side of (24) can be described as

$$\mathbf{Q}_i = {}^B\mathbf{l}_{ni} f_i + \mathbf{f}_{pi}. \quad (34)$$

Substituting (25), (33), and (34) into (24) yields

$$\begin{aligned} \mathbf{f}_{pi} &= \mathbf{M}_{leg}^i \ddot{\mathbf{q}}_{pi} + \mathbf{C}_a^i \dot{\mathbf{q}}_{pi} - {}^B\mathbf{l}_{ni} f_i \\ &= \mathbf{M}_{leg}^i {}^{pi}\mathbf{J}_q \ddot{\mathbf{q}} + \mathbf{C}_a^i {}^{pi}\mathbf{J}_q \dot{\mathbf{q}} + \mathbf{M}_{leg}^i \tilde{\boldsymbol{\omega}}_P^B \mathbf{R}^P \mathbf{P}_i - {}^B\mathbf{l}_{ni} f_i, \quad (35) \end{aligned}$$

where  $\mathbf{C}_a^i$  is a  $3 \times 3$  matrix, which is given by

$$\begin{aligned} \mathbf{C}_a^i &= \frac{m_{rci} r_{rci}}{l_i^2} \\ &\quad \cdot \left( {}^B\mathbf{l}_{ni} \dot{\mathbf{q}}_{pi}^T {}^{B\bar{\mathbf{l}}}_{ni} {}^{B\bar{\mathbf{l}}}_{ni} + {}^B\mathbf{l}_{ni}^T \dot{\mathbf{q}}_{pi} {}^{B\bar{\mathbf{l}}}_{ni} {}^{B\bar{\mathbf{l}}}_{ni} + {}^{B\bar{\mathbf{l}}}_{ni} {}^{B\bar{\mathbf{l}}}_{ni} \dot{\mathbf{q}}_{pi} {}^B\mathbf{l}_{ni}^T \right) \\ &\quad - \frac{\left( m_{rci} r_{rci}^2 + m_{tci} r_{tci}^2 + I_r^i + I_t^i \right)}{l_i^3} \\ &\quad \cdot \left( {}^B\mathbf{l}_{ni}^T \dot{\mathbf{q}}_{pi} {}^{B\bar{\mathbf{l}}}_{ni} {}^{B\bar{\mathbf{l}}}_{ni} + {}^{B\bar{\mathbf{l}}}_{ni} {}^{B\bar{\mathbf{l}}}_{ni} \dot{\mathbf{q}}_{pi} {}^B\mathbf{l}_{ni}^T \right). \quad (36) \end{aligned}$$

**3.2.2. The Completed Dynamic Equations.** Assuming that the axial stiffness coefficients of the actuators are equal and letting  $k$  denote the axial stiffness coefficient, then for the  $i$ th actuator

$$f_e^i = -k \cdot \Delta l_i, \quad (37)$$

where  $f_e^i$  is the force needed to cause a  $\Delta l$  change in the  $i$ th actuator length. Assembling the equations for all the actuators and considering (8), (37) becomes

$$\mathbf{f}_e = -k \cdot \mathbf{J} \cdot \Delta \mathbf{q}, \quad (38)$$

where  $\mathbf{f}_e$  is the general elastic force,  $\mathbf{f}_e = [f_e^1 \ f_e^2 \ f_e^3 \ f_e^4 \ f_e^5 \ f_e^6]^T$ .

Similarly, the general damping force  $\mathbf{f}_c$  can be described as

$$\mathbf{f}_c = -c \cdot \mathbf{J} \cdot \dot{\mathbf{q}}, \quad (39)$$

where  $\mathbf{f}_c$  is a  $6 \times 1$  matrix and  $c$  is the damping coefficient of the actuator.

Based on the virtual work principle, the dynamic equation of the moving platform under the external forces of the loads can be described as

$$\boldsymbol{\Gamma}^T \cdot \delta \mathbf{q} = (\mathbf{f}_e^T + \mathbf{f}_c^T + \mathbf{F}^T) \cdot \delta \mathbf{L}, \quad (40)$$

where  $\boldsymbol{\Gamma} = [\tau_1, \tau_2, \tau_3, \tau_4, \tau_5, \tau_6]^T$  is the applied generalized force exerted on the moving platform,  $\delta \mathbf{q} = [\delta x, \delta y, \delta z, \delta \gamma, \delta \beta, \delta \alpha]^T$  is virtual displacement of the moving platform,  $\mathbf{F} = [f_1, f_2, f_3, f_4, f_5, f_6]^T$  describes the actuator forces, and  $\delta \mathbf{L} = [\delta l_1, \delta l_2, \delta l_3, \delta l_4, \delta l_5, \delta l_6]^T$  gives the virtual displacement of the actuators.

$$\delta \mathbf{L} = \mathbf{J} \cdot \delta \mathbf{q}. \quad (41)$$

Substituting (41) into (40), the external force  $\Gamma$  acting on the moving platform can be written as

$$\Gamma = \mathbf{J}^T (\mathbf{f}_e + \mathbf{f}_c + \mathbf{F}). \quad (42)$$

Substituting (38) and (39) into (42) yields

$$\Gamma = -\mathbf{K} \cdot \Delta \mathbf{q} - \mathbf{C} \cdot \dot{\mathbf{q}} + \mathbf{J}^T \mathbf{F}, \quad (43)$$

where  $\mathbf{K} = k\mathbf{J}^T\mathbf{J}$  is the matrix for generalized stiffness and  $\mathbf{C} = c\mathbf{J}^T\mathbf{J}$  is the matrix for generalized damping.

The dynamic model for upper platform as a rigid body ignoring the inertia of the actuators can be derived using the Newton-Euler method [14]:

$$\begin{aligned} m \cdot {}^B \ddot{\mathbf{p}}_c &= \mathbf{F}_{3 \times 1}, \\ {}^B \mathbf{R} \cdot {}^P \mathbf{I} \cdot {}^B \mathbf{R}^T \cdot \dot{\omega} + \tilde{\omega} \cdot {}^B \mathbf{R} \cdot {}^P \mathbf{I} \cdot {}^B \mathbf{R}^T \cdot \omega + m \\ &\cdot ({}^B \mathbf{R} \cdot {}^P \mathbf{p}_c) \times \dot{\mathbf{i}} = \mathbf{M}_{3 \times 1}, \end{aligned} \quad (44)$$

where  $m$  is the payload mass,  ${}^P \mathbf{I}$  is the inertia matrix with respect to frame  $\{P\}$ ,  $\mathbf{F}_{3 \times 1} = [\tau_1, \tau_2, \tau_3]^T$  and  $\mathbf{M}_{3 \times 1} = [\tau_4, \tau_5, \tau_6]^T$ .

$$\begin{aligned} \mathbf{H}_p &= \begin{bmatrix} \mathbf{E}_3 & \mathbf{E}_3 & \mathbf{E}_3 & \mathbf{E}_3 & \mathbf{E}_3 & \mathbf{E}_3 \\ {}^B \mathbf{R}^P \tilde{\mathbf{p}}_1 {}^B \mathbf{R}^T & {}^B \mathbf{R}^P \tilde{\mathbf{p}}_2 {}^B \mathbf{R}^T & {}^B \mathbf{R}^P \tilde{\mathbf{p}}_3 {}^B \mathbf{R}^T & {}^B \mathbf{R}^P \tilde{\mathbf{p}}_4 {}^B \mathbf{R}^T & {}^B \mathbf{R}^P \tilde{\mathbf{p}}_5 {}^B \mathbf{R}^T & {}^B \mathbf{R}^P \tilde{\mathbf{p}}_6 {}^B \mathbf{R}^T \end{bmatrix}, \\ \mathbf{F}_p &= [\mathbf{f}_{p1}^T \ \mathbf{f}_{p2}^T \ \mathbf{f}_{p3}^T \ \mathbf{f}_{p4}^T \ \mathbf{f}_{p5}^T \ \mathbf{f}_{p6}^T]^T. \end{aligned} \quad (47)$$

Substituting (35) and (47) into (46) produces the complete dynamic equation of the vibration simulator, which can be described as

$$\mathbf{M}(\mathbf{q}) \ddot{\mathbf{q}} + \mathbf{C}(\mathbf{q}, \dot{\mathbf{q}}) \dot{\mathbf{q}} + \mathbf{K} \cdot \Delta \mathbf{q} = \mathbf{J}^T \mathbf{F}, \quad (48)$$

where  $\mathbf{M}(\mathbf{q})$  is a  $6 \times 6$  mass matrix,  $\mathbf{C}(\mathbf{q}, \dot{\mathbf{q}})$  is a  $6 \times 6$  matrix of the centrifugal and Coriolis force terms,  $\mathbf{K}$  is a  $6 \times 6$  matrix of the generalized stiffness, and  $\mathbf{F}$  is a  $6 \times 1$  vector representing actuator forces. They are given by

$$\begin{aligned} \mathbf{M}(\mathbf{q}) &= \begin{bmatrix} m\mathbf{E}_3 & m \cdot {}^B \mathbf{R} \cdot {}^P \tilde{\mathbf{p}}_c \cdot {}^B \mathbf{R}^T \\ m \cdot {}^B \mathbf{R} \cdot {}^P \tilde{\mathbf{p}}_c \cdot {}^B \mathbf{R}^T & {}^B \mathbf{R} \cdot {}^P \mathbf{I} \cdot {}^B \mathbf{R}^T \end{bmatrix} \\ &+ \sum_{i=1}^6 {}^{pi} \mathbf{J}_i^T \mathbf{M}_{leg}^i {}^{pi} \mathbf{J}_i, \end{aligned}$$

Substituting (43) into (44) yields

$$\begin{aligned} &\begin{bmatrix} m\mathbf{E}_3 & m \cdot {}^B \mathbf{R} \cdot {}^P \tilde{\mathbf{p}}_c \cdot {}^B \mathbf{R}^T \\ m \cdot {}^B \mathbf{R} \cdot {}^P \tilde{\mathbf{p}}_c \cdot {}^B \mathbf{R}^T & {}^B \mathbf{R} \cdot {}^P \mathbf{I} \cdot {}^B \mathbf{R}^T \end{bmatrix} \ddot{\mathbf{q}} \\ &+ \left( \begin{bmatrix} 0 & 0 \\ 0 & \tilde{\omega} {}^B \mathbf{R} \cdot {}^P \mathbf{I} \cdot {}^B \mathbf{R}^T \end{bmatrix} + c \cdot \mathbf{J}^T \mathbf{J} \right) \dot{\mathbf{q}} \\ &+ \begin{bmatrix} m\mathbf{E}_3 \\ \mathbf{0} \end{bmatrix} \tilde{\omega}^2 \cdot ({}^B \mathbf{R} \cdot {}^P \tilde{\mathbf{p}}_c) + k \cdot \mathbf{J}^T \cdot \mathbf{J} \cdot \Delta \mathbf{q} = \mathbf{J}^T \mathbf{F}. \end{aligned} \quad (45)$$

Considering the inertia of the actuators, (45) can be written as

$$\begin{aligned} &\begin{bmatrix} m\mathbf{E}_3 & m \cdot {}^B \mathbf{R} \cdot {}^P \tilde{\mathbf{p}}_c \cdot {}^B \mathbf{R}^T \\ m \cdot {}^B \mathbf{R} \cdot {}^P \tilde{\mathbf{p}}_c \cdot {}^B \mathbf{R}^T & {}^B \mathbf{R} \cdot {}^P \mathbf{I} \cdot {}^B \mathbf{R}^T \end{bmatrix} \ddot{\mathbf{q}} \\ &+ \left( \begin{bmatrix} 0 & 0 \\ 0 & \tilde{\omega} {}^B \mathbf{R} \cdot {}^P \mathbf{I} \cdot {}^B \mathbf{R}^T \end{bmatrix} + c \cdot \mathbf{J}^T \mathbf{J} \right) \dot{\mathbf{q}} \\ &+ \begin{bmatrix} m\mathbf{E}_3 \\ \mathbf{0} \end{bmatrix} \tilde{\omega}^2 \cdot ({}^B \mathbf{R} \cdot {}^P \tilde{\mathbf{p}}_c) + k \cdot \mathbf{J}^T \cdot \mathbf{J} \cdot \Delta \mathbf{q} \\ &= -\mathbf{H}_p \mathbf{F}_p. \end{aligned} \quad (46)$$

Expressions for  $\mathbf{H}_p$  and  $\mathbf{F}_p$  are given by

$$\begin{aligned} \mathbf{C}(\mathbf{q}, \dot{\mathbf{q}}) \dot{\mathbf{q}} &= \left( \begin{bmatrix} 0 & 0 \\ 0 & \tilde{\omega} {}^B \mathbf{R} \cdot {}^P \mathbf{I} \cdot {}^B \mathbf{R}^T \end{bmatrix} + c \cdot \mathbf{J}^T \mathbf{J} \right) \dot{\mathbf{q}} \\ &+ \sum_{i=1}^6 ({}^{pi} \mathbf{J}_i^T) \mathbf{C}_a^{pi} \mathbf{J}_i \dot{\mathbf{q}} + \begin{bmatrix} m\mathbf{E}_3 \\ \mathbf{0} \end{bmatrix} \tilde{\omega}^2 ({}^B \mathbf{R} \cdot {}^P \mathbf{p}_c) \\ &+ \sum_{i=1}^6 {}^{pi} \mathbf{J}_i^T \mathbf{M}_{leg}^i \tilde{\omega}^2 ({}^B \mathbf{R} \cdot {}^P \mathbf{p}_i). \end{aligned} \quad (49)$$

Pre-multiplying both sides of (48) with  $\mathbf{J}^{-T}$ , the actuator forces are given by

$$\mathbf{F} = \mathbf{J}^{-T} [\mathbf{M}(\mathbf{q}) \ddot{\mathbf{q}} + \mathbf{C}(\mathbf{q}, \dot{\mathbf{q}}) \dot{\mathbf{q}} + \mathbf{K} \cdot \Delta \mathbf{q}]. \quad (50)$$

**3.3. Calculation of Disturbance Forces and Moments.** As we know, the object of this study is to develop a micro-vibration simulator which can reproduce desired disturbance

forces and moments. So this subsection will calculate the disturbance forces and moments when the actuator forces are applied to the MMVS.

The calculation of the disturbance forces and moments is based on the Newton-Euler method. For the convenience of analysis, a frame of reference is attached to the actuator with its origin at the lower joint points,  $x$ -axis ( $\mathbf{h}_i$ ) along the actuator,  $y$ -axis ( $\mathbf{y}_i$ ) along the rotation axis (axis fixed to the actuator) of the universal joint, and  $z$ -axis ( $\mathbf{k}_i$ ) perpendicular to the  $x$ - and  $y$ -axes according to the right hand rule. Figure 1 shows the frame. Considering the rotational equilibrium of the entire actuator, Euler's equation for the actuator is obtained as

$$\begin{aligned} & \left( {}^B\mathbf{I}_{rci} + {}^B\mathbf{I}_{tci} \right) \boldsymbol{\varepsilon}_{ai} + \boldsymbol{\omega}_{ai} \times \left[ \left( {}^B\mathbf{I}_{rci} + {}^B\mathbf{I}_{tci} \right) \boldsymbol{\omega}_{ai} \right] \\ & + m_{rci} \mathbf{r}_{rci} \times {}^B\mathbf{a}_{rci} + m_{tci} \mathbf{r}_{tci} \times {}^B\mathbf{a}_{tci} \\ & = {}^B\mathbf{I}_i \times \mathbf{f}_{pi} + M_{ui} \mathbf{h}_i, \end{aligned} \quad (51)$$

where  $\mathbf{r}_{rci} = (l_i - r_{rci}) {}^B\mathbf{I}_{ni}$ ,  $\mathbf{r}_{tci} = r_{tci} {}^B\mathbf{I}_{ni}$ , and  $M_{ui}$  is the magnitude of the constraint moment at the universal joint acting about the  $\mathbf{h}_i$  axis.

Taking cross products of both sides of (51) with  $\mathbf{h}_i$ , the scalar unknown  $M_{ui}$  is given by

$$M_{ui} = \frac{{}^B\mathbf{I}_{ni}^T \mathbf{C}_i}{\left( {}^B\mathbf{I}_{ni}^T \mathbf{h}_i \right)}, \quad (52)$$

where  $\mathbf{C}_i$  is a  $3 \times 1$  matrix, which is given by

$$\begin{aligned} \mathbf{C}_i &= \left( {}^B\mathbf{I}_{rci} + {}^B\mathbf{I}_{tci} \right) \boldsymbol{\varepsilon}_{ai} + \boldsymbol{\omega}_{ai} \times \left[ \left( {}^B\mathbf{I}_{rci} + {}^B\mathbf{I}_{tci} \right) \boldsymbol{\omega}_{ai} \right] \\ &+ m_{rci} \mathbf{r}_{rci} \times {}^B\mathbf{a}_{rci} + m_{tci} \mathbf{r}_{tci} \times {}^B\mathbf{a}_{tci}. \end{aligned} \quad (53)$$

Ignoring the damping forces of the actuator and considering the upper leg of the actuator, Newton's equation can be given by

$$f_i + {}^B\mathbf{I}_{ni}^T \mathbf{f}_{pi} - k \cdot \Delta l_i - m_{rci} {}^B\mathbf{I}_{ni}^T \cdot {}^B\mathbf{a}_{rci} = 0. \quad (54)$$

Solving (54), the constraint force at the spherical joint can be rewritten as

$$\mathbf{f}_{pi} = X_i {}^B\mathbf{I}_{ni} + \mathbf{D}_i. \quad (55)$$

Expressions  $X_i$  and  $\mathbf{D}_i$  are given by

$$\begin{aligned} X_i &= m_{rci} {}^B\mathbf{I}_{ni}^T \cdot {}^B\mathbf{a}_{rci} + k \cdot \Delta l_i - f_i, \\ \mathbf{D}_i &= \frac{\left( \mathbf{C}_i \times {}^B\mathbf{I}_{ni} - M_{ui} \mathbf{h}_i \times {}^B\mathbf{I}_{ni} \right)}{l_i}. \end{aligned} \quad (56)$$

Considering the translational equilibrium, Newton's equation for the entire actuator can be written as

$$m_{rci} {}^B\mathbf{a}_{rci} + m_{tci} {}^B\mathbf{a}_{tci} - \mathbf{f}_{pi} = \mathbf{f}_{ui}, \quad (57)$$

where  $\mathbf{f}_{ui}$  is the constraint force at the universal joint.

Substituting (55) into (57), the constraint force  $\mathbf{f}_{ui}$  is given by

$$\mathbf{f}_{ui} = m_{rci} {}^B\mathbf{a}_{rci} + m_{tci} {}^B\mathbf{a}_{tci} - X_i {}^B\mathbf{I}_{ni} + \mathbf{D}_i. \quad (58)$$

Consequently, the disturbance forces acting on the center of the bottom of the base plane, which are produced by the simulator, can be written as

$$\mathbf{F}_m = \sum_{i=1}^6 \mathbf{f}_{ui}. \quad (59)$$

Similarly, the disturbance moments acting on the center bottom of the base plane, produced by the simulator, which are shown in Figure 6, can be written as

$$\mathbf{M}_m = \sum_{i=1}^6 \left( \mathbf{r}_{OBi} \times \mathbf{f}_{ui} + M_{ui} \mathbf{h}_i \right), \quad (60)$$

where  $\mathbf{r}_{OBi}$  is the vector from the origin  $O_g$  to the lower joint point  $B_i$ .

**3.4. Planning of Disturbance Forces and Moments.** In the last subsection, the relationships between the disturbance forces and moments and the actuator forces are derived. This subsection will deduce the relationship between the deduced forces and moments and the generalized acceleration of the moving platform and then plan the disturbance forces and moments.

Because micro-vibrations have the characteristics of a wide frequency range and small amplitudes, a few approximations can be adopted to plan the disturbance forces and moments. For example, the third term on the right side of (13) is a square term of angular velocity, so it can be ignored when the angular velocity of the moving platform is small. The simplified acceleration of the upper joint  $P_i$  can be described as

$${}^B\ddot{\mathbf{p}}_i \cong {}^B\dot{\mathbf{t}} + \dot{\boldsymbol{\omega}} \times {}^B\mathbf{R} \cdot {}^P\mathbf{p}_i \cong \left[ \mathbf{E}_3 \quad {}^B\tilde{\mathbf{p}}_i^T \right] \begin{bmatrix} {}^B\dot{\mathbf{t}} \\ \dot{\boldsymbol{\omega}} \end{bmatrix} = \mathbf{T}_{pi} \ddot{\mathbf{q}}, \quad (61)$$

where  $\mathbf{T}_{pi} = \left[ \mathbf{E}_3 \quad {}^B\tilde{\mathbf{p}}_i^T \right]$ .

Similarly, ignoring the second terms of (19) and (21), respectively, the acceleration of the upper and lower legs is given by

$$\begin{aligned} {}^B\mathbf{a}_{rci} &= {}^{rci}\mathbf{J}_{pi} \cdot \ddot{\mathbf{q}}_{pi}, \\ {}^B\mathbf{a}_{tci} &= {}^{tci}\mathbf{J}_{pi} \cdot \ddot{\mathbf{q}}_{pi}. \end{aligned} \quad (62)$$

Substituting (61) into (62) yields

$$\begin{aligned} {}^B\mathbf{a}_{rci} &= {}^{rci}\mathbf{J}_{pi} \left[ \mathbf{E}_3 \quad {}^B\tilde{\mathbf{p}}_i^T \right] \begin{bmatrix} {}^B\dot{\mathbf{t}} \\ \dot{\boldsymbol{\omega}} \end{bmatrix} = {}^{rci}\mathbf{J}_{pi} \mathbf{T}_{pi} \ddot{\mathbf{q}}, \\ {}^B\mathbf{a}_{tci} &= {}^{tci}\mathbf{J}_{pi} \left[ \mathbf{E}_3 \quad {}^B\tilde{\mathbf{p}}_i^T \right] \begin{bmatrix} {}^B\dot{\mathbf{t}} \\ \dot{\boldsymbol{\omega}} \end{bmatrix} = {}^{tci}\mathbf{J}_{pi} \mathbf{T}_{pi} \ddot{\mathbf{q}}. \end{aligned} \quad (63)$$

The angular velocity of the actuator is very small, so it can also be ignored. The angular acceleration of the actuator can be described as

$$\boldsymbol{\varepsilon}_{ai} \cong \frac{{}^B\bar{\mathbf{I}}_{ni}^B \mathbf{a}_{pi}}{l_i}. \quad (64)$$

After obtaining the simplified expressions presented as (61), (63), and (64), the following expressions are obtained:

$$\begin{aligned} X_i &\cong m_{rci} {}^B\mathbf{I}_{ni}^T \cdot {}^{rci}\mathbf{J}_{pi} \mathbf{T}_{pi} \ddot{\mathbf{q}} + k \cdot \Delta l_i - f_i, \\ \mathbf{C}_i &\cong \left[ ({}^B\mathbf{I}_{rci} + {}^B\mathbf{I}_{tci}) \cdot \frac{{}^B\bar{\mathbf{I}}_{ni}}{l_i} + m_{rci} \bar{\mathbf{r}}_{rci} \cdot {}^{rci}\mathbf{J}_{pi} + m_{tci} \bar{\mathbf{r}}_{tci} \cdot {}^{tci}\mathbf{J}_{pi} \right] \mathbf{T}_{pi} \ddot{\mathbf{q}}, \\ \mathbf{D}_i & \\ &\cong - \frac{{}^B\bar{\mathbf{I}}_{ni}}{l_i \left[ ({}^B\mathbf{I}_{rci} + {}^B\mathbf{I}_{tci}) / l_i \cdot {}^B\bar{\mathbf{I}}_{ni} + m_{rci} \bar{\mathbf{r}}_{rci} \cdot {}^{rci}\mathbf{J}_{pi} + m_{tci} \bar{\mathbf{r}}_{tci} \cdot {}^{tci}\mathbf{J}_{pi} \right]} \mathbf{T}_{pi} \ddot{\mathbf{q}} \\ &= \Lambda_i \ddot{\mathbf{q}}, \end{aligned} \quad (65)$$

where  $\Lambda_i = -{}^B\bar{\mathbf{I}}_{ni}/l_i \left[ ({}^B\mathbf{I}_{rci} + {}^B\mathbf{I}_{tci}) / l_i \cdot {}^B\bar{\mathbf{I}}_{ni} + m_{rci} \bar{\mathbf{r}}_{rci} \cdot {}^{rci}\mathbf{J}_{pi} + m_{tci} \bar{\mathbf{r}}_{tci} \cdot {}^{tci}\mathbf{J}_{pi} \right] \mathbf{T}_{pi}$ .

Therefore, the constraint forces at the spherical and universal joints can be rewritten as

$$\begin{aligned} \mathbf{f}_{pi} &= X_i {}^B\mathbf{I}_{ni} + \Lambda_i \ddot{\mathbf{q}}, \\ \mathbf{f}_{ui} &= \left[ \left( m_{rci} {}^{rci}\mathbf{J}_{pi} + m_{tci} {}^{tci}\mathbf{J}_{pi} - m_{rci} {}^B\mathbf{I}_{ni} {}^B\mathbf{I}_{ni}^T {}^{rci}\mathbf{J}_{pi} \right) \mathbf{T}_{pi} \right. \\ &\quad \left. - \Lambda_i + {}^B\mathbf{I}_{ni} \mathbf{e}_i \mathbf{J}^{-T} \mathbf{M}(q) \right] \ddot{\mathbf{q}} = \Theta_{ui} \ddot{\mathbf{q}}, \end{aligned} \quad (66)$$

where  $\mathbf{e}_i = [0 \ \dots \ 1 \ \dots \ 0]$  is a  $1 \times 6$  matrix, the  $i$ th element is 1, and the other elements are 0, and  $\Theta_{ui}$  is  $3 \times 1$  matrix,  $\Theta_{ui} = (m_{rci} {}^{rci}\mathbf{J}_{pi} + m_{tci} {}^{tci}\mathbf{J}_{pi} - m_{rci} {}^B\mathbf{I}_{ni} {}^B\mathbf{I}_{ni}^T {}^{rci}\mathbf{J}_{pi}) \mathbf{T}_{pi} - \Lambda_i + {}^B\mathbf{I}_{ni} \mathbf{e}_i \mathbf{J}^{-T} \mathbf{M}(q)$ .

The disturbance forces and moments acting on the center of the base plane's bottom can be rewritten as

$$\begin{aligned} \mathbf{F}_m &= \sum_{i=1}^6 \mathbf{f}_{ui} = \sum_{i=1}^6 \Theta_{ui} \ddot{\mathbf{q}} = \Theta_T \ddot{\mathbf{q}}, \\ \mathbf{M}_m &= \sum_{i=1}^6 (\mathbf{r}_{OBi} \times \mathbf{f}_{ui} + M_{ui} \mathbf{h}_i) = \sum_{i=1}^6 \bar{\mathbf{r}}_{OBi} \Theta_{ui} \ddot{\mathbf{q}} = \Theta_R \ddot{\mathbf{q}}. \end{aligned} \quad (67)$$

Equation (67) can be written in a matrix form as

$$\begin{bmatrix} \mathbf{F}_m \\ \mathbf{M}_m \end{bmatrix} = \begin{bmatrix} \Theta_T \\ \Theta_R \end{bmatrix} \ddot{\mathbf{q}}. \quad (68)$$

Taking both sides of (68) with  $[\Theta_T^T \ \Theta_R^T]^{-T}$ , the generalized acceleration of the moving platform can be given by

$$\ddot{\mathbf{q}} = \begin{bmatrix} \Theta_T \\ \Theta_R \end{bmatrix}^{-1} \begin{bmatrix} \mathbf{F}_m \\ \mathbf{M}_m \end{bmatrix}. \quad (69)$$

Let  $\mathbf{F}_m^d$  and  $\mathbf{M}_m^d$  denote the desired disturbance forces and moments, respectively; the desired generalized acceleration of the moving platform can be described by

$$\ddot{\mathbf{q}}_d = \begin{bmatrix} \Theta_T \\ \Theta_R \end{bmatrix}^{-1} \begin{bmatrix} \mathbf{F}_m^d \\ \mathbf{M}_m^d \end{bmatrix}. \quad (70)$$

Assuming that the generalized velocities and generalized displacements of the moving platform are, respectively, the time integral and time double integral of the generalized acceleration, the following equations can be obtained:

$$\begin{aligned} \dot{\mathbf{q}}_d &= \int \ddot{\mathbf{q}}_d dt, \\ \mathbf{q}_d &= \iint \ddot{\mathbf{q}}_d dt. \end{aligned} \quad (71)$$

Substituting (70) and (71) into (50) yields the desired actuator forces, which are given by

$$\mathbf{F}_d = \mathbf{J}^{-T} [\mathbf{M}(\mathbf{q}_d) \ddot{\mathbf{q}}_d + \mathbf{C}(\mathbf{q}_d, \dot{\mathbf{q}}_d) \dot{\mathbf{q}}_d + \mathbf{K}(\mathbf{q}_d) \mathbf{q}_d]. \quad (72)$$

So far, the relations between the actuator forces and the desired disturbance forces and moments are obtained.

## 4. Numerical Simulation and Analysis

**4.1. Normal Mode Analysis.** It is very important to consider the dynamic characteristics at an earlier design stage, such as the natural frequencies. As described in (48), the whole dynamic equations of the MMVS are developed. The Coriolis and centrifugal force terms as the square terms of velocity may be neglected when the velocity is small. Thus, the free vibration of the MMVS may be described as

$$\mathbf{M}(\mathbf{q}) \ddot{\mathbf{q}} + \mathbf{C}(\mathbf{q}, \dot{\mathbf{q}}) \dot{\mathbf{q}} + \mathbf{K}(\mathbf{q}) \mathbf{q} = \mathbf{0}. \quad (73)$$

It should be noted that the mass matrix  $\mathbf{M}(\mathbf{q})$  is given in a concise matrix form, which considers the impact of the payload decent ration and mass of the actuator. The natural frequencies and mode shapes (or eigenvectors) of the MMVS can be obtained by solving this equation with numerical methods. The structural parameters and mass properties of the MMVS are shown in Tables 1 and 2, respectively.

The finite element method is also adopted to calculate the natural frequencies and mode shapes of the MVVS. The aim here is to compare and cross-check the theoretically obtained results with a totally different method (in this case a NASTRAN® simulation). The reference MVVS modeled in the simulation has exactly the same characteristics as it does in the theoretical model. Table 3 shows a comparison between the six natural frequencies obtained by the analytical equations formulated in this paper and the simulation. The comparison shows an excellent agreement between the results in terms of modal properties.

The mode shapes in the work space directly represent the position and orientation of the moving platform corresponding to each natural frequency. Substituting the design parameters and natural frequencies of the MVVS into (73),

TABLE 1: Structural parameters of the multi-degree-of-freedom micro-vibration simulator.

Notation	Specification	Value
$R_p$	Moving platform radius	0.127 m
$R_b$	Base plane radius	0.18 m
$H$	Height of the origin of the body frame in the base frame	0.22 m
$\varphi$	Moving platform central angle	30°
$\theta$	Base plane central angle	90°
$r_{rci}$	Length from the upper joint to the centroid of the upper leg of the actuator	85.9 mm
$r_{tci}$	Length from the lower joint to the centroid of the lower leg of the actuator	84.8 mm
$z_{cm}$	Height of the centroid of the moving platform in the body frame	27.8 mm
$k$	Axial stiffness of membrane	$1.6 \times 10^4 \text{ N m}^{-1}$

TABLE 2: Mass properties of the multi-degree-of-freedom micro-vibration simulator.

Notation	Specification	Value
$m$	Mass of the moving platform	4.934 kg
$I_{xx}$	Moment of inertia of the moving platform about $x$ -axis	$3.0 \times 10^{-2} \text{ kg m}^2$
$I_{yy}$	Moment of inertia of the moving platform about $y$ -axis	$3.0 \times 10^{-2} \text{ kg m}^2$
$I_{zz}$	Moment of inertia of the moving platform about $z$ -axis	$5.9 \times 10^{-2} \text{ kg m}^2$
$m_{rci}$	Mass of the upper leg of the actuator	0.443 kg
$m_{tci}$	Mass of the lower leg of the actuator	1.797 kg
$I_r^i$	Moment of inertia of the upper leg	$9.0 \times 10^{-4} \text{ kg m}^2$
$I_t^i$	Moment of inertia of the lower leg	$2.3 \times 10^{-3} \text{ kg m}^2$

TABLE 3: Natural frequencies obtained by the developed analytical model and the simulation.

Method	$f_1$ (Hz)	$f_2$ (Hz)	$f_3$ (Hz)	$f_4$ (Hz)	$f_5$ (Hz)	$f_6$ (Hz)
Theoretical	4.79	4.79	7.33	16.43	17.45	17.45
Simulation	4.86	4.86	7.32	15.99	16.73	16.73
Relative error	1.5%	1.5%	0.1%	2.7%	4.3%	4.3%

the modal matrix is obtained using MATLAB and rearranged according to the natural frequencies sequence as described with expression (74). Having normalized the modal matrix, the mode shapes obtained by the theoretical method and the simulation are exactly in correspondence; see Figure 7.

$$\phi = \begin{bmatrix} 1 & 0 & 0 & 0 & 0 & -0.01 \\ 0 & -1 & 0 & 0 & -0.01 & 0 \\ 0 & 0 & 0 & 1 & 0 & 0 \\ 0 & -0.89 & 0 & 0 & -1 & 0 \\ 0.89 & 0 & 0 & 0 & 0 & 1 \\ 0 & 0.02 & 1 & 0 & 0 & 0 \end{bmatrix}. \quad (74)$$

**4.2. Cosimulation Verification.** In this section, a cosimulation using ADAMS and MATLAB/Simulink is adopted to verify the validity of the dynamic model and the feasibility of the MMVS [22, 23]. The control system is constructed in the MATLAB/Simulink environment and the virtual prototype of the MMVS is built in ADAMS. The six actuator forces of the

actuators are used as inputs to drive the ADAMS model and the disturbance forces and moments of the base plane acting on the ground are used as the outputs of the ADAMS plant model. Figure 8 shows the simplified ADAMS model and the cosimulation block diagram. The corresponding Simulink model is shown in Figure 9. The model has seven blocks on the top level. The first, leftmost block is the command generator block which can generate the desired disturbance forces and moments that we design. The second is the configuration parameters block used to assign the structural parameters of the MMVS. The third block is used to assign the actuator parameters, and the third block is used to assign the stiffness coefficient of the membrane, damping coefficient of the single actuator, and the mass properties of payload. The desired actuator forces are obtained from the output of the fifth block which is the MATLAB *Fcn* block including the dynamic equations of the MMVS. The sixth is a subsystem block representing the virtual prototype building in ADAMS. The seventh is used to plot the actual disturbance forces and moments measured by “sensors” in ADAMS.

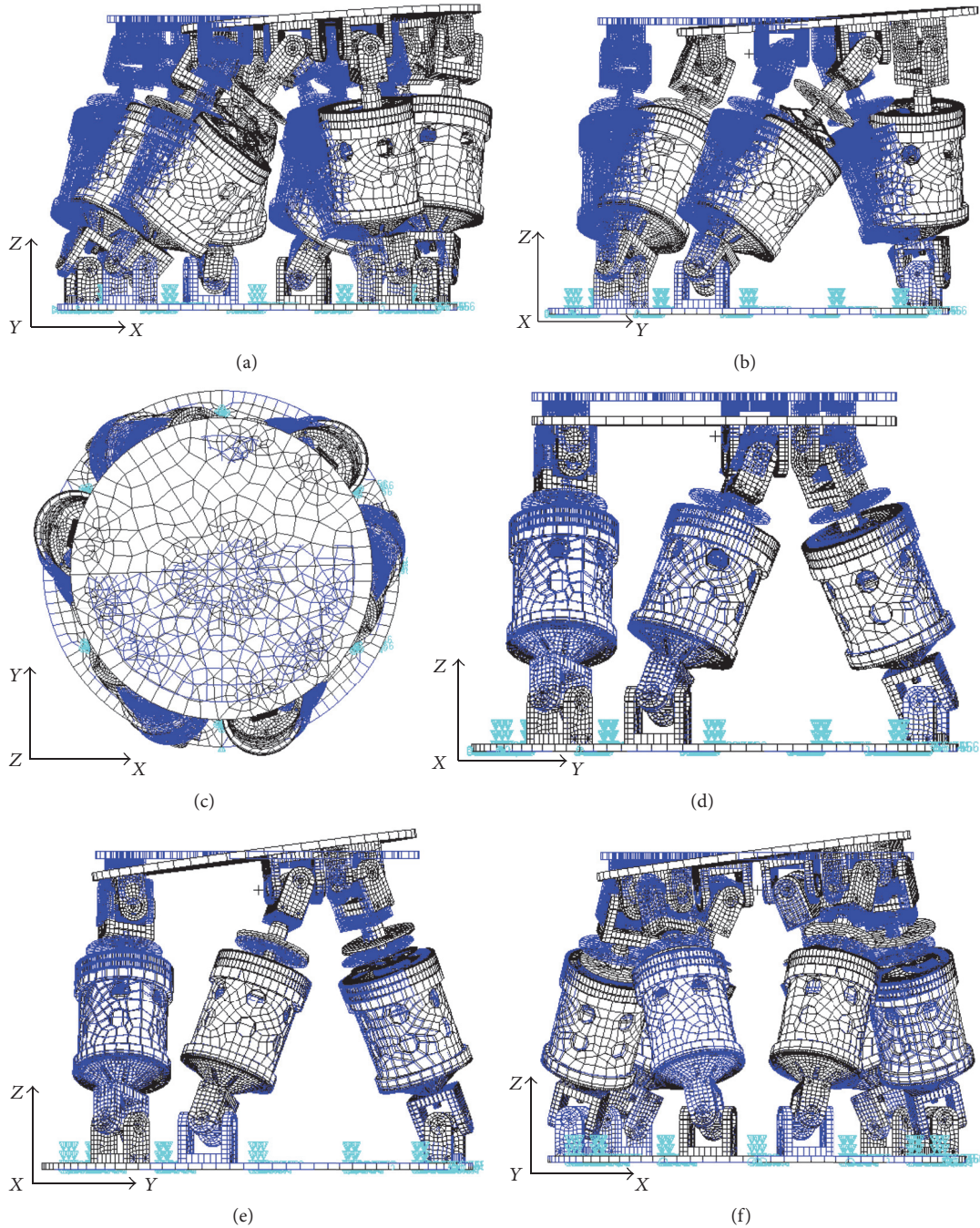


FIGURE 7: The first six mode shapes of the simulator: (a) shearing mode along  $x$  at 4.86 Hz, (b) shearing mode along  $y$  at 4.86 Hz, (c) twisting mode around  $z$  at 7.32 Hz, (d) piston mode along  $z$  at 15.99, (e) tilting mode around  $x$  at 16.73 Hz, and (f) tilting mode around  $y$  at 16.73 Hz.

According to the initial design goal, the MMVS needs to generate the frequency spectrum of the disturbance forces and moments produced by real flight R/MWAs. Table 4 shows the target disturbance forces and moments, which are the experimental data reported in [4].

Figures 10 and 11 show the disturbance forces and moments produced by the MMVS in the time and frequency domains, respectively. From Figure 11, it is clear that the disturbance forces and moments generated by the simulator

are quite consistent with the target MWA disturbance data reported in [4]. Moreover, there is no coupling between the generated disturbance forces and moments. This indicates that the micro-vibration simulator can reproduce the disturbance forces and moments along any arbitrary direction. Table 5 shows the frequency spectrum difference between the MWA disturbance and the simulator disturbance. As shown in Table 4, the frequency components of their disturbance forces and moments are identical. The greatest differences

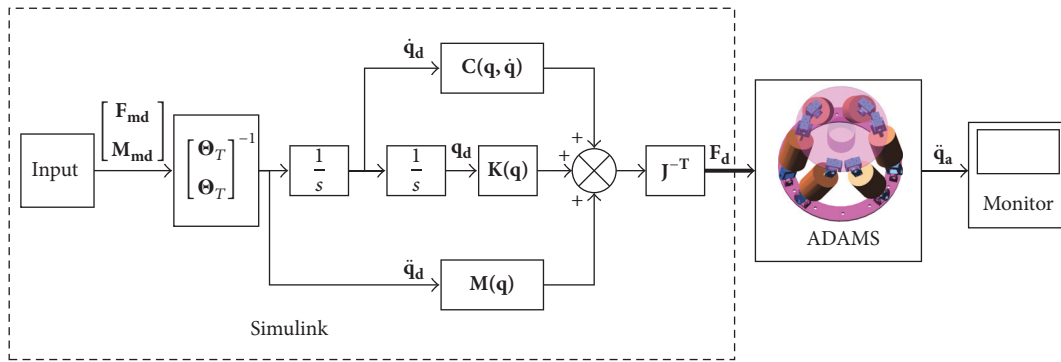


FIGURE 8: Cosimulation block diagram.

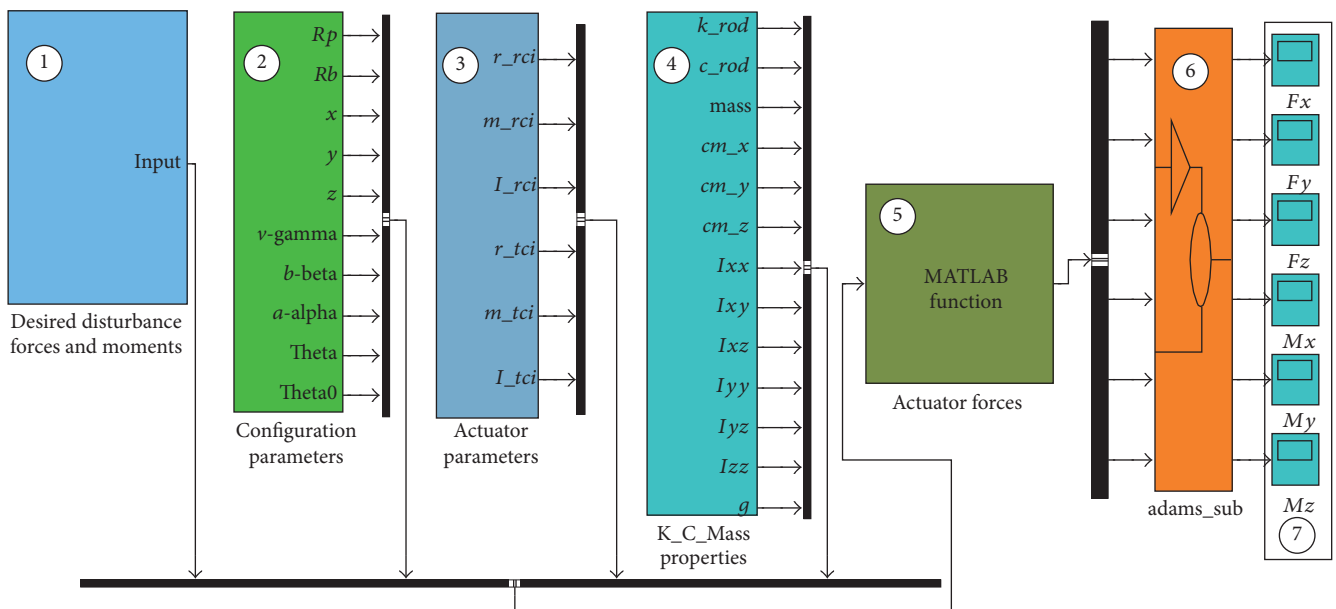


FIGURE 9: Simulink model of cosimulation of the MMVS.

TABLE 4: Target disturbance forces and moments.

Frequency (Hz)	$F_x$ (N)	$F_y$ (N)	$F_z$ (N)	$M_x$ (N·m)	$M_y$ (N·m)	$M_z$ (N·m)
50	0.1	0.1	0	0.05	0.05	0
100	0.2	0.5	0	0.15	0.15	0
200	0.2	0.2	1.2	0.05	0.05	0
250	1.8	1.8	3.2	0.4	0.38	0.05

TABLE 5: Frequency spectrum difference between MWA disturbance and simulator disturbance.

Frequency (Hz)	Difference (%)					
	$F_x$	$F_y$	$F_z$	$M_x$	$M_y$	$M_z$
50 Hz	3.20	4.19	0.00	2.56	4.42	0.00
100 Hz	1.25	0.08	0.00	3.67	2.73	0.00
200 Hz	0.35	0.40	0.58	7.30	2.42	0.00
250 Hz	0.44	0.50	0.44	7.50	3.29	1.68

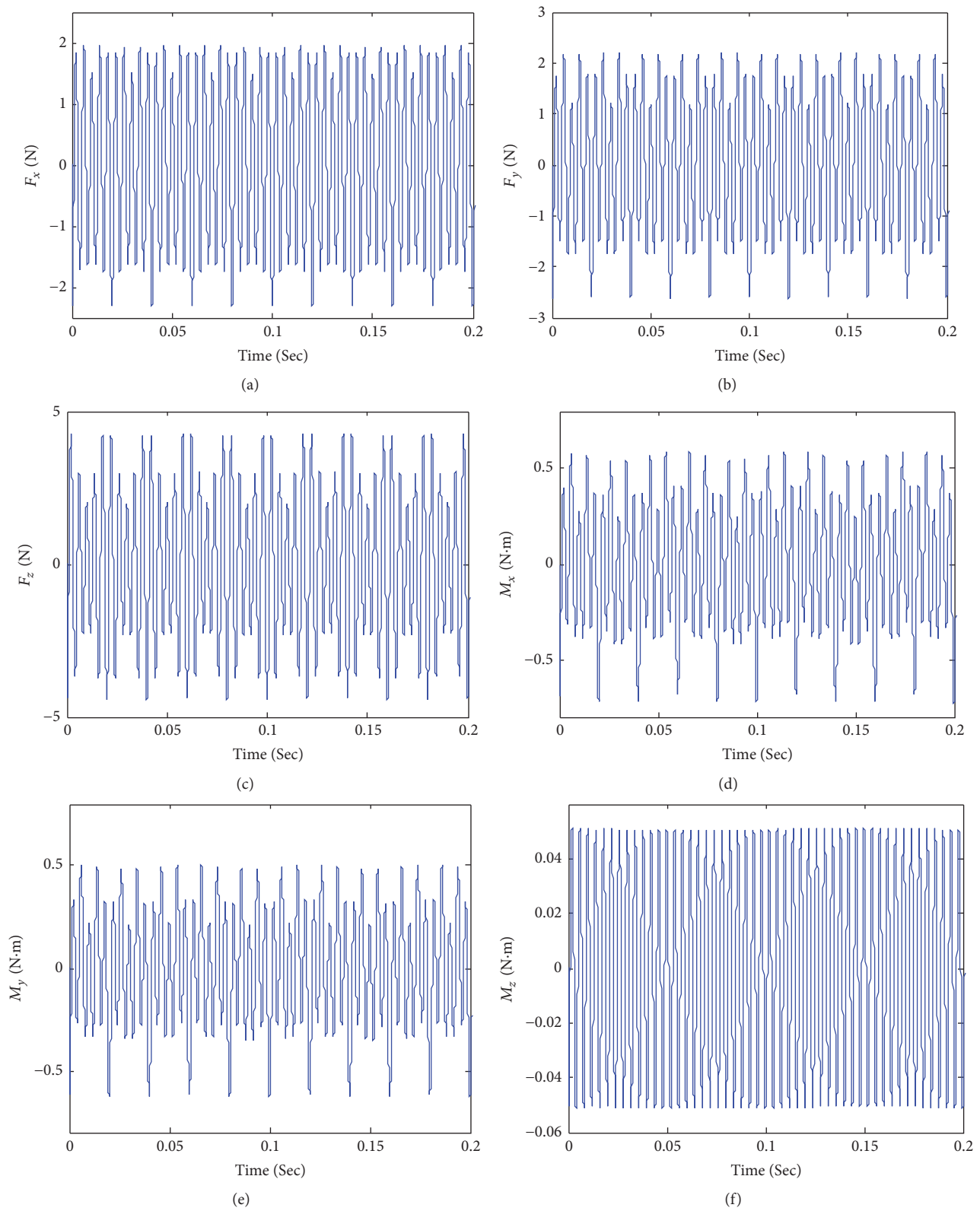


FIGURE 10: Disturbance forces and moments in the time domain: (a) disturbance forces along the  $x$ -axis, (b) disturbance forces along the  $y$ -axis, (c) disturbance forces along the  $z$ -axis, (d) disturbance moments around the  $x$ -axis, (e) disturbance moments around the  $y$ -axis, and (f) disturbance moments around the  $z$ -axis.

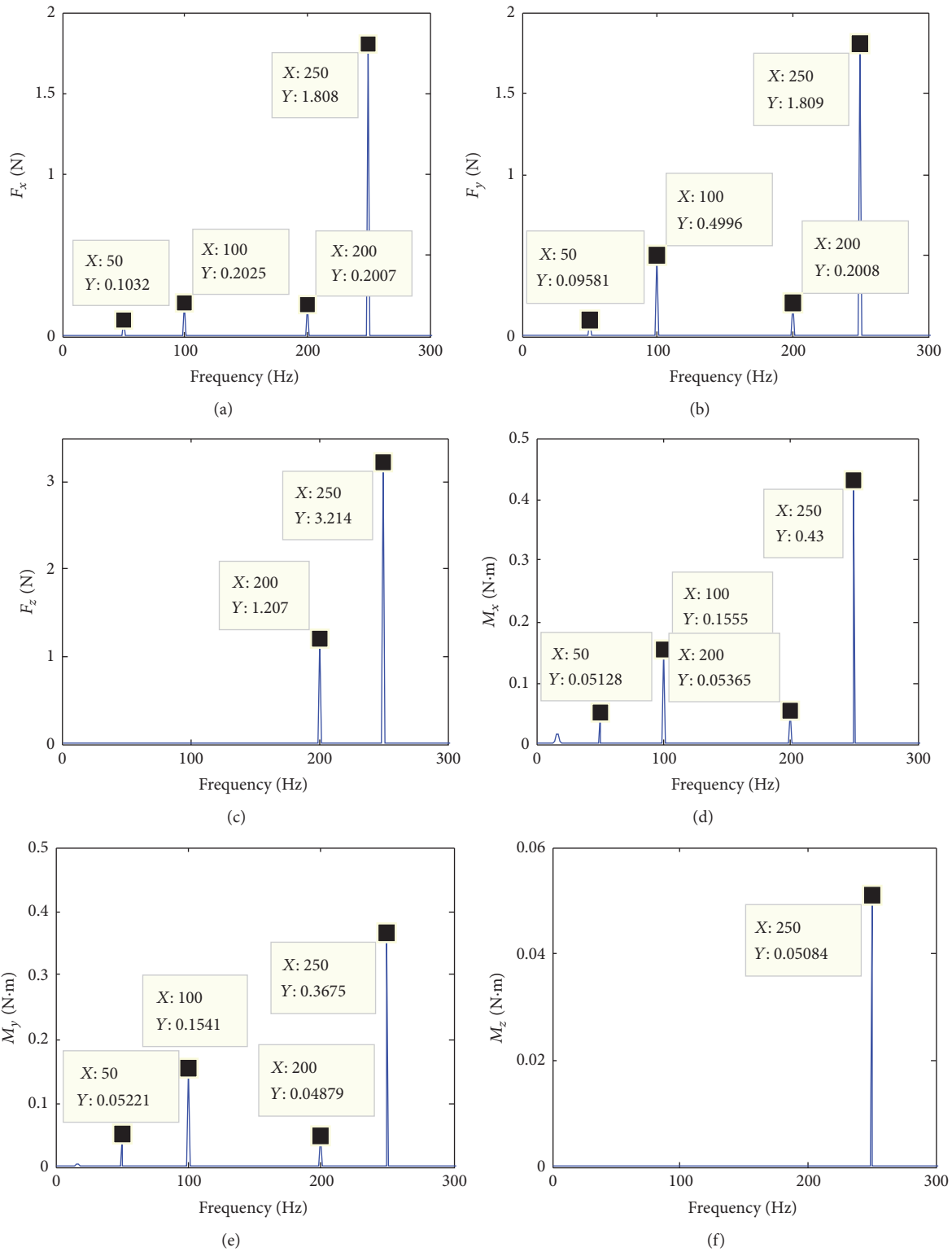


FIGURE 11: Disturbance forces and moments in the frequency domain: (a) disturbance forces along the x-axis, (b) disturbance forces along the y-axis, (c) disturbance forces along the z-axis, (d) disturbance moments around the x-axis, (e) disturbance moments around the y-axis, and (f) disturbance moments around the z-axis.

in the disturbance force amplitude and the disturbance moment amplitude are 4.19% and 7.5%, respectively. The smallest differences in the disturbance force amplitude and the disturbance moment amplitude are 0.08% and 1.68%, respectively.

## 5. Conclusions

In this study, a multi-degree-of-freedom micro-vibration simulator (MMVS) based on the Gough-Stewart platform, which can generate the disturbance frequency spectrum of a real flight reaction/momentum wheel assemblies (R/MWAs), is proposed. The complete inverse kinematic and dynamic equations of the simulator were derived using the Newton-Euler method and Lagrange approach. These kinematic and dynamic models were proved to be valid. By approximation of a feasible model, a disturbance planning method to calculate the excitation forces of the actuators was deduced. To verify the feasibility of this micro-vibration simulator, cosimulation was adopted. The simulation results show that the simulator induced disturbances were almost identical to those of a real flight R/MWAs, and there was no coupling between the disturbance forces and moments.

In this study, valuable findings for a micro-vibration simulator of the R/MWAs were obtained. However, the dynamic models of the simulator were derived based on considering the simulator as a rigid system. In future studies, the structure resonance caused by flexing will be taken into account while planning the excitation forces of the actuators.

## Conflicts of Interest

The authors declare that they have no conflicts of interest.

## Acknowledgments

This work was supported by the National Natural Science Foundation of China under Grant no. 11672290, the Jilin Scientific and Technological Development Program under Grant no. 20160520074JH, and the Youth Innovation Promotion Association, Chinese Academy of Sciences under Grant no. 2014195.

## References

- [1] W.-Y. Zhou and D.-X. Li, "Design and analysis of an intelligent vibration isolation platform for reaction/momentum wheel assemblies," *Journal of Sound and Vibration*, vol. 331, no. 13, pp. 2984–3005, 2012.
- [2] R. A. Masterson, D. W. Miller, and R. L. Grogan, "Development and validation of reaction wheel disturbance models: Empirical model," *Journal of Sound and Vibration*, vol. 249, no. 3, pp. 575–598, 2002.
- [3] K.-C. Liu, P. Maghami, and C. Blaurock, "Reaction wheel disturbance modeling, jitter analysis, and validation tests for solar dynamics observatory," in *Proceedings of the AIAA Guidance, Navigation and Control Conference and Exhibit*, August 2008.
- [4] W. Zhou, D. Li, Q. Luo, and K. Liu, "Analysis and testing of microvibrations produced by momentum wheel assemblies," *Chinese Journal of Aeronautics*, vol. 25, no. 4, pp. 640–649, 2012.
- [5] D.-K. Kim, "Micro-vibration model and parameter estimation method of a reaction wheel assembly," *Journal of Sound and Vibration*, vol. 333, no. 18, pp. 4214–4231, 2014.
- [6] C. Liu, X. Jing, S. Daley, and F. Li, "Recent advances in micro-vibration isolation," *Mechanical Systems and Signal Processing*, vol. 56, no. 1, pp. 55–80, 2015.
- [7] W.-Y. Zhou, D.-X. Li, Q. Luo, and J.-P. Jiang, "Design and test of a soft suspension system for cantilevered momentum wheel assembly," *Proceedings of the Institution of Mechanical Engineers, Part G: Journal of Aerospace Engineering*, vol. 227, no. 7, pp. 1144–1160, 2013.
- [8] W. Zhou and D. Li, "Experimental research on a vibration isolation platform for momentum wheel assembly," *Journal of Sound and Vibration*, vol. 332, no. 5, pp. 1157–1171, 2013.
- [9] D. Kamesh, R. Pandiyan, and A. Ghosal, "Modeling, design and analysis of low frequency platform for attenuating micro-vibration in spacecraft," *Journal of Sound and Vibration*, vol. 329, no. 17, pp. 3431–3450, 2010.
- [10] D. Kamesh, R. Pandiyan, and A. Ghosal, "Passive vibration isolation of reaction wheel disturbances using a low frequency flexible space platform," *Journal of Sound & Vibration*, vol. 331, no. 6, pp. 1310–1330, 2012.
- [11] I. Hostens, J. Anthonis, and P. Kennes, "Six-degrees-of-freedom test rig design for simulation of mobile agricultural machinery vibrations," *Journal of Agricultural Engineering Research*, vol. 77, no. 2, pp. 155–169, 2000.
- [12] I. Hostens, J. Anthonis, and H. Ramon, "New design for a 6 dof vibration simulator with improved reliability and performance," *Mechanical Systems and Signal Processing*, vol. 19, no. 1, pp. 105–122, 2005.
- [13] B. Dasgupta and T. S. Mruthyunjaya, "The Stewart platform manipulator: a review," *Mechanism and Machine Theory*, vol. 35, no. 1, pp. 15–40, 2000.
- [14] R. Oftadeh, M. M. Aref, and H. D. Taghirad, "Explicit dynamics formulation of Stewart-Gough platform: a Newton-Euler approach," in *Proceedings of the 23rd IEEE/RSJ 2010 International Conference on Intelligent Robots and Systems, IROS 2010*, pp. 2772–2777, October 2010.
- [15] B. Dasgupta and T. S. Mruthyunjaya, "A Newton-Euler formulation for the inverse dynamics of the Stewart platform manipulator," *Mechanism and Machine Theory*, vol. 33, no. 8, pp. 1135–1152, 1998.
- [16] S. Pedrammehr, M. Mahboubkhah, and N. Khani, "Improved dynamic equations for the generally configured Stewart platform manipulator," *Journal of Mechanical Science and Technology*, vol. 26, no. 3, pp. 711–721, 2012.
- [17] B. Dasgupta and T. S. Mruthyunjaya, "Closed-form dynamic equations of the general Stewart platform through the Newton-Euler approach," *Mechanism and Machine Theory*, vol. 33, no. 7, pp. 993–1012, 1998.
- [18] S. Staicu, "Dynamics of the 6-6 Stewart parallel manipulator," *Robotics and Computer-Integrated Manufacturing*, vol. 27, no. 1, pp. 212–220, 2011.
- [19] Z.-F. Shao, X. Tang, X. Chen, and L.-P. Wang, "Research on the inertia matching of the Stewart parallel manipulator," *Robotics and Computer-Integrated Manufacturing*, vol. 28, no. 6, pp. 649–659, 2012.

- [20] T. Tian, H. Jiang, Z. Tong, J. He, and Q. Huang, "An inertial parameter identification method of eliminating system damping effect for a six-degree-of-freedom parallel manipulator," *Chinese Journal of Aeronautics*, vol. 28, no. 2, article 418, pp. 582–592, 2015.
- [21] G. Park, D.-O. Lee, and J.-H. Han, "Development of multi-degree-of-freedom microvibration emulator for efficient jitter test of spacecraft," *Journal of Intelligent Material Systems and Structures*, vol. 25, no. 9, pp. 1069–1081, 2014.
- [22] Y. Yun and Y. Li, "A general dynamics and control model of a class of multi-DOF manipulators for active vibration control," *Mechanism and Machine Theory*, vol. 46, no. 10, pp. 1549–1574, 2011.
- [23] K.-C. Lee, D.-K. Hong, Y.-H. Jeong, C.-Y. Kim, and M.-C. Lee, "Dynamic simulation of radial active magnetic bearing system for high speed rotor using ADAMS and MATLAB co-simulation," in *Proceedings of the 2012 IEEE International Conference on Automation Science and Engineering: Green Automation Toward a Sustainable Society, CASE 2012*, pp. 880–885, August 2012.

## Research Article

# Sensitivity Analysis of a CPAM Inverse Algorithm for Composite Laminates Characterization

**Farshid Masoumi and Ahmad Ghasemi Ghalebahman**

*Department of Mechanical Engineering, Semnan University, Semnan 35131 19111, Iran*

Correspondence should be addressed to Ahmad Ghasemi Ghalebahman; ghasemi@semnan.ac.ir

Received 12 April 2017; Accepted 28 May 2017; Published 10 July 2017

Academic Editor: Naveed Ahmad

Copyright © 2017 Farshid Masoumi and Ahmad Ghasemi Ghalebahman. This is an open access article distributed under the Creative Commons Attribution License, which permits unrestricted use, distribution, and reproduction in any medium, provided the original work is properly cited.

Using experimental data and numerical simulations, a new combined technique is presented for characterization of thin and thick orthotropic composite laminates. Four or five elastic constants, as well as ply orientation angles, are considered as the unknown parameters. The material characterization is first examined for isotropic plates under different boundary conditions to evaluate the method's accuracy. The proposed algorithm, so-called CPAM (Combined Programs of ABAQUS and MATLAB), utilizes an optimization procedure and makes simultaneous use of vibration test data together with their corresponding numerical solutions. The numerical solutions are based on a commercial finite element package for efficiently identifying the material properties. An inverse method based on particle swarm optimization algorithm is further provided using MATLAB software. The error function to be minimized is the sum of squared differences between experimental and simulated data of eigenfrequencies. To evaluate the robustness of the model's results in the presence of uncertainty and unwanted noises, a sensitivity analysis that employs Gaussian disorder model is directly applied to the measured frequencies. The results with high accuracy confirm the validity and capability of the present method in simultaneous determination of mechanical constants and fiber orientation angles of composite laminates as compared to prior methods.

## 1. Introduction

In many engineering applications, such as design or quality control of advanced composite structural systems, it is particularly important to have correct understanding of mechanical constants of composites [1]. It is more complicated to determine the mechanical constants of fiber-reinforced polymer composites than to determine those of homogenous and isotropic materials, because, in such materials, which may include a variety of constituent materials mixed together, the number of elastic constants is increased and also some additional complexity due to their nonhomogenous nature may occur. When static test methods such as simple tensile test are used for composites, they will be faced with some problems. Special problems such as effects of supports, dependence on samples size, and nonuniform fields of stress-strain in the experiments usually cause a wide scatter and unwanted errors in the test results. In addition, the destructive nature of these tests and inability to repeat the test for a specific sample are

other disadvantages of conventional experimental methods for determining the material properties. Thus, a powerful and useful technique that is able to be utilized for characterizing the real structures needs to be introduced. To resolve aforementioned problems, among previously proposed methods, the nondestructive evaluations of material parameters based on inverse computational techniques look promising for composite materials [2].

In the inverse computational methods, there are complex relationships between material properties and structural behavior which allow us to characterize the material properties of composites. These relationships are usually represented by a typical computational and mathematical model known as direct simulated solution. In the direct problem, measurable data are determined from model parameters. So, if there is a certain set of measured experimental data for evolution of structural behavior, the composite plates' properties can be determined by solving an inverse problem [3]. But, in general, it cannot be measured exactly and the measured data are often

diverted from real measurable quantities. This deviation can be as small as rounding error that is created by computer estimations. In fact, the deviation can be completely innate in measuring process, which means it is due to existing errors in the measurement process. So, data from model parameters are obtained without any errors in the direct process but, in general, data are in the deviated form.

Extraction of natural frequencies through modal analysis has been considered as experimental data in the inverse methods. Literature reveals that, in order to investigate the stability of solution to small changes imported to the experimental data, a sensitivity analysis needs to be applied accompanied with the various inverse methods proposed for determination of parameters of composite plates. When laminated composites are designed, design variables for a specific kind of material are fibers directions, number of layers, and thickness of each layer. Because of restrictions on the manufacture and use of these composite plates, choosing of fibers direction is usually limited to a set of definite discrete values and also layers' thickness is specific [4]. Moreover, among the various factors, stacking sequence of layers is one of the most important parameters that can increase structures' resistance to the damage caused by different loads. The orientation of the fibers in layers highly affects the mechanical strength of laminated composites, so identification of the stacking sequence of layers for theoretical research and practical applications seems worthy [5]. Sepahvand and Marburg [6] attempted to determine elastic constants of orthotropic plates by expansion of Polynomial Chaos theory and also experimental data resulting from modal analysis. Parameters of their model are obtained by expansion of generalized Polynomial Chaos and the corresponding unknown constants are calculated using inverse stochastic problem. Ip et al. [7] determined elastic constants of cylindrical orthotropic shells by using Bayesian estimation based on natural frequencies obtained from a model with free boundary conditions. Their model is formulated by using Rayleigh-Ritz method that is based on the characteristic functions of the beam. Then they succeeded to realize the high dependence of circumferential wave pattern of vibrational mode and in-plane shear modulus on the natural frequencies of cylindrical shells. To simplify the modeling process and reduce the complexity of numerical modeling, Hwang and Chang [8] used an FEM model with an optimization process to determine just elastic constants of thin and thick composite laminates and also aluminum plates. Deobald and Gibson [9] determined four independent elastic constants of thin orthotropic plates. The Classical Lamination Theory and three-mode Rayleigh formulation optimized with objective function of sum of square difference of experimental and numerical frequencies are used in their work. Liu et al. [10] used an advanced neural network algorithm as optimization algorithm in their proposed inverse method to determine nonhomogenous properties of composite laminates. They used displacement response of surfaces due to linear loading as experimental data and Hybrid Numerical Method (HNM) as direct solution for evaluating the dynamic response of surfaces. Finally, by applying three disorder levels of 1, 3, and 10 percent to the measured experimental data, they could use these simulated

data to evaluate the amount of solution stability. Mohan Rao and Arvind [11], in their first case study, determined stacking sequence of the layers of hybrid laminated composite panels in order to maximize critical buckling load under thermal loading using a metaheuristic optimization algorithm known as scatter search. They used a same algorithm in order to determine stacking sequence of the multilayer plates in their second case study and minimize the weight and manufacturing cost of these plates by considering constraints on the buckling load and the first natural frequency.

As it is evident from the literature, simultaneous identification of mechanical constants and stacking sequence of composite plates has not been reported and the presented study tries to perform this task. In the present study, natural frequencies extracted from vibration analysis of structure are considered as experimental results. Accuracy of the obtained results by inverse method depends commonly on some issues like sufficient accuracy of the method used in vibration analysis and solution of eigenproblem. In this study, the commercial FEM code of ABAQUS is used for vibration modeling and calculation of natural frequencies of thin and thick homogenous and orthotropic plates. In order to determine four elastic constants and stacking sequence of such composite plates by inverse method, the PSO algorithm in MATLAB software is employed. The sum of squared difference of experimental and numerical frequencies is used as the objective function. By linking MATLAB software and ABAQUS software, it is possible to perform this alternating optimization process. In order to apply sensitivity analysis, the Gaussian noise is added directly to the (simulated) measured frequencies and then robustness of the proposed inverse method to the unwanted disorders is evaluated. Outcomes show that the proposed inverse method is properly stable towards adding noise. Results obtained from the present method are validated by comparing those obtained from other previously proposed methods.

## 2. Vibration Analysis of the Composite Plates (Direct Solution)

A modeling method which assumes that the structural properties of the material are known and consequently predicts the physical behavior of the structure through them is usually referred to as direct modeling or forward solution [3]. As an example, for a transversely isotropic composite plate, direct modeling of a vibration problem can consist of a model which is able to provide natural frequencies and mode shapes of a two-dimensional thin composite plate with four independent elastic constants and also arbitrary fiber orientation angle for each layer. For this purpose, an available commercial finite element code can be used for undamped free vibration modeling of the plate.

In the present study, natural frequencies and modes shapes of the considered composite plates have been extracted using modal analysis in ABAQUS software (version 6.12-1). All models are meshed by eight-node plate element (S8R element) with six degrees of freedom for each node. This element can be used for both thin and thick composite plates

and also can be utilized for homogenous and orthotropic materials [13].

### 3. Optimization Design Based on PSO Algorithm

The problem of determining the parameters of composite plates by inverse method can be discussed as an optimization problem. One of the most powerful algorithms that get noticed by researchers is PSO algorithm [14, 15]. In this algorithm, each design variable of the population that is known as particle possesses a velocity that enables it to move through the problem space and is replaced instead of crossover and mutation of other population-based algorithms (which search more than one initial solution of the search space for design variables) like genetic algorithms [14]. Velocity can be defined by a vector in the problem space. So, each particle is characterized by a location (solution) and velocity. Relocation of a particle is done by means of the present location of the particle and its velocity. It means that resultant of the current location (solution) and velocity vector denotes the location of each particle in the next iteration. Each particle maintains its current location, velocity, and a memory of its previous best location, as well as the global best location of the entire swarm that all particles have achieved so far at each iteration. The velocity vector and displacement of each particle in the next iteration can be estimated, respectively, through the following relations:

$$v_i^{n+1} = wv_i^n + c_1r_1(p_i^n - x_i^n) + c_2r_2(p_g^n - x_i^n) \quad (1)$$

$$x_i^{n+1} = x_i^n + v_i^{n+1}, \quad (2)$$

where  $w$  is the inertia weight,  $c_1$  and  $c_2$  are positive constants whose names are social and self-cognitive parameters, respectively, and  $i = 1, 2, \dots, m$  in which  $m$  is the population size.  $r_1$  and  $r_2$  are uniformly distributed random values within  $[0, 1]$ , and  $n = 1, 2, \dots, N$  indicates the repetition number and  $N$  is the maximum allowable iteration. The first right-hand term in (1) is previous velocity of the particle which enables it to move through the problem space. The second and third terms show the velocity difference based on the best solution of each particle and the best solution of all particles, respectively [15]. Obviously, the greater social parameter value of the particle is, the more velocity vector approaches the best answer of all particles and also the greater self-cognitive parameter is, the more velocity vector approaches the best answer that the particle has experienced. In general, PSO algorithm can be summarized in three phases: evaluation, comparison, and imitation. Evaluation phase measures desirability of each particle error. Comparison phase determines the best particle among all particles and, in the imitation phase, the new location of the particles based on knowledge that has been obtained until now is determined. These three phases are allowed to continue until the end-up condition is satisfied. The ultimate goal is to find the particle that has the best answer for investigation problem.

FPSO (Fuzzy-Particle Swarm Optimization) is another type of PSO algorithm for identification of discrete parameters. In this case, the set of location vectors can be expressed in a fuzzy matrix where its elements represent fuzzy logic membership functions. How to use this algorithm for job scheduling problem is briefly explained here.  $J = \{J_1, J_2, \dots, J_n\}$  is assumed to be a set of jobs that must be processed on a set of machines  $M = \{M_1, M_2, \dots, M_m\}$ . All jobs of set  $J$  must be carried out and so the total cost of jobs is minimized.

In FPSO algorithm, the relations between jobs and machines can be defined in a matrix form as

$$X = \begin{bmatrix} x_{11} & x_{12} & \cdots & x_{1n} \\ x_{21} & x_{22} & \cdots & x_{2n} \\ \vdots & \vdots & \ddots & \vdots \\ x_{m1} & x_{m2} & \cdots & x_{mn} \end{bmatrix}_{m \times n}, \quad (3)$$

where  $x_{ij}$  is fuzzy logic and represents dependency of  $J_j$  on  $M_i$ . So, amount of elements of matrix  $X$  must be in range  $[0, 1]$ . In another view,  $x_{ij}$  shows the possibility that  $M_i$  carries out job  $J_j$ . In other words, sum of each column's elements of the matrix must be equal to 1. In a similar way, the velocity matrix can be defined as

$$V = \begin{bmatrix} v_{11} & v_{12} & \cdots & v_{1n} \\ v_{21} & v_{22} & \cdots & v_{2n} \\ \vdots & \vdots & \ddots & \vdots \\ v_{m1} & v_{m2} & \cdots & v_{mn} \end{bmatrix}_{m \times n}. \quad (4)$$

Equations (1) and (2) can be rewritten for FPSO algorithm as

$$V_i^{n+1} = wV_i^n + c_1R_1 \otimes (P_i^n - X_i^n) + c_2R_2 \otimes (P_g^n - X_i^n) \quad (5)$$

$$X_i^{n+1} = X_i^n + V_i^{n+1},$$

where  $R_1$  and  $R_2$  are of  $m \times n$  order matrix and their elements are uniformly distributed random variables in range  $[0, 1]$ . Operator  $\otimes$  multiplies the corresponding elements of matrixes together. There is not any changes in other variables. According to the constraints on the elements of matrix  $X$ , the illegal values of  $X$  that may be generated after updating the fuzzy matrix must be modified. To this end, first, all elements of matrix  $X$  must be positive. So, the negative elements generated in matrix  $X$  are intentionally set to zero. Second, sum of each column's elements must be equal to 1. So each element of this matrix must be divided to the sum of its column elements.

### 4. Definition of the Optimization Problem

Design variables considered in this study are four independent elastic constants of thin transversely isotropic plates and also fiber orientation angles. These constants are  $E_1, E_2, \nu_{12}, G_{12}$  which represent Young's modulus parallel and

perpendicular to the fiber orientation, in-plane Poisson's ratio, and the shear modulus, respectively. Constants  $G_{13}$ ,  $G_{23}$  are required for FE modeling in ABAQUS, which can be defined by the following equations for transversely isotropic material system [15]:

$$\begin{aligned} G_{12} &= G_{13}, \\ G_{23} &= \frac{E_2}{2(1 + \nu_{23})}; \\ \nu_{23} &= \frac{\nu_{12}(1 - \nu_{12}E_2/E_1)}{1 - \nu_{12}}. \end{aligned} \quad (6)$$

For thick plates,  $G_{23}$  is conceded as fifth independent constant and (6) should not be used to evaluate this constant. The objective function that must be minimized by the optimization algorithm is defined as

$$F = \sum_{i=1}^6 (\bar{\omega}_i - \omega_i)^2, \quad (7)$$

where  $\bar{\omega}_i$  represent the measured experimental frequencies and  $\omega_i$  are the corresponding frequencies calculated from the numerical solution. The search space that stands between upper and lower bounds of elastic constants is represented as

$$\begin{aligned} 10 < E_1 \text{ (GPa)} < 200 \\ 5 < E_2 \text{ (GPa)} < 40 \\ 5 < G_{12} \text{ (GPa)} < 30 \\ 0.15 < \nu_{12} < 0.4 \\ 2 < G_{23} \text{ (GPa)} < 30 \quad (\text{for thick plates}). \end{aligned} \quad (8)$$

It is to be noted that the stiffness matrix (constitutive relationships between stress and strain components) must be positive definite. Therefore, there are some relations between elastic constants of the composite material. These relations are defined as the following constraints for the algorithm [12]:

$$\begin{aligned} & [1 - (\nu_{23})^2] \left[ 1 - \nu_{12}^2 \frac{E_2}{E_1} \right] \\ & - \left[ \nu_{12} \frac{E_2}{E_1} \sqrt{\frac{E_1}{E_2}} + \nu_{12} \nu_{23} \sqrt{\frac{E_2}{E_1}} \right]^2 > 0, \\ & \left| \frac{\nu_{12}(1 - \nu_{12}(E_2/E_1))}{1 - \nu_{12}} \right| < 1, \\ & |\nu_{12}| < \sqrt{\frac{E_1}{E_2}}, \\ & \frac{E_1}{E_2} > 1. \end{aligned} \quad (9)$$

As it is mentioned, fibers' orientation is limited to some definite values; so they are considered as discrete parameters

in this study. The fiber orientation angles between which the algorithm is allowed to search are given in the following equation:

$$[0, \pm 5, \pm 10, \pm 15, \dots, \pm 75, \pm 80, \pm 85, 90]. \quad (10)$$

## 5. Settings for Optimization Algorithm

**5.1. Initial Population.** For generating the initial starting particles, the first value of  $E_2$  is randomly generated within the specified constraints. Since range of  $E_1$  is wider than  $E_2$  and according to the fourth constraint of (9),  $E_1$  should be larger than  $E_2$ ; its value is randomly generated between  $E_2$  and the upper limit of  $E_1$ . In order to determine the reasonable amount of  $\nu_{12}$ , according to the third constraint, it is also randomly determined within interval  $[-\sqrt{E_1/E_2}, \sqrt{E_1/E_2}]$ . Because there is not any constraint for orientation of fibers' angles, the initial population of them is created randomly.

**5.2. Evaluation of Solution and Error Analysis.** According to initial solution of particles which has been generated within the feasible region of the third and fourth constraints, it is not necessary to check satisfaction of these two constraints in the initial evaluation. But because there is no guarantee that they remain valid in the next iterations, feasibility of them must be also checked alongside the two other constraints in the evaluation process. Then if any constraint is violated, error of solutions will accept a great value and thus the corresponding particle will be penalized. But if the solution is reasonable, it will be sent to ABAQUS solver for proceeding the calculations. Sum of squared deviation of outputs from the target values is shown as error of the desired solution.

## 6. Employing the Inverse Method for Determination of Parameters

For determination of parameters, it is essential that the direct modeling explained in the previous sections be linked with code written in MATLAB for optimization algorithm. In other words, there must be an ability to make a linking bridge between ABAQUS and MATLAB software in order to call both frequencies provided by ABAQUS in MATLAB and also parameters provided by MATLAB in ABAQUS. This alternating process is therefore repeated between ABAQUS and MATLAB software until the error function defined in (7) is minimized. In the following, how ABAQUS and MATLAB software work is explained. To have better perception of the optimization procedure, the inverse solution algorithm is explained here step by step, and its corresponding flowchart is represented in Figure 1; it does not necessarily mean the time priority of these steps' operation during performing the algorithm.

In Step 1, parameters are generated by code written in MATLAB software. In Step 2, a text file is created by this code and these generated parameters are saved in this file according to commands written in this code. In Step 3, ABAQUS software is run (without GUI) by python language that is explained in the next step (Step 4). Commands required for operating of this step are also utilized in code

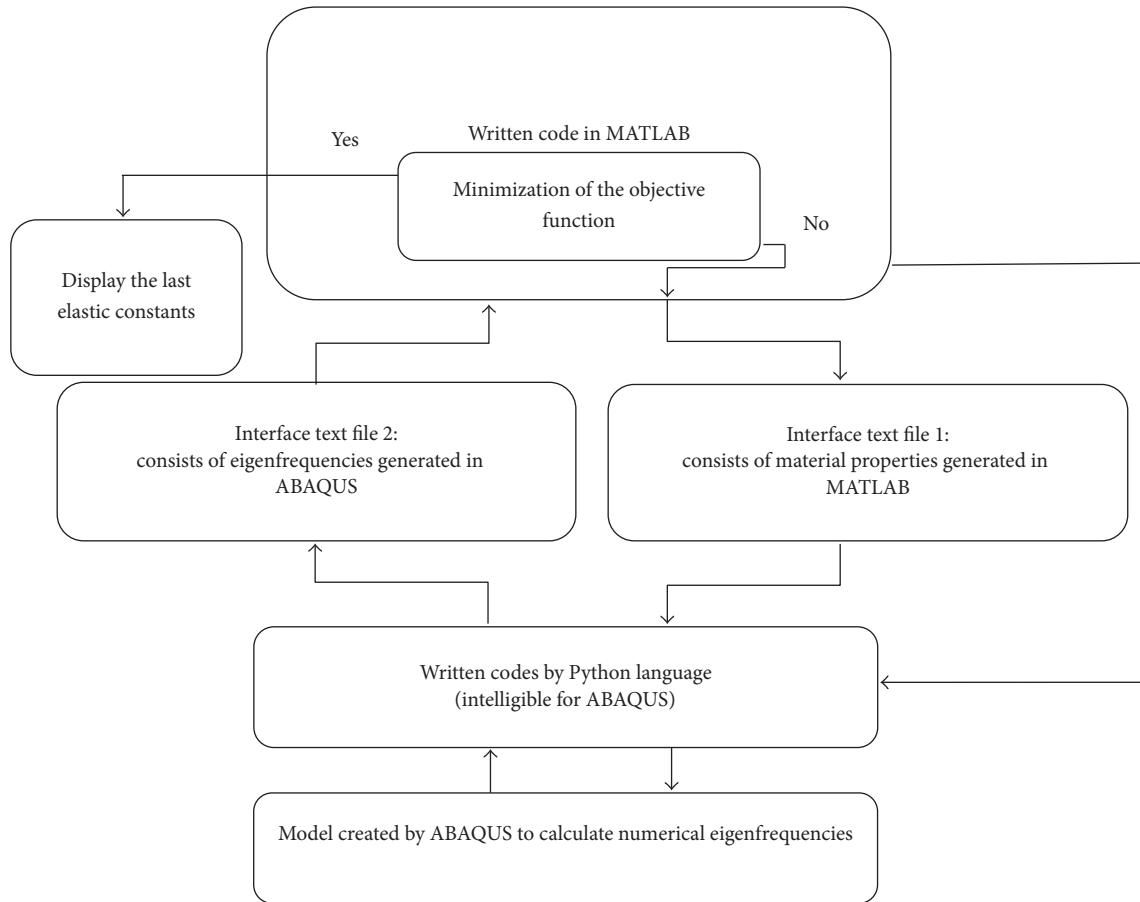


FIGURE 1: Flowchart of the CPAM inverse solver algorithm.

written by MATLAB software. In Step 4, a python code that is intelligible for ABAQUS is written beforehand for ABAQUS software. The required commands for calling parameters in the text file of Step 2, importing them into ABAQUS, getting the natural frequencies generated by the model in ABAQUS, creating another text file, and finally saving these frequencies in this file, are written in this code. In Step 5, the model that is previously created in ABAQUS to determine the natural frequencies of plates is run. In Step 6, the code that is written by python language calls natural frequencies that are obtained by the model created in ABAQUS in the previous step. In Step 7, the code that is written by python programming language saves frequencies called by ABAQUS (previous stage) in a second interface text file. In Step 8, the code that is written in MATLAB calls frequencies saved in the second interface text file and then the error function in (7) is checked. Whenever this error function is minimized in every iteration of this alternating process, the process will be stopped and the corresponding parameters that generate these frequencies and make the error function be minimized are chosen as the set of optimal solutions; otherwise, this process will continue unless the error function is minimized. So, this algorithm that is capable of linking PSO algorithm in MATLAB to the model in ABAQUS is briefly called CPAM.

## 7. Result and Discussion

**7.1. Validation of FEM Modeling.** Due to use of natural frequencies calculated from numerical solution in objective function and the importance of their accuracy in determination of the parameters, first it is necessary to be sure of accuracy of direct solution for providing desired natural frequencies that are obtained by modeling in ABAQUS software. In order to validate the FEM modeling, an aluminum plate has been considered and its first six natural frequencies have been compared with those obtained by Rayleigh-Ritz method presented by Deobald and Gibson [9]. Hwang and Chang [8] have extracted them again to validate their FEM modeling in ANSYS software. Dimensions of the considered square aluminum plate are  $25.4 \text{ cm} \times 25.4 \text{ cm} \times 0.316 \text{ cm}$ , density is  $2.77 \text{ gr/cm}^3$ , Young's modulus is  $72.4 \text{ GPa}$ , shear modulus is  $28 \text{ GPa}$ , and Poisson's ratio is  $0.33$ . In order to match mesh size of this plate with the mesh size reported in [8, 9], the  $10 \times 10$  in-plane mesh sizes that totally give 100 elements are considered for the plate. Natural frequencies obtained from modal analysis and impact technique [9] are shown in Table 1. In addition, natural frequencies obtained by Rayleigh-Ritz method [9] are also displayed in this table in comparison with those extracted by ANSYS [8] and ABAQUS solvers,

TABLE 1: Natural frequencies (Hz) of the aluminum plate.

Frequencies	$f_1$	$f_2$	$f_3$	$f_4$	$f_5$	$f_6$
Experimental [9]	156.7	232.5	300.4	411.7	411.7	744.9
ABAQUS soft	160.0	233.1	297.3	412.6	412.6	741.8
ANSYS soft [8]	161.2	231.9	294.6	413.7	413.7	728.6
Rayleigh-Ritz [9]	163.2	237.6	299.9	424.3	424.3	749.4

TABLE 2: Dimensions and density of the aluminum and carbon/epoxy plates [8].

	Length (cm)	Width (cm)	Thickness (cm)	Density (gr/cm <sup>3</sup> )	Arrangement
Aluminum					
A1 (F-F-F-F)	30.00	28.00	0.30	2.70	
A2 (C-F-F-F)	28.00	25.00	0.30	2.70	
Carbon/epoxy					
B1	28.15	24.55	0.20	1.54	[0 <sub>20</sub> ]
B2	24.50	15.30	0.20	1.54	[0 <sub>20</sub> ]
C1	26.00	26.00	0.32	1.59	[(0/90) <sub>8</sub> ] <sub>S</sub>
C2	24.30	15.30	0.32	1.59	[(0/90) <sub>8</sub> ] <sub>S</sub>
D1	10.10	5.30	0.35	1.55	[0 <sub>20</sub> ]
D2	10.00	5.20	0.32	1.59	[(0/90) <sub>8</sub> ] <sub>S</sub>
Glass/epoxy					
C3 (F-F-F-F)	20	16	0.20	1.59	[(0/90) <sub>8</sub> ] <sub>S</sub>
C4 (F-F-F-F)	20	16	0.20	1.59	[(45/-45) <sub>8</sub> ] <sub>S</sub>
D3 (C-F-F-F)	12	6	0.35	1.59	[(0/90) <sub>8</sub> ] <sub>S</sub>
D4 (C-F-F-F)	12	6	0.35	1.59	[(45/-45) <sub>8</sub> ] <sub>S</sub>

TABLE 3: Elastic constants obtained by the tensile test and handbook.

Mechanical properties	$E_1$ (GPa)	$E_2$ (GPa)	$\nu_{12}$	$G_{12}$ (GPa)	$G_{23}$ (GPa)
Aluminum [12]	69	69	0.33	25.94	
Glass/epoxy	40.1	8.9	0.23	4.23	
Carbon/epoxy [8]	121.2	9.34	0.23	6.25	3.0

respectively. The actual elastic constants are used in all of these three methods.

As can be seen, the natural frequencies obtained from these three methods are very close together in average. However, there is still natural frequencies that are not matched well together and it can lead to creation of inherent errors for determination of parameters of plates inversely. Nevertheless, as it is obvious from Table 1, natural frequencies obtained by modeling in ABAQUS software are closer to the experimental frequencies resulting from modal analysis than those obtained by modeling by ANSYS solver and Rayleigh-Ritz method; this means more accuracy for the present method in modeling and direct solution and finally leads to providing a higher accuracy in identifying the parameters.

For more complete validation of the present method, several examples were examined here, referring to the research work of Hwang and Chang [8] to determine the natural frequencies of homogenous and orthotropic plates with various boundary conditions and stacking sequence. Dimensions, density, and stacking sequence of these plates are available in Table 2 and their mechanical properties are in Table 3.

Presented values for the mechanical properties of aluminum plates are obtained from metals handbook [12] and those for composite panels from static tests available in the literature [8]. Natural frequencies obtained from vibration test are shown in Table 4 and those obtained from modeling in ABAQUS software are shown in Table 5. The composite plates chosen from Hwang and Chang's paper have free boundary condition at all edges. In aluminum plate A1, boundary conditions of all edges are also free but, in aluminum plate A2, boundary conditions of bigger edge are clamped and other ones are free.

Moreover, in order to include experiment in the presented study, 4 thick and thin glass/epoxy plates are investigated in modal laboratory (Figure 2). To reduce the errors of production process, these plates are placed in a vacuum condition. Dimensions, density, and stacking sequence of these plates are shown in Table 2. Plates C3 and C4 are laid on the foam devices (Figure 3) and because natural frequencies are independent of position and rigidities of these devices, boundary conditions of these plates are considered completely free [9, 16]. For thick plates D3 and D4, one edge

TABLE 4: Natural frequencies (Hz) of the aluminum, carbon/epoxy [8], and glass/epoxy plates obtained by modal test.

Frequencies	$f_1$	$f_2$	$f_3$	$f_4$	$f_5$	$f_6$	$f_7$	$f_8$	$f_9$	$f_{10}$
Aluminum										
A1	114	167	218	289	300	497				
A2	39	91	237	261	337	545				
Carbon/epoxy										
B1	60	82	143	218	232	257				
B2	111	202	290	310	370	555				
C1	102	311	342	364	390	612				
C2	183	370	535	870	944	1050				
D1	1670	3480	3860	4400	5100	6300	8800	9900	10500	11000
D2	1240	2170	3310	5350	6880	7030	7530	8910	11340	11710
Glass/epoxy										
C3	188	385	555	594	669	1076				
C4	261	279	573	635	682	1002				
D3	154	471	968	1626	2025	2743	3439	4658	5394	5819
D4	136	654	833	1792	2112	2410	3968	4025	5175	5824

TABLE 5: Natural frequencies of the aluminum and carbon/epoxy plates obtained by ABAQUS solver.

Frequencies	$f_1$	$f_2$	$f_3$	$f_4$	$f_5$	$f_6$	$f_7$	$f_8$	$f_9$	$f_{10}$
Aluminum										
A1	115	166	218	292	307	500				
A2	40	91	240	266	340	556				
Carbon/epoxy										
B1	61	84	150	230	231	261				
B2	113	216	304	314	378	560				
C1	100	306	338	360	381	600				
C2	181	370	529	865	938	1033				
D1	1661	3478	3855	4368	5059	6243	8769	9830	1029	10959
D2	1238	2169	3315	5320	6844	7015	7561	8910	10986	11650

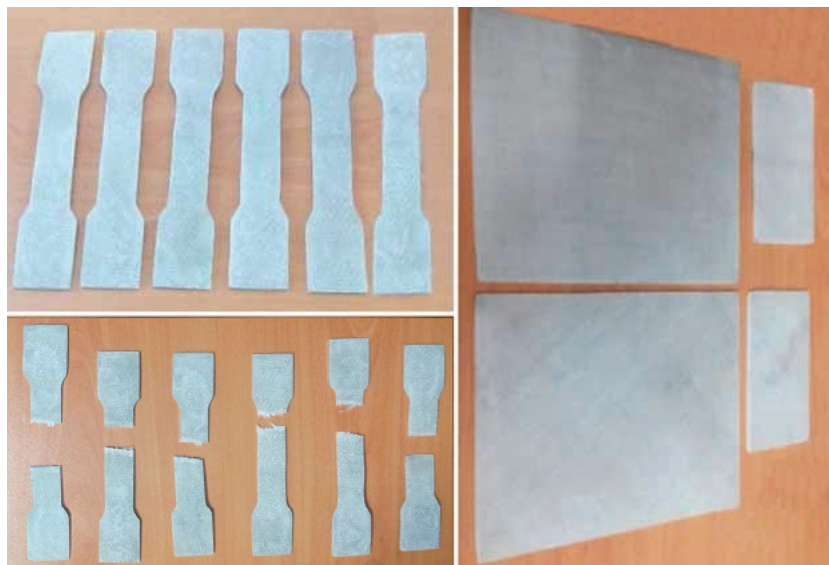


FIGURE 2: Glass/epoxy specimens for modal and tensile tests.



FIGURE 3: Modal test for thin glass/epoxy plates (F-F-F-F).



FIGURE 4: Modal test for thick glass/epoxy plates (C-F-F-F).

is clamped and other ones are free (Figure 4). Because, for this kind of boundary condition, frequencies of all modes shift down, frequencies of higher mode can be investigated more accurately. As can be seen from Figures 3 and 4, laser test is used in this experiment to reduce experimental errors. Plates in this study are excited by an impulse hammer equipped with force transducer. By using a signal analyzer, frequency response can be calculated. Natural frequencies obtained by modal test for these plates are listed in Table 4.

In order to promote validation of the present study, mechanical constants of these glass/epoxy plates are also obtained by investigating tensile test specimens in laboratory

(Figure 2). Tensile test machine is attached by a force sensor and also a strain gauge in direction of the applied force. As it is obvious from Figure 5, two other strain gauges are installed on the specimens in direction of  $90^\circ$  and  $45^\circ$  relative to direction of applied force. So, by recording the amount of strains in 3 different directions and also amount of applied force, 4 independent constants are obtained by the tensile test which are listed in Table 3.

*7.2. Validation of CPAM Method for Determination of Homogenous Plates (Aluminum) Constants.* In order to validate CPAM method described in the previous sections, first, an attempt is made to determine mechanical properties of the discussed aluminum plates in the work of Deobald and Gibson [9]. Deobald and Gibson considered these plates as a transversely isotropic material and tried to determine their four elastic constants by modal analysis and Rayleigh-Ritz method. Four elastic constants have been investigated in their study, while aluminum plates are homogenous and it is enough to determine their two constants; therefore, Hwang and Chang [8] determined these two constants beside determining the four ones and compared their results with those reported by Deobald and Gibson. Results for determination of four elastic constants by using the presented approach and also comparison of them with the average results of Deobald and Gibson and Hwang and Chang's study are shown in Table 6. Table 7 represents comparison between the results provided in this study for investigation of two elastic constants and the average of corresponding ones, obtained by Hwang and Chang.

It is obvious that considering just two elastic constants results in a more accurate estimation and is less time-consuming than considering four ones. So, if it is guaranteed that experimented material is homogenous, just two elastic constants should be determined and even if four elastic constants are investigated, the results will be reliable. If two constants are investigated, the following restrictions must be also applied to the optimization algorithm; however, the CPAM inverse method with four elastic constants can be usable for both homogenous and orthotropic materials.

$$E_1 = E_2$$

$$G_{12} = \frac{E_1}{2(1 + \nu_{12})}. \quad (11)$$

In order to assure the accuracy of the CPAM inverse method for determination of parameters of isotropic and orthotropic plates with various boundary conditions and stacking sequence, more cases are investigated by Huang and Chang. Dimensions, density, and layout of considered plates, their mechanical properties, and obtained natural frequencies are presented in Tables 2, 3, and 4, respectively. Using the frequencies given in Table 4, two and four elastic constants are obtained by the present approach for plates A1 and A2; Table 8 shows these results in comparison with the corresponding ones reported by Huang and Chang.

Although four constants determined for both specimens A1 and A2 have a high accuracy like aluminum plates investigated by Deobald and Gibson [9], characterization of

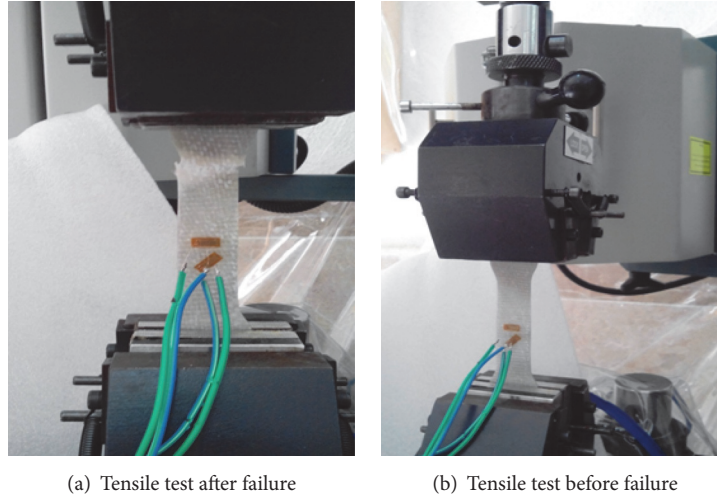


FIGURE 5: Tensile test done for glass/epoxy specimens.

TABLE 6: Four determined elastic constants for the aluminum plate.

Elastic constants	$E_1$ (GPa)	$E_2$ (GPa)	$\nu_{12}$	$G_{12}$ (GPa)
Reference value [12]	72.4	72.4	0.33	28.0
Deobald and Gibson's paper [9]	69.5 (-4.0%)	69.9 (-3.5%)	0.361 (9.4%)	25.6 (-8.6%)
Hwang and Chang's paper [8]	73.5 (1.5%)	69.1 (-4.5%)	0.34 (3%)	26 (-7.1%)
Present method	74.2 (2.5%)	73.8 (1.9%)	0.338 (2.6%)	29.6 (5.6%)

TABLE 7: Two determined elastic constants for the aluminum plate.

Elastic constants	$E_1$ (GPa)	$\nu_{12}$
Reference value [12]	72.4	0.33
Hwang and Chang's paper [8]	72.2 (-0.3%)	0.356 (7.3%)
CPAM method	72.6 (0.35%)	0.34 (3%)

two constants is done faster and more accurately than characterization of four constants. Elastic constants of specimen A1 are obtained with higher accuracy than the ones obtained for specimen A2. This is mainly because, for the case of free boundary condition at all edges in comparison with other considered boundary conditions, the natural frequencies predicted from numerical solution are closer to the experiment frequencies. This viewpoint is exactly evident in Table 5. It can also be because implementation of free boundary conditions in practice (experiment) is definitely closer to the theoretical case (finite element modeling in ABAQUS) in comparison with the other conditions such as clamped or supported conditions.

Elastic constants obtained from inverse solution presented in this study have higher accuracy than elastic constants obtained by Huang and Chang [8] and Deobald and Gibson [9]. As it is clear from Table 1, natural frequencies obtained from ABAQUS are closer to the experimental frequencies than those obtained from Rayleigh-Ritz method and ANSYS. Also the physical constraints given in (9) cause the optimization algorithm to generate parameters closer to

reality and therefore lead to more accurate elastic constants determined in this study.

*7.3. Validation of CPAM Method for Determination of Orthotropic Plates (Composite) Parameters.* As it has been already mentioned, carbon/epoxy composite plates studied in Hwang and Chang's paper [8] with free boundary conditions on their all edges as well as glass/epoxy plates tested in the modal laboratory are considered here for characterization of composite plates. Parameters of these plates are elastic constants and fiber orientation angles. As mentioned before, these parameters are obtained simultaneously and the results of this simultaneous investigation for mechanical constants are presented in Table 9(a) and those for stacking sequence in Table 9(b). Specimen B1 has approximately square shape and B2 is a rectangular plate. These plates are approximately similar to plates C1, C2, C3, and C4 in terms of dimensions. These six specimens, as their length/thickness ratio is about more than 50, are considered as thin plates. Dimensions of D-type specimens are different; so, they are considered as thick plates [8]. As can be seen from Table 9(a), elastic constants determined by the presented method for carbon/epoxy plates are compared with those investigated by Hwang and Chang [8]. These constants are compared with results of static tensile test (Table 3) for glass/epoxy plates and amount of error percentage is also calculated for them.

As seen from Table 9(a) for carbon/epoxy plates, elastic constants obtained for square and rectangular B-type and C-type plates are not so different from each other. So, using such square or rectangular plates does not make much difference

TABLE 8: Elastic constants determined for the aluminum specimens.

Elastic constants	$E_1$ (GPa)	$E_2$ (GPa)	$\nu_{12}$	$G_{12}$ (GPa)
Reference value [12]	69	69	0.33	25.94
Hwang and Chang [8]				
A1	71.4 (3.5%) 68.8 (-0.3%)	64.9 (-5.9%)	0.28 (-15%) 0.32 (-3%)	24.67 (-4.9%)
A2	63.2 (-8.5%) 67 (-2.9%)	70.5 (2.2%)	0.365 (10.6%) 0.32 (-3%)	25.1 (-3.2%)
CPAM method				
A1	70.8 (2.6%) 69.14 (0.2%)	70.7 (2.5%)	0.36 (9%) 0.34 (3%)	26.9 (3.7%)
A2	73.6 (6.7%) 70.4 (2.1%)	71.1 (3%)	0.36 (9.1%) 0.34 (3%)	26.7 (3%)

TABLE 9: Simultaneous determination of material constants and stacking sequence for composite specimens.

(a)

Specimens	$E_1$ (GPa)	$E_2$ (GPa)	$\nu_{12}$	$G_{12}$ (GPa)	$G_{23}$ (GPa)
Reference [12]	121.2	9.34	0.23	6.25	3.6
Hwang and Chang [8]					
B1	125.5 (4%)	8.55 (-8.4%)	0.34 (47.8%)	5.4 (-13.6%)	
B2	128.7 (6.2%)	8.10 (-13.2%)	0.33 (43.4%)	6.05 (-3.2%)	
C1	123.7 (2%)	9.96 (6.6%)	0.35 (52.2%)	6.85 (9.6%)	
C2	120.2 (-1%)	9.96 (6.6%)	0.35 (52.2%)	6.85 (9.6%)	
D1	120.0 (-1%)	9.60 (2.8%)	0.21 (-8.6%)	5.70 (-8.8%)	2.9 (-19.4%)
D2	120.0 (-1%)	9.00 (-3.6%)	0.30 (30.4%)	7.10 (13.6%)	2.5 (-3.5%)
Present method					
Carbon/epoxy					
B1	122.3 (1%)	9.12 (-2.3%)	0.25 (8.6%)	6.43 (2.8%)	
B2	123.8 (2.1%)	9.63 (3.1%)	0.26 (13.4%)	6.48 (3.7%)	
C1	126.5 (4.3%)	9.47 (1.3%)	0.24 (4.3%)	6.58 (5.3%)	
C2	125.7 (3.7%)	9.44 (1%)	0.25 (8.6%)	6.57 (5.1%)	
D1	120.6 (-1%)	9.86 (5.5%)	0.22 (-4.3%)	5.87 (9.9%)	3.3 (-8.3%)
D2	120.2 (-1%)	9.01 (-3.5%)	0.25 (8.6%)	6.36 (1.7%)	3.4 (-5.55%)
Glass/epoxy					
C3	41.7 (4%)	8.71 (-2.1%)	0.25 (8.7%)	4.41 (4.3%)	
C4	41.3 (2.9%)	8.53 (-4.1%)	0.24 (4.3%)	4.38 (3.5%)	
D3	39.4 (-1.7%)	9.14 (2.7%)	0.25 (8.7%)	4.18 (-1.1%)	3.3
D4	39.6 (-1.2%)	9.26 (4%)	0.26 (13%)	4.12 (-2.6%)	3.2

(b)

Thin plates	Stacking sequence	Thick plates	Stacking sequence
B1	[0, 0, 0, 0, 0]	D1	[0, 0, 0, 0, 0]
B2	[0, 0, 0, 0, 0]	D2	[0, 90, 0, 90]
C1	[0, 90, 0, 90]	D3	[0, 90, 0, 90]
C2	[0, 90, 0, 90]	D4	[45, -45, 45, -45]
C3	[0, 90, 0, 90]	G1	[0, 90, 0, 90, 0, 90]
C4	[45, -45, 45, -45]	G2	[45, -45, 45, -45, 45, -45]
F1	[0, 90, 0, 90, 0, 85]		
F2	[45, -45, 45, -45, 50, -45]		

in outcomes for determination of these constants. Results for elastic constants obtained from CPAM inverse method show a good agreement with corresponding ones obtained from static tests available in the literature for B1, B2, C1, and C2 [8]. The differences between estimated constants from presented inverse method and those measured from experiment cannot necessarily just be due to error associated with vibration modeling in ABAQUS software or PSO algorithm. Hwang and Chang [8] also showed that such differences can be caused by the sources of noises created by test and measurement equipment. As it is explicitly evident from Table 9(a), results obtained from the presented method are relatively more accurate than those reported by Hwang and Chang [8]. As it is noted previously, this fact is because the natural frequencies predicted by ABAQUS solver are closer to the values measured experimentally than frequencies obtained by ANSYS. Moreover, the appropriate constraints for elastic constants given in (9) make optimization algorithm generate parameters that are closer to reality. For glass/epoxy plates, amount of errors of these constants obtained for C3 and C4 (in comparison with tensile test) shows high accuracy of this method and also experiment. There is no difference between results of C3 and C4 which means that differences in stacking sequence of plates do not affect accuracy of the present method.

As it was also mentioned in previous sections, four independent elastic constants must be predicted for thin plates, but constant  $G_{23}$  is considered as another independent constant that must be investigated for thick plates D1, D2, D3, and D4 and, therefore, the second part of (6) should be omitted from algorithm code. Because high-frequency modes affect more transverse shear deformation of plates than low modes, the first ten frequencies presented in Table 4 are used in error function in order to determine the elastic constants of specimens D1, D2, D3, and D4.

Stacking sequence identification of plates B1 and B2 is done by considering just five unknown angles. It means that stacking sequence is assumed as  $[(\theta_1, \theta_2, \theta_3, \theta_4, \theta_5)_4]_s$  in which  $\theta_i$  ( $i = 1, 2, 3, 4, 5$ ) must be determined and due to the presence of the repetition pattern of sublaminates in this lay-up configuration, it is enough to identify just these five unknown angles instead of twenty ones. In order to evaluate ability of CPAM method for identification of five angles, these five angles are considered unknown. Similarly, for plates C1, C2, C3, and C4, stacking sequence is considered as  $[(\theta_1, \theta_2, \theta_3, \theta_4)_4]_s$  such that four angles must be evaluated. In another case of plates C2 and C4, all angles are considered to be known for identification system except 6 angles  $[(\theta_1, \theta_2, \theta_3, \theta_4, \theta_5, \theta_6)]$ . Results obtained from this identification for C2 and C4 are indicated by F1 and F2, respectively. Results obtained from this stacking sequence identification for plates B1, B2, C1, C2, C3, C4, F1, and F2 are presented in Table 9(b). It can be seen from Table 9(b) that CPAM method can identify accurately fibers' angle of the plates with eight and ten layers and provide acceptable results. However, for cases F1 and F2, all angles are identified accurately except one of them. This can be because of difference between experimental and theoretical frequencies. It is clearly noted that, according to the results of Tables 4 and 5, natural frequencies

obtained from experiment deviated a little from numerical solution and there is a difference between these two types of frequencies. As it is mentioned previously, it can cause inborn error in the inverse solution system.

Here, five angles are considered unknown for thick plates D1 in addition to four ones for plates D2, D3, and D4 to investigate parameters of them and their results for stacking sequence identification for them are presented in Table 9(b). The way that the number of angles is chosen for both of these plates is similar to the way explained for B-type and C-type plates previously. In addition, symbols G1 and G2 are also used for calculation of six angles for plates D2 and D4 (like symbols F1 and F2 for thin plates C2 and C4). As it is clear from Table 9(b), CPAM method can identify angles of these eight-layer, ten-layer, and six-layer plates with high accuracy.

For thin plates, four independent elastic constants have been considered in the identification process. But, for thick plates D1, D2, D3, and D4, the constant  $G_{23}$  is also considered as fifth independent variable in the identification algorithm. So, the second part of (6) is not used for thick plates. For thin plates, first six natural frequencies are used in the error function (see (7)). Since the frequencies of higher modes have more effects on the transverse shear deformation of plates in comparison with lower modes and also due to being more sensitive to this effect in thicker plates, instead of considering the first six frequencies, the first ten frequencies that are presented in Table 4 are used in construction of the error function; it can be another important reason for high accuracy of G-type cases in comparison with F-type ones.

**7.4. Sensitivity Analysis.** Study of stability of an inverse problem which results in smooth movement of all parameters to the real response of the problem is an especially important issue that must be considered in inverse methods. The inverse solution may diverge by moving from initial chosen points in the solution space. It means that the difference between measured experimental data (real responses) and those evaluated from direct solution (simulated model) is increased. It is essential that all parameters generated in solution space move towards the real responses when the process continues; under such circumstances, inversion of solution is stable [17]. As it is defined by Hadamard [17], an inverse problem will be termed well-posed if

- (1) there is a solution for data in solution space,
- (2) solution in model space (model parameters) is unique,
- (3) solution remains stable to the small changes in the input data.

If these three tests are not satisfied, the problem will be called ill-posed. If data are sufficient, in other words, data space is larger than model space, the first test will be satisfied. The proposed inverse method has used six and ten experimental natural frequencies for determination of the four and five elastic constants (along with fibers angles), respectively. Also, due to capability of the inverse solution for correct identification of the model space, the first two

TABLE 10: Elastic constants determined for specimen A2 for different levels of disorder.

Material constants	Free disorder		1% disorder		5% disorder		10% disorder	
	CPAM method	Amount	Percentage error	Amount	Percentage error	Amount	Percentage error	
$E_1$ (GPa)	70.4	69.2	-1.7%	68.2	-3.1%	65.9	-6.4%	
$\nu_{12}$	0.34	0.348	2.3%	0.364	7.2%	0.38	11.9%	

TABLE 11: Elastic constants determined for specimen C1 for different levels of disorder.

Material parameters	Free disorder		1% disorder		5% disorder		10% disorder	
	CPAM method	Amount	Percentage error	Amount	Percentage error	Amount	Percentage error	
$E_1$ (GPa)	126.5	127.6	0.88%	129.5	2.37%	132.65	4.86%	
$E_2$ (GPa)	9.47	9.61	1.48%	9.9	4.45%	10.35	9.3%	
$\nu_{12}$	0.24	0.25	4.1%	0.26	8.33%	0.28	16.66%	
$G_{12}$ (GPa)	6.58	6.69	1.62%	6.17	-6.17%	5.88	-10.63%	
Stacking sequence	[0, 90, 0, 90]	[5, 90, 0, 90]		[-10, 85, 0, 90]		[-10, 80, 5, 90]		

TABLE 12: Elastic constants determined for specimen C3 for different levels of disorder.

Material parameters	Free disorder		1% disorder		5% disorder		10% disorder	
	CPAM method	Amount	Percentage error	Amount	Percentage error	Amount	Percentage error	
$E_1$ (GPa)	41.7	42	0.81%	42.6	2.23%	43.5	4.34%	
$E_2$ (GPa)	8.71	8.88	2.02%	9.11	4.65%	9.41	8.12%	
$\nu_{12}$	0.25	0.26	4%	0.27	8%	0.29	16%	
$G_{12}$ (GPa)	4.41	4.45	1.12%	4.16	-5.64%	3.85	-12.53%	
Stacking sequence	[0, 90, 0, 90]	[-5, 85, 0, 90]		[5, 80, 0, 90]		[-15, 80, -10, 90]		

tests are passed well and the problem is expected to be well-posed for determination of parameters. But the third test of Hadamard is about the stability of inverse solution. In a well-posed problem, a small disturbance (disorder) in the model parameters causes small disturbance in the data space and vice versa. In other words, if a small disturbance in data space creates a large disturbance in model space, an ill-posed problem will be faced. One way to evaluate the stability of inverse solution system is to directly import some disorders to the measured experimental data and recalculate the model parameters (elastic constants and fibers' angles) by using these noisy data comprising disorders (simulated data) [18].

One of the artificial disorders that may be used by inverse problems is creating Gaussian disorder. In order to create this disorder, a vector of some quasi-random numbers (using a Gaussian distribution with average  $a$  and standard deviation  $b$ ) is generated by Box-Muller method. For applying this disorder to the data, the average  $a$  is set to zero and the standard deviation  $b$  is obtained from following relation [18]:

$$b = p_e \times \left[ \frac{1}{(n_s (\sum_{i=1}^{n_s} \omega_i^m)^2)} \right]^{1/2}, \quad (12)$$

where  $\omega_i^m$  is  $i$ th natural frequency,  $n_s$  is total number of measured frequencies for  $i$ th mode, and  $p_e$  quantifies the level of disorder; as an example,  $p_e = 0.5$  means disorder level is 0.5%. Using a test by different levels of simulated disorder can provide an appropriate criterion for the stability of the inverse method against being polluted with disturbances.

Thus, frequencies polluted with disturbances and obtained by adding Gaussian disorder to the measured experimental values are utilized for simulating experimental data that are measured with noise. If Hadamard tests for simulating data with an appropriate level of disorder are passed well by an inverse method, then this method can be employed everywhere for scientific and practical usage. So, effect of different levels of disorder (1, 5, and 10 percent) is investigated for specimens A2, C1, C3, D1, and D3 and consequently the obtained results are presented in Tables 10, 11, 12, 13, and 14, respectively. Ten groups of frequencies are simulated for each level of disorder and the presented results in these tables are the average of this ten-time operation of inverse solution (solution must run once for each group of simulated frequency to obtain material properties). Percentage errors presented in these tables for different levels of disorder are calculated in comparison with the free disorder values obtained from the presented method (it is not calculated in comparison with reference values for elastic constants).

The results of Tables 10, 11, 12, 13, and 14 show that Young's modulus  $E_1$  has the least sensitivity to disturbances and disorders in the system and relatively remains with good accuracy, even in high levels of the disorder. Young's modulus  $E_2$  is a little sensitive to disorders in the system; however, results obtained for this modulus are again stable and satisfactory. Poisson's ratio is more sensitive than the other constants to disorders appearing in the system because it has a smaller value than others; so a small change and disorder in the

TABLE 13: Elastic constants determined for specimen D1 for different levels of disorder.

Material parameters	Free disorder	1% disorder		5% disorder		10% disorder	
	CPAM method	Amount	Percentage error	Amount	Percentage error	Amount	Percentage error
$E_1$ (GPa)	120.6	121.5	0.76%	124.9	3.53%	127.4	5.63%
$E_2$ (GPa)	9.86	9.97	1.16%	10.3	4.85%	10.4	7.41%
$\nu_{12}$	0.22	0.23	4.54%	0.24	9.09%	0.26	18.18%
$G_{12}$ (GPa)	5.87	5.78	-1.53%	5.5	-6.25%	5.39	-8.23
$G_{23}$ (GPa)	3.3	3.45	4.68%	3.57	8.18%	3.88	17.57%
Stacking sequence	[0, 0, 0, 0, 0]	[5, 5, 0, 0, 0]		[10, -5, 5, 0, 0]		[-10, -10, 10, -5, 0]	

TABLE 14: Elastic constants determined for specimen D3 for different levels of disorder.

Material parameters	Free disorder	1% disorder		5% disorder		10% disorder	
	CPAM method	Amount	Percentage error	Amount	Percentage error	Amount	Percentage error
$E_1$ (GPa)	39.4	39.6	0.74%	40.5	2.89%	41.7	5.94%
$E_2$ (GPa)	9.14	9.25	1.28%	9.60	5.12%	9.88	8.14%
$\nu_{12}$	.25	0.24	-4 %	0.27	8%	0.29	16%
$G_{12}$ (GPa)	4.18	4.11	-1.64%	3.91	-6.34%	3.83	-8.26
$G_{23}$ (GPa)	3.3	3.44	4.31%	3.54	7.27%	3.92	18.79%
Stacking sequence	[0, 90, 0, 90]	[5, 85, 0, 90]		[5, 80, -5, 90]		[10, 80, -10, 90]	

system cause it to be changed with high percentage due to its small amount. This factor is well evident in the results of other constants. As it is mentioned above,  $E_2$  which is smaller than  $E_1$  has higher percentage of error (and so does modulus  $G_{12}$  in comparison with  $E_1$ ). High percentage of error for out-of-plane shear modulus  $G_{23}$  in thick plates D1 and D3 indicates that this material constant shows more sensitivity than other constants to changes in natural frequencies in transverse vibration. As it is mentioned previously, since high-mode frequencies influence more the transverse shear deformation than low-mode frequencies, this sensitivity in thick plates seems reasonable. The fibers' angles of both thin and thick plates show acceptable resistance against disorders and the obtained results are reasonable. As can be seen from Tables 11, 12, 13, and 14, angles that are closer to the mid-planes (inner stacking sequence) are more sensitive than angles further away from them (outer stacking sequence). The reason is that outer stacking sequence changes more stiffness matrix (and, consequently, natural frequencies) of the plates in comparison with inner stacking sequence. According to the results presented in Tables 10, 11, 12, 13, and 14, because the deviations for the estimated parameters (that are obtained with disorders in the system) are in an acceptable domain and also in the same range of disorders, the proposed inverse method passes the third test of Hadamard successfully and is appropriate to use in practical applications.

## 8. Conclusion

In this paper, a new combined FEM optimization method is presented to determine the elastic constants and stacking sequence of composite plates concurrently by using natural frequencies measured experimentally. To determine the parameters of aluminum, carbon/epoxy, and glass/epoxy

composite plates, this rapid, convergent, and accurate method is employed with applying proper constraints and choosing appropriate parameters. It is shown that the proposed method can predict well the parameters of such materials. Furthermore, implementation of free boundary condition at all edges of the plates in vibrational experiment leads to better results. Although four elastic constants can be investigated for homogenous materials, determination of two elastic constants increases the accuracy and quickness of results. No obvious dependence on the laminate dimensions has been observed for determination of parameters of carbon/epoxy and glass/epoxy composite laminates. By comparing the results obtained through this method with those obtained by similar methods available in the literature, the high accuracy of the proposed method is properly confirmed. This method can predict out-of-plane shear modulus with agreeable accuracy for thick orthotropic plates. Finally, by applying sensitivity analysis with three levels of disorder (1, 5, and 10 percent), the stability of the method is evaluated and, as a result, the proposed inverse solution shows high and good resistance against unwanted disorders.

## Conflicts of Interest

The authors declare that they have no conflicts of interest.

## References

- [1] S.-F. Hwang, J.-C. Wu, and R.-S. He, "Identification of effective elastic constants of composite plates based on a hybrid genetic algorithm," *Composite Structures*, vol. 90, no. 2, pp. 217–224, 2009.
- [2] E. O. Ayorinde and L. Yu, "On the elastic characterization of composite plates with vibration data," *Journal of Sound and Vibration*, vol. 283, no. 1-2, pp. 243–262, 2005.

- [3] G. R. Liu, X. Han, and K. Y. Lam, "A combined genetic algorithm and nonlinear least squares method for material characterization using elastic waves," *Computer Methods in Applied Mechanics and Engineering*, vol. 191, no. 17-18, pp. 1909–1921, 2002.
- [4] F. S. Almeida and A. M. Awruch, "Design optimization of composite laminated structures using genetic algorithms and finite element analysis," *Composite Structures*, vol. 88, no. 3, pp. 443–454, 2009.
- [5] M. E. Ibrahim, "Nondestructive evaluation of thick-section composites and sandwich structures: a review," *Composites Part A: Applied Science and Manufacturing*, vol. 64, pp. 36–48, 2014.
- [6] K. Sepahvand and S. Marburg, "On construction of uncertain material parameter using generalized polynomial chaos expansion from experimental data," *Procedia IUTAM*, vol. 6, pp. 4–17, 2013.
- [7] K.-H. Ip, P.-C. Tse, and T.-C. Lai, "Material characterization for orthotropic shells using modal analysis and Rayleigh-Ritz models," *Composites Part B: Engineering*, vol. 29, no. 4, pp. 397–409, 1998.
- [8] S.-F. Hwang and C.-S. Chang, "Determination of elastic constants of materials by vibration testing," *Composite Structures*, vol. 49, no. 2, pp. 183–190, 2000.
- [9] L. R. Deobald and R. F. Gibson, "Determination of elastic constants of orthotropic plates by a modal analysis/Rayleigh-Ritz technique," *Journal of Sound and Vibration*, vol. 124, no. 2, pp. 269–283, 1988.
- [10] G. R. Liu, W. B. Ma, and X. Han, "An inverse procedure for determination of material constants of composite laminates using elastic waves," *Computer Methods in Applied Mechanics and Engineering*, vol. 191, no. 33, pp. 3543–3554, 2002.
- [11] A. R. Mohan Rao and N. Arvind, "A scatter search algorithm for stacking sequence optimisation of laminate composites," *Composite Structures*, vol. 70, no. 4, pp. 383–402, 2005.
- [12] American Society for Metals, "Properties and selection: non-ferrous alloys and pure metals," in *Metals Handbook*, vol. 2, 9th edition, 1979.
- [13] Abaqus User's Manual, Abaqus Version 6.12-1 Documentation, Dassault Systemes SIMULIA Corporation, Providence, RI, USA, 2012.
- [14] R. C. Eberhart and Y. Shi, "Particle swarm optimization: developments, applications and resources," in *Proceedings of the Congress on Evolutionary Computation*, vol. 1, pp. 81–86, IEEE, Seoul, Republic of Korea, 2001.
- [15] A. K. Bledzki, A. Kessler, R. Rikards, and A. Chate, "Determination of elastic constants of glass/epoxy unidirectional laminates by the vibration testing of plates," *Composites Science and Technology*, vol. 59, no. 13, pp. 2015–2024, 1999.
- [16] F. Moussu and M. Nivoit, "Determination of elastic constants of orthotropic plates by a modal analysis/method of superposition," *Journal of Sound and Vibration*, vol. 165, no. 1, pp. 149–163, 1993.
- [17] A. L. Dontchev and T. Zolezzi, *Well-Posed Optimization Problems*, vol. 1543 of *Lecture Notes in Mathematics*, Springer, Berlin, Germany, 1993.
- [18] E. R. Golder and J. G. Settle, "The Box-Muller method for generating pseudo-random normal deviates," *Applied Statistics*, vol. 25, pp. 12–20, 1976.

## Research Article

# Numerical Evaluation on Dynamic Response of Existing Underlying Tunnel Induced by Blasting Excavation of a Subway Tunnel

Jixue Zhou,<sup>1,2,3</sup> Yi Luo,<sup>1</sup> XinPing Li,<sup>1</sup> Yunhua Guo,<sup>1</sup> and Tingting Liu<sup>1</sup>

<sup>1</sup>Hubei Key Laboratory of Roadway Bridge & Structure, Wuhan University of Technology, No. 122 Luoshi Rd., Wuhan 430070, China

<sup>2</sup>School of Civil Engineering and Architecture, Wuhan University of Technology, No. 122 Luoshi Rd., Wuhan 430070, China

<sup>3</sup>China Railway 20 Bureau Group Co., Ltd., No. 89 Taihua Road, Xi'an 710016, China

Correspondence should be addressed to Yi Luo; [ylo@whut.edu.cn](mailto:ylo@whut.edu.cn)

Received 1 April 2017; Accepted 7 May 2017; Published 19 June 2017

Academic Editor: Abdul Qadir Bhatti

Copyright © 2017 Jixue Zhou et al. This is an open access article distributed under the Creative Commons Attribution License, which permits unrestricted use, distribution, and reproduction in any medium, provided the original work is properly cited.

In Southwest China, most regions are mountainous, where traditional drill-and-blast method is adopted to excavate relatively harder rocks. However, blasting would cause vibration to adjacent structures and might result in damage or even failure. This paper considers a case where subway tunnel is overlying an existing railway tunnel, while the excavation requires blasting method. Vibration and stress distribution are calculated via Dynamic Finite Element Method (DFEM) for both full-face excavation and CD method. Result shows that vibration induced by CD method is only 28% of that caused by full-face blasting with same distance. Peak vibration is located on the lining facing the blasting source, while peak tensile stress is on the other side of the contour due to the reflection of stress wave on strata boundary. And peak value of tensile stress induced by full-face blasting is capable of causing lining failure; thus full-face blasting is not suggested within 40 m beyond the underlying tunnel axis. However, CD method has shown much advantage, since blasting within 25 m is also considered safe to the underlying tunnel. But when the blasting source is as near as 12 m within the underlying tunnel, the CD method is no longer safe.

## 1. Introduction

World population growth is encouraging massive request on convenient traffic and large residential settlement, which results in fast development in subway system [1, 2]. For example, more than 410 km subway is in operation beneath London, UK [3], and 293 km beneath Madrid, Spain [4]. Developed regions such as Hong Kong are making good use of their underground space for not only subway tunnels but also other underground caverns [5], which makes it common to have different tunnels or underground spaces overlapping each other at different elevations. Similar situations are also encountered in fast developing cities in China during recent years, while great investments are made in subway construction before cities are too crowded.

Usually, the subway tunneling is achieved by shield machines [6, 7], but due to the turning curvature limitation and geological or economical issues, the drill-and-blasting

method has to be adopted [8] in many cases, which will inevitably cause vibration problem on surrounding rock mass and adjacent structures. For existing tunnels near subway tunneling, possible dynamic damage to their lining should be evaluated before any hazard occurs, especially in the mountainous area Southwest China, where drill-and-blasting is more commonly used.

While developing the public transit systems, associated geohazards such as water and soil ingress, ground surface settlement, and sinkholes are likely to be encountered due to unforeseen ground conditions or other reasons that are not apparent in the preliminary design phase [9–12]. A better mechanical understanding of the effects of the overcrossing tunneling on the existing tunnels would provide a quick but low cost assessment alternative method for evaluating the behavior of underlying tunnels prior to construction.

Dynamic damage or failure during subway blasting excavation might cause fatal damage to surrounding rock mass

and structures. Ren et al. [13] summarized the tectonic structure, geomorphology, hydrogeology, and engineering geology in Guangzhou, China, and reported a collapse of the tunnel face resulting from a blast operation in construction of Guangzhou Subway, which led to a serious sinkhole of 690 m<sup>2</sup>, and the collapse of two buildings. Actually, many drill-and-blast practices have been conducted during hydraulic tunnels or mining shafts [14–19], which indicated that blasting vibration has critical influence on damage or failure of surrounding rock mass and lining.

Ma et al. [16] monitored the vibration velocities of surface particles after the blasting of auxiliary holes and showed that vibration isolation can be achieved by the existing blasting cavity. Zhang et al. [20] studied the vibration intensity and frequency at the ejective direction during drill-and-blasting. Dong et al. [21] found that the vibration velocities were different at different points even though the points were in the same distance or elevation to blasting source.

However, fewer research literatures were focusing on the influence of blasting on existing tunnels nearby. Zhao et al. [19] adopted a Finite Element Method (FEM) to study blasting vibration velocity and vibration frequency on existing tunnel. Result shows that field monitoring experiment and numerical simulation can optimize blasting excavation program and provide a reference for other similar engineering projects. Shin et al. [22] studied effect of blast-induced vibration on existing tunnels in soft rocks. Other studies were conducted on damage of surrounding rock mass induced by blasting excavation of adjacent hydraulic tunnels or shafts [17, 23] (Zhao and Long, et al., 2016b), but subway tunnels are usually buried shallower than hydraulic tunnels or shafts.

## 2. Methodology

The principal purpose of this paper is to carry out a dynamic stability evaluation for underlying tunnels under the influence of drill-and-blast tunneling of an overlying subway tunnel, as a case example for subways with similar situations. Analytical solutions for tunnel bending moment and axial force evaluation are studied by Abate and Massimino [25], and the response of a tunnel lining was expressed as a function of the compressibility and flexibility ratios of the tunnel and the overburden pressure and at-rest coefficient of the earth pressure of the soil. However, for tunnels in irregular shape or complex construction procedure, numerical methods have to be adopted especially for dynamic problems [26].

In recent years, numerical methods such as the finite difference method (FDM) and Finite Element Method (FEM) have been employed to analyze the stress and perform deformation analyses of underground excavations [27, 28] and have been widely employed by researchers to investigate deformations and stress distributions in tunnel intersections and in bifurcation tunnels [29] investigating the influence of a new obliquely crossing tunnel on an existing main tunnel using a 3D finite element analysis. And few investigations

have been conducted on dynamic interaction between underground tunnel and ground or adjacent tunnels. Mobaraki and Vaghefi [30] have analyzed the dynamic response of underground tunnel induced by ground blasting. Rebello et al. [31] used FDM to analyze dynamic response of ground structures induced by underground tunnel blasting. Lu et al. [15] adopted FEM to study the dynamic influence on ground airport runway induced by tunnel blasting excavation. It is a growing trend of evaluating dynamic problems in blasting tunneling.

Considering Dynamic Finite Element Method (DFEM) being a more effective measure for this type of dynamic problem, and the most mature and widely adopted in blasting simulation, it is adopted in this study. Given that the coordinate of a particle is  $X_i$  ( $i = 1, 2, 3$ ) at the beginning and  $x_i$  ( $i = 1, 2, 3$ ) at time  $t$ , then the motion equation is as follows:

$$x_i = x_i(X_j, t), \quad (1)$$

with initial condition at  $t = 0$  as

$$\begin{aligned} x_i(X_j, 0) &= X_i \\ \dot{x}(X_j, 0) &= V_i(X_j, 0), \end{aligned} \quad (2)$$

where  $V_i$  is initial velocity.

In DFEM, explicit equation is adopted as follows:

$$[\mathbf{M}] \delta + [\mathbf{C}] \dot{\delta} + [\mathbf{K}] \ddot{\delta} = \mathbf{P}. \quad (3)$$

where  $[\mathbf{M}]$ ,  $[\mathbf{C}]$ , and  $[\mathbf{K}]$  are mass matrix, damping matrix, and stiffness matrix of the whole system,  $\delta$ ,  $\dot{\delta}$ , and  $\ddot{\delta}$  are displacement vector, velocity vector, and acceleration vector, and  $\mathbf{P}$  is the load vector.

## 3. Evaluation for Kunming Subway

**3.1. Project Overview.** The Number 3 Kunming Subway (KS3) tunnel section between Xishan Park Station and Chejiabi Station is designed to be excavated by drill-and-blasting CD method. This section of tunnel is in length of 301.5 m, in radius of 450 m, with inclination of 2‰ from Xishan Park Station to YDK0+535, and with inclination of -28‰ to shield machine well, shown in Figure 1.

This section of subway tunnel is overlying three tunnels, namely, YDK0+492.92 (Newly Built Bijiguan Tunnel, NBB), YDK0+551.61 (Old Pilot Tunnel, OP), and YDK0+578.69 (Expended Bijiguan Tunnel, EB). The top elevations of existing tunnels are, respectively, 7.19 m, 14.5 m, and 6.358 m beneath the tunneling subway bottom. It is obvious that the NBBT has the largest section area and span, so it is chosen as the main object for dynamic evaluation.

Figure 2 shows section contour and dimension of NBBT and geological condition. Mechanical parameters are shown in Table 1. The maximum burial depth of subway tunnel is 20 m, while the minimum is 6.5 m. Main stratas around the tunnel from top to bottom are fully, highly, and intermediary weathered basalt, with RQD from 60% to 80%. And seepage is not obvious in this region.

TABLE 1: Material parameters.

Type	Natural density/kg/m <sup>3</sup>	Deformation modulus/GPa	Cohesiveness/kPa	Internal friction angle	Poisson ratio
Plain fill	$1.96 \times 10^3$	0.035	15	10	0.3
Fully weathered basalt	$2.1 \times 10^3$	0.055	17	35	0.27
Highly weathered basalt	$2.6 \times 10^3$	0.075	20	45	0.25
Intermediate weathered basalt	$2.7 \times 10^3$	9	460	65	0.2
Concrete C35	$2.39 \times 10^3$	14	4500	62.2	0.3
Concrete C20	$2.37 \times 10^3$	11	2600	60	0.3

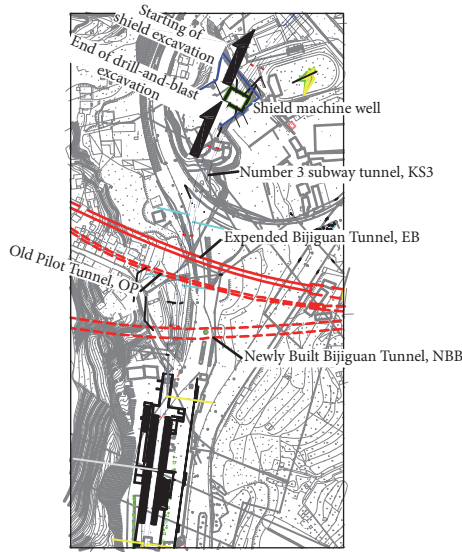


FIGURE 1: Plan of KS3 tunneling overlying three existing tunnels.

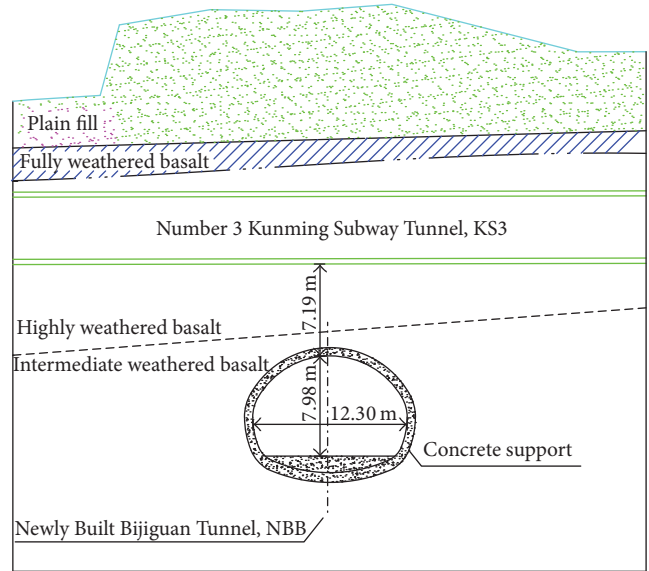


FIGURE 2: Section contours for underlying NBBT.

Since less weathered basalt is relatively difficult for shield excavation, drill-and-blasting excavation method is considered for this section to shield well. As rock mass between subway tunnel and NBBT is relatively thin, thus drill-and-blasting excavation method would cause vibration on adjacent tunnel, as well as potential damage or even failure. So the stability evaluation during subway tunnel excavation should be carried out on the underlying tunnels. The underlying NBB tunnel is designed as comprehensive lining section, as shown in Figure 2.

**3.2. Excavation Method.** Since the distance between KS3 and NBB is as small as 7.19 m, it is very difficult to avoid damaging underlying tunnel; thus careful excavation must be adopted in the section of KS3 tunnel near the axis of NBB tunnel. However, the section further away from the axis can still be excavated with other methods so as to accelerate excavation rate.

Section contour of KS3 with full-face excavation is shown in Figure 3, while excavation procedure of CD method is shown in Figure 4. In full-face excavation, most part of the whole contour is formed by one blasting operation, and the inverted arch at the bottom is formed by the second operation. So, most of the time, the step length of full-face excavation is below 3 m, while it is as small as 0.6 m in this

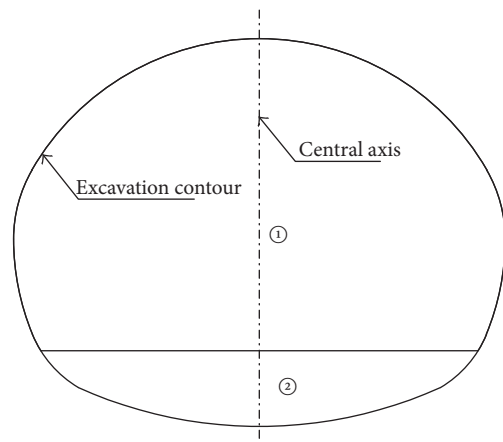


FIGURE 3: Full-face excavation contours for KS3 subway tunnel.

project. However, in CD method, the section is divided into four parts, which are excavated by four individual blasting operations and temporary supports are installed after each blasting operation. In CD method, excavation area is smaller and supporting makes the tunnel more stable. Temporary support is to be filled with C20 concrete, to enhance its stiffness and strength.

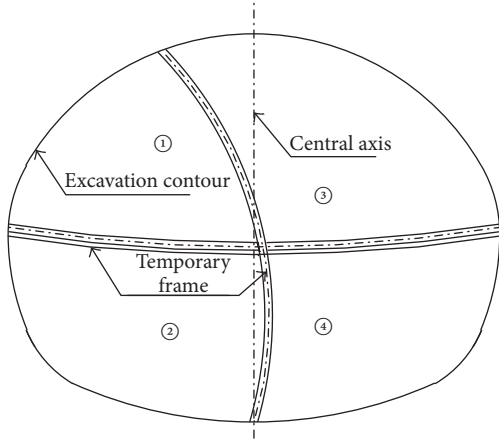


FIGURE 4: CD method excavation contours for KS3 subway tunnel.

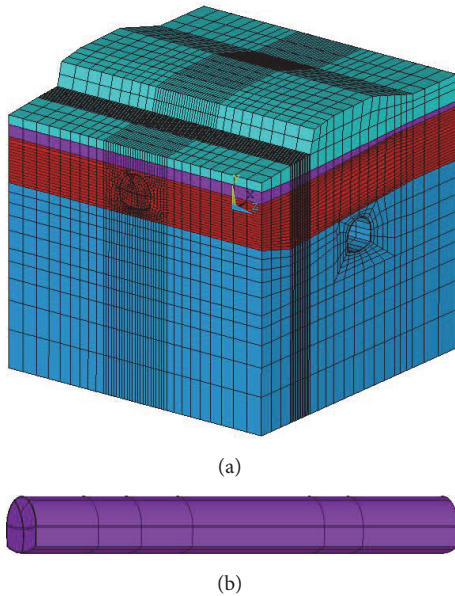


FIGURE 5: Modeling of KS3 subway tunneling over NBBT ((a) model with elements; (b) volume being excavated in subway tunnel).

**3.3. Numerical Modeling.** Dynamic Finite Element Method (DFEM) is adopted for numerical calculation. The whole model is meshed into 89382 elements and 98210 nodes, shown in Figure 5, and the volume to be excavated includes four different parts in CD method, which can also be considered together as full-face method.

Different layers of strata are modeled according to field investigation result. The topography of ground surface is simplified, since the detail is not significant to numerical calculation focusing on the underground structures.

Four side surfaces and the bottom surface are set as nonreflection surfaces, to simulate the transmission of blast-induced vibration to further field, while the vibration should be reflected at the top surface.

Both existing tunnel lining and surrounding rock were assumed to be elastoplastic materials with incremental stress-strain relations obeying the Mohr-Coulomb yield criteria and associated flow rule. However, all parameters are tested for static calculation, while dynamic parameters are required for calculating blasting influence.

According to the relative study (Zhao and Long, et al., 2016b) the relationship between dynamic elasticity modulus ( $E_d$ ) and static elasticity modulus ( $E_s$ ) is as follows:

$$E_d = 8.7577E_s^{0.5822}. \quad (4)$$

According to the view of Dai [33], in a blasting loading frequency range, the relationship between dynamic Poisson ratio ( $\mu_d$ ) and static Poisson ratio ( $\mu_s$ ) is as follows:

$$\mu_d = 0.8\mu_s. \quad (5)$$

However, during the blasting operation, surrounding rock mass would respond in high strain rate, so it is necessary to consider the high strain rate effect. Therefore, the kinematic hardening constitutive model is adopted. It can be explained by the following equation:

$$\sigma_y = \left[ 1 + \left( \frac{\dot{\epsilon}}{C} \right)^{1/P} \right] (\sigma_0 + \beta E_p \epsilon_{\text{eff}}^p), \quad (6)$$

where  $\sigma_0$  is initial yield stress and  $C$  and  $P$  are Cowper-Symonds strain rate coefficients, relating only to material type.  $\beta$  is a coefficient, where  $\beta = 0$  means plastic kinetic hardening and  $\beta = 1$  means equivalent hardening model. The static yield stress is the combination of initial yield stress and additional part,  $\beta E_p \epsilon_{\text{eff}}^p$ , and  $E_p$  is plastic hardening modulus, as in

$$E_p = \frac{E_t E_{\text{tan}}}{E - E_t}, \quad (7)$$

where  $E_0$  is Young's modulus and  $E_{\text{tan}}$  is tangent modulus and  $\epsilon_{\text{eff}}^p$  is effective plastic strain and  $\epsilon_{ij}^p$  is component plastic strain, which are defined as follows:

$$\begin{aligned} \epsilon_{\text{eff}}^p &= \int_0^t d\epsilon_{\text{eff}}^p \\ d\epsilon_{\text{eff}}^p &= \sqrt{\frac{2}{3}} d\epsilon_{ij}^p d\epsilon_{ij}^p. \end{aligned} \quad (8)$$

**3.4. Blasting Load Application.** After the detonation of explosives, there is a complex thermodynamical process in the borehole, accompanied by shock wave on the borehole wall. Peak load on the borehole wall can be calculated as follows, according to the classical Chapman-Jouguet theory [34]:

$$P_0 = \frac{\rho_0 V_d^2}{2(\gamma + 1)} \left( \frac{d_c}{d_b} \right)^{2m} \left( \frac{l_c}{l_b} \right)^m n, \quad (9)$$

where,  $P_0$ ,  $\rho_e$ ,  $V_d$ , and  $\gamma$  are average initial pressure, density, detonation velocity, and isentropic index of explosive,  $d_c$  and  $d_b$  are diameter of explosive and borehole, respectively,  $l_c$  and

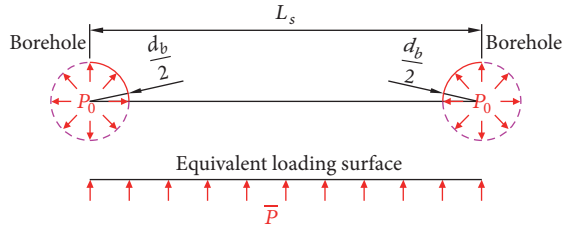


FIGURE 6: Equivalent application of blasting load.

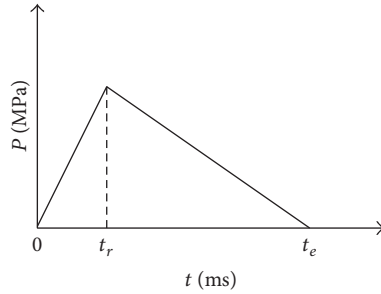


FIGURE 7: Blasting load applied to excavation contour. (Note. Peak load at  $t_r$  is 53.6 MPa, and  $t_r = 2.3$  ms and  $t_e = 17.0$  ms, as calculated according to Lu et al. [24].)

$l_b$  are length of borehole and explosive, respectively, and  $l_c = l_b$  in shallow borehole blasting.  $m$  and  $n$  are calculation parameters for loading and should be 3 and 10 for this case.

In standard blasting design, the diameter of boreholes and spacing have the following relationship:

$$L_s = 30d_b. \tag{10}$$

Therefore equivalent blasting load on the line joining holes, shown in Figure 6, is

$$\bar{P} = \delta = \frac{P_0}{30}. \tag{11}$$

And blasting load applied on to the excavation contour is simplified to triangle load as in Figure 7.

All elements are 8-node elements, in average size of 1 m. In this numerical calculation, explicit equations (as (3)) are calculated with Ls-dyna program. And a sensitivity analysis has been carried out on element size, with the same excavation situation of CD method blasting excavation 37 m away. It is indicated that when element size varies from 1 m to 0.2 meters, calculation time is increased by almost 12 times, to 43.5 hours, while vibration response waveforms on monitoring points are quite similar, peak vibration velocity difference is within 2%. Waveforms calculated with different element sizes are compared in Figure 8.

### 4. Calculation Results and Discussion

4.1. Evaluation Standards. Different countries usually have their own criteria about blasting vibration, such as those specified in AS2187 (Australia, 1983) and DIN 4150 (GOS,

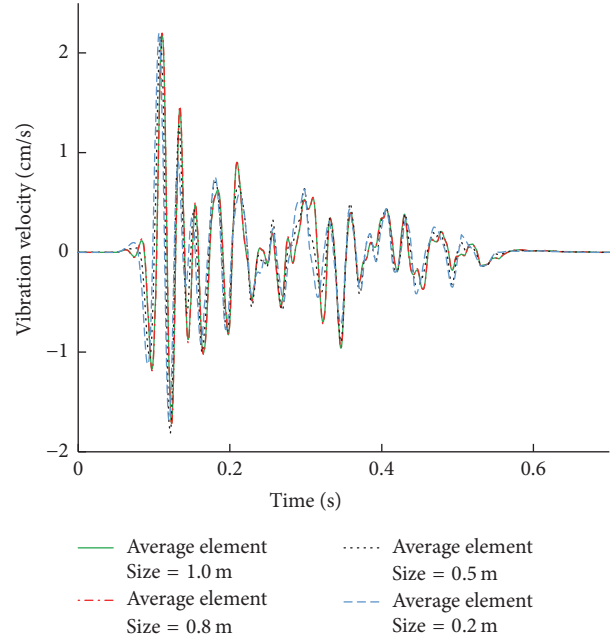


FIGURE 8: Waveforms calculated with different element sizes.

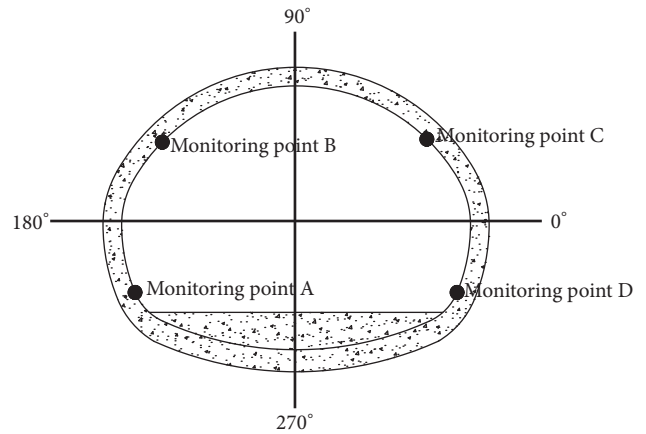


FIGURE 9: Monitoring points and division on lining of NBB tunnel.

1984). But these standards in developed countries are not updated frequently, while Chinese standard is updated every few years [24]. In most standards vertical vibration velocity is required below 3~8 mm, when frequency is below 10 Hz. According to Chinese “Safety Regulation for Blasting” [32], the vibration limitation for tunnels is listed below in Table 2. And relative safety criteria for lining structures are listed in Table 3.

4.2. Vibration on Lining of NBB Tunnel. As the vertical vibration velocity of short footage blasting is larger than the horizontal [35, 36], which conforms calculation result, the vertical vibration velocity is mainly investigated. Furthermore, since concrete is more likely to be damaged by tensile stress, the analysis is focusing on the maximum stress on the lining.

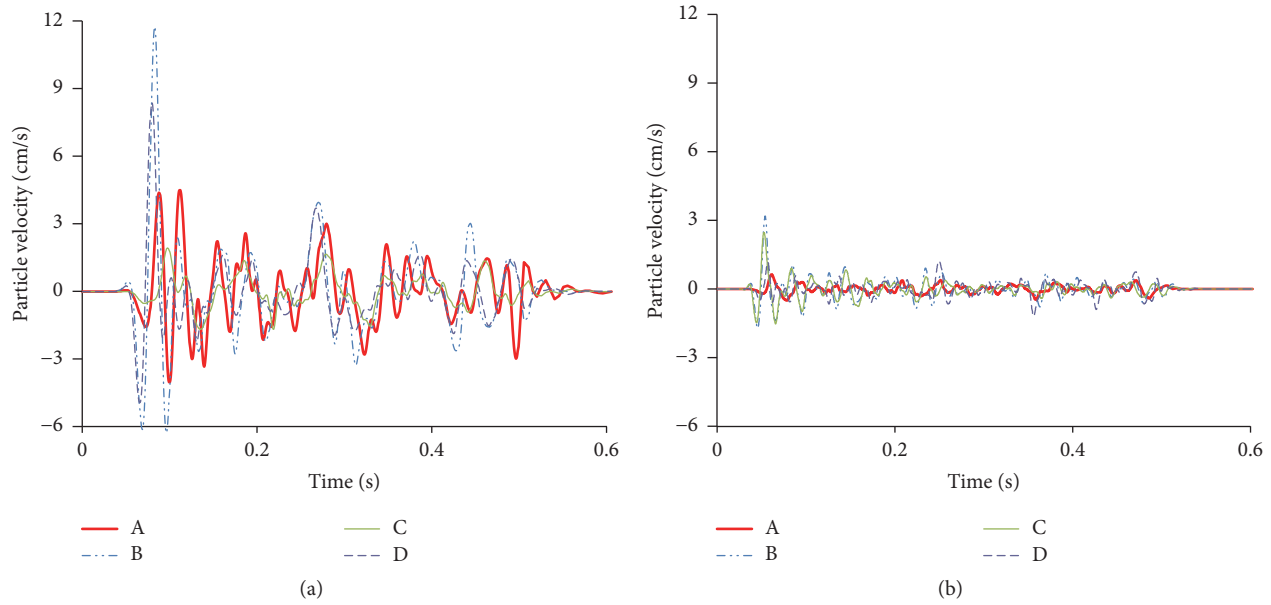


FIGURE 10: Vertical vibration response on monitoring points induced by full-face blasting (a) and CD method (b).

TABLE 2: Safety vibration limitation for tunnels and shafts in China [32].

Structure type	Allowable safety peak particle velocity/cm/s		
	$f \leq 10$ Hz	$10 \text{ Hz} \leq f \leq 50$ Hz	$f > 50$ Hz
Hydraulic tunnels	7~8	8~10	10~15
Traffic tunnels	10~12	12~15	15~20
Mining shafts	15~18	18~25	20~30

In order to make the analysis more clear, the lining of NBB tunnel is divided into angles and four monitoring points (MP) are focused on as shown in Figure 9, for vertical vibration and dynamic stress response.

Figure 10 shows vertical vibration on lining of NBB tunnel at four different monitoring points, induced by full-face excavation (Figure 10(a)) and Part ③ (shown in Figure 4) of CD method (Figure 10(b)) individually. The blasting source distance in both situations is 37 m from tunnel axis. From Figure 10, it is obvious that largest vibration occurs at MP B in both situations, which is in accordance with the vibration attenuated via distance. However, the peak vibration values induced by full-face blasting or CD method are quite different, with the former being 2.5 times larger. Actually, in blasting operation of Part ③, the blasting contour is no longer a full area, since the left half of the tunnel section is already excavated. Therefore, the perimeters of the blasting counters in two situations are quite different in length, thus making the explosive weight detonated in one delay much less (approximately 40%) than full-face blasting. On the other hand, the free surface on Part ③ is also influencing the propagation of blasting wave, resulting in less vibration velocity on lining of underlying tunnel. It is also interesting that Figure 10 revealed different wave frequencies

in both situations, as well as a slight difference in vibration duration.

Comparison shows very large difference in vibration response on lining of the underlying tunnel and suggests that CD method is much safer to adjacent structure.

**4.3. Dynamic Stress Variation.** Although vibration is considered as evaluation value in most standards, it is tensile stress that controls fundamental damage in dynamical process. Analysis is conducted on dynamical subsidiary stress, as shown in Figure 11.

Comparison between Figures 11(a) and 11(b) also shows advantage of CD method, since the peak value of dynamic tensile stress is approximately only 25% of that induced by full-face blasting. However, different from vibration distribution, the maximum tensile stress on section contour is at MP C. In the radar graph of max tensile stress induced by full-face blasting, shown in Figure 12, the peak tensile stress is located at approximately  $65^\circ$  angle. Actually, this phenomenon is caused by special strata condition of this area, where the subway tunnel is in highly weathered basalt while the underlying tunnel is in intermediate weathered basalt, causing a ratio of 0.075 versus 9 in deformation modulus. This large difference in deformation modulus has influenced the propagation of blast-induced stress wave; thus stress wave reflects at strata boundary and overlaps at MP C with later wave propagating directly from the source.

This process is obvious by observing maximum principle stress distribution versus time, as shown in Figure 13. In the early stage of dynamic stress distribution, the peak tensile stress is at angle of about  $270^\circ$  and then goes to angle of about  $330^\circ$ . But the peak value is about 156.5 ms after detonation. In early stages, tensile stress is not large and is below 1 MPa most of the time. However, the peak value is 1.283 MPa, which just

TABLE 3: Relevant safety criteria for tunnel lining structures [32].

Structure type	Allowable safety peak particle velocity/cm/s		
	$1 d \leq CA \leq 3 d$	$3 d \leq CA \leq 7 d$	$7 d \leq CA \leq 28 d$
Concrete	1.2	1.2~5.0	5.0~7.0
Shot concrete		5.0	
Grouting	1	1.5	2~2.5
Bolts and anchor cables	1	1.5	5~7

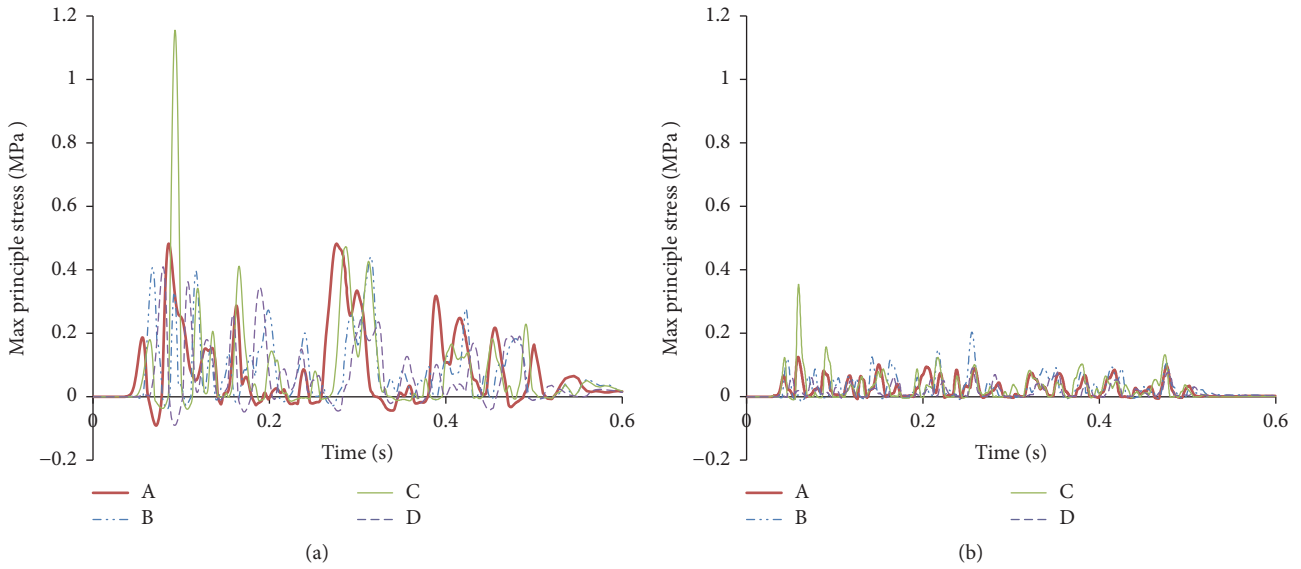


FIGURE 11: Maximum principle stress response on monitoring points induced by full-face blasting (a) and CD method (b).

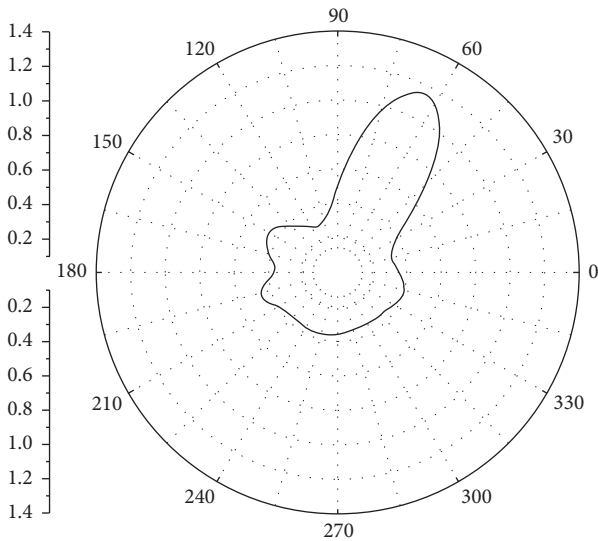


FIGURE 12: Distribution of peak tensile stress on underlying tunnel induced by full-face blasting.

might cause tensile damage on the lining. Therefore, full-face blasting might be able to apply approximately 40 m beyond

the axis of underlying tunnel, with further confirmation from field blasting tests.

Tensile stress distribution variation induced by CD method 25 m away through time is shown in Figure 14, which shows similar peak tensile stress distribution to Figure 13. However, although blasting distance is 33% smaller, the peak tensile stress is only about 50% of that induced by full-face blasting excavation.

More calculations have been carried out to determine a safe distance for CD method and results are listed in Table 4. It is revealed that, even 37 m beyond the blasting source, the vibration induced by full-face excavation reached 12.4 cm/s, which exceeds allowable value of vibration within relevant frequency. So it is reasonable to adopt CD method, in which tunnel section is divided into 4 parts with smaller contour and thus would cause less blasting load on the excavation contour in each blasting operation. Optimized blasting source distance to NBBT should be larger than 12 m and smaller than 25 m.

### 5. Conclusion

Considering the problem in subway tunneling in mountainous area Southwest China, the number 3 subway construction

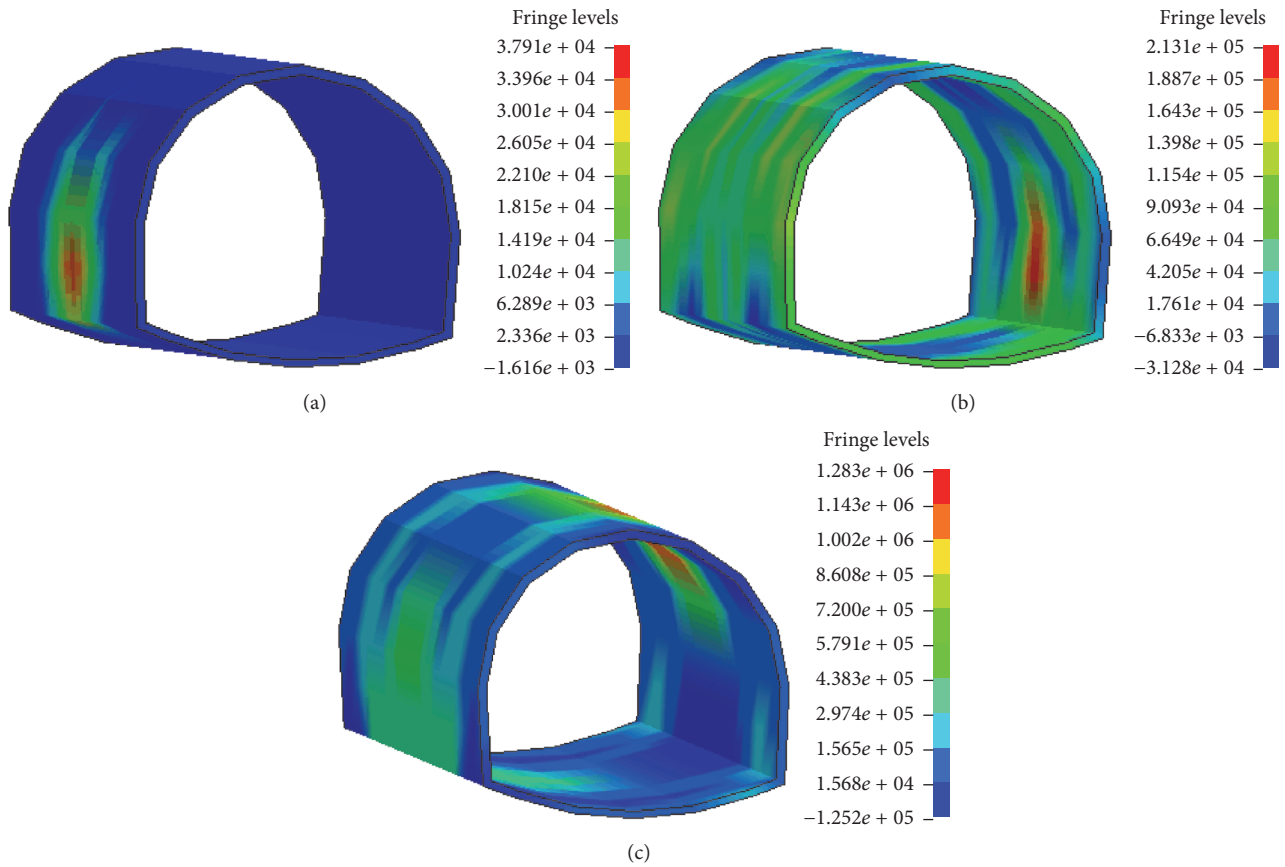


FIGURE 13: Maximum principle stress distribution variation induced by full-face blasting 37 m away. (Note. Positive value for tensile stress. (a) Time = 47.5 ms, (b) time = 91.5 ms, and (c) time = 156.5 ms.)

TABLE 4: Dynamic response on NBBT lining induced by tunneling.

	Full-face excavation		CD method excavation	
Blasting source distance/m	37	37	25	12
Maximum peak tensile stress/MPa	1.28	0.45	0.63	1.83
Maximum peak particle velocity/cm/s	12.6	3.5	5.8	15.8
Frequency at peak particle velocity/Hz	35.7	54.3	61.1	63.9

in Kunming is taken as a case study. In order to evaluate the potential damage or failure on the existing underlying tunnel, calculations have been carried out with Dynamic Finite Element Method. Following conclusions can be drawn.

Drill-and-blast method would cause different extent of vibration to underlying tunnel depending on specific method and distance between blasting source and object tunnel. Vibration velocity induced by CD method to the underlying tunnel axis is only 28% of that caused by full-face blasting with same distance.

Peak value of tensile stress induced by full-face blasting is capable of causing lining failure at approximately 37 m beyond the underlying tunnel axis. However, CD method has shown much advantage, since blasting within 25 m is also considered safe to the underlying tunnel. But when the blasting source is as near as 12 m beyond the underlying

tunnel, the CD method is no longer safe, which still should be confirmed by field blasting tests.

Peak vibration is located on the lining facing the blasting source, while peak tensile stress is on the other side of the contour due to the reflection of stress wave on strata boundary. It is also the key location to be monitored during field blasting tests.

### Conflicts of Interest

The authors declare that they have no conflicts of interest.

### Acknowledgments

This work was supported by the National Natural Science Foundation of China (51378500 and 51609183) and the Key

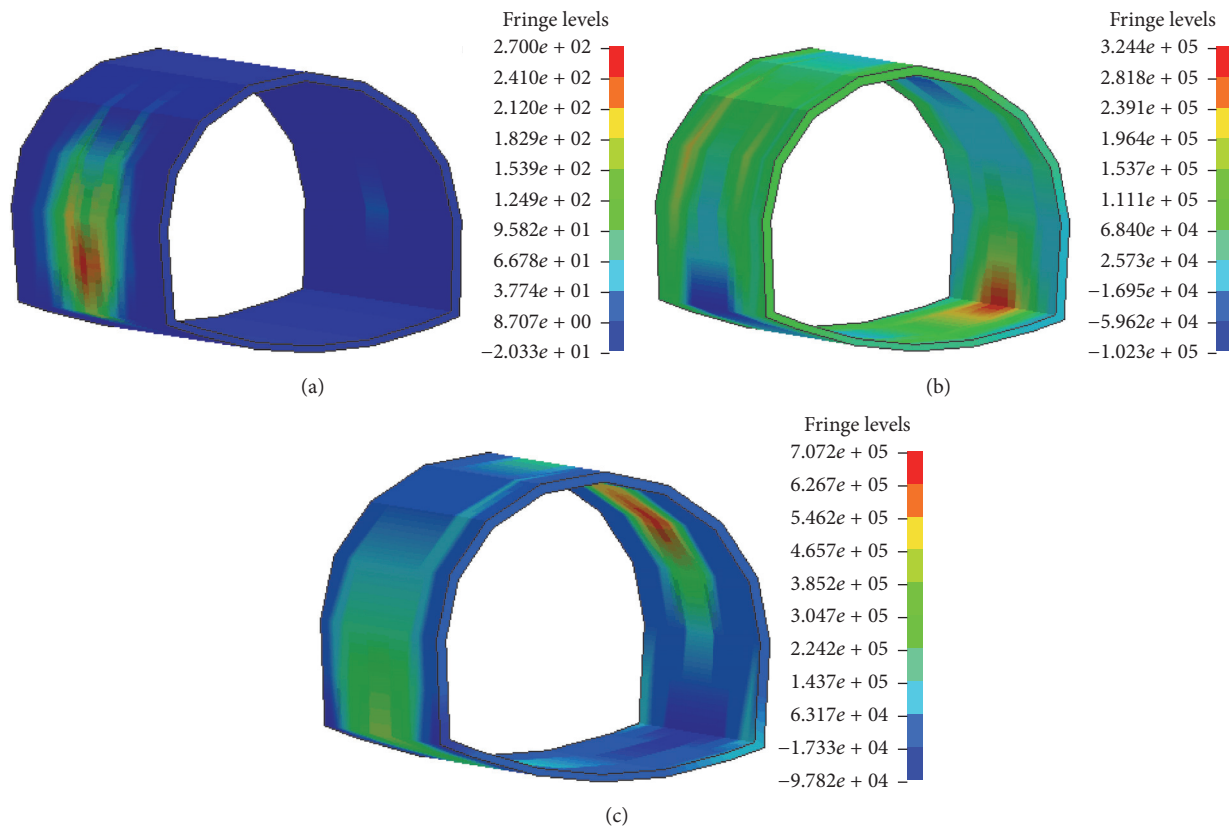


FIGURE 14: Maximum principle stress distribution variation induced by CD method 25 m away. (Note. Positive value for tensile stress. (a) Time = 47.5 ms, (b) time = 91.5 ms, and (c) time = 156.5 ms.)

Natural Science Foundation of Hubei Province of China (2015CFA136).

## References

- [1] S.-L. Shen, H.-N. Wu, Y.-J. Cui, and Z.-Y. Yin, "Long-term settlement behaviour of metro tunnels in the soft deposits of Shanghai," *Tunnelling and Underground Space Technology*, vol. 40, pp. 309–323, 2014.
- [2] Y. Tan, X. Li, Z. Kang, J. Liu, and Y. Zhu, "Zoned excavation of an oversized pit close to an existing metro line in stiff clay: case study," *Journal of Performance of Constructed Facilities*, vol. 29, no. 6, article 04014158, 2015.
- [3] Z. Guo and N. H. M. Wilson, "Assessing the cost of transfer inconvenience in public transport systems: a case study of the London Underground," *Transportation Research Part A: Policy and Practice*, vol. 45, no. 2, pp. 91–104, 2011.
- [4] M. J. M. Maynar and L. E. M. Rodríguez, "Discrete numerical model for analysis of earth pressure balance tunnel excavation," *Journal of Geotechnical and Geoenvironmental Engineering*, vol. 131, no. 10, pp. 1234–1242, 2005.
- [5] M. I. Wallace and K. C. Ng, "Development and application of underground space use in Hong Kong," *Tunnelling and Underground Space Technology*, vol. 55, pp. 257–279, 2016.
- [6] F. Ji, J. Lu, Y. Shi, and C. Zhou, "Mechanical response of surrounding rock of tunnels constructed with the TBM and drill-blasting method," *Natural Hazards*, vol. 66, no. 2, pp. 545–556, 2013.
- [7] H.-N. Wu, S.-L. Shen, S.-M. Liao, and Z.-Y. Yin, "Longitudinal structural modelling of shield tunnels considering shearing dislocation between segmental rings," *Tunnelling and Underground Space Technology*, vol. 50, pp. 317–323, 2015.
- [8] B. Li, L. Wu, C. Xu, Q. Zuo, S. Wu, and B. Zhu, "The detection of the boulders in metro tunneling in granite strata using a shield tunneling method and a new method of coping with boulders," *Geotechnical and Geological Engineering*, vol. 34, no. 4, pp. 1155–1169, 2016.
- [9] J. Du, R. He, and V. Sugumarán, "Clustering and ontology-based information integration framework for surface subsidence risk mitigation in underground tunnels," *Cluster Computing*, vol. 19, no. 4, pp. 2001–2014, 2016.
- [10] R. Liang, T. Xia, Y. Hong, and F. Yu, "Effects of above-crossing tunnelling on the existing shield tunnels," *Tunnelling and Underground Space Technology*, vol. 58, pp. 159–176, 2016.
- [11] J. C. Ni and W.-C. Cheng, "Characterising the failure pattern of a station box of taipei rapid transit system (TRTS) and its rehabilitation," *Tunnelling and Underground Space Technology*, vol. 32, pp. 260–272, 2012.
- [12] Y.-S. Xu, Y. Yuan, S.-L. Shen, Z.-Y. Yin, H.-N. Wu, and L. Ma, "Investigation into subsidence hazards due to groundwater pumping from Aquifer II in Changzhou, China," *Natural Hazards*, vol. 78, no. 1, pp. 281–296, 2015.
- [13] D.-J. Ren, S.-L. Shen, W.-C. Cheng, N. Zhang, and Z.-F. Wang, "Geological formation and geo-hazards during subway construction in Guangzhou," *Environmental Earth Sciences*, vol. 75, no. 11, pp. 1–14, 2016.

- [14] J. X. Lai, H. B. Fan, J. X. Chen, J. L. Qiu, and K. Wang, "Blasting vibration monitoring of undercrossing railway tunnel using wireless sensor network," *International Journal of Distributed Sensor Networks*, vol. 2015, Article ID 703980, 7 pages, 2015.
- [15] S. Lu, C. Zhou, N. Jiang, and X. Xu, "Effect of excavation blasting in an under-cross tunnel on airport runway," *Geotechnical and Geological Engineering*, vol. 33, no. 4, pp. 973–981, 2015.
- [16] H. Ma, H. Wang, C. He, Z. Zhang, and X. Ma, "Influences of Blasting sequence on the vibration velocity of surface particles: a case study of qingdao metro, China," *Geotechnical and Geological Engineering*, vol. 35, no. 1, pp. 485–492, 2017.
- [17] P. C. Xu, Q. Dong, X. P. Li, and Y. Luo, "Influence research of underground caverns blasting excavation on excavation damage zone of adjacent cavern," *Advanced Materials Research*, vol. 838-841, pp. 901–906, 2014.
- [18] J. Yang, W. Lu, Q. Jiang, C. Yao, S. Jiang, and L. Tian, "A study on the vibration frequency of blasting excavation in highly stressed rock masses," *Rock Mechanics and Rock Engineering*, vol. 49, no. 7, pp. 2825–2843, 2016.
- [19] H. B. Zhao, Y. Long, X. H. Li, and L. Lu, "Experimental and numerical investigation of the effect of blast-induced vibration from adjacent tunnel on existing tunnel," *KSCE Journal of Civil Engineering*, vol. 20, no. 1, pp. 431–439, 2016.
- [20] N. Zhang, X. Fang, L. Fan, K. Ding, Z. Hua, and P. University, "The influence of initiation sequences on blasting vibration in millisecond blasting," *Explosive Materials*, 2013.
- [21] Q. Dong, X. Li, and H. Zhao, "Study on damage characteristic of underground cavern blasting excavation based on dynamic damage constitutive model," in *Proceedings of the International Conference on Advances in Energy, Environment and Chemical Engineering*, Changska, China, September 2015.
- [22] J.-H. Shin, H.-G. Moon, and S.-E. Chae, "Effect of blast-induced vibration on existing tunnels in soft rocks," *Tunnelling and Underground Space Technology*, vol. 26, no. 1, pp. 51–61, 2011.
- [23] X. Xia, H. B. Li, J. C. Li, B. Liu, and C. Yu, "A case study on rock damage prediction and control method for underground tunnels subjected to adjacent excavation blasting," *Tunnelling and Underground Space Technology*, vol. 35, pp. 1–7, 2013.
- [24] W.-B. Lu, Y. Luo, M. Chen, and D.-Q. Shu, "An introduction to Chinese safety regulations for blasting vibration," *Environmental Earth Sciences*, vol. 67, no. 7, pp. 1951–1959, 2012.
- [25] G. Abate and M. R. Massimino, "Numerical modelling of the seismic response of a tunnel–soil–aboveground building system in Catania (Italy)," *Bulletin of Earthquake Engineering*, vol. 15, no. 1, pp. 469–491, 2017.
- [26] Y. Li, X. Jin, Z. Lv, J. Dong, and J. Guo, "Deformation and mechanical characteristics of tunnel lining in tunnel intersection between subway station tunnel and construction tunnel," *Tunnelling and Underground Space Technology*, vol. 56, pp. 22–33, 2016.
- [27] H. Liu, P. Li, and J. Liu, "Numerical investigation of underlying tunnel heave during a new tunnel construction," *Tunnelling and Underground Space Technology*, vol. 26, no. 2, pp. 276–283, 2011.
- [28] J. Shi, C. W. W. Ng, and Y. Chen, "Three-dimensional numerical parametric study of the influence of basement excavation on existing tunnel," *Computers and Geotechnics*, vol. 63, pp. 146–158, 2015.
- [29] G. M. Gaspari, O. Zanoli, and M. Pescara, "Three-dimensional modelling of the tunnel intersections in weak rock mass on the kadikoy-kartal metro line of istanbul," in *Proceedings of the European Rock Mechanics Symposium, EUROCK 2010*, pp. 491–494, June 2010.
- [30] B. Mobaraki and M. Vaghefi, "Effect of the soil type on the dynamic response of a tunnel under surface detonation," *Combustion, Explosion and Shock Waves*, vol. 52, no. 3, pp. 363–370, 2016.
- [31] N. E. Rebello, R. Shivashankar, and V. R. Sastry, "Response of strata and buildings to blast induced vibrations in the presence and absence of a tunnel," *Geotechnical and Geological Engineering*, vol. 34, no. 4, pp. 1013–1028, 2016.
- [32] Standardization Administration of China. Chinese National Standard GB6722-2014: Safety regulation for blasting. 2015.
- [33] J. Dai, *Dynamic Behaviors and Blasting Theory of Rock*, Metallurgical Industry Press, Beijing, China, 2002.
- [34] M. Saif, W. Wang, A. Pekalski, M. Levin, and M. I. Radulescu, "Chapman-Jouguet deflagrations and their transition to detonation," *Proceedings of the Combustion Institute*, vol. 36, no. 2, pp. 2771–2779, 2015.
- [35] J.-H. Hu, X.-J. Yan, K.-P. Zhou, and L.-H. He, "Study on the deformation and safety in the process of shallow buried tunnel construction," in *Proceedings of the 2009 International Conference on Engineering Computation, ICEC 2009*, pp. 123–126, May 2009.
- [36] L. Wang and H. L. Wang, "Influence of different direction vibration peak velocity of tunnel blasting on building," *Blasting*, vol. 29, no. 4, pp. 6–9.

## Research Article

# Vibration of a Cylindrical Tunnel under a Centric Point-Source Explosion

Yuetang Zhao,<sup>1,2</sup> Cheng Chu,<sup>1,2</sup> Anastasios Vafeidis,<sup>3</sup> and Jie Li<sup>1,2</sup>

<sup>1</sup>College of Defense Engineering, PLA University of Science and Technology, Nanjing, Jiangsu 210007, China

<sup>2</sup>State Key Laboratory of Disaster Prevention & Mitigation of Explosion & Impact, PLA University of Science and Technology, Nanjing, Jiangsu 210007, China

<sup>3</sup>Laboratory of Mechanics and Materials, Polytechnic School, Aristotle University of Thessaloniki, Thessaloniki, Greece

Correspondence should be addressed to Cheng Chu; iamcci@163.com

Received 15 March 2017; Accepted 30 April 2017; Published 18 June 2017

Academic Editor: Abdul Qadir Bhatti

Copyright © 2017 Yuetang Zhao et al. This is an open access article distributed under the Creative Commons Attribution License, which permits unrestricted use, distribution, and reproduction in any medium, provided the original work is properly cited.

Underground tunnels are vulnerable to terrorists' bombing attacks, which calls for studies on tunnel's response to internal explosive loading. In this paper, the dynamic response of a cylindrical tunnel to an ideal centric point explosion was treated as an axisymmetric 2-dimensional problem, in which the tunnel was modeled with a continuous anisotropic shell, while the ground medium's effect was accounted for with linear elastic Winkler springs and the explosive loading described by a temporal and spatial function. The governing equation of the motion is a fourth-order partial differential equation, for which a numerical method combining finite difference with the implicit Newmark- $\beta$  method was adopted. This method avoided complicated integral transform and numerical inverse transformation, thus allowing efficient parameter study. The maximum radial displacement was found on the circle of the center of explosive, where hoop stress is the maximum principal stress. The anisotropy showed little influence on maximum hoop stress. Within the range of ground medium's modulus, minor influence on maximum hoop stress was incurred. This research may be helpful to hazard assessment and protective design for some critical subway tunnels.

## 1. Introduction

In recent years, increased terrorist bombing attacks on subway system have been observed [1–3]; the most recent one was the notorious 2017 Saint Petersburg subway bombing [4]. Besides threats from terrorism, accidental explosion may be another potential hazard. The aftermath of an internal blast may include casualties and structural damage [5]. A deformation beyond threshold may cause the collapse of the structure. Also many of these tunnels may be built across beneath water bodies, such as these in New York, London, Shanghai, and Paris. A blast may breach or tear apart the wall of the tunnel lining and cause a flooding, for which the aftermath may be intractable [6, 7]. Thus the resistance of a tunnel structure to an internal blast should be studied.

In the designing of tunnels, the effects from some natural hazards and man-made disturbances such as seismic events and fires are generally considered, whereas blast loads are

rarely considered for civilian tunnels [8]. Therefore, under the background of increasing probability of terrorist bombing attacks, safety of municipal tunnels under explosions needs more attention.

So far experimental study on tunnel's response to internal explosion can be scarcely found in literature. Preece et al. [9] and Liu and Nezili [10] conducted a series of scale model tests using centrifuge facility, where the tunnel was simulated by monolithic aluminum tube. Their results may not be applicable to reinforced concrete tunnel since mechanical behaviors of metals like aluminum are quite different from that of reinforced concrete. Bonalumi et al. [11] conducted internal blast tests on a concrete pipe embedded in soft soil purposed to study internal blast loading in cylindrical enclosure, whereas the response of structure is not accounted for. Zhao et al. [12] carried out a few full-scale tests on staggered segmental tunnel's response to internal point-source explosions, concluding that damage mainly concentrated in

joint areas; however, no theoretical study was made on the tests.

Tunnels' response to blast loading was more studied with finite element modeling. Based on the results of numerical simulation with ABAQUS, Colombo et al. [13, 14] plotted pressure-impulse (P-I) diagrams, which is also called iso-damage diagram for segmental tunnels in case of an internal explosion. This provided a useful tool for damage assessment and antiexplosion design of segmental tunnel lining. However, their results were obtained on the presumption of an axisymmetric plane problem, that is, the blast loading keeps constant along the tunnel axis, which is unlikely the true case. Choi et al. [15, 16] did nonlinear finite element analyses on internal explosion of tunnels and evaluated the vulnerability of lining structure, only concluding with some descriptive remarks. Yu et al. [17] also simulated internal explosion effects on tunnel in soil, and the influences from the soil and charge location were analyzed; however, there were no clear conclusions. These FEM analyses allowed for reproduction of the process involving blast wave propagation and its interaction with the tunnel and the structure's response. However, these researches rely much on commercial finite element code, and the validity of the results depends on the material models' parameters they used. Until now, no validation against any test results can be found in literature. Also it is not efficient to do parameter studies when the model scale is big.

As for theoretical investigation, a tunnel's response to internal blast loads is generally treated as an axisymmetric plane strain problem, where the blast loading is simplified as uniformly distributed loading which keeps constant along the axial direction, and the tunnel is modeled with continuous isotropic thin shell [18–20], but this can hardly be the real case since the explosion could not be a centric infinite line charge detonation. Among those theoretical studies, Gao et al. [21] studied a 3D problem of point-source explosion's effects on a long straight cylindrical tunnel in soil. However, the method includes complicated integral transform and numerical inverse transforms, which makes their research inconvenient for engineering use. Another problem in their research is that the orthogonal anisotropy of tunnel structure, that is, the difference in mechanic behavior between the circumferential and axial directions, which might be important in its overall dynamic response, was seldom accounted for.

In this paper a 3-dimensional problem of a long cylindrical thin-walled tunnel under a point-source explosion was studied, where both the lining structure and the blast loading were described more realistically. To begin with, a description of the blast loading on the inner wall of the structure with simplified spatial and temporal function was elaborated. Then the tunnel structure was modeled as a long straight anisotropic cylindrical thin shell, of which the governing equation of its motion was established on the basis of classical theory of shell. Thereafter a solving method combining finite difference method and Newmark- $\beta$  implicit integration method was developed and some numerical results of shell's dynamic response and parameter study were displayed and discussed. At last some concluding remarks were given on the basis of the analyses and discussions. The method developed

in this paper may aid in both blast hazard assessment and protective design for some critical part of subway tunnel systems.

## 2. The Description of Blast Loads due to a Centric Point-Source Explosion

Considering a point charge of explosive locating on the centre axis. After detonation, the blast wave's propagation and its loading effects can be categorized into two phases. First is a period of spherical pressure wave propagation and its interaction with the structure in the near-field. After a distance of 4~6 times' radii from the explosive centre, it evolves into second phase; that is, after complicated interactions in first phase the blast wave propagates along tunnel axis like a 1-dimensional plane wave [22, 23]. Therefore, the loading on the tunnel from inner explosion is quite complicated.

Blast wave with pressure of  $p(x, t)$  propagates at a velocity of  $D$  along the inner surface of a cylindrical shell with a certain length; the overpressure of incident blast wave could be described by a temporal and spatial function [21] as follows:

$$p(x, t) = \Delta P_\phi e^{-\alpha t - \beta|x|}, \quad (1)$$

where  $\alpha$ ,  $\beta$  are attenuation parameters of blast waves with respect to time and space, respectively; the centric point source of explosion is chosen as the origin of the coordinate system;  $\Delta P_\phi$  is overpressure of incident blast wave, which could be estimated with empirical equation given by M. A. Sadovskii [24]:

$$\Delta P_\phi = 10g \left( \frac{7}{\bar{Z}^3} + \frac{2.7}{\bar{Z}^2} + \frac{0.84}{\bar{Z}} \right), \text{ kPa}, \quad (2)$$

where  $\bar{Z} = Z/W^{1/3}$  is scaled distance, with  $Z$  and  $W$  denoting stand-off distance (m) to the centre of explosive charge and weight of the charge (kg).

Knowing incident blast wave loading in confined space of tunnel's enclosure, the effective loading acts on inner wall of the lining due to the wave's reflection, that is, reflected overpressure can be calculated with the following empirical formula for normal reflection [25]:

$$\Delta P_r = 2\Delta P_i + \frac{6\Delta P_i^2}{\Delta P_i + 0.7P_0}, \quad (3)$$

where  $\Delta P_i$  is incident overpressure and  $P_0$  is ambient atmospheric pressure.

Pokrovsky [24] proved by experimental data that when incidence pressure is smaller than 0.3 MPa, reflected pressure of an oblique reflection can be calculated by the formula for normal reflection.

## 3. Governing Motion Equation and Its Solution

Taking account of the stiffness difference between circumferential and axial directions, the circular tunnel lining

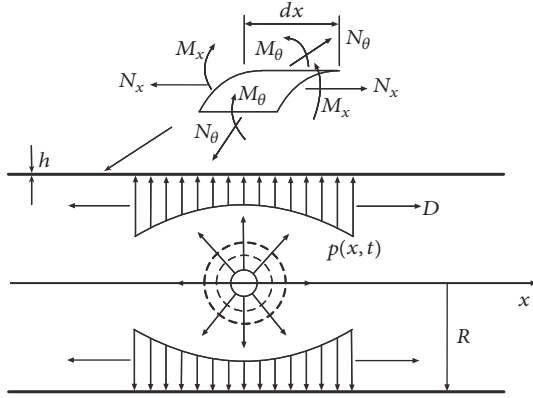


FIGURE 1: A cylindrical shell under blast loading from a centric point-source explosion.

structure could be treated as an anisotropic cylindrical shell, as graphically shown in Figure 1, and the ground resistance effects are modeled with radial linear elastic Winkler springs.

**3.1. Governing Equation of Motion.** As aforementioned, an explosive charge is detonated on centre axis of a circular tunnel with radius of  $R$ . The lining undergoes radial deflection fluctuation under the drive of radial explosive loading. For the axisymmetric problem of a shell's radial vibration, imagine cutting a unit element for forces' analysis, and all the forces acting on this unit element are diagramed in Figure 1, where  $M_x$  denotes axial moment acting on the shell surface,  $M_\theta$  denotes circumferential moment,  $N_\theta$  denotes circumferential force, and  $N_x$  denotes axial force. Due to the axisymmetry, other forces and moments vanish.

For elastic soils the lining-ground interaction could be described by linear elastic Winkler spring; therefore the resistance force is

$$f_R = k_s u(x, t) R dx d\theta, \quad (4)$$

where  $k_s$  is dilatational stiffness of ground springs, for which Penzien [26] gave the method of calculation as

$$k_s = \frac{E_s}{2R(1 + \nu_s)}, \quad (5)$$

where  $E_s$  and  $\nu_s$  are Young's modulus and Poisson's ratio of the ground medium. Soils' damping in structure-soil interaction was neglected for the simplicity of the problem, also because this approach leads to bigger amplitude of response, thus making the assessment more conservative.

Considering the balance equation of all the forces acting on the unit element and projecting all the forces to radial direction we can get

$$\begin{aligned} \rho h R d\theta dx \frac{\partial^2 w}{\partial t^2} + \frac{\partial N_x}{\partial x} dx R d\theta + 2N_\theta dx \sin \frac{d\theta}{2} \\ = P(x, t) R d\theta dx - k_s w R d\theta dx, \end{aligned} \quad (6)$$

where  $w$  denotes radial displacement of the shell.

Taking account of  $\sin(d\theta/2) \cong d\theta/2$  and  $\partial N_x / \partial x = -\partial^2 M_x / \partial x^2$  and simplifying (5) we reach the following:

$$\rho h \frac{\partial^2 w}{\partial t^2} + \frac{\partial^2 M_x}{\partial x^2} + \frac{1}{R} N_\theta = p(x, t) - k_s w. \quad (7)$$

Suppose  $E_x$ ,  $E_\theta$ ,  $\nu_x$ , and  $\nu_\theta$  are axial and circumferential elastic module and passion ratio of anisotropic shell material, respectively;  $\rho$  is the material's mass density.

According to classical theory of shell [27] we have

$$\begin{aligned} N_\theta &= K \gamma \frac{w}{R}; \\ M_x &= -D \frac{\partial^2 w}{\partial x^2}; \\ M_\theta &= -\nu_\theta D \frac{\partial^2 w}{\partial x^2}; \\ N_x &= \nu_x N_\theta, \end{aligned} \quad (8)$$

where  $\gamma = E_\theta / E_x = \nu_x / \nu_\theta$ ,  $K = E_x h / (1 - \nu_x^2 / \gamma)$ , and  $D = E_x h^3 / 12(1 - \nu_x^2 / \gamma)$ .

Also maximum stress can be calculated as follows:

$$\begin{aligned} \sigma_{x \text{ Max}} &= \frac{M_x}{W_x} + \frac{N_x}{h}, \\ \sigma_{\theta \text{ Max}} &= \frac{M_\theta}{W_\theta} + \frac{N_\theta}{h} \end{aligned} \quad (9)$$

$$W_x = W_\theta = \frac{h^2}{6}.$$

Substituting (8) into (6) we get forced vibration equation of a thin cylindrical shell:

$$\begin{aligned} D \frac{\partial^4 w}{\partial x^4} + \rho h \frac{\partial^2 w}{\partial t^2} + K' w = p(x, t), \\ K' = \left( \frac{K \gamma}{R^2} + k_s \right). \end{aligned} \quad (10)$$

At the beginning time  $t = 0$ , the structure is stationary before the loading takes effects; therefore, the system has initial conditions as

$$w = \dot{w} = 0, \quad \text{when } t = 0. \quad (11)$$

Supposing that the shell is straight and infinitely long, however it is unrealistic; we simply take a far enough boundary that within the period of computation keeps stationary. Here we choose the boundary condition at  $x = \pm L$  where  $L \gg R$  as follows:

$$\begin{aligned} w &= 0; \\ M_x &= 0; \\ N_x &= 0. \end{aligned} \quad (12)$$

Together with (11) the problem becomes a system of mixed initial initial conditions and boundary conditions.

3.2. *Solution of the Problem.* In this subsection, a numerical method for solving the problem is explained. With finite difference of 2-order accuracy, the partial derivatives in (10) can be written as follows.

For  $i = 1, 2$ , with forward finite difference

$$\begin{aligned} \frac{\partial^4 w(x_i, t)}{\partial x^4} &= \frac{3w_i - 14w_{i+1} + 26w_{i+2} - 24w_{i+3} + 11w_{i+4} - 2w_{i+5}}{\Delta x^4}. \end{aligned} \quad (13)$$

For  $i = 3, \dots, n-2$ ,

$$\frac{\partial^4 w(x_i, t)}{\partial x^4} = \frac{w_{i+2} - 4w_{i+1} + 6w_i - 4w_{i-1} + w_{i-2}}{\Delta x^4}. \quad (14)$$

For  $i = n-1, n$ , with backward finite difference

$$\begin{aligned} \frac{\partial^4 w(x_i, t)}{\partial x^4} &= \frac{3w_i - 14w_{i-1} + 26w_{i-2} - 24w_{i-3} + 11w_{i-4} - 2w_{i-5}}{\Delta x^4}, \end{aligned} \quad (15)$$

where  $i$  is the index of spatial points.

The initial conditions are

$$\begin{aligned} w(x, t)|_{t=0} &= 0; \\ \frac{\partial w(x, t)}{\partial t} \Big|_{t=0} &= 0; \\ \frac{\partial^2 w(x, t)}{\partial t^2} &= \frac{p(x, t)}{a}; \\ \frac{\partial^2 w(x, t)}{\partial t^2} \Big|_{t=0} &= \frac{p(x, t)}{a} \Big|_{t=0}. \end{aligned} \quad (16)$$

And the boundary condition is

$$w(x, t)|_{x=\pm L} = 0. \quad (17)$$

The unconditionally stable implicit Newmark- $\beta$  method [28] was incorporated into this problem to solve the time integration.

For a general dynamic problem, we have  $[\mathbf{M}][\mathbf{U}'''] + [\mathbf{C}][\mathbf{U}'] + [\mathbf{K}][\mathbf{U}] = [\mathbf{F}]$ , where  $[\mathbf{M}]$ ,  $[\mathbf{U}]$ ,  $[\mathbf{U}']$ ,  $[\mathbf{U}'']$ ,  $[\mathbf{K}]$ ,  $[\mathbf{C}]$ ,  $[\mathbf{F}]$  denote matrix of masses, displacements, velocities, accelerations, stiffness, damping coefficients, and forces.

The finite difference approximations for the Newmark- $\beta$  method can be written as follows:

$$\begin{aligned} u_{i+1} &\approx u_i + \dot{u}_i \Delta t + \left[ \left( \frac{1}{2} - \beta \right) \ddot{u}_i + \beta \ddot{u}_{i+1} \right] \Delta t^2, \\ \dot{u}_{i+1} &\approx \dot{u}_i + [(1 - \gamma) \ddot{u}_i + \gamma \ddot{u}_{i+1}] \Delta t. \end{aligned} \quad (18)$$

If  $\beta = 1/4$  and  $\gamma = 1/2$ , then the Newmark- $\beta$  method is implicit and unconditionally stable, with at least two-order accuracy.

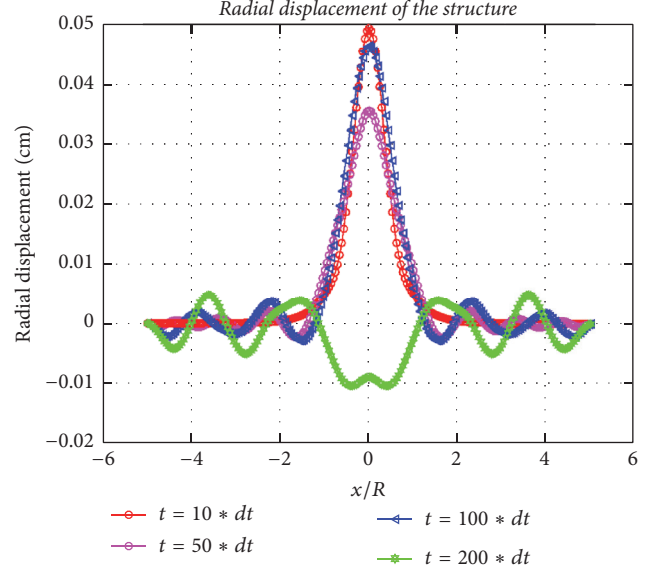


FIGURE 2: Radial displacement of the shell at varied times ( $dt = 0.2$  msec, the curves correspond to 2 msec, 10 msec, 20 msec, and 40 msec).

## 4. Numerical Results and Parameter Studies

4.1. *Basic Numerical Results.* Concerning a numerical calculation case of a cylindrical tunnel shell of reinforced concrete, the parameters are

$$\begin{aligned} R &= 3.0 \text{ m}, \\ h &= 0.3 \text{ m}, \\ L &= 5R, \\ \rho &= 2650 \text{ kg/m}^3, \\ E_x &= 3.45 \times 10^4 \text{ MPa}, \\ \nu_x &= 0.25, \\ \gamma &= \frac{E_\theta}{E_x} = \frac{\nu_x}{\nu_\theta} = 0.75. \end{aligned} \quad (19)$$

Blast wave parameters are  $\Delta P_\phi = 5 \times 10^5$  Pa,  $p_0 = 1 \times 10^5$  Pa,  $\alpha = 30$ , and  $\beta = 0.85$ .

The surrounding ground was at first treated as homogeneous soil, and its Young modulus was taken as  $E_s = 25$  MPa,  $\nu_x = 0.3$ . Later, more stiff soils will also be accounted for as surrounding media in this section.

The results of radial displacement of the shell at varied times is plotted in Figure 2; it can be seen that radial vibration of the shell is symmetrical with respect to the location of charge; that is,  $x = 0$ . The radial expansion of the centre point rises to maximum value very shortly after the acting of the explosive loading and then gradually decays. After it return to its initial location, there is a process of rebounding, that is, vibrating inwards, causing a radial contraction of the shell, which is evident from the curve of displacement at 40 msec.

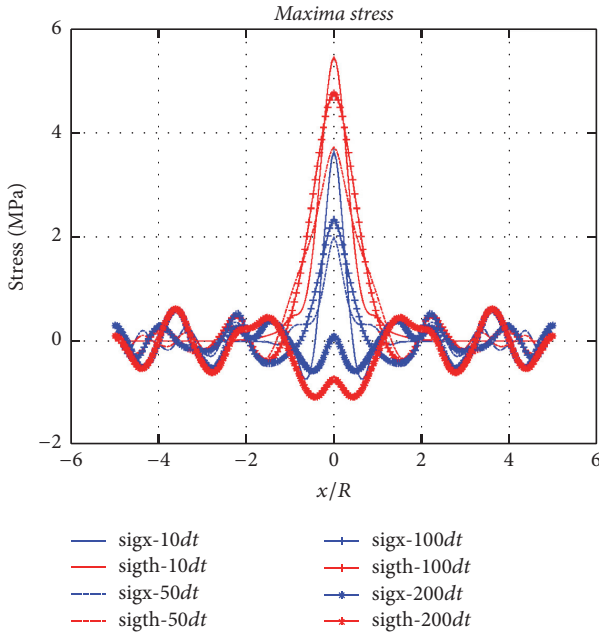


FIGURE 3: Maximum axial stress (blue) and hoop stress (red) at varied times ( $dt = 0.2$  msec, corresponding to 2 msec, 10 msec, 20 msec, and 40 msec).

Therefore, the vibration of the shell includes two different phases, that is, radial expansion and contraction. Also it can be found that as the amplitude of vibration of centre point decays, the nearby points begin to vibrate, and this vibration propagates along the axis in two symmetric directions like a wave.

With the time history of radial displacement of all the points on the shell along the axial direction, the maximal axial stress and hoop stress on all points can be obtained, which are plotted in Figure 3. With both symmetric geometry of structure and the loading condition, it is intuitive to deduce that the stress outcomes are also symmetric. Like the displacement curves, the maximal stress was reached at centre point, which is most close to the explosion. Also the evolution profiles are similar to that of displacement. Notice that on all the points hoop stress values generally outweighed axial stress, no matter during expansion or contraction. This proved that hoop, i.e., circumferential direction of the shell, was more strained during this process.

For clarity, the centre point was given special attention and its axial stress and hoop stress components were compared in Figure 4, which shows clearly that hoop stress and axial stress components fluctuated like two waves synchronically, while the amplitude of the former is always nearly two times as big as the latter one.

4.2. Parameter Studies. Since it is already clear that the most intense response happens on a circle centred by the explosive charge, we only need to check the stress response on centre points.

First the influence of anisotropy of shell, which is accounted for by the coefficient of  $\gamma = E_\theta/E_x = \nu_x/\nu_\theta$ , is

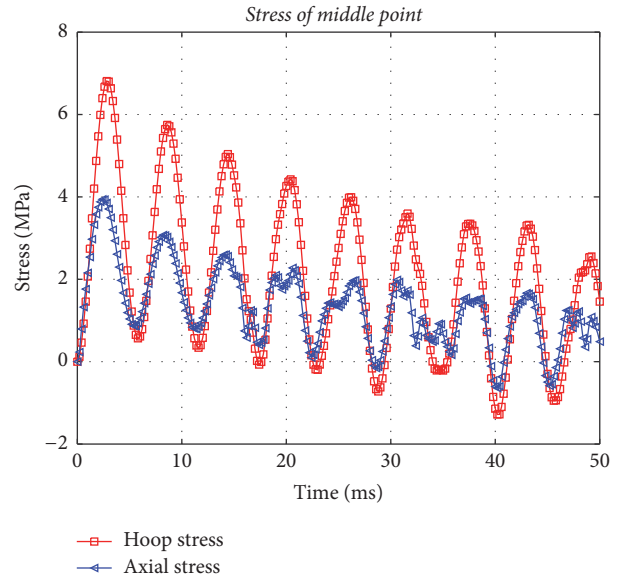


FIGURE 4: Maximum hoop stress and axial stress of shell's centre point.

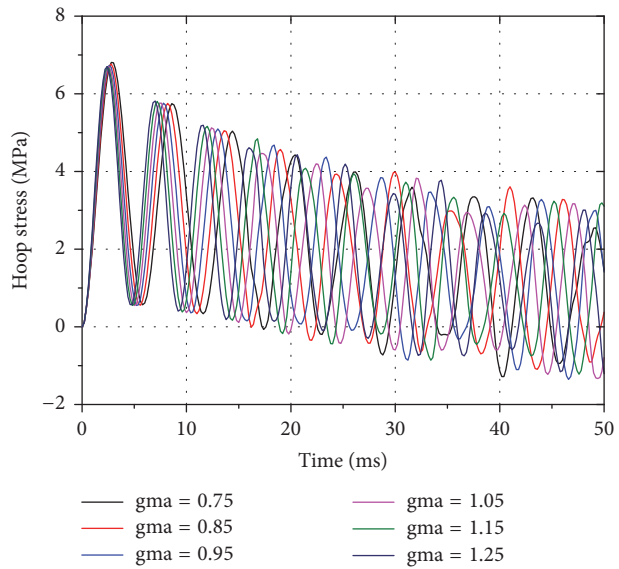


FIGURE 5: The influence of anisotropy on hoop stress of centre point.

studied; the comparison of the hoop stress on centre point is plotted in Figure 5. It can be seen that, within the range of  $\gamma = 0.75 \sim 1.25$ , the influence of anisotropy on hoop stress of centre point is not pronounced at the beginning; only a minor influence on response magnitude can be observed. The influence however grows more manifest in the later part of the motion, which can be found from the lags between the series of curves. As a convention, the maximum response is more concerned in engineering; thus the anisotropy might be neglected in analysis of limit response.

Another factor may be the stiffness of the surrounding ground materials like rock or soil where the cylindrical tunnel was embedded in. Since Young's modulus of elastic soils

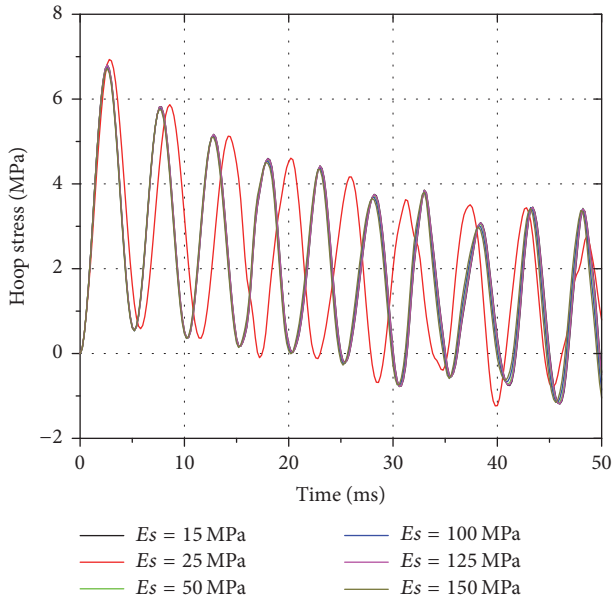


FIGURE 6: The influence of ground material's Young's modulus on hoop stress of centre point.

can vary in a big range, a range of  $E_s = 15\sim 50$  MPa was considered for homogeneous soils in this analysis, while a range of  $E_s = 120\sim 150$  MPa was tested for more stiff rocks. The results are plotted in Figure 6. It can be seen that, within the ranges of values we checked, the influence from ground medium's elastic parameter is also negligible. As we see this,  $E_s/E_x = 15\sim 150/(3.45 \times 10^{10}) \approx 4.5 \times (10^{-10} \sim 10^{-9})$  is too small to affect the response significantly.

## 5. Discussion and Conclusions

In this paper, an ideal centric point explosion in a cylindrical thin tunnel was simplified as an axisymmetric 2-dimensional problem, in which the tunnel was modeled with a continuous anisotropic shell, while the surrounding ground medium's effect was accounted for with linear elastic Winkler springs. The damping of the ground medium in structure-ground interaction was neglected for the simplicity of the problem, also because this approach leads to bigger amplitude of response, thus making the assessment more conservative. The explosive loading produced by a centric point-source detonation was described by a temporal and spatial function. The governing equation of the motion was established and a numerical method combining finite difference with the implicit Newmark- $\beta$  method was developed for solving the problem. Some discussions and concluding remarks could be made as follows.

(1) A long straight anisotropic shell model was adopted to model dynamic vibration of a cylindrical tunnel under a centric point-source explosion, and the governing equation of the motion was established.

(2) Combining finite difference method with Newmark- $\beta$  method, a numerical procedure was developed for solving the governing equation of shell's vibration problem.

(3) Numerical results were given to show some profiles of the vibration response of the anisotropic shell to centric point-source explosion, from which a vibration propagation and decay from charge centre to far end were shown.

(4) The shell's vibration consists of an expansion phase and a contraction phase, during which the maximum hoop stress always outweigh axial stress, suggesting a possible failure mode of axial cracks due to a tensile strength criterion met by hoop stress, since, for engineering materials like concrete, the tensile strength is much lower than compressive strength.

(5) Parameter studies showed that the coefficient of anisotropy does not influence the response amplitude significantly when changing in the range of 0.75 to 1.25; however, it generally alters the period of the vibration.

(6) From our investigation, Young's modulus of surrounding elastic medium shows limited influence on the shell's dynamic response, even when we check the value from 15 MPa to 150 MPa.

This research may be helpful to blast hazard assessment and protective design for some critical subway tunnels.

## Conflicts of Interest

The authors declare that they have no conflicts of interest.

## Acknowledgments

This research is financially supported by Natural Science Foundation of China (Projects no. 51478469 and no. 51021001); the support from CSC scholarship (no. 201503170208) is also acknowledged by the authors.

## References

- [1] Wikipedia, London bombings, July 2005.
- [2] Wikipedia, Moscow Metro bombings, 2010.
- [3] Wikipedia, Brussels bombings, 2016.
- [4] Wikipedia, Saint Petersburg Metro bombing, 2017.
- [5] Wikipedia, "List of terrorist incidents involving railway systems, 2017," [https://en.wikipedia.org/wiki/List\\_of\\_terrorist\\_incidents\\_involving\\_railway\\_systems](https://en.wikipedia.org/wiki/List_of_terrorist_incidents_involving_railway_systems).
- [6] D. M. Reporter, "New York subway tunnels to be made terror-proof with \$600m ring of steel," Daily Mail Report, 2010.
- [7] T. Namako, *MTA Terror-Proofs Bridges & Tunnels*, New York Post, New York, NY, USA, 2010.
- [8] Working Group No. 2 and International Tunnelling Association, "Guidelines for the design of shield tunnel lining," *Tunnelling and Underground Space Technology*, vol. 15, no. 3, pp. 303–331, 2000.
- [9] J. R. Weatherby, T. K. Blanchat, N. T. Davie, J. J. Calderone, T. C. Togami, and R. A. Benham, *Computer and Centrifuge Modeling of Decoupled Explosions in Civilian Tunnels*, Sandia National Labs, Albuquerque, NM, USA, 1998.
- [10] H. Liu and S. Nezili, "Centrifuge modeling of underground tunnel in saturated soil subjected to internal blast loading," *Journal of Performance of Constructed Facilities*, vol. 30, no. 2, Article ID 06015001, 2016.

- [11] P. Bonalumi, M. Colombo, and M. Di Prisco, "Internal explosions in embedded concrete pipes," *Applied Mechanics and Materials*, vol. 82, pp. 452–457, 2011.
- [12] Y. Zhao, C. Chu, and Y. Yi, "Study on an engineering measure to improve internal explosion resistance capacity of segmental tunnel lining structures," *Journal of Vibroengineering*, vol. 18, no. 5, pp. 2997–3009, 2016.
- [13] M. Colombo, P. Martinelli, and R. Huaping, "Pressure-Impulse Diagrams for SFRC Underground Tunnels," in *Proceedings of EURO-C Conference*, St. Anton am Alberg, Austria, March 2014.
- [14] M. Colombo, P. Martinelli, and M. Di Prisco, "A design approach for tunnels exposed to blast and fire," *Structural Concrete*, vol. 16, no. 2, pp. 262–272, 2015.
- [15] S. Choi, I. Chaney, and T. Moon, "Blast and post blast behavior of tunnels," in *Proceedings of the North American Tunneling*, M. E. F. Lawrence, R. Eckert, M. F. Smithson, and B. F. Townsend, Eds., pp. 655–663, Society for Mining, Metallurgy, and Exploration, 2010.
- [16] S. Choi, J. Wang, G. Munfakh, and E. Dwyre, "3D nonlinear blast model analysis for underground structures," in *Proceedings of the GeoCongress*, pp. 1–6, Atlanta, Ga, USA, 2006.
- [17] H. Yu, Z. Wang, Y. Yuan, and W. Li, "Numerical analysis of internal blast effects on underground tunnel in soils," *Structure and Infrastructure Engineering*, vol. 12, no. 9, pp. 1090–1105, 2016.
- [18] V. R. Feldgun, A. V. Kochetkov, Y. S. Karinski, and D. Z. Yankelevsky, "Internal blast loading in a buried lined tunnel," *International Journal of Impact Engineering*, vol. 35, no. 3, pp. 172–183, 2008.
- [19] V. R. Feldgun, A. V. Kochetkov, Y. S. Karinski, and D. Z. Yankelevsky, "Blast response of a lined cavity in a porous saturated soil," *International Journal of Impact Engineering*, vol. 35, no. 9, pp. 953–966, 2008.
- [20] T. Senjuntichai and R. K. N. D. Rajapakse, "Transient response of a circular cavity in a poroelastic medium," *International Journal for Numerical and Analytical Methods in Geomechanics*, vol. 17, no. 6, pp. 357–383, 1993.
- [21] M. Gao, J. Y. Zhang, Q. S. Chen, G. Y. Gao, J. Yang, and D. Y. Li, "An exact solution for three-dimensional (3D) dynamic response of a cylindrical lined tunnel in saturated soil to an internal blast load," *Soil Dynamics and Earthquake Engineering*, vol. 90, pp. 32–37, 2016.
- [22] A. M. Benselama, M. J.-P. William-Louis, F. Monnoyer, and C. Proust, "A numerical study of the evolution of the blast wave shape in tunnels," *Journal of Hazardous Materials*, vol. 181, no. 1-3, pp. 609–616, 2010.
- [23] A. M. Benselama, M. J.-P. William-Louis, and F. Monnoyer, "A 1D-3D mixed method for the numerical simulation of blast waves in confined geometries," *Journal of Computational Physics*, vol. 228, no. 18, pp. 6796–6810, 2009.
- [24] G. Pokrovsky, *Explosion*, Nedra, Moscow, Russia, 1980.
- [25] J. Henrych and G. R. Abrahamson, "The dynamics of explosion and its use," *Journal of Applied Mechanics*, vol. 47, no. 1, p. 218, 1980.
- [26] J. Penzien, "Seismically induced racking of tunnel linings," *Earthquake Engineering and Structural Dynamics*, vol. 29, no. 5, pp. 683–691, 2000.
- [27] S. Timoshenko and S. Woinowsky-Krieger, *Theory of Plates and Shells*, McGraw-Hill, New York, NY, USA, 1959.
- [28] N. M. Newmark, "A method of computation for structural dynamics," *Proceedings of the American Society of Civil Engineers*, pp. 67–94, 1959.